C55.602:So 4/v.4

Solar-Terrestrial Predictions Proceedings

Volume 4: Prediction of Terrestrial Effects of Solar Activity

Richard F. Donnelly, Editor

Space Environment Laboratory

Boulder, Colorado

PENNSYLVANIA STATE UNIVERSITY
JUN 13 1980
DOCUMENTS COLLECTION

U.S. DEPARTMENT OF COMMERCE

National Oceanic and Atmospheric Administration

Environmental Research Laboratories

SOLAR-TERRESTRIAL PREDICTIONS PROCEEDINGS

VOLUME IV

PREDICTION OF TERRESTRIAL EFFECTS OF SOLAR ACTIVITY

Edited by

Richard F. Donnelly
Space Environment Laboratory
Boulder, Colorado 80303, U.S.A.

March 1980

The International Solar-Terrestrial Predictions Proceedings and Workshop Program was hosted by the NOAA Space Environment Laboratory. The workshop was held April 23-27, 1979, at the College Inn in Boulder, Colorado.

Science co-sponsors of the program:

AGU: American Geophysical Union
AMS: American Meteorological Society
COSPAR: Committee on Space Research
IAGA: International Association of Geomagnetism and Aeronomy
IAU: International Astronomical Union
IUWDS: International URSIGRAM and World Days Service
SCOSTEP: Scientific Committee on Solar-Terrestrial Physics
URSI: Union Radio Scientifique Internationale; Commissions E and G

Science and financial co-sponsors of the program:

Air Force Geophysics Laboratory
Air Force Office of Scientific Research
Department of Energy
National Aeronautics and Space Administration
National Science Foundation
NOAA Environmental Research Laboratories

U.S. Depository Copy

NOTICE

The papers in this volume express the opinions and suggestions of the authors. They are presented here in the spirit of encouraging further study, testing and development of solar-terrestrial predictions. The presentation of the papers in this volume does not constitute endorsement or approval by the Environmental Research Laboratories or by the cosponsors of the International Solar-Terrestrial Predictions Proceedings and Workshop Program.

The Environmental Research Laboratories do not approve, recommend, or endorse any proprietary product or proprietary material mentioned in this publication. No reference shall be made to the Environmental Research Laboratories or to this publication furnished by the Environmental Research Laboratories in any advertising or sales promotion which would indicate or imply that the Environmental Research Laboratories approve, recommend, or endorse any proprietary product or proprietary material mentioned herein, or which has as its purpose an intent to cause directly or indirectly the advertised product to be used or purchased because of this Environmental Research Laboratories publication.

For sale by the Superintendent of Documents, U.S. Government Printing Office, Washington, D.C. 20402

(Order by SD Stock No. 003-017-00479-1)

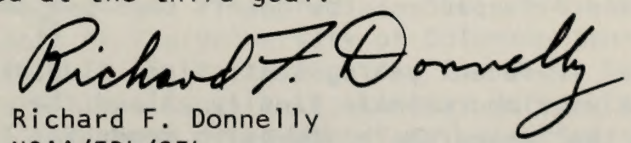
PREFACE

The International Solar-Terrestrial Prediction Proceedings and Workshop Program (ISTP/P-W Program) included the following: (1) an open call for contributed papers on solar-terrestrial predictions; (2) invited review papers about (a) the prediction, warning and monitoring services of groups that regularly issue solar-terrestrial predictions; (b) the current and future needs for predictions by groups that use solar-terrestrial predictions, and (c) current knowledge of selected topics in solar-terrestrial physics and applications; (3) working groups on fourteen areas of interest for solar-terrestrial predictions; (4) a preprint exchange from October, 1978 through March, 1979; (5) a workshop of representatives of the working groups; and (6) the Solar-Terrestrial Predictions Proceedings. These proceedings consist of four volumes:

	U.S. Government Printing Office, Superintendent of Documents Stock No.
Volume I. Prediction Group Reports	(003-023-00041-9)
Volume II. Working Group Reports and Reviews	(003-017-00471-6)
Volume III. Solar Activity Predictions	(003-017-00473-2)
Volume IV. Predictions of Terrestrial Effects of Solar Activity	

Volume I reviews the current practice in solar-terrestrial predictions. Volume II presents the recommendations and reports developed by the working groups at the workshop. Topical reviews and papers on the current and future needs for predictions are also included. The program did not include a conference where the authors presented their papers orally. Working group participants were asked to read the preprints and correspond with the authors and other group members before meeting at the workshop. Participants included forecasters, scientists and prediction users. Volumes III and IV present individual suggestions for particular prediction schemes.

The goals of the program were as follows: (1) to determine and document the current state-of-the-art of solar-terrestrial predictions, the applications of these predictions, and the future needs for solar-terrestrial predictions, (2) to encourage research, development and evaluation of solar-terrestrial predictions, and (3) to provide indepth interaction of prediction users, forecasters and scientists involved in the research and development of prediction techniques. To achieve the first goal, we invited forecast groups and user groups to review their activities. The working groups concentrated on deriving recommendations for future needs pertinent to solar-terrestrial predictions. The early call for contributed papers was made to achieve the second goal, i.e. authors had more than a year to orient their work towards a paper on predictions. The workshop was aimed at the third goal.



Richard F. Donnelly
NOAA/ERL/SEL
Boulder, Colorado 80303 USA

March 21, 1980

OVERVIEW

Volumes III and IV include papers contributed in response to an open call for papers about solar-terrestrial predictions. Whereas Volume III involves solar activity predictions, Volume IV involves the prediction of the terrestrial effects of solar activity. Chapter A includes papers about geomagnetic activity predictions ranging from solar cycle variations, solar rotation variations to the disturbances following sudden commencements or sudden impulses. The use of interplanetary data to predict geomagnetic activity is discussed in several papers and is currently a very active topic in research and development of geomagnetic predictions. Geomagnetic activity can be set off both by solar flare disturbances and the interplanetary magnetic field sector structure passages. During the declining phase of a solar cycle, long lasting coronal holes can cause recurrent geomagnetic activity related to the solar rotation rate. Studies of geomagnetic activity have had a marked influence on studies of the solar cycle by emphasizing the strong role of long lasting solar structure (recurring over several solar rotations) during the decay of a solar cycle.

Chapter B includes papers about predicting energetic magnetospheric particles. Predictions of substorm-related particles, ring current development and electron precipitation into the Earth's atmosphere are discussed.

Volume IV includes many papers about predicting ionospheric and radio propagation conditions, which reflects the continued importance of this traditional applications area of solar-terrestrial predictions. Physicists tend to assume that the way to predict the ionospheric and radio propagation effects of solar activity is to try to predict the solar activity and then estimate the interplanetary, magnetospheric, geomagnetic and then the ionospheric and radio propagation effects. However, many of these papers for radio propagation predictions are based primarily on empirical or statistical relations. Predictions of sporadic E, spread F, and scintillations generally involve statistical or empirical predictions and still seem quite far removed from the physical-prediction approach.

Chapter C includes ionospheric predictions, including storm effects, sporadic E, solar-flare induced sudden ionospheric disturbances, and high latitude particle precipitation induced disturbances. Chapter D includes radio propagation predictions. Predictions for transionospheric propagation is a relatively new and growing area within radio propagation predictions. Chapter E includes satellite drag applications and geomagnetic activity effects on long-line electric power systems at high latitudes. Chapter F involves climate predictions involving solar activity. The papers in Chapters E and F supplement the papers on these topics in Volume II.

In recent years, statistical studies of the correlation between solar activity and climate finally raised that subject to a level of respectability so that research is now being conducted to try to systematically determine the physical processes involved. However, it still is a controversial subject area. The arguments against such correlative subjects, where the physical processes involved are not clear, tend to initially involve questions of whether the correlations are statistically significant. Such subjects tend

to involve several fields of science where the experts in each of the fields are naturally skeptical of papers that link their area of expertise with another distant subject area with which they are unfamiliar. Editors find it difficult to obtain competent overall reviews. In the reviews of papers on the relation between solar activity and climate, one group of participants systematically recommended that the papers be accepted with little or no need for revisions. A second group systematically recommended that the same papers be rejected outright without considering further revisions. In other words, there was a marked polarization among the participants. Fortunately the workshop activities in this area were peaceful and constructive.

Chapter G includes some controversial topics, namely the correlation between solar-activity and terrestrial seismic activity and the possible relation between solar activity and biological effects. Numerous papers correlating human behavior or biological effects with solar activity exist scattered through the literature in the past three decades. These are mainly ignored by the mainstream of science or criticized as appearing to lack statistical significance. Seldom is the criticism published and presented in a logical scientific way. Perhaps both the variations in seismic activity and solar activity are modulated by the same unknown galactic force. Such speculation doesn't count for much in science. Many physicists, including this editor, do not place much significance on correlative studies even if they are supposed to be statistically significant unless a reasonable explanation of a possible physical link exists. Controversial papers have been included to point out these topics of research within the broad field of solar-terrestrial predictions and to encourage further research and constructive scientific criticism of these topics.

Most of the papers in these proceedings were reviewed by participants in the Solar-Terrestrial Predictions Proceedings and Workshop Program, where the reviews were used to try to improve the papers. About a dozen papers were rejected. Almost all papers required revisions. In some cases, we have tried to improve the English presentation of the paper and hope that the meaning intended by the author has not been accidentally distorted.

Richard F. Donnelly

Richard F. Donnelly, March 20, 1980
ISTP/P-W Program Chairman

ACKNOWLEDGEMENTS

The editor wishes to thank the many persons who helped conduct the workshop or produce and distribute the proceedings. I appreciate the professional help of Larry Christiansen and his staff of the University of Colorado Center for Conferences and Management and the staff of the College Inn for their help in conducting the workshop. I am grateful to Sandy Rush, Lindsay Murdock and Dorothy Burdick for their help in editing these proceedings and preparing them for the printer. I wish to thank Judy Jasan for her typing and David Klock and Linda Kishimoto for help in distributing the proceedings to the workshop participants. I thank Steve Suess for his help on the Editorial Review Committee.



Digitized by the Internet Archive
in 2012 with funding from
LYRASIS Members and Sloan Foundation

http://archive.org/details/solarterrestr00inte

SOLAR TERRESTRIAL PREDICTIONS PROCEEDINGS

VOLUME IV PREDICTION OF THE TERRESTRIAL-EFFECTS OF SOLAR ACTIVITY

TABLE OF CONTENTS

Page

Preface.....iii

Overview.....iv

Acknowledgements.....v

A. GEOMAGNETIC ACTIVITY PREDICTIONS

Prediction of Geomagnetic Activities From Solar Wind Parameters Based on the Linear Prediction Theory — T. Iyemori and H. Maeda.....A - 1

The 21st Solar Cycle: aa Index of Geomagnetic Activity — J. Feynman.....A - 8

Computer Forecasting of Geomagnetic Disturbances — T.V. Gaivoronskaya and V.P. Kuleshova.....A - 19

Interplanetary Magnetic Field and Polar Cap Magnetic Disturbances: Using the Data for Prediction of Auroral Electrojet Activity — O.A. Troshichev, N.P. Dmitrieva, B.M. Kuznetsov, and V.P. Vasiliev...A - 24

Short-Term Forecasting of Geomagnetic Storms Associated With High-Speed Solar Wind Streams — V.M. Mishin, V.V. Shelomentsev, A.D. Bazarzhapov, and L.P. Sergeeva.....A - 37

Solar Cycle Effect of 27-Day Recurrent Geomagnetic Storm — T. Ondoh and Y. Nakamura.....A - 46

Short-Term Predictions of a Sudden Geomagnetic Impulse Value on the Basis of the Interplanetary Data — S.A. Grib.....A - 53

Prediction of Substorm Activities — T. Saito.....A - 61

Short-Term Forecasting of the Substorm Breakup Phase Based on Ground Magnetic Observations in the Zone of Magnetospheric Cleft Projection — V.V. Shelomentsev, V.M. Mishin and T.I. Saifudinova.....A - 69

Development of Disturbances After SC and SI — I.N. Men'shutina.....A - 80

Working Group Report on Geomagnetic Storms - S.I. Akasofu.....A - 91

Addendum: Workshop Report on Geomagnetic Disturbance Predictions - J.A. Joselyn.....A - 115

B. MAGNETOSPHERIC PARTICLE PREDICTIONS

Prediction of High-Energy (>0.3 MeV) Substorm-Related Magnetospheric Particles - D.N. Baker, R.D. Belian, P.R. Higbie, and E.W. Hones, Jr.....B - 1

The Use of > 30 keV Electron Anisotropies At 6.6 R_E to Predict Magnetospheric Substorms — D.N. Baker, P.R. Higbie, E.W. Hones, Jr., and R.D. Belian.....B - 12

Evolution of Substorm and Quiet — Time Electron Anisotropies ($30 \leq E_e \leq 300$ keV) at 6.6 R_E — P.R. Higbie, D.N. Baker, R.D. Belian and E.W. Hones, Jr.....B - 23

Predicting Partial Ring Current Development — C.R. Clauer and R.L. McPherron.....B - 44

On the Predictability of Radiation Belt Electron Precipitation Into the Earth's Atmosphere Following Magnetic Storms — W.N. Spjeldvik, and L.R. Lyons.....B - 59

C. IONOSPHERIC PREDICTIONS

Geomagnetic Activity Control of Ionospheric Variability — M. Mendillo, F.X. Lynch, and J.A. Klobuchar.....C - 1

A Morphology-Based Prediction Scheme for the Coupled Latitudinal and Local-Time Development of F-Region Storms — M. Mendillo and J.A. Klobuchar.....C - 15

On the Possibility to Predict Variations in the F2-Region Parameters as a Function of the IMF Direction — R.A. Zevakina and E.V. Lavrova..C - 27

Forecasting of δfoF2-Variations for Ionospheric Disturbances — V.P. Kuleshova, E.V. Lavrova and L.N. Lyakhova.....C - 37

Fundamentals of the Physical Forecast of Ionospheric Plasma — M.N. Vlasov.....C - 41

Self-Consistent Model of the Ionospheric Plasma and the Hydrodynamic Forecast — M.N. Vlasov and A.G. Kolesnik.....C - 47

Prediction of the Parameters of the Maximum of the Vertical Electron Density Gradient — T.A. Anufrieva, T.L. Gulyaeva, G.F. Kadukhin, T.N. Soboleva, and A.G. Shlionsky.....C - 57

Model Calculations of Electric Fields and Currents in the High-Latitude E Region for Predictions of Ionospheric Variations — S. Matsushita and Y. Kamide.....C - 65

Statistical Prediction of E_s-Layer Parameters and Echo-Signal Characteristics - T.S. Kerblay and G.S. Nosova.....C - 77

Forecast of Critical Frequency and Height of Maximum Density of Mid-Latitude E-Layer — G.S. Ivanov-Kholodny and A.A. Nusinov.....C - 82

Daytime Sporadic-E Blanketing Frequency Prediction — A.E. Giraldez...C - 87

Short Term Prediction of Ionospheric Disturbances — S.N. Mitra and M. Sain..... C - 107

The Inference of Severe Night-Time Disturbances of the D Region From High-Latitude Riometer Observations — J.K. Hargreaves.....C - 110

The Possible Prediction of SID's Using the Slowly Varying Component of the Solar Radio Flux at 3.2 CM — Z.Y. Zhu, A.H. Zhou and S.R. Zhou..... .....C - 114

D. RADIO PROPAGATION PREDICTIONS

1. Transionospheric Propagation Predictions

An Improved Ionospheric Irregularity Model — D.G. Singleton.....D1 - 1

Predicting Transionospheric Propagation Conditions — D.G. Singleton..D1 - 16

Model of Phase and Amplitude Scintillations From In-Situ Measurements — S. Basu and S. Basu.....D1 - 32

A Resume of Anticipated Fleetsatcom and Gapfiller Scintillation Effects During the Peak of Solar Cycle 21 (1980-1982) — J.M. Goodman.....D1 - 50

Ionospheric Refractive Correction Using an Adaptive Procedure — D.E. Donatelli and R.S. Allen.....D1 - 65

Prediction of Transionospheric Signal Time Delays at Widely Separate Locations Using Correlative Techniques — H. Soicher.....D1 - 81

2. HF Ionosphere-Reflected Propagation Predictions

HF Communications Predictions 1978 (An Economical Up-To-Date Computer Code, AMBCOM) — V.E. Hatfield.....D2 - 1

The Statistical Properties of the Disturbed High-Latitude Ionosphere in Radio Wave Propagation Computations — E.M. Kovalevskaya and E.M. Zhulina.....D2 - 16

Prediction of HF Communication Disturbances by Pre-SC HF Field Increases on Polar Paths Crossing the Auroral Zone — T. Ondoh and K. Obu.....D2 - 21

Minicomputer Simulation of Ionospheric Radiowave Propagation at Decametric Wavelengths — D.D. Meisel, B. Duke and W.D. Savedoff.....D2 - 31

A Simplified Computer Method For Long-Term Calculation of HF Sky-Wave Circuits — A.A.E. Picquenard and E. Rodriques de Paula.....D2 - 41

Prediction of foF2 by the Monthly Ratio (MR) Method — P.S. N. Murthy C.S.R. Rao, and M. Sain.....D2 - 54

HF Communication Problems at Low Latitudes Due to Steep Spatial and Temporal Gradients — D.R. Lakshmi, S. Aggarwal, P.K. Pasricha and B.M. Reddy.....D2 - 58

Prediction of the Characteristics of a Radio Signal Reflected from Horizontally-Inhomogeneous Ionosphere and the Relevant Requirements for Prediction of Ionospheric Parameters — T.S. Kerblay, E.M. Kovalevskaya, E.M. Zhulina and L.M. Ishkova.....D2 - 65

Using Solar Flux Index Predictions to Forecast HF Radio Wave Propagation — D.J. Snyder.....D2 - 74

Grafex Predictions — J.F. Turner.....D2 - 85

3. Absorption, Field Strength and Radio Noise Predictions

Prediction of Radio Wave Absorption in the Ionosphere — J.O. Oyinloye.....D3 - 1

On the Short-Term Prediction of the Space-Time Distribution of Auroral Absorption — R.A. Zevakina and M.V. Kiseleva.....D3 - 14

Determination of the Solar Cycle Variation of HF Radio Wave Absorption at Low Latitude — K.M. Kotadia, A Gupta and R.M. Kotak.....D3 - 20

Prediction of Riometer Absorption from Solar Flare Radio Burst Characteristics — P. Bakshi and W.R. Barron.....D3 - 26

A Method of Predicting Skywave Field Strength in HF Bands in Tropical Zones — O.P. Sehgal and H.O. Agrawal.....D3 - 31

Unpredicted Variations in D-Region Response to Solar X-Ray Events — R.H. Doherty.....D3 - 35

Secular Variation of Occurrence Rate and Dispersion of Low-Latitude Whistlers During the Solar Cycle Nos. 19 and 20 — Y. Tanaka, M. Hayakawa, J. Ohtsu and A. Iwai.....D3 - 48

Atmospheric Radio Noise Measurements in LF/MF Bands — A.K. Bhatnagar and M. Sain.....D3 - 55

Prediction of Waveguide Propagation of Radio Waves Using the Extremal-Parametric Method Based on Predicted Ionospheric Parameters — A.G. Shlionsky.....D3 - 60

E. SATELLITE AND ELECTRIC POWER APPLICATIONS

Anamalous Satellite Drag and the Green-Line Corona — R.C. Altrock....E - 1

Effects of Magnetospheric Disturbances on the Geoelectric Field in Auroral and Sub-Auroral Regions, and Interactions With HV-DC/AC Electric Power Lines: Large-scale man-made effects on the global aeronmic environment — W.M. Boerner, J.B. Cole and W.R. Goddard.....E - 5

F. SUN → WEATHER PREDICTIONS

The Solar Prediction of Climatic Changes — H.C. Willett.....F - 1

Weather and Climate Predictions in the Northern Hemisphere Based on Solar-Terrestrial Relations — V. Bucha.....F - 18

The Effects of Changing the Solar Constant on the General Circulation of the Earth's Atmosphere — T. Asakura and Y. Tanaka.....F - 44

Meteorological Microseisms and Sun-Weather Relationships — J. Lastovicka.....F - 54

On the Variation of the Annual Mean Sea - Level Pressure in Latitude Zones of the Northern Hemisphere — J. Xanthakis, B. Tritakis and B. Petropoulos.....F - 63

The 13.6-Day Oscillation in the Stratosphere — A. Ebel.....F - 77

A Consideration of the Possible Use For Weather Forecasting of a Particular Sun-Weather Relation — R.G. Williams and M.J. Rycroft.....F - 85

G. MISCELLANEOUS PREDICTIONS

A Prediction of the Influence of T, [NO] and $q(O_2)$ on the Positive Ion Composition at the Mesopause Region — D.K. Chakrabarty and P. Chakrabarty.....G - 1

On Predicting the Parameters of Medium Scale Gravity Waves With the Onset of Tropospheric Jet Stream — O.P. Nagpal.....G - 8

Solar Relationship and Prediction of Seismic Activity of the Earth — Y.D. Kalinin, and V.M. Kiselev.....G - 23

Solar Terrestrial Prediction - Aspects for Preventive Medicine — E. Stoupel.....G - 29

A. GEOMAGNETIC ACTIVITY PREDICTIONS

PREDICTION OF GEOMAGNETIC ACTIVITIES FROM SOLAR WIND PARAMETERS BASED ON THE LINEAR PREDICTION THEORY

Toshihiko Iyemori and Hiroshi Maeda
Geophysical Institute, Kyoto University,
Kyoto 606, Japan

Geomagnetic activity described by the Dst, AL and AU indices is predicted from solar wind parameters (i.e. interplanetary magnetic field southward component Bz(<0), wind velocity V, and particle density N). The hourly value data are used. The prediction technique is based on the Wiener's linear prediction theory. That is, first we calculate the impulse response function of one of the geomagnetic indices to the interplanetary electric field, -V·Bz, from both the index and the solar wind parameters, and then we predict the geomagnetic index using the impulse response function thus calculated and the data of the solar wind parameters. It is emphasized that the impulse response functions of the indices differ from each other and the effect of the interplanetary electric field, -V·Bz, lasts for more than several hours.

1. INTRODUCTION

Since the close relationship between the geomagnetic activity and the north-to-south component of the interplanetary magnetic field(IMF-Bz) was recognized, several attempts to get a quantitative relationship between them have been made. For example, Arnoldy(1971) showed the linear relationship between the auroral electrojet activity index AE and the IMF southward component(Bz<0), and predicted the AE index from the solar wind data for two hours before the prediction time. Burton et al.(1975) showed empirically a simple relationship between the Dst index and the interplanetary electric field dawn-to-dusk component, -V·Bz, where V denotes the solar wind bulk velocity, and predicted the Dst index from the solar wind data preceding twenty-five minutes.

In this paper, we try to predict these geomagnetic indices, AL, AU and Dst, from the solar wind data by somewhat different method. That is, by the method based on the Wiener's linear prediction theory. The AL and AU indices are regarded as a measure of the intensity of the westward and the eastward auroral electrojet, respectively. The Dst index is mainly a measure of the

ring current intensity, but the intensity of the solar wind pressure and that of the magnetopause current also contribute to the Dst index (Davis and Sugiura,1966).

2. PREDICTION TECHNIQUE

We assume that the magnetosphere acts as a linear system to the interplanetary electric field dawn-to-dusk component, $-V \cdot Bz$, and causes the geomagnetic disturbances. That is, we consider a linear system with constant coefficients, the input of it is $-V \cdot Bz$ and the output is one of the geomagnetic indices, AL, AU or Dst.

If we have sufficient knowledge of the system, we will be able to predict the output of the system from the input data. In the case of a linear system with constant coefficients, the property of the system can be completely expressed by the impulse response function $h(\tau)$, and the output data $w(t)$, where 't' denotes the time and is connected with the input data $f(t)$ through eq.(1).

$$w(t) = \int_0^\infty h(\tau) f(t-\tau) d\tau \qquad (1)$$

The function $h(\tau)$ can be calculated from $w(t)$ and $f(t)$ by the method of root-mean-square(RMS) error criterion by Wiener(1949) and the algorithm of calculation for the discrete time series was given by Levinson(1949) in Wiener's book.

In our case, the input $f(t)$ is the interplanetary electric field, $-V \cdot Bz$, where we put Bz equal to zero when Bz is positive(i.e. northward), the output $w(t)$ is one of the geomagnetic indices, Dst, AL or AU, and the impulse response function $h(\tau)$ is calculated for each index (Iyemori et al.,1978).

3. CALCULATION AND CHARACTER OF $h(\tau)$

All the data used in this study are hourly values and the periods that the data cover are listed in Table 1, the total being 250 days. These non-continuous periods are connected next to each other and regarded as one continuous time series having the length of 250 days. The interplanetary data used are ; (a) IMF data book(king,1975) and (b) the composite interplanetary plasma data tape, both of which were supplied from WDC-A for Solar Terrestrial Physics. The IMF data are used in a geocentric solar-magnetospheric coordinate system (GSM) (Russell,1971). The geomagnetic indices used are ; (c) Dst index by Sugiura and Poros(1971) and (d) AE(AL and AU) index by Allen et al.(1973,1974).

Figure 1 shows the impulse response function thus calculated for Dst°, AL and AU, where the Dst° is defined by eq.(2) to remove the effect of compression of the magnetosphere caused by the kinetic pressure change of the solar wind (Burton et al.,1975).

$$Dst^\circ = Dst - a\sqrt{NV^2} + b \qquad (2)$$

Here N is the number density (particles/cm^3) of the solar wind, V is the bulk velocity (km/sec), 'a' and 'b' are constants, and we used the numerical values 0.0255 and 20.6 for 'a' and 'b' respectively. The symbol 'M' and 'EM' in Figure 1 indicate the length of the impulse response function which is calculated and the efficiency as a predictor. That is, if EM is nearly equal to unity, it shows that the output data (e.g. geomagnetic indices) is almost completely predicted by the impulse response function from the input data (e.g. interplanetary parameters), and if EM is nearly zero, the output data is little predicted (Levinson,1949).

The response function of Dst°(top panel in Figure 1) is roughly consistent with what is expected from the result of Burton et al.(1975), but our result shows a more complex feature of the response. That is, after the main development appearing in about one hour, there exist a second development with a time lag of about five hours. Similar second developments are seen in the response function of AL index (middle panel in Figure 1) and, though slight, in that of AU index. These are indicated by arrows in Figure 1. This result means that the effect of the interplanetary electric field lasts for more than several hours for the development of geomagnetic disturbances (cf. Arnoldy, 1971).

The other point of emphasis is the difference between the response functions of AL index and that of AU index. This means that the mechanism of development of the westward auroral electrojet, a measure of it is AL index, is different from that of the eastward auroral electrojet(AU index) (Iyemori et al.,1978).

TABLE 1. Periods and each time span that the data cover.

PERIOD (month/day/year)			SPAN (day)
1/19/67	-	1/31/67	13
2/ 3/67	-	2/13/67	11
2/16/67	-	2/27/67	12
3/ 3/67	-	3/13/67	11
7/25/67	-	8/ 9/67	16
8/24/67	-	9/17/67	25
9/24/67	-	10/13/67	20
10/16/67	-	11/20/67	36
11/23/67	-	12/10/67	18
12/21/67	-	1/ 9/68	20
1/23/68	-	2/ 1/68	10
2/ 5/68	-	2/19/68	15
2/23/68	-	3/ 9/68	16
3/13/68	-	3/26/68	14
3/30/68	-	4/11/68	13
		TOTAL	250

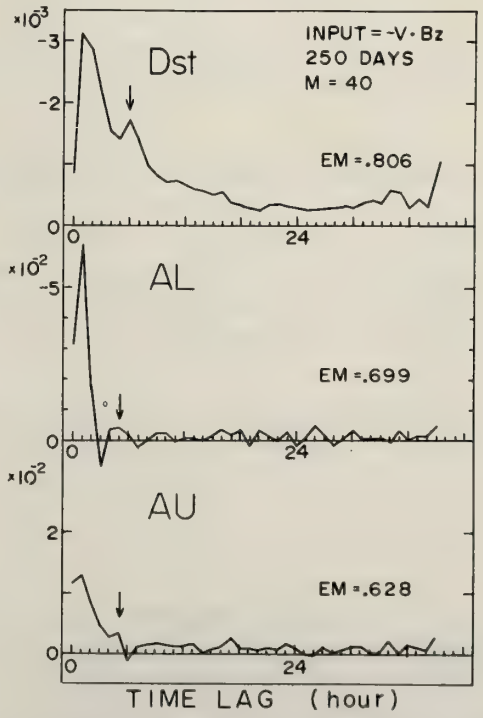


Fig.1 Impulse response functions for geomagnetic indices, Dst, AL, and AU. The input data for the system is interplanetary electric field, -V·Bz, where we put Bz equal to zero when Bz is positive. The data used have the length of 250 days.

4. EXAMPLE

Figure 3 to 5 show some examples of prediction. The solid lines denote the data of the solar wind (number density N, bulk velocity V, and IMF-Z component Bz in GSM coordinate system) and the geomagnetic indices (AU, AL, and Dst). The broken lines denote the predicted values for each index calculated by the impulse response function in Figure 1 using the solar wind parameters covering from forty hours before up to the time when the index is predicted. This time span (40 hours) of the impulse response function for prediction is long enough, because the value of EM (i.e. the efficiency of prediction) in Figure 2 are nearly saturated before 40 hours (M=40). Each figure (Figure 3 to 5) covers the time span of ten days and the number above the base line of the Dst index denotes the number of days counted from the first of January.

Figure 3 covers the period from February 26 to March 6 in 1968, when the geomagnetic activities are moderately high. The predicted values of AL and Dst index coincide with the observed values fairly well, but those of AU index do not coincide so well. Figure 4 covers the period from October 18 to October 27 in 1967, when the geomagnetic activities are comparatively quiet.

Figure 5 covers the period from November 29 to December 8 in 1967, when the geomagnetic activities are moderately high similar, to the period in Figure 3. But in this case, the velocity of the solar wind, V, is rather high after the day 339 when the predicted values are much smaller than the observed values for all indices. The tendency for the predicted values from interplanetary electric field, $-V \cdot Bz$, to be smaller than the observed values when the solar wind velocity is high (i.e. more than 500 km/sec) is rather commonly seen.

The difference between the predicted and the observed values during such a high velocity period can be reduced to some extent if $V^2 \cdot Bs$ is used as the input (Murayama and Hakamada,1975; Maezawa,1978); here, Bs denotes the hourly mean of the southward component alone, and differs from Bz when the variance is large and Bz is around zero. However, this tendency still remains. So, this may suggest that the solar wind energy is transferred into the magnetosphere not only in a form proportional to $-V \cdot Bz$ (or $V^2 \cdot Bs$) but also in other forms of the solar wind velocity V, for example, in a form of viscous-like interaction.

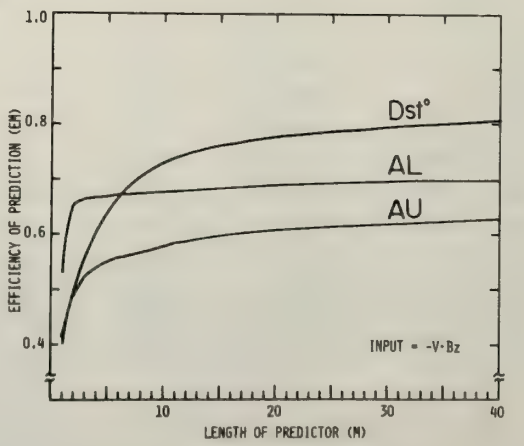


Fig.2 Relation between the length of the impulse response (M-hours) and the efficiency of prediction (EM). The values of EM are nearly saturated before M becomes 40.

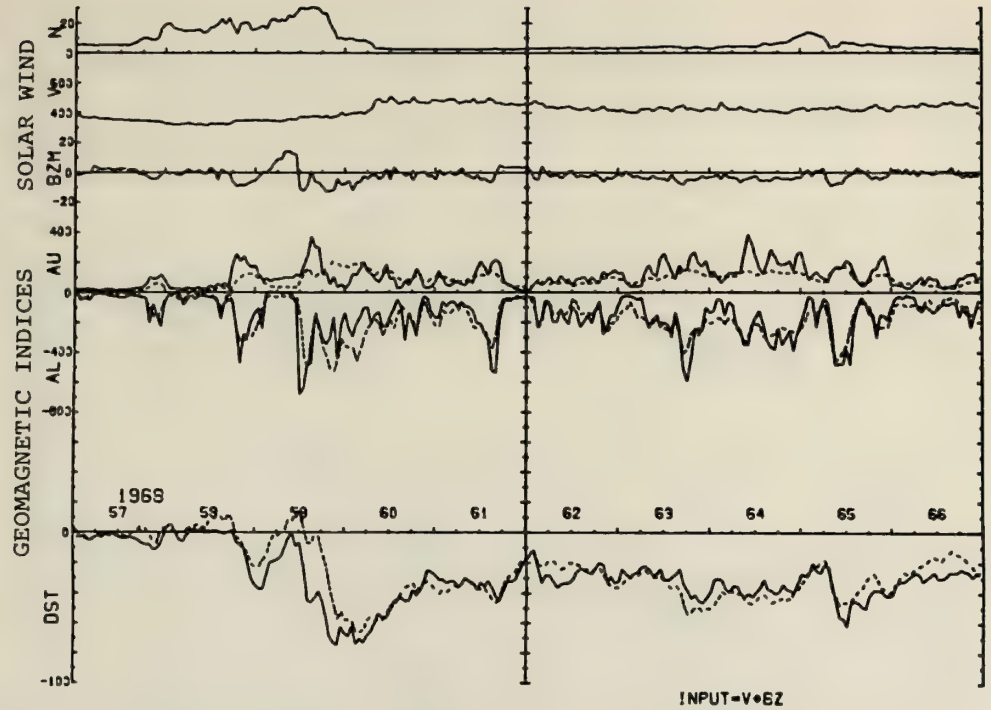


Fig.3 Data(solid line) and predicted values(broken line). This figure covers the period from February 26(day 57) to March 6(day 66) in 1968. The predicted values are calculated from the solar wind parameters using the impulse response functions in Figure 1.

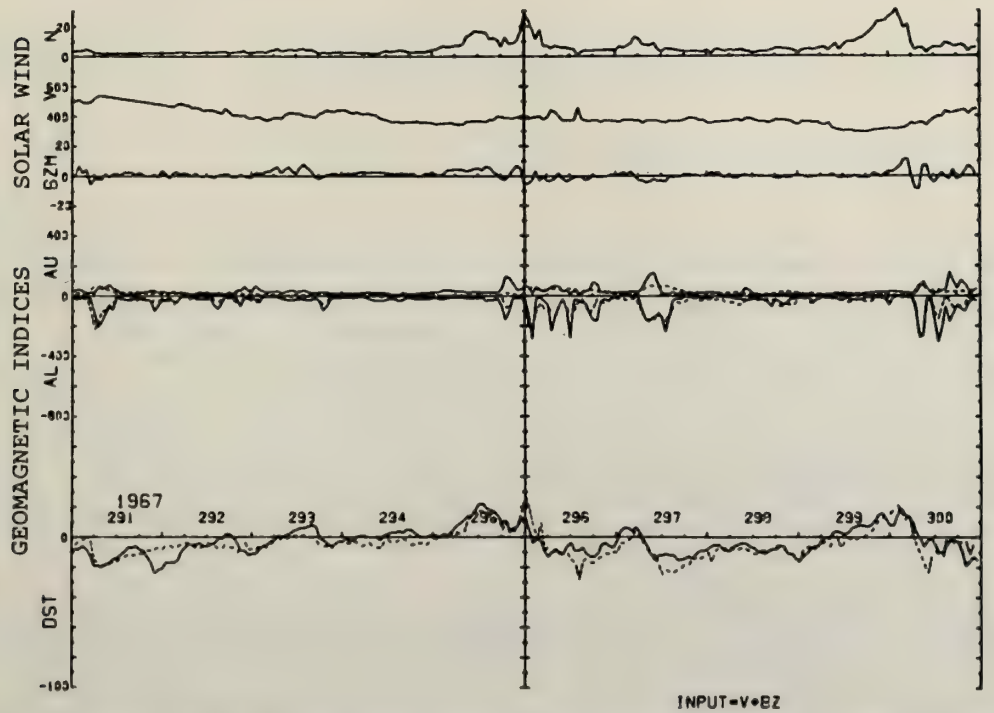


Fig.4 Data(solid line) and predicted values(broken lines). The day 291 is October 18 and the day 300 is October 27 in 1967. Geomagnetic activities are quiet comparatively in this period.

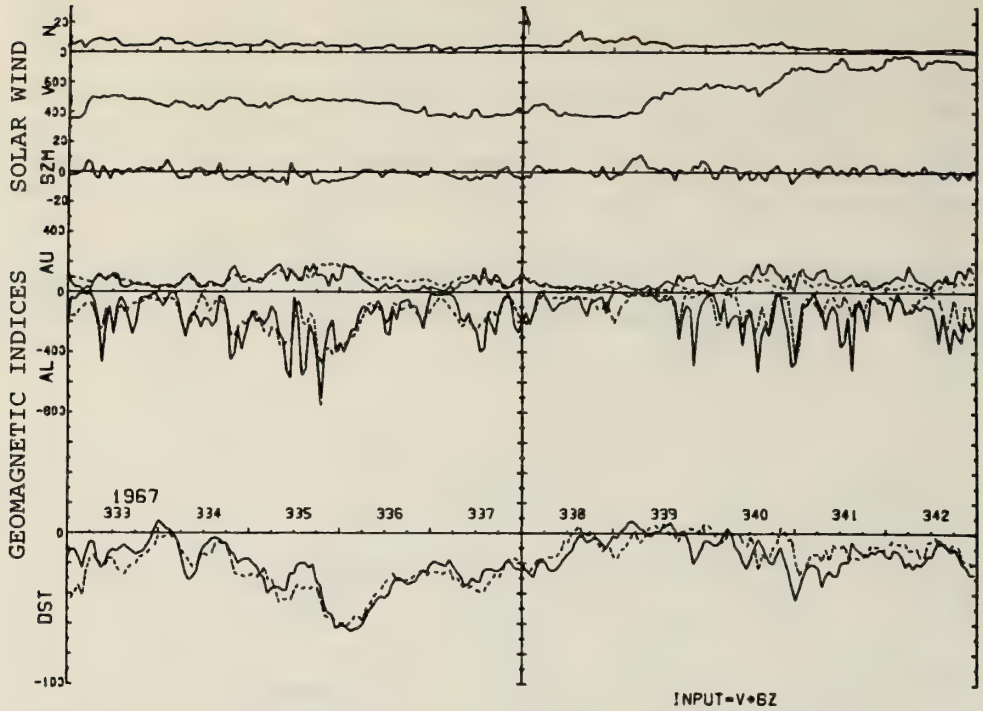


Fig.5 Data(solid line) and predicted values(broken line). The day 333 is November 29 and the day 342 is December 8 in 1967. The solar wind velocity is rather high after the day 339, when the predicted values are smaller than the observed values. This tendency is rather commonly seen in the other periods.

5. SUMMARY

We applied the Wiener's prediction theory to the prediction of geomagnetic activities from the solar wind parameters. The result was successful in the first approximation, and the impulse response functions brought some important information about the mechanisms of geomagnetic disturbances. But sometimes, for example when the solar wind velocity was high, the prediction was not so successful. This result may suggest another possibility for the mechanism of the transfer of the solar wind energy into the magnetosphere. Therefore, to predict the geomagnetic disturbances more precisely by the linear prediction theory, we should treat the magnetosphere as a multiple input system and/or as a system with time dependent coefficients.

ACKNOWLEDGEMENTS

We wish to thank prof.Y.Inoue at Kyoto Industrial University, and Dr.T. Araki and other members at our Institute for their useful discussions. The interplanetary data have kindly been provided by the National Space Science Data Center through the World Data Center-A for Rocket and Satellites, NASA.

REFERENCES

Allen, J. H., C. C. Abston, and L. D. Morris (1974): Auroral electrojet magnetic activity indices AE(10) for 1967, Rep. UAG-33, World Data Center-A for Solar-Terrestrial Physics.

Allen, J. H., C. C. Abston, and L. D. Morris (1973): Auroral electrojet magnetic activity indices AE(11) for 1968, Rep. UAG-29, World Data Center-A for Solar-Terrestrial Physics.

Arnoldy, R. L. (1971): Signature in the interplanetary medium for substorm, J. Geophys. Res., 76: 5189.

Burton, R. K., R. L. McPherron, and C. T. Russell (1975): An empirical relationship between interplanetary conditions and Dst, J. Geophys. Res., 80: 4204.

Davis, T. N., and M. Sugiura (1966): Auroral electrojet activity index AE and its universal time variations, J. Geophys. Res., 71: 785.

Iyemori, T., H. Maeda, and T. Kamei (1978): Impulse response of geomagnetic indices to interplanetary magnetic field, J. Geomag. Geoelectr., 30: to be published.

King, J. H. (1975): Interplanetary Magnetic Field Data Book, National Space Science Data Center.

Levinson, N. (1949): The Wiener RMS(root-mean-square) error criterion in filter design and prediction, Appendix B in N.Wiener's book (see below).

Maezawa, K. (1978): Dependence of geomagnetic activity on solar wind parameters: a statistical approach, Solar Terrestrial Enviromental Res. in Japan, 2: 103.

Murayama, T., and K. Hakamada (1975): Effects of solar wind parameters on the development of magnetospheric substorms, Planet. Space Sci., 23: 75.

Russell, C. T. (1971): Geophysical coordinate transformation, Cosmic Electrodyn., 2: 184.

Sugiura, M., and D. J. Poros (1971): Hourly values of equatorial Dst for years 1957 to 1970, Rep. X-645-71-278, Goddard Space Flight Center, Greenbelt, Maryland.

Wiener, N. (1949): Extrapolation, interpolation, and smoothing of stationary time series with engineering applications, Published by the Tech. Press of the M.I.T. and John Wiley & Sons,Inc., New York.

THE 21ST SOLAR CYCLE: aa INDEX OF GEOMAGNETIC ACTIVITY

Joan Feynman
National Science Foundation
Washington, D. C. 20418, USA

Analysis and prediction of geomagnetic activity and its relation to long term variations in the interplanetary medium have been hampered, until recently, by frequent changes of indices used to describe geomagnetic variations. However, Mayaud has re-examined the old geomagnetic records and produced a series of commensurate data, the aa index, available since 1868 until the present. Feynman and Crooker have shown that the variation of aa consists of a long term (80 $\sim$ 100 year) trend on which is superposed an eleven year variation. The trend increased roughly 60% from the 1900's to 1960. The yearly average <aa> can be considered as made up of two terms, the trend term (probably related to the "80 year cycle" in sunspots) and the 11 year solar cycle variation. In this paper I discuss the properties of the 11 year variation and the trend from 1868 to the present. This information is then used to attempt to estimate the yearly values of <aa> that might be expected in cycle 21. I tentatively estimate that the maximum <aa> will be about 27. However, I point out that we may be entering the declining phase of the "80 year cycle" which is expected to be marked by decades of erratic but generally declining geomagnetic activity. If the "80 year cycle" is indeed cyclic, then <aa> as small as 5 or 10 may be expected within the next few decades.

1. INTRODUCTION

Although the relationship between the solar cycle and geomagnetic activity is very close, there are many interesting and important differences between the solar cycle variations of sunspot number and the solar cycle variation of geomagnetic activity. The sunspot cycle and the geomagnetic cycle both show the same solar cycle periodicity, but the phase of the geomagnetic cycle lags the sunspot cycle by 18 months (Fraser-Smith, 1972). Maximum geomagnetic activity typically occurs at a different period of the solar cycle than maximum sunspot number. A second peak appears late in the geomagnetic cycle, usually well after sunspot maximum. This activity is made up of recurrent storms and the peak in the yearly average activity index is frequently higher than that due to the non-recurrent activity appearing earlier in the cycle (Newton, 1948). In addition the general level of geomagnetic activity rose by about 60% between 1900 and 1960 (Russell, 1975).

Feynman and Crooker (1978) have pointed out that this rising trend appears strongly in the activity occurring at the minimum of the geomagnetic cycle and is not directly related to the increase in sunspot number at sunspot maximum that occurred during this same period.

In this paper I discuss patterns that have occurred in the solar cycle variation of geomagnetic activity. These patterns are then projected to cycle 21 to estimate the geomagnetic activity expected for that cycle. The results are crude but are a first attempt to predict geomagnetic activity year by year throughout a solar cycle.

1.1 Patterns of Geomagnetic Activity

At this stage of our understanding of geomagnetic activity, and its relation to the solar wind, the predictions of geomagnetic activity must be purely empirical. The best indicator of future activity is past activity. Geomagnetic activity has been monitored since 1832 (Bartels, 1932). Auroral activity and sunspot records extend the record well back into the 18th century. Recent historical studies (c.f. Eddy, 1976) are now expanding the record into earlier times but will not be of concern to this study.

The longest term pattern of interest here that seems to exist in the sunspot cycle and in geomagnetic activity is the 80 to 100 year cycle which is seen in the amplitude of the sunspot cycle. Of course, since the sunspot cycle record extends from about 1700 to the present, only three minima of the 80-100 year cycle have occurred. Since the record is so short it is not established that those minima of the amplitude of the sunspot cycle actually represent cyclic behavior. Thus, although from past experience there is reason to expect that small sunspot cycles may occur circa the year 2,000, this cannot be predicted with any confidence. In addition, even if the amplitude modulation of sunspot cycles is cyclic, its period is uncertain to at least 20 years, so that the minimum could well develop within the next decades or not for almost a half century.

Geomagnetic activity exhibited a minimum in 1900 (Russell, 1975) which may well have been related to the minimum in the amplitude of the sunspot cycle (Feynman and Crooker, 1978). This association of minimum geomagnetic disturbances with minima in the 80 $\sim$ 100 year solar cycle is strengthened by observations of auroral frequencies. Fritz (1873) noted that there were marked minima in auroral activity in 1700, 1760 and 1810. The two minima of 1700 and 1810 correspond to periods of minimum sunspot cycle amplitude. Since auroral activity and geomagnetic activity are closely related, this suggests that geomagnetic activity minima occur at times of sunspot amplitude minima. Then the arguments that led to the expectation of a sunspot amplitude minimum circa 2,000 lead also to a geomagnetic minimum during the same epoch.

As mentioned earlier, geomagnetic activity has been monitored since 1832. Analysis has been hampered by the frequent changes in the index used to describe the activity. However, Mayaud (1973) has re-examined the magnetic records from two antipodal stations and generated a commensurate set of data, the aa index, available for the period from 1868 to the present. This data will be used to establish further patterns of past geomagnetic activity.

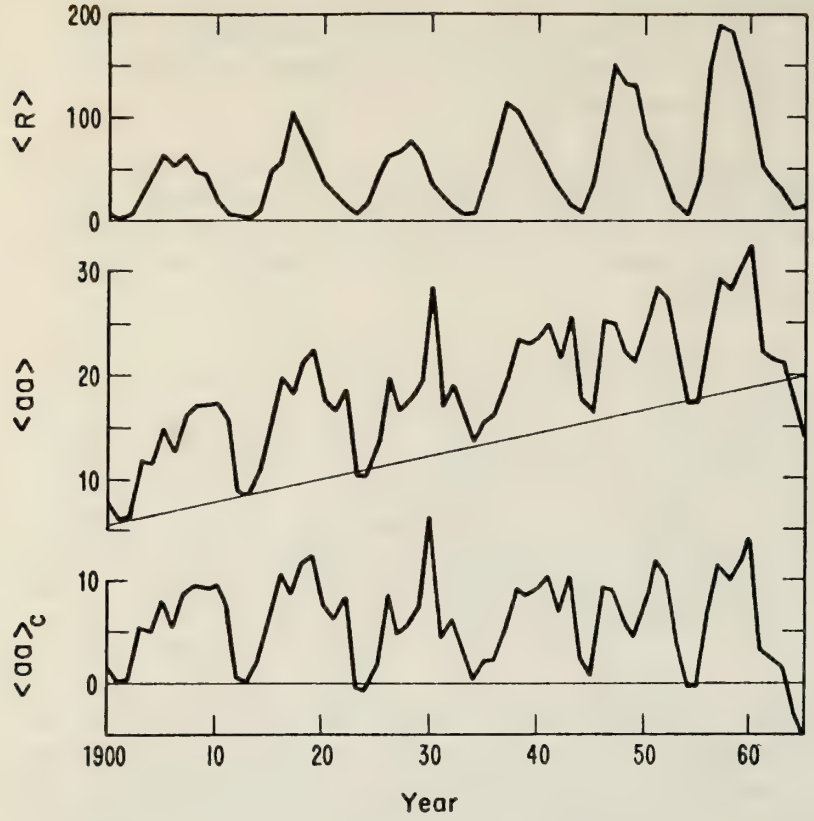


Fig. 1 Sunspot and geomagnetic activity 1900-1964 (from Feynman and Crooker, 1978). The top panel gives the yearly averaged sunspot number <R>. The middle panel shows the yearly averaged geomagnetic index <aa>. The straight line is the trend and is discussed in the text. The bottom panel shows <aa> minus the trend.

The activity from 1900 to 1960 will be discussed in some detail. This period is chosen because, as shown by Feynman and Crooker (1978), the solar cycle variation of geomagnetic activity is particularly simple. Figure 1, from their paper, shows the sunspot number and geomagnetic activity for that period. The top panel gives the yearly average sunspot number R with its tendency toward rising amplitudes. The second panel gives the yearly averages of the aa values, <aa>. Feynman and Crooker divided the <aa> variation into two parts, a long term trend and a solar cycle variation. The long term trend was monotonically increasing between 1900 and 1960 and is shown by the straight line in the middle panel. The equation of the line is

$$\langle aa \rangle_t = 0.22\ (T-1900) + 5.7 \qquad (1)$$

where T is the time in years. The bottom panel of Figure 1 shows the remainder when the values of $\langle aa \rangle_t$ given by (1) are subtracted from the measured <aa>. This remainder, denoted by $\langle aa \rangle_c$ exhibits the eleven year solar cycle variation during this sixty year period.

Feynman and Crooker point out that the changes in $\langle aa \rangle_c$ are much the same in each cycle. The cycle averaged $\langle aa \rangle_c$ varies from 5.8 to 7.2 with a mean of 6.4 and a root mean square deviation from the mean of 0.4. A scatter plot of the cycle averaged sunspot number and the cycle averaged $\langle aa \rangle_c$ shows no relation between the variables. The average solar cycle variation of geomagnetics during this period is calculated by superposing the data using years of minimum $\langle aa \rangle_c$ as zero epoch and averaging. Figure 2a shows the results for 8 years after minimum and Figure 2b shows results for 8 years before minimum. The values in Figure 2a and 2b are not the same because the duration

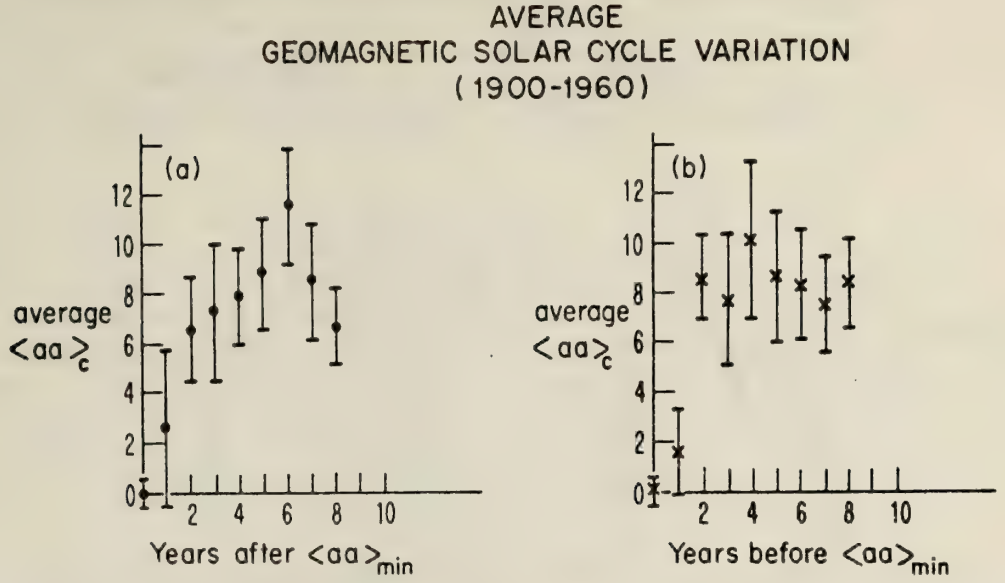


Fig. 2 The average solar cycle variation of geomagnetic activity $\langle aa \rangle_c$ for 1900-1960. The vertical bars give the root mean square deviation from the mean.

of solar cycles varies by a year or two. Both a and b are necessary for prediction. Note that both the rise and the decline of $\langle aa \rangle_c$ is quite sharp so the geomagnetic cycle has a much squarer shape than the sunspot cycle. The rise after geomagnetic minimum is about seven units in two years, while the drop to minimum is even more precipitous.

Geomagnetic activity during this period shows the 22 year double-sunspot cycle found by Chernosky (1966). Figure 3a and b are superpositions of $\langle aa \rangle_c$ for the three even cycles 14, 16 and 18 and for the two and a half odd cycles 15, 17 and half of 19. In the even cycles the activity during the first half of the cycle is relatively reduced and during the last half of the cycle it is enhanced. The reverse is true for the odd cycles. Russell and McPherron (1973) attribute this effect to the varying heliographic latitude dependence of the interplanetary magnetic field caused by the tip of the sun's poles to the plane of the ecliptic. Incidently, this explanation seems at first to present a paradox since the intensity of geomagnetic activity during the recurrent part of the cycle is now being used as a predictor of sunspot number maximum in the next cycle (Ohl, 1968; Sargent, 1978). However, the modulation of the even and odd cycles is too small to effect the predictions appreciably.

Returning now to study the long term trend in geomagnetic activity more extensively, we will assume that the 5 1/2 solar cycle variations of geomagnetic activity between 1900 and 1960 are typical of all solar cycle variations. The long term trend can be estimated crudely by subtracting the mean value for the solar cycle variation shown in Figure 2 from the measured values of $\langle aa \rangle$. The results are given in Figure 4. The general increase from 1900 to 1960 is clearly evident. The scatter of the points is a measure of the

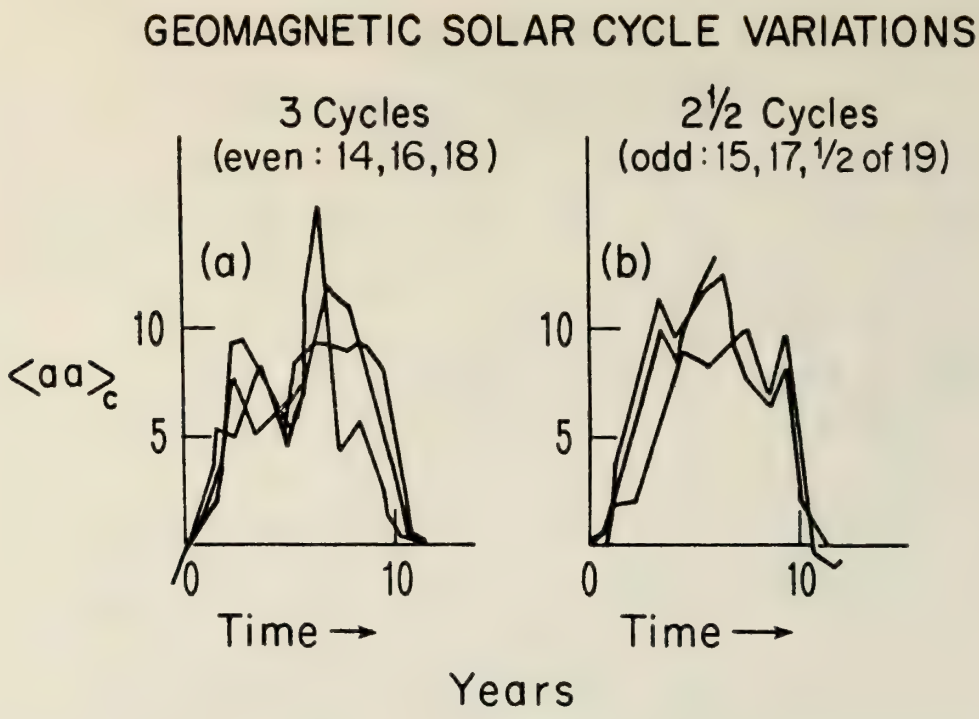


Fig. 3 A superposition of the solar cycle variation $\langle aa \rangle_c$ for even and odd numbered solar cycles separately. The late period even cycles and early period odd cycles are more disturbed than the early period even cycles or late period odd cycles.

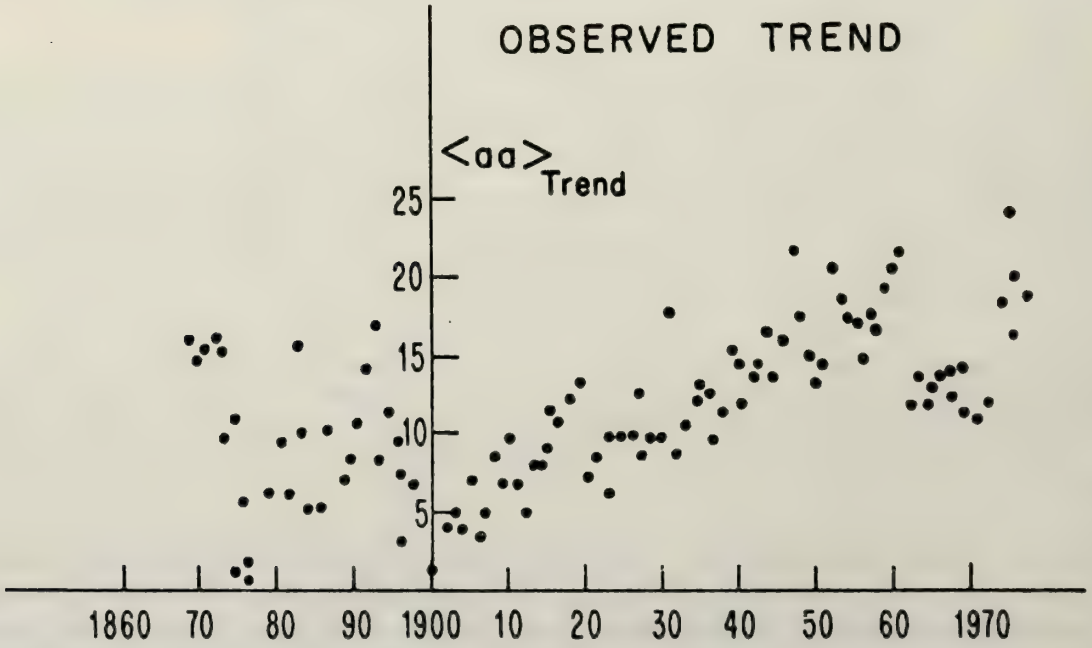


Fig. 4 The trend in aa determined by subtracting the average solar cycle variation in Figure 2 from the observed $\langle aa \rangle$.

variation of the behavior from cycle to cycle. Note that in 1960 there is a precipitous drop followed by an equally sharp recovery in 1974. This is another view of the observation reported by Gosling et al. (1977) that geomagnetic activity in the 20th solar cycle was unusual. Note that from this view the first part of the cycle might be considered more atypical than the last half.

During the period before 1900 the estimated trend is very erratic. This is equivalent to saying that the solar cycle variation of <aa> does not always follow the pattern established between 1900 and 1960. The period from 1868 to 1900 covers three solar cycles, the first of which has the highest yearly sunspot number of any between 1800 and 1900 and the second is as low as the small cycle beginning in 1901. If the 80-100 year cycle is really cyclic, the period from 1868 to 1900 is the decay period of a cycle whereas the period from 1900 to 1960 was a buildup period. If we are entering another decay period we may expect the trend in geomagnetic activity to be declining and erratic.

There are several other patterns in geomagnetic activity that are useful in making predictions. For example, Figure 1 shows that geomagnetic activity <aa> averaged over a cycle more or less followed changes in the intensity of the sunspot cycle. To quantify this relationship and extend it to cover the entire period for which <aa> are available, Figure 5 shows the cycle average sunspot number plotted against the cycle average <aa>. For each variable, the cycle average is taken from minimum to minimum of that variable. Data for the period between 1900 and 1960 is shown as circles. The crosses indicate cycles earlier or later than this period. There is, of course, clearly a relationship although there is considerable scatter in the points. The same plot was made using the maximum sunspot number instead of the cycle averaged values, however the scatter was increased. If the trend $\langle aa \rangle_t$ is is used instead of <aa> the scatter is about the same as shown in Figure 5. Since recurrent geomagnetic activity is being used to predict the sunspot number in the following cycle, the cycle averaged <aa> was also plotted against the cycle averaged sunspot number in the next cycle. The scatter was considerably increased. Part of the reason that Figure 5 shows a relationship is the persistance of trends from cycle to cycle. This is particularly true for the period between 1900 and 1960, shown as circles. However, the cycles which did not take place during this period seem to show the same relationship as seen from the points marked as crosses.

Although a rough estimate of geomagnetic activity in cycle 21 could be made from Figure 5, a more satisfactory process is to consider the non-recurrent geomagnetic activity early in the cycle separately from the late recurrent activity. In Figure 6 the cycle averaged sunspot number is plotted against the average of the <aa> from the first, second and third year before the minimum of the preceding sunspot cycle. The relationship is quite strong, as has been pointed out by Ohl (1968) who studied the recurrent geomagnetic activity and the maximum of the sunspot number in the next cycle. Sargent (1978) uses the relationship discussed by Ohl, corrected by a factor proportional to the sunspot number at minimum to predict that the maximum sunspot number in cycle 21 will be about 150. That prediction will be used later in this paper as the expected sunspot number for cycle 21.

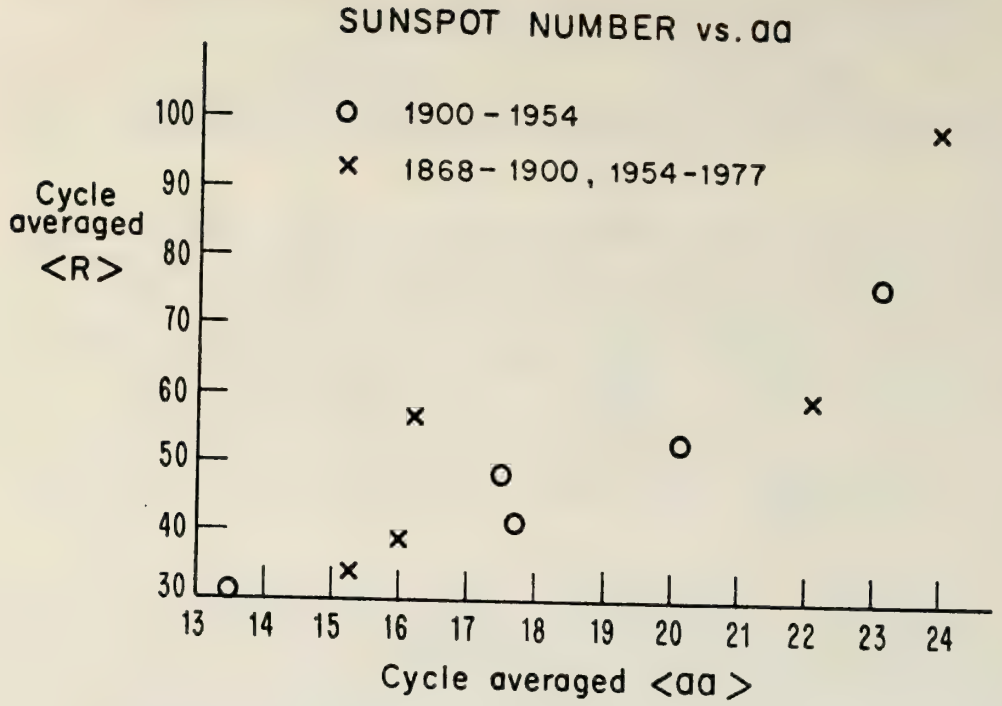


Fig. 5 The cycle averaged sunspot number versus the cycle averaged <aa>. Note the data from 1868-1900 and 1954-1977 show much the same relationship as the data from 1900-1954.

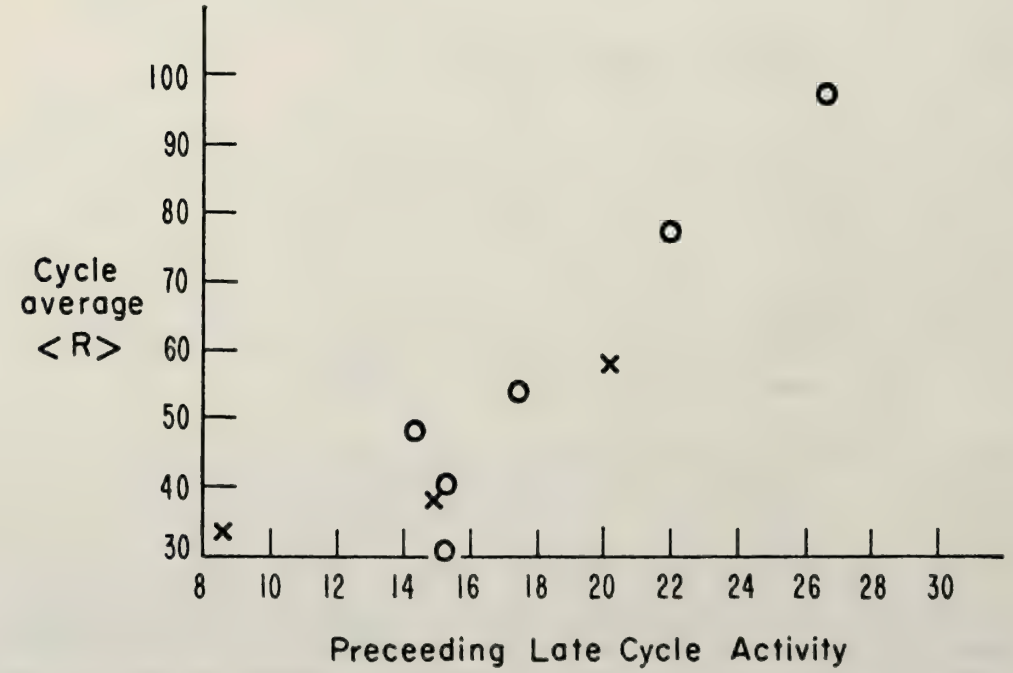


Fig. 6 A comparison between the cycle averaged sunspot number and the average of the activity during the first, second and third year before the minimum of the preceding sunspot cycle. The circles and crosses have the same meaning as in Figure 5.

The relationship in Figure 6 cannot, of course, be used to predict magnetic activity in cycle 21. However, the magnetic activity early in the cycle is roughly proportional to the sunspot number of that same cycle. This is shown in Figure 7 where the cycle averaged sunspot number is plotted against the average of the <aa> values for the fourth, fifth and sixth year after the sunspot minimum which initiated the corresponding sunspot cycle. The circles and crosses have the same meaning as in Figures 5 and 6. The shaded region shows a range of predicted <aa> for cycle 21 which has been included from an estimate of the mean sunspot number expected for cycle 21. The cycle averaged sunspot number in cycle 21 was arrived at by noting that the ratio of the cycle averaged sunspot number to the maximum sunspot number ranged from 0.41 to 0.56 for the ten cycles from 1867 to 1976. The mean of the ratios was .50 and the root mean square deviation from the mean was .04. Assuming the next sunspot cycle maximum is 150, this gives a cycle averaged value of 74 $\pm$ 6. The estimate of the uncertainty in <aa> is made by eye from the other points on the graph. The star marks the middle of the region of the prediction as an aid to the eye.

Another useful relationship is obtained from Figure 8 which shows the <aa> average for the three years before sunspot minimum versus <aa> average for the fourth, fifth and sixth year after that same minimum. Note that the activity after minimum is smaller than that before minimum in 8 cycles out of 9.

1.2 Application to Cycle 21

In this section I will project the patterns discussed above to cycle 21. A serious difficulty appears at once. If we are now entering the declining phase of the 80 year cycle, the trend will be erratic and declining. However, since we cannot be sure if the 80-100 year variation is indeed cyclic, (or if it is, when the minimum will come) we have no way of telling whether or not the break in the trend in 1960 represented the beginning of a decline. Since the decline cannot be predicted, the discussion in the remainder of this section will be made under the assumption that the trend remains at the level of the last geomagnetic minimum in 1977. Needless to say, this is a very shaky assumption.

Then assuming the trend remains constant at 20, the first approximation to the activity in cycle 21 is given in Table I where the average shape given in Figure 2 is simply added to the constant trend. These values can be refined and checked by using additional aspects of the patterns discussed in the previous section. For example, the average for the fourth, fifth and sixth year after minimum is 28 $\pm$ 3 in Table I, but from Figure 7 it is estimated to be between 22 and 26. The best estimate then is about 25 or 26. This agrees with Figure 8 in which it is shown that the late activity of cycle 20 during which <aa> averaged 27 should be greater than the first half of cycle 21. Now, since cycle 21 is an odd cycle, the last half of the cycle is expected to be lower than in the first half. In Table I the average of the last three years before solar minimum is 26·3 $\pm$ 2·5. Since this period should be lower than 25-26, the lower part of this range is more probable, say perhaps 23 or 24. Carrying this line of argument yet further, since the first half of a cycle is expected to be lower than the preceding last half, the activity during the first half of cycle 22 should be lower than 23 or 24.

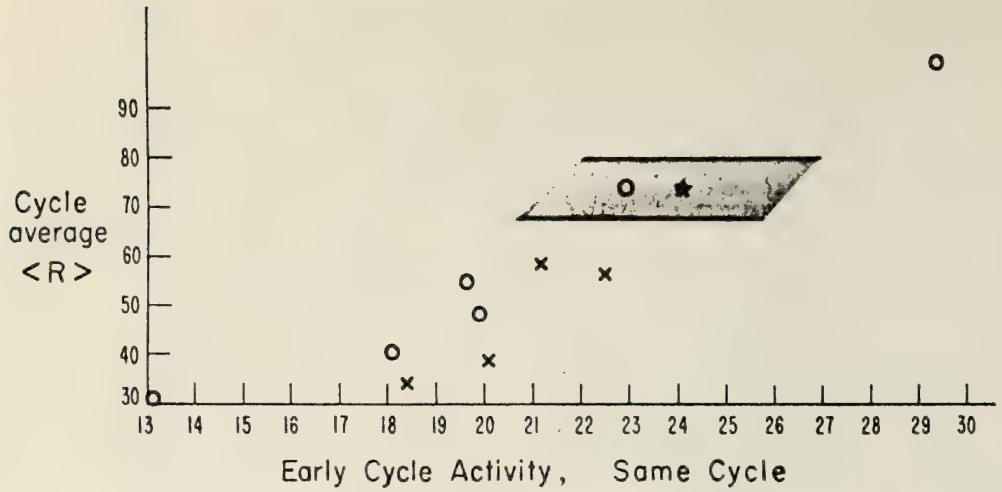


Fig. 7 A comparison between the cycle averaged sunspot number and the average of the activity during the fourth, fifth and sixth year after minimum sunspot number. In this figure minimum is counted as year one. The solar and geomagnetic activity are in the same cycle. The shaded region shows the predicted values for cycle 21 assuming the maximum sunspot number is 150.

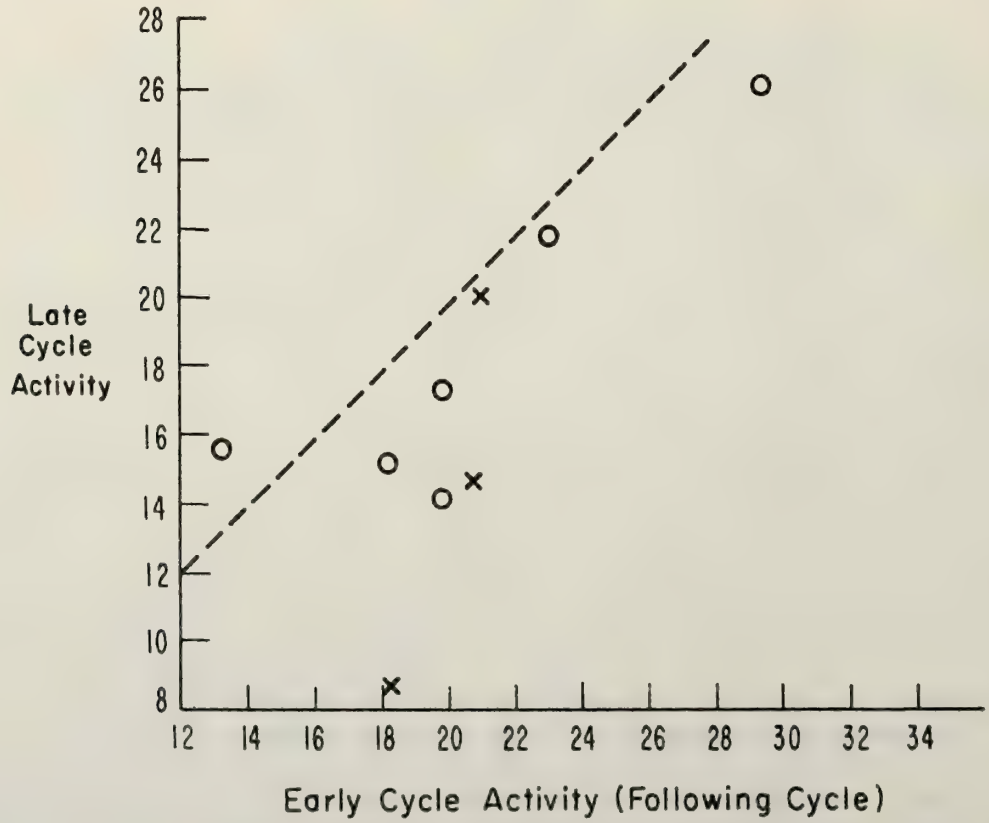


Fig. 8 A comparison between the average of the activity during the first, second and third year before the minimum of a sunspot cycle and the average activity during the fourth, fifth and sixth year after that minimum. The dashed line indicates equal activity.

Table I

Year	<aa>
1978	23 ± 3
1979	27 ± 2
1980	27 ± 3
1981	28 ± 2
1982	29 ± 2
1983	32 ± 3
-	
-	
-	
min - 3 yr.	29 ± 3
min - 2 yr.	29 ± 3
min - 1 yr.	22 ± 2

Table II

Year	<aa>
1978	23 ± 3
1979	27 ± 2
1980	25
1981	26
1982	27
-	
-	
-	
min - 3 yr.	24-25
min - 2 yr.	23-24
min - 1 yr.	22

Since cycle 22 is an even cycle, the last half is expected to be higher than the first half and the line of predictions is broken.

The final predictions are shown in Table II. Since all the assumptions and uncertainties that have gone into them have been outlined, it is clear that they are on very shaky ground. However, with our present knowledge, they are the best that can be done. The contribution of this paper is to provide a status report on our ability to predict geomagnetic activity. The major difficulty stems from our lack of understanding of the 80-100 year cycle. It is therefore important that the solar wind and geomagnetic activity continue to be monitored and studied during the coming period when the sunspot cycle, the solar wind and geomagnetic activity are expected to decline.

Acknowledgments

I thank Dr. Murray Dryer and Dr. Donald J. Williams and the Space Environment Laboratory, NOAA for their hospitality while this work was being carried out. I also thank H. H. Sargent for interesting and informative discussions and Dr. JoAnn Joselyn for reviewing the manuscript.

REFERENCES

Bartels, J. (1932): Terr. Magn. and Atm. Elec., 37, 1.

Chernosky, E. J. (1966): J. Geophys. Res., 71, 965.

Eddy, J. A. (1976): Science, 192, 1189.

Feynman, J. and N. U. Crooker (1978): Nature, 275, 626.

Fraser-Smith, A. C. (1972): J. Geophys. Res., 77, 4209.

Fritz, Hermann (1873): Verzeichnis beobachter Polarlichten, Wein, Poland, Akademie.

Gosling, J. T., J. R. Asbridge, S. J. Bame (1977): J. Geophys. Res., 82, 3311, 1977.

Newton, H. W. (1948): Mon. Not. of the R. Astr. Soc. Geophys. Suppl. 5, 159.

Mayaud, P. N. (1973): IAGA Bull. 33.

Ohl, A. I. (1968): Problems of the Arctic and Antarctic, 28, 137.

Russell, C. T. (1975): Solar Phys., 42, 259.

Russell, C. T. and R. L. McPherron (1973): J. Geophys. Res., 78, 92.

Sargent, H. H. (1978): Conference Record, Vehicular Tech. Soc., 28th IEEE. Vehicular Tech. Conference, Denver, Colorado.

COMPUTER FORECASTING OF GEOMAGNETIC DISTURBANCES

T. V. Gaivoronskaya and V. P. Kuleshova
Institute of Terrestrial Magnetism,
Ionosphere and Radio Wave Propagation
of the USSR Academy of Sciences
Moscow, USSR

The forecasting of geomagnetic disturbances by computer is considered. Disturbances caused by chromospheric flares and active regions on the solar disk are predicted. The solar data are used to obtain the signs that precede the magnetic storms. The forecast is accomplished by one of the methods of pattern recognition, allowing about 70% of the flares and 30% of the active regions to be recognized.

1. INTRODUCTION

In this report we consider geomagnetic storms caused by chromospheric flares (Gaivoronskaya and Kuleshova, 1977) and active regions on the solar disk and try to forecast these storms by computer. The computer forecast depends on defining the geoefficiency of the chromospheric flare or the active region independently of the magnetic disturbance value. The flare or active region is considered as geoeffective if it is followed by a magnetic storm. Prediction consists of forecasting the storms according to the preceding signs of the flares and active regions. The classification of the signs as geoeffective and non-geoeffective depends on correct recognition of the patterns (Vapnik and Chervonenkis, 1974). We make use of the "Kora" method (Bongard, 1967; Vanzvaig, 1973), the most simple one to realize.

2. FORECAST OF THE FLARE GEOMAGNETIC DISTURBANCES

In considering the geomagnetic disturbances caused by flares the list of the chromospheric flares during 1967-70 (Solar-Geophysical Data) has been considered. We chose flares of importance 2B and more; the number of these flares is 137. Each flare is described by its importance, duration, and position on the solar disk in regard to the central meridian. For each flare, we have noted the sudden ionospheric disturbance (SID) and the burst at 3000 MH_z, if there are any. SID and radio burst are then described by their duration,

intensity and type, and are connected with the flare by the time of commencement.

All data have been distributed into three groups according to three types of information (optical flare, SID, radio wave). The signs of geoeffectiveness and non-geoeffectiveness are chosen in each group. In the group of optical data the choice is made in the following way. The more prolonged and intensive the flare, and the less its distance from the central meridian, the more probable that the flare is geoeffective. Therefore, some values of duration, longitude, and importance can be found to be geoeffective signs. The choice of these signs is supported by means of comparison of durations, longitudes, and importance of all flares. The duration, the longitude, and the importance of the geoeffective flare are taken as signs of geoeffectiveness; no non-geoeffective flares have a greater importance and duration or a lesser longitude. By such comparison the region of geoeffectiveness for three values, duration, longitude, and importance have been determined. In the same manner, non-geoeffective signs are found.

Figure 1 shows the regions of geoeffectiveness and non-geoeffectiveness determined by the signs for each flare's importance. Longitudes are plotted versus the durations of the flares. The geoeffective region has the dense shade; the non-geoeffective region has no shade. It is impossible to separate the flares that are not in these regions.

Similarly, the signs for SID and radio wave data are obtained. These results are shown in Figures 2 and 3.

3. FORECASTING OF GEOMAGNETIC DISTURBANCES CAUSED BY ACTIVE REGIONS

The list of plages during solar minimum (1963-65) has been taken in order to forecast geomagnetic disturbances. The plages are described by the following data (the first three are given at the moment of passage of central meridian):

1. heliographic latitude
2. area in millionths of the solar hemisphere
3. intensity
4. development of the plage during the current transit of the disk (1 = passes to or from invisible hemisphere, b = bears on disk, d = dies on disk)
5. stage of the area evolution (/ = increasing, — = stable, \ = decreasing, ⌐ = increasing and stable, etc.)
6. age in solar rotations
7. duration of plage in disk given in days.

All data are distributed into groups so that signs can be determined:

1. latitude, area, intensity
2. development of plage and its area evolution
3. age and duration in disk.

In the case of forecasting a geomagnetic disturbance, it is impossible to determine the influence of each active region on the geomagnetic field. Therefore the longitude band of plages is taken as the active region independently of the solar hemisphere (N and S). To determine signs, the plage with the greatest area of each active region is taken into account. We consider 315 active regions with 158 geoeffective regions. Figure 4 and Table 1 show the geoeffective and non-geoeffective signs of plages for the three groups of data.

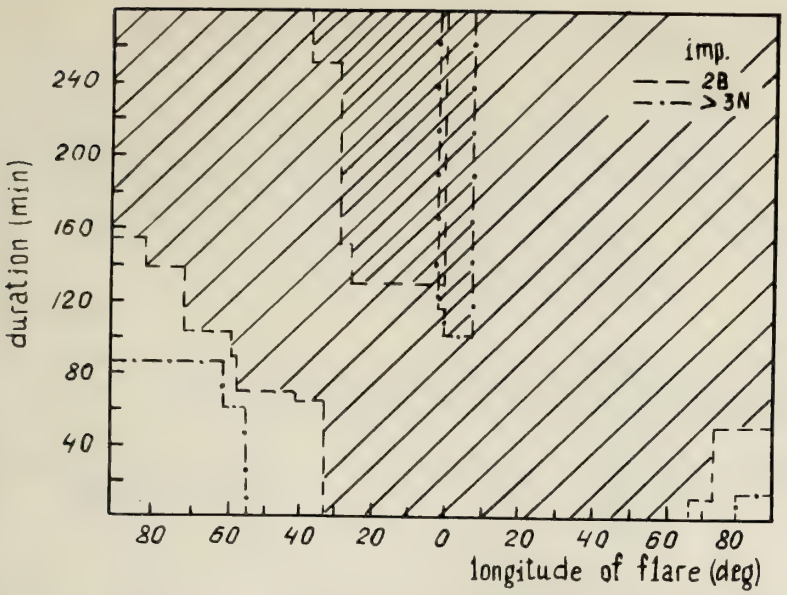


Figure 1. Geoeffective and non-geoeffective regions, according to longitude and duration of flare.

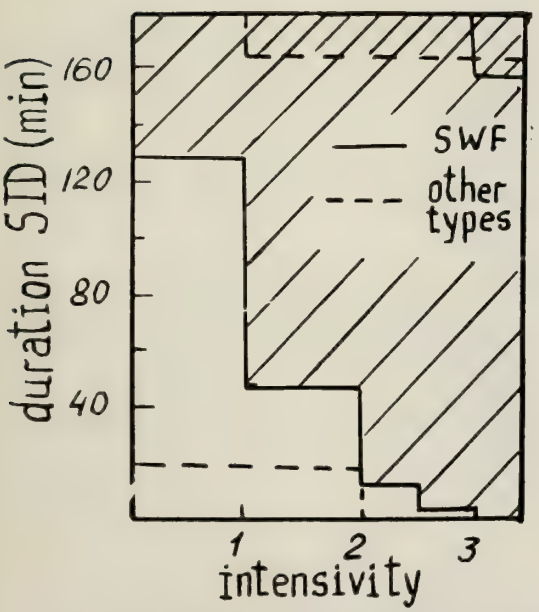


Figure 2. Geoeffective and non-geoeffective regions, according to intensity and duration of SID.

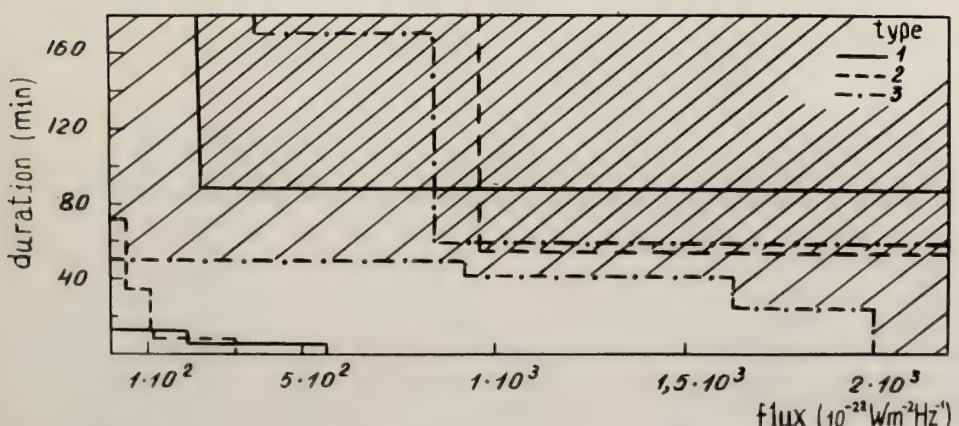


Figure 3. Geoeffective and non-geoeffective regions, using radio wave data.

Type 1 is a microwave simple burst; type 2 indicates a rise of intensity after the burst (microwave range); and type 3 is a microwave complex burst.

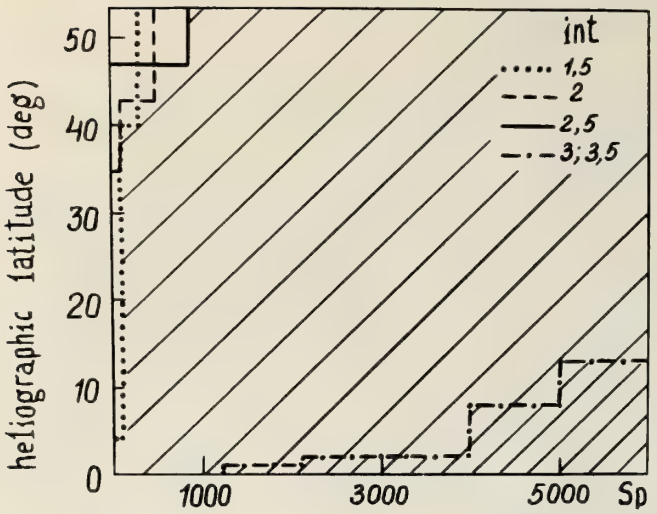


Figure 4. Geoeffective and non-geoeffective signs of plages for the three groups of data.

Thus, the computer distributes the phenomena in the following way: the flare or the active region is geoeffective if the flare or the plage with the greatest area belongs to the geoeffective region for some group of data; on the contrary, it is non-geoeffective if it gets into a non-geoeffective one. The obtained signs are verified with data that are not in the primary list of data (flares 1971-73, plages 1966-67). It confirms the possibility of forecasting storms by computer. The "Kora" method allows recognition of about 30 percent of the active regions and 70 percent of the flares, in spite of the small amount of data used.

Table 1. Geoeffective and Non-Geoeffective Signs of Plages

Geoeffective Signs		Non-Geoeffective Signs	
Plage's development	Area evolution	Plage's development	Area evolution
b - 1		b - 1	
b - 1		b - d	
b - 1		1 - d	
b - d		1 - d	
1 - 1			
1 - d			

Age in rotation	Duration on disk (in days)	Age in rotation	Duration on disk (in days)
1	15	1	6
2	4	2	3, 6, 9
3	5, 10-12, 14, 15	3	3, 4, 8
4	14, 15		
5	9, 12, 14		
6	5, 9, 13, 14		

REFERENCES

Bongard, M. M. (1967): Problem of recognition, Nauka, Moscow.

Gaivoronskaya, T. V. and V. P. Kuleshova (1977): The forecasting of flare magnetic disturbances by computer. In: Ionospheric disturbances and methods of their forecast, Nauka, Moscow, 168-173.

Solar-Geophysical Data, Boulder (1963-73).

Vantsvaig, M. N. (1973): Algorithm "Kora" of teaching the pattern recognition. In: Algorithm of teaching the pattern recognition, Soviet Radio, Moscow.

Vapnik, V. N. and A. Ya. Chervonenkis (1974): Theory of pattern recognition, Nauka, Moscow.

INTERPLANETARY MAGNETIC FIELD AND POLAR CAP MAGNETIC DISTURBANCES: USING THE DATA FOR PREDICTION OF AURORAL ELECTROJET ACTIVITY

O. A. Troshichev
Arctic and Antarctic Institute
Leningrad, 192104, USSR

N. P. Dmitrieva
Polar Geophysical Institute
Murmansk, 183023, USSR

B. M. Kuznetsov and V. P. Vasiliev
Institute of Physics, Leningrad University
Leningrad, 198904, USSR

The relationship between the IMF variations and geomagnetic disturbances at the polar cap in summer and winter is analyzed. The distribution of the space and amplitude characteristics of the DP_2, DP_3, and DP_4 disturbances generated, respectively, by the southward (B_{ZS}), northward (B_{ZN}) and azimuthal (B_Y) components of the IMF are examined and a simple method for their separation is proposed. The DP_2 disturbances at the polar cap in summer precede substorm activity, while similar disturbances at the polar cap in winter develop synchronously with the westward auroral electrojet. The indices of the IMF and polar cap magnetic activity suitable for substorm prediction are developed.

The southward component of the IMF is the most significant parameter affecting magnetospheric activity (Pudovkin et al., 1977; Kamide et al., 1977). The variability of the IMF seems to be another geoefficient characteristic (Garrett et al., 1974). In order to forecast magnetospheric substorms, it is necessary to determine effective precursors of substorms, not only in the IMF characteristics but also in the ground magnetic data. The most suitable precursors are the polar cap magnetic disturbances induced as a result of permanent interaction between the IMF and geomagnetic field (Nishida, 1968; Svalgaard, 1968; Mansurov, 1969; Iwasaki, 1971; Mishin et al., 1973; Friis-Christensen and Wilhjelm, 1975; Kuznetsov and Troshichev, 1977; and Levitin et al., 1977). The DP_2 disturbances are related to the southward component ($B_Z < 0$) of the IMF. The others are concerned with the northern or the azimuthal components of IMF (the DP_3 and DP_4 disturbances, respectively, according to terminology by Kuznetsov and Troshichev (1977)). The main difficulty in applying the DP_2 variation to predictions is the problem of their separation from other polar cap magnetic disturbances.

In this paper we analyze the relationship between the IMF parameters and polar cap magnetic disturbances and propose a simple procedure for estimating the disturbance intensity of the southward component of the IMF. New indices of the polar cap magnetic activity and the IMF characteristics are examined.

1. DATA AND METHOD OF ANALYSIS

To analyze individual events we have used the magnetograms of five stations in the northern hemisphere (Alert, Resolute, Mould Bay, Godhavn, and Baker Lake), three stations in the southern hemisphere (Vostok, Dumont d'Urville, and Mirny), and IMF observations obtained from the IMP-3 satellite for July and August 1965. The correlation analysis was based on the hourly values of the three components of the geomagnetic field for the same stations and the Interplanetary Medium Data Book (King, 1977) for the period of July-August, 1965 and 1966.

In the case of a three-dimensional distribution of probabilities, the regression relation between the B_X, B_Y, B_Z components of the IMF and X, Y, Z geomagnetic elements for a given station for each hour UT can be represented as follows (Troshichev and Tsiganenko, 1978):

$$\begin{aligned} X &= \overline{X} + K_{XX}B_X + K_{XY}B_Y + K_{XZ}B_Z \\ Y &= \overline{Y} + K_{YX}B_X + K_{YY}B_Y + K_{YZ}B_Z \\ Z &= \overline{Z} + K_{ZX}B_X + K_{ZY}B_Y + K_{ZZ}B_Z \end{aligned} \qquad (1)$$

where the K's are the regression coefficients and $\overline{X}$, $\overline{Y}$, $\overline{Z}$ are hourly values of the three elements averaged for the period of July-August, 1965 and 1966. From the regression coefficients and the values of X, Y, Z, it is possible to obtain the direct relationship between the IMF components and the δX, δY, δZ elements of the geomagnetic disturbance vector at each station and to construct the appropriate distribution of $\delta F = \sqrt{(\delta X)^2 + (\delta Y)^2}$ and the equivalent current systems.

2. THE RELATIONSHIP BETWEEN THE IMF VARIATIONS AND POLAR CAP MAGNETIC DISTURBANCES DURING SUMMER

We have examined the distribution of disturbance vectors, δF, and the current systems for different values of the IMF components. The current system for the condition $B_X = B_Y = 0$, $B_Z = -I\gamma$ is shown in Figure 1(a). There is a typical two-vortex DP_2 current system with sunward currents near the pole. The focuses of these vortices are located at latitudes $\Phi' \simeq 75°-78°$, when $B_Z = -I\gamma$.

In the case of the northward (B_{ZN}) component ($B_X = B_Y = 0$, $B_Z = I\gamma$), the DP_3 shows a two-vortex current system (Fig. 1(b)) in agreement with the results of Maezawa (1976) and Kuznetsov and Troshichev (1977). In this system, currents flow in the opposite direction; that is, currents are anti-sunward near the pole. The focuses of the DP_3 current vortices are located at latitude $\Phi' \simeq 80°$. Maximum values of δF and maximum current intensity are ob-

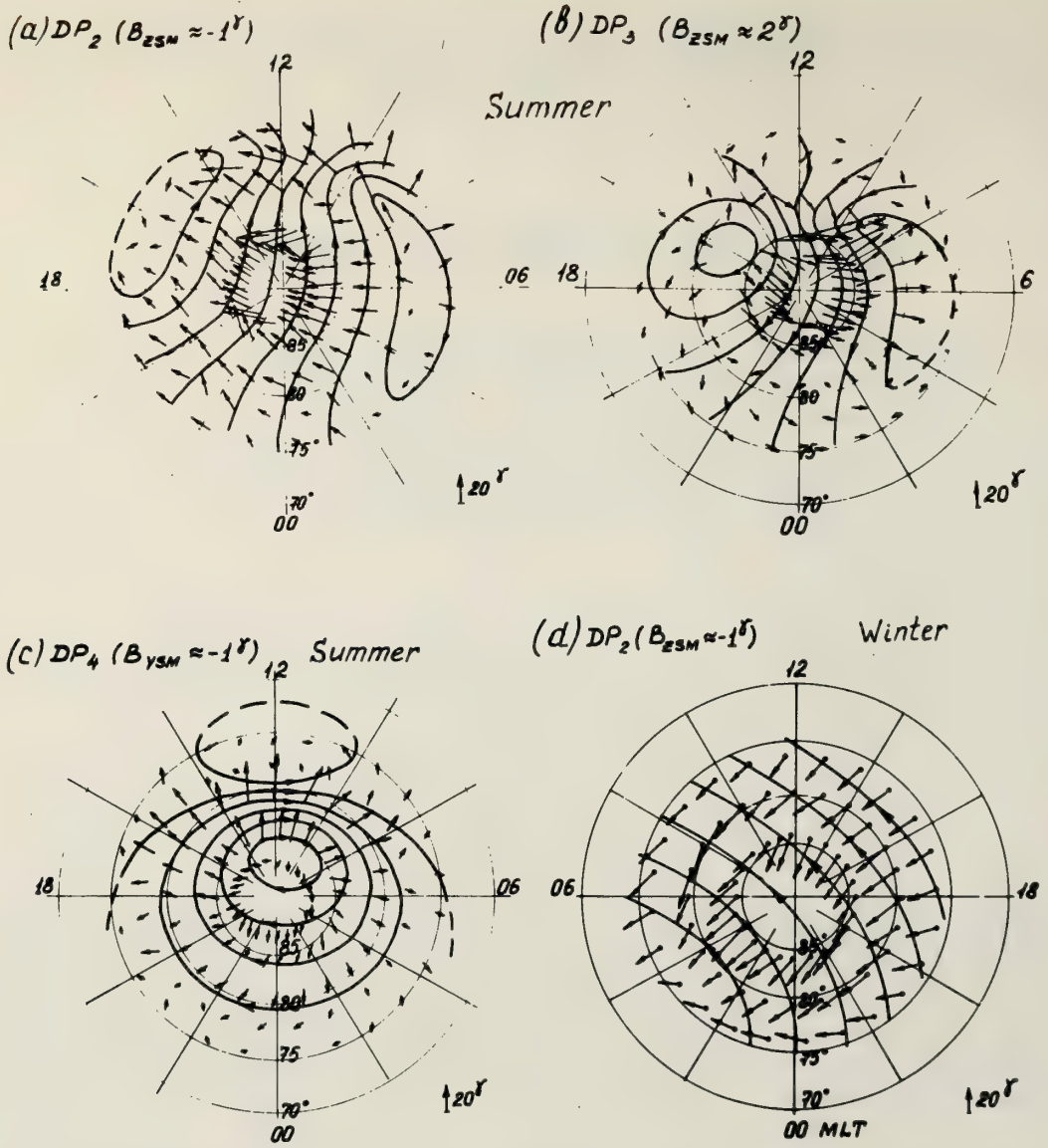


Figure 1. The magnetic disturbances related to the IMF component variations: (a) DP_2, (b) DP_3, (c) DP_4 at the summer polar cap and (d) DP_2 at the winter polar cap.

served at daytime at latitude $\Phi' \simeq 85°$. The intensity of the current decreases rapidly in the equatorward direction.

The equivalent current system of DP_4 disturbances, related to the azimuthal component of the IMF ($B_X = B_Z = 0$, $B_Y = -I\gamma$) is shown in Figure 1(c). As distinct from the DP_2 and DP_3 systems, the DP_4 equivalent system consists only of one polar-cap current vortex connected with the polar electrojet in the daytime cusp region. At latitudes lower than those of the cusp, there is a tendency towards formation of the second vortex in the day sector.

The influence of the radial (B_X) component of the IMF at the geomagnetic field is negligible almost everywhere. The correlation coefficients are near zero for all hours UT, and the regression coefficients differ from zero only

in the daytime cusp region. We interpret such regularity as being a result of the close relationship of the B_X and B_Y components within the framework of the IMF sector structure.

The ionospheric current systems of the DP_2, DP_3, and DP_4 disturbances may be generated as a result of field-aligned currents flowing in and out of the ionosphere. Troshichev and Gizler (1978) have computed the ionospheric effects produced by field-aligned currents using the Triad data (Iijima and Potemra, 1976a,b) and a realistic model of the ionospheric conductivity (Vanyan and Osipova, 1975). The results obtained by Troshichev and Gizler show that systems of the ionospheric electric fields and Hall currents generated by field-aligned currents are in good agreement with the experimental data on electric fields and current systems of the DP_2, DP_3, and DP_4 disturbances.

3. DEPENDENCE OF THE DP_2 AND DP_3 DISTURBANCE INTENSITY ON THE B_Z COMPONENT

According to Kuznetsov and Troshichev (1977), the dependence of both DP_2 and DP_3 disturbances on the magnitude of the vertical component B_Z may be regarded as linear. The straight line which represents this dependence will intersect the B_Z axis at the point $B_Z \simeq 1.5\gamma$. This conclusion is confirmed by the present analysis.

Figure 2 shows the relationship between the intensities of DP_2 and DP_3 disturbances at the polar station Alert during periods of low magnetic activity (AE < 120γ) for different directions of the azimuthal component

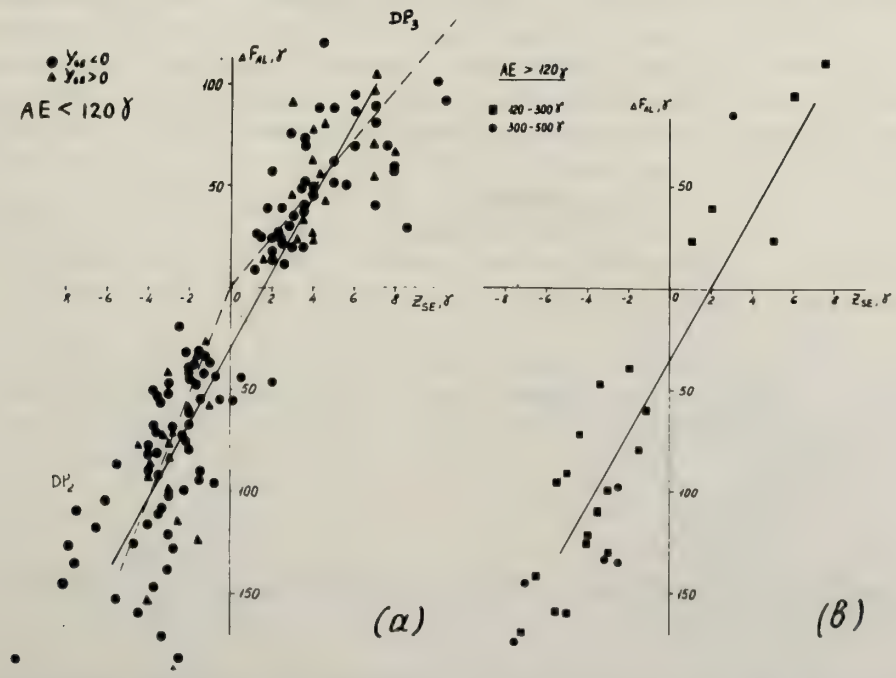


Figure 2. The relationship between the magnitude of the B_Z component of the IMF and the intensities of DP_2 and DP_3 disturbances at the nearpole station Alert during the periods of low (a) and high (b) magnetic activity.

($B_Y < 0$ and $B_Y > 0$). The solid lines represent the linear dependence obtained by a least squares fit to the whole array of data, and the dotted lines represent dependences obtained separately for $B_Z > 0$ and $B_Z < 0$.

As Figure 2 includes data for all hours, we have examined the dependence $\delta F(B_Z)$ for local morning, noon, evening, and night sectors separately. Our analysis shows that the linear relation between the B_Z component of the IMF and the DP_2 and DP_3 disturbances is valid for any local time, but the character of this relationship changes from day to night. Approximating the dependence $\delta F(B_Z)$ by

$$\delta F = K_0 + K_1 B_Z \qquad (2)$$

we obtain the results presented in Table 1 (where B_{0Z} is the value of B_Z for $|\delta F| = 0$).

Table 1. The parameters of the linear relation between the B_Z component of the IMF and the DP_2, DP_3 disturbances

	morning	noon	evening	night	overall (Fig. 2)
$K_0(\gamma)$	-13	-50	-29	-28.5	-30
K	15	20	17	19	18.5
$B_{0Z}(\gamma)$	0.9	2.5	1.7	1.5	1.6

It may be seen that for fixed B_Z values, the daytime intensity of the DP_2 disturbances is twice that of the dawn-time one. But in any case the magnitude δF appears to be equal to zero only for the northward component $B_Z \simeq (1 \div 2.5)\gamma$. This agrees with the results of Maezawa (1976) and Kuznetsov and Troshichev (1977). The influence of the azimuthal components on the relationship $\delta F(B_Z)$ may be observed only in the daytime sector, where the intensity of the DP_2 disturbances tends to be higher for $B_Y > 0$ than for $B_Y < 0$.

It is significant that the intensity of the DP_2 and DP_3 disturbances in the summer polar cap does not show obvious dependence on the activity of the auroral electrojets. According to our results, the pattern of the function $\delta F(B_Z)$ is the same for both low (Fig. 2(a), AE < 120γ) and high (Fig. 2(b), AE > 120γ) activity.

Thus we conclude that the intensity of DP_2 and DP_3 disturbances in the summer polar cap is determined mainly by the B_Z component and therefore the DP_2 and DP_3 disturbances in the summer polar cap may be a good indicator of this IMF component.

4. VARIATION OF THE RESIDUAL GEOMAGNETIC FIELD (S_q^p VARIATION)

The values $\overline{X}$, $\overline{Y}$, $\overline{Z}$ in equation (1) represent the geomagnetic field remaining after exclusion of variations generated by the IMF components (if the linear relation between the IMF parameters and geomagnetic disturbances is real). Our analysis shows that the $\overline{X}$, $\overline{Y}$, $\overline{Z}$ elements undergo a regular varia-

tion with respect to their mean daily values. This variation may be presented by a two-vortex current system similar to that of the DP_2 disturbance (Fig. 3). However, the variation of the residual geomagnetic field has evidently another origin than the DP_2 variation as (1) it is observed after the exclusion of variations related to the IMF and the pattern is the same for both $B_Z < 0$ and $B_Z > 0$, and (2) it is a daily variation.

We suppose this variation to be identified with the S^P_q variation by Nagata and Kokubun (1962). It may result from the stationary magnetospheric convection due to the nonmagnetic interaction of the solar wind with the magnetosphere. In accordance with the hypothesis of Axford (1969), the mechanism of the quasiviscous friction may be proposed as a basic one in this interaction.

5. ESTIMATION OF THE ELECTRIC FIELDS OF THE S^P_q VARIATION AND THE DP_2, DP_3 DISTURBANCES

If the magnetic disturbances in the summer polar cap are generated by the ionospheric Hall currents, the intensity of currents and therefore the electric field E may be easily estimated by

$$E(mV/m) \simeq \frac{\delta F}{2\pi\Sigma} 10\,(\gamma) \qquad (3)$$

where δF is the magnitude of the magnetic disturbance and Σ is the Hall ionospheric conductivity, $\Sigma \simeq 10$ mhO.

For the S^P_q variation, when δF is near 50γ near the pole we obtain the dawn-dusk electric field, $E \simeq 8$ mV/m. For DP_2 disturbances, the estimation gives also the dawn-dusk field, $E \simeq 4$ mV/m for $B_Z = -I\gamma$ and the growth of this field is about 4 mV/m per $I\gamma$ increase of the southward component B_{ZS}. In the case of the DP_3 disturbance, the electric field has the opposite direction (dusk-dawn) with a maximum intensity in the daytime cusp region equal

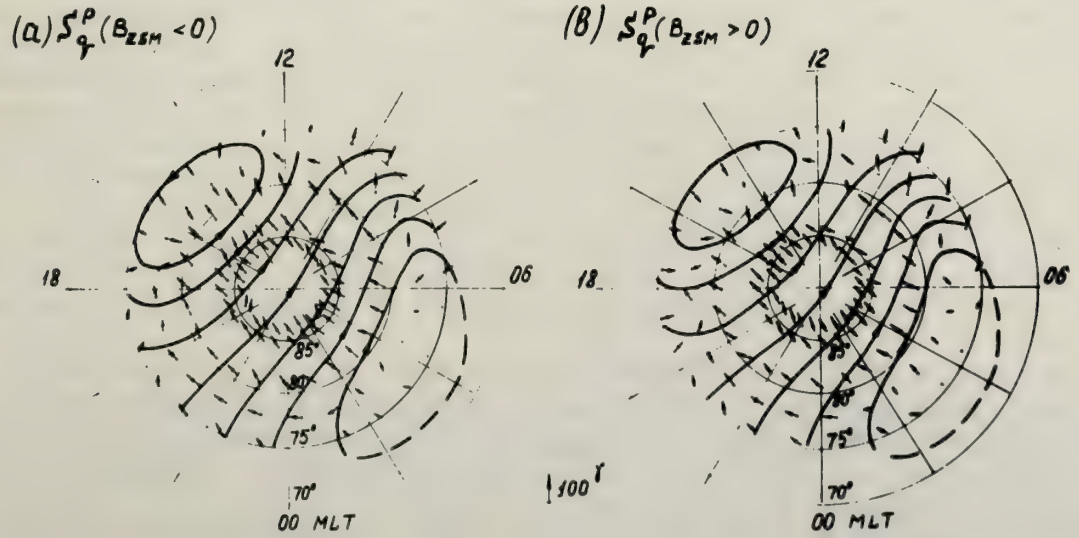


Figure 3. The equivalent current systems of the residual geomagnetic field variation (S^P_q variation) for $B_Z < 0$ (a) and $B_Z > 0$ (b).

to about 8 mV/m for $B_z = 2\gamma$. Estimated values appear to confirm the experimental data.

In the case of the southern component of the IMF, the electric field of DP_2 and S^p_q variation are added together and the total field near the pole is about 15 mV/m for $B_z = -2\gamma$ and $E \simeq 25 \div 30$ mV/m for $B_z = -(4 \div 5)\gamma$. These are typical values of the polar cap electric fields during periods of low and moderate magnetic activity. In the case of the northern component B_{ZN}, the DP_3 electric field is cancelled by the S^p_q electric field until the northern component becomes very large. That is why the DP_2 disturbance pattern (or S^p_q) may be observed at the polar cap for $B_z = 0$.

6. THE RELATIONSHIP BETWEEN THE IMF VARIATIONS AND POLAR CAP MAGNETIC DISTURBANCES IN THE WINTER POLAR CAP

It has been noted already (Sumaruk and Feldstein, 1973; Friis-Christensen and Wilhjelm, 1975) that the geomagnetic disturbances related to the northward and azimuthal components of the IMF have maximum intensity in summer and tend to zero in winter. Our analysis leads to the same results. As the field-aligned currents seem to be the main source of the DP_2 and DP_3 disturbances (Troshichev and Gizler, 1978), the evident seasonal dependence of these disturbances indicates that the occurrence and intensity of the daytime cusp field-aligned currents is regulated by the ionospheric conductivity near the pole.

The seasonal dependence of the DP_2 disturbances is not so clear. According to a common point of view, they may be observed in the winter polar cap as well as in the summer one. However in this case, the question arises about the origin of the DP_2 disturbance under conditions of low conductivity in the winter ionosphere.

To solve this problem we analyzed the development of disturbances at stations in both the summer (Alert) and winter (Vostok) polar caps, when the B_z component of the IMF turns to the south. The onset of the southward B_{ZS} component appears not to affect the geomagnetic field at Vostok until the substorm begins, in contrast with the summer polar cap where DP_2 disturbances start 10-20 minutes after B_z turns to the south and only then does the substorm develop. We noted 110 events of DP_2 disturbances at Alert during July-August 1965, but synchronous geomagnetic variations at Vostok were found in only 23 events. Moreover, only 8 of them occurred when the AE-index was below 100γ and for the other 15, the activity index was higher. This allows us to conclude that there is a close connection between the development of auroral electrojets and the occurrence of "DP_2" disturbances in the winter polar cap.

The results of the correlation analysis confirm this conclusion. We calculated the regression coefficients and constructed the appropriate current systems for disturbances in the winter polar cap related to the B_{ZS} component (Fig. 1(d)) and for disturbances in both summer and winter polar caps related to the westward electrojet (Fig. 4).

The current patterns in Figures 1(a), 1(d), and 4 show the following. The equivalent current systems of the polar cap disturbances related to the westward electrojet are similar in summer and in winter (Fig. 4). The equivalent current system of the "DP_2" disturbances in the winter polar cap

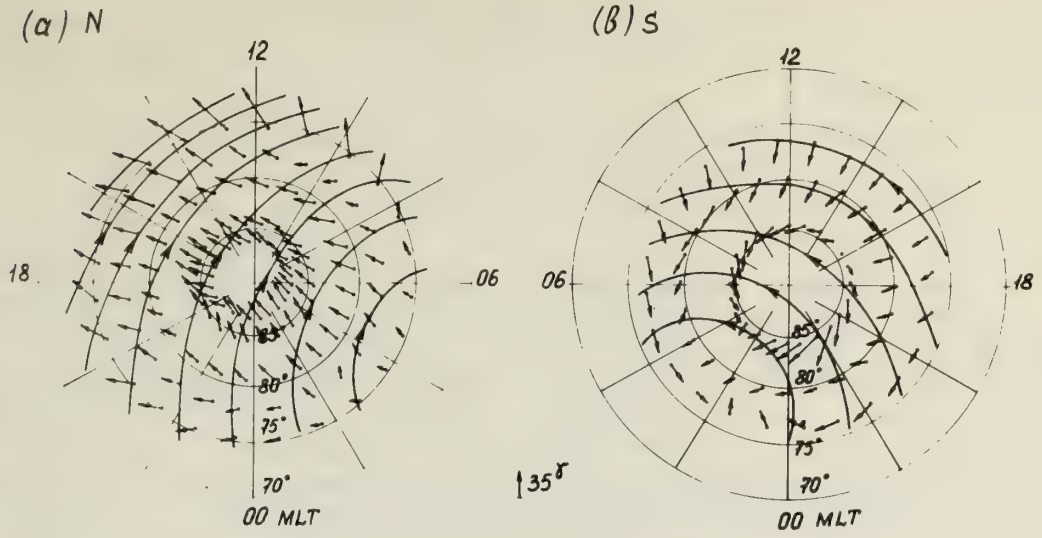


Figure 4. The equivalent current systems of the magnetic disturbances related to the westward electrojet at the summer (a) and winter (b) polar cap.

(Fig. 1(d)) differs from the standard DP_2 system (Fig. 1(a)) but is similar to systems in Figure 4. Taking into account the low conductivity and therefore the small contribution of the ionospheric currents to the winter polar cap disturbances, we conclude that the distant effects of the field-aligned currents are represented in Figure 1(d) and Figure 4(b). (The same interpretation is valid for disturbances in the summer polar cap related to the westward electrojet, Figure 4(a).)

This means that the field-aligned DP_2 currents in the winter polar cap are closed only through the highly conducting auroral oval. If the ionospheric conductivity in the auroral oval is as low as in the polar cap, the DP_2 field-aligned currents will close up. As the increased conductivity in the auroral oval depends directly on the substorm activity, the disturbances in the winter polar cap due to DP_2 field-aligned currents will be seen only during the substorm development.

On the basis of these results it may be concluded that the "DP_2" disturbances in the winter polar cap cannot be used as precursors of the auroral electrojet activity.

7. PROCEDURE OF THE FORECAST INDICES DERIVATION

Figure 1 shows that the fields of the DP_2, DP_3, and DP_4 disturbances are most homogeneous near the pole. The geomagnetic disturbance vector δF is directed approximately from dawn to dusk in the case of the DP_2 and DP_3 variations, but it lies along the noon-midnight meridian under the influence of the azimuthal component of the IMF. Therefore we can assume that near the pole at any moment of universal time (UT), the projection of the δF on the axis 0600-1800 LT corresponds to the disturbances generated by the north-south

(B_Z) component of the IMF, while the projection on the axis 1200-2400 LT corresponds to the disturbances due to the azimuthal (B_Y) component, that is, in the northern hemisphere.

$$\begin{aligned} F_i(B_Z) &= dX_i \sin \alpha_i - dY_i \cos \alpha_i \\ F_i(B_Y) &= dX_i \cos \alpha_i + dY_i \sin \alpha_i \\ \alpha_i &= \lambda_i + (UT)_i \cdot 15^\circ \end{aligned} \tag{4}$$

where λ is the geographical longitude and dX and dY are the deviations of the X and Y elements from their quiet level.

According to equation (4), the value $F_i(B_Z)$ is positive when $B_Z < 0$ (the disturbance vector directed from dawn to dusk), and is negative when $B_Z > 0$ (direction to dawn); the value $F_i(B_Y)$ is positive when $B_Y > 0$ (direction to noon) and is negative when $B_Y < 0$ (direction to midnight). The values dX and dY were determined for every three minutes. The quantities F_i calculated according to equation (4) were summarized for 15 minutes:

$$F_\Sigma(B_Z) = \sum_1^5 F_i(B_Z); \quad F_\Sigma(B_Y) = \sum_1^5 F_i(B_Y) \tag{5}$$

The magnitudes of F_Σ attributed to the end of the appropriate 15-minute intervals were plotted on a graph. Intervals of 15 minutes duration were chosen for the reason that these impulses in the IMF appear to be the shortest time period for which polar cap magnetic variations may be traced (Garrett et al., 1974; Kuznetsov and Troshichev, 1977).

In order to take into account the variability of the polar cap geomagmetic field within the 15-minute intervals, we calculated the successive differences

$$\Delta X_i = dX_i - dX_{i-1}; \quad \Delta Y_i = dY_i - dY_{i-1} \tag{6}$$

On the basis of these differences (defined with regard to their signs) the quantities δF_i and F'_Σ were computed from

$$\begin{aligned} \delta F_i(B_Z) &= \Delta X_i \sin \alpha_i - \Delta Y_i \cos \alpha_i \\ \delta F_i(B_Y) &= \Delta X_i \cos \alpha_i + \Delta Y_i \sin \alpha_i \end{aligned} \tag{7}$$

$$F'_\Sigma = \frac{\Delta F_\Sigma}{\Delta t} = \frac{\sum_1^5 \delta f_i}{\Delta t}$$

where Δt = 15 minutes. Thus for every 15-minute interval we have four characteristics: $F_\Sigma(B_Z)$, $F'_\Sigma(B_Z)$, and $F_\Sigma(B_Y)$, $F'_\Sigma(B_Y)$. The first pair represents the 15-minute sum of the disturbance vectors and the 15-minute averaged rate of change of these vectors for DP_2 (when $F_\Sigma > 0$) or DP_3 (when $F_\Sigma < 0$) disturbances; the second pair represents the similar quantities for the DP_4 disturbances. The signs of the F_Σ and F'_Σ may be the same as well as opposite. For example, the intensity of the DP_2 disturbance ($F_\Sigma(B_Z) > 0$) within the 15-minute interval can either increase ($F'_\Sigma(B_Z) > 0$) or decrease ($F'_\Sigma(B_Z) < 0$).

For the interplanetary magnetic field, the 15-minute sum of the southward component ($\sum B_{ZS}$) and the 15-minute sum of the negative gradients of the vertical component ($\sum(-\delta B_Z)$) were likewise determined.

The IMF data and magnetograms of the observatory Alert for July 1965 were used in our analysis.

8. EFFICIENCY OF THE FORECAST INDICES

We examine the relationship between the AE-indices of the substorm activity and the values $\sum B_{ZS}$, $\sum(-\delta B_Z)$, $F_\Sigma(B_Z)$, $F'_\Sigma(B_Z)$, $F_\Sigma(B_Y)$ and $F'_\Sigma(B_Y)$ for 25 days of July 1965. The first peculiarity which is obvious from the examination is the following: the rise of the AE-index almost always succeeds the increase of the values of $\sum B_{ZS}$. There is a certain similarity between the time course of the $\sum B_{ZS}$ and the changes in the AE-index. However, sometimes the parameters $\sum(-\delta B_Z)$ seem to be more effective. Figure 5 gives an example of such an event (see the period 1500-1800 UT, July 13). To take into account these situations, it is reasonable to examine any combination of $\sum B_{ZS}$ and $\sum(-\delta B_Z)$. In our analysis we take the product

$$\sigma(B_Z) = \sum B_{ZS} \cdot \sum (-\delta B_Z) \qquad (8)$$

Unfortunately in many cases, the parameters $\sigma(B_Z)$ are less clear than $\sum B_{ZS}$. We consider the sum of these values where $\sum B_{ZS}$ and $\sum(-\delta B_Z)$ are given different weights, to be a better parameter.

Among the polar cap magnetic characteristics, the value $F_\Sigma(B_Z)$ is the most effective for forecasting. The intensive enhancements of the magnitude of $F_\Sigma(B_Z)$ are followed by magnetic substorms with a time delay of 0.3-3 hours. After the decrease of $F_\Sigma(B_Z)$, there is a decrease of activity in the auroral zone. Apparently there is a threshold for the response of $F_\Sigma(B_Z)$ about the value of 200γ: the substorms do not develop when $F_\Sigma(B_Z)$ is below this quantity. This threshold indicates that the S^p_q variation contributes to the value of F_Σ.

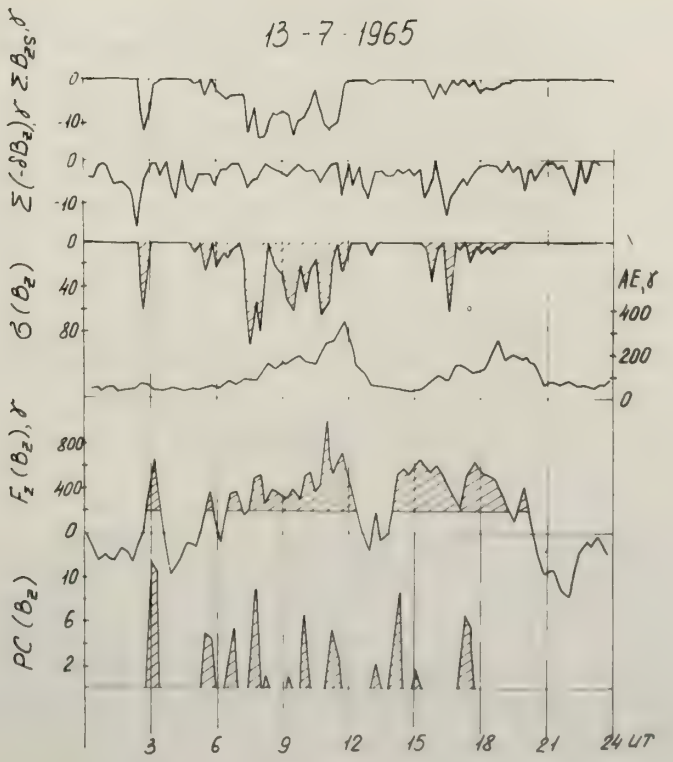


Figure 5. The relation between the AE-indices of substorm activity and various characteristics of the IMF and the polar cap magnetic activity, July 13, 1965.

It is typical that the correspondence between AE and $F_{\Sigma}(B_Z)$ is present not only in isolated substorms (which develop on the background of the quiet geomagnetic field), but also in cases of the substorm sequence, when maxima are observed one after another with periodicity about one hour or more. Sometimes the striking similarity is seen even in such details as the time sequence and shape of the small spikes.

The characteristic $F'_{\Sigma}(B_Z)$ examined separately from $F_{\Sigma}(B_Z)$ appears to be poorly correlated with AE indices. The product of the values $F_{\Sigma}(B_Z)$ and $F'_{\Sigma}(B_Z)$ (that is the $PC(B_Z)$-index) gives the better result, because almost every magnetic substorm seems to be preceded by enhancements in the value of PC. But this characteristic undergoes constant changes in magnitude and in sign and therefore it is difficult to use for forecasting.

Figure 5 shows also an unusual instance in which a very intensive enhancement of all values of the southward component of the IMF ($\sum B_{ZS}$, $\sigma(B_Z)$, $F_{\Sigma}(B_Z)$, $PC(B_Z)$) is not followed by any activity in the auroral zone. It may be assumed that in this case, the auroral electrojet activity occurs at latitudes higher than typical auroral zone latitudes.

The values related to the azimuthal components $F_{\Sigma}(B_Y)$ and $F'_{\Sigma}(B_Y)$ are evidently useless for predicting. In any case they do not appear to cause changes in the above regularities.

For 25 days of July 1965, we recorded 46 substorms with the intensity of more than 200γ (according to AE-indices). This number includes the isolated bays as well as intensive peaks of activity in the substorm sequences. The results of the analysis are presented in Table 2, where all events and predicted substorms (on the basis of the polar cap data) are shown.

Table 2. The results of forecast analysis.

Indices of the polar cap magnetic activity	Amount of substorms			Amount of false precursors
	all examined	with precursors	without precursors	
$F_{\Sigma}(B_Z)$	46	40	6	11
$F_{\Sigma}(B_Z) \cdot F'_{\Sigma}(B_Z)$	46	39	7	15
Both indices are used	46	41	5	5

9. CONCLUSIONS

From the above results, it is concluded that most (>85%) moderate and large substorms can be predicted on the basis of the IMF data as well as the polar cap magnetic variations. The characteristics related to the southward component of the IMF can be used as substorm predictors. The method proposed in the present study will not predict those substorms which develop under the northward component of the IMF. This method may also be used for diagnosis of the IMF sector structure.

Acknowledgments. We thank Dr. N. F. Ness whose interplanetary magnetic field data were used in this paper.

REFERENCES

Axford, W. I. (1969): Viscous interaction between the solar wind and the Earth's magnetosphere. Planet. Space Sci., 12:45.

Friis-Christensen, E., and J. Wilhjelm (1975): Polar cap currents for different directions of the interplanetary magnetic field in the Y-Z plane. J. Geophys. Res., 80:1248.

Garrett, H. B., A. J. Dessler, and T. W. Hill (1974): Influence of solar wind variability on geomagnetic activity. J. Geophys. Res., 79:4603.

Iijima, T., and T. A. Potemra (1976a): The amplitude distribution of field-aligned currents of northern high latitudes observed by Triad. J. Geophys. Res., 81:2165.

Iijima, T., and T. A. Potemra (1976b): Field-aligned currents in the dayside cusp region observed by Triad. J. Geophys. Res., 81:5971.

Iwasaki, N. (1971): Localized abnormal geomagnetic disturbances near the geomagnetic pole and simultaneous ionosphere variation. Rep. Ionosph. Space Res. Japan, 25:163.

Kamide, Y., P. D. Perreault, S.-I. Akasofu, and J. D. Winningham (1977): Dependence of substorm occurrence probability on the interplanetary magnetic field and on the size of the auroral oval. J. Geophys. Res., 82:5521.

King, J. H. (1977): Interplanetary medium data book. Greenbelt, NSSDC, N 77-04.

Kuznetsov, B. M., and O. A. Troshichev (1977): On the nature of polar cap magnetic activity during undisturbed periods. Planet. Space Sci., 25:15.

Levitin, A. E., B. A. Belov, R. G. Afonina et al. (1977): Three-dimensional current systems of geomagnetic field variations in north polar cap connected with component of the IMF. Preprint IZMIRAN, N 17 a.

Maezawa, K. (1976): Magnetospheric convection induced by the positive and negative Z components of the interplanetary magnetic field: quantitative analysis using polar cap magnetic records. J. Geophys. Res., 81:2289.

Mansurov, S. M. (1969): New data about relation between space and Earth magnetic fields. Geomagn. Aeronomy, 9:768.

Mishin, V. M., A. D. Bazarzhapov, E. I. Nemtsova et al. (1973): Influence of the interplanetary magnetic field on magnetospheric convection and electric currents in the ionosphere. In: Substorms and magnetospheric disturbances, Nauka, Leningrad, 191.

Nagata, T., and S. Kokubun (1962): An additional geomagnetic daily variation (S^{p}_{q}-field) in the polar region on a geomagnetically quiet day. Rep. Ion. Space Res. Japan, 16:256.

Nishida, A. (1968): Coherence of geomagnetic DP_2 fluctuations with interplanetary magnetic variations. J. Geophys. Res., 73:5549.

Pudovkin, M. I., V. P. Kozelov, L. L. Lazutin, O. A. Troshichev, and A. D. Chertkov (1977): Physics principles of magnetospheric disturbance forecasting. Ed. S. I. Isaev, Nauka, Leningrad, 312 p.

Sumaruk, P. V., and Feldstein, Ya. I. (1973): IMF sector structure and geomagnetic disturbances in the nearpole region. Kosmitch. Issled., 9:155.

Svalgaard, L. (1968): Sector structure of the interplanetary magnetic field and daily variation of the geomagnetic field at high latitudes. Danish. Meteor. Inst. Geophys. Paper, R-6.

Troshichev, O. A., and V. A. Gizler (1978): Field-aligned electric currents and polar magnetic disturbances. In: Geomagnetic Research, Moscow, N 23, 24.

Troshichev, O. A., and N. A. Tsiganenko (1978): Correlation relationship between parameters of the interplanetary magnetic field and polar cap magnetic variations. In: Geomagnetic Research, Moscow, N 24.

Vanyan, L. L., and I. L. Osipova (1975): Conductivity of the polar ionosphere. Geomagn. Aeronomy, 15:847.

SHORT-TERM FORECASTING OF GEOMAGNETIC STORMS ASSOCIATED WITH HIGH-SPEED SOLAR WIND STREAMS

V. M. Mishin, V. V. Shelomentsev, A. D. Bazarzhapov,
and L. P. Sergeeva
Siberian Institute of Terrestrial Magnetism,
Ionosphere and Radio Wave Propagation (SibIZMIR)
Irkutsk-33, P.B.4, USSR

At the front of high-speed solar wind streams, density bursts are observed with peak values $n \geq 10$ cm^{-3}. Such bursts produce a characteristic geomagnetic response in the polar cap. In principle, this effect may be used to predict, 0.5-1 day beforehand, the geomagnetic storms observed when the high-speed part of the stream crosses the Earth.

1. INTRODUCTION

Global geomagnetic storms are usually classified as two types: sporadic (flare-associated) and recurrent. Sporadic storms are distinguished by the presence of a sudden commencement (SC), small duration (≃1-2 days), absence of a 27-day recurrence, and coherence with cyclic variations of the Wolf numbers. Recurrent storms are characterized by the absence of SC, long duration, and recurrence. They achieve the greatest frequency and intensity at the decline of the solar cycle phase, 1-2 years prior to the epoch of solar minimum.

Available techniques for magnetic storm prediction are well improved only for flare-associated storms, whereas for recurrent ones the improvement is insufficient. This can be explained, probably, by the fact that for the flare-associated storms a whole number of ground precursors is known: magnetic effects (SC) and crochet (SFE), ionospheric effects (SID), absorption effects in the polar caps (PCA), etc. At the same time obvious and distinct precursors of recurrent storms are not well established, and the forecasting of such disturbances is based on their recurrence that enables us to predict only the successive storms (at multiples of 27 days after the initial one) but not the initial storm of the succession itself.

Thus, there is no available technique for forecasting geomagnetic storms with respect to recurrent storms. This is significant since the flare-associated disturbances are only ≃3-4 percent of the total number of storms at solar cycle minimum and ≃10-30 percent at solar cycle maximum, i.e., the recurrent storms are predominant. Therefore, a discovery of precursors of

recurrent storms is extremely desirable.

In the present paper some possibilities for short-term forecasting of both recurrent and flare-associated storms are discussed in terms of ground geomagnetic observations in the high-latitude region.

2. RELATION OF RECURRENT STORMS TO HIGH-SPEED SOLAR WIND STREAMS

For a long time the possibility of hypothetical M-regions on the sun (a term introduced by Bartels, 1932) as being the sources of recurrent geomagnetic storms and displaying no apparent signatures on the solar disk was discussed. Recently, it was stated that these storms are associated with the high-speed solar wind streams (HS) whose formation takes place mainly in the regions of the solar surface with open configuration of magnetic field lines where the so-called "coronal holes" are observed in X-ray emissions (Krieger et al., 1973; Neupert and Pizzo, 1974; and Gulbrandsen, 1975). In view of this relation of recurrent storms to high-speed streams, improvement of geomagnetic storm forecasting should involve the following:

1. detection of coronal holes with the help of solar observations;
2. detection of HS in the interplanetary medium;
3. discovery of ground signatures of HS and of their precursors.

A technique for the direct observation of coronal holes is not well developed as yet and sometimes requires special cosmic instrumentation. The detection of the HS while it is passing from the sun toward the Earth is also possible with the help of cosmic instruments, although in the recent paper of Roelof et al. (1977), the possibility, uniting points (2) and (3) above, was shown of detecting density jumps, surpassing HS (and the geomagnetic disturbance prediction $\simeq$1 day beforehand) by means of ground observations of the interplanetary radio scintillation (IPS).

We shall examine the possibility of detecting the precursors of HS using ground geomagnetic observations. For this purpose it is necessary first of all to consider the structure of HS. According to the available models by Hundhausen (1972) and by Ivanov and Mikerina (1974), HS has a complex structure in the form of alternating layers, differing in physical characteristics and producing, according to Ivanov and Mikerina (1974), different geomagnetic responses. Nevertheless, we think that to improve the technique for the prediction of storms, it is sufficient to divide HS into only two parts—a "core" and a "periphery."

Figure 1 is a schematic illustration of the time variations of solar wind velocity (V), density (n), IMF module (B), and the D_{st}-index; all observed when a typical HS passes through the Earth's orbit. At the front of HS the enhancement of n and B of a burst type are observed, the n-burst surpassing the B-burst (this behavior of wind parameters in the typical stream is well known).

From the analysis of 36 HS detected in the 1967-68 data of STAC-B (1971) and of King (1977), we have estimated the mean delay times of onsets of B,V increase and the main storm phase decrease seen by D_{st} with respect to the n-burst onset. It turned out that Δt (n,B) $\simeq$ 6 hours, Δt (n,V) $\simeq$ 12 hours, Δt (n,D_{st}) $\simeq$ 24 hours, i.e., the beginning of the storm's main phase takes place, on the average, a day after the onset of the n-burst. It should be noted also that the occurrence of storms having considerable magnitude

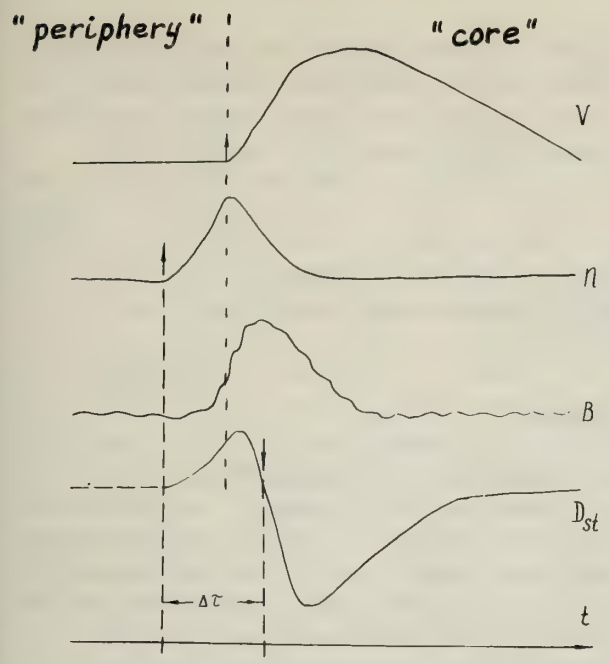


Figure 1. Typical profiles of velocity, V, density, n, a module of the IMF, B, in the high-speed solar wind stream and associated geomagnetic storm in D_{st} index. $\Delta\tau$ is the delay time of the main storm phase with respect to the onset of the growth of n.

($D_{st} \leq -40\gamma$ in the maximum of the main phase) is observed in ≃80 percent of the cases in the sample.

On the basis of these data, by "core" we shall mean the high-speed part of a stream and by "periphery," the front region wherein V has background values but n and B are enhanced (Fig. 1).

Taking into account the time estimates given above, one can assume that the possibilities of short-term forecasting of the main phase lie in the discovery of specific responses of the magnetosphere and the ionosphere to bursts of n and B.

The role of the IMF in the generation of magnetospheric substorms and storms is well known. According to a theoretical reconnection hypothesis by Dungey (1961) and to numerous experimental studies, the most geoeffective solar wind parameter is the south IMF Z-component. A technique for definition of geoefficiency of streams (mainly flare-associated) and for the prediction of geomagnetic storms made possible by the discovery of a regular direction of the IMF Z-component observed in large-scale magnetic fields in the solar photosphere, is described in detail in a monograph by Pudovkin et al. (1977) and is, undoubtedly, of great interest (see also Rosenberg and Coleman, 1978). However, it is reasonable as well to study the geoefficiency of wind density bursts.

The role of this parameter in ground geomagnetic disturbances is as yet but little understood, although it is emphasized in some works. The relation of n to DCF-disturbances and to the initial storm phase SC has been established (see, for example, Verzariu et al., 1972; Kane, 1974; Pudovkin et al., 1977). In addition, Kane (1974) has shown that the presence of high values of $n \geq 10$ cm^{-3} is one of the necessary conditions for development of the main storm phase (along with the presence of the south IMF Z-component). Correlation coefficients of D_{st} and n during the initial storm phase are higher than of D_{st} and V (~0.8-0.9 and 0.2-0.4, respectively).

Since the onset of the main storm phase, associated with HS, is

appreciably delayed with regard to the onset of the n-burst, a study of the geomagnetic effects of wind density may provide the basis for predicting storms about a day beforehand. Below we shall consider the results obtained for this purpose from the analysis of high-latitude magnetic data.

3. A GEOMAGNETIC RESPONSE OF THE POLAR CAP TO THE PASSAGE OF A HIGH-SPEED STREAM PERIPHERY

3.1 Analysis of Geomagnetic Indices

In order to reveal the high-latitude geomagnetic response to the HS passage, it is reasonable, first of all, to examine the behavior of specific activity indices. In the polar cap they are the index PC, derived from data from stations near the pole ($\Phi \gtrsim 85°$) (see, for example, Iijima and Nagata, 1972; Kuznetsov and Troshichev, 1977) and the index PE, from data of magnetospheric cleft projection stations ($\Phi \simeq 75\text{-}81°$) (Shelomentsev and Mishin, 1977). These indices reflect the dynamics of polar disturbances such as S_qP, DP-2, PEJ and others, and yield, according to Shelomentsev and Mishin (1977), good results in the current forecasting of magnetic substorms (expansion phase) $\simeq$1-3 hours beforehand.

A method of superimposed epochs was used for this analysis of the data for 1967-68. Figure 2 presents the profiles of PC, PE, and D_{st}, averaged over 20 streams where the zero time moment (τ=0) is the onset of the main storm phase in D_{st}.

The stable growth of the polar cap indices begins $\simeq$6-10 hours prior to τ = 0. It is of interest to note that the index PE displays considerable dynamics in the earlier period also. This may testify to the fact that the

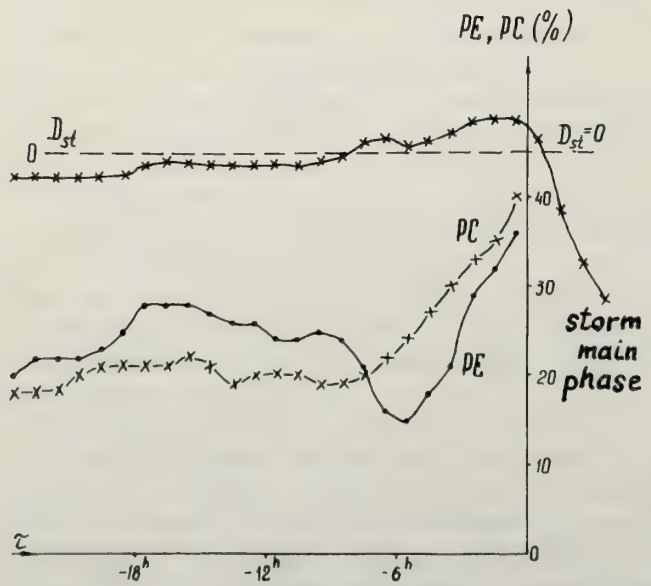


Figure 2. Changes of polar cap indices PC and PE before the main phase onset in D_{st} (a superimposed epoch method for 20 streams).

characteristic activity fluctuations in the magnetospheric cleft zone begin a long time before (of an order of a day) the main phase onset that is important for predicting.

The results show evidence that the polar cap responds, in a definite manner, to the HS passage (including its "periphery") before the onset of a geomagnetic storm related to HS. However, these data do not explain anything about the effect of the wind density jump at the stream front. Therefore we have selected 16 specific n-bursts that surpass the proper HS (its "core"), i.e., observed during the background values of wind velocity ($V \simeq V_b \simeq$ constant) and we have used a superimposed epoch method. The zero moment ($\tau = 0$) corresponds to the n-burst onset. All bursts are reduced to a mean value of $\Delta\tau$ from the growth onset up to the maximum of n (contraction or expansion in the time axis). Only the cases with $\Delta\tau \lesssim 10$ hours were selected. A mean value is $\langle\Delta\tau\rangle \simeq 6$ hours. Values of the H-component at stations near the pole, Resolute Bay (N), and Vostok (S), were taken as a geomagnetic measure (a rough analog of index PC). Results are given in Figure 3. It is seen that the passage of the density burst through the Earth is, in fact, accompanied by the enhancement of a transpolar current in the ionosphere.

Since the present sample corresponds to a stream "periphery" (<V> lies within 380-390 km/s; i.e., it is practically constant during the time interval under consideration), only the parameters n and B may be geoeffective. To clarify the role of the IMF, a profile of the Z-component is presented in Figure 3. (For the convenience of comparison with geomagnetic data, the ordinate axis, Z_{SM}, is reversed.) This figure shows that at the period when $\tau = -2 \div +2$ hours, Z_{SM} is southward and for $\tau > +2$ hours, it is northward.

For the reason given, the growth of H at $\tau = -2 \div +2$ hours may be associated with the presence of the southern IMF. However, the influence of parameter n is also well seen from the inequality of values H at $\tau < 0$ and

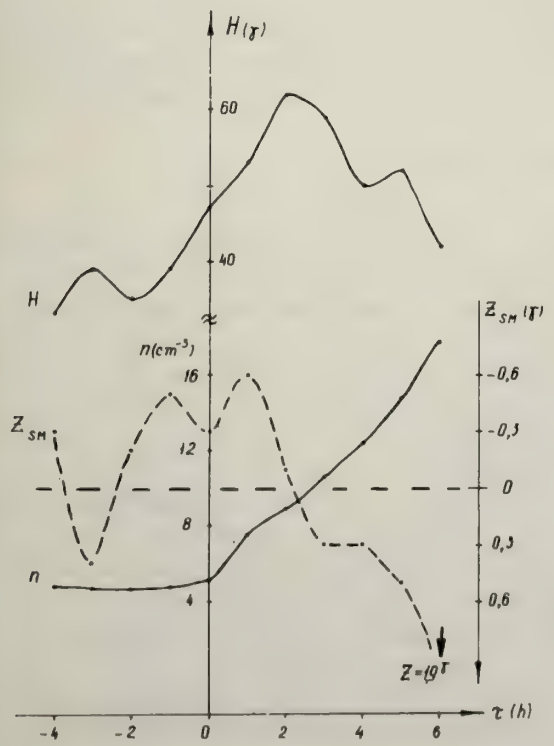


Figure 3. Changes of a transpolar current in the ionosphere (H), of Z_{SM}-component of the IMF and of solar wind density (n), derived by the superimposed epoch method for 16 n-bursts at the HS-fronts. A zero time moment corresponds to the n-burst onset.

$\tau > 0$ at equal Z_{SM}. For example, for $Z_{SM} = 0$, $H \simeq 35\gamma$ at $\tau = -2$ hours, and $H \simeq 60\gamma$ at $\tau = +2$ hours. On the whole, values of H at the increased values of n are considerably higher than those before the burst. An additional analysis in which the given sample was divided into two according to the predominant sign of Z_{SM} (southern or northern) supported this conclusion.

Thus, the behavior of polar cap indices testifies to the fact that the magnetosphere responds, in a certain manner, to the passage of the "periphery" of the stream where there is a density burst (as well as the growth of modules and fluctuations of the IMF). According to the above data, the lead time for forecasting storms associated with HS is not great ($\simeq$6-10 hours). However, these ciphers probably define only the lower limit as the indices were based on data from only a few stations; i.e., they may not be representative. It would be reasonable to study the effect using more precise characteristics like the equivalent current patterns based on data from the entire available network of observatories. This could elucidate a type of current system that produces the geomagnetic response of n-variations.

3.2 The Analysis of High-Latitude δ-Currents

In order to draw the equivalent current patterns that describe the effect of solar wind parameters, we have used the data from a global network of stations for 8 quiet summer days in 1968; the hourly values of solar wind parameters (King, 1977); and a modified method of a spherical harmonic analysis by Bazarzhapov et al. (1975). The original spectrum of spherical functions that describes a magnetic potential and an external current function

$$J = -\frac{10R}{4\pi}E\sum_{n}\sum_{m}\frac{2n+1}{n+1}\left(\frac{R_E}{R}\right)^{n}\left(E_n^m \cos mt + e_n^m \sin mt\right)P_n^m(\cos\theta) \qquad (1)$$

involves 15 zonal and 14 tesseral harmonics. The coefficients $E = \{E_n^m, e_n^m\}$ were expanded in series by the solar wind parameters (density, velocity, and IMF components):

$$E = a_0 + a_1 n + a_2 V + a_3 B_z + a_4 B_y + \ldots \qquad (2)$$

where the dots involve multiplicative terms (products with respect to V and the IMF components describing the interplanetary electric field $\vec{E} = -\vec{V} \times \vec{B}$). The coefficients a_i were determined by the least-squares method for each coefficient E separately. By means of equation (1), isolines, J_i, were drawn, representing the systems of equivalent currents. These are reflected by the individual terms in the expansion equation (2) and describe the effects of n (δ_n currents), V (δ_V currents), etc.

The current patterns for δ_V (at V = 400 km/s), δ_z (at $B_z = -3\gamma$) and δ_y (at $B_y = 4\gamma$) are presented in Figure 4. As expected, the δ_V and δ_z systems are similar to the S_q^P and the DP-2 currents. It is well known that the southern IMF component affects the development of the DP-2 currents (Nishida, 1968; and Iijima and Nagata, 1972), and, probably, the velocity effect is caused by "viscous friction" mechanisms, which produce large-scale magnetospheric convection. The ionospheric reflection is represented by Hall currents of the S_q^P or DP-2 type (Axford and Hines, 1961). The δ_y currents, as distinct from δ_V and δ_z, are zonal ones, in agreement with Friis-Christensen

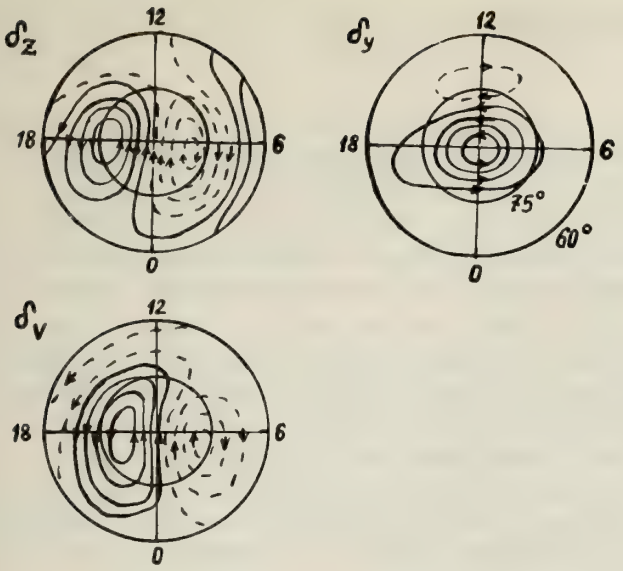


Figure 4. Equivalent δ-currents in the polar region, reflecting the effect of solar wind velocity (δ_V at V = 400 km/s) and IMF (δ_z at B_z = -3γ and δ_y at B_y = 4γ). Current lines are drawn for intervals of 10kA.

and Wilhelm (1975), Mishin et al. (1975), and Sumaruk and Feldstein (1975). The similarity of these patterns with the known ones indicates that this is the correct technique for the computation of δ-currents. Such confidence in the technique is necessary for understanding the unknown effects of solar wind density.

Currents δ_n are given in Figure 5 for two values: n = 4 cm^{-3} and 6 cm^{-3}. They are similar in form to the currents δ_V and δ_z, i.e., to the $S_q P$ and the DP-2 currents. This probably shows evidence for the effect of "viscous friction" mechanisms also. The value of the transpolar current is ≃30-50 kA (kiloamperes) for the given values of n, and ≃80-90 kA at n ≃ 10 cm^{-3} (the latter is consistent with the minimal peak value observed in bursts at the HS-front). The value of the ground magnetic disturbance caused by currents of similar strength is ≥20-40γ; i.e., it should be distinguished on magnetograms with standard sensitivity (≃5-10 γ/mm).

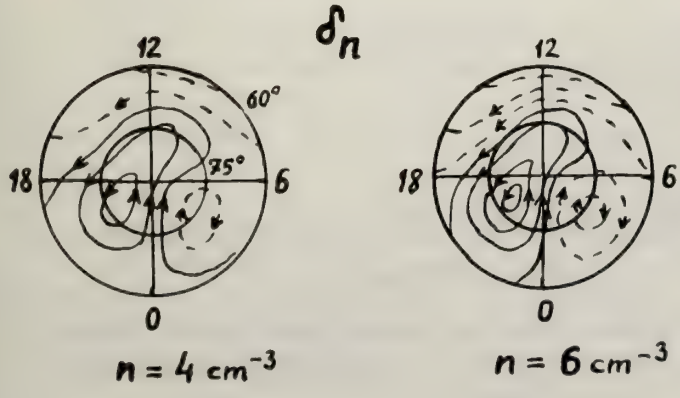


Figure 5. Equivalent δ-currents in the polar region, reflecting the effect of solar wind density (δ_n at n = 4 cm^{-3} and 6 cm^{-3}). The interval between current lines is 5 kA.

4. CONCLUSION

From the analysis of the behavior of the geomagnetic indices PC and PE as well as the computation of δ-currents in the polar cap produced by fluctuations of different solar wind parameters, it is concluded that the density bursts observed at the front ("periphery") of high-speed solar wind streams result in characteristic geomagnetic responses. The δ_n-current system is similar in form to the S_q^P and DP-2 currents and has an appreciable intensity at values $n \gtrsim 5$ cm^{-3}. In principle, this effect may be used for the short-term forecasting of geomagnetic (both recurrent and flare-associated) storms with a lead time of the order of 0.5-1 day. Although the prompt computation of the δ-currents is hardly possible at present, the results indicate that the detection of δ_n-disturbances, which in $\simeq$ 80 percent of the cases are precursors of strong storms ($D_{st} \lesssim -40\gamma$) can be realized with a more simple treatment of magnetograms or indices from polar cap stations. Further detailed studies are necessary for the development of this technique.

REFERENCES

Axford, W. I., and C. O. Hines (1961): A unifying theory of high latitude geophysical phenomena and geomagnetic storms. Can. J. Phys., 39:1433.

Bartels, J. (1932): Terrestrial magnetic activity and its relation to solar phenomena. Terr. Magn., 37:1.

Bazarzhapov, A. D., V. M. Mishin, and G. B. Shpynev (1975): A mathematical analysis of geomagnetic variation fields. Gerl. Beitr. Geophys. 84:918.

Dungey, J. W. (1961): Interplanetary magnetic field and the auroral zones. Phys. Rev. Lett., 6:47.

Friis-Christensen, E., and J. Wilhelm (1975): Polar cap currents for different direction of the interplanetary magnetic field in the YZ-plane. J. Geophys. Res., 80:1248.

Gulbrandsen, A. (1975): The solar M-region problem—an old problem now facing its solution? Planet. Space Sci., 23:143.

Hundhausen, A. J. (1972): Coronal Expansion and Solar Wind. Springer-Ferlag, Heidelberg-N.Y.

Iijima, T., and T. Nagata (1972): Signatures for substorm development of the growth phase and expansion phase. Planet. Space Sci., 20:1095.

Ivanov, K. G., and N. V. Mikerina (1974): A structure of the interplanetary plasma streams and geomagnetic disturbances. In: Solar Wind and Magnetosphere, Moscow, IZMIRAN, p. 3 (in Russian).

Kane, R. P. (1974): Relationship between interplanetary plasma parameters and geomagnetic D_{st}. J. Geophys. Res., 79:64.

King, J. H. (1977): Interplanetary Medium Data-Book-Appendix, ed. by NSSDC/WDC-A.

Krieger, A. S., A. F. Timothy, and E. C. Roelof (1973): A coronal hole and its identification as the source of a high velocity solar wind stream. Solar Phys., 23:123.

Kuznetsov, B. M., and O. A. Troshichev (1977): On the nature of polar cap magnetic activity during undisturbed periods. Planet. Space Sci., 25:15.

Mishin, V. M., A. D. Bazarzhapov, E. I. Nemtsova, G. V. Popov, and V. V. Shelomentsev (1975): The effect of the IMF on magnetospheric convection and electric currents in the ionosphere. In: Substorms and Disturbances in the Magnetosphere, Leningrad, Nauka, p. 191 (in Russian).

Neupert, W. M., and V. Pizzo (1974): Solar coronal holes as sources of recurrent geomagnetic disturbances. J. Geophys. Res., 79:3701.

Nishida, A. (1968): Geomagnetic DP-2 fluctuations and associated magnetospheric phenomena. J. Geophys. Res., 73:1795.

Pudovkin, M. I., V. P. Kozelov, L. L. Lazutin, O. A. Troshichev, and A. D. Chertov (1977): Physical Basis for the Magnetospheric Disturbance Forecasting, Leningrad, Nauka (in Russian).

Roelof, E. C., B. L. Gotwols, D. G. Mitchell, W. M. Cronyn, and S. D. Shawhan (1977): Use of interplanetary radio scintillation power spectra in predicting geomagnetic disturbances, preprint of Johns Hopkins University, AFGL-TR-77-0244.

Rosenberg, R. L., and P. J. Coleman, Jr. (1978): Solar cycle-dependent north-south field configurations observed in solar wind interaction regions, preprint No. 1804, University of California.

Shelomentsev, V. V., and V. M. Mishin (1977): A magnetospheric cleft index PE and short-term forecasting of the substorm breakup phase. Abstracts of the Symposium on Geomagnetospheric Physics, Irkutsk, p. 28 (in Russian).

"Solar-Terrestrial Activity Charts (STAC-B) for 1967-1968," ed. by the Science Council of Japan, under T. Obayashi (1971).

Sumaruk, P. V., and Y. I. Feldstein (1975): Magnetic field variations in the polar cap. In: Substorms and Disturbances in the Magnetosphere, Leningrad, Nauka, p. 170 (in Russian).

Verzariu, P., M. Sugiura, and I. B. Strong (1972): Geomagnetic field variations caused by changes in the quiet-time solar-wind pressure. Planet. Space Sci., 20:1909.

SOLAR CYCLE EFFECT OF 27-DAY RECURRENT GEOMAGNETIC STORM

T. ONDOH and Y. NAKAMURA
Radio Research Laboratories, Tokyo, 184, JAPAN

The 27-day autocorrelation coefficients of ΣK_p and mean ΣK_p over 5 solar rotations have been computed at solar rotation numbers from 1550 (Aug. 1946) to 1975 (Feb. 1978). These results are compared with the solar cycle variation of smoothed sunspot numbers.
The general features of the 18th sunspot cycle are very similar to those of the 20th sunspot cycle. This fact suggests the 22 year period as the basic solar cycle. In the declining phase of the 20th sunspot cycle, 27-day autocorrelation coefficients of ΣK_p above 0.4 have continued from Dec. 1972 to Oct. 1976 being longer than those in the 18th sunspot cycle. These recurrent geomagnetic disturbances in the 20th cycle occur in association with long-lived coronal holes and high-speed solar wind streams. The 27-day autocorrelation coefficients of ΣK_p above 0.4 occur for smoothed sunspot numbers ranging from 82.2 to 6.3 in the declining phase of the 18th sunspot cycle. This range of smoothed sunspot number for recurrent geomagnetic disturbances in the 18th cycle is very close to that of 80.4 - 13.4 in the declining phase of the 20th cycle except for the solar flare events in August,1972. Hence, we may forecast occurrences of long-lived coronal holes, high-speed solar wind streams, and recurrent geomagnetic storms by estimating time variation of the sunspot number.

1. Introduction

Newton and Milsom (1954) showed a close accordance between the averaged sunspot curve and the averaged curve for geomagnetic storms, and also reported recurrence peaks of the non-sc storms around +27 and +54 days. Chernosky (1966) found from the superposition analysis of the daily magnetic character figure C_i that the declining phase of the even sunspot cycle is more active in geomagnetic activity than the ascending phase, and that the converse is true for the odd cycle. Recently, long-lived coronal holes have been identified as the origin of solar wind high-speed streams and their associated recurrent geomagnetic disturbances (Krieger et al.,1973, 1974 ; Neupert and Pizzo,1974 ; Sheeley et al.,1976).

In this paper, we compare the smoothed sunspot number with the 27-day autocorrelation coefficient of ΣK_p during Aug. 1946 to Feb. 1978, and discuss on the prediction of recurrent geomagnetic storms and high-speed solar wind by the time variation of smoothed sunspot number.

2. 27-Day Recurrent Tendency of Geomagnetic Activity in the Solar Quiet Period

The 27-day autocorrelation coefficient Ac(n) of ΣK_p at the solar rotation number of "n" over five solar rotations can be computed by

$$Ac(n) = \frac{\sum_{t=t_1}^{t_2} \left\{P(t) - \overline{P(t)}\right\} \cdot \left\{P(t+27) - \overline{P(t+27)}\right\}}{\left[\sum_{t=t_1}^{t_2} \left\{P(t) - \overline{P(t)}\right\}^2 \cdot \sum_{t=t_1}^{t_2} \left\{P(t+27) - \overline{P(t+27)}\right\}^2\right]^{1/2}} ,$$

$$\overline{P(t)} = \frac{1}{27 \times 5} \sum_{t=t_1}^{t_2} P(t) , \text{ and } \overline{P(t+27)} = \frac{1}{27 \times 5} \sum_{t=t_1}^{t_2} P(t+27) , \text{ where } P(t)$$

denotes the daily sum of three-hour geomagnetic activity indices, ΣK_p, $t_1 = 27 \times (n - 3) + 1$ and $t_2 = 27 \times (n + 2)$. Ac(n) is computed from ΣK_p data observed during solar rotation number of (n - 3) to (n + 2).

Fig. 1 shows 27-day autocorrelation coefficients of ΣK_p, mean ΣK_p over 5 solar rotations, and smoothed sunspot numbers from solar rotation number (SRN) of 1550 (Aug. 1946) to 1750 (June 1961). The time variation of sunspot number in Fig. 1 indicates that the sunspot cycle 18th ended around SRN of 1653 (April 1954). The 27-day autocorrelation coefficients of ΣK_p between SRN 1603 and 1650 are higher (above 0.4) than those in other periods. This high recurrent tendency of geomagnetic activity occurs corresponding to the decrease of sunspot number from 82.2 at SRN 1603 to 6.3 at SRN 1650, although the 27-day autocorrelation coefficient deeply decreased down to 0.1 at SRN 1615 (June 1951) corresponding to a short term enhancement of the sunspot number or solar activity around SRN 1615. Except for the above period between SRN 1603 and 1650, the 27-day autocorrelation coefficients are mostly below 0.3 in the solar cycle 18th and 19th as shown in Fig. 1.

The time variation of smoothed sunspot number in Fig. 1 shows the 18th cycle maximum of 151.8 in May, 1947, the minimum of 3.4 in April, 1954, and the 19th cycle maximum of 201.3 in March, 1958 respectively. The 27-day autocorrelation coefficients of ΣK_p are higher than 0.4 from the middle of declining phase of the solar activity to the vicinity of solar activity minimum in the 18th sunspot cycle. However, there occurred no such effect in the 19th cycle untill June, 1961. The smoothed sunspot number in June,1961 is 55.8 which is far below a half of the maximum in the 19th cycle (201.3). Concerning this respect and also the maximum sunspot number, solar characteristics in the 18th cycle are considerably different from those in the 19th cycle.

Fig. 2 illustrates time variations of the smoothed sunspot number, mean ΣK_p over 5 solar rotations, and 27-day autocorrelation coefficient of ΣK_p observed during SRN 1750 (June,1961) to SRN 1975 (Feb. 1978). The time variation of smoothed sunspot number in Fig. 2 shows a minimum of 9.6 at SRN 1795 (Oct. 1964), a maximum of 110.6 at SRN 1851 (Nov. 1968), and a minimum of 12.2 at SRN 1950 (March 1976) respectively. The maximum sunspot number of 110.6 in the 20th sunspot cycle (Aug. 1964 - March 1976) is about one half of that (201.3) in the 19th cycle, and it is also smaller than the maximum sunspot number of 151.8 in the 18th cycle.

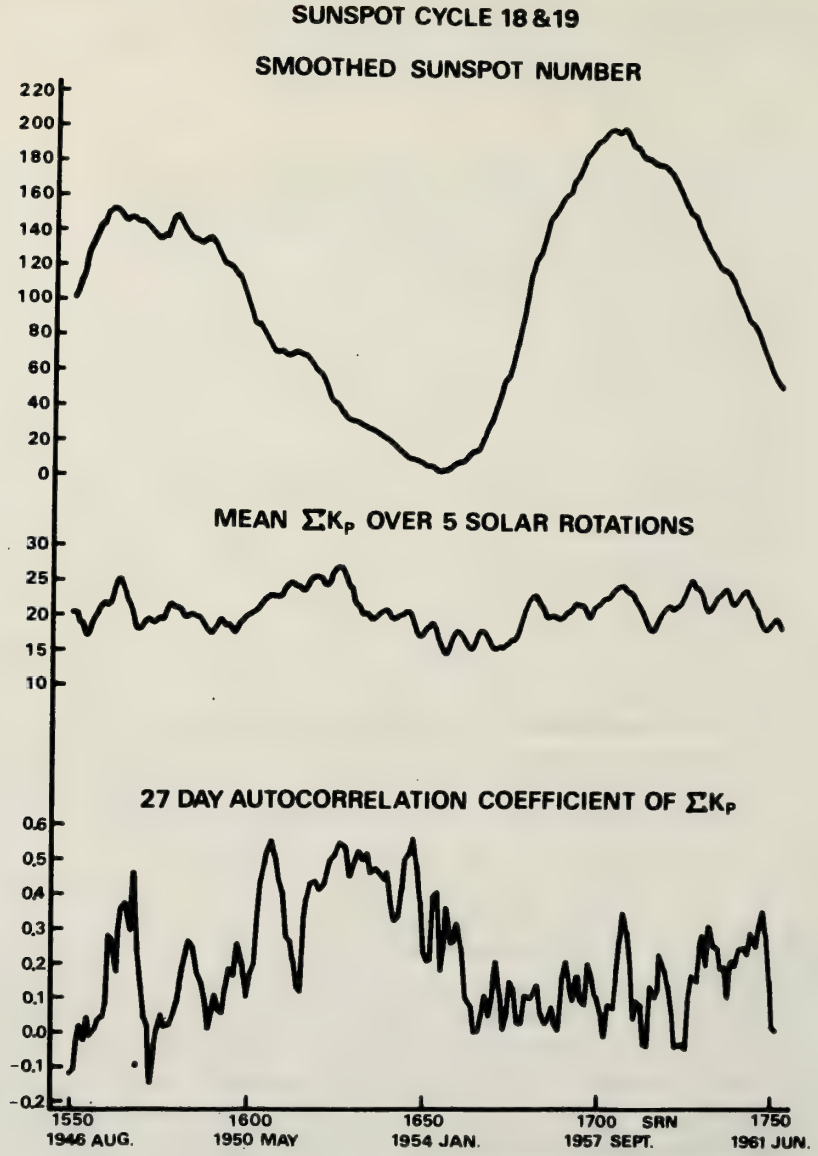


Fig. 1 Solar-cycle variations of the smoothed sunspot number, mean ΣK_p over five solar rotations, and 27-day autocorrelation coefficient of ΣK_p during August,1946 to June, 1961.

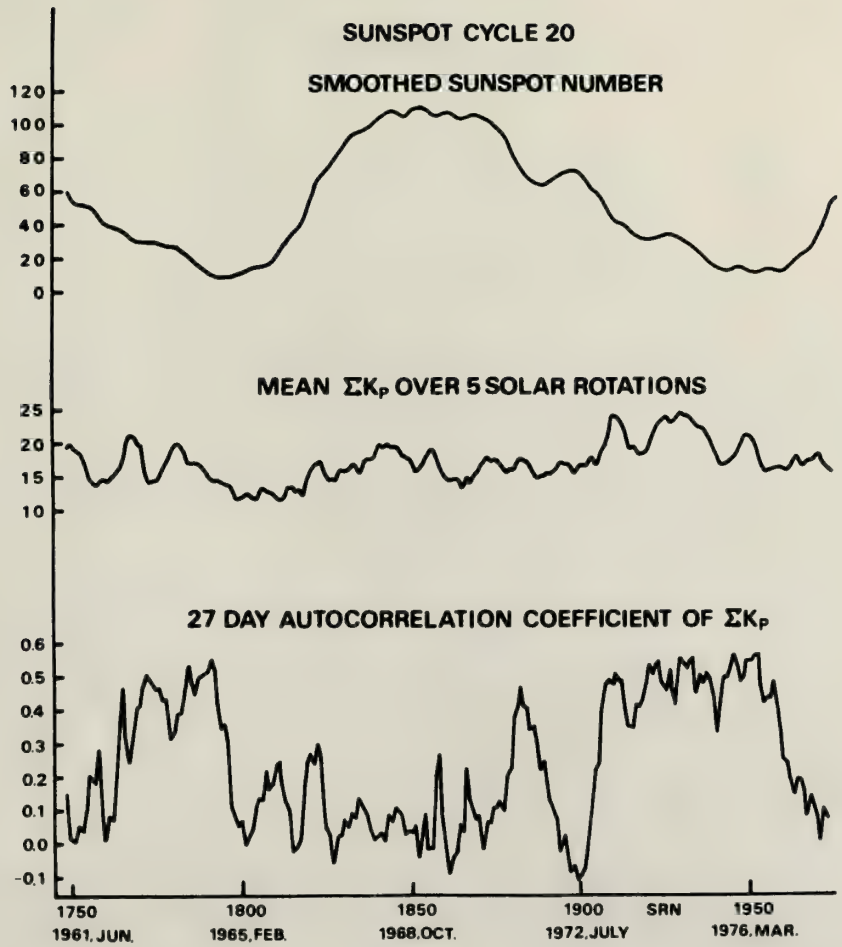


Fig. 2 Solar-cycle variations of the smoothed sunspot number, mean ΣK_p over five solar rotations, and 27-day autocorrelation coefficient of ΣK_p during June 1961 to February 1978.

In the 19th sunspot cycle (SRN 1653 ; April 1954 - SRN 1793 ; Aug. 1964), 27 day autocorrelation coefficients above 0.4 of ΣK_p occur in a period between SRN 1769 (June 1962) and SRN 1793 (Aug. 1964),corresponding to the sunspot number of 38 and 10 respectively. Thus, the high recurrent period of geomagnetic activity in the 19th cycle is much shorter than that in the 18th cycle. In the 20th sunspot cycle (SRN 1793 ; Aug. 1964 - SRN 1950 ; March 1976), the 27-day autocorrelation coefficient of ΣK_p once became above 0.4 between SRN 1880(Jan. 1971) and SRN 1884(May,1971),corresponding to smoothed sunspot number decrease from 80.4 to 68.1, but it decreased down to -0.09 at SRN 1899 (June 1972). Then, the 27-day autocorrelation coefficient increased rapidly up to 0.4 at SRN 1906 (Dec.,1972).

This deep valley of 27-day autocorrelation coefficient of ΣK_p around June, 1972 results from a short-term enhancement of the smoothed sunspot number which is associated with the solar active center causing the August event, in 1972. The deep decrease of 27-day autocorrelation coefficient of ΣK_p around June, 1972 in the 20th sunspot cycle (Fig. 2) is very similar to that around June, 1951 in the 18th cycle (Fig. 1) which is also associated with a short-term enhancement of the sunspot number. It should be noted that the short-term degradation of 27-day recurrent tendency of the geomagnetic activity occurs simultaneously with the sunspot increase halfway during the sunspot declining phase in both of the 18th and 20th cycles.

The 27-day autocorrelation coefficients of ΣK_p were above 0.4 in a long period between SRN 1906(Dec. 1972) and SRN 1958 (Oct. 1976) during which the smoothed sunspot number decreased from 55.1 to 13.4. The high recurrent period of geomagnetic disturbances in the 20th cycle is longer than those in both of the 19th and 18th cycles. This is a remarkable thing in the 20th sunspot cycle,together with a low value (110.6) of the maximum sunspot number. In summary, the general features of the 20th sunspot cycle are very similar to those of the 18th sunspot cycle, but not to the 19th cycle, though the maximum smoothed sunspot number in the 18th cycle is higher than that in the 20th cycle. This fact suggests that the basic solar cycle is the 22 year period rather than the 11 year period.

3. Application of the 27-day Recurrent Tendency of the Geomagnetic Activity to the Forecast of Solar-terrestrial Disturbances in the Solar Quiet Period

Solar images derived from HeII 304 Å and HeI 10830 Å spectroheliograms or wideband XUV images during the Skylab mission (Bohlin and Rubenstein,1975 ; Tousey et al.,1973) have revealed that coronal holes in low latitudes (so called the M region) are the origin of solar wind high-speed streams and 27-day recurrent geomagnetic disturbances. Sheeley et al.(1976) have added 3 days to the occurrence times of both the coronal holes and solar wind streams to maximize the correlation of the holes and high-speed streams above 600 km/sec with the geomagnetic disturbances as a sequence of 27-day Bartels rotations. In Table 1, we compare solar wind velocities with smoothed sunspot numbers and 27-day autocorrelation coefficients of ΣK_p from May,1970 (SRN 1871) to May, 1973 (SRN 1911) in order to forecast the occurrence of high-speed solar plasma streams and recurrent geomagnetic disturbances. Solar wind data in Table 1 are taken from the Interplanetary Medium Data

Book published by NSSDC/WDC-A (1977).

Table 1 Comparison of solar wind velocity, 27-day autocorrelation coefficient of ΣK_p and smoothed sunspot number

SRN	Month/Day/Year	Ac(n)	Solar Wind km/sec			Smoothed Sunspot Number
			V_{max}	V_{av}	V_{min}	
1871	5/5 - 5/31/'70	-0.01	669	398	291	105.8
1872	6/1 - 6/27/'70	0.06	706	420	266	105.3
1882	2/26 -3/24/'71	0.47	696	441	300	74.4
1884	4/21 -5/17/'71	0.40	678	408	310	68.1
1899	5/30 -6/25/'72	-0.11	485	378	290	70.5
1900	6/26 -7/22/'72	-0.09	510	377	285	68.2
1910	3/23 -4/18/'73	0.50	785	572	342	42.7
1911	4/19 -5/15/'73	0.49	797	583	351	40.7

The maximum velocity, average velocity, and minimum velocity of the solar wind in a period of SRN 1911 are the highest of all solar wind velocities in Table 1. The SRN 1911 belongs to the period of highly recurrent geomagnetic activities (Ac(n) > 0.4) which have continued long from Dec. 1972 to Oct. 1976. In fact, Sheeley et al.(1976) have shown high correlations of long-lived coronal holes, high-speed solar winds, and recurrent geomagnetic activities during Jan.,1973 to Jan.,1976 in a familiar 27-day Bartels format. At SRN 1899 and 1900, the three kind speeds of solar wind are the lowest of all solar wind speeds in Table 1. This low-speed solar wind corresponds well to the lowest 27-day autocorrelation coefficient of ΣK_p (-0.1) and the solar active center producing the August event in 1972. The three kind speeds of solar wind at SRN 1882 and 1884 are again higher compared with those at SRN 1899 and 1900. This reflects well high values of the 27-day autocorrelation coefficient of ΣK_p (> 0.4) in a period between SRN 1880 and 1884. However, at SRN 1871 and 1872 (May - June,1970) when the 27-day autocorrelation coefficients of ΣK_p are below 0.1, solar wind speeds are relatively high. This may result from random occurrences of solar flares during the solar active phase of the 20th sunspot cycle, but not from coronal holes. Thus, it becomes clear that long-lived coronal holes and high-speed solar wind streams produce 27-day recurrent geomagnetic disturbances only during the declining phase of the sunspot cycle.

In the declining phase of the 18th sunspot cycle, 27-day autocorrelation coefficients of ΣK_p above 0.4 occur for smoothed sunspot numbers ranging from 82.2 to 6.3 except for the solar-flare events around June, 1951 (SRN 1651). Also, in the declining phase of the 20th sunspot cycle, 27-day autocorrelation coefficients of ΣK_p above 0.4 occur for smoothed sunspot numbers ranging from 80.4 to 13.4 except for the solar-flare events around August,1972(SRN 1901). In summary, high-speed solar wind streams above 600-700 km/sec originating from low-latitude coronal holes caused recurrent geomagnetic storms corresponding to smoothed sunspot numbers for about 80 to 10 in the declining phase of the 18th and 20th sunspot cycles, except for solar flare events. Further comparative study between 27-day autocorrelation coefficients of ΣK_p and smoothed sunspot numbers is needed to apply the above results to the storm forecast in the solar quiet period.

References

Bohlin, J. D. and D. M. Rubenstein (1975) : Report UAG-51, World Data Center A for Solar - Terrestrial Physics, NOAA, Boulder,Colorado.

Chernosky , E. J. (1966) : Double sunspot-cycle variation in terrestrial magnetic activity, 1884 - 1963, J. Geophysical Research, 71, 965.

Interplanetary Medium Data Book (1977) : National Space Science Data Center, World Data Center A for Rockets and Satellites, NASA.

Krieger, A. S., A. F. Timothy, and E. C. Roelof (1973) : A coronal hole and its identification as the source of a high velocity solar wind stream, Solar Physics, 37, 469.

Krieger, A. S., A. F. Timothy, G. S. Vaiana, A. J. Lazarus, and J. D. Sullivan (1974) : Solar Wind Three, Edited by C. T. Russell, 132.

Neupert, W. M. and V. Pizzo (1974) : Solar coronal holes as sources of recurrent geomagnetic disturbances, J. Geophysical Research, 79, 3701.

Newton, H. W. and A. S. Milsom (1954) : The distribution of great and small geomagnetic storms in the sunspot cycle, J. Geophysical Research, 59, 203.

Sheeley, JR. N. R., J. W. Harvey, and W. C. Feldman (1976) : Coronal holes, solar wind streams, and recurrent geomagnetic disturbances : 1973 - 1976, Solar Physics, 49, 271.

SHORT-TERM PREDICTIONS OF A SUDDEN GEOMAGNETIC IMPULSE VALUE ON THE BASIS OF THE INTERPLANETARY DATA

S. A. Grib
LOIZMIRAN, 23, Line 2, V.O.
199053 Leningrad, USSR

A new method for the prediction of a sudden geomagnetic impulse value and the sudden storm commencement impulse resulting from the study of solar wind shock wave collision with the bow shock wave-magnetosphere system is proposed. The interplanetary data for the discontinuity are taken as initial. The calculation is done within the limits of the theory of the splitting of arbitrary magneto-hydrodynamic discontinuity. Satisfactory agreement between the calculated and the observed value of the geomagnetic impulse during SSC is obtained. The thermal anisotropy value may be used as the perturbation index for the solar wind flow. The correlation between the mhd evaluations and "Prognoz" satellite data is shown.

1. INTRODUCTION

The propagation of shock waves through the interplanetary space has been investigated by many authors (Hundhausen, 1972; Dryer, 1975; Zastenker et al., 1975). The tangential discontinuities often observed in the solar wind are considered also in the context of a strong discontinuity model (Burlaga, 1971; Grib, 1977). These discontinuities as they go through space effect the bow shock wave (Brunelli and Grib, 1972; Völk and Auer, 1974) and the magnetosphere of the Earth (Grib, 1973; Shen, 1973).

Ivanov (1965) and Dryer et al. (1967), in their studies of the solar wind shock waves interaction with "the bow shock S_1-magnetopause C_m" system, did not consider the interplanetary magnetic field and the mobility of the magnetopause. Grib (1971, 1972, 1973) and Shen and Dryer (1971) showed that when the solar wind wave collides with a bow shock two new shock waves, S_3 and S_4, and a contact surface are generated. They show that as the shock wave collides with the magnetopause, then the rarefaction wave, R, and the shock wave refracted inside the magnetosphere appear simultaneously.

Völk and Auer (1974) obtained results identical to those of Grib (1971) and Brunelli and Grib (1971); i.e., that the interaction of the tangential discontinuity $\underset{\sim}{I}$ (its proton concentration increases) with the shock wave results in two shock waves. But the tangential discontinuity $\underset{\sim}{I}$ (which decreases the proton concentration) produces the rarefaction wave: $\underset{\sim}{IS} - \underset{\sim}{SIR}$. These

authors also indicated that the rarefaction wave reflected from the magnetopause appears to result from the influence of the nonstationary shock wave. Völk and Auer used the gas dynamic relations, which are invalid in this case, to change the gas pressure to the total pressure without considering the integral $\tau_n(\alpha) = \int_0^1 (1 + \alpha x^{n-2})dx$, where $\alpha = v_A^2/a^2$, the square of Alfven velocity divided by the sonic velocity.

Neubauer (1975) considered the collision of a flat tangential discontinuity with locally flat shock front limiting himself to the fast shock waves refracted inside the magnetosheath. This author also indicated that the rarefaction wave appears as a result of the interaction $\overleftarrow{IS}$.

The purpose of this paper is to evaluate the sudden impulse SI^+ and the impulse of the sudden geomagnetic storm ΔB_{ssc} on the basis of the magnetohydrodynamic consideration of the solar wind shock wave collision with the bow shock-magnetosphere system. In other words, we predict the magnitude of the geomagnetic effect from the interplanetary data.

2. PREDICTION TECHNIQUE

The problem is to obtain the value of the abrupt change of the geomagnetic field using experimental data that characterize the shock jump-like change of the solar wind parameters. In other words, given the value $d/dt(\rho u^2)$ and the derivative of total pressure $(d/dt)(\overline{p}) = dp/dt + (B/\overline{ur})(dB/dt)$, where $d/dt = \partial/\partial t + \vec{u}\nabla$, in the solar wind we want to evaluate the geomagnetic impulse, ΔB.

The nonstationary shock wave S_2 propagating through the nonperturbed flow (this region has the index "0" in Figure 1) causes the abrupt increase of all parameters charaterizing the flow condition: the concentration, the temperature, the bulk velocity, u, and the intensity of the magnetic field. After interacting with the bow shock wave S_1 the nonstationary magnetohydrodynamic shock wave perturbs the flow inside the magnetosheath (indicated by index "1" in Figure 1) and afterwards collides with the magnetopause, C_m, contracting the magnetosphere of the Earth (region "m" in Figure 1). The interaction of

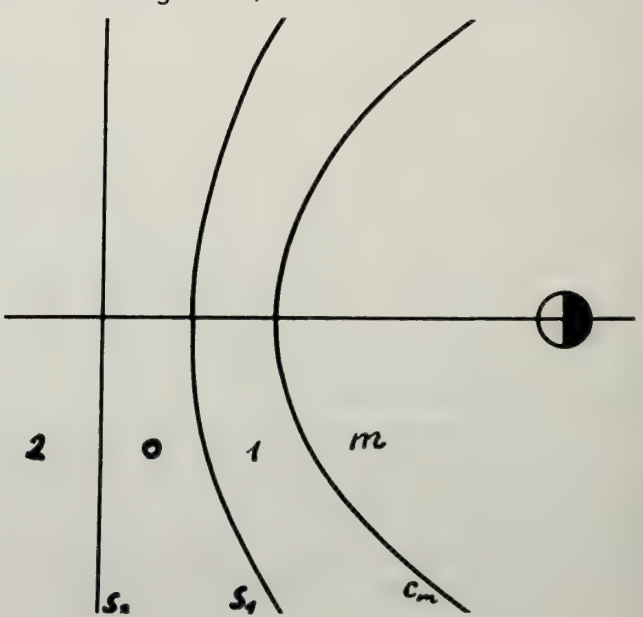


Figure 1. Diagram of the interaction.

the nonstationary solar wind shock wave with the bow shock is calculated from the theory of the splitting of arbitrary discontinuity using the method described by Brunelli and Grib (1972).

Given the ordinary Mach number, M_2, for the running shock wave, we find from the table of Brunelli and Grib (1972) the corresponding intensity (Mach number) of the shock wave refracted inside the magnetosheath, M_4.

We assume that the interaction of the shock waves is regular, and that for the current line in the magnetosheath, the equation of Bernoulli is valid:

$$u^2/2 + i + B^2/\rho + (\nu_m/\rho u^2)(\mathrm{curl}\,\vec{B} \times \vec{B})\vec{u} = \mathrm{const.} \qquad (1)$$

where u is the bulk velocity, i is the enthalpy, B is the magnetic induction, ν_m is the magnetic viscosity, and ρ is the density.

From the change of concentration at the shock front, we obtain the increase of pressure from the mhd adiabate of Hugoniout:

$$p/p_0 = \{(h\eta - 1) + (\gamma\alpha_0/2)(\eta - 1)^3\}/(h - \eta) \qquad (2)$$

Here, $\alpha = v_A^2/a^2 = B_0^2/4\pi\rho_0 a_0^2$, $\eta = n/n_0$, a_0 is the sonic speed in the nonperturbed region, $h = (\gamma + 1)/(\gamma - 1)$, γ is the politropic exponent, and n is the concentration.

Taking the value of the pressure close to the stagnation point of the magnetosphere calculated from the generalized equation of Bernoulli (1), we obtain the change of pressure in the stagnation point (Grib, 1973):

$$\Delta p_s = 1 + (1 - 1/\eta)\gamma M^2/(1 + 1/\beta_0) \qquad (3)$$

where $\beta_0 = 8\pi p_0/B^2$. The time of the shock wave passing through the magnetosheath may be evaluated from

$$\Delta t = \int_0^{\delta} dx/[u_1(1 - \tfrac{x}{\delta}) + a_1 M_4] \qquad (4)$$

where δ is the thickness of the nonperturbed magnetosheath, u_1 is the flow velocity immediately after the shock front, and a_1 is the sonic speed in this region.

From Δp_s we evaluate the change of geomagnetic intensity by the empirical formula of Siscoe et al. (1968):

$$\Delta B_{ssc} = k\,(\sqrt{p_s} - \sqrt{p_{s0}}) \qquad (5)$$

in which $k = 1.35 \times 10^5$.

At the same time, Δp_s may be diminished as a result of the rarefaction wave being reflected from the magnetosphere (Grib, 1972). For this case, the changes in the velocity components are:

$$\begin{aligned} \Delta u_x &= \mp (v_A/\gamma p_0^{1/2}) \int_{p_1}^{p_0} (p/p_0) q_{\pm}\, dp \\ \Delta u_y &= \mp X_{\pm}\ \mathrm{sign}\ (B_y/B_x) \\ X_{\pm} &= (v_A/\gamma p_0^{1/2}) \int_{p_1}^{p_0} (p/p_0)^{-(\gamma+1)/2\gamma}\, [(1 - q_{\pm})/(1 - pq_{\pm})]^{1/2} dp \end{aligned} \qquad (6)$$

Here the upper sign before the value corresponds to the waves which are going to the right, and the lower sign to the waves going to the left. In the lower index, the plus sign corresponds to a fast wave (R_+) and the minus sign to a slow wave, and $q_{\pm} = a_{\pm}^2/a_0^2$. Here a_+ is the fast magnetosonic speed and a_- is the slow speed.

The sharp increase of the magnetic field intensity inside the magnetosphere may be found also from the generalized law of Crussard-Landau for the

refracted shock wave which was obtained by Grib (1968, 1975):

$$(B/B_m)^2 = 1 + [(B_0/B_m)^2 - 1][(1 + 2\, v_{Am}/3A_1x_0)(x/x_0 + 2v_{Am}/3A_1x_0)]^{\frac{1}{2}} \quad (7)$$

where $B_0 = B\big|_{x=x_0}$, B_m is the intensity of the geomagnetic field before the front, $F_1(\xi) = A_1\xi + B$ is the shock wave profile, and $\xi = x - (u + v_A)t$. This law may be used for determining the wave going from the magnetopause to the plasmasphere. But beyond this the task is more complicated and the shock wave degenerates to magnetohydrodynamic waves.

3. EXAMPLE

Let us take for an example the sudden commencement of the geomagnetic storm of 15-16 February 1967. At that time two satellites, Vela 3 and Expl.-33, were in the free flow of the solar wind outside the magnetosphere.

The SSC was registered on the ground at 23^h48^m UT, February 15, 1967. The satellite Expl.-33 registered the arrival of the shock wave four minutes later. This testifies to the inclination of the shock front. On the shock front, an abrupt change of the solar wind parameters was observed: the temperature increased from 2.1×10^4 to 12.7×10^4K and the bulk velocity from 271 to 388 kms^{-1}. These data are from Hirshberg and Colburn (1969) and Hundhausen (1970). (See Figure 2.)

Let us consider the interaction of the nonstationary shock wave of the solar wind with the bow shock determined by the theory of the splitting of arbitrary discontinuity as it has been described. For the moving shock wave we have the Mach number, $M_2 \simeq 6.9$ and from examination of the shock wave colli-

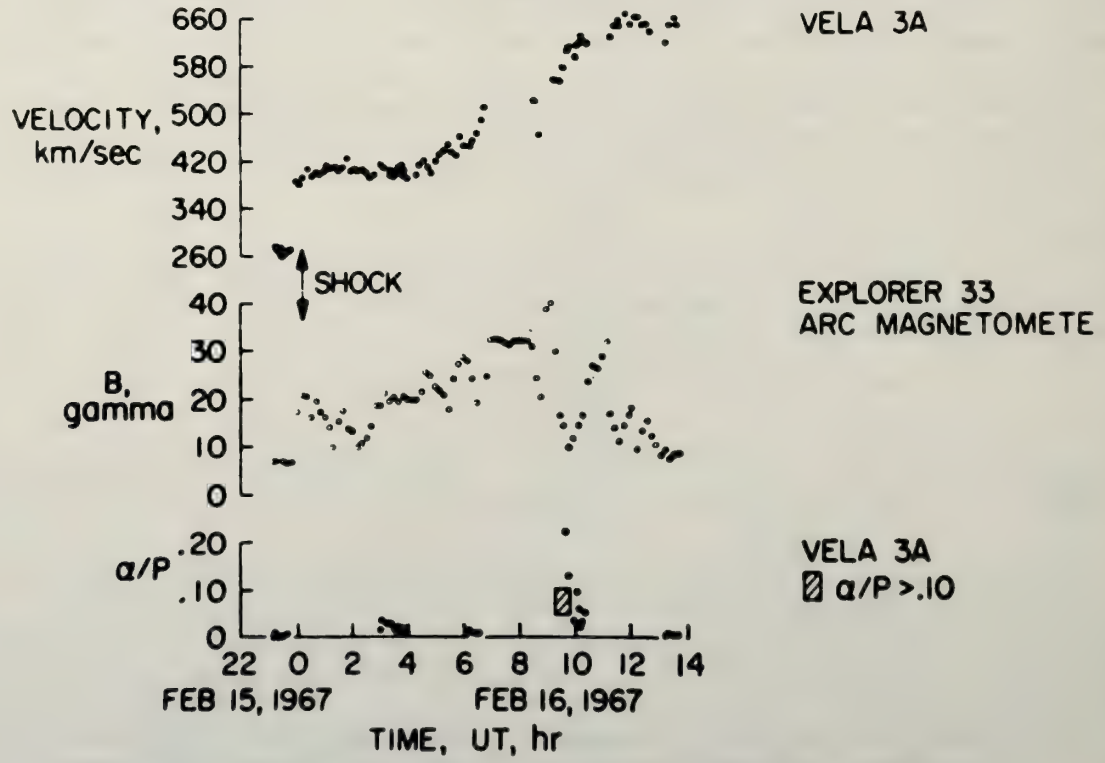


Figure 2. The solar wind parameters at the shock front.

sion with the bow shock (Brunelli and Grib, 1972) we have for the shock wave refracted inside the magnetosheath, $M_4 \simeq 1.9$ for $B_0 = 3.5\gamma$ (B_0 is the interplanetary magnetic field).

Further we obtain the changes in the pressure in the magnetopause from equation (3) and $\Delta B_{scc} \simeq 30\gamma$ from equation (5). This is the average value for the midlatitude region. At the same time the observed increase of the H-component at the San Juan observatory on February 15, 1967, was 38γ; and at other observatories it varied from 35 to 48 γ. The observed value is higher than the calculated one because we assumed a frontal collision but, in reality, it was an oblique one, which causes a smaller decrease in the wave intensity.

In Figure 3, we see explicitly the smooth decrease of the geomagnetic field intensity after the rapid increase. This decrease may be connected with secondary wave interactions inside the magnetosheath (Grib, 1973).

If we take into consideration the oblique component of the interplanetary field for the oblique shock waves, we have, in addition, slow shock waves and slow rarefaction waves. But it is easy to show that for the typical interplanetary conditions their intensity is small in comparison with the fast waves appearing in both the normal and oblique cases.

Let us apply this method to the August 1972 events. For the SSC of August the fourth (0119 UT) we have (Dryer et al., 1976): $M_2 = 17.3$, $\beta = 0.16$, the ratio of gas pressure to magnetic. In this case, the calculated $\Delta B = 35\gamma$. At the same time, ΔB at Moscow is 24γ and at Leningrad, $\Delta B = 26\gamma$.

For the August 8 event (2354 UT), we have $M_2 = 10.3$ and $\beta = 0.24$. Then the calculated ΔB is 30γ and the observed ΔB is 48γ for Moscow and 41γ for Leningrad.

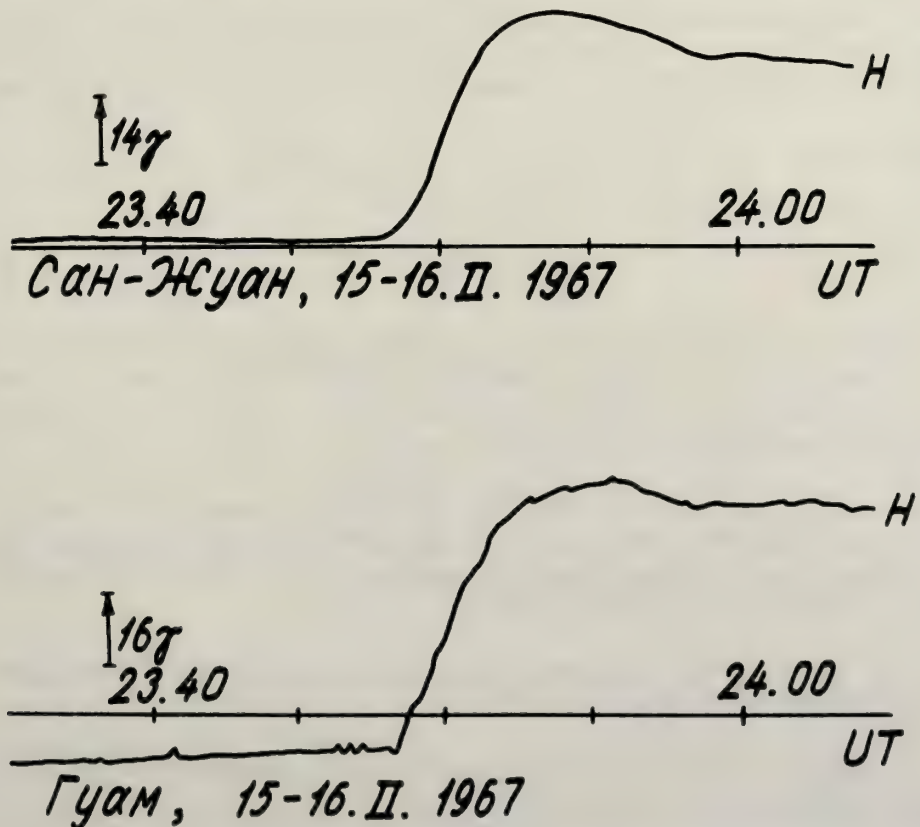


Figure 3. The continuous magnetograms for the SSC on February 15, 1967: San Juan (above), Guam (below).

We know that the solar wind flow has thermal anisotropy considering the direction of the magnetic field: $T_{\parallel} \neq T_{\perp}$. From the method described by Grib (1976) it is possible to find the change of concentration on the shock front, $\tau = n/n_0$, dependent on the field change, $k = B_y/B_{y0}$ for the given value of the nonperturbed flow anisotropy $\lambda = (T_{\parallel} - T_{\perp})/(B^2/4\pi)$. The change of plasma concentration may differ significantly from the field change at the front (Grib, 1976). Meanwhile, from the laws of conservation, it is determined that the degree of anisotropy is increasing after the shock wave front.

From the data of the Prognoz and Prognoz 1 satellites (Bloch et al., 1975) on May 9, 1972, we see that on the shock front $k = 1.96$, $\tau = 0.44$; on August 8, $k = 1.3$, $\tau = 0.65$. All these values for $\lambda > 0$ satisfy the formulae given by Grib (1976).

4. SUMMARY

The proposed method may predict the magnitude of the geomagnetic impulse on the basis of the interplanetary data. For the present level of the data the error of calculation is rather satisfactory.

With this method it is possible to predict the magnitude of the geomagnetic impulse both some minutes and some hours before the event--depending on the distance of the space vehicle from the Earth. The data on radio bursts may be used to determine the shock wave velocity close to the sun.

The thermal anisotropy parameter λ may serve as the characteristic of the space perturbation degree.

The author would like to acknowledge Professor V. A. Troitskaya for useful comments.

REFERENCES

Bloch, G. M., G. N. Zastenker, B. M. Kuzhevskii, S. B. Likin, N. F. Pisarenko, I. A. Savenko, and V. A. Stiazhkin (1975): The intensity bursts for the low energetic charged particles connected with interplanetary shock waves. Space Res., 13:695.

Brunelli, B. E., S. A. Grib (1972): On the interaction of solar wind shock waves with the magnetosphere of the Earth. In: Research in geomagnetism, aeronomy and the physics of the sun, 23:369. English transl.: NASA tech. transl. NAS 3-2481 (1973).

Burlaga, L. F. (1971): Hydromagnetic waves and discontinuities in the solar wind. Space Sci. Rev., 12:600.

Dryer, M. (1975): Interplanetary shock waves: Recent developments. Space Sci. Rev., 17:277.

Dryer, M., D. L. Merritt, and P. M. Aronson (1967): Interaction of plasma cloud with the Earth's magnetosphere. J. Geophys. Res., 72:2955.

Dryer, M., Z. K. Smith, R. S. Steinolfson, J. D. Mihalov, J. H. Wolfe, and J.-K. Chao (1976): Interplanetary distrubances caused by the August 1972 solar flares as observed by Pioneer 1. J. Geophys. Res., 81:4651.

Grib, S. A. (1968): The attenuation of flat shock waves in the transversal magnetic field. Vestnik LGU, 1:77.

Grib, S. A. (1971): On the interaction of the shock waves with the magnetosphere of the earth during geomagnetic storms with sudden commencement. In: Program and Abstracts for the XV IUGG General Assembly. Moscow, 472.

Grib, S. A. (1972): The interaction of solar wind shock waves with the magnetosphere of the Earth. DAN BSSR, 16:493.

Grib, S. A. (1973): Some aspects of the interaction of solar wind shock waves with the magnetosphere of the Earth. Geomagn. i. Aeronom., 13:788.

Grib, S. A. (1975): On the shock wave propagation through the magnetospheric plasma. Geomagn. Issledovania, 14:47.

Grib, S. A. (1976): The effect of anisotropic shock waves on the parameters of interplanetary plasma. In: coll. The Materials of International Seminar: Active Processes on the Sun and the Problem of Solar Neutrino. Leningrad, 170.

Grib, S. A. (1977): Nonstationary interactions of the solar wind discontinuities with the bow shock-magnetosphere system. In: Symposium on the Physics of the Magnetosphere. Irkutsk, 12.

Hirshberg, J., and D. S. Colburn (1969): Interplanetary field and geomagnetic variations--a unified view. Planet. Space Sci., 17:1183.

Hundhausen, A. J. (1970): Solar wind properties and the state of the magnetosphere. Ann. Geophys., 26:427.

Hundhausen, A. J. (1972): Coronal Expansion and Solar Wind. Springer-Verlag, New York.

Ivanov, K. G. (1965): On the interpretation of the observations of ssc of geomagnetic storms in space. Geomagn. i. Aeronom., 5:471.

Neubauer, F. M. (1975): Nonlinear oblique interaction of interplanetary tangential discontinuities with magnetogasdynamic shocks. J. Geophys. Res., 80:1213.

Shen Wen Wu, and M. Dryer (1972): Magnetohydrodynamic theory for the interaction of an interplanetary double-shock ensemble with the Earth's bow shock. J. Geophys. Res., 77:4627.

Shen Wen Wu (1973): Interaction of interplanetary MHD shock waves with the magnetopause. Astrophys. Space Sci., 24:51.

Siscoe, G. L., V. Formisano, and A. J. Lazarus (1968): Relation between geomagnetic SI and solar wind pressure changes--an experimental investigation. J. Geophys. Res., 73:4869.

Völk, H. J., and R.-D. Auer (1974): Motions of bow shock induced by interplanetary disturbances. J. Geophys. Res., 79:40.

Zastenker, G. N., V. V. Temny, C. d'Uston, and I. M. Bosqued (1978): The form and energy of the shock waves from the solar flares of August 2, 4, and 7, 1972. J. Geophys. Res., 83: 1035.

PREDICTION OF SUBSTORM ACTIVITY

TAKAO SAITO
Onagawa Magnetic Observatory and Geophysical Institute
Faculty of Sciences, Tohoku University
Sendai 980, JAPAN

A technique to predict magnitude of a substorm and orientation to which the substorm disturbances expand is proposed by utilizing the associated Pi2-type ULF wave. A background model for the prediction technique is given. The longer-term predictions of substorm activity is discussed in the last section by classifying the term into several hours, one year, and eleven years.

1. INTRODUCTION

One of the most fundamental and important disturbances of the earth's magnetosphere is the substorm. All substorm activity is associated with Pi2-type magnetic pulsations. This type of pulsation starts simultaneously with onset of the expansion phase of the substorm. In this sense, the onset of every Pi2 and the onset of every substorm have a one-to-one relationship (Saito, 1961; Saito et al., 1976a). Although Pi2 is numerically defined as a type of pulsation with irregular waveform having the periods of 45-150 seconds according to the 1963 Berkeley classification, Pi2 is observationally in a period range from 30 to 300 seconds according to the physical classification (Saito 1978a). Substorm activity can be predicted by utilizing various characteristics of Pi2 pulsation as will be explained in Sections 2, 3, and 4. A basic model for this Pi2-substorm relation will be given in Section 5. The longer-term predictions of substorm activity will be discussed in Section 6.

2. PREDICTION OF SUBSTORM MAGNITUDE

Generally, substorm range maximizes about 30 minutes and recovers about 90 minutes after the onset of the substorm. The maximum range of a substorm observed at a midlatitude station (Fredericksburg, Virginia, for example) is called *magnitude* of the substorm. Magnitude M of a substorm is closely related with the period T of the associated Pi2 as shown in Fig.1C.

This relation means that magnitude of a substorm can be predicted by measuring the period of the initial two-three pulses of the associated Pi2

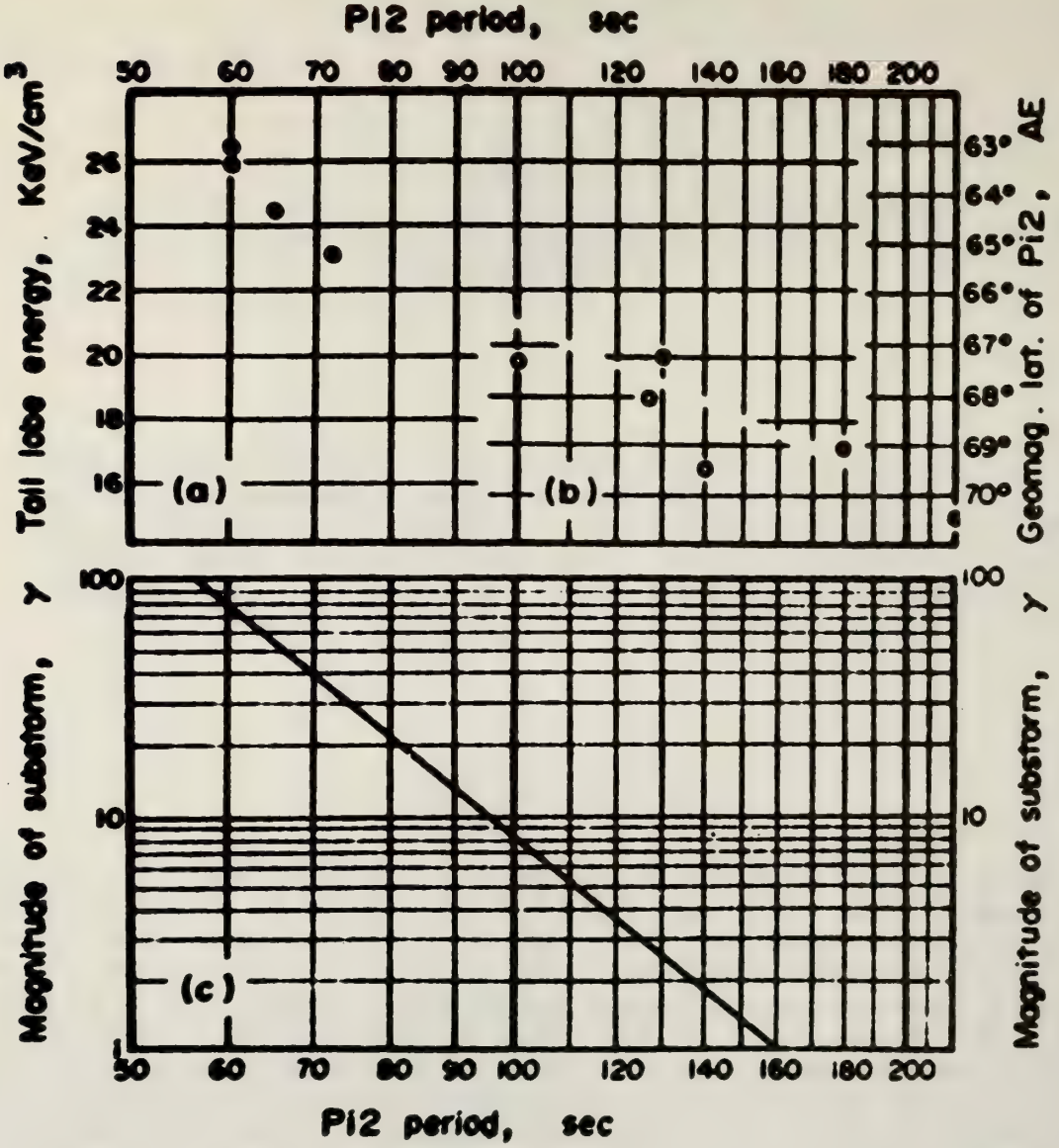


Fig.1 Observed relation between Pi2 period and (a) tail lobe energy (solid circles), (b) geomagnetic latitude of both maximum amplitude of Pi2 and the instantaneous position of the auroral electrojet (open circles), and (c) magnitude of the associated substorm, respectively. The tail lobe energy just before the onset of substorm is measured from the magnetic field data obtained by Explorer 34. The position of AE is inferred from the distribution of ΔZ and ΔH obtained at meridian chain stations. Since the M-T relation is dependent on the phase of the solar cycle, an averaged relation obtained from the data from 1957 to 1965 is exhibited here.

pulsation. Hence, prediction of the magnitude can be executed within only the initial two-three-minute duration for a substorm with M=100nT(γ), for example, as shown in Fig.1C. Actually a substorm with M=17nT was observed being associated with a Pi2 with T=80 sec that commenced at 21h20m LT at Fredericksburg on December 16, 1961 (Saito and Matsushita, 1968). In this sense the prediction on which we will discuss in the present paper will not mean the prediction of substorm *onset*, but of substorm *activity* as is expressed in the title of this paper.

This kind of prediction is really useful to find a chance to launch a rocket to aurora, to command a scientific observation to a polar-orbiting satellite, to select a radio-propagation path for the transpolar telecommunications, etc.

3. PREDICTION OF LATITUDE TO WHICH SUBSTORM DISTURBANCES EXPAND

The amplitude of a Pi2 maximizes at the latitude where the instantaneous main electrojet flows (Olson and Rostoker, 1975; Saito et al., 1976a; Kuwashima, 1978; Oguti et al., 1978). The period T of the Pi2 is also related to the latitude Φ of the electrojet; T is longer for the larger Φ as shown in Fig.1B. Since the waveform of Pi2 becomes simplified in the lower latitudes, T can be measured strictly at low-latitude stations. Therefore, Φ can be inferred from T of low-latitude Pi2. When Φ is estimated to be small, we can predict that the substorm which is now expanding will develop further from Φ to the higher latitudes, since the larger substorm makes generally a prominent poleward expansion from the lower latitudes. Actually the latitude Φ was 65° geomagnetic latitude when a substorm was observed to start together with a Pi2 with T=60sec at 21h30m UT on August 26, 1970 (Saito, et al. 1976a).

4. PREDECTION OF LONGITUDES TO WHICH SUBSTORM DISTURBANCES DEVELOP

Magnetic disturbances during substorms are expressed by systematic hodographs on the horizontal plane (Fukushima, 1953). Hodographs of the initial kick of Pi2-type magnetic disturbances are also governed by a systematic rule: initial kicks at stations in the northern hemisphere orient statistically toward the *convergent* point on the northern auroral oval on the midnight meridian (Saito, 1961; Rostoker, 1967; Saito and Matsushita, 1968). Oguti et al. (1978) confirmed by using the observed data of sequential Pi2-substorm events that this convergent point coincides with the substorm ignition region to which auroral particles precipitate initially. Then activity of the substorm develop from this region toward both longitudes via westward travelling surges and eastward travelling loops (Kisabeth and Rostoker, 1973; Fig.15 of Saito, 1974).

In actual cases the convergent point, namely the ignition region, is sometimes situated far from the averaged midnight auroral oval (Fig.4 of Saito, 1961). This conclusion that had been derived in 1961 was confirmed afterwards by satellite auroral photographs, according to which the substorm ignition region that is identified by an initial auroral brightening was also frequently far from the midnight meridian (for example, see Figs. 4c and 4e in Snyder et al., 1974).

Hence, we can locate the longitude of the substorm ignition region (and can predict the longitudes to which the substorm disturbances develop) by using the associated Pi2 disturbance at a low-latitude station, if the orientation of the initial kick of the Pi2 is combined with Φ as obtained in the previous section (Saito et al., 1976a). Triangulation of initial kicks of a Pi2 event observed simultaneously at many well-distributed stations promises a more precise locating of the ignition region (Saito, 1961).

Actually the geomagnetic longitude Λ of the convergent point was about 280° for a substorm event that commenced at 11h35.5m UT on August 29, 1957 (Kato et al., 1962).

5. BASIC MODEL FOR THE PREDICTION THCHNIQUE

Various Pi2 models have been proposed by various researchers (Doobov and Mainstone, 1973; Olson and Rostoker, 1977; Nishida, 1979; and others), but the basic model which will be used here is the one by Saito et al. (1976a) that Pi2 is due to a damped-type standing Alfvén wave on the field lines anchored in the auroral oval in the midnight sector. In this model the Alfvén wave is considered to be excited by the abrupt formation of the X-type neutral line in the magnetotail (Sakurai et al., 1976). In the case when a large magnetic energy is stored in the magnetotail, the radius of the auroral oval (namely, of the polar cap) becomes large. Hence, if the large amount of energy is suddenly released by the formation of the X-type neutral line, a substorm with large magnitude commences associating with a poleward expansion from the low-latitude auroral oval. In this case the period of the standing Alfvén wave is short, since the path-field line is short and the magnetic fields along the field line are intense. The M-T relation as described in Section 2 and the Φ - T relation in Section 3 are interpreted in this way by this model. As for the more comprehensive description on this Pi2 model, the reader may refer to Saito et al. (1976a) or Kuwashima et al., (1980).

The convergent characteristic in the distribution of the initial kick of the Pi2-type magnetic fluctuations (see Section 3 and4) is interpreted as due to the repulsion forces among the field-aligned currents that are suddenly intensified in association with the onset of the substorm (Saito, 1977).

6. LONG-TERM PREDICTIONS OF SUBSTORM ACTIVITY

In the previous sections a technique to predict the substorm activity before the activity reaches its maximum was described. Then let us discuss on long-term predictions of substorm activity before its onset classifying the term into various time lengths.

In the first place let us consider the prediction several hours before substorm onset. When the orientation of the interplanetary magnetic field (IMF) is southward, the solar wind energy is stored more in the magnetotail via the reconnection between IMF and MMF (magnetospheric magnetic field) on the dayside magnetopause. Hence, when IMF turns from northward to southward, we can expect that a substorm with large M will break within a few hours. However, we cannot predict the *precise* duration from the southward turning to the substorm onset (Saito et al., 1976b). In the case of southward IMF (Saito

et al. 1980), prediction of substorm becomes much more difficult.

Next, let us consider a prediction of substorm activity within the coming one year. A recurrent-type magnetic storm is regarded as an assembly of substorm events modulated by the sector structure of IMF (Saito, 1972a). According to the Russell-McPherron effect, IMF tends to be southward near around April 5 and October 5 (Russell et al.,1973). Since the Russell-McPherron model is a one-dimensional model, a more realistic two dimensional model was proposed with the name of SEQSM model (Saito, 1972b). Since the axial effect is decisively observable on geomagnetic disturbances, this effect is called the ARS effect, which becomes maxima at March 8 and September 8 because heliolatitude of the subearth point maximizes. Hence, the ARS-SEQSM model derived from a combination of two effects was regarded as the cause of the seasonal variation and the 27-day recurrent variation of magnetic activity. We can expect from a combined model that magnetic activity becomes maximum near around March 21 and September 21 as observed (Saito, 1972b). According to the ARS-SEQSM model, the epoch of magnetically active days in some solar rotation number can be fairly predicted by surveying the magnetic activity data of one year ago (Saito, 1972b).

As for the solar-cycle term prediction of recurrent-type magnetic(namely, substorm) activity, the dynamic auto-correction analysis of the past magnetic activity indices (Fig.2 of Saito, 1972b) may offer a useful information. The figure shows that 27-day recurrent disturbances are statistically predicted to occur from 3.5 years before to 0.5 years before sunspot minimum. This interval is explained by the two-hemisphere model on the three dimensional interplanetary magnetic structure (Saito, 1975). According to this model, a warped neutral sheet of the helionagnetosphere turns over once every solar cycle (Saito et al., 1978) and makes an *apparent* sector structure in the

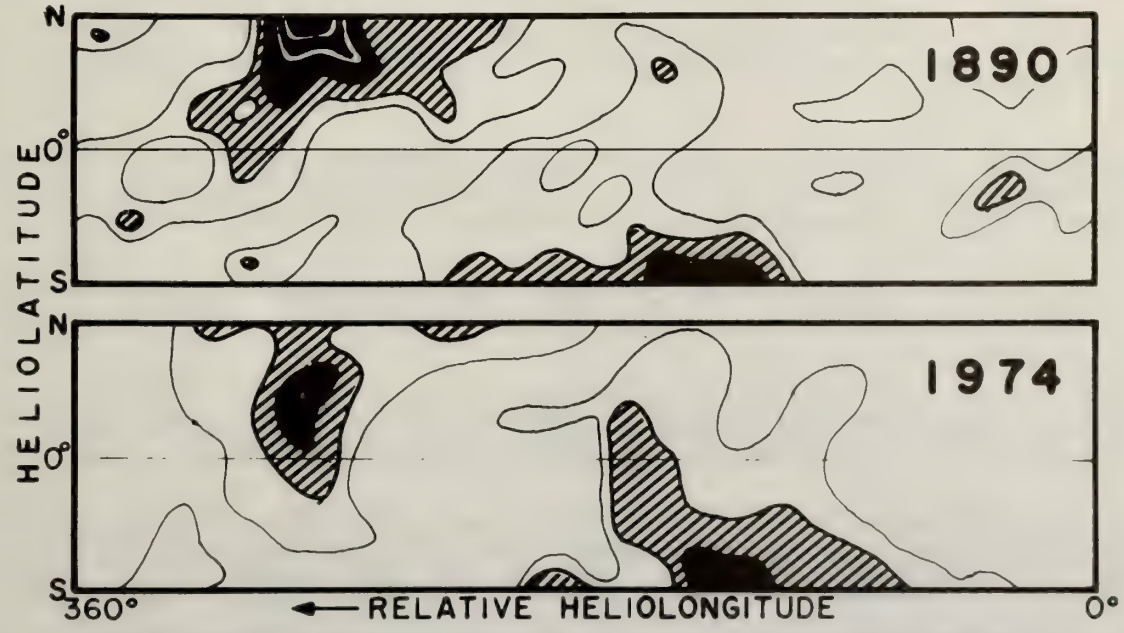


Fig.2 Stable antipodal relation of the two solar M-regions that appeared simultaneously on the sun. The black area in the northern hemisphere and that its antipodal position mean the M-regions from Ci and C9 indices (cf. Fig. 1 of Saito, 1972b). Note the strikingly stable antipodal relation has been held from 1890 (upper panel) to 1974 (lower panel).

sunspot declining-minimum years. Recurrent-type Sc and Si as observed (Saito, 1972c) is also expected from this two-hemisphere model (Saito, 1978b). The recurrent-type magnetic storm is closely related to the coronal-hole tongue that is regarded to be the solar M-region. Saito (1978c) analyzed geomagnetic Ci and C9 indices during almost one century and found a very stable antipodal relation in the two M-regions that tend to appear simultaneously on the sun. Fig.2 shows that the antipodal relation of the two M-regions derived from the Ci indices in 1890 is strikingly similar to that in 1974 (Saito, 1978C).

Since the main purpose of the present paper is to propose a technique to predict substorm activity by means of Pi2, the reader may refer to the following references.

REFERENCES

Doobov,A.L. and J.S. Mainstone (1973); Investigations of Pi2 micropulsations-(I) Frequency spectra and polarization, Planet. Space Sci., 21 : 721.

Fukushima,N.(1953) : Polar magnetic storms and geomagnetic bays. J. Fac. Sci. Univ. Tokyo, Section II, 8:293.

Kato, Y. and T. Saito (1962) : Morphological study of geomagnetic pulsations. J. Phys. Soc. Japan, 17:(Suppl. A-II)34.

Kisabeth, J.L. and G. Rostoker (1973) : Current loops in auroral loops and surges inferred from ground-based magnetic observations. J. Geophys. Res., 78:5573.

Kuwashima, M. (1978) : Wave characteristics of magnetic Pi2 plusations in the auroral region. Spectral and polarization studies. Memoirs of the National Polar Research Institute. Series A. Aeronomy. 15:1.

Kuwashima, M. and T. Saito (1980) : Spectral characteristics of magnetic Pi2 pulsations in the auroral region and lower latitudes. Submitted to J. Geophys. Res.

Nishida, A.(1979); Possible origin of transient dusk-to-dawn electric field in the nightside magnetosphere, J. Geophys. Res., 84, 3409.

Oguti, T., K. Hayashi, S. Kokubun, K. Tsuruda, T. Watanabe, and R. E. Horita (1978) : Local auroral expansion and Pi2. Abstracts for the 64th Assembly of Japanese Society of Geomagnetism and Geoelectricity. 42 p.

Olson, J.V. and G. Rostoker (1975); Pi2 pulsations and the auroral electrojet Planet. Space Sci., 23:1129.

Olson, J.V. and G. Rostoker (1977); Latitude variation of the spectral components of auroral zone Pi2, Planet Space Sci., 25:663.

Rostoker, G. (1967); The polarization characteristics of Pi-2 micropulsations and their relation to the determination of possible source mechanisms for the production of nighttime impulsive micropulsation activity, Can. J. Phys., 45:1319.

Russell, C.T. and R.L. Mcpherron (L973) : Semiannual variation of geomagnetic activity. J. Geophys. Res. 78:92.

Saito, T. (1961) : Oscillation of geomagnetic field with the progress of pt-type pulsation. Sci. Rept. Tohoku Univ., Ser.5, Geophys., 13:53.

Saito, T. (1972a) : Structure of the interplanetary magnetic field and occurrence of magnetospheric substorms——Examination of hypotheses on semiannual variation in substorm activity. Proc. 4th MagnetosphereSymp. (on Magnetospheric Substorm), Publ. by Inst. Space Aeronaut. Sci., Univ. Tokyo, 72 pp.

Saito, T. (1972b) : Recurrent magnetic storm in relation to the structure of solar and interplanetary magntic fields. Rept. Ionos. Space Res. Japan, 26:245.

Saito, T. (1972c) : Recurrent-type magnetic disturbances and prehistoric solar magnetic field. Proc. IASY-IMS Symp., Publ. by Inst. Space Aeronaut. Sci., Univ. Tokyo, 167 pp.

Saito, T. (1974) : Examination of the Models for the Substorm-Associated Magnetic pulsation, Ps6. Sci. Rept. Tohoku Univ. Ser.5, Geophys., 22:35.

Saito, T. (1975) : Two-hemisphere model on the three-dimensional magnetic structure of the interplanetary space, Sci. Rept. Tohoku Univ., Ser.5, Geophys., 23:37.

Saito, T. (1977) : Study of mini-substorm as a suitable research theme during IMS, Proc. IMS Symp. held at ISAS, Tokyo Univ. on 14-16. July, 1977. 203 pp.

Saito, T. (1978a) : Long-period irregular magnetic pulsation, Pi3, Space Sci. Rev., 21:427.

Saito, T. (1978b) : Destruction of corotation shock by a solar flare. In: Summary of Japanese IMS Observations presented at IMS Working Conferense, Innsbruck, 46 pp.

Saito, T. (1978c) : Antipodal characteristics of solar M-regions that have been observed for the past one century. Abstracts for the 63th Assembly of Japanese Society of Geomagnetism and Geoelectricity. 70 pp.

Saito, T. and S. Matsushita (1968) : Solar cycle effects on geomagnetic Pi2 pulsations. J. Geophys. Res., 73:267.

Saito, T., T. Sakurai and Y. Koyama (1976a) : Mechanism of association between Pi2 pulsation and magnetospheric substorm, J. Atmos. Terrestr. Phys., 38:1265.

Saito, T., K. Yumoto and Y. Koyama (1976b) : Magnetic pulsation Pi2 as a sensitive indicator of magnetospheric substorm, Planet. Space Sci., 24:1025.

Saito, T., T. Sakurai and K. Yumoto (1978) : The earth's paleomagnetosphere as the third type of the planetary magnetosphere, Planet. Space Sci., 26:413.

Saito, T., and T. Sakurai (1980) : N-type reconnection model to interpret the mechanism of mini-substorm. Submitted to Planet. Space Sci.

Sakurai, T. and T. Saito (1976) : Magnetic pulsation Pi2 and substorm onset, Planet. Space Sci., 24:573.

Snyder, A.L., S.-I. Akasofu, and T.N.Davis (1974) : Auroral substorms observed from above the north polar region by a satellite. J. Geophys. Res., 79:1393.

SHORT-TERM FORECASTING OF THE SUBSTORM BREAKUP PHASE BASED ON GROUND MAGNETIC OBSERVATIONS IN THE ZONE OF MAGNETOSPHERIC CLEFT PROJECTION

V. V. Shelomentsev, V. M. Mishin, and T. I. Saifudinova
Siberian Institute of Terrestrial Magnetism,
Ionosphere and Radio Wave Propagation (SibIZMIR)
Irkutsk-33, P. Box 4, USSR

A new geomagnetic index, PE, is introduced, based on the records of stations located within the zone of magnetospheric cleft projection ($\Phi \simeq 75$-$81°$). At the pre-breakup substorm period the PE-index reflects the intensification of two current modes in the polar cap: DP-2, associated with the enhancement of large-scale magnetospheric convection, and PEJ (a polar electrojet), producing a high-latitude effect of the IMF Y-component. This defines the applicability of the index for short-term forecasting of the breakup phase. The estimates obtained provide evidence of a high degree of forecasting accuracy with the help of the adopted technique (~80-90% for isolated substorms and ≳60% for substorms in a sequence ~2-3 hours prior to breakup onset).

1. INTRODUCTION

A geomagnetic substorm is a complex phenomenon, accompanied by magnetic field reconfiguration, formation and decay of plasma regions, and other large-scale magnetospheric processes, resulting in the release of considerable energy (~10^{21}-10^{22} erg) in the low ionosphere. This energy creates strong ionospheric disturbances that often cause interference in normal operation of radio communication lines, power lines, and other communication means. In addition, there is some evidence that geomagnetic disturbances are closely connected with the Earth's climatic conditions and its biosphere.

The above circumstances demonstrate the importance of improving substorm forecasting techniques. Since the most remarkable substorm signatures are detected during the breakup phase, the forecasting should, obviously, be based on the discovery of specific changes in magnetospheric and/or ionospheric parameters during the prebreakup period (i.e., during the so-called "growth phase").

The present paper describes the results of the development of the short-term forecasting technique for a substorm breakup phase, inferred from ground magnetic observations in the zone of magnetospheric cleft projections (Φ~75-81°).

2. GROUND SIGNATURES OF THE GROWTH PHASE OF THE MAGNETIC SUBSTORM

One is faced with some difficulties when selecting the ground substorm signatures, especially at the prebreakup period. This is due, in many respects, to the fact that a modern network of magnetic observatories is extremely sparse and nonuniform, particularly at high latitudes where the disturbances, generated during substorms, are most intense. Thus, the use of data from auroral (AE-indices) and midlatitude stations to define the beginning of the breakup phase and other substorm characteristics often results in ambiguity due to discreteness and multiplicity of "elementary" breakups, forming a single substorm (Clauer and McPherron, 1974; Sergeev, 1974; Vorobjev and Rezhenov, 1975; Wiens and Rostoker, 1975). This leads to contradictory interpretation of the growth phase and even to rejection of its existence and is a subject of considerable controversy (see, e.g., Akasofu and Snyder, 1972; Vasyliunas and Wolf, 1973; McPherron, 1974).

At the same time the use of polar cap data ($\Phi \gtrsim 75°$) in the analysis of substorms allows one to show that the most significant ground signatures of the prebreakup period take place only at very high latitudes. Thus, in the dayside polar cusp region ($\Phi \sim 75$-$80°$) there is activization and equatorward motion of background aurorae (Starkov and Feldstein, 1967) and auroral particle precipitation regions (Burch, 1972). In the polar cap, DP-2 disturbances are developed (Nishida, 1971; Iijima and Nagata, 1972). The occurrence of DP-2 is of particular interest for forecasting because it can be detected with the help of a special magnetic index PC, drawn by means of magnetograms from stations near the pole ($\Phi \gtrsim 85°$) (Fairfield, 1967; Iijima and Nagata, 1972). According to the conclusions of Kuznetsov and Troshichev (1977), forecasting the substorm breakup phase on the basis of the PC-index enables one to achieve accuracy of about 70%.

Nevertheless, it should be noted that DP-2 is not a unique current mode, characteristic of the prebreakup period in the polar region. The other important element of this period is a polar (not auroral!) electrojet, PEJ, responsible for the high-latitude effect of the IMF Y-component (Mishin et al., 1975; Sumaruk and Feldstein, 1975). It is localized in the zone of a magnetospheric cleft projection ($\Phi \sim 75$-$80°$) and is most intense in its dayside sector, corresponding to the polar cusp projection. PEJ takes place at quiet times too, but during substorms it is sharply intensified (as shown by Mishin et al., 1974, 1977). Figure 1 shows the changes of equivalent current density in the midnoon sector versus substorm time (moment $\tau=5$ corresponds to the breakup phase onset). On the average, the enhancement of current starts ~1-1.5 hours prior to the breakup, so that, together with DP-2, the intensification of PEJ may serve as an indicator of a substorm growth phase.

The additional evidence in favor of this conclusion is presented in Figure 2 where the motion of disturbance onset in coordinates (Φ, t) is shown. It is seen that the zone of the growth phase onset (moments $\tau=1$-2) just corresponds to the magnetospheric cleft projection region where a polar electrojet is localized.

From all of the above facts, one can infer that the magnetic records from stations of magnetospheric cleft projection may serve as the basis for introducing a new index, suitable for short-term forecasting of a substorm breakup phase.

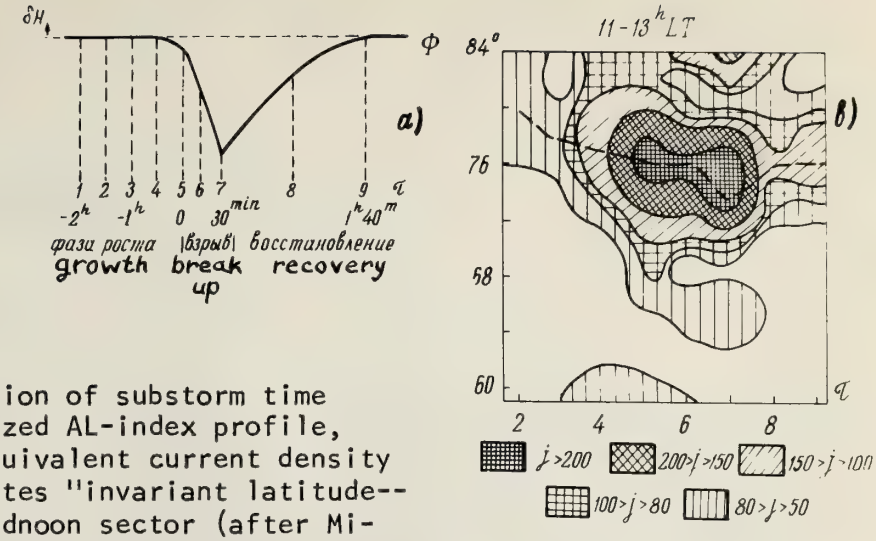


Figure 1. (a) Definition of substorm time moments τ by the idealized AL-index profile, (b) Distribution of equivalent current density (in amp/km) in coordinates "invariant latitude--substorm time" for a midnoon sector (after Mishin et al., 1974). Data are obtained for a "statistical" substorm, comprising a great number of individual cases.

3. A MAGNETOSPHERIC CLEFT INDEX, PE

3.1. A Technique for Index Drawing

To draw the index PE (abbreviated from "polar electrojet") the data of six permanent magnetic observatories (three in the Northern and three in the Southern Hemisphere, Table 1) were used for spring and fall of 1968. Equinox seasons were selected because at these periods the solar illumination of both polar caps is approximately equal and there is no need to introduce corrections for seasonal variations.

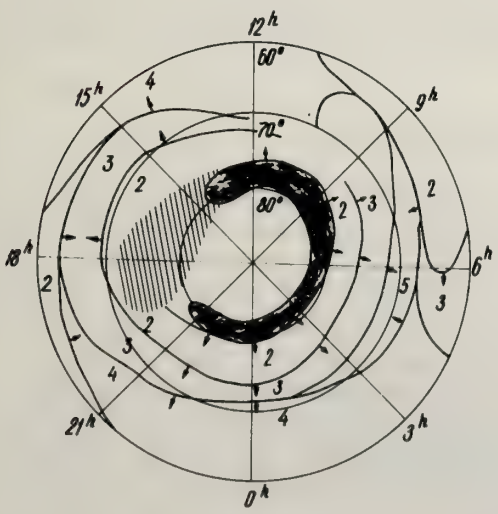


Figure 2. A diagram of disturbance onset movement in the polar region at the substorm growth phase (moment τ= 1-5 are determined on the left side of Figure 1). A zone of the initial disturbance is hatched (after Mishin et al., 1974). Data are obtained for a "statistical" substorm, comprising a great number of individual cases.

Table 1. A network of stations for drawing PE-index.

Station	coordinates			
	geographic		corrected geomagnetic	
	ζ	λ	Φ	Λ
Godhavn	69.2	306.5	77.6	43.3
Mirny	-66.6	93.0	-76.6	127.4
Dumont D'Urville	-66.7	140.9	-80.1	228.7
Mould Bay	76.2	242.6	80.7	264.0
Baker Lake	64.3	264.0	75.1	320.4
Scott Base	-77.8	166.8	-80.5	323.4

It was found by experience that the best results for forecasting substorms were obtained from the integral PE index, determined as a total of disturbance amplitudes of the horizontal component at all stations used:

$$PE = \sum_{i=1}^{6} |H_i - H_i^0| \qquad (1)$$

where H_i^0 is the background level of quiet days. The proposed technique for index drawing is analogous to that for determining the AE-index (Davis and Sugiura, 1966) and differs from the latter only in smoothing of sharp peaks in the magnetograms of some stations. In the present paper we have confined ourselves only to computations of hourly indices because of simplicity of original data processing, though the time resolution of the index may be improved up to standard resolution of magnetograms, i.e., 2.5-minute values.

3.2. Physical Meaning of the Index

The PE index determined by equation (1) is integral not only in its method of calculation but also in its physical sense, because it reflects the dynamics of all current modes in the polar cap, causing fluctuations of the H component. During the most interesting (for forecasting) prebreakup period the predominant contribution to PE is made by two main elements of the growth phase current system--the one-vortex mode with electrojet PEJ and the two-vortex mode DP-2. Their development is controlled, respectively, by a meridional electric field (across a polar cusp) and by a "dawn-dusk" one (across a polar cap). Therefore, to describe the physical meaning of the PE index, its correlation with the theoretical measures of these electric fields should be studied.

According to Gonzalez and Mozer (1973, 1974) the time variations of the "dawn-dusk" field in the polar cap are well described by a model potential

according to a theory of reconnection between interplanetary and geomagnetic fields at the dayside magnetospheric boundary. A formula for the potential has the following form:

$$\Phi(\text{rel, unit}) = \begin{cases} \dfrac{VB_i\,(S-\cos\alpha)}{(1+S^2-2S\,\cos\alpha)^{\frac{1}{2}}} & \text{at } S > \cos\alpha \\ 0 & \text{at } S \leq \cos\alpha \end{cases} \qquad (2)$$

where V is solar wind velocity, B_i is the magnitude of the IMF, $S(=B_i/B_m)$ is a ratio of interplanetary and geomagnetic field magnitudes at the lobe magnetopause, α is an angle between these fields ($\alpha=\pi/2 - tn^{-1}(Z_{SM}/|Y_{sm}|)$, where Z_{SM} and Y_{SM} are the vertical and azimuthal IMF components, respectively, in the solar-magnetospheric coordinates). For further computations we have adopted S = 0.6, based on the results of a correlation analysis of the magnetic activity with the IMF (Svalgaard, 1975; Shelomentsev, 1976).

Figure 3 illustrates an average picture for changes of Φ, AE and PE, obtained by means of a superimposed epoch method for a sample involving 19 isolated substorms. Here and further a zero time ($\tau=0$) is consistent with the beginning of a sharp AE-index increase, i.e., agrees with the definition of the breakup phase onset (Akasofu; 1968). Note that this definition of τ differs from that adopted in Figures 1 and 2.

Figure 3. Normalized mean profiles of changes of Φ (dashes), AE (solid) and PE (dot-and-dash) for isolated substorms. $\tau=0$ corresponds to the breakup phase onset. ["Isolated" means a substorm, developing after the quiet background (AE<100γ) and lasting for at least 6 hours].

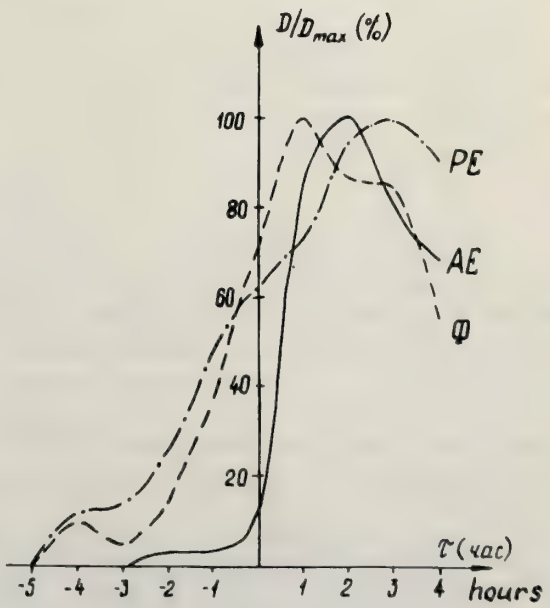


Figure 3 shows a significant correlation between potential, Φ, and PE index. At the same time certain differences are observed, particularly the lack of coincidence of times of maxima. This is in agreement with the integral character of the PE index, involving the contribution not only of DP-2 whose measure is Φ but also of the electrojet PEJ. Unfortunately, the theoretical description of meridional electric fields in the ionosphere, controlling the generation of PEJ, is not yet developed sufficiently to study the correlation in more detail.

From Figure 3 it follows that the growth of Φ and PE starts long before the breakup onset (τ=0)--in some cases as much as five hours before. A significant increase of the PE index (~10% of the amplitude) is already observed four hours prior to the breakup. This shows eivdence for the fact that one can really detect the precursors of the substorm breakup phase with the help of the PE index.

3.3. Forecasting the Breakup Phase by Means of the PE Index

Figures 4 and 5 give a representation of profiles Φ, AE, and PE for single substorms. Arrows show the beginnings of characteristic changes of the PE index, precursors of the breakup phase.

3.3.1. Isolated substorms

Typical examples of isolated substorms are given in Figure 4. In each individual case it is evident that the beginning of the changes of PE precedes a breakup onset by several hours. Prebreakup time variations of PE are of three types: (1) a smooth growth (Figure 4a); (2) oscillations with a quasi-period ~2-3 hours (Figure 4b); and (3) superposition of types 1 and 2 (Figure 4c). The characteristic values of PE corresponding to a substorm (involving the growth phase) are hundreds of gammas. In fact, the stable condition PE>100γ points in most cases to the fact that the breakup will start in several hours.

3.3.2. Nonisolated substorms

Substorms often occur in a sequence rapidly affecting each other and forming, when they are of sufficient numbers, the strongest worldwide disturbances--global magnetic storms. Examples of such successions are given in Figure 5, in which the characteristic prebreakup changes of the PE index are also observed. Almost every single breakup of a succession (AE burst) is preceded by a PE burst. This means that observations in the magnetospheric cleft zone can give information about the continuation or cessation of disturbances that have begun in the auroral zone.

The accuracy of forecasting nonisolated substorms is less compared to that for isolated substorms. Indeed, the observed changes of PE index before an individual breakup of a succession is a superposition of a decreasing disturbance, corresponding to the preceding substorm, and of an increasing one, corresponding to a new substorm. Therefore, a moment of the PE growth onset (a point of minimum), taken as a precursor of a new breakup, shifts toward the moment of a new AE burst onset, as compared with the situation that would be observed for substorms separated by a durable quiet interval.

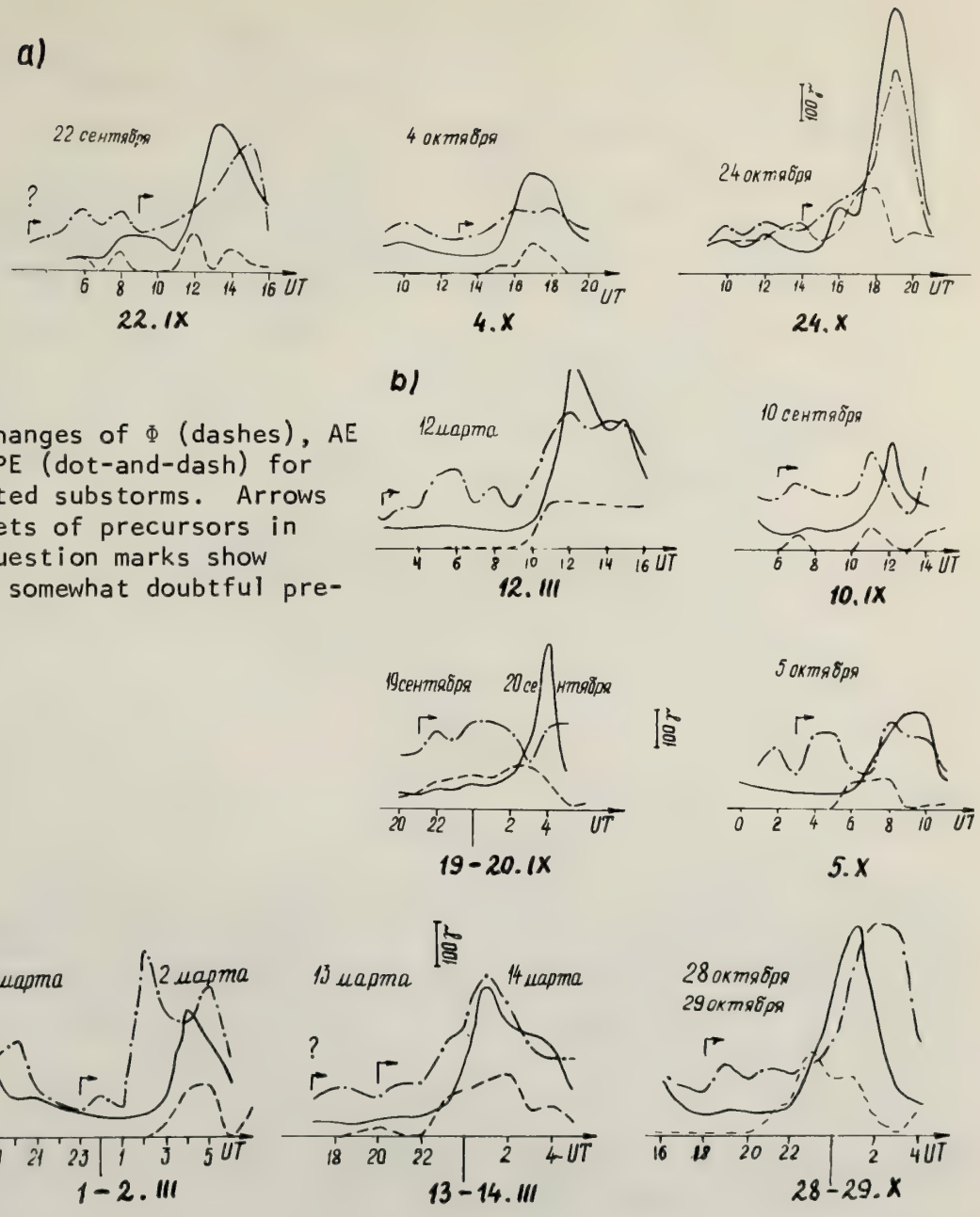


Figure 4. Changes of Φ (dashes), AE (solid) and PE (dot-and-dash) for single isolated substorms. Arrows show the onsets of precursors in PE index. Question marks show possible but somewhat doubtful precursors.

3.3.3. Accuracy of forecasting

Not being able to carry out the substorm prediction based on the PE index in real-time, we have confined ourselves to the epignosis of the known substorms during the time periods including 19 isolated and 21 nonisolated substorms. To reveal the breakup precursors in the PE index we used the criteria previously described (the character of time variations of PE and the quantitative condition, PE>100γ). The results are presented in Figure 6 where the time dependence of the forecasting accuracy percentage preceding the breakup onset $\tau=0$ is shown. These data yield a quantitative estimation of the forecasting accuracy, achieved by introducing the PE index. The proposed technique enables us to predict ~80 percent of isolated substorms ~3 hours

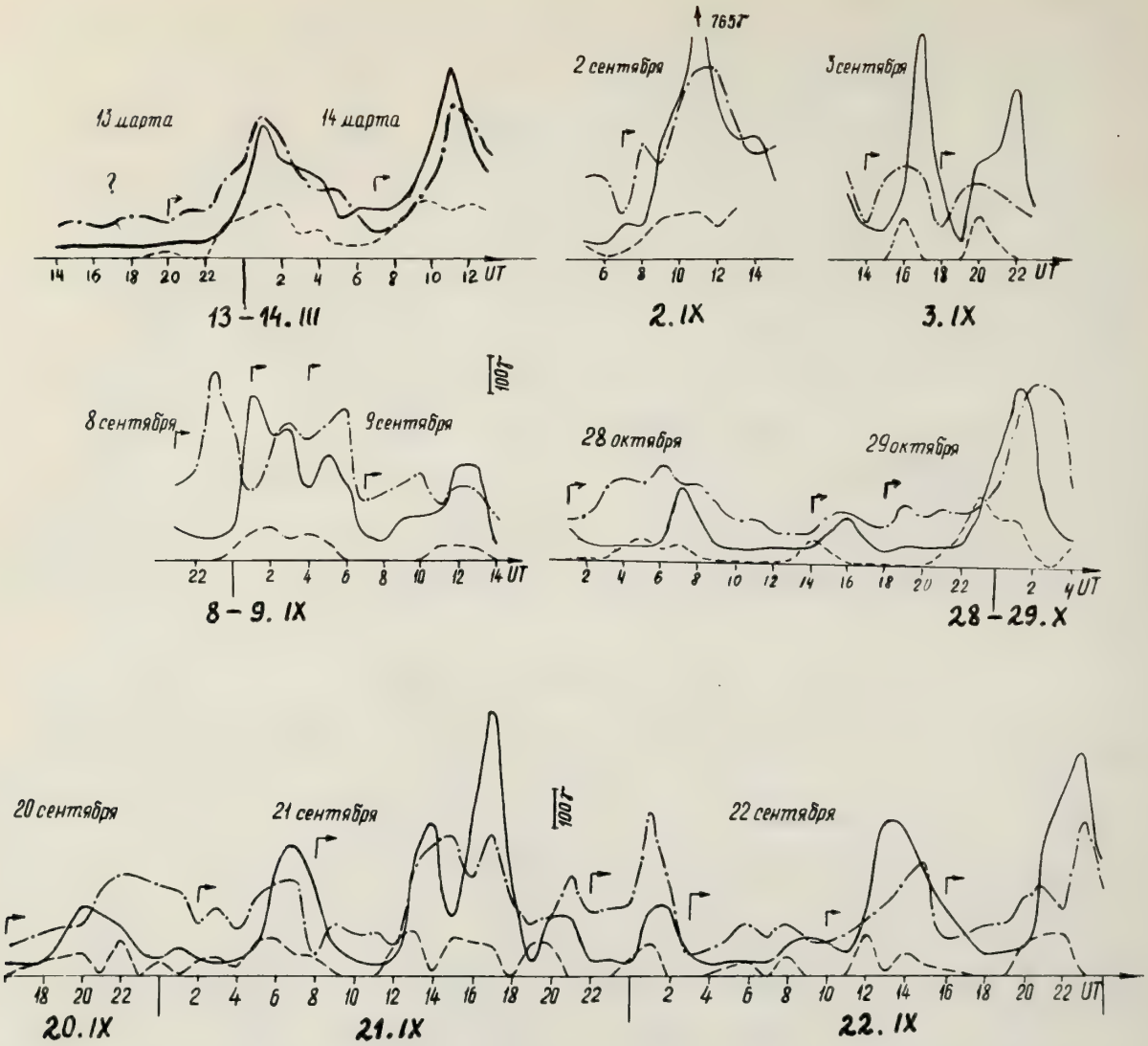


Figure 5. Changes in Φ (dashes), AE (solid), and PE (dot-and-dash) for substorm successions.

beforehand and almost all of them (95 percent) 1-2 hours prior to the breakup. The forecasting accuracy of nonisolated substorms is lower due to the reasons mentioned above. However, in this case a good enough accuracy (≥60 percent) may be achieved ~2 hours beforehand. Note that the quoted results should be considered only preliminary. To obtain more accurate estimates it is necessary to expand the time period under consideration to take into account the number of the "false alerts" and so on. Of course, the final testing of the prediction method should be made in real-time.

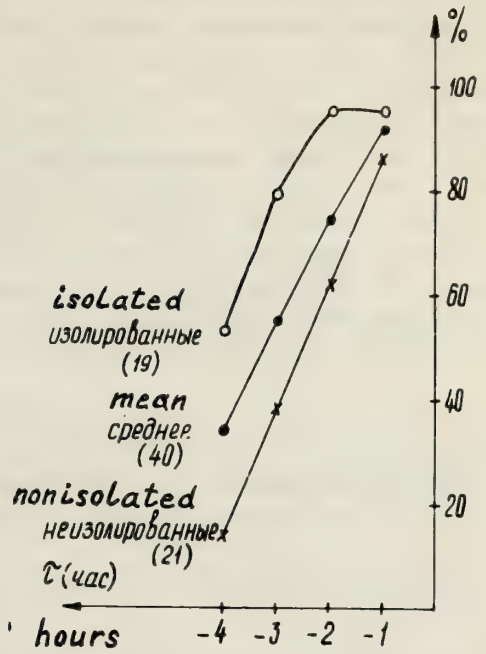


Figure 6. Accuracy of breakup phase forecasting versus the time preceding the breakup onset $\tau=0$ (in percentage).

4. CONCLUSION

In the present paper a new geomagnetic index PE is introduced, based on magnetic records of the H-component at stations located in the zone of magnetospheric cleft projection ($\Phi \sim 75\text{-}81°$). At the prebreakup substorm period the changes of PE index reflect, mainly, the intensification of two current modes in the polar cap: a two-vortex DP-2 system and a polar electrojet, PEJ. This observation is supported by the results of the analysis both of single cases and a "statistical" substorm (Mishin et al., 1974, 1977) as well as by correlation of PE with the "dawn-dusk" electric field potential, computed by means of the reconnection model of Gonzalez and Mozer (1974).

The presence of the breakup precursors in the region of a magnetospheric cleft, revealed with the help of the PE index, gives evidence in favor of the substorm growth phase existence. The signatures of the growth phase are observed both for single (isolated) substorms and for those forming a succession. Note that in some cases the disturbances of the PE index begin 4-5 hours prior to the breakup onset that exceeds mean known duration of the growth phase (~1-2 hours). In such cases we deal either with the very durable growth phase or with specific events in the magnetospheric cleft zone, reflecting, probably, the variations of solar wind parameters (particularly IMF), overtaking the substorm development. Finally, there are few cases when it is difficult (or impossible) to select the precursors with the help of the PE index. It is possible that a certain negative role is played here by the sparseness and nonuniformity of the network of magnetic observatories (shown in Table 1).

The approbation of PE index for short-term forecasting of the substorm

breakup phase shows that a high degree of accuracy may be achieved. Therefore, a new index may be recommended for various applied problems, including forecasting of the breakup phase, together with the PC index and other measures of the substorm growth phase signatures.

Subsequent improvement of the proposed index is probably possible by the accounting of not only amplitudes but also changeability of magnetic variations in the polar region. According to Kuznetsov and Troshichev (1977) a similar modification, approbed with PC index, results in significant improvement of forecasting data. It is necessary also to make the analysis during the solstice seasons to avoid introducing corrections for seasonal variations when computing the PE index. In addition, the problems of further improvement of the forecasting technique yield the necessity to expand the network of magnetospheric cleft stations in Arctic and Antarctic.

Acknowledgment

The authors express their thanks to A. D. Bazarzhapov, V. Kh. Kompanets and N. Ja. Naidenova for their help in this work.

REFERENCES

Akasofu, S.-I. (1968): Polar and Magnetospheric Substorms. D. Reidel Pub. Co., Dordrecht, Holland.

Akasofu, S.-I., and A. L. Snyder (1972): Comments on the growth phase of magnetospheric substorms. J. Geophys. Res., Vol. 77, p. 6275.

Burch, J. L. (1972): Precipitation of low-energy electrons at high latitudes: Effects of IMF and dipole tilt angle. J. Geophys. Res., Vol. 77, p. 6696.

Clauer, C. R., and R. L. McPherron (1974): Variability of midlatitude magnetic parameters used to characterize magnetospheric substorms. J. Geophys. Res., Vol. 79, p. 2898.

Davis, T. N., and M. Sugiura (1966): Auroral electrojet activity index AE and its universal time variation. J. Geophys. Res., Vol. 71, p. 785.

Fairfield, D. H. (1967): Polar magnetic disturbances and the IMF. Space Res., Vol. 8, p. 107.

Gonzalez, W. D., and F. S. Mozer (1973): Response of polar cap convection to the IMF. J. Geophys. Res., Vol. 78, p. 6784.

Gonzalez, W. D., and F. S. Mozer (1974): A quantitative model for potential resulting from reconnection with an arbitrary IMF. J. Geophys. Res., Vol. 79, p. 4186.

Iijima, T., and T. Nagata (1972): Signatures for substorm development of the growth phase and expansion phase. Planet. Space Sci., Vol. 20, p. 1095.

Kuznetsov, B. M., and O. A. Troshichev (1977): On the nature of polar cap magnetic activity during undisturbed periods. Planet. Space Sci., p. 15.

McPherron, R. L. (1974): Current status of the growth phase controversy. EOS Trans. of AGU, Vol. 55, p. 994.

Mishin, V. M., A. D. Bazarzhapov, T. I. Saifudinova, V. D. Urbanovich and V. V. Shelomentsev (1974): Development of magnetic substorms. I. Issled. po Geomagn., Aeron. i Fizike Solntsa, issue 30, Moscow, Nauka, p. 107 (in Russian).

Mishin, V. M., A. D. Bazarzhapov, M. I. Matveev, T. I. Saifudinova and V. V. Shelomentsev (1975): Polar electrojet. Issled. po Geomagn., Aeron. i Fizike Solntsa, issue 36, Moscow, Nauka, p. 46 (in Russian).

Mishin, V. M., A. D. Bazarzhapov, T. I. Saifudinova, V. V. Shelomentsev and G. B. Shpynev (1977): Development of magnetic substorms. II. Issled. po Geomagn., Aeron. i Fizike Solntsa, issue 43, Moscow, Nauka, p. 23 (in Russian).

Nishida, A. (1971): DP-2 and polar substorm. Planet. Space Sci., Vol. 19, p. 205.

Sergeev, V. A. (1974): On longitudinal localization of the substorm active region. Planet. Space Sci., Vol. 22, p. 1341.

Shelomentsev, V. V. (1976): On functional dependence of planetary magnetic activity upon "viscous friction" and IMF components. Issled. po Geomagn., Aeron. i Fizike Solntsa, issue 39, Moscow, Nauka, p. 122 (in Russian).

Starkov, G. V., and Y. I. Feldstein (1967): A scheme of elementary disturbance in aurorae at the day side of the Earth. Geomagnetism & Aeronomy, Vol. 7, p. 367 (in Russian).

Sumaruk, P. V., and Y. I. Feldstein (1975): Magnetic field variations in the polar cap. In: Substorms and Disturbances in the Magnetosphere, Leningrad, Nauka, p. 170 (in Russian).

Svalgaard, L. (1975): On the cause of geomagnetic activity, SUIPR Rept. No. 646, Stanford Univ., California.

Vasyliunas, V. M., and R. A. Wolf (1973): Magnetospheric substorms: some problems and controversies. Rev. Geophys. Space Phys., Vol. 11, p. 181.

Vorobjev, V. G., and B. V. Rezhenov (1975): Jump-like westward motion of the region of auroral substorm localization at the impulse magnetic field change. In: Substorms and Disturbances in the Magnetosphere, Leningrad, Nauka, p. 103 (in Russian).

Wiens, R., and G. Rostoker (1975): Characteristics of the development of the westward electrojet during the expansive phase of magnetospheric substorms. J. Geophys. Res., Vol. 80, p. 2109.

DEVELOPMENT OF DISTURBANCES AFTER SC AND SI

I. N. Men'shutina
Polar Geophysical Institute
Apatity, USSR

The difference between SI and SC is assumed to be determined by the states of the magnetosphere and solar wind at the time of the appearance of discontinuities and shock waves to the magnetosphere. The behavior of solar wind parameters (B, B_x, B_y, B_z, V, and den) and the state of the magnetosphere both before and after SC and SI are studied to find the parameters that are important for SC and SI. The determination of such parameters allows prediction of the disturbances connected with solar wind discontinuities and shock waves since the SCs are accompanied by disturbances the SIs are not.

1. INTRODUCTION

Two types of sudden changes of the geomagnetic field with large amplitudes are known presently: sudden commencements (SC) and sudden impulses (SI). [The sharp changes in the geomagnetic field with a small amplitude ($A < 16\gamma$) are termed sudden worldwide changes (Rigby and Mainstone, 1975).] SC and SI were originally determined by using the ground geomagnetic field observations. The essential difference between them, taken as the basis for the determination, was the behavior of the magnetic field after the impulse: the impulses followed by a magnetic storm were called sudden commencements, the others were sudden impulses. According to the IAGA Bulletin, the SCs as a rule are immediately followed by disturbances. These disturbances were observed by most stations. The SIs are not accompanied by these disturbances at most stations.

Thus, the definitions of SC and SI are based on the different behaviors of the geomagnetic field. However, there are many investigations where the difference between SC and SI is not taken into account, for example Ondoh's (1970) work considering the SC and SI amplitude distribution. Furthermore, the cosmic noise absorption characteristics are shown to be the same for SCs and SIs by Brown (1967).

SCs and SIs cannot be connected with the principally different solar wind phenomena. It has been shown that both SCs and SIs can be associated both with shock waves and with discontinuities of solar wind (however, the probability is not the same)(Burlaga, 1975; Burlaga and Ogilvie, 1969; Chao and Lepping, 1974; Gosling et al., 1967; Hirsberg et al., 1970; Moldovanu, 1974; and Nishida, 1964, 1975). Since SCs and SIs are associated with the same group of solar wind phenomena, the geoefficiency of these phenomena, that is the development of the disturbances immediately after the impulse and the de-

velopment of the magnetic storm (and in this way the determination of SC and SI) is determined by the state of the magnetosphere at the time of the discontinuities or shock wave and also by a number of parameters of solar wind that influence the state of the magnetosphere. The determination of such parameters allow prediction of the geoactivity associated with the solar wind discontinuities, shock waves, and irregularities.

The other side of this problem concerns the triggering of substorms by SC. Taking into account the results of the investigations considering the SC-triggering problem (Akasofu et al., 1973; Burch, 1972, Jijima, 1973; Kawasaki et al., 1971; Kokubun, 1972; Kokubun et al., 1977; and Shieldge and Siscoe, 1970), it is possible to find sufficient and necessary conditions for triggering both substorms (accompanied by all its features) and other disturbances. SC investigations can be useful for studying the connection between substorms, disturbances, and magnetic storms.

2. RESULTS

The principal factors determining the geoefficiency of shock waves and solar wind discontinuities, according to the results of the present investigation, are the interplanetary magnetic field; the velocity and number density of the solar wind; the state of the magnetosphere characterized by D_{st} and AE indices; and the angle between the interplanetary magnetic field and the dipole axis of the Earth.

Accordingly, both hourly average values for solar wind parameters published by King (1977) and the hourly averaged magnitudes of the D_{st} and AE indices were studied. The state of the solar wind one hour before the impulse and for one hour during the impulse were studied. Changes in the above-mentioned parameters connected with the existence of shock waves and discontinuities were considered. The SC and SI data represented by the IAGA Bulletin (1969) were used for investigation. For this period, graphs showing the behavior of the solar wind and magnetosphere before and after SC and SI, depending on UT, were constructed (Figs. 1 and 2). There were no evident UT dependencies of any parameter both for SC and SI. According to the figures the behaviors of a number of parameters were different for SC and SI.

The principal statistical results of the graphs are given in Table 1, which contains the median values of all the parameters for one hour before SC and SI and for the hour including SC and SI, the quarter values indicating the value scatter. The changes of the parameters are also estimated: the probability of change occurrence (in percent) and the values of changes are given.

As can be seen from Figures 1 and 2 and Table 1, the following features are characteristic for SC (average values):

a. The magnitude of the interplanetary magnetic field changes substantially. As a rule, B values increase during the hour including SC. The probability of the increase is 85%. The change equals 2.8γ.

b. The B_y component undergoes the largest change among components of the interplanetary magnetic field. Though both an increase and decrease of the B_y component are possible, the decrease is observed more often (65%). However, the value of the change is larger at B_y increasing during the hour of SC ($\Delta B_y = 2.9\gamma$). The median values of B_y are negative.

c. The B_x component changes are not essential. The B_x decrease and increase probabilities due to SC are nearly equal. The median magnitudes before

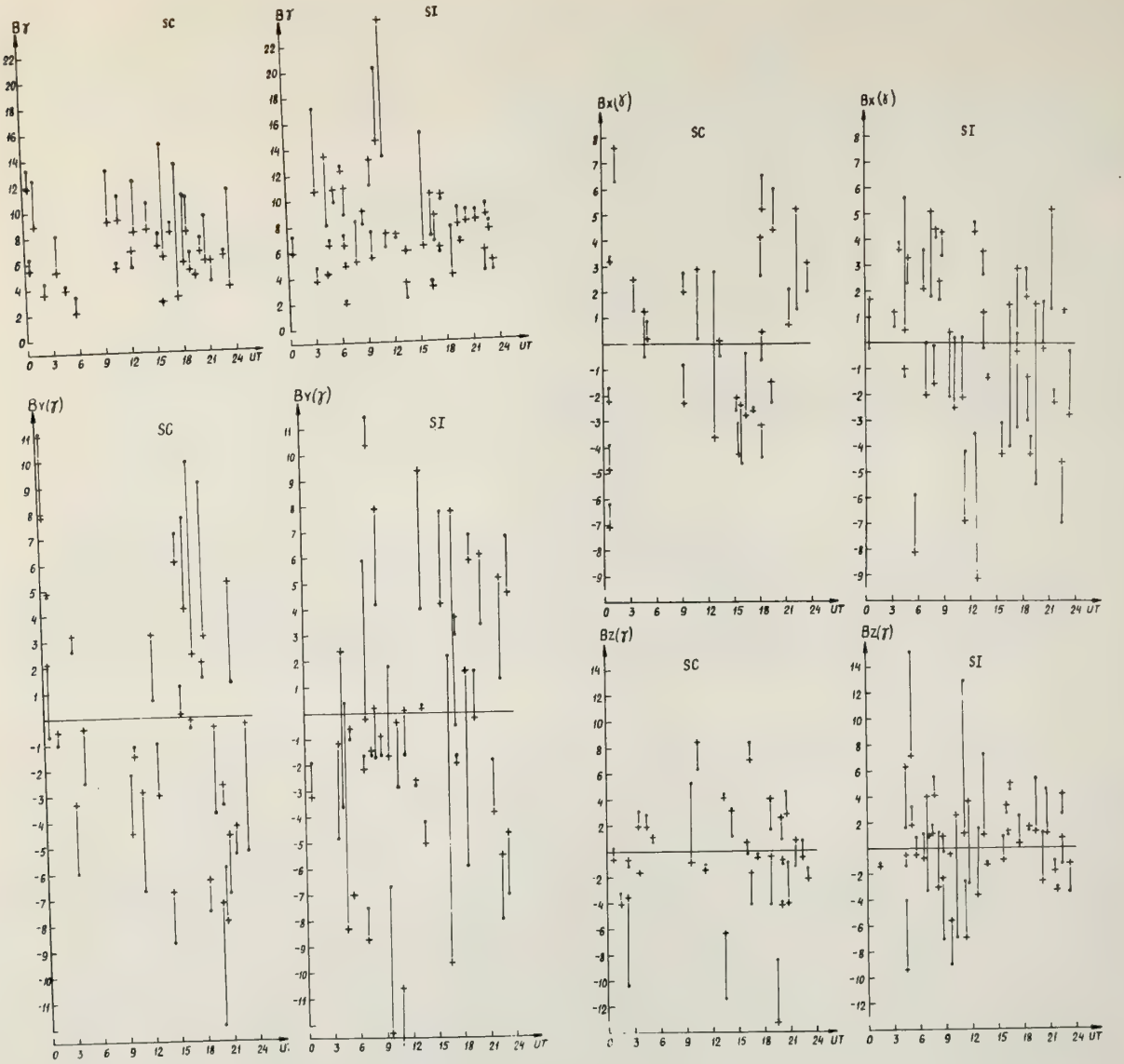


Figure 1. Behavior of B, B_x, B_y, and B_z before and after SC and SI.

and after SC are positive and approximately the same. This sector of the interplanetary magnetic field is unchanged, with the primary direction toward the sun. However, SC does change the ratio of B_x to B_y.

d. The median magnitude of B_z is negative both before and after SC. B_z both increases and decreases; however, the amplitude of the decrease is larger than that of the increase and is equal to -2.5γ.

e. The median velocity is 400 km/sec before SC, corresponding to the quiet solar wind velocity. The probability that there is no change in velocity is 54%; that the velocity increases is 45%. The median velocity after SC is equal to 440 km/sec.

f. The number density either decreases or stays constant. The median values are 3 cm^{-3} and 3.8 cm^{-3} before and after SC, respectively.

g. Before SC the median D_{st} value is negative (-2γ). As a rule, the D_{st} increases during SC. The average D_{st} change is 7.6γ, with D_{st} becoming

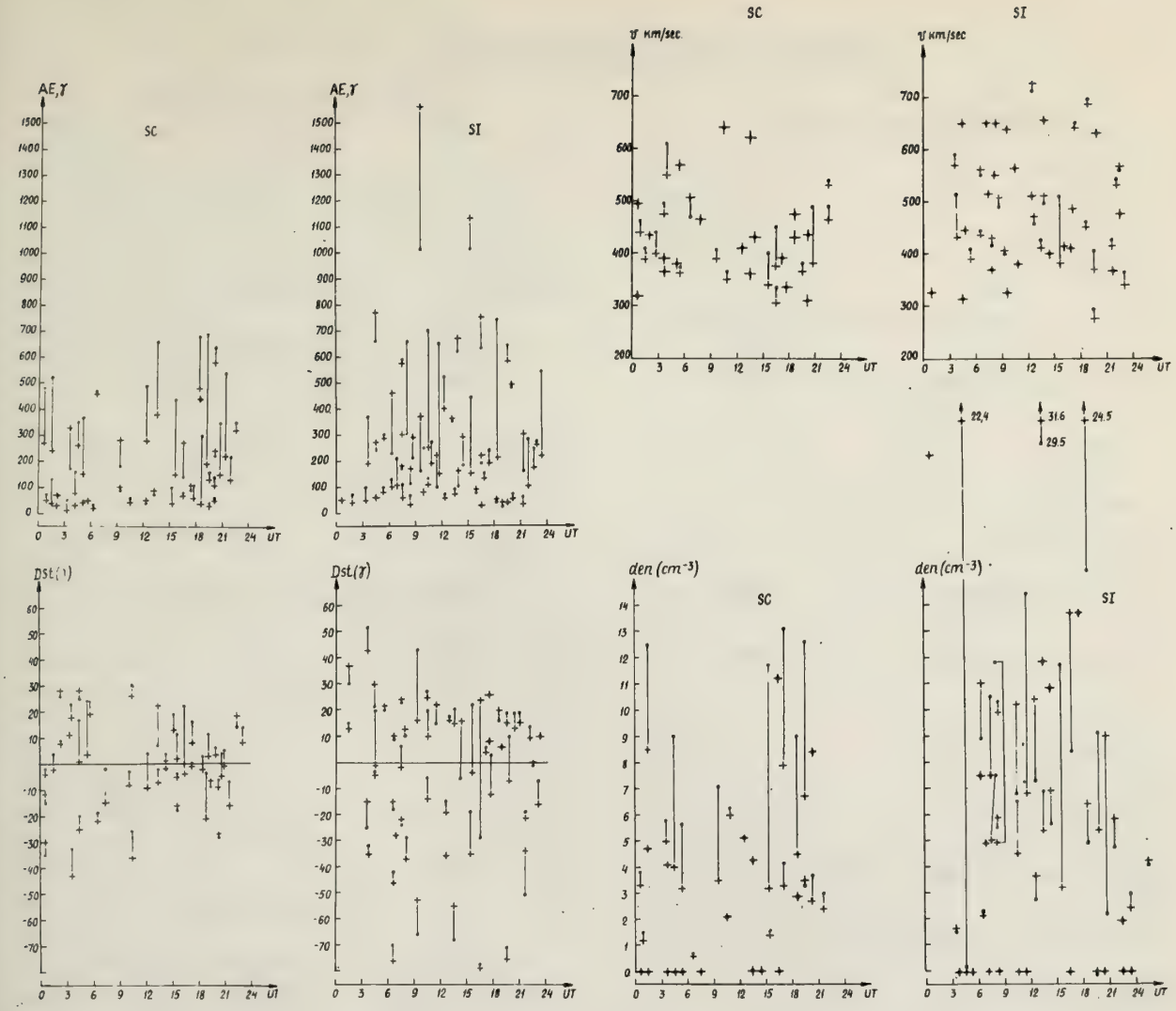


Figure 2. Behavior of AE, D_{st}, V, and den before and after SC and SI.

positive. In this case either a large magnetospheric compression or DR current disappearance can occur. Sometimes D_{st} decreases; however, the decreasing value is 4.3γ. That may correspond to simultaneous development of the two processes: increasing DR current and magnetospheric compression. The first process is more intensive.

h. The auroral zone disturbance is not large. The median AE index is equal to 120γ. The change of disturbances due to SC is not considerable. AE is 150 γ. The AE index can increase and decrease after SC.

The following features are typical for sudden impulses:

a. The median value of IMF increases after SI, probably due to the increase of the B field after SI. Increase and decrease values are approximately equal.

b. B_y is negative before as well as after SI.

c. B_x can either increase or decrease after SI, with the decrease value of B_x exceeding the increase value after SI. The sector remains unchanged.

d. The median B_z values are positive. B_z more often increases (55%)

Table 1. Statistical Results.

Considered parameters	SC	SI
Bx med +	0.2 γ	0.5 γ
Bx quart +	2.7 γ; -2.0 γ	2.6 γ; -2.2 γ
Bx med (.)	0.5 γ	0.0 γ
Bx quart (.)	3.6 γ; -1.5 γ	2.5 γ; -3.1 γ
$\overline{\Delta Bx} < 0$	-1.45 γ	-2.25 γ
occurrence probability of $\Delta B_x < 0$	50%	50%
$\overline{\Delta Bx} > 0$	1.43 γ	1.79 γ
occurrence probability of $\Delta Bx > 0$	50%	50%
By med +	-0.5 γ	-0.5 γ
By quart +	3.1 γ; -3.9 γ	4.1 γ; -3.3 γ
By med (.)	-1.0 γ	-1.9 γ
By quart (.)	2.7 γ; -5.3 γ	3.9 γ; -4.9 γ
$\overline{\Delta By} < 0$	-2.13 γ	-3.1 γ
occurrence probability of $\Delta By < 0$	65%	49%
$\overline{\Delta By} > 0$	2.90 γ	3.05 γ
occurrence probability of $\Delta By > 0$	35%	51%
Bz med +	-0.5 γ	0.6 γ
Bz quart +	2.5 γ; -1.9 γ	1.7 γ; -1.4 γ
Bz med (.)	-0.3 γ	1.0 γ
Bz quart (.)	2.7 γ; -2.5 γ	3.4 γ; -3.2 γ
$\overline{\Delta Bz} < 0$	-2.5 γ	-3.2 γ
occurrence probability of $\Delta Bz < 0$	45%	37%
$\overline{\Delta Bz} > 0$	1.6 γ	3.4 γ
occurrence probability of $\Delta Bz > 0$	55%	55%
Bmed +	6.0 γ	7.2 γ
Bquart +	8.2 γ; 4.8 γ	10.6 γ; 5.2 γ
Bmed (.)	8.2 γ	7.6 γ
Bquart (.)	11.6 γ; 5.8 γ	9.6 γ; 6.0 γ
$\overline{\Delta B} < 0$	-1.5 γ	-2.2 γ
occurrence probability of $\Delta B < 0$	7%	41%
$\overline{\Delta B} > 0$	2.8 γ	2.0 γ
occurrence probability of $\Delta B > 0$	85%	54%
Vmed +	400 km/sec	465 km/sec
Vquart +	460; 365 km/sec	570; 400 km/sec
Vmed (.)	440 km/sec	480 km/sec
Vquart (.)	490; 390 km/sec	560; 415 km/sec
$\overline{\Delta V} < 0$	-40 km/sec	-12 km/sec
occurrence probability of $\Delta V < 0$	2%	18%
$\overline{\Delta V} > 0$	35 km/sec	29 km/sec
occurrence probability of $\Delta V > 0$	43%	32%
occurrence probability of $\Delta V = 0$	54%	50%

Table 1. Statistical Results--continued.

Considered parameters	SC	SI
den med +	3.0 cm^{-3}	5.0 cm^{-3}
den quart +	4.9; 0.0 cm^{-3}	7.2; 0 cm^{-3}
den med (.)	3.8 cm^{-3}	5.0 cm^{-3}
den quart (.)	7.1; 0.0 cm^{-3}	9.0; 0 cm^{-3}
Δden < 0	-0.2 cm^{-3}	-4.0 cm^{-3}
occurrence probability of Δden < 0	2%	33%
Δden > 0	2.6 cm^{-3}	3.3 cm^{-3}
occurrence probability of Δden > 0	49%	24%
occurrence probability of Δden = 0	49%	42%
Dst med +	-2 γ	2 γ
Dst quart +	7 γ; -12 γ	16 γ; -20 γ
Dst med (.)	4 γ	10 γ
Dst quart (.)	13 γ; (-3)γ	21 γ; -27 γ
ΔDst < 0	24.3 γ	-9.4 γ
occurrence probability of ΔDst < 0	20%	34%
ΔDst > 0	7.6 γ	8.2 γ
occurrence probability of ΔDst > 0	76%	55%
occurrence probability of ΔDst = 0	2%	11%
AE med +	120 γ	190 γ
AE quart +	270 γ; 50 γ	290 γ; 90 γ
AE med (.)	150 γ	210 γ
AE quart (.)	370 γ; 70 γ	470 γ; 100 γ
ΔAE < 0	64 γ	99.5 γ
occurrence probability of ΔAE < 0	17%	40%
ΔAE > 0	128 γ	132 γ
occurrence probability of ΔAE > 0	71%	55%
occurrence probability of ΔAE = 0	12%	5%

Notations used in Table 1:

x med +	median value of x parameter one hour before SC (SI)
x quart +	quarter value of x parameter one hour before SC (SI)
x med (.)	median value of x parameter during an hour including SC (SI)
x quart (.)	quarter value of x parameter during an hour including SC (SI)
$\overline{\Delta x}$	average change of x parameter

than decreases after SI with the values of change in both cases being approximately equal.

e. The changes in velocity are not essential. The velocity value before SI is 465 km/sec, i.e., the solar wind is weakly disturbed. The velocity either remains constant or increases.

f. The density does not change, but it is large (5 cm^{-3}).

g. D_{st} is positive before SI, i.e., DR current is small or absent. D_{st} more frequently increases due to SI, i.e., the magnetosphere is compressed. When a small DR current exists before SI, it decreases still more due to SI. However, one can observe the D_{st} decreasing. The decreasing value is considerable and equal to -9.4γ. In this case appearance (or increasing) of DR current is possible.

h. The AE index value is equal to 190γ before SI and 210γ after SI.

According to these obtained and formulated results, shown in Figures 1 and 2 and Table 1, the principal differences between the behaviors of the average parameters for SC and SI consist of the following:

a. The interplanetary magnetic field preceding SI is more intensive. The B value is equal to 7.2γ, exceeding the B value for the quiet solar wind. However, the change of interplanetary magnetic field is larger in the case of SC.

b. The B_z component is negative before SC and positive before SI.

c. The B_x component increases after SC and decreases after SI. The B_x value preceding SC is equal to the one preceding SI.

d. There is a sharp distinction in the behavior of the B_y component due to SC and SI. B_y changes after SI but not after SC.

e. The solar wind velocity before SI exceeds the solar wind velocity before SC. However, more considerable velocity changes are observed after SC, analogous to B behavior.

f. The number density is larger for SI and its value is constant. After SC the number density increases.

g. D_{st} is negative before SC, i.e., the DR current exists and the magnetsophere compression is not too large. Before SI, D_{st} is positive and DR current is small or absent. As a rule D_{st} increases both after SC and after SI.

Thus, before SI the solar wind is weakly disturbed and DR current is either weak or absent. The changes of parameters are not considerable in the case of SI, but the situation is opposite for SC: the parameter changes that take place in the initially quiet solar wind have the largest value.

3. DISCUSSION AND SPECULATION

Individual cases show that there are deviations from the average in the behavior of parameters; however, as a rule, one can observe variations of a range of parameters, and the variations of one of them is compensated by the variation of the others. Taking into account the correlation between the solar wind parameters and the state of the magnetosphere and the cause-effect connection, one can consider another parameter determined by a combination of the above described parameters. The distance to the subsolar point (R_o) and its variation (ΔR_o) may be taken as such a parameter, as the R_o is determined by the state of the solar wind and its variation is proportional to the energy transmitted to the magnetosphere tail independently on the mechanism of

transference (Aubry et al., 1970). Thus, the difference between SI and SC is that for SI the transferred energy is less than for SC (i.e., $\Delta R_{oSC} > \Delta R_{oSI}$).

The estimations of R_o and R_o made for median parameter values according to Shin and Konradi (1975) indicate that the above is true when SC develops in quiet conditions and SI in weakly disturbed ones. This is the average case in which $\Delta R_o \geq 1R_E$ and it is equal to $0.6R_E$ for SI.

If sharper change of solar wind parameters is taken into account, corresponding to the change from the quiet conditions to disturbed ones, the difference in ΔR_o for SC and SI increases and is about $3R_E$. It should be noted that the approximate values of R_o and ΔR_o correspond to real ones, because B_z is positive for SI and its negative value for SC is small, so the field line reconnection and the R_o change due to this process can be neglected.

The existence of the considerable negative B_z component after SC provides the continuous energy transference and makes disturbance development possible during a longer period of time. It probably leads to the magnetic storm. This is the average picture. Individual cases differ variously. For example, one can observe SC when $B_z > 0$. The various individual cases may be explained at least qualitatively in the frame of the following picture. The change of the convection regime occurs due to the changes of the solar wind characteristics including the total magnetic field, its heterogeneity and velocity, density, and viscosity at the magnetospheric boundary. It leads to the electric field directed from dawn to dusk. The existence of electric field results in the accumulation of energy in the magnetospheric tail. Along with this process the energy accumulation is controlled by the sign and magnitude of the B_z component of IMF.

The existence of positive B_z leads to carrying away the magnetospheric plasma to the distant tail due to the plasma drift in perpendicular magnetic and electric fields. The latter appears due to $\vec{E} = (-1/C)[\vec{B} \times \vec{V}]$ and has the opposite direction in comparison with the E field of the convection. Thus, the condition $B_z < 0$ always provides the development of disturbance after SC and SI, in agreement with the results of Jijima (1973), Kokubun (1972), and Kokubun et al. (1977). The development of disturbances when $B_z > 0$ depends on intensity correlation of both processes considered above. The value and the direction of the summarized electric field will determine both the possibility of development of disturbances and the magnetosphere distance at which the region of maximum energy will be localized. One can suggest that this region will be displaced at a large distance from the Earth (to higher latitudes). The characteristics of these disturbances may differ from those of the auroral substorm occurring at auroral latitudes. The displacement of the disturbed region influences the AE index behavior but AE index changes may not be substantial. Such behavior of AE can be observed in any cases of SC and SI. It should be noted that when the activity region is displaced to very high latitudes SC cannot be marked in the IAGA Bulletin because the latitudinal distribution of the station is not uniform.

4. CONCLUSION

Preconditions and changes in solar wind parameters, which lead to an energy increase in the Earth's magnetopshere, are necessary for triggering disturbances after SC and SI. On the average the preconditions and solar wind changes for SC provide the energy increase due to convection strengthening, which is not connected with the existence of negative B_z (the change of R_o

is more than 1 R_E). The quiet solar wind and negative D_{st} (DR current existence) before the impulse are essential in this case for convection strengthening.

Before SI the solar wind is disturbed, D_{st} is either absent or small, and B_z is positive. The change of parameters (D_{st} and solar wind parameter) provides a smaller ΔR_o than in the SC case. The average value of ΔR_o is equal to 0.6 R_E and it is not sufficient for a critical energy increase in the magnetosphere tail.

In certain cases there are deviations from the average values in the investigated parameters (B, B_x, B_y, B_z, V, den, AE, D_{st}). In these cases the possibility of triggering is determined by the correlation between the energy connected with the convection strengthening and that connected with the B_z component. The values of the R_o, B_z, and V magnitudes determines both the probability of triggering and the latitudes at which the maximum disturbance will be observed [with $B_z < 0$ at the ΔR_o value, estimated according to Shin and Konradi (1975), can be considered effective, not including the R_o change caused by the negative B_z existence]. One can observe the displacement of the active region to higher latitudes when B_z is positive and ΔR_o is large.

According to Boller and Stolov (1970), and Russell and McPherron (1973), at certain UT moments the significance of the B_z component can be taken by B_y, expecially when there are considerable changes in the B_y component. However, using data of one year, we did not find any UT dependence for SC or SI.

If $B_z > 0$ for a long time after SI a magnetic storm is impossible because there are no sources and the energy due to convection strengthening due to the impulse is depleted.

The obtained results may be used for the prediction of geomagnetic activity after the impulses. The main points are estimations of the solar wind state and D_{st} value (DR current existence) before impulse and their changes, which permit a determination of R_o and ΔR_o (real or effective). The ratio of the R_o, ΔR_o and B_z values determines the probability of a disturbance developing and the character of the disturbance after the impulse: with $B_z < 0$ the substorm accompanied by all known features is triggered; with $B_z > 0$ the character of the disturbance will be determined by the convection strengthening. The intensity of both disturbance types may be the same (Domingo, 1978).

REFERENCES

Akasofu, S. I., P. D. Perreault, F. Yasuhara, and C. I. Meng (1973): Auroral substorms and interplanetary magnetic field. J. Geophys. Res., 78:7498-7508.

Aubry, M. F., C. T. Russell, and M. G. Kivelson (1970): Inward motion of the magnetopause before a substorm. J. Geophys. Res., 75:7018-7031.

Boller, B. R., and H. T. Stolov (1970): Kelvin-Helmholtz instability and the semiannual variation of geomagnetic activity. J. Geophys. Res., 75:6073-6083.

Brown, R. R. (1967): Auroral-zone electron precipitation accompanying a sudden impulse in the geomagnetic field. J. Geophys. Res., 72: 2448-2451.

Burch, J. L. (1972): Preconditions for the triggering of polar magnetic substorms by storm sudden commencement. J. Geophys. Res., 77: 5629-5632.

Burlaga, L. F. (1975): Interplanetary streams and their interaction with Earth. Space Sci. Rev., 17:327-352.

Burlaga, L. F., and K. W. Ogilvie (1969): Causes of sudden commencements and sudden impulses. J. Geophys. Res., 74:2815-2825.

Chao, J. K., and R. Lepping (1974): A correlative study of SCs, interplanetary shocks and solar activity. J. Geophys. Res., 79:1799-1807.

Domingo, V. (1978): Interplanetary magnetic field and geomagnetic activity. COSPAR: Space Research, Volume 18, Pergamon Press, Oxford and New York, p. 325-328.

Gosling, J. T., J. R. Asbridge, S. J. Bame, A. J. Hundhausen, and I. B. Strong (1967): Discontinuities in the solar wind associated with sudden geomagnetic impulses and storm commencements. J. Geophys. Res., 72: 3357-3363.

Hirsberg, J., A. Alksne, D. S. Colburn, S. J. Bame, and A. J. Hundhausen (1970): Observation of a solar flare indiced interplanetary shock and helium enriched driver gas. J. Geophys. Res., 75:1-15.

IAGA Bulletin (1969): Geomagnetic data, rapid variations, no. 12.

Jijima, T. (1973): Interplanetary and ground magnetic conditions preceding SSC-triggering substorms. Rept. Ion. Space Res. Japan, 27:205-208.

Kawasaki, K., S.-I. Akasofu, F. Yasuharu, and C. I. Meng (1971): Storm sudden commencements and polar magnetic substorms. J. Geophys. Res., 76:6761-6789.

King, J. H. (1977): Interplanetary medium data book--appendix, NSSDC/WDC-A-R&S 77-04 A.

Kokubun, S. (1972): Relationship of the interplanetary magnetic field structure with development of substorm and storm main phase. Plan. Space Sci., 20:1033-1050.

Kokubun, S., R. L. McPherron, and C. T. Russell (1977): Triggering of substorms by solar wind discontinuities. J. Geophys. Res., 82: 74-85.

Moldovanu, A. (1974): Geomagnetic effects of interplanetary sector structure. Planet. Space Sci., 22:193-208.

Nishida, A. (1975): Interplanetary field magnetic effect on the magnetosphere. Space Sci. Rev., 17:353-389.

Nishida, A. (1964): Sudden impulses in the magnetosphere observed by Explorer 12. J. Geophys. Res., 69:2243-2255.

Ohdoh, T. (1970): Magnetospheric sudden impulses. J. Rad. Res. Lab., 17: 199-213.

Rigby, B. J., and J. S. Mainstone (1975): Characteristics of sudden worldwide changes in the geomagnetic field. J. Atmos. Terr. Phys., 78:92-108.

Russell, C. T., and R. L. McPherron (1973): Semiannual variation of geomagnetic activity. J. Geophys. Res., 78:92-108.

Shieldge, J. P., and G. L. Siscoe (1970): A correlation of the occurrence of simultaneous sudden magnetospheric compressions and geomagnetic bay onset with selected geophysical indices. J. Atmos. Terr.Phys., 32:1819-1830.

Shin, Yi-su, and A. Konradi (1975): Magnetic field depression at the Earth surface calculated from the relationship between the size of the magnetosphere and D_{st} values. J. Geophys. Res., 80:195-199.

WORKING GROUP REPORT ON GEOMAGNETIC STORMS

Dr. S.-I. Akasofu
Geophysical Institute, University of Alaska
Fairbanks, Alaska 99701

1. Task definition

The task of WGB2 is to provide the scheme for the best prediction procedures of the occurrence, intensity and time development of a geomagnetic storm for a given flare and a given coronol hole by using the presently available knowledge. The group is charged to provide a set of recommendations for improving the prediction procedures. For practical purposes, a geomagnetic disturbance is defined as a geomagnetic storm when the local K index exceeds K = 5 and/or when the Dst value exceeds 100γ.

2. Solar flare associated storms

2.1 Prediction of the onset time

According to an extensive statistical study, the transit time of the blast wave, namely the time interval between flare onset and storm onset (defined by onset time of the storm sudden commencement, SSC), is about 43 hrs; (see Fig. 1). However, when solar flares are successively generated, the blast wave generated by the second and later flares propagate much faster than the first wave. Thus, the transit time can become as short as 25 hrs. There does not seem to be any significant dependence of the transit times on the central meridian distance of the responsible flares, suggesting that the blast wave is, as a first approximation, a spherical wave.

2.2 Expected maximum intensity of the main phase decrease

Fig. 2 gives the dependence of the Dst decrease as a function of the central meridian distance of the responsible solar flares. The envelope of the plot can provide the expected maximum intensity of the Dst decrease. Solar flares associated with PCA are marked by a circle with a dot. Note that Dst decreases of more than 100γ are caused by flares which are located roughly between 45° E and 70° W. It can also be seen that PCA flares tend to produce more intense Dst decreases than those without PCA.

2.3 Time-development of geomagnetic storms

The arrival of the blast wave to the magnetosphere (thus, the occurrence of SSC) does not necessarily mean that a (typical) geomagnetic storm develops. There is a great variety of the development of geomagnetic storms. Some storms are associated with a large SSC (see the top example in Fig. 3), but with no main phase. Some other storms develop a large Dst decrease

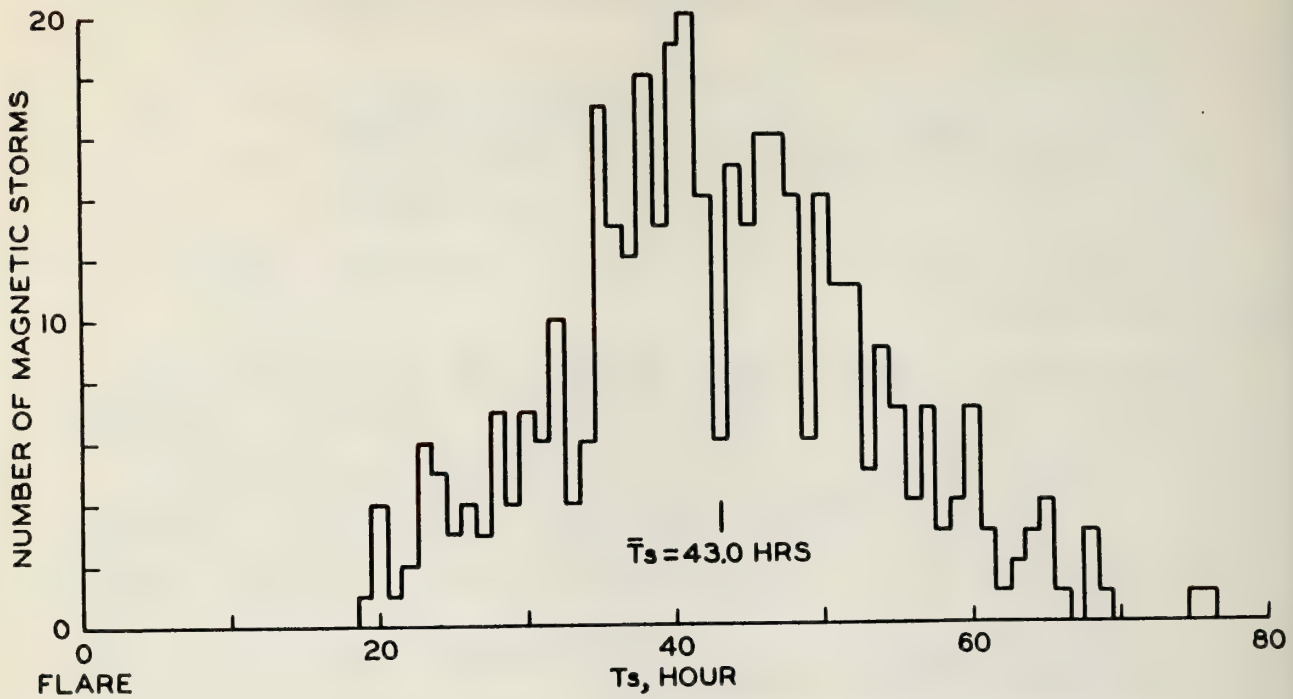


Fig. 1 Akasofu, S.-I. and S. Yoshida, Planet. Space Sci., 15, 39, 1967.

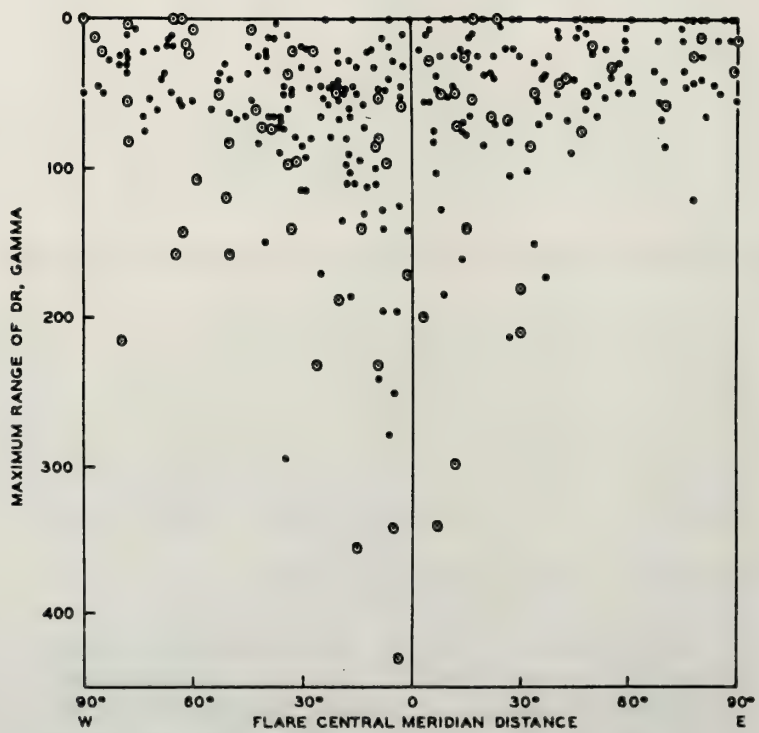


Fig. 2 Akasofu, S.-I. and S. Yoshida, Planet. Space Sci., 15, 39, 1967.

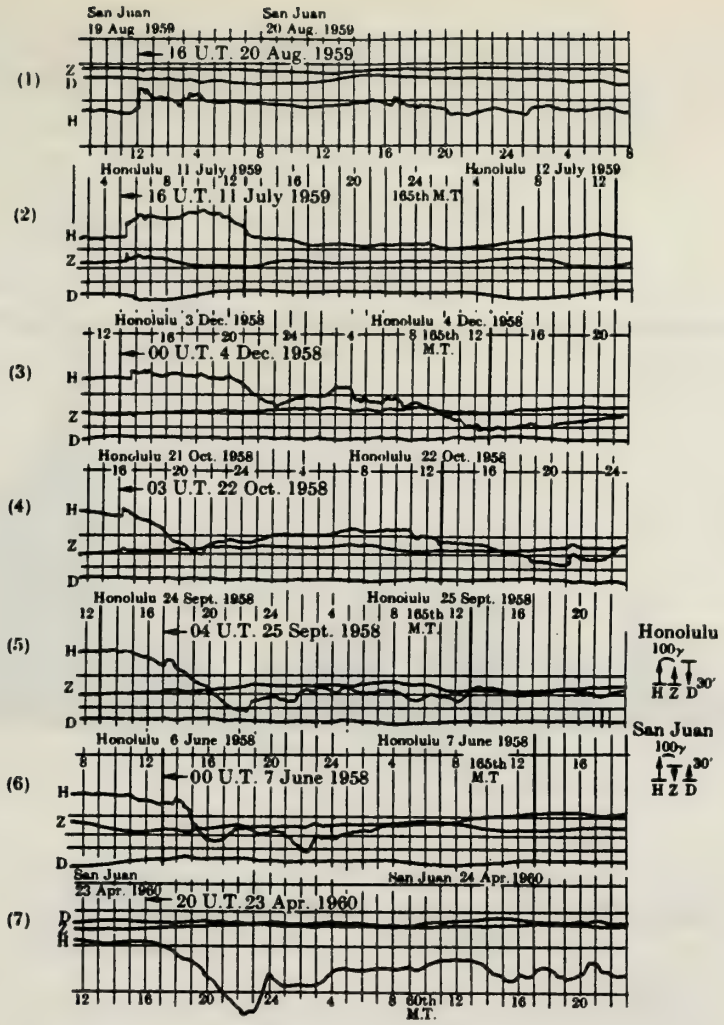


Fig. 3. Akasofu, S.-I. and S. Chapman, Solar-Terrestrial Physics, Oxford Univ. Press, 1972.

without any distinct SSC (See the bottom example in Fig. 3). Between these two extreme cases, there is a variety of time developments. The period between the SSC and the main phase onset is called the initial phase during which a low latitude H component record shows a steady positive change (like a step-function). Some geomagnetic storms have more than 10 hrs. of the initial phase, and some others have the initial phase of only 1 hr. or less.

An important task of our WG is to find out whether or not one can predict how a geomagnetic storm will develop for a given flare. This is because major auroral activity is concentrated during the main phase of a geomagnetic storm, in particular during the period when the main phase is rapidly growing and because major auroral activity causes serious ionospheric disturbances, power line disturbances, etc.

This can be seen in Fig. 4 in which both auroral activity (expressed by the AE index) and the development of the main phase (expressed by the DST index) for the July 8-9, 1958, storm are shown.

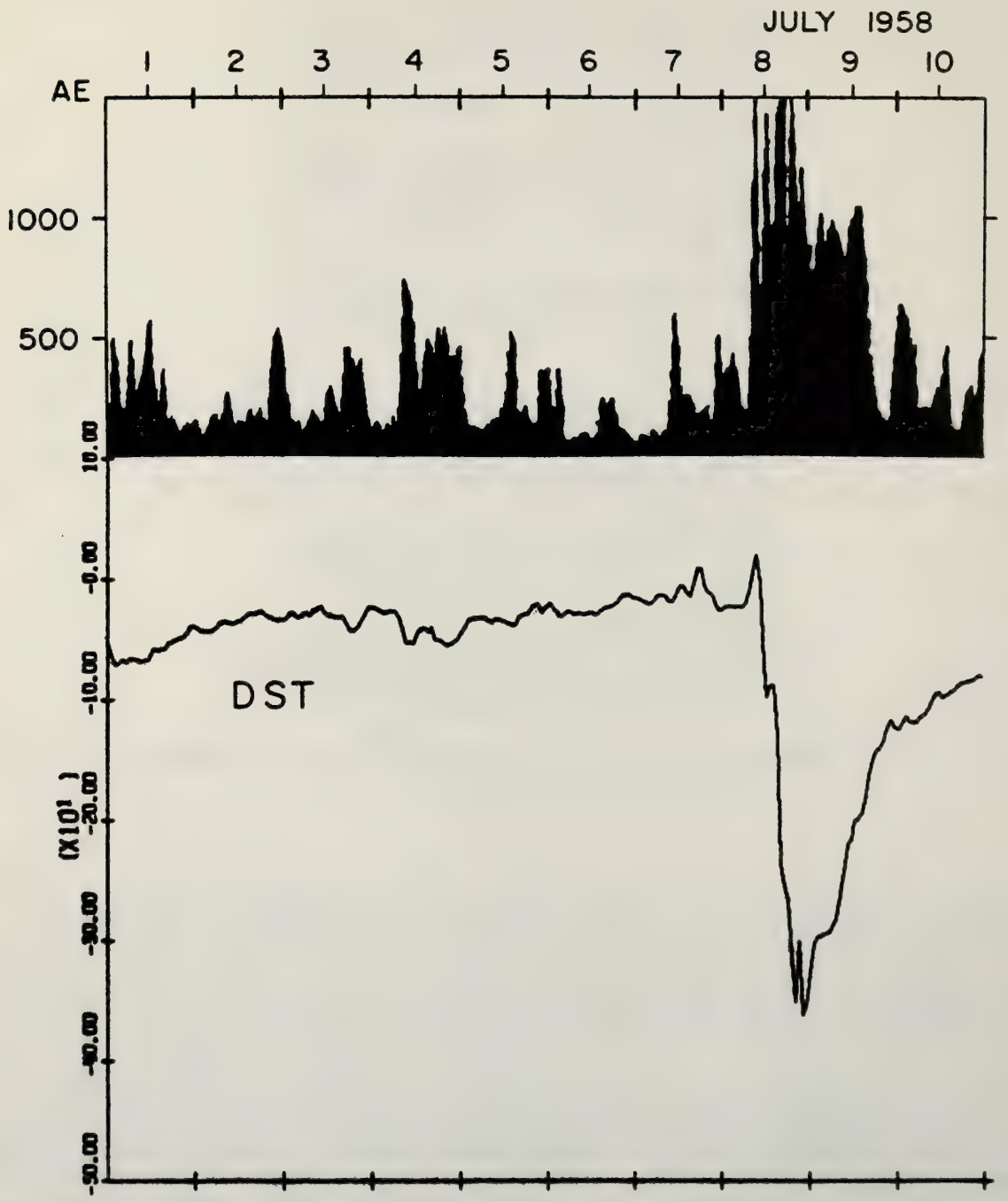


Fig. 4 Akasofu, S.-I. and S. Chapman, Solar-Terrestrial Physics, Oxford Univ. Press, 1972.

The importance of predicting the onset of the main phase can be seen in Figs. 5a and 5b. They show from the top, the power line fluctuations (the GVEA line near Fairbanks, Alaska; 138KV, 100 A; 166km length, approximately stretched along a gm meridian), the so-called 'earth current' record measuring the ground electric field induced by auroral activity) and the H component records on September 29, 1978, 02 - 19UT, (16-24 Alaska Standard Time (AST), Sept. 28; 0 - 9 AST, September 29). One can see, first of all, that most of the power line fluctuations were caused by auroral activity. Secondly, the main phase of this particular storm began at about 07 - 08UT Sept. 29, and the power line fluctuations began to increase considerably at about 07 UT.

2.4 Solar wind parameters controlling the development of the main phase

One can see from the above discussion that our task is reduced to find a solar wind parameter which controls the development of the main phase during which auroral activity becomes intense.

It is important, first of all, at this point to examine the most appropriate magnetospheric quantities which represent the intensity of geomagnetic storms. The two important 'products' of a geomagnetic storm are the Joule heat produced in the auroral ionosphere ring current particles. Here, we denote the Joule heat production rate by U_J and the ring current injection rate by U_R.

It has been found that the solar wind parameter ε defined (see Fig. 6) by $\varepsilon = VB^2 \sin^4\frac{\theta}{2} \ell_0^2$ (erg/sec) is reasonably well correlated with $U = U_J + U_R$ (erg/sec) where:

V = the solar wind speed

B = the magnitude of the interplanetary magnetic field

$\theta = \tan^{-1}(|By/Bz|)$ for $Bz>0$

$\theta = 180° - \tan^{-1}(|By/Bz|)$ for $Bz<0$

Fig. 7 shows an example of this correlation for the storm of Feb. 7-8, 1967. Fig. 8a is a good example to show that the solar wind parameter ε does indeed control the development of the main phase. After the SSC of Sept. 23, 1966, storm at 09 UT, the main phase did not develop until about 15 UT (see the AE index). A large increase of the AE index was associated with the simultaneous increase of ε at that time. One should keep in mind that in searching the solar wind parameter it is essential to correlate it with $U = U_J + U_R$. A good prediction must be based on sound physics, and it is physically meaningless to correlate it with U_J alone, since $U_R \geq U_J$.

2.5 Need of monitoring the solar wind parameter

The above study indicates strongly that one can predict the time development of geomagnetic storms by monitoring the solar wind parameter ε.

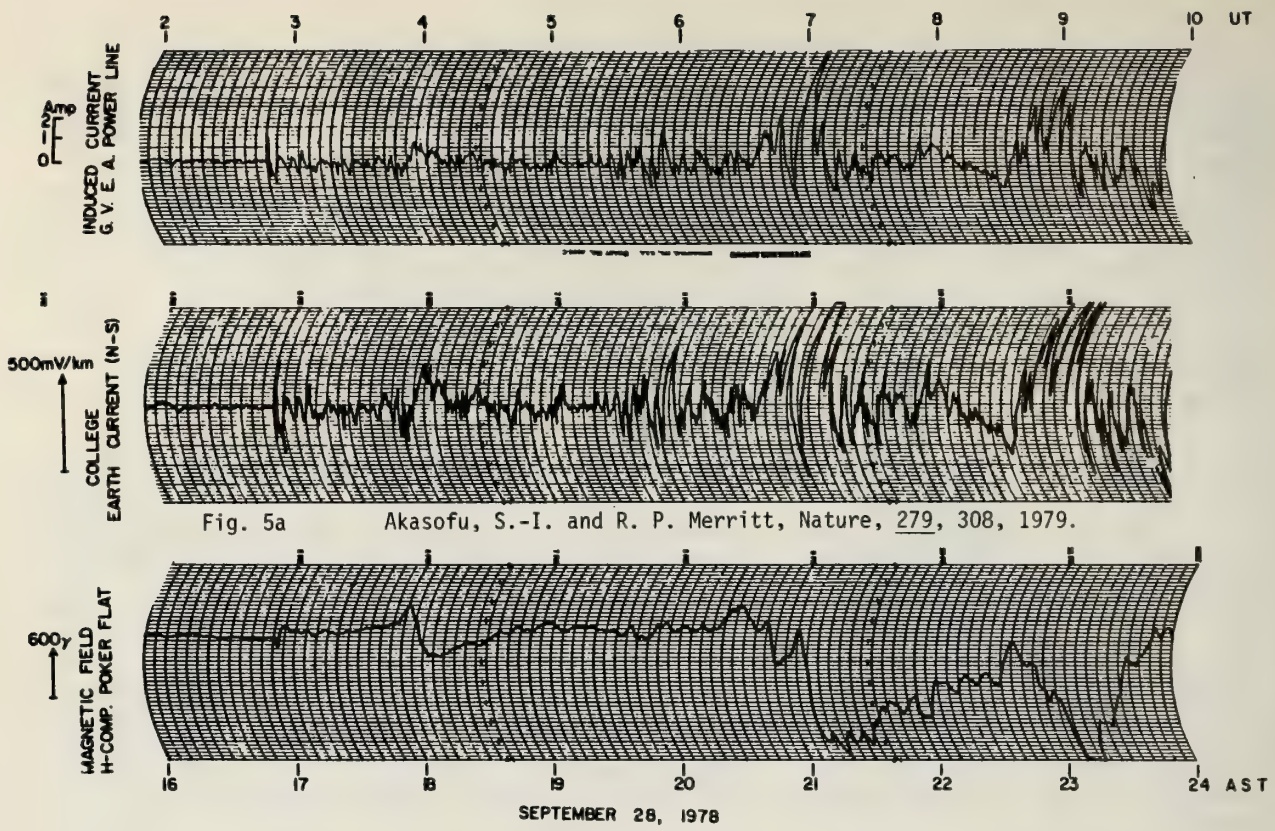


Fig. 5a Akasofu, S.-I. and R. P. Merritt, Nature, 279, 308, 1979.

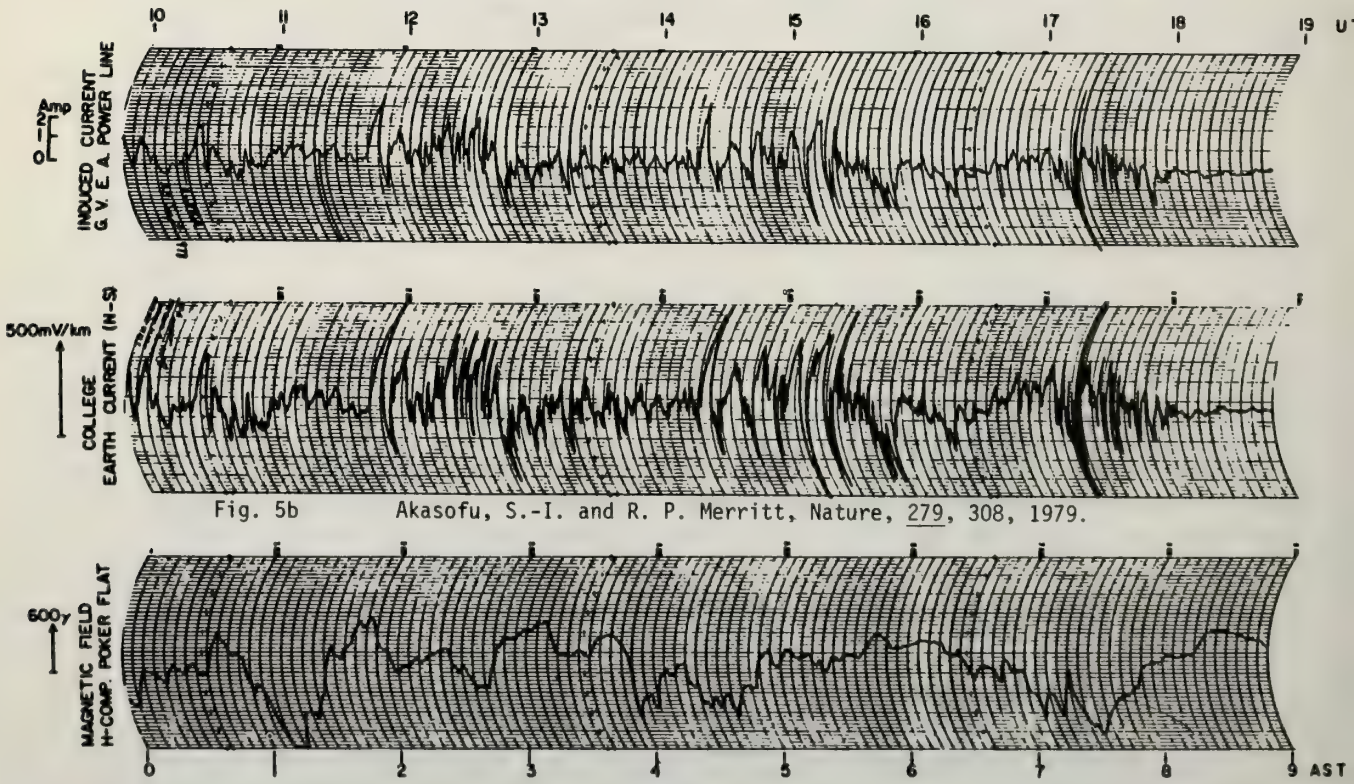


Fig. 5b Akasofu, S.-I. and R. P. Merritt, Nature, 279, 308, 1979.

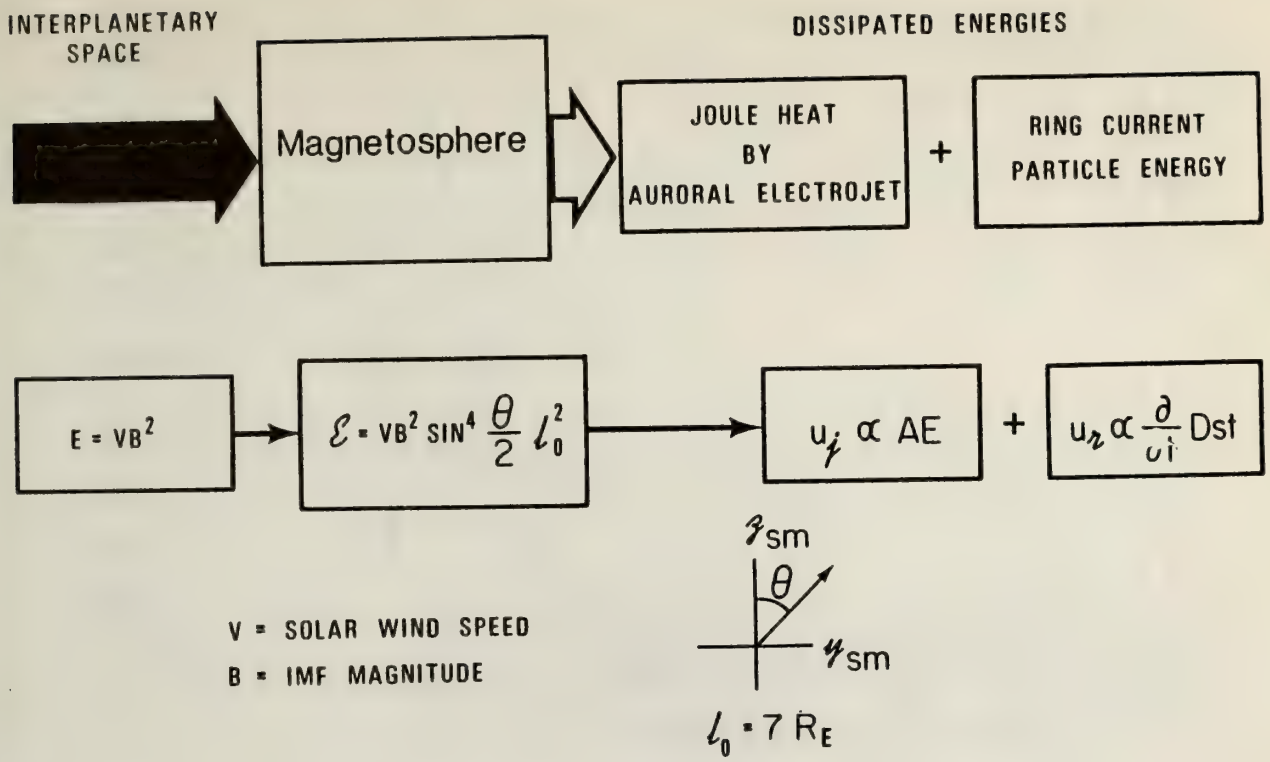


Fig. 6

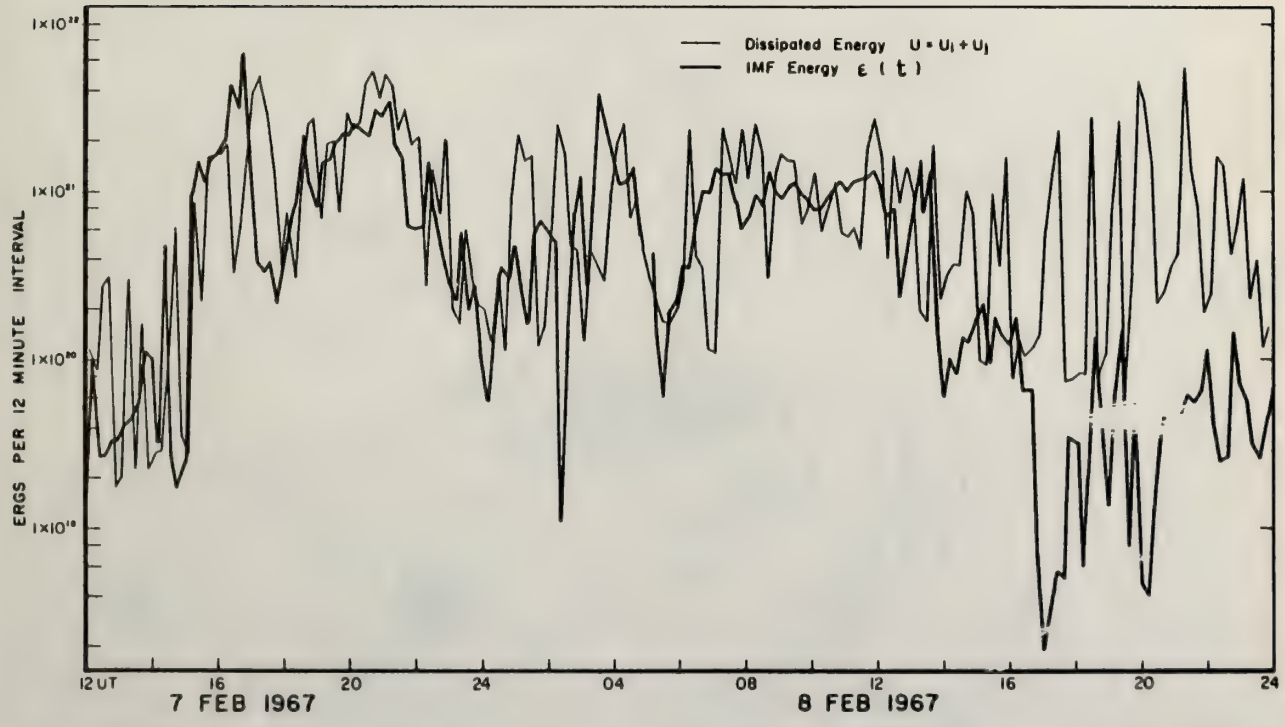


Fig. 7 Perreault, P. and S.-I. Akasofu, Geophys. J. Roy. Astr. Soc., 54, 547, 1978.

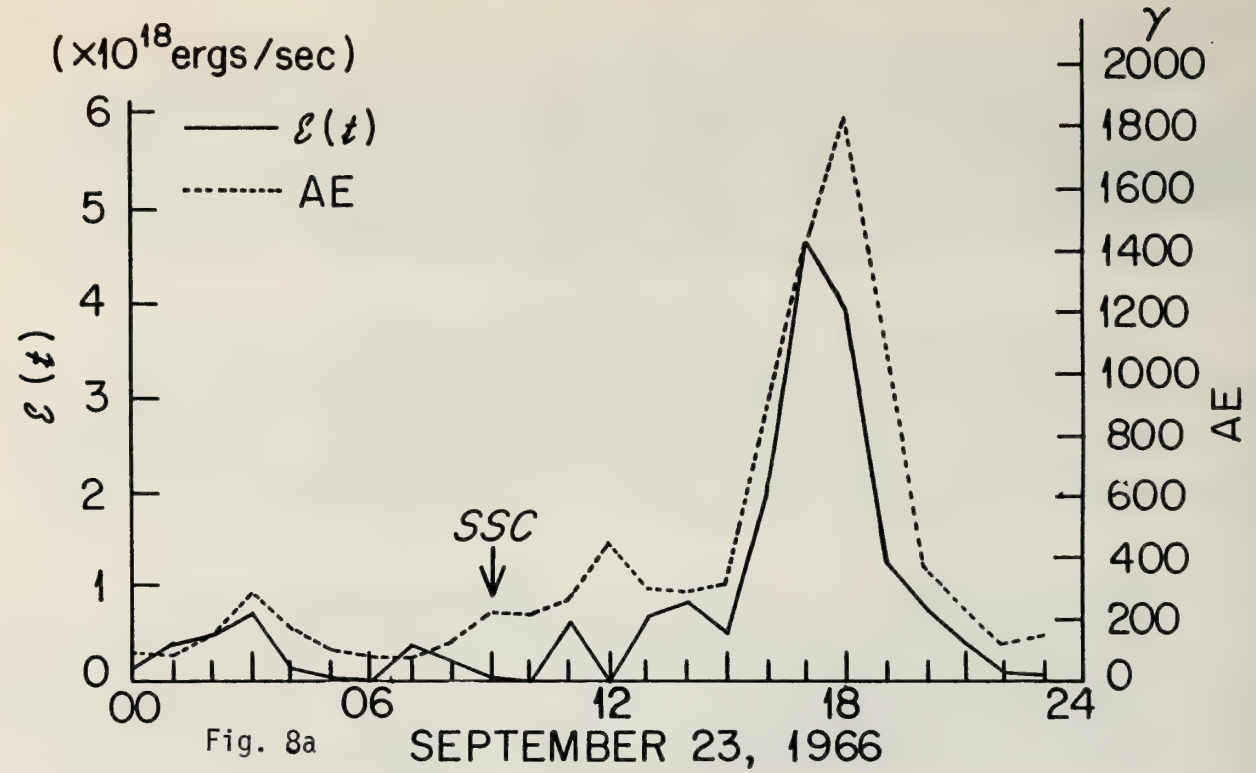


Fig. 8a

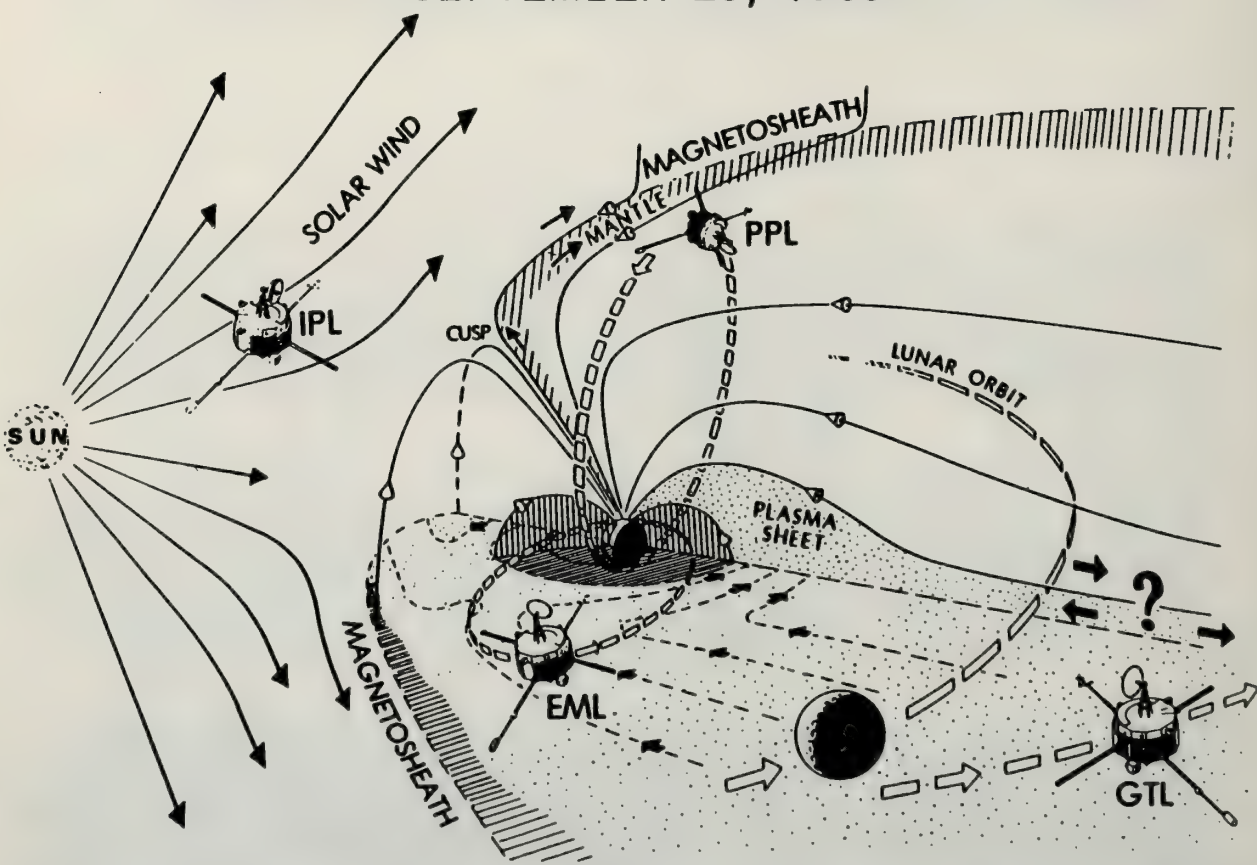


Fig. 8b Origin of Plasmas in Earth's Neighborhood, Goddard Space Flight Center, NASA, April, 1979.

Although it is not shown here, a number of geomagnetic storms were examined in terms of time variations of ε. Geomagnetic storms with a large SSC, but without a significant main phase, were associated with small values of ε.

It is recommended that the ISEE/C satellite data be released for monitoring ε on real time basis. It is recommended also that the IPL satellite of the OPEN program is partly dedicated in monitoring ε (See Fig. 8). It is also proposed that the exact functional form of this energy coupling function be determined by future effort, in proving the expression of ε.

3. Numerical simulation technique

It was shown in the previous section that we have now the first approximation expression for the energy coupling function ε and that it is possible to predict the development of geomagnetic storms by monitoring ε. The ISEE/C satellite at the libration point will be an ideal location for the purpose.

However, the solar wind 'signal' from the libration point to the magnetosphere will take only about one hour or so. Therefore, it is desirable to find other methods to infer the development of geomagnetic storms, if possible, well before the arrival of the blast wave. It is suggested here that the numerical simulation technique should be developed for this purpose.

Before explaining this technique, some preparation is needed. First of all, it has become increasingly apparent that the sun has a Jupiter-like magnetosphere, together with an extensive equatorial current disk (see Fig. 9). However, the solar current disk is not flat. It has an azimuthal large-scale wave structure, so that as the sun rotates with a period of 27, the earth will be located above the current disk during certain periods and below it during the rest. This seems to be a better way of explaining the so-called 'sector structure' of the interplanetary magnetic field. Furthermore, the 'root' of the current disk is not located along the solar equator (Hundhausen). Fig. 10 shows the root of the current disk during the Carrington Rotation period 1616 (the thick line which connects the brightest region of the solar corona in the lower figure). It shows also the distribution of the magnetic polarity on the solar disk and at 1 au (together with the solar wind speed).

When a blast wave is generated on the solar disk by a solar flare (Fig. 11), it will generate a large-scale wave in the radial direction. Fig. 12a shows schematically the wavy current disk at about 15 UT on July 5, 1974. The inferred meridian cross-section of the solar current disk during the July 4 - 5, 1974, storm is shown in Fig. 12b. Note that the situation in Fig. 12a is shown in the fourth cross-section from the top. When the root of the current disk is located in the southern hemisphere, a large main phase develops if the earth is located below the wavy current disk (because the B_z component is negative and θ in ε become large); See Fig. 13. On the other hand, if the root of the current disk is located in the northern hemisphere, a large main phase tends to develop if the earth is located above the current disk for the same reasons.

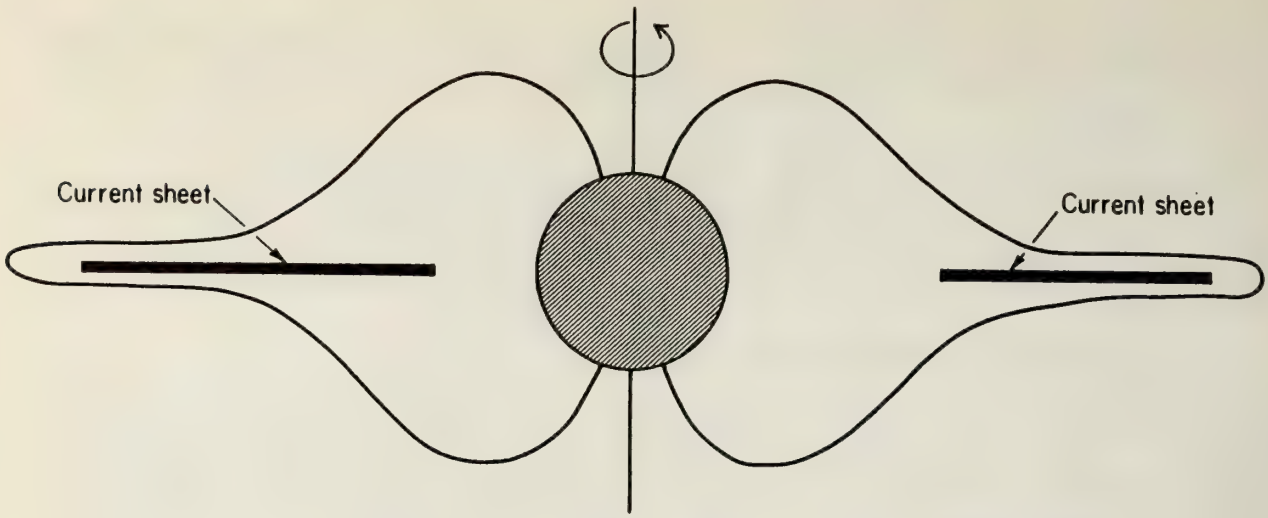


Fig. 9 Akasofu, S.-I., Space Sci. Rev., 21, 489, 1978.

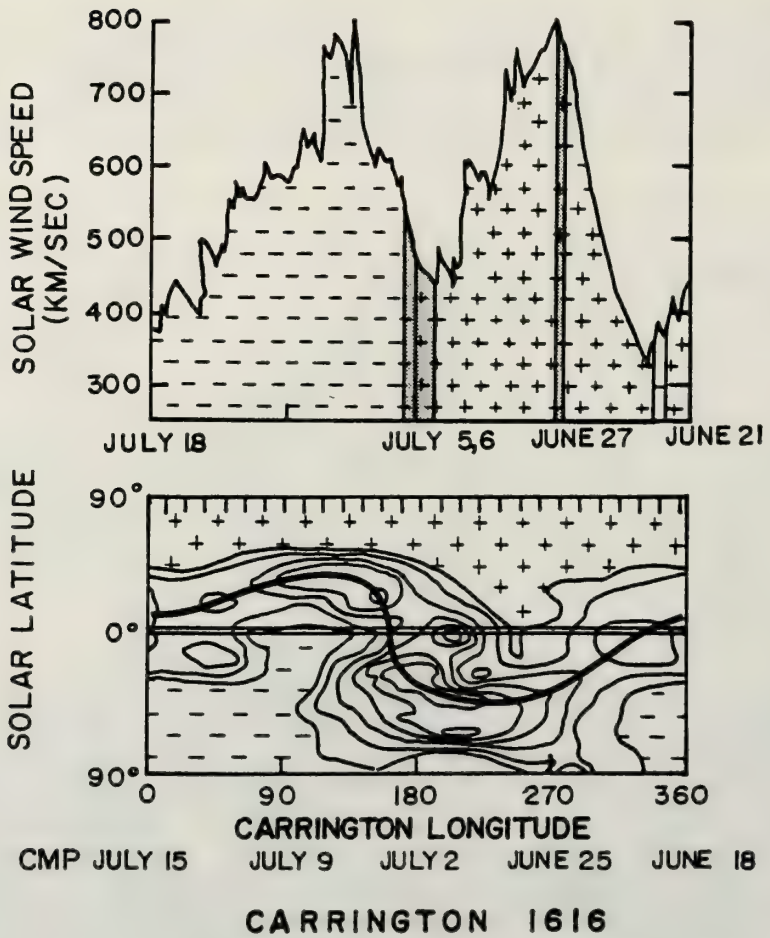


Fig. 10 Hundhausen, A. J., Coronal Holes and High Speed Wind Streams, Colorado Assoc. Univ. Press, 1977.

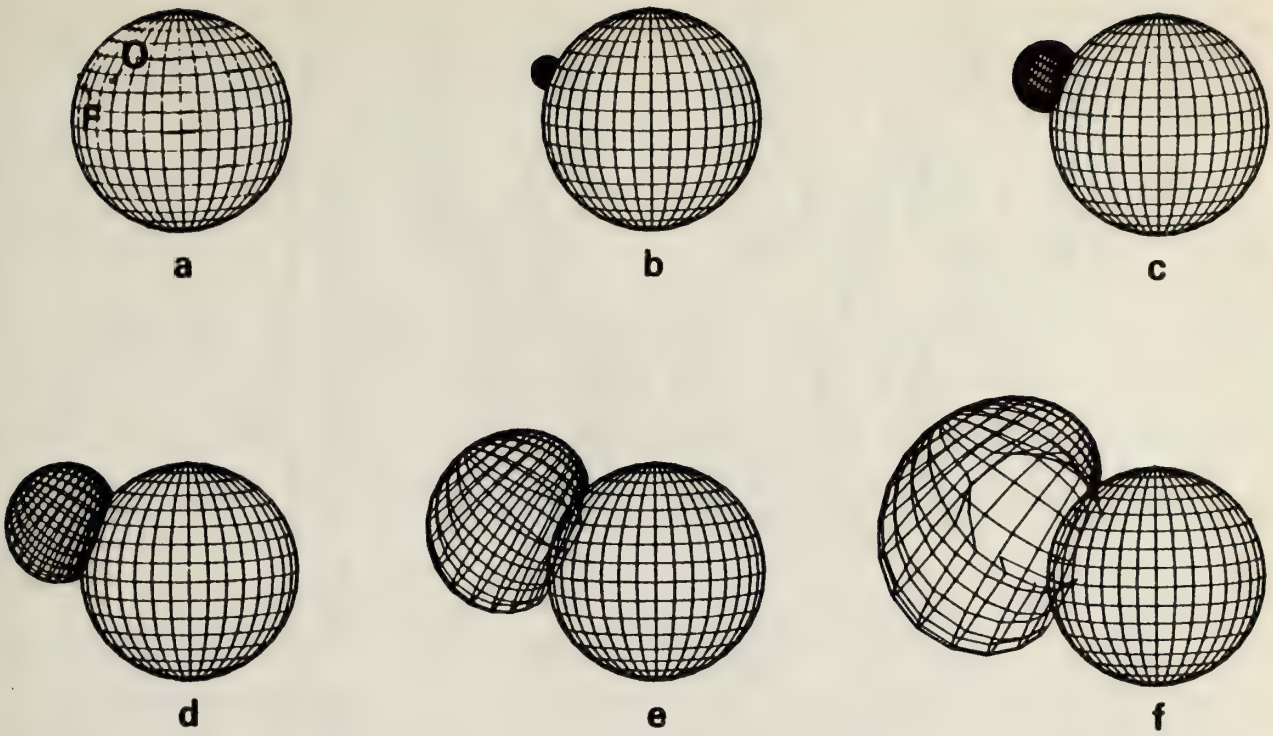
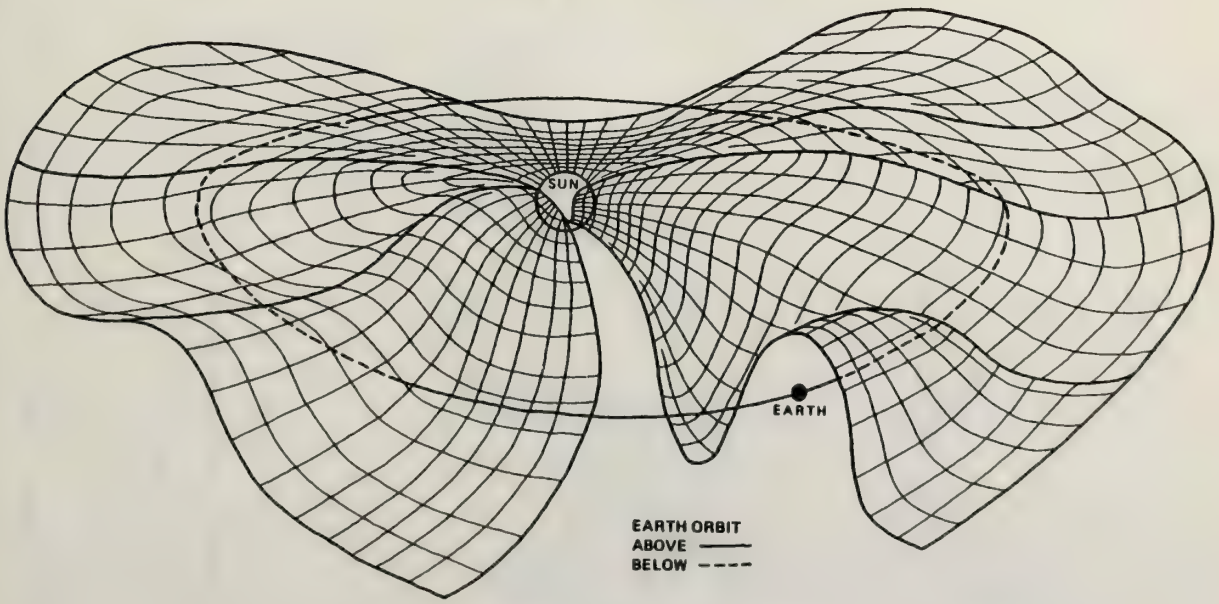


Fig. 11 Uchida, Y., M. D. Altschuler and G. Newkirk, Jr., Solar Phys., 28, 495, 1973.



THE SOLAR CURRENT SHEET

Fig. 12a Akasofu, S.-I., Planet. Space Sci., 27, 1055, 1979.

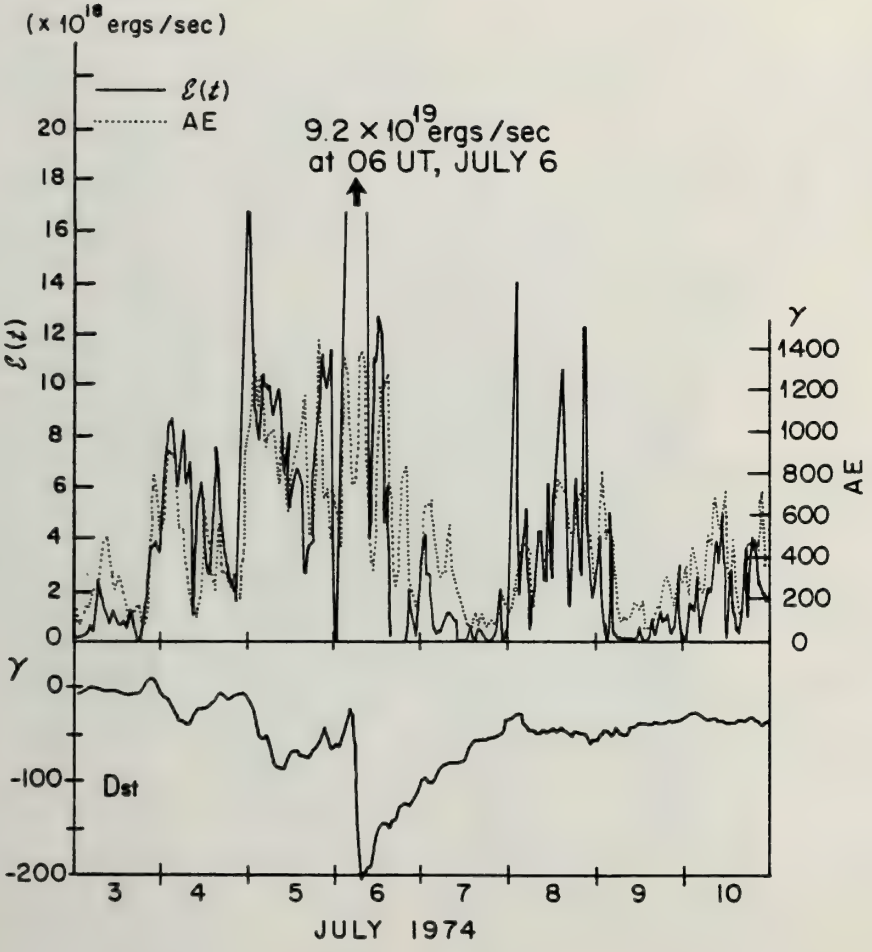


Fig. 13

Akasofu, S.-I., Planet. Space Sci., 27, 1039, 1979.

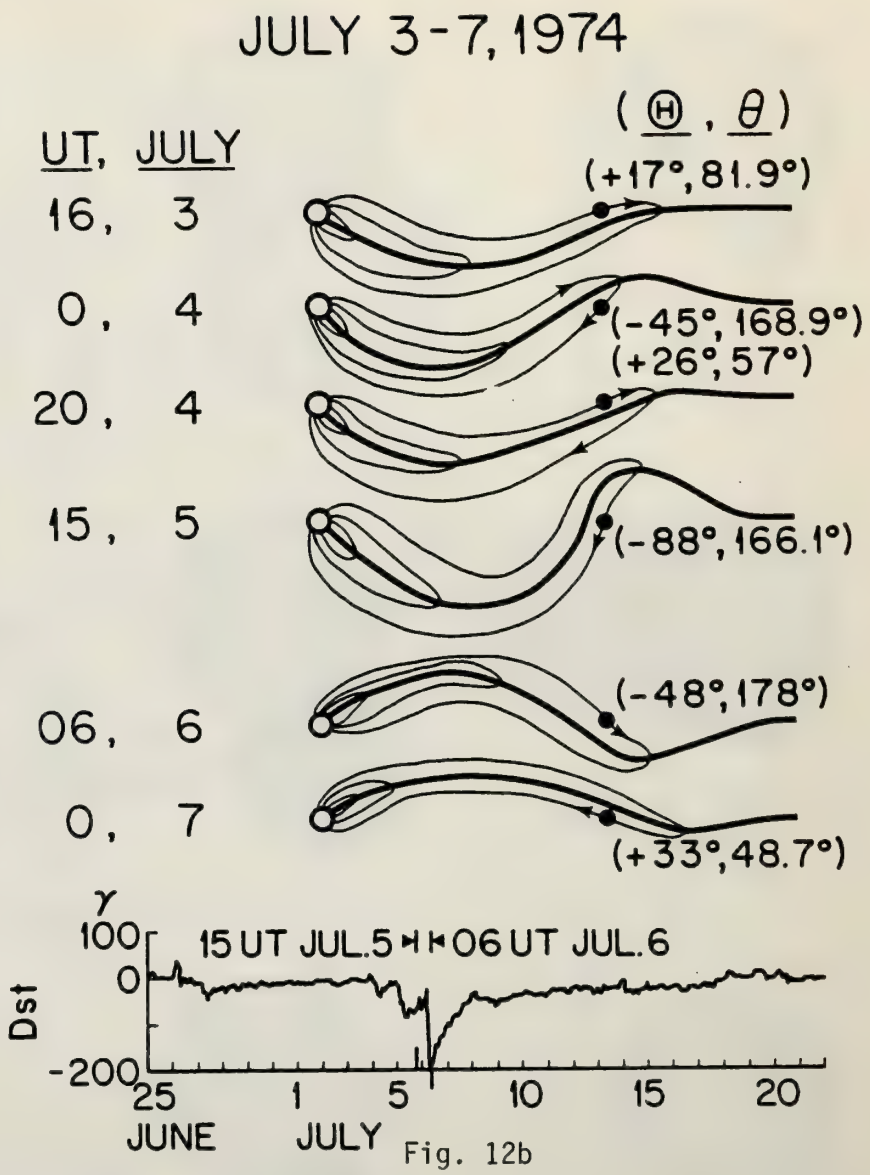


Fig. 12b

Akasofu, S.-I., Planet. Space Sci., 27, 1055, 1979.

Interplanetary magnetic field variations during a number of geomagnetic storms were examined, and it has been demonstrated that is 'wave' interpretation is more consistent with other interpretations, such as 'tangled magnetic fields' in the ejected cloud from the sun or the 'stretched sunspot fields' by the solar stream. The presence of the suggested magnetic field configuration of the sun has recently been demonstrated by tracing solar magnetic field lines by using the Type III burst field line tracing technique (Fig. 14).

The above study suggests that if one could successfully simulate numerically the generation of the waves on the solar current disk, it will become possible to predict the development of a geomagnetic storm well before the arrival of the blast wave. If so, one could estimate time variations of $\varepsilon(t)$ well before the arrival of the blast wave and thus of the time development of geomagnetic storms on the basis of the numerical simulation. In fact, the monitoring of $\varepsilon(t)$ at the libration point will become the 'last check' for the prediction.

In the next section, it will be shown that such a simulation technique has successfully made in the equatorial plane (Dryer and Wu).

It is recommended therefore that every possible information on interplanetary, solar wind condition and the geometry of the solar disk be obtained as initial conditions in the numerical simulation (the interplanetary scintillation method, Solar radio Type II, IV bursts, solar protons, type IV burst field line tracing, etc.). Soon after the flare onset, the numerical simulation can be initiated by generating the blast wave from the flare location.

4. Coronal-hole associated storms

The solar wind structure associated with a high-speed solar wind stream originating from the coronal hole has extensively been studied (Fig. 15). However, there is no obvious relationship of the solar wind quantities, such as T, N, V, F and P independently with the AE index. This lack of correlation is illustrated in Fig. 16.

However, there is a good correlation between ε and the AE index (see Fig. 17). Therefore, coronal hole-associated storms can also be monitored by monitoring ε at the libration point. It is important to note that the solar wind parameter ε is applicable to both flare-generated storms and coronal hole-generated storms.

Coronal hole-associated storms are relatively easier to predict because of its 27-day recurrence tendency (compared with flare-generated storms). Therefore, by monitoring carefully previous recurrence of a high speed solar wind stream (Fig. 18), one can infer approximately the onset date. Actually, the cause of a coronal hole-associated storm is basically the same as a flare-generated storm in terms of the wavy structure of the solar current disk (Fig. 19). The numerical simulation of the high speed solar wind streams in the equatorial plane has been conducted by Dryer and Wu. Their results can reproduce well the observed change in the equatorial

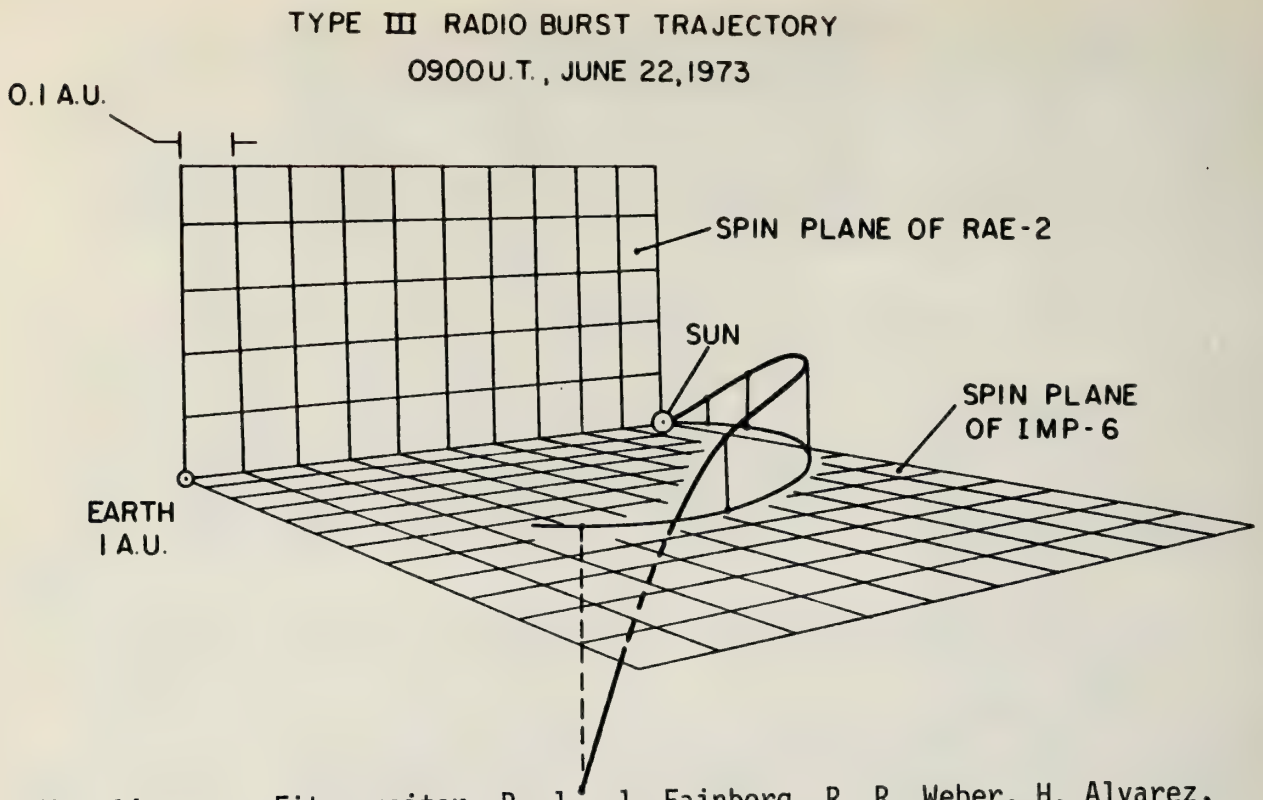


Fig. 14 Fitzenreiter, R. J., J. Fainberg, R. R. Weber, H. Alvarez, F. T. Haddock and W. H. Potter, Solar Phys., 52, 477, 1977.

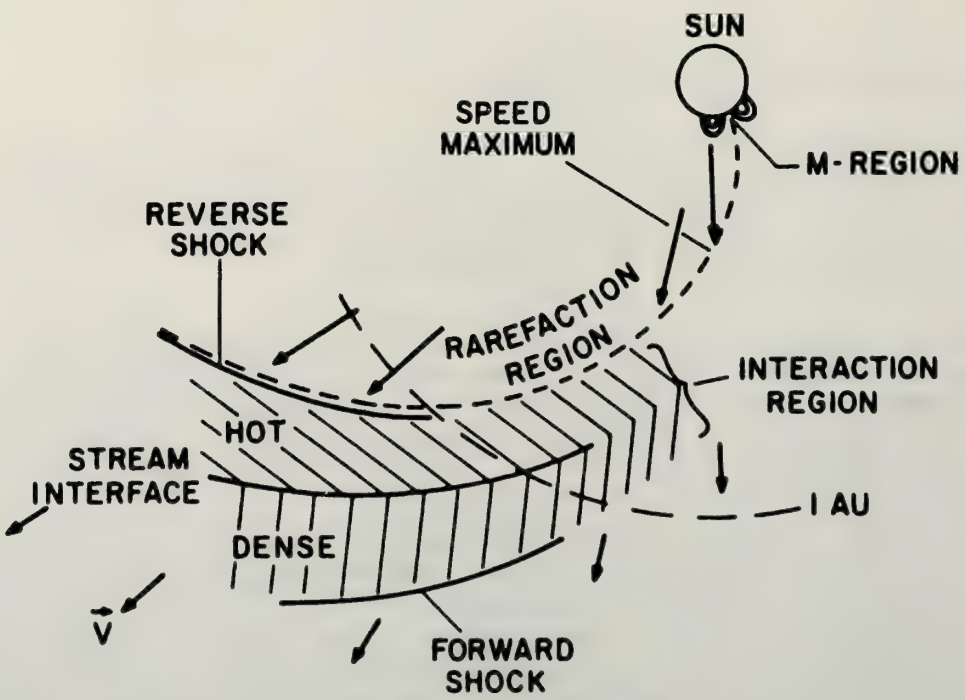


Fig. 15 Burlaga, L. F., Space Sci. Rev., 17, 327, 1975.

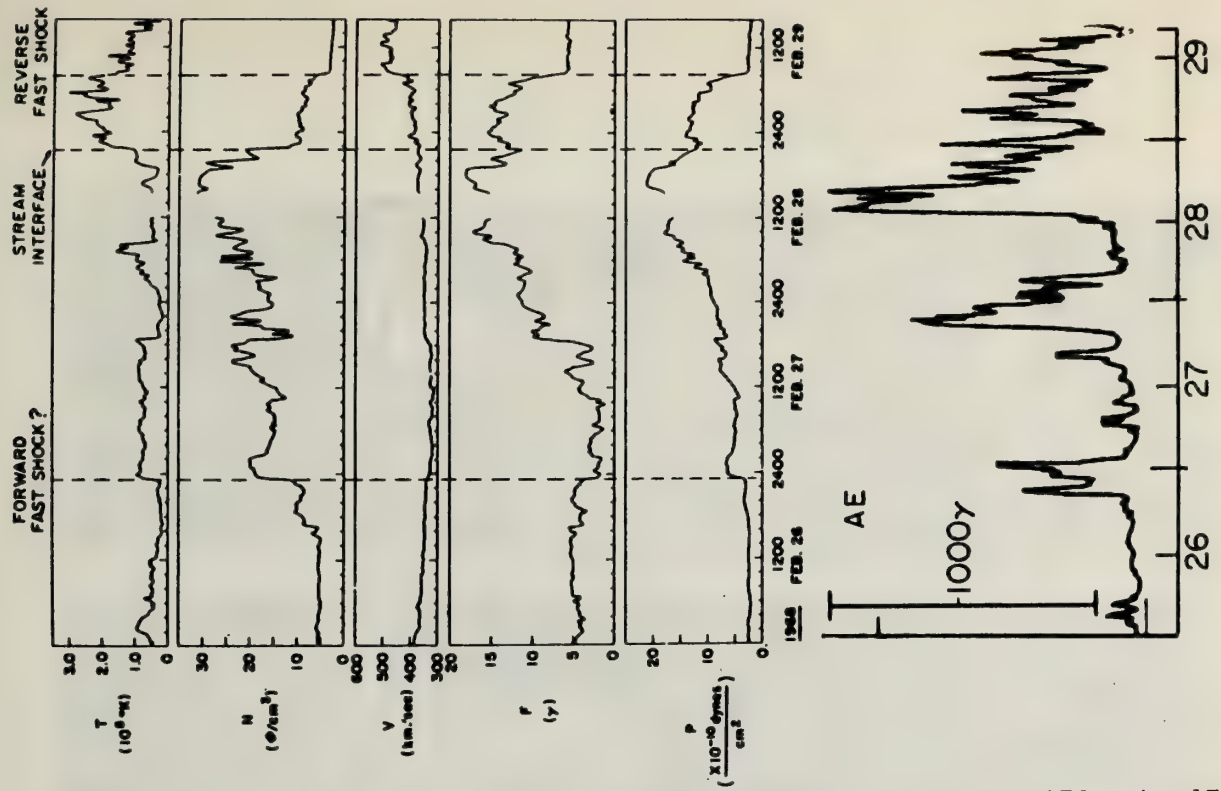


Fig. 16 Burlaga, L. F., J. Geophys. Res., 79, 3717, 1974; the AE index is added.

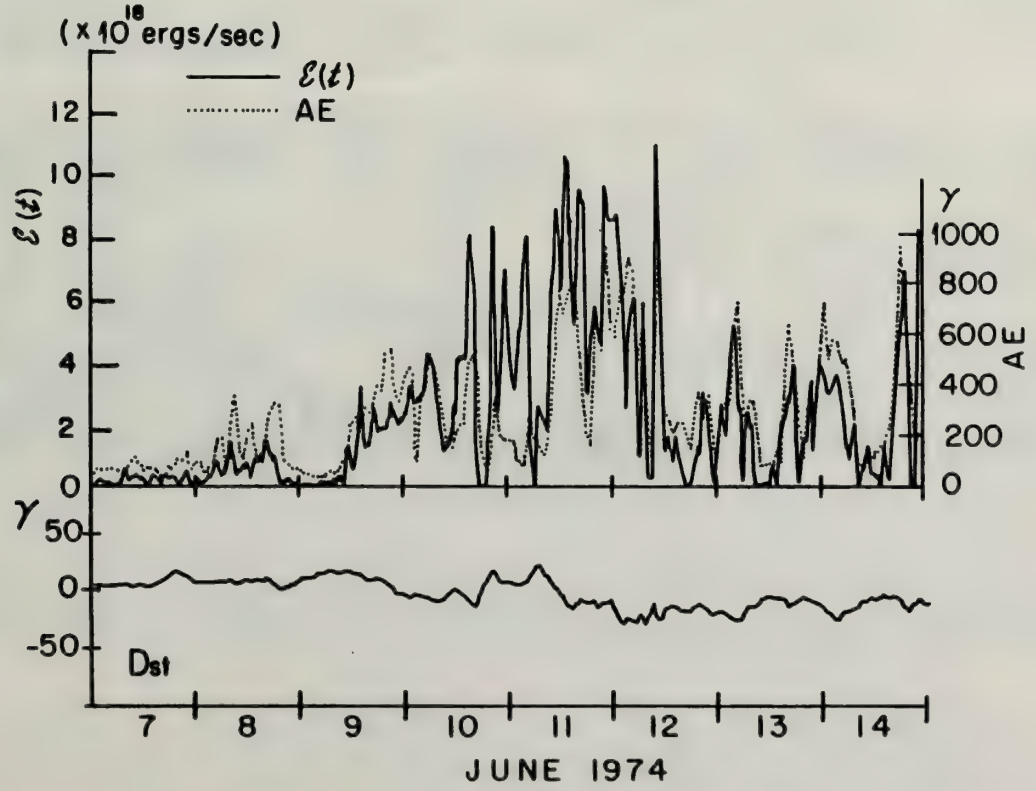


Fig. 17 Akasofu, S.-I., Planet. Space Sci., 27, 1039, 1979.

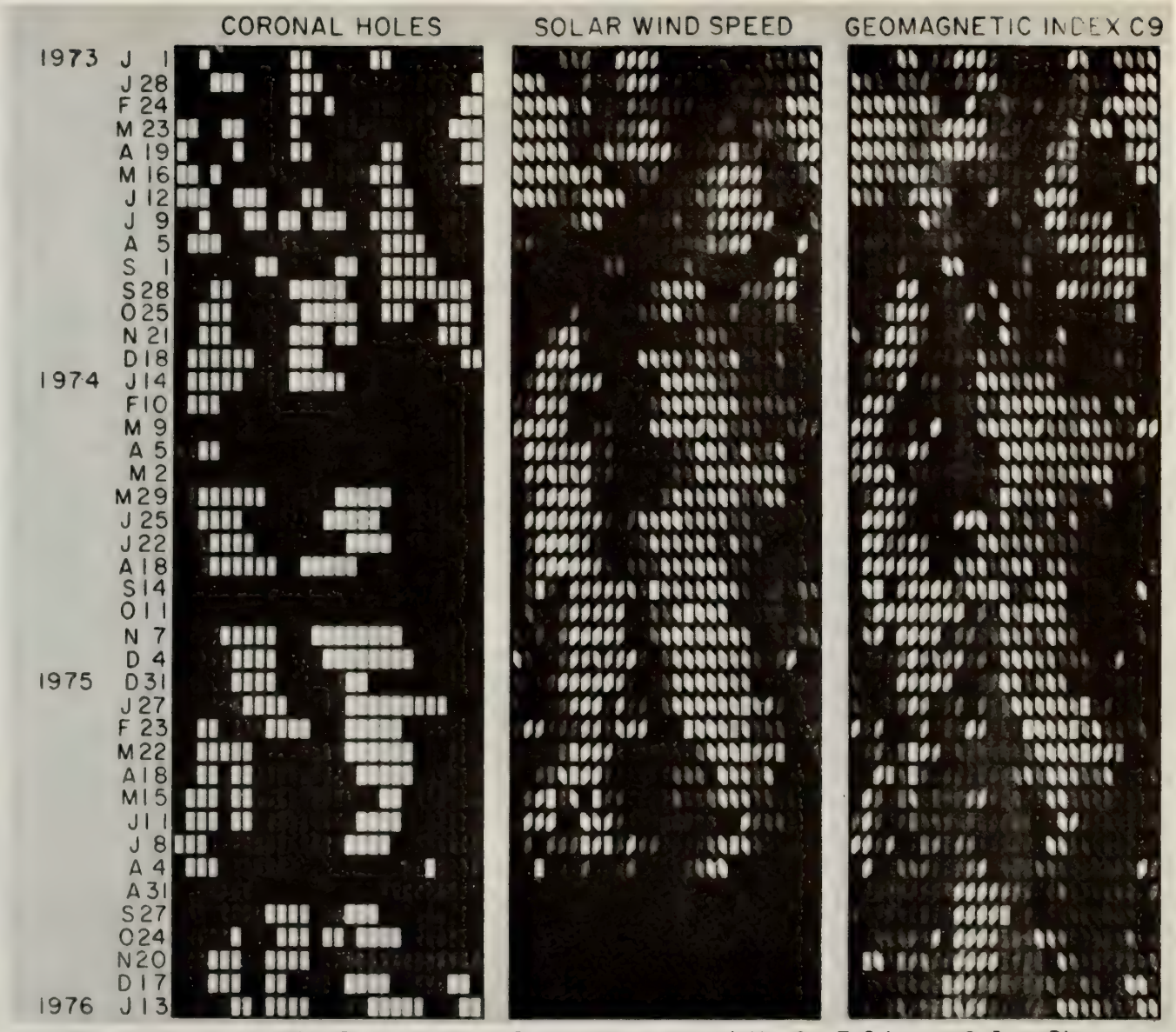


Fig. 18 Sheeley, N. R., J. W. Harvey and W. C. Feldman, Solar Phys., 49, 271, 1976.

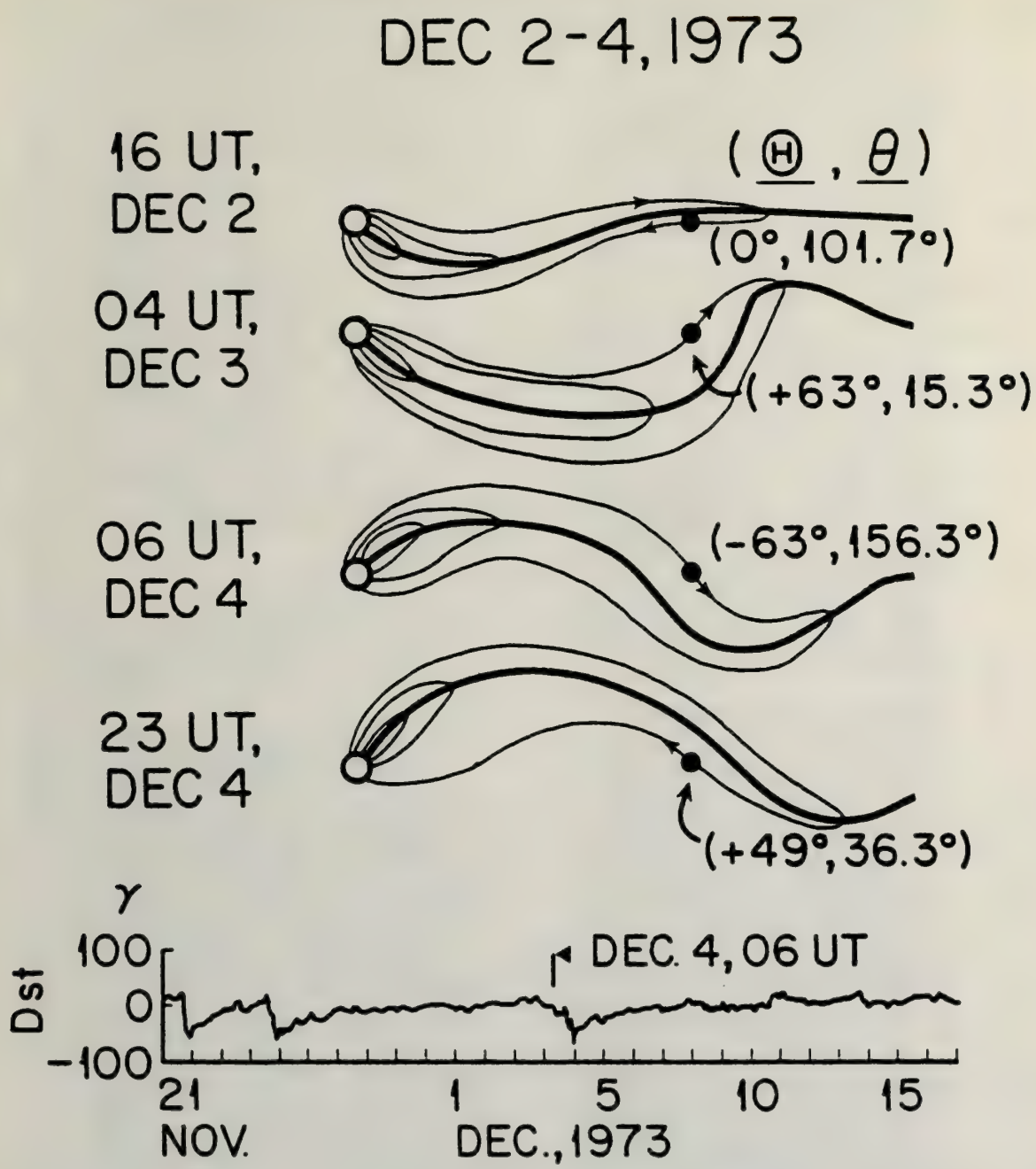


Fig. 19 Akasofu, S.-I., Planet. Space Sci., 27, 1055, 1979.

plane. Therefore, it is recommended that similar numerical simulation efforts be made in the meridian plane.

5. Magnetospheric quantities related to substorm occurrence and intensity

It has been suggested that there are several magnetospheric quantities which are related to the occurrence and intensity of magnetospheric substorms. Some of them are:

(a) The size of the auroral oval

The size of the oval is related to the intensity of magnetospheric substorms. The size of the oval can be determined and/or inferred from the following observations:

(i) Satellite image of auroral oval (Fig. 20)

(ii) Particle flux distribution from polar orbiting satellites

(iii) Meridian chain of magnetic observatories (Fig. 21)

(b) Tail-like distortion of the magnetic field at the geosynchronous distance

6. Substorm monitoring

The AE index is the most important substorm index at the present time. However, it will be a difficult task to monitor the AE index on real time basis (though not impossible). A great international effort is needed to achieve this purpose, by standarizing magnetometers, installing radio sets, transmitting data to the WDC via satellites.

It has been shown that the auroral kilometric radiations correlate well with the AE index. Fig. 22 shows an example of this correlation.

It is thus recommended that the GTL satellite of the OPEN program carries the necessary equipment to monitor continuously the auroral kilometric radiations in the magnetotail.

Fig. 23 shows another example of this correlation. Note that there were two 'distinct' substorms on this particular day. However, the correlation is not as good as one would wish. A close examination of the AE index by the combined H component high latitude record shows that only one of the AE stations was contributing to the two peaks. This example suggests that there is needed for the improvement of the AE index (Rostoker).

7. Prediction of the lowest overhead latitude of the auroral oval

It is well known that the auroral oval expands considerably equatorwards during geomagnetic storms. Fig. 24 shows the distribution of aurorals during the historic storm of Feb. 11, 1958. It is important to predict the

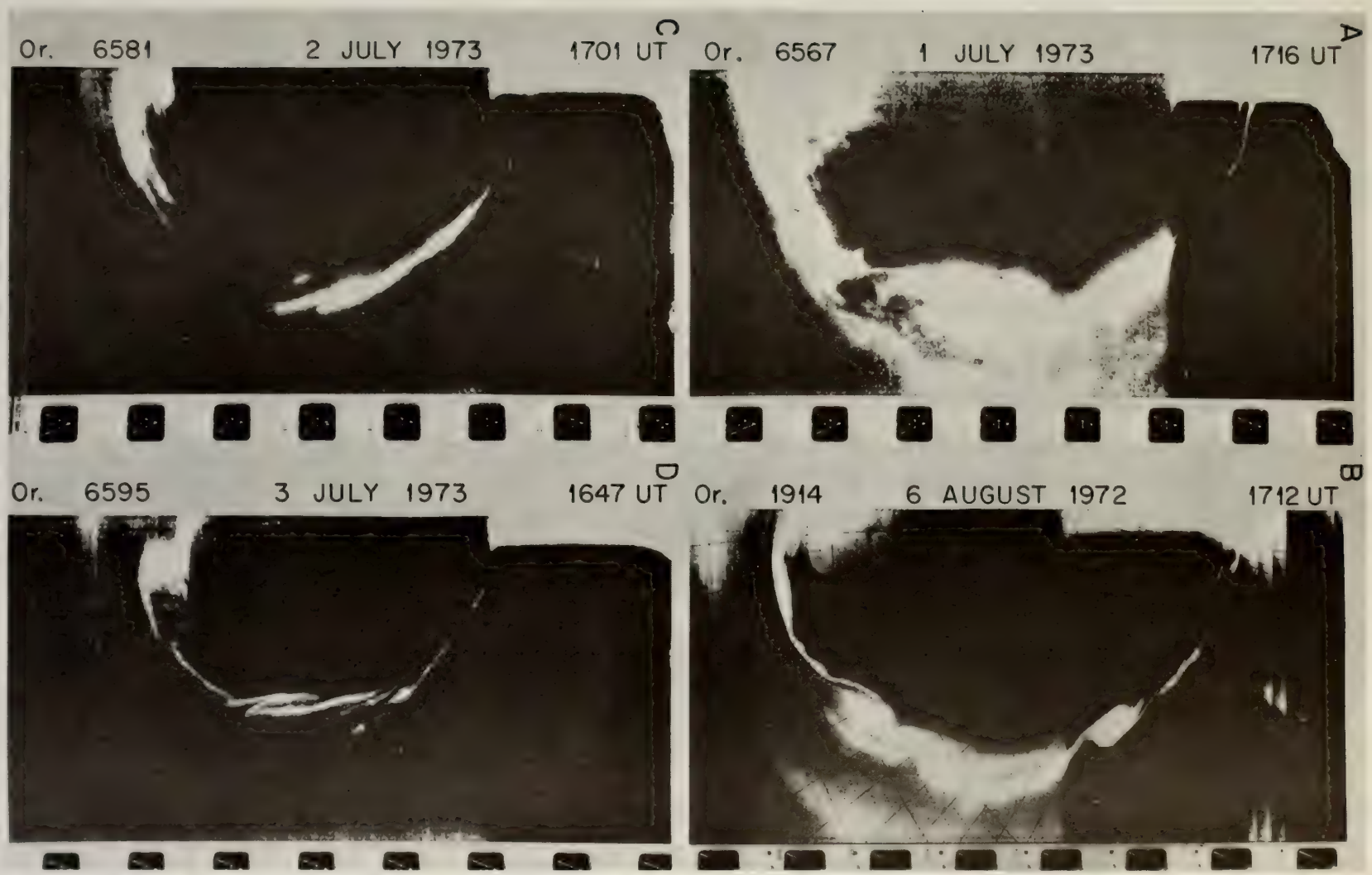
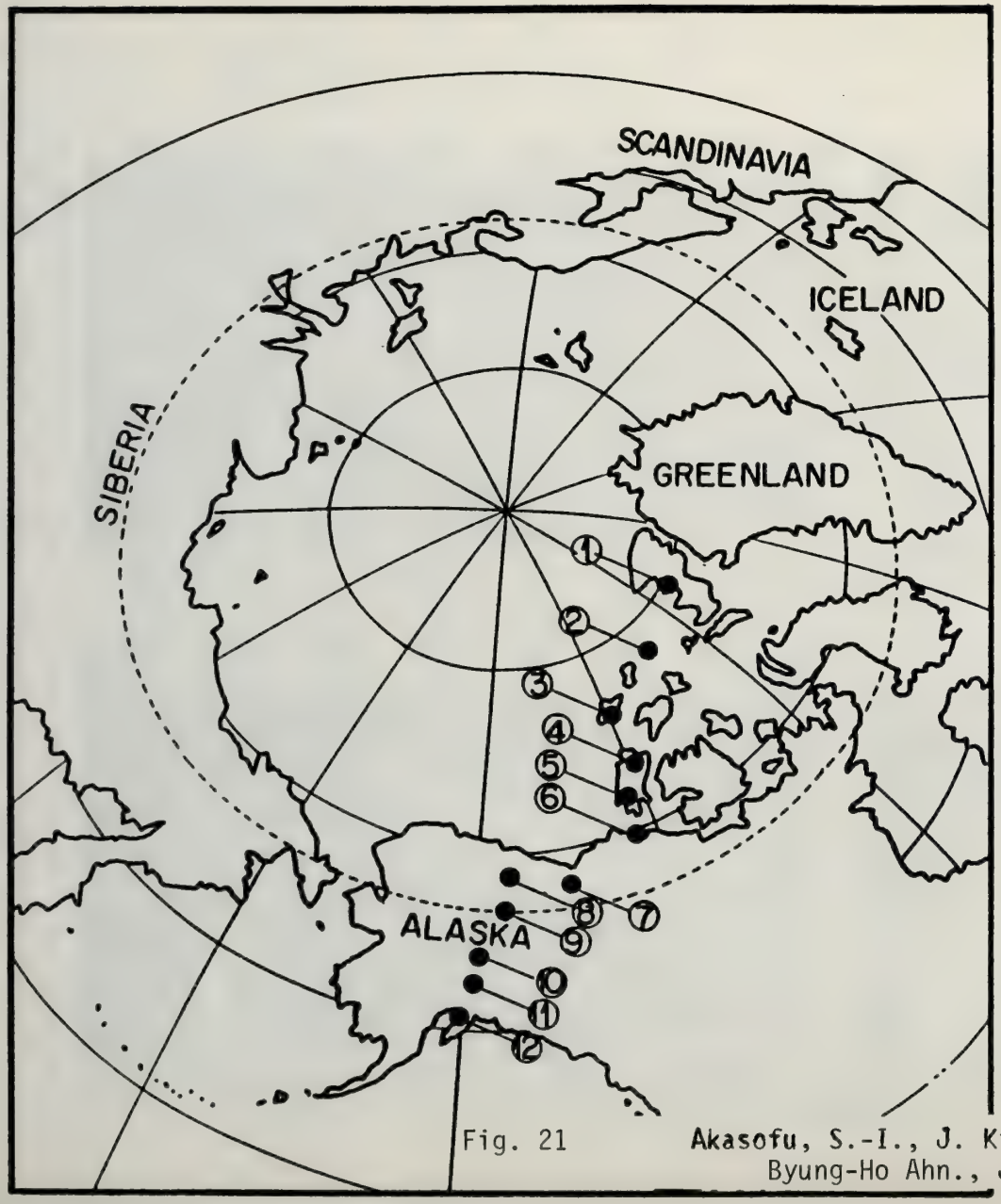

Or. 6581
2 JULY 1973
1701 UT
C
Or. 6567
1 JULY 1973
1716 UT
A
Or. 6595
3 JULY 1973
1647 UT
D
Or. 1914
6 AUGUST 1972
1712 UT
B

Fig. 20



IMS Alaska Meridian Chain of Geophysical Observatories

		Invariant Latitude
1	EUREKA	89°
2	ISACHSEN	86°
3	MOULD BAY	81°
4	JOHNSON POINT	78°
5	SACHS HARBOUR	76°
6	CAPE PARRY	74°
7	INUVIK	71°
8	ARCTIC VILLAGE	69°
9	FORT YUKON	67°
10	FAIRBANKS	65°
11	TALKEETNA	62°
12	ANCHORAGE	61°

Fig. 21 Akasofu, S.-I., J. Kisabeth, G. J. Romick, H. W. Kroehl and Byung-Ho Ahn., J. Geophys. Res., (in press), 1980.

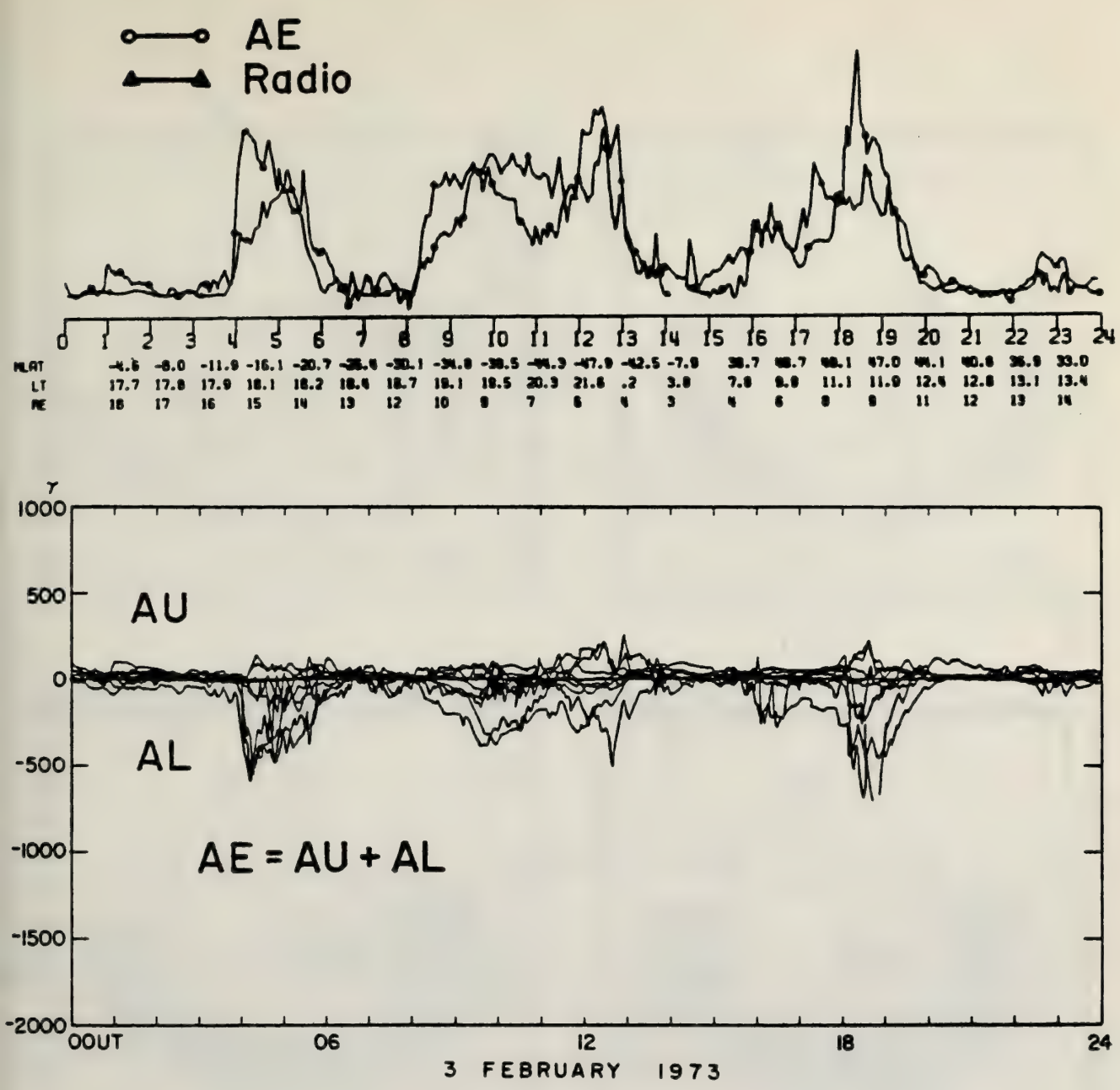


Fig. 22 Voots, G. R., D. A. Gurnett and S.-I. Akasofu, J. Geophys. Res., 82, 2259, 1977.

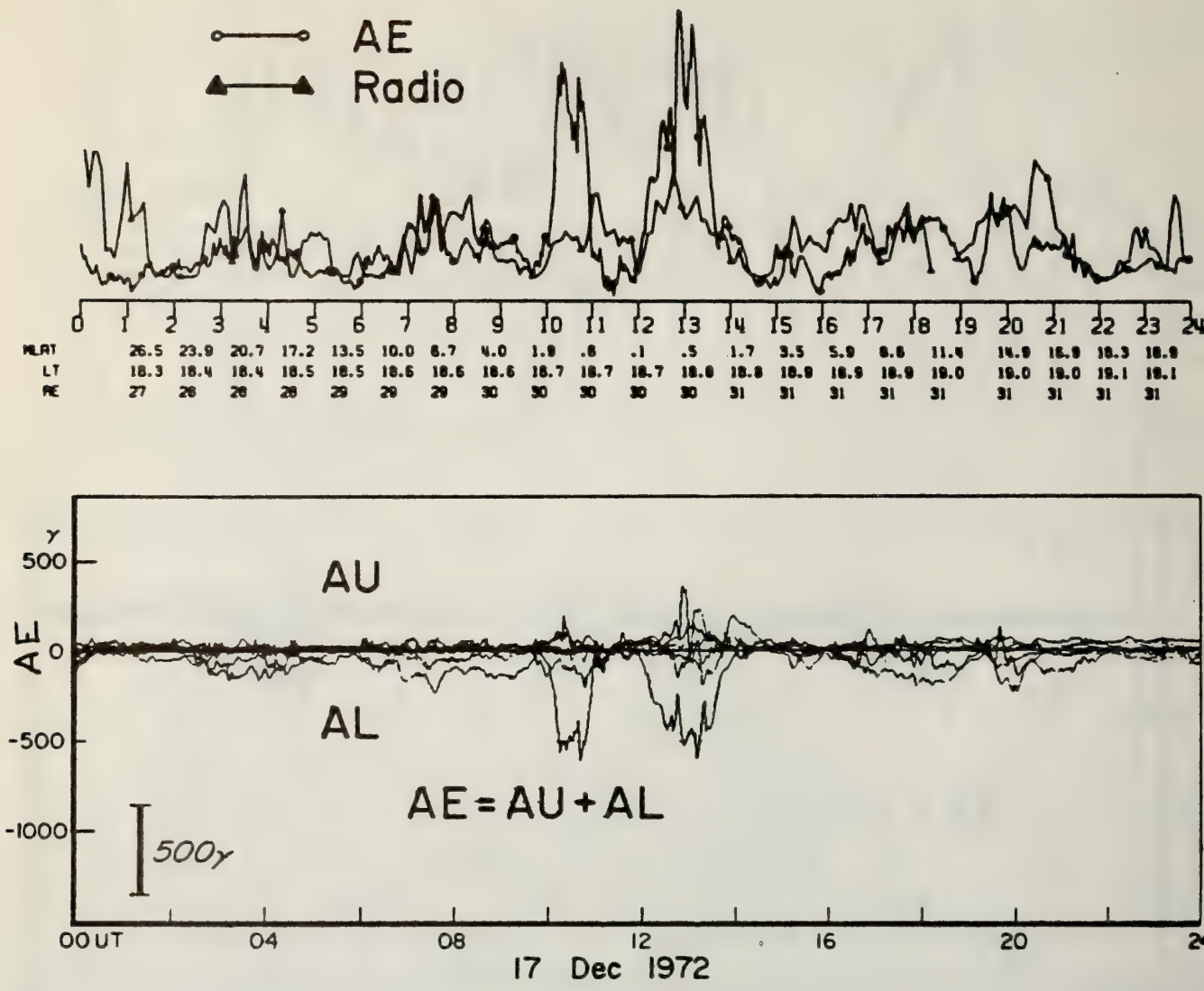


Fig. 23 Voots, G. R., D. A. Gurnett and S.-I. Akasofu, J. Geophys. Res., 82, 2259, 1977.

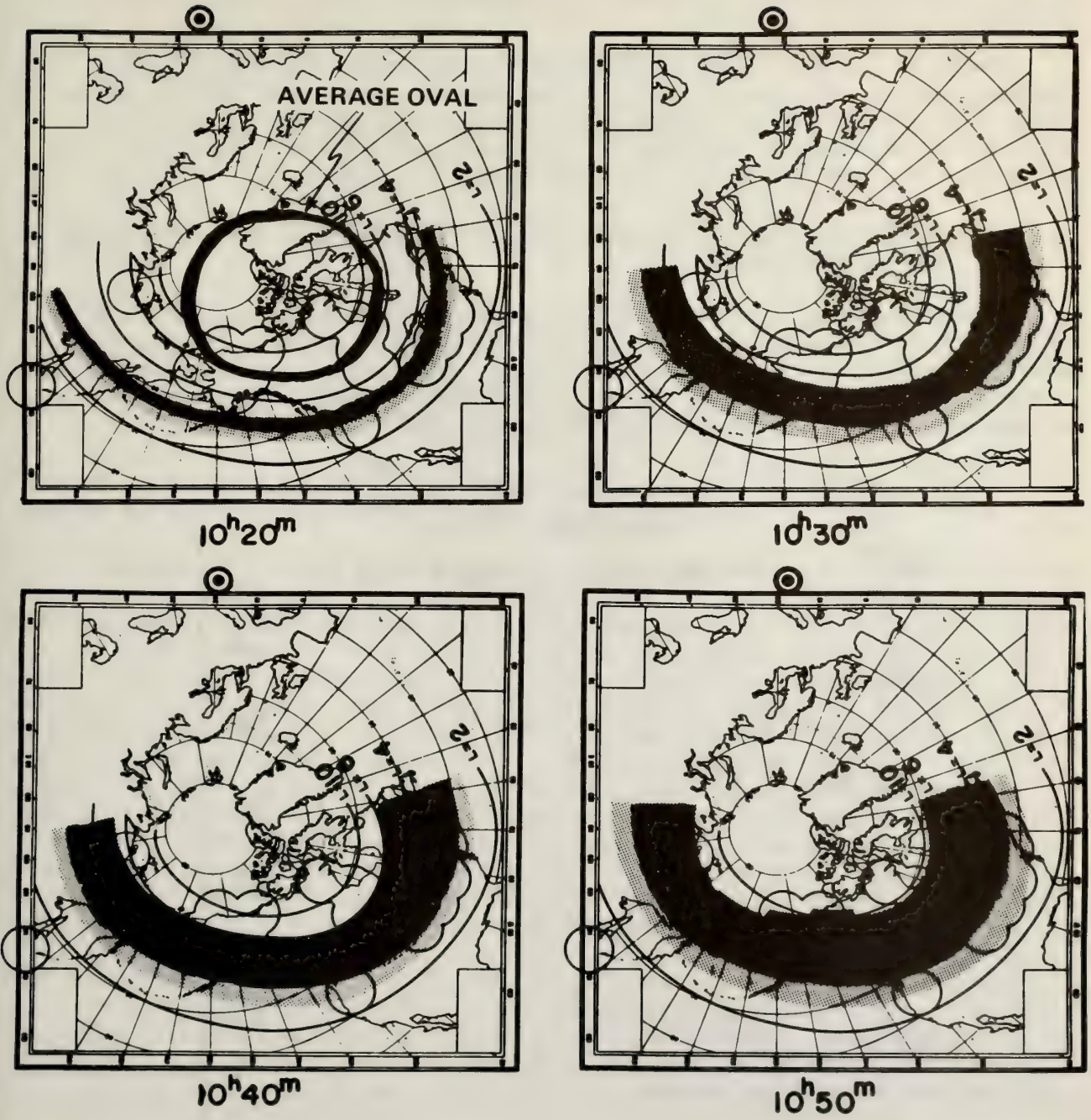


Fig. 24 Akasofu, S.-I. and S. Chapman, J. Atmos. Terr. Phys., 24, 785, 1962.

location of the auroral oval, since most intense ionospheric currents are confined in the vicinity of the auroral oval and most intense particle precipitation takes place there.

There is a simple relationship between the lowest overhead latitude (geomagnetic) of the auroral oval in the midnight sector and the Dst index (Fig. 25). If one could predict time variations of $\varepsilon(t)$ by the numerical simulation, it would be possible to infer the expected Dst value. Then, by using Fig. 25, one can infer the lowest overhead latitude.

8. Identification of the source regions of the solar wind associated with geomagnetic storms

Although solar flares and coronal-holes are identified as the source regions of the solar wind associated with geomagnetic storms, there are many geomagnetic storms of which the source regions on the solar disk is not obvious at the present time. One of the recent examples of this type of geomagnetic storms is the storm of August 28, 1978.

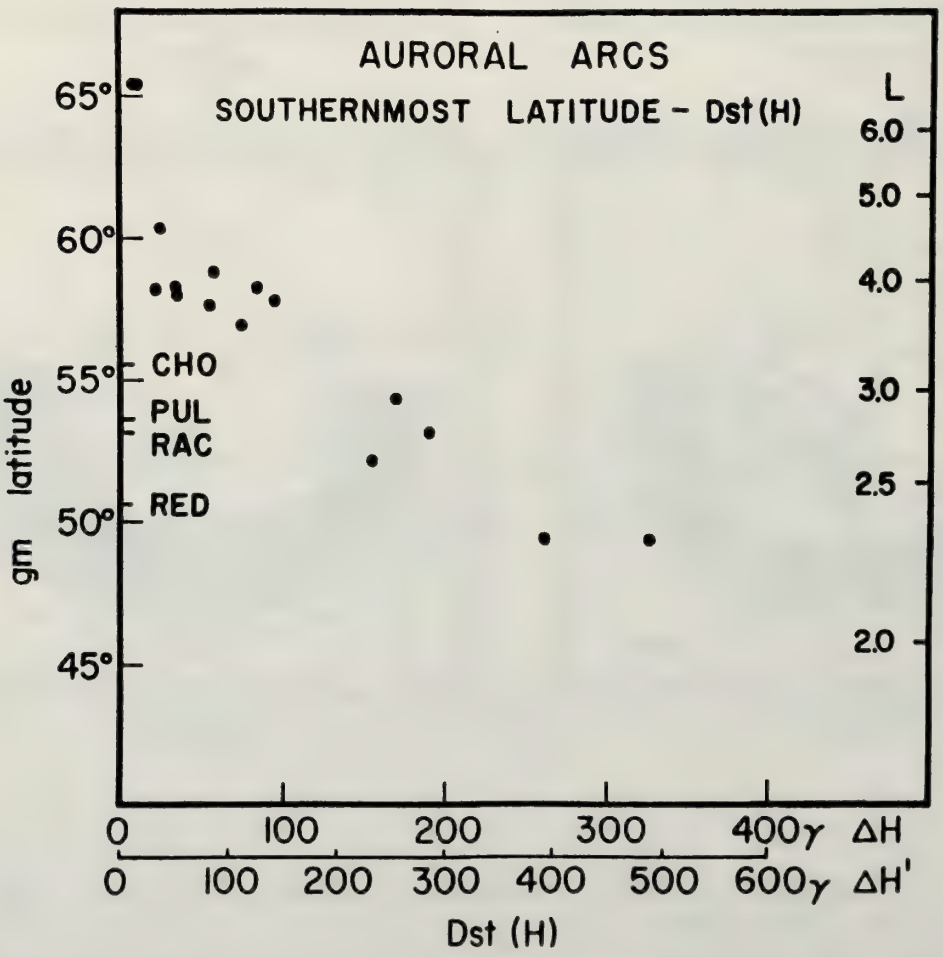


Fig. 25 Akasofu, S.-I. and S. Chapman, J. Atmos. Terr. Phys., 24, 785, 1962.

ADDENDUM

WORKSHOP REPORT ON GEOMAGNETIC DISTURBANCE PREDICTIONS

J.A. Joselyn
Space Environment Laboratory
NOAA/ERL
Boulder, Colorado 80303, U.S.A.

As expressed in the previous paper, this working group sought to provide the best available scheme for the prediction of the occurence, intensity, and time development of a geomagnetic storm for a given flare or coronal hole. As a result of the deliberations of the working group, which was chaired by S.I. Akasofu and included S. Matsushita, F.Cook, M. Dryer, T. Watanabe, and J.A. Joselyn, a summary logic diagram, shown in Figure 1, was drawn. The following remarks were presented with the diagram at the closing plenary session of the Solar-Terrestrial Predictions Workshop.

Geomagnetic effects from solar sources are extremely variable. If there is a resultant geomagnetic storm, it may or may not have an associated sudden commencement. Sudden impulses in the geomagnetic field associated with shocks propagating through the interplanetary medium may or may not be followed by a storm main phase. The actual terrestrial result of a solar cause is apparently regulated by details at the solar source and by the ambient and propagation characteristics of the interplanetary medium. Considering first the possible geomagnetic impact of a solar flare, several optical, x-ray, radio, and particle data inputs must be evaluated. These inputs are conveniently organized by the CFI (Comprehensive Flare Index) defined by Dodson and Hedeman (note their report in this Proceedings). The bigger the CFI, the bigger the potential storm and the earlier the arrival time. Arrival times are typically on the order of 43 hours, but the range is from 25 hours to 60 or more hours. Flare location has some statistical importance to flare intensity (the largest storms are identified with flares occurring between 45°E and 70°W solar helio longitude), but not to transit times. There is essentially no data available at this time to assist in predicting storm intensity (maximum DST) and the expected length of the disturbance. Such predictions would be useful because major auroral activity and the attendant serious space craft, ionospheric, and long-line disturbances are concentrated during the main phase of a geomagnetic storm.

As a possible immediate aid to short-term storm prediction, we suggest that the solar wind plasma be monitored on a real-time basis. The ISEE-C satellite, now orbiting the sun-earth libration point at approximately .01 AU in front of the earth, is ideally suited for such monitoring, even though it was not initially intended for real-time use. Solar wind plasma parameters such as density, velocity, and magnetic field intensity and orientation could be obtained and analyzed from 30-60 minutes in advance of the arrival of that

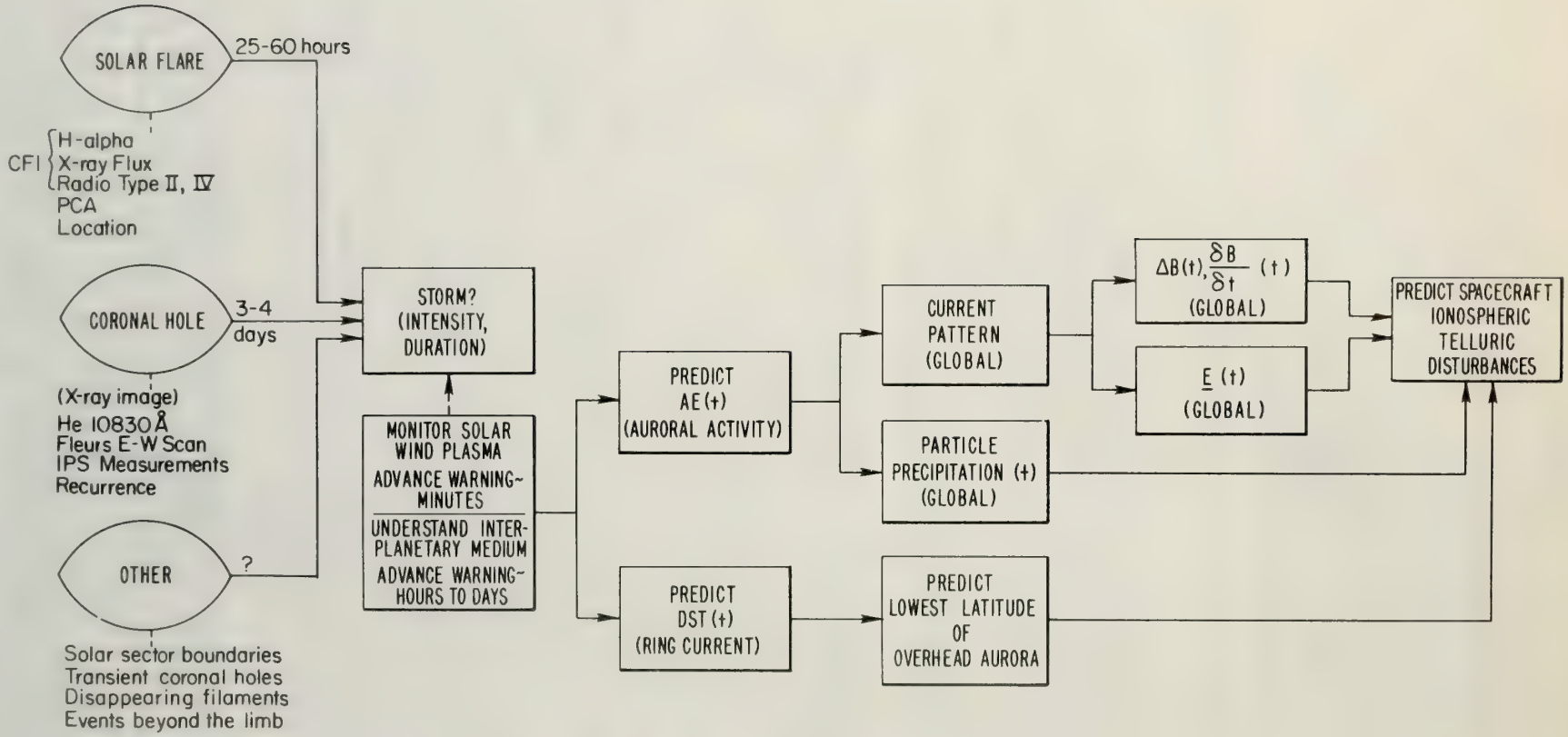


Figure 1. Schematic for prediction of geomagnetic disturbances

plasma at earth. Several functional forms have been suggested as algorithms relating solar wind parameters to geomagnetic indices. These will not be listed here except to note that there is encouraging evidence that such algorithms are sufficiently successful that we can expect operationally useful advance warnings, not only that a geomagnetic storm will shortly occur, but also how large the storm will be and when it will end.

A more fundamental prediction aid, which is now being developed, is a 3-dimensional understanding of the ambient interplanetary medium. This understanding is required to explain why some major flares, even though suitably located, do not precipitate geomagnetic effects. A comprehensive model of the interplanetary medium would require the continuous integration of all available solar observations (optical, radio, x-ray, particles, interplanetary scintillation data, etc.) so that the interplanetary topology could be known and the interaction of this pre-existing topology with flare ejecta could be calculated.

The logical sequence for geomagnetic effects originating in coronal holes goes along the same lines as for flares. Here, the observational inputs are ideally a soft x-ray image, but coronal holes can also be inferred from He 10830 Å data from Kitt Peak, 'Fleurs', Australia, east-west scans at 692 and 1415 MHz, interplanetary scintillation indications of high speed streams, and the traditional method of recurrence. High-speed, low density plasma is associated with a geomagnetic disturbance three to four days following the central meridian passage of a coronal hole. The latitudinal location of the hole is a factor - the closer to the ecliplic, the more likely that magnetic effects will be observed. As with flares, a real-time solar wind monitoring platform between the earth and the sun would be beneficial for short-term predictions. And clearly, an understanding of the three-dimensional topology of the interplanetary medium would allow much improved long-term (days or even months) prediction of coronal hole disturbances.

There are undoubtedly other solar sources of geomagnetic disturbances which are yet to be fully investigated. Some of these are solar sector boundaries, transient coronal holes, rapidly disappearing filaments, and events beyond the visible solar limb which are still able to propagate to earth. Work on all of these additional sources of disturbance is in progress. An interplanetary monitoring platform is even more important for the prediction of these events for which optical and other data may be uncertain or absent.

The final goals of an understanding of the relationship between the solar plasma outputs and the terrestrial magnetosphere are the successful prediction of Auroral activity (AE) and the Ring Current (DST) as inputs for global models of currents and particle precipitation patterns. From these, spatial and temporal gradients in the local geomagnetic field could be calculated resulting in the detailed prediction of space craft, ionospheric, and telluric disturbances.

Obviously, a great deal of research and technique development is necessary before this prediction scheme can become operational. However, much of the theoretical understanding implicit in the diagram now exists in at least a rudimentary form, and additional development may allow significant improvement in the near future toward the prediction of geomagnetic disturbances.

B. MAGNETOSPHERIC PARTICLE PREDICTIONS

PREDICTION OF HIGH-ENERGY (> 0.3 MeV) SUBSTORM-RELATED MAGNETOSPHERIC PARTICLES

D.N. Baker, R.D. Belian, P.R. Higbie and E.W. Hones, Jr.
University of California, Los Alamos Scientific Laboratory
Los Alamos, New Mexico 87545

Measurements both at 6.6 R_E and in the plasma sheet ($\geq$ 18 R_E) show that high-energy substorm-accelerated particles occur preferentially when the solar wind speed (V_{SW}) is high. Virtually no > 0.3 MeV protons, for example, are observed in association with substorms that occur when V_{SW} is < 400 km/sec. On the other hand, the probability of observing high-energy protons is very large, both at geostationary orbit and in the plasma sheet, when V_{SW} is > 700 km/sec. These results suggest that realtime monitoring of interplanetary conditions could allow simple, effective prediction of high-energy magnetospheric particle disturbances.

INTRODUCTION

Measurable intensities of high-energy (0.3-2.0 MeV) substorm-related particles appear to be produced in only a small fraction (10-20%) of all substorms [Hones et al., 1976; Belian et al., 1978; Baker et al., 1978]. This occurrence frequency is generally found both for electrons [e.g. Paulikas and Blake, 1978] and for protons. Furthermore, particles of these energies occur with similar frequency both at synchronous altitude (6.6 R_E) in the outer radiation zone and in the distant plasma sheet ($\geq$ 18 R_E).

Absolute intensities of the high-energy particle component are generally rather low when compared to the fluxes of other substorm-accelerated particles. Nonetheless, the very energetic particles can be quite disruptive, when present, due to their penetrating character. Recent work has shown rather clearly the conditions under which such particles are produced, and in this paper we discuss simple methods for prediction of high-energy substorm particles from a knowledge of interplanetary plasma and magnetic field conditions.

INSTRUMENTATION

The measurements to be discussed in this paper were made with Los Alamos Scientific Laboratory instruments aboard several different earth-orbiting spacecraft. The Charged-particle Analyzer (CPA) instruments are on board spacecraft 1976-059A and 1977-007A which are both at the geostationary orbit. Energetic proton measurements made by various Vela spacecraft ($\sim$ 18 R_E) have been described previously by Hones et al. [1976].

The CPA instrument measures low-energy electrons (LoE) and low-energy protons (LoP). The respective energy ranges for the LoE and LoP subsystems are $30 \leq E_e \leq 300$ keV and $0.15 < E_p < 0.6$ MeV. The CPA also measures high-energy electrons (HiE) and high-energy protons (HiP). The HiE and HiP energy ranges are, respectively, $0.2 \leq E_e \leq 2.0$ MeV and $0.4 \leq E_p \leq 150$ MeV. Because the geostationary spacecraft under discussion here have no onboard magnetometers, pitch angle distributions of > 30 keV electrons are calculated in a self-consistent manner (see Higbie and Moomey [1977] and Higbie et al., [1978]). Using a spherical harmonic analysis and least-squares fitting technique, the symmetry axis of the second-order (pancake" or "cigar") pitch angle distribution of the > 30 keV electrons defines the local magnetic field direction. The colatitude (or meridional tilt) of the local field line calculated in this way is called θ_B; the second-order electron anisotropy amplitude is called C_2. ($C_2 < 0$ corresponds to a pancake distribution, whereas $C_2 > 0$ corresponds to a cigar distribution.)

BASIS OF THE METHOD

Figure 1 shows an example of one kind of high-energy proton enhancement commonly observed at the geostationary orbit. Early on October 2, 1976 several substorm "injections" of lower energy (< 300 keV) protons and electrons were detected by CPA instrumentation aboard spacecraft 1976-059. Notable among these injections was that which occurred at ∿ 0420 UT when spacecraft 76-059 was at ∿ 0200 LT. As seen in Figure 1, this injection event had associated with it protons extending in energy up to at least ∿ 1.0 MeV.

At the higher energies (generally > 300 keV) the injected protons appeared in the form of rather narrow, well-defined pulses of particles. Significant dispersion is seen since higher energy channels show flux increases before similar increases are seen at lower energies. Note that in each energy range there are several clear pulses, or "echoes," as the protons drift azimuthally around the earth [Belian et al. 1978].

As seen by the parameter θ_B the local magnetic field was in a very stretched, or taillike, configuration prior to ∿ 0430 UT, but this relaxed toward a somewhat more dipolar configuration after the particle injection.

The highly disturbed geomagnetic conditions observed during the early portion of October 2 are seen in the Meanook and Great Whale River magnetogram traces shown in Figure 2. Especially noteworthy is the very large negative bay in the Great Whale H-component beginning at ∿ 0420 UT. This substorm enhancement is plausibly related to the proton injection observed at 6.6 R_E.

We find both drift-echo (DE) and nondrift echo (NDE) types of proton enhancements at geostationary orbit. In contrast to the DE type of event shown after ∿ 0420 UT in Figure 1, NDE events show clear flux enhancements but by definition there is not a very evident pulsed behavior of high-energy protons in these cases.

In Figure 3 we show several different kinds of data. The upper two panels of the figure show daily averages, respectively, of the proton and electron intensities measured by the CPA aboard spacecraft 76-059. Selected energy

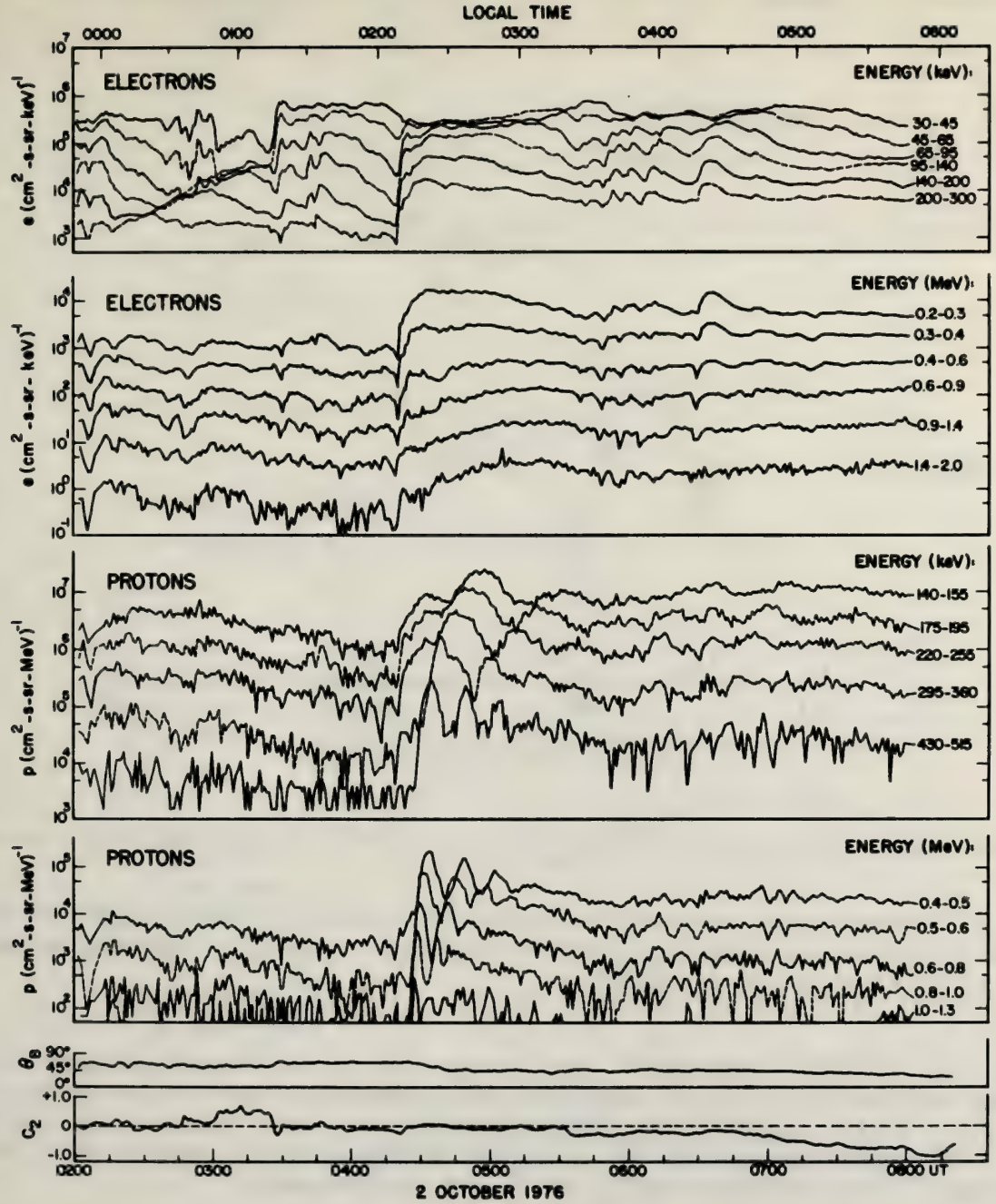


Figure 1. Selected CPA data from spacecraft 1976-059A for a portion of October 2, 1976 including electrons in various energy ranges (as labeled) in the upper two panels and protons in the third and fourth panels from the top. The bottom two panels contain information (as described in the text) obtained from the low-energy electron anisotropies: θ_B is the inferred local magnetic field direction and C_2 is the > 30 keV electron second-order anisotropy amplitude. A major feature seen in these data is high-energy proton drift-echo event beginning at ∿ 0420 UT (and at a spacecraft local time of ∿ 0200).

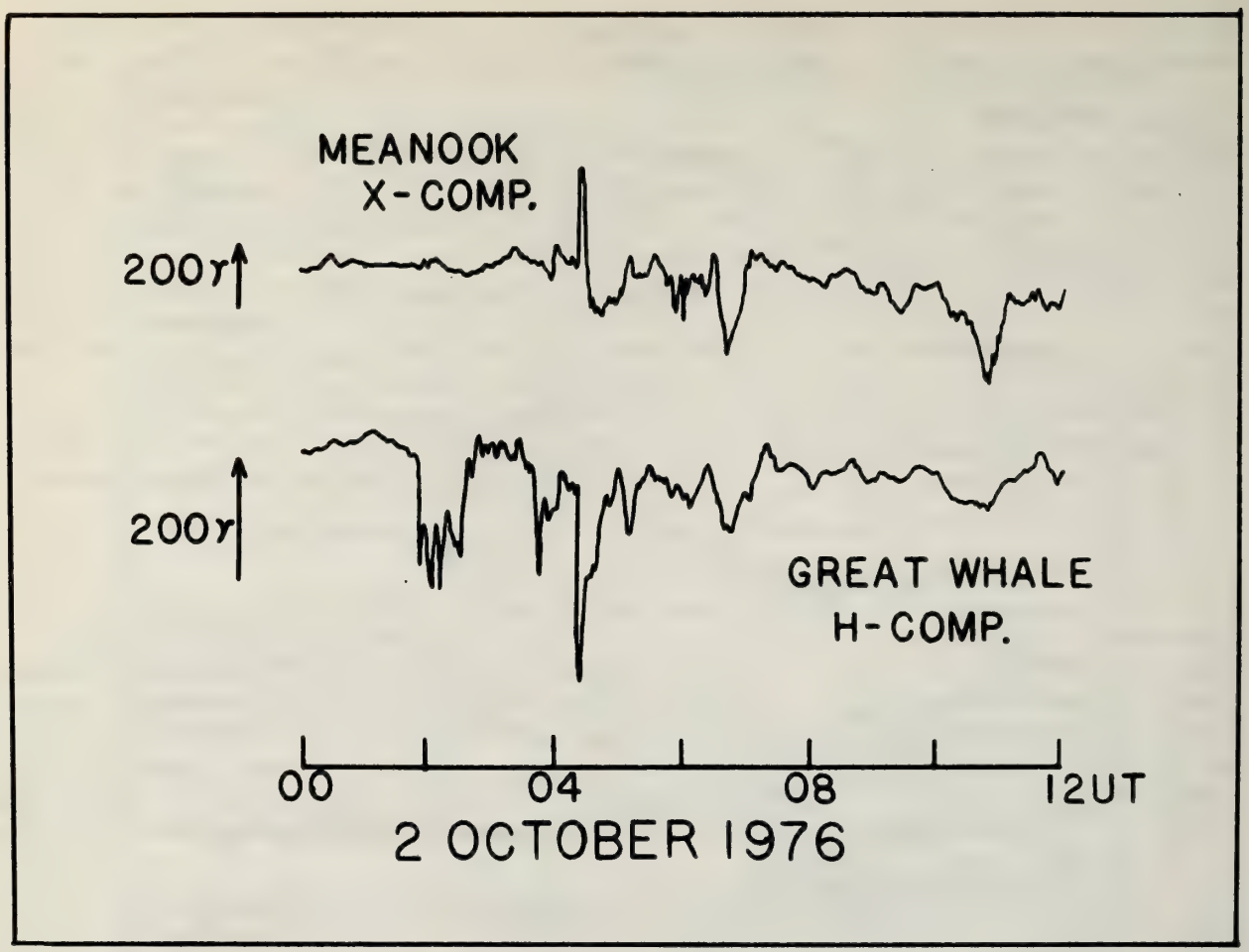


Figure 2. Ground-based magnetogram traces from Meanook (reaches magnetic midnight at 0900 UT) and Great Whale River (midnight at 0600 UT) showing substorm activity early on October 2, 2976.

ranges (out of many available) are shown for a two month period, viz., November-December 1976. Also shown are the 12-hour averages of the solar wind speed, V_{sw} (third panel), the interplanetary $\sim$ 1 MeV proton flux (fourth panel), the daily number of DE plus NDE events seen at spacecraft 76-059 (fifth panel), and finally, the K_p daily sum (sixth panel).

As may be seen, K_p generally correlates with V_{sw}. More importantly here, however, it is also suggested by Figure 3 that synchronous altitude high-energy proton and electron flux profiles, the number of DE and NDE proton events, and even interplanetary energetic proton bursts correlate fairly well with V_{sw}.

The correlation of high-energy proton enhancements at 6.6 R_E with solar wind speed is summarized in a statistical fashion in Figure 4. The upper panel of the figure shows the solar wind speed occurrence distribution for a one-year period (July 1976-June 1977). The raw numbers of DE and NDE events seen during various solar wind speed intervals are shown in the second panel. Finally, by normalizing the panel 2 distributions by the distribution in panel

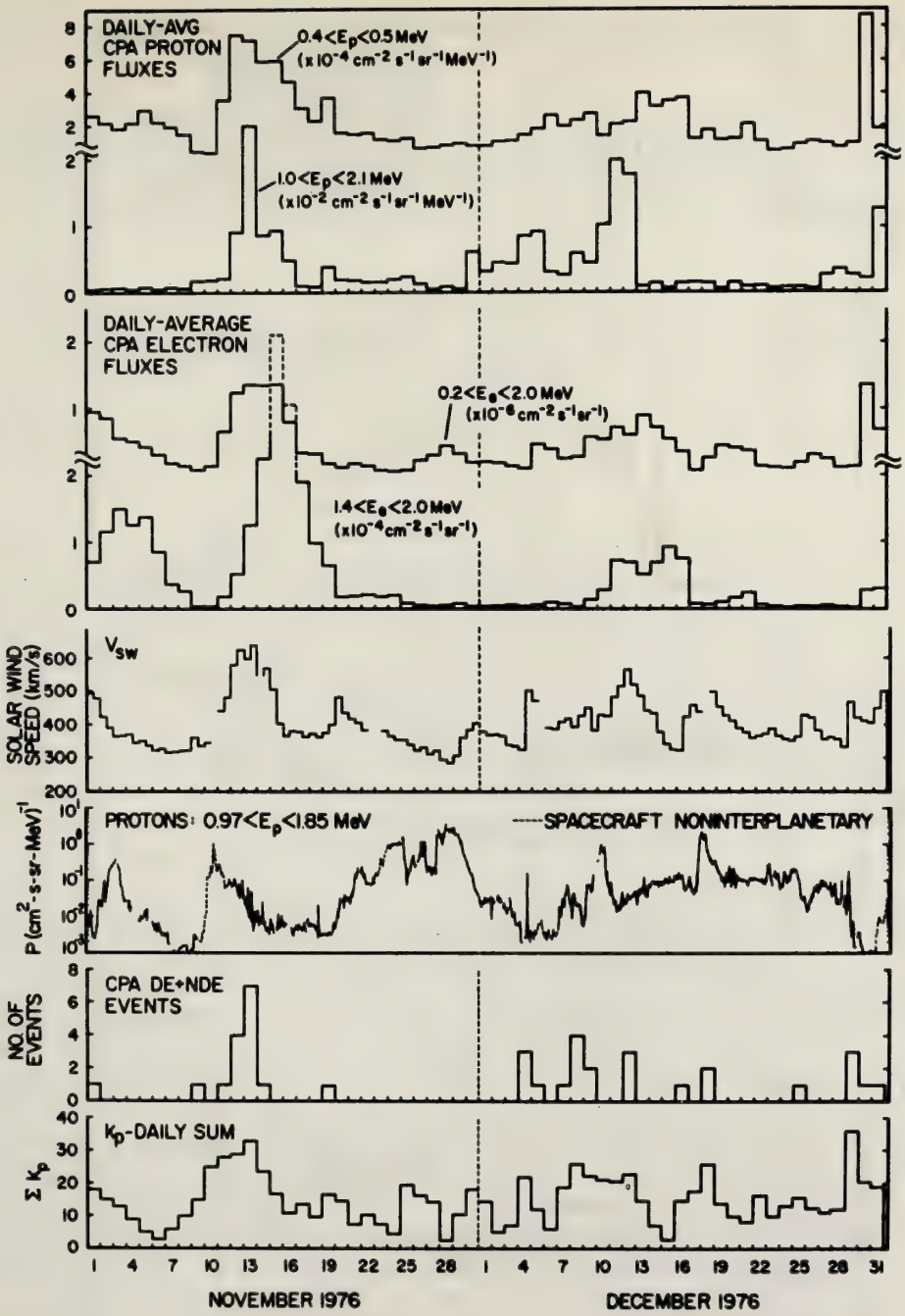


Figure 3. A composite plot of various data sets for November and December of 1976. The upper two panels show, respectively, CPA proton and electron flux profiles at 6.6 R_E. The third panel shows the 12-hour solar wind speed averages (courtesy of J. R. Asbridge, S. J. Bame, W. C. Feldman, and J. T. Gosling). The fourth panel shows the interplanetary flux of 0.97-1.85 MeV protons (Solar-Geophysical Data). The fifth panel shows the daily number of CPA high-energy proton events observed during the period. Finally, the bottom panel shows the November-December K_p daily sum, ΣK_p. As discussed in the text, several correlations between the various data sets are evident.

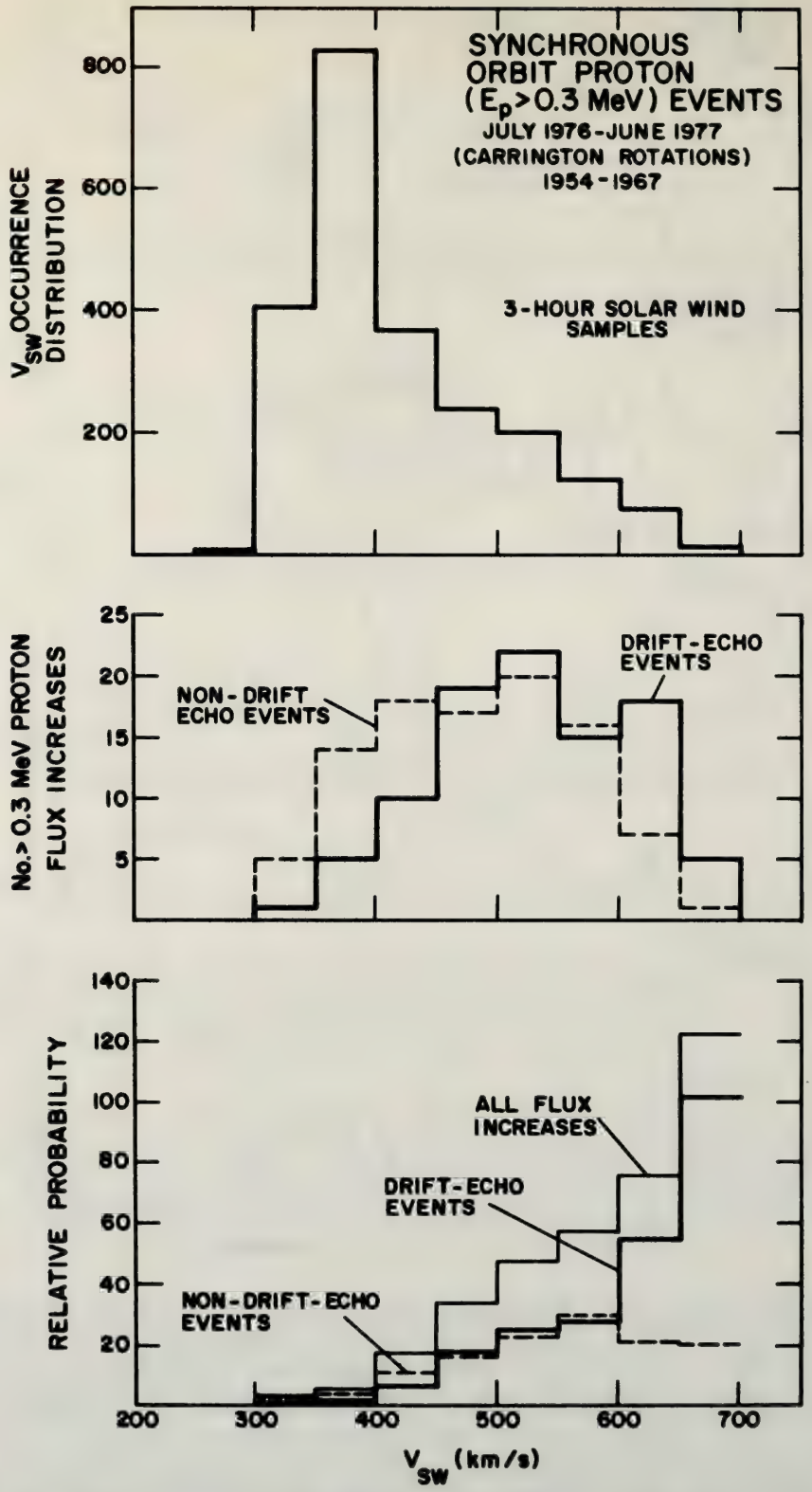


Figure 4. The upper panel shows that between July 1976 and June 1977 the bulk solar wind speed occurrence distribution peaked strongly between 350 and 400 km/sec. The second panel shows that most DE and NDE events occurred when V_{SW} was > 400 km/sec. When panel 2 data are normalized by the data of panel 1, a strong positive correlation is found between proton flux increases at 6.6 R_E and solar wind speed as shown in panel 3.

1, we get the relative occurrence probability of high-energy proton events at synchronous orbit.

We see that although V_{sw} is < 400 km/sec much of the time during 1976-77, relatively speaking almost no high-energy proton enhancements occur during these low-speed conditions. However, as V_{sw} increases above 400 km/sec the probability of observing a high-energy proton enhancement increases dramatically.

This dependence on solar wind speed is not restricted to 6.6 R_E. As seen in Figure 5, very similar results obtain for high-energy proton events observed in the plasma sheet by Vela instrumentation. In the third panel of Figure 5 we have normalized the probability to 100 for the 650-700 km/sec interval. Notice the change in scale and the very strong increase in relative probability when V_{sw} > 700 km/sec.

Not only the number of substorm-related events depends on solar wind speed, but also the absolute intensity of each event depends on the associated V_{sw}. This is demonstrated in Figure 6 which shows the observed peak proton intensities measured by the CPA plotted versus V_{sw}. We have broken the observations into three sectors according to the spacecraft location at the time the drift-echo events were detected. As discussed by Baker et al. [1978], the local time variation seen in Figure 6 may be related to dispersion effects as particles move away from injection regions and also may reflect drift-shell effects due to strong cross-magnetospheric electric fields. Nonetheless, a substantial positive correlation between peak flux and solar wind speed is seen in each local time sector.

Finally, we also find magnetospheric high-energy proton enhancements to have a noticeable tendency to occur when the interplanetary magnetic field (IMF) is southward. As shown by the statistical results related to Vela observations in Figure 7, the total IMF magnitude is not abnormally large during these events (panel (a)). However, panel (b) shows that ~ 95% of the Vela events occurred following at least a one-hour period of predominantly southward IMF (B_z < 0). Panels (c) and (d) show the occurrence frequency and median observed 0.5 MeV fluxes, respectively, plotted versus the combination of the observed V_{sw} and B_z for each event (i.e., the Y-component of the interplanetary electric field, IEF). Substantial dependences on the magnitude of the dawn-to-dusk component of the interplanetary electric field (IEF) are suggested.

DISCUSSION AND POSSIBLE USES

The foregoing results suggest rather strongly that realtime monitoring of the interplanetary plasma and magnetic field could permit a quite simple and useful prediction scheme. As a minimum, users who wished to know whether or not substorm-related particles of hundreds of keV (or above) could be expected need only find out the solar wind velocity. This seems to be the simplest and most fundamental correlation: if V_{sw} is low, say < 400 km/sec, then high-energy, substorm-accelerated particles are extremely unlikely throughout the outer magnetosphere; conversely, if V_{sw} is very high, say ≥ 700 km/sec, then

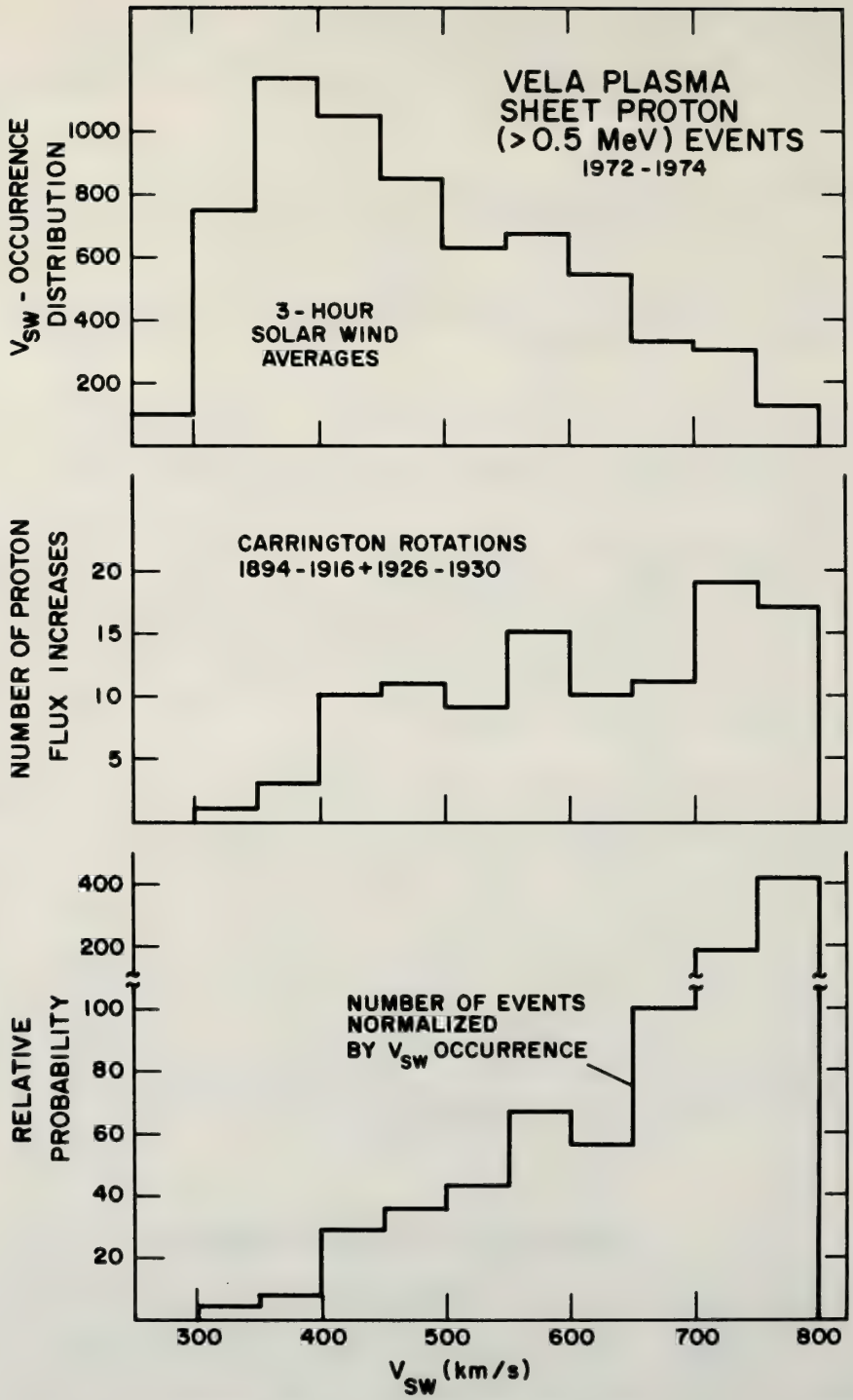


Figure 5. Data similar to Figure 4, but for Vela plasma sheet proton enhancements. In the lower panel we have normalized the relative probability to 100 between 650 and 700 km/sec. The relative probability of a high-energy proton event increases dramatically at high V_{SW}.

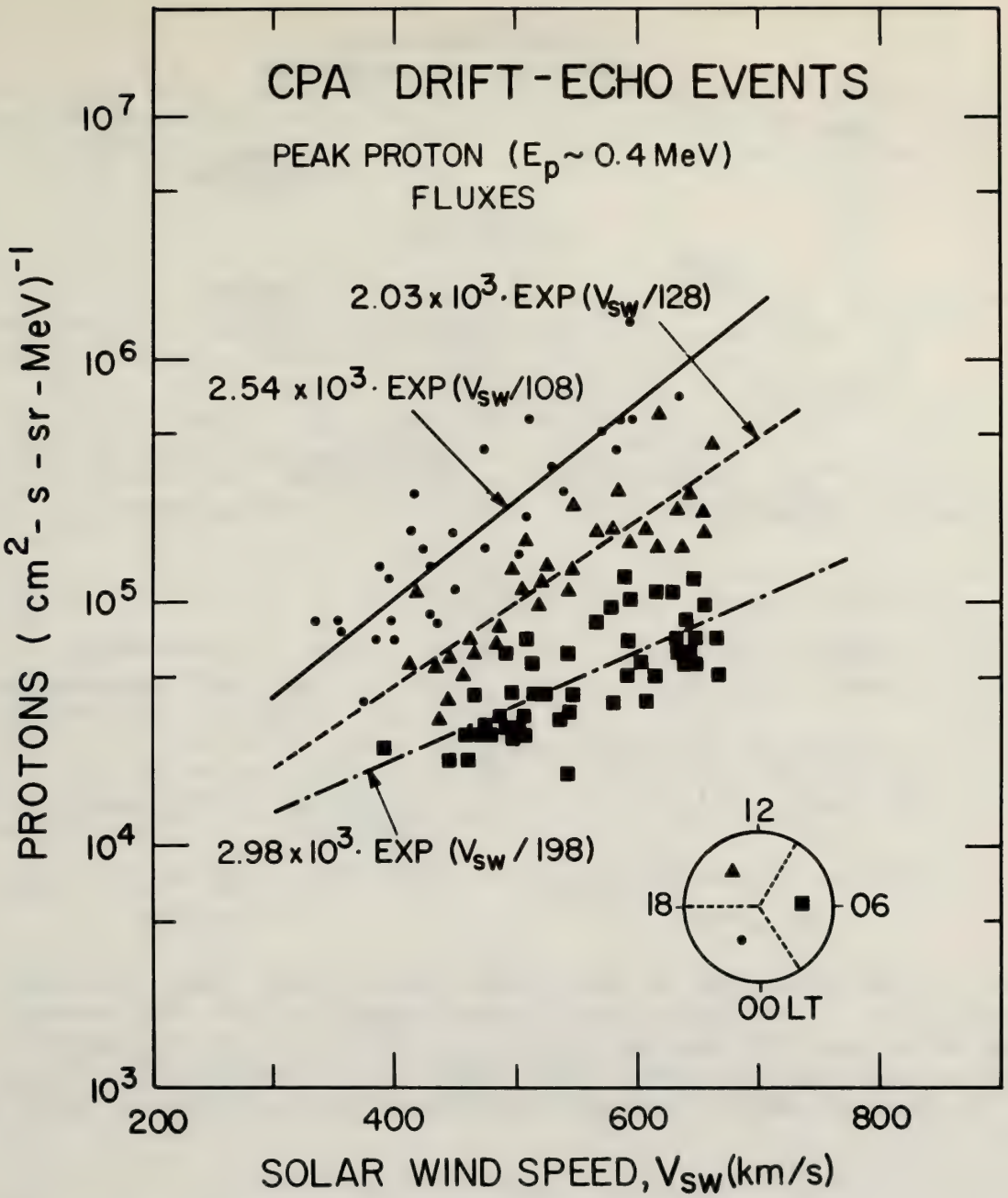


Figure 6. Peak observed CPA proton fluxes (at $E_p \sim 0.4$ MeV) versus bulk solar wind speed. A positive correlation is shown by the linear regression fits to data from each local time sector.

the probability is very high that a substorm will produce copious quantities of high-energy protons and electrons.

There may be deeper and more detailed correlations that can be inferred (cf., Figure 7). These more quantitative correlations appear to require knowledge of the IMF, as well as V_{sw}. Furthermore, there may be some specific feature, such as the fluctuation spectrum of the IMF, the IEF, etc., which

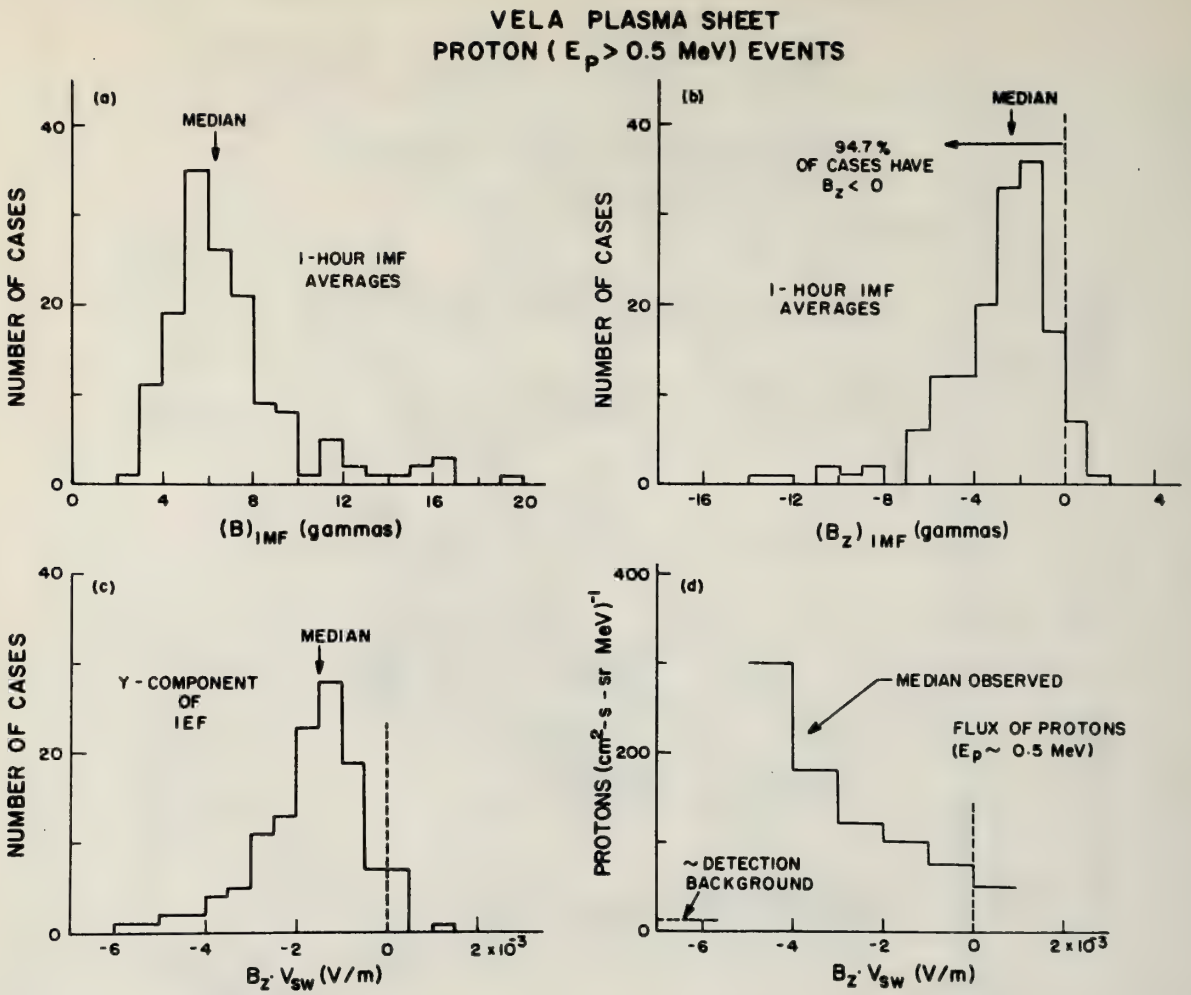


Figure 7. The dependence of Vela plasma sheet proton event occurrence frequencies: (a) on the total interplanetary mangetic field (IMF) strength; (b) on the north-south IMF component, $(B_z)_{IMF}$; and (c) on the Y-component of the interplanetary electric field (IEF) which is the negative of $(B_z)_{IMF} V_{sw}$. Part (d) shows the median observed peak proton flux in the plasma sheet versus $B_z V_{sw}$.

actually "produces" the large acceleration events observed when V_{sw} is high. Nonetheless, our results suggest that whatever the mechanism, it occurs only when solar wind speed is high; other IP changes appear to contribute in a secondary way to this feature.

In summary, it appears that a real time monitoring of V_{sw} and the IMF could provide both a qualitative and a quantitative prediction of the probability for the occurrence and intensity of > 0.3 MeV substorm related energetic particles. These predictions would seem to have validity both in the outer radiation zones (L ~ 5-8) and in the magnetotail.

ACKNOWLEDGMENTS

We particularly thank S. J. Bame, J. R. Asbridge, W. C. Feldman, and J. T. Gosling for providing us with solar wind data used in this study. This work was done under the auspices of the United States Department of Energy.

BIBLIOGRAPHY

Baker, D.N., R. D. Belian, P. R. Higbie, and E. W. Hones, Jr., High-energy magnetospheric protons and their dependence on geomagnetic and interplanetary conditions, submitted to J. Geophys. Res., 1978.

Belian, R. D., D. N. Baker, P. R. Higbie, and E. W. Hones, Jr., High-resolution energetic particle measurements at 6.6 R_E, 2, High-energy proton drift-echoes, J. Geophys. Res., 83, 1978.

Higbie, P. R. and W. R. Moomey, Pitch angle measurements from satellites using particle telescopes with multiple view directions, Nucl. Instr. and Meth., 146, 439, 1977.

Higbie, P. R., R. D. Belian, and D. N. Baker, High-resolution particle measurements at 6.6 R_E, 1, Electron micropulsations, J. Geophys. Res., 83, 1978.

Hones, E. W., Jr., I. D. Palmer, and P. R. Higbie, Energetic protons of magnetospheric origin in the plasma sheet associated with substorms, J. Geophys. Res., 81, 3866, 1976.

Paulikas, G. A., and J. B. Blake, Energetic electrons at synchronous altitude 1967-1977, Aerospace Corporation Rep. No. TR-0078 (3960-05), March 1978.

Solar Geophysical Data, Environmental Data Service, NOAA, Nos. 393 and 394, May-June, 1977.

THE USE OF > 30 keV ELECTRON ANISOTROPIES AT 6.6 R_E TO PREDICT MAGNETOSPHERIC SUBSTORMS *

D. N. Baker, P. R. Higbie, E. W. Hones, Jr., and R. D. Belian
University of California, Los Alamos Scientific Laboratory
Los Alamos, New Mexico 87545

Observations at the geostationary orbit show that > 30 keV electron pitch angle distributions begin to develop a cigarlike (field-aligned) character typically one to two hours prior to the onset of the injection of substorm-produced energetic particles into the outer radiation zone. Conversely, when no substorm is imminent the low-energy electrons remain nearly isotropic in the nighttime magnetosphere. The direct substorm injection of particles is usually detected near local midnight whereas the cigarlike anisotropies are generally detected when the spacecraft is in the (pre)midnight sector (18-02 local time). These results suggest that 30 keV electron field-aligned anisotropies at 6.6 R_E may serve as a short-term (0.5-3.0 hour) predictor of substorms. Real time monitoring of a simple electron anisotropy parameter from a network of well-instrumented spacecraft could aid in the operation of military and communications satellites and could also help predict ionospheric disturbances.

1. Introduction

Accurate, short-term (0.5-3.0 hour) prediction of magnetospheric substorms and substorm-related effects would be of great potential benefit. For example, spacecraft charging events and other operational anomalies often occur in association with substorm injection events at the synchronous orbit of 6.6 R_E [Garrett et al., 1977]. Thus, a simple, reliable method of forecasting the imminence of a substorm could allow spacecraft operation personnel time to prepare for these difficulties and possibly take alternative or preventive measures.

The primary disruption due to substorm-produced hot plasma and energetic particles generally occurs in the 23-06 local time (LT) sector [Garrett et al., 1977]. Hence the danger to spacecraft operations, and also for ionospheric disturbances resulting from substorms, occurs with highest probability as the spacecraft (or the conjugate ionospheric region) moves into the midnight sector. Of course, injected plasmas and energetic particles may readily drift in azimuth around the earth, but the first impulsive appearance of the disturbance is near midnight [Parks et al., 1968; Arnoldy and Chan, 1969; Baker et al., 1978].

*Work performed under the auspices of the U.S. Department of Energy, Washington DC

As will be discussed in this paper, we find that in situ measurements of the anisotropy of > 30 keV electrons at synchronous orbit appears to provide a tool for assessing the probability of an impending substorm. The method may be viewed as either a very limited technique or as a general predictive scheme. In the limited sense, the anisotropy measurements could simply aid in the operations of a given spacecraft bearing electron detectors similar to those to be discussed below. As part of a more expanded technique, however, more general information for substorm prediction may be obtained from energetic electron anisotropies and therefore the method could be of general predictive utility.

2. Instrumentation

The observations to be discussed in this paper were obtained with the low-energy electron (LoE) detector portion of the Los Alamos Scientific Laboratory Charged-Particle Analyzer (CPA) experiments. Identical CPA instruments are onboard spacecraft 1976-059A and spacecraft 1977-007A both of which are located in geostationary orbit. For the period under discussion here, 77-007 was at $\sim$ 135° W longitude, while 76-059 was first at $\sim$ 35° W and then was at $\sim$ 70° W longitude.

The LoE sensors measure energetic electrons in the energy range 30 to 300 keV with six fixed energy discrimination thresholds. Each LoE detector consists of five identical sensor-collimator units arranged at 0°, $\pm$30°, and $\pm$60° to the spacecraft equatorial plane. The spacecraft rotates with a ten-second period around an axis that points continually toward the center of the earth. Given the fan detector arrangement and given the high sampling rate of the instrument, we obtain a set of 200 data points at each energy level during each ten-second rotation. Furthermore, these points are spread rather uniformly over the unit sphere and this allows complete, continuous pitch angle coverage for all magnetic field orientations.

Since the spacecraft under consideration here have no onboard magnetometers, pitch angle distributions are computed in a self-consistent manner from the > 30 keV electrons using a spherical harmonic analysis and least-squares fitting technique [Higbie and Moomey, 1977]. Quite accurate field directions can be inferred by this technique, but no information about field magnitudes is obtained.

The spherical harmonic analysis includes terms up to, and including, the fourth order. Of particular relevance here is the character of the second-order anisotropy. The amplitude of the second-order anisotropy is called C_2: if C_2 is > 0, this corresponds to a field-aligned type of anisotropy which we generally designate as a "cigar" distribution; if C_2 is < 0, this corresponds to a trapped type of distribution (j_{max} at $\alpha = 90°$) which we call a "pancake" distribution. The symmetry axis of the second-order, trapped distribution (cigar or pancake) defines the local magnetic field direction. The colatitude (or meridional tilt) of the field line calculated in this way is designated as θ_B. In a dipolar magnetic field, θ_B would be expected to be twice the magnetic latitude of the geostationary spacecraft (i.e., 10°-20°). As will be seen below, significant "stretching" of the field lines (θ_B > 20°) often occurs in the nightside magnetosphere.

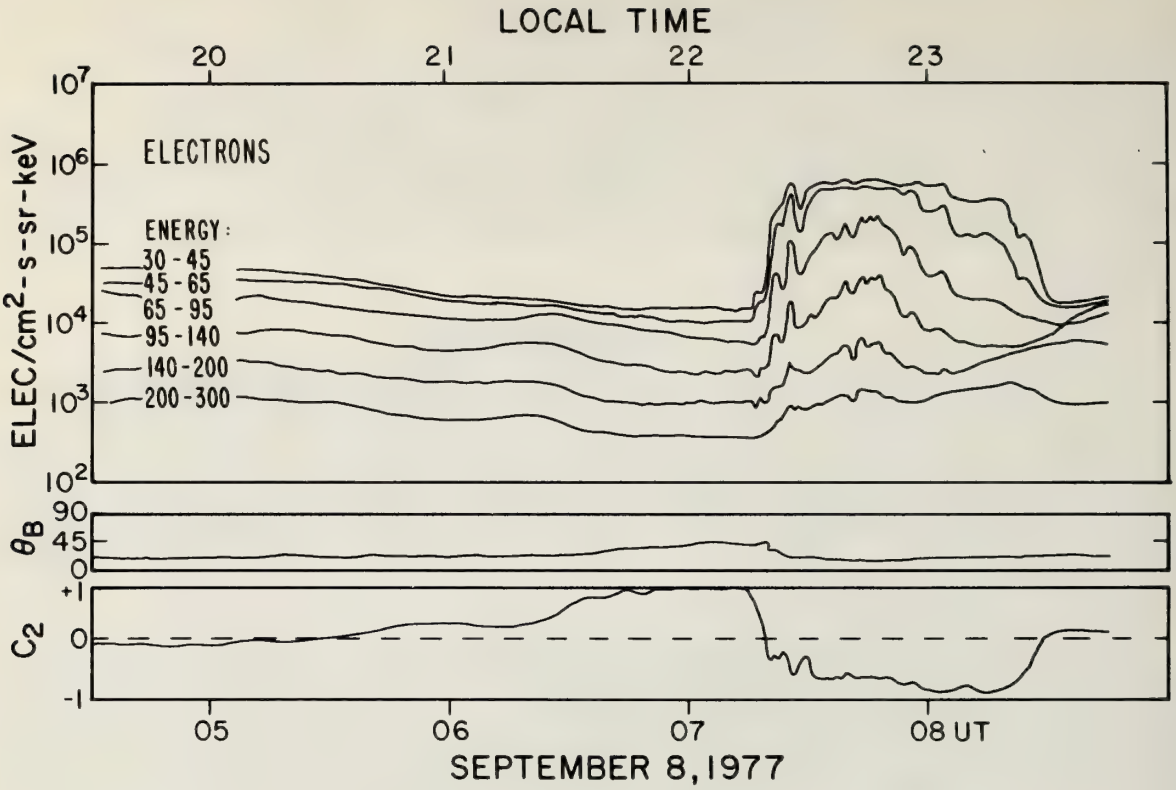


Fig. 1. Charged-particle analyzer low-energy electron data for a portion of September 8, 1977 as measured by spacecraft 1977-007A at geostationary orbit. The upper panel shows differential electron fluxes in the energy ranges (keV) as labeled. The second panel shows the inferred meridional tilt (θ_B) of the local magnetic field line, while the third panel shows the $>$ 30 keV electron second-order anisotropy parameter (C_2).

3. Basis of the Method

Figure 1 shows data obtained from the CPA aboard spacecraft 1977-077 for a portion of September 8, 1977. The top panel shows differential electron intensities between 30 and 300 keV as labeled. The second panel shows the inferred tilt, θ_B, of the local magnetic field line. The bottom panel shows the second-order anisotropy parameter, C_2. Universal time (UT) of the data acquisition is shown along the bottom of the figure, while spacecraft geographic local time (LT) is shown along the top of the figure.

Electron fluxes as observed by spacecraft 77-007 had been approximately constant since 0300 UT (1800 LT). Beginning at $\sim$ 0530 UT (2030 LT) the C_2 parameter increases substantially indicating the progressive development of a cigarlike electron anisotropy. Concurrent with the increase of C_2, the spin-averaged electron flux at all energy levels diminishes gradually and nearly monotonically.

At ∿ 0620 UT, C_2 increases more rapidly and reaches +1.0 by 0700 UT. During this same time interval θ_B increases substantially to ∿ 50°. Prior to 0500 UT θ_B was ∿ 15° which would be only a slightly larger field line tilt than expected in a dipolar field (i.e., θ_B ∿ 10° at the spacecraft magnetic latitude of ∿ 5°). Hence, throughout the "cigar phase" of this event there was a progressive development of a more stretched or "taillike" field in the premidnight sector of the magnetosphere.

At ∿ 0720 UT we observe an injection of energetic electrons in essentially all energy ranges up to 300 keV. At nearly the same time C_2 decreases abruptly and goes negative indicating that the > 30 keV electron anisotropy has become of the pancake, or trapped, variety with peak fluxes perpendicular to the local field line. Concurrent with these flux and anisotropy changes, it is seen that θ_B relaxes from ∿ 50° back to 15° ∿ 20°. Hence a more dipolar configuration of the field accompanies the injection process.

In Figure 2 we show the detailed character of the pitch angle distributions of the electrons at several points during the event shown in Figure 1. Each vertical column of Figure 2 shows pitch angle distributions at selected energy levels (as labeled to the right of the figure) and each column corresponds to data acquired during one 10-second spacecraft rotation beginning at the time indicated at the top of the figure. Each individual distribution corresponds to the number of counts per 8-msec sample plotted versus $\mu \equiv \cos\alpha$.

As shown by the 0604:43 UT samples, the > 30 keV anisotropies early in the precursory phase begin by showing a mild, but clear, flux minimum at $\mu = 0$ ($\alpha = 90°$). Later at 0701:23 UT when the field is rather taillike (θ_B ∿ 50°) and C_2 is large (+1.0), the flux minimum at $\mu = 0$ is very pronounced. We find the cigar anisotropies prior to substorms to be readily detectable with the CPA even for θ_B values approaching 80°-90° [Baker et al., 1978].

After the substorm onset and the concomitant flux injection, we see strong flux maxima at $\mu = 0$. As illustrated by the third column of Figure 2 (0802:49 UT), this pancake character extends, in this case, only up to ∿ 100 keV whereas at higher energies the electrons merely resume an approximately isotropic distribution.

The relationship that these energetic electron variations bear to substorms is shown by Figure 3. Leirvogur (∿ 22° W geographic longitude) shows two periods of substorm activity beginning at ∿ 2200 UT of September 7 and ∿ 0120 UT of September 8. At Meanook (∿ 113° W geographic longitude) slight disturbances are seen after ∿ 2200 and ∿ 0100 UT. There is only one clear substorm signature at Meanook, however, and the onset time for this event is ∿ 0720 UT. Thus the energetic electron injection seen at spacecraft 77-007 (∿ 135° W longitude) corresponds almost precisely to the small, 100 γ bay onset seen at Meanook. Furthermore, the cigar anisotropy phase (0530-0720 UT) occurs well after substorm activity has ceased at magnetometer stations near midnight at that time.

Most energetic electron injections which we observe near midnight at 6.6 R_E follow a pattern similar to that illustrated in Figure 1. That is, there is a "precursory" phase in which significant taillike stretching of the field lines occurs and a substantial cigar type of anisotropy is observed in the >

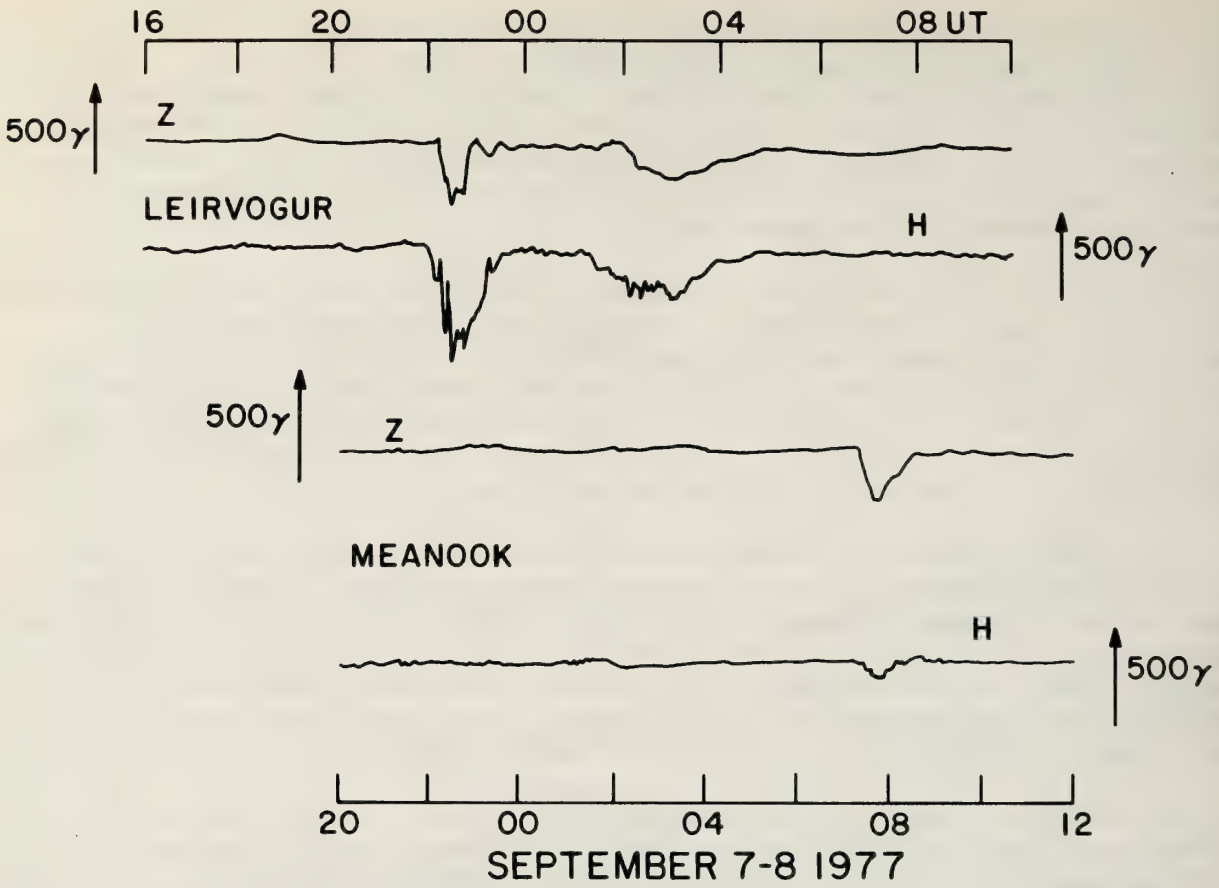


Fig. 2. Pitch angle distributions observed at selected times during the event shown in Figure 1. Several electron energies, as labeled on the right, are shown and each plot corresponds to the number of counts per 8 msec sample versus μ, the cosine of the pitch angle (α).

30 keV electrons. At the time of the flux injection (which is usually very close to the substorm expansion onset as determined from ground-based magnetometer data) the 30 keV electrons exhibit a strong pancake distribution.

We have examined several month's worth of data to assess the statistical association of the cigar phase (in > 30 keV electrons) at 6.6 R_E with substorms. Table 1 is a matrix representation which summarizes our results from available data during July-December 1976. Included are substorms which occurred when the spacecraft was within several hours of local midnight.

Several points should be noted in Table 1. First, we had no AE indices available for this study and thus we had to rely on standard auroral zone magnetograms (Kiruna, Leirvogur, Narssarssuaq, Great Whale River) to judge whether or not a substorm had occurred. Secondly, the 17 cases in which no cigar phase was observed correspond to passages of the spacecraft completely through the nighttime sector of the magnetosphere. Hence the numbers in row 1

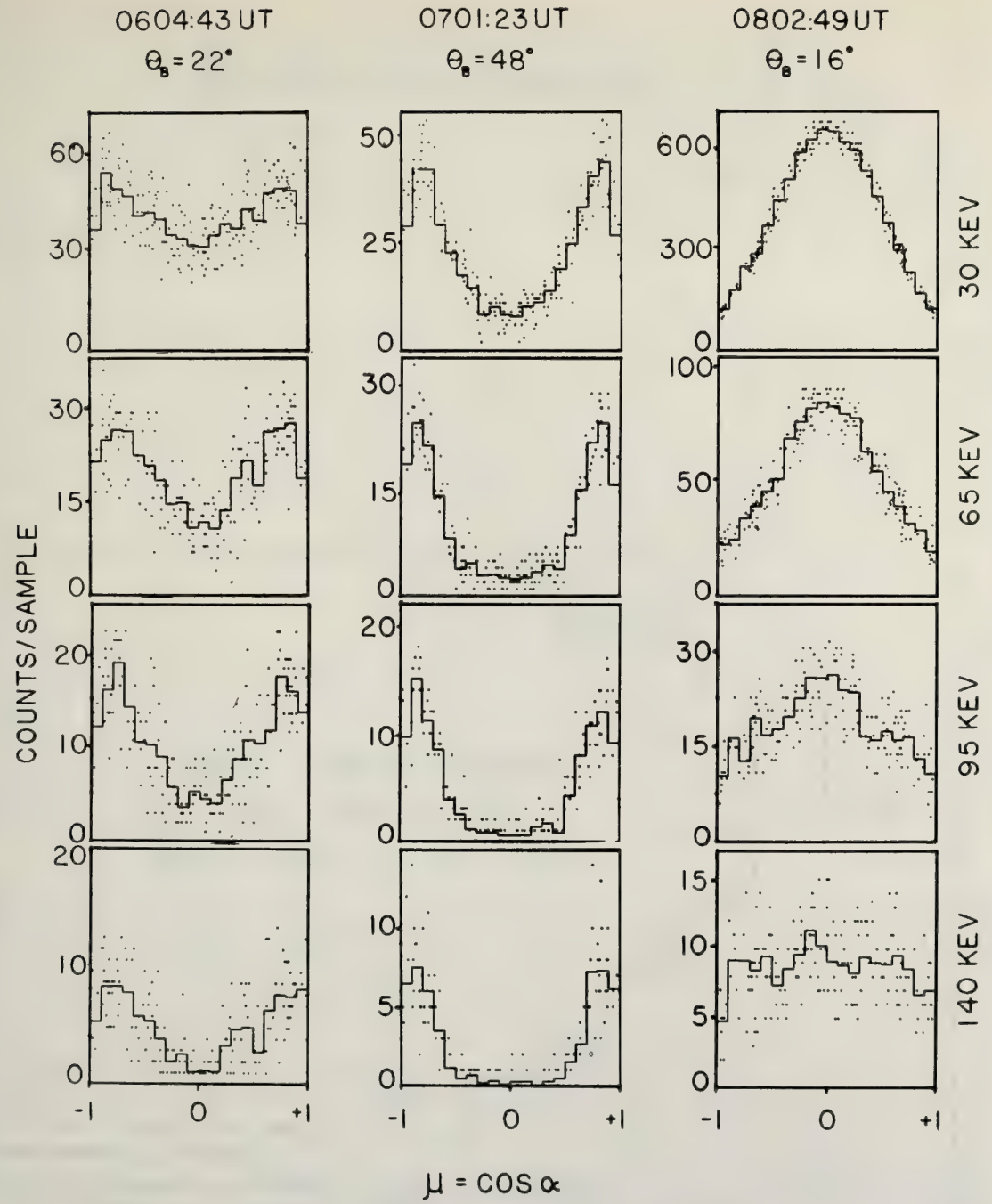


Fig. 3. Ground-based magnetogram traces for 7-8 September, 1977 showing auroral zone substorm activity associated with the period shown in Figure 1.

of the table are a different entity than the event-related numbers of row 2. Nonetheless, the rather highly diagonal character of the matrix in Table 1 suggests a firm relationship between the cigar phase and substorms.

To further assess the statistical relationship of the cigar phase to substorm onset we have generated distributions such as that shown in Figure 4. For approximately 85 events in which we observed flux injections at the

TABLE 1

PRECURSORY CIGAR-PHASE ASSOCIATION WITH SUBSTORMS.

	No Substorm	Substorm Observed
No Cigar-Phase Observed	15	2
Cigar-Phase Observed	4	97

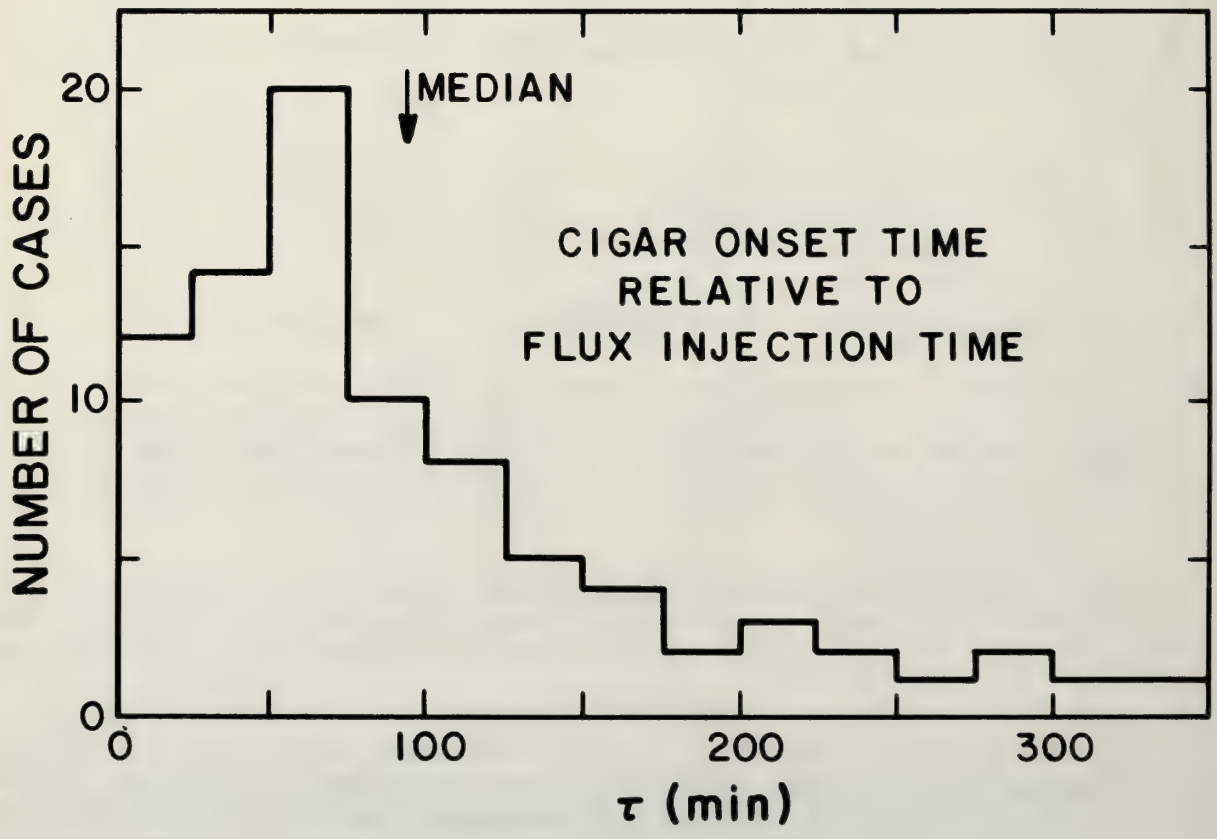


Fig. 4. The statistical relationship of the onset of the cigar phase in the > 30 keV electrons at 6.6 R_E to the observed flux injection time on the same spacecraft. The value of τ is the flux injection time minus the cigar phase onset time.

synchronous orbit satellite in the midnight sector and in which we could assign a clear cigar-phase onset time, we have found the time, τ, between the onset of the cigar phase and the injection time. At least as far as the spacecraft at 6.6 R_E is concerned, "flux injection time" is synonymous with "substorm onset time." As shown by Figure 4, $\gtrsim$ 85% of the substorm injection events had cigar phases < 3 hours in duration. (The significance or importance of the extended tail of the distribution in Figure 4 remains to be assessed.) The typical (median) time of duration of the cigar precursory phase was found to be $\sim$ 1.5 hours.

We conclude from these results that the observation of cigarlike anisotropies in > 30 keV electrons at 6.6 R_E implies with high probability that a substorm will occur shortly. Similarly we conclude that absence of cigar anisotropies implies, again with high probability, that no substorm is imminent. Observation of the onset of the cigar phase (which occurs primarily only in the 18-02 LT sector) can mean that the disruption associated with energetic particle and hot plasma injection can occur any time between $\sim$ 0.5 and $\sim$ 3.0 hours later. However, the highest probability is that the next injection of particles will occur in about one to two hours.

4. Discussion and Possible Uses

As described in the Introduction, one of the major impacts of substorms is the disruption of spacecraft operations due to energetic particle (and hot plasma) disturbances generated during the substorm. Many other impacts (such as ionospheric disturbances, communications interruption, etc.) of a very practical nature also occur as a result of these energetic particle substorm effects. Thus it seems reasonable that all methods of predicting such events (and thus alleviating their impact) should be employed.

We feel that we have a reasonably good theoretical understanding of why a "cigar phase" should accompany most substorm events. The reason is that in the nightside magnetosphere the synchronous altitude is right on the borderline at which $\sim$ 30 keV electrons are ordinarily nearly isotropic (or else have a pancake distribution) in the undistorted, quiescent magnetosphere. As the magnetosphere becomes more distorted with the development of a stretched, taillike magnetic field geometry on the nightside, the $\sim$ 30 keV electrons respond very sensitively. In the stretched field topology, small pitch angle electrons drift further from the earth than they normally would in the quiescent magnetosphere, while large pitch angle electrons drift nearer to the earth than normal. Both of these populations drift in this way in an attempt to preserve their adiabatic invariants [Roederer, 1972]. Since there are weak (but noticeable) radial gradients in the 30 keV electron population in the outer radiation zone, the net result of the distorted drift paths discussed above is to produce cigarlike anisotropies at $L \simeq 6.6$. This ordinarily occurs if, and only if, substantial stresses have built up in the outer magnetosphere, i.e., if, and only if, a substorm is imminent. Eventually the accumulated magnetic stress in the magnetotail is released by the substorm and the field at 6.6 R_E relaxes toward a more dipolar configuration.

Our observations are generally consistent with the well-known model [McPherron et al., 1973] of substorms in which a southward IMF causes dayside magnetopause erosion, flux transport to the tail lobes (with an increase in

tail lobe field strength), and an increase and inward motion of the cross tail current. This latter inward motion of the tail current then produces a more taillike field geometry in the vicinity of 6.6 R_E and energetic electrons respond as described above.

Energetic electrons, we feel, offer certain advantages over synchronous orbit magnetometers in observing substorm-induced magnetospheric effects: (1) Electrons, in a sense, average over a broad range of magnetospheric longitudes by virtue of their eastward azimuthal gradient and curvature drifts, whereas individual magnetometers make very localized measurements; and (2) Electron anisotropies can often show enhanced cigarlike character even when concomitant significant taillike field stretching is not observed at a given spacecraft location. The latter effect may well reflect the fact that electron cigarlike anisotropies may often result (or be enhanced) by the losses of $\alpha \lesssim 90^\circ$ particles at the dayside due to the dayside magnetopause erosion mentioned in the model above. Magnetometers cannot show such evidence of dayside erosion directly. We point out that the electron measurements discussed here can be made by suitably instrumented spacecraft on which energetic particle background levels are routinely and importantly measured. This can be done without the additional requirements of high magnetometer telemetry rates and extreme spacecraft cleanliness. We certainly would not, however, wish to argue that magnetometer data are not desirable and important for most scientific endeavors at any magnetospheric location.

Although we are advocating use of electron anisotropies to predict substorms, we are not arguing for causality. Certainly, cigarlike energetic electron anisotropies do not "cause" substorms, nor does a certain degree of taillike magnetic field stretching necessarily imply that a substorm will occur in some specific period of time. Our observations do, however, suggest that once magnetospheric stresses have been built up they will, in general, only be relieved by a substorm occurrence. Thus our results show a statistical relationship between the time of cigar phase onset and the time of substorm expansion phase onset with a typical difference in these times of 1-2 hours. Embedded within this statistical relationship may well be a direct physical causality associated with time scales of instability onsets or times for certain sequences of processes to lead to the eventual energy release of a substorm. Further research will hopefully answer this question.

The results reported here appear to support the concept of a substorm "growth phase" [McPherron, 1970], at least for substorms which we are able to observe at synchronous orbit. There is apparent disagreement at this time as to whether every individual substorm has a growth phase as described by McPherron, or whether there is only a single growth phase (following a southward turning of the IMF) which precedes a sequence of substorms (see Pytte and West [1978] for a recent discussion of the growth phase). Our results seem to indicate that nearly every observed substorm is preceded by the 'cigar phase'. Whether this phenomenon indicates a growth phase for individual substorms, or simply the reestablishment of conditions (say by electrons newly drifting to the spacecraft location) due to an earlier addition of energy to the magnetotail, is a subject for further research. We again note that the cigar phase may be quite evident in the 30 keV electrons even though there is little apparent progressive taillike magnetic field stretching at 6.6 R_E and even

though ground-based magnetometers may show little departure from quiet-time behavior.

Observations relating specifically to the growth phase of substorms have been presented, for example, in the series of papers about the August 15, 1968 substorms (see McPherron [1973] and the papers thereafter). Detailed electron anisotropy information is given for these cases by West et al. [1973b] and Kivelson et al. [1973]. OGO 5 observations of two substorms, made near midnight at a greater geocentric distance than our own observations, showed a transition of the electron pitch angle distributions ($E > 50$ keV) from field-aligned to approximately isotropic during the substorm growth phase identified by a variety of other observations. Thus, our results at 6.6 R_E for a very large number of cases would indicate an association of the growth of the cigar distributions of electrons ($E > 30$ keV) with a substorm "growth phase," whereas the previous observations at generally greater geocentric distances have associated the disappearance of cigar anisotropies with the growth phase. It is felt that all of these observations are generally consistent with the expected behavior of drifting electrons in a distorted magnetospheric field.

As in Figure 1 above, we have studied many examples of fairly "isolated" substorms. We observe quite frequently, however, many substorms in rapid succession each with accompanying energetic particle injection. Ordinarily the period prior to each of these several injections is accompanied by the return or re-establishment of the cigar phase. This continues, apparently, until all of the available free energy has been dissipated and the magnetospheric ground state is approached. Thus, even under very disturbed conditions the cigar phase or the time derivative of the C_2 parameter may be used to indicate that yet another substorm onset and flux injection is imminent.

Recently it has been proposed [Akasofu, 1978] that realtime monitoring of the solar wind velocity (V) and the interplanetary magnetic field (IMF) magnitude and direction could predict substorms (or at least the AE index) with 50-60% probability. This seems, indeed, to be a very promising approach. This corresponds to an external monitor of the energy input function. From our present results, we would suggest that low-energy electron anisotropies appear to act as a rather sensitive internal magnetospheric "barometer." To achieve the highest success in substorm prediction, it would seem profitable to use several effective means of prediction including both external and internal assessment methods.

A set of several well-instrumented synchronous altitude satellites separated from each other by several hours in local time could form a very useful substorm monitoring network. Real time readout and assessment of a very simple electron parameter (such as C_2) in the local nighttime sector could give a reasonably good handle on the probability of an imminent substorm. This information could be used not only in the operation of military and communications satellites, but also to predict ionospheric disturbances associated with the drifting injected energetic particles.

Bibliography

Akasofu, S.-I., Interplanetary energy flux assoociated with magnetospheric substorms, Univ. of Alaska Geophys. Inst. preprint, 1978.

Arnoldy, R. L., and K. W. Chan, Particle substorms observed at geostationary orbit, J. Geophys. Res., 74, 5019, 1969.

Baker, D. N., P. R., Higbie, E. W. Hones, Jr., and R. D. Belian, High-resolution energetic particle measurements at 6.6 R_E, 3, Low-energy electron anisotropies and short-term substorm predictions, J. Geophys. Res., 83, 4863, 1978.

Garrett, H. B., A. L. Pavel, and D. A. Hardy, Rapid variations in spacecraft potential, Air Force Geophys. Lab., Rep. AFGL-TR-77-0132, 1977.

Higbie, P. R., and W. R. Moomey, Pitch angle measurements from satellites using particle telescopes with multiple view directions, Nuc. Inst. and Meth., 14. 439, 1977.

Kivelson, M. G., T. A. Farley, and M. P. Aubry, Satellite studies of magnetospheric substorms on august 15, 1968, 5, Energetic electrons, spatial boundaries, and wave particle interactions at Ogo 5, J. Geophys. Res., 78, 3079, 1973.

McPherron, R. L., Growth phase of magnetospheric substorms, J. Geophys. Res., 75, 5592, 1970.

McPherron, R. L., Satellite studies of magnetospheric substorms on August 15, 1968, 1, State of the magnetosphere, J. Geophys. Res., 78, 3044, 1973.

McPherron, R. L., C. T. Russell, and M. P. Aubry, Satellite studies of magnetospheric substorms on August 15, 1968, 9, Phenomenological model for substorms, J. Geophys. Res., 78, 3131, 1973.

Parks, G. K., R. L. Arnoldy, T. W. Lezniak, and J. R. Winckler, Correlated effects of energetic electrons at the 6.6 R_E equator and the auroral zone during magnetospheric substorms, Rad. Sci., 3, 715, 1968.

Pytte, T., and H. I. West, Jr., Ground-satellite correlations during presubstorm magnetic field configuration changes and plasma sheet thinning in the near-earth magnetotail, J. Geophys. Res., 83, 3791, 1978.

Roederer, J. G., Geomagnetic field distortions and their effects on radiation belt particles, Rev. Geophys. Space Phys., 10, 599, 1972.

West, H. I., Jr., R. M. Buck, and J. R. Walton, Satellite studies of magnetospheric substorms on August 15, 1968, 6, Ogo 5 energetic electron observations - Pitch angle distributions in the nighttime magnetosphere, J. Geophys. Res., 78, 3093, 1973.

EVOLUTION OF SUBSTORM AND QUIET-TIME ELECTRON ANISOTROPIES ($30 \leq E_e \leq 300$ keV) AT 6.6 R_E

P. R. Higbie, D. N. Baker, R. D. Belian, and E. W. Hones, Jr.
University of California, Los Alamos Scientific Laboratory
Los Alamos, New Mexico 87545

Work using the Charged Particle Analyzer (CPA) instruments aboard spacecraft 1976-059A and 1977-007A in synchronous orbit has shown that ∿ 30 keV electron anisotropies may act as a sensitive indicator of the buildup of stresses in the outer magnetosphere. The development of such stresses is evidenced in the premidnight sector by the formation of field-aligned (cigar) anisotropies in the 30 keV electrons one to two hours prior to the onset of the expansion phase of the substorm. Using the complete three-dimensional pitch angle measurement capability of the CPA, we show in a movie format the detailed development of electron anisotropies during the course of substorm growth, expansion, and recovery phases. In contrast, we also show detailed examples of quiet-time behavior of electron anisotropies at several energy levels between 30 and 300 keV. Such periods with no substorm activity show that 30 keV electrons remain ∿ isotropic (outside the loss cone) throughout the nighttime sector, even though the higher energy (> 100 keV) electrons show the development of cigar anisctropies associated with normal drift-shell splitting. These results emphasize the substorm predictive capabilities of the low-energy electron anisotropies and illustrate how the data might be used in a real-time monitoring mode.

INTRODUCTION

Numerous authors have studied the correlations between the interplanetary magnetic field (IMF) and ground based observations of geomagnetic activity. Caan et al. [1977] examined 18 clear events for which the IMF turned southward after being directed northward for at least two hours. Such turnings were followed in about one hour by substorms as determined from magnetograms recorded at nightside auroral or midlatitude stations. The beginning of some negative bays were correlated with momentary northward excursions of the IMF and the recovery phases of the substorms, as indicated by the magnetograms, seemed to be controlled by the northward turning of the IMF.

Kamide et al. [1977] examined electron precipitation data from Isis 1 and 2 as well as all-sky camera data to determine if the substorm occurrence probability was related to the B_z component of the IMF or to the size of the auroral. They found that the "storm time" probability increased from a low but appreciable value for distinctly northward fields to 100% for strongly southward fields. Conversely, the "quiet time" probability decreased to zero for even weakly southward fields.

Burton et al. [1975] developed an empirical equation relating Dst to interplanetary conditions. They found that Dst, which is mainly responsive to the ring current and is calculated from an average of the perturbations of the H component at mid-latitude stations, could be approximated by a function of the solar wind dynamic pressure and the Y component of the interplanetary field (rectified to correspond to B_z southward) in solar magnetospheric coordinates. They also introduced a filter function to account for delays in the response of the magnetosphere to changing solar wind conditions. This served the same purpose as the typical one hour time lags used by other authors investigating such correlations.

In an earlier paper by Hirshberg and Colburn [1969], the magnitude of the three-hour averaged B_z component was found to be correlated with K_p regardless of the sign of B_z. On the other hand, the variance in B was found to be positively correlated with K_p when B_z was negative.

The preconditions for triggering of a substorm by solar wind discontinuities were examined by Kokubun et al. [1977]. They compared ground magnetograms and AE indices with interplanetary field data for 125 storm sudden commencement (SSC) and sudden impulse (Si) events. They found that the probability of a substorm being triggered increased with the amplitude of the SSC and was strongly dependent on the previous AE activity and the (southward) direction of the IMF. They also cited a few cases in which the energy required for a substorm occurrence was not stored effectively although the IMF was southward.

McPherron [1970] established the concept of a growth phase for a geomagnetic substorm. While the signature in the magnetograms for a given substorm may be subjective, the idea that the build-up, prior to a substorm, of magnetic stresses or the inflow of magnetic energy to the magnetotail might have observable consequences is quite reasonable.

Kamide and Matsushita [1978] presented a summary of the growth phase controversy and attempted to reconcile the differences in a consistent manner. They view the source (dayside merging), energy storage (excess flux in the magnetotail), and drain (reconnected nightside flux) as separate processes. The drain process may proceed quietly (as by plasma convection) or catastrophically (as in substorms). The source, storage and drain processes are related, but not in a simple deterministic way. In Kamide and Matsushita's view, the growth phase narrowly defined applies to very few substorm occurrences, and broadly defined applies to almost all configurations of the magnetosphere.

Perreault and Kamide [1976] cited a number of cases for which the IMF was not uniform across the face of the magnetosphere. Several cases were found when the field was oppositely directed upstream of the dawn and dusk sectors respectively. This result implies care should be taken in relating magnetospheric effects to possible external driving forces.

Svalgaard [1977] gave a very detailed treatment of the am index and was able to synthesize a function using solar wind parameters (plasma density, bulk speed, the angle between the IMF and the dipole axis, the dipole tilt

angle, and the magnitude and variance of the IMF) which replicated the index almost exactly.

The phenomenon of drift-shell splitting is well known and analyzed (Pfitzer et al. [1969], Roederer [1972]). The fact that particles of the same energy but having different initial pitch angles have orbits lying on different drift shells in a nonazimuthally symmetric magnetic field will play a key role in the analysis given below. In our remarks below we will suggest that stored magnetic energy or stresses in the magnetotail indeed has observable consequences for energetic electron distributions.

A number of groups have observed particles at geostationary altitudes and have studied their relation to substorms as well as their typical behavior.

Parks et al. (1972) summarized a number of features of energetic particle variations observed at the geostationary orbit and suggested a model of magnetospheric substorms. They found that the intensity of fluxes of electrons in the 500 keV to 1 MeV energy range are well organized by the quantity $(0.311/B)^{1/3}$ where B is the locally measured magnetic field. Temporal variations are more apparent in the 50-150 keV energy range. The intensity of precipitated fluxes (inferred from x-ray observations from balloons) are intimately related to the intensity of these particles at the equator. After being accelerated in the morning hours, these electrons gradient drift eastward, but are nearly all precipitated before reaching the evening hours in local time.

Parks et al. further suggest that the recovery of the magnetic field to a more dipolar orientation is a consequence of the removal of a high β plasma from the lines of force as the electrons ($E \sim 10$ keV) are precipitated. Precipitation is due to the growth of whistlers (Kennel-Petschek mechanism). The recovery of the field accelerates the electrons by betatron action and enhances the pitch-angle anisotropy. As the local electron fluxes are depleted the field becomes more dipolar and field lines further out in the tail begin to dump their associated hot electrons. This corresponds to the poleward auroral expansion phase. This model thus suggests that substorms are initiated by strong precipitation of energetic electrons on the morning side of the magnetosphere. This process depends on the state of the magnetosphere and the constantly changing solar wind parameters and ionospheric parameters.

Pitch angle distributions at geostationary altitudes have been studied by several authors (Bogott and Mozer, 1971; Kaye et al., 1978; Higbie et al., 1978b). In general they find evidence for drift shell splitting effects. In addition Kaye et al. find evidence for strict local control of the pitch angle distributions in that the distributions respond adiabatically to changes in the local magnetic field.

Baker et al. (1978a) observed that the existence of cigar anisotropies in the late evening to midnight range at the geostationary orbit could be taken as a prediction of substorm onsets. In some 97 cases cigar anisotropies were seen to preceed substorms, whereas for 17 cases when no cigars were seen, only two were accompanied by (weak) substorm activity. This paper illustrates in a movie format the evolution of typical observations of this type.

INSTRUMENTS AND MOVIE FORMAT

The charged particle analyzer has been described in some detail previously (Higbie, et al. 1978b). Briefly, five collimated sensors are arranged at 30°, 60°, 90°, 120° and 150° to the spacecraft spin axis which is always pointed toward the earth. Each sensor is sampled, for each of six energy windows, forty times per ten second rotation period. Thus for each energy there are two hundred samples which cover the unit sphere rather uniformly. The energy windows have 30, 45, 65, 95, 140, and 200 keV thresholds with a common upper energy cutoff of 300 keV. Since there is no on-board magnetometer the pitch angle distributions must be calculated in a self consistent manner (Higbie and Moomey, 1977).

In the movie the pitch angle distributions are plotted as a function of the cosine of the pitch angle (measured from the symmetry axis of the distribution) and are illustrated at the top of each frame. The six energy windows corresponding to each distribution increase from left to right and top to bottom. The normalized counting rate (or square root for compression) is plotted in each box.

The spin-averaged counting rate corresponding to the lowest energy window is plotted in the lowest panel. Since each movie frame corresponds to one spacecraft rotation, the movie proceeds at approximately 180 to 240 times real time for silent or sound projection rates. One point is added to the spin-averaged counting rate curve for each movie frame so that the end point of the curve serves as a time reference.

Also plotted for certain examples are the B_z component of the IMF in solar magnetospheric coordinates and the auroral zone magnetometer readings for a ground station near the spacecraft meridian.

OBSERVATIONS

October 31, 1976 Event

Prior to the start of the movie the IMF had gone through a two and one-half hour period (2100-2300) of strong negative B_z, an hour and a half episode of positive B_z and then another half-hour of negative B_z. At the start of the movie B_z has just turned northward. The C_2 parameter is very large and positive indicating strong cigar development. All energy channels show well developed cigar shapes, as illustrated in Figure 1a. Close inspection of these distributions reveals a small loss cone very near $\mu = +1$. The distributions evolve slowly during the next two hours. The spin averaged counting rate does not change appreciably, but by 0400 UT there has been an appreciable relative increase of 90° pitch angle particles at all energies (Figure 1b). At 0409 UT there is a slight decrease in the spin average counting rate which occurs $\sim$ 2 minutes after the IMF has turned southward momentarily. During the next hour the velocity of the solar wind increases from $\sim$ 450 to $\sim$ 480 km/sec and its density decreases by a factor of three. 90° pitch angle particles begin to appear at 18310 sec UT, apparently at all energies simultaneously. These particles are particularly evident in channels 3 and 4 in Figure 1c. By 18420 sec UT (Figure 1d), the cigar shapes have been transformed into pancake distributions and the counting rate begins to decrease. A negative bay in the

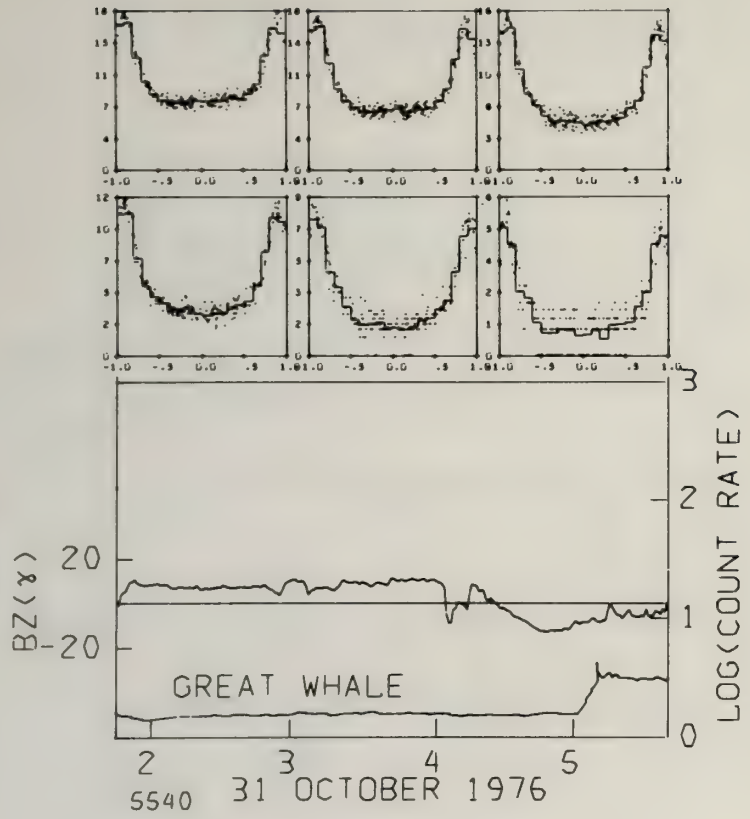


Figure 1a.

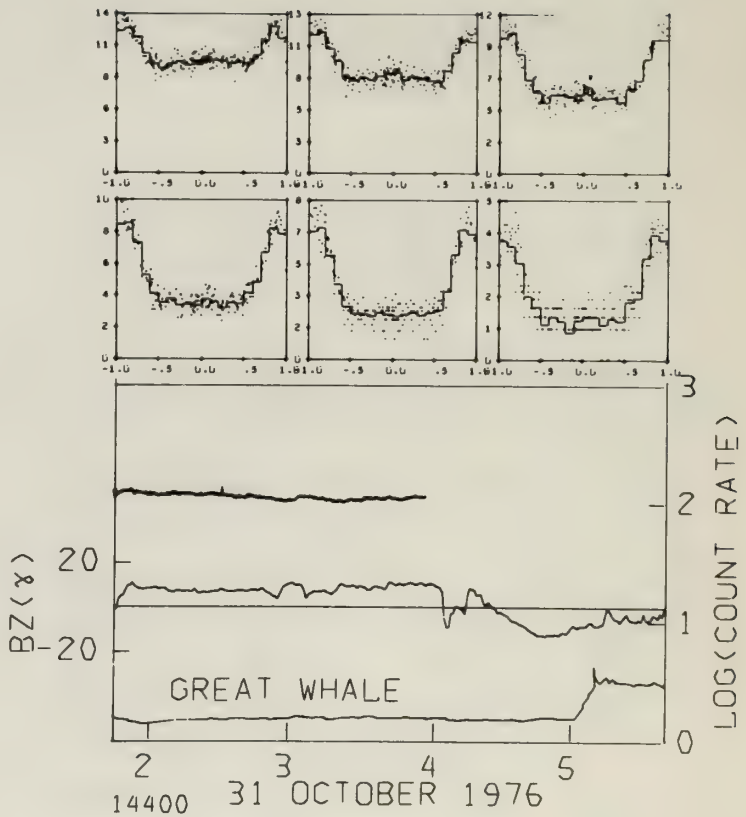


Figure 1b.

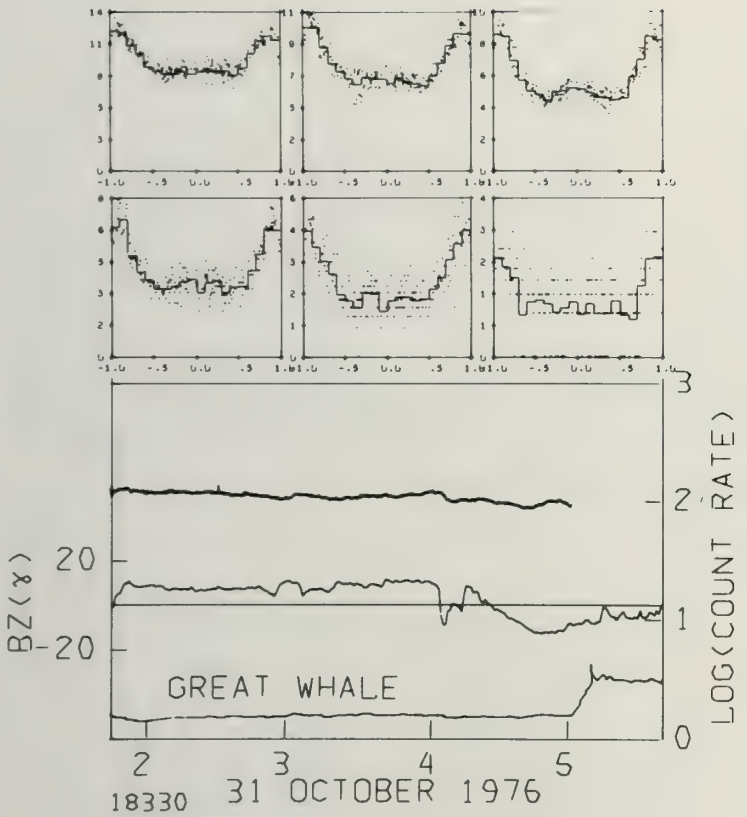


Figure 1c.

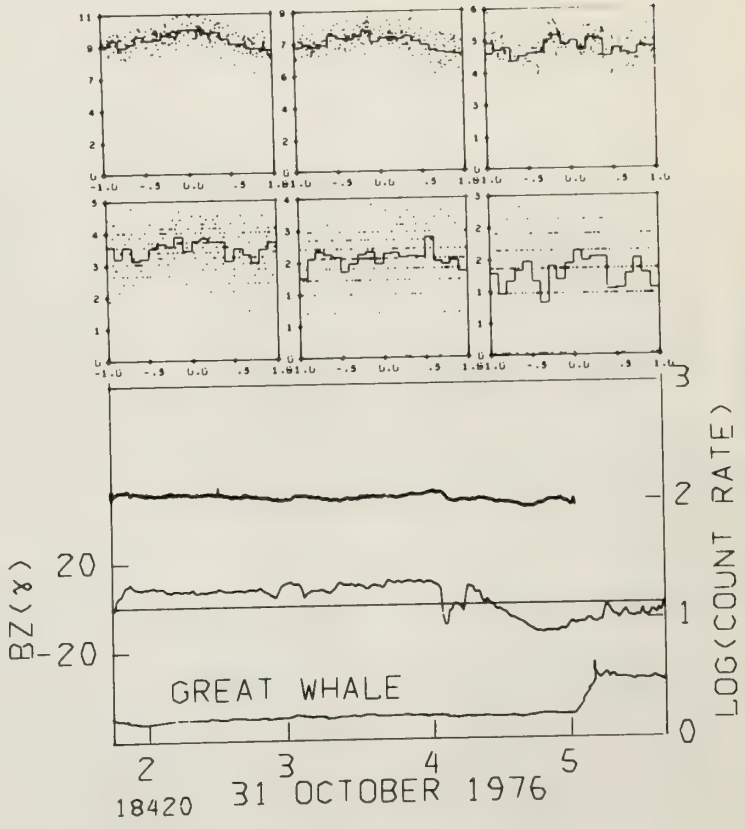


Figure 1d.

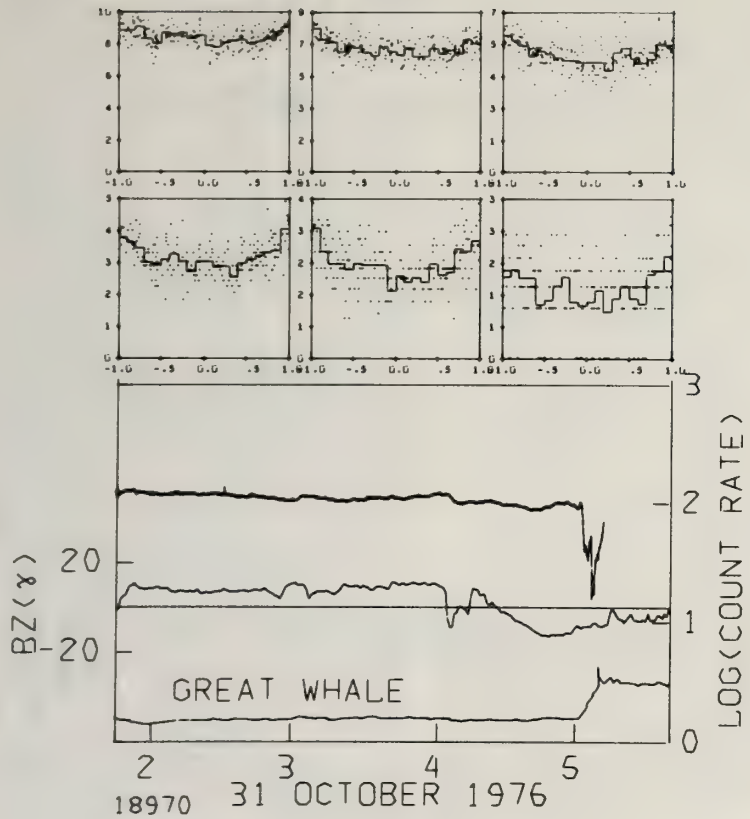


Figure 1e.

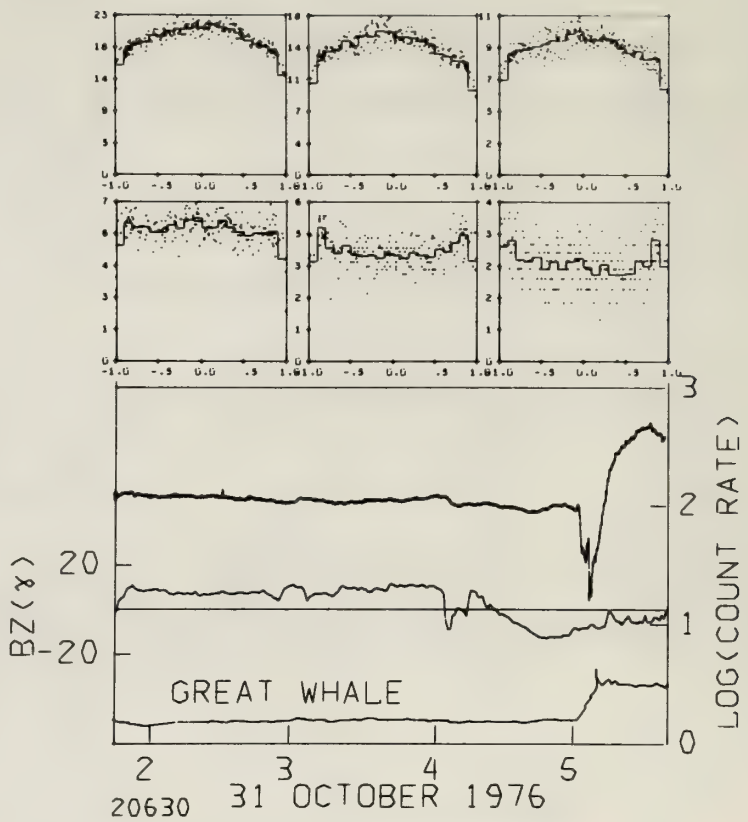


Figure 1f.

H-component recorded at Great Whale River begins at ~ 0508 UT ≈ 18480 sec UT. A series of chaotic distributions ensue but when the flux recovers at 18970 sec UT the distributions have clear cigar like characteristics at all energies (Figure 1e). Eventually (~ 0530) pancakes form in the lowest four energy channels, but cigar distributions remain in the highest energy channels (Figure 1f). This situation obtains until the end of the film.

December 14, 1976 Event

This event is an example of an extremely quiet day. Before the start of the film the IMF had a small southward component (in solar ecliptic coordinates) for several hours. Auroral zone stations (Leirvogur in particular) show essentially no geomagnetic activity. The three hour Kp values were: December 14 (1^+, 2^+, 1^-, 1^-, 1^-, 0^+, 0^+, 1^-) and December 15 (0^+, 1^-, 0^+, 1^+, 0, 0, 0^+, 0). The movie starts at 2300 UT on December 14. There are no discernable variations in the pitch angle distributions during the course of the film. The lower energy channels all show very weak pancake distributions; there are hints of a cigar distribution in the highest energy channel. Representative frames are shown in Figures 2a and 2b for times near the beginning and the end of this time interval.

September 2, 1976 Event

Prior to the start of the movie at 0300 UT, the B_z component (in solar magnetospheric coordinates) had been nearly zero with small northward and southward excursions. At 0300 UT the Great Whale magnetogram indicates a substorm recovery was in progress. 1976-059 was near the midnight meridian. The C_2 parameter was decreasing, corresponding to an increasingly pancake-shaped distribution. θ_2 showed a slight decrease corresponding to a less taillike configuration of the magnetic field. The azimuthal angle of the field which had been 20° west was returning to 0° indicating a field lying in the local meridian. At approximately 0338 UT the C_2 parameter began to increase. The B_z component, which had been strongly northward since ~ 0240 UT, showed no change near this time. Plasma data from IMP-J shows a high speed stream starts at about this time. The increase in C_2 continues until a strong cigar distribution develops just prior to a series of particle injections beginning at ~ 0520 UT. A very large injection which reaches a saturated flux level starts at 0545 UT [cf. Baker et al. (1978[b]) for a discussion of the stable trapping limit (Kennel-Petschek limit) observed by our instruments]. A negative bay develops at Great Whale starting at ~ 0530 when the station was only a few minutes past local midnight.

At the beginning of the movie (Figure 3a), the three lowest energy channels show a pancakelike distribution, the highest two channels show a weak cigarlike distribution and the 95-300 keV channel is more or less isotropic. By 0350 UT, well before the southward turning of the IMF, the highest four channels show pancake distributions, the 45-300 keV channel has appreciably flattened, and the 30-300 keV channel still retains the initial pancakelike shape (Figure 3b). Within ~ 25 minutes after the IMF is directed south, all channels display cigarlike distributions (Figure 3c).

The cigarlike shapes become more accentuated as time progresses until ~ 0512 when the 30-300 keV channel recovers to an isotropic state (Figure 3d). In the next five to six minutes all channels become pancakelike (Figure 3e). After the pancake shapes are well established the spin-averaged counting rate

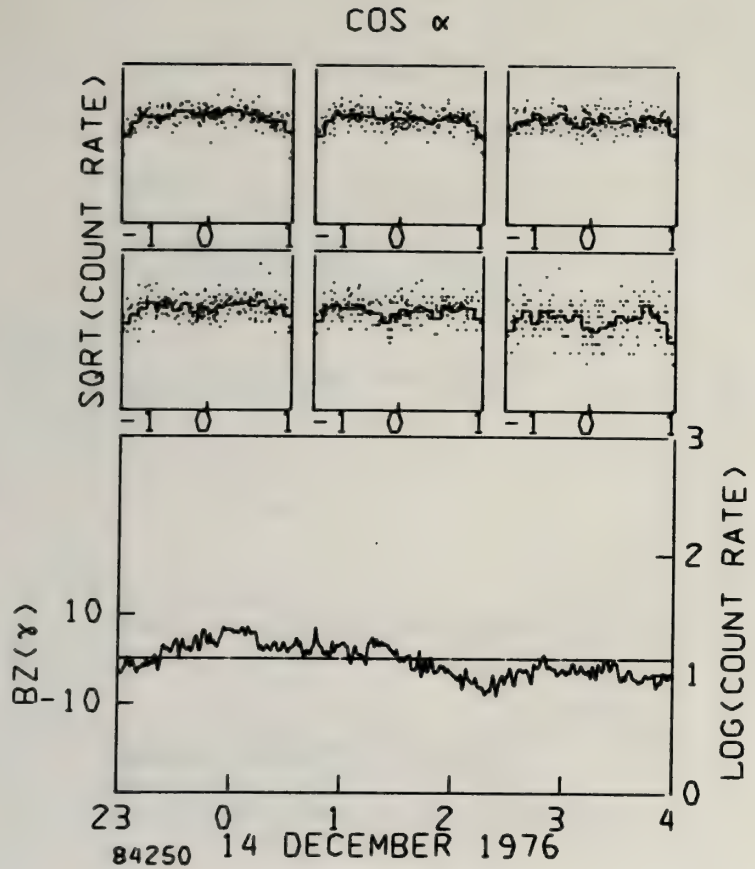


Figure 2a.

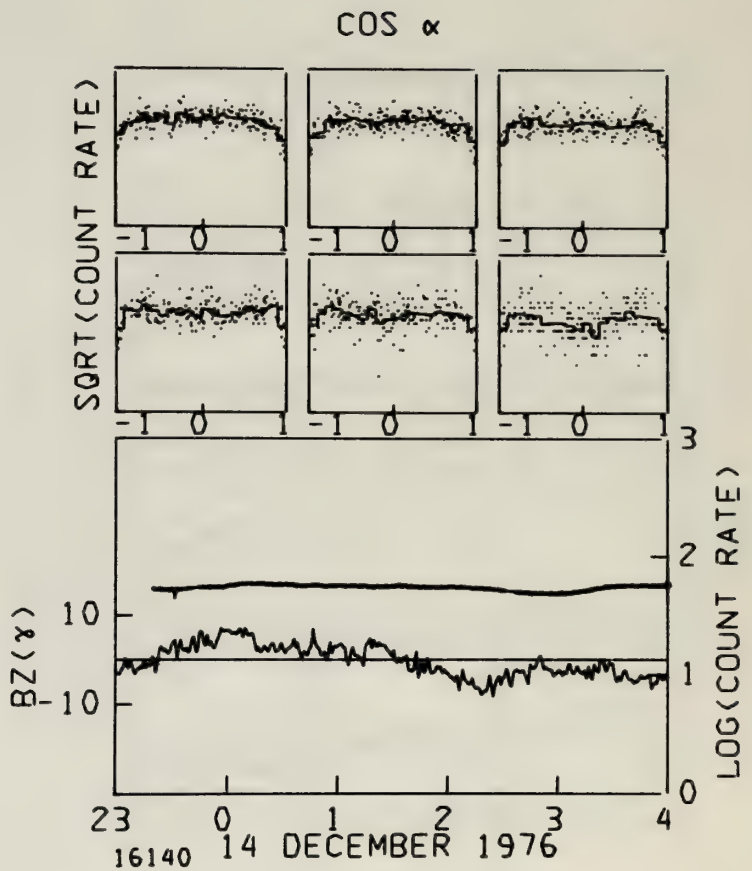


Figure 2b.

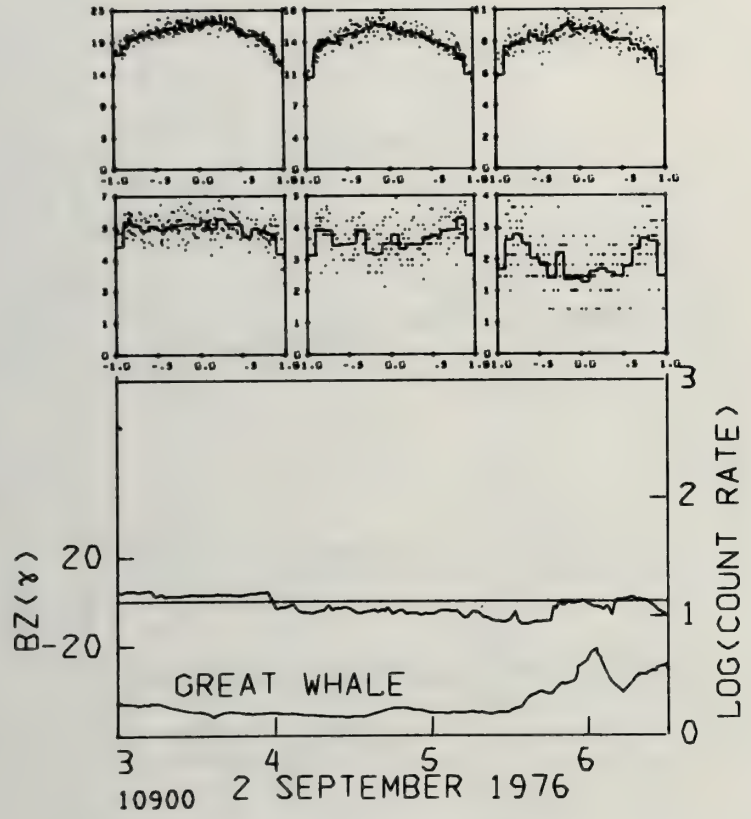


Figure 3a.

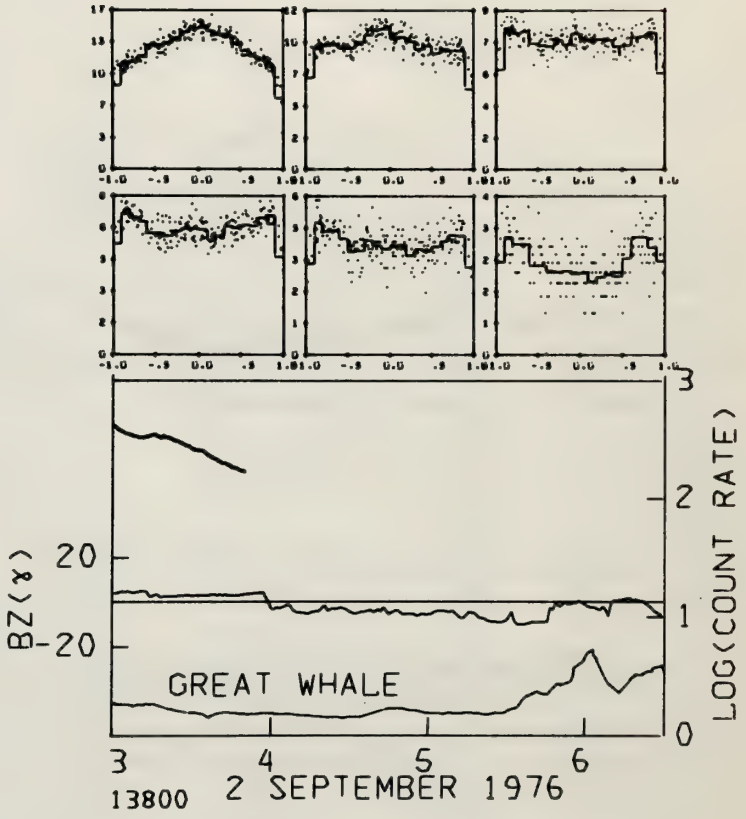


Figure 3b.

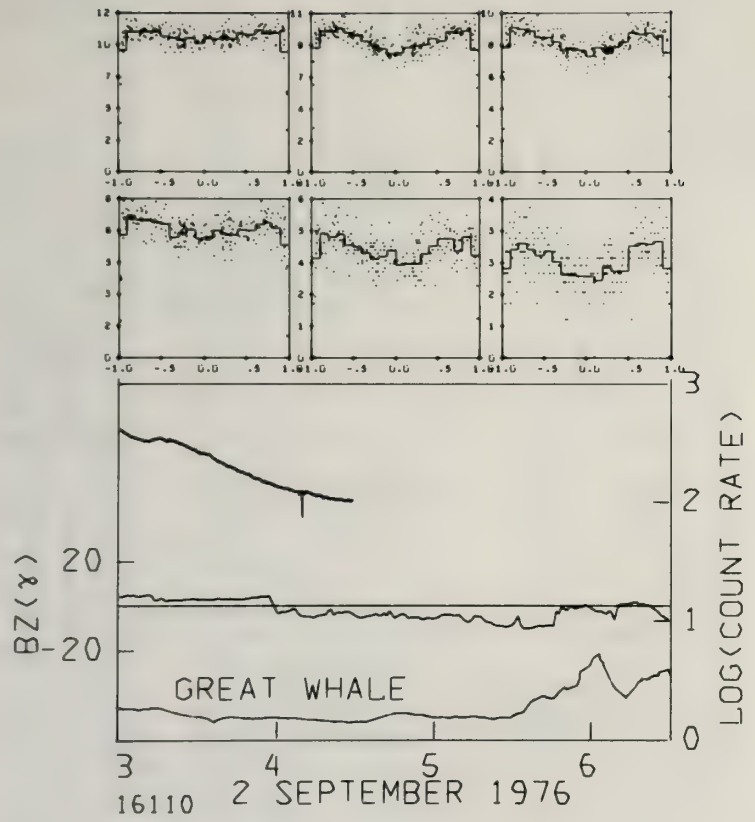


Figure 3c.

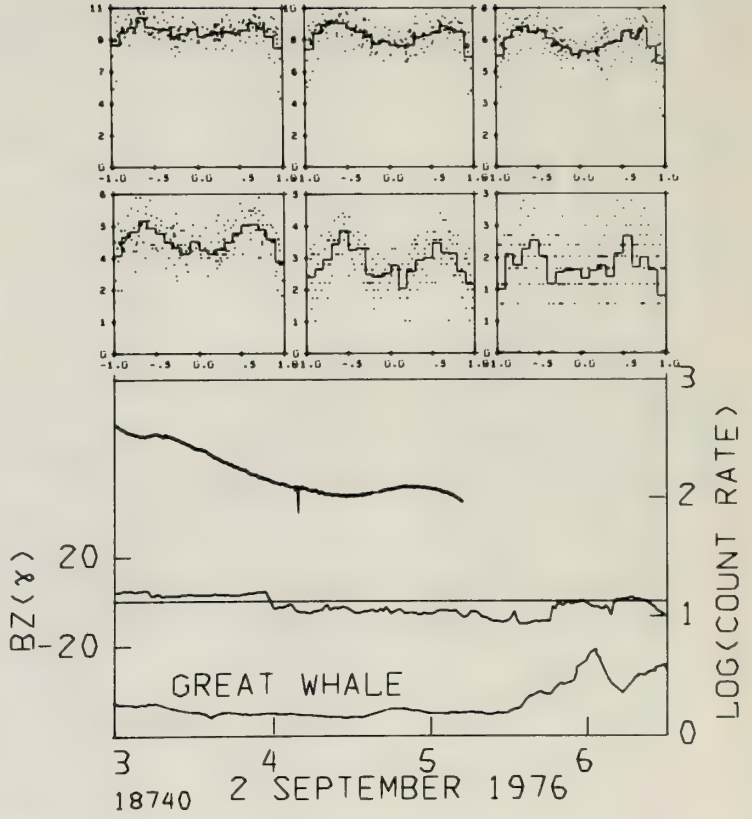


Figure 3d.

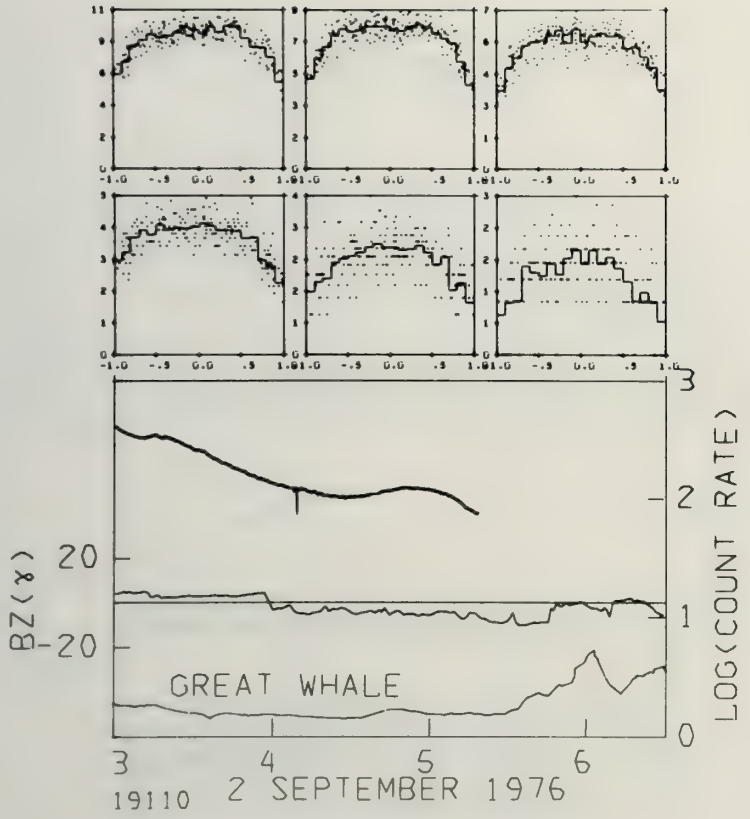


Figure 3e.

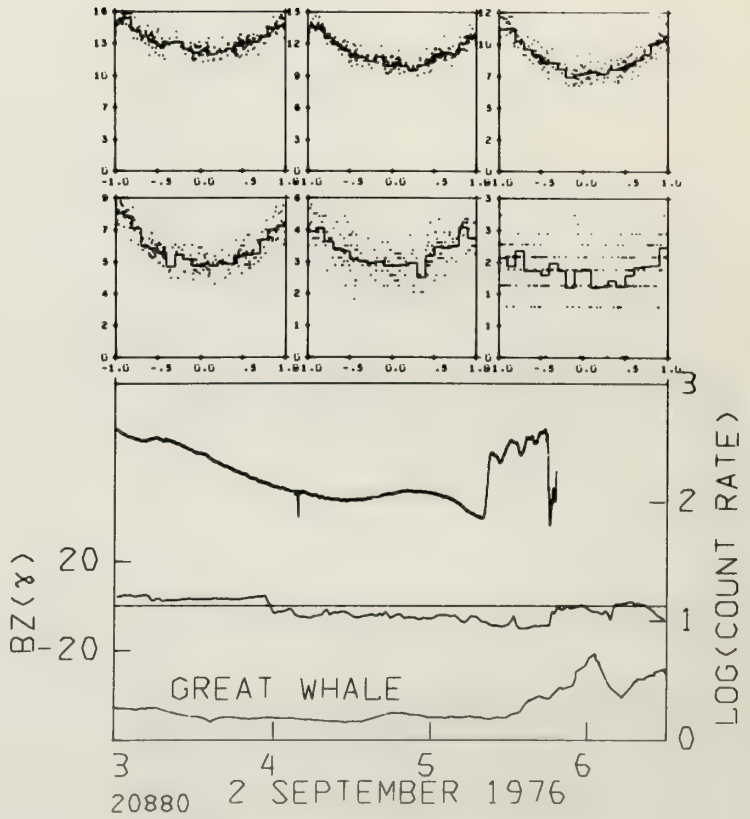


Figure 3f.

increases by a factor of four. This increase showed some evidence of energy dispersion on a time scale of ∿ 1 minute.

After the increase there were quasiperiodic oscillations of the spin-averaged 30-300 keV electron flux with a period of ∿ 5 minutes. However, the higher energy channels show that there must have been a series of injections since these peaks occur at earlier times in successively higher channels. At ∿ 0545 a large decrease occurs and a new cigar distribution is observed (Figure 3f). The omnidirectional flux climbs to a quite high value in about one half hour and slowly forms a pancake distribution at all energies (Figure 3g).

In summary, the magnetosphere seemed to be relaxing somewhat from 0300 to 0338 UT. At that time, before the field becomes directed southward, cigar distributions begin to form. Pancakelike distributions reform a few minutes before the first of a series of injections reach the spacecraft. A complex series of events follow the first injection.

The formation of cigarlike distributions is in accord with our notion that such distributions are indicators of stresses in the magnetosphere. In this particular case, the stresses may have been induced by the high speed solar stream and then increased when the IMF turned south. The change to pancake-like distributions just prior to the large injection may have been due to energy dispersion effects, adiabatic changes (the field direction did not change at the time of the first injection), or some form of wave-particle interaction which isotropized the distribution. It should be noted that the spacecraft is moving away from midnight where the pitch angle distribution is usually most cigarlike.

August 4, 1976 Event

Prior to turning south at 2226 UT the IMF had been directed north for 5 hrs 19 min. There was a 16 min data gap starting at 1736 UT but the field was strongly north before and after the gap. Before the gap there were a ten-minute and a five-minute period when the field was at ∿ 0° to the ecliptic. At 2226 UT the field turned south for approximately 25 minutes, then remained north for the duration of the film except for a few southward excursions. (There is a data gap from 0132 to 0150 UT which is given as a straight line in the movie.)

The pitch angle anisotropy was very pancakelike when 1976-059 was near local noon (∿ 1515-1615 UT) and, after a data gap, in the local time range 18-20 hr (∿ 2015-2215 UT). In fact the quiet time ($K_p \leq 1+$) anisotropy would be more pancakelike only 10% of the time (Higbie et al. 1978) compared with data in the above local time intervals. After 2215 UT the anisotropy, began to rise until it was above the 90% percentile line by 0000 UT on August 5. The solar wind conditions showed no unusual changes during this period except for an increase in the temperature by a factor of two at ∿ 2230.

The movie starts (Figure 4a) with all energy channels showing well developed pancakelike distributions. Then distributions slowly flatten out with the highest energy channels showing occasional weak cigarlike distributions. By 2325 UT all channels show well developed cigar distributions which are most accentuated at higher energies, e.g. the peak to valley ratio is 1.1 for the

30-300 keV channel, but 2.8 for the 200-300 keV channel. There are two brief dropouts in the spin-averaged flux at 2356 on 4 August and then at 0035 UT on 5 August and a weak enhancement at 0101 UT. The distributions remain reasonably well organized during the second dropout (Figure 4c) and during the enhancement (Figure 4d) and demonstrate that they retain their cigarlike character. Thus these three excursions may be due to boundary motion combined with a radial gradient in the electron flux. The cigar shapes are well established prior to the flux enhancement at 0147 UT. The cigar distributions remain, despite the increased flux until 0157 UT when the 30-300 keV distribution becomes weakly pancakelike as illustrated in Figure 4e. This condition persists for only three minutes before the flux returns to about the level that had been established prior to 0147 UT and a cigarlike distribution is established in the lowest energy channel. There is another increase at 0207 UT and a large injection at 0210 UT. The omnidirectional flux increases by a factor of approximately eight during this injection. Well-formed pancakelike distributions develop in the lowest three channels, but cigarlike distributions persist in the highest two channels (Figure 4f). As the counting rate slowly decreases over the next 45 minutes the cigar distributions slowly reform until by the end of the movie all channels show cigars. During this entire sequence the local field line direction, as determined from the symmetry axis of the distribution, changed very little. The colatitude was 40° in magnetic dipole coordinates at the start of the movie and increased to 50° which implies that the field was quite stretched. The magnetogram at Narssarssuaq shows several distinctive features during this period. A case could be made for identifying all the flux dropouts and increases at 6.6 R_E except for the dropout at 2356 UT, with various rapid changes in the H component displayed in the magnetogram.

To summarize, there are a number of flux enhancements and dropouts that do not significantly change the basic cigarlike distributions observed. Thus these changes may be due to boundary motions or local adiabatic effects only. The flux injection at 0210 UT was accompanied by pancakelike distributions and may thus reflect a true injection and reconfiguration of a portion of the magnetosphere. No dramatic associations with parameter changes in the solar wind were noted.

December 21, 1976 Event

There was a data gap in the Imp J interplanetary field data from $\sim$ 2230 UT on 20 December to $\sim$ 0100 UT on 21 December. During the period covered by the movie the B_z component of the IMF was very weak ($\leq$ 2.5 γ) and varied both north and south. The plasma analyzer on Imp J showed a few minutes of coverage just after 0100 UT and continuous coverage after 0400 UT. The solar wind speed was $\sim$ 390 km/sec for both periods. Except for two samples of bad data at 7770 sec and 8150 sec UT that were unfortunately not edited out of the movie, the spin averaged counting rate shows essentially no variations. Auroral zone magnetograms, Narssarssuaq in particular, show no substorms but essentially flat traces. The pitch angle distributions are essentially isotropic at all energies throughout the movie. Suggestions of pancake or cigar shapes can be seen in individual frames and the loss cone is evident, but no significant anisotropy is observed. Typical frames for the beginning and end of this period are shown in Figure 5.

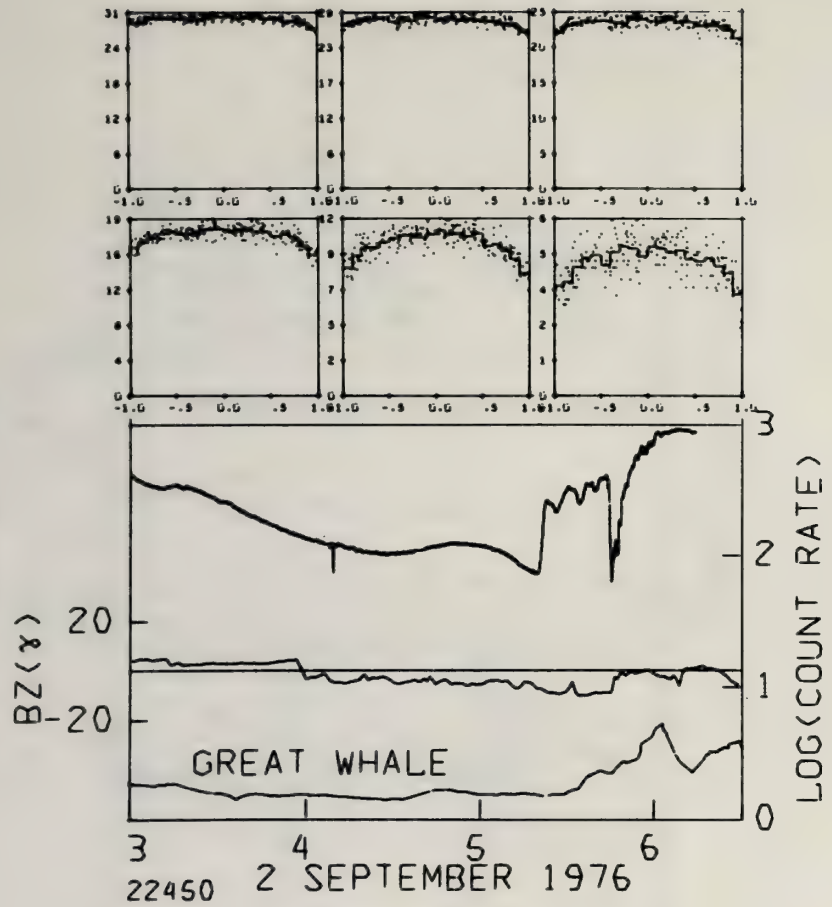


Figure 3g.

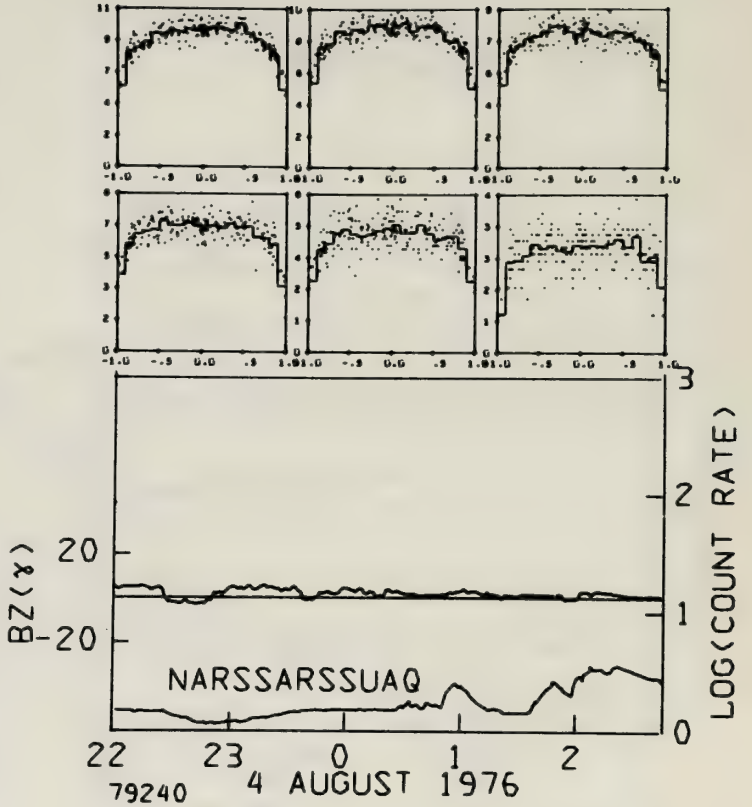


Figure 4a.

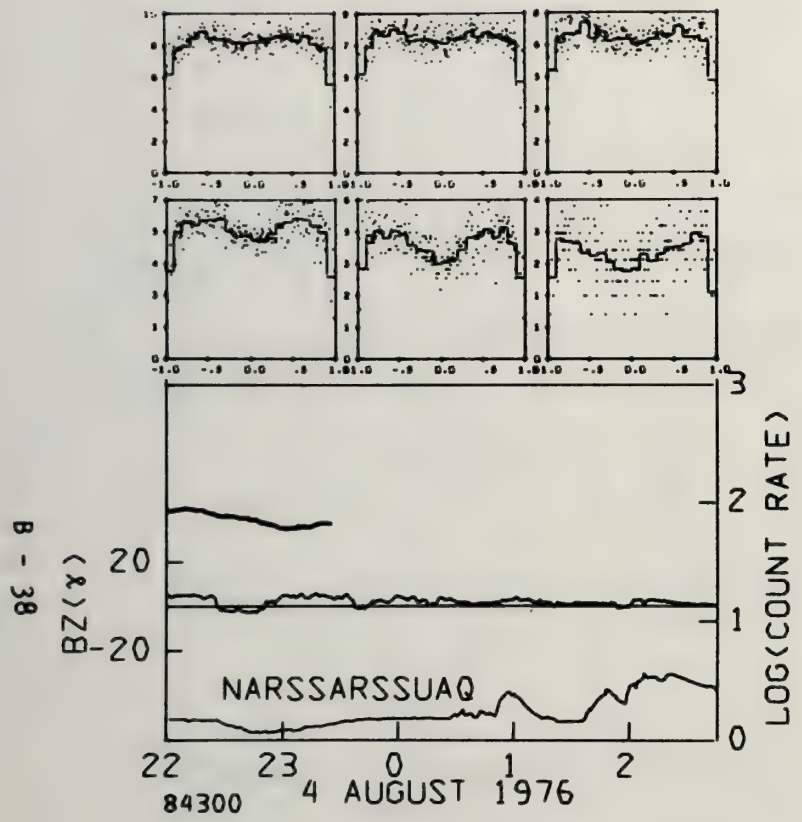


Figure 4b.

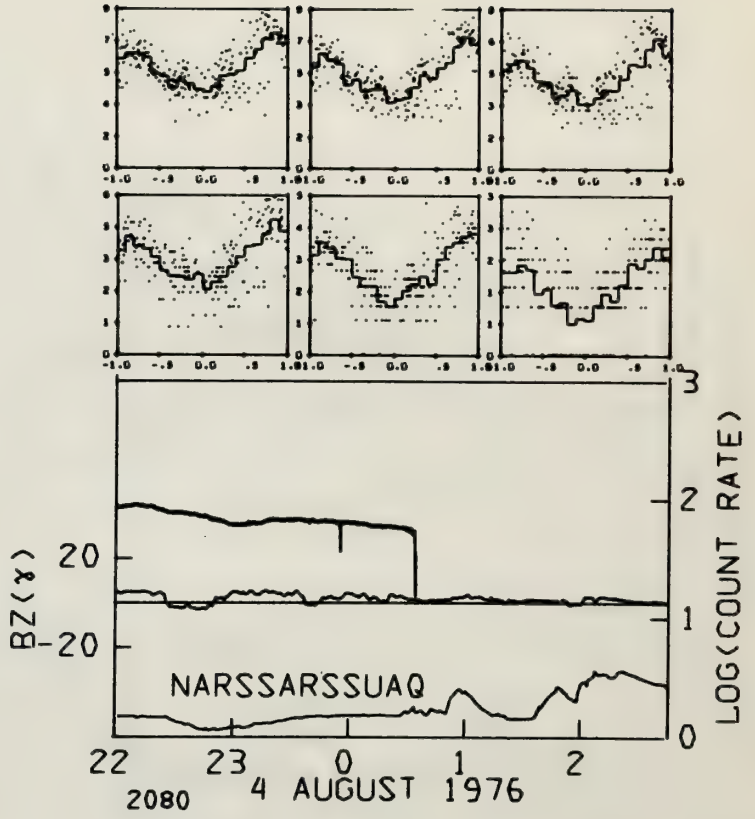


Figure 4c.

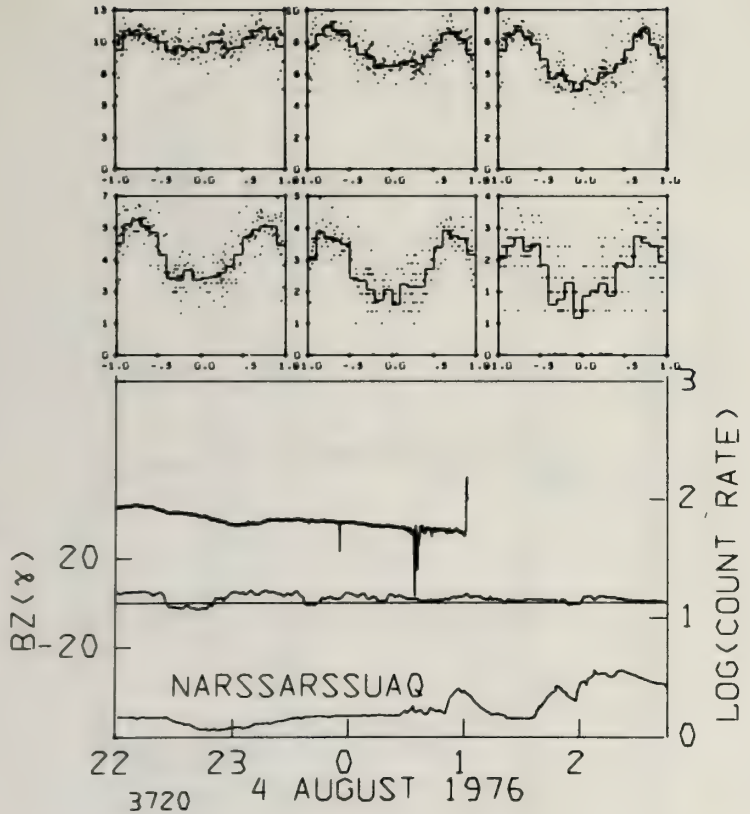


Figure 4d.

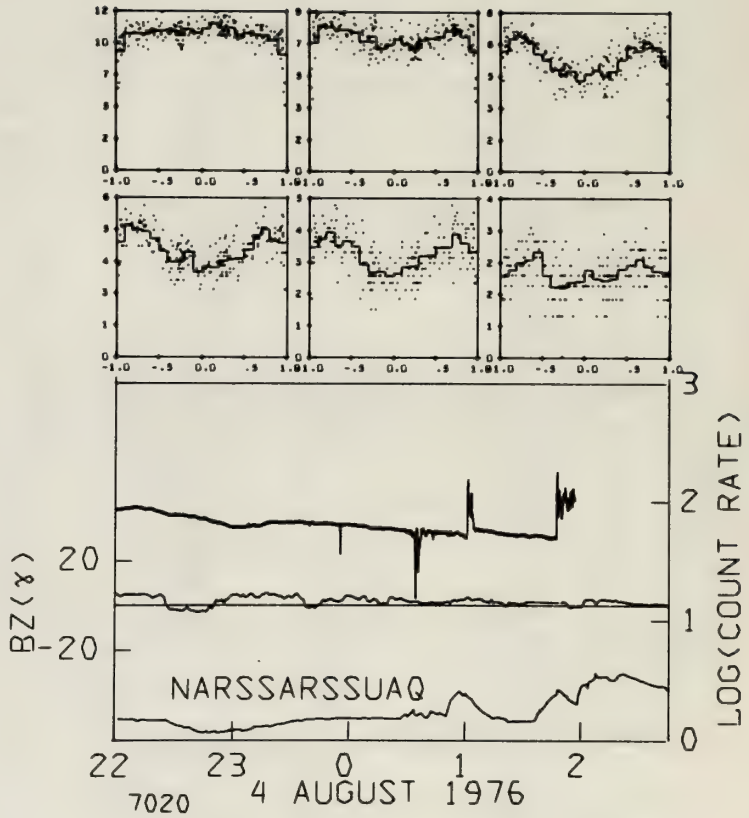


Figure 4e.

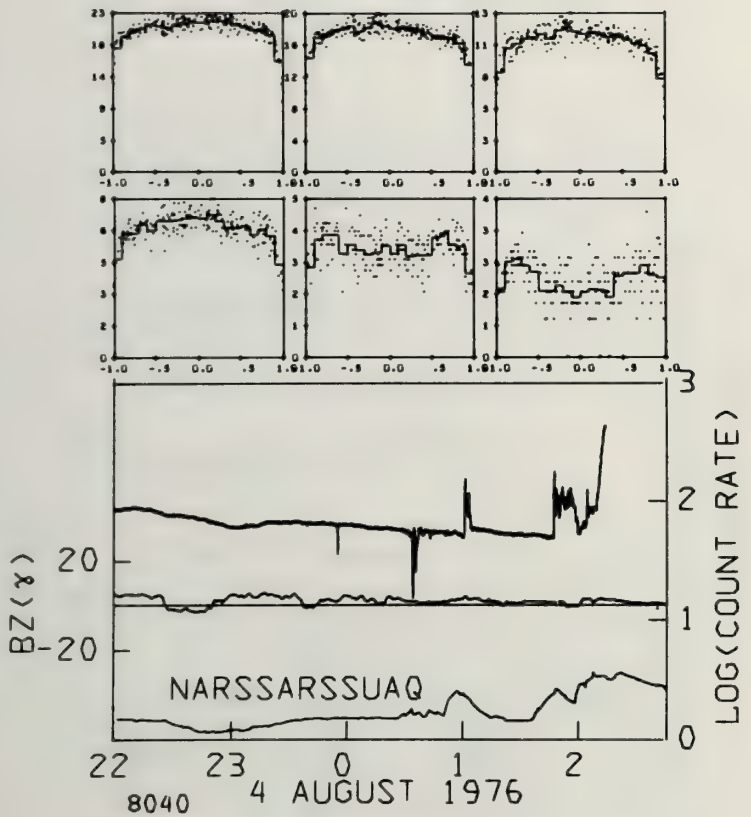


Figure 4f.

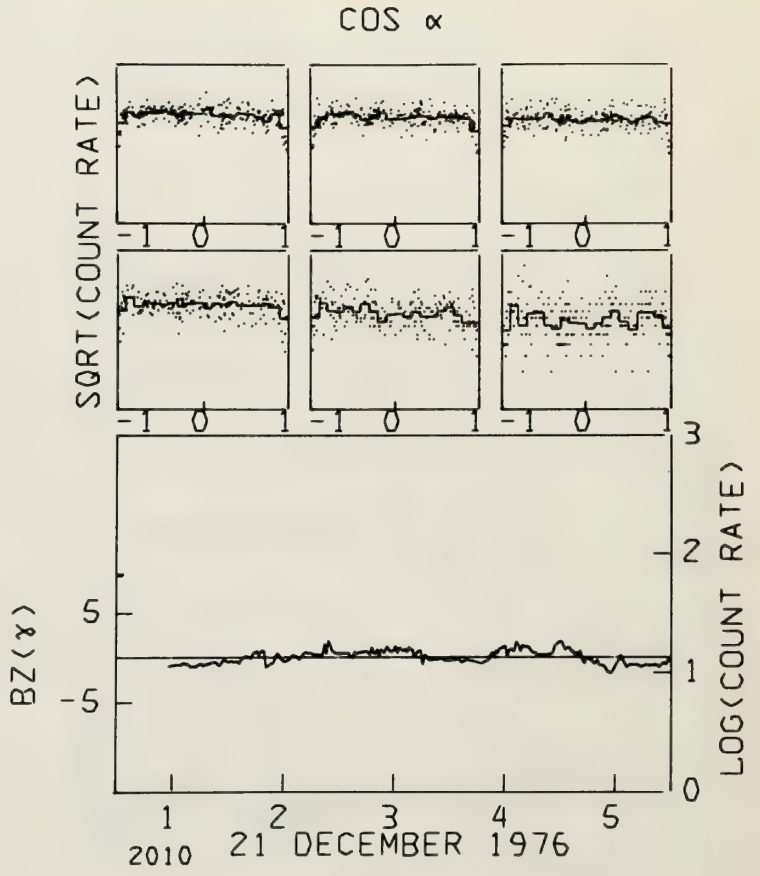


Figure 5a.

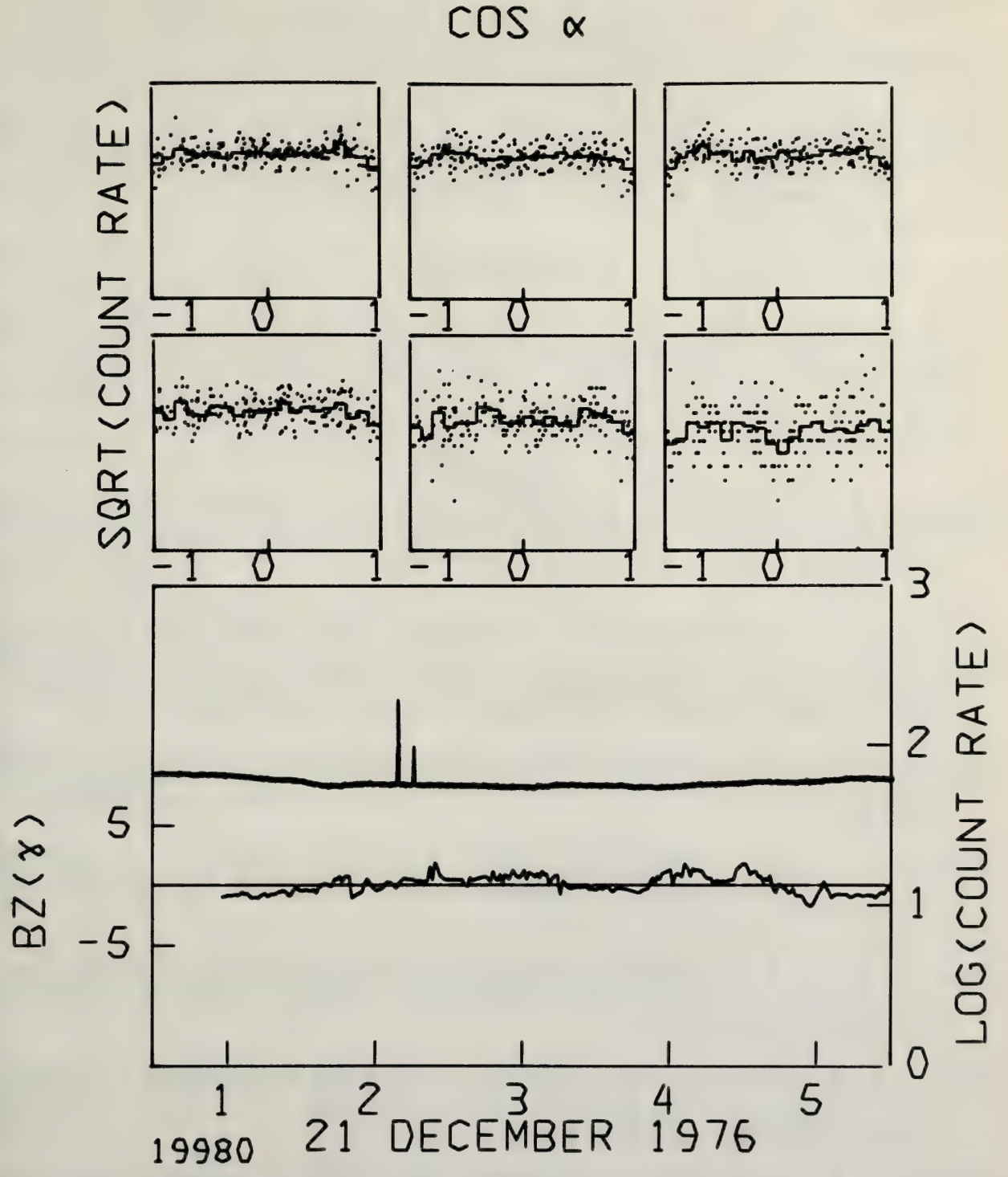

COS α
SQRT(COUNT RATE)
-1
0
1
BZ(γ)
5
-5
LOG(COUNT RATE)
3
2
1
0
1
2
3
4
5
19980 21 DECEMBER 1976

Figure 5b.

DISCUSSION

Examples have been given illustrating a prediction technique for substorms. A movie format was used which shows the low energy pitch angle distributions and their evolution in time for several energies. It is conceivable that such distributions might be displayed in real time for the use of ground personnel to monitor conditions at geostationary orbit. When the spacecraft is in the correct interval of local time ($\sim$ 2000 to 0300 hours) the character of the pitch angle distributions can be used to gauge the probability of the occurence of a substorm. A limited number of copies of this film are available for loan.

ACKNOWLEDGMENTS

We express our appreciation to Drs. R. Lepping and N. F. Ness for the use of the flux gate magnetometer data from Imp-J obtained through the National Space Science Data Center. Our particular thanks goes to Patricia A. Max who ran the computer codes. This work was performed under the auspices of the U.S. Department of Energy.

REFERENCES

Baker, D. N., P. R. Higbie, E. W. Hones, Jr., and R. D. Belian (1978a): High resolution energetic particle measurements at 6.6 R_E, 3, low-energy electron anisotropies and short-term substorm predictions, J. Geophys. Res., (in press).

Baker, D. N., E. W. Hones, Jr., P. R. Higbie, R. D. Belian, and P. Stanning (1978b): A correlation study of > 30 keV electrons at 6.6 R_E with high latitude riometer measurements. The AGU Chapman Conference on Magnetospheric Substorms and Related Plasma Processes, Los Alamos.

Bogott, F. H. and F. S. Mozer (1971): Equatorial proton and electron angular distributions in the loss cone and at large angles. J. Geophys. Res., 76:6790.

Burton, R. K., R. L. McPherron, and C. T. Russell (1975): An empirical relationship between interplanetary conditions and Dst. J. Geophys. Res., 80:4204.

Caan, M. N., R. L. McPherron, and C. T. Russell (1977): Characteristics of the association between the interplanetary magnetic field and substorms, J. Geophys. Res., 82:4837.

Higbie, P. R. and W. R. Moomey (1977): Pitch angle measurements from satellites using particle telescopes with multiple view directions. Nucl. Instru. and Meth., 146:439.

Higbie, P. R., D. N. Baker, E. W. Hones, Jr., and R. D. Belian (1978): Pitch angle distributions of > 30 keV electrons at geostationary altitudes. AGU Chapman Conference on Quantitative Modeling of Magnetospheric Processes, La Jolla.

Higbie, P. R., R. D. Belian, and D. N. Baker (1978): High-resolution energetic particle measurements at 6.6 R_E, 1, electron micropulsations. J. Geophys. Res., (in press).

Hirshberg, J. and D. S. Colburn (1969): Interplanetary field and geomagnetic variations - a unified view. Planet. Space Sci., 17:1183.

Kamide, Y., P. D. Perreault, S. I. Akasofu, and J. D. Winningham (1977): Dependence of substorm occurrence probability on the interplanetary magnetic field and on the size of the auroral oval. J. Geophys. Res., 82:5521.

Kamide, Y. and S. Matsuskita (1978): A unified view of substorm sequences. J. Geophys. Res., 83:2103.

Kaye, S. M., C. S. Lin, G. K. Parks, and J. R. Winckler (1978): Adiabatic modulation of equatorial pitch angle anisotropy. J. Geophys. Res., 83:2675.

Kokubun, S., R. L. McPherron, and C. T. Russell (1977): Triggering of substorms by solar wind discontinuities. J. Geophys. Res., 82:74.

McPherron, R. L. (1970): Growth phase of magnetospheric substorms. J. Geophys. Res., 75:5592.

Parks, G. K., G. Laval, R. Pellat (1972): Behavior of outer radiation zone and a new model of magnetospheric substorm. Planet Space Sci, 20:1391.

Perreault, P. D. and Y. Kamide (1976): A dusk-dawn asymmetry in the response of the magnetosphere to the IMF B_z component. J. Geophys. Res., 81:4773

Pfitzer, K. A., T. W. Lezniak, and J. R. Winckler (1969): Experimental verification of drift-shell splitting in the distorted magnetosphere. J. Geophys. Res., 74:4687.

Roederer, J. G. (1972): Geomagnetic field distortionns and their effects on radiation belt particles. Rev. Geophys. Space Phys., 10:599.

Svalgaard, L. (1977): Geomagnetic activity: dependence on solar wind parameters. Coronal Holes and High Speed Streams, J. B. Zinker, ed., Colorado Associated University Press, 371-441.

PREDICTING PARTIAL RING CURRENT DEVELOPMENT

C. Robert Clauer and R. L. McPherron
University of California, Los Angeles
Institute of Geophysics and Planetary Physics
Los Angeles, California 90024

Analysis of midlatitude ground magnetograms during periods of substorm activity reveals that some substorms are associated with a large decrease in the northward (X) component of the geomagnetic field near dusk but that many other substorms are not. The dusk depression of the field is interpreted as the magnetic signature of the asymmetric (or partial) ring current. The development and decay of the partial ring current is shown to be strongly dependent on the B_Z (northward) component of the interplanetary magnetic field (IMF). The partial ring current develops only during periods of sustained southward IMF of several gammas or greater. A subsequent change to northward IMF will be followed by a rapid (two or three hour) decay of partial ring current. Thus, measurements in the IMF can be used to predict the development and decay of the partial ring current. It may eventually be possible to infer the solar wind electric field based on partial ring current parameters. This method of inference would lend itself to real time monitoring using a worldwide chain of midlatitude observatories similar to the partial chain established for the IMS. In general, midlatitude data coverage is more complete than coverage at high latitudes. The use of this more complete data set to monitor the development of the partial ring current offers greater sensitivity than obtained with the D_{ST} index and may eventually prove more reliable than high latitude indices for monitoring the IMF.

I. INTRODUCTION

The southward component of the interplanetary magnetic field (IMF) has been shown to exhibit a fundamental relationship with geomagnetic activity (Hirshberg and Colburn, 1969). The high correlation between IMF orientation and geomagnetic activity has generally been regarded as confirmation of the open magnetospheric model introduced by Dungey (1961). In the open model of the solar wind-magnetosphere interaction, the strength of the electrostatic field imposed across the magnetosphere is proportional to the dawn-dusk component of the interplanetary electric field (IEF). The IEF depends upon the solar wind velocity $\underset{\sim}{V}_{sw}$ and the IMF through the relation $\underset{\sim}{E} = - \underset{\sim}{V}_{sw} \times \underset{\sim}{B}$. A southward component of the IMF gives rise to a dawn to dusk component of the IEF.

Recently, much effort has been directed toward improving our understanding of the effects of the potential drop imposed across the magnetosphere by its interaction with the solar wind. The suggestion was made by Dungey (1961) and concurrently by Axford and Hines (1961) that geomagnetic activity was directly related to plasma convection. In general, plasma in the magnetosphere is convected by two processes. The most spatially uniform and temporarily stable component of the convection is driven by the externally imposed electrostatic field while a more intense and localized component is thought to result from the induced electric fields produced during substorm expansions. This second component of the convection, substorm expansions, has generally been considered the principle mechanism by which plasma is energized and transported to the inner magnetosphere to form the ring current (Davis and Parthasarathy 1967, Davis 1969).

The results which are presented in this report indicate that the development of the partial ring current is more closely related to the IMF and, therefore, to the strength of the electrostatic field than to individual substorms. This result suggests a direction for prediction research. In particular, it may be possible to infer conditions in the solar wind using ground determined partial ring current parameters. Alternatively, measurements of the IEF could be used to predict the development and decay of the partial and symmetric ring currents.

II. EXPERIMENTAL RESULTS

The magnetic signatures of the symmetric and partial ring currents are best observed with midlatitude ground magnetic observations. Using a worldwide network of observatories, one can observe the spatial and temporal development of these large scale current systems (Troshichev and Feldstein, (1972), Clauer and McPherron, (1978).

Figure 1 is a schematic illustration of a very simple model of the partial ring current system and substorm expansion phase current system having field aligned closure through the eastward and westward electrojets respectively. The magnetic effect of these currents at midlatitudes as a function of the local time or position around the earth is illustrated at the top of the figure. The X or northward component of the field is depressed by the partial ring current and enhanced by the substorm expansion current. The Y or eastward component is enhanced in regions of outward field aligned current and decreased in regions of earthward field aligned current. A number of parameters which characterize these current systems may be obtained from the local time magnetic perturbation profile. They include the magnitude of the disturbance, the extent and the central meridian.

To compute these profiles, we use digital data from a chain of midlatitude magnetic observatories, listed in Table 1. The average quiet

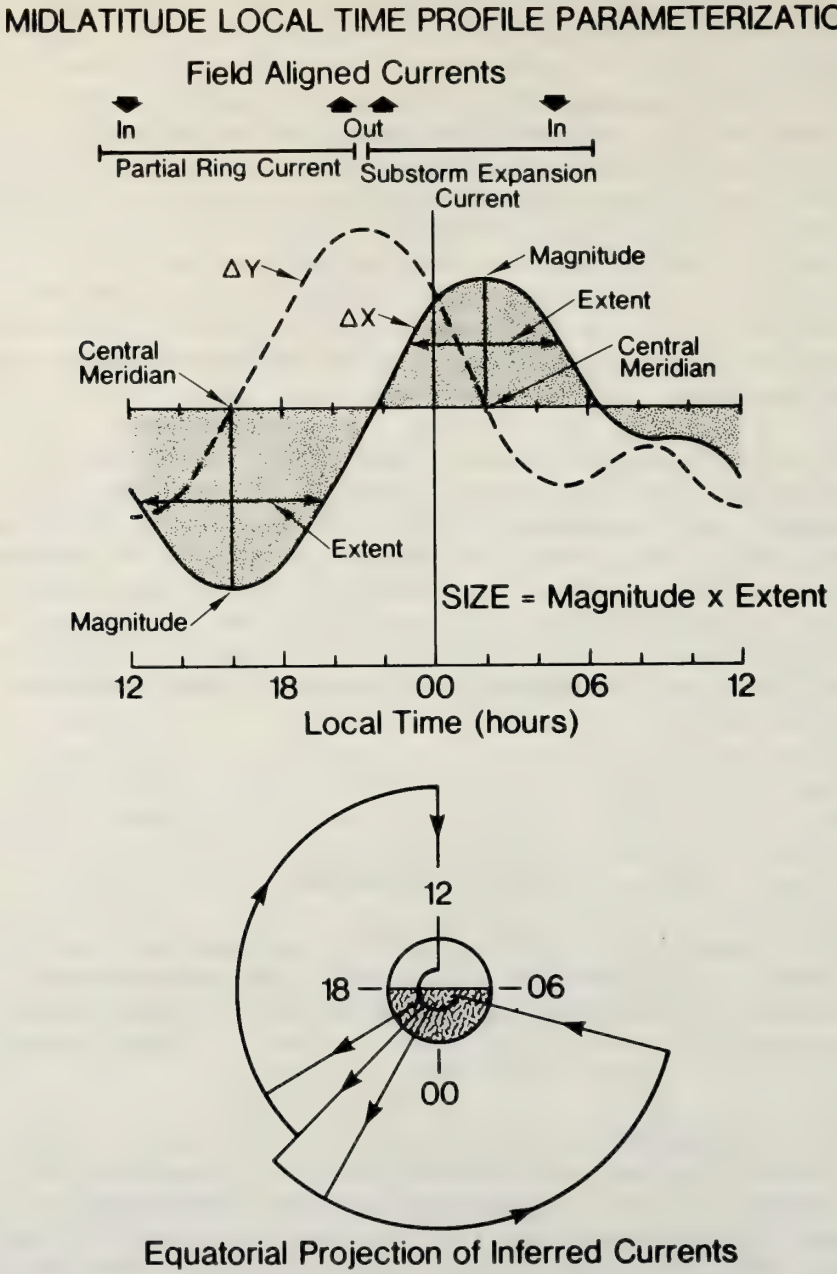


Figure 1. Schematic representation of local time magnetic perturbation profile due to simple wire model substorm expansion phase current and partial ring current with field aligned closure through the auroral electrojets ΔX is the perturbation in the northward component, ΔY is the perturbation in the eastward component

TABLE 1

MIDLATITUDE OBSERVATORIES

STATION	GEOGRAPHIC COORDINATES WEST LONGITUDE	LATITUDE	GEOMAGNETIC COORDINATES LONGITUDE	LATITUDE
Toledo	4.05°	39.87°N	75.6°	43.8°
San Fernando	5.20	36.40 N	71.3	40.9
M'Bour	16.97	14.40 N	55.0	21.3
Paramaribo	55.22	5.82 N	14.3	17.0
Pilar	63.88	31.67 S	4.6	-20.2
Trelew	65.32	43.25 S	3.2	-31.8
San Juan	66.15	18.12 N	3.1	29.6
Cuba	82.13	22.97 N	345.4	34.1
Dallas	96.75	32.98 N	327.7	43.0
Boulder	105.23	40.13 N	316.5	49.0
Tucson	110.83	32.25 N	312.2	40.4
Tahiti	149.62	17.55 S	282.7	-15.3
Honolulu	158.00	21.32 N	266.5	21.1
Port Moresby	212.85	9.42 S	217.9	-18.6
Kakioka	219.82	36.23 N	206.0	26.0
Kanoya	229.20	31.40 N	198.0	20.5
Gnangara	244.05	31.78 S	185.8	-43.2
Tangerang	253.37	6.17 S	175.4	-17.6
Irkutsh	255.55	52.17 N	174.7	40.7
Hyderabad	281.45	17.42 N	148.9	7.6
Tashkent	290.37	41.30 N	144.0	32.3
Tananarive	312.45	18.92 S	112.5	-23.7
Tbilisi	315.28	42.07 N	122.0	36.6
Odessa	329.12	46.77 N	111.1	43.6
Hermanus	340.77	34.42 S	80.5	-33.3

day field, which includes diurnal, seasonal and secular variations, is removed from the data and a smooth profile is fitted through the result using cubic splines.

Successive local time profiles are computed at 2.5 minute intervals in Universal Time and the result is displayed in the form of Local Time - Universal Time (LT - UT) contour maps. These maps display the temporal and spatial development of magnetic disturbances. We also compute parameters which characterize the successive profiles. These include the maximum and minimum value of magnetic perturbation, D_{ST} the worldwide average midlatitude perturbation, the asymmetry defined as the difference between the maximum and minimum perturbations. We will illustrate our results and the mapping procedure with two examples.

Figure 2 shows the high latitude activity on Feb. 11, 1967, a day characterized by a large isolated substorm. It was quiet prior to 0515 UT at which time a substorm onset occurred. Local midnight at each station is indicated by a cross above the trace. Table 2 gives the station locations.

Figure 3 shows the midlatitude observations along with the interplanetary data. The center panel is a LT-UT map of the magnetic disturbance in the X component. The vertical axis is local time or position around the earth relative to the earth-sun line. Local midnight is at the center and local noon at the top and the bottom edges. Contours of the magnetic deviation from a quiet day are drawn at 5γ intervals. A vertical line is drawn at 0515 UT. The average field prior to 0515 was -10γ and contours above that level have been shaded. A positive field enhancement centered near 0300 LT begins at 0515 UT and is the signature of the substorm expansion. A simultaneous depression in the field develops near dusk. This is the partial ring current signature.

Parameters derived from the mapping procedure are plotted in the bottom panel. The top three traces are the maximum, average (D_{ST}), and minimum midlatitude, field perturbation. There is a clear increase in the maximum due to the substorm while the minimum decreases as a result of the partial ring current. The bottom three traces are the asymmetry index defined as the difference between the maximum and minimum, and the local time position of the maximum and minimum.

The top panel displays the solar wind density and velocity and the north-south component of the IMF (B_Z) in solar magnetospheric coordinates. The data gap in the density and velocity measurements is partially filled in with hourly average values from the interplanetary medium data book by King (1977)1 Note that the partial ring current indicated by the depression of the minimum continues to develop during the substorm recovery indicated by a decrease of the maximum. The development of the partial ring current is occurring during a period of sustained southward B_Z. A vertical line is drawn at the onset of partial ring current decay. Note that the decay follows the northward turning of B_Z.

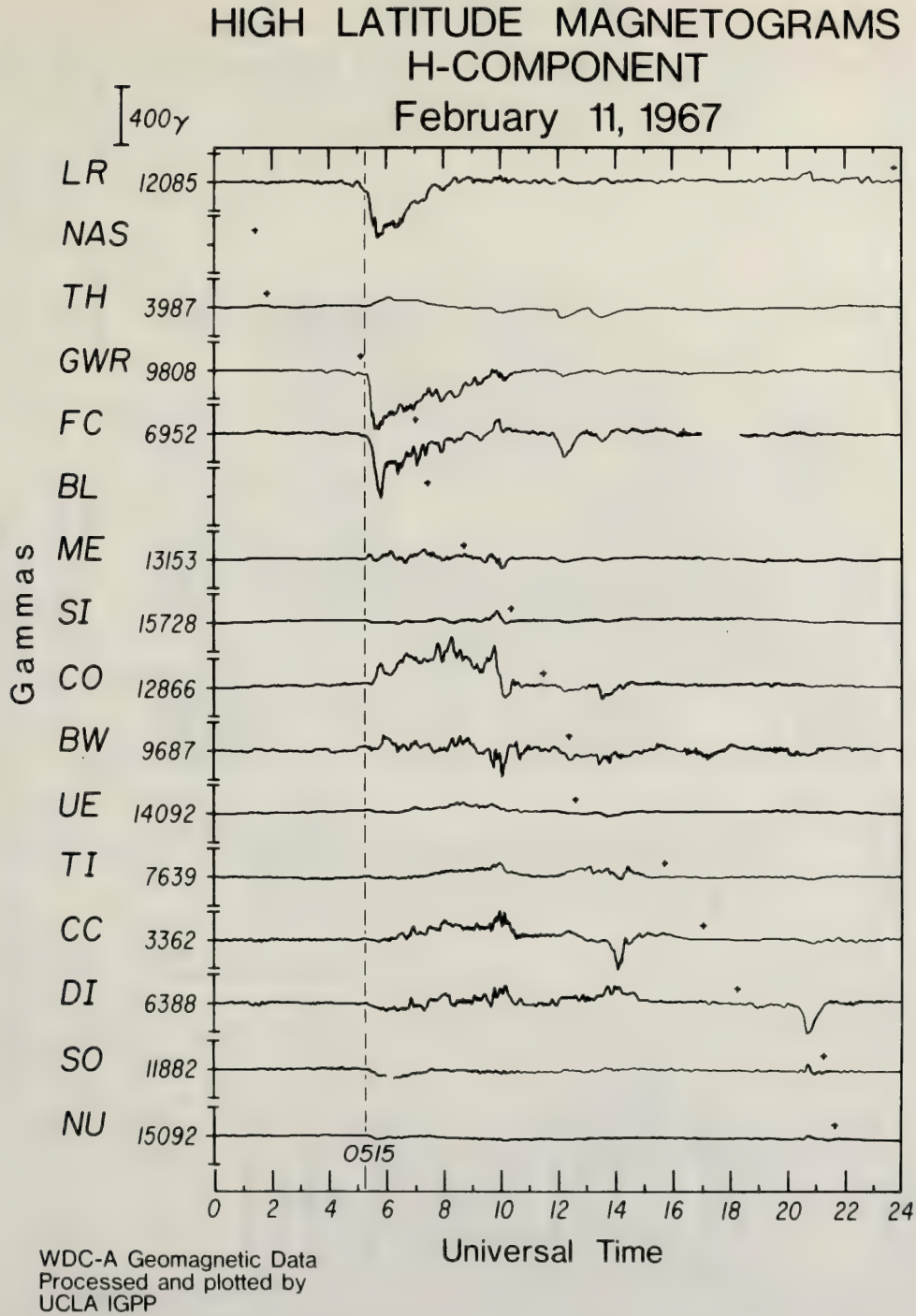


Figure 2. High latitude magnetograms of H component for Feb. 11, 1967. Vertical line at 0515 UT marks substorm onset. Cross above trace marks local midnight at observatory.

TABLE 2

STATION CODE	STATION NAME	GEOGRAPHIC LATITUDE	(EAST) LONGITUDE	GEOMAGNETIC LATITUDE	GEOMAGNETIC LONGITUDE
LR	Leirvogur	64.18°	338.30°	70.22°	71.04°
NAS	Narssarssuaq	61.20	314.60	71.21	36.79
TH	Thule	76.55	291.17	88.05	01.16
GWR	Great Whale River	55.27	282.22	66.58	347.36
FC	Fort Churchill	58.80	265.90	68.70	322.77
BL	Baker Lake	64.33	263.97	73.77	315.23
ME	Meanook	54.62	246.67	60.00	301.02
SI	Sitka	57.06	224.67	60.00	275.34
CO	College	64.86	212.15	64.63	256.52
BW	Barrow	71.30	203.25	68.54	241.15
UE	Cape Wellen	66.17	190.17	61.79	237.10
TI	Tixie Bay	71.58	129.00	60.44	191.41
CC	Cape Chelyuskin	77.72	104.30	66.26	176.46
DI	Dixon	73.50	80.57	63.02	161.57
SO	Sodankyla	67.37	26.63	63.76	119.99
AI	Abisko	68.36	18.82	66.04	115.08
NU	Nurmijarvi	60.52	24.65	57.87	112.58

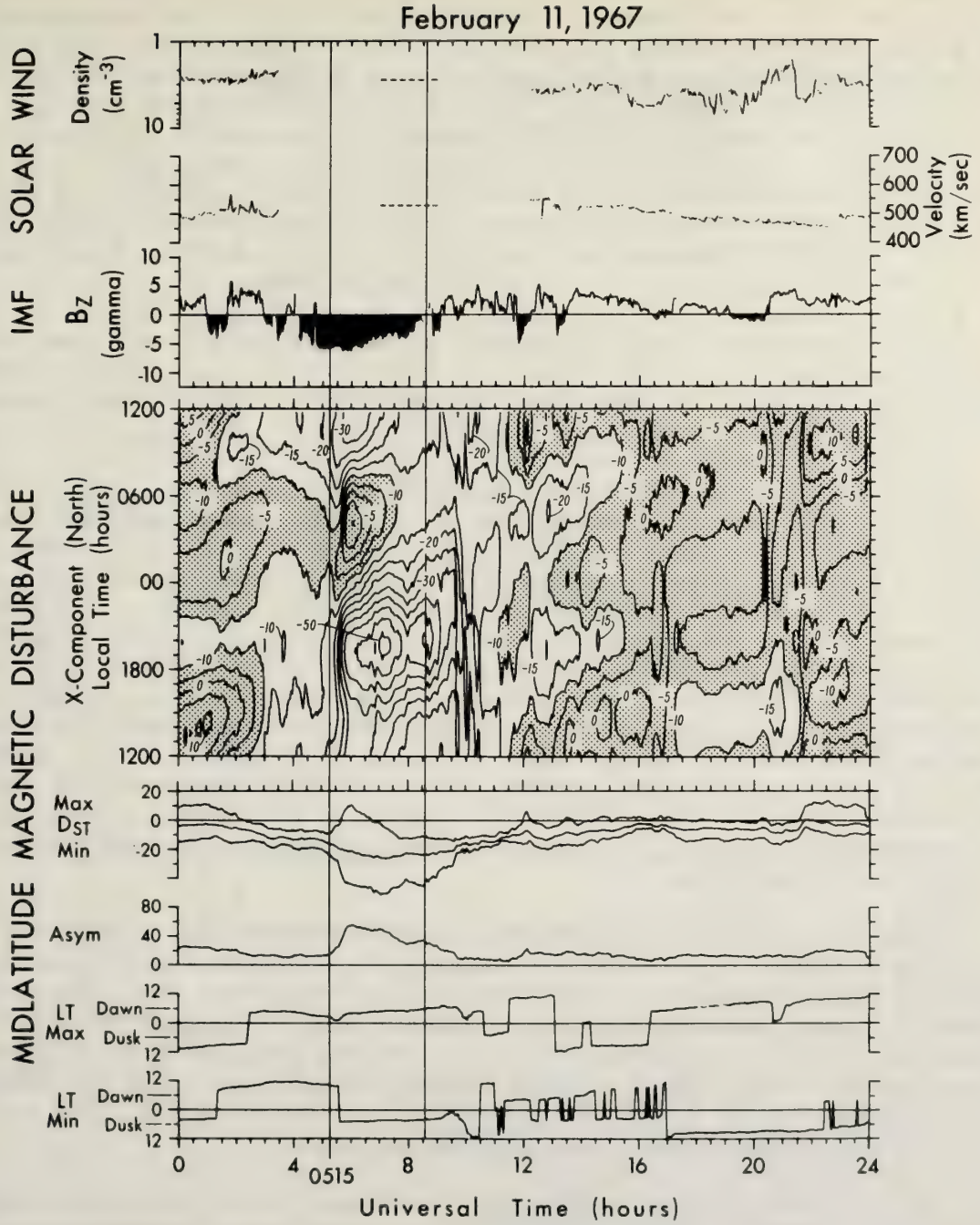


Figure 3. Interplanetary data and midlatitude ground data for Feb. 11, 1967. (From top to bottom) Solar wind proton number density, solar wind velocity, north-south component of interplanetary magnetic field (southward field is shaded), LT - UT map of magnetic perturbations measured in north-south component of midlatitude field and parameters of the midlatitude disturbance: ΔX_{max}, D_{ST}, ΔX_{min}, asymmetry, local time position of ΔX_{max} and local time position of ΔX_{min}. Vertical lines mark substorm onset (0515UT) and onset of partial ring current decay (0835UT).

Figure 4 shows the high latitude activity for Jan. 23, 1968, a day characterized by a small amount of activity early in the day culminating with a large substorm having an onset at 20 UT. Figure 5 shows the solar wind and midlatitude ground observations. The activity during the earlier part of the day was small and did not result in any large midlatitude disturbance. The substorm at 20 UT, however, is comparable in size to the substorm on Feb. 11. Little, if any, partial ring current development is shown either on the map or by the midlatitude minimum parameter. A difference between this event and the one on Feb. 11 can be seen in the character of the B_Z component of the IMF. For this event the field was fluctuating north and south for short periods of time.

Of the twenty-five events examined thus far, 5 events had clear large southward turnings of the IMF associated with the development of a distinct partial ring current. In each case, when the IMF turned northward, decay of the partial ring current was observed.

It appears that two classes of substorm activity are distinguishable using midlatitude magnetic observations - substorms associated with clear large partial ring currents and substorms associated with little or no partial ring current magnetic signature. Figure 6 shows superposed epoch averages of the midlatitude parameters and B_Z timed relative to the substorm onset for the two groups of events. The average local time position of the maximum and minimum is also shown. The panel on the left presents the results for substorms in which the dusk depression was less than the noise level due to S_q variability. At dusk this level is about 15γ (Clauer, McPherron and Kivelson, 1979). There is a small depression of the minimum associated with the substorm, however, it is probably the result of the substorm associated Birkland currents since it is very close to the substorm maximum and slightly to the east. The B_Z component averages about 3γ prior to the substorm.

The panel on the right shows the results for substorms associated with clear partial ring current signatures. Each of these events was associated with a decrease of the dusk field of more than 20γ. The events followed a large southward turning by about 1 hour. The partial ring current measured by the minimum begins to develop about 15 minutes after the southward turning and 45 minutes before the substorm. The substorm position appears to be centered near 0400 LT while the partial ring current center is 2100 LT one hour after the substorm onset.

Figure 7 shows further analysis of the events which had well defined partial ring currents. In the left panel the superposed averages were timed relative to the onset of the partial ring current development. The B_Z component reached - 4γ 30 minutes before the onset time and remained substantially southward. The panel on the right shows the averages superposed relative to the onset of partial ring current decay. The decay begins shortly after the B_Z component reaches -2.5γ.

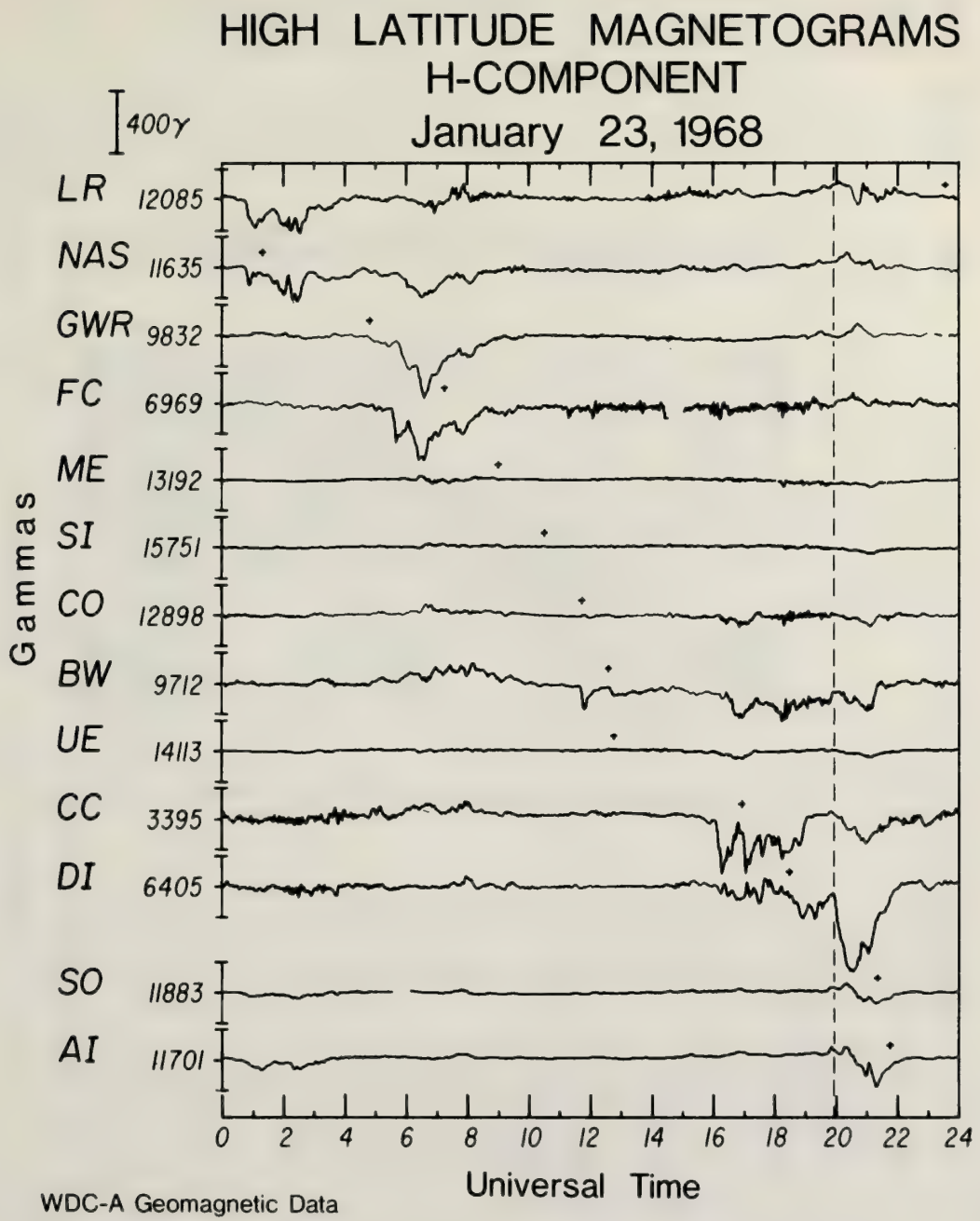


Figure 4. High latitude magnetograms of H component for Jan. 23, 1968. Vertical line at 2000 UT marks substorm onset.

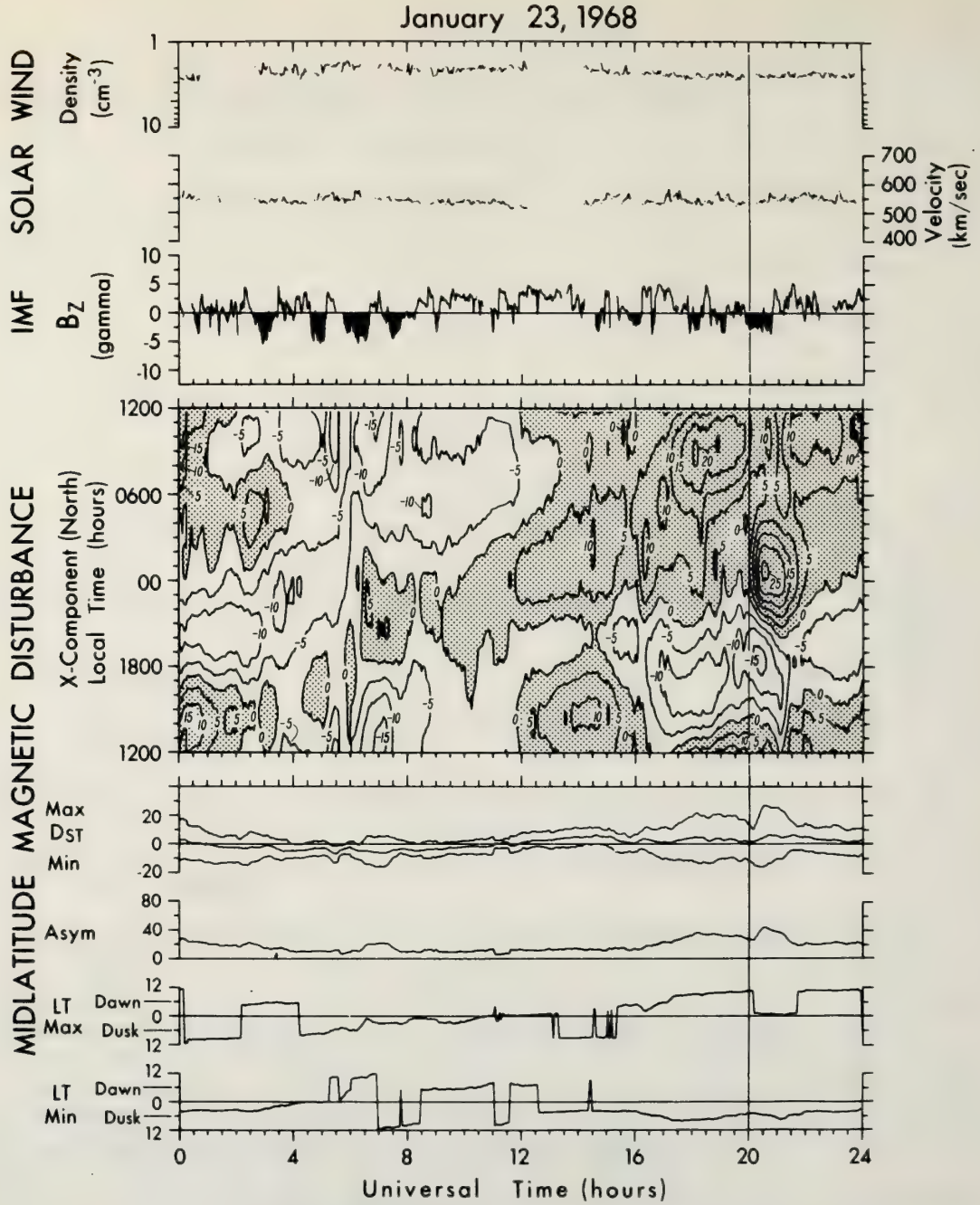


Figure 5.. Interplanetary data and midlatitude ground data for Jan. 23, 1968. Format is the same as Figure 3. Vertical line at 2000 UT marks substorm onset.

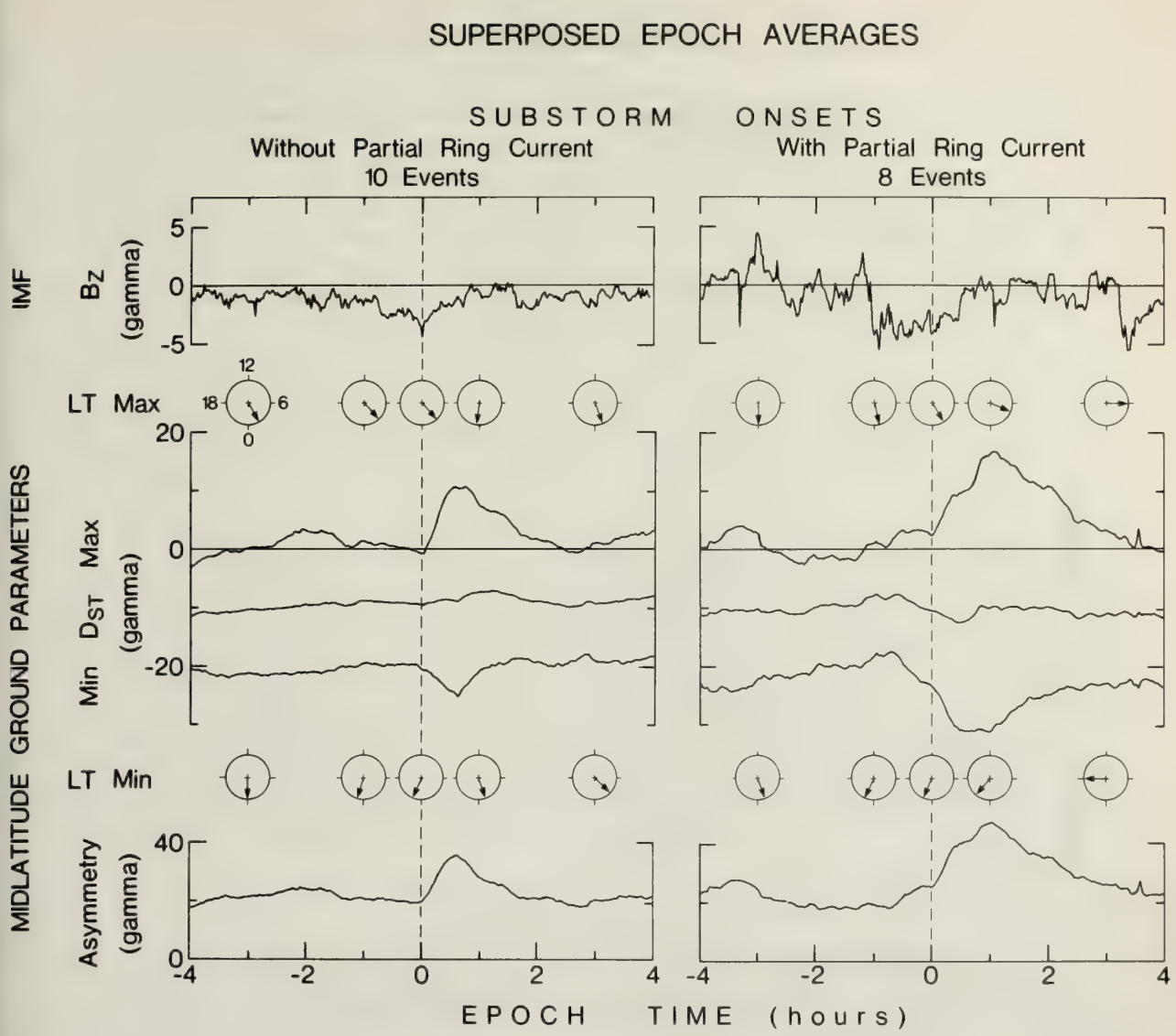


Figure 6. Superposed epoch averages of parameters timed relative to substorm onset for events with little or no partial ring current (left) and events with a clear large partial ring current (right). Parameters are (from top to bottom) north south component of interplanetary magnetic field, ΔX_{max}, D_{ST}, ΔX_{min} and asymmetry. Clocks indicate average local time position of ΔX_{max} and ΔX_{min} during epoch.

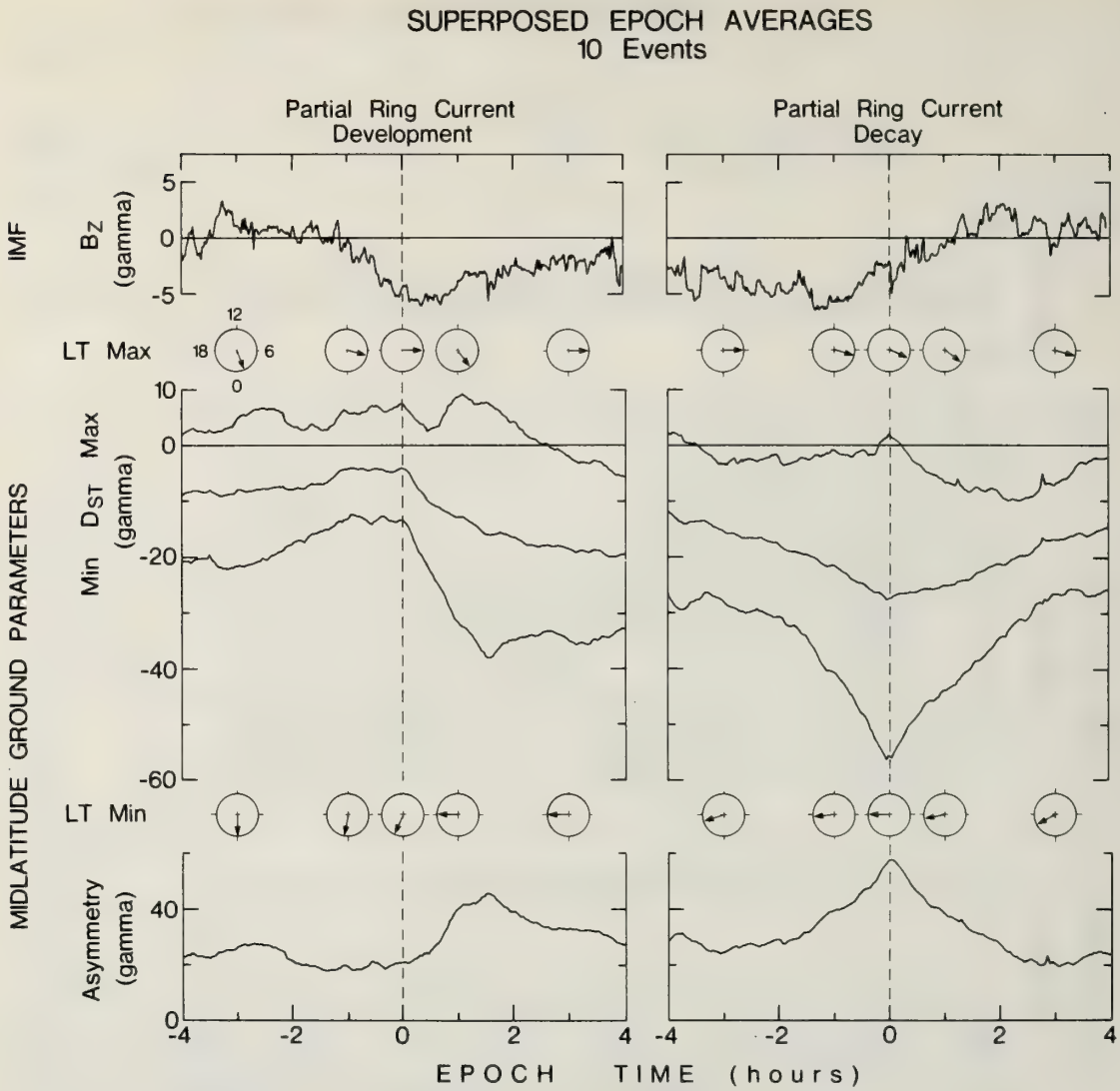


Figure 7. Superposed epoch averages of parameters of events with distinct large partial ring currents. Epoch averages are timed relative to the onset of partial ring current development (left) and onset of partial ring current decay (right). The format is the same as Figure 6.

CONCLUSIONS

Among the principal goals of magnetospheric research are to develop methods which can use ground based measurements to monitor the conditions in space and develop parameters which can predict magnetospheric activity. Burton, et al., 1975, developed an empirical relationship using the solar wind electric field and dynamic pressure which predicted the development and decay of the symmetric ring current measured by the D_{ST} index. The prediced and measured D_{ST} values were extremely similar for several storms tested. From Figure 3 it is clear that the midlatitude minimum index is more responsive to smaller events than D_{ST}. There is also sufficient evidence to suggest that it may be possible to develop a relation between the midlatitude minimum and solar wind parameters similar to the Burton result but with the advantage of greater sensitivity. Inversion of the relationship would permit midlatitude magnetic parameters to act as monitors of the solar wind electric field.

The use of midlatitude data as a real time diagnostic tool for the magnetosphere has several advantages over similar use of auroral zone and polar cap data. Real time data acquisition using synchronous satellites offers better reliability over the tenuous radio or telephone data links at high latitudes, particularly during disturbed conditions. Operation of midlatitude observatories in general tends to be easier than operation of stations in remote areas of the arctic. The important result of this is a more complete data base at midlatitudes. As our understanding of the physics of the dynamical processes of the solar-magnetospheric interaction develops, the use of midlatitude geomagnetic data as a diagnostic and predictive tool will become more important.

ACKNOWLEDGEMENTS

This research has been supported by the Office of Naval Research through grant N00014-75-C-0396. We thank the World Data Center A for supplying the digital ground magnetograms and C. P. Sonett and D. S. Colbrun for supplying the Explorer 33, 35 magnetic field data.

REFERENCES

Axford, W.I. and C.O. Hines (1961): A unifying theory of high latitude geophysical phenomena and geomagnetic storms. Can. J. Phys., 39: 1433.

Burton, R.K., R.L. McPherron and C.I. Russell (1975): An empirical relationship between interplanetary conditions and D_{ST}. J. Geophys. Res., 80: 4204.

Clauer, C.R. and R.L. McPherron (1978): On the relationship of the partial ring current to substorms and the IMF, J. Geomag. Geoelect., 30: 195.

Clauer, C.R., R.L. McPherron and M.G. Kivelson (1979): How does the variability of S_q currents affect midlatitude determination of ring current development, to be presented at 1979 spring AGU meeting, Washington, D.C.

Davis, T.N. and R. Parthasarathy (1967): The relationship between polar magnetic activity DP and growth of the geomagnetic ring current, J. Geophys. Res., 72: 5825.

Davis, T.N. (1969): Temporal behavior of energy injection into the geomagnetic ring current, J. Geophys. Res., 74: 6266.

Dungey, J.W. (1961): Interplanetary magnetic field and the auroral zone, Phys. Rev. Lett., 6: 47.

King, J.H. (1977): Interplanetary medium data book - appendix, National Space Science Data Center, NASA, GSFC, Greenbelt, Md. 20771

Troshichev, O.A. and Ya I. Feldstein (1972): The ring current in the magnetosphere and polar magnetic substorms, J. Atm. Terr.-Phys., 34: 845.

ON THE PREDICTABILITY OF RADIATION BELT ELECTRON PRECIPITATION INTO THE EARTH'S ATMOSPHERE FOLLOWING MAGNETIC STORMS

Walther N. Spjeldvik and Lawrence R. Lyons
NOAA/ERL, Space Environment Laboratory
Boulder, Colorado 80303, USA

The earth's radiation belts are subject to drastic structural changes during magnetic storms. Fluxes of energetic electrons at hundreds of keV are increased by orders of magnitude during the storm main phase. During the recovery phase the trapped fluxes decay back to quiet time levels by precipitating the excess electrons into the middle latitude atmosphere where they profoundly enhance the ionization rates in the D and E regions. The present report emphasizes the operating physical mechanism and seeks to establish a preliminary prediction scheme based on causal interrelations rather than purely statistical correlations. Although it is possible to make an order-of-magnitude prediction for the disturbed period following magnetic storms, more detailed work is needed to develop a precise quantitative forecast. In particular, greater emphasis on the source and distributions of plasmaspheric ELF whistler mode wave turbulence (hiss) is called for. The predictions of the ionospheric electron density enhancements may be used to forecast VLF to MF ionospheric radio wave propagation disturbances.

1. INTRODUCTION

It has long been established that the D and E regions of the earth's ionosphere become severely disturbed following the onset of major magnetic storms (e.g. Lauter and Knuth, 1967; Belrose and Thomas, 1968). During such times the lower ionosphere exhibits enhanced absorption of LF and MF ($\sim$ 0.2 MHz) radio waves that reflect from the E-layer, and lower frequency waves that reflect from D-region heights ($\sim$ 80 km) show substantial phase disturbances generally with significant phase advance during the post storm events (Belrose and Thomas, 1968). In a recent work Lauter et al. (1977) have found that the post storm absorption events occur rather simultaneously in both hemispheres on subauroral latitudes down to $\sim 50^0$ geomagnetic latitude. In contrast they found that D-region absorption enhancements during the main phase of magnetic storms can show strong transient latitudinal dependence.

This difference between the post storm and main phase absorption enhancements may be qualitatively understood in terms of storm-time displacement of the plasmapause. During the storm main phase enhancements of the dawn-to-dusk convection electric field makes

the plasmasphere shrink to a size where middle latitude geomagnetic field lines ($L \sim 3$-5 or $\Lambda \sim 50$-65^0) can map outside the plasmasphere. Any wave-particle interaction induced electron precipitation under such conditions is likely to be highly transient, perhaps in analogy with auroral characteristics. As the main phase of the storm subsides, the plasmasphere starts to recover and extends towards higher invariant latitudes. Thus the post storm middle latitude ionospheric effects map along magnetic field lines within the high density plasmasphere where plasma wave propagation and wave-particle resonance conditions are quite different from the conditions outside. It has been found that the plasmapause separates the region of intermittent ELF chorus emissions beyond the plasmasphere and the quasi-steady ELF broadband (0.1-1 KHz) whistler mode hiss within the plasmasphere (e.g. Thorne et al., 1973).

The D-region effects associated with the recovery phase of magnetic storms are found to be caused by radiation belt electron precipitation (e.g. Spjeldvik and Thorne, 1975a, b, 1976). There are other known classes of D-region disturbances. X-ray solar flares can cause Sudden Ionospheric Disturbance (SID) events and solar proton emissions can give rise to Polar Cap Absorption (PCA) at latitudes sometimes extending well southward of the auroral zone. Predictions of such occurrences must come from solar physics (e.g. Krivsky, 1977) and is beyond the scope of this report. A catalog of D-region absorption presented as daily averages for the period 1948-1976 is now available (Lauter, 1977). In this paper we will concentrate on the post storm ionospheric disturbances associated with the electron precipitation.

A practical application of prediction of these storm after-effects stems from the fact that the enhanced energetic electron precipitation is durable over time scales of days. Since some naval navigation systems utilize VLF wave propagation properties, it is conceivable that severe and persistent ionospheric modification leading to significant VLF phase advances may, if not corrected for, lead to misnavigation.

2. RADIATON BELT ELECTRONS

It is clear that the observed ionospheric radio wave absorption and phase effects may be explained in terms of an enhanced D and E region free electron concentration. The physical mechanisms responsible for ionization by precipitating energetic electrons have been studied extensively in recent years. Thorne et al. (1973) have presented observations showing that a class of ELF whistler mode wave turbulence, known as plasmaspheric hiss, in the frequency range 0.1 to 1 kHz exhibits a fairly persistent substantial intensity level of tens of milligammas on L-shells below the plasmapause location.

Lyons et al. (1971, 1972) used such hiss observations within the plasmasphere to model the efficiency of radiation belt electron-plasmaspheric hiss interaction for energetic electrons at 20 keV to 2 MeV. In a subsequent paper Lyons and Thorne (1973) demonstrated that the radial structure of the earth's quiet time electron belts can be understood in terms of inward radial diffusion from an outer zone electron source and losses due to pitch angle scattering into the atmospheric bounce loss cone. Their most significant result was the unambiguous explanation of the separation of the two Van Allen radiation zones of energetic electrons.

The quiet time, storm time and post storm morphology of energetic radiation belt electrons within the location of the quiet time plasmapause ($L \sim 5$) is illustrated in Figures 1 and 2 (from Lyons and Williams, 1975). The data shown are from Explorer 45 and include the geomagnetic storm period in December 1971. Figure 1 gives the radial profiles; notice the pronounced quiet time "slot" region located just beyond $L = 3$ (dashed lines). With the onset of the storm the slot region becomes filled with freshly injected electrons (orbit 101 in Figure 1), and during the storm recovery phase the fluxes decay down to the normal quiet time two-zone structure. The progress of the observed decay is shown as the electron

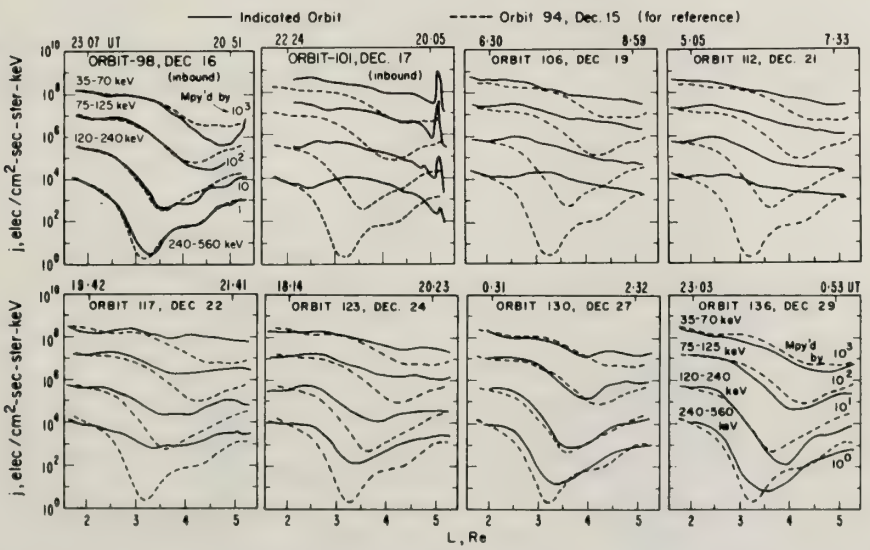


Figure 1. Observed radial profiles of the perpendicular (90° local pitch angle) electron flux obtained near the geomagnetic equator for the periods preceding, during and following the storm of December 17, 1971. Solid curves give the profiles from the orbit indicated in each panel, and the dashed curves give the pre-storm profiles from orbit 94 outbound (December 15, 1971) for comparison. To clearly display the data, the 120-240 keV, 75-125 keV, and 35-70 keV fluxes have been multiplied by 10^1, 10^2, and 10^3, respectively. Note the relaxation of the post-storm profiles to their pre-storm shapes and intensities.

flux versus time in Figure 2. Notice that at high L-shells ($L \gtrsim 5$) injections, possibly by substorm activity, take place during the recovery phase. On lower L-shells a rather clear cut decay following the main phase injection is seen. On very low L-shells in the inner radiation zone, $L \lesssim 2$, the electron fluxes are seen to be very stable, presumably because the main phase injection did not reach this close to the earth.

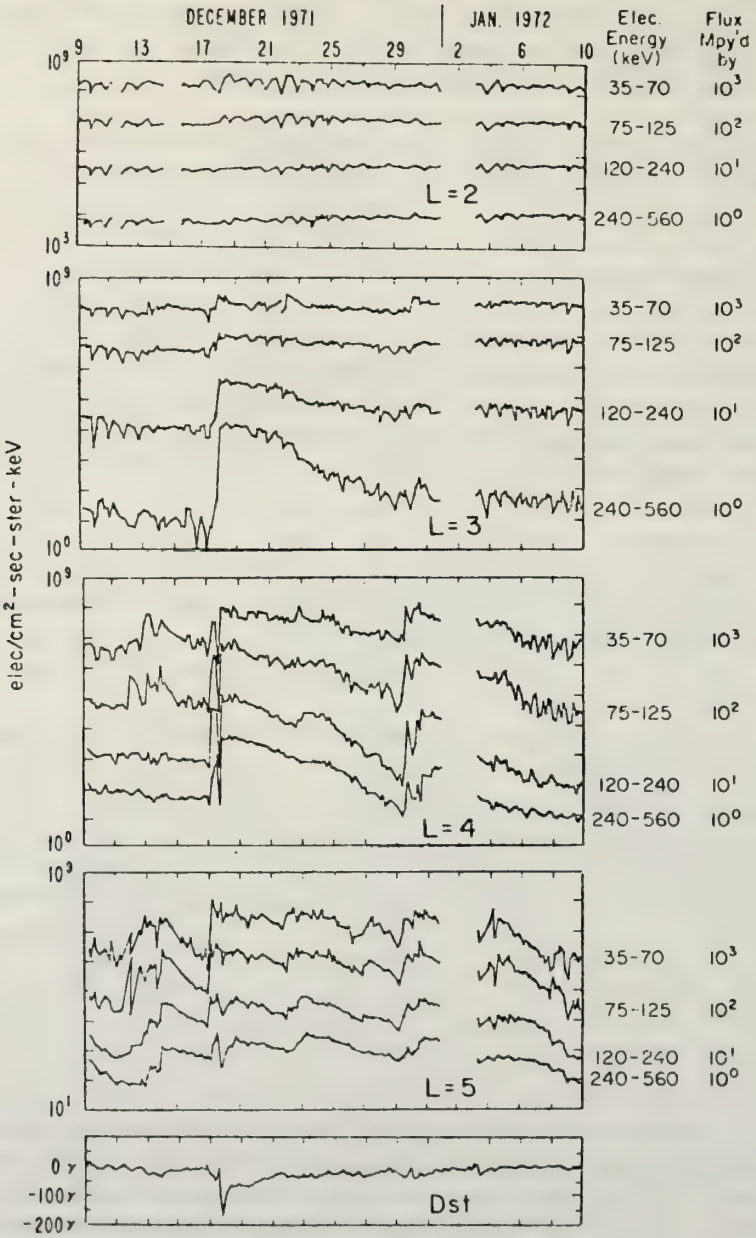


Figure 2. Fluxes of equatorially mirroring electrons versus universal time for the period Dec. 9, 1971-Jan. 9, 1972. All available data points from both inbound and outbound portions of the Explorer 45 are shown. Each panel shows the observations at the indicated L-value for the four energy channels. The 120-240 keV, 75-125 keV, and 35-70 keV fluxes have been multiplied by 10^1, 10^2, 10^3, respectively. Dst is also shown.

3. ELECTRON SCATTERING

Plasmaspheric hiss can resonate with energetic radiation belt electrons when:

$$\omega = k_{\parallel} v_{\parallel} - n\Omega \qquad (1)$$

where ω is the plasma wave frequency, $k_{\parallel}$ and $v_{\parallel}$ are the components of the wave propagation vector parallel to the local magnetic field direction, Ω is the electron cyclotron frequency and n is an integer ($n = 0, \pm 1, \pm 2, \pm 3, \ldots$). Measurements have shown that the ELF hiss exists almost continuously throughout the plasmasphere (e.g. Russell et al., 1969; Thorne et al., 1973; Parady and Cahill, 1973; Smith et al., 1974; Parady et al., 1975). The waves frequently exhibit a sharp lower frequency cut-off near 100 to 200 Hz, a more diffuse upper-frequency cut-off located near 1 kHz and a well-defined maximum intensity at a few hundred Hz. During quiet time the wide band average wave amplitude range from $\sim$ 3 mγ to $\sim$ 60 mγ, and the wave intensity is increased during the recovery phase of a magnetic storm (Parady et al., 1975; Smith et al., 1974); this is illustrated in Figure 3.

The waves are always found to be highly turbulent with wave energy distributed over all wave normal angles with respect to the magnetic field. Since these waves can propagate obliquely to the magnetic field, they are most frequently found to be distributed throughout the plasmasphere (Thorne et al., 1973). Indeed the ELF

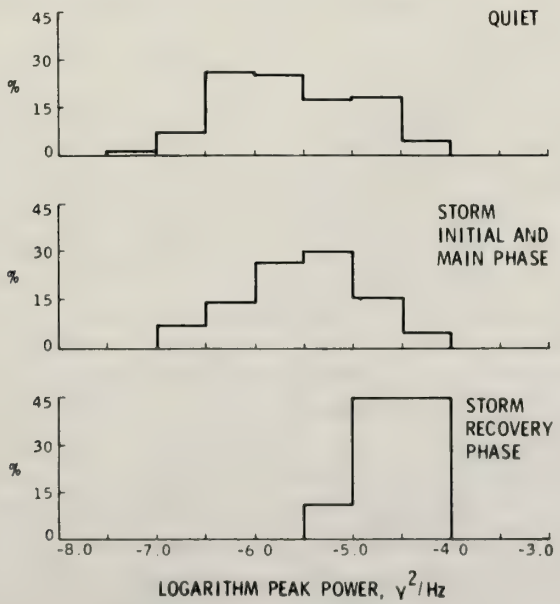


Figure 3. Histograms of peak spectral power during various phases of magnetic storms deduced from OGO-6 observations (from Smith et al., 1974). A definite intensification during the storm recovery phase is seen.

hiss appears to be the predominant wave mode within the plasmasphere. Current theories consider the plasmaspheric hiss to be generated in the plasmapause region by ring current energy (tens of keV) outer zone electrons penetrating into the plasmasphere (Lyons et al., 1972; Thorne et al., 1973; Thorne and Barfield, 1976). Once generated, these waves, because of their low frequencies, undergo a nearly perfect reflection within the magnetosphere so that little wave energy is lost to the earth's ionosphere (e.g. Kimura, 1966; Thorne and Kennel, 1967).

Substorm associated variations in the ELF hiss are known to occur (Thorne and Barfield, 1976), however, sufficient analysis to allow forecast of such variability has not yet been accomplished. On the other hand, a well defined perturbation of the plasmaspheric hiss has been found to occur during the recovery phase of magnetic storms. Figure 3, which is taken from Smith et al. (1974) clearly demonstrates that the hiss is highly intensified at such times and Smith et al. (1974) found that this intensity remains high during most of the post storm recovery phase. In contrast, there is little difference between the hiss intensities during quiet times and during the magnetic storm main phase. The post storm ELF amplitude increase is typically a factor of three or four and this corresponds to over an order of magnitude increase in the wave energy.

Using the observed properties of the plasmaspheric hiss, Lyons et al. (1972) calculated the lifetimes for radiation belt electrons at energies which can resonate with the waves (20 keV to 2 MeV). Some of their results for an assumed wave amplitude of 35 mγ are shown in Figure 4; here a wave intensity maximum at 600 Hz is used

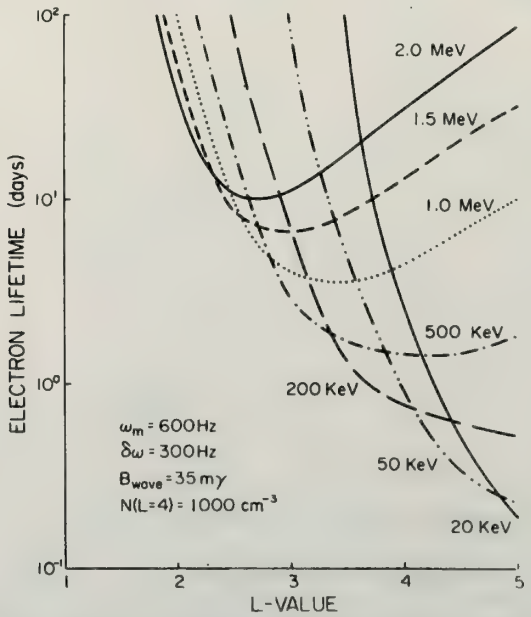


Figure 4. Theoretical electron precipitation lifetimes versus L-value for a range of electron energies: 20 keV to 2 MeV. The results are valid within the plasmasphere (from Lyons et al., 1972).

together with an effective bandwidth of 300 Hz. It should be noted that these electron precipitation lifetimes are proportional to the square of the wave amplitude and therefore scale with the wave intensity such that

$$\tau_p = \tau_{po} \left(\frac{B_{WO}}{B_W} \right)^2 \qquad (2)$$

where B_{WO} is the nominal value of the average wave amplitude at which the lifetimes τ_{po} are given as function of energy and L-shell. Similarly, for a given trapped electron spectrum the rates of energetic electron precipitation scale inversely with τ_p (for details, see Lyons and Thorne, 1971, 1972, and for applications see Spjeldvik and Thorne, 1975a, b).

Notice that for all electron energies there exists a relatively sharply defined L-shell below which these lifetimes become very long. This marks the outer edge of the stable inner radiation zone and is effectively a separator between the wave-particle interaction dominated outer electron belt and the Coulomb collision controlled inner belt. From Figure 4 we see that this boundary moves to higher L-shells with decreasing electron energy, and this accounts for the observed fact that the inner zone extends to higher L-shells with decreasing electron energy. Using radiation belt electron data Lyons et al. (1972) also demonstrated that the wave particle scattering into the atmospheric bounce loss cone accounts for the post storm decay of the radiation belts as function of L-shell and electron energy beyond the inner radiation zone.

4. ENERGY DEPOSITION IN THE ATMOSPHERE

Once pitch angle scattering of energetic radiation belt electrons has lowered the electron pitch angle to the immediate vicinity of the atmospheric bounce loss cone, the electrons encounter the denser parts of the earth's atmosphere within the next half bounce period. Let $\alpha_{0L}(E)$ be the (energy dependent) nominal loss cone angle defined such that an incident electron with equatorial pitch angle $\alpha_0 \leq \alpha_{0L}$ has 50% or more probability that its kinetic energy will be degraded to 1/e of its incident energy during the next atmospheric encounter. The equatorial pitch angle range of the loss cone spans only a small fraction of pitch angle space, at L = 4 typically from 0^0 to 5.5^0 giving a total loss cone of $\sim 11^0$. The idealized case of isotropic electron precipitation has been studied by Potema and Zmuda (1970) and Potemra (1973). However, during the storm recovery phase the radiation belt electron pitch angle diffusion rate practically always remains below the strong diffusion limit (e.g. Lyons et al., 1972; Spjeldvik and Thorne, 1975a). As a consequence the loss cone will exhibit the characteristics of a steep down-step from the trapped flux level ($\alpha_0 > \alpha_{0L}$) to the precipitated flux level ($\alpha_0 \lesssim \alpha_{0L}$). The fine details of the narrow transition region have been studied (Spjeldvik and Thorne, 1975a; Davidson and Walt, 1977) but some controversy still remains

as to the preciseness of the analytical and numerical approximations (Spjeldvik, 1977; Walt and Davidson, 1978; Spjeldvik, 1978). Fortunately, such details are not of great importance for the height distributions of the energy deposited in the atmosphere by the energetic electrons. An electron losing 1-1/e or more of its incident kinetic energy is also so substantially scattered by the atmosphere that practically all "memory" of the incident pitch angle becomes lost. At radiation belt energies the backscattered electron flux may be in the range 10-30% of the incident flux, depending on energy (e.g. Spjeldvik and Thorne, 1975a; Davidson and Walt, 1977). The major portion of the precipitated ($\alpha_0 \lesssim \alpha_{0L}$) flux becomes stopped in the atmosphere, and in the process the incident electron energy is deposited as local excitation and ionization of the atmospheric constituents and, at several MeV and above, also in the generation of Bremsstrahlung X-rays. Although 13 eV energy is sufficient to ionize an atmospheric molecule, energy absorption by bound electron excitation makes an average of 35 eV necessary to produce a free ion-electron pair in air. Thus, as a rule of thumb a 350 keV precipitated electron produces 10,000 ion-electron pairs along its trajectory. It is the magnitude and height distribution of this precipitation source that is of prime concern. A numerical code for simulating the energy deposition has been developed by Walt et al. (1968) and has been applied by Spjeldvik and Thorne (1975a) and by Davidson and Walt (1977) where details can be found. Further analysis of the associated VLF ionospheric wave propagation has been made by Larsen et al. (1976, 1977) and by Davis (1976).

Figure 5 gives an example of the calculated ionospheric ion-electron pair production rates due to energetic radiation belt electron precipitation on September 6, 1966 using trapped electron measurements made with the OV3-3 satellite early in the recovery phase of a major magnetic storm. These results which are taken from Spjeldvik and Thorne (1975a) are given for a wide range of ELF intensities; the most probable post storm wave amplitudes are in the range 30-60 mγ although intensification to hundreds of mγ may occur.

5. PREDICTABILITY OF THE ELECTRON PRECIPITATION

In the present context there are three levels at which forecasts of post storm energetic electron precipitation into the atmosphere may be made:

(1) Qualitative assessment of the size and timing of the ionospheric storm after-effects.

(2) Semiquantitative predictions of the overall magnitude and temporal evolution with a probable error better than an order of magnitude.

(3) Precise quantitative forecasts of the precipitation flux including perturbations due to ELF hiss variability.

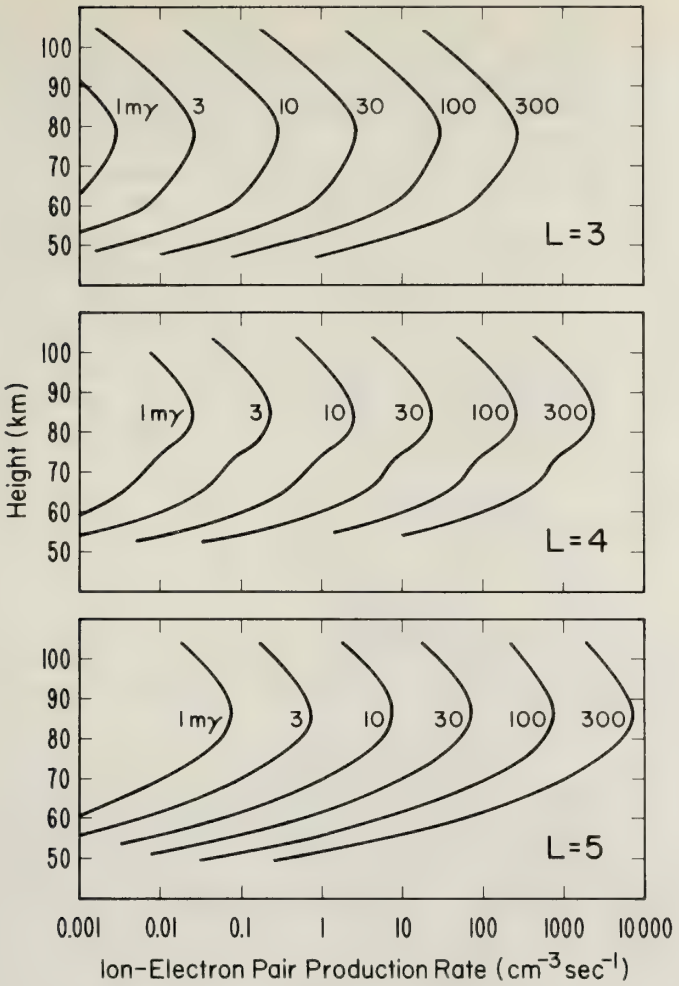


Figure 5. Ion-electron pair production rates in the lower ionosphere due to radiation belt electron precipitation on September 6, 1966. The results are given using the pitch angle diffusion coefficients of Lyons et al. (1972) and the energy deposition program of Walt et al. (1968). The dependence on the ELF mean amplitude is given for the range 1 mγ to 300 mγ (for details see Spjeldvik and Thorne, 1975a).

In general, the qualitative aspects of the operating physical mechanisms are fairly well established. We know that with the magnetic storm refilling of the radiation belt "slot" region the effective rates of energetic electron precipitation will be correspondingly enhanced even in the complete absence of ELF whistler mode hiss intensification. Thus, qualitative estimates (category 1) may readily be made. However, using satellite measurements of the precise extent to which the electron "slot" is being refilled during the storm main phase together with the empirical knowledge of the most probable ELF hiss intensification during the recovery phase from the quiet time levels to 10-150 mγ or more (e.g. Parady and Cahill, 1973) it is possible to make at least a semi-quantitative (category 2) prediction.

The magnitude of the electron flux injection into the radiation belt "slot" region varies from storm to storm. We do not yet know how this varies with the minimum Dst during the storm; however, it is reasonable to surmise that these quantities should show co-variation. For post storm prediction we will therefore rely on radiation belt observations during the storm main phase. If the spectral shapes of the injected electron fluxes do not change substantially from storm to storm it is possible to establish a prediction scheme for the D and E region production profiles by a simple scaling of the detailed computations presented in Figure 5. Let j_{OBS} be the observed differential energy electron flux at a pitch angle α_o ($>\alpha_{OL}$) and energy E early in the recovery phase at time t_o; and let j_{OLD} be the corresponding quantity established for the September 6, 1966 magnetic storm already studied (Spjeldvik and Thorne, 1975a). We then have the scaling relation

$$Q = Q_{OLD} \left(\frac{j_{OBS}}{j_{OLD}} \right) \left(\frac{B_W}{B_{W-OLD}} \right)^2 \qquad (3)$$

where Q and Q_{OLD} are the predicted and previously (e.g. Figure 5) computed ionospheric ion-electron pair production rates, and B_W and B_{W-OLD} are the corresponding ELF whistler mode mean wave amplitudes of the plasmaspheric hiss.

As time progresses through the recovery phase the electrons will decay on time scales given in Figure 4 and scaled according to Eqn. (3) for other wave amplitudes. The time evolution of radiation belt electrons following a magnetic storm will then be similar to the time evolution exemplified in Figure 2, and the precipitation induced D and E region ionization rates will decay correspondingly. If j_{OBS} in Eqn. (3) is replaced by $j_{OBS} \exp(-(t-t_o)/\tau_p)$ where τ_p is the mean electron precipitation lifetime for the energy of an electron which deposits its energy primarily at height h (e.g. Potema, 1973), then the time evolution of the ionization rates are forecastable.

Of course, this simplified precipitation prediction scheme makes assumptions on:

(a) Intensity of the ELF whistler mode plasmaspheric hiss.

(b) The spectral shapes of the radiation belt electron injection flux.

The use of (a) to upgrade the predictability to category 3 requires further research on the hiss generation, particularly its association with substorms. In principle, there is no difficulty in using (b). However, this would require the use of an extensive computer code (such as the one of Walt et al., 1968 or Monte Carlo Methods) on a real time basis for each storm period.

6. D REGION IONIZATION CHANGES

The D region ionosphere has been found to contain a number of different charged particles. Free electrons and light positive ions (N_2^+, O_2^+ and NO^+) are formed by the ionization mechanism. Heavier ions are formed through the attachment processes, ion-molecule reactions and formation of hydrated cluster ions.

Realizing that the positive ions appear to fall into two classes, light ions with small recombination coefficient and heavier ions with substantially larger recombination coefficient, and that the negative ions likewise can be divided into the high electron affinity heavy species and the lower affinity light species, Spjeldvik and Thorne (1975b) developed a simplified multi-species ionic model that has been used to study the storm after effects.

Using this model we have determined the value of the effective recombination coefficient α_{eff} defined such that

$$\frac{d[N]}{dt} = Q - \alpha_{eff} [e]^2 \qquad (4)$$

where [N] is the number density sum of all negative particles, Q is the ion-electron pair production rate and [e] is the number density of free electrons. The analytic form of α_{eff} can easily be deduced from the model of Spjeldvik and Thorne (1975b). The α_{eff} height profile for daytime conditions is given in Figure 6. At night the atomic oxygen concentration below 80 km becomes very small and the chemistry favors the high affinity negative species. On the other

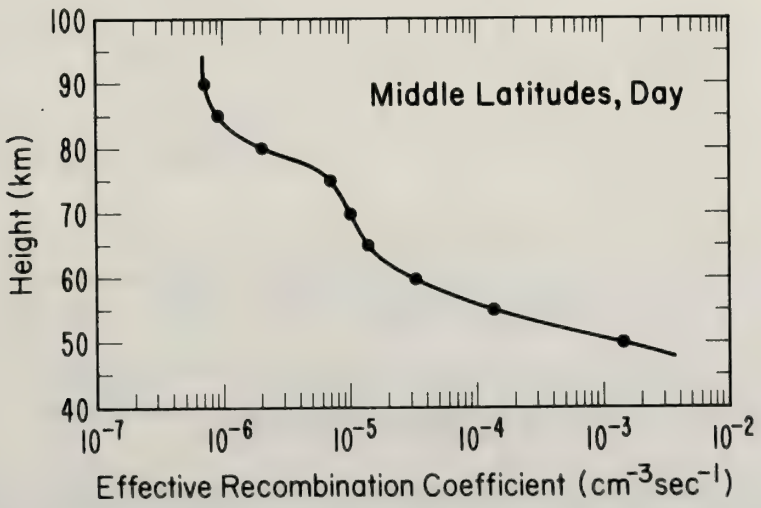


Figure 6. Effective recombination coefficient for the daytime lower ionosphere calculated from the ionic chemistry model of Spjeldvik and Thorne (1975b).

hand, substantially increased ion-electron pair production at night tends to favor the lighter species. Consequently, the nocturnal values of α_{eff} are dependent on Q, or for the case of radiation belt electron precipitation on the trapped flux level of energetic electrons (with $\alpha_0 > \alpha_{0L}$) and the scattering ELF hiss amplitude. For the trapped fluxes of September 6, 1966 we present in Figure 7 the dependence of α_{eff} on the plasmaspheric hiss intensity. This dependence is of course strongest below 80 km and above $\sim$ 50 km (below which the electron precipitation effects are weak).

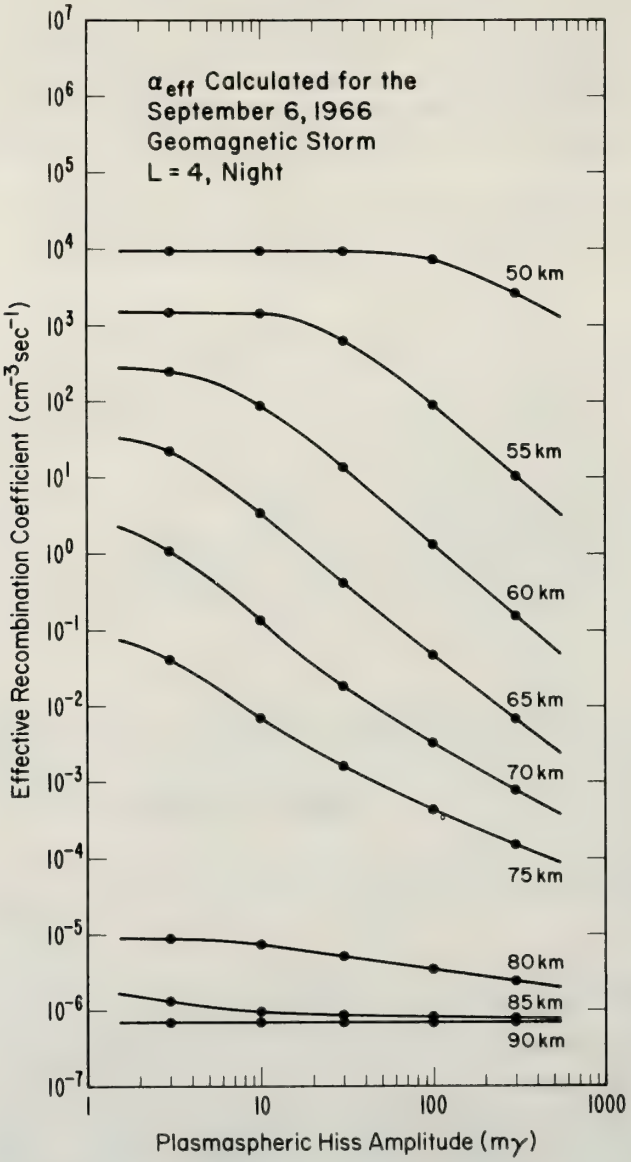


Figure 7. Effective recombination coefficient for the nighttime lower ionosphere calculated from the ionic chemistry model of Spjeldvik and Thorne (1975b). The α_{eff} values are found to be dependent on the ion-electron pair production rate Q and therefore for a given magnetic storm (Sept. 6, 1966 in this example) on both the trapped radiation belt flux level and the ELF wave intensity B_W.

It should be noted that the simplified formula (4) really represents a carryover from earlier considerations of only one kind of D-region ion. With the recognition of a variety of ions (4) may still be used provided α_{eff} is considered a variable with atmospheric composition and production rate Q (and consequently with [e]). For example, Haug and Landmark (1970) have demonstrated restrictive conditions under which $\alpha_{eff} \sim [e]^{-1}$ near 80 km and similar features are found by others (e.g. Haug and Thrane, 1970; Folkestad et al., 1972; Lastovička, 1975).

For steady state conditions ($d/dt \to 0$) the electron density is just given by $[e] = \sqrt{Q/\alpha_{eff}}$ where the appropriate values of Q and α_{eff} may be obtained from Figures 5, 6, and 7.

This is valid if Q remains unchanged for tens of minutes during the day and typically 1-2 hours during the night. Thus, in a very simplified fashion it is possible to predict the D region chemical response in free electrons by a simple scaling of the detailed calculations already carried out (e.g. Spjeldvik and Thorne, 1975b).

ACKNOWLEDGEMENTS

One of us (W.N.S.) was supported by a NASA grant W13952.

REFERENCES

Belrose, J. S. and L. Thomas (1968): "Ionization Changes in the Middle Latitude D-Region Associated with Geomagnetic Storms", Journal of Atmospheric and Terrestrial Physics, 30, 1397.

Davidson, G. T. and M. Walt (1977): "Loss Cone Distribution of Radiation Belt Electrons", Journal of Geophysical Research, 82, 48.

Davis, J. R. (1976): "Localized Nighttime D-Region Disturbances and ELF Propagation", Journal of Atmospheric and Terrestrial Physics, 38, 3674.

Folkestad, K., E. V. Thrane and B. Landmark (1972): "A Study of Ion-Pair Production Rates and Electron Number Densities in the Ionospheric D-Region", Journal of Atmospheric and Terrestrial Physics, 34, 963.

Haug, A. and B. Landmark (1970): A Two-Ion Model of Electron-Ion Recombination in the D-Region," Journal of Atmospheric and Terrestrial Physics, 32, 405.

Haug, A. and E. V. Thrane (1970): The Diurnal Variation in the Mid-Latitude D-Region" Journal of Atmospheric and Terrestrial Physics, 32, 1641.

Kimura, I. (1966): "Effects of Ions on Whistler-Mode Ray Tracing", Radio Science, 1, 269.

Krivsky, L.(1977): "Solar Proton Flares and Their Prediction", Czechoslovak Academy of Sciences Astronomical Institute Publication #52, Prague.

Larsen, T. R., J. B. Reagan, W. L. Imhof, L. E. Montbriand and J. S. Belrose (1976): "A Coordinated Study of Energetic Electron Precipitation and D-Region Electron Concentrations over Ottawa During Disturbed Conditions", Journal of Geophysical Research, 81, 2200.

Larsen, T. R., T. A. Potemra, W. L. Imhof and J. B. Reagan (1977): "Energetic Electron Precipitation and VLF Phase Disturbances at Middle Latitudes Following the Magnetic Storm of December 16, 1971", Journal of Geophysical Research, 82, 1519.

Lasstovička, J. (1975): "On the Linearity of the Dependence of the A3 Ionospheric Absorption at 2775 kHz on the Intensity of Ionizing Radiation", Journal of Atmospheric and Terrestrial Physics, 37, 1505.

Lauter, E. A. (1977): "A Catalog of Excessive Absorption (Post-Storm Ionization Enhancements) in the Mid-Latitude D-Region 1948-1976", Akademie der Wissenschaften der DDR, HHI-STP-Report 10, Berlin.

Lauter, E. A. and R. Knuth (1967): "Precipitation of High Energy Particles into the Upper Atmosphere at Medium Latitudes after Magnetic Storms", Journal of Atmospheric and Terrestrial Physics, 29, 411.

Lauter, E. A., J. Bremer, A. Grafe, I. Deters and K. Evers (1977): "The Post-Storm Ionization Enhancements in the Mid-Latitude D-Region and Related Electron Precipitation from the Magnetosphere", Akademie der Wissenschaften der DDR, HHI-STP-Report 9, Berlin.

Lyons, L. R., R. M. Thorne and C. F. Kennel (1971): "Electron Pitch Angle Diffusion Driven by Oblique Whistler-Mode Turbulence", Journal of Plasma Physics, 6, 589.

Lyons, L. R., R. M. Thorne and C. F. Kennel (1972): "Pitch Angle Diffusion of Radiation Belt Electrons within the Plasmasphere", Journal of Geophysical Research, 77, 3455.

Lyons, L. R. and R. M. Thorne (1973): "Equilibrium Structure of Radiation Belt Electrons", Journal of Geophysical Research, 78, 2142.

Lyons, L. R., and D. J. Williams (1975): The Storm and Poststorm Evolution of Energetic (35-560 keV) Radiation Belt Electron Distributions", Journal of Geophysical Research, 28, 3985.

Parady, B. K. and L. J. Cahill, Jr. (1973): "ELF Observations during the December 1971 Storm", Journal of Geophysical Research, 78, 4765.

Parady, B. K., D. D. Eberlein, J. A. Marvin, W. W. L. Taylor and L. J. Cahill, Jr. (1975): "Plasmaspheric Hiss Observations in the Evening and Afternoon Quadrants", Journal of Geophysical Research, 80, 2183.

Potemra, T. A. and A. J. Zmuda (1970): "Precipitating Energetic Electrons as an Ionization Source in the Midlatitude Nighttime D-Region", Journal of Geophysical Research, 75, 7161.

Potemra, T. A. (1973): "Precipitating Energetic Electrons in the Mid-Latitude Lower Ionosphere", In: Physics and Chemistry of Upper Atmospheres, Ed.: B. M. McCormac, p. 67.

Russell, C. T., R. E. Holzer and E. J. Smith (1969): "Observations of ELF Noise in the Magnetosphere: I. Spatial Extent and Frequency of Occurrence", Journal of Geophysical Reseach, 74, 755.

Smith, E. J., M. A. Frandsen, B. T. Tsurutani, R. M. Thorne and K. W. Chan (1974): "Plasmaspheric Hiss Intensity Variations During Magnetic Storms", Journal of Geophysical Research, 79, 2507.

Spjeldvik, W. N. and Thorne, R. M. (1975a): "The Cause of Storm After Effects in the Middle Latitude D-Region", Journal of Atmospheric and Terrestrial Physics, 37, 777.

Spjeldvik, W. N. and R. M. Thorne (1975b): "A Simplified D-Region Model and its Application to Magnetic Storm After Effects", Journal of Atmospheric and Terrestrial Physics 37, 1313.

Spjeldvik, W. N. and R. M. Thorne (1976)): "Maintenance of the Middle Latitude Nocturnal D-Layer by Energetic Electron Precipitation", Journal of Pure and Applied Geophysics, 114, 497.

Spjeldvik, W. N. (1977): "Radiation Belt Electrons: Structure of the Loss Cone", Journal of Geophysical Research, 82, 709.

Spjeldvik, W. N. (1978): "Reply to the Comment of Walt and Davidson", Journal of Geophysical Research, 83, 226.

Thorne, R. M. and C. F. Kennel (1967): "Quasi-Trapped VLF Propagation in the Outer Magnetosphere", Journal of Geophysical Research, 72, 857.

Thorne, R. M., E. J. Smith, R. K. Burton and R. E. Holzer (1973): "Plasmaspheric Hiss", Journal of Geophysical Research, 78, 1581.

Thorne, R. M., and J. N. Barfield (1976): "Further Observational Evidence Regarding the Origin of Plasmaspheric Hiss", Geophysical Research Letters, 3, 29.

Walt, M., W. M. MacDonald and W. E. Francis (1968): "Penetration of Auroral Electrons into the Atmosphere", in: Physics of the Magnetosphere, Ed: Carovillano, R. C.

Walt, M. and G. T. Davidson (1978): "Comment on 'Radiation Belt Electrons: Structure of the Loss Cone' by W. N. Spjeldvik", Journal of Geophysical Research, 83, 225.

C. IONOSPHERIC PREDICTIONS

GEOMAGNETIC ACTIVITY CONTROL OF IONOSPHERIC VARIABILITY

Michael Mendillo
and
Francis X. Lynch
Astronomy Department
Boston University
Boston, MA 02215 USA

John A. Klobuchar
Air Force Geophysics Laboratory
Hanscom AFB
Bedford, MA 01731 USA

1. INTRODUCTION

Every ionospheric parameter varies in space and time. Given the sparcity of ionospheric observing stations and the cost factors associated with creating new ones, one must often resort to prediction schemes in order to have an estimate for a particular parameter. Given the fact that an observed parameter ($P_o(t)$) is not the same every day, one can define a mean or median diurnal pattern $\overline{P_o(t)}$ for each month. The standard deviations for the observed $P_o(t)$ may be denoted $\sigma_o(t)$, and thus a month's worth of observations at a given site $\{P_o(t)\}$ may be described in the average as $\overline{P_o(t)} \pm \sigma_o(t)$.

The crux of the problem facing ionospheric forecasters centers on the need to know the diurnal values of P at a site where observations are not available. The main approach to this problem has centered on the use of large ionospheric data bases, $\Sigma\{P_o(t)\}$, which are analyzed in statistical ways to search for trends and correlations which may aid the long and short term needs of forecasters. The main goals a statistical analysis of ionospheric data can hope to achieve with respect to the formulation of prediction schemes are:

(1) Specification of the magnitudes of the standard deviations for each parameter, and thus the determination of whether or not predictions of average monthly behavior $(\overline{P(t)})$ can realistically address the needs of individual users.

(2) A search for statistically significant patterns of ionospheric variability and thus reduce the uncertainty implied by the $\pm \sigma_o$ values attached to any predicted $\overline{P(t)}$ curve.

(3) An examination of the correlations between ionospheric variability seen at different sites in order to extend individual measurements to cover a wider geographical area.

A great many studies have been carried out in each of these areas, and thus approaches toward realistic prediction schemes have been formulated for several ionospheric parameters. Rush (1973) has reviewed the situation for short-term predictions of radio propagation conditions at mid-latitudes by examining hourly critical frequencies for the E, F1 and F2 regions (i.e., f_oE, f_oF1 and f_oF2, respectively). For the E-region during the 0900-1500 LT period, the observed standard deviations for f_oE (σ_o expressed in percent with respect to a monthly median) were generally less than 6% -- implying that 95% of all observations lie within ± 12% of their median value. For f_oF1, the σ_o (%) were found to be only slightly more variable with the difference being greatest during solar maximum years. The conclusion reached by Rush was that for most needs the day-to-day variability of f_oE and f_oF1 is such that monthly median (or mean) values can be used to represent the diurnal variations. This implies that forecasters' attention should be given to the methods of predicting average behavior, rather than to ways of taking into account the inherent variability of the E and F1 regions. This has, in fact, been a fruitful avenue in that the median values of f_oE and f_oF1 at mid-latitude can, for the most part, be predicted to within an accuracy of ± 5% (Muggleton, 1972; DuCharme et. al, 1971).

For the F2 region, the situation is quite the opposite. Rush (1976), for example, suggests that an average value of ±15% provides a good estimate for the standard deviations observed in f_oF2 behavior at mid-latitudes, regardless of local time, season or solar cycle conditions. It should be emphasized that while the experimentally measured and propagation system dependent parameter is often a critical frequency, e.g., f_oF2 (in MHz), the physically important parameter from a modeling point of view is the electron density (N_e, in #el/cm^3). Since a critical frequency or plasma frequency, f_p, is related to electron density by $f_p(\text{MHz}) \simeq [9\ N_e(10^6 \text{el/cm}^3)]^{\frac{1}{2}}$, the variabilities in the maximum electron density, σ_o(Nm), of each ionospheric region (NmE, NmF1, NmF2) are proportionally larger than those quoted for their respective critical frequencies (f_oE, f_oF1, f_oF2).

Some ionospherically-affected propagation systems depend on the electron densities themselves and thus their relatively large standard deviations about average monthly conditions become the variability factor of prime concern. For example, satellite navigation and detection radar systems can be limited in accuracy by the time delay imposed upon their RF signal's passage through the entire ionosphere. The total number of electrons contained along a vertical ray path through the ionosphere is called the Total Electron Content (TEC), a parameter capable of being measured routinely by satellite radio beacon techniques (Titheridge, 1972). Since 90% or more of the TEC occurs in the F2 region, the large TEC data base which has been assembled since the mid-1960's is a valuable source for F2

region studies. Recently, Johanson et. al. (1977) described a study of TEC day-to-day variability effects by analyzing the observed standard deviations, σ_o (%), from monthly mean TEC behavior recorded at an 11-station network in the northern hemisphere. They concluded that TEC variability, as described by σ_o (%), was approximately ± 25% with only small additional dependences upon local time, season, latitude and solar flux conditions. Hawkins and Klobuchar (1974) showed that for a single mid-latitude site (Sagamore Hill/Hamilton MA), the monthly mean diurnal curve for TEC may be predicted via a simple relationship between TEC and solar flux which has a correlation coefficient higher than 0.9 for all months. This suggests that, at least for mid-latitudes, a forecaster's attention should not be directed toward improved prediction schemes for average behavior, but rather toward the search for ways to predict (or correct for) the inherent day-to-day variability of the F-region. This, as we have seen, is precisely the opposite view facing E and F1 region prognosticators.

2. POSSIBLE APPROACHES TO THE VARIABILITY PROBLEM

As discussed in the previous section, we may assume that a prediction for the monthly mean diurnal behavior of an F2-region parameter (Nmax or TEC) is available. We denote this prediction P(t) and attach to it some error (±e) from the observed mean behavior $\overline{P}_o$(t). Associated with $\overline{P}_o$(t) is an observed standard deviation $\pm\sigma_o$; it is generally agreed that $|e| < |\sigma|$ by approximately a factor of 2. Thus, as a first approach to modifying a monthly prediction P(t) for day-to-day variability effects, it makes good sense to concentrate on reducing the impact of the magnitude of σ_o.

Rush (1976) considered the case for short-term predictions of f_oF2 via real-time updates from a network of stations. Correlation coefficients for Δf_oF2 were obtained as a function of station separation distances for a full range of local time, seasonal and north-south vs. east-west conditions. These results were used to test the concept of using real-time measurements at one site to update monthly median-based predictions at another site. Thus, consider the case that at site A data are available while at site B only $P(t)\pm\sigma_o$ exists. Based on percentage departures from median conditions at A, $P(t) \rightarrow P'(t)$ at B. Depending upon the separation between A and B, this update can reduce the uncertainty at B associated with its monthly median prediction, that is, $\sigma_o \rightarrow \sigma'$. Rush found that for σ_o to be reduced by 50%, the approximate separation distances for such an extrapolation/update had to be less than 500 km for north-south sites and 1000 km for east-west sites. Thus, it was

concluded that to achieve this degree of improvement under most conditions at mid-latitudes an observational network would be required capable of reporting real-time ionospheric measurements from a global grid 10° in latitude and 20 degrees in longitude. In a broad sense, this represents "state of the art" conclusions for the day-to-day variability problem.

An aspect of F-region behavior long associated with the variability question is the role geomagnetic activity plays in determining the magnitudes of σ_{φ} at any given site. A great many studies have been carried out concerning ionospheric storms, and so the crucial points concerning storm effects vis à vis the more general problem of ionospheric variability are known. These include:

(1) The "worst case" departures of an F-region parameter from average monthly conditions invariably occur during geomagnetic disturbance.

(2) At most ionospheric sites, storm-time departures from average conditions exhibit well defined positive and negative phases, which themselves often have pronounced local time, seasonal and solar cycle dependencies.

(3) Ionospheric disturbances associated with geomagnetic storms often show long-lived effects in comparison to geomagnetic parameters.

The ionospheric TEC parameter is well-suited for studying storm effects. Superimposed-epoch types of analyses have been applied to the problem and well-defined, quantitative "correction schemes" for updating monthly median predictions are available (Mendillo and Klobuchar, 1979). The standard deviations of the storm-time characteristic correction curves for a 4-day storm period are, almost without exception, much larger than the standard deviations associated with a monthly mean or median pattern. This implies that for days that are <u>not</u> associated with strong geomagnetic activity, the artificial restriction of using <u>monthly</u> statistics may be exploited to yield quantitative and potentially useful information about day-to-day forecasting. Consider, for example, a 30-day month for which we have ordered the days by a suitable geomagnetic parameter into six 5-day categories ranging from very quiet to very disturbed conditions. We denote these 5-day periods as QQ, Q, q, d, D and DD days. Results of storm effects in the TEC data (essentially the DD and D days) implicitly tell us something about the remaining days. For example:

(1) The standard deviations for the QQ to d days must be smaller than the observed σ_{φ} for the entire month.

(2) If the amplitudes and phases (+ or -) of storm-time corrections are reasonably well-defined, then at least the dominant phase of the variations for the non-disturbed days can be inferred.

We have tested these approaches in several ways using TEC obtained from the AFGL latitudinal network of observing sites near the 70 W meridian. The data base available covered the declining and minimum portions of the past solar cycle (≃1971-1976). Four stations are selected for discussion in order to cover the geomagnetic sites characterized by L = 5 (Narssarssuaq), L = 4 (Goose Bay), L = 3 (Sagamore Hill/Hamilton) and L = 2 (Kennedy Space Flight Center). In the following section, we describe results of a preliminary analysis which attempts to use geomagnetic activity as a key to specifying the hierarchy of F-region variability contained in statistically-based ionospheric forecasts.

3. RESULTS

The initial search for a geomagnetically-controlled hierarchy to F-region variability should concentrate on extreme cases, and thus our first analysis centered on defining the essential differences between very quiet days (QQ) and very disturbed days (DD). Hourly values of ionospheric TEC data for each site were used to form percentage variations from monthly mean conditions for the 5-QQ and DD-days of each month. The average diurnal behaviors (QQ and DD), averaged over all months, are given in Figure 1 (a) Narssarssuaq, (b) Goose Bay, (c) Hamilton and (d) KSFC. When examined in this way, a remarkable degree of consistency emerges in that the QQ and DD curves are virtually "mirror images" for all local times at all four stations. This dichotomy does not always extend to precise magnitudes and phases, nor to the zero percentage line as the "mirror point" -- but nevertheless it does suggest a strong ordering influence related to geomagnetic activity. Previous studies have shown that ionospheric storm morphologies are best ordered by a superimposed-epoch scheme carried out for several days, and thus a single curve labeled "Disturbed Day Variation" cannot capture the true and often multi-phase development of an ionospheric storm (Mendillo, 1978). The DD curves presented here thus point to the most long-lived effects associated with storms -- and therefore the QQ curves describe the absence of these perturbations. Consider, for example, daytime effects over the L = 2-5 range. At high latitudes, the DD curves show essentially negative effects while enhancements appear at L = 2. Consequently, the QQ variations also exhibit a latitudinally dependent phase change. Thus, if one considers "QQ-like behavior" versus "DD-like behavior" then the spatial extent over which correlations occur may be greatly enhanced. The implication to forecasters is obvious, as will be discussed more fully below.

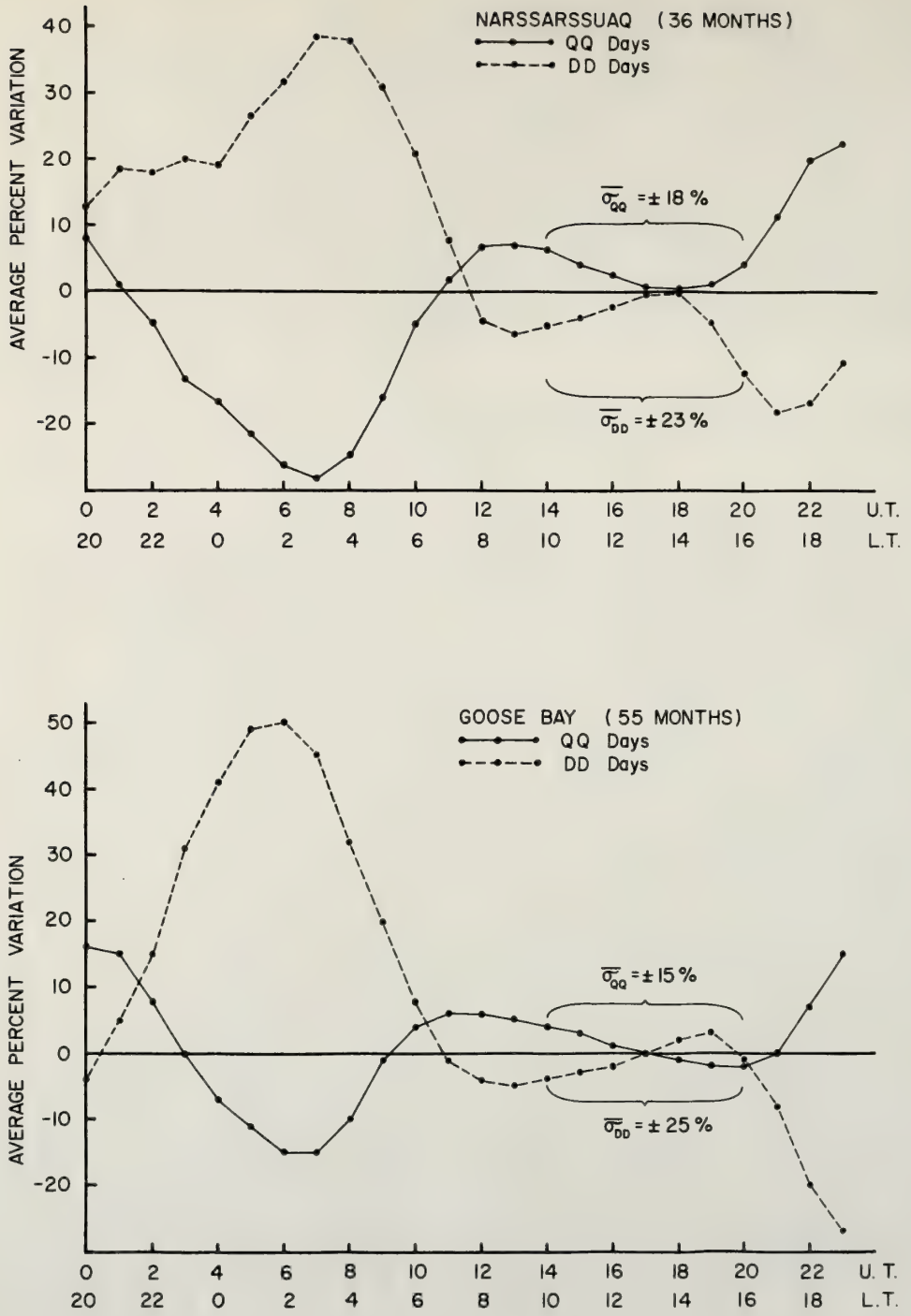
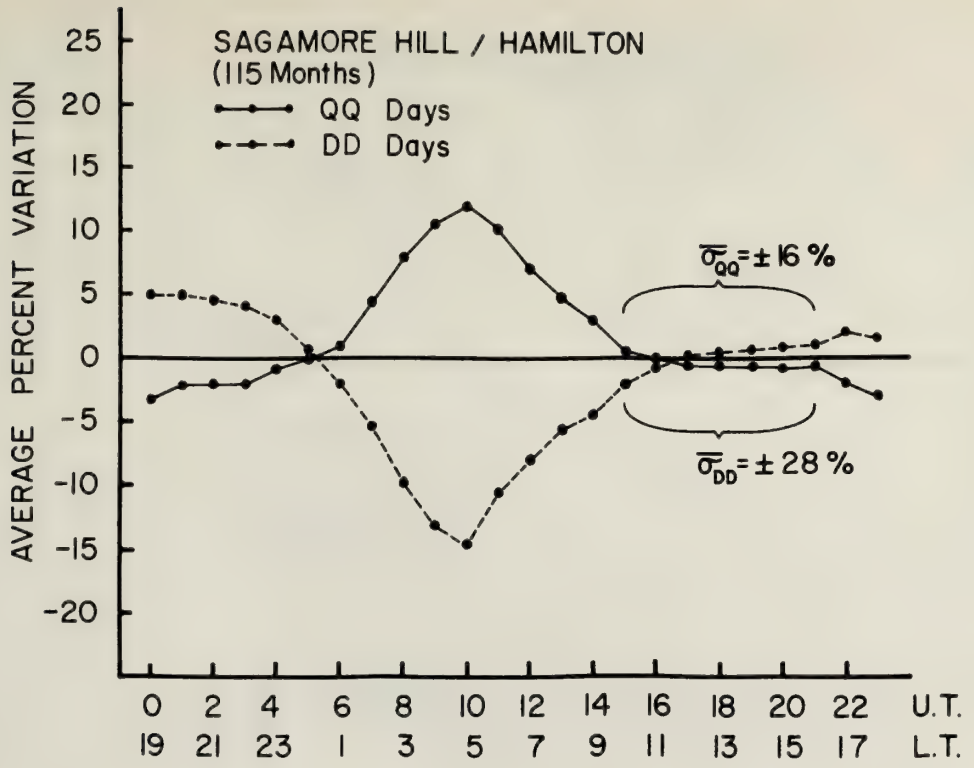


Figure 1.
Average diurnal behavior of ΔTEC(%) for the 5 QQ-days and the 5 DD-days of a month for (a) Narssarssuaq and (b) Goose Bay.



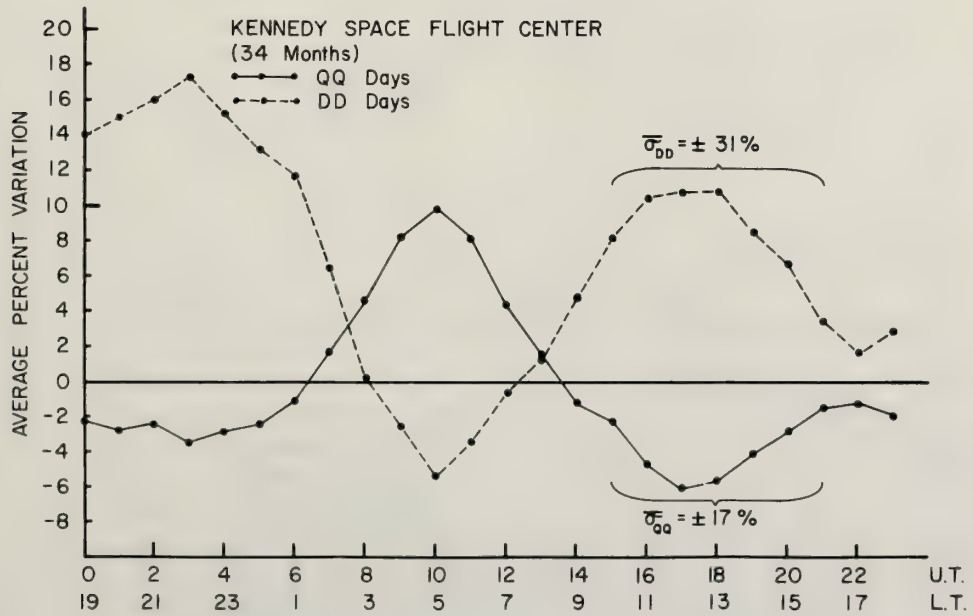


Figure 1.
Average diurnal behavior of ΔTEC(%) for the 5 QQ-days and the 5 DD-days of a month for (c) Hamilton and (d) Cape Kennedy.

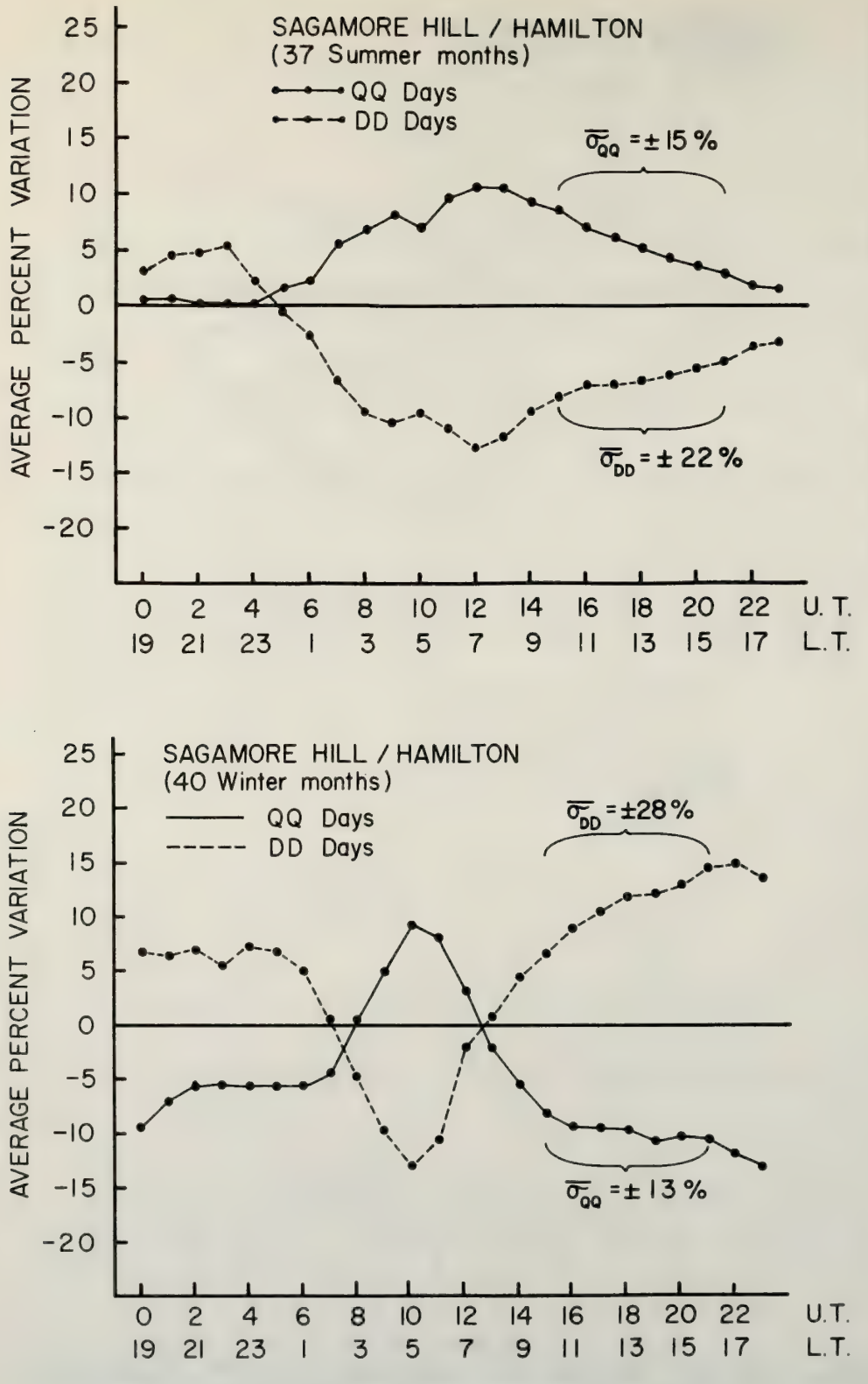


Figure 2.
Average diurnal behavior of ΔTEC(%) for the QQ-days and DD-days for Summer and Winter months at Hamilton (L ≃ 3).

Since ionospheric storm effects have well-known seasonal variations, it is not surprising that the QQ behavior also follows a seasonal control. For example, in Figure 1 (c), the Hamilton QQ/DD curves for all months averaged together show very little variation from monthly mean conditions during the 10:00 - 16:00 LT period. Figure 2 contains a Summer versus Winter breakdown of the same data base; the amplitudes of the curves are much larger and of different sign and thus an accurate description of QQ behavior at L = 3 requires a seasonal analysis simply because the storm effects at L = 3 are strongly seasonal dependent. This is not necessarily the case, however, for all latitude regions (Mendillo, 1978).

The results presented in Figure 1 and 2 suggest that a knowledge of ambient geomagnetic conditions may be sufficient to achieve a meaningful real-time update to monthly mean predictions of F-region behavior. It would appear that several implementation schemes for this information should be considered and tested. For illustration purposes, we concentrate here on the case where geomagnetic information is available to predict that a day is probably one of the 5 QQ-days of the month. For the site in question, where $\bar{P}(t) \pm \sigma_o(t)$ is the predicted monthly mean pattern and associated variability, one could update this value in several possible ways:

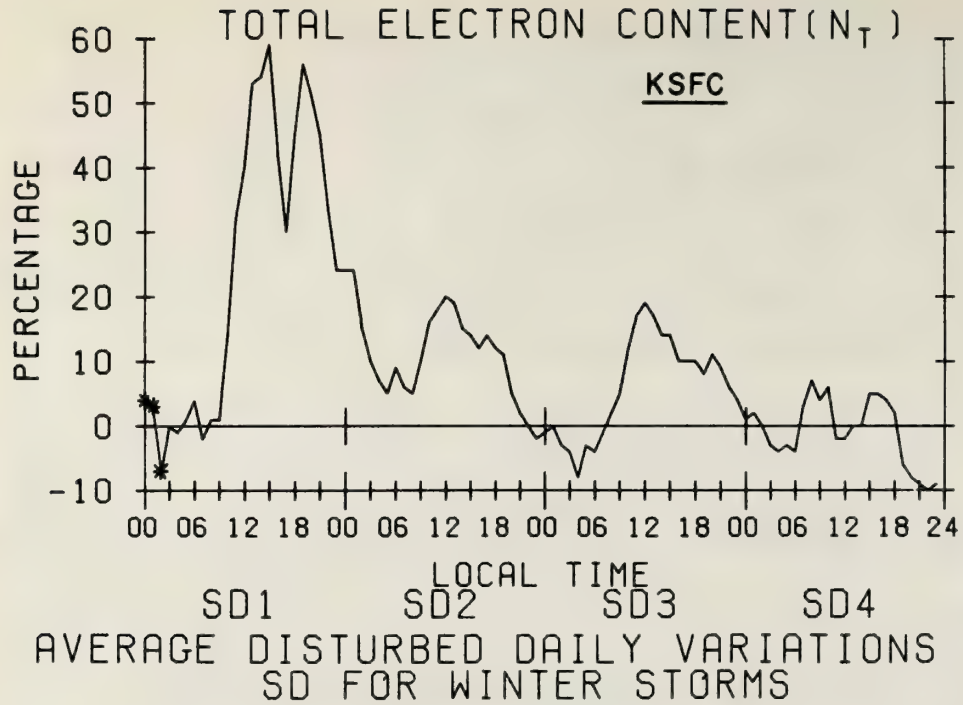
(1) Using curves similar to those shown in Figures 1 and 2, one could update $\bar{P}(t)$ by the appropriate $\Delta P_{QQ}(\%)$ and assign a new uncertainty $\pm\sigma_{QQ}$. This type of scheme would require interpolation according to geomagnetic latitudes, with a full breakdown of seasonal effects in the QQ(t) patterns and their associated standard deviations σ_{QQ}. Thus, each of the QQ days would have a predicted diurnal pattern changed from $\bar{P}(t) \pm \sigma_o(t)$ to $\bar{P}(t) + \Delta P_{QQ}(t) \pm \sigma_{QQ}(t)$. Since $\sigma_{QQ}(t)$ is demonstrably smaller in magnitude than σ_o (usually quoted to be ± 25%), an updated value with reduced uncertainty (say to ± 15%, i.e., a 40% improvement) has been achieved.

(2) An alternate scheme could take advantage of the fact that Figures 1 and 2 show that during certain local time periods and seasons, the QQ patterns fall well to the positive or negative side of the mean behavior. Thus, knowledge that a certain day is a QQ day implies that only the positive or negative half of the excursion associated with $\pm \sigma_o$ is likely to occur and updates should be made accordingly. Under such conditions, the monthly mean based prediction $\bar{P}(t) \pm \sigma_o(t)$ would be changed to:

$$\bar{P}(t)\left[1 + \frac{\sigma_o}{2}\right] \pm \frac{\sigma_o}{2} \quad \text{for positive effects} \qquad (1)$$

or

$$\bar{P}(t)\left[1 - \frac{\sigma_o}{2}\right] \pm \frac{\sigma_o}{2} \quad \text{for negative effects.} \qquad (2)$$



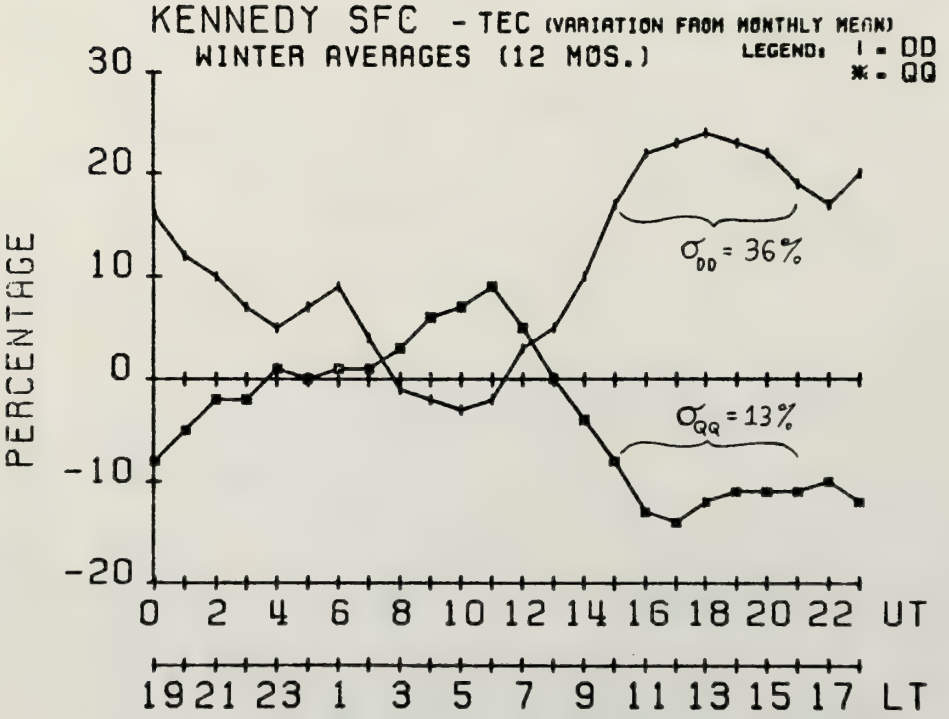


Figure 3.
(a) Average Disturbed Daily Variations of ΔTEC(%) for Winter Storms at Cape Kennedy (L ≃ 2).
(b) Average diurnal behavior of ΔTEC(%) for the QQ-days and DD-days for Winter months at Cape Kennedy (L ≃ 2).

The end result is again a value updated in magnitude, but now with an uncertainty reduced by 50%. The possibility thus exists for using simple positive or negative QQ-pattern sectors to achieve a 50% improvement in forecasting without recourse to a large network of real-time observing sites. If real-time measurements can be made, the additional possibility exists of using a single observation in conjunction with QQ patterns (which may be either positively or negatively correlated over wide latitude spans) to forecast F-region updates over regions far in excess of simple in-phase correlation distances.

4. CASE STUDIES

As an example of the concepts discussed in the previous sections, Figures 3 and 4 describe geomagnetic hierarchy effects in the day-to-day variability patterns observed at the lower mid-latitude site Cape Kennedy (KSFC, L = 2) for the winter season. The average local time disturbance pattern (SD(TEC,%) for winter storms at KSFC is given in Figure 3a (Mendillo, 1978). This is a relatively simple pattern of daytime enhancements with only small nighttime depletions for each day of the storm pattern. The absence of both positive and negative daytime phases causes the DD-day pattern for Winter months (Fig. 3b) to describe this simple pattern with a 5-day average of approximately ±20% during the daytime hours. While this type of correction would suffice for days 2 and 3 of a storm period, it is factors of 2 to 3 too small a correction for the first day of a storm. This re-emphasizes the fact that SD_i(TEC,LT), i = 1,4 patterns should be used to update storm periods and not DD-curves.

The character of the QQ curve represents a more realistic description for day-to-day effects because (1) the standard deviations are lower and (2) the 5 QQ-days of a month are not usually sequential. To test for the consistency of the QQ vs. DD descriptions implied by Figure 3b, we examined several Winter month's worth of KSFC total content data. Figure 4 summarizes the analysis for the Winter months of 1975 (January, February, November, December). The days of the month were ordered by ΣKp and percentage deviations from the monthly mean were computed for each UT-hour. The vertical scale in Figure 4 shows 5-day groupings according to ΣKp and the horizontal axis gives UT/LT steps. To separate the positive excursions from the negative excursions for easy visual inspection, cross-hatchings were used for any hour where the deviation was zero or positive (i.e., Δ TEC$\geq$ 0). The clear areas of Figure 4 therefore describe hourly/daily periods where Δ TEC $<$ 0. Note that the phases of the Δ TEC (%) variations in the top portion of Figure 4 are very

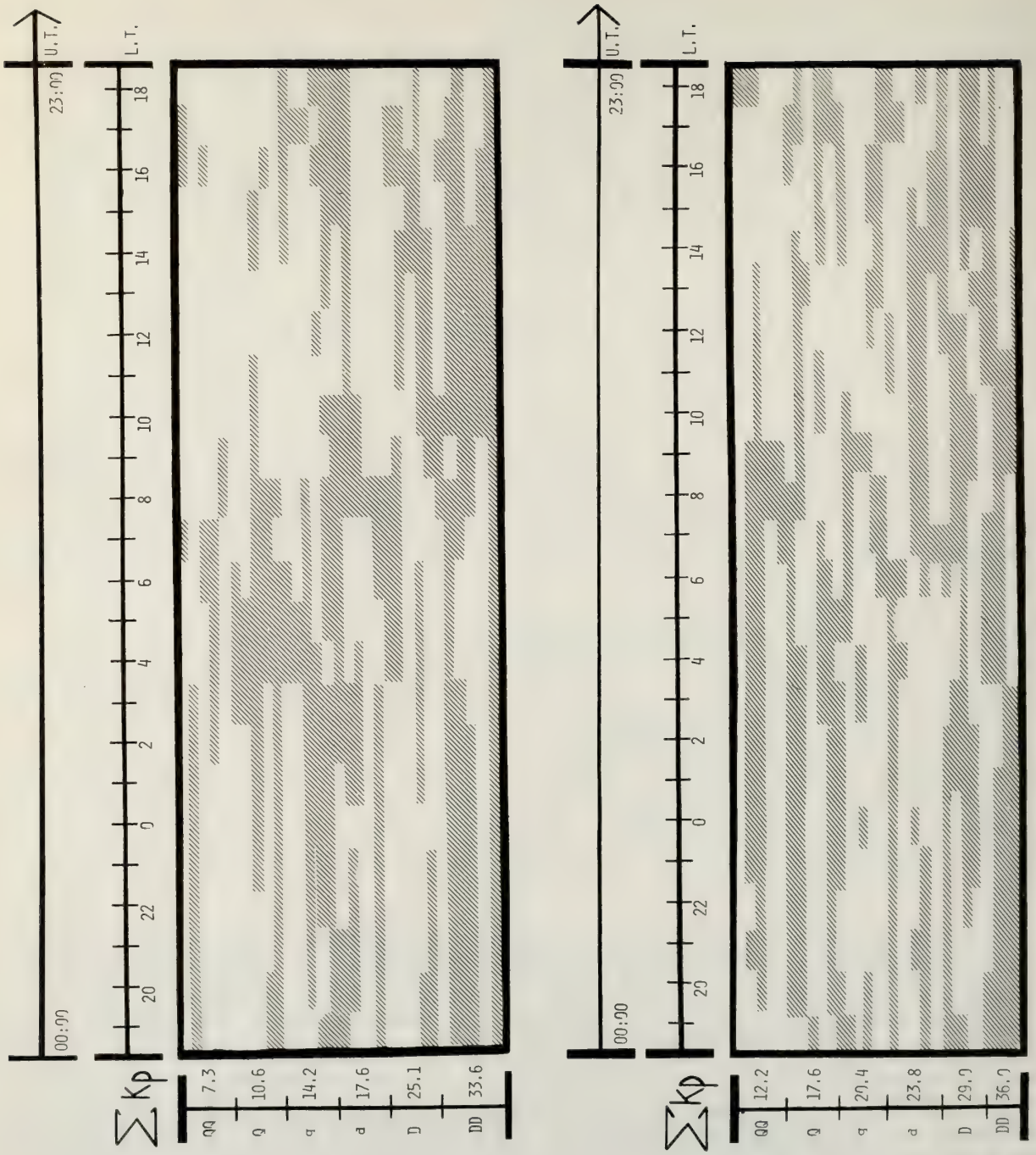


Figure 4.
Examples of geomagnetic ordering of TEC variability for Winter months at Cape Kennedy for January (top) and February (bottom), 1975. Shaded areas give periods where $\Delta TEC(\%) \geq 0$.

similar to those predicted by the QQ-curve in Figure 3b. For example, during the daytime period (10:00-16:00 LT) when the F-region generally attains its largest density values (and therefore uncertainties are most important), the negative values persist on virtually all of the QQ-days shown. As pointed out in the previous section, a simple knowledge of the plus or minus side of $\pm \sigma_o$ leads to an updated F-region prediction with a 50% reduction in uncertainty.

5. SUMMARY

We have presented a summary of preliminary findings concerning the search for a geomagnetic activity control of ionospheric variability. The results are encouraging in that the division of a month's worth of F-region data into a geomagnetically ordered hierarchy may lead to a satisfactory forecasting scheme for day-to-day variability. The five geomagnetically quietest days of the month (QQ-days) were seen to behave in a consistent way for a season and station where the disturbed days had a well-defined pattern. The geomagnetic storm associated disturbed days within a month are themselves best handled by superimposed epoch derived average storm patterns, $SD[\Delta TEC(\%), LT]$, for each day of a storm period. Thus, if storm days and QQ days are removed from a monthly distribution, the remaining 15-20 days may either fall within acceptable variability limits or lend themselves to "QQ-like" or "DD-like" classifications.

REFERENCES

DuCharme, E.D., Petrie, L.E. and R. Eyfrig (1971): A method for predicting the F1 layer critical frequency, Radio Science, 6, 369.

Hawkins, Gerald S. and John A. Klobuchar (1974): Seasonal and diurnal variations in the total electron content of the ionosphere at invariant latitude 54 degrees, AFCRL-TR-0294, Air Force Geophys. Lab., Hanscom AFB.

Johanson, J.M., Buonsanto, M.J. and J.A. Klobuchar (1978): The variability of ionospheric time delay, Proc. Symp. Effect of the Ionosphere on Space and Terrestrial Systems, 24-26 January, 1978, J. Goodman, ed., Naval Res. Lab (in press, 1978).

Mendillo, Michael (1978): Behavior of the Ionospheric F-Region During Geomagnetic Storms, AFGL-TR-78-0092 (II), Astron. Contrib. Boston Univ., Ser. III, No. 6, March.

Mendillo, Michael and John A. Klobuchar (1979): A morphology-based prediction scheme for the coupled latitudinal and local-time development of F-region storms; Proceedings of the Symposium on Solar-Terrestrial Predictions, April.

Muggleton, L.M. (1972): A describing function of the diurnal variation of $N_m(E)$ for solar zenith angles from 0 to 90^o, J. Atmos. Terr. Phys., 34, 1374.

Rush, Charles M. (1976): An ionospheric observation network for use in short-term propagation predictions, Telecom. J., 43, VIII, 544.

Rush, Charles M. and Joseph Gibbs (1973): Predicting the day-to-day variability of the mid-latitude ionosphere for application to HF propagation predictions, AFCRL-TR-73-0335, Air Force Geophysics Lab., Hanscom AFB.

Titheridge, J.E. (1972): Determination of ionospheric electron content from the Faraday rotation of geostationary satellite signals, Planet. Space Sci., 20, 353.

A MORPHOLOGY-BASED PREDICTION SCHEME FOR THE COUPLED LATITUDINAL AND LOCAL-TIME DEVELOPMENT OF F-REGION STORMS

Michael Mendillo
Astronomy Department
Boston University
Boston, MA 02215 USA

John A. Klobuchar
Space Physics Division
Air Force Geophysics Laboratory
Hanscom AFB
Bedford, MA 01731 USA

1. INTRODUCTION

The ionospheric F-region often experiences noticeable perturbations during geomagnetic storms. The variations encountered generally include several periods during which the storm effects far exceed day-to-day variability, and thus prediction schemes for "ionospheric storms" would be useful to many F-region supported radio propagation links and trans-ionospheric satellite navigation systems. To date, only statistical or morphology-based studies of ionospheric storms as seen at various specific sites have been developed, but little attention has been given to using these results in any sort of real or near real-time prediction scheme. Part of the reason for this lies in the fact that poorly conceived or excessive averaging techniques used in early ionospheric storm studies tended to make the resultant "average storm pattern" very small in magnitude and poorly resolved in local time. Any familiarity with the often drastic effects seen during individual storms then tended to reinforce the notion that average storm patterns containing only small-scale detail offer little useable advice to the radio propagation community.

In this brief report, we summarize an F-region storm analysis which yields a coupled latitude/local time description of average storm effects. The results differ from past studies in that the selection of events studied and averaging techniques employed allow the characteristic storm patterns to capture the essential features of individual storms. The average storm patterns are thus sufficiently defined in amplitude and resolved in local time to make the overall morphologies a realistic prediction scheme for F-region disturbance effects.

2. ANALYSIS

The full analysis of ionospheric storms used for this study

has been described by Mendillo (1978). In brief, the study relies exclusively upon the ionospheric parameter total electron content (TEC). The ionospheric TEC refers to the height integral of the ionospheric electron density profile, $N_e(h)$, and therefore contains contributions from all of the various ionospheric regions (D,E,F1 and F2). Since the F-region N_e values easily account for more than 90% of the integral, TEC is rightly considered a measure of the F-region total plasma content. This columnar content is obtained by continuously monitoring the amount of Faraday rotation (polarization twist) a VHF radiowave wave experiences in traversing the ionosphere. Since the amount of Faraday rotation depends on the geomagnetic field strength, most of the rotation occurs within the first few thousand kilometers above the Earth's surface. It is generally agreed that, within an accuracy of 5-10%, the Faraday technique gives the ionospheric content up to a height of approximately 2000 km. Further details of the interpretation and data reduction methods of Faraday rotation observations are given by Titheridge (1972), Mendillo and Klobuchar (1974) and Papagiannis et al. (1975).

The TEC parameter is a quantity well suited for storm studies. The major reason for this is that the occurrence of a disturbed ionosphere does not interfere with the continuous monitoring of the Faraday effect. Thus, while severe distortions of the $N_e(h)$ profile may occur, while the VHF signal may suffer amplitude scintillations due to N_e irregularities or absorption effects, the measurement is basically unaffected by these often drastic processes. Conventional ionosonde measurements, on the other hand, can suffer severe degradations during storm periods, and thus the events of most interest can be lost to the very effects under study.

All of the TEC data used in the study were taken from the AFGL-sponsored chain of geostationary satellite observing sites at (1) Narssarssuaq, Greenland, (2) Goose Bay, Labrador, (3) Sagamore Hill/Hamilton, Massachusetts and (4) The Kennedy Space Flight Center (KSFC), Florida. The 420-km ionospheric point used to fix the latitudinal coordinates for the TEC measured from each site refer to geomagnetic L-shell values of approximately 5, 4, 3 and 2 for Narssarssuaq, Goose Bay, Hamilton and KSFC, respectively.

The TEC data base available at each site covered the periods (1) April 1971-December 1975 (Narssarssuaq), (2) November 1971-April 1975 (Goose Bay), (3) January 1971-December 1975 (Hamilton) and (4) November 1973-September 1976 (KSFC). The geomagnetic storm selection criterion was $Ap \geq 30$ for at least one day of the storm period or $Kp(max) \geq 5$. The method for determining average storm patterns in percent on a local time basis ($SD_i(TEC,LT), i=1,4$) has been described in previous studies (Mendillo, 1971; Mendillo and Klobuchar, 1974). For the present case, the monthly median diurnal pattern was used as the control

curve, and the storm-associated perturbations were followed over a 4-day period using hourly resolution in local time. The relatively large data base yielded a total number of solar-minimum-epoch storms of 70, 67, 109 and 70 for the L=5, 4, 3 and 2 sites. In addition to computing the average storm patterns at each site for the entire data set, a subdivision by season was also used: Summer (May, June, July, August), Winter (November, December, January, February), Spring (March, April) and Fall (September, October).

Once the average storm pattern for a given period is obtained at each site, the results are combined by constructing iso-level contour maps of the percentage deviations on a grid of invariant latitude versus local time. A contour-plot representation for TEC quiet and storm-time variations seen along the 70° W meridian chain was described by Mendillo and Klobuchar (1975). Its generalization to percentage variations is straight forward, and the procedure offers a compact way of presenting simultaneous storm patterns obtained over a wide latitude range.

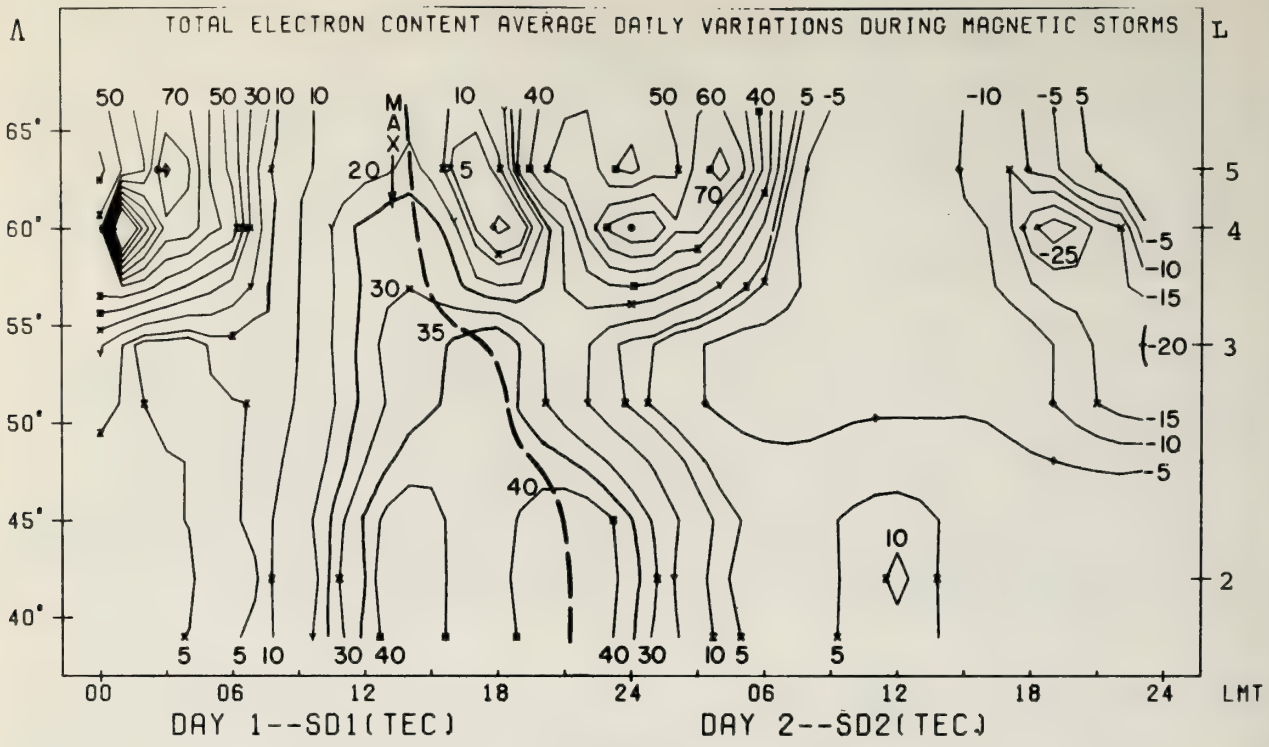
3. RESULTS

Figures 1 through 5 present the unified storm morphology patterns obtained for all storms, with a seasonal break-down according to Summer, Fall, Winter and Spring. In Figure 1, the results for all storms taken together show how the "characteristic features" seen at the individual sites may be unified into a composite representation of the essential storm features encountered over the $L \simeq 2 - 5$ latitude range. In particular, the following points may be noted:

(1) On the day of the storm commencement (SC), the SD_1 (TEC,LT) pattern shows that the daytime positive phase grows in magnitude and peaks at a later local time as one progresses from high to low latitudes in the $L = 2 - 5$ domain. At low latitudes ($L \simeq 2$), the positive phase has both a noontime and post-sunset component not seen at the $L > 2$ sites.

(2) Auroral-oval associated TEC enhancements maximize near $L = 4$ during the post midnight hours on Days 1 and 2. Depressed TEC values occur equatorward of the auroral enhancements, beginning prior to 18:00 LT at $L \simeq 5$ and reaching midlatitudes after midnight. This trough-associated disruption of the normal latitude gradients maximizes during the 00-06:00 LT period on Day 3. The pattern repeats on subsequent nights, showing that persistent storm effects dominate the nighttime ionosphere in the $L = 3 - 5$ range long after the daytime perturbations have subsided.

Figures 2 through 5 contain storm morphology patterns according to season. One can see that all of the characteristic



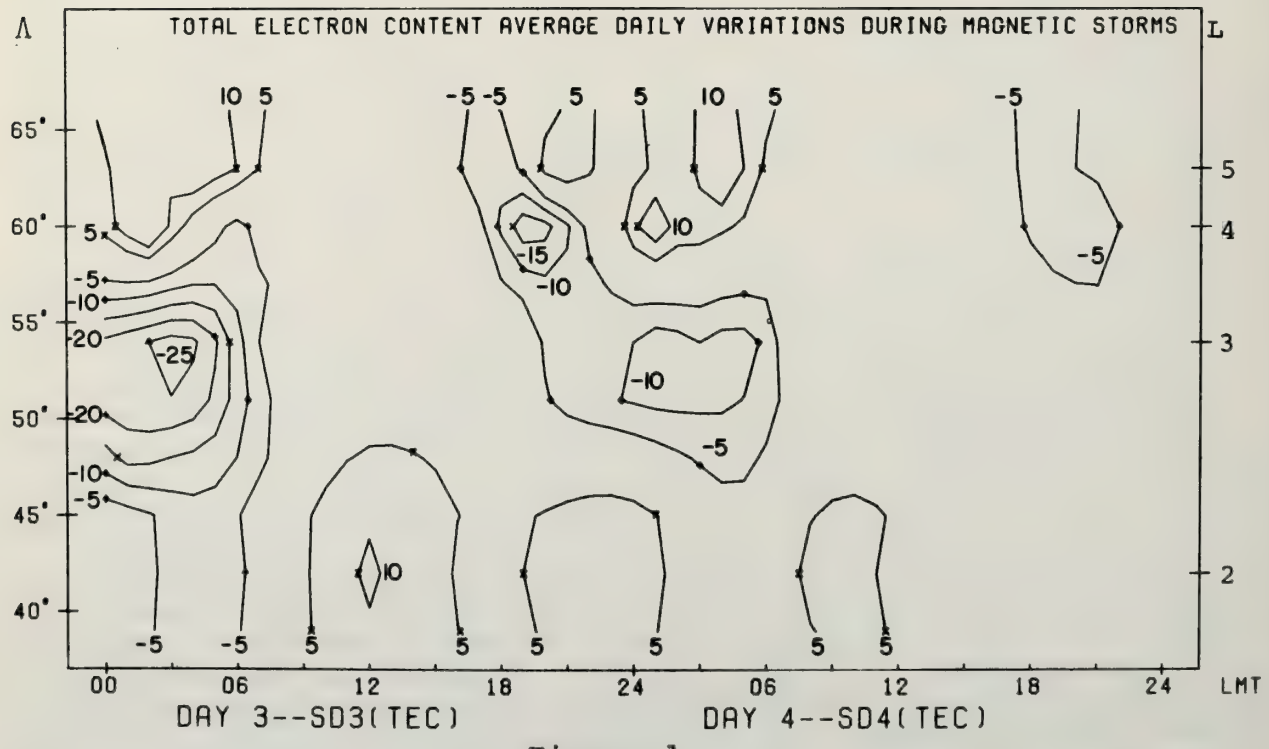


Figure 1.

Average storm patterns for all storms. Contours give ΔTEC(%) as a function of invariant latitude (Λ) and local time (LT).

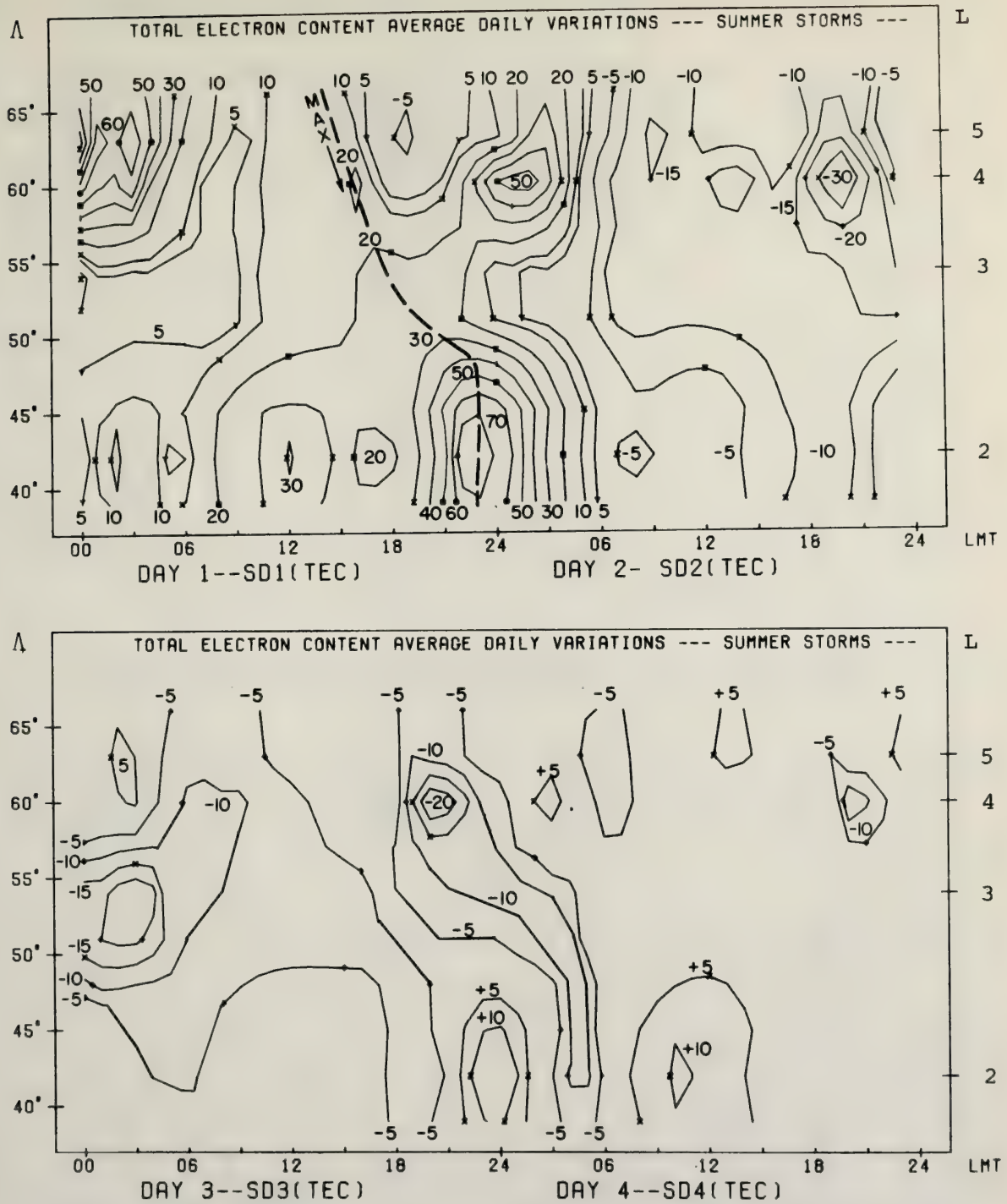


Figure 2.

Average storm patterns for Summer storms. Contours give ΔTEC(%) as a function of invariant latitude (Λ) and local time (LT).

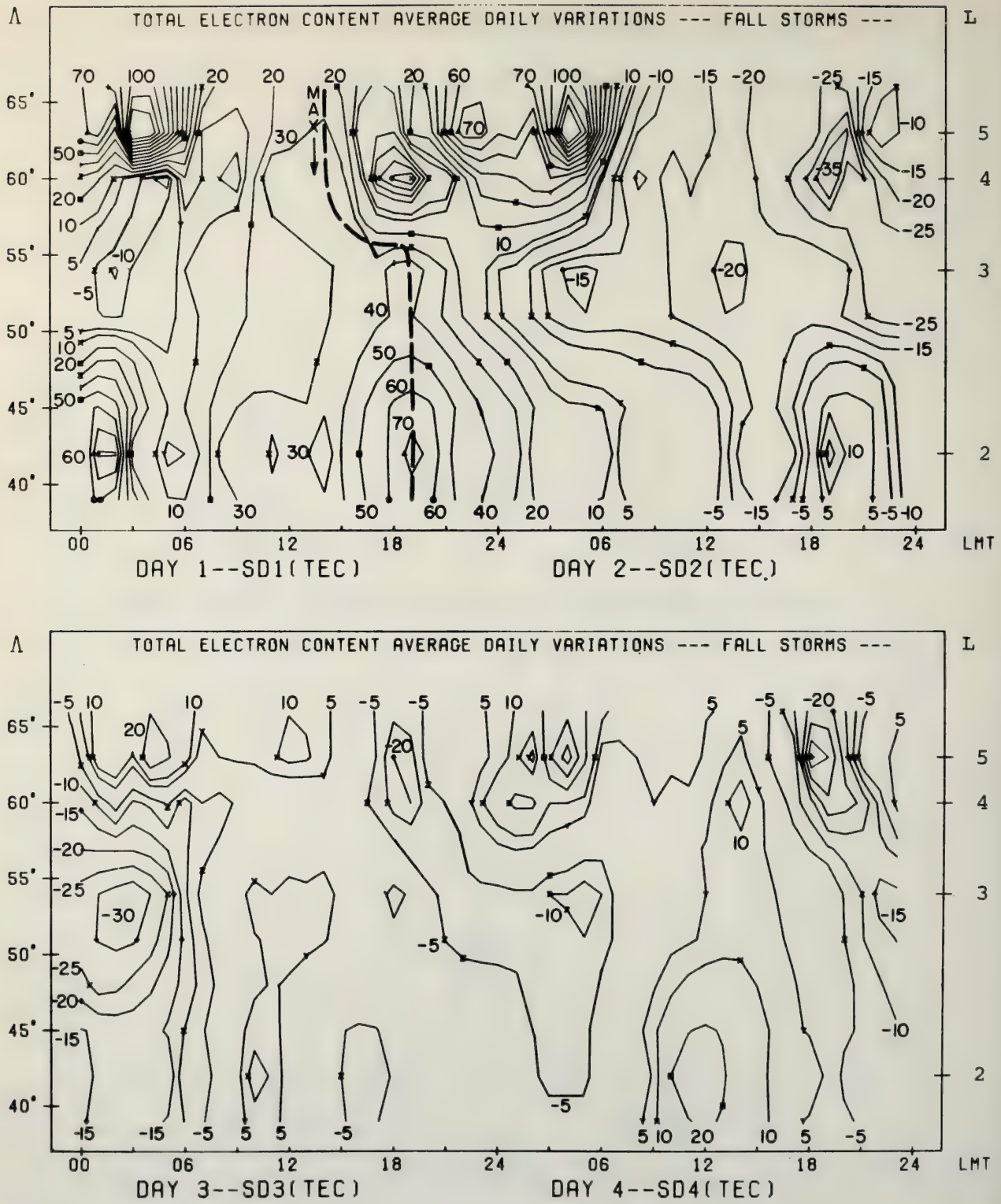


Figure 3.

Average storm patterns for Fall storms. Contours give ΔTEC(%) as a function of invariant latitude (Λ) and local time (LT).

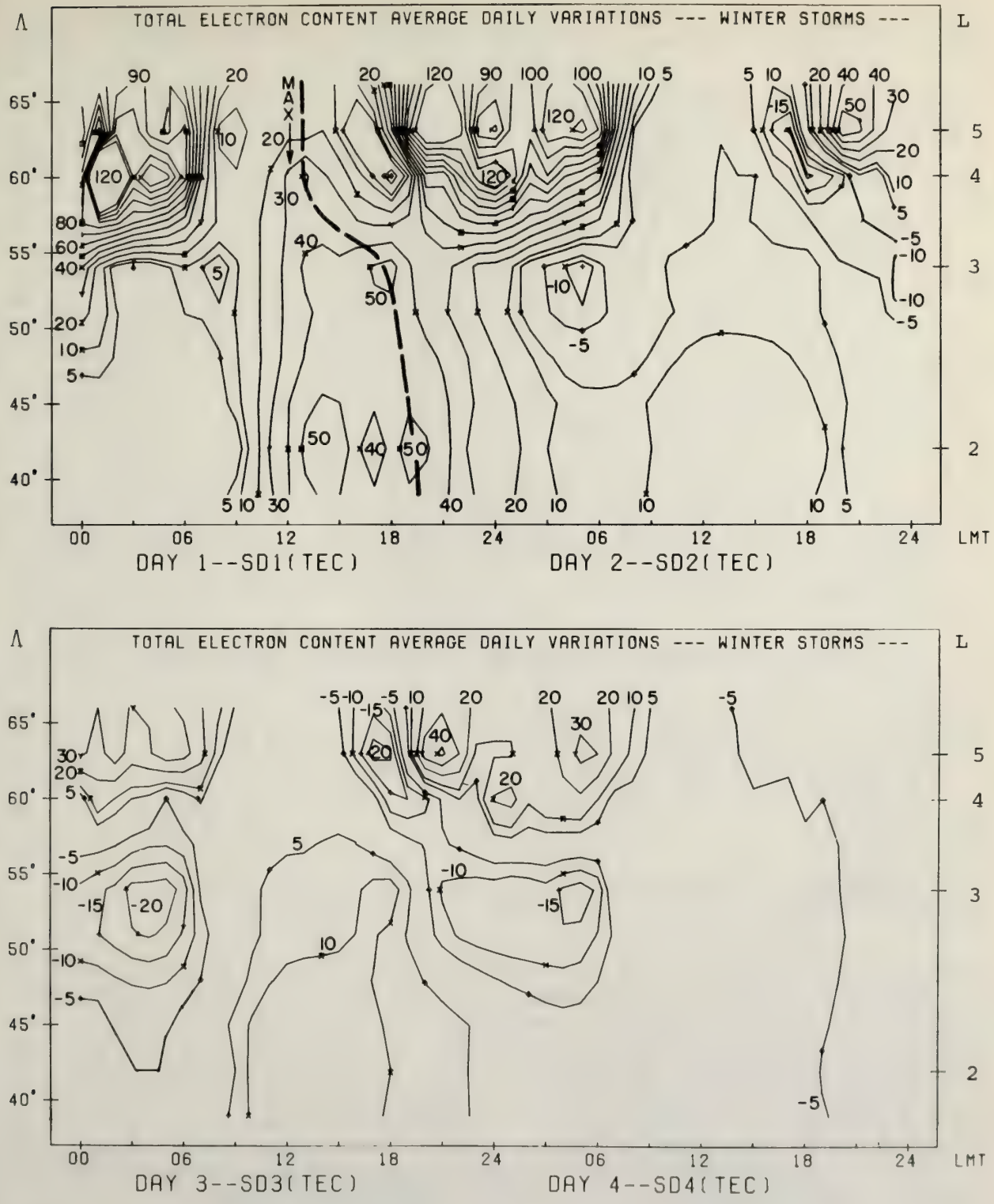


Figure 4.

Average storm patterns for Winter storms. Contours give ΔTEC(%) as a function of invariant latitude (Λ) and local time (LT).

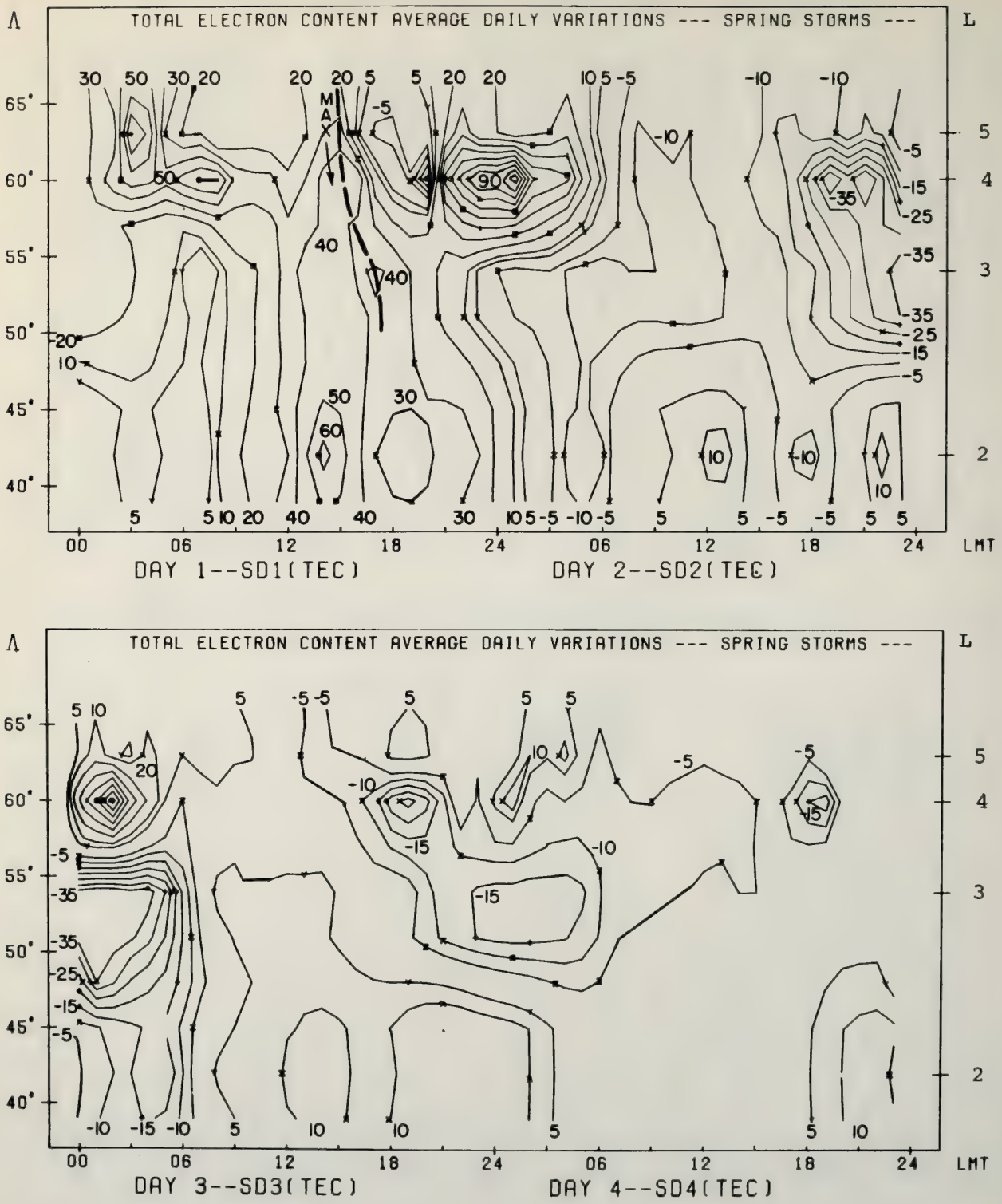


Figure 5.

Average storm patterns for Spring storms. Contours give ΔTEC(%) as a function of invariant latitude (Λ) and local time (LT).

features summarized in Figure 1 occur in each season, and that clear modulations of those patterns are present. These include:

I. VARIATIONS IN THE AFTERNOON ENHANCEMENTS

(1) The positive phase enhancements on Day 1 maximize at a later local time in Summer (Fig. 2) than in Winter (Fig. 4), over the entire L = 2 - 5 latitude range. During Spring and Fall storms (Fig. 3 and 5), the latitudinal progression of the local time of the afternoon enhancement does not extend below L = 3.

(2) The magnitude of the afternoon enhancement is relatively insensitive to season at L = 4 - 5, it varies in step with the so-called seasonal anomaly near L = 3 (i.e., maximum in Winter, minimum in Summer), while at L = 2, the seasonal trend is one of peak enhancements during Summer and Fall, minimum enhancements during Winter and Spring.

(3) At L $\simeq$ 2, where twin maxima occur on Day 1, the initial enhancement is strongly confined to the 12-15:00 LT period. Only during Spring storms does it exceed the magnitude of the late afternoon enhancement.

II. VARIATIONS IN THE NEGATIVE PHASE

(1) For L $\gtrsim$ 3, a daytime negative phase occurs during all seasons except Winter; it extends to L $\simeq$ 2 during Summer and Fall.

(2) The intrusion of auroral oval and trough effects to lower latitudes occurs during all seasons. The nighttime F-region enhancements at L > 3 associated with particle precipitations are largest during the SD 1 and SD 2 periods, with lingering effects still seen on Day 4. The depletion effects seen at L $\lesssim$ 3 are due to trough migrations upsetting the normal latitude gradients. The maximum effect occurs during 00-03:00 LT period on Day 3 for all seasons, with the strongest depletions extending to L < 2 during both equinox periods. The persistence of nighttime effects again occurs for all seasons.

4. ASSESSMENT OF THE AVERAGE STORM PATTERN CONCEPT

Any casual observer of ionospheric storms knows that, quite literally, no two storms exhibit identical behavior. Indeed, one of the main reasons for publishing the AFCRL ATLAS of Sagamore Hill storm effects (Mendillo and Klobuchar, 1974) was the goal of displaying the great variety of F-region responses which occur at a single site due to increases in geomagnetic activity. The question naturally arises, then, of the real usefulness (and meaning) of average storm patterns. The answer to this dilemma may be approached along two avenues:

I. From the point of view of understanding the physical processes most responsible for storms, it would be foolish to concentrate on a single event, given the realization that single events differ so from one another. The notion of specifying the mechanism which causes storm effects is now known to be a relatively naive concept. The fact that perturbations exhibit

positive and negative phases, with considerable variations according to season and latitude, shows that a blend of mechanisms operates, with perhaps a dominance of one over the others from event to event and site to site. If, however, the average behavior of a set of storm events exhibits a clear and recognizable pattern--and one reminiscent of many individual events--then the average pattern must point to features and processes truly characteristic of that site. Thus, the average pattern will identify the features most common at a given site or latitude range and the search for operative processes will be limited to those capable of causing such effects. Clearly, individual storms will exhibit characteristic features much more pronounced than they appear in the average, and these therefore set the limiting tests for the identification of correct mechanisms.

II. From the point of view of wishing to update F-region morphology models, there is little choice from using average storm patterns. To base predictions upon individual events would be clearly unjustifiable, for the reasons mentioned above. Average patterns, constructed on a local time basis with seasonal breakdown, offer the only reasonable way of providing an estimate of how a model predicting the median or average behavior should be modified to include disturbance effects. The correct role of individual events is, once again, to set the limit of "worst-case" conditions for a given parameter and/or site.

Finally, it would be good to comment on the absolute values of the percentage variations presented in the previous figures. Perhaps the most frustrating aspect of storm investigations is the realization that, once the goal of obtaining clear and characteristic storm patterns is achieved, the absolute values of the patterns are often small and, moreover, the standard deviations of those values are invariably greater than the perturbation values themselves. We suggest that results characterized, for example, by variation values of +35% ±45% or -5% ±30% are not necessarily vague or meaningless numbers. One must realize that the standard deviations of a typical mid-latitude monthly mean diurnal pattern are generally near ±25%. Thus, if an SD(%) value is obtained which is larger than this "normal variability" --even if its standard deviation is large--a significant storm-associated feature has been identified. As in the above case, a ΔTEC of say +35% ±45% surely points to the likelihood of a substantial TEC enhancement--a potentially valuable update to an ionospherically-supported propagation system. Similarly, a small average value with a large uncertainty (such as the ΔTEC = -5% ±30% quoted above) provides the information that while a monthly mean pattern cannot be significantly updated, the normal variability of ≃25% should now be taken with caution.

Both examples treated above referred to the interpretation of a single storm-associated SD(%) value. A third case exists, namely a string (from several hours to a few days) of consis-

tently positive or negative SD values of small absolute value (say $\lesssim |10\%|$). This typically happens, for example, during the negative phase of mid-latitude storm effects when daytime SD values might be characterized by -5 to -10% for two to three days. Such consistencies point to the reality of the negative phase and its longevity. Yet, in striving to theoretically model neutral atmospheric effects upon F-region loss processes, one would clearly not aim to produce only a -5% effect.

The best evidence we have for believing in the meaning and utility of Average Storm Patterns is once again a return to the Sagamore Hill/Hamilton studies of the past decade. Few sites on Earth have received more scrutiny than this $L \simeq 3$ location near 70° W during periods of geomagnetic activity. Characteristic features, first seen in 1965 storm data, followed during subsequent solar maximum and minimum years, repeated in average patterns for 1968-1969 (Mendillo, 1971), 1968-1972 (Mendillo and Klobuchar, 1974), and now 1971-1975 (Mendillo, 1978), always point to a consistency between average and individual storm effects. And finally, the reality and utility of our average storm patterns were never more obvious than in the correct identification of the "SKYLAB effect" of the large-scale F-region "hole" which occurred during a severe geomagnetic storm (Mendillo et al., 1975).

Acknowledgements

This work was supported in part by contracts F19628-75-C-0044 and F19628-77-R-0310 from the Air Force Geophysics Laboratory to Boston University. We thank Mr. Michael Buonsanto and Mr. Francis Lynch for their assistance in many of the technical aspects of this study.

References

Mendillo, Michael, Ionospheric Total Electron Content Behavior During Geomagnetic Storms, Nature, 234, 23, 1971.

Mendillo, Michael (1978) Behavior of the Ionospheric F-Region During Geomagnetic Storms, AFGL Tech. Report. AFGL-TR-78-0092(II), Astron. Contrib. Bos. Univ., Ser. III, No. 6, March, 1978.

Mendillo, M., Hawkins, G.S. and Klobuchar, J.A., A sudden vanishing of the ionospheric F-region due to the launch of Skylab, J. Geophys. Res., 80, 2217, 1975.

Mendillo, M. and J.A. Klobuchar, An Atlas of the Midlatitude F-Region Response to Geomagnetic Storms, AFCRL Tech. Report No. 0065, Hanscom AFB, Bedford, Ma. 01731, USA, 1974.

Mendillo, M. and J.A. Klobuchar, Investigations of the Ionospheric F-Region Using Multi-Station Total Electron Content Observations, J. Geophys. Res., 80, 643, 1975.

Papagiannis, M.D., Hajeb-Hosseinich, H. and M. Mendillo, Changes in the ionospheric profile and the Faraday M factor with K_p, Planet. Space Sci., 23, 107, 1975.

Titheridge, J.E., Determination of ionospheric electron content from the Faraday rotation of geostationary satellite signals, Planet. Space Sci., 20, 353, 1972.

ON THE POSSIBILITY TO PREDICT VARIATIONS IN THE F2-REGION PARAMETERS AS A FUNCTION OF THE IMF DIRECTION

R.A.Zevakina, E.V.Lavrova
Institute of Terrestrial Magnetism,
Ionosphere and Radio Wave Propagation
of the USSR Academy of Sciences
Moscow, USSR

Variations in the F2-region parameters depending on the direction of the vertical and radial components of the IMF are examined. It is shown that using data on the IMF direction or those on geomagnetic variations in subpolar regions one can predict the sign of deviation of f_0F2 from the medians.

In the existing short-term predictions of the ionospheric state (Zevakina, 1975) the changes of the ionosphere due to anomalous radiation from active solar regions are estimated. In the present paper, we consider the possibility of predicting the sign of δf_0F2 variations under magnetically quiet conditions ($\pm$20%). The cause of these variations has not yet been established. It is supposed that they are due to the variability of the various processes in the ionosphere. In recent years, their relation to the solar wind parameters has begun to be investigated (Kolomiitsev, 1975; Potapova, 1974; Zevakina, 1974; Berezin, 1974; Lyatskaya, 1974). Potapova (1974) and Zevakina (1974) deal with the variations in f_0F2 and h_{max} at the different directions of the radial component of the interplanetary magnetic field (IMF). It has been shown that on days with off-Sun (+) IMF direction the fluctuations of f_0F2 at high and middle latitudes are in most cases higher than the median values, whereas on the days characterized by the sunward (-) IMF direction it is lower. The variability of f_0F2 has

been found to increase when the Earth intersects the sectorial IMF boundaries (Zevakina, 1974).

Bearing in mind that the magnetic variations are the most significant in the presence of the southward IMF component (Ivanov, 1972), we have considered here, apart from the effect of the radial IMF component, the influence upon the F2-region variations of the IMF component vertical relative to the ecliptic. With this purpose, we have studied the mean $\delta\overline{f_oF2}$ and $\Delta\overline{hp\ F2}$ variations separately for the days with the southward (S) and northward (N) IMF components and for the off-Sun and sunward IMF directions and also the $\delta\overline{f_oF2}$, $\Delta\overline{h_pF2}$ and $\Delta\overline{h'F}$ variations in intersecting the sectorial IMF boundaries and in the period of the change of the northward component for the southward one.

The present study has been carried out using the data of the ionospheric stations Druzhnaya, Resolute Bay, Murmansk, Yakutsk, Moscow, Khabarovsk, Alma-Ata, Yamagawa, Delhi, Lwiro, Rarotonga, Canberra, Hobart, Mawson, and Scott Base obtained during the years of low (1964, 1972 and 1973) and high (1958, 1967 and 1968) solar activity. The data on the IMF have been taken from (Wilcox, 1965; Solar T.A.Chart, 1967; Mansurov, 1973), δf_oF2, Δh_pF2 and $\Delta h'F$ being determined from the medians on quiet days.

Fig. 1 illustrates the diurnal variations of $\delta\overline{f_oF2}$ at different latitudes during 1964 and 1958, depending on the direction of the radial IMF component. From this figure it follows that for the sunward direction of the IMF component, the $\delta\overline{f_oF2}$ in the northern hemisphere were predominantly negative, whereas in the southern hemisphere, positive. For the off-Sun direction of the IMF component, the reverse picture was observed. When the IMF was directed away from the Sun, however, the opposite-in-phase $\delta\overline{f_oF2}$ variations in the two hemispheres are less pronounced than in the case of the sunward direction and are not always present. Thus, in 1958, when the IMF direction was off-Sun, the $\delta\overline{f_oF2}$ in the northern and southern

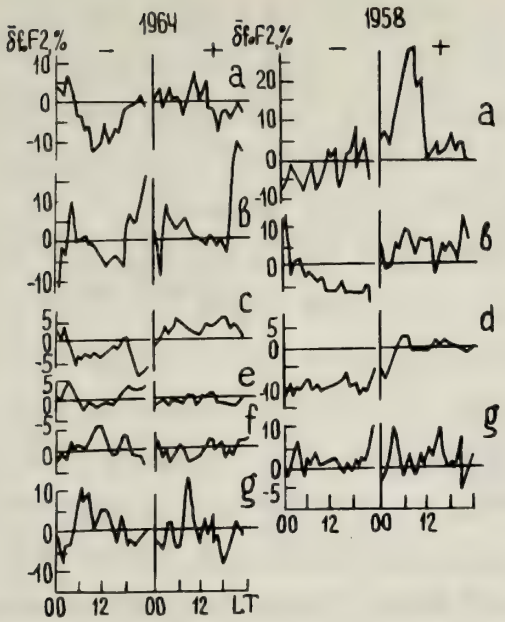


Fig. 1. Mean diurnal variations of δf_0F2 for the sunward (-) and off-Sun (+) IMF directions at the stations:
a) Resolute Bay, winter;
b) Murmansk, equinox;
c,d) Moscow, equinox and summer respectively;
e) Khabarovsk, winter;
f) Canberra, winter;
g) Scott Base, winter.

hemispheres were positive. But at Resolute Bay they were considerably higher than at Scott Base. The limits of $\delta\overline{f_0F2}$ variations in 1958 were greater ($\pm$ 20%) than in 1964 ($\pm$ 10%).

The influence of the IMF upon f_0F2 is more pronounced in winter and on equinoxes, at the near-noon time. The effect is the most significant within the polar caps, in the region of the dayside cusp.

We have compared the diurnal variations of $\delta\overline{f_0F2}$ during 1967 and 1968 at various radial directions of the IMF with those of $\delta\overline{f_0F2}$ on days with the southward and northward IMF components. As an illustration, fig. 2 shows such diurnal variations in the equinox periods of 1967 for the stations Resolute Bay, Murmansk, Moscow, and Huancayo.

From this figure and similar ones it follows that for the sunward IMF direction the $\delta\overline{f_0F2}$ variations are similar to those of $\delta\overline{f_0F2}$ on the days of the southward IMF component and, for the off-Sun IMF direction, it varies in the same manner as on the days with the northward component. In Moscow, δf_0F2 was, on average, negative on days with the southward

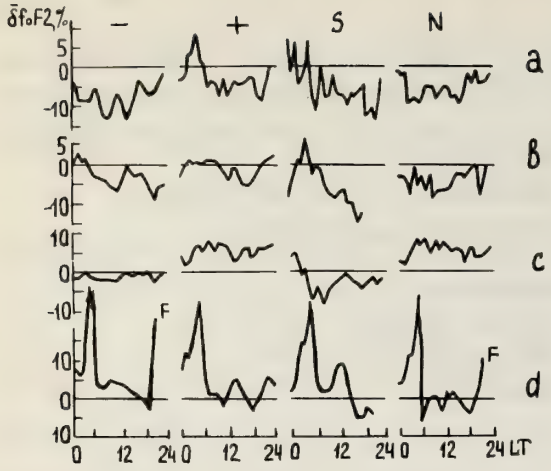


Fig. 2. Mean diurnal variations of δf_0F2 in the equinox period of 1967 for the different directions of the radial vertical IMF components at the stations:
a) Resolute Bay; b) Murmansk; c) Moscow; d) Huancayo.

IMF component and for the sunward direction, and positive on days with the northward compenent and for the off-Sun IMF direction. At high and equatorial latitudes, the sign of $\delta \overline{f_0F2}$ in 1967 and 1968 did not change with the change in IMF direction, but for the southward and sunward direction, $\delta \overline{f_0F2}$ was lower than for the northward and off-Sun direction. At equatorial latitudes the effect of IMF is small, though noticeable; it manifests itself in that, on days with the southward component and the sunward direction of the IMF, δf_0F2 is on average somewhat higher than on days with the northward component and the off-Sun IMF direction.

The variations in the altitude of the F2-region at different IMF directions have been examined using the data of Moscow. With this purpose, Δh_pF2 characterizing variations in h_{max} have been determined. Table 1 presents Δh_pF2 during 1968 over the seasons at different IMF directions at night (21 - 02 hrs LT) and in daytime (10 - 15 hrs LT) hours.

From the table it follows that in winter and on equinoxes Δh_pF2 is 2 to 3.5 times higher on days with the southward IMF component than on days with the northward component. In summer at night Δh_p is not much higher at the southward component than at the northward one, whereas in the daytime it is higher by a factor of 3, though Δh_p themselves are small. On days with the sunward IMF direction, both in winter and spring, Δh

is 1.4 times higher at night, and 2 to 3.5 times higher in the daytime than on days with the off-Sun IMF direction. During summer nights the values of Δh_p are not significantly different for the sunward and off-Sun directions, but in the daytime, Δh_p^- is three times as high as Δh_p^+. Therefore, the altitude of the F region, just as f_oF2, undergoes the most significant change with the change in the direction of the vertical IMF component.

Table 1

Season	Δh_pF2								Δ_-/Δ_+		$\Delta S/\Delta N$	
	Night				Day							
	+	−	N	S	+	−	N	S	Night	Day	Night	Day
Winter	22	32	19	43	2	7	3	11	1.4	3.5	2.2	3.6
Spring	23	33	11	49	7	18	7	23	1.4	2.5	4.4	3.2
Autumn	36	24	24	51	3	5	5	16	0.6	1.6	2.1	3.3
Summer	14	15	12	16	7	22	9	24	1.0	3.1	1.3	2.6

In what follows, the variations of the F2 region at different latitudes, which occur when the Earth passes through the sectorial boundaries of the IMF, are examined. Using the method of epoch superposition, we have determined the $\delta\overline{f_oF2}$ and $\Delta h'F$ variations during near-noon (11-13 hrs LT) and near-midnight (21-23 hrs LT) hours for five days before and after the Earth passes through the sectorial boundaries, for 1958 and 1964. The variations in the average $\delta\overline{f_oF2}$ and $\Delta h'F$ during the daytime and nighttime hours occurring when the Earth passes through the boundary separating the sector with the off-Sun field direction and that with the sunward direction during 1964 are presented in fig. 3. The first day of the new sector is taken as zero.

From fig. 3 it follows that at high and middle latitudes $\delta\overline{f_oF2}$ is higher, when the Earth passes through the end of the

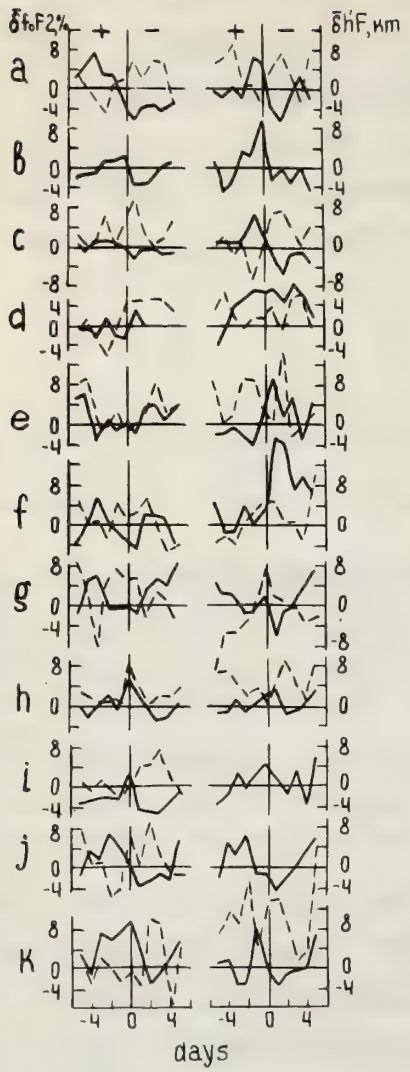


Fig. 3. Mean variations in δf_oF2 (1) and $\Delta h'F$ (2) during five days before and after the intersection by the Earth of the IMF sectorial boundaries at the stations: a) Resolute Bay; b) Murmansk; c) Moscow; d) Khabarovsk; e) Yamagawa; f) Lwiro; g) Rarotonga; h) Canberra; i) Hobart; k) Mawson; l) Scott Base.

positive sector, than it is in the beginning of the negative sectors during the daytime and nighttime hours. At low latitudes (Khabarovsk, Yamagawa, Lwiro, and Rarotonga) $\delta\overline{f_oF2}$ is lower, in the daytime for two days before and after the intersection of the sector boundaries, than during the nearest days, while at night it is higher in the beginning of the sector than at the end. Thus, the $\delta\overline{f_oF2}$ variations in the daytime and at night in the positive sector occurred in phase within the polar cap and at low latitudes, while in the negative sector, in the opposite phase.

It should be noted that when the Earth goes over from the negative sector to the positive no reverse picture is observed, but the same one. This effect appears to be due to a change in not only the sign of IMF on the sectorial boundary, but also other solar-wind parameters, because it is known (Wilcox, 1965; 1968) that the solar wind speed and the value of IMF are higher in the beginning of the sector than at its end, whereas the number of solar protons is larger at the end of the sector than at its beginning (Nishida, 1966).

The variations in latitudes of the F region that occur at the intersection of sectorial boundaries are on average opposite to frequency variations, i.e. in the periods of increase in $\delta \overline{f_0F2}$, the altitudes in most cases decreased by 5 to 10 km, whereas in the periods of decreasing $\delta \overline{f_0F2}$ they increase by 10 to 20 km (the dashed curve in fig. 3).

For 1967 and 1968, we have examined, aside from the variations in the F-region occurring when the sign of the radial component changes, the $\delta \overline{f_0F2}$ variation in periods when the northward IMF component changes for the southward one. It has been shown that the change in the sign of the vertical IMF component leads to the same δf_0F2 variations as the change in the sign of the radial IMF component. When the northward IMF component changes for the southward one during the daytime, there occurs a decrease of δf_0F2 at high and middle latitudes and an increase of δf_0F2 at equatorial latitudes. At night δf_0F2 at middle latitudes changes, with the changing sign of IMF, in the same manner as in the daytime, while within the polar cap the values of $\delta \overline{f_0F2}$ increase in the period of changing sign and on the subsequent day. The $\delta \overline{f_0F2}$ variations in the daytime and at night are the most considerable during the day on which the sign of IMF changes and during two or three days after the change.

From what we have stated above it follows that the variability of the F-region at all latitudes is significantly dependent on the direction of the interplanetary magnetic field. The magnitude and sign of $\delta \overline{f_0F2}$ and Δh_pF2 under quiet conditions are determined, to a considerable degree, by the IMF direction. The change in the sign of the vertical component of IMF brings about more significant variations in the F-region than the change in the sign of the radial component. However, the character of $\delta \overline{f_0F2}$ and Δh_pF2 variations in the case of the southward component is analogous to that of variations in the case of the sunward IMF direction, while variations for the northward component are similar to those for the off-Sun

IMF direction.

The change in the sign of the radial and vertical IMF components produces in the F2 region effects similar to disturbances but of lower intensity. The effects due to the IMF are different from those due to disturbances also in that they are maximum within the polar cap, at latitudes of the dayside cusp, whereas the disturbance effects are maximum within the auroral zone.

The possibility to use the obtained results for predictions has been tested utilizing the data of five stations, used in short-term predictions (Zevakina, 1967) as the reference ones. From the data on $\delta \overline{f_0 F2}$ obtained at the stations Druzhnaya, Murmansk, Yakutsk, Moscow and Alma-Ata we have determined the diurnal variations of $\delta \overline{f_0 F2}$ during 1972-1973 over the seasons for days with the sunward and off-Sun directions. The $\delta f_0 F2$ used in ionospheric forecasting services are different from those considered above in that they are determined using not the median for quiet days, but the sliding ten-day medians (Zevakina, 1967). Therefore, it was necessary to find out whether the IMF effect would be pronounced for such data. The direction of the radial IMF component over the indicated period has been determined using geomagnetic data (Mansurov, 1973).

Table 2 presents the probabilities for the positive and negative $\delta f_0 F2$ at the different IMF directions.

From the table it follows that the IMF effect is clearly pronounced in the periods of equinox, but in winter and summer it is not so evident.

So, the use of the real time data on the IMF direction is important for the prediction of the $\delta f_0 F2$ sign especially in the periods of equinox.

The data presented above suggest that the variability of the F-region under both quiet and disturbed conditions may be connected with the variability of the solar wind parameters.

Table 2

Station	Probability of appearance of $\delta f_0F2 < 0$ and > 0, %											
	Equinox				Summer				Winter			
	+		-		+		-		+		-	
	>0	<0	>0	<0	>0	<0	>0	<0	>0	<0	>0	<0
Druzhnaya	90	10	25	75	40	60	35	65	-			-
Murmansk	78	22	22	78	40	60	42	58	55	45	31	69
Yakutsk	85	15	30	70	38	62	47	53	57	43	60	40
Moscow	90	10	28	72	48	52	40	60	60	40	42	58
Alma-Ata	78	22	43	57	57	43	38	62	55	45	50	50

The ionospheric effects, just as the geomagnetic ones, appear to be due to the rearrangement of convection and electric currents in the magnetosphere (Sorgensen, 1978; Bassolo, 1972) and ionosphere during the change in the IMF direction (Dungey, 1961).

REFERENCES

Bassolo, V.S., S.M.Mansurov and V.P.Shabansky (1972): In: Investigations on geomagnetism,aeronomy and solar physics, issue 23, Irkutsk, 125.

Berezin, Yu.M., N.P.Ben'kova and G.V.Bukin (1974): Abstracts to the reports for the All-Union Conference on the Physics of Ionosphere held in Rostov-on-Don, Moscow, IZMIRAN,96.

Bobrov, M.S. (1973): Astronomicheskii Vestnik, 13, 177.

Dungey, J.W. (1961): Phys. Rev. Letts., Vol. 6, 47.

Ivanov, K.G. and N.I.Mikerina (1972): Geomagnetism and aeronomy, Moscow, USSR Academy of Sciences, 12, 688.

Kolomiitsev, O.P., S.M.Mansurov and L.G.Mansurova (1975): In: Physics and simulation of ionosphere, Moscow, USSR, Nauka, 179.

Lyatskaya, A.M. and V.B.Lyatskii (1974): Abstracts to the reports for the All-Union Conference on the Physics of Ionosphere Held in Rostov-on-Don, Moscow, IZMIRAN, 99.

Mansurov, S.M. and L.G.Mansurova (1973): Geomagnetism and Aeronomy, Moscow, USSR Academy of Sciences, 13, 794.

Nishida, A. (1966): Rept. Ionosphere and Space Res. Japan, 20, 36.

Potapova, N.I. and B.S.Shapiro (1974): Geomagnetism and aeronomy, Moscow, USSR Academy of Sciences, 14, 1101.

Solar Terrestrial Activity Chart for 1967, 1968. Science Council of Japan, 1973, 1974.

Sorgensen, F.S., E.Friis-Christennsen and J.Wilhjem (1972): J. Geophys. Res., Vol. 77, 1976.

Wilcox, J.M. and N.F.Ness (1965): J. Geophys. Res., Vol. 70, 5793.

Wilcox, J.M. (1968): Space Sci. Rev., Vol. 8, 258.

Zevakina, R.A., E.V.Lavrova and L.N.Lyahova (1967): Principles of predicting the ionospheric-magnetic disturbances and the short-term radioforcast service, Moscow, USSR, Nauka.

Zevakina, R.A. (1974): Abstracts to the reports for the All-Union Conference on the Physics of Ionosphere Held in Rostov-on-Don. Moscow, USSR, IZMIRAN, 93.

Zevakina, R.A., V.P.Kuleshova, E.V.Lavrova, and L.N.Lyakhova (1975): Methods of short-term predictions of magnetic activity and the state of the ionosphere. (Instruction), Moscow, USSR, IZMIRAN.

FORECASTING OF δ foF2-VARIATIONS FOR IONOSPHERIC DISTURBANCES

V. P. Kuleshova, E. V. Lavrova, L. N. Lyakhova
Institute of Terrestrial Magnetism
Ionosphere and Radio Wave Propagation of
the Academy of Sciences of the USSR
Moscow, Union of Soviet Socialist Republics

Different types of ionospheric disturbances are distinguished. The regular variations (Dst and SD) of δ foF2 for each type are derived. A good agreement between (Dst+SD) with real δ foF2 changes during ionospheric disturbances is obtained. These regular variations of δ foF2 are presented in the form of Dst and SD maps, and the application of these maps to short-term forecasting is recommended.

It is well known that every individual ionospheric disturbance has its own peculiar behavior (Kane, 1973). Nevertheless, the study of mean disturbance patterns continues to attract attention, both for disturbance-predicting needs, as well as for studying physical causes of disturbances. One of the methods used is to distinguish disturbance storm-time (Dst) and solar local time (SD) variations from the observed value of δ foF2. In most early studies (e.g., Matsushita, 1959), the Dst and SD-variations were obtained for magnetic storm periods. Because of the variety of ionospheric disturbances, the resulting Dst and SD variations were very small and the irregular (DI) part was dominant. The purpose of the present paper is to distinguish regular components of δ foF2 variations in such a way that they include the most typical variations of δ foF2 during ionospheric disturbances connected with magnetic storms.

As a first step, the most typical ionospheric disturbances were distinguished:

1. Negative disturbances with one active period, D_{-1} ;
2. Negative disturbances with several active periods, D_{-2} ;
3. Two-phase disturbances (the initial phase a positive disturbance), D_{+-} ;
4. Negative disturbances in night hours only, D_{-n} ;
5. Unstable state of ionosphere (the mixing of positive and negative δ foF2, D_{mix} ; and
6. Positive disturbances, D_{+} .

In contrast to the paper by Mednikova (1957) where ionospheric disturbances were picked out without taking into account geomagnetic activity, the present paper deals with some additional types of ionospheric disturbances. The ionospheric disturbances have been divided into strong ($|\delta foF2| \geq 30\%$) and weak ($|\delta foF2| < 30\%$), and into SC and GC, depending on the character of geomagnetic storm commencement (sudden or gradual). The distribution of the disturbances according to season has shown that the dominant types of disturbances are characteristic of different seasons. Thus, D_{-1} and D_{-2} ionospheric disturbances are dominant during the equinoxes, when they are observed with a probability of 84% during large SC-type geomagnetic storms; in winter, all types of ionospheric disturbances have almost equal probability.

The Dst (δ foF2) and SD (δ foF2) variations have been determined for the dominant types of ionospheric disturbances of each season. In calculating the Dst (δ foF2) variations, the duration of each storm was taken as the unit time period for that storm. So the horizontal axis in figure 1a is divided into storm parts rather than in hours. Figure 1a, b present examples of the resultant SD and Dst variations for the most frequently observed type (D_{-1}) found during equinox months (solid curves). Figure 1a, b have for comparison the same variations obtained for periods of magnetic storms (dotted curves), as calculated by previous authors (Matuura, 1972). The regular variation of δ foF2 is thus readily seen to be increased essentially by calculating SD and Dst variations for different types of ionospheric storms.

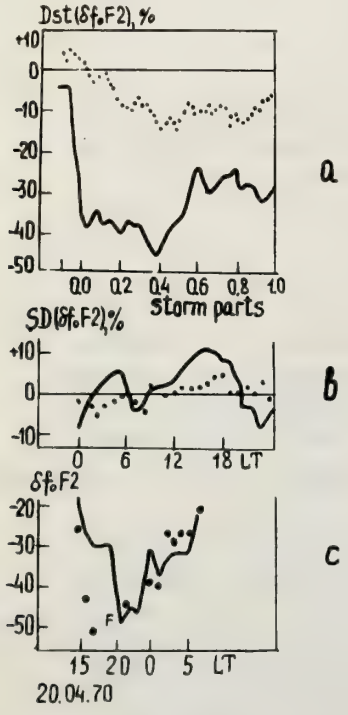


Figure 1. (a) Dst (δ foF2) and (b) SD (δ foF2) variations for D_{-1} ionospheric disturbances in equinox; (c) (Dst+SD) and real δ foF2 for 20.04.70 storm (see text).

The resultant SD and Dst variations can be made use of for δ foF2 forecasting during disturbances. Figure 1c shows the real δ foF2 during the disturbance of April 20, 1970 (points) and the forecast of the storm (Dst+SD)-variation (solid curve). The mean square difference between these variations is $\pm$ 7%. For all storms considered, the mean square difference per storm fluctuates between $\pm$5% and $\pm$15%.

For forecasting purposes, one must know the expected onset time of an ionospheric disturbance. Present research has shown that the delay time of an ionospheric disturbance onset (the steady decrease of δ foF2 to - 15% and more) in Moscow, with respect to the magnetic storm onset, is determined by the local time of the magnetic storm's main phase onset (MPO). The delay time is small (0-2 hours) in the evening and at night. In the daytime it has a linear dependence given by $\Delta Tm = 17.2 - 0.8\ Tm$, where ΔTm is the delay time (in hours) of the ionospheric disturbance onset from the magnetic storm's main phase onset, and Tm is local time of the MPO.

It is natural to expect that for different types of ionospheric disturbances, the preceding solar-terrestrial conditions have to be taken

into consideration. But in spite of some differences in the distribution of ionospheric disturbance types with respect to solar characteristics (see Figure 2, where (1) denotes disturbances connected with flares, (2) with recurrent active regions and (3) with new regions), it is evident that the observable solar characteristics are not the only cause of different ionospheric disturbances types.

It can be supposed that just as is the case with the fine structure of magnetic disturbances (Ivanov, 1974), so is the character of the ionospheric disturbance determined by the structure of interplanetary magnetic fields and by their interactions with the Earth's magnetosphere. This assumption is confirmed by comparison of the ionospheric disturbance development with geomagnetic variations. For example, the D_{-1} type is observed for the case of a very well developed main phase immediately after the SC of a magnetic storm, while the D_{-n} type is associated with large delay times of the main phase onset relative to its SC.

Results of the present analysis demonstrate that the types of ionospheric disturbances are connected mostly with the development of the main phase of a magnetic storm, which is itself determined by the structure of the solar wind and by its interaction with the magnetosphere.

The dividing of ionospheric disturbances into types and picking out regular variations help in the estimation of the contribution of individual processes which lead to ionospheric disturbances. There are, for example, some hypotheses (Matuura, 1972) about the cause of SD- (ionospheric currents in the polar region) and Dst-variations (changes of atmospheric composition due to global convective motion).

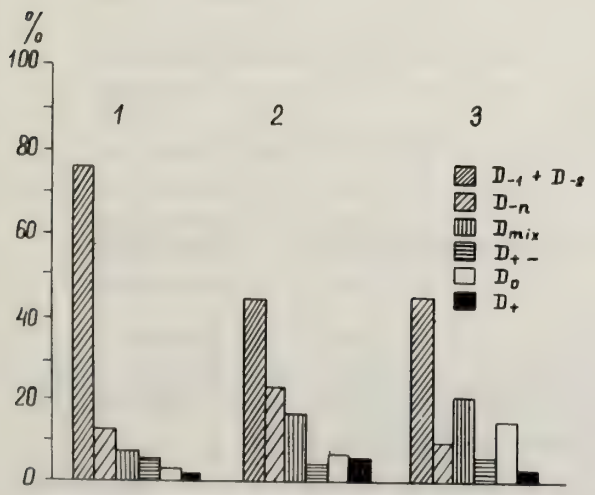


Figure 2. Distribution of ionospheric disturbances types depending on heliophysical situation: 1-flares; 2-recurrent active regions; 3-new active regions.

The irregular DI-variation can be interpreted as the superposition of the different oscillations associated with individual processes. The contribution of these oscillations can be different for each individual disturbance.

Preliminary research on the spectral composition of the ionospheric DI-variation showed that the observed maximum of the spectrum occurred in the frequency range 0.33-0.38 hr^{-1} (period about 3 hours); for some storms this is identified with a similar maximum in the AE index spectrum. This indicates that an auroral electrojet intensity change gives a contribution to the DI-variation.

The calculated regular storm variations for ionospheric stations

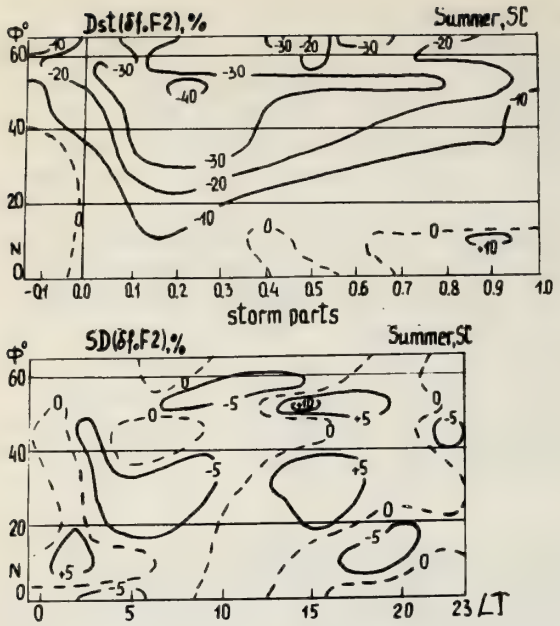


Figure 3. Dst and SD maps for D_{-1} ionospheric disturbances in summer.

of different latitudes in the eastern hemisphere can be presented in the format of maps of SD- and Dst variations for the dominant types of ionospheric disturbances. Figure 3 shows examples of Dst and SD maps for ionospheric disturbances of the D_{-1} type in summer.

By means of these maps, it is possible to prepare a forecast of the development of an ionospheric disturbance (it is, of course, necessary to know the real or predicted onset of the magnetic storm main phase). The mean-square error of such a forecast is ± 15%. This error is the mean irregular (DI) part of ionospheric disturbance.

REFERENCES

Ivanov, K. G., and N. V. Mikerina (1974): Composition of the interplanetary plasma stream and the magnetospheric storms. In: Solar Wind and Magnetosphere, Moscow, USSR Academy of Sciences, 3.

Kane, R. P. (1973): Global evolution of F2 region storms. J. Atm. Terr. Phys., Vol. 35, N1, 1953-1966.

Matsushita, S. (1959): The study of ionospheric storms morphology. J. of Geophys. Res., Vol. 64, N3.

Matuura, N. (1972): Theoretical models of ionospheric storm. Space Sci. Revs., Vol. 13, N1, 124.

Mednikova, N. V. (1957): Ionospheric disturbances in middle latitudes. In: Physics of solar corpuscular flows and their influence on the upper atmosphere, reports of the Conference of Committee on Investigation of Sun, 1955, 22-24 XI, Moscow, USSR Academy of Sciences, 183.

FUNDAMENTALS OF THE PHYSICAL FORECAST OF IONOSPHERIC PLASMA

M. N. Vlasov
Institute of Applied Geophysics
USSR Goscomgidromet
Moscow, USSR

A new method of forecasting the ionospheric plasma based on a physical model is considered. The physical forecast must solve two main problems simultaneously: the prediction of the ionospheric parameters that determine radiowave propagation of the prediction of the parameters that influence the flight of cosmic objects. There are two main requirements for the physical forecast: first, the forecast must include the results of current investigations of ionospheric plasma physics, and second, a common physical basis of the plasma forecast and of the meteorological forecast is necessary because of the strong coupling between the upper and lower atmosphere. The system of hydrodynamic equations is considered as the basis of the physical forecast of the ionospheric plasma. The theoretical, empirical, and semi-empirical models of the ionospheric plasma are discussed with a view to using these models for the physical forecast. It is shown that the self-consistent theoretical model based on the hydrodynamic equation system may be used for the physical forecast of the ionospheric plasma at middle latitudes. The main advantage of the model is the self-consistent description of the behavior of the neutral and charged constituents. Analysis of the preliminary results of the ionospheric forecast based on the self-consistent model indicates that the theoretically calculated parameters of the radiowave propagation are very close to the values deduced from vertical-incidence sounder data. The development of theoretical models of the ionospheric plasma in the future is discussed.

Recently the development of ionospheric and upper atmospheric investigations has made possible the detailed theoretical description of ionospheric plasma behavior. A comprehensive study by Stubbe (1970) attempted, for the first time, the simultaneous theoretical treatment of the neutral and charged constituents, and thereby constructed a realistic ionospheric model. At present, a number of ionospheric models are available (Polyakov et al., 1975; Namgaladze et al., 1972; Kolesnik, 1976; and Vlasov and Kolesnik, 1979). The comparison of these models with experimental data indicates that the main features of the ionosphere are reflected in detail by these models. Recently,

attempts at the creation of two- and three-dimensional models have been made (Straus and Schultz, 1976). The successful theoretical description of the ionospheric plasma appears to be necessary for use in current ionospheric forecasting.

The forecast has two main purposes: prediction of those ionospheric plasma parameters that determine radiowave propagation, and prediction of the parameters that influence flights of cosmic objects. The parameters of the first group are mainly connected with charged particles and the parameters of the second group are connected with neutral components of the ionospheric plasma. All current investigations indicate a very strong coupling between neutral and ionized species. The close connection between neutral and ionized species is due to the photochemical processes of production and loss of neutral and charged particles by the dynamical transport processes, e.g., the drift charged particles induced by the neutral wind and electrodynamic drifts of neutral particles induced by collisions with ionized species. This means that the two main problems of the ionospheric plasma forecast must be solved simultaneously by using theoretical models.

The purpose of this paper is a discussion of a new method of ionospheric plasma forecasting based on the physical models. The statistical ionospheric forecast based on vertical-incidence sounder data does not satisfy modern practical demands. First, information about the height distribution of electron density is necessary for predicting radiowave propagation, but this information cannot be deduced from vertical-incidence sounder data. Also, information about the electron and ion temperature is very important and these parameters cannot be deduced from sounder data. Second, a statistical forecast has all the disadvantages characteristic of a statistical description of a variable phenomenon. Third, it is impossible to include modern ionospheric plasma physics in the creation of a physical forecast.

The development of a new method of ionospheric forecasting based on a physical model of the ionospheric plasma may overcome many of the above-mentioned difficulties. Recently a physical model based on the hydrodynamic description of air motion in the lower atmosphere was developed for forecasting weather. Taking into account the close relationship between the upper and the lower atmosphere, it is very desirable that physical models for forecasting the ionospheric plasma and the weather be based on the same theoretical fundamentals. The hydrodynamic treatment may be used for describing the behavior of the lower atmosphere as well as the upper atmosphere (below 400-500 km). In this case, the physical model of the ionospheric plasma is similar to the hydrodynamic model of the meteorological forecast. Due to this common basis, our understanding of the relationship between both models may be developed in the future.

The difference between the hydrodynamical description of the lower atmosphere and magnetohydrodynamical description of the ionospheric plasma is very significant. The main difference is that in the ionospheric plasma the elementary processes as well as the collective processes are important but the behavior of the lower atmosphere is controlled only by the collective processes. Electromagnetic forces play an important role in the ionospheric plasma but these forces are neglected in the lower atmosphere. The principal problem of the lower atmosphere is the description of the atmospheric gas interaction with the ground surface.

It is clear that the modern ionospheric plasma description based on the solution of the hydrodynamic equation system might not present the total pic-

ture of the behavior of the neutral and charged constituents for different conditions. First of all, we assume that this description is very comprehensive for the middle-latitude ionospheric plasma under undisturbed conditions.

For other conditions, the coupling between the ionosphere and magnetosphere is very important and in this case, the theoretical description becomes very difficult. We do not have any realistic theory which describes the ionosphere-magnetosphere coupling. Therefore, the self-consistent theoretical description of the ionospheric plasma may be developed in detail only for the middle latitudes for undisturbed conditions. The hydrodynamical equation system, by characterizing the neutral and charged constituents of the ionospheric plasma for different levels of solar activity, may be used to predict the diurnal, annual, and semiannual variations of the height distribution of the main parameters.

It is necessary to emphasize that this theoretical description does not require additional information about any parameters of the plasma. The boundary conditions may be induced from the measured data but this fact does not violate the theoretical description when the behavior of the plasma about these boundaries is not represented by the theory. Consequently, the ionospheric plasma model based on this self-consistent theoretical description may be named the theoretical model. By contrast, there are semi-empirical ionospheric plasma models in which a number of the plasma parameters are given by experimental data.

In most of the semi-empirical models, the parameters connected with the neutral atmosphere are given by experimental data but the parameters of ionized constituents are theoretically calculated. However, there is a set of models in which parameters of the charged particles are given by measurements. These plasma parameters are the electron and ion temperatures.

The determination of ionospheric parameters from experimental data makes it possible to eliminate a number of theoretical equations. However, in this case, agreement between the parameters given by experimental data and the parameters deduced from theory may be obtained only by using different indexes. It is known that the indexes represent the ionospheric plasma state very roughly but are not self-consistent with the semi-empirical models.

First of all, in the semi-empirical model, the parameters of the neutral atmosphere do not agree with the ionospheric parameters, and consequently, in this model, the connection between the neutral and ionized constituents is violated. In spite of the improvement of the empirical models of the neutral atmosphere resulting from a large number of satellite measurements, these models do not reflect a number of features of the upper atmosphere and there is no agreement between them (Hedin et al., 1977; and Barlier et al., 1978). The creation of an empirical model of the neutral atmosphere reproducing all variations is impossible because of the enormous number of measurements necessary. Therefore, whenever it is possible, we must construct the semi-empirical and theoretical models of the neutral atmosphere because this model may be in best agreement with the ionospheric model.

The theoretical model of the ionospheric plasma is the best generalization of the experimental data. Whenever the relationship between the neutral and charged constituents is very important, the self-consistent theoretical model of the ionospheric plasma must be developed.

However, it is clear that, at present, only a semi-empirical model may be constructed to describe the polar ionospheric plasma as well as the disturbed ionospheric plasma for middle latitudes and the equatorial latitudes.

An empirical ionospheric model based on available satellite, rocket, and ground-based measurements may be applied to ionospheric forecasting, but in this case the forecast is statistical. However, innumerable measurements are necessary for the empirical description of the ionospheric plasma (Nisbeth, 1975).

For the development of the physical model, the empirical models are very necessary, first of all, for the comparison of the theory with the measurements, and for the improvement of the theoretical model. The main purpose of the experimental investigation of the ionospheric plasma is to reveal and to study the plasma features which are important for the construction of the self-consistent theoretical models. Therefore, the difficulties of the theoretical description must determine the direction of the experimental investigations.

For estimation of the physical forecast, the self-consistent time-dependent model based on the solution of the coupled momentum, energy balance, and continuity equations has been developed. This model is discussed in the paper by Vlasov and Kolesnik (1979), where the comparison with the experimental data is presented. Only the ionospheric forecast parameters deduced from the model are considered. The plasma frequency, foF2, has been computed from the self-consistent model and compared with the vertical-incidence sounder data. The comparison has been made for a number of ionospheric stations at middle latitudes: Ashkabad, 37.9°N; Boulder, 40°N; Alma-Ata, 43.5°N; Tbilisi, 41.7°N; Irkutsk, 52°N; Tomsk, 56.5°N; Moscow, 55.6°N; Sverdlovsk, 56.7°N; and Monte-Capellino, 44.5°N.

For these stations, the discrepancy between the theoretical plasma frequency and the vertical-incidence sounder data is about 20 percent in the daytime. However, the discrepancy increases in the twilight and nighttime. The description of the variation of ionospheric parameters at twilight is a very complex problem.

The theoretical height distributions of the electron density and the values of $h_{max}F2$ have been compared with the incoherent scatter data from Millstone Hill (Evans, 1975) and the vertical-incidence sounder data from the ionosphere stations. The theoretical profiles are in good agreement with the experimental data. Thus, the primary results indicate that it is possible to create a physical model based on the self-consistent time-dependent model of the ionospheric plasma and this model can predict the behavior of the neutral and charged constituents.

However, the creation of physical hydrodynamical forecasts of the ionospheric plasma is a very difficult problem and it requires the development of ionospheric models. Three main aspects of the development of the self-consistent theoretical models may be pointed out. First, the two-dimensional model is necessary for the calculation of the neutral wind that influences the ionospheric plasma behavior at twilight and nighttime. Second, the excited species processes are necessary to take into account the calculation of the energy balance of the ionospheric plasma because the excited species store a very considerable amount of energy and then transfer the energy to the ambient gas. For example, it is evident now that the vibrational temperature of the ionospheric plasma is an important parameter as well as the electron, ion, and neutral temperatures (Vlasov, 1976). The excited species processes play an important role in the explanation of the winter anomaly (Vlasov and Izakova, 1979). Thirdly, the development of the model of the ionospheric plasma of the lower thermosphere and mesosphere is very important due to two reasons: this model may be used as the lower boundary condition

for the self-consistent model, and may be useful for understanding the relationship between the upper and lower atmosphere. The main problem of this model is the eddy diffusion transport. It appears that a number of experimental investigations and further development of the theory are very necessary for resolution of this problem.

As for the experimental investigations of the upper atmosphere, the vibrational temperature measurements are necessary. Unfortunately, we do not have direct methods for measuring this parameter. An indirect method of determining the vibrational temperature is based on the mass-spectrometric measurements of the air release in the upper atmosphere (Danilov et al., 1977).

Summarizing all the above, the following main conclusions may be drawn:

1. At present an ionospheric plasma forecast is necessary to resolve two main problems: the prediction of the variations of the plasma parameters that determine radiowave propagation and the prediction of the parameters controlling the satellite flights. The resolution of these problems requires a detailed description of the spatial and temporal variations of the ionospheric plasma parameters. The statistical forecast cannot resolve these problems.

2. Resolution of this forecast problem is possible only by using physical models of the ionospheric plasma. In this case, the model is based on the hydrodynamical equation system that describes the behavior of the neutral and charged constituents.

3. The relationship between the upper and lower atmosphere can be taken into account if the meteorological forecast and the ionospheric plasma forecast are based on the same conception. The hydrodynamical treatment must describe the behavior of the upper and lower atmosphere so far as the ionospheric plasma physical forecast may be connected with the meteorological hydrodynamical forecast that is developed at present.

4. In contrast to the statistical forecast, the physical forecast based on the self-consistent time-dependent model of the ionospheric plasma can include modern and future advances of ionospheric physics.

5. The primary results indicate that the semi-consistent model may be used for the physical forecast of the ionospheric plasma. The plasma frequency deduced from the model is in very good agreement with the vertical-incidence sounder data at middle latitudes.

6. The main problems of the theoretical modelling for the forecast are the following: the development of a two-dimensional model; the inclusion of the excited species processes; the construction of the model of the lower thermosphere and mesosphere as the low boundary condition for the self-consistent model.

It should be emphasized that the problem of the physical hydrodynamical forecast of the ionospheric plasma is very complicated and international investigations of it would be desirable.

REFERENCES

Barlier, F., et al. (1978): Ann. Geophys., 34:9.

Danilov, A. D., et al. (1977): COSPAR Space Res., 17:465.

Evans, J. V. (1975): Millstone Hill Thompson Scatter Results, Tech. rpt. 513.

Hedin, A. E., et al. (1977): J. Geophys. Res., 82:2139.

Kolesnik, A. G. (1976): V sb. "Fizika ionosfery," M., Nauka, s. 139.

Namgaladze, A. A., C. S. Latyshev, and M. A. Nikitin (1972): Preprint IZMIRAN, N. 7, Moskova.

Nisbet, J. S. (1975): Atmosph. Earth and Planets, Proc. Summer Adv. Study, Dordrech, Boston, 245.

Polyakov, V. M., M. A. Koen, and G. V. Hazanov (1975): V sb. "Issledovaniya po geomagnetizmu, aeronomii i fizike Solnza," vyp. 33, 9.

Straus, J., and M. Schulta (1976): J. Geophys. Res., 81:5822.

Stubbe, P. (1970): J. Atmosph. Terr. Phys., 32:865.

Vlasov, M. N. (1976): J. Atmosph. Terr. Phys., 38:807.

Vlasov, M. N., and T. M. Izakova (1979): COSPAR Space Res., 19 (submitted).

Vlasov, M. N., and A. G. Kolesnik (1979): Paper presented at this workshop.

SELF-CONSISTENT MODEL OF THE IONOSPHERIC PLASMA AND THE HYDRODYNAMIC FORECAST

M. N. Vlasov
Institute of Applied Geophysics, Goskomgidromet of the USSR
Moscow, USSR
and
A. G. Kolesnik
Tomsk University, the USSR Academy of Sciences
Tomsk, USSR

The system of hydrodynamic equations has been used to construct a self-consistent theoretical model. In the model, the simultaneous behavior of the neutral and charged constituents is described. A self-consistent model of the ionospheric plasma has been made for the height region from 120 to 500 km at middle latitudes. The comparison of the theoretical model with experimental data and empirical models indicates a good agreement. The theoretical model reflects well the annual, semiannual, and diurnal variations of the ionospheric plasma. This indicates that the model may be used for the forecast of ionospheric plasma parameters. The maximum discrepancy between the plasma frequency deduced from this model and obtained from vertical incidence sounding data is equal to 20 percent in the daytime.

Vlasov (1979) has suggested a new method of forecasting the ionosphere and upper atmosphere based on a physical model of the ionospheric plasma processes.

According to Vlasov (1979), this method may be based on the ionospheric plasma model produced by the solution of the hydrodynamic equation system for the neutral and charged constituents. This model can be developed to forecast disturbed conditions at middle latitudes.

The purpose of this paper is to present a self-consistent theoretical model of the middle latitude ionospheric plasma from 120 to 500 km and to estimate the forecast possibility of this model.

1. BASIC EQUATIONS AND PROCESSES

The total equation system of the model includes the continuity equations:

$$\frac{\partial n_i}{\partial t} = q_i - \ell_i - \frac{\partial}{\partial z_i}(n_i w_i); \quad i = 4, \ldots 10 \qquad (1)$$

where n_i is the concentration of O^+, O_2^+, NO^+, N_2^+, $N(^4S)$, NO, $N(^2D)$; $i = 4, 5, 6, 7, 8, 9, 10$, respectively; w_i is the vertical component of the ith partial velocity which is supposed to be equal to zero for $i = 5$-10.

For the O^+ ion,

$$W_4 = -D_a \left[\frac{1}{n_e}\frac{\partial n_e}{\partial z} + \frac{1}{T_p}\frac{\partial T_p}{\partial z} + \frac{1}{H_p}\right] \sin^2 I - u_n \sin I \cos I \qquad (2)$$

where D_a is the ambipolar diffusion coefficient; I is the geomagnetic declination; $n_e = \Sigma n_i$ ($i = 4, 5, 6, \ldots 10$) is the electron concentration; $T_p = T_e + T_i$; $H_p = \kappa T_p / m_4 g$; and u_n is the meridional component of the neutral gas velocity.

The ion production and transformation rate (q_i) and the loss rate (ℓ_i) are determined by the following photochemical processes:

(a) the ionization and dissociation by solar radiation

$$O + h\nu \rightarrow O^+ + e^-; \quad N_2 + h\nu \rightarrow N_2^+ + e$$

$$O_2 + h\nu \rightarrow O_2^+ + e^-; \quad NO + h\nu \rightarrow N + O$$

(b) ionization and dissociation by photoelectrons

$$O + e_{ph} \rightarrow O^+ + e; \quad N_2 + e_{ph} \rightarrow N_2^+ + e$$

$$O_2 + e_{ph} \rightarrow O_2^+ + e; \quad N_2 + e_{ph} \rightarrow N(^4S) + N(^2D)$$

(c) ion-molecule reactions

$$O^+ + N_2 \rightarrow NO^+ + N(^4S); \quad O^+ + O_2^+ \rightarrow O_2^+ + O$$

$$O_2^+ + NO \rightarrow NO^+ + O_2; \quad N(^4S) + NO \rightarrow N_2 + O$$

$$N_2^+ + O \rightarrow \begin{cases} NO^+ + N(^4S); & N_2^+ + O_2 \rightarrow O_2^+ + N_2 \\ NO^+ + N(^2D); & N(^2D) + O_2 \rightarrow NO + O \end{cases}$$

(d) dissociative-recombination reactions

$$O_2^+ + e \rightarrow \begin{cases} O(^3P) + O(^1D) \\ O(^1D) + O(^1D); \\ O(^3P) + O(^3P) \end{cases} \quad NO^+ + e \rightarrow \begin{cases} N(^2D) + O(^3P) \\ N(^4S) + O(^3P) \end{cases}$$

$$N_2^+ + e \rightarrow \begin{cases} N(^2D) + N(^2D) \\ N(^4S) + N(^4S) \end{cases}$$

This scheme of the ionospheric processes corresponds to that of Danilov and Vlasov (1973). The calculations of photoelectron spectra and ionization rates are from Kolesnik and Chernishov (1978). The change of ultraviolet radiation spectrum ($\lambda < 1027$Å) with solar activity is taken from Chernishov (1978).

The distributions of the main neutral components are determined from the barometric law

$$n_\alpha = \frac{n_{\alpha 0} T_{n0}}{T_n} \exp\left(-\int_{z_0}^{z} \frac{dZ'}{H_\alpha}\right), \quad \alpha = 1, 2, 3 \qquad (3)$$

where $\alpha = 1, 2, 3$ for O, O_2, N_2, respectively; and $H_\alpha = \kappa T_n/m_\alpha g$. A very important part of the total system is the equation for heat balance of the ionospheric plasma. The equation for the neutral temperature is

$$n_n \bar{c}_p \frac{\partial T_n}{\partial t} = \lambda_n \frac{\partial^2 T_n}{\partial z^2} + \left[\frac{\partial \lambda_n}{\partial z} - n_n \bar{c}_p (W_B + W_D)\right] \frac{\partial T_n}{\partial z} - m_n n_n g W_D + Q_n - L_n \qquad (4)$$

where

$$n_n = \sum_{\alpha=1}^{3} n_\alpha, \qquad m_n = \frac{1}{n_n} \sum_{\alpha=1}^{3} m_\alpha n_\alpha, \qquad \bar{c}_p = \frac{1}{n_n} \sum_{\alpha=1}^{3} c_{p\alpha} n_\alpha,$$

λ_n is the heat conductivity according to Banks and Vockarts (1973); Q_n and L_n are the local heating and cooling rates, respectively, of the neutral gas according to Kolesnik and Chernishov (1978), Chernishov et al. (1978), and Stubbe and Warnuum (1972); W_B and W_D are the vertical components of the neutral gas drift due to the "breathing" of the atmosphere and the horizontal wind divergency are equal, respectively, to

$$W_B = T_n \int_{z_0}^{z} \frac{1}{T_n^2} \frac{\partial T_n}{\partial t} dz' \qquad (5)$$

$$W_D = \frac{1}{n_n} \int_{z}^{\infty} \left[\frac{\partial}{\partial x}(n_n V_n) + \frac{\partial}{\partial y}(n_n U_n)\right] dz' \qquad (6)$$

according to Rishbeth et al. (1969). The X- and Y-axes are coincident with the zonal and meridional directions, respectively; and V_n and U_n are the zonal and meridional components of the neutral gas velocity.

The equation for the electron temperature is

$$\frac{\partial T_e}{\partial t} = \frac{2}{3} \frac{\lambda_e}{\kappa n_e} \frac{\partial^2 T_e}{\partial z^2} + \frac{2}{3\kappa n_e} \frac{\partial \lambda_e}{\partial z} \frac{\partial T_e}{\partial z} + \frac{2}{3} \frac{T_e}{n_e} \frac{\partial n_e}{\partial t} + \frac{2}{3\kappa n_e} (Q_e - L_e) \qquad (7)$$

where λ_e is the electron heat conductivity as given in Banks and Kockarts (1973); κ is Boltzman's constant; Q_e and L_e are the local heating and cooling rates, respectively, of the electron gas (Kolesnik and Chernishov, 1978; Chernishov and Kolesnik, 1978; and Stubbe and Warnuum, 1972). For the Q_e and Q_n calculations, the intensity of the Schuman-Runge radiation and the O_2 absorption cross section according to Ackerman (1970) are used.

Neglecting the heat conductivity in the heat balance of the ion gas, the T_i equation may be presented in the form

$$T_i = (T_n + \theta T_e^{-1/2}) / (1 + \theta T_e^{-3/2}) \qquad (8)$$

where

$$\theta = 1.7 \cdot 10^8 \, n_e T_n^{-1/2} / n_n$$

In our model, the equations for the zonal and meridional components of the neutral gas velocity are (Gerschman, 1974; and Geisler, 1966):

$$\frac{\partial V_n}{\partial t} = \frac{\mu_n}{\rho_n} \frac{\partial^2 V_n}{\partial z^2} - \frac{1}{\rho_n} \frac{\partial P_n}{\partial x} + 2\Omega U_n \sin\phi - \frac{n_e}{n_n} \nu_{in} V_n \sin^2 I \qquad (9)$$

$$\frac{\partial U_n}{\partial t} = \frac{\mu_n}{\rho_n} \frac{\partial^2 U_n}{\partial z^2} - \frac{1}{\rho_n} \frac{\partial P_n}{\partial y} - 2\Omega V_n \sin\phi - \frac{n_e}{n_n} \nu_{in} U_n \qquad (10)$$

where Ω is the Earth's rotation velocity; μ_n is the molecular viscosity coefficient; $\rho_n = m_n n_n$; P_n is the pressure; and ν_{in} is the ion-neutral collision frequency.

The values of $\partial P_n/\partial x$ and $\partial P_n/\partial y$ are calculated using the OGO-6 model (Hedin et al., 1974). The initial conditions are given by the periodical solution of $U(t) = U(t + T)$, where $T = 24$ hours.

At the lower boundary ($z_0 = 120$ km), the O, O_2, N_2 concentrations are given by an empirical model (Kolesnik, 1975); the O^+ concentration is given by equation (1) for $w_4 = 0$; the electron temperature is found from equation (7) neglecting heat conductivity ($\lambda_e = 0$); the neutral temperature is according to the OGO-6 model (Hedin et al., 1974); the V_n and U_n values are taken to be zero. At the upper boundary ($z_\infty = 500$ km), the O^+ flux is given by Thompson scatter measurements (Evans, 1971a, 1971b, and 1975); the electron temperature is given as the gradient $\partial T_e/\partial z$, using the results of Evans (1975, 1967, 1971c, and 1970). A neutral temperature condition is taken as $\partial T_n/\partial z = 0$, and the V_n and U_n condition is $(\partial V_n/\partial z) = (\partial U_n/\partial z) = 0$.

Equations (1) through (10) are solved by the numerical method and the calculation of photoelectron spectrum and the local heating are included.

2. MODEL AND EXPERIMENTAL DATA

The results of the calculation of the main plasma parameters are compared with the satellite and experimental rocket data and ground-based measurements. Figure 1 gives a comparison of the calculated atomic oxygen concentration using both the theoretical model and the empirical model (Kolesnik, 1975) and with the CIRA-72 model.

Good agreement between the theoretical prediction and the empirical atomic oxygen concentration (Kolesnik, 1975) is shown in Figure 1. However, the atomic oxygen concentration from the CIRA-72 model at the height of 150 km at equinox is three times higher than the concentration from the theoretical model, but at a height of 200 km, the calculated concentrations are smaller than the concentration from the CIRA-72 model by a factor of 2-3. The discrepancy for the concentration of O_2 and N_2 is smaller. Differences between the CIRA-72 model and a number of experimental data are well known and have been discussed (Mikhnevich et al., 1976; and Tricke et al., 1976).

Figure 2 shows the variations of the neutral gas temperature with solar activity. The temperatures $T_{n\,max}$ and $T_{n\,min}$ are maximum and minimum temperatures of the diurnal variations ($r = T_{n\,max}/T_{n\,min}$). The values of $T_{n\,min}$ and r deduced from the satellite drag data (Roemer, 1971) and calculated by Stubbe (1970) are given in Figure 2 for the latitude $\phi = 52°N$ at equinox. The variations of $T_{n\,max}$ and $T_{n\,min}$ with solar activity agree well with experimental data (Waldteufel and Coggen, 1971). The winter increase of $T_{n\,max}$ with solar activity is smaller than in summer due to the very significant role of the Schuman-Runge continuum radiation in the winter heat balance. A similar result has been obtained by Kolesnik (1976) for a stationary model.

Figure 3 shows the diurnal variation of T_n at equinox deduced from the theoretical model. For comparison, the OGO-6 data, Stubbe's model (1970), and the Thompson scattering results (Evans, 1975; Salach and Evans, 1973) are also presented in Figure 3.

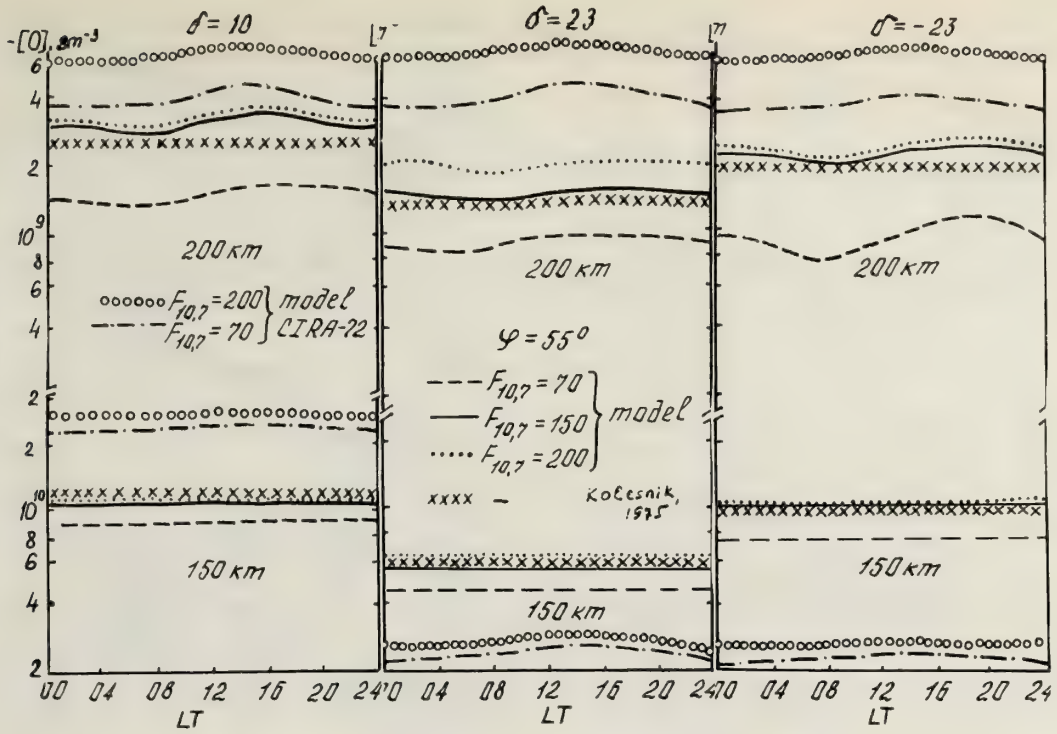


Figure 1. The diurnal variation of O concentration at height 150 km and 200 km.

The T_n latitude variation is about 130° K for the latitude range from 40°N to 55°N and this variation depends on season. In winter, the value of T_n for 40°N is higher than the value for 55°N at equinox. This latitudinal discrepancy decreases at equinox and is neglected in summer. Similar results have been deduced from the AEROS-A satellite data (Rawer, 1976).

In our model the time of the daily maximum of the neutral temperature is two hours after the time of maximum in the experimental data. This fact may be connected with a one-dimensional approximation (Baily and Moffett, 1972; Straus et al., 1975).

The theoretical and experimental height distributions of T_e and T_i are given in Figure 4. The comparison of the theoretical height profiles of T_e with the incoherent measurement data (Evans, 1970) indicates good agreement. For high solar activity, the maximum of the theoretical electron temperature appears at an altitude near $h_{max}F2$. This effect has been observed by Bauer (1976) and may be explained by the energy transfer to ions. Thus the electron and ion temperatures calculated in the model are reliable for different ionospheric conditions.

Figure 5 shows the plasma frequency variation with height, season, and solar activity at latitudes ϕ = 55°N and ϕ = 70°N. There are annual and semi-annual variations. Figure 5 illustrates the behavior of the winter anomaly in the F2 region and the $h_{max}F2$ variations and a number of other features.

Therefore the comparison of the theoretical model with experimental data and empirical models (MSIS model, CIRA-72 model) indicates that this self-consistent model reflects the main features of the ionospheric plasma be-

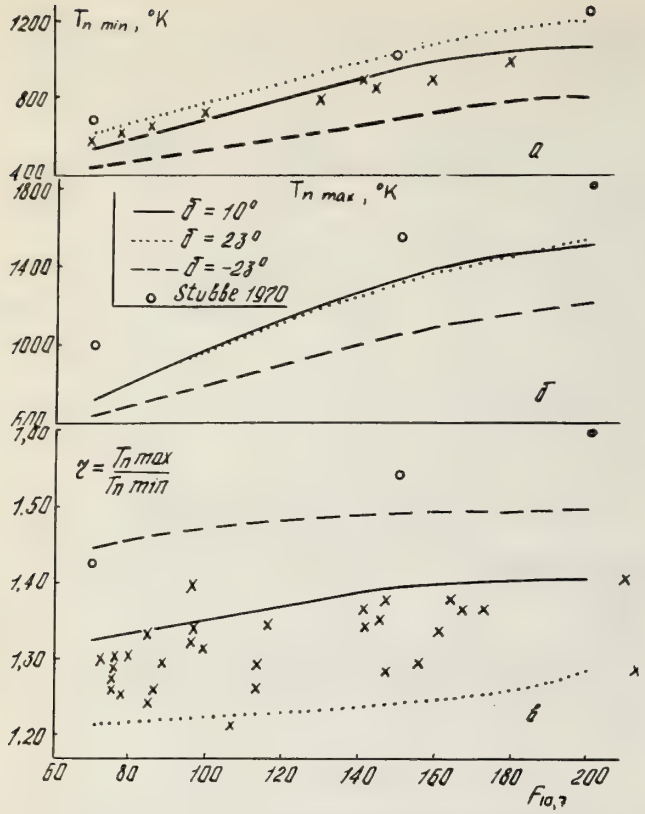


Figure 2. The neutral temperature variation with solar activity.

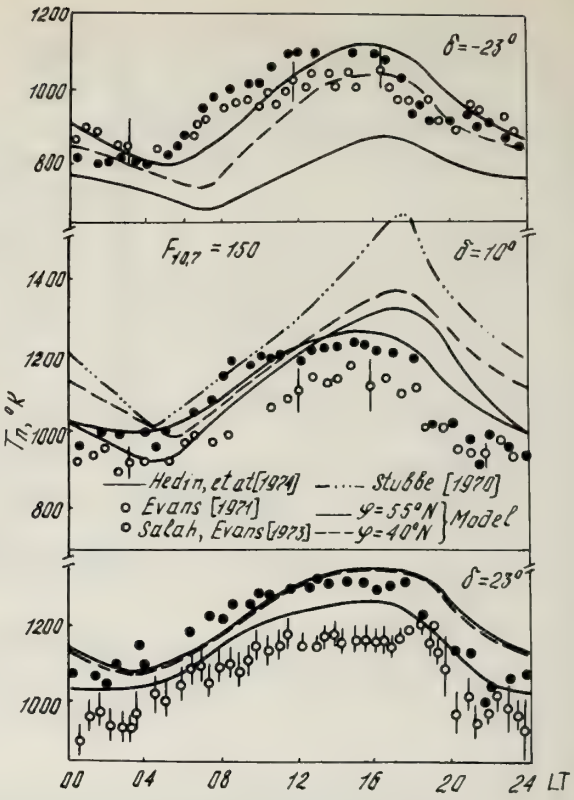


Figure 3. Diurnal variation of neutral temperature.

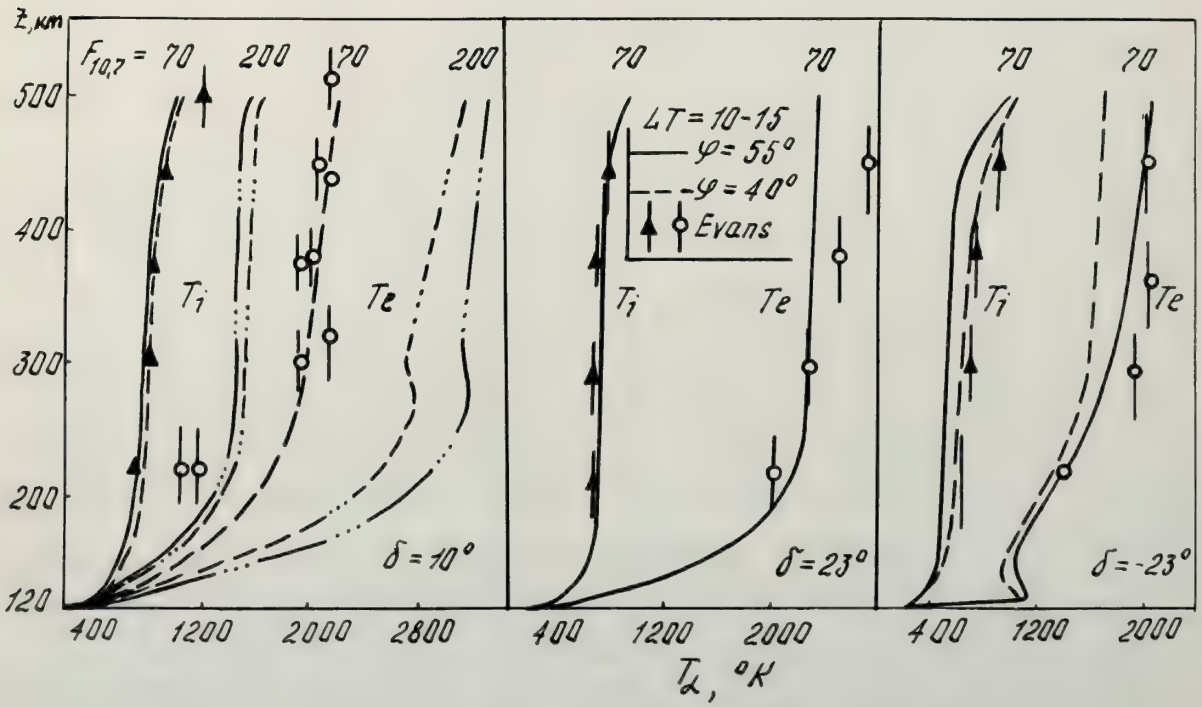


Figure 4. Height profiles of electron and ion temperature.

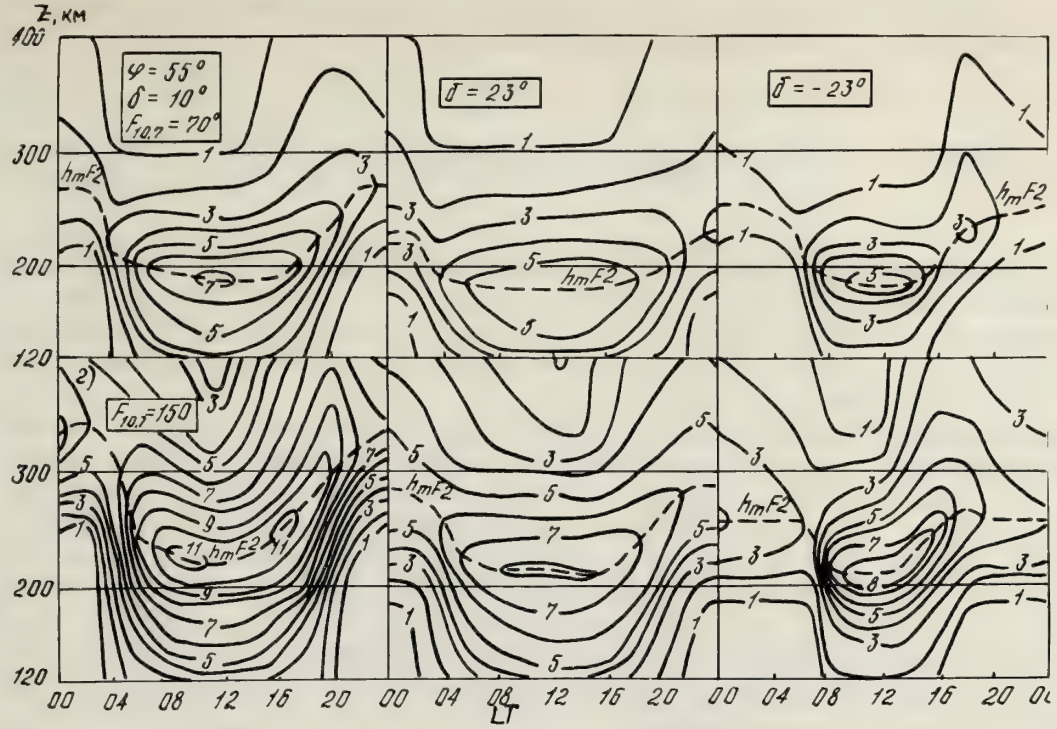


Figure 5. Plasma frequency variations.

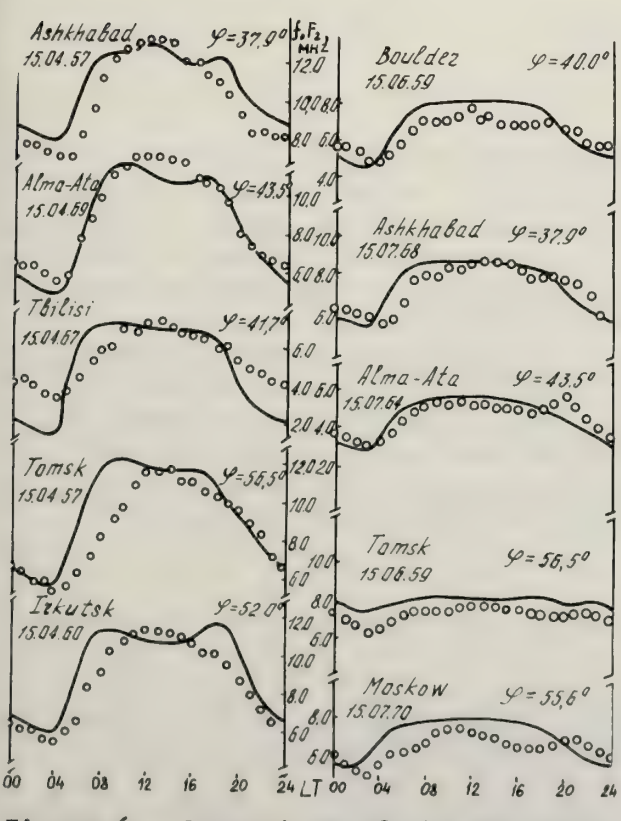


Figure 6. Comparison of the frequency calculated from the model with vertical sounder data for different ionospheric stations.

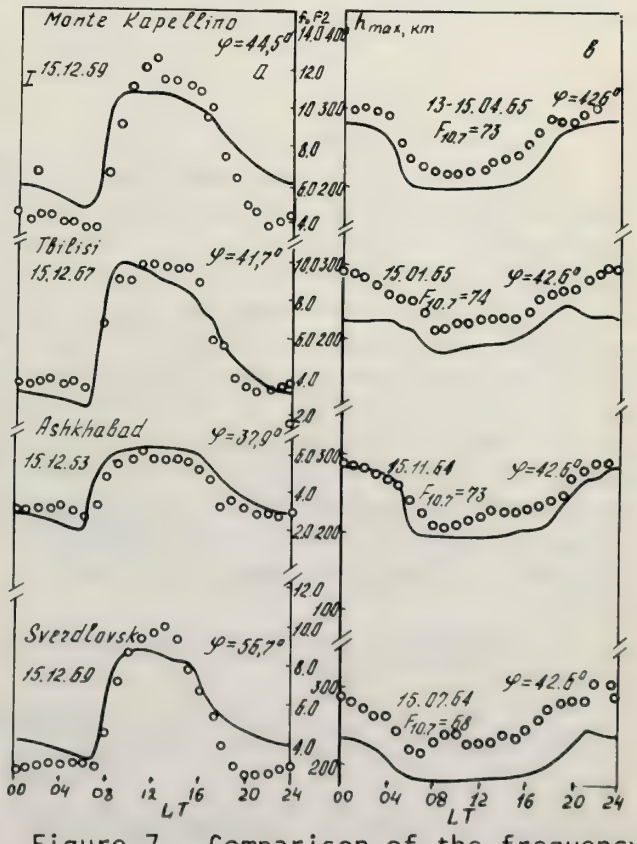


Figure 7. Comparison of the frequency and $h_{max}F2$ values deduced from the model with ionospheric station data.

havior. It is very important that the model describes the simultaneous behavior of the neutral and charged constituents.

3. MODEL AND FORECAST

Calculations of foF2 from the model have been made and the values compared with the vertical incidence sounder data of ionospheric stations.

For example, the comparison of the theoretically calculated values of foF2 with the ionospheric data for the midlatitude stations in the north hemisphere is presented in Figures 6 and 7.

Averaged values of foF2 were used for the comparison. Figure 7 shows also the values of $h_{max}F2$ in comparison with the incoherent scatter data (Evans, 1967, 1970, 1971b). In the daytime the error of the forecast is about 20 percent. The error increases greatly for twilight conditions. This may be explained by the very strong influence of the upper boundary conditions on the ionospheric behavior in twilight and nighttime. In the daytime this influence is neglected. At nighttime and twilight the thermospheric wind strongly influences the electron density height distribution but the wind calculation is based on the horizontal gradients from the OGO-6 model, which are not reliable for this purpose.

4. CONCLUSION

The system of hydrodynamic equations makes it possible to construct a theoretical model of the ionospheric plasma without including empirical parameters. In this model, the simultaneous behavior of the neutral and charged constituents is described. A self-consistent model of the ionospheric plasma for altitudes from 120 up to 500 km at middle latitudes may be constructed. The comparison of the theoretical model with experimental data and empirical models indicates good agreement. The theoretical model reflects well the main features of the ionospheric plasma indicating that it may be used to forecast ionospheric plasma parameters. The maximum discrepancy between the plasma frequency calculated from the model and deduced from vertical-incidence sounder data is equal to 20 percent in the daytime. The development of a self-consistent model is necessary to develop a physical forecast of the ionospheric plasma.

REFERENCES

Ackerman, A. (1970): Aeronomica Acta, A, 77.

Banks, P. M., and G. Kockarts (1973): Aeronomy, Academic Press, New York, London.

Bauer, Z. (1976): Fizika nebesnikh atmosfer, Moscow, "Mir."

Bailey, G. T., and R. T. Moffett (1972): Planet. Space Sci., 20:1085.

Chernishov, V. I., A. G. Kolesnik, and M. N. Vlasov (1978): Geomagnetizm i Aeronomiya, 18, 2.

Chernishov, V. I. (1978): Geomagnetizm i Aeronomiya, 18, 5.

CIRA-72, COSPAR International Reference Atmosphere, (1972): Academie-Verlag, Berlin.

Danilov, A. D., and M. N. Vlasov (1973): Fotokhimiya ionizovannykh i vozbyzhdennikh chastis v nizhnei ionosfere. Leningrad, Gidrometeoizdat.

Evans, J. V. (1967): Planet. Space Sci., 15:1387.

Evans, J. V. (1970): Planet. Space Sci., 18:1225.

Evans, J. V. (1971a): Radio Sci., 6:843.

Evans, J. V. (1971b): Radio Sci., 6:609.

Evans, J. V. (1975a): Millstone Hill Thompson Scatter Results 1968, Technical Report 513, Millstone Hill, Massachusetts.

Evans, J. V. (1975b): Planet. Space Sci., 23:1611.

Evans, J. V. and J. Holt (1971): Radio Sci., 6:855.

Fricke, K., et al. (1976): COSPAR Space Res., 16, 265.

Geisler, Y. E. (1966): J. Atmospher. Terr. Phys., 28:703.

German, B. N. (1974): Dinamika ionosfernoi plasmi, Moscow, "Nauka."

Hedin, A. E., et al. (1974): J. Geophys. Res., 79:215.

Kolesnik, A. G. (1965): Geomagnetizm i aeronomiya, 15, 2.

Kolesnik, A. G. (1976): V sb. "Fizika ionosferi," Moscow, "Nauka."

Kolesnik, A. G., and V. I. Chernishov (1978): Geomagnetizm i aeronomiya, 18, 1.

Mikhnevich, V. V., et al. (1976): V sb. "Sutochnie variatsii i korpuskulyarnoe izluchenie," L. Gidrometeoizdat, 119.

Rawer, K. (1976): Space Res., 16:211.

Rishbeth, H., R. J. Moffett, and G. L. Wailey (1969): J. Atmospher. Terr. Phys., 31:1035.

Roemer, M. (1971): Space Res., 11:761.

Salach, I. E., and I. V. Evans (1973): Space Res., 13:268.

Stubbe, P. J. (1970): J. Atmospher. Terr. Phys., 32:865.

Stubbe, P., and W. S. Warnuum (1972): Planet. Space Sci., 20:1121.

Straus, T., et al. (1975): J. Atmospher. Terr. Phys., 37:1545.

Vlasov, M. N. (1979): Proceedings of International Solar-Terrestrial Predictions Workshop Program, Boulder, Colorado.

Waldteufel, P., and L. Cogger (1971): J. Geophys. Res., 76:5322.

PREDICTION OF THE PARAMETERS OF THE MAXIMUM OF THE VERTICAL ELECTRON DENSITY GRADIENT

T. A. Anufrieva, T. L. Gulyaeva, G. F. Kadukhin,
T. N. Soboleva, and A. G. Shlionsky
Institute of Terrestrial Magnetism
Ionosphere and Radio Wave Propagation Academy of Sciences, USSR
142092, Troitsk, Moscow Region, USSR

The results of a study of the spatial and temporal variations of the parameters of the maximum of the vertical ionization gradient (height level, plasma frequency and the value of $(dN/dh)_{max}$) are presented. The corresponding prediction maps were developed from N(h) profile data. It is possible to use planetary maps of the critical frequencies and the F2 layer geometric parameters for this purpose also.

1. GLOBAL DISTRIBUTION OF THE MAXIMUM HEIGHT GRADIENT

Available ionospheric predictions do not provide all of the data necessary for predicting long distance radio wave propagation. For instance, there are no data available on the inter-layer valley parameters and those of the vertical ionization gradient maximum upon which the frequencies and the determination of some waveguide characteristics by the extremal-parametric method (Shlionsky, 1971) depend.

Model N_e profiles have been used in the present paper to analyze the variations of $(N'h)_{max}$ parameters (Soboleva, 1972 and 1973; Kadukhin and Soboleva, 1978a; and Rawer and Rama Krishnan, 1972) as well as electron density profiles calculated from vertical incidence ionograms (Kadukhin and Soboleva, 1978b) using analogous searching methods (Kadukhin and Shlionsky, 1970).

The calculation of N(h) profiles from hourly ionograms has been carried out for 13 stations: Huancayo, Talara, Bogota, Jamaica, Grand Bahama, Wallops Island, Winnipeg, Colledge, Churchill, Narsarssuaq, Godhavn, Resolute Bay, and Thule. Equinox conditions (March) at solar activity minimum and quiet geomagnetic activity have been considered: $F_{10.7} = 75$, $R_z = 10$, $K_p = 0$.

Figure 1 shows, in terms of geomagnetic latitude and local time, the global distributions of the following parameters (the north and south hemispheres are approximately symmetrical relative to the geomagnetic equator): $(dN/dh)_{max}$ in the F region; the values of electron concentration, Ng; and the heights at this point, h_g.

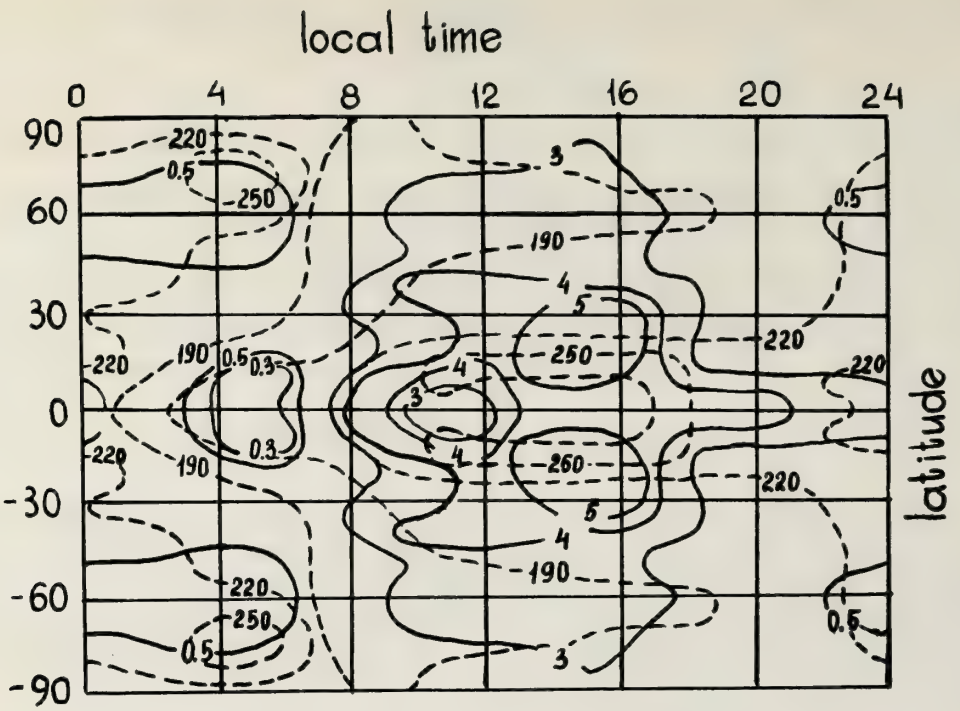


Fig.1a Isoline of parameters $10^{-5} N_g$, e/cm^3 (-)
h_g, km (---).

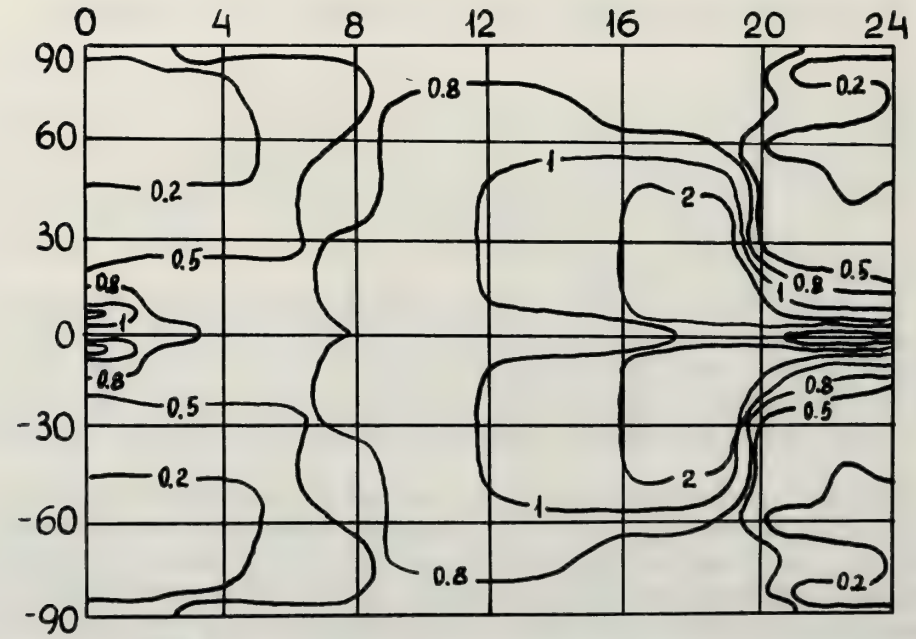


Fig.1b
Isoline of parameters $\left(\frac{dNe}{dh}\right)_{max} \cdot 10^{-4} \frac{e}{cm^3}$

To investigate the changes in the parameters of gradient maximum these data were complemented by empirical N(h) profiles, the latter being compiled by generalizing the N_e measurements from rocket flights and those of the incoherent radio wave scatter method for two levels of solar activity: (1) $F_{10.7} = 75$, $R_z = 10$, $K_p = 0$; and (2) $F_{10.7} = 175$, $R_z = 100$, $K_p = 2 \div 3$.

Figures 2a and 2b and Tables 1 and 2 give the results of the comparative analysis of $(dN/dh)_{max}$ values calculated from the different profiles: the circles indicate the results of the N(h) profile analysis of ionograms (Kadukhin and Soboleva, 1978b). The solid line shows the calculation from the empirical model profiles (Soboleva, 1972, 1973) at solar activity minimum for different hours of LT at $\Phi = 50°N$ and along the noon-midnight meridian.

Numerical data obtained from both types of profiles fit well enough and their relative changes are similar notwithstanding some differences in details. This allows us to study further the diurnal, latitudinal and cyclic variations using only the empirical model profiles. The results for two levels of solar activity and equinox conditions are shown in Figures 2c and 2d and in Tables 1 and 2.

The maximum values of daytime height gradients in the diurnal distributions of N'_{max} at middle latitudes (Figure 2c) are about twice as great as those of the night hours, small extrema are observed at morning and evening hours, the evening one being more distinct. A geomagnetic daytime anomaly is observed in the latitude distribution of N'_{max} (Figure 2d), when the equatorial values are smaller than those observed at $\Phi = 20°N$. The value of N'_{max} decreases at high latitudes. The minimum values of the gradient are observed near the trough latitudes at night similar to those of the F2 layer critical frequencies while N'_{max} increases towards low latitudes.

As solar activity changes from $F_{10.7} = 75$ to $F_{10.7} = 175$, N'_{max} increases on an average by the order of 1.5 times (Figures 2c, 2d, Tables 1 and 2).

Seasonal variations of the gradient maximum are tabulated in Table 3. These are from the tentative table of Electron Density for Temperate Latitudes (Rawer and Rama Krishnan, 1972). Noon and midnight for two solar activity levels ($R_z = 10$ and 100) and for four months (March, June, September, December) have been considered. Maximum values of N'_{max} in daytime are observed in March and December and they are minimal in summer. The nighttime seasonal differences are small; maximum values are observed during the summer months. As solar activity increases, these regularities remain inchanged.

Knowing the maximum of the vertical electron concentration gradient, it is possible to predict the maximum frequencies, f_{max}, of the ionospheric duct using the extremal parametric method (Shlionsky, 1971, 1978):

$$f_{max} = 0.9 \cdot \sqrt{\left[Ng + \frac{6370\, h_g}{2} (dN/dh)_{max}\right] \cdot 10^{-4}} \qquad (1)$$

The global distribution of f_{max} at equinox for minimum solar activity (Figure 3) has been obtained from equation (1) and the N(h) profiles. Latitudinal, diurnal, cyclic, and seasonal f_{max} variations have been calculated from the empirical model profiles using equation (1). These are given in Tables 1, 2, and 3. The calculations show that the maximum frequency variations are determined mainly by the variations of the maximum of the electron concentration gradient and have the same peculiarities as $(N_h')_{max}$. The maximum frequencies exceed considerably the MUF of the F2 layer. Comparing f_{max} with MUF for equinox conditions at solar activity minimum along the zero geomagnetic meridian (Chernyshow and Vasilyeva, 1976), we have shown that in

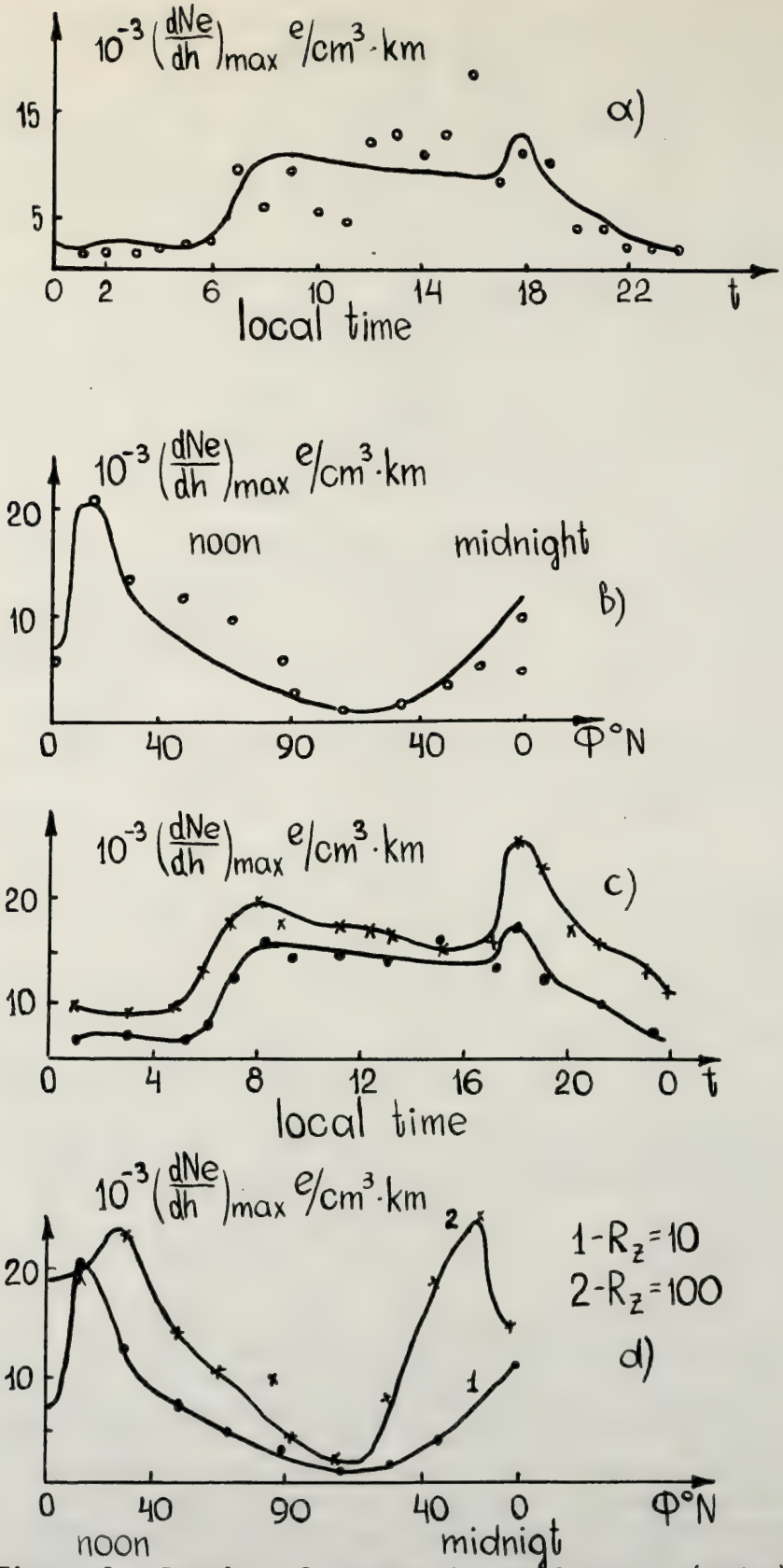


Figure 2. Results of comparative analyses of $(dN/dh)_{max}$ values calculated from different profiles.

Table 1. Diurnal variations of extremal parameters at two solar conditions.

Minimum solar activity $F_{10,7}=75$, $R_z=10$, $K_p=0\div1$					Moderate solar conditions. $F_{10,7}=175$ $R_z=100$ $K_p=2\div3$					
From N(h)-profiles ionogram Cadukhin, Soboleva 1978					From empirical model profiles ne(h) Soboleva 1972, 1973				Cadukhin, Soboleva, 1978				
LT	$(\frac{dNe}{dh})_{max}$ e/cm³·km	h_g km	$10^{-4}N_g$ e/cm³·km	f_{max} MHz	$(\frac{dNe}{dh})_{max}$ e/cm³·km	h_g km	$10^{-4}N_g$ e/cm³·km	f_{max} MHz	$(\frac{dNe}{dh})_{max}$ e/cm³·km	h_g km	$10^{-4}N_g$ e/cm³·km	f_{max} MHz	
00	1,93	228	(5,30)	22,4	-	-	-	-	-	-	-	-	
01	1,50	248	5,30	20,4	2,24	258	6,85	24,6	5,40	328	29,8	38,6	1,56
03	1,50	218	3,00	19,7	2,56	218	2,66	26,2	4,20	308	18,8	33,9	1,29
05	2,30	218	3,10	24,8	1,80	213	3,54	21,9	4,80	288	19,9	36,2	1,65
06	-	-	-	-	3,40	213	10,9	30,3	8,00	233	27,4	46,5	1,53
07	9,40	188	15,7	50,1	7,60	208	17,8	45,2	13,0	243	53,0	59,4	1,31
08	5,60	188	20,3	41,7	-	-	-	-	15,0	243	63,0	63,8	-
09	9,50	193	24,2	50,5	9,00	198	25,8	49,1	13,0	233	56,2	59,3	1,21
11	3,80*	193	28,5	32,2	10,0	198	38,7	51,9	13,0	248	70,7	59,5	1,15
13	12,7	195	28,9	58,2	9,0	188	29,8	49,1	12,0	302	84,0	57,5	1,17
15	12,7	198	29,0	58,3	11,6	193	25,0	55,5	10,0	303	86,2	52,7	0,95
17	11,5	203	21,8	64,4	8,6	203	26,6	48,1	11,2	238	50,0	55,1	1,15
18	12,3	203	15,8	57,4	12,5	220	28,0	58,0	21,6	267	68,5	76,6	1,32
19	9,80	203	16,4	51,3	7,2	228	21,2	44,1	18,2	253	38,7	70,1	1,59
20	4,30	208	13,7	34,0	-	-	-	-	13,0	258	26,4	59,3	-
21	3,50	213	11,0	30,8	5,0	228	7,10	36,6	12,4	263	17,8	57,6	1,58
23	2,20	243	4,60	24,5	1,76	238	3,20	21,8	7,6	293	2,58	45,1	2,06

Table 2. Latitude and cycle variations of extremal parameters.

noon

Minimum solar activity $F_{10,7}=75$, $R_z=10$, $K_p=0\div1$					Moderate solar conditions $F_{10,7}=175$, $R_z=100$, $K_p=2\div3$				
From N(h)-profiles ionogram Cadukhin, Soboleva 1978					From empirical model profiles ne(h) Soboleva 1972, 1973				Cadukhin, Soboleva, 1978				f_2/f_1
t	$10^{-3}(\frac{dNe}{dh})_{max}$ e/cm³·km	h_g km	$10^{-4}\cdot N_g$ e/cm³·km	f_{max} MHz	$10^{-3}(\frac{dNe}{dh})_{max}$ e/cm³·km	h_g km	$10^{-4}\cdot N_g$ e/cm³·km	f_{max} MHz	$10^{-3}(\frac{dNe}{dh})_{max}$ e/cm³·km	h_g km	$10^{-4}\cdot N_g$ e/cm³·km	f_{max} MHz	
0	5,23	220	34,3	37,6	6,60	278	59,5	42,7	19,0	282	94,5	72,1	1,69
16	21,0	258	47,7	75,3	20,6	263	77,0	75,8	20,0	292	145	74,3	0,99
30	13,7	218	44,6	60,8	12,4	238	53,1	57,9	24,0	292	141	81,2	1,40
50	14,0	193	25,2	61,1	7,60	198	34,4	45,3	14,0	252	75,0	59,6	1,32
60	8,00	193	32,0	46,1	-	-	-	-	-	-	-	-	-
69	8,9	193	27,0	48,9	7,80	193	32,6	45,8	9,00	240	42,4	49,4	1,10
89	3,3	197	16,8	29,5	3,40	183	15,1	30,2	10,00	213	28,9	51,2	1,72

midnight

0	(10-4)	214	41,2	51,9-33,2	11,8	232	18,8	56,3	20,1	272	79,3	73,8	1,31
16	4,80	257	16,1	36,1	-	-	-	-	25,2	297	100	82,2	-
30	3,40	212	3,00	30,1	4,20	263	7,93	33,7	23,0	312	50,0	78,9	2,34
50	2,2	243	4,60	24,5	1,98	223	1,58	23,0	7,60	315	21,2	45,6	1,98
60	0,6	228	3,20	13,1	-	-	-	-	-	-	-	-	-
69	(2-1,8)	223	5,60	23,2	0,94	248	8,40	16,1	2,70	305	17,2	23,6	1,47
89	2,3	207	6,30	24,9	2,80	234	26,6	27,4	5,0	305	29,8	37,1	1,35

*Numbers underlined correspond to high deflection.

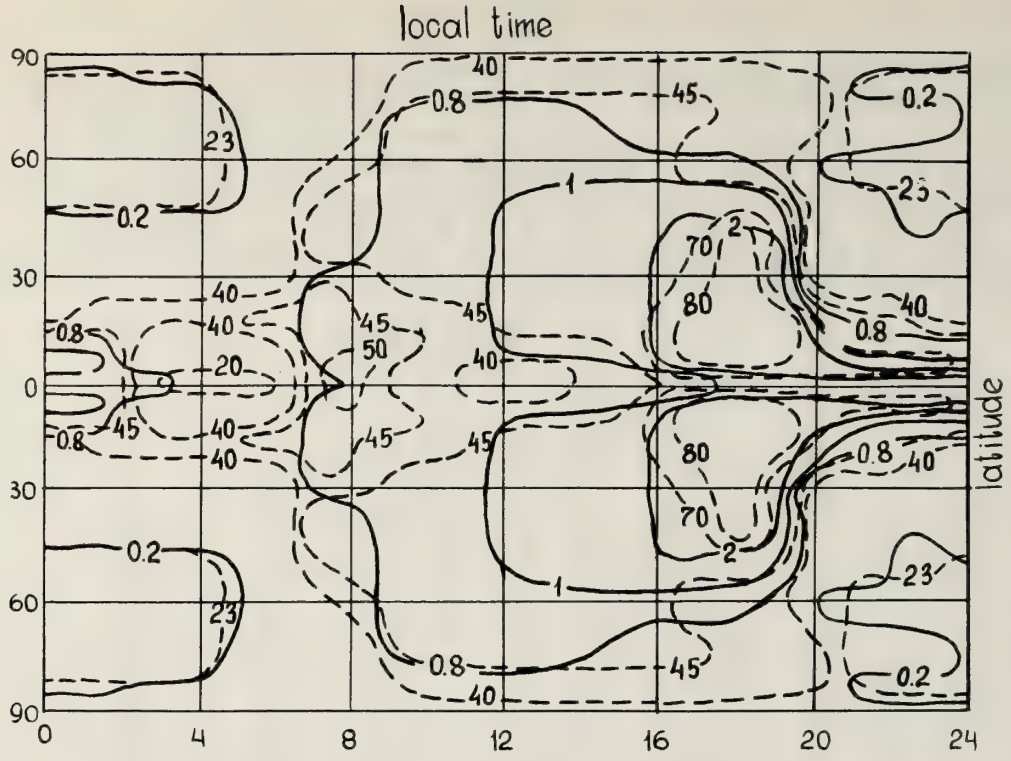


Figure 3. Isoline of parameters $10^{-4}(\frac{dNe}{dh})_{max}$ $\frac{e}{cm^3}$ · km (——); f_{max}, MHz (---).

Table 3. Seasonal variation of extremal ionosphere parameters based on tables of electron density for temperate latitudes.

Activity	R_z = 10				R_z = 100			
Month	3	6	9	12	3	6	9	12
				noon				
$10^{-3}(\frac{dN}{dh})_{max}$ e/cm³·km	8,40	6,00	7,40	10,0	21,6	9,00	11,7	19,1
h_g·Km	198	203	208	208	198	222	208	208
$N_g \cdot 10^{-4}$ e/cm³	24,4	25,8	21,2	28,2	57,8	51,5	49,4	54,0
f_{max}, MHz	47,6	40,2	44,6	51,8	76,1	49,4	56,2	71,6
				midnight				
$10^{-3}(\frac{dN}{dh})_{max}$ e/cm³·km	1,50	2,80	1,30	1,54	4,20	6,00	4,30	3,00
h_g·Km	265	225	268	275	288	252	273	303
$N_g \cdot 10^{-4}$ e/cm³	6,67	8,33	6,47	5,70	18,3	17,2	14,5	9,70
f_{max}, MHz	20,2	27,5	18,8	20,5	33,8	40,3	34,2	28,6

Source: K. Rawer and S. Rama Krishnan (1972).

the night hours $f_{max}/MUF = 3 \div 4$ at $\Phi = (16 - 50)°N$. This ratio is equal to 6 at $\Phi = 6°N$, $f_{max}/MUF = 7 \div 8$ at $\Phi = (6 - 50)°$ and 3.5 at the equator in the daytime.

2. USE OF THE F2-LAYER GEOMETRIC PARAMETERS FOR THE PREDICTION OF THE GRADIENT'S MAXIMUM

Calculating the parameters of the maximum of the vertical gradient from the analysis of ionograms is a tedious process. Some attempts have been made to obtain these parameters using the derivatives of an ionogram trace (Gulyaeva and Shlionsky, 1976). It was shown that the maximum of the gradient occurs at the plasma frequency, f_g, corresponding to the minimum of the second derivative of an ionogram trace, $(d^2h/df^2)_{min}$. However, the other parameters of this point, namely, the true height, h_g, and the maximum value of the gradient $(dN/dh)_{max}$ cannot be estimated directly from an ionogram.

To determine those, it is suggested to use the maps of the planetary distribution of the F2-layer parabolic model geometric parameters (Anufrieva and Shapiro, 1976) widely used for predicting N(h) profiles and h'f curves. The height of the gradient's maximum is determined by fitting a parabola to the peak of the F2 layer:

$$h_g = h_mF2 - y_mF2 \cdot \sqrt{1 - f_g^2/f_o^2F2} \qquad (2)$$

where h_mF2 is the peak height of the F2 layer, y_mF2 is the semithickness of the layer, foF2 is the critical frequency, and f_g is as defined above. For the same parabola, the expression of the vertical ionization gradient at the height, h_g, is as follows:

$$(dN/dh)_{max} = \frac{2}{y_mF2} \sqrt{N_m(N_m - N_g)} \qquad (3)$$

where N_m is the peak ionization at the F2 layer, and $N_g = 1.24 \times 10^4 f_g^2$ (f_g is in MHz and N is in cm^{-3}).

Thus, using the predictions of the F2 critical frequencies (Chernyshow and Vasilyeva, 1976); the geometric parameters, h_mF2 and y_mF2 (Anufrieva and Shapiro, 1976); the plasma frequency, f_g, at the point $(dN/dh)_{max}$ as derived from the ionograms; and equations (2) and (3), the planetary distribution of the height, h_g, and the gradient maximum value $(dN/dh)_{max}$ may be predicted.

REFERENCES

Anufrieva, T. A., and B. S. Shapiro (1976): Geometric parameters of the F2 layer of the ionosphere. Moscow, Nauka.

Chernishov, O. V., and T. N. Vasilyeva (1976): Prediction of the maximum usable frequencies. Moscow, Nauka.

Gulyaeva, T. L., and A. G. Shlionsky (1976): Identification of the maximum of the vertical ionization gradient from the derivatives of an ionogram trace. Geomagn. i Aeronomiya, 16:698.

Kadukhin, G. F., and A. G. Shlionsky (1970): Method to search N(h) profiles by analogous computer techniques. Geomagn. i Aeronomiya, 10:268.

Kadukhin, G. F., and T. N. Soboleva (1978a): Latitudinal variations of electron concentration for radio wave propagation. Proceedings of Propagation of Short Radio Waves, Moscow, IZMIRAN, p. 140.

Kadukhin, G. F., and T. N. Soboleva (1978b): Latitude-temporal variation of the main parameters of N(h) profiles of a quiet ionosphere. Proceedings of the Ray Tracing Characteristics of Radio Wave Propagation, Moscow, Nauka, p. 130.

Rawer, K., and S. Rama Krishnan (1972): Tentative tables of electron density for temperate latitudes. Freiburg, FRG.

Soboleva, T. N. (1972): The empirical model of the diurnal distribution of electron concentration $N_e(h)$ in a geomagnetically quiet ionosphere for temperate latitudes. Preprint no. 20, Moscow, IZMIRAN.

Soboleva, T. N. (1973): A latitude model of electron concentration distribution in a geomagnetically quiet ionosphere. Preprint no. 16, Moscow, IZMIRAN.

Shlionsky, A. G. (1971): About reflecting MUF of radio waves at the over-the-earth ionosphere. Preprint no. 12, Moscow, IZMIRAN.

Shlionsky, A. G. (1978): The influence of the main parameters and N(h) profiles on the characteristics of radio wave propagation in ionospheric ducts. Proceedings of Ionospheric Research 26:80.

MODEL CALCULATIONS OF ELECTRIC FIELDS AND CURRENTS IN THE HIGH-LATITUDE E REGION FOR PREDICTIONS OF IONOSPHERIC VARIATIONS

S. Matsushita and Y. Kamide*
High Altitude Observatory, NCAR
Boulder, Colorado 80307, U.S.A.

Model calculations of ionospheric electric fields and currents in relation to field-aligned currents are briefly discussed to aid in predictions (at least for development of prediction techniques) of ionospheric variations caused by the fields and currents.

1. INTRODUCTION

Electric fields and currents in the high-latitude E region are important physical parameters for ionospheric variations, because they produce electromagnetic drifts and joule heating which cause ionospheric height and density changes (e.g., Anderson and Matsushita, 1974; Richmond and Matsushita, 1975; Matsushita, 1976; many references therein). Accordingly, predictions of electric fields and currents for various geomagnetic conditions may contribute greatly to ionospheric predictions. In order to attain this goal, model calculations of ionospheric electric fields and currents in relation to field-aligned currents for both quiet periods and substorms (Kamide and Matsushita, 1979a, b) may deserve a brief introduction here.

By changing ionospheric conductivity distributions as well as field-aligned current densities and configurations, which depend upon geomagnetic conditions, various patterns for electric field and current distributions in the ionosphere have been obtained. In other words, electric fields and currents can be estimated (or predicted) as soon as the conductivity distributions and field-aligned currents are either observed directly or assumed from geomagnetic conditions. (Conversely, field-aligned currents can roughly be estimated from electric field and current observations with a conductivity model.)

Many diagrams of electric equi-potential distributions and of electric current vectors in the ionosphere are placed together specially for the present report to aid in predictions. Some of the diagrams have never been published before. Two examples of electric field vector distributions are provided to help the readers in estimating the electric fields from equi-potential diagrams.

*Present address: Kyoto Sangyo (Industrial) University, Kamigamo, Kita-Ku, Kyoto 603, Japan

2. CONDUCTIVITY MODELS

For the centered-dipole spherical earth in the equinoctial season, θ is colatitude and λ is longitude measured eastward from midnight. Height-integrated conductivities are given by $\Sigma_{\theta\theta}$, $\Sigma_{\lambda\lambda}$, and $\Sigma_{\theta\lambda}$, where $2\Sigma_{\theta\theta}=\Sigma_{\theta\lambda}/\sin\Phi$ and $2\Sigma_{\lambda\lambda}=\Sigma_{\theta\lambda}\sin\Phi$. Here, Φ is the inclination angle of a geomagnetic field line with respect to the horizontal ionosphere. They are assumed to have the following values and distributions for various models:

1. Simplest Model No conductivity variation with θ and λ (see straight lines for Model 1 in Figure 1).

2. Very Quiet Gradually varying conductivity distributions with no local enhancement (see smooth curves for Model 2 in Figure 1).

3. Quiet Exponentially-distributed enhanced conductivities at ($20^o<\theta<30^o$, $-90^o<\lambda<90^o$) with a peak at ($\theta=22.5^o$, $\lambda=0^o$) (see curves for Model 3 in Figure 1).

4. Typical Substorm As shown in Figure 2, four auroral regions are as follows:
   - Region I $20^o<\theta<25^o$ & $0^o<\lambda<90^o$ with a peak value of 10 mhos for $\Sigma_{\theta\lambda}$ at ($\theta=22.5^o$, $\lambda=+45.0^o$)
   - Region II $20^o<\theta<25^o$ & $-90^o<\lambda<0^o$ with a peak value of 40 mhos for $\Sigma_{\theta\lambda}$ at ($\theta=22.5^o$, $\lambda=-45.0^o$)
   - Region III $25^o<\theta<30^o$ & $0^o<\lambda<90^o$ with a peak value of 20 mhos for $\Sigma_{\theta\lambda}$ at ($\theta=27.5^o$, $\lambda=+45.0^o$)
   - Region IV $25^o<\theta<30^o$ & $-90^o<\lambda<0^o$ with a peak value of 20 mhos for $\Sigma_{\theta\lambda}$ at ($\theta=27.5^o$, $\lambda=-45.0^o$).

5. Field-Aligned Current Intensity Variations Same as Model 4.

6. Field-Aligned Current Location Shifts Same as Model 4.

7. Conductivity Variations
   - 7.1 Same as Model 4 except $\Sigma_{\theta\lambda}/\Sigma_{\theta\theta}=4$.
   - 7.2 Same as Model 4 except $\Sigma_{\theta\lambda}=0$ mho at Region IV.

8. Additional Field-Aligned Current Same as Model 4.

The exponentially-distributed enhanced conductivity can be shown by $\Sigma_{\theta\lambda}=\Sigma(\max)\exp\left[-(\theta-\theta'_o)^2/D_\theta^2-(\lambda-\lambda'_o)^2/D_\lambda^2\right]$, where ($\theta'_o$, λ'_o) gives the center location of the enhanced conductivity region at which $\Sigma_{\theta\lambda}$ is maximum. The constants D_θ and D_λ are taken in such a way that $\Sigma_{\theta\lambda}$ becomes approximately 0.2 $\Sigma(\max)$ at latitudinal and longitudinal boundaries.

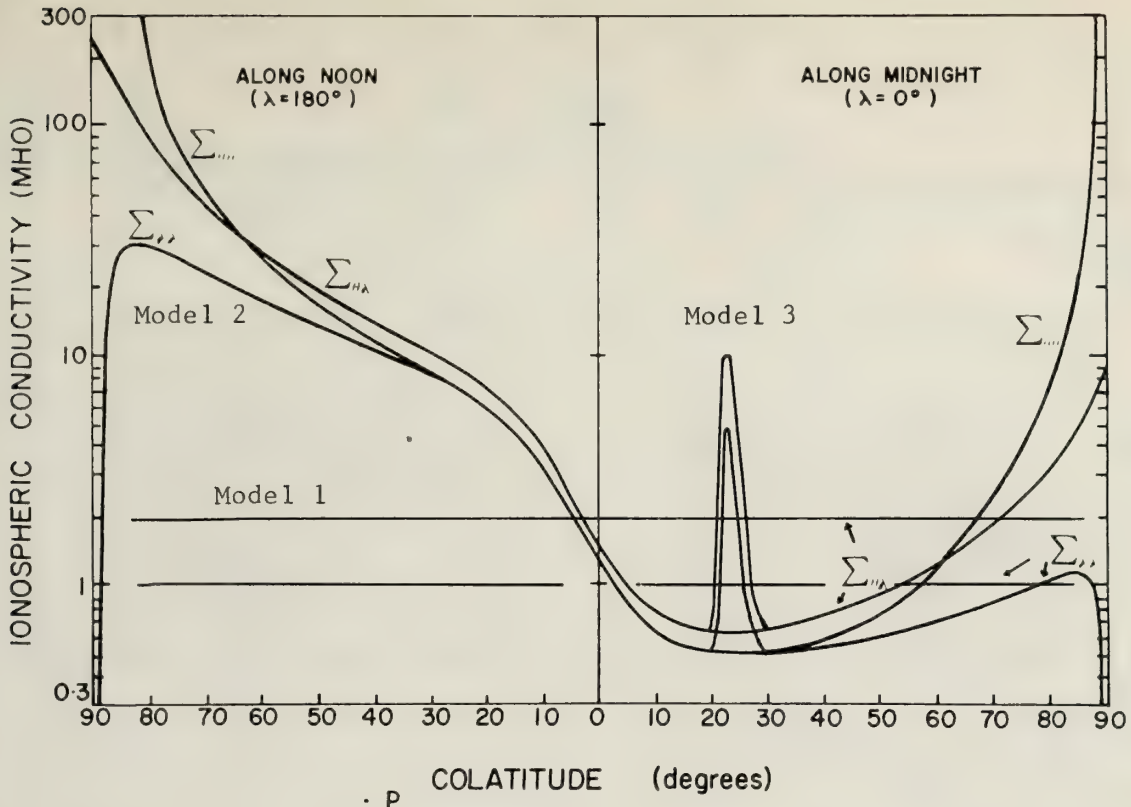


Fig. 1. Height-integrated conductivity distributions along the noon-midnight meridian for Models 1, 2, and 3.

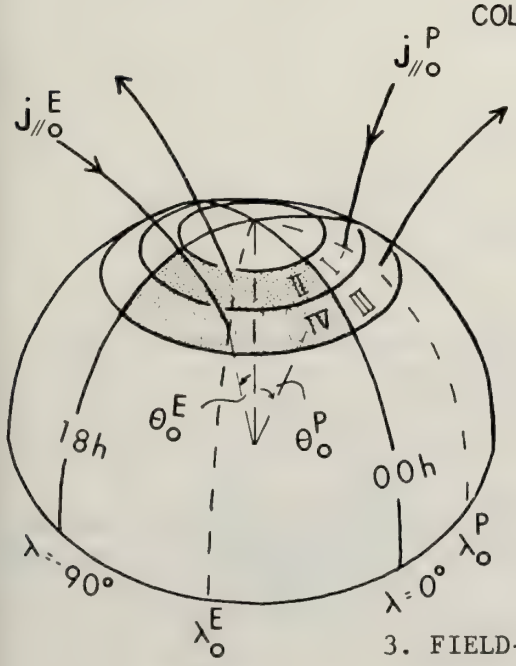


Fig. 2. Schematic diagram to show the field-aligned currents $j_{||}$ and auroral regions I, II, III, and IV with different amounts of electric conductivities.

3. FIELD-ALIGNED CURRENT MODELS

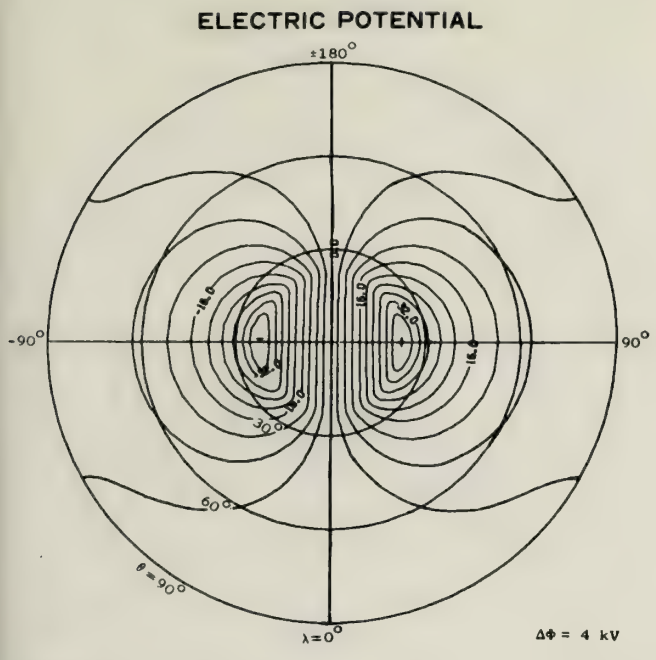
As shown in Figure 2, the maximum current density for the poleward-half (or equatorward-half) of the exponentially-distributed field-aligned currents is $j_{||o}^{P}$ (or $j_{||o}^{E}$) at the colatitude θ_o^P (or θ_o^E) and the longitude λ_o^P (or λ_o^E) with the total downward field-aligned current intensity $I_{||}^{P}$ (or $I_{||}^{E}$). Actual numbers of these parameters for the eight main models discussed in section 2 are shown as follows:

	θ_o^P	λ_o^P	$j_{\|\|o}^P$ $x10^{-6}$ A/m^2	$I_{\|\|}^P$ $x10^6$ A	θ_o^E	λ_o^E	$j_{\|\|o}^E$ $x10^{-6}$ A/m^2	$I_{\|\|}^E$ $x10^6$ A
1. Simplest Model	22.5°	90.0°	0.1	0.19	-	-	-	-
2. Very Quiet	"	"	"	"	-	-	-	-
3. Quiet								
3.1 Slight auroral enhancement	"	"	0.2	0.38	-	-	-	-
3.2 Double $I_{\|\|}$	"	"	"	"	27.5°	-90.0°	0.1	0.21
4. Typical Substorm	"	45.0	2.0	1.9	"	-45.0	1.0	1.1
5. $I_{\|\|}^P = I_{\|\|}^E$	"	"	"	"	"	"	1.7	1.9
6. λ_o Location Shifts								
6.1 Intense substorm	"	67.5	"	2.8	"	-67.5	1.0	1.6
6.2 Expansive phase	"	90.0	"	3.7	"	-45.0	"	1.1
6.3 Recovery phase	"	45.0	"	1.9	"	-90.0	"	2.0
7. Σ Variations								
7.1 $\Sigma_{\theta\lambda}/\Sigma_{\theta\theta} = 4$	"	"	"	"	"	-45.0	"	1.1
7.2 $\Sigma_{\theta\lambda} = 0$ at IV	"	"	"	"	"	"	"	"
8. Additional $I_{\|\|}$	"	"	"	1.9	"	"	"	"
($=4x10^5$ A) at $\theta=19.0°$				(morning)				
$\lambda=-45.0°$				2.3 (evening)				

4. RESULTS

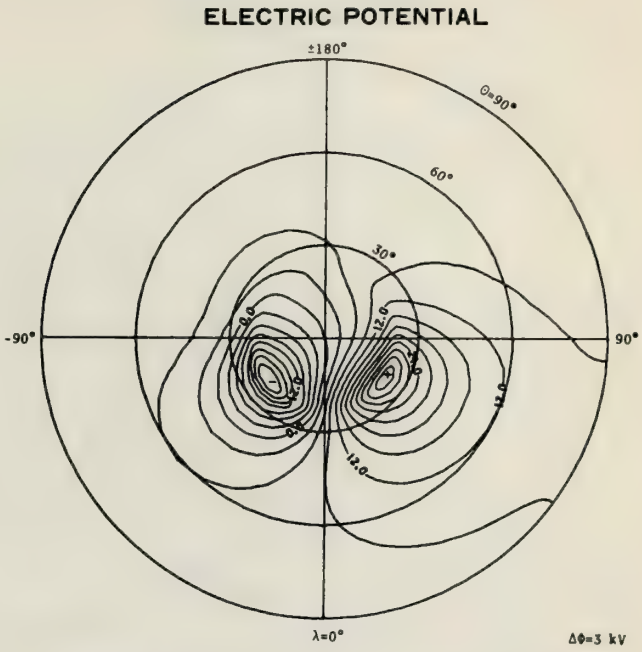
The steady-state equations for electric current conservation are solved numerically for the various models of the electric conductivity and field-aligned current mentioned in the previous sections (see section 2 in Kamide and Matsushita, 1979a for the detail). Obtained results of this model calculation are as follows:

Model	Electric Equi-Potential Distribution	Electric-Field Vector Distribution	Ionospheric Current Vector Distribution
1	Fig. 3		Fig. 17
2	Fig. 4	Fig. 15	Fig. 18
3.1	Fig. 5		Fig. 19
3.2	Fig. 6		Fig. 20
4	Fig. 7		Fig. 21
5	Fig. 8	Fig. 16	Fig. 22
6.1	Fig. 9		Fig. 23
6.2	Fig. 10		Fig. 24
6.3	Fig. 11		Fig. 25
7.1	Fig. 12		Fig. 26
7.2	Fig. 13		Fig. 27
8	Fig. 14		Fig. 28



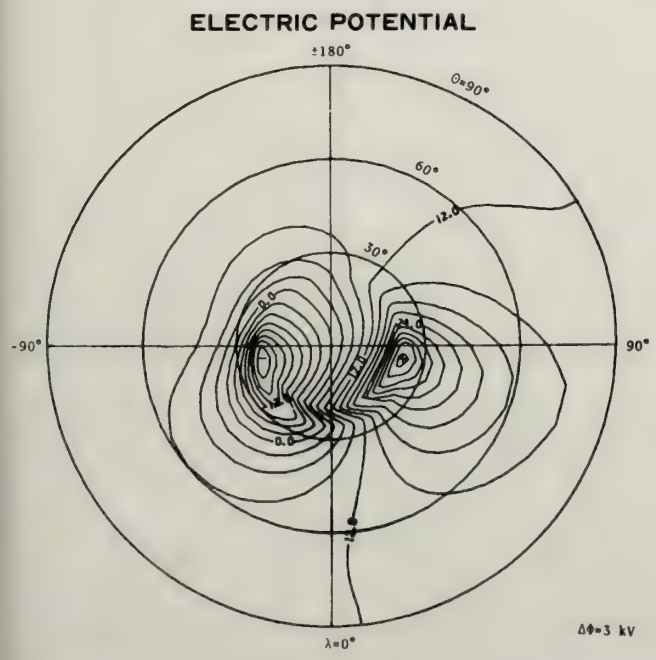
Simple Case

Fig. 3



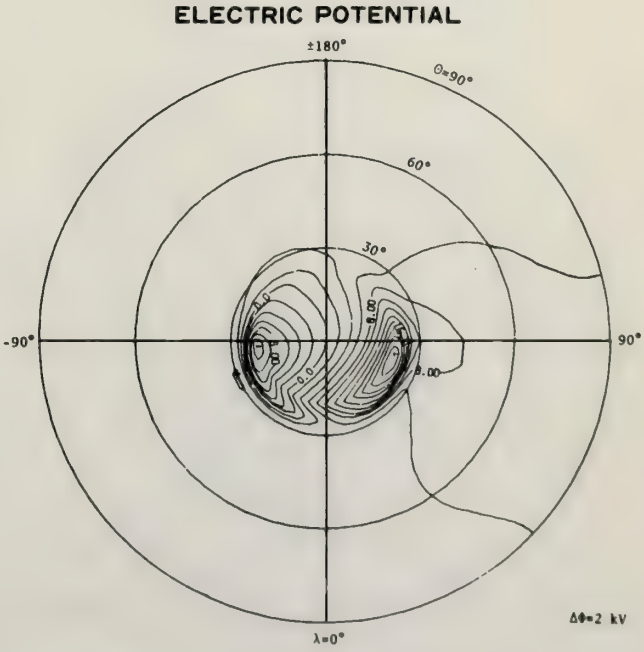
Extremely Quiet

Fig. 4



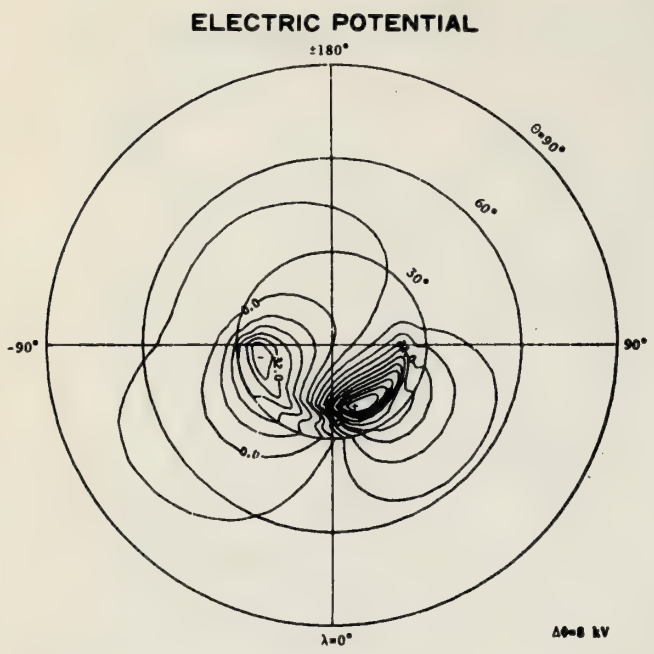
Quiet Case with Slight
Auroral Enhancement

Fig. 5



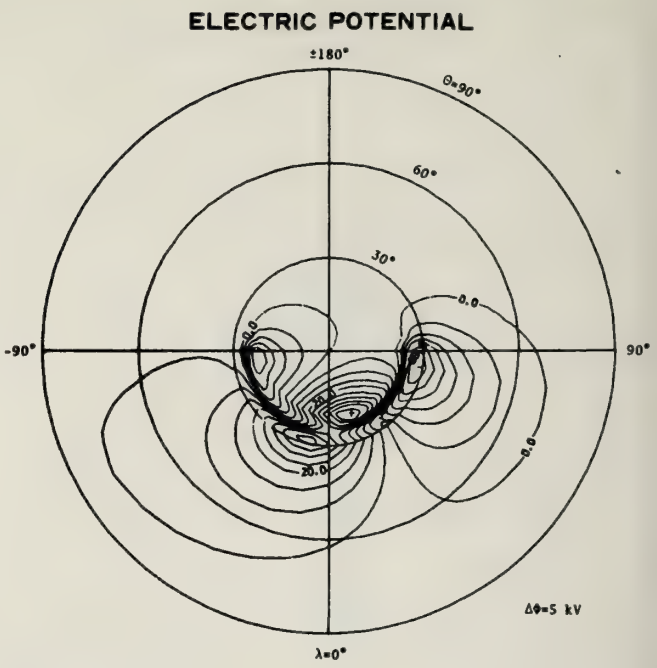
Quiet Case: Double Field-Aligned
Currents

Fig. 6



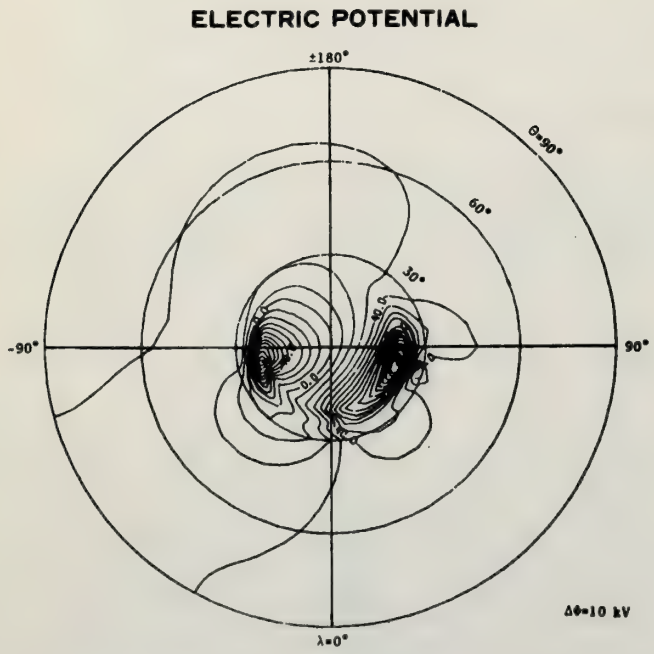
Typical Substorm

Fig. 7



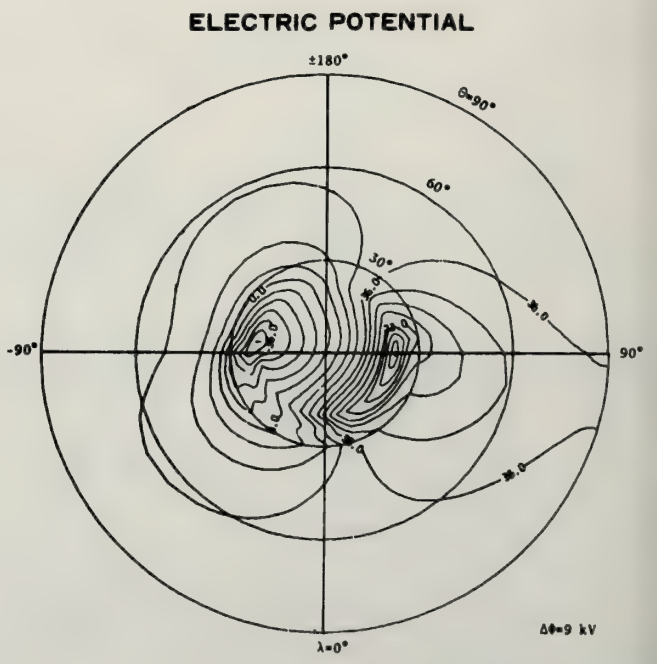
$I_{\parallel}P/I_{\mu}E = 1$

Fig. 8



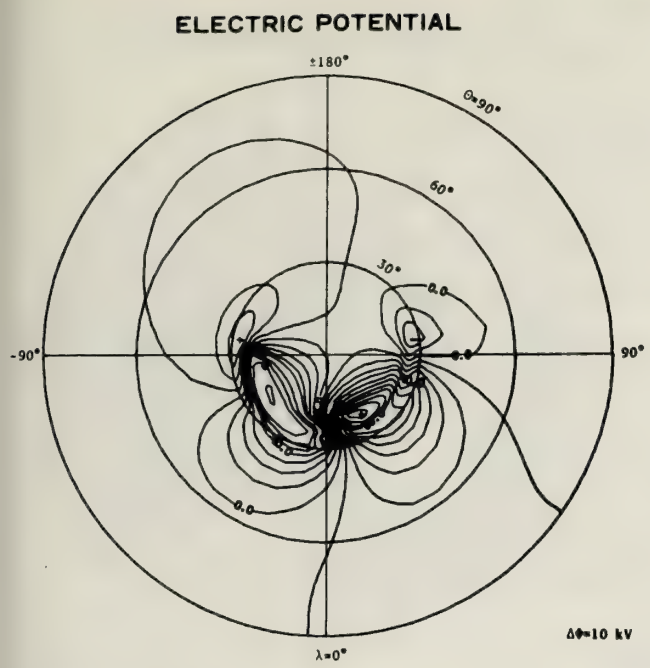
Field-Aligned Current Center $\lambda=67.5^{\circ}$

Fig. 9



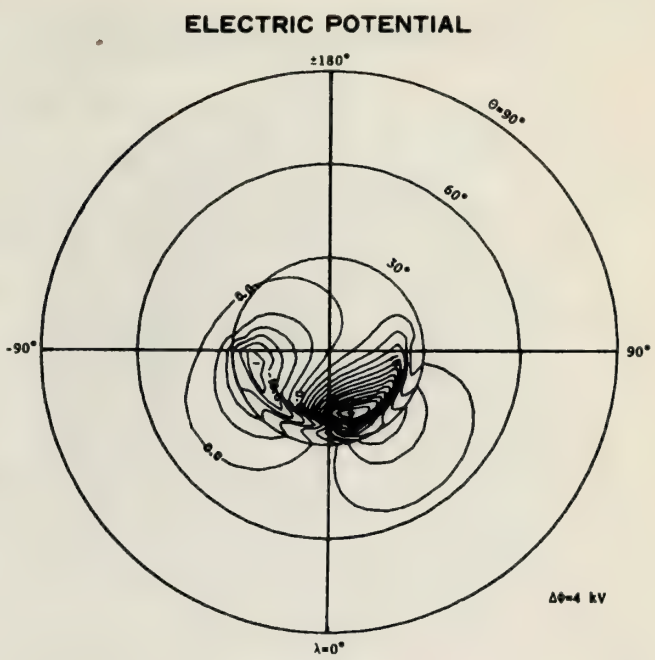
Different Longitudes of Poleward-side and Equatorward-side Field-Aligned Currents

Fig. 10



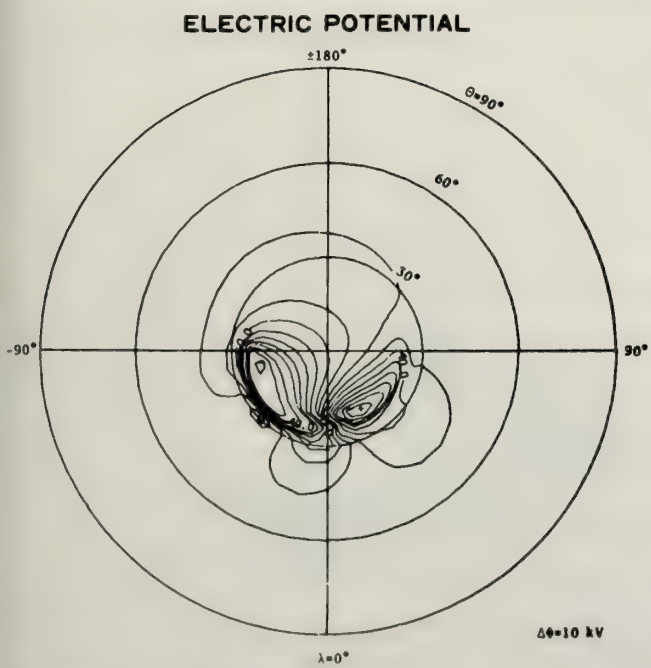
Different Longitudes of Poleward-side and Equatorward-side Field-Aligned Currents

Fig. 11



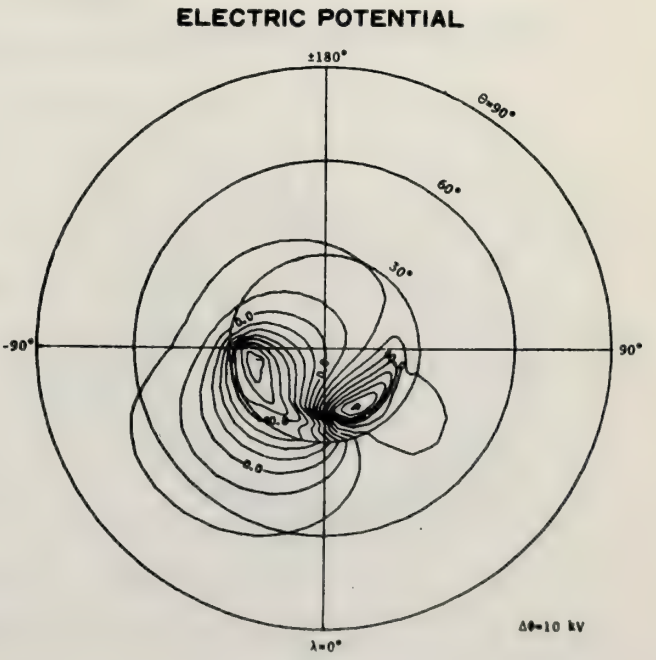
Hall to Pedersen Ratio ~ 4

Fig. 12



No Conductivity Enhancement in Eastward Electrojet Region

Fig. 13



Downward Field-Aligned Current at Poleward Edge of Evening Oval

Fig. 14

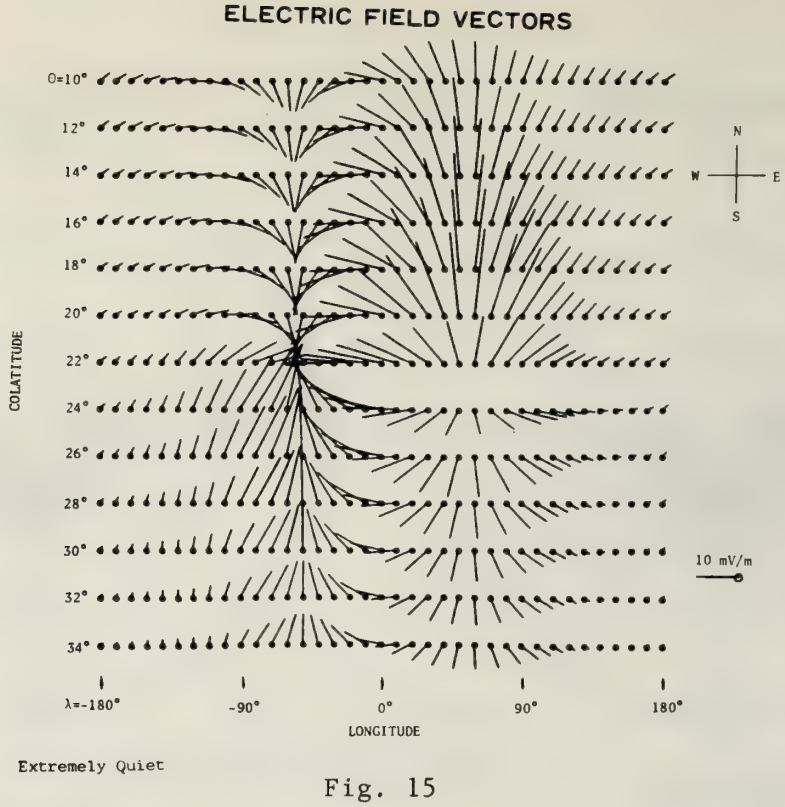

ELECTRIC FIELD VECTORS
θ=10°
12°
14°
16°
18°
20°
22°
24°
26°
28°
30°
32°
34°
COLATITUDE
N
W
E
S
10 mV/m
λ=-180°
-90°
0°
90°
180°
LONGITUDE
Extremely Quiet

Fig. 15

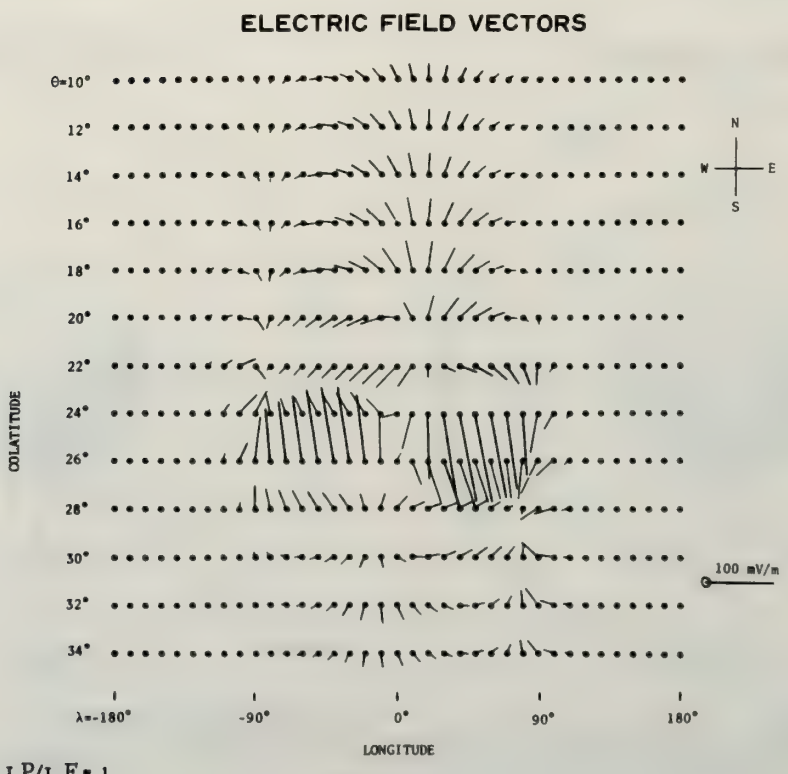
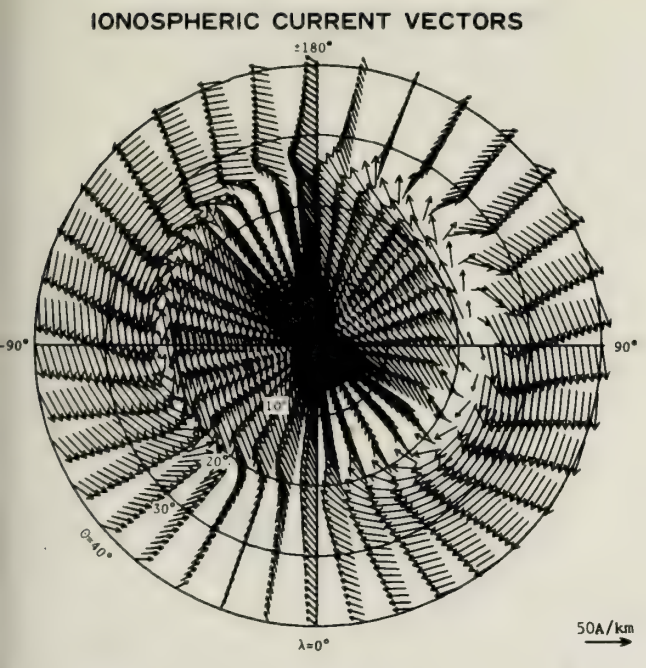
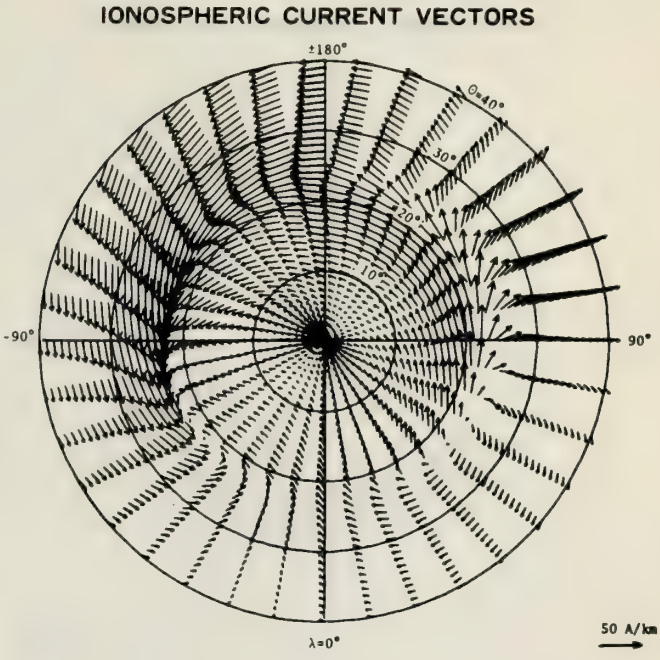

ELECTRIC FIELD VECTORS
θ=10°
12°
14°
16°
18°
20°
22°
24°
26°
28°
30°
32°
34°
COLATITUDE
N
W
E
S
100 mV/m
λ=-180°
-90°
0°
90°
180°
LONGITUDE
$I_H P/I_H E = 1$

Fig. 16



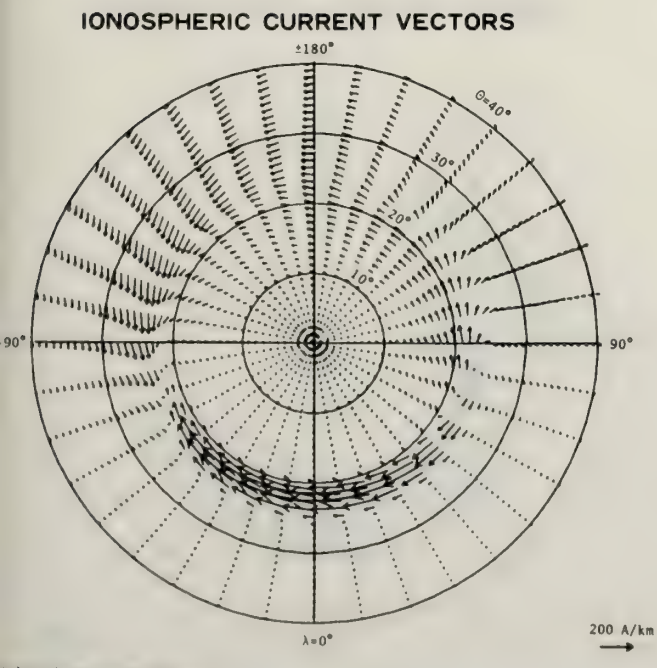
Simple Case

Fig. 17



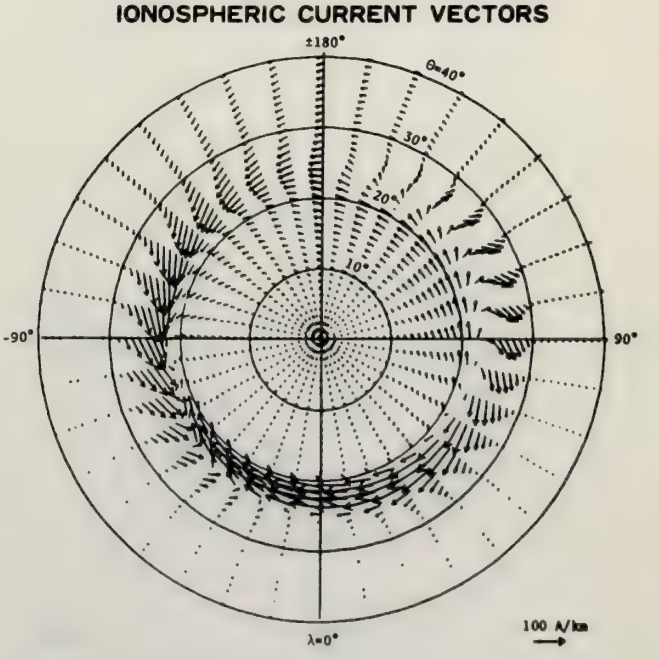
Extremely Quiet

Fig. 18



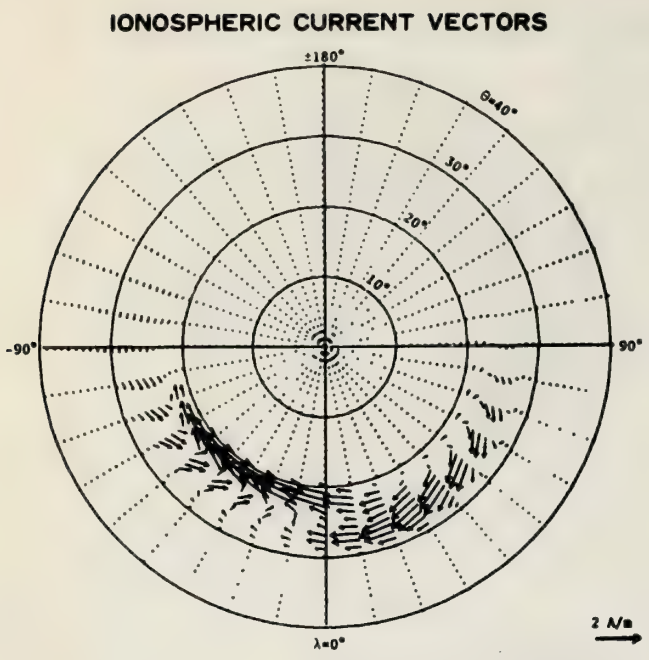
Quiet Case with Slight Auroral Enhancement

Fig. 19



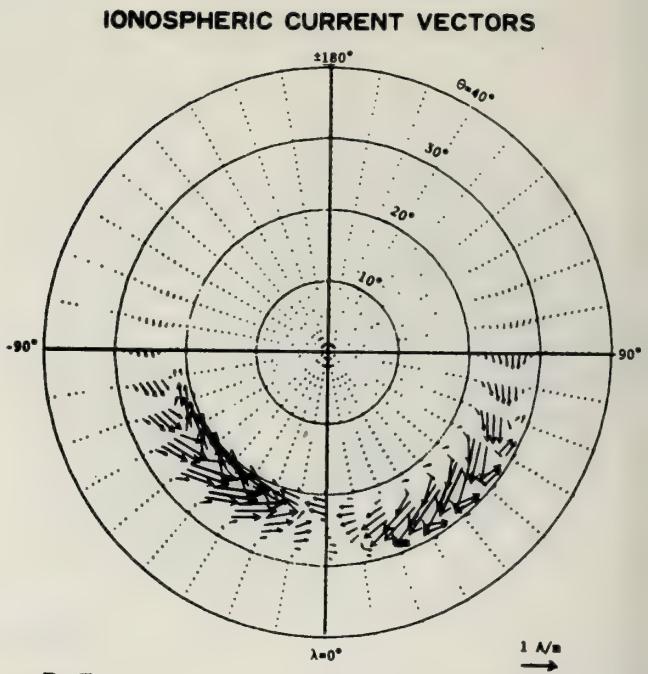
Quiet Case: Double Field-Aligned Currents

Fig. 20



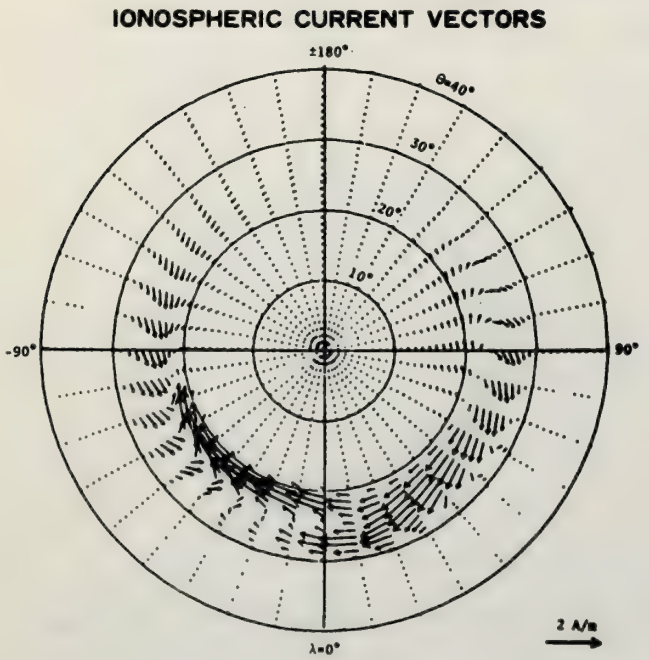
Typical Substorm

Fig. 21



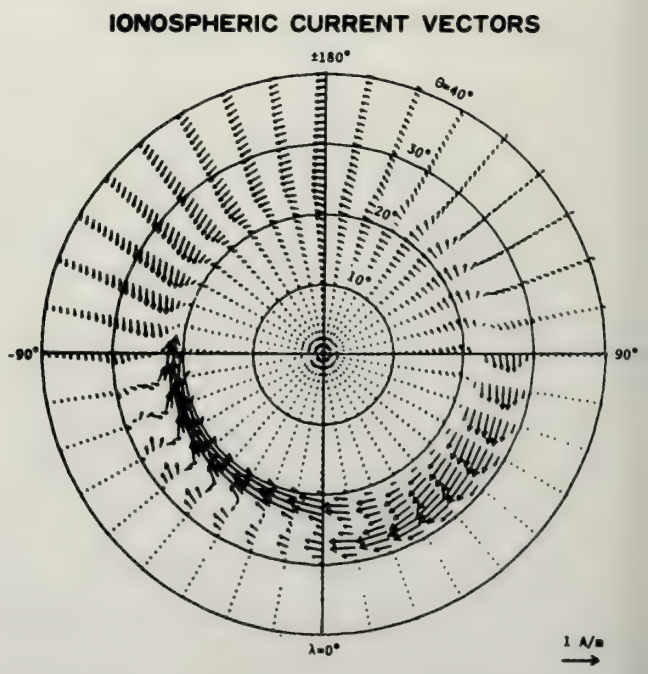
$I_1^P/I_1^E = 1$

Fig. 22



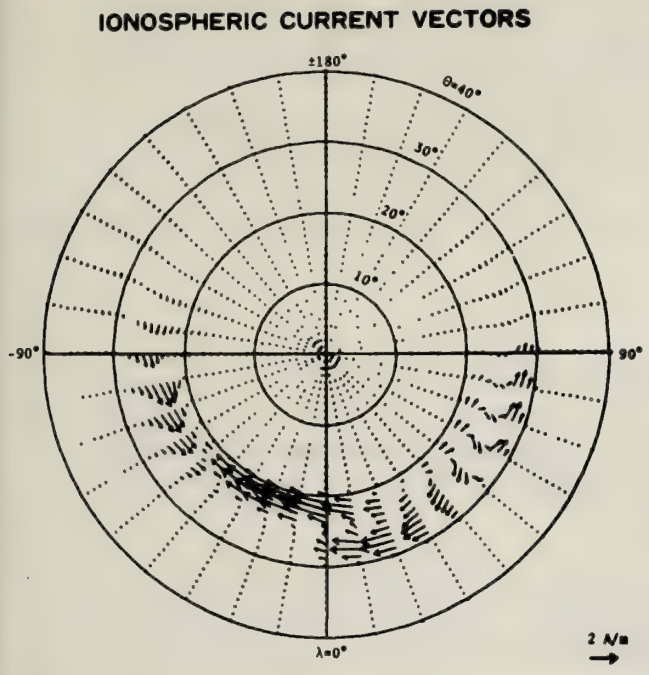
Field-Aligned Current Center $\lambda=67.5^{\circ}$

Fig. 23



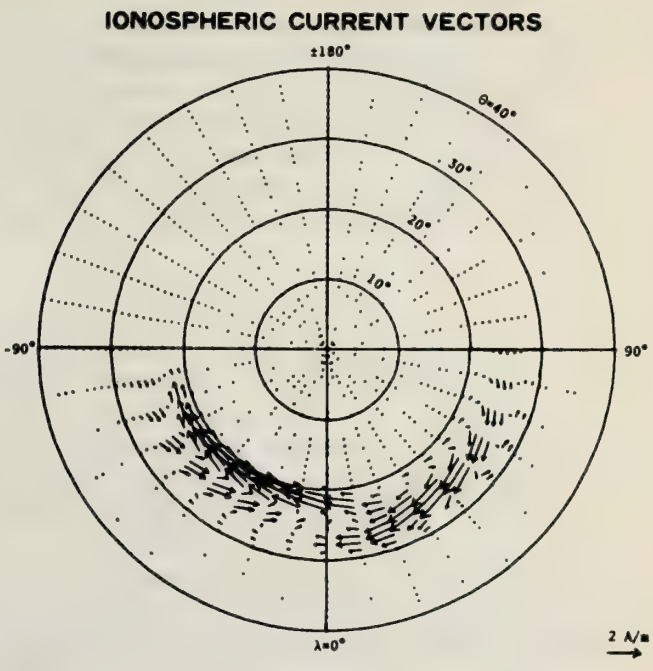
Different Longitudes of Poleward-side and Equatorward-side Field-Aligned Currents

Fig. 24



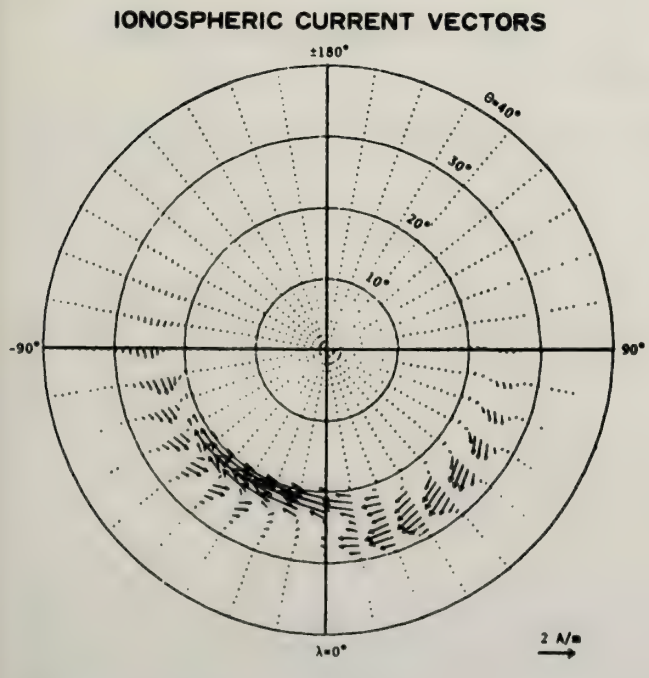
Different Longitudes of Poleward-side and Equatorward-side Field-Aligned Currents

Fig. 25



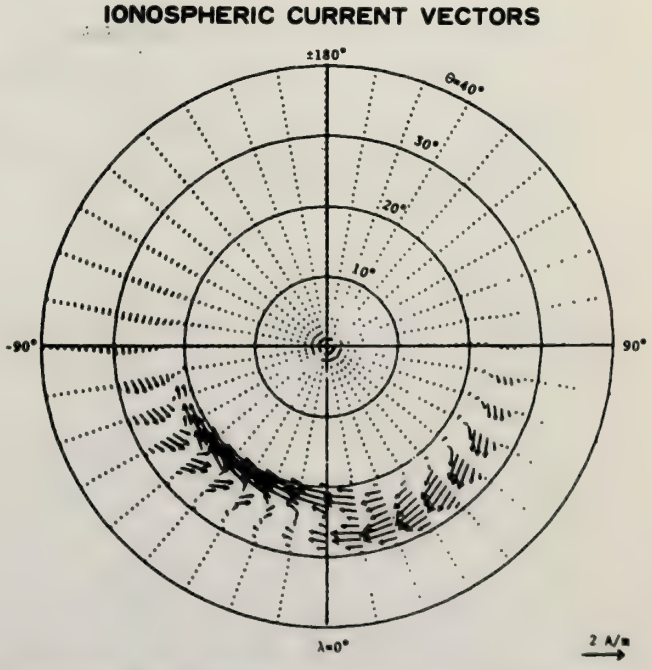
Hall to Pedersen Ratio ~ 4

Fig. 26



No Conductivity Enhancement in Eastward Electrojet Region

Fig. 27



Downward Field-Aligned Current at Poleward Edge of Evening Oval

Fig. 28

5. CONCLUSION

Since computed results are in satisfactory agreement with observations, those diagrams shown for different geomagnetic conditions may aid in predictions. Studies of time sequences of the electric potential and current-vector distributions in the form of movies are under preparation.

We are grateful to Drs. T. Holzer, A. D. Richmond, and R. G. Roble for their helpful discussions and to Dr. J. C. Adams for his able assistance in computer programming during an early phase of the present study. The National Center for Atmospheric Research is sponsored by the National Science Foundation.

REFERENCES

Anderson, D. N., and S. Matsushita (1974): Seasonal differences in the low-latitude F2-region ionization density caused by $\bar{E}x\bar{B}$ drift and neutral wind. J. Atmos. Terr. Phys., 36:2001.

Kamide, Y., and S. Matsushita (1979a): Simulation studies of ionospheric electric fields and currents in relation to field-aligned currents, 1. Quiet periods. J. Geophys. Res., submitted.

Kamide, Y., and S. Matsushita (1979b): Simulation studies of ionospheric electric fields and currents in relation to field-aligned currents, 2. Substorms. J. Geophys. Res., submitted.

Matsushita, S. (1976): Ionospheric and thermospheric responses during August 1972 storms - A review. Space Sci. Rev., 19:713.

Richmond, A. D., and S. Matsushita (1975): Thermospheric response to a magnetic substorm. J. Geophys. Res., 80:2839.

STATISTICAL PREDICTION OF E_s-LAYER PARAMETERS AND ECHO-SIGNAL CHARACTERISTICS

T. S. Kerblay, G. N. Nosova
Institute of Terrestrial Magnetism, Ionosphere and Radio Wave Propagation of the Academy of Sciences of the USSR
Moscow Region, USSR

To calculate and predict E_s echo-signal characteristics, an analytical expression describing the spatial structure of the E_s-layer is suggested. On the basis of published experimental results, statistical estimations of the model parameters have been obtained.

An empirical-statistical basis is expedient to use at present when making predictions of the E_s-layer since an unambiguous relationship between the solar emission, the aeronomical and other characteristics of the ionospheric E-layer, and the parameters of the E_s-layer has not been established. Further, the significant variability of the E_s-layer parameters makes it necessary to apply the statistical method in their description.

To make predictions for the E_s-layer, therefore, a model should be selected that can satisfactorily describe the spatial structure of the layer and the empirical and statistical variations in the model parameters. It should be noted that the number of parameters that may characterize the ionization intensity in the E_s-layer and its spatial distribution is much higher than the number of parameters for the regular layers.

The following expression has been adopted (Kerblay and Nosova, 1976) to use when simulating the large-scale structure (ℓ of about the order of 100 km) of the E_s-layer to calculate the characteristics of signal reflected from that layer:

$$N = N_o \frac{4e^{hZ}}{(1+e^{hZ})^2}\left[1 - K\sin\left(\frac{2\pi X}{\ell_1} + \phi\right)\cos\left(\frac{2\pi Y}{\ell_2} + \psi\right)\right]^2 \qquad (1)$$

where X, Y, and Z are the Cartesian coordinates with the origin at the maximum of the layer; N_o is the mean electron number density in the layer maximum which may be estimated by f_bE_s, $N_o = A(f_bE_s)^2$; K is the value characterizing the amplitude of plasma frequency fluctuations in a horizontal plane; ℓ_1 and ℓ_2 are the scales of inhomogeneity along the X and Y axes, respectively; ϕ and ψ are the phase shifts determining the position of the periodic structure relative to the coordinate origin.

The distribution of the electron number density in the layer as a function of altitude is represented by the model of thin layer (the Epstein layer). The advantage of the model is that it provides an analytical solution for the reflection coefficient that may be used to estimate the energy characteristics of a signal reflected from the layer.

The half-thickness of such a layer, ξ, is related to the parameter h by $\xi = 0.56\ \pi/h$.

Thus, the prediction of the E_s-layer includes the prediction of the parameters contained in expression (1), namely N_o, ℓ_1, ℓ_2, h, K, ϕ, and ψ. The statistical estimates of these parameters have been obtained by analyzing the published experimental results on the basis of the methods of vertical sounding, backscattering, incoherent scattering, etc. The distribution laws were determined, and the most probable values and variances were estimated for the various parameters.

The value N_o is estimated by using one of the probability-statistic methods for determining the frequency parameters of the E_s-layer (f_oE_s and f_bE_s) (Kerblay, 1964; Mikhailova and Ovezgeldyev, 1976; Minullin and Eliseeva, 1976). Such methods make it possible to determine the diurnal, seasonal, and global variations in the occurrence probabilities of f_oE_s and f_bE_s above a set value. Since clear variations of f_oE_s and f_bE_s with the solar cycle have not been found, the calculation methods give the values averaged over the solar cycle. According to modern concepts, the maximum electron number density in the E_s-layer is determined through f_bE_s.

We shall refrain from dwelling on the well-known diurnal, seasonal, and global variations of f_bE_s. The parameter characterizing the layer thickness ξ has been obtained mainly from the published results of rocket measurements. Figure 1 shows the histogram of the ξ distribution for 93 observations. It follows from the figure that the most probable value of ξ is of the order of 1 km, and $\overline{\xi} = 1.2$ km.

The time variations in f_bE_s at vertical soundings permit the value of K to be estimated by assuming that the time variations are relevant to the passage of a series of inhomogeneities over the measurement point at a velocity V = 80-100 m s^{-1}.

The value of K was determined by using the simultaneous measurements of E_s from 1972, when more frequent vertical soundings with 10- and 15-min observations of the E_s-layer were carried out at the European network of stations. (The analysis was made using the data from the stations listed in Table 1.)

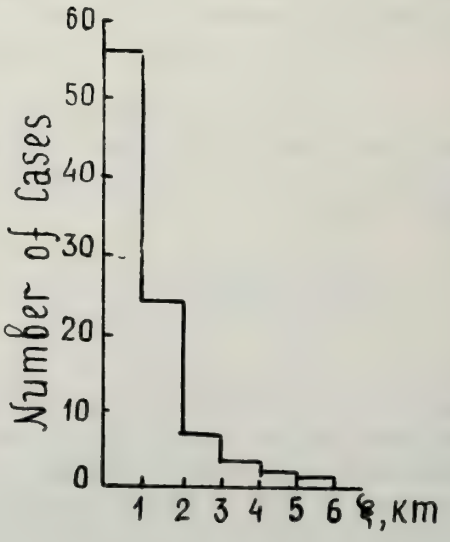


Figure 1. Distribution of semi-thickness of layer E_s.

Table 1. Measurement stations by location.

Station	φ	λ	ϕ
Moscow	55.5	37.9	50.8
Rugen	54.6	13.6	54.5
De Bilt	52.1	5.2	54.0
Slough	51.5	0.6	54.3
Dourbes	50.6	4.6	56.3
Kiev	50.5	30.5	47.5
Pruhonice	50.5	14.5	60.4
Freiburg	48.1	7.8	48.4
Rostov-Don	47.0	41.5	42.5
Garchi	47.3	3.1	49.6
Graz	47.1	15.5	47.0
Bekescsaba	46.7	21.2	46.0

Note: ϕ - geomagnetic latitude
φ - geographic latitude
λ - geographic longitude

Figure 2 shows the histogram based on observations of f_bE_s from the middle-latitude ionospheric stations listed in Table 1. The histogram presents the most probable value of K = 0.25 and $\overline{K}$ = 0.3.

The scales of inhomogeneous structure ℓ_1 and ℓ_2 can also be characterized. It should first be noted that the two scales, ℓ_1 (lateral) and ℓ_2 (longitudinal), of the structure have been inserted to increase the generality of expression (1). It is impossible to obtain the two scales from the available experimental results or theoretical works because of the absence of a unified opinion about the degree of anisotropy of the large-scale structure of E_s and about the orientation of the inhomogeneities. It is necessary, therefore, to characterize only the mean value $\overline{\ell} = 1/2\ (\ell_1 + \ell_2)$. $\overline{\ell}$ is determined from several sources, including radar measurements, backscattering, incoherent scattering, vertical sounding, etc. The data from the various sources are in a satisfactory agreement and give $\overline{\ell}$ ranging from 100 km to 1000 km, with the most probable values in the 100-300 km region. Figure 3 presents the histogram of ℓ obtained from the data of vertical sounding. The periods with increased f_bE_s were scaled to ℓ on the assumption that they are the effect of passage of the E_s inhomogeneity over the station at a velocity of 100 m s^{-1}. Similar values of ℓ have been obtained by comparing the moments of

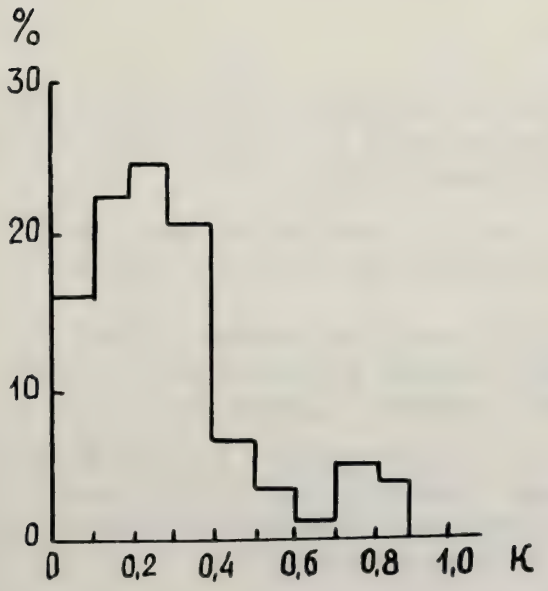


Figure 2. Distribution of parameter K.

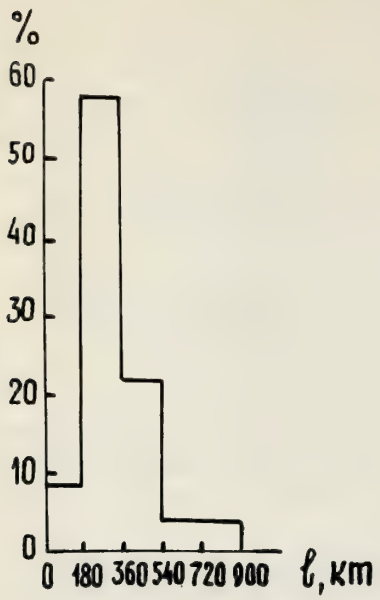


Figure 3. Distribution of horizontal size of E_s.

simultaneous observations of E_s in vertical and inclined soundings (Kerblay et al., 1978a). When the radio wave propagation characteristics are calculated, the values of ϕ and ψ are determined as functions of the position of the E_s-layer inhomogeneity center relative to the region of radio signal reflection. The method for calculating the trajectory characteristics of the signal reflected from the E_s-layer is based on the above described model using the mathematical formalism developed at the laboratory for calculating the ray trajectories in three-dimensionally inhomogeneous medium (see the reports of Kerblay et al., 1978b).

The method developed as applied to the E_s-layer permits the distance D, elevations Δ_1 and Δ_2 and azimuth deviation to be calculated at the parameters of the layer model set statistically or determined experimentally in vertical soundings.

Calculation results were compared with the values measured along the lines of inclined sounding on the basis of published data (Miya and Sasaki, 1966) and using the experimental results obtained along the Arkhangelsk-Kazan path. Despite the statistical setting of the majority of model parameters, a satisfactory agreement has been obtained between the calculated results and experimental data, which indicates the developed method may be used to estimate the characteristics of a signal reflected from the E_s-layer.

REFERENCES

Kerblay, T. S., and G. N. Nosova (1976): About the model of the large-scale spatial structure of the middle-latitude sporadic E. In: The Physics and Empirical Simulation of the Ionosphere, Nauka, Moscow, 104.

Kerblay, T. S. (1964): Instruction Manual: Calculations of the Short Wave Radio Communication Frequencies Reflected from the E_s-layer. Nauka, Moscow.

Kerblay, T. S., R. A. Kurganov, R. G. Minullin, and G. N. Nosova (1978a): Horizontal sizes and velocities of the E_s-clouds by experiment carried out on the radio paths Salekhard-Tumen. Ionospheric Research, 26:64.

Kerblay, T. S., G. N. Nosova, R. G. Minullin, R. A. Kurganov, A. M. Nasirov, and N. V. Leshenko (1978b): Experimental investigations of E_s-signals for radio paths about 1000 km long. International Symposium on Radio Waves and Ionosphere, URSI, Helsinki, Finland, August 21.

Mikhailova, G. V., and O. O. Ovezgeldyev (1976): An empirical model of the middle-latitude sporadic E. Izv. Akad. Nauk Turkm. SSR, ser. fiz-thehn., Khim, geol., 3:65.

Minullin, R. G., and T. Ya. Eliseeva (1976): Regularities of integral distributions of the top frequencies of the sporadic E. Geomagn. i Aeron., 16(4):726.

Miya, K., and T. Sasaki (1966): Characteristics of ionospheric E_s propagation and calculation of E_s signal strength. Radio Science 1(1):99.

FORECAST OF CRITICAL FREQUENCY AND HEIGHT OF MAXIMUM DENSITY OF THE MID-LATITUDE E-LAYER

Ivanov-Kholodny G.S. and Nusinov A.A.
Institute of Applied Geophysics, Goscomhydromet
Moscow
USSR

The scheme of forecasting of E-layer critical frequency, height of maximum and scale height is proposed. The scheme is based on main physical processes responsible for the layer formation and includes Solar ultraviolet and X-ray emission fluxes as initial parameters.

The methods of forecasting the E-layer parameters are based at present on some empirical relations obtained as a result of statistical data processing of the vertical ionospheric sounding (see e.g., Ching and Chiu, 1968; Tchernishov and Vasilieva, 1975). The initial parameters for calculation of critical frequencies are as a rule the sunspot number and the solar zenith angle. Such methods of forecasting give some average ionospheric parameters, but they neither account for specific helio-geophysical conditions, nor reflect the connections between these parameters and causes of their variations. For computation of radio wave propagation at middle distances, it is necessary to know the main E-layer parameters, i.e. critical frequency, the height of maximum and effective thickness. These parameters are determined mainly by Solar ultraviolet and X-ray fluxes varying significantly from day to day. Though the solar activity indices mainly used for ionospheric forecasts (the sunspot number and radio flux at 10,7 cm) give the average levels of fluxes, they do not reflect short-time variations of their values. So approximate mean ionospheric parameter values calculated by means of present methods appear to be insufficiently accurate and can be used only for mean value evaluations.

A forecast where physical processes in the ionosphere are taken into account does not have such drawbacks. For day-time mid-latitude E-layer the processes determining layer's parameters are photoionization and complex of charge-exchange reactions and recombination. Ionization rate is determined by Sun ultraviolet and X-ray emission, as well as neutral atmosphere parameters. The development of satellite means of observations allows to obtain regularly emission flux data even now. However, accurate data on neutral atmosphere variations at E-layer heights have not been obtained yet. Thus the problem of the comprehensive calculation of E-layer parameters cannot be solved at present. Therefore, in order to predict the E-layer parameters, we have to use the forecast consisting of both determinated part based on

the knowledge of physical processes resulting in layer formation and part based on statistical processing.

Ionization rate computations for E-layer using spectrum of Ivanov-Kholodny and Firsov (1974) and atmosphere model (Jacchia, 1971) show that the main part of E-layer ionization is caused by the Sun radiation in the Ly β (1026 Å) and CIII (977 Å) lines. This conclusion is confirmed by statistical analysis of E-layer critical frequency behavior both during the year (Ivanov-Kholodny and Nusinov, 1976) and during the time of some X-ray bursts on the Sun (Ivanov-Kholodny et al., 1976). In order to reveal E-layer main variations, it is useful to introduce a structure parameter R_0. It is a ratio of ionization rate by X-ray (30-100 Å) radiation to that of ultraviolet radiation at the E-layer maximum height: $R_0 = q_x / q_u$ under a certain state of Sun activity, when ultraviolet and X-ray emission fluxes are equal to U_0 and X_0 correspondingly, and ionization rate in the layer maximum is q_0. Then ionization rate q under arbitrary solar activity is as follows:

$$q = q_0 \left(\frac{R_0}{1+R_0} \cdot \frac{X}{X_0} + \frac{1}{1+R_0} \cdot \frac{U}{U_0} \right) \qquad (1)$$

where X and U - the radiation fluxes in the period to be forecasted.

The study of ionosphere behaviour at the moments of X-ray bursts (Ivanov-Kholodny et al., 1977) have shown that R_0 value monotonously varied for a year period from $R_0 = 0.16$ in wintertime to 0.22 in equinoxes and 0.32 in summer. Ionization rate computations demonstrate that such variation is caused by changing atmosphere structure at the turbopause level. This changing is connected with a sharp decrease of molecular oxygen effective height scale in wintertime. Simultaneously this changing causes some other effects inherent in E-layer seasonal variations. As it is known critical frequency f_0E varies with zenith angle z as $\cos^p z$ at daytime, where the power $p \approx 1.07$ in summer and $p \approx 1.23$ in winter (see e.g. Ivanov-Kholodny and Nusinov, 1977). Variations of p-values have also been obtained as a result of ionization rate computations (Ivanov-Kholodny and Nusinov, 1977) providing for atmosphere seasonal variations at the turbopause level. The same computations give also the value of winter anomaly (Appleton, 1963), which coincides with the observed one: the q_0 value extrapolated to the same zenith angle decreases as much as 12 per cent from winter to summertime. Thus E-layer critical frequency at an arbitrary moment can be found in accordance with (1) from equation:

$$(f_0E)^4 = I \cos^p z \left(\frac{R_0}{1+R_0} \cdot \frac{X}{X_0} + \frac{1}{1+R_0} \cdot \frac{U}{U_0} \right) \qquad (2)$$

where the phase factor depending on the day number D can be introduced to account for seasonal changes of p, R and I values:

$$\Phi(D) = \sin \left[\frac{2\pi}{365} (D-80) \right] \qquad (3)$$

Then these values are the following:

$$R_0 = 0.23 + 0.07\ \Phi\ (D) \tag{4a}$$

$$p = 1.15 - 0.08\ \Phi\ (D) \tag{4b}$$

$$I = I_0[\ 1-0.06\ \Phi\ (D)] \tag{4c}$$

I_0 depends on the absolute values of radiation fluxes, ionizing the atmosphere at the heights of 100:120 km, as well as on a number of atmospheric parameters. Uncertainties in determination of these values do not permit to calculate I_0 immediately. Therefore I_0 can be found by means of statistical analysis of ionospheric data, where equation (2) is used as a regression equation. Estimation based on Moscow station data gives $I_0 = 190\ MHz^4$. From the processing of data obtained in other stations the value might be made more precise. Just equations (2-4) give formulae to forecast E-layer critical frequency.

It is well known that f_0E decreases by the value about 0.1 MHz under strong magnetic disturbances (Beynon and Brown, 1959; Appleton and Lyon, 1961). Analysis made in Ivanov-Kholodny and Nusinov (1977b) showed that these f_0E variations could be due to both change of atmosphere composition (the increase of nitric oxyde concentration, advected from polar regions) and considerable increase of its density. Data available now are not sufficient to calculate these phenomena. Therefore to forecast the effect caused by magnetic disturbances it is possible to use the results of statistical analysis made in Ivanov-Kholodny and Nusinov (1977b). In accordance with Ivanov-Kholodny and Nusinov (1977b), to evaluate the effect of geomagnetic disturbance with a given Ap-index, it is necessary to subtract value 0,4 Ap from equation (2), with Ap-index being taken for previous day.

Formula (2) includes only relative values of radiation fluxes, so the forecast does not need a precise calibration of detectors installed onboard the satellite observatory. According to Schmidtke et al. (1977) fluxes in lines 1026 Å and 977 Å causing ionization in E-layer and a flux in line 304 Å vary identically. Therefore the 304 Å line for which we have the most reliable data may be used to forecast the critical frequency. Moreover, instead of X-ray flux within the range of 30-100 Å, which cannot be easily measured, now it is possible to use 8-20 Å flux data. Measurements of such a flux are more reliable and do not require complicated instruments. It was shown in Ivanov-Kholodny et al. (1976) that the ratio X/X_0 in (2) ought to be replaced by square root relative intensity within 8-20 Å range.

For accurate calculation of radio transmission frequencies, it is necessary to know not only the critical frequency of the layer, but also its main geometric parameters, i.e. height of maximum h and scale height H. So far these values either have not been used in forecasts at all, or have been considered to be constant (for example in Ching and Chiu (1968) h=110 km and H=10 km). Analysis of ionospheric observations (see e.g. Robinson, 1959) shows that the simple Chapman's equation

$$h=h_0 - H \ln \cos Z \tag{5}$$

can be used to forecast the height of maximum. However, both the results of observations (Robinson, 1960; Butcher, 1970; Whitehead, 1973) and computations (Ivanov-Kholondy and Nusinov, 1977a) prove, that h_0 and H values are changed with seasons: from summer to winter h_0 value changes from $\sim$ 107 km to $\sim$ 103 km and H value - from 6:9 km in summer to 3:4 km in winter. Using seasonal factor (3) it is possible to write approximate formulae for h_0 and H for different seasons:

$$h_0 = 105 + 2 \cdot \Phi\ (D) \qquad (6a)$$

$$H = 56 + 2 \cdot \Phi\ (D) \qquad (6b)$$

These expressions agree with both observations and computations. Their accuracy is about 1:1.5 km, and it is sufficient for calculations of M2000-coefficient with relative error of 2:3 percent.

Thus a forecast of critical frequency and geometric parameters of E-layer can be given due to simple calculations according to (2-6). Initial data for such forecast are values characterizing conditions of E-layer formation for a certain day, i.e. fluxes of ionizing radiation and magnetic activity indices. Hence it is sufficient to know only relative values of the fluxes. A number of values in such as p, I and R describes seasonal variations of atmosphere structure. The average values of p, I and R may be obtained by statistical data processing and their annual variations - by model computations.

The scheme of forecast under consideration is intermediate between exact computation and statistical model. This method has some advantages as compared with existing ones. Above all it allows to forecast (or to calculate through the data available) the state of ionosphere for a concrete moment, characterized by a given set of helio-geophysical parameters. Further it includes only the values immediately determining the E-layer formation and dynamics. It should be noted that the existing schemes of forecasting give only the monthly mean f_0E value depending on average sunspot number. The method also allows to forecast variations of E-layer critical frequency during geomagnetic disturbances. Moreover, this forecasting scheme gives an opportunity to calculate seasonal variations as well as short-time variations caused by rapid changes of solar radiation flux (bursts). In many cases there are no visible changes on the Sun's surface during these rapid variations, so they do not take place in the existing schemes of forecasting.

REFERENCES

Appleton, E. (1963): J. Atmos. Terr. Phys., 25:577.

Appleton, E. V., and A. J. Lyon (1961): J. Atmos. Terr. Phys., 21:73.

Beynon, W. Y. G., and G. M. Brown (1959): J. Atmos. Terr. Phys., 14:138.

Butcher, E. (1970): J. Atmos. Terr. Phys., 32:97.

Ching, B. K., and Y. T. Chiu (1968): J. Atmos. Terr. Phys., 35:1615.

Ivanov-Kholodny, G. S., and V. V. Firsov (1974): Geomagn. i aeronomy, 14:188.

Ivanov-Kholodny, G. S., and A. A. Nusinov (1976): Geomagn. i aeronomy, 16:76.

Ivanov-Kholodny, G. S., L. H. Lestchenko, and I. N. Odintsova (1976): Geomagn. i aeronomy, 16:246.

Ivanov-Kholodny, G. S., L. N. Lestchenko, A. A. Nusinov, and I. N. Odintsova (1977): Geomagn. i aeronomy, 17:839.

Ivanov-Kholodny, G. S., and A. A. Nusinov (1977a): Geomagn. i aeronomy, 17:1018.

Ivanov-Kholodny, G. S., and A. A. Nusinov (1977b): Geomagn. i aeronomy, 17:423.

Jacchia, L. G. (1971): Spec. Rept. No. 332. Smithsonian Inst. Astrophys. Observ., Cambridge, Mass.

Robinson, B. J. (1959): Reports on Progress in Physics, 22:241.

Robinson, B. J. (1960): J. Atmos. Terr. Phys., 18:215.

Schmidtke, G., K. Rawer, H. Botzek, D. Norbert, and K. Holzer (1977): J. Geophys. Res., 82:2423.

Tchernishov, O. V., and T. N. Vasilieva (1975): "The forecast of MUF". "Nauka", Moscow.

Whitehead, J. D. (1973): J. Atmos. Terr. Phys., 35:183.

DAYTIME SPORADIC-E BLANKETING FREQUENCY PREDICTION

A. E. Giraldez
LIARA, Avda. Libertador 327
Vicente Lopez, Buenos Aires, Argentina

A prediction method for the daytime median hourly values of the Sporadic-E layer blanketing frequency (fbEs) in particular for the South American sector, is presented. The fbEs values show dependence on Wolf number (R), solar zenith angle (X) and geographic latitude (λ). This method calculates the frequency value (fbEs) for midlatitudes provided that R, local time, geographic latitude and month number are given as input conditions.
Comparisons with scaled data from ionosondes between 20 and 55° latitude, for an R excursion from 10 up to 200 are shown. This prediction method provides daytime fbEs values within 10% error for the South American sector. Northern hemisphere, Africa and Australia also show good agreement, within 10% error except for latitudes higher than 40° in Winter time.

1.- INTRODUCTION

Sporadic-E layers, due to their special characteristics, permit a narrow margin of prediction, but only during quiet time conditions.
The formation mechanism at midlatitudes seems to be the wind-shear mechanism (Whitehead, 1960, 1961, 1962 ; Axford, 1961, 1963; Hall, 1964; Hines, 1964; Chimonas and Axford, 1968), assumption which is supported by experimental findings (Rosenberg and Edwards, 1964; Bowen et al, 1964; Rosenberg et al, 1964; MacLeod, 1966; Wright, 1967; Wright et al, 1967; Wright and Fedor, 1969; Miller and Smith, 1975; Harper et al, 1975).
The fact that Es layers are formed by metallic ions has been widely established by mass-spectrometer measurements between 90 and 130 km (Istomin, 1963; Narcisi and Bailey, 1965; Narcisi, 1968, 1973; Young et al, 1967; Anderson and Barth, 1971; Johanessen and Krankowsky, 1972; Zbinden et al, 1975; Goldberg, 1975) and recently also using backscatter by Behnke and Vickrey, 1975.
Processes which produce the ionization of metal ions necessary to form Es layers have been investigated in detail (Swider, 1969; Ferguson, 1972; Brown, 1973; Baggaley and Cummack, 1974; Poole and Nicholson, 1975), and the diurnal variation of metal-ions is mainly determined by the concentrations of O_2^+ and NO^+ (Miller and Smith, 1976). Based on the above mentioned assumptions about the mechanism of formation and the source of the metal-ions, the next point to be considered is the opportunity of formation of an Es layer. Taking into account that wind-shear theory requires a horizontal shear of neutral winds, gravity waves and tidal winds are the most appropriate phenomena to give rise to a Es layer. As the magnitudes of tides and gravity waves are comparable, (Hines, 1963) the persistence of the tidal winds and the random nature of the gravity wave spectrum indicates that long-term features of Sporadic-E layers should be dominated by the tidal modes (Smith and Mil-

ller, 1977). The observation of Es layers by means of ionosondes, provides information about virtual height (h'Es), and two maximum frequencies, namely fbEs, foEs.
This paper deals only with fbEs, which is the nearest Es critical frequency to the mean plasma density of the layer. (Rawer, 1962; Reddy and Rao, 1968; Whitehead, 1972), and therefore the least influenced by short duration wind variability, as is the case of foEs.
Due to the arguments expressed, three main variables must be taken into account if a prediction of fbEs is attempted. Solar zenith angle, which governs O_2^+ and NO^+ concentrations and R (Wolf) number, or any other solar activity index which proves to be related to significant E region ion concentration. A third variable to take into account is geographic latitude, due to Es dependence on tides, because the current knowledge on solar tides (Volland and Mayr, 1974, 1972, 1977; Volland and Grellman, 1977; Richmond, 1971, 1977; Richmond et al, 1976; Evans, 1976; Lindzen, 1974;) would indicate that at E region heights, semidiurnal tideswith a strong latitudinal variability are important. Also magnetic field vector is fundamental, according to wind shear theory (Reddy & Matsushita, 1968; 1969), and geomagnetic coordinates necessary. In this case geographic coordinates are being used, for simplicity, and assumed that geographical coordinates also take account the wind shear parameters at least aproximately. The prediction method developed in this paper shows that the daytime dependence of fbEs with the R value is roughly the same as the one obtained by Bosolasco and Elena (1963) and Heisler and Whitehead (1964) for foEs. Also the mean value of fbEs had a diurnal variation similar in phase and amplitude to foE, a result consistent with the idea that the Es is due to a redistribution of existing ionization. The practical applications of this method are related with HF radio propagation predictions. HF links predicted through the use of the F layer ionization might be seriously disturbed by Es ionization up to 2000 km distance from the transmitter, as Es layers can act as a low altitude reflecting layer which renders the MUF F2 factor meaningless. As percent of time with presence of Es layers at midlatitudes is, during daytime higher than 30% of time (CCIR 1976), an estimation of maximum frequency reflected by Es layers is a necessary tool to be taken into account as a perturbation factor in HF propagation predictions. (CCIR, Doc. 6/177 (1976); CCIR, Study Program 4A-2/6).

2.- PREDICTION TECHNIQUE

2.1.- STATIONS INFORMATION

Hourly mean values of fbEs scaled at four South American stations located between 23.5° S and 51.7° S geographic latitude and with a small longitudinal dispersion are used. The period of analysis covers from 1957 up to 1974. Detailed station information is provided in table 1.

TABLE 1

Station name	Geographic		Geomagnetic	
	long.	latit.	long.	latit.
Sao Paulo	313.4	-23.6	21.09	-12.8
Tucumán	294.6	-26.9	3.33	-15.4
Buenos Aires	301.2	-34.6	9.4	-23.2
Port Stanley	302.2	-51.7	9.09	-40.4

2.2.- Data handling

The data are arranged by geographic latitude, R number and cos (X) values rather than hour, season and year.
Data corresponding to months with severe geomagnetic perturbations (Ap > 50) covering more than half the month are not considered.
There have been made a two dimensional array in R and cos (X) values for each station under study. Each line goes from cos (X) = 0 up to cos (X) = 1. Each cell in the line includes data within Δ cos(X) = 0.1. Each column goes from R = 10 up to R = 200, and each cell in the column includes data within Δ R = 20.
Thus, a 10x10 array of data is obtained for each station.
A mean value in each cell is calculated, together with the corresponding standard deviation of data in the cell. It is remarcable to point out that in each cell the dispersion from the mean does not rise over 10%, and in most cases lays below 5%, as shown in Figure 1.

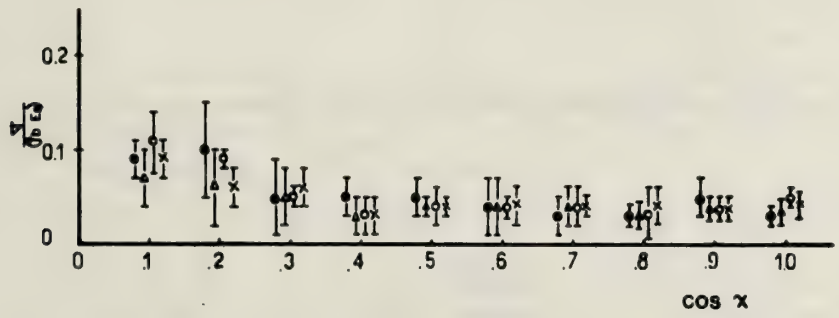


Fig. 1. Average standard deviation (σ) over the mean value fbEs for the four stations under analysis, against cos X. Bars indicate dispersion limits. ● , R = 50; Δ , R = 100; o , R = 150; x , R = 200.

2.3.- Analysis of data

There have been assumed a functional dependence of fbEs on R and cos (X) such as:

$$fbEs(R,X) = F(R).(\cos(X))^n \qquad (1)$$

2.3.1.- Solar zenith angle dependence

For constant R values in the two dimmensional array made for each station mentioned before, an exponential curve fitting by the least squares method is performed for each R interval value and each station for the function:

$$fbEs = a.(\cos X)^b \qquad (2)$$

with the following results:
The exponent is almost constant during all the excursion over R values for each station, but grows with latitude, as shown in Figure 2.
The correlation coefficient in the exponential curve fit results $r > 0.967$ for cells between $0.1 \leq \cos X < 1.$ in every case.

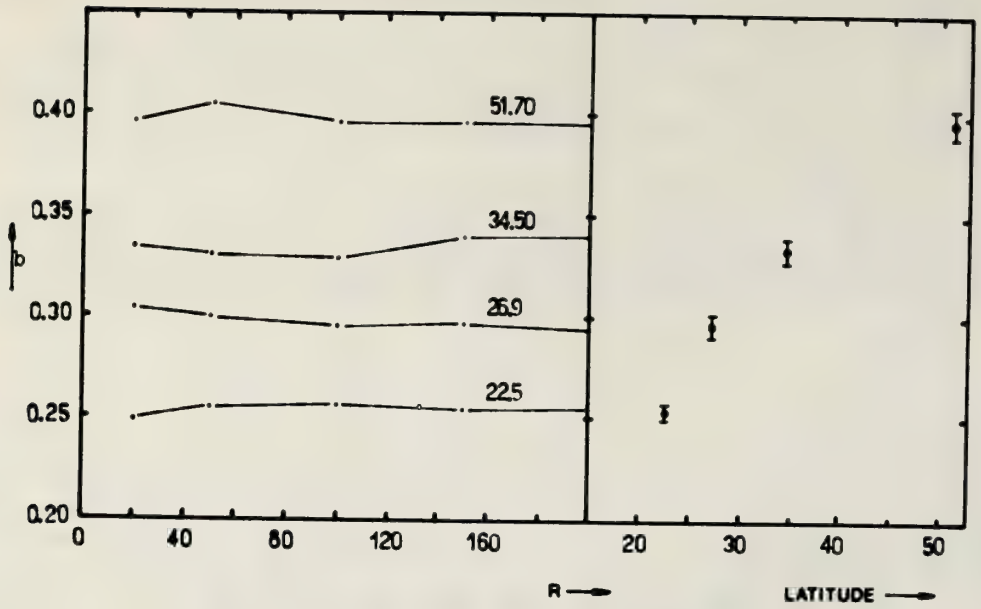


Fig. 2. Left figure shows b against R for the four latitudes. The numbers on each curve are the corresponding South latitude of the station. The figure on the right shows b against South latitude. Dots are mean values, bars are standard deviation.

In order to avoid a latitudinal dependent exponent in the $(\cos X)^b$ expression, it will be adopted a constant b value, and the latitudinal dependence will be treated as a different term. The exponent adopted is $b \simeq 0.25$ as for the Normal E layer (K. Davies, 1965), to permit further comparison between normal E and Sporadic-E frequency expressions.

2.3.2.- R (Wolf number) dependence

The analysis of data to find out the functional dependence of fbEs upon R follows similar lines as those of paragraph 2.3.1.
Linear, logaritmic and exponential curve fitting is performed for each cos X value along the columns of the array. Results show that exponential curve fitting have a poor correlation, but linear and logaritmic fitting presents similarly good correlation coefficients ($r > 0.9$).

$$\text{log.curve fit :} \quad a + b.\log(R) = F(R) \qquad (3)$$
$$\text{linear curve fit:} \quad a + b.R = F(R) \qquad (4)$$

The election between log and linear function is then made through the analysis of their independence on cos X.
The comparison of (b/a) coefficients as a function of cos X for both curves, as shown in Figure 3, indicates that linear regression is almost independent on X value, while log is not. Thus, linear dependence of frequency on R values is adopted, with a functional depen-

dence:

$$fbEs\,(R) \simeq 1 + 1.7374\times10^{-3}\,.R \qquad (5)$$

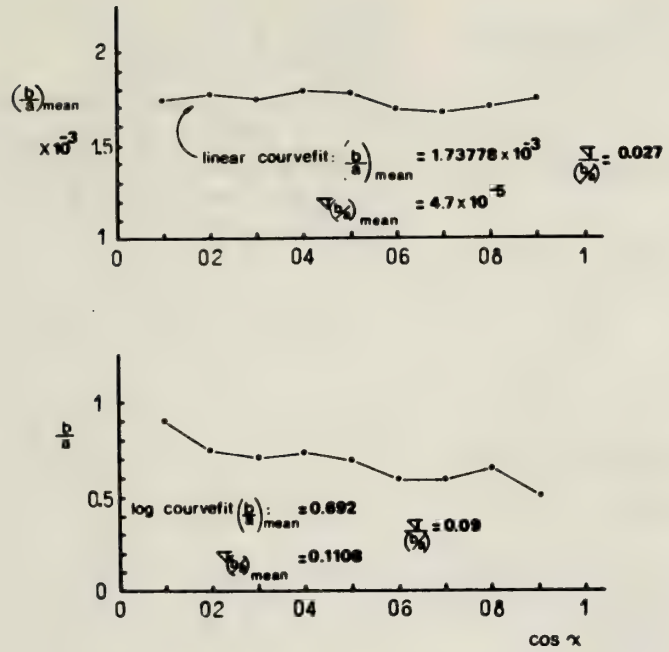


Fig. 3.- Top figure shows experimental values (dots) as well as dispersion (σ) and relative error $\sigma/(b/a)$ for the linear curve fit as function of cos X values. Bottom figure shows the same data for log curve fit.

2.3.3.- Latitudinal dependence

As it is observed in fig. 2, there is a strong latitudinal influence upon the critical layer frequency. This section is devoted to find out the third term of the equation, which relates cos X and latitude.
The analysis of the equation,

$$fbEs(observed)/(\cos X^{\frac{1}{4}}.\ F(R)) \;=\; F(X,\lambda) \qquad (6)$$

where λ = geographic latitude
for each cell of the 10x10 array, results in a group of values for $F(X,\lambda)$ as function of latitude and X angle values, after evaluating the mean value of each column. (R values) Those values obtained are shown in fig. 4 (crosses).
Intermediate points on fig. 4 are obtained by Lagrange interpolation method. This procedure visualizes the corresponding latitude of the maximum $F(X,\lambda)$ function for each value of cos X. As is observed in the same figure, $F(X,\lambda)$ is a single maximum function for each cos X value, with a different maximum position for each one.
Figure 5 shows those maximum from Fig. 4, as a function of cos X, together with the empirical function which fits the curve.
This is not the most appropriate place to analyze the physical meaning of Fig. 5, but anyway, it means that independently of the solar activity and the charge exchange mechanism efficiency, there is a semidiurnal symetric effect which drives maximum wind-shear mechanism efficiency towards the pole and after towards the equator in the morning, and which repeats in the afternoon. This effect requires a deeper analysis to be adequately explain-

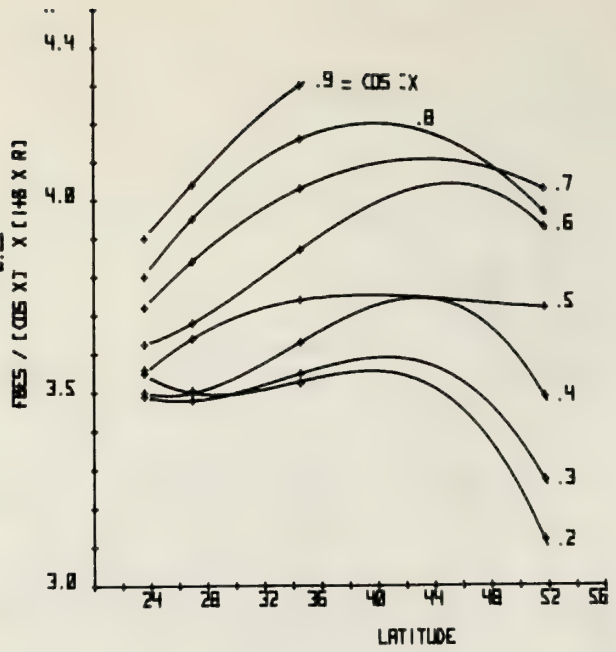


Fig. 4.- Figure 4 shows formula (6) above as a function of latitude, with cos X as a parameter Crosses indicate experimental values. The continuous line results from Lagrange interpolation.

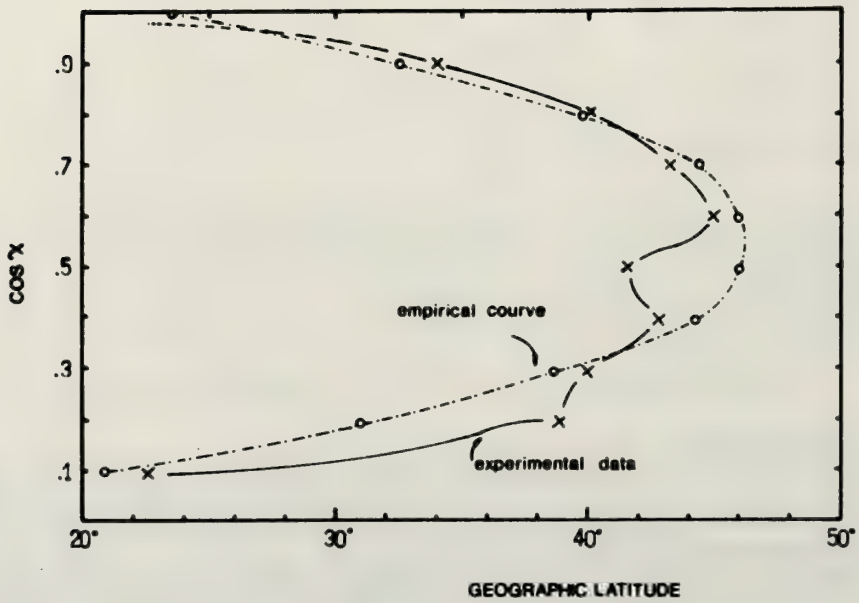


Fig. 5.- Maximum values of Fig. 4 for each cos X value (crosses) and empirical curve (cicles) as a function of geographic latitude.

ed, but as pointed out in the introduction, this effect is related to E region tidal wind system.

The expression obtained to fit Fig. 5 data is:

$$\Phi = \text{lat}_{(\max.F(X,\lambda))} = 150^{\circ}(\cos X - \cos^2 X + \cos^3 X/9) + 7^{\circ} \qquad (7)$$

$F(X,\lambda)$ is reasonably good fitted by a function of the form:

$$F(X_i,\lambda) = A(X_i) \cdot \exp\left(- (|\lambda| - \Phi)^2 / S(X_i) \right) \qquad (8)$$

with:

$$A(X_i) = \text{maximum value of } F(X_i,\lambda)$$

All data on expression (8) are known, except S(X).
The solution of equation (8) for S(X) as function of latitude and cos X values gives a set of values shown in Fig. 6 (crosses). Curve fitting for those values (full line) is shown in the same figure.

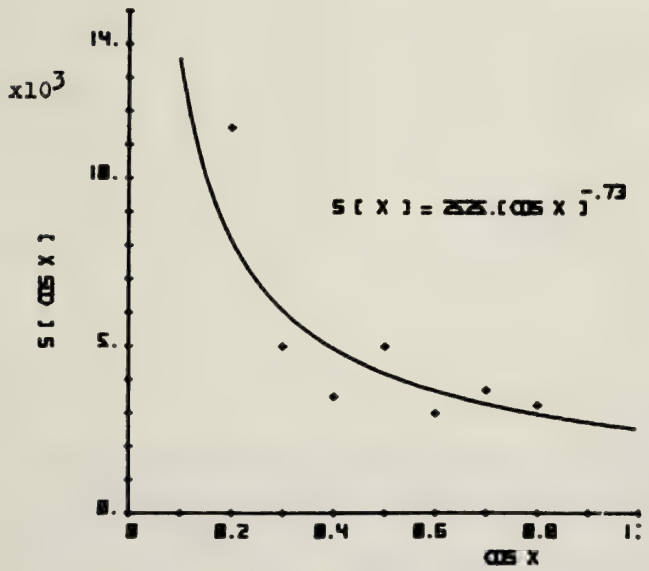


Fig. 6.- Values of S(cos X) as function of cos X values corresponding to equation (8) (crosses), and the least squares curve fit (full line) with the corresponding equation of the curve.

with:

$$S(X) = 2525 \cdot (\cos X)^{-.73} \qquad (9)$$

Thus, the latitudinal term is:

$$F(X,\lambda) = \exp - \left(\frac{|\text{lat}| - \Phi}{50.26^0} \right)^2 \cdot (\cos X)^{0.73} \qquad (10)$$

2.3.4.- fbEs Prediction Equation

The single term which remains to be determined is the constant of proportionality (A) which takes into account the cos X, R and $F(X,\lambda)$ coefficients which have not been chosen independently. Then;

$$A = fbEs(obs)./\cos^{\frac{1}{4}}X, F(R).F(X,\lambda) \qquad (11)$$

Figure 7a shows the A value for the four latitudes under study for all R and cos X values, while Fig. 7b shows A value as function of cos X values, for all latitudes and R values.

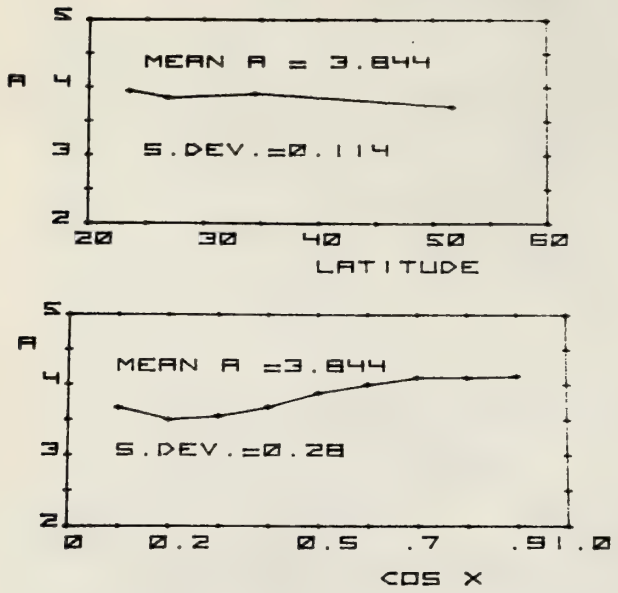


Fig. 7.- Experimental values on the proportionality constant to be adopted in order to obtain a good fbEs value. Crosses indicate mean value of the proportionality constant averaged on cos X values, an R number for the fall set of data, for each station (upper figure). Crosses indicate mean values of A averaged on latitude and solar activity for the full set of data for each cos X value cells.

to make the equation (11) easier to handle, the X variable might be replaced by local time, with the help of the declination equation:

$$\delta = 23.45 \sin \frac{360}{365} (n + 284^{\circ}) \qquad (12)$$

where n = number of the day of the year
and cos X(δ, λ, local time) equation:

$$\cos X = \sin\delta \sin\lambda + \cos\delta \cos\lambda \cos h \qquad (13)$$

where h = number of the hour x $\frac{360^{\circ}}{24} - 180^{\circ}$

Results
Fig. 8 shows the comparison between experimental and calculated frequency values as:

$$(fbEs_{observed} - fbEs_{calculated}) / fbEs_{observed} \qquad (14)$$

for the South American sector under study, as mean values over cos X, for all the period considered.

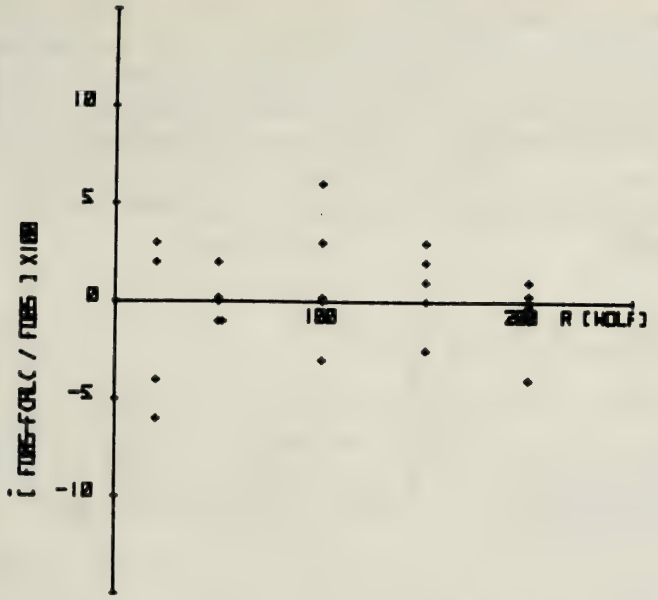


Fig. 8.- Estimation of the relative error of the method for the South American sector for the four stations under study (crosses) it have been obtained by calculating equation (14) for each data column and each station for solar R values = 20, 50, 100, 150 and 200.

3.- BASES FOR TECHNIQUE

The empirical formula obtained to reproduce experimental values is based on physical arguments for the selection of the variables and on mathematical and statistical arguments to obtain the equations.

The selection of R, X and λ as variables, is based on the dependence of Es layers on Normal E layer ionization for reasons already mentioned in the introduction, for the two first variables (R and X); and in the special nature of Es formation (neutral wind-shears) for the third variable (latitude).

As Sporadic-E layer formation in a particular isolated case depends on meteorological conditions prevailing in E region heights (Whitehead, 1972), it is impossible to predict isolated cases, but a mean value of several cases, eliminates to a certain amount, the particular and ocassional conditions surrounding each case, and leaves only the general pattern, which is predicted in this paper. This prediction of median hourly values for fbEs is based on the assumption of predictability of mean conditions for the data of a whole month.

4.- SAMPLE PREDICTIONS

Median hourly values published in "Ionospheric Data" booklets for fbEs are used as experimental data in the foregoing section for the world wide test of the method.

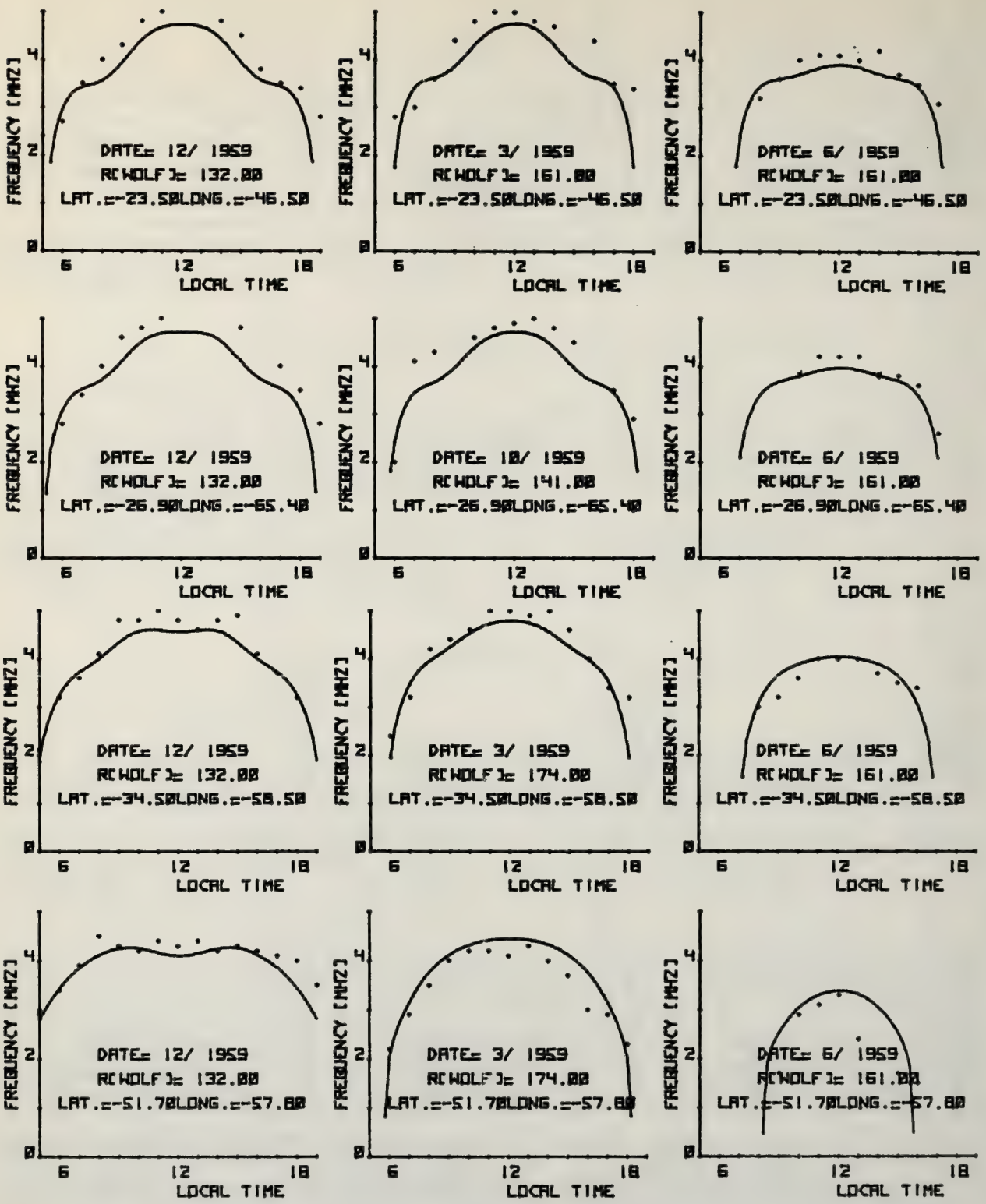


Fig. 10.- South American Sector, the same as Fig. 9 but for high solar activity level

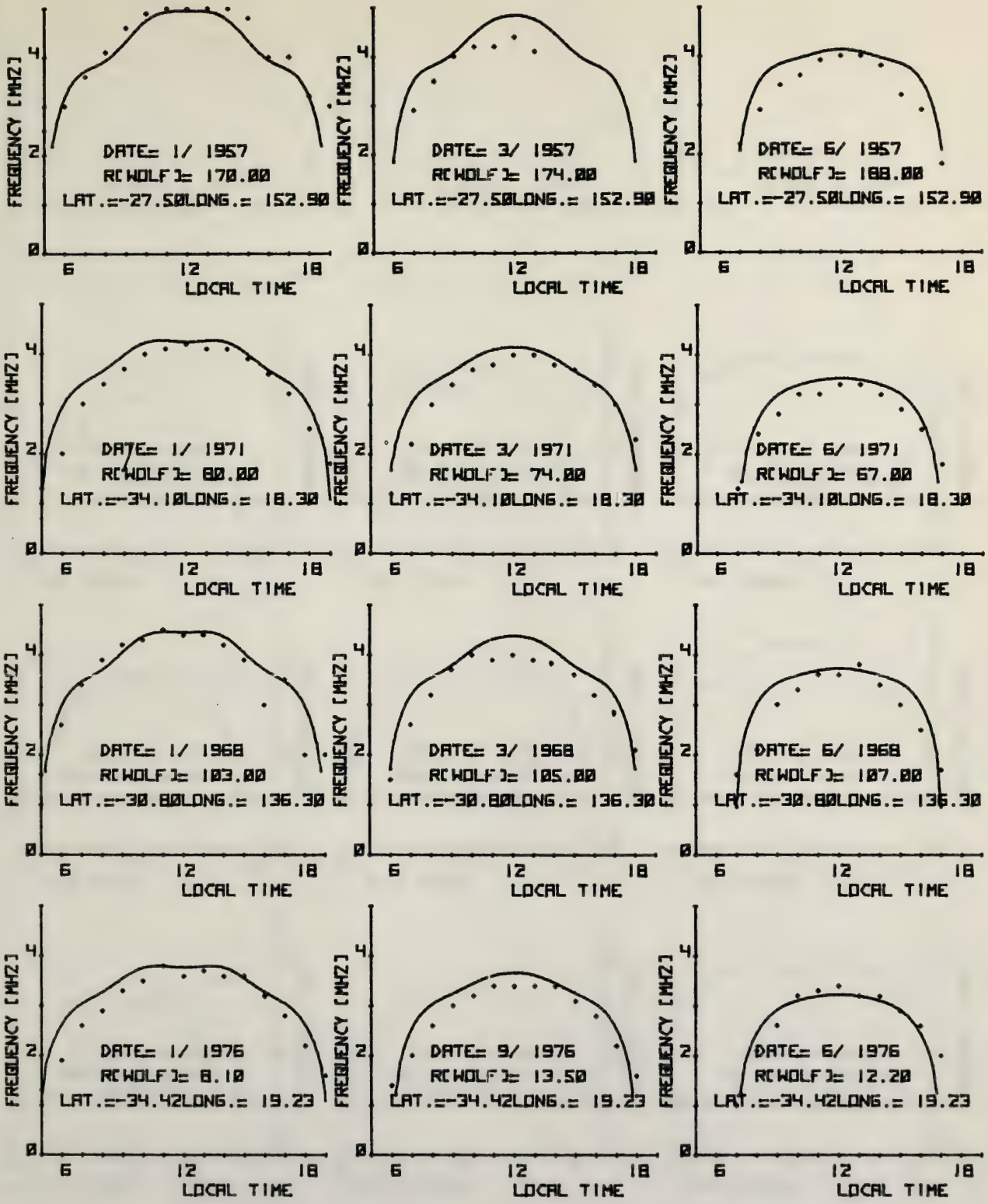


Fig.- 11.- Australia and South Africa. Dotts: observed median hourly values (MHz); full line: predicted values (MHz). From left to right, Summer Equinox, Winter; from top to bottom, Brisbane (Australia); Capetown (S. Africa); Woomera (Australia) and Hermanus (S. Africa). Date = month/year; R (Wolf) = R sunspot value; lat. - long. = geographic latitude and longitude.

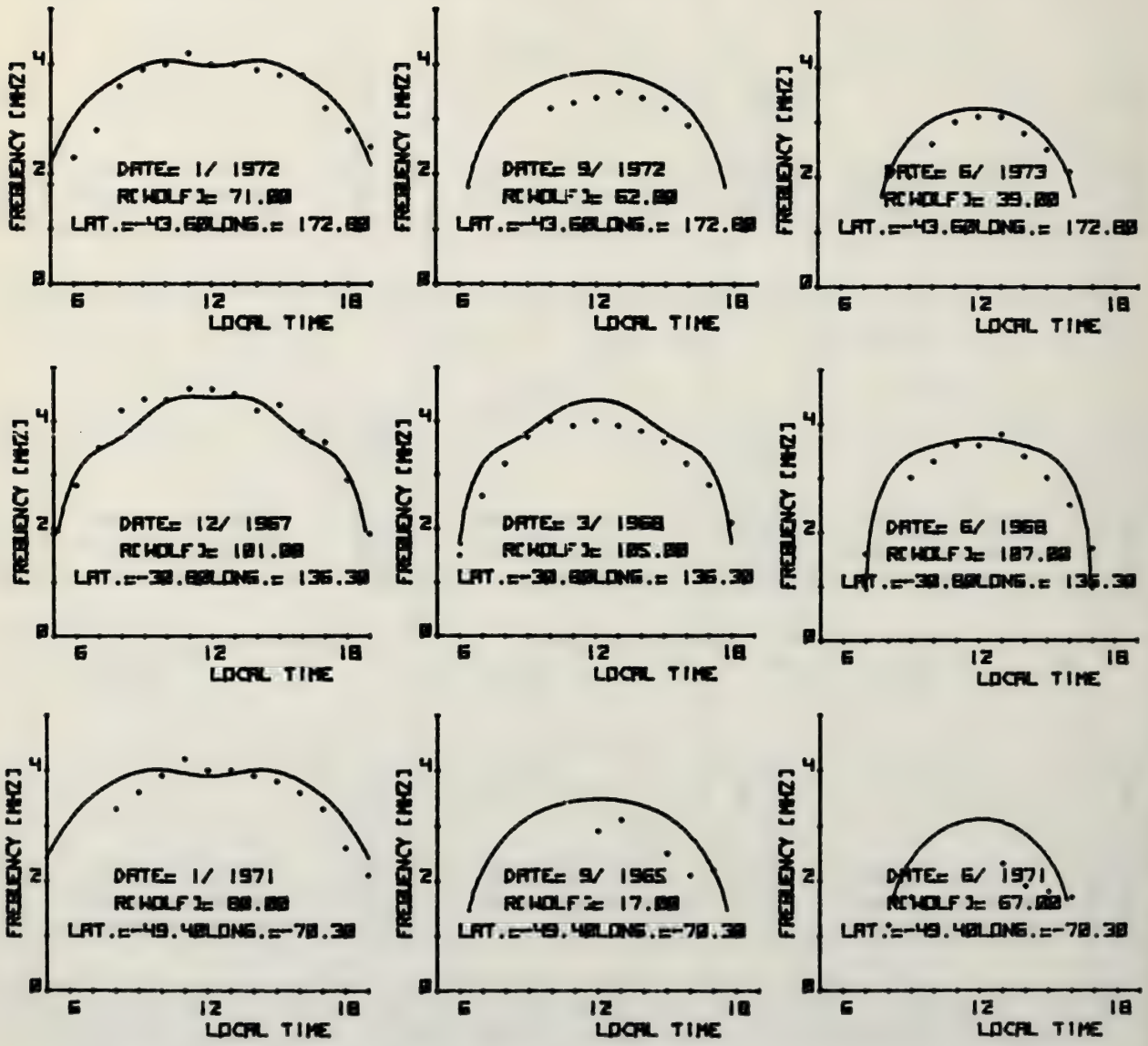


Fig. 12.- Australian sector; from top to bottom Christchurch, Woomera and Kerguelen.

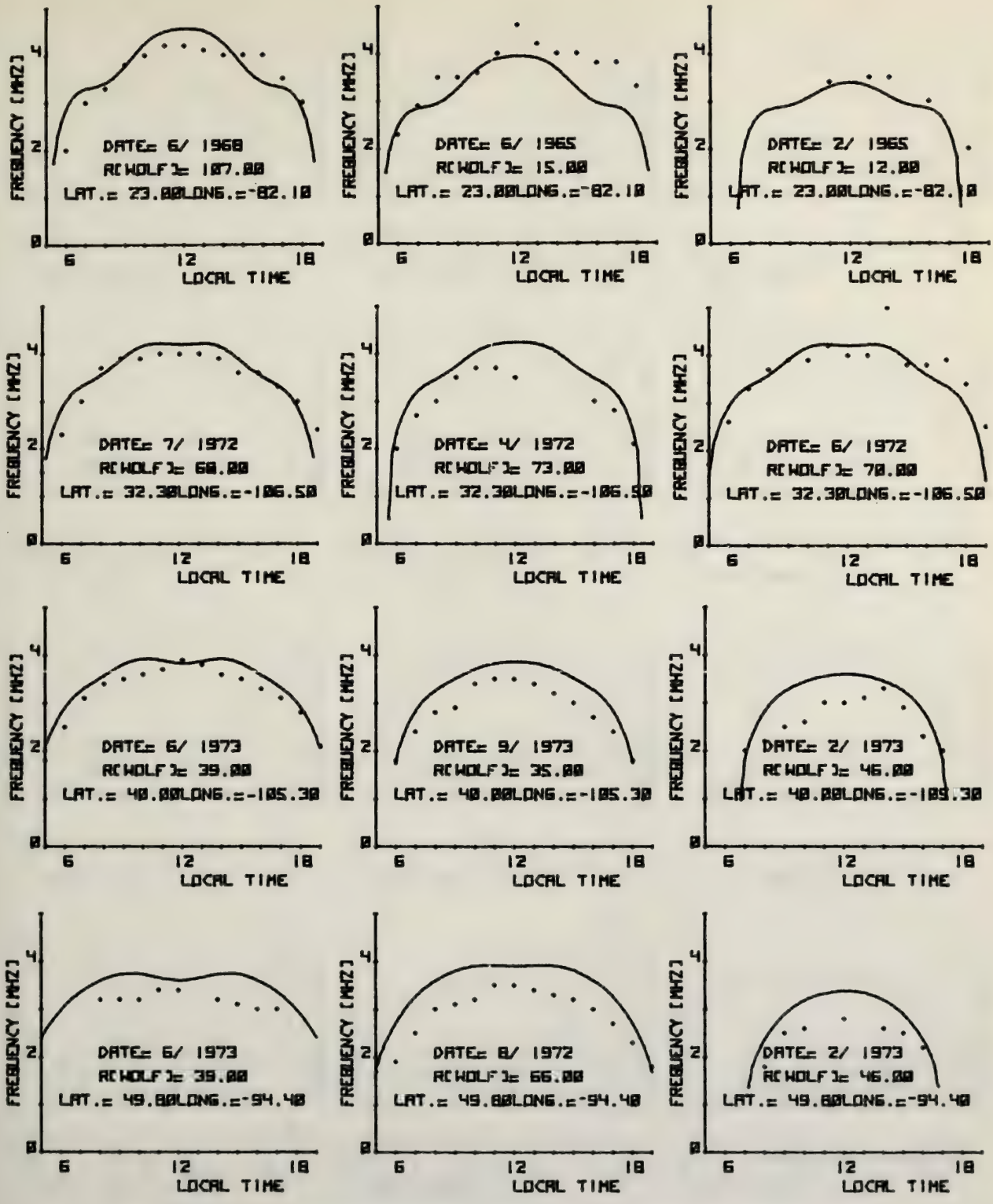


Fig. 13.- North American sector. From top to bottom Cuba, White Sands, Boulder and Winnipeg. Dotts: observed median hourly values (MHz); full line: predicted values (MHz) legends with the same meaning as fig. 9 and 11.

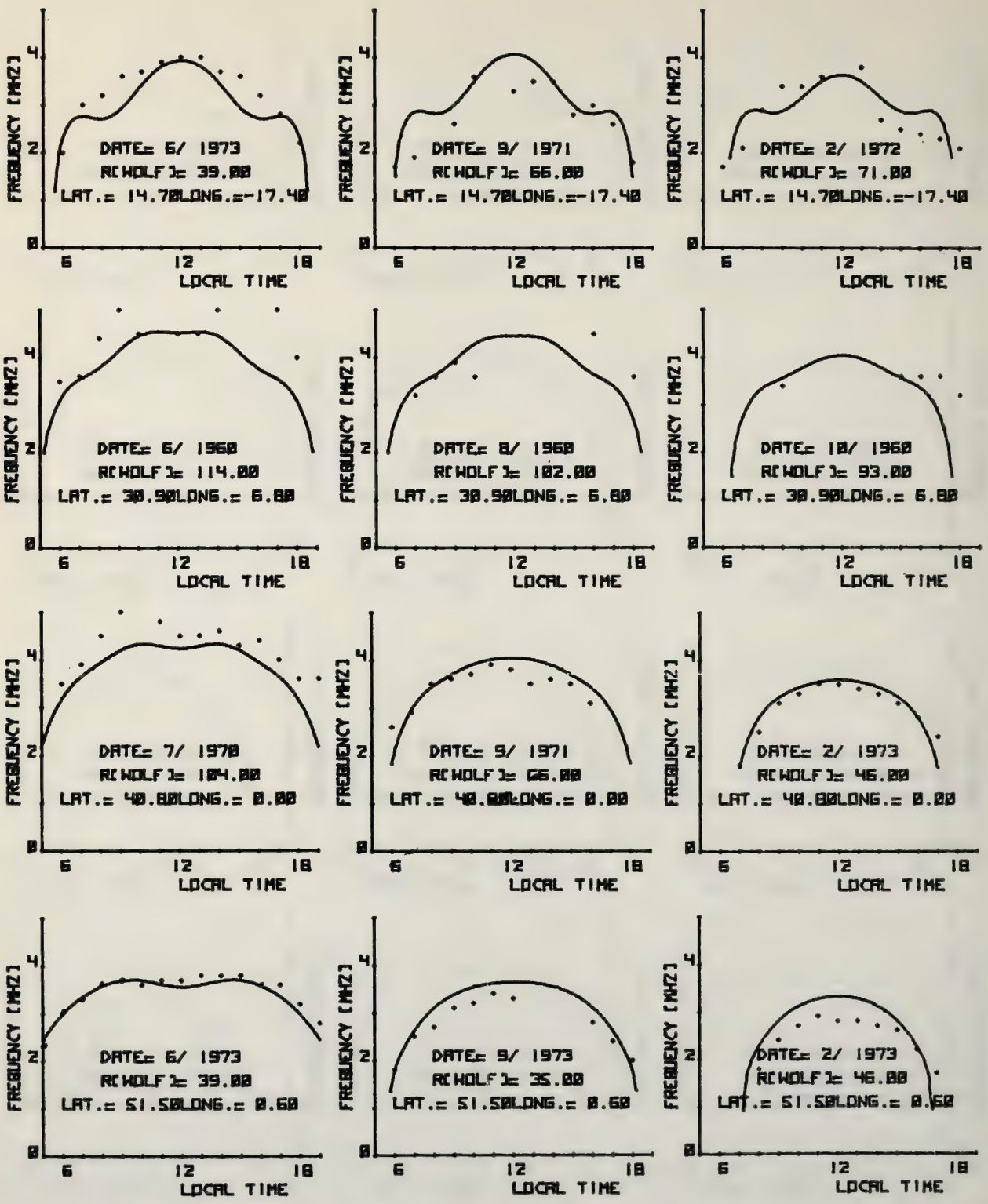


Fig. 14.- Europe and North Africa. From top to bottom Dakar, Rabat, Fortosa and Slough; legends similar to figs. 9 and 11.

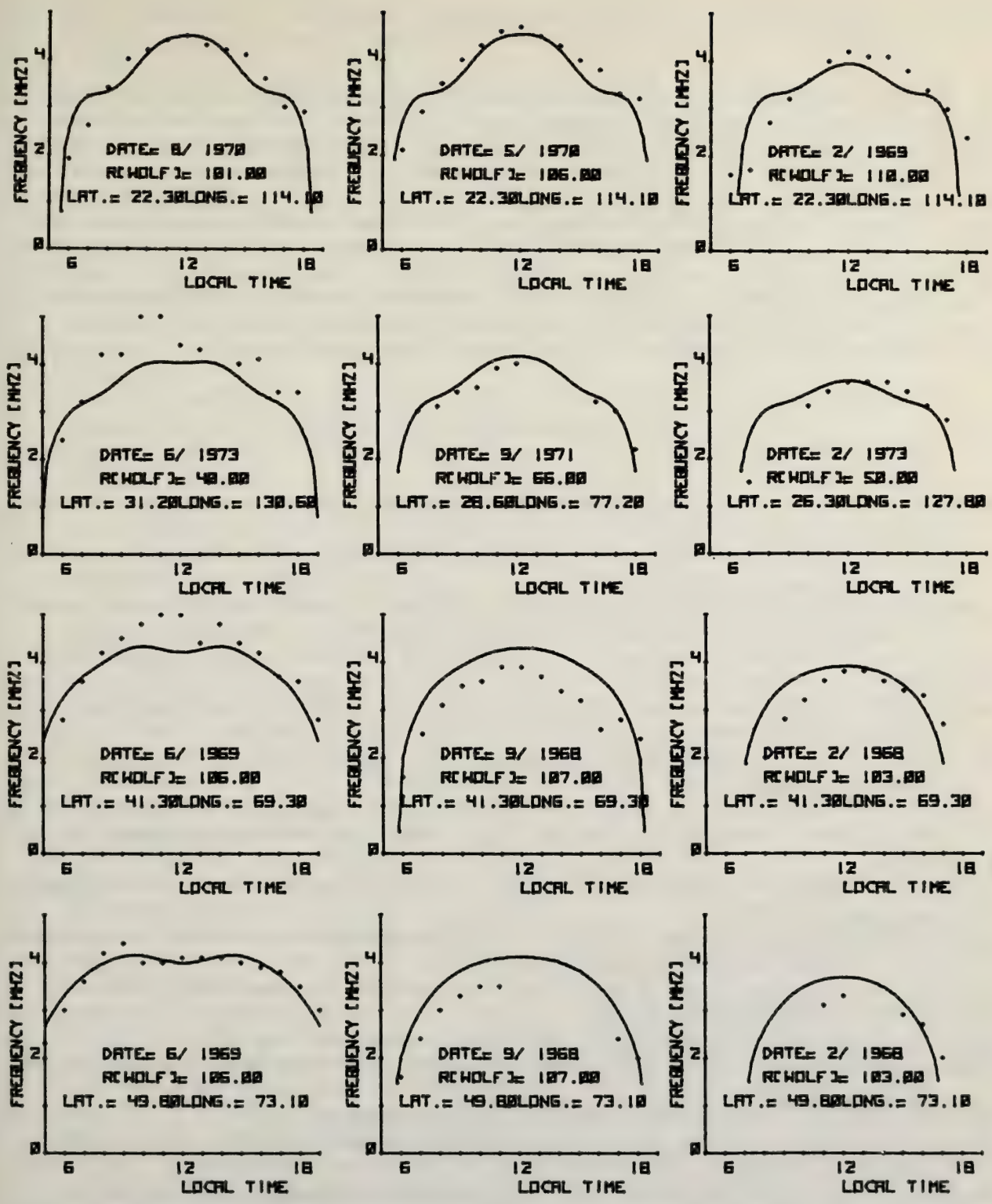


Fig. 15.- Asia (Northern Hemisphere). Legends similar to figures 9 and 11. Top line (3 figures) from Hong Kong. Second line from top: left Okinawa, center Delhi, right Yamagawa. Third line from top: Tashkent, bottom Karaganda.

5.- CONCLUSIONS

The prediction method presented reproduces within a reasonably good margin the observed daytime fbEs data for ionospheric stations between 20° and 40° latitude (North and South Hemispheres). There is observed that fbEs values might be predicted as function of month number, solar activity level and geographical latitude, as is suggested by theoretical and experimental evidence of Es layers dynamics. For latitudes higher than 40° during Winter time, the prediction method is not adequate nor for latitudes where Dip angle is higher than ± 50°. The empirical formula reached have a strong resemblance with the corresponding foE prediction formuli in the terms corresponding to solar zenith angle and solar activities parameters. There is a third term, a latitudinal term, wich does not appear in foE prediction, but that is of fundamental importance for Sporadic-E prediction formuli, due to the formation mechanism which is its distinct characteristic.

BIBLIOGRAPHY

Anderson, J. G., and C. A. Barth (1971): Rocket investigation of the MgI and MgII dayglow J.G.R. 76, 3723 - 3732.

Axford, W. I. (1961): Note on a mechanism for the vertical transport of ionization in the ionosphere. Can. J. Phys. 39, 1393.

Axford, W. I. (1963): The formation and vertical movement of dense ionized layers in the ionosphere due to vertical wind-shear. J. G. R. 68, 769-779.

Baggaley, W. J., and C. H. Cummack (1974): Meteor train ion chemistry. J.A.T.P. 36, 1759-1773.

Behnke, R. A., and J. F. Vickrey (1975): Radar evidence for Fe^+ in a Sporadic-E layer. Radio Sci. 10, 325-327.

Bossolasco, M., and A. Elena (1963): Sporadic-E layer ionization and the sunspot cycle. Geofis. pura appl. 56 (3), 142.

Bowen, P. J., K. Norman, A. P. Willmore, J. M. Baguette, F. Murtin and R. O. Storey (1964): Rocket studies of Sporadic-E ionization and ionospheric winds. Planet. Space Sci. 12, 1173.

Brown, T. L. (1973): The chemistry of metallic elements in the ionosphere and mesosphere Chem. Rev. 73, 645-667.

CCIR Doc 6/177-E (1976): Report 259-3 (Rev. 76) VHF propagation by irregular layers, Sporadic-E or other anomalous ionization. 230-259.

CCIR Doc 6/177-E (1976): Question 4-1/6 (Rev. 76) Propagation by way of Sporadic-E and other anomalous ionization. 349.

CCIR Study programms 4A-2/6 and 4B-2/6, 249, CCIR Comission VI (1974).

Chimonas, G., and W. I. Axford (1968): Vertical movement of temperate-zone Sporadic-E layers. J. G. R. 73, 111-117.

Davies, K. (1965): Ionospheric radio propagation. NBS Monograph 80.

Evans, J. V. (1976): The dynamics of the ionosphere and upper atmosphere. AGU - ISSTP, Boulder, Co. Vol. II.

Ferguson, E. E. (1972): Atmospheric metal ion chemistry. Radio Sci. 7, 397-401.

Goldberg, R. A. (1975): Silicon ions below 100 km: A case for SiO_2^+. Radio Sci. 10, 329-334.

Hall, R. B. (1964): The formation of the Sporadic-E layer. J. A. T. P. 26, 1143-1146.

Harper, R. M., R. H. Wand, and J. D. Whitehead (1975): Comparison of Arecibo E-region data and Sporadic-E theory: A measurement of the diffusion coefficient. Radio Sci. 10, 357-62.

Heisler, L. H., and J. D. Whitehead (1964): The correlation between the occurrence of Sporadic-E and the horizontal component of the earth's magnetic field. J. A. T. P. 26, 439-444.

Hines, C. O. (1963): The upper atmolphere in motion. Quart. J. Roy. Meterolog. Soc. 89, 1-42.

Hines, C. O. (1964): The formation of midlatitude Sporadic-E layers. J. G. R. 69, 1018-9.

Istomin, V. G., (1963): Ions of extra-terrestrial origin in the earth's ionosphere. Space Res. 3, 209-220.

Johanessen, A., and D. Krankowsky (1972): Positive-ion composition measurements in the upper mesosphere and lower thermosphere at high latitude during Summer. J. G. R. 77, 2888-2901.

Lindzen, R. S. (1974): Tides and internal gravity waves in the atmosphere. F. Verniani (ed) Structure and dynamics of the upper atmosphere. Elsevier Press, N. Y., 1974.

MacLeod, M. A. (1966): Sporadic-E theory; collision-geomagnetic equilibrium. J. Atmos. Sci. 23, 96.

Miller, K. L., and Smith, L. G. (1975): Horizontal structure of midlatitude Sporadic-E layers observed by incoherent scatter radar. R. Sci. 10, 271-276.

Miller, K. L., and L. G. Smith (1976): Midlatitude Sporadic-E layers. Aeronomy Report 76, Univ. of Illinois.

Narcisi, R. S., and A. D. Bailey (1965): Mass spectrometric measurements of positive ions at altitudes from 64 to 112 km. J. G. R. 70, 3687-3700.

Narcisi, R. S. (1968): Processes associated with metal ion layers in the E-region of the ionosphere. Space Res. 8, 360-369.

Narcisi, R. S. (1973): Mass spectrometer measurements in the ionosphere. Phys. and Chem. of Upper Atmosphere, B. M. McCormac (Ed.), D. Reidel Publ. Co. Dordrecht, Holland, 171-183.

Poole, L. M. G., and T. F. Nicholson (1975): The effect of ionic processes on the characteristics of radio echoes from meteor trains. Planet. Spa. Sci. 23, 1261-1277.

Rawer, K. (1962): Structure of Es at temperature latitudes. Ionosp. Sporadic-E, E. K. Smith and S. Matsushita (Ed.), Mc Millan Co. N. York, 292-343.

Reddy, C. A., and M. Rao (1968): On the physical significance of the Es parameters fbEs, fEs, and foEs. J. G. R. 73, 215-224.

Reddy, C. A. and Matsushita, S. (1968): The variations of neutral wind shears in the E-region as deduced from blanketing Es. J. A. T. P. 30, 747-762.

Reddy, C. A. and Matsushita, S. (1969): Time and latitude variations on Blanketing Es of different intensities. J. G. R. 74, 824-843.

Richmond, A. D. (1971): Tidal winds at ionospheric heights. Radio Sci. 6, 175-189.

Richmond, A. D. (1977): Ionospheric winds: Dynamo theory: A review. Submitted to J. Geomag. Geoelect. (Japan).

Richmond, A. D., S. Matsushita and J. D. Tarpley (1976): On the production mechanism of electric currents and fields in the ionosphere. J. G. R. 81, 547-555.

Rosenberg, N. W., and H. D. Edwards (1964): Observations of ionospheric wind patterns through the night. J. G. R. 69, 2819-2826.

Rosenberg, N. W. and H. D. Edwards, and J. W. Wright (1964): Ionospheric winds: motions into night and Sporadic-E. Space Res. 4, 171.

Smith, L. G., and Miller, K. L. (1977): Sporadic-E layers and unstable wind-shears. Submitted to J. of Geomag. and Geoelect. (Japan).

Swider, Jr., W. (1969): Processes for meteoritic elements in the E-region. Planet. Space. Sci. 17, 1233-1242.

Volland, H., and H. G. Mayr (1972): A three dimensional model of themospheric dynamics: I, II and III. J. A. T. P. 34, 1745-1816.

Volland, H., and H. G. Mayr (1974): Tidal waves within the thermosphere. R. Sci. 9, 263-73.

Volland, H., and H. G. Mayr (1977): Theoretical aspects of tidal and planetary wave propagation at thermospheric heights. Rev. Geophys. Space Phys. 15, 203-225.

Volland, H., and L. Grellmann (1977): A hydromagnetic dynamo of the atmosphere. Submitted to J. Geomag. Geoelect. (Japan).

Whitehead, J. D. (1960): Formation of the Sporadic-E layer in the temperate zones. Nature 188, 567.

Whitehead, J. D. (1961): The formation of the Sporadic-E layer in the temperate zones. J. A. T. P. 20, 49-58.

Whitehead, J. D. (1962): The formation of a Sporadic-E layer from a vertical gradient in horizontal wind. Ionos. Sporadic-E, Smith, E. K., and Matsushita, S.

Whitehead, J. D. (1970): Production and prediction of Sporadic-E. Rev. Geophys. Space Phys. 8, 65-144.

Whitehead, J. D. (1972): The structure of Sporadic-E from a radio experiment. Radio Sci. 7, 355-358.

Wright, J. W. (1967): Sporadic-E as an indicator of wind structure in the lower ionosphere and the influx of meteors. J. G. R. 72, 4821-4830.

Wright, J. W., C. H. Murphy and G. U. Bull (1967): Sporadic-E and the wind structure of the E-region. J. G. R. 72, 1443-1460.

Wright, J. W., and L. S. Fedor (1969): The interpretation of ionospheric radio drift measurements, 2. Kinesonde observations of micro structure and vertical motion of Sporadic-E. J. A. T. P. 31, 925.

Young, J. M., C. Y. Johnson and J. C. Holmes (1967): Positive ion composition of a temperate-latitude Es layer as observed during a rocket flight. J. G. R. 72, 1473-1497.

Zbinden, P. A., M. A. Hidalgo, P. Eberhardt and J. Geiss: (1975) Mass spectrometer measurements of the positive ion composition in the D- and E-regions of the ionosphere. Planet. Space Sci. 23, 1621-1624.

SHORT TERM PREDICTION OF IONOSPHERIC DISTURBANCES

S. N. MITRA
All India Radio
Akashvani Bhavan
Parliament Street
New Delhi 110001, INDIA

MANGAL SAIN
All India Radio
Research Department
Indraprastha Estate
New Delhi 110002, INDIA

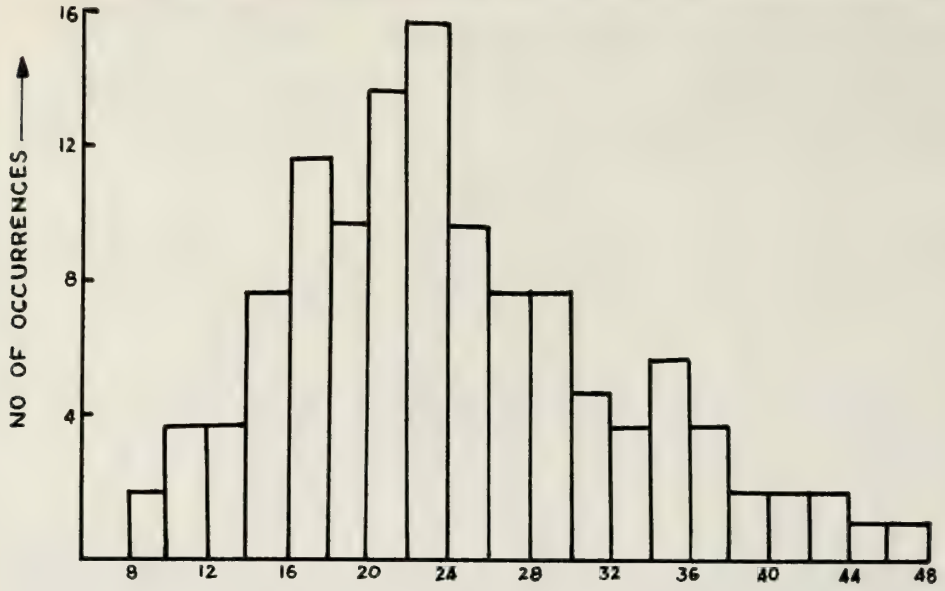
The CCIR in its Study Program 10A-1/6(1974) has asked for indentification of precursors to forecast short-term disturbances of the ionsphere arising out of solar phenomena. The only solar happening that can cause ionospheric disturbance is a flare on the sun's chromosphere and its accurate observation will be needed to make such short-term forecasts of propagation conditions which may be needed for the development of appropriate Technical Standards used by IFRB (Recommendation 4, RR). A method for such forecasts is described in this document.

A simple, reliable and unambiguous radio method of detecting a flare through propagation of longwaves was developed in the Research Department of All India Radio in August, 1958 (Mitra, 1959) at Delhi (77°05'E, - 28°35'N). This method, based on the continous recording of field strength of a distant longwave station, makes use of the fact that a sudden change occurs in longwave signal during a solar flare. This effect has been designated as SCL (Mitra, 1970). An explanation for the above-mentioned changes in longwave intensity has been offered (Mitra, 1970, 1973, 1974).

Based on extensive field strength recordings at Delhi (77°05'E, - 28°35'N) of Radio Tashkent (69°22'E, 41°25'N) operating on 164 kHz at a distance of 1630 Km from Delhi and Radio Alma - Ata (77°00'E, 43°17'N) operating on 182 kHz at a distance of 1660 Km from Delhi, it has been established that this method is very effective for the detection of solar flares (Mitra, 1964, 1973, 1974). A procedure for classification of solar flares detected by this method has been suggested (Mitra, 1964).

A practical utility of the SCL observation of a solar flare is in short-term forecasting of magnetic storms, a delayed effect caused by corpuscular emissions from flares. Such magnetic storms affect adversely shortwave propagation and an accurate forecast would be important for radio communications. The magnetic storms are caused by the incidence of charged corpuscles emitted during a flare when they impinge upon the ionosphere with concentration in the polar regions. The beginning of the storm will depend upon the arrival of these particles, which in turn depends upon their speed of travel. Data on principal magnetic storms collected during IGY (1958-60) recorded at Alibag (India) Magnetic Observatory have been analysed with a view to finding the most probable delay (Mangal Sain, 1968). Figure 1 shows one such histogram where this delay is found to be 23 hours.

FIGURE 1. HISTOGRAM SHOWING THE DELAY BETWEEN THE BEGINNING OF SILs AND BEGINNING OF CORRESPONDING MAGNETIC STORM.



A study has also been made to determine the most probable value of the duration of a magnetic storm corresponding to an SCL and it has been found to be 26 hours (Figure 2). However, when SCL's corresponding to type 3 and 3+ flares are only considered, the duration is 34 hours.

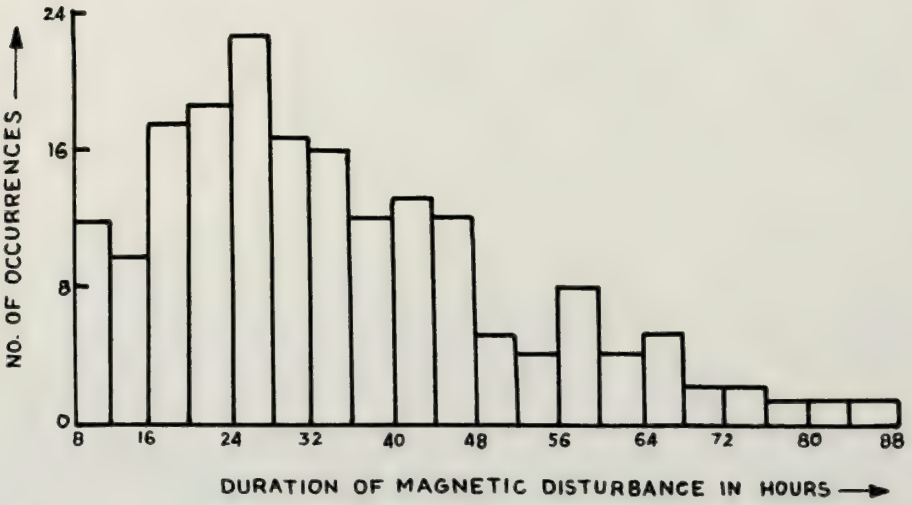


Figure 2. Histogram showing the Duration of Magnetic Storm for all types of Flares observed through Sil.

On further analysis, it has been observed that the probablity of occurrence of a magnetic storm is high where the relative increase in signal in an SCL is large. Any increase by 10 dB or greater is very likely to be associated with a magnetic storm within 20 to 24 hours of its occurrence. A systematic world wide patrol and study of SCL could provide a useful tool for short term prediction of ionosheric disturbances and the resulting propagation conditions.

REFERENCES

Mangal Sain. (1968): Ph. D. Thesis on 'Investigation of Lower Ionoshere through the Study of Longwave Propagation and SID Effects', submitted to the University of Delhi (India).

Mitra, S. N. (1959): Some Investigations on Longwave Propagation, J. Inst. Elec. Telecomm. Engrs (India), 5, 121.

Mitra, S. N. (1964): A Radio Method of Dectecting Solar Flares, J. Atmos. Terr. Phys., 26, 375.

Mitra, S. N. (1970): SCL - A New Nomencature to Denote the Effect of Solar Flares on Longwave Propagation Intensity, Solar Physics, 15, 249.

Mitra, S. N. (1973): SCL and its Associations with Solar & Geophysical Activity, Indian Journal of Radio and Space Physics, 2, 193.

Mitra, S. N. (1974): SCL and its Dependence on Season and X-ray Flux Density From a Solar Flare, J. Inst. Elec. Telecomm. Engrs (India), 20, 141.

THE INFERENCE OF SEVERE NIGHT-TIME DISTURBANCES OF THE D REGION FROM HIGH-LATITUDE RIOMETER OBSERVATIONS

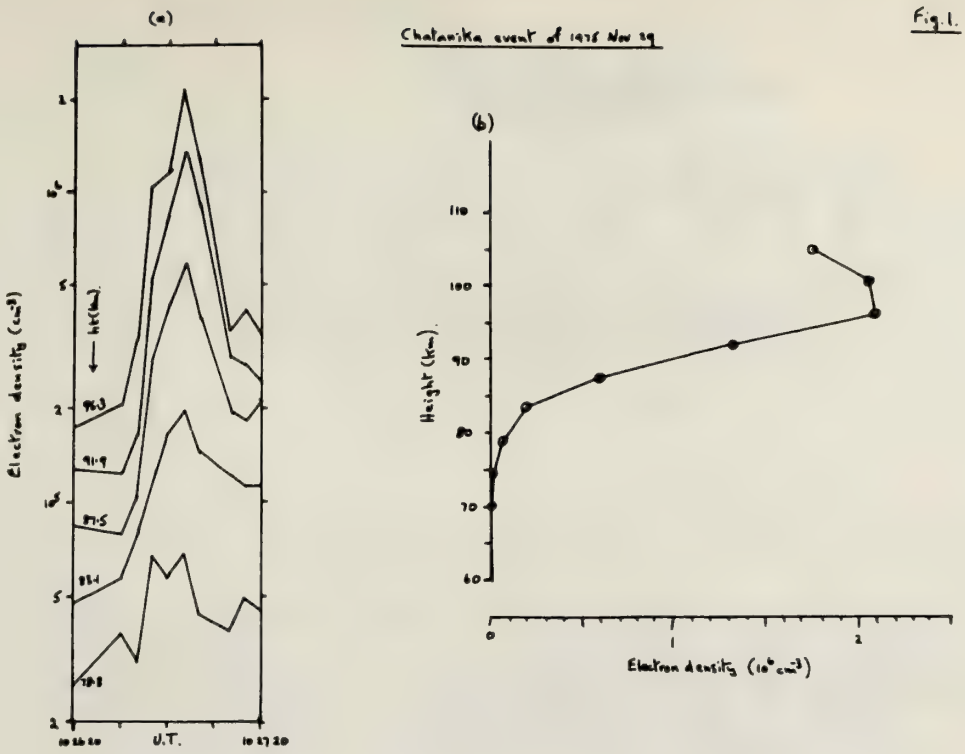
J.K. Hargreaves
Ionosphere and Magnetosphere Unit
Dept. of Environmental Sciences
University of Lancaster
Lancaster
LA1 47Q
England

The short-duration "spike" events, often seen at the beginning of substorms with high-latitude riometers, are much more intense than is indicated by measurements with a standard wide-beam riometer system. The ionospheric event may be less than 50 km across, but the electron density at 90 km may rise to over 10^6 cm^{-3} in less than a minute, leading to strong horizontal gradients of electron density. The local energy input to the D-region is considerable during these events. A real-time system for the rapid detection of the events is proposed, based on the use of riometers with different beamwidths.

The auroral D and E regions are sometimes perturbed by precipitation events of quite remarkable intensity, in which the electron density at 90 km altitude may for a short time exceed 10^6 cm^{-3}. The events occur most frequently during the few hours before midnight, and are most easily recognized on a riometer record where they appear as sharp-onset "spike events". In some cases the spike clearly marks the beginning of a substorm, but at other times it occurs in isolation. It does not usually appear after a substorm has been in progress for several minutes, however.

The properties of the spike event are unusual by comparison with other precipitation events. Not only is it particularly intense, but also it is more spatially confined than most other auroral absorption events and is subject to more rapid motion -- generally, like the substorm onset, in a poleward direction.

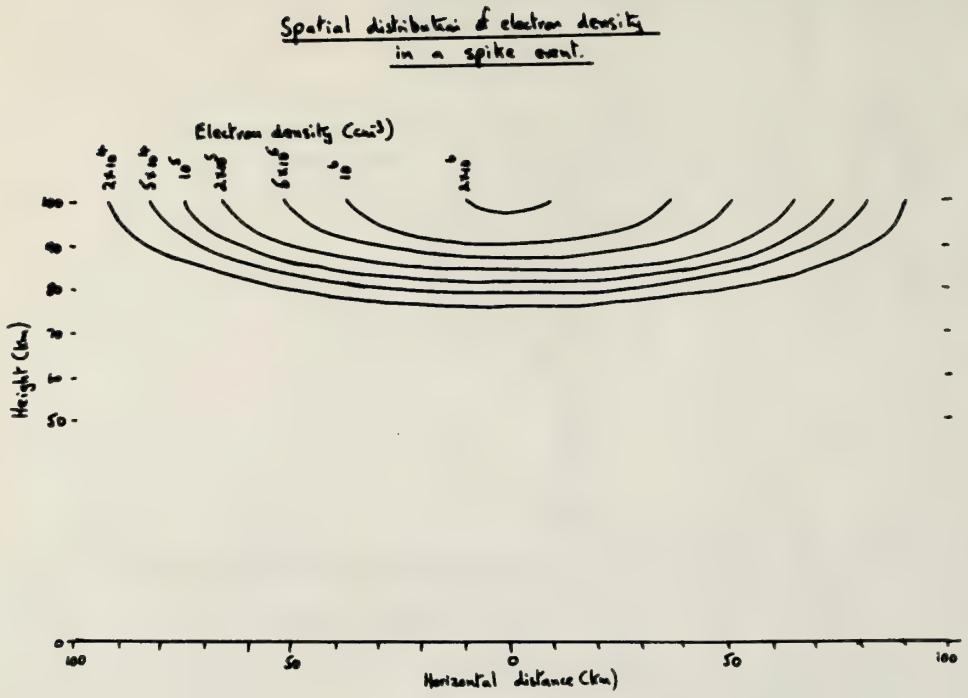
Figure 1 shows an example of such an event as observed by incoherent scatter radar from Chatanika, Alaska. This event rose to a maximum in 20 sec. and its duration between electron densities of half the peak value was also 20 sec. (Figure 1a). At the peak of the event the electron density was 10^6 cm^{-3} at 90 km and over $2x10^6$ cm^{-3} at the layer maximum at about 98 km



1. SPIKE EVENT SEEN AT CHATANIKA ON 1975 NOV 29.
(a) ELECTRON DENSITY AT FIXED HEIGHT. (b) ELECTRON DENSITY PROFILE AT THE PEAK OF THE EVENT.

(Figure 1b). At the same time the 30 MHz riometer at Chatanika registered a spike absorption event with maximum absorption 3.0 dB. Recent studies (Nielsen and Axford, 1977; Hargreaves, Chivers and Nielsen, 1979.) have shown that the spike events are narrower than the region observed by a standard wide-beam riometer antenna and typically, if represented by a gaussian model, have a characteristic width (x_0) of some 20 - 40 km if the absorbing layer is at 90 km altitude. (The relatively narrow width explains why there is a marked discrepancy between the observed and calculated absorption values, 3.0 and 13.8 dB respectively, for the event of Figure 1.)

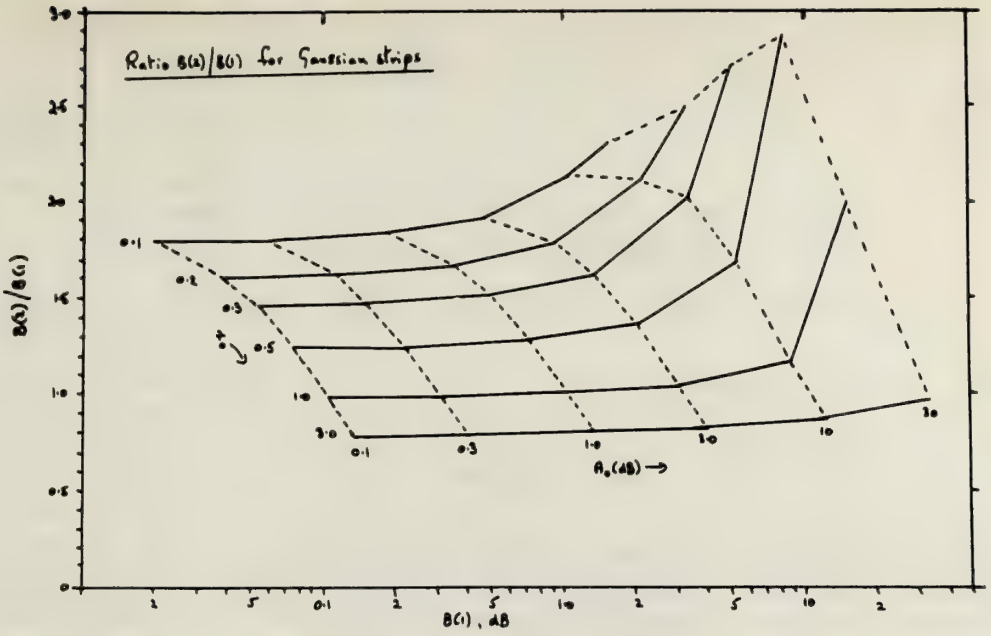
The intensity of the spike event as a disturbance of the D and E regions makes it a phenomenon of some interest. For instance, assuming the variation of event intensity seen at a fixed site to be due to movement of the precipitation region, the spatial distribution of D- and E-region ionization can be estimated for a typical case (width x_0 = 30 km, peak electron density 10^6 cm^{-3} at 90 km altitude). As shown in Figure 2, the contours of constant electron density may be considerably tilted during the passage of the disturbance. The ionospheric event corresponds to large field- aligned fluxes of energetic (above 20 kev) electrons at geostationary orbit, and the energy deposition below 90 km can reach 40 erg/cm^2-sec.



2. ESTIMATED SPATIAL DISTRIBUTION OF ELECTRON DENSITY IN A SPIKE EVENT, WITH HORIZONTAL AND VERTICAL DISTANCES PLOTTED ON THE SAME SCALE. A GAUSSIAN VARIATION OF ELECTRON DENSITY AT GIVEN HEIGHT HAS BEEN ASSUMED.

The spatial confinement of the events provides a possible method for their rapid detection, using riometers with antennas of different beamwidths. Calculations have been made of the response of various riometer antennas to absorption events in the form of a gaussian strip, in which the absorption varies as $A_0 \exp(-x^2/2x_0^2)$ in the x-direction but with no variation in the y-direction. Figure 3 compares the responses due to a wide-beam antenna of width 64° between half-power points, B(1), and a "medium-beam" antenna of beamwidth 32°, B(2). It is seen that the ratio of the responses, B(2)/B(1), as a function of B(1) provides an estimate of the width, x_0, as well as of the true intensity of the event, A_0. (The true intensity is the absorption that would be measured by a riometer with a zenithal pencil-beam antenna.) For most events, a ratio exceeding 1.3 will indicate a narrow event, whereas for widespread absorption events the ratio will be less than unity.

Operationally, the above possibility could be implemented using the I.M.S. riometer chain in Alaska, whose output is transmitted to the Space Environment Laboratory, Boulder, almost in real time (actually at 12-minute intervals). In addition to the construction of a riometer system with narrower antenna beam in Alaska, computer software would have to be developed to convert the riometer readings to absorption values and then to derive the ratios B(2)/B(1)



3. RATIO OF APPARENT ABSORPTION WITH WIDE (B(1)) AND MEDIUM (B(2)) RIOMETER ANTENNAS, BASED ON A GAUSSIAN STRIP MODEL, THE WIDE AND MEDIUM ANTENNAS HAVING BEAMWIDTHS OF 64° AND 32° RESPECTIVELY. THE RATIO WOULD BE ABOUT 2 FOR THE EVENT OF FIGURE 1, COMPARED WITH UNITY OR LESS FOR A WIDESPREAD EVENT.

continuously. Such a system would provide a rapid warning of intense, spatially confined, auroral precipitation events. It is suggested that such a system might also provide the possibility of early detection of substorm occurrence. The chance of a substorm following a spike event is fairly high, and although the actual probability is not known this could be readily evaluated from existing data.

Acknowledgements

I am indebted to the radar group at the Aeronomy Center, Utah State University, for making available observations from Chatanika, to Drs. H.J.A. Chivers and E. Nielsen for discussions on spike events, and to Mrs. S. Hargreaves for assistance with the computations.

References

Hargreaves, J. K., H. J. A. Chivers, and E. Nielsen (1979): Properties of spike events in auroral radio absorption. J. Geophys. Res., 84, 4245.

Nielsen, E., and W.I. Axford (1977): Small-scale auroral absorption events associated with substorms. Nature, 267:502.

THE POSSIBLE PREDICTION OF SID'S USING THE SLOWLY VARYING COMPONENT OF THE SOLAR RADIO FLUX AT 3.2CM

Zhu Zu Yan, Zhou Ai Hua, and Zhou Shu Rong
中国科学院紫金山天文台
Purple Mountain Observatory, Nanking, China

1. INTRODUCTION

There is a fairly good correlation between SID's and the slowly varying component (SVC) at 3.2cm. Using the solar radio total flux density at 3.2cm and the data of sudden disturbance in the ionosphere, the statistical correlation was made. It has been found that the relative continuous increase of SVC at 3.2cm can be used to predict SID events.

2. DATA

The radio data used were the daily antenna temperature observed with the 3.2cm radio telescope of the Purple Mountain Observatory. The activities of all solar active regions on the solar surface contribute to the peaks and valleys of the curves of variation of daily antenna temperature.

The SID data are the records of communication circuits in our country during December 1966 to February 1975. According to the coincidence between 3.2cm solar bursts and communication events, the latter can be identified as SID events. The SID events which took place during periods of no solar observations were not used.

3. THE POSSIBLE PREDICTION METHOD

According to the variation of daily antenna temperature, we judged the possibility that solar bursts would occur that give rise to SID events. An analysis of 95 peaks on the antenna temperature curves was made, and the relative continuous increase of antenna temperature for each peak, $(T\overset{3}{a}-T\overset{0}{a})/T\overset{0}{a}$ or $(T\overset{4}{a}-T\overset{0}{a})/T\overset{0}{a}$, was calculated, where $T\overset{4}{a}$ and $T\overset{3}{a}$ are antenna temperature values observed on the third and fourth days, respectively, after the beginning day t_o of successive antenna temperature increase. Comparing the calculated values with SID data, the results are given in Figure 1, where dots indicate that there are SID events during the peak period and circles indicate no SID at all. It has been found that the peaks corresponding to SID events satisfy the following criteria:

$$(T_a^3 - T_a^0)/T_a^0 \geq 5.5\% \qquad \text{or} \qquad (T_a^4 - T_a^0)/T_a^0 \geq 7.0\%$$

and most of the dates which have SID events occur within seven days later than the date on which the foregoing criteria are satisfied. Then we obtained the prediction criteria: when the relative continuous increase of antenna temperature satisfies the criteria

$$(T_a^3 - T_a^0)/T_a^0 \geq 5.5\% \qquad \text{or} \qquad (T_a^4 - T_a^0)/T_a^0 \geq 7.0\%$$

there will appear SID events within seven days caused by solar bursts.

The data was analyzed for 98 days of SID's. Consider Figure 2, where Δt indicates the days between the date of an SID and the date of the preceding valley of the radio flux curve. The vertical coordinate indicates the number of days with SID events. It can be seen from Figure 2 that most SID events take place within 7 days after satisfying the criteria (from the 3rd to 9th days), which is 76.5% of the total days of SID events. There is only 18.4% Δt in 6 days (10th to 15th days) and 5.1% Δt in 1st - 2nd and 16th - 17th days as shown in Table 1.

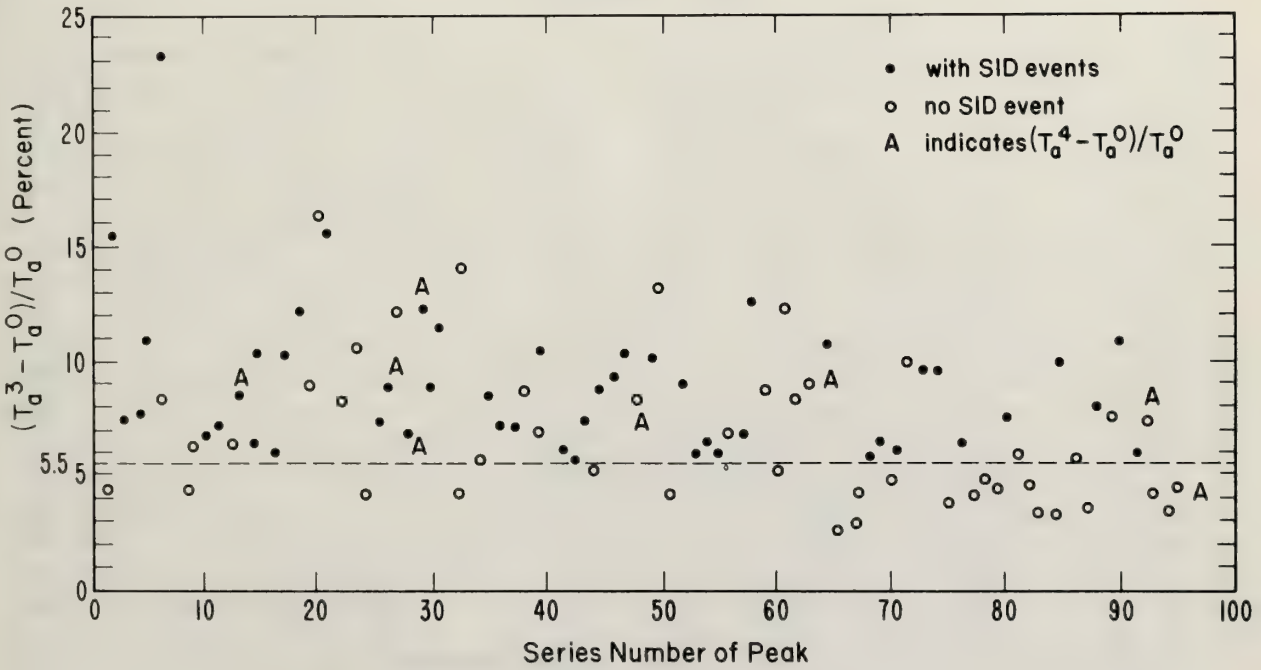


Figure 1. Distribution of three-day percentage change in the slowly varying component of 3.2cm solar radio flux.

Table 1.

Time Interval Δt (days)		days with SID	days with SID (%)
1-17	(day) (total days)	98	100
1-2	(2 days)	3	3.1
3-9	(7 days)	75	76.5
10-15	(6 days)	18	18.4
16-17	(2 days)	2	2.0

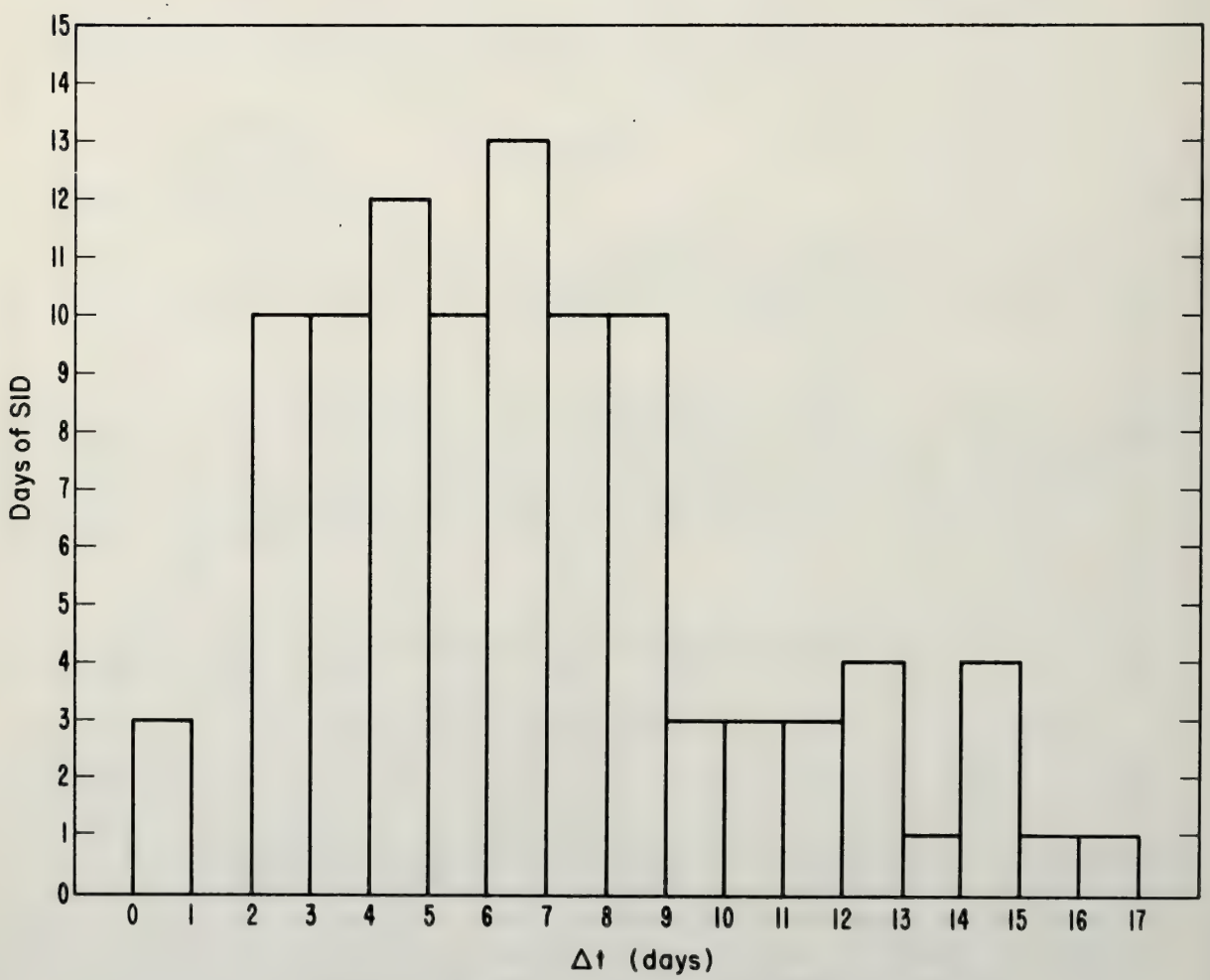


Figure 2. Distribution of SID's.

D. RADIO PROPAGATION PREDICTIONS

1. TRANSIONOSPHERE PROPAGATION PREDICTIONS

AN IMPROVED IONOSPHERIC IRREGULARITY MODEL

D.G. Singleton
Defence Science and Technology Organization,
Electronics Research Laboratory,
Salisbury, S.A., Australia

Modifications are made to the global model developed by Fremouw et al. for the incremental electron density of F-layer irregularities in order to force the model into agreement with a considerable body of scintillation and spread-F data. While special attention is given to the equatorial region, where the original model was particularly lacking, the results of other studies are used to update the model in the other latitude regions and so provide a model of general application.

1. INTRODUCTION

Fremouw and Bates (1971) and later Fremouw and Rino (1973) were the first to attempt to produce an irregularity model by collating the data available in the literature on the occurrence, strength, size, etc. of F-region ionization density irregularities. They proposed an empirical model of global scintillation behaviour taking into account variations due to time of day, season, sunspot-cycle and latitude. An extension of this model to allow simulation of spread-F occurrence as well as scintillation index was proposed by Singleton (1975). This spread-F adaption of the model was used subsequently to better define the sunspot cycle dependence (Singleton, 1977). The need for the model to allow for the effects which magnetic activity have on the behaviour of the irregularities was first addressed by Pope (1974). He proposed a modification to the model to achieve this at high latitudes. Singleton (1978) recently indicated how the model can be further modified so as to allow the simulation of the effect of magnetic activity on the irregularities at the low latitudes. He also considered a further effect, hitherto neglected in the modelling process, namely variations in irregularity occurrence with longitude. This paper briefly outlines this model and its derivation.

2. IRREGULARITY SIZE AND SHAPE

The early scintillation observations, which were carried out in the VHF region, seemed to be explicable in terms of a Gaussian distribution of irregularity size (Briggs and Parkin, 1963) which appeared to peak at about 1km. This corresponds to the scale size to which the scintillation mechanism is most sensitive at these frequencies, being approximately equal to the radius of the first Fresnel zone. The reliability of the Gaussian distribution was first thrown into doubt with the unexpected observation of scintillation at gigahertz frequencies near the magnetic equator (Craft and

Westerlund,1972). Subsequent in-situ measurements (Dyson et al., 1974) and scintillation spectral studies (Singleton, 1974) have shown that the irregularities in the F-region have a power law spectrum involving a wide range of wavenumbers corresponding to dimensions ranging from a few metres to tens of kilometres. Consequently, it is important that a model of irregularity behaviour intended for universal application should both be evaluated in terms of, and employ, a power law irregularity spectrum. A wavenumber spectrum of monotonic power-law form involving an outer scale size of 10km is assumed.

It is convenient to define the scintillation index S_4 of a fluctuating radio wave (whose amplitude is R) by

$$S_4 = [\{\overline{R^4} - (\overline{R^2})^2\} / (\overline{R^2})^2]^{\frac{1}{2}} \qquad (1)$$

In this case, it can be shown (Rufenach, 1975) that, for weak scattering conditions, S_4 is a function of the excess or deficiency of electron density in the irregularities (ΔN), the thickness of the irregular layer (Δh), the axial ratio of the field-aligned irregularities (α), the angle between the direction of propagation and the Earth's magnetic field (ψ), the outer scale wavenumber of the irregularity spectrum (k_o), the observing wavelength (λ), the distance between the observer and the irregularities (z) and the angle of incidence of the radiation on the ionosphere (χ) (vide equations (A1) to (A6) of the Appendix).

Fremouw and Bates (1971) and Fremouw and Rino (1973) in their original models assumed a constant value of ten for the elongation factor (α) at all latitudes. This figure is probably justified in the equatorial region where values of α in excess of 7.5 have been observed (Koster, 1963). However, at the high latitudes (50° geomagnetic and above) values of α in the vicinity of 5 have been observed (Singleton, 1973). Consequently, in the present model α is represented by equation (A9). This gives α = 10 for geomagnetic latitudes (θ) from 0° to 15°, α = 5 for $50^\circ < \theta < 90^\circ$ and a smooth transition of α from 10 to 5 between 15° and 50° geomagnetic latitude.

3. HIGH LATITUDE MAGNETIC ACTIVITY BEHAVIOUR

Fremouw's original model of global scintillation behaviour suffered from the limitation that it took no account of the well established correlation of scintillation occurrence with magnetic activity. This correlation is negative in the equatorial region and positive at magnetic latitudes in excess of 50°. The high latitude effect is largely due to the equator-wards movement of the edge of the polar region of high scintillation activity (the scintillation boundary) with increasing magnetic activity. Pope (1974) modified Fremouw's model so as to adequately represent these movements of the scintillation boundary. This variant of the model will now be outlined.

The model of ΔN consists of four additive terms, the influence of each being dominant in different regions of geomagnetic latitude, namely equatorial, mid, high and auroral latitudes. These terms are functions of some or all of the following parameters: local time (t hours), day of year (D days), geomagnetic latitude (θ degrees), three hourly planetary magnetic index (Kp) and the monthly smoothed Zurich sunspot number (R). In order to retain the option of adding variations involving other variables into the expression, a factor m has been included in each term which allows the

adjustment of its magnitude. Thus the model is represented by equation (A17) in which the subscripts e,m,a and h refer to the equatorial, middle, auroral and high latitude regions respectively.

Using units of electrons/m^3 for electron density, the ΔN terms in equation (A17) are

$$\Delta N_e = 5.5\times10^9(1+0.05R)[1-0.4\cos\{4\pi(D+10)/365\}].$$
$$[\exp\{-(t/4)^2\}+\exp\{-(t-23.5)^2/3.5^2\}]\exp\{-(\theta/\theta_e)^2\} \quad (2)$$

and as given by equations (A23), (A24) and (A25) of the Appendix, where $\theta_e = 12^\circ$, $\theta_m = 10^\circ$ and $\theta_o = 32.5^\circ$.

Singleton (1977) noted that the sunspot cycle variation of ΔN implied by spread-F morphology (Singleton, 1960; 1968) is inadequately modelled by the above equations. This position can be rectified however, if sunspot number variations of θ_e, θ_m, θ_o, m_e, m_m, m_h and m_a as given by equations (A32), (A35), (A34) and (A18) to (A21) inclusive, are incorporated in the model.

4. LOW LATITUDE MAGNETIC ACTIVITY BEHAVIOUR

At low latitudes increased magnetic activity tends to inhibit the occurrence of both spread-F and scintillation (Lyon, Skinner and Wright, 1960). The nature of the correlation between scintillation index and magnetic activity was investigated by Koster (1972) whose results for Legon are reproduced in figure 1. Here scintillation-index observations, obtained between July and December in a year of high sunspot activity (1969), were first normalized so as to remove the seasonal and diurnal variations and then plotted against the 24 hour sum of the appropriate day's Kp indices (S_K). Though there is considerable scatter, the diagram suggests that there is some value of S_K below which scintillation index is independent of S_K and above which scintillation index decreases with increasing S_K. Koster suggested a Kp sum of 30 as the boundary between these two regimes.

4.1 The model employed

Section 4.2 considers the effect of magnetic activity on spread-F occurrence season by season. The Kp sum which separates the regime of constant response from that of inhibition is found to vary with season. In fact, the modelling process is best served by the three lines drawn on figure 1, one for each of the seasons as indicated. Each of the lines is accommodated by the scatter and indeed they suggest one plausible reason for the scatter at the higher S_K values. This variation is incorporated in the model by including in m_e (equation (A17)) a factor F_K which is an appropriate function of S_K (Section 4.2).

The modified model can be tested against some scintillation index data obtained at 45 MHz, at Accra (Koster and Wright, 1960). Diurnal distributions obtained from this data for both the international magnetically quiet days (circles) and disturbed days (crosses) during sunspot maximum is shown in figure 2(a). Employing the model, together with the published Kp and sunspot number values, to simulate the degree of scintillation at Accra during the quiet and disturbed periods involved,

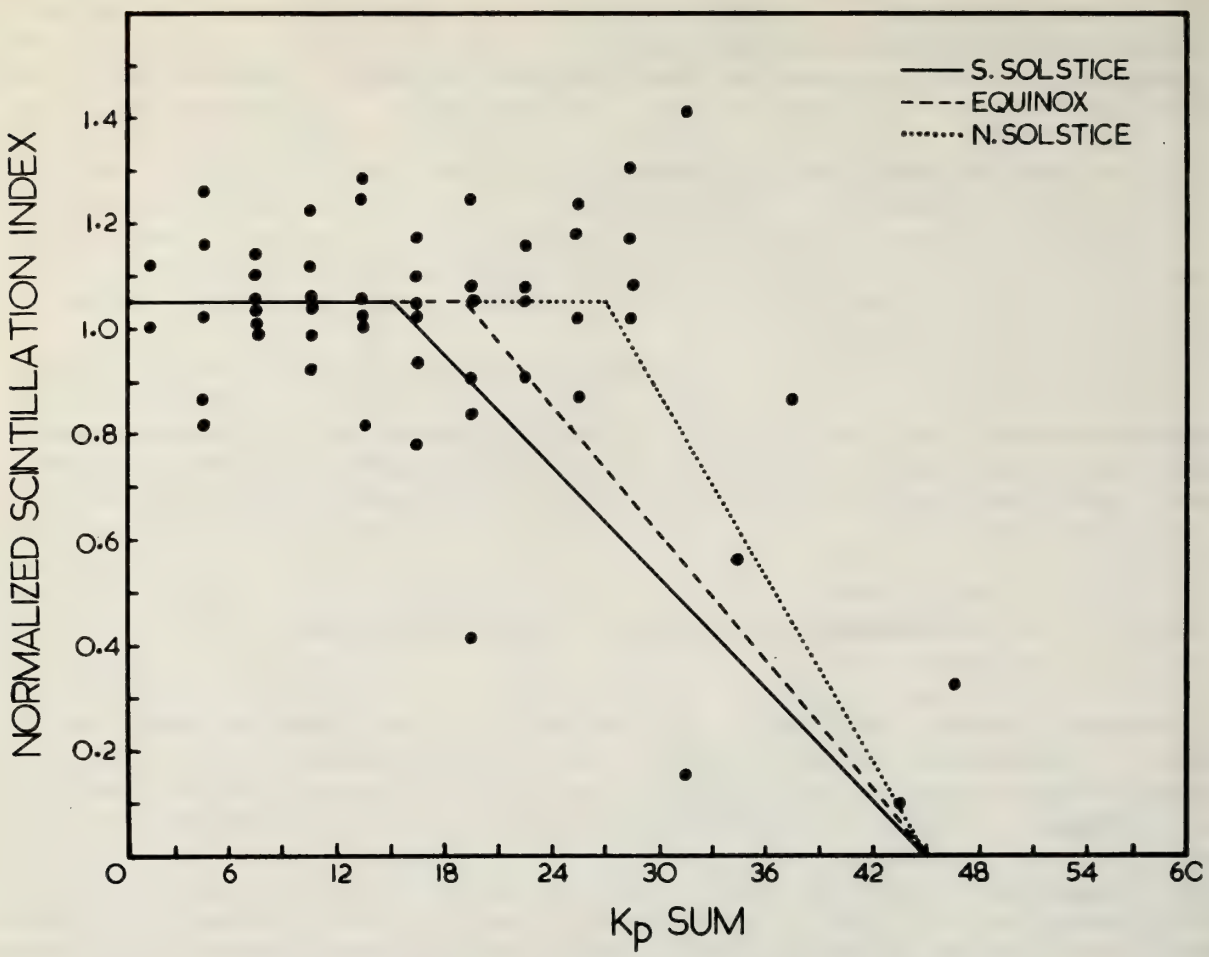


Fig.1: Normalized scintillation index as a function of Kp sum.

gives the diurnal curves shown as full and broken lines respectively in figure 2(a). The success of the modified model in predicting the levels of scintillation activity under magnetic quiet and disturbed conditions is obvious.

Fremouw and Rino employed an equatorial diurnal factor of the form (equation (2))

$$F_d = \exp[-(t/4)^2] + \exp[-\{(t-23.5)/3.5\}^2] \quad (3)$$

However, in order to obtain a good fit throughout the night between the predicted curves and the experimental points in figure 2(a), this diurnal factor had to be modified to be

$$F_d = \exp[-(t/3)^2] + \exp[-\{(t-22)/7\}^9] \quad (4)$$

Koster and Wright (1960) also carried out an analysis using spread-F occurrence data obtained at Ibadan which was similar to that described above for their Accra scintillation data. The resulting diurnal distributions are shown in figure 2(b). In order to simulate this data, it is necessary to employ the spread-F adaption of the scintillation model (Singleton, 1975).

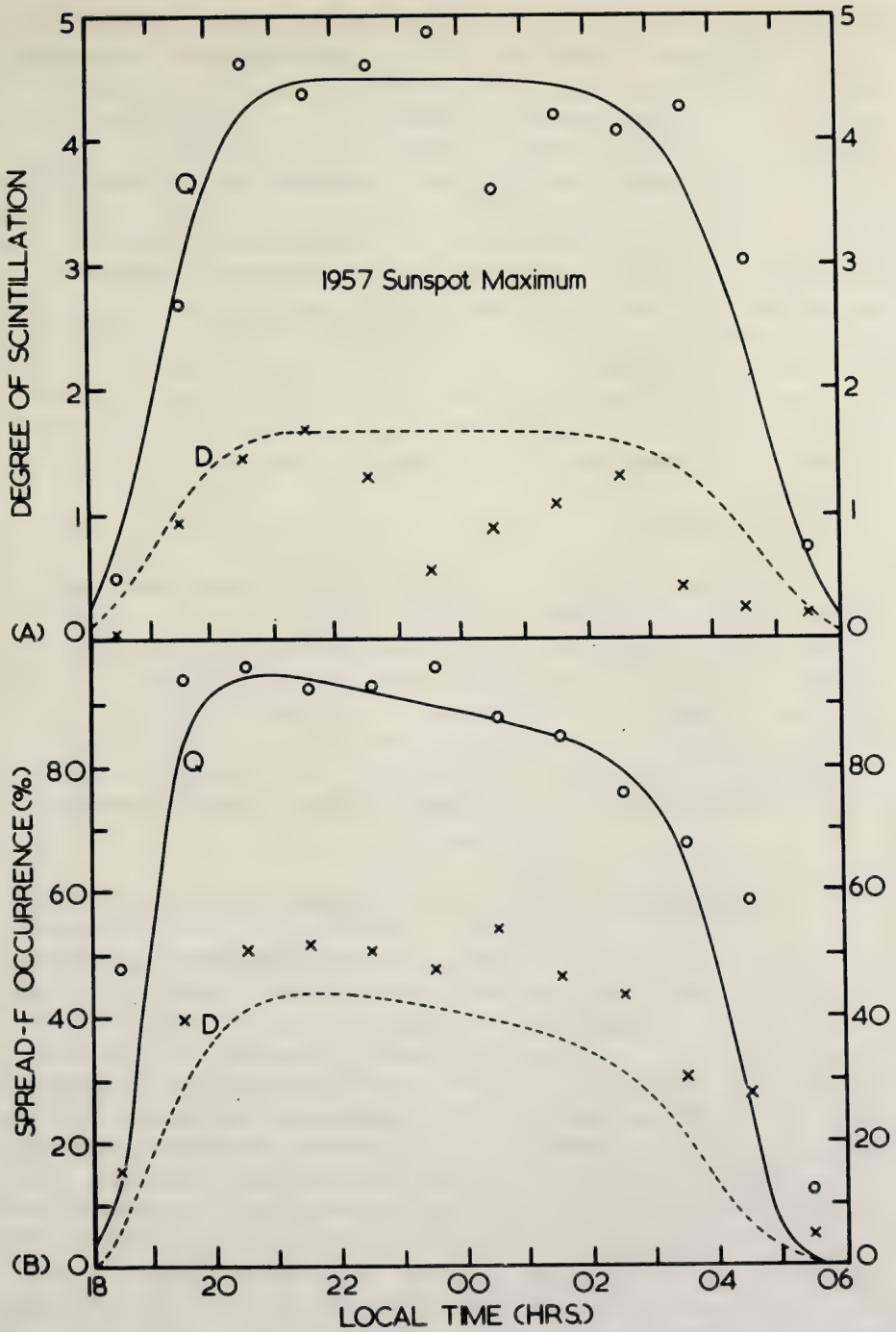


Fig.2: Magnetically quiet and disturbed levels (circles and crosses respectively) of scintillation observed at Accra and spread-F occurrence at Ibadan at sunspot maximum.

This adaption employs an empirical model of the maximum electron density of the F layer N (Chiu, 1975) in combination with $\triangle N$ to simulate both the mean spread in critical frequency $\triangle f$ (equation (A8)) and the percentage occurrence of spread F P_s (equation (A7)). This procedure (Briggs, 1964) removes the apparent modulation of the occurrence of irregularities by the strength of the background layer when spread F is used as an indicator of

irregularity presence (Singleton, 1962). This is the same modulation which results in the frequently reported anticorrelation of the occurrence of spread F and scintillations. The curves for magnetically quiet and disturbed days resulting from such a simulation of the Ibadan data are shown as the full and broken lines respectively in figure 2(b).

The scintillation modelling process depends on a simulation of the product $\Delta N(\Delta h)^{\frac{1}{2}}$, while the spread-F adaption of the model does not involve Δh. Consequently, a diurnal variation in ΔN implied from scintillation data may be confused by a diurnal variation in Δh. However, this will not be the case for diurnal variations of ΔN obtained from spread-F data. It has been customary in F-region irregularity modelling to use a constant value of Δh, namely 100km, when considering scintillation data. However, the degree of fit between the model and the spread-F data illustrated in figure 2(b) can only be obtained if the ΔN diurnal variation, based on the scintillation data, is altered to accommodate a Δh, which, in the equatorial region, is assumed to vary as

$$\Delta h = 10^{(1+t_{18}/6)} \qquad (5)$$

where t_{18} is local time in hours from 1800 LMT. Consequently, the diurnal factor in the equatorial term of the Fremouw and Rino model of ΔN is modified so that when combined with this nocturnal variation of Δh, no change is made to $\Delta N(\Delta h)^{\frac{1}{2}}$. In this way, the modelling of scintillation index remains unaltered while allowing a successful modelling of spread-F occurrence. Because of the ad hoc nature of this variation of Δh, the possibility that it may also encompass real differences between the irregularities responsible for spread F and scintillations cannot be dismissed.

4.2 Choice of the seasonal magnetic factors

Figure 3 shows some further occurrence results for equatorial spread F (Lyon et al. 1960). Here sunspot maximum data were used to produce diurnal percentage occurrence diagrams for magnetic quiet days (circles) and disturbed days (crosses). The data were obtained at several observing stations in the Afro-Indian zone (20°W to 80°E longitude), while the curves simulated with the modified model are appropriate to Ibadan (3.9°E).

Two changes to the seasonal dependence of the Fremouw and Rino model were found to be necessary in order to obtain the fit between the simulated diurnal variations and the experimental variations illustrated in figure 3. The first involves adopting the magnetic inhibition relationships already mooted in Section 4.1. These are given by equations (A28), (A29) and (A30) where F_C is 1.05, B_K is 17 in the southern solstice, 19 in the equinox and 27 the northern solstice and where $(B_K + F_C/A_K)$ is 45. The second modification involves the overall seasonal variation in ΔN. Fremouw and Rino model the seasonal variation as a simple sinusoidal semi-annual variation peaking in the equinoxes (equation (2)). However, as Koster (1972) points out, there is also a considerable annual variation in scintillation index as observed at Legon and such a variation has been included in the modified model. The seasonal term in equation (2), namely

$$F_s = [1 - 0.4 \cos\{4\pi(D+10)/365\}] \qquad (6)$$

was replaced by

$$F_S = [\,1 - 0.36\cos\{4\pi(D+10)/365\} + 0.25\cos\{2\pi(D+10)/365\}\,] \quad (7)$$

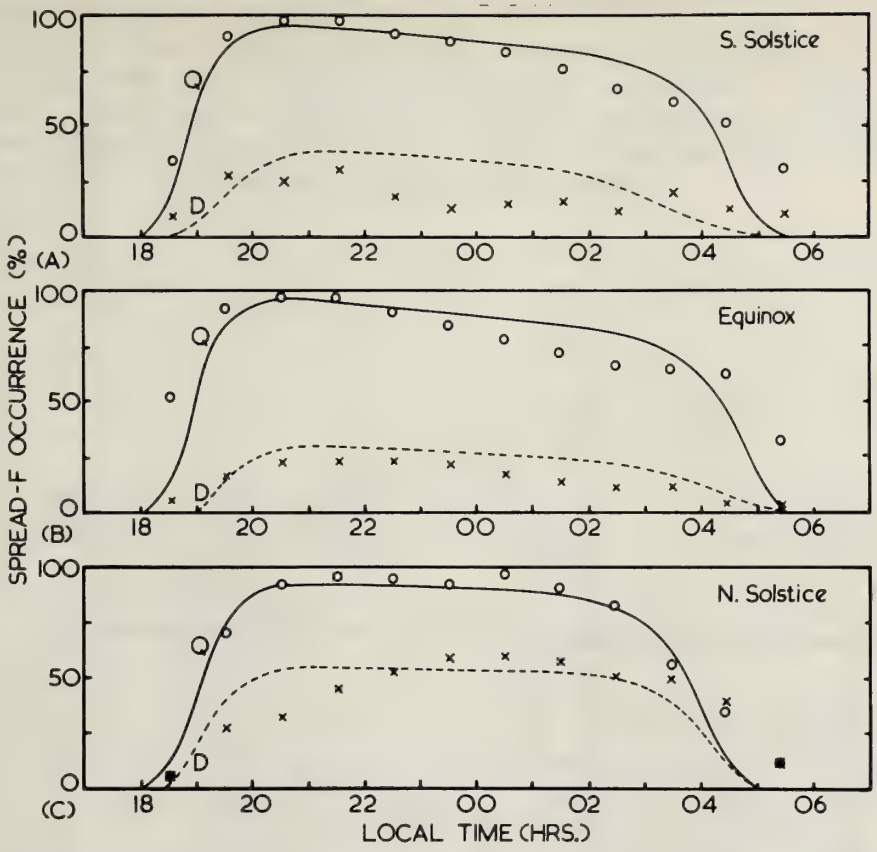


Fig.3: Magnetically quiet and disturbed levels (circles and crosses respectively) of spread-F occurrence at Ibadan in each of the seasons at sunspot maximum.

4.3 Sunspot cycle effect

The investigation of scintillation at Accra and spread-F at Ibadan by Koster and Wright (1960), besides giving the sunspot maximum results of figure 2, also presents similar results under sunspot minimum conditions (figure 4). Only two changes are found to be necessary to produce the illustrated degree of fit between the simulation and experiment. The first involves the diurnal distribution factor which is required to take the form

$$F_d = \exp[-(t/3)^4] + \exp[-\{(t-21.5)/6\}^2] \quad (8)$$

The second modification involves the variation of the thickness of the disturbed region through the night. This is required to be of the form

$$\Delta h = 10^{(1+t_{18}/18)} \quad (9)$$

Equations (5) and (9) can be generalized to give

$$\Delta h = 10^{(1+t_{18}/\tau_{18})} \quad (10)$$

Also, the diurnal function (F_d) can be generalized to give equation (A26), the variation from sunspot maximum to minimum conditions being accounted for by employing t, τ_m, q and τ_{18} as given in equations (A38) to (A41).

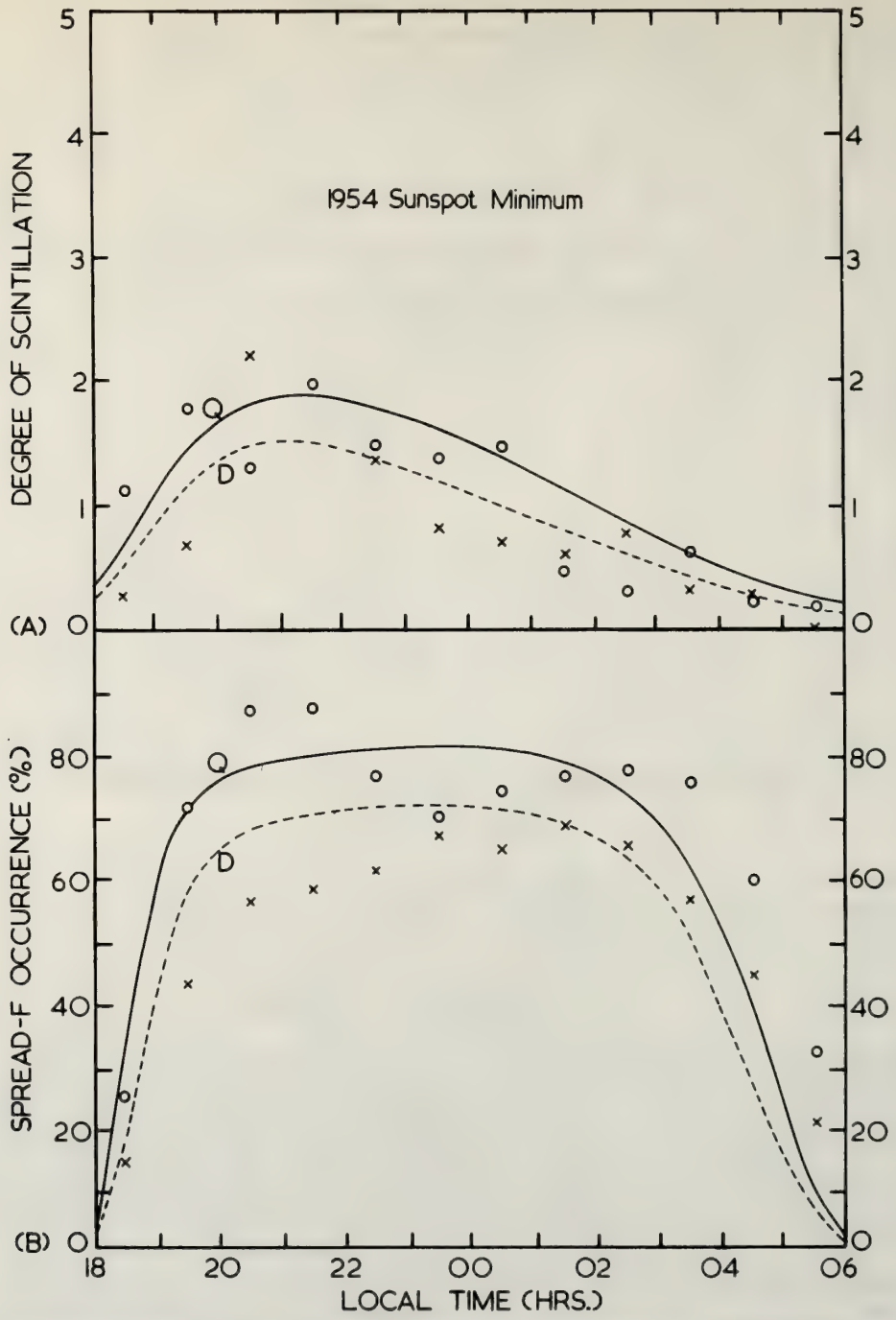


Fig.4: Magnetically quiet and disturbed levels (circles and crosses respectively) of scintillation observed at Accra and spread-F occurrence at Ibadan at sunspot minimum.

5. THE LONGITUDE DEPENDENCE AT LOW LATITUDE

Lyon et al. (1960) analysed spread-F data obtained during the I.G.Y. at fifty-seven equatorial stations. They divided the stations into three geographic longitude zones, the American zone (longitudes 45° W to 85° W), the

African zone (longitudes 20°W to 80°E) and the Asian zone (100°E to 160°E) and produced magnetic latitude variations of occurrence, season by season, for each zone. Their data points are reproduced in figure 5. The filled circles represent the observed occurrence situation during magnetically quiet days and the crosses correspondingly for magnetically disturbed days. The curves drawn on figure 5 are not those drawn by Lyon et al. and should be neglected for the moment.

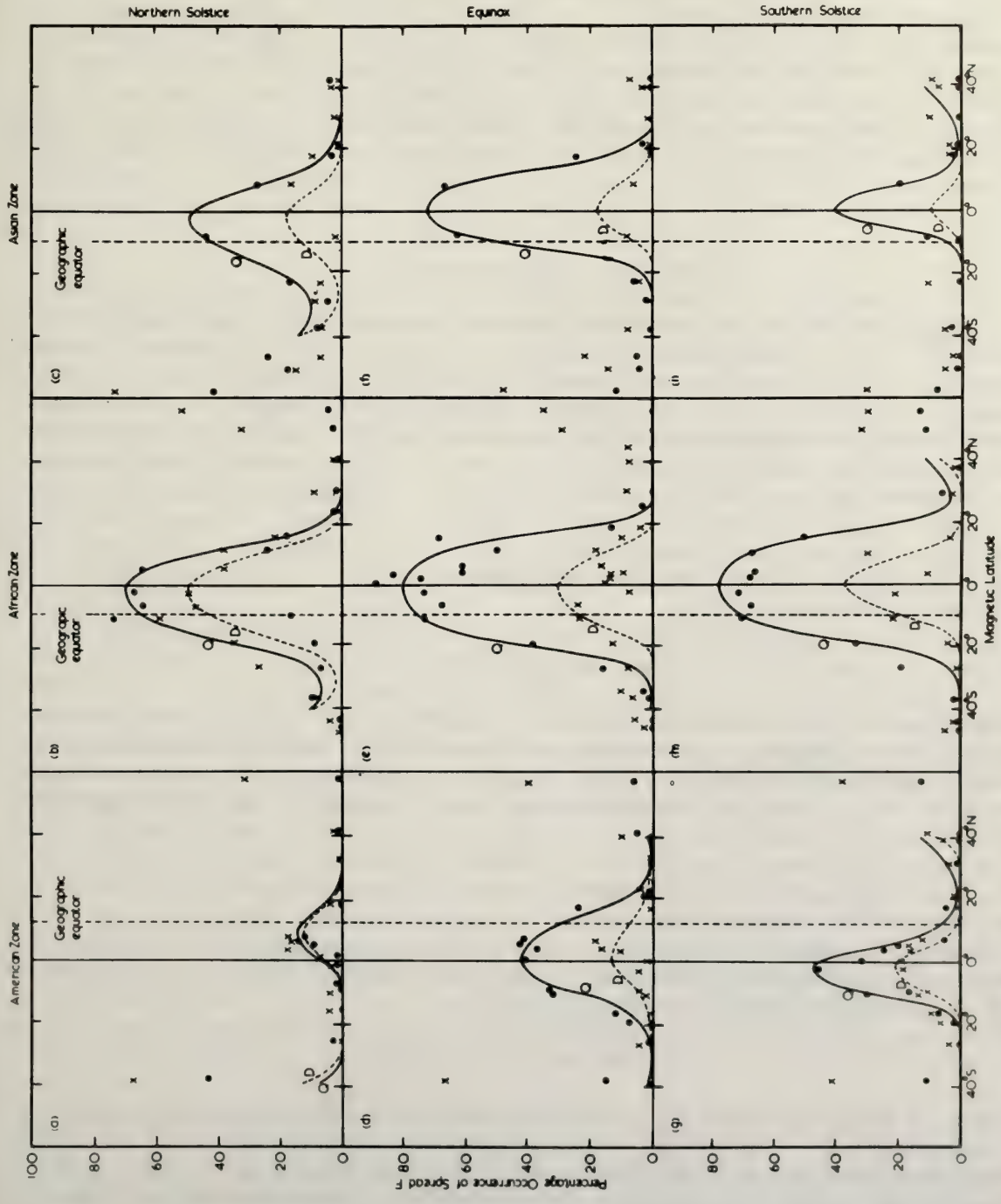


Fig.5: The variation of spread-F occurrence with magnetic latitude for the seasons and longitude zones indicated. The points and crosses refer to magnetically quiet and disturbed conditions.

As Lyon et al. point out, the points on figure 5 show that there are longitudinal and seasonal variations in (a) the overall occurrence of spread F, (b) the extent of the occurrence reduction accompanying magnetic activity, (c) the width of the equatorial region of enhanced spread-F activity, and (d) the position of the region with respect to either the magnetic or geographic equator. These variations will now be included in the model.

It should be noted that the results for the African zone (figures 5(b),(e) and (h)) were derived from the same data used to produce the diurnal variations of figure 3. As these diurnal variations have been accommodated by the model already (Section 4.2), the model as described above should predict the occurrence levels of the peaks of the latitude distributions for both quiet and disturbed days in figures 5(b), (e) and (h). This is found to be the case. Of course the model, at this point, also predicts similar levels for all other longitudes (Ω) which is obviously erroneous.

5.1 Quiet-day occurrence

In order to establish a basis on which to model the longitudinal-seasonal variation (figure 5), the seasonal factor (equation (7)) was replaced in equation (2) by a particular value which will be called a peak occurrence factor (F_s). For each of the nine combinations of season and longitude displayed in figure 5, peak occurrence factors were chosen so as to cause the model's prediction of spread-F occurrence to fit the observed quiet day occurrence peaks. These calculations employed the values of Kp and sunspot number observed during the appropriate periods. As expected in the African zone, the peak occurrence factors are as given by equation (7). Mathematical expressions were found which describe the seasonal and longitudinal variations of the peak occurrence factors. These are equations (A27), (A42), (A43) and (A44).

5.2 Critical value of Kp sum

From figure 5 it is obvious that the extent of the reduction in spread-F occurrence accompanying increased magnetic activity varies with both season and longitude. In Section 4.1 it was suggested that the occurrence reduction occurs when the 24-hour Kp sum surpasses some critical value. Variation of this critical value with season and longitude therefore, provides the basis for a model of the magnetic activity effect. The critical Kp sum (B_K) for each of the combinations of longitude and season represented in figure 5 can be determined by forcing the model to reproduce the disturbed day peak occurrences. A set of mathematical expressions were derived which describe the seasonal and longitudinal variations of the critical Kp sums (B_K). These are equations (A45), (A52), (A53) and (A54).

5.3 Incremental width

Fremouw's original model of ΔN assumed that the equatorial region of high activity was centred on the geomagnetic equator and fell off with latitude according to $\exp\{-(\theta/\theta_e)^2\}$ where θ_e is a constant "width" of 12°. Examination of figure 5 suggests this is an approximation with regard to both the position of the peak and its width. While the question of width

will be examined in this section and that of peak position in the next section, in practice these quantities were necessarily modelled in concert.

A value of θ_e' was found which, when subtituted for θ_e in equation (2) allowed the model to adequately represent the spread-F data for each of the seasons and longitudes represented in figure 5. The corresponding incremental widths ($\Delta\theta_e = \theta_e' - \theta_e$) were found to be adequately modelled by equations (A33), (A49), (A50) and (A51).

5.4 Latitude of the occurrence peak

As indicated in Section 5.3, the peak of irregularity activity in the equatorial region is not always on the geomagnetic equator and the model should allow for the deviations. This, together with the variations in width just discussed, is taken into account by replacing the $\exp\{-(\theta/\theta_e)^2\}$ term in equation (2) by $\exp[-\{(\theta+\theta_d)/(\theta_e+\Delta\theta_e)\}^2]$. Deviations ($\theta_d$) were found for each of the seasons and longitudes represented in figure 5. These were modelled by equations (A31), (A46), (A47) and (A48).

5.5 Total longitude dependence

When the four longitude variations discussed above are included in the model, which is also supplied with the observed values of Kp and sunspot number, the resulting latitude distributions for each of the seasons and longitudes of figure 5 are as shown by the curves on that figure. The full-line curves represent the quiet day situation, while the broken lines are for disturbed days. As expected, the model provides a good simulation of the experimental situation.

6. BLACKOUT FACTOR

At latitudes in excess of a critical value θ_c (about 70° geomagnetic), the adaption of the ΔN model to simulate spread-F occurrence requires the inclusion of a blackout factor (Singleton, 1975). This factor, which is applied directly to the occurrence probability predicted by equation (A7), is believed to be due predominantly to the effect of polar blackout on an ionosonde's ability to detect spread F. The blackout factor (B) is given in equations (A11) to (A16) inclusive (Singleton, 1977).

7. MODEL VALIDATION

The major modifications made to the model affect the equatorial region. Consequently, it is essential to test it against independent data obtained in this region. This has been done successfully with regard to the simulation of both scintillation and spread-F activity (Singleton, 1978).

8. CONCLUSION

The model has been developed considerably by incorporating in it information from a number of published data bases other than those used originally by Fremouw and his co-workers. Scintillation data has been

supplemented by spread-F data in those areas of the modelling process in which the scintillation data was found to be inadequate. The model's validity has been demonstrated by testing it against a number of other data bases. Consequently, the improved model can be used with confidence as a simulation technique in engineering studies of propagation configurations affected by F-region irregularities.

REFERENCES

Briggs, B.H. (1964): Observatios of Radio Star Scintillations and Spread-F Echoes Over a Solar Cycle, J. Atmos. Terr. Phys., 26:1.

Briggs, B.H. and J.A. Parkin (1963): On the Variation of Radio Star and Satellite Scintillation with Zenith Angle. J. Atmos. Terr. Phys., 25:339.

Chiu, G.J. (1975): An Improved Phenomenological Model of Ionospheric Density. J. Atmos. Terr. Phys., 37:1563.

Craft, H.D., and L.H. Westerlund (1972): Scintillation at 4 and 6 GHz Caused by the Ionosphere, AIAA Paper No. 72-179, American Inst. of Aeronautics and Astronautics Library, 150 Third Ave., New York.

Dyson, P.L., J.P. McClure, and W.B. Hanson (1974): In-Situ Measurements of the Spectral Characteristics of F-Region Ionospheric Irregularities, J. Geophys. Res., 79:1495.

Fremouw, E.J.,and J.F. Bates (1971): Worldwide Behaviour of Average VHF-UHF Scintillation, Radio Sci., 6:863.

Fremouw, E.J., and C.L. Rino (1973): An Empirical Model for Average F-layer Scintillation at VHF-UHF, Radio Sci., 8:213.

Koster, J.R., and R.W. Wright (1960): Scintillation, Spread F and Transequatorial Scatter, J. Geophys. Res., 65:2303.

Koster, J.R. (1963): Some Measurements of the Irregularities Giving Rise to Radio Star Scintillations at the Equator, J. Geophys. Res., 68:2579.

Koster, J.R. (1972): Equatorial Scintillation, Planet. Space Sci., 20:1999.

Lyon, A.J., M.J. Skinner, and R.W.H. Wright (1960): The Belt of Equatorial Spread-F, J. Atmos. Terr. Phys., 19:145.

Pope, J.H. (1974): High Latitude Ionospheric Irregularity Model, Radio Sci., 9:675.

Rufenach, C.L. (1975): Ionospheric Scintillation by a Random Phase Screen: Spectral Approach, Radio Sci., 10:155.

Singleton, D.G. (1960): The Geomorphology of Spread F, J. Geophys. Res., 65:3615.

Singleton, D.G. (1962): Spread F and the Perturbations of the Maximum Electron Density of the F-Layer, Aust. J. Physics., 15:262.

Singleton, D.G. (1968): The Morphology of Spread-F Occurrence Over Half a Sunspot Cycle, J. Geophys. Res., 73:295.

Singleton, D.G. (1973): The Dependence of High-Latitude Ionospheric Scintillations on Zenith Angle and Azimuth, J. Atmos. Terr. Phys., 35:2253.

Singleton, D.G. (1974): Power Spectra of Ionospheric Scintillation, J. Atmos. Terr. Phys., 36:133.

Singleton, D.G. (1975): An Empirical Model of Global Spread-F Occurrence, J. Atmos. Terr. Phys., 37:1535.

Singleton, D.G. (1977): The Reconciliation of an F-Region Irregularity Model with Sunspot Cycle Variations in Spread-F Occurrence, Radio Sci., 12:107.

Singleton, D.G. (1978): An Improved Ionospheric Irregularity Model, ERL-46-TR, Electronics Res.Lab., Dep.of Def., Australia.

APPENDIX: THE PROPOSED MODEL

The following is a concise statement of the model. The scintillation index S_4 is given by

$$S_4 = 2^{\frac{1}{2}}\varphi_o F f(\beta) \tag{A1}$$

where

$$\varphi_o = [\pi^{\frac{1}{2}}(r_e\lambda)\Delta N(\Delta h\alpha)^{\frac{1}{2}}/2^{\frac{1}{4}}(\beta k_o)^{\frac{1}{2}}](\sec\chi)^{\frac{1}{2}} \tag{A2}$$

$$F = \{1-\exp(-\mu)\}^{\frac{1}{2}} \tag{A3}$$

$$f(\beta) = (3\beta^4+2\beta^2+3)\ /\{2(2)^{\frac{1}{2}}\} \tag{A4}$$

$$\mu = (\lambda z/2\pi)k_o^2 \tag{A5}$$

$$\beta^2 = \cos^2\psi + \alpha^2\sin^2\psi \tag{A6}$$

The probability of occurrence of spread-F is given by

$$P_s = 50\ [1-\mathrm{erf}\{\sqrt{2}(\Delta f_c/\Delta f_o-1)\}] \tag{A7}$$

where

Δf_c = ionosonde frequency resolution (typically 0.1MHz),

$$\Delta f_o = 8.98\times10^{-6}\{(N+\Delta N)^{\frac{1}{2}} - N^{\frac{1}{2}}\} \tag{A8}$$

The following parametric variations constitute the model. The elongation factor α is given by

$$\alpha = 10-2.5[1 + \mathrm{erf}\{(\theta-35)/10\}] \tag{A9}$$

The effective thickness Δh is given by

$$\Delta h = 10^{(1+t_{18}/\tau_{18})} \quad \text{(A10)}$$

The blackout factor B is given by

$$B = \left\{1 + A[\cos\{2\pi(t-\tau)/24\} - 1] + C[\cos\{4\pi(t-\tau)/24\} - 1]\right\}\exp\{-(\theta-\theta_c)^2/\theta_p^2\} \quad \text{(A11)}$$

where

$$A = (0.14-0.000275R)[1-(0.7857-0.000987R)\cos\{2\pi(D+10)/365\} - (0.2143-0.000777R)\cos\{4\pi(D+10)/365\}] \quad \text{(A12)}$$

$$C = (0.025+0.0003R)[1+(2-0.01R)\cos\{2\pi(D+10)/365\} + (1-0.01R)\cos\{4\pi(D+10)/365\}] \quad \text{(A13)}$$

$$\tau = (2.75+0.005R)[1+0.0073R\cos\{2\pi(D+10)/365\} + (0.091+0.0032R)\cos\{4\pi(D+10)/365\}] \quad \text{(A14)}$$

$$\theta_c = (66.25-0.0063R)[1+(0.0377-0.0096R)\cos\{2\pi(D+10)/365\} + (0.0189-0.00048R)\cos\{4\pi(D+10)/365\}] \quad \text{(A15)}$$

$$\theta_p = (229.5+0.019R)[1+(0.6144-0.00021R)\cos\{2\pi(D+10)/365\} - (0.307-0.00011R)\cos\{4\pi(D+10)/365\}] \quad \text{(A16)}$$

The F-layer peak electron density N is given by a model due to Chiu(1975) and the incremental electron density in the irregularities ΔN is given by:

$$\Delta N = m_e\Delta N_e(R,D,t,\theta,\Omega,S_K) + m_m\Delta N_m(t,\theta) + m_h\Delta N_h(t,Kp,\theta) + m_a\Delta N_a(t,R,\theta) \quad \text{(A17)}$$

where

$$m_e = 3.2 - 0.011R \quad \text{(A18)}$$

$$m_m = 8.6 - 0.032R \quad \text{(A19)}$$

$$m_h = 11.0 - 0.041R \quad \text{(A20)}$$

$$m_a = 15.0 - 0.066R \quad \text{(A21)}$$

$$\Delta N_e = 5.5\times10^9 F_d F_s F_K(1+0.05R)\exp\{-(\theta+\theta_d)^2/(\theta_e+\Delta\theta_e)^2\} \quad \text{(A22)}$$

$$\Delta N_m = 6.0\times10^8\{1+0.4\cos(\pi t/12)\}\exp\{-(\theta-\theta_o)^2/\theta_m^2\} \quad \text{(A23)}$$

$$\Delta N_h = 2.7\times10^9[1+\mathrm{erf}\{(\theta-\theta_b)/\theta_h\}] \quad \text{(A24)}$$

$$\Delta N_a = 5.0\times10^7 R\exp[-\{\theta-70+2\cos(\pi t/12)\}^2/\{0.03R\}^2] \quad \text{(A25)}$$

$$F_d = 10\left\{\exp[-(t/3)^4] + \exp[-\{(t-t_m)/\tau_m\}^q]\right\}/10^{(1+t_{18}/\tau_{18})/2} \quad \text{(A26)}$$

$$F_s = P\{1 + S\cos\Omega - H\cos(2\Omega)\} \quad \text{(A27)}$$

$$F_K = F_C \qquad \text{for } 0<S_K<B_K \quad \text{(A28)}$$

$$= F_C - A_K(S_K - E_K) \qquad \text{for } B_K \leq S_K < (B_K + F_C/A_K) \tag{A29}$$

$$= 0 \qquad \text{for } S_K \geq (B_K + F_C/A_K) \tag{A30}$$

$$\theta_d = V[1 - AV\cos\{2\pi(D+10)/365\} - SV\cos\{4\pi(D+10)/365\}] \tag{A31}$$

$$\theta_e = -11.5R + 34.5 \tag{A32}$$

$$\Delta\theta_e = T[1 - AT\cos\{2\pi(D+10)/365\} - ST\cos\{4\pi(D+10)/365\}] \tag{A33}$$

$$\theta_o = -0.085R + 49 \tag{A34}$$

$$\theta_m = 6.75 + 0.0165R - (3.25 - 0.0165R)\cos(2\pi D/365) \tag{A35}$$

$$\theta_b = 68 - [0.75 + 0.25\cos\{\pi(t-21)/12\}]Kp - 7.5\cos\{\pi(t-21)/12\} \tag{A36}$$

$$\theta_h = 7 - 3\cos\{\pi(t-21)/12\} \tag{A37}$$

$$t_m = 21.5 + 0.0025R \tag{A38}$$

$$\tau_m = 6.0 + 0.005R \tag{A39}$$

$$q = 2.0 + 0.035R \tag{A40}$$

$$\tau_{18} = 18.0 - 0.06R \tag{A41}$$

$$P = 0.628[1 + 0.170\cos\{2\pi(D+10)/365\} - 0.402\cos\{4\pi(D+10)/365\}] \tag{A42}$$

$$S = -0.08[1 - 1.375\cos\{2\pi(D+10)/365\} - 1.25\cos\{4\pi(D+10)/365\}] \tag{A43}$$

$$H = 0.5[1 + 0.08\cos\{2\pi(D+10)/365\} + 0.06\cos\{4\pi(D+10)/365\}] \tag{A44}$$

$$B = K[1 - AK\cos\{2\pi(D+10)/365\} - SK\cos\{4\pi(D+10)/365\}] \tag{A45}$$

$$V = -0.508 - 1.74\cos\Omega + 3.30\sin\Omega \tag{A46}$$

$$SV = (-0.873 - 1.13\cos\Omega + 3.47\sin\Omega)/V - 1 \tag{A47}$$

$$AV = (-2.721 - 5.78\cos\Omega + 5.0\sin\Omega)/V \tag{A48}$$

$$T = 4.86 + 3.14\cos\Omega - 0.994\sin\Omega \tag{A49}$$

$$ST = (6.16 + 6.84\cos\Omega - 3.72\sin\Omega)/T - 1 \tag{A50}$$

$$AT = (1.98 - 0.98\cos\Omega - 1.75\sin\Omega)/T \tag{A51}$$

$$K = 24.61 + 6.88\cos\Omega - 6.89\sin\Omega \tag{A52}$$

$$SK = (22.57 + 8.43\cos\Omega - 6.87\sin\Omega)/K - 1 \tag{A53}$$

$$AK = (-1.09 + 2.09\cos\Omega + 5.72\sin\Omega)/K \tag{A54}$$

Quantities not specified above are defined in the main text.

PREDICTING TRANSIONOSPHERIC PROPAGATION CONDITIONS

D. G. Singleton
Defence Science and Technology Organization,
Electronics Research Laboratory,
Salisbury, S.A., Australia.

A method is developed for predicting propagation conditions on transionospheric circuits. The method combines a realistic model of F-region irregularity behaviour with thin screen scintillation theory in order to simulate both the mean scintillation index and the probability of the signal falling below a nominated level. Consideration is given to the application of the prediction method to transionospheric circuits terminated by a synchronous satellite at 176.5°E (e.g. MARISAT II) and by points on the Earth's surface within an area bounded in latitude by 30°N and 65°S and in longitude by 75°E and 270°E. A partial validation of the model is provided by a comparison of its prediction of scintillation index with observational data obtained at Manus Island.

1. INTRODUCTION

The most serious cause of disruption to space-Earth radio communications is of natural origin. It results from the phenomenon known as scintillation. In this phenomenon the steady signal at the receiver is replaced by one which is fluctuating in amplitude, phase and apparent direction of arrival. Early investigation (Booker, 1958) established that the signal fluctuations were introduced as the result of the passage of the radio wave through an irregular ionosphere. In particular, electron-density irregularities in the F-layer of the ionosphere are now known to be the prime cause of the fluctuations.

In the last two decades considerable effort has been expended in establishing the properties of the electron density irregularities in the F-layer (Getmantsev and Eroukhimov, 1969). Sufficient is now known so as to allow the behaviour of the irregularities to be modelled in an empirical way. The early models (Fremouw and Bates, 1971; Fremouw and Rino, 1973) were based on a limited amount of scintillation data and neglected such important aspects as the dependence of the irregularity occurrence on magnetic activity and longitude. Recently, the ability to use spread-F data obtained from ionograms (Singleton, 1975) has added another dimension to the modelling process (Singleton,1977;1978) and more realistic models of the behaviour of the irregularities now exist (Singleton, 1978).

The next section outlines a model by means of which the nature and behaviour of the F-region irregularities can be simulated. It is shown that

this model, coupled with the thin-screen theory of scintillation, leads to a means of predicting propagation conditions on transionospheric circuits. A partial validation of the model is carried out by comparison of its prediction of scintillation index at Manus Island with data obtained there. Section 3 then examines the application of the prediction scheme to circuits operating between a synchronous satellite at 176.5 °E and the Earth's surface. Particular attention is paid to variations in latitude, longitude, day-of-year, time-of-day and the effects of changes in magnetic activity and sunspot number. The significence of these predictions is discussed in Section 4.

2. THE MODEL

2.1 The propagation mechanism

If a plane radio wave is incident on a smooth horizontally stratified ionosphere it emerges as a plane wave. On the other hand, if there are irregularities of electron density embedded in the F layer, neighbouring parts of the wave traverse regions of different refractive index and the emerging wave wavefront is distorted due to the correspondingly different phase propagation times. As the wave propagates away from the irregular layer, the phase distortions give rise to amplitude fluctuations (Briggs and Parkin, 1963). That is, a diffraction pattern is developed. The depth of the amplitude fluctuations in this pattern increases with increasing distance from the irregular layer up to a limiting value, which persists as the wave travels on further. Passage of the irregularities overhead and/or movement of the source causes the diffraction pattern to move and hence a fluctuating signal is presented to a point receiver.

In order to quantify the fluctuations in the amplitude (R) of the scintillating signal, a quantity called the scintillation index (S) is defined as follows.

$$S = [\{\overline{R^4} - (\overline{R^2})^2\} / (\overline{R^2})^2]^{\frac{1}{2}}$$

By considering first the properities of the wavefront on emergence from the irregular region in terms of the properites of the ionization density irregularities, and then dealing with the subsequent diffraction problem, it is possible to show (Briggs and Parkin, 1963; Singleton, 1970) that

$$S = f\{\lambda, (\overline{\Delta N^2})^{\frac{1}{2}}, \Delta h, K_o, p, \alpha, i, \psi, z_1, z_2\} \qquad (1)$$

where λ = transmitting wavelength,

$(\overline{\Delta N^2})^{\frac{1}{2}}$ = the rms deviation of electron density in the irregularities.

Δh = thickness of the irregular layer,

K_o = outer-scale wavenumber of the irregularity spectrum,

p = spectral index of the irregularity spatial spectrum,

α = irregularity elongation factor along the Earth's magnetic field,

i = angle of incidence of the wave on the ionosphere,

ψ = angle between the direction of propagation and the Earth's magnetic field,

z_1 = distance of the receiver from the irregularities and

z_2 = distance of the transmitter from the irregularities.

This expression is valid if the deviations of phase across the emergent wavefront are less than one radian. For phase deviations greater than this, a strong scattering approximation must be used and values of S greater than one may be encountered. This condition is referred to as saturation (Singleton, 1970).

The variables λ, i, ψ, z_1 and z_2 in the function f (equation (1)) are directly dependent on the transmitter, ionosphere and receiver configuration and can be easily determined in any particular case. On the other hand, the quantities $(\overline{\Delta N^2})^{\frac{1}{2}}$, $\Delta h, K_o, p, \alpha$ describe the nature of the irregular region.

2.2 The nature of the irregularities

The gross features of the nature and behaviour of ionospheric irregularities have been determined by means of innumerable studies involving scintillations (Getmantsev and Eroukhimov, 1969), spread F (Herman, 1966) and in-situ measurements (Basu et al., 1976). Initially Fremouw and Bates (1971) and Fremouw and Rino (1973) summarized those properties of F-region irregularities, which can be determined by means of the scintillation phenomenon, in terms of a set of empirical equations. These expressed $(\overline{\Delta N^2})^{\frac{1}{2}}$ as a function of year, day-of-year, time-of-day, latitude and running average sunspot number (RASN). By employing spread-F data (Herman, 1966), which is more plentiful than scintillation data, Singleton (1975;1977) was able to further define the role of the sunspot cycle in these equations, as well as include effects due to changing magnetic activity and longitude. Temporal variations of Δh and latitude variations of K_o and α were also included in this model. The result (Singleton, 1978) is a set of empirical relations which give, in analytic form, a realistic expression of the nature of the irregularities responsible for scintillation on transionospheric circuits.

2.3 Predicting scintillation index

By combining the results of the scintillation theory (equation (1)) with the model of irregularity behaviour described in Section 2.2, it is possible to give analytic expression to the manner in which the scintillation index, observed on any transionospheric circuit, varies with such parameters as the positions of the terminals of the circuit, year, day-of-year, hour-of-day, magnetic activity, sunspot number and operating frequency. Computer programs have been written which embody this analytic formulation and which thereby allow the prediction of scintillation index for various transionospheric propagation circuits.

Figure 1 shows an output from one such program. Here a transmitting satellite at synchronous height over the equator at 176.5° E is considered. Contours of equal scintillation index are drawn for reception points on a

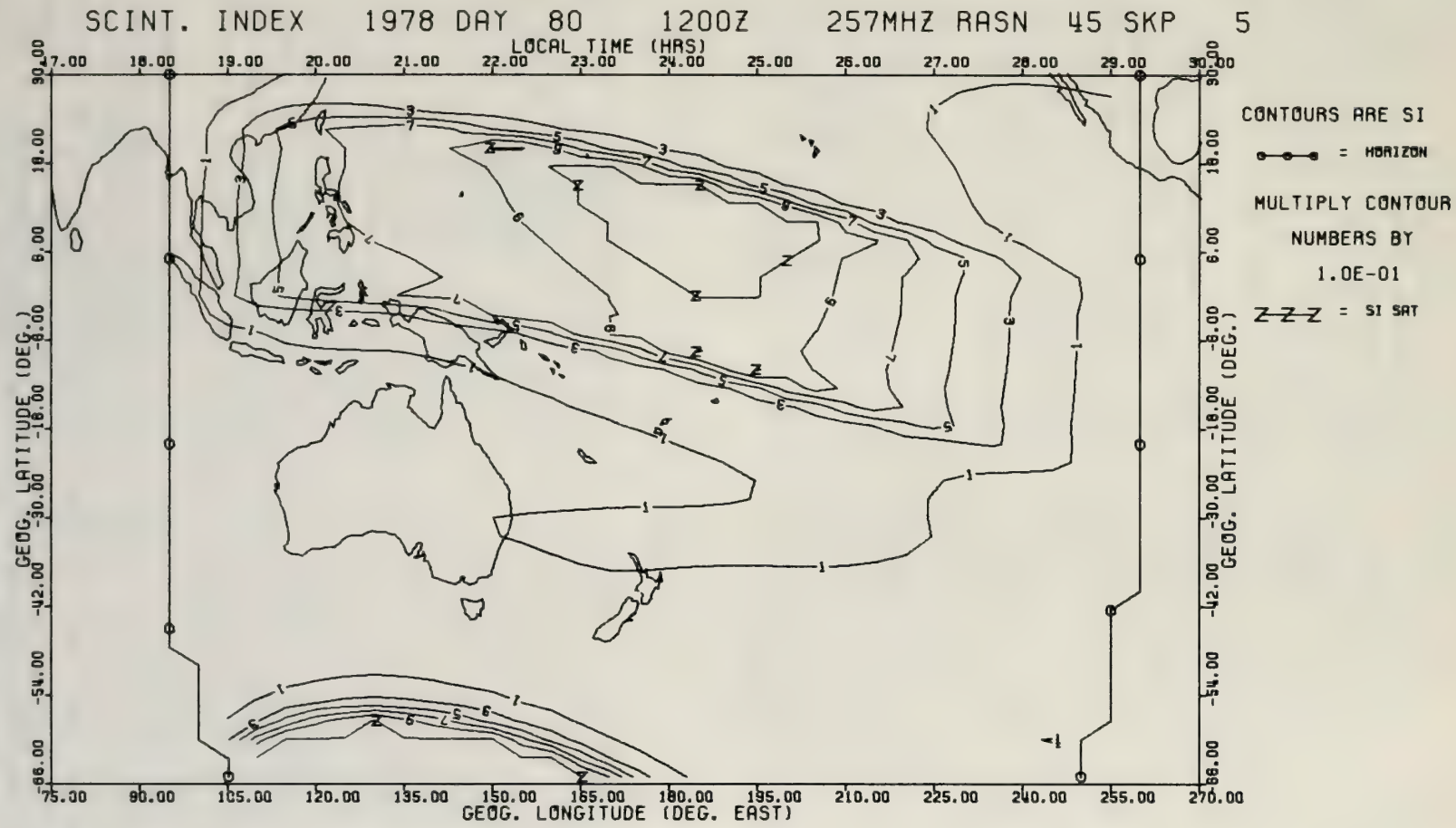


Fig. 1: Contours of scintillation index (S) on a geographic latitude versus longitude map.

map of the area between 30° N and 66°S geographic latitude and 75° to 270°E geographic longitude. Note the contours are limited necessarily to that part of the Earth's surface in view of the satellite (i.e. within the horizon curves on the figure). This particular diagram represents the predicted behaviour of all possible transionospheric circuits operating on day 80 of 1978 at 1200 hours UT. A frequency of 257 MHz, which corresponds to the down-link frequency of MARISAT II, was employed in the calculations. The expected running average sunspot number (RASN) at this time was 45 and the sum of the Kp figures for the day (SKp) was taken as 5. Local time is indicated across the top of the diagram.

Two regions of high scintillation activity are indicated in figure 1: one along the geomagnetic equator and a second at high latitudes. There is only slight activity in the middle latitudes. Note that at this time the scintillation index becomes saturated rather rapidly at the high geomagnetic latitudes, while saturation is limited to an area over the mid-Pacific Ocean in the equatorial region. It should be recalled that the figure is a prediction of the mean scintillation index. No indication is given as to the extent of the scatter individual observations of scintillation index might have about the mean at this time.

Equation (1) shows that the scintillation index depends on the distance of the receiver from the irregularities (z_1) and the distance of the transmitter from the irregularities (z_2). However, the nature of this dependence is such that, in any particular case, the interchange of z_1 and z_2 does not alter the value of S. Thus for a two way communication system, the scintillation index expected on the up-link should be the same as that predicted for the down-link.

2.4 Model Validation

In order to completely validate the model throughout the area shown in figure 1, observations at a number of points would be required. At present, only MARISAT data from Manus Island (147.37°E, 2.04°S) is available, though other observations are planned. This site is strategically placed however, being just inside the equatorial region of high activity. A favourable comparison of the model's predictions with data from this site would add considerable credence to the usefulness of the model.

Digitized signal-strength data from Manus Is. has been reduced to provide half-hourly S values during the period August to November 1976. For each of these months diurnal distributions of scintillation activity have been produced and are given in figure 2. Each plot shows the diurnal variation of each of the following: the mean scintillation index (full line curve), the range of observed values of S (vertical full lines) and an index value one standard deviation of the hourly distribution of S from the mean index for that hour (points on the vertical lines).

The model was employed to provide a detailed prediction of scintallation activity during each of these months. Actual values of sunspot number and Kp were employed to predict the scintillation index for each hour of each day and this data was then used to form diurnal distributions of mean index. These diurnal distributions are shown as the broken-line curves on figure 2.

Figue 2 indicates that the model provides a good simulation of the actual observations, the predicted mean index generally being within one standard deviation of the observed mean index.

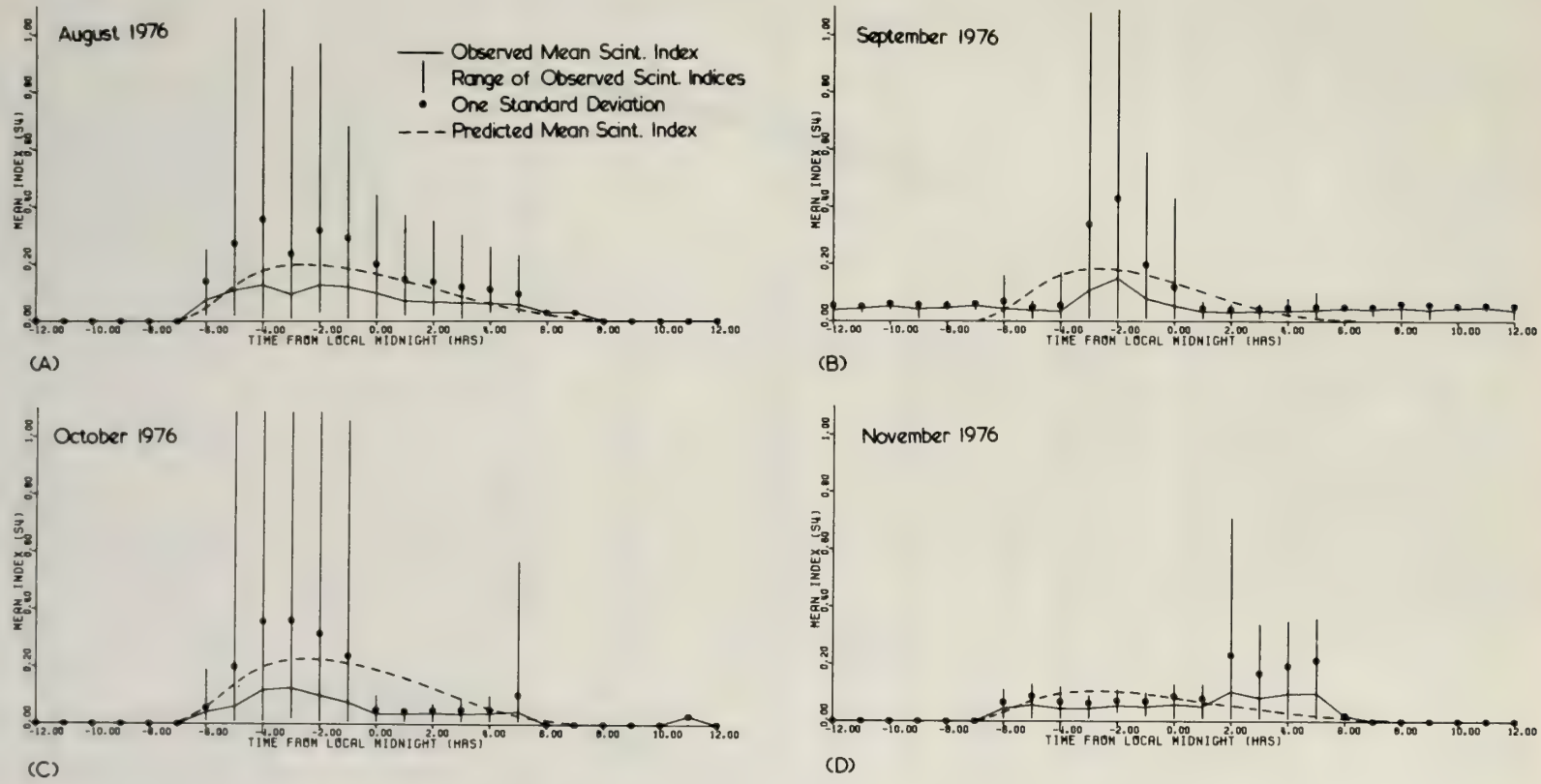


Fig. 2: Comparison of predicted and observed mean scintillation index at Manus Is.

2.5 Predicting disruption probability

Scintillation index proves to be a convenient measure of scintillation activity when the observation of scintillation is used as a technique for studying ionospheric irregularities. However, in the engineering of communication circuits employing transionospheric propagation, a more system oriented measure is needed, such as the probability of communication being lost due to scintillation effects. For most communication systems, the "outage" probability can be defined quantitatively as the probability of the signal level falling below some designated value. This threshold signal level is usually the noise level and, in this case, the maximum allowable fade margin is equal to the signal-to-noise ratio in dB. Hereafter, the probability of the signal falling below the fade margin will be called the disruption probability and its relationship to the scintillation index will now be examined.

Whitney et al. (1972) demonstrated that the probability distribution of signal amplitude (R) for a scintillating signal is closely represented by the Nakagami m distribution (Nakagami, 1960). This is

$$p(R) = \frac{2m^m R^{2m-1}}{\Gamma(m)(\overline{R^2})^2} \exp(-mR^2/\overline{R^2})$$

where m can be shown to be $1/S^2$. Defining signal level χ as

$$\chi = 10 \log_{10}(R^2/\overline{R^2})$$

it follows from the Nakagami distribution that the probability of the signal level falling below some specified level χ_o is

$$P(\chi_o) = \int_{-\infty}^{\chi_o} \frac{2m^m}{M\Gamma(m)} \exp[m\{2\chi/M - \exp(2\chi/M)\}]d\chi \qquad (2)$$

where $M = 20 \log_{10} e$. Thus, if χ_o is the threshold of the fade margin, then $P(\chi_o)$ corresponds to the disruption probability.

The integral in equation (2) is readily evaluated and since $S = m^{-\frac{1}{2}}$, it allows predictions of mean scintillation index to be converted to predictions of disruption probability. Figure 3 is the disruption-probability prediction corresponding to the scintillation-index prediction of figure 1. Here disruption probability (expressed as a percentage) for a fade margin of -6dB is plotted as a series of contours on the same map as that used for figure 1.

As expected, figure 3 has similar characteristics to figure 1. The areas affected by scintillation appear to be slightly reduced in terms of signal level probability as compared with the scintillation index indication. This merely reflects the fact that, under weak scintillation conditions, the probability of 6dB fades is low. Note also that the scintillation index to disruption probability conversion is only possible where the scintillation index $\lesssim 1$. The model is unable to comment on disruption probability where the scintillation index is saturated, except to say that the disruption probability in the saturated region will be higher than the disruption probability just outside this region. Thus at high latitudes immediately

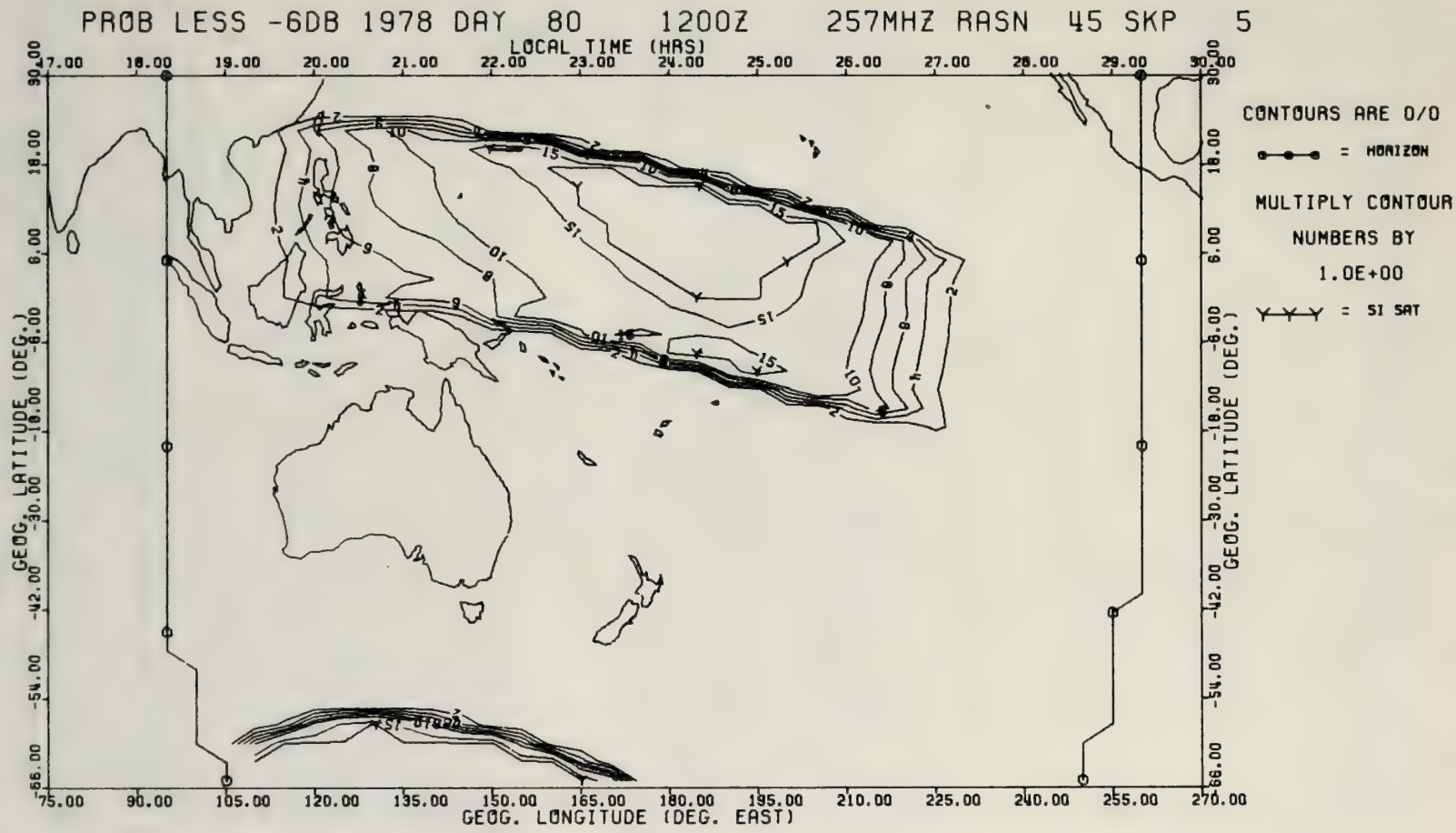


Fig. 3: Contours of disruption probability (expressed as a percentage) for a fade margin of -6dB on a geographic latitude versus longitude map.

south of Australia, the disruption probability rapidly increases to values in excess of the saturation value which is itself in excess of 15%.

From the above it will be seen that equation (2), coupled with equation (1) and the model of ionospheric irregularities discussed in Section 2.2, provides the engineer designing a transionospheric propagation circuit with a means of determining the fading margins necessary to overcome scintillation effects under various conditions. In order to evaluate the performance of a proposed system, disruption probabilities for various critical signal levels are usually needed as a function of latitude, longitude, time-of-day, season, level of magnetic activity and phase of the sunspot cycle. The next section illustrates such a performance evaluation for MARISAT II.

3. THE MODEL'S PREDICTIONS

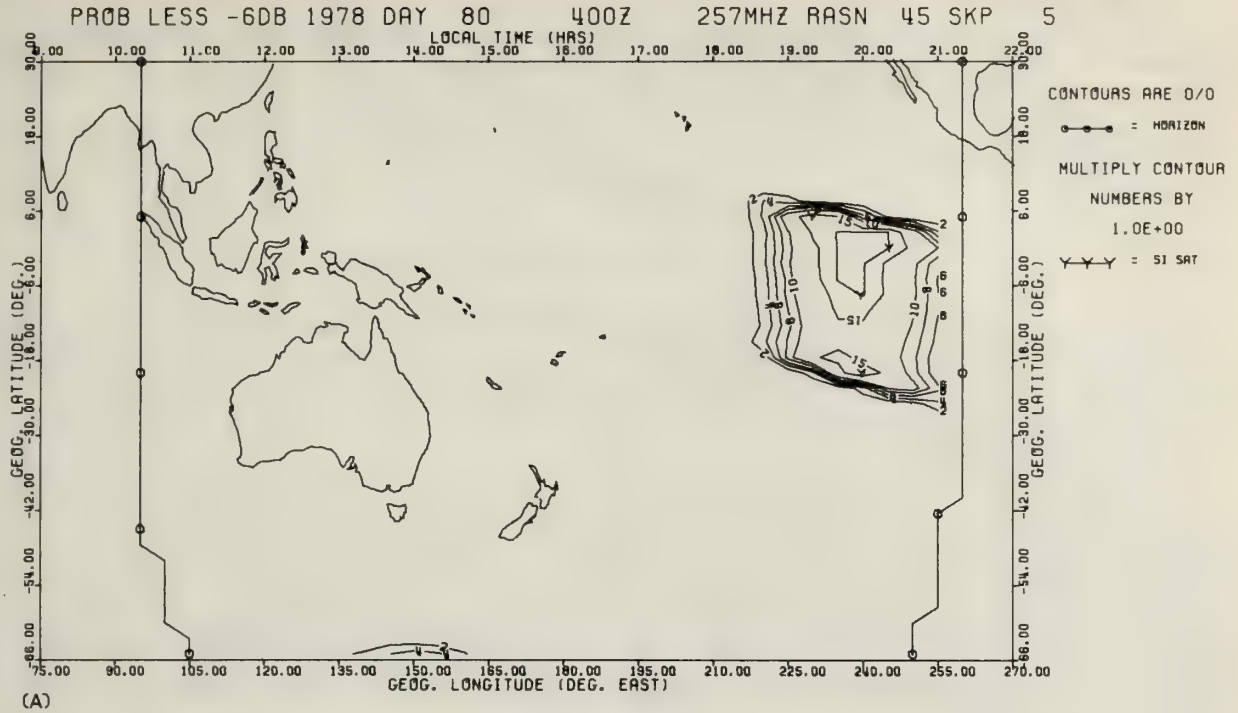
3.1 Variations with latitude and longitude

Consider the case of a communications satellite at synchronous height over the equator at 176.5°E with up-link and down-link frequencies near 257 MHz. If the fade margin allowed is 6dB, then the instantaneous picture at 1600 hours UT of the likelihood of disruption to both the down- and up-link transmissions over a wide geographical area is as shown in figure 3. As indicated earlier, the likelihood of disruption to these circuits is limited to those terminating in the equatorial and high latitude regions. This style of presentation will be used in the following sections to examine how the geographic distribution of circuit performance varies with time-of-day, season, magnetic activity, sunspot cycle and critical level.

3.2 Diurnal variations

The diurnal development of the equatorial and high latitude areas of scintillation activity can be gauged by a comparison of figures 3 and 4. In figure 4(a) the western half of the diagram is experiencing late morning, noon and afternoon conditions for which there is little scintillation activity in either the equatorial or high latitude regions. Activity in the equatorial region rapidly builds up on the satellite's eastern horizon however, where late evening conditions prevail.

The instantaneous picture eight hours later at 1200 hours UT (figure 3) shows that the equatorial region of high activity has moved out over the mid-Pacific Ocean and circuit disruption at the 6dB level is experienced over a wide area. At the high latitudes during the eight hours between the instantaneous pictures of figures 4(a) and 3, the affected region moves equator-wards and the maximum disruption probability increases from 4% to something in excess of 15%. By 1800 hours UT (figure 4(b)), the equatorial activity has retreated into the western horizon of the satellite's field of view and the high latitude activity has started to fall back towards the South Pole. Thus the high activity in the equatorial region moves along the geomagnetic equator being roughly centred on local midnight.



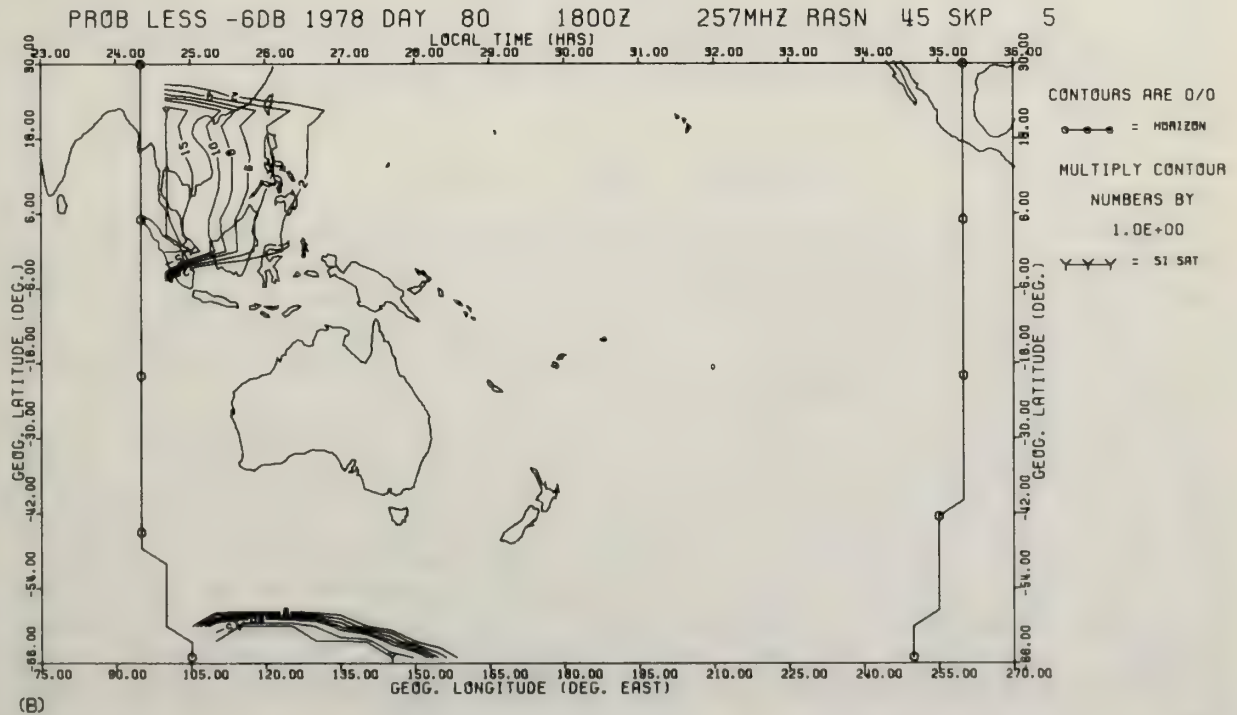


Fig. 4: An illustration of the diurnal development of the equatorial and high latitude disturbed regions.

3.3 Seasonal variations

In the equatorial region of high scintillation activity, the likelihood of disturbance to a transionospheric circuit is greatest in the equinoxes (figure 3). In the solstice periods it is found that, there is little likelihood of circuit disruption in the equatorial region.

In the high latitude region of high scintillation activity there is little seasonal effect.

3.4 Magnetic activity variations

Magnetic activity affects the low and high latitude regions of high activity differently. The measure of the degree of magnetic activity used here is the sum (SKp) of the eight three-hourly planetary K figures for a day. In figure 3 SKp is 5. This is increased to 30 and 50 in figures 5(a) and (b) respectively.

An increase of SKp from 5 to about 20 affects the equatorial activity little. However, at the high latitudes, this SKp increase causes the active region to move some 2° towards the equator. Increasing SKp from 20 to 30 takes the high latitude region only about 1° nearer the equator but causes a marked decrease in equatorial activity (figure 5(a)). A further increase of SKp by 10 (figure 5(b)) sees the equatorial activity disappear altogether, while there is a further slight movement of the high latitude active region towards the equator.

It is clear that magnetic activity ranks with geographic position, time-of-day and season as a factor which needs to be taken into account in determining the usefulness of a transionospheric circuit.

3.5 Sunspot cycle variation

Figures 3 and 6 illustrate the effect of the changing sunspot cycle on the disruption probability under equinoxial conditions. The disturbed equatorial region not only expands in size with increasing sunspot number but also increases in intensity. Increasing the sunspot number (RASN) from 10 to 40 (figures 6(a) and 3) causes the peak disruption probability to increase from 4% to something in excess of 15%.

In the present sunspot cycle these values of RASN will be exceeded by mid 1978 and values well in excess of 100 will be encountered by 1980. Figure 6(b) gives an indication of the severe conditions which can be expected at that time. The whole equatorial (magnetic) region of the area of interest will be subject to circuit dislocations for much more than 15% of the time.

At the high latitudes the disturbed region appears to be altered little by increasing values of sunspot number when these are moderate values (figures 3 and 6(a)). At the higher sunspot numbers (figure 6(b)) there appears to be a slight contraction of the disturbed region towards the South Pole.

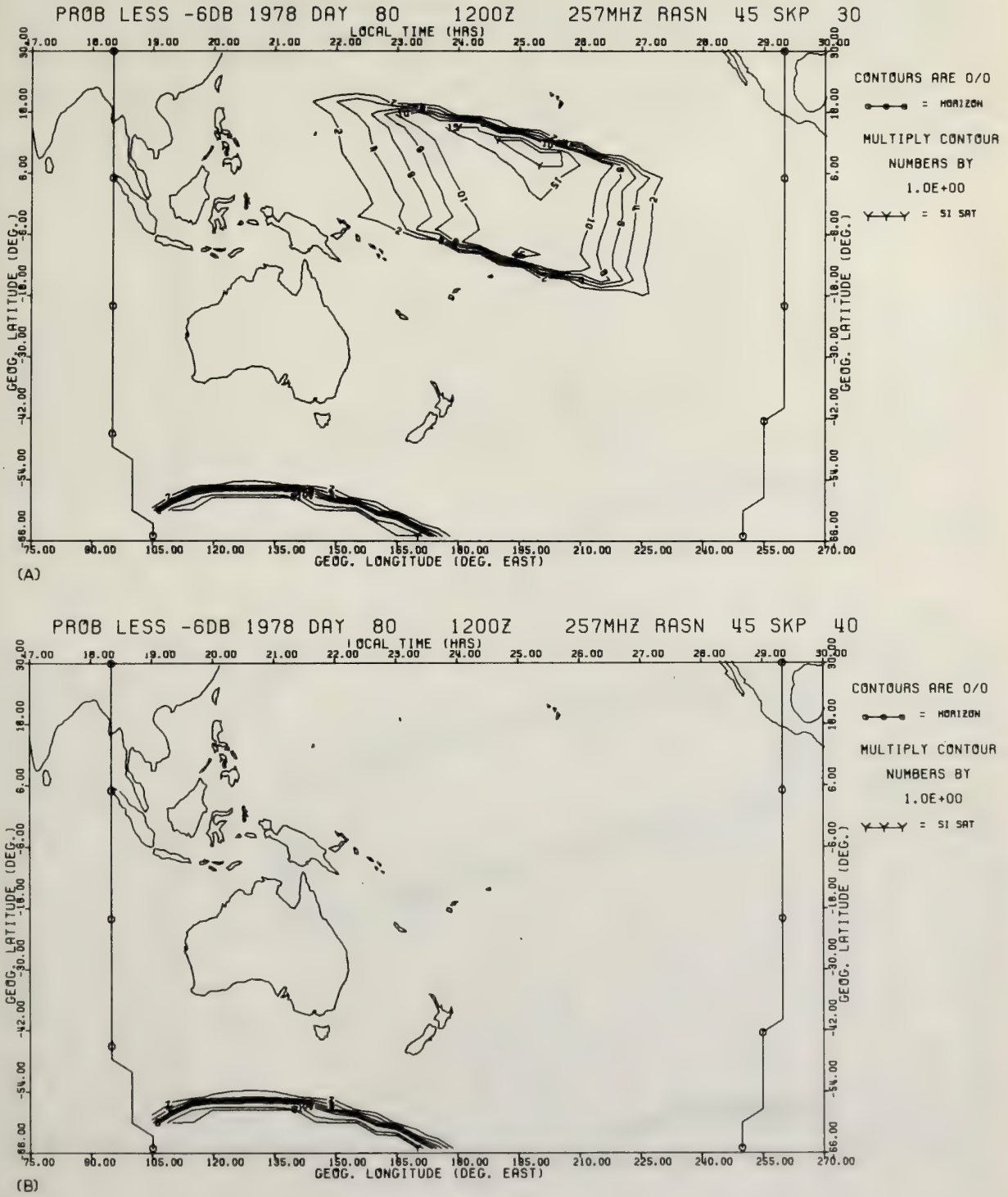


Fig. 5: The effect of magnetic activity on the disruption probability in the disturbed regions.

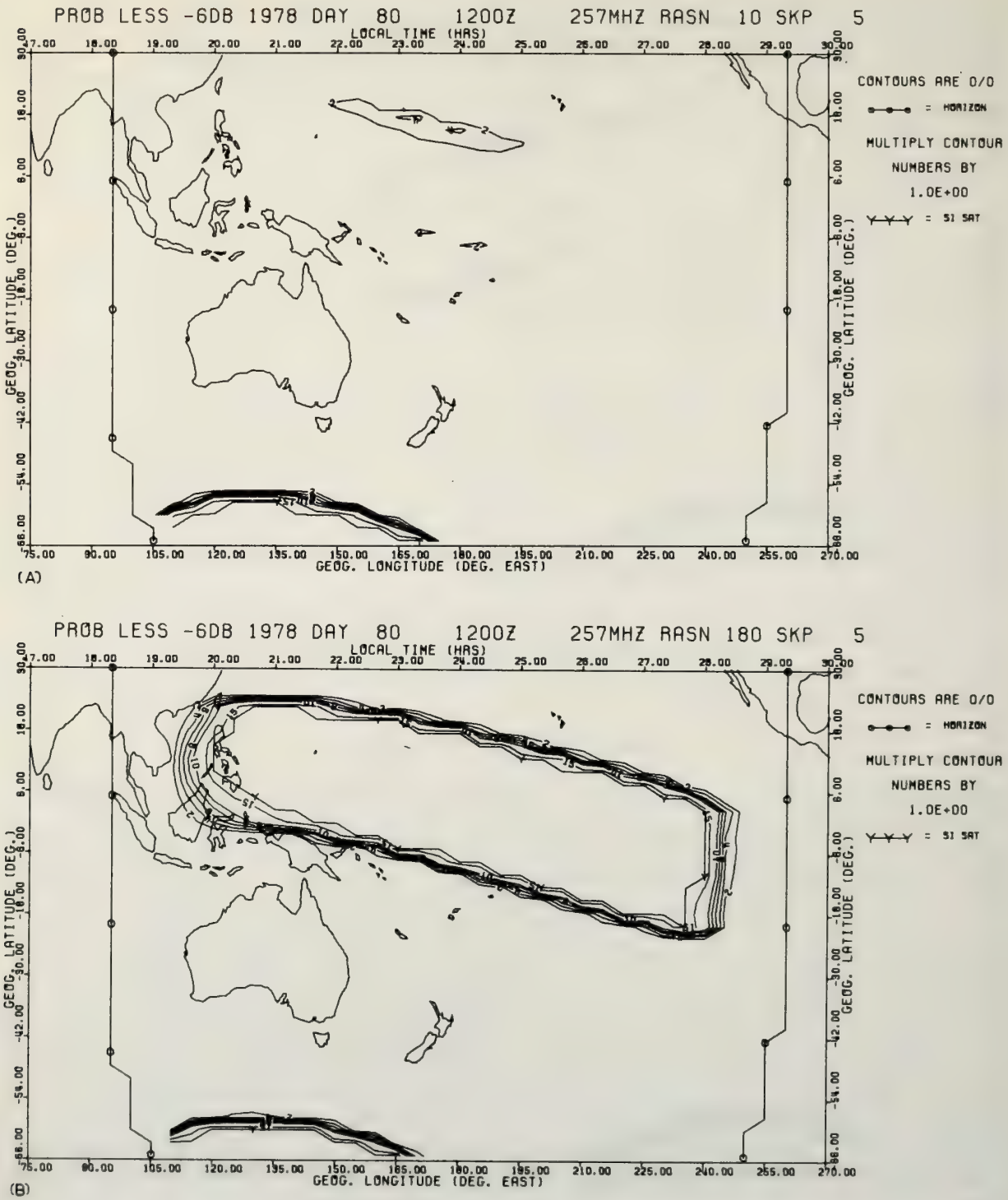


Fig. 6: The effect of sunspot activity on the disruption probability in the disturbed regions during the equinoxes.

3.6 Changes in the critical level

Figures 3 and 7 illustrate the effect of changing the critical level or fade margin (χ_o) in the disruption probability calculations (equation (2)). These figures represent the same situation except for the critical level. As expected, increasing the critical level or fade margin decreases both the area in which transionospheric propagation is likely to be disturbed by scintillation effects and the probability of such disturbance. This is true for both the equatorial and high latitude regions of high scintillation activity.

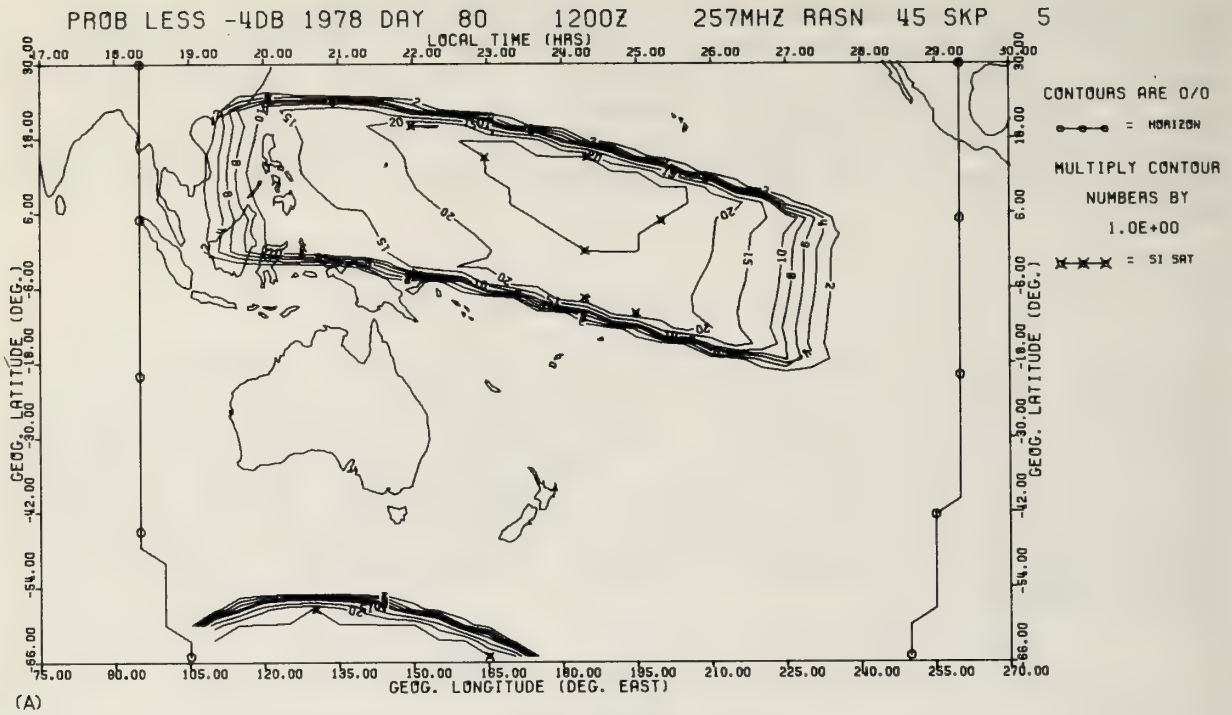
3.7 Single circuit investigations

Besides obtaining instantaneous pictures of disruption probability over a large geographic area at various times of day, season, etc., it is also possible to employ the prediction scheme outlined in Section 2 to examine a particular circuit in detail. Here the two terminals of the transionospheric circuit are fixed at known positions so the disruption probability can be examined as a function of time-of-day and day-of-year for various operating frequencies, critical signal levels, SKp values and sunspot numbers.

4. DISCUSSION

The prediction scheme used in the circuit performance evaluations described above finds a mean scintillation index which is then converted to a disruption probability (Section 2). No attempt is made to account for the scatter individual scintillation index observations will have about the predicted value. The whole process of irregularity and propagation simulation is aimed at reducing this scatter. For instance, the present scheme is a vast improvement, in this respect, over using a simple estimate of mean index involving only a latitude variation. This is underscored by the partial validation of the model as discussed in Section 2.5. Obviously this scatter will be reduced further and the prediction scheme correspondingly improved as more variables are taken into account in the irregularity model. Even so, as the result of improvements which have recently been made, the model is now quite realistic and allows meaningful simulations of transionospheric propagation circuits to be made.

The examples of the use of the prediction scheme employed to illustrate the discussion in the previous sections have all been based on a satellite at synchronous height. It should be noted that the prediction scheme and, indeed, the current computer programs embodying this scheme, are equally applicable to orbiting satellites at any height.



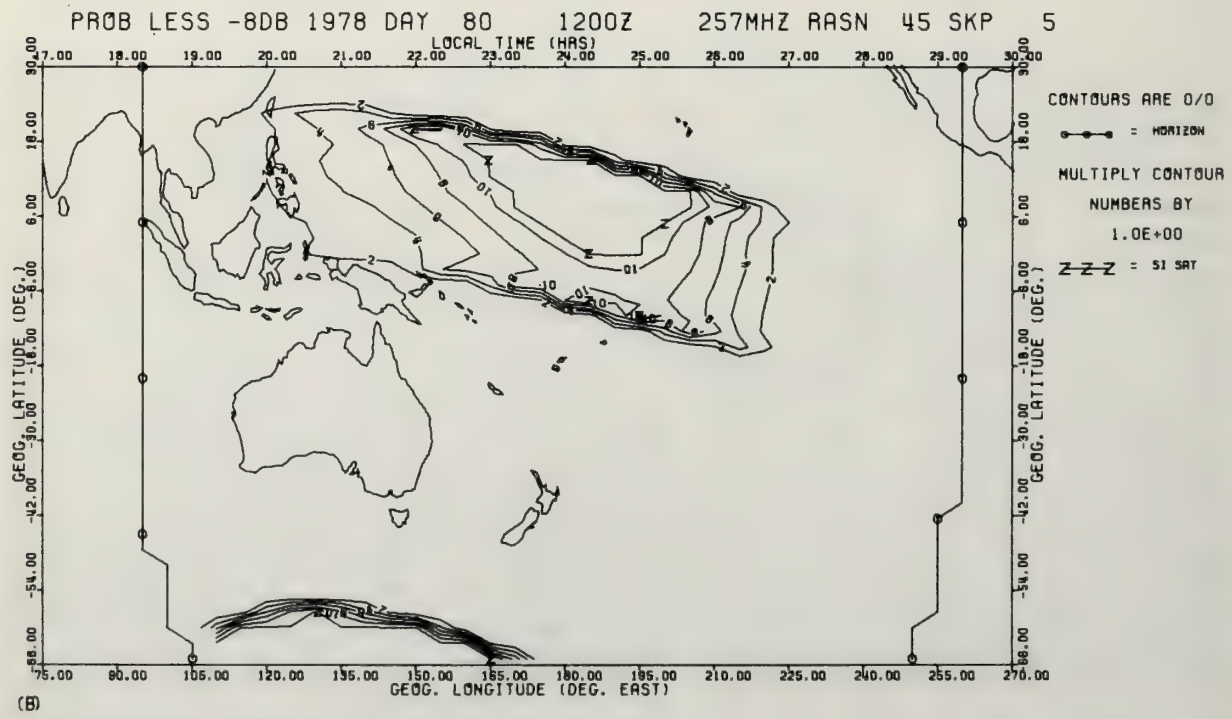


Fig. 7: The effect of changing the critical level in the disruption probability calculations.

REFERENCES

Basu,Sunanda, S.Basu and B.K.Khan (1976): Model of Equatorial Scintillations from In-Situ Measurements. Radio Sci., 11:821.

Booker,H.F. (1958): The Use of Radio Stars to Study Irregular Refraction of Radio Waves in The Ionosphere. Proc.I.R.E., 46:298.

Briggs,B.H. and I.A.Parkin (1963): On the Variation of Radio Star and Satellite Scintillations with Zenith Angle. J.Atmosph.Terr.Phys., 25:339.

Fremouw,E.J. and H.F.Bates (1971): Worldwide Behaviour of Average VHF-UHF Scintillations. Radio Sci., 6:863.

Fremouw,E.J. and C.L.Rino (1973): An Empirical Model for Average F-Layer Scintillation at VHF/UHF. Radio Sci., 8:213.

Getmantsev,G.G. and L.M.Eroukhimov (1969): Radio Star and Satellite Scintillations. Annals of the IQSY, 5:229.

Herman,J.R (1966): Spread F and Ionospheric F-region Irregularities. Rev. of Geophys., 4:255.

Nakagami,M. (1960): Statistical Methods in Radio-Wave Propagation. Edited by W.C.Hoffman (Pergamon Press, New York) 3-36.

Singleton,D.G. (1970a): Saturation and Focusing Effects in Radio-Star and Satellite Scintillations J.Atmosph. Terr.Phys., 32:187.

Singleton,D.G. (1970b): The Effect of Irregularity Shape on Radio Star and Satellite Scintillations J.Atmosph. Terr.Phys., 32:315.

Singleton,D.G. (1975): An Empirical Model of Global Spread-F Occurrence. J.Atmosph.Terr.Phys., 37:1535.

Singleton,D.G. (1977): The Reconciliation of an F-Region Irregularity Model with Sunspot-Cycle Variations in Spread-F Occurrence. Radio Sci., 12:107.

Singleton,D.G. (1978): An Improved Ionospheric Irregularity Model. ERL-46-TR, Electronics Res. Lab., Dep. of Defence, Australia.

Whitney,H.E., J.Aarons, R.S.Allen and D.Seeman (1972): Estimation of the Cumulative Amplitude Probability Distribution Function of Ionospheric Scintillations. Radio Sci., 7:1095.

MODEL OF PHASE AND AMPLITUDE SCINTILLATIONS FROM IN-SITU MEASUREMENTS

Santimay Basu and Sunanda Basu
Emmanuel College, Boston, MA 02115

In-situ measurements of F-region irregularity amplitude and ambient electron density made by Ogo-6 and AE-C satellites are utilized for modelling phase and amplitude scintillations in the equatorial region during two solstice periods. Considerable differences in the longitude variation is noted during the two solstices. The model estimates are in good agreement with available ground-based phase and amplitude scintillation measurements. Problems associated with the use of bottomside spread-F data for transionospheric propagation modelling at VHF/UHF are also discussed.

1. INTRODUCTION

F-region irregularities are the cause of intense scintillations (irregular phase and amplitude fluctuations) of signals transmitted through the ionosphere over the frequency range VHF to 1 GHz at high latitudes and VHF to S-band at equatorial latitudes. While the causative mechanisms of these irregularities remain unresolved and continue to be a subject of multi-technique experiments (Aarons et al., 1978; Basu and Aarons, 1977; Basu and Kelley, 1977; 1978), their effects are a cause of serious concern to communications engineers. This is because amplitude scintillations can degrade the performance of high data rate satellite communication links while phase scintillations can impair the performance of satellite systems that use synthetic aperture processing to achieve high angular resolution.

Ground-based measurements over two decades have established the broad morphological features of three major scintillation regions, two covering the polar caps and a third one approximately centered on the magnetic equator (Aarons, 1975). That spread-F observations broadly show similar occurrence maxima have been documented in many studies (Shimazaki, 1959; Singleton, 1960, 1968; Penndorf, 1962; Herman, 1966; Chandra and Rastogi, 1970). While undoubtedly both scintillations and spread-F are caused by irregularities in the F-region, there are definite differences in the occurrence pattern of each as a function of sunspot cycle, season and longitude. These will be discussed further in Section 2. Thus the use of bottomside spread-F data to modify scintillation models at VHF/UHF must be treated with caution. Furthermore, both scintillation and spread-F measurements are performed primarily on the ground and thus cannot provide coverage over ocean surfaces. Clustering of geostationary satellites at preferred longitudes has also contributed to

uneven scintillation coverage.

Satellites carrying out in-situ observations of irregularity parameters present a viable alternative for mapping the irregularity morphology at both high and low latitudes. At high latitudes this technique has been used by Dyson (1969) and Sagalyn et al., (1974) to map irregularity characteristics. Good agreement was obtained between the scintillation boundary (Aarons and Allen, 1971) and the in-situ irregularity boundary. However no attempt has yet been made to convert the observed irregularity morphology into a high latitude scintillation model. At the equator, Basu et al., (1976a,b) used in-situ irregularity data obtained from Ogo-6 to map the equatorial irregularity morphology and convert it into a scintillation model for the December solstice. A pronounced longitude variation of equatorial scintillations was evident and comparison with available ground scintillation measurements was very encouraging, indeed. In Section 3, the principle of utilizing the in-situ technique for estimating phase and amplitude scintillations is presented. In Section 4 we shall discuss earlier published results obtained with the Ogo-6 satellite and present more recent results obtained with the Atmosphere Explorer satellites. Available ground based scintillation data are used to compare the model with actual observations. A brief summary is provided in Section 5.

2. DIFFERENCES BETWEEN SPREAD-F AND SCINTILLATION MORPHOLOGY

The general association of spread-F and scintillations has been noted by a large number of authors as mentioned before. The morphology of spread-F, however, is better documented because of the large global network of ionosondes that was set up during the IGY period in 1957-58, many of which have been kept operating subsequently. Scintillation morphology, in comparison, is still inadequately explored and there are large gaps in our knowledge. Thus in their first attempt at providing a global morphology of amplitude scintillations, Fremouw and Rino (1973) found that more than 60% of their thirty modelling categories had to remain untested because of a lack of data. While it is probable that additional data may have been accumulated within the last five years, we are still far from amassing a comprehensive scintillation data bank. Thus, an effort has been made to utilize spread-F data to modify scintillation models (Singleton, 1975; 1977; 1978). In this section, we propose to discuss the geophysical parameters that control spread-F and scintillation phenomena leading to differences in their occurrence pattern.

It is well known that scintillations are directly related to the rms fluctuations of electron density, ΔN, and the thickness, L, of such irregularity layers (Briggs and Parkin, 1963; Rufenach, 1975). Spread-F, on the other hand, is generally characterized by Δf_0, where f_0 is the critical frequency of the F-layer. Since the electron density at the maximum of the F-layer, N, is proportional to f_0^2, the deviation of the electron density from the mean, ΔN, should be proportional to $f_0 \Delta f_0$. Thus this latter quantity should be used to compare with scintillation observations. Briggs (1964) could thus resolve the conflicting morphologies of spread-F data as observed at Slough, and radio-star scintillation data observed at Cambridge over a

solar cycle. As a result of this study Briggs (1964) came to the conclusion that the variation of the spread-F index with season and solar cycle reflects mainly the variation of critical frequency with season and solar cycle. It is interesting to note that Singleton (1962) using a different technique, namely estimating f_0 and Δf_0 from a number of stations at widely separated geomagnetic latitudes, came to the same conclusion. He found that at all latitudes the magnitude of Δf is greatest when critical frequency is lowest. Thus, we find that background conditions dominate the quantitative measure of the spread-F index whereas the scintillation index is not similarly affected. A quantitative relationship between in-situ irregularity measurements and spread-F index was reported in a recent study by Wright et al., (1977). They showed that on a statistical basis, the magnitude of $\Delta N/N$ obtained by Ogo-6 can be related to $2\Delta f/f$ read from frequency spread ionograms. This is in agreement with the arguments given above.

Another major problem of using spread-F as an ionospheric irregularity index is the great variation of equipment and convention used to measure and classify spread-F. This point was discussed at some length by Lyon et al., (1960), where they pointed out that the 50 percent reduction of spread-F occurrence during the equinoxes in the American zone as compared to the Afro-Indian zone shown in their Figure 1 is due to equipment differences. The fast-sweep high-power ionosondes being used at Huancayo and Chimbote in the American sector were reponsible for obtaining better quality ionograms from which f_0F could be read even in the presence of spreading and hence a smaller number of occurrences of spread-F were reported. A careful analysis of the Huancayo and Ibadan (in the African sector) ionograms by the authors themselves showed no significant variation. However, the results of Lyon et al., (1960) have been used by Singleton (1978) to modify the Fremouw-Rino scintillation model leading to a prediction of much lower equinoctial occurrence of scintillations in the American sector as compared to a station in the African sector. This is contrary to scintillation observations as may be noted by comparing Figures 3 and 6 of Aarons (1977). It is thus quite probable that large errors will be introduced into existing scintillation models by modifying them in such a way as to reproduce faithfully tabulated bottomside spread-F occurrence characteristics.

The problems associated with the modelling of scintillations based on spread-F data can be further recognized by a discussion of several known instances of anti-correlation in their occurrence characteristics. At high latitudes studies conducted by Penndorf (1962), Tao (1965) and Olesen and Jepsen (1966) have all conclusively proved that spread-F in all sectors of the northern hemisphere auroral oval show a winter maximum and summer minimum. Scintillations in the North Atlantic sector of the auroral oval, on the other hand, show a consistent summer maximum and winter minimum as shown in Figure 1 for data from Narssarssuaq, Greenland. This diagram reproduced from Basu (1975) was obtained by updating the data analysis made by the Air Force Geophysics Laboratory group (Aarons, 1973a,b; Whitney et al., 1973) and converting to S_4 using Whitney's (1974) method. Analysis of more recent data upto 1976 shows an exactly similar seasonal variation (J. Aarons, private communication, 1977).

Basu (1975) showed that the two-to-one variation of the S_4 index is in keeping with the same magnitude of variation of the auroral electrojet index AL (Davis and Sugiura, 1966) in the North Atlantic sector which itself may be caused by the variation of the orientation angle χ of the earth's magnetic

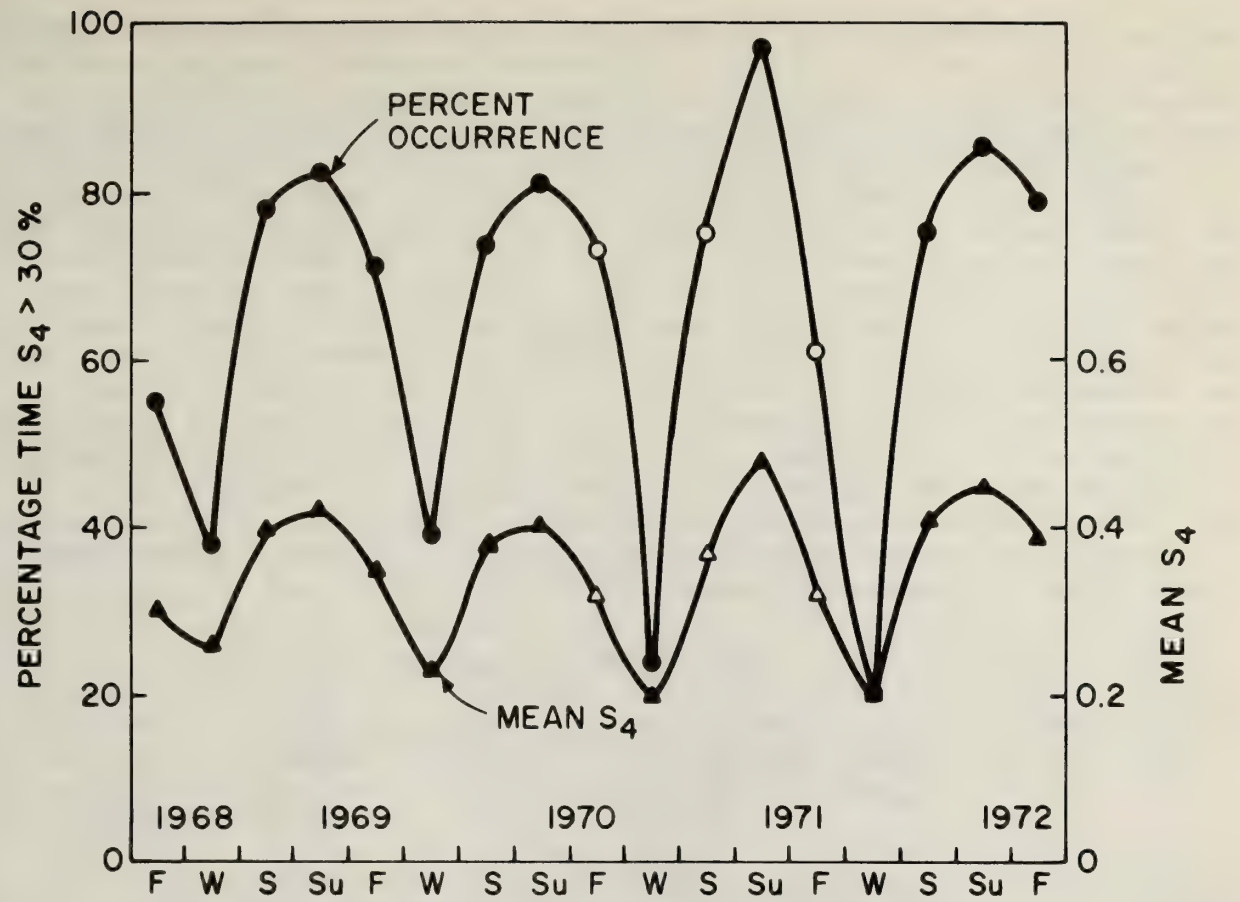


Fig. 1 The seasonal behaviour of percentage occurrence of S_4 > 0.3 (SI > 6dB) shown by circles and mean S_4 index (triangles) recorded at Narssarssuaq, Greenland from ATS-3 at 137 MHz between Sept 1968 and Oct 1972 for Kp = 0-3. The mean of the two highest hourly values of percentage occurrence and S_4 index in the 2200-0200 LT period in each season has been plotted (after Basu, 1975).

dipole with respect to the solar wind flow. It was further pointed out that such a pronounced seasonal variation may not be expected in the Scandinavian and Alaskan sectors of the auroral oval where the seasonal variation of the dipole tilt angle χ is much smaller. In agreement with the above prediction, earlier radio star measurements in the Alaskan sector (E.J. Fremouw, private communication, 1975) and satellite scintillation measurements in the Scandinavian sector (Liszka, 1963) and more recent WIDEBAND satellite observations in Alaska (C.L. Rino, private communication, 1978) failed to show any noticeable seasonal variation. Thus there is a longitudinal control of the seasonal pattern of scintillation occurrence in the auroral oval which is not possible to model on the basis of spread-F observations.

Other examples of major discrepancy between scintillation and spread-F data may be found in the equatorial region. The seasonal spread-F occurrence maximizes at African longitudes during the June solstice (Lyon et al., 1960). This is in contrast to the minimum of scintillation occurrence observed at Legon, Ghana as shown in Figure 2 which is reproduced from Koster (1978). This data has been obtained at high elevation angles using Marisat trans-

missions at 257 MHz and unambiguously shows the minimum occurrence of scintillations during the June solstice. Differences in sunspot cycle variation are also observed. For example, spread-F shows a negative correlation with sunspot cycle at Huancayo (Chandra and Rastogi, 1970) while scintillations show a positive correlation (Aarons, 1977). Chandra and Rastogi's work did not distinguish data on the basis of magnetic activity but a more recent analysis has shown that the negative correlation holds even for magnetically quiet days (J. Aarons, private communication, 1979). Further, to simultaneously model scintillation and spread-F characteristics observed at Legon by Koster and Wright (1960), Singleton (1978) found that a variation of L, the thickness of the irregularity layer, from 10 km at 1800 LT to 100 km at 2400 LT and finally to 1000 km at 0600 LT is necessary. There is no physical basis for postulating such an irregularity layer thickness variation, indeed, it is contrary to Jicamarca radar measurements which show that irregularity layer thickness is maximum in the evening hours when scintillations also maximize (Basu et al., 1977; 1978). Such ad-hoc parameter variations to match observed spread-F and scintillation characteristics in one region is liable to cause large errors in scintillation modelling at another location.

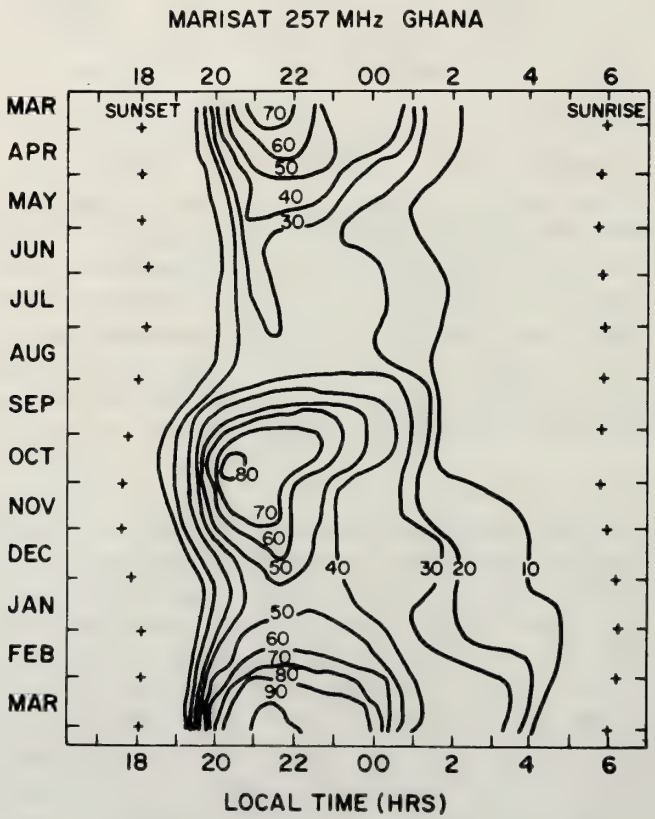


Fig. 2 Percentage occurrence contours of scintillation index $S_4 \geq 0.3$ (SI $\geq$ 6 dB) at 257 MHz obtained at Ghana from Marisat observations (after Koster, 1978).

3. THE TECHNIQUE OF MODELLING SCINTILLATIONS FROM IN-SITU DATA

A measure of the temporal fluctuations or scintillations of signal phase and amplitude which is recorded by a receiver on the ground is provided by the scintillation index (Briggs and Parkin, 1963). The normalized second central moment of signal intensity (I) is used to represent the S_4 index of amplitude fluctuations given by

$$S_4^2 = \frac{\overline{I^2} - (\overline{I})^2}{(\overline{I})^2} \qquad (1)$$

On the other hand, the index of temporal phase fluctuations is represented by the variance in phase, σ_ϕ^2.

In the framework of diffraction theory, the indices of phase (σ_ϕ) and amplitude (S_4) fluctuations can be related to the irregularity parameters in the ionosphere. Initially, the above relationship was developed for an assumed gaussian form of irregularities. However, Dyson et al., (1974) and Phelps and Sagalyn (1976) showed by the use of in-situ data that the irregularities at F-region heights do have a power law type of irregularity power spectrum with one-dimensional spectral index of 2 corresponding to a 3-dimensional index of 4. For such a 3-dimensional irregularity power spectrum with an outer scale wavenumber K_0, the variance of phase (σ_ϕ^2) and amplitude scintillation index (S_4) in the case of weak scattering have been obtained (Rino and Matthews, 1978) as

$$\sigma_\phi^2 = \frac{1}{2\pi^2} \cdot (r_e\lambda)^2 \cdot (L\sec\theta) \langle\Delta N^2\rangle K_0 G (\tau v_{eff})^2 \qquad (2)$$

$$S_4^2 = 4\pi^2 \cdot (r_e\lambda)^2 \cdot (L\sec\theta) \langle\Delta N^2\rangle \frac{\lambda Z \sec\theta}{2\pi} K_0 F \qquad (3)$$

where

- r_e - the classical electron radius (2.8×10^{-15} m)
- λ - the wavelength of probing radio wave
- Z, L - irregularity layer height and thickness respectively
- θ - zenith angle at irregularity height
- $\langle\Delta N^2\rangle$ - mean square electron density deviation
- K_0 - outer scale wavenumber
- τ, v_{eff} - detrend interval and effective scan velocity of the propagation path across the irregularities
- G, F - geometrical parameters for anisotropic irregularities.

Equation (3) shows that the S_4 index of scintillation can be modelled if information on electron density deviation, ΔN, and the outer scale wavenumber, K_0 and irregularity layer thickness are available. The axial ratios pertinent to the three dimensional shape of the irregularities (rod or sheet) enter into the geometrical factors G and F in equations (2) and (3)

respectively. The available in-situ data do not provide information on G and F and the shape of the irregularities have to be assumed. The modelling of phase variance in equation (2) is related to two additional parameters v_{eff} and τ as discussed by Rino and Matthews (1978). The parameter, v_{eff}, depends not only on the relative velocity between the propagation path and the irregularities but for anisotropic irregularities, on the direction of motion with respect to the shortest autocorrelation distance of electron density deviation as well. The detrend interval τ is set by the time interval over which the phase variance is to be computed. Thus v_{eff} and τ are set by the particular system for which the phase modelling is to be done.

The major geophysical parameters involved in the modelling of S_4 and σ_ϕ are thus the rms electron density deviation, ΔN, the form of irregularity power spectrum, the outer-scale wavenumber, K_0, and the irregularity layer thickness, L. Various types of analyzers on board the satellites have been used to measure the ion concentration (or electron concentration for charge neutrality) at F-region heights (Hanson et al., 1970; Sagalyn et al., 1974). Currently, it is possible to sample the ion or electron concentration (N) with an accuracy of .01% at a sampling rate as high as 200 per sec corresponding to a spatial resolution of 35 m (McClure and Hanson, 1973; McClure et al., 1977). Such high resolution data have been used to obtain the irregularity power spectrum which, as already mentioned, indicate that at F region heights power-law type of irregularity power spectrum is obtained with a 3-dimensional spectral index of 4. This type of spectrum forms the basis of model equations (2) and (3) given above.

For the development of a morphological model of scintillations, measurements of irregularity amplitude, $\Delta N/N$, as computed from T sec of data are utilized in conjunction with simultaneous measurement of electron density N. A combination of $\Delta N/N$ and N data provides the required ΔN parameter as a function of position and time. In case the satellite altitude is much lower than the height of maximum ionization, proper allowance should be made in deriving ΔN estimates. The in-situ measurements of irregularity spectrum (Dyson et al., 1974; Phelps and Sagalyn, 1976; McClure, private communication, 1978) and phase scintillation measurements (Rino and Matthews, 1978) with Wideband satellite indicate that the outer scale at F region heights is large, probably on the order of tens of km. In view of this, the spatial length corresponding to T sec time interval when projected in the direction of shortest correlation distance of electron density deviation sets the apparent outer scale length q_0. The outer scale wavenumber is, therefore, $K_0=2\pi/q_0$. For the equatorial scintillation model that we developed from the Ogo-6 in-situ observations, the time interval was T=5 secs and the outer scale length was considered to be 20 km corresponding to an outer-scale wavenumber of $K_0 = 0.3\ km^{-1}$.

The satellite in-situ measurements pertain to a single altitude and cannot directly provide any information on irregularity layer thickness (L). However, it is possible to obtain estimates of this parameter from in-situ data obtained by satellites in elliptic orbit or direct radar backscatter observations (Basu et al., 1976; Woodman and LaHoz, 1976). Based on these measurements, it is found that L = 200 km is appropriate for equatorial scintillation modelling. It should be emphasized that the electron density devation (ΔN) of the irregularities is the single parameter which is most variable and controls scintillations. The importance of the in-situ technique stems from the fact that it directly samples the fluctuations of

electron density.

4. SCINTILLATION MODEL DEVELOPED FROM IN-SITU DATA

4.1 Equatorial Model during the December Solstice

Based on the Ogo-6 in-situ irregularity data obtained during November-December, 1969 and 1970 when the satellite perigee (400 km altitude) was located over the equatorial region, an occurrence contour of $\Delta N = 10^{10}$ m^{-3} was derived during the early evening hours (1900-2300 MLT) between $\pm 24°$ dip latitudes at all longitudes (Basu et al., 1976a,b). Considering an outer scale wavenumber $K_0 = 0.31$ km^{-1}, equatorial irregularity layer thickness of 200 km and median altitude of 450 km, the above level of ΔN was translated to an amplitude scintillation index of $S_4 = 0.24$ (or a peak-to-peak fluctuation of 4.5 dB) at 140 MHz for overhead propagation geometry. The percentage occurrence contour of the above level of equatorial scintillation during the D months (November-December) in the early evening hours under sunspot maximum conditions is shown in Figure 3. The pronounced longitude variation of scintillation predicted by this model and its agreement with ground scintillation measurements have been discussed at length in Basu et al., (1976a,b).

Since we consider that the data length providing ΔN dictates the value of K_0, we may put $v_{eff}\ \tau = 2\pi/K_0 = 20 \times 10^3$ m in equation (2) and derive that for $\Delta N = 10^{10}$ m^{-3} under overhead propagation condition $\sigma_\phi = 2.2$ radians at 140 MHz. For nighttime geostationary satellite observations in the equatorial region, $v_{eff} = 100$ m/sec corresponding to the irregularity drift and therefore, Figure 3 may represent the occurrence contours of $\sigma_\phi \geq 2.2$ radians at 140 MHz with a detrend interval of $\tau = 200$ secs. Since σ_ϕ scales linearly with τ and the radio wavelength, the above statistics are equivalent to $\sigma_\phi \geq 0.01$ radian at 1400 MHz with $\tau = 10$ secs. These estimates will also apply to an orbiting satellite if the flight path is aligned parallel to the geomagnetic field when v_{eff} becomes equal to the E-W drift of the irregularities. This is nearly achieved by the Wideband satellite in the Peruvian sector. A limited set of phase scintillation data obtained from the Wideband satellite at Ancon, Peru (kindly made available to us by C.L. Rino of SRI International) during 1977 indicate that the average value of $\sigma_\phi \simeq .05$ radian at 1239 MHz with $\tau = 10$ secs at the magnetic equator for near overhead propagation conditions. This is in fair agreement with our estimates.

4.2 Equatorial Model during the June Solstice

The Ogo-6 satellite, during its two=year lifetime, did not achieve a suitable perigee-cum-local time combination for equatorial irregularity modelling during the June solstice. Recently, it has been possible to utilize the Atmospheric Explorer-C (to be abbreviated as AE-C) in-situ

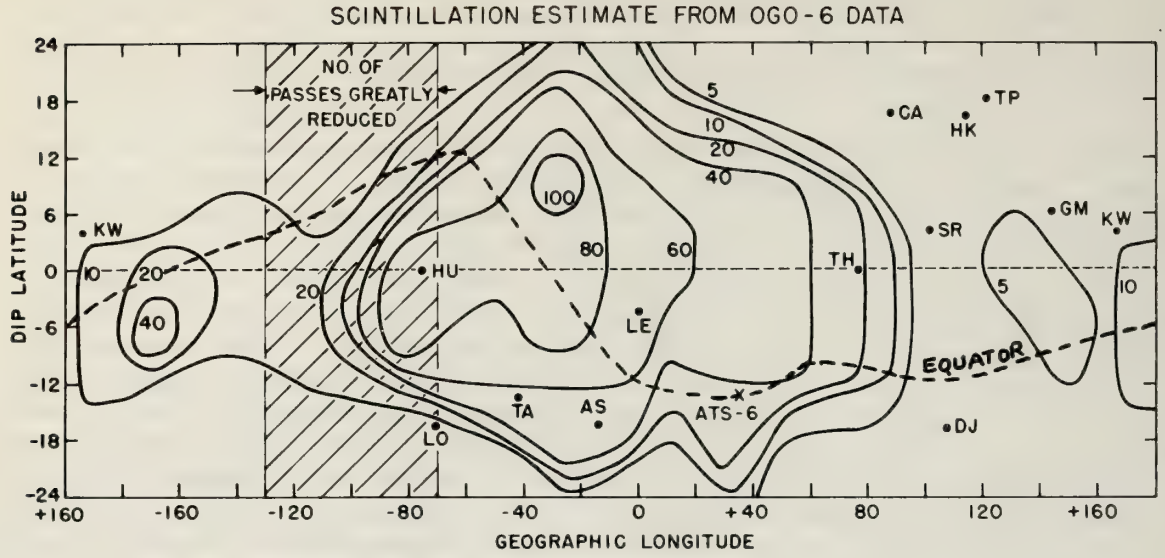


Fig. 3 Percentage occurrence contours of amplitude scintillation index $S_4 \geq 0.24$ (SI $\geq$ 4.5 dB) or phase scintillation index $\sigma_\phi \geq 0.1$ radian with a detrend interval of τ = 10 secs at 140 MHz (1900-2300 MLT, Nov-Dec, 1969 and 1970) obtained from Ogo-6 in-situ irregularity data for overhead geometry.

irregularity data for developing an equatorial scintillation model during the J months (June-July). The satellite altitude varied from about 200 - 600 km over the equatorial region and provided an ideal platform for the study of F region irregularities. Unfortunately, however, the longitude coverage of AE-C satellite was not uniform and only a few orbits were obtained on a specific night. This resulted in a great reduction of the total number of transits available within a specific local time period. Employing a similar technique as outlined in the previous subsection, the percentage occurrence contours of electron density deviation $\Delta N \geq 10^{10}$ m^{-3} was obtained within $\pm 24°$ dip latitude at all longitudes in the J months during 1900-2330 MLT under magnetically quiet conditions (Kp = 0-3) and is shown in Figure 4. As discussed before, the above level of $\Delta N = 10^{10}$ m^{-3} corresponds to an amplitude scintillation index of $S_4 = 0.24$ (or a peak-to-peak fluctuation of 4.5 dB) at 140 MHz for overhead propagation conditions which is equivalent to phase scintillations of $\sigma_\phi = 0.1$ radian at 140 MHz with a detrend interval of τ = 10 secs or $\sigma_\phi = 0.01$ radian at 1400 MHz with τ = 10 secs for geostationary satellite observations near the magnetic equator.

Figure 4 indicates that there is a drastic reduction of scintillaltion occurrence in the pre-midnight period during the J months as compared to the occurrence characteristics shown in Figure 3 for the same time interval during the D months, particularly in the African and American sectors. It should, however, be noted that Figures 3 and 4 represent respectively the sunspot maximum and minimum conditions. The reduction of scintillation occurrence in the pre-midnight period at African and American longitudes during the J months as predicted by Figure 4 is in good agreement with the ground scintillation observations at Huancayo (HU) and Legon (LE) during the same period as will be discussed later. Figure 5 shows the occurrence statistics of an identical level of scintillation obtained from AE-C in-situ data during the J months but in the near and post-midnight period. The observing period encompassed two magnetic storms but due to paucity of data separation on the basis of magnetic activity levels was not possible. The longitude sectors shown shaded indicate that due to reduced number of

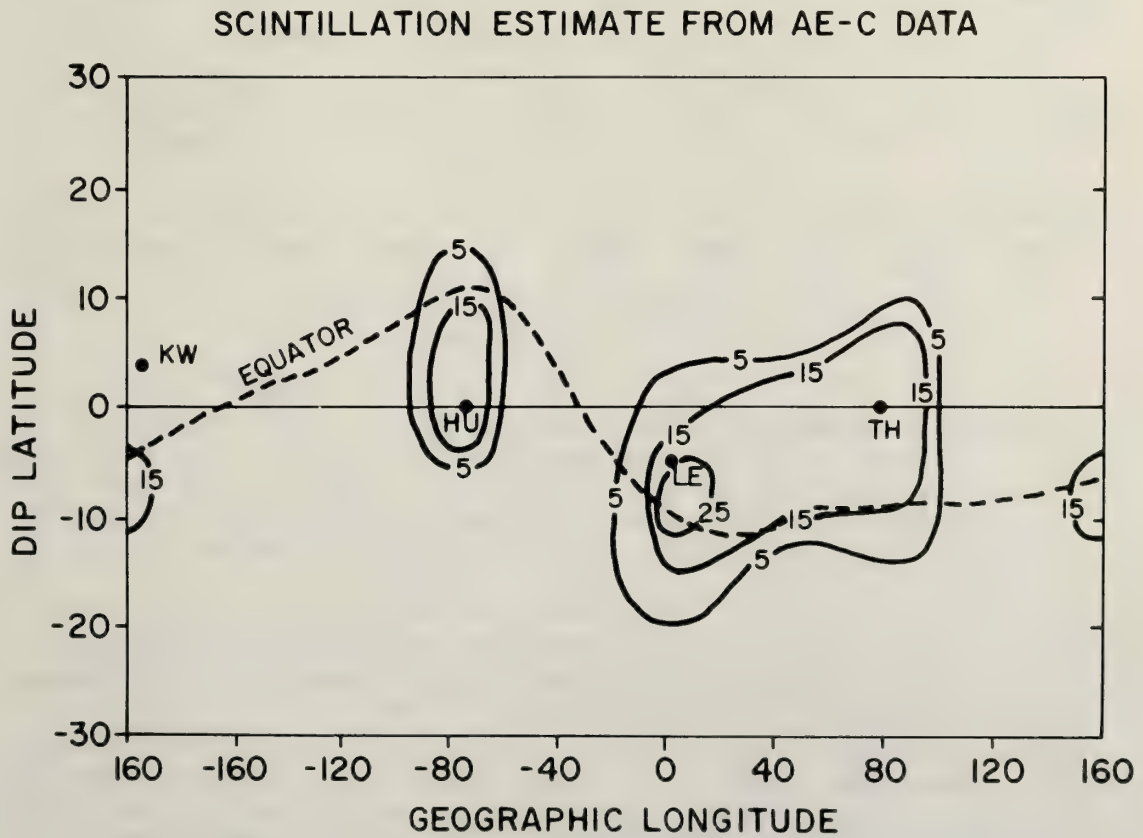


Fig. 4 Percentage occurrence contours of amplitude scintillation index $S_4 \geq 0.24$ (SI $\geq$ 4.5 dB) or phase scintillation index $\sigma_\phi \geq 0.1$ radian with a detrend interval of τ = 10 secs at 140 MHz (1900-2330 MLT, July 11-Aug 4, 1974, magnetically quiet conditions) obtained from in-situ irregularity measurements by Atmospheric Explorer-C (AE-C) satellite for overhead geometry.

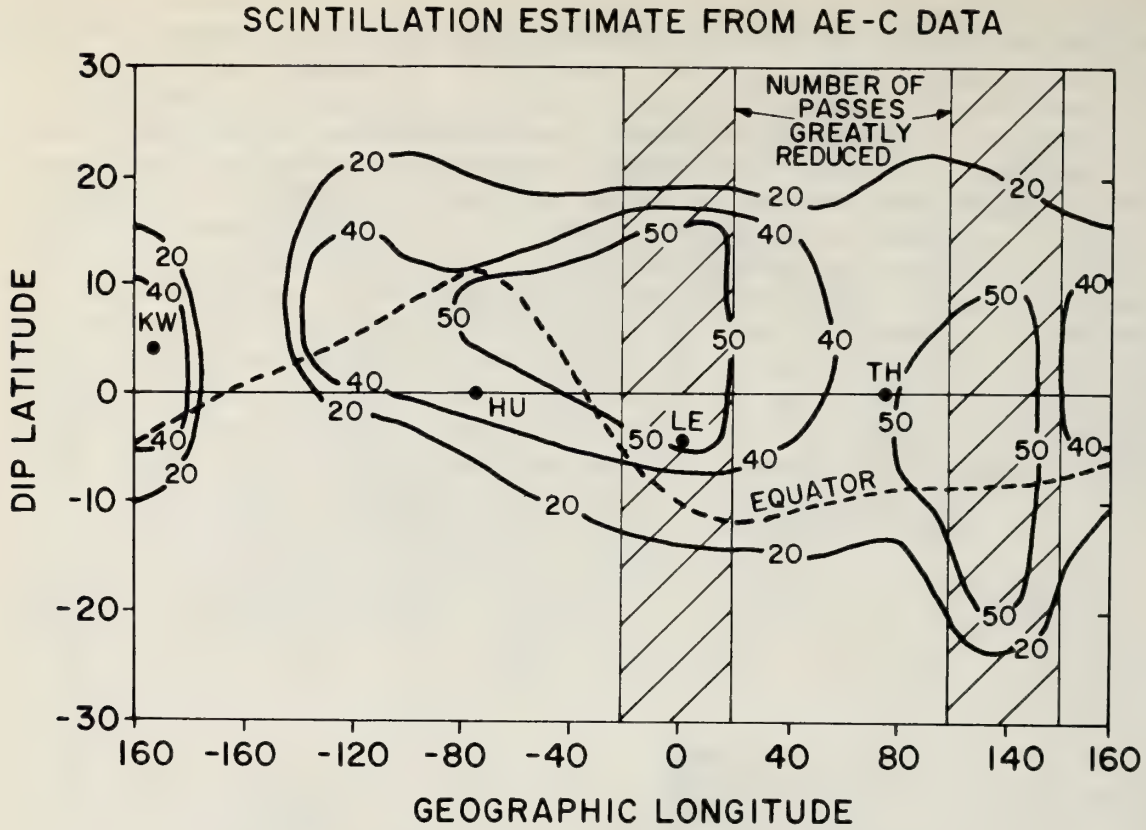


Fig. 5 Percentage occurrence contours of amplitude scintillations with $S_4 > 0.24$ (SI > 4.5 dB) or phase scintillations with $\sigma_\phi > 0.1$ radian with a detrend interval of $\bar{\tau} = 10$ secs at 140 MHz (2330-0300 MLT, June 20-July 9, 1974, magnetically quiet and disturbed conditions) obtained from AE-C in-situ data for overhead geometry.

transits the statistics over these regions is unreliable. Considering the remaining portions of the diagram, a general enhancement of scintillation occurrence may be noted at all longitudes.

In order to compare the occurrence statistics of scintillations during the J-months developed from in-situ data (Figures 4 and 5) with ground observations we present in Figures 6 and 7 the nighttime patterns of scintillation occurrence for the low (Kp = 0-3) and high (Kp = 4-9) magnetic indices observed during the same period at Huancayo, Peru and Legon, Ghana, respectively. Figure 6 shows the statistics of SI > 4 dB obtained at Huancayo during June-July, 1974 from 137 MHz transmissions of ATS-3 whereas Figure 7 shows the statistics of SI > 6 dB observed at Legon from the same satellite. A higher level of scintillation index was chosen for Legon to account for the lower elevation angle of ATS-3 satellite when viewed from this station. Figure 6 indicates that at Huancayo, the occurrence of scintillations is as low as 10% in the pre-midnight period during the J months under magnetically quiet conditions. This is in good agreement with the 15% occurrence near Huancayo derived from in-situ data under quiet periods

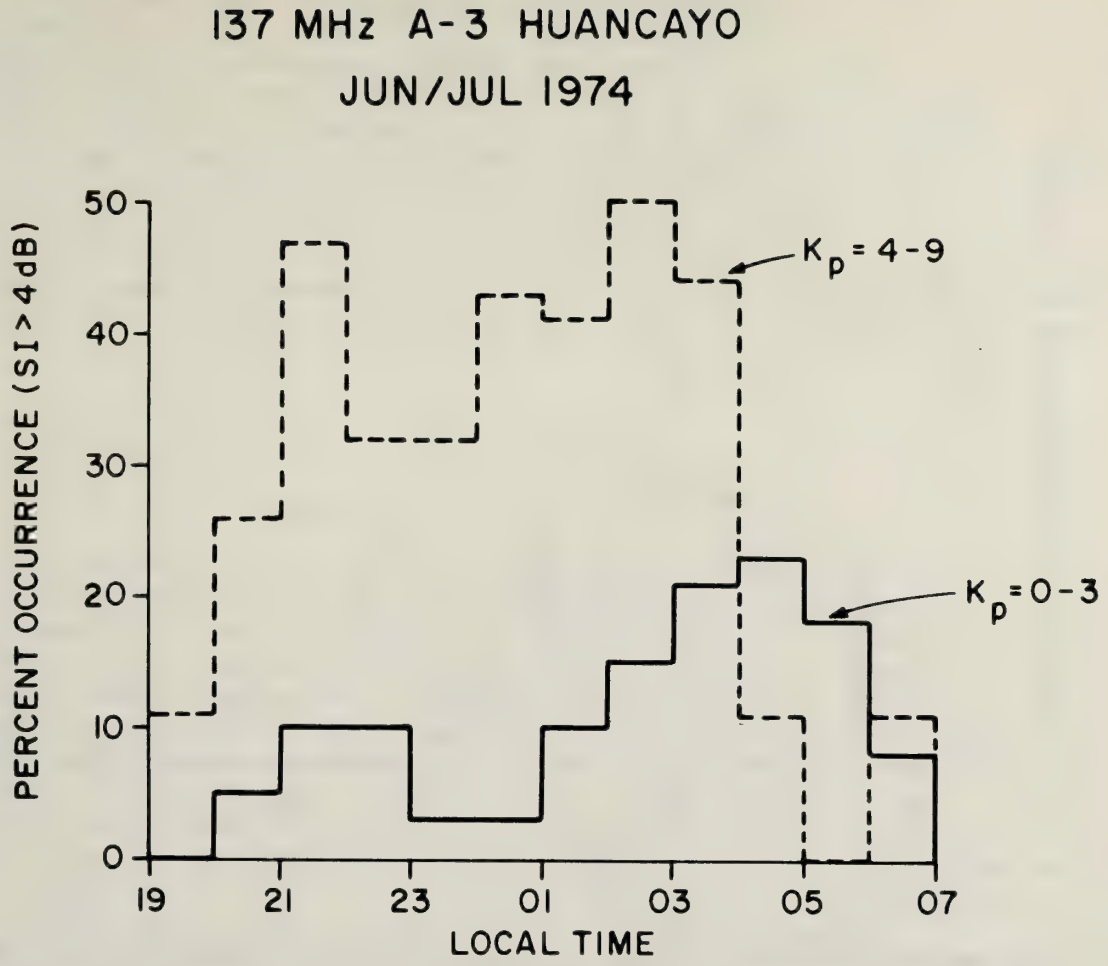


Fig. 6 Variation of the percentage occurrence of scintillations SI > 4 dB at 137 MHz observed at Huancayo with ATS-3 satellite at 70° elevation during June-July, 1974, for magnetically quiet (Kp ∿ 0-3) and disturbed (Kp ∿ 4-9) conditions (data courtesy of Instituto Geophysico del Peru).

(Kp = 0-3) and shown in Figure 4. Figure 6 shows that under magnetically active conditions, the occurrence of scintillation is greatly enhanced. The increase of scintillation with magnetic activity in the Huancayo sector during the J months has been documented before (Mullen, 1973; Aarons, 1977). As mentioned earlier, the statistics of scintillations obtained from in-situ data during the midnight and post-midnight period for all magnetic conditions (Kp = 0-9) and shown in Figure 5 encompassed two magnetic storms. In fact, all the AE-C transits in this figure that recorded irregularities between -20° and -100° longitudes occurred during disturbed period. The enhanced scintillation in the Huancayo sector predicted by Figure 5 thus corresponds very well with the observational results shown in Figure 6.

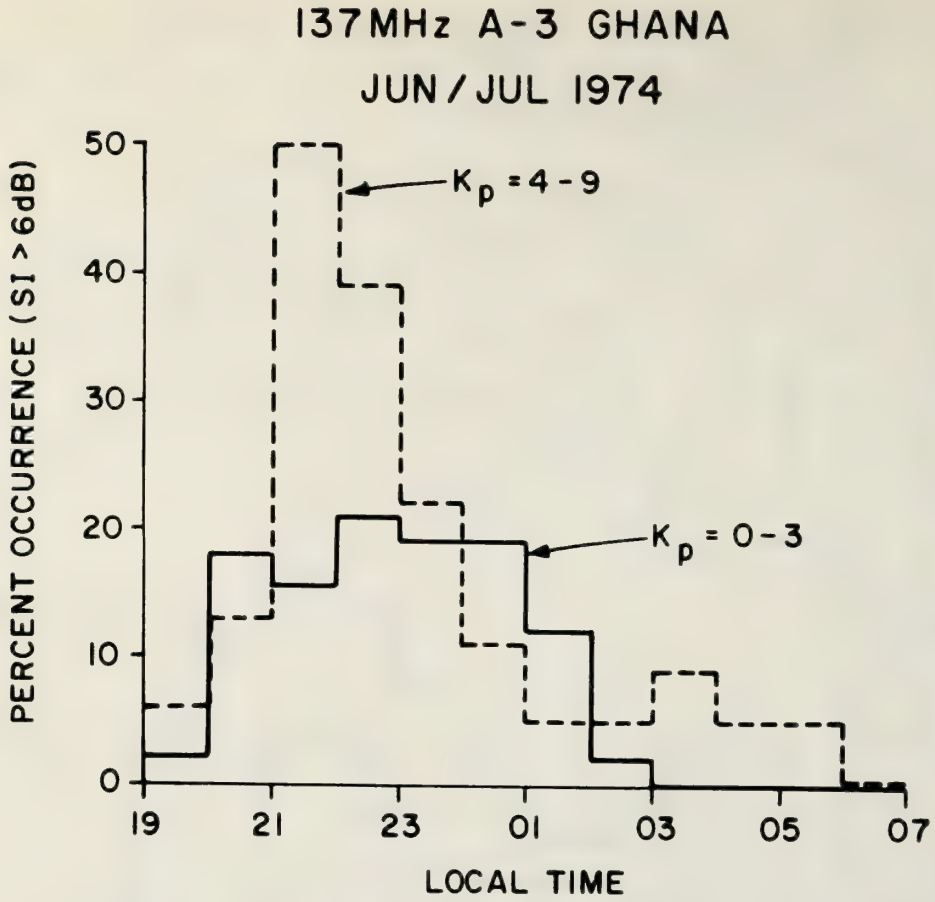


Fig. 7 Variation of the percentage occurrence of scintillations SI > 6 dB at 137 MHz observed at Legon with ATS-3 satellite at 12° elevation during June-July, 1974, for magnetically quiet (Kp ∿ 0-3) and disturbed (Kp ∿ 4-9) conditions. In view of the low elevation angle of the satellite, the occurrence diagram for SI > 6 dB in this diagram is compatible with SI > 4 dB in Figure 6 (data courtesy of J.R. Koster).

Figure 7 shows the behavior of ground scintillation results at Legon (J.R. Koster, private communication, 1978) during June-July, 1974 and indicates that under magnetically quiet conditions (Kp = 0-3), a scintillation occurrence of about 20% is obtained primarily in the pre-midnight period. Contrary to the usual inverse correlation with magnetic activity (Aarons, 1977), Figure 7 shows enhanced scintillation occurrence during magnetic activity. The enhancement observed in the present data set is confined to the pre-midnight hours. This behavior is somewhat different from that noted in the Huancayo sector (Figure 6) where enhancement of scintillation occurred during both pre- and post-midnight periods. The quiettime occurrence of scintillation observed at Legon and shown in Figure 7 is in agreement with the quiettime statistics obtained with the in-situ data around Legon (LE) as shown in Figure 4. The behavior of scintillations in this sector obtained from in-situ data during the post-midnight period (Figure 5)

could not, however, be compared with the observational results as the number of AE-C transits over the Legon sector was very small.

Combining Figures 3, 4, and 5, it may be noted that the occurrence of scintillations at Kwajalein (KW) is highest in the J-months during the post-midnight period. This is in agreement with the observations of SRI International performed at Kwajalein during 1977 (Rino et al., 1977).

It should, however, be noted that while Figure 3 providing the statistics of scintillation during the D-months was based on 250 transits of Ogo-6 satellite, Figures 4 and 5 providing the occurrence statistics during the J-months were based on a total of only 105 transits of AE-C satellite. The estimates should therefore be considered preliminary and we are currently attempting to enlarge the data base by using other available satellites.

5. CONCLUSIONS

The satellite in-situ irregularity measurements provide a direct measurement of electron density deviation (ΔN) parameter which can be used to develop models for amplitude and phase scintillations. In view of the insufficient coverage of ground scintillation observations caused by either the absence of suitable ground locations or satellites, the usefulness of in-situ probing with unlimited latitude and longitude coverage cannot be overemphasized. The evaluations made in the previous section show that scintillation models based on the quantitative measure of electron density deviation (ΔN) by satellites provide realistic estimates. Although, the models that we have developed so far pertain to the equatorial region, it is by no means limited to this region. Currently, a high latitude scintillation model based on AE-C and AE-D data is being developed.

It should, however, be mentioned that our current efforts are based on satellites whose primary function was not concerned with irregularity measurements at F region heights for scintillation modelling. As such, the constraints imposed on satellite altitude, time of transit, etc., limited our data base. A dedicated satellite performing such measurements at F-region altitudes with suitable orbital characteristics will be an ideal vehicle for the development of a world-wide model of phase and amplitude scintillations.

6. ACKNOWLEDGMENTS

The Ogo-6 and AE-C satellite data were kindly made available to us by W.B. Hanson and J.P. McClure. Phase and amplitude scintillation data were kindly provided by C.L. Rino, J.R. Koster and A. Bushby. A helpful critique of the manuscript by J. Aarons is gratefully acknowledged. We wish to thank J. Freni for help with AE-C data analysis.

This work was partially supported by AFGL contract F19628-78-C-0005 and NASA contract S-41843B.

7. REFERENCES

Aarons, J. (1973a): A descriptive model of F-layer high-latitude irregularities as shown by scintillation observations. J. Geophys. Res., 78: 7441.

Aarons, J. (1973b): A graphical description of scintillation occurrence patterns, in Agardograph No. 166 on Total Electron Content and Scintillation Studies of the Ionosphere, edited by J. Aarons, North Atlantic Treaty Organization, Neuilly Sur Seine, France.

Aarons, J. (1975): Global morphology of ionospheric scintillations II, AFCRL Report No. TR-75-0135, Air Force Cambridge Research Laboratories, Hanscom AFB, MA 01731.

Aarons, J. (1977): Equatorial scintillations: A review. IEEE Trans. Ant. & Propagat., 25:729.

Aarons, J., and R.S. Allen (1971): Scintillation boundary during quiet and disturbed magnetic conditions. J. Geophys. Res., 76:170.

Aarons, J., J. Buchau, S. Basu, and J.P. McClure (1978): The localized origin of equatorial F-region irregularity patches. J. Geophys. Res., 83:1659.

Basu, S. (1975): Universal time seasonal variations of auroral zone magnetic activity and VHF scintillations. J. Geophys. Res., 80:4725.

Basu, S., and J. Aarons (1977): Equatorial irregularity campaigns, Part I: Correlated scintillation and radar backscatter measurements in October, 1976. AFGL Report No. TR-77-0264, Air Force Geophysics Laboratory, Hanscom AFB, MA 01731.

Basu, S., and M.C. Kelley (1977): Review of equatorial scintillation phenomena in light of recent developments in the theory and measurement of equatorial irregularities. J. Atmos. Terr. Phys., 39:1229.

Basu, S., and M.C. Kelley (1978): A review of recent observations of equatorial scintillations and their relationship to current theories of F-region irregularity generation. Accepted by Radio Sci.

Basu, S., S. Basu, J.N. Bhar, and B.K. Guhathakurta (1976a): Equatorial irregularity morphology in the Afro-Asian sector with Ogo-6. Space Res., 16:427.

Basu, S., S. Basu, and B.K. Khan (1976b): Model of equatorial scintillations from in-situ measurements. Radio Sci., 11:821.

Basu, S., J. Aarons, J.P. McClure, C. LaHoz, A. Bushby, and R.F. Woodman (1977): Preliminary comparisons of VHF radar maps of F-region irregularities with scintillations in the equatorial region. J. Atmos. Terr. Phys., 39:1251.

Basu, S., S. Basu, J. Aarons, J.P. McClure, and M.D. Cousins (1978): On the coexistence of km- and m-scale irregularities in the nighttime equatorial F-region. J. Geophys. Res., 83:4219

Briggs, B.H. (1964): Observations of radio star scintillations and spread-F echoes over a solar cycle. J. Atmos. Terr. Phys., 26:1.

Briggs, B.H., and I.A. Parkin (1963): On the variation of radio star and satellite scintillation with zenith angle. J. Atmos. Terr. Phys., 25: 339.

Chandra, H., and R.G. Rastogi (1970): Solar cycle and seasonal variation of spread-F near the magnetic equator. J. Atmos. Terr. Phys., 32:439.

Davis, T.N., and M. Sugiura (1966): Auroral electrojet activity index AE and its universal time variations. J. Geophys. Res., 71:785.

Dyson, P.L. (1969): Direct measurements of the size and amplitude of irregularities in the topside ionosphere. J. Geophys. Res., 74:6291.

Dyson, P.L., J.P. McClure, and W.B. Hanson (1974): In-situ measurements of the spectral characteristics of F-region ionospheric irregularities. J. Geophys. Res., 79:1495.

Fremouw, E.J., and C.L. Rino (1973): An empirical model of average F-layer scintillation at VHF/UHF. Radio Sci., 8:213.

Hanson, W.B., S. Sanatani, D. Zuccaro, and T.W. Flowerday (1970): Plasma measurements with the retarding potential analyzer on Ogo-6. J. Geophys. Res., 75:5483.

Herman, J.R. (1966): Spread-F and ionospheric F-region irregularities. Rev. Geophys. Space Phys., 4:255.

Kelleher, R.F. (1976): Morphology of equatorial spread-F irregularities in Proceedings of Fifth International Equatorial Aeronomy Symposium, Townsville, Australia.

Koster, J.R. (1978): Phase and amplitude scintillation at the equator, Final Scientific Report on Grant No. AFOSR-78-3516, University of Ghana, Legon, Ghana,

Koster, J.R., and R.W.H. Wright (1960): Scintillation, spread-F and trans-equatorial scatter. J. Geophys. Res., 65:2303.

Liszka, L. (1963): A study of ionospheric irregularities using transmissions at 54 Mc/s. Ark. Geofys., 4:227.

Lyon, A.J., N.J. Skinner, and R.W.H. Wright (1960): The belt of equatorial spread-F. J. Atmos. Terr. Phys., 19:145.

McClure, J.P., and W.B. Hanson (1973): A catalog of ionospheric F-region irregularity behavior based on Ogo-6 retarding potential analyzer data. J. Geophys. Res., 78:7431.

McClure, J.P., W.B. Hanson, and J.H. Hoffman (1977): Plasma bubbles and irregularities in the equatorial ionosphere. J. Geophys. Res., 82: 2650.

Mullen, J.P. (1973): Sensitivity of equatorial scintillation to magnetic activity, J. Atmos. Terr. Phys., 35:1187.

Olesen, J.K., and S.B. Jepsen (1966): Some characteristics of spread-F in very high latitudes, in Spread-F and Its Effects upon Radiowave Propagation and Communications, edited by P. Newman, Technivision, Maidenhead, England.

Penndorf, R. (1962): Diurnal and seasonal variation of spread-F in the Arctic. J. Geophys. Res., 67:2289.

Phelps, A.D.R., and R.C. Sagalyn (1976): Plasma density irregularities in the high latitude top side ionosphere. J. Geophys. Res., 81:515.

Rino, C.L., and S.J. Matthews (1978): On the interpretation of ionospheric scintillation data using a power law phase screen model - weak scatter. SRI Report No. 4606T, SRI International Menlo Park, CA 94025.

Rino, C.L., E.J. Fremouw, R.C. Livingston, M.D. Cousins, and B.C. Fair (1977): Wideband satellite observations, SRI Report No. DNA 4399F, SRI International, Menlo Park, CA 94025.

Rufenach, C.L. (1975): Ionospheric scintillation by a random phase screen: Spectral approach. Radio Sci., 10:155.

Singleton, D.G. (1960): The geomorphology of spread F. J. Geophys. Res., 65:3615.

Singleton, D.G. (1962): Spread-F and the perturbations of the maximum electron density of the F-layer. Aust. J. Phys., 15:262.

Singleton, D.G. (1968): The morphology of spread-F occurrence over half a sunspot cycle. J. Geophys. Res., 73:295.

Singleton, D.G. (1975): An empirical model of global spread-F occurrence. J. Atmos. Terr. Phys., 37:1535.

Singleton, D.G. (1977): The reconciliation of an F-region irregularity model with sunspot cycle variations in spread-F occurrence. Radio Sci., 12:107.

Singleton, D.G. (1978): Improving the ionospheric irregularity model. Sumbitted to J. Geophys. Res.

Tao, K. (1965): Worldwide maps of the occurrence percentage of spread-F in years of high and low sunspot numbers. J. Radio Res. Lab., 12:317.

Whitney, H.E., J. Aarons, R.S. Allen, and D.R. Seeman (1973): Cumulative amplitude probability distribution functions for three observatories, in Agardograph No. 166 on Total Electron Content and Scintillation Studies of the Ionosphere, edited by J. Aarons, North Atlantic Treaty Organization, Neuilly Sur Seine, France.

Whitney, H.E. (1974): Notes on the relationship of scintillation index to probability distributions and their uses for system design, Report No. AFCRL-TR-74-0004, Air Force Cambridge Research Laboratories, Bedford, MA.

Woodman, R.F., and C. LaHoz (1976): Radar observations of F-region equatorial irregularities. J. Geophys. Res., 81:5447.

Wright, J.W., J.P. McClure, and W.B. Hanson (1977): Comparisons of ionogram and Ogo-6 satellite observations of small-scale F-region inhomogeneities. J. Geophys. Res., 82:548.

A RESUME OF ANTICIPATED FLEETSATCOM AND GAPFILLER SCINTILLATION EFFECTS DURING THE PEAK OF SOLAR CYCLE 21 (1980-1982)

John M. Goodman
Head, Telecommunications Environmental Effects Branch
Communications Sciences Division
Naval Research Laboratory
4555 Overlook Ave., S.W.
Washington, D. C. 20375, USA

A brief review of UHF scintillation data obtained worldwide, and particularly over the magnetic equator, combined with projections for a significant peak in solar activity occurring in 1981 implies that significant degradation in communication performance will occur under certain conditions. This paper describes some of the characteristics of amplitude and phase scintillation as we know them, examines the trends with solar and magnetic activity, and projects the trends into the near future.

1.0 Prospectus

The amplitude scintillation of radiostar emissions and transmissions from artificial earth satellites has been of considerable interest to radio engineers for several decades. Generally speaking it has been found that amplitude scintillation increases with both increasing solar activity and magnetic activity, but it has marked variations with latitude and time of day. There have been found to exist two intense zones of scintillations; one at high latitudes, and the other centered over the geomagnetic equator. Apart from these latitudinal-referenced zones, a longitudinal variation in the occurrence of amplitude scintillation has also been detected for fixed universal times. Weak scintillation has been observed at mid-latitudes but this is predominantly a summer-daytime phenomenon which is likely the result of sporadic E-ionization. It is thought that high latitude scintillation results from particle precipitation events concommitant with substorms and that equatorial scintillation derives from an instability (Rayleigh-Taylor) in that region, which is most pronounced

during nocturnal and equinoctial periods. Scintillation has been observed to decrease with increasing radio frequency ($f^{-1.5}$) and increasing elevation angle. Strong UHF scintillation has been observed at high latitudes and scintillation at GHz frequencies has been observed over the geomagnetic equator. There is an equatorward expansion of the high-latitude scintillation zone and a poleward expansion of the equatorial zone suggested by recent NTS-2 data at both UHF and L-band following geomagnetic storms. Since geomagnetic storms ultimately derive from solar activity, the globally-averaged scintillation is typically expected to increase as we approach the high in solar activity. As a result disrupted UHF communication may occur at certain midlatitude stations and almost certainly will involve communication stations and ships at high latitudes.

The amplitude distributions associated with scintillation events are typically observed to be approximated by a Nakagami-m function which allows for Rayleigh fading with m=1. It has been observed that Rayleigh (essentially worst-cast) fading is the rule, rather than the exception during peak scintillation periods at UHF.

The power spectra are dominated by contributions near the Fresnel-zone frequency $v.(\lambda Z)^{-\frac{1}{2}}$ when v is the relative velocity of ionospheric motion, λ is the radio wavelength and Z is the distance to the scintillation region of inhomogeneities, which have been found to exhibit a power law spectral behavior. As deduced from various experimental techniques, the height distribution of inhomogeneities favors a mean height of $\sim$ 400 kilometers for its centroid, but this varies widely depending both upon geography and forcing function dependencies. Thus at a FLEETSATCOM or MARISAT/GAPFILLER frequency of $\sim$ 250 MHz and a relative velocity of 200 meters/sec, we anticipate that most of the scintillation power will occur at roughly 0.3 Hz which implies an average fading interval of the order of 3 seconds but may become significantly shorter as the intensity of the scatter becomes larger in the Rayleigh regime (due to multiple scattering). This periodicity is clearly expected to vary with solar activity (i.e., fades to become faster as well as deeper with increasing activity) because of enhanced motion of the inhomogeneities (i.e., dependence on v, above). The scintillation power spectra typically have a power-law behavior, ν^{-p}, above the Fresnel frequency where ν is the fluctuation frequency and the index p ranges between about 2 and 4 (p is taken to around 3 on the average but may be slightly lower at high latitudes and higher at low latitudes, depending on geomagnetic activity.) This behavior is brought about by the fact that the intrinsic spectra of inhomogeneities is of a power-law form rather than being Gaussian, as originally supposed, and it accounts at least in part for the larger than predicted values of scintillation which were observed with TACSAT over the Pacific in the early 70's. The occurrence of GHz scintillation over the geomagnetic equator may be due to an additional source (of outer scales) which is not easily observed from spectral analysis at lower frequencies.

The bandwidth of scintillation is exceptionally broad and as a result frequency diversity is not a practical possibility. Polarization diversity is also found to be impractical as a mitigation scheme. On the other hand, time diversity and space diversity hold considerable promise. The space diversity concept operates on the proposition that fading is independent if two ray trajectories are sufficiently separated. Work at NOSC has shown that the minimum separation is 700 to 1000 meters but is dependent upon the height of the inhomogeneities or equivalently the Fresnel zone radius. Larger spacings are required for periods of higher solar activity according to the NOSC studies. This relatively significant receiver spacing requirement to achieve diversity gain suggests that disadvantaged users such as ships operating at low latitudes cannot be accomodated through use of spaced antennas on the ship structure.

Time diversity schemes have been examined by several groups including MIT/Lincoln Laboratory. Burst errors arising during scintillation are randomized by interleaving, and convolutional encoding is employed for forward error corrections. This procedure, upon de-interleaving and decoding (Verterbi), has been tested under simulated Rayleigh fading conditions and appears to operate successfully. However, it is an additional expense, and a sacrifice in throughput and timeliness is imposed due to the delay in processing the data (around 2 minutes).

Remarks presented so far have been made in the framework of amplitude scintillation effects, since very limited amounts of phase scintillation data have been obtained upon which generalizations could be based. This problem is being circumvented through use of recent experiments aboard ATS-6 but most principally using transmissions from WIDEBAND DNA-002. In these experiments, a UHF or GHz channel is used as phase reference and differential phase data have been obtained at a lower set of frequencies. Data of this type have also been obtained using TRANSIT satellites and U.S. NAVY TIMATIONs (NTS 1 and 2). Concern had been raised that PSK modulation schemes would suffer additional degradation if phase scintillation were severe. Isolated events have been reported which lend some credance to this fear. However at the data rates employed by FLEETSATCOM, the COSTAS phase lock loop in the standard receivers (viz, AN/SSR-1) typically responds to the challenge so that phase scintillations may be ignored during periods of low solar activity. During the more virulent periods of activity in which inhomogeneities are in more rapid motion and fade (and phase change) rates are enhanced, the matter is open at this time.

Statistical models of world-wide scintillation effects have been constructed by workers at Stanford Research Institute using data obtained principally at VHF, and localized empirical models have been developed by a group at AFGL for both high and equatorward latitudes. Since these models are statistical and subject to all the usual

problems associated with attempts to represent complex (and poorly understood or measured) phenomena with simple functions, they are not particularly desirable for use in forecasting. Nevertheless they may be used provided caution is observed.

A general review of all aspects of scintillation is being prepared by the author of this note and will not be covered herein. We shall presently concentrate only upon the solar and magnetic activity aspects of UHF transmissions from a geostationary satellite.

2.0 Dependence of Scintillation on Solar Activity

As has already been noted, most evidence clearly points to the fact that during epochs of higher solar activity a higher occurrence rate of scintillation is to be expected. Furthermore in regions where the occurrence rate is already high, the intensity of scintillation is increased. In general both properties operate simultaneously except, naturally, whenever amplitude scintillation is already saturated. Even in this case the scintillation rate will be observed to increase.

Models have been developed which indicate the increase in scintillation with solar activity both directly and indirectly (through magnetic activity indices). Stanford Research Institute [1.,2.,3.], NOAA, [4.] and AFGL [5.,6.,7] have published models and reviews have been provided by a number of authors,[8.,9.]. It is noteworthy that there are well over 300 papers which have been published by various scientists dealing with various aspects of scintillation, and it would be impossible to cite them here. However certain aspects of how the sun controls scintillation have begun to emerge from detailed morphological studies and modelling attempts.

The general view held is that solar activity enhances scintillation over the equator, that magnetic activity enhances scintillation at high latitudes and the auroral zone, and that midlatitude scintillation is independent of both sources. Indeed the Fremouw-Pope-Rino Model (F-P-R Model) as described by Fremouw et al [3.] expresses this view analytically. The F-P-R model indicates:

$$S_4 \sim S_4^M (\lambda_m, T) + S_4^H (\lambda_m, T, K_p) + S_4^A (\lambda_m, T, K_p) + S_4^E (\lambda_m, \lambda_g, T, D, R) \quad (1)$$

where S_4 is the scintillation index
λ_m is the geomagnetic latitude
λ_g is the geographic latitude
D is the day of year
T is the local time of day
K_p is the planetary K index
R is the mean sunspot number
and the superscripts M, H, A, and E refer to Midlatitude, High latitude, Auroral, and Equatorial respectively.

Figures 1-4 show how the S_4 index appears for a sunspot number of 100 near vernal equinox at subsatellite local times of 0000, 0600, 1200, and 1800 hours using the model of Fremouw et al (F-P-R Model). These graphics are intensity modulated (gray-scale) representations of S_4 for a transmitting synchronous satellite located at 75° W longitude with the scaled values projected back to the geographical positions of all surface points in view of the satellite. These representations are for F-region scintillation only and are, of course, only mean values. Nevertheless, they show the two principal scintillation zones rather clearly.

It is worth mentioning again that solar and magnetic activity dependencies are difficult to separate. Provided appropriate solar-related observables are selected (not necessarily R but some other parameter such as EUV, X-ray, or radio flux, solar wind velocity, etc.) and suitable time constants are considered, it might be possible to exclude K_p in future correlation analyses altogether (or alternatively R if K_p is desired). In this connection the F-P-R model is observed to exclude a joint dependence upon K_p and R; this is to avoid correcting for the same effect twice.

Let us now examine the predictions of the F-P-R model for a radio frequency of 250 MHz and a sunspot number of 200. Figure 5 shows the location of the four major communication area master stations (NAVCAMS) on a grid in which a set of (300 kilometer altitude-referenced) invariant latitude isopleths is overlaid and the zones of scintillation are depicted. It would appear that we should consider the term $S_4^E(\lambda_m,\lambda_g, T, D, R)$ for Honolulu and Guam, $S_4^M(\lambda_m, T)$ for Naples, and possibly $S_4^M(\lambda_m,T)$ and $S_4^H(\lambda_m,T,K_p)$ for Norfolk.

Honolulu and Guam are roughly 20° and 10° above the geomagnetic equator respectively. Evidence exists that equatorial scintillation peaks at $\pm$ 10° of the equator. It has a dependence above the equator of the form[3]:

$$\exp - \frac{(\lambda_m - 10°)^2}{(10°)^2} \qquad (2)$$

A similar term exists south of the equator.

Hence S_4 is maximized for Guam and reduced to $\frac{1}{e}$ at Honolulu; at the equator itself S_4 is equal to $\frac{2}{e}$ of its maximum value because of the sum of two terms.

Curves due to Fremouw et al [3] for Ancon, Peru and Kwajalein Atoll have been modified by the author of this paper to reflect a radio frequency of 250 MHz and a sunspot number of 200. The original curves were for f = 138 MHz and R = 21; translations in frequency for amplitude and phase scintillation were

$$S_4 \sim f^{-1.5}$$
$$\phi_{rms} \sim f^{-1} \qquad (3)$$

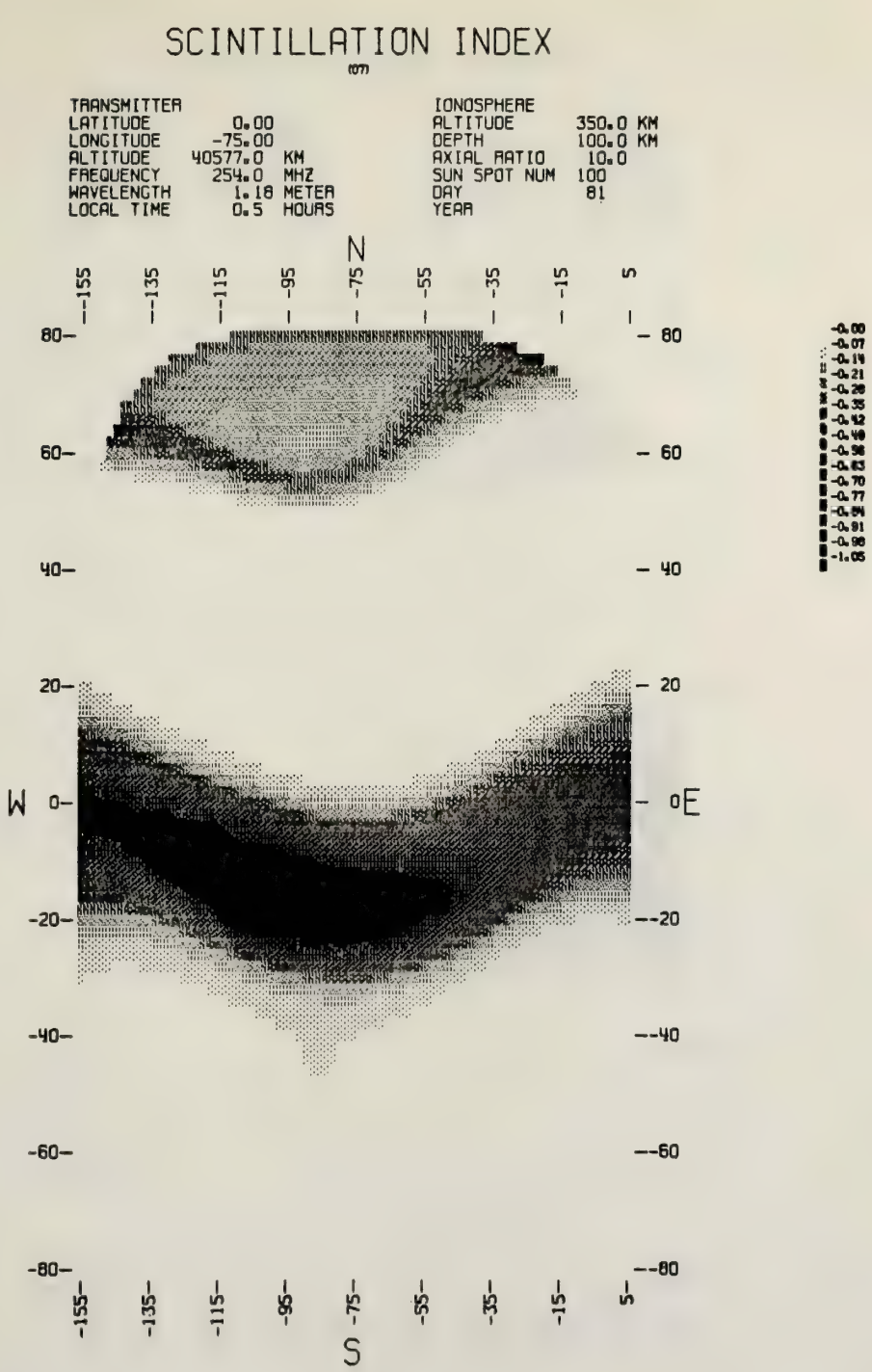

SCINTILLATION INDEX
TRANSMITTER
LATITUDE 0.00
LONGITUDE -75.00
ALTITUDE 40577.0 KM
FREQUENCY 254.0 MHZ
WAVELENGTH 1.18 METER
LOCAL TIME 0.5 HOURS
IONOSPHERE
ALTITUDE 350.0 KM
DEPTH 100.0 KM
AXIAL RATIO 10.0
SUN SPOT NUM 100
DAY 81
YEAR
N
S
W
E
-155
-135
-115
-95
-75
-55
-35
-15
5
80
60
40
20
0
-20
-40
-60
-80

Fig. 1

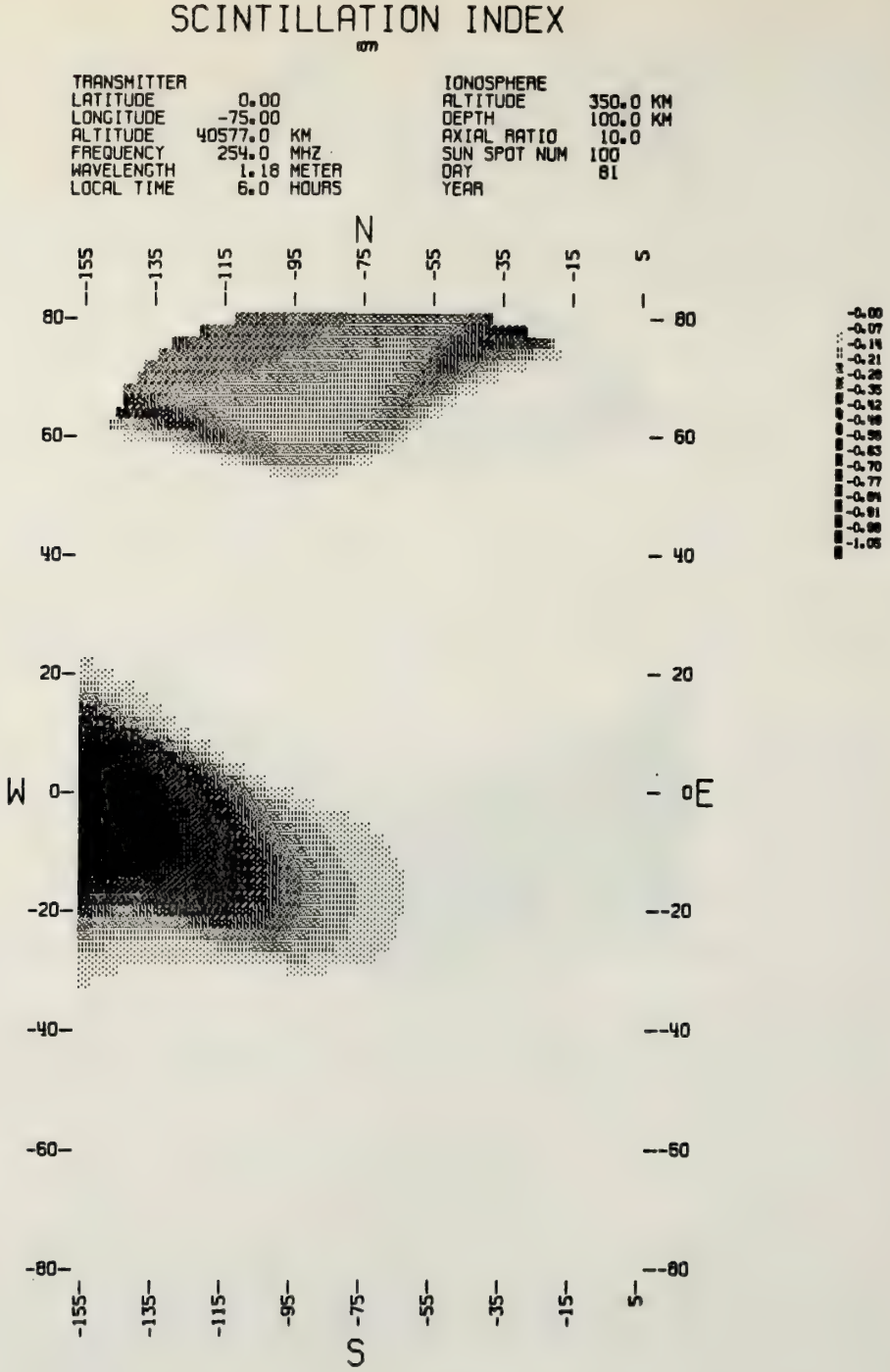

SCINTILLATION INDEX
TRANSMITTER
LATITUDE 0.00
LONGITUDE -75.00
ALTITUDE 40577.0 KM
FREQUENCY 254.0 MHZ
WAVELENGTH 1.18 METER
LOCAL TIME 6.0 HOURS
IONOSPHERE
ALTITUDE 350.0 KM
DEPTH 100.0 KM
AXIAL RATIO 10.0
SUN SPOT NUM 100
DAY 81
YEAR
N
S
W
E
-155
-135
-115
-95
-75
-55
-35
-15
5
80
60
40
20
0
-20
-40
-60
-80

Fig. 2

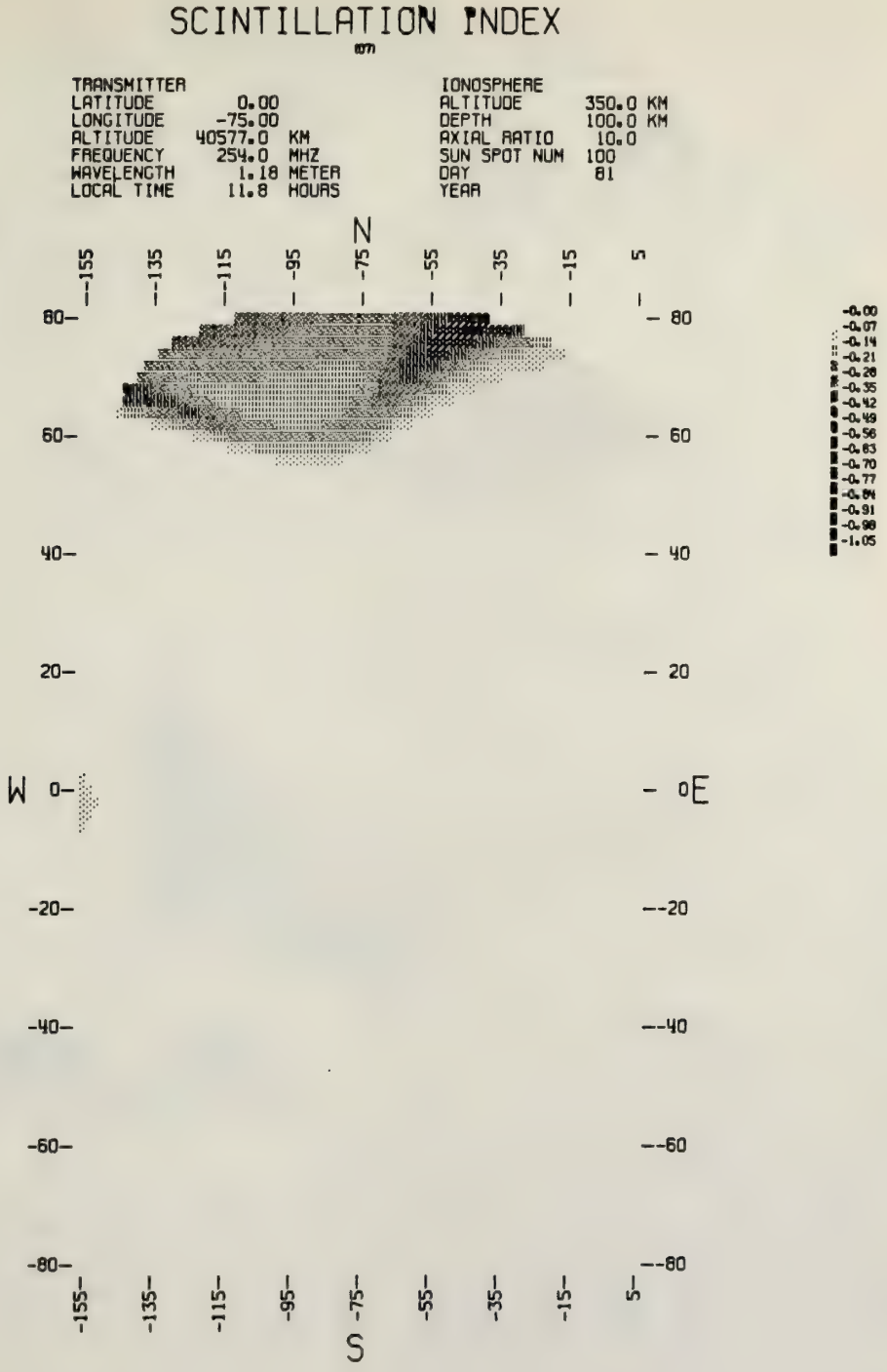

SCINTILLATION INDEX
TRANSMITTER
LATITUDE 0.00
LONGITUDE -75.00
ALTITUDE 40577.0 KM
FREQUENCY 254.0 MHZ
WAVELENGTH 1.18 METER
LOCAL TIME 11.8 HOURS
IONOSPHERE
ALTITUDE 350.0 KM
DEPTH 100.0 KM
AXIAL RATIO 10.0
SUN SPOT NUM 100
DAY 81
YEAR
N
S
W
E
-155
-135
-115
-95
-75
-55
-35
-15
5
80
60
40
20
0
-20
-40
-60
-80
-1.05

Fig. 3

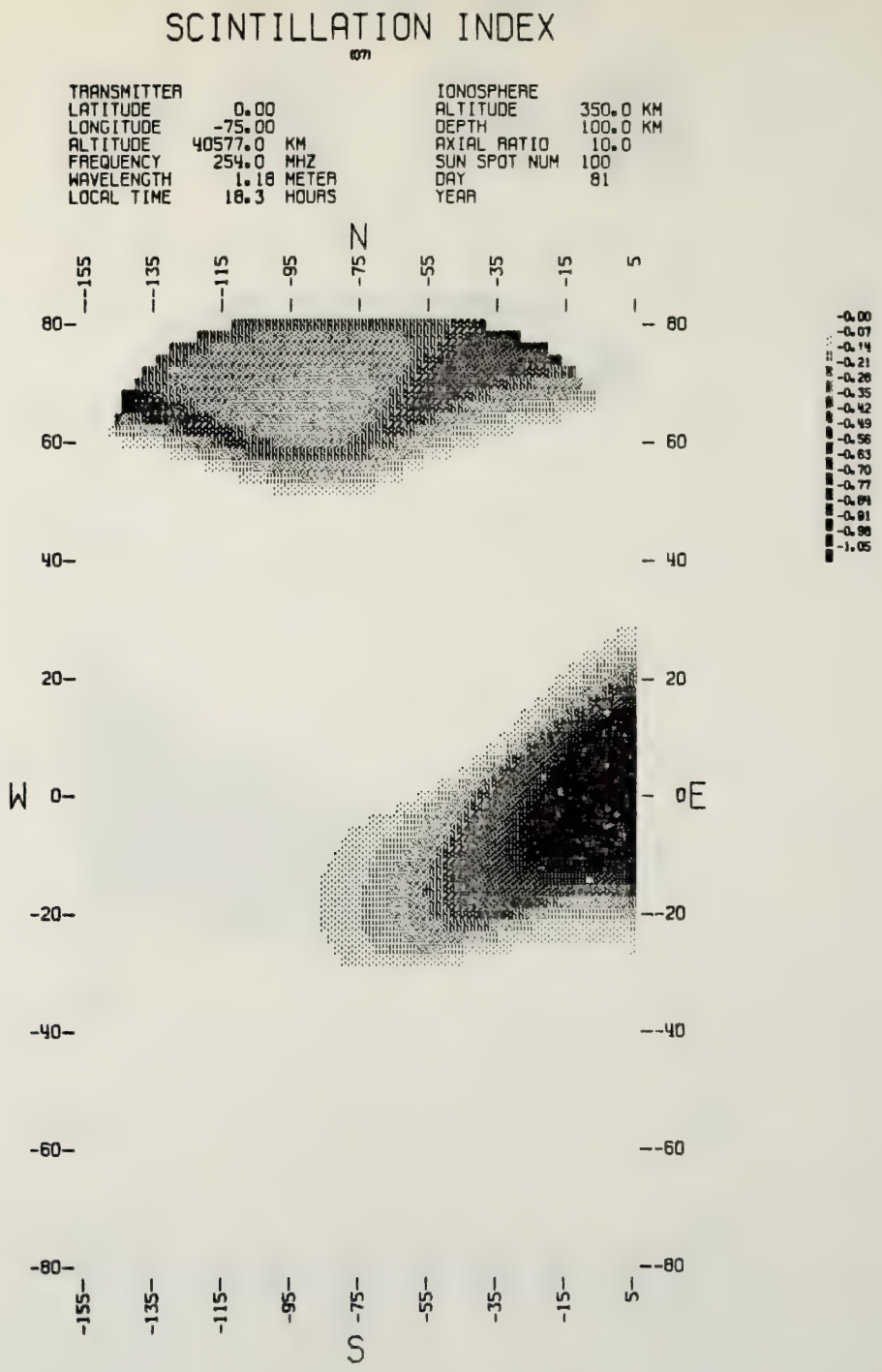

SCINTILLATION INDEX
TRANSMITTER
LATITUDE 0.00
LONGITUDE -75.00
ALTITUDE 40577.0 KM
FREQUENCY 254.0 MHZ
WAVELENGTH 1.18 METER
LOCAL TIME 18.3 HOURS
IONOSPHERE
ALTITUDE 350.0 KM
DEPTH 100.0 KM
AXIAL RATIO 10.0
SUN SPOT NUM 100
DAY 81
YEAR
N
S
W
E
-155
-135
-115
-95
-75
-55
-35
-15
5
80
60
40
20
0
-20
-40
-60
-80

Fig. 4

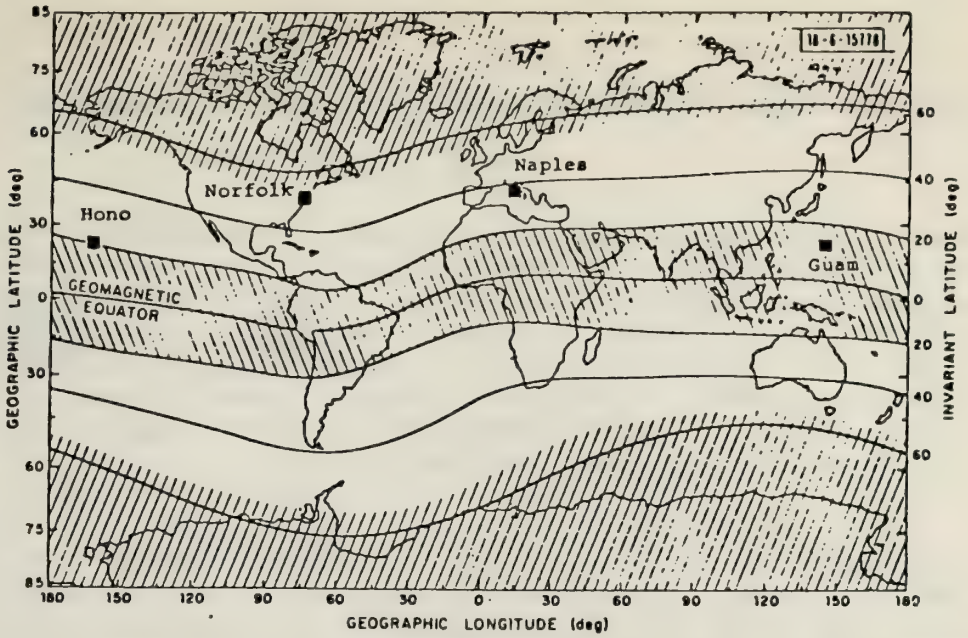
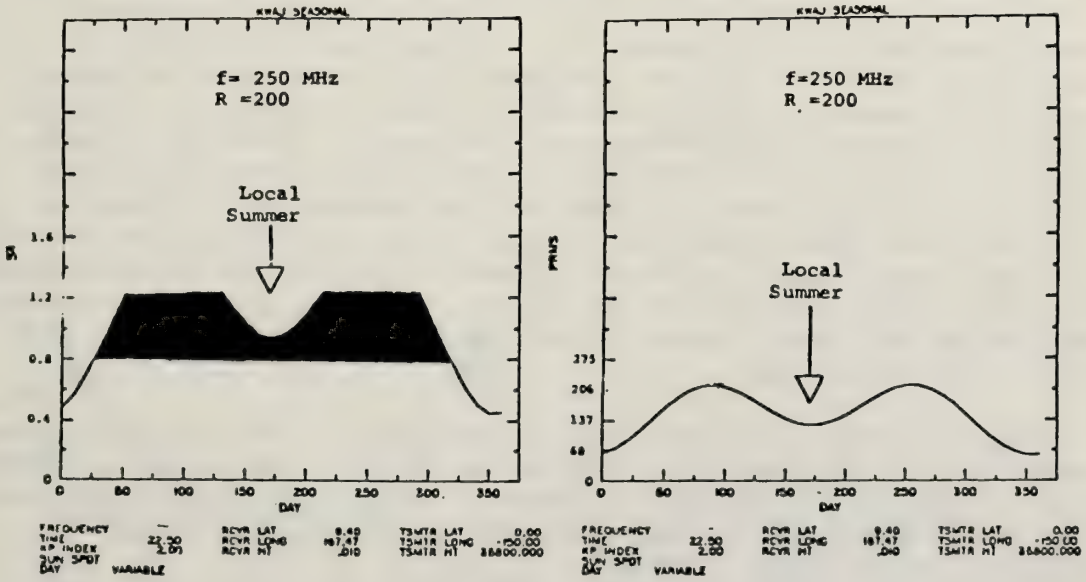


Fig. 5 - Location of the Four Major NAVCOMSTAS with respect to the regions of strong F-region scintillation (shaded).



6A 6B

Fig. 6A - Seasonal Dependence of Scintillation Index S_4 during nocturnal hours (2200 local) for Kwajalein Atoll and at a frequency of 250 MHz and for a sunspot no. of R=200.

6B - RMS ϕ scintillation (same conditions as A) (Curves adapted from Ref 3)

and translations in sunspot numbers were made using the linear relation 3.

$$S_4 \sim \phi_{rms} \sim 1 + 0.04\ R \qquad (4)$$

which is applicable in the non-saturated regions. Figures 6 and 7 show the projected seasonal variations in S_4 and rms phase fluctuations for Ancon and Kwajalein respectively. Figure 8 shows the diurnal variation to be expected at Ancon at equinox. It has been shown [9.,10.] that if $S_4 \geq 0.8$ then the 1-99% fading range in dB is approximately 19dB. This area is shaded. Under this condition the FLTBCST channel of MARISAT/GAPFILLER will suffer a bit error rate $\geq 10^{-3}$ and corrupted messages will occur[11].

We see that corrupted messages will be observed on the average every night for sites similar to Ancon and Kwajalein except during local wintertime. Furthermore it will persist for approximately six(6) hours. It is odd that the APL report[10.] does not allow for any appreciable solar activity effect.

Figure 9 is a NOSC prediction of the magnitude of equatorial scintillations to be expected at sunspot maxiumum. Their assertion of a projected 30% occurrence of scintillations ($\sim$ 7.5 hours/day for worst month conditions and $S_4 \geq 0.3$ or fading $\geq$ 6dB) is somewhat lower than the 42% occurrence (i.e. $\sim$ 10 hours/day for $S_4 \geq 0.3$) implied by Figure 8. Furthermore Ancon is virtually on the magnetic equator and would be subject to somewhat less intense scintillation than that observed at GUAM because of relation 2 above (by a factor of $\frac{2}{e}$ or 1.4dB). In sum, the F-P-R model predicts that equatorial scintillation for sites like Guam will be greater than or equal to $\sim$ 20dB (based upon Ancon projections) 6 hours/day on the average for the worst month case. Further, at least 1 hour/day of scintillation $\leq$ 20dB willbe observed for 60% of the year (i.e. all year excluding the period near local winter). Scintillation is reduced by 4.4dB on the average at Honolulu.

Scintillation at Naples, which is strictly in the midlatitude zone, should not be particularly severe except possibly during local summer when sporadic E ionization is enhanced. The probability of sporadic E-induced ionization has been examined recently by the author[12.] based on earlier work at VHF[13.].

Scintillation at Norfolk may be severe during nocturnal hours following magnetic storms. This is due to the southward expansion of the equatorward edge of the scintillation boundary. There is little data presently available to provide a projection for large solar activity epochs. However the occurrence of major magnetic storms is known to be related to the occurrence of large solar flares and enhancements in solar wind velocity. Scintillation, as observed from Washington, D.C., following magnetic storms has been reported both at VHF and UHF[14.,15.]. Projections of difficulty in interpretations of

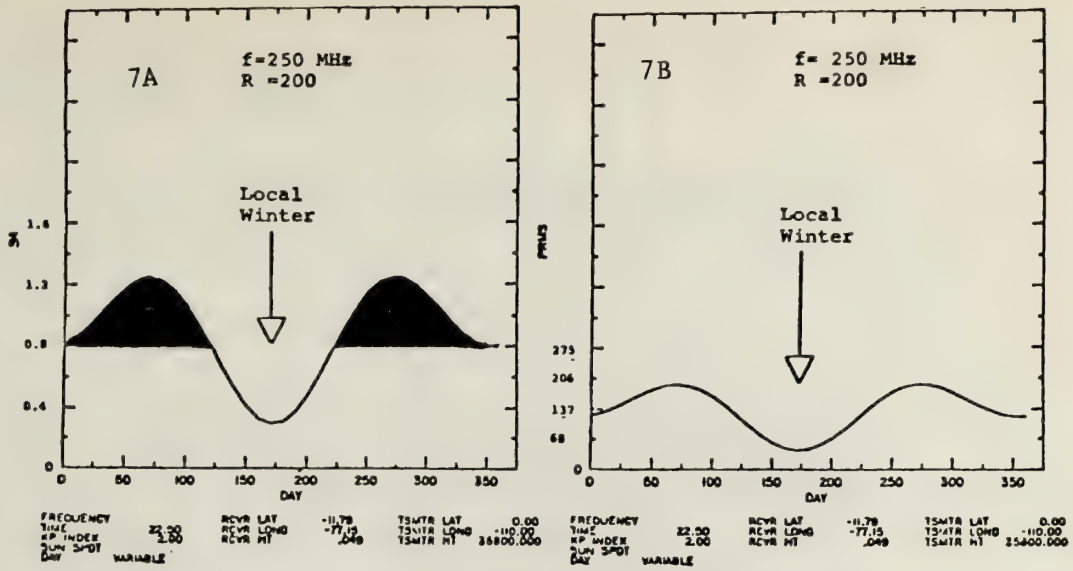


Fig. 7A - Seasonal Dependence of Scintillation Index S4 during Nocturnal Hours (2200 Local) for Ancon, Peru and at a frequency of 250 MHz and for a sunspot No. of R=200.

7B - RMS ϕ scintillation. (same conditions as A) (Curves adapted from Ref 3)

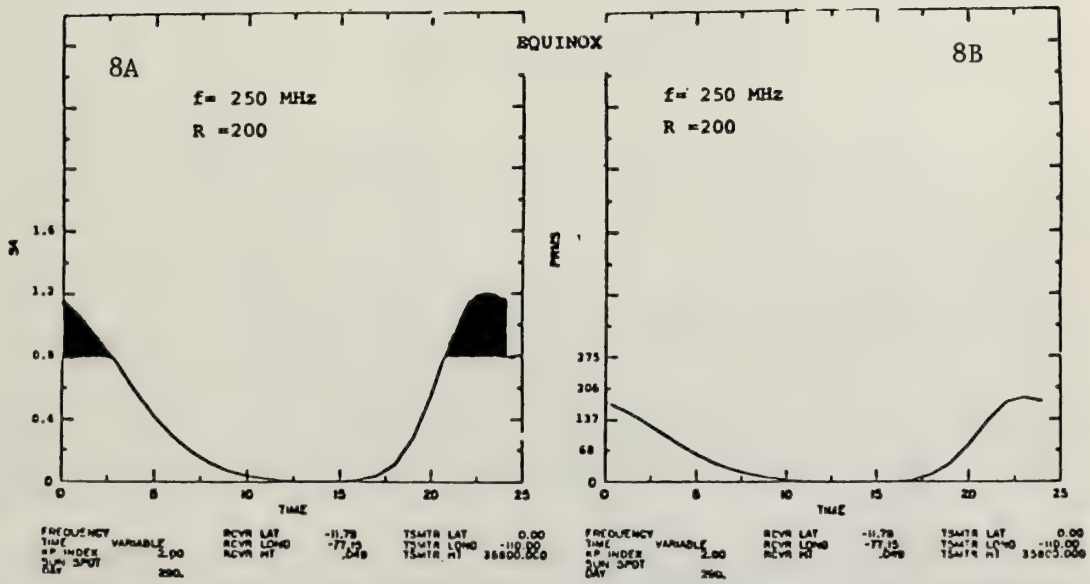
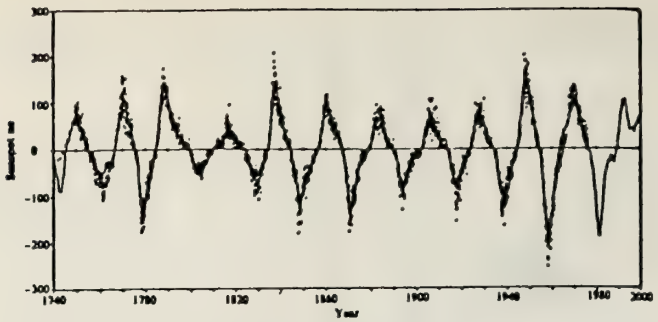


Fig. 8A - Diurnal Variations of S4 Index for Ancon, Peru for f=250 MHz and R=200.

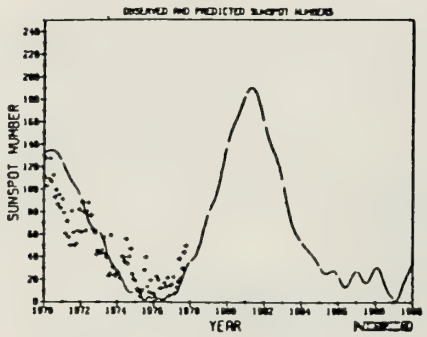
8B - Diurnal Variations of RMS ϕ for Ancon, Peru for f=250MHz and R=200.

Fig. 9A



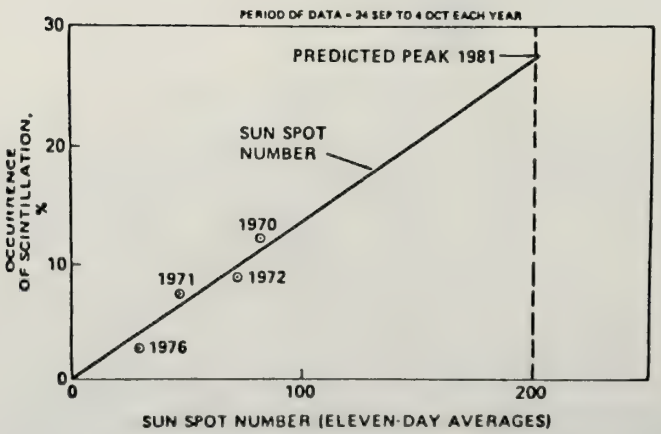
Observed and Predicted Solar Activity Indices (Sunspot No.) from 1740. Absolute values of the extrema are to be interpreted as the peak sunspot numbers. The smooth curve (prediction) near 1981 is seen to be as large as the 1959 peak, the largest in recorded history. (Ref 16)

9B



- Detailed plot of solar cycle 21 predictions. (Ref 16)

9C



Predicted Scintillation at 250 MHz for GUAM at equinox (Ref 16) (Also from several papers by R.U.F. Hopkins at NOSC)

FLTBCST messages at solar maximum in the Norfolk area roughly translates to projecting the number of major magnetic storms. This is a difficult and risky business.

Scintillation at high latitudes is slightly less severe than that over the equator but is essentially omni-present, exhibiting little variation with season or time of day at fixed invariant latitudes and fixed values of K_p. However the auroral oval (and scintillation boundary) sweeps out different geographic latitudes as a function of time and as a result a ship positioned at a fixed high latitude point will observe a diurnal dependence of scintillation. At operationally important oceanic regions between Greenland, Iceland, and the United Kingdom (termed GIUK gap), for example, scintillation will be enhanced during the night and least (but not zero) during the day[10]. Ships in the North Atlantic will be particularly vulnerable to scintillation following magnetic storms, even during daytime hours due to the southward movement of the various circumpolar features.

3.0 Resume of U.S. Navy Position Vis-A-Vis Scintillation

The U.S. Navy is now considering various options for mitigation of UHF scintillation, specifically for fleet broadcast (FLTBCST) channels and these are presently being considered from a broad systems viewpoint. The various techniques are typically evaluated with due consideration for whether the Fleet asset is either a ship or a ground station. As would be expected, space diversity is only applicable to the FLTBCST downlink to the communication area master stations (CAMS) since considerable real estate is required. As a result its incorporation will not generally be of service to the Fleet except as a monitoring system. The use of time diversity schemes (interleaving and forward error correction) is useful for both uplink protection from the CAMS and downlink to the ships or the CAMS, provided special decoding and de-interleaving equipment is available. However, it is generally concluded that coding schemes cannot be practicably employed for high data rate (2400 BPS) channels in a polled net or in Demand Assigned Multiple Access (DAMA) scenarios. These systems are also quite expensive. Brute force techniques such as increasing uplink effective isotropic radiated power (EIRP) or downlink shore G/T are also being explored; these options are also not without drawbacks.

One of the more viable long term possibilities is to avoid UHF scintillation altogether by inserting FLTBCST into the SHF channels of future synchronous satellite systems such as FLTSATCOM or LEASAT. This option will require acquisition of SHF receiving equipment by the Fleet and such plans are now being formulated. However, these plans will not be brought to fruition during the 1980 to 83 epoch during which time scintillation may be at its peak levels. In summary, the downlink protection for ships against scintillation is less than complete, and there is no short term solution to this problem. The intermediate solution involves protection of links to major flag ships and carriers

using SHF equipment. A short term solution for the more critical circuits located at the CAMS might involve several options not the least of which is SHF relay of FLTBCST to an alternate site using the Defense Satellite Communications System (DSCS) channels. This alternate site, hopefully being located in a non-scintillation region, would copy UHF FLTBCST from FLTSATCOM and would retransmit the traffic to the CAMS via the relatively non-vulnerable DSCS links at 7-8 GHz.

The role of forecasting and prediction of scintillation would appear therefore to be of some practical interest in resource management in the near term and may extend into the intermediate and long terms.

4.0 Summary

We have shown in this brief note that scintillation effects at UHF (250 MHz) have the potential to be extremely deleterious during the upcoming epoch of solar activity, predicted to be as high as 200 (See Figure 9).[16].

This is a preliminary assessment. Work is continuing to refine the estimates.

The author would like to thank LCDR Claude LaVarre, Dep. Director Naval Electromagnetic Spectrum Center, Naval Communications Unit, for suggesting this topic. LCDR C. French of NAVELEX is acknowledged for his comments and Dr. E. Fremouw made several helpful suggestions in reviewing this paper.

REFERENCES

1. Fremouw, E. J. and C. L. Rino, 1973, Radio Sci. 8, 213.
2. Rino, C. L., E. J. Fremouw, A. R. Hessing, and V. E. Hatfield, 1978, RADC-TR-78-87.
3. Fremouw, E. J., C. L. Rino, A. R. Hessing, and V. E. Hatfield, 1978, RADC-TR-78-88.
4. Pope, J. H., 1974, NOAA TR ERL 308-SEL 30.
5. Aarons, J., J. Muller, H. Whitney, E. Martin, K. Bhavnani, L. Whelan, 1976, AFGL-TR-76-0210.
6. Basu, Sunanda, Santimay Basu, B.R. Khan, 1976, AFGL-TR-76-0080.
7. Aarons, J., E. MacKenzie, and K. Bhavnani, 1978, Proc. AGARD NATO Specialists Conference, Ottowa, Canada. (papers 5-1).
8. Aarons, J., 1976, AFGL-TR-76-0078.
9. Crane, R. K., 1974, MIT Lincoln Lab Report 1974-29.
10. Goodman, J. M., P.L. Watkins, C.G. Myers, R. Hogg, 1978, NRL Report 8160
11. _____, 1976, Johns Hopkins APL, SDO-4380.6
12. Goodman, J.M., 1976, NRL Memo Report 3396
13. Goodman, J.M., 1967, J. Atmospheric Terrest. Phys. 29, 607
14. Goodman, J.M., 1968, J. Planet. Space Sci. 16, 951
15. Goodman, J.M., R. Zirm, R. Beard, 1978, URSI Proc. Helsinki
16. Argo, P.E., and J. R. Hill, 1978, IES'78 Proc., paper 5-1

IONOSPHERIC REFRACTIVE CORRECTION USING AN ADAPTIVE PROCEDURE

D.E. Donatelli
Regis College Research Center
Weston, Massachusetts

R.S. Allen
Air Force Geophysics Laboratory
Hanscom AFB, Mass. 01731

The time and space variability of the ionosphere as it impacts range correction for radar, navigation and communication systems is considered. An adaptive technique for reducing this impact is examined using TEC data from locations representative of the extent of a typical radar coverage area. Results indicate the procedure is successful during periods when the absolute residual error in range correction is maximum.

1. INTRODUCTION

Radar, navigation and communication systems are able to achieve greater precision through advancements in technology, but daily variability of the ionosphere constrains achievement of their desired accuracy. Numerical maps which provide monthly median corrections have been derived from a world-wide climatology of ionospheric parameters; their use alone reduces the residual in range or time delay measurements to about 20 - 25 percent of the median correction in day time and 30 - 35 percent at night. It is this residual which proposed adaptive techniques attempt to reduce.

Here we will examine the results of using a scaling procedure with a numerical map of median correction within a radar coverage area. The scaling is obtained from real-time measurements of total electron content (TEC) compared with the median TEC for the time and location of the measurement. The refractive correction, which is directly proportional to the electron content along the ray path, is then scaled by this factor. Both temporal and spatial growth of residual error is examined. The zero-point of error is set by the time and place of calibration; the maximum, by the time-space interval required to achieve the magnitude of the median residual error. This interval, and the magnitude of the error within it, determines the effectiveness of the procedure.

2. PROCEDURE

For an operational-type assessment of this procedure, a radar location is hypothesized in the central U.S. Its coverage area is represented in Figure 1. The locations marked are the subionospheric points for stations at which TEC archive data were available. Those marked "x" had simultaneous data for the 1968-69 solar maximum; those marked "o" for the 1974-76 solar minimum. Data from Hamilton, Mass. (HAM) were available for the entire 1968-76 period, and from Goose Bay, Labrador (GSB) for 1972-76. The TEC data are reduced measurements of Faraday rotation of the VHF beacons from the geostationary satellites (Titheridge, 1972): ATS-3 for Hamilton, Goose Bay, Kennedy Space Flight Center, Florida (KSF), Urbana, Illinois (URB); ATS-1 for Stanford, California (STA), Edmonton, Alberta (EDM). The entire set of HAM data were used to examine the temporal variability over season and solar cycle (DuLong, 1977) and the GSB data were used for a comparison of results at two locations (Donatelli and Allen, 1978).

To initiate the procedure, a real time observation is obtained from one of the data stations. The calibration consists of a scaling factor determined by comparing the observation with the expected median. This factor is used to scale the median at 15-minute intervals throughout the day. Figure 2 demonstrates this procedure with calibration occurring every 2 hours, on the hour, for the case where the calibration is made along the same ray path to which the adaptive procedure is applied. Each curve originating at the calibration time demonstrates the average effect over the month of using the scaling factor from this time for 12 succeeding hours. It is obvious that the maximum time interval for which a scaling factor is useful, or, at least, not detrimental, is bound by the time of calibration on one end and the succeeding solar terminator on the other.

3. TIME VARIABILITY

A summary of the HAM data study is provided in Table I, representing the solar maximum conditions, $\bar{S} = 155$, $\overline{R_z} = 110$, and the solar minimum conditions, $\bar{S} = 71$, $\overline{R_z} = 10$, where $\bar{S}$ and $\bar{R}$ represent the twelve-month running mean solar flux at 2800 Mhz and sunspot number, respectively. The values, in meters, of the parameters for range correction and the residual errors are listed at the local times of the daily mean maxima and minima for the periods representing the seasonal maxima and minima, in simulation of actual use by a 425 Mhz radar on a target at 1000 km altitude, 5^{o} elevation angle. To estimate the range correction for other values of $\bar{S}$ it is possible to interpolate or extrapolate to a reasonable approximation by assuming a linear relationship between $\bar{S}$ and TEC.

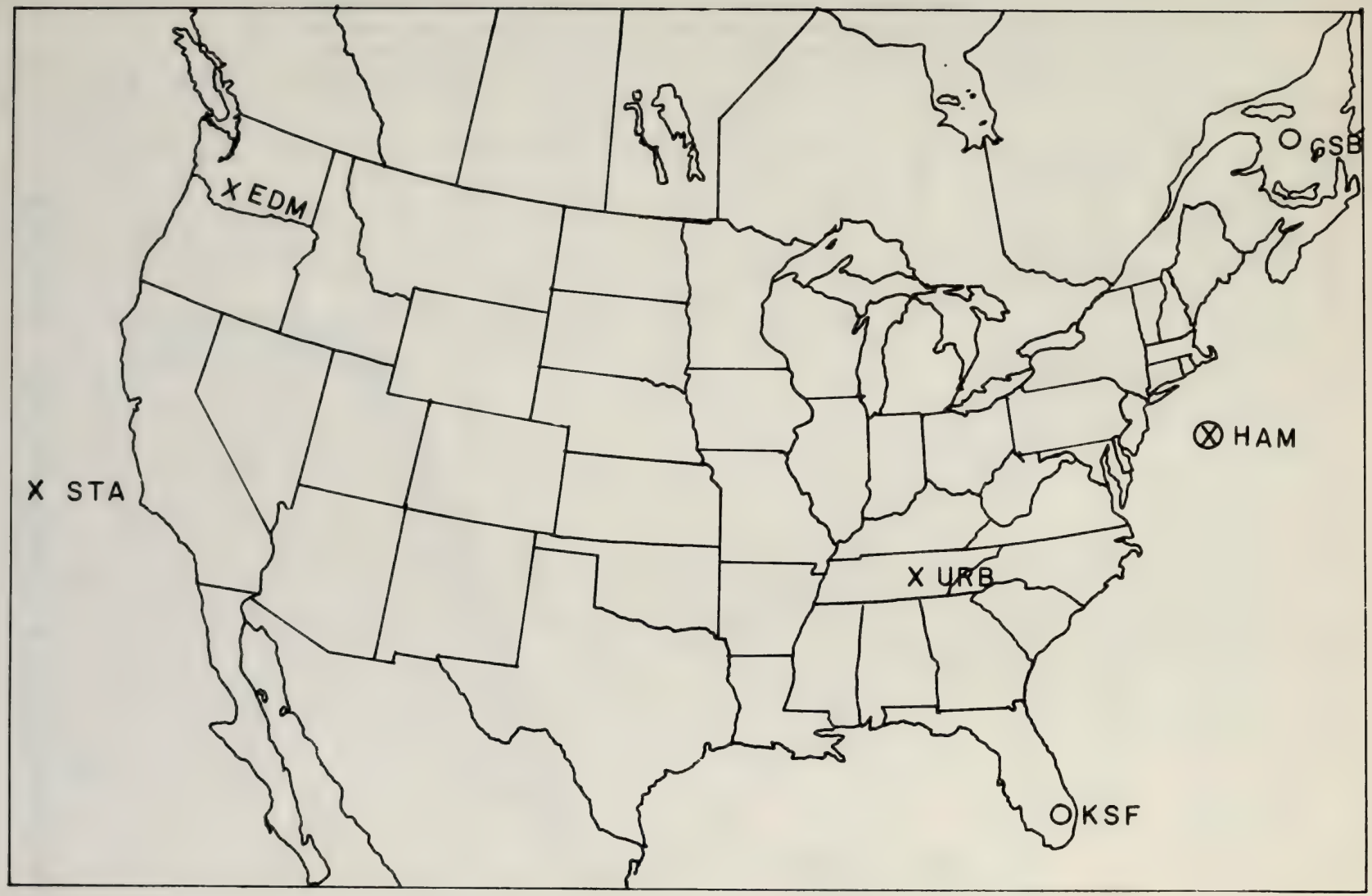


Figure 1. Map showing the locations of the sub-ionospheric points of the stations at which the TEC data were taken.

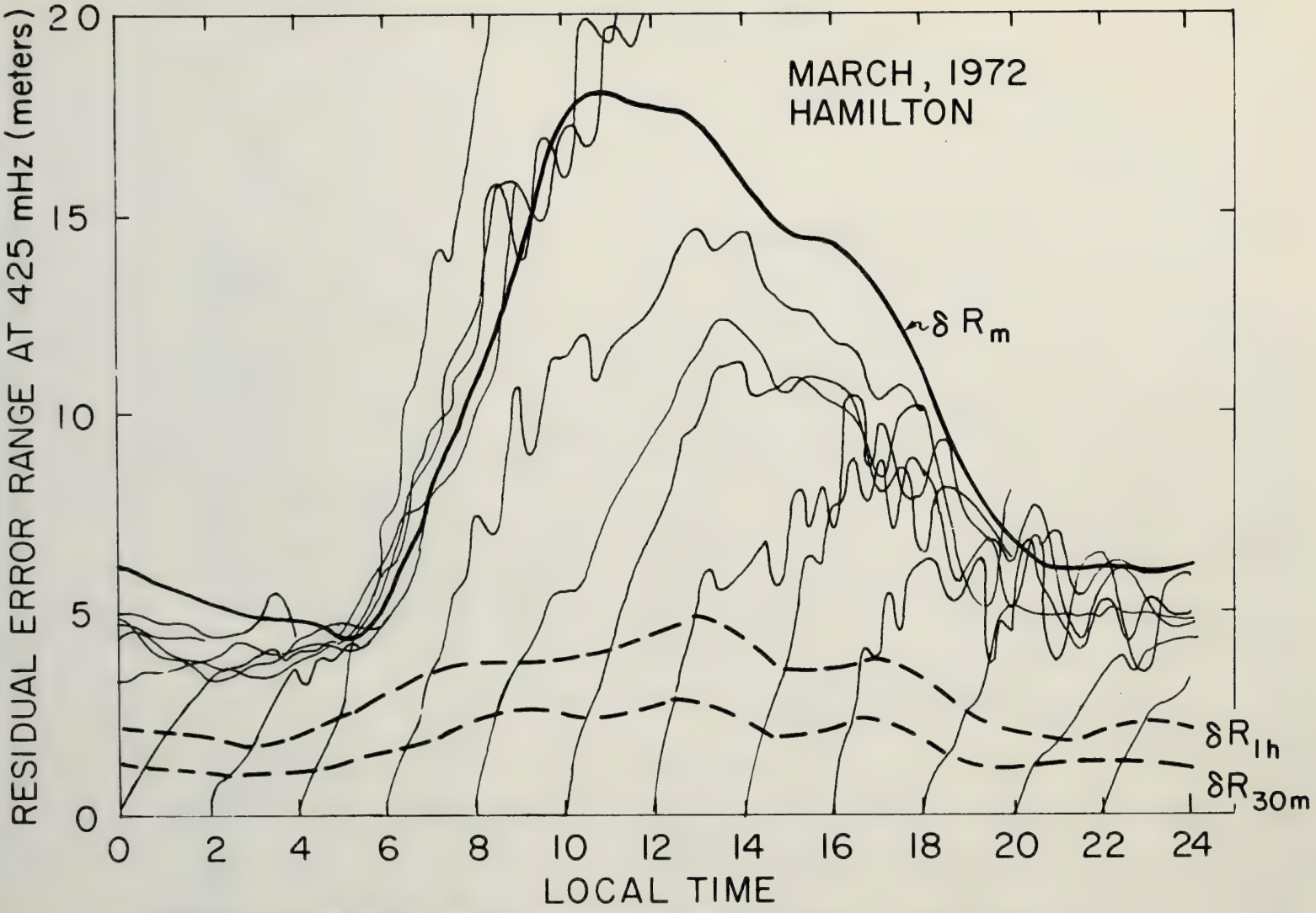


Figure 2. The residual error in range correction using an updating technique ranging from 0-residual error at the time of calibration to the residual error using only the median correction, δR_m, at a time depending primarily on the interval between calibration and subsequent terminator.

The parameters listed are:

ΔR -the ionospheric component of range measurement

δR_m -the residual error in range correction using a median prediction, caused by the day-to-day variability of the ionosphere

δR_{3h} -the residual error in range correction using a scaled median prediction three hours after updating

δR_{1h} -the residual error in range correction using a scaled median prediction one hour after updating

δR_{30m} -the residual error in range correction using a scaled median prediction thirty minutes after updating

TABLE I

	WINTER		VERNAL EQUINOX		SUMMER		AUTUMNAL EQUINOX	
	MAX	MIN	MAX	MIN	MAX	MIN	MAX	MIN
	Solar Maximum ($\bar{R}_z$ = 110; $\bar{S}$ = 155)							
ΔR	230	38	300	55	170	55	275	45
δR_m	40	12	50	17	27	15	50	15
δR_{3h}	27	10	30	10	18	10	27	12
δR_{1h}	15	7	17	7	11	8	11	5
δR_{30m}	10	4	10	4	8	4	9	4
	Solar Minimum ($\bar{R}_z$ = 10; $\bar{S}$ = 71)							
ΔR	70	10	70	10	60	14	75	14
δR_m	12	4	17	4	10	3	10	4
δR_{3h}	12	6	14	3	10	3	14	4
δR_{1h}	8	2	8	1	4	2	8	2
δR_{30m}	6	1	4	1	3	1	4	1

This table shows that an updated prediction of median range correction can reduce the residual error by 60 percent after one hour, and by 30 percent in daytime at solar maximum even after three hours. It appears that at solar maximum there are large amplitude long period variations that are readily corrected with updating. Shorter period smaller amplitude fluctuations superimposed on these, exist at both solar maximum and minimum and impose a limit on effectiveness.

Near sunrise and sunset and during severe magnetic disturbances, periods of rapid changes in TEC, the same degree of reduction in error can be maintained by reducing the interval for updating to about 15 - 30 minutes. This is demonstrated in Figure 3, using the adaptive procedure on a highly disturbed day. Calibration in 30-minute intervals would allow a 65 percent reduction in the maximum error of the day despite the steep gradients in TEC.

The comparison of HAM results with those for the same procedure applied at GSB is presented in Figure 4 using the parameters as defined in Table I, with the addition of:

δR_{15m} -the residual error in range correction using a scaled prediction fifteen minutes after updating

The curves are comprised of the maximum value each month of the designated parameter. The results are similar for both stations, indicating the latitude variation, in this case, may not be significant in day time when the maxima occur.

It must be emphasized that the time interval for effective updating is determined by the rate of change of TEC. Since these data are reduced at 15-minute intervals, fluctuations with a period less than 30 minutes are not observable. The amplitude of these is assumed to be much smaller than the monthly average variability. Therefore, it is the effects of the longer period, and presumably larger amplitude, variations that are being reduced here. The amplitude of the shorter period variations determine the limits for minimizing residual error.

During sunrise and sunset periods, the effects of production and loss, respectively, create gradients that dominate all other fluctuations. Similar gradients may occur during magnetic disturbance. There may be large rapid variations, particularly in the region of the auroral zone and the trough in high and mid-latitudes. It is the rate at which these changes occur that must set the calibration interval at these times.

4. TIME - SPACE VARIATION

Time and space variations cannot be viewed independently. Even if a calibration is used instantaneously, there are likely to be local time variations, for at any longitude, actual sun time varies over latitude, except briefly at the equinoxes. Therefore, any spatial variation includes temporal effects. Spatial variations have been examined in previous work (Allen, 1977; Leitinger et al, 1978) using data from the TRANSIT satellites reduced to provide TEC along the satellite path. The variation of ionospheric features and some of the implications of attempting to track these features in space and time were examined, and the conclusions are confirmed by this present study.

The work discussed up to this point assumes the adaptive procedure

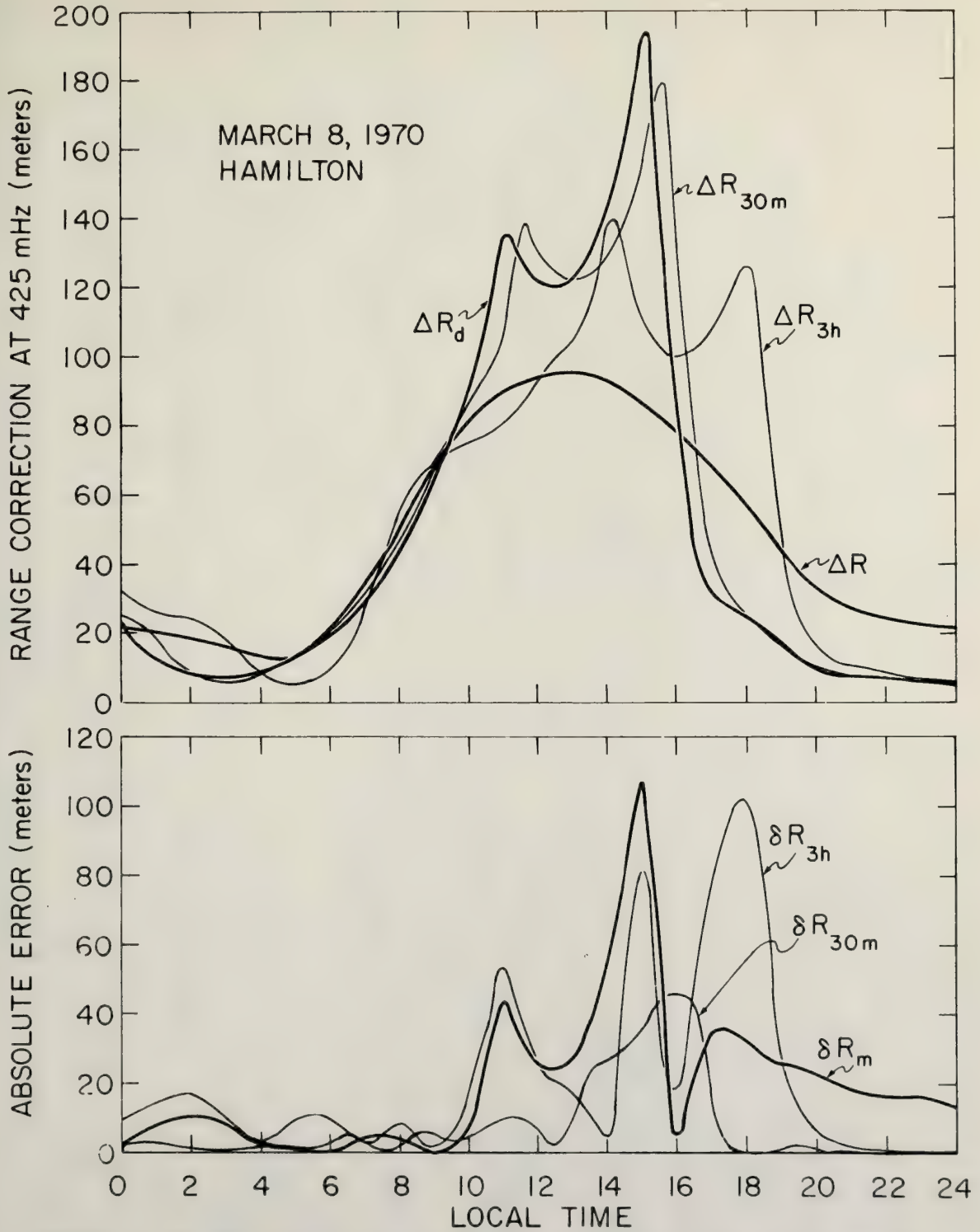


Figure 3. The effectiveness of an updating procedure during a severe magnetic disturbance, comparing the actual required range correction, ΔR_d, with the predicted median, ΔR, and the 30 minute, $\Delta R_{30\ m}$, and 3 hour, $\Delta R_{3\ h}$, updated predictions. The differences in the range correction curves of the upper scale are presented as absolute error on the lower scale.

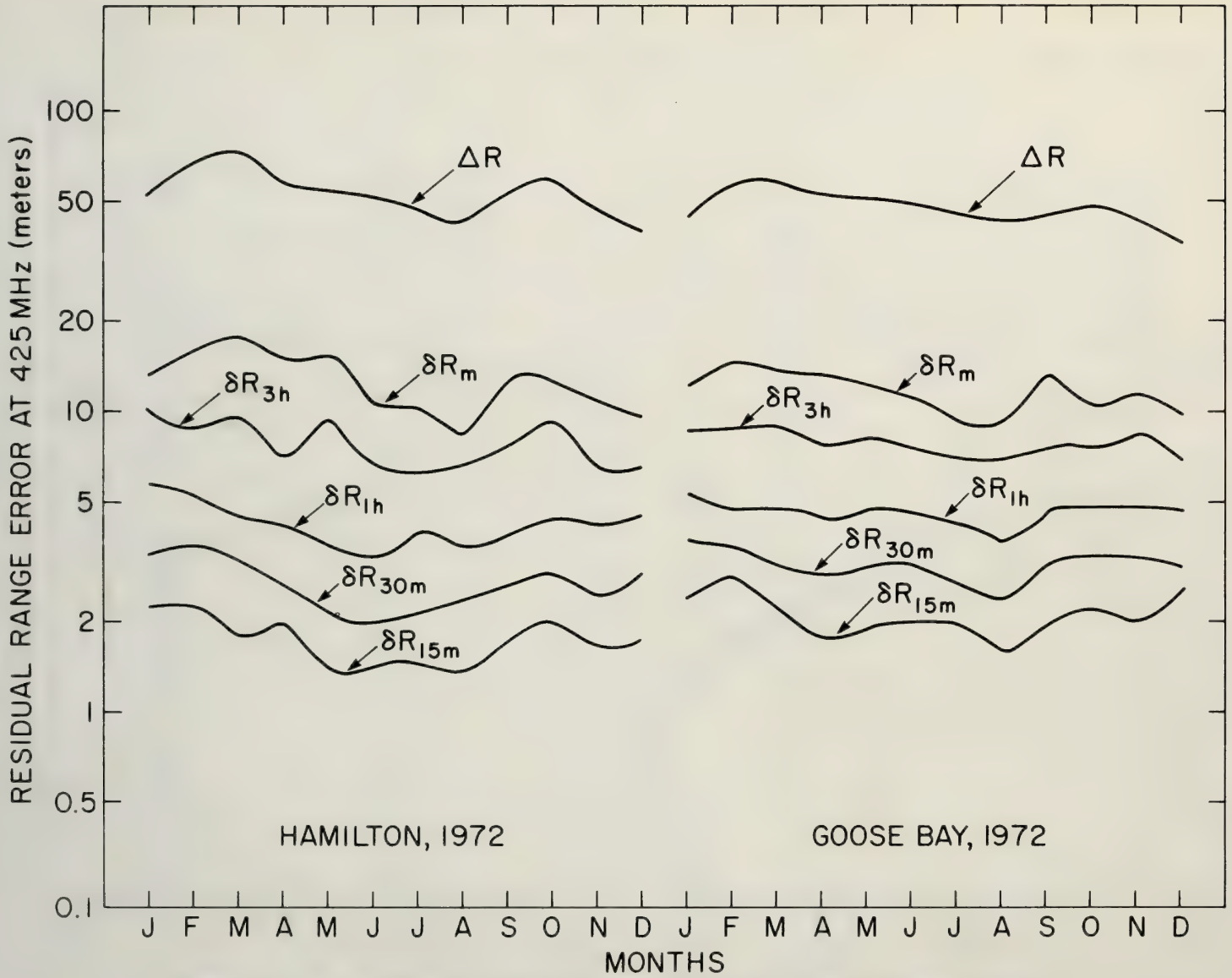


Figure 4. The reduction in maximum monthly residual error in range correction at two different stations, Hamilton, Mass. and Goose Bay, Labrador, for 1972 using the parameters as defined for Table I.

would be applied along the same path as the observation. In actual use this would occur rarely. A valid assessment of an adaptive procedure requires examination of error growth across a region comparable to a system coverage area. The stations shown in Figure 1 provide the best available data for this purpose.

Data availability required that the procedure be examined in two segments: the 68-69 solar maximum period data from HAM, URB, STA AND EDM; and the 74-76 solar minimum period data from GSB, HAM AND KSF. The first segment includes longitudinal variations between the station pairs HAM-URB and URB-STA, and primarily latitudinal effects between EDM-STA. For the second segment, latitudinal effects dominated the station pairs GSB-HAM and HAM-KSF.

Preliminary results, presented in Figures 5-7 show that the degree of success (or failure) of the adaptive procedure depends on the difference in the percentage variability along the ray path used for calibration and the ray path of the applied correction. The upper two sets of curves compare the means and the standard deviations, respectively, for the station pair. Figure 5 is the Stanford-Edmonton pair for the 1969 April and October equinox months and Figure 6, the Stanford-Urbana pair for the same period, showing latitude and longitude effects, respectively. Figure 7 is the Goose Bay-Hamilton pair for the same months, but near solar minimum, 1975. The latitudinal extent is similar to Stanford-Edmonton. The standard deviation represents the variability at each station; the comparative percentage variability can be determined from the differences between the mean and standard deviation (δR_m) curves for each station. If there is a large difference in the percentage variability between the two stations, the one with the lesser is preferred for calibrating. It should also be noted that the night time variability often differs considerably between stations and this may be attributed, in part, to conjugate effects.

In applying the adaptive procedure a calibration at one station is used to determine the factor to update the mean of the other. The process is applied reciprocally between each pair of stations. The lower two sets of curves compare δR_m at the station which is being updated, with the residual error when the adaptive procedure is applied 15 minutes (δR_{15m}) and 3 hours (δR_{3h}) after calibration. Thus, the set labeled EDM → STA, in Figure 5, implies that the calibration was made at Edmonton and the adaptive procedure was applied at Stanford; vice-versa for STA→EDM; similarly for URB→STA and STA→URB in Figure 6, and GSB-HAM AND HAM-GSB for Figure 7. At solar maximum δR_{15m} and δR_{3h} are comparable indicating that the residual error can be effectively reduced after 3 hours in daytime. Note that the implied local time difference in the STA→URB δR_{3h} curve is approximately 6 hours, but the residual error is comparable to δR_{15m} which is a 3-hour local time variation, thus, inferring that the correction is for large scale spatial, not temporal effects. This result does not apply at solar minimum however, as Figure 7 shows. The curve for residual error when the adaptive procedure is applied one hour after calibration (δR_{1h}) is included here to emphasize that at solar minimum a measurement can be used for about one hour. Unlike the solar maximum period, the residual error continues to increase to the degree that δR_{3h} is comparable to δR_m, implying it may be preferable to revert to a median correction after one hour if a new calibration is not available. This is consistent with results presented in the section on time-variability.

The diagram of Figure 8 shows the relative location of station pairs as difference in degrees latitude from South to North and from West to East

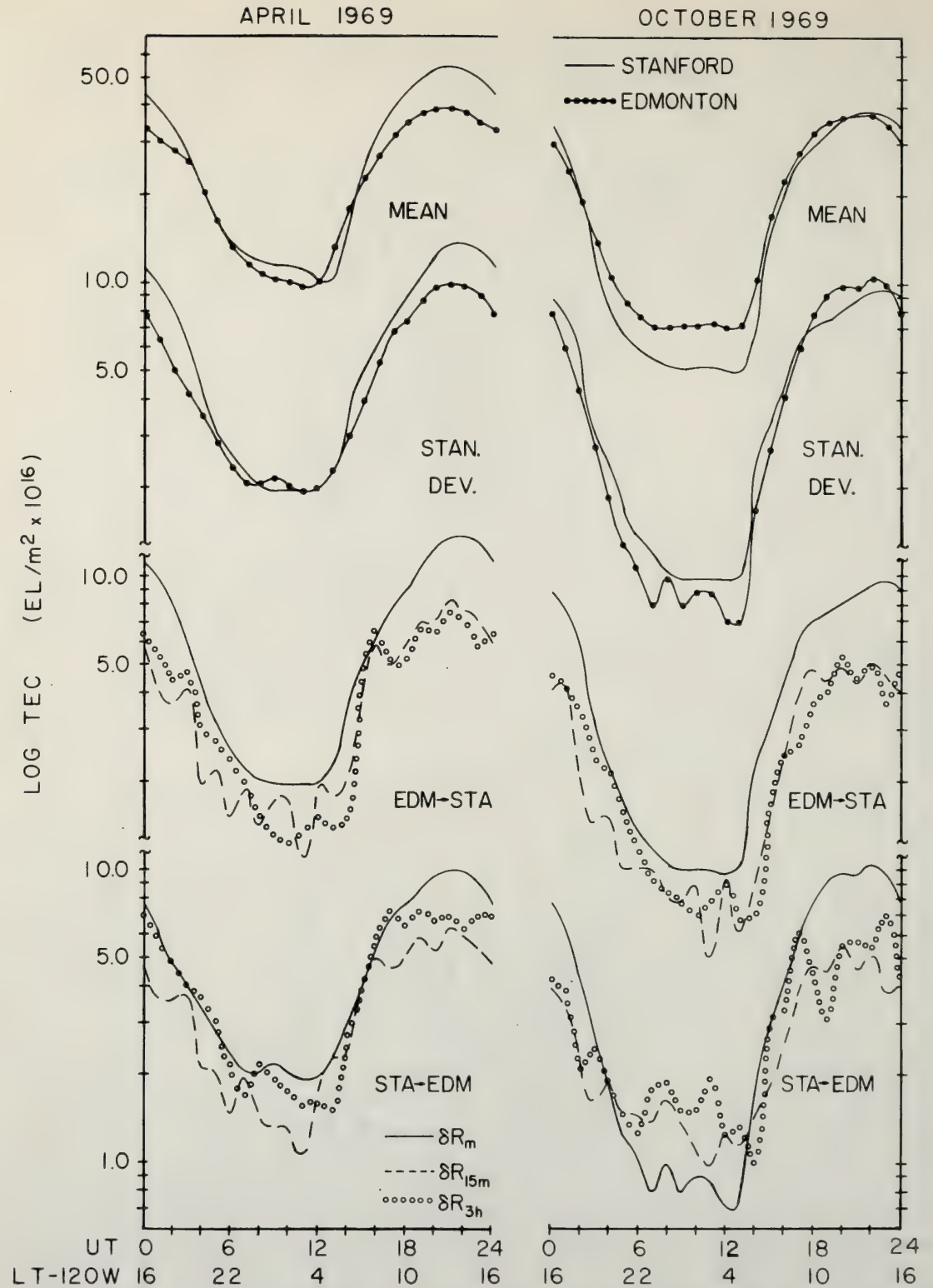


Figure 5. The mean and standard deviations are compared to determine the relative percentage variability for the Stanford-Edmonton station pair in the upper two sets of curves. The lower two sets compare the results of applying the adaptive procedure at each station using 15-minute and 3-hour calibration intervals in April and October 1969.

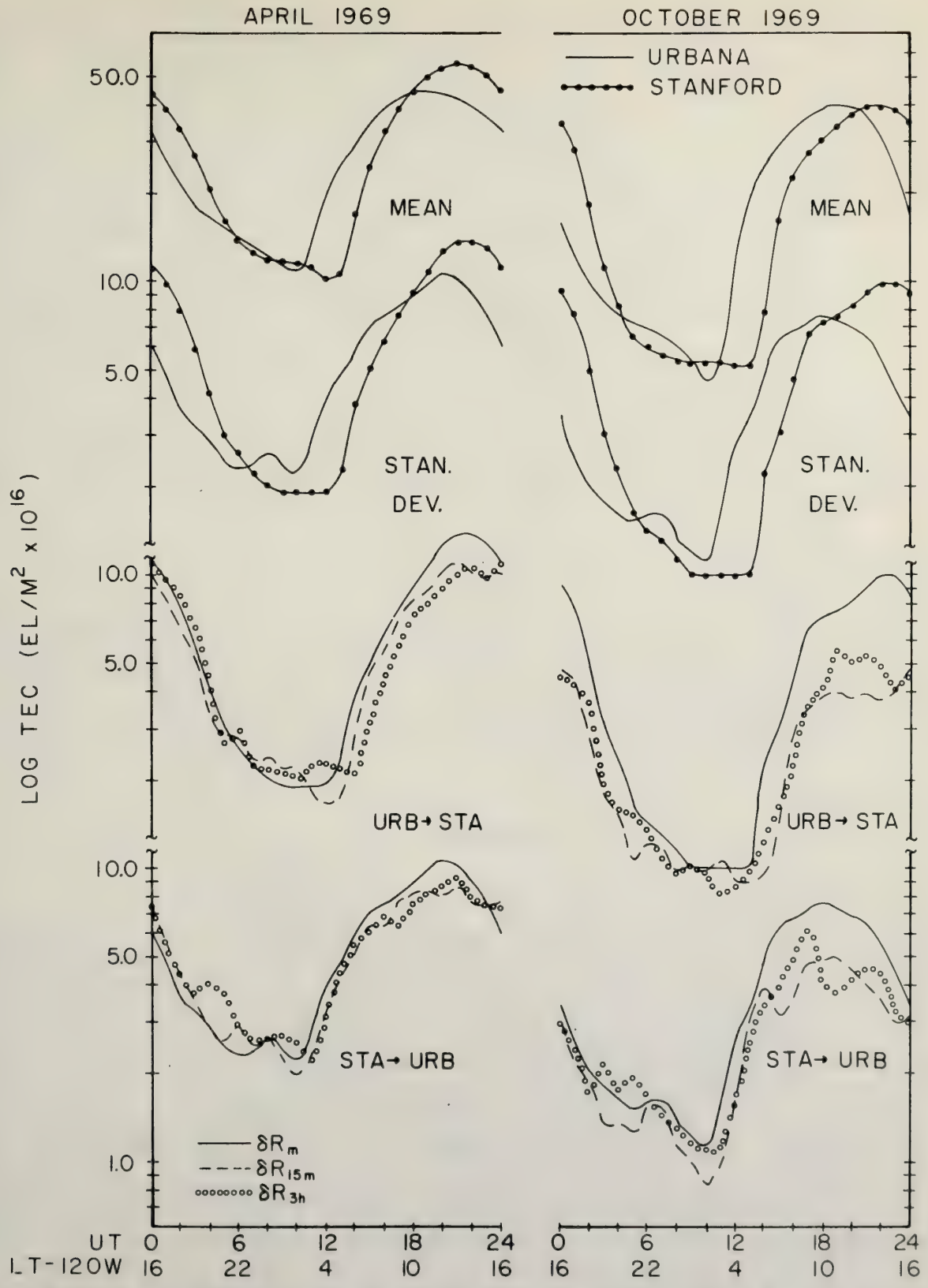


Figure 6. Same as Figure 5, but comparing the Stanford-Urbana station pair.

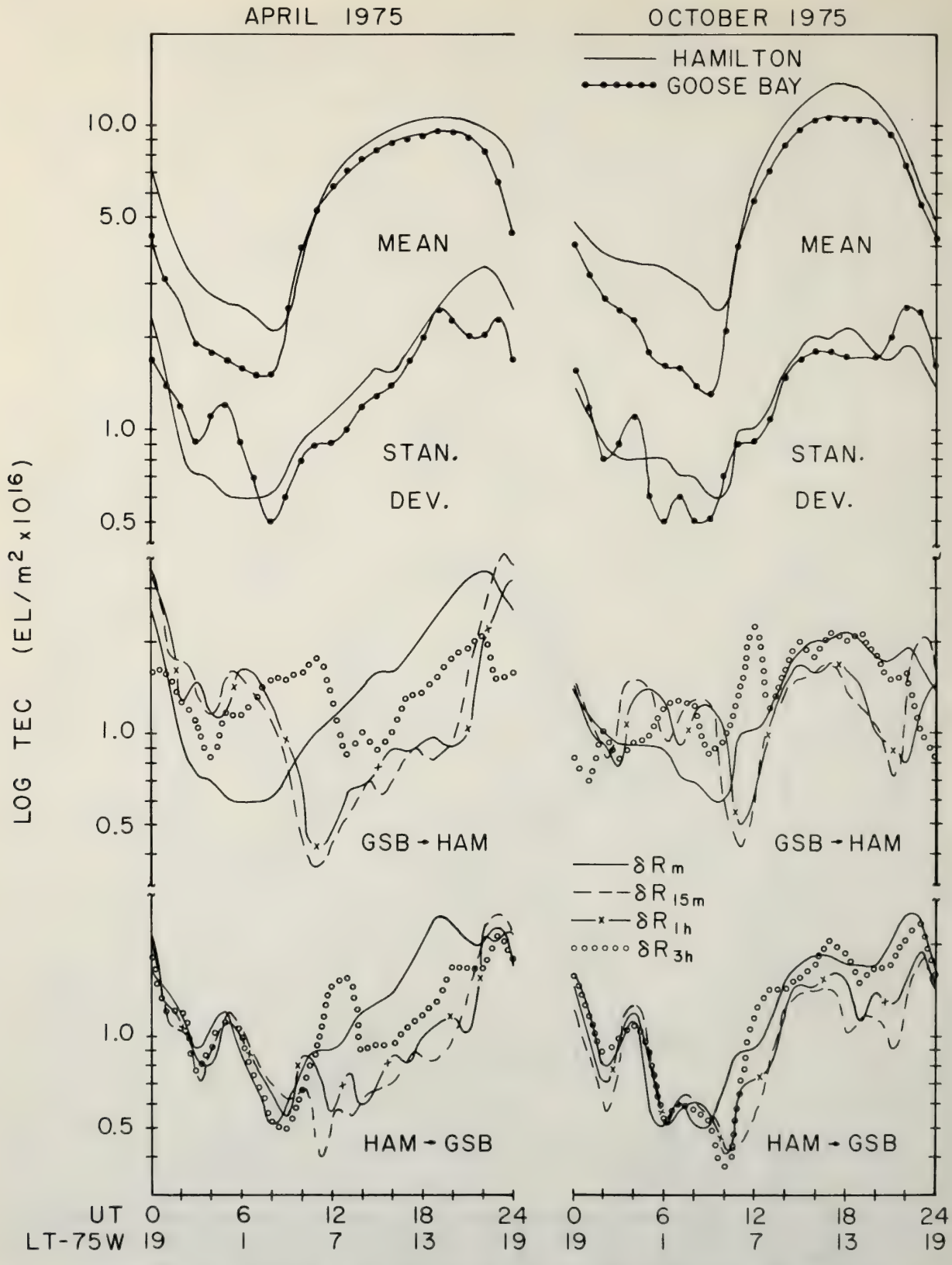


Figure 7. Same as Figure 5 but comparing the Goose Bay-Hamilton station pair for April and October 1975, also including the results for a 1-hour calibration interval.

longitude. The STA-EDM and KSF-HAM pairs have the greatest latitude separation while STA-URB has the greatest separation in longitude. The effects of these latitude and longitude differences are illustrated in Figure 9 where the stations Stanford, Urbana and Hamilton are used to represent target locations. The curves demonstrate the dependence of residual error on the ray path used for calibration in the adaptive procedure: the δR_m are again the standard deviation at the station for the month of October; the δR_{15m}, δR_{1h}, δR_{3h} are for the time interval of applied update as in previous figures, but here they represent calibration along the ray path to the target. Each of the two curves labelled δR, with a station name, is the 15-minute applied update with calibration from that station, both from different directions.

In Figure 9a, δR_{URB} and δR_{EDM} give results comparable to δR_{3h}, with δR_{EDM} producing better night time and δR_{URB} better day time results. A 50 percent reduction is possible in day time in both cases.

With only a few degrees variation in latitude but a large longitudinal variation, the time-space equivalence in longitude becomes apparent. In Figure 9b, δR_{STA}, which includes a 2 hour 45 min local time difference, is comparable to δR_{3h}, while δR_{HAM}, with a 1 hour local time difference, compares with the δR_{1h}. The differences in results using different ray paths represent spatially localized uncorrelated variations as shown by Davies et al, 1978.

In the case of equal degree-longitude separation but unequal degree-latitude separation as in Figure 9c, δR_{GSB} and δR_{KSF} are comparable to δR_{3h} as is δR_{EDM} of Figure 9a. The calibrations are from opposing directions with δR_{GSB} producing better day time results than δR_{KSF} which includes a greater latitude distance. The nighttime results are poor in either case, with δR_{GSB} the worse, perhaps because of its proximity to the auroral zone.

A lower limit to the residual error is represented by δR_{15m} for each target location in Figures 9a, b and c. This is set by the amplitude of daily variations with a period less than 30 minutes

5. DISCUSSION

In the procedure examined here a simple scaling method was used to reduce the residual error in ionospheric correction that exists because of daily variability about the mean behavior. This scheme is most successful when the scaling factor is determined, and the update applied, along the same ray path. This is generally not the case, however, and problems arise when the variability differs considerably across a system coverage area. A greater spatial incoherence is found in latitudinal separation as opposed to longitudinal separation as has been shown previously in correlation studies using TEC and foF2 (Klobuchar and Johanson, 1977; C. Rush, 1976). At solar maximum the large scale, long period variations predominate, while at solar minimum it is the smaller scale, shorter term variations that contribute to the greater percentage of the daily variability. These are less likely to be correlated over large distances. The possible causes of consistent differences in variability need to be understood in order to develop a weighting scheme to compensate for them. In determining the space-time interval for this adaptive correction scheme the important factors are: location of the terminators, frequency and scale size of large amplitude

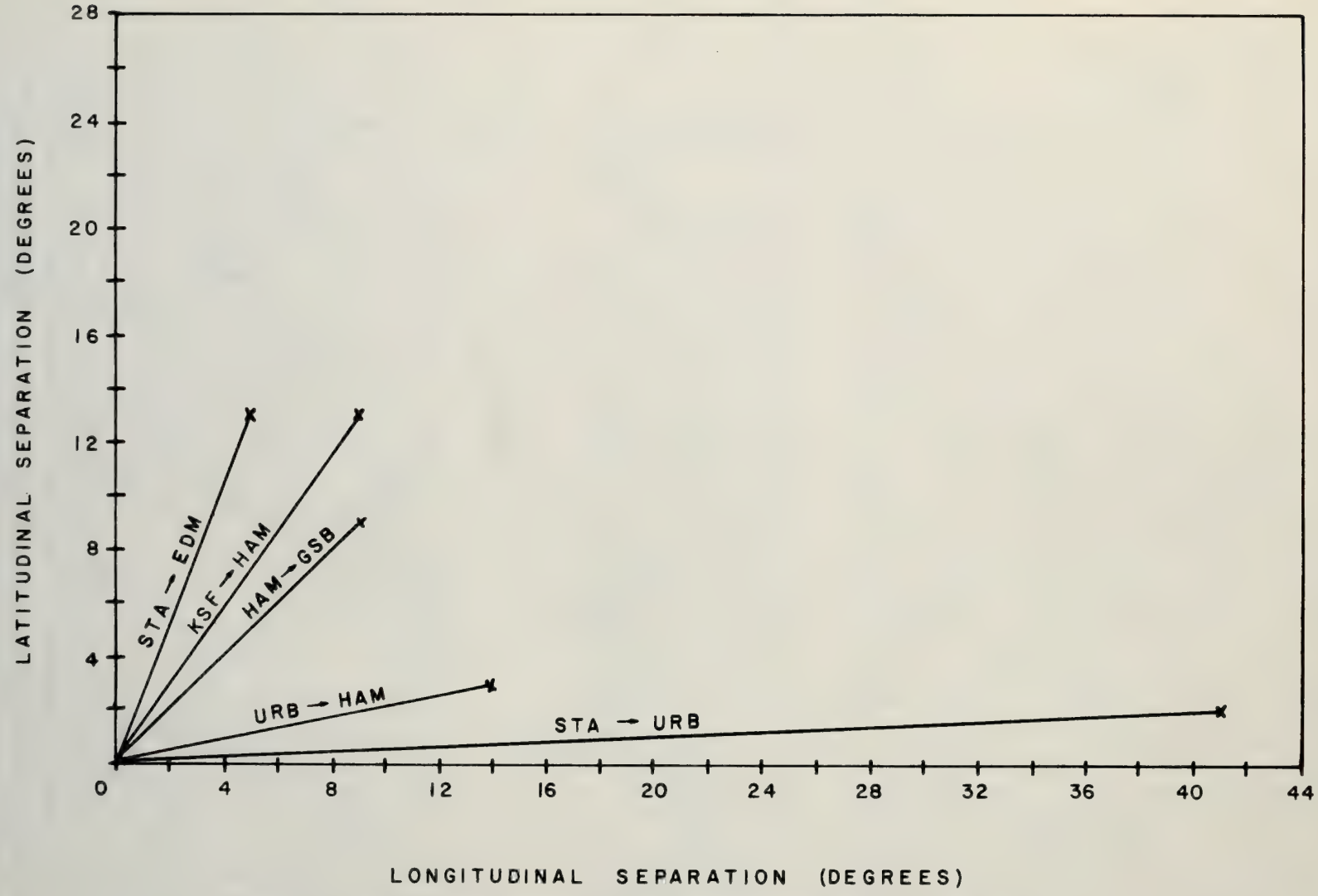


Figure 8. The relative location of the station-pairs as difference in degrees latitude from South to North and longitude from West to East.

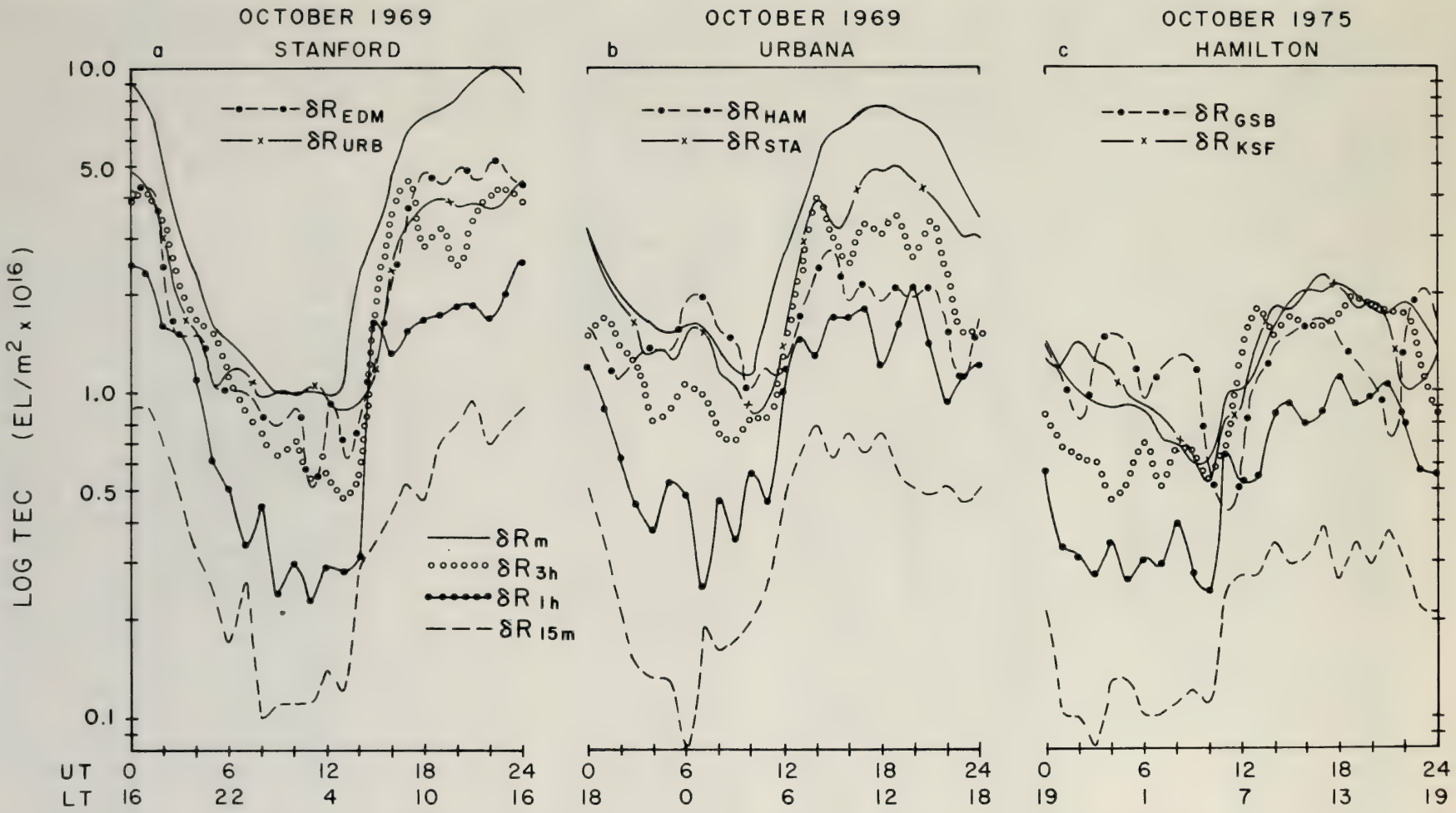


Figure 9. Comparing the residual error that results using the adaptive procedure on a target with calibration along three different ray paths: to the target itself and two points in differing directions. For 9a, target is at Stanford with calibration at Edmonton and Urbana; 9b target is Urbana, calibration at Hamilton and Stanford; 9c target at Hamilton, calibration at Goose Bay and Kennedy Space Flight Center.

fluctuations and their rate of change in time and space define the boundary of the calibration intervals with precedence given to the terminators. During sunrise, sunset and magnetic disturbances these intervals may be as short as 15-30 minutes of time and space equivalence. At solar minimum a significant reduction may require a one hour interval while at solar maximum a comparable percentage reduction in residual error is possible using a 3-hour interval.

6. ACKNOWLEDGEMENTS

The authors would like to thank Mr. J. Klobuchar of AFGL for the use of the TEC data and for many helpful suggestions.

This work was supported by Air Force Contract F 19628-76-C-0255.

7. REFERENCES

Allen, R.S. (1977): Considerations Relative to Adapting TRANSIT Observations to Predicting Radar Range Corrections. AFGL-TR-77-0004, DDC# ADA 038238.

Davies, K., W. Degenhardt, G.K. Hartmann, R. Leitinger (1978): Electron Content Measurements over the U.S. Joint Radio Beacon Program NOAA/MPAE/GRAZ, Station Report ATS-6 ^{o} W.

Donatelli, D.E. and R.S. Allen (1978): Temporal Variability of Ionospheric Refraction Correction. Effect of the Ionosphere on Space and Terrestial Systems, Editor J.M. Goodman, January 1978: 490-496.

DuLong, D.D. (1977): Reduction of the Uncertainty of Radar Range Correction. AFGL-TR-77-0125, DDC# ADA 046166.

Klobuchar, J.A. and J.M. Johanson (1977): Correlation Distance of Mean Daytime Electron Content. AFGL-TR-77-0185, DDC# ADA 048117.

Leitinger, R., R.S. Allen, D.E. Donatelli, G.K. Hartmann (1978): Adaptive Mapping of Ionospheric Features. Effect of the Ionosphere on Space and Terrestrial Systems, Editor J.M. Goodman, January 1978: 530-537.

Rush, C.M. (1976): An Ionospheric Observation Network for use in Short-Term Propagation Predictions. Telecommunication Journal, 43 (VIII): 544-549.

Titheridge, J.E. (1972): Determination of Ionospheric Electron Content from the Faraday Rotation of Geostationary Satellite Signals. Planetary and Space Science, 20: 353-369.

PREDICTION OF TRANSIONOSPHERIC SIGNAL TIME DELAYS AT WIDELY SEPARATE LOCATIONS USING CORRELATIVE TECHNIQUES

HAIM SOICHER
COMMUNICATIONS SYSTEMS CENTER
US ARMY COMMUNICATIONS R&D COMMAND
FORT MONMOUTH, NJ 07703

Excess time delays of transionospheric radio signals introduce ranging errors in satellite-navigation and radar systems, which are directly proportional to the total electron content (TEC) along the propagation path. Correlations of TEC values (based on linear regression analysis) at Fort Monmouth, NJ (40.18°N, 74.06°W) and Richmond, FL (25.60°N, 80.40°W), as well as at Richmond, FL and Anchorage, AK (61.04°N, 149.75°W) were previously determined. The correlation analysis was performed at monthly and daily intervals for winter periods during the quiet phase of the solar cycle.

Average regression lines obtained by the analysis were then used to try to determine TEC at Richmond, assuming the availability of TEC in Fort Monmouth, and at Anchorage, assuming the availability of TEC at Richmond. In most cases, the "predicted" TEC was within one standard deviation of actual observed data for the former case, and within two standard deviations for the latter case.

INTRODUCTION

The effects of the ionization along the satellite-to-ground signal-ray-path on the propagation time of such a signal was previously discussed. (Soicher, 1977). The excess time delay introduced by the ionization is directly proportional to the total electron content (TEC) along the signal path. In view of the stringent accuracy requirement of modern satellite-navigation and radar systems, the excess time delay must be compensated for either by real time measurements or through empirical modeling techniques. The former requires that the user possess dual frequency reception capabilities, while the latter (which utilizes a single frequency) depends on how well TEC and its temporal and spatial variability can be modeled and/or predicted. For improved accuracy, the forecasting techniques should be supported by periodic updating of data (preferably in real time) at specified locations. The question arises as to the extent of the geographic area, surrounding a station

having real-time TEC-determination capabilities, within which TEC values could be interpolated with acceptable accuracy. In other words, could TEC be determined at Location A if a real-time measurement was taken at a different location, B, and what would be the geographic constraints of A and B?

To this end, a specific investigation designed to determine the correlation (based on linear regression analysis) between TEC values at Fort Monmouth, NJ (40.18°N, 74.06°W) and at Richmond, Florida (25.60°N, 80.40°W) (Soicher, 1978a), and between TEC values at Richmond, Florida and Anchorage, Alaska (61.04°N, 149.75°W) (Soicher, 1979) was undertaken. Beacon transmissions from geostationary satellites were used to determine the TEC at the stations by means of the Faraday rotation technique.

The subionospheric points for the Richmond-Fort Monmouth stations (i.e., the geographic locations where the ray paths to the ATS-6 (located at 94°W) intersect a "mean" altitude of 420 Km) were 36.5°N, 76.6°W, and 23.6°N, 81.6°W, respectively. Thus, the "representative" TEC for the two stations was separated by $\sim 13^{\circ}$ in latitude and by $\sim 5^{\circ}$ in longitude corresponding to a 20-minute difference in local time). The subionospheric points for the Richmond-Anchorage monitoring the SMSI (located at 105°W), and the ATS-6 (located at 140°W), respectively, were 22.5°N, 82.7°W and 54.3°N, 147.3°W respectively. The "representative" TEC was separated by $\sim 31.8^{\circ}$ in latitude and $\sim 63.8^{\circ}$ in longitude (corresponding to a 4 hr 15 minute difference in local time).

The correlation data indicated that TEC, or equivalently, ionospheric signal time-delays, are highly correlatable at the two sets of locations. When daily data sets were compared at approximately the same local time the correlation coefficients were, in general, $\gtrsim 0.9$ for the Fort Monmouth-Richmond locales, and $\gtrsim 0.7$ for the Richmond-Anchorage locales.

The next phase of the investigation was the effort to determine whether it is possible to accurately predict TEC at one locale from TEC at the other, using average regression lines obtained for the corresponding data sets. The technique employed was as follows: Average monthly regression lines were computed. In one case, average slopes as well a average intercepts of the regression lines at monthly intervals were computed. In a second case, average slopes were computed while the intercepts were forced to pass through a common data point for the two sets at a specific predawn time for each day. Having determined the average regression lines, TEC at one locale was calculated for a given TEC at the corresponding other locale. The deviation (D_i) of the calculated TEC from its actual value at a particular time is then determined. This deviation, D_i is then divided by σ_i , the monthly TEC standard deviation value at the same time. The average absolute value of this ratio, i.e., $\left|\frac{D}{\sigma}\right|$ was then computed for each day.

The results for the Fort Monmouth-Richmond data sets (i.e., predicting TEC at Richmond from TEC at Fort Monmouth) using average slopes and intercepts of the monthly regression lines are shown in Fig. 1. The results for the Richmond-Anchorage data sets (i.e., predicting TEC at

Anchorage from TEC at Richmond for the same local time) using average slopes and intercepts of the monthly regression lines are shown in Fig.2.

DISCUSSION

As Fig. 1 indicates, the daily average of the ratios $\frac{|D|}{\sigma} = \frac{1}{N}\sum_{i=1}^{N}\frac{|D_i|}{\sigma_i}$, $N \leq 96$ for Richmond is, for the most part, smaller than one, i.e., on the average, the deviation of the computed Richmond TEC values from Fort Monmouth TEC values is, in general, within the monthly standard deviation of the Richmond data. The diurnal behavior of the ratio is such that the ratio is higher during the night (when σ is small) than during the day. Some of the high values of this ratio are attributable to ionospheric effects during magnetically active period, e.g., on September 15 and 18, 1974, large enhancement of TEC were observed in response to magnetic sudden commencements; on March 11, the K_p index ranged from 4^o to 7^-. The results of the figure also indicate that the ratio appears larger during the equinoctial period (September, March) than during the winter and spring months. This is observed despite the fact that the standard deviation during the equinoctial months was considerably higher than during the other months. The ratio, in general, does not change substantially (as compared to the above case) when the average regression slopes are forced to pass through the actual data points at the two locations at specific time. (Soicher 1978b).

As Fig. 2 indicates, the daily average of the ratios $|D|/\sigma$ for Anchorage is for the most part, smaller than two, i.e., on the average, the deviation of the computed Anchorage TEC values from the corresponding Richmond TEC values, is, in general, within two standard deviations of the Anchorage data. As in the Fort Monmouth-Richmond data sets the diurnal behavior of the ratio is such that the ratio is higher during the night than during the day. In addition, the figure indicates that the ratio is larger on the average in October than in the following two months. This occurs despite the fact that the correlation coefficient was, on the average, higher in October, declined in November and declined further in December (due to changes in TEC diurnal shapes associated with changing separation in sunrise and sunset times at the two locales) (Soicher 1979). As with the Fort-Monmouth case, the ratio here does not change substantially (as compared to the above case) when the average regression lines are forced to pass through the actual data points at the two locations.

Since total signal time-delays are largest during the day and thus, introduce significant errors in navigation and radar systems, it is appropriate to examine the ratio $|D|/\sigma$ during the time when TEC is diurnally larger, i.e., between 1500 and 2100 UT (Richmond, Fort Monmouth times and corresponding Anchorage time).

For the Fort Monmouth case the data indicates that the ratio $|D|/\sigma$ obtained by average regression lines computed by the two techniques for the day period, are substantially lower than the corresponding ratios for the full diurnal periods. The fact that the bulk of the data indicates that the ratio falls below 1 is encouraging since both correlation

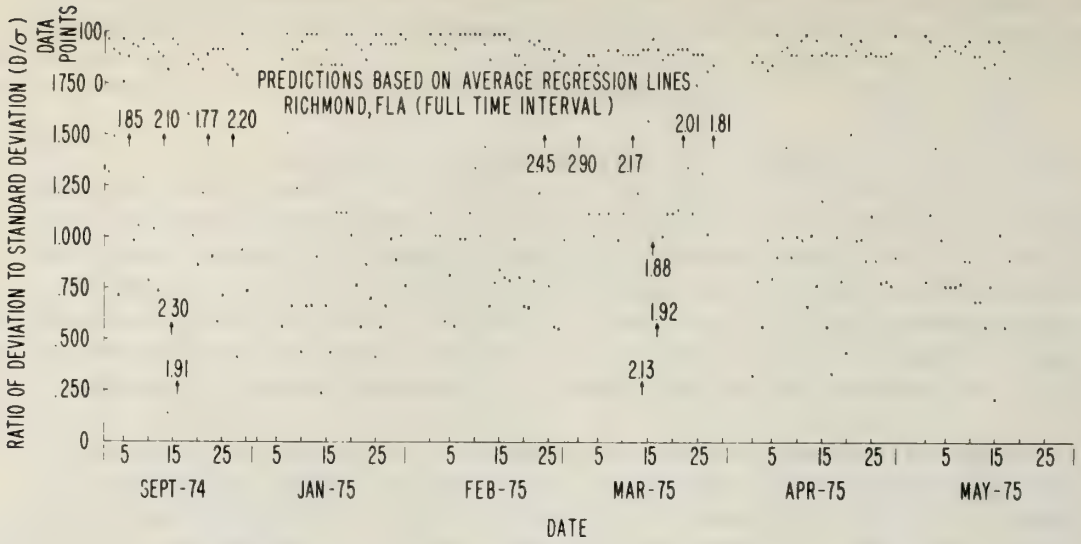


FIG. 1. THE VARIATION OF THE RATIO $|D|/\sigma$ FOR RICHMOND, FLORIDA, FOR THE TIME PERIOD SEPTEMBER 1974, AND JANUARY 1975-MAY 1975, CALCULATED FOR FULL DIURNAL PERIODS BY AVERAGE REGRESSION LINES OBTAINED BY FORT MONMOUTH, NJ-RICHMOND, FLORIDA DATA SETS. ($|D| \equiv$ DIURNAL AVERAGE OF THE DEVIATIONS OF THE COMPUTED TEC VALUES FROM OBSERVED ONES; $\sigma \equiv$ MONTHLY STANDARD DEVIATION OF THE RICHMOND DATA). THE ARROWS AND THE CORRESPONDING NUMERICAL VALUES ARE FOR THOSE VALUES OF THE RATIO WHICH EXCEED THE SCALE OF THE FIGURE. ALSO INDICATED IN THE UPPER PORTION OF THE FIGURE ARE THE NUMBER OF TEC DATA PAIRS AT 15-MINUTE INTERVALS USED IN THE ANALYSIS.

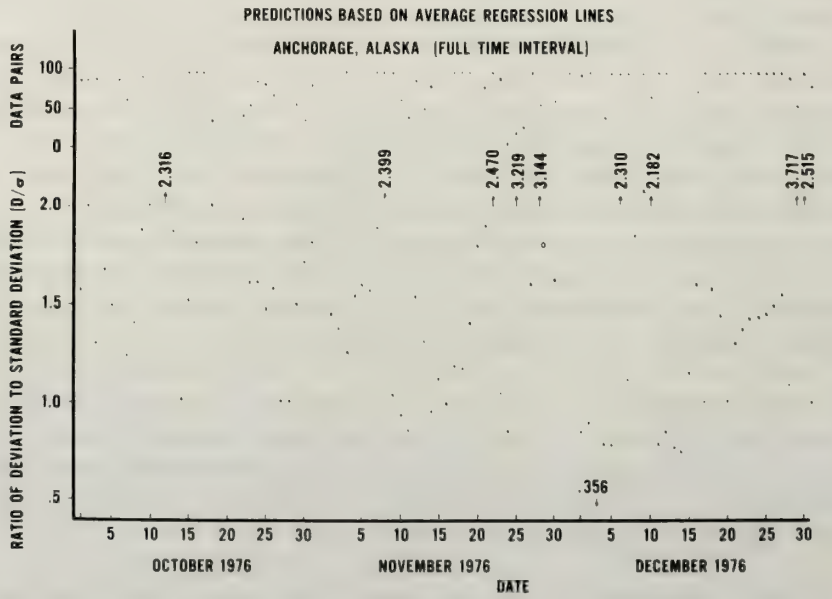


FIG. 2. THE VARIATION OF THE RATIO $|D|/\sigma$ FOR ANCHORAGE, ALASKA, FOR THE TIME PERIOD OCTOBER 1976-DECEMBER 1976, CALCULATED FOR FULL DIURNAL PERIODS BY AVERAGE REGRESSION LINES OBTAINED BY RICHMOND, FLORIDA-ANCHORAGE, ALASKA DATA SETS.

methods yield "predicted" TEC values that fall within the monthly standard deviation of the data during the time period when the presence of TEC poses the source of largest error.

For the Richmond-Anchorage case a similar statement cannot be made. On the average, the ratio is not markedly different for the full time interval and for the time interval for maximum values of TEC.

CONCLUSIONS

The high correlation of signal time delay variation at two sets of locale separations, one widely separated by latitude, and the other widely separated by latitude and longitude (and hence by local time), prompted the examination as to whether time-delay data at one locale may be "predicted" if continuous corresponding data were available at the other locale. The correlation is high, in part, due to the 24 hour periodicity of the data. It is precisely this periodicity, however, that gives the "prediction" technique employed here its accuracy. The variation of the time delay is the highly correlatable quantity, and thus, the whole data set - if available, should be used in the prediction scheme.

Monthly average regression lines were used in the analysis. The slopes of the average monthly regression lines were within $\pm 20\%$ from their average for the whole period. The intercepts of the monthly lines of regression were considerably more scattered.

For the two locales separated mainly in latitude (Fort Monmouth-Richmond) the deviation of the "predicted" data from the observed data was for the most part, within one standard deviation of the monthly data set. For the daytime period, when the error introduced by the time-delay is greatest, the ratio $|D|/\sigma$ was even lower. When the average regression line for the entire period considered was calculated (i.e., the average of six monthly averages), the bulk of the "predicted" data was still within one standard deviation of the monthly data set. The ratio is often high during time periods characterized by ionospheric disturbances.

For the two locales widely separated by latitude and longitude (Richmond-Anchorage), the deviation of the "predicted" data from the observed data was, for the most part, within two standard deviations of the monthly data set. When the average regression line for the entire period was used, the bulk of the "predicted" data was still within the two standard deviations of the monthly data set.

Since the monthly value of the standard deviation is $\sim 25\%$ of the absolute value of the time delay, the method of prediction outlined here appears to have the capability of correcting the time delay due to the ionosphere to within $\sim 25\%$ for stations separated in latitude, and $\sim 50\%$ for stations widely separated in latitude and longitude.

REFERENCES

Soicher, H. (1977): Ionospheric and plasmaspheric effects in satellite navigation systems. IEEE Trans. Antennas & Propagation, Vol AP-25, No. 5.

Soicher, H. (1978a): Spatial correlation of transionospheric signal-time-delay. IEEE Trans. Antennas & Propagation, Vol AP-26, No. 2.

Soicher, H. (1978b): Prediction of transionospheric signal time-delays using correlative techniques. Proceedings of the Symposium of the COSPAR Satellite Beacon Group on "Beacon Satellite Measurements of Plasmaspheric and Ionospheric Properties", 22-25 May 1978, Florence, Italy.

Soicher, H. (1979): Correlation of satellite signal time-delays at widely separated locations. IEEE Trans. Antennas & Propagation, Vol AP-27, No. 6.

2. HF IONOSPHERE-REFLECTED PROPAGATION PREDICTIONS

HF COMMUNICATIONS PREDICTIONS 1978 (AN ECONOMICAL UP-TO-DATE COMPUTER CODE, AMBCOM)

V.E. Hatfield
SRI International, 333 Ravenswood Avenue
Menlo Park, California 94025 USA

An existing economical HF prediction code has been extended to incorporate the following features: sporadic E modes and losses on reflection and transmission, a model of the auroral ionosphere, and a model of auroral absorption that varies with magnetic activity. In addition to the homing procedure that was available in the original program for point-to-point communications, a surveillance capability (for OTH radar or other purposes) has been included. New output options include contour maps of signal-to-noise ratio plus raypath and wavefront plots.

1. INTRODUCTION

Recent program development at SRI International on the computer code AMBCOM has incorporated the latest information on ionospheric features that affect communications at HF into a predictions code that is both easy and economical to use. It was also considered important to provide output that would give useful information to communication planners and data analysts. The computer code (called AMBCOM for ambient ionospheric communication predictions at HF) has been tested extensively in connection with a recent contract for the U.S. Army Ballistic Missile Defense Advanced Technology Center.

2. GENERAL DESCRIPTION OF THE CODE

The AMBCOM computer code uses as its basis the NUCOM code developed by SRI during the 1960s under sponsorship of the Defense Nuclear Agency. NUCOM predicts the performance of HF communication systems under normal and nuclear conditions (Nielson, 1967).* AMBCOM employs the raytracing and communication system concepts of NUCOM, but it is intended primarily for ambient ionospheric communication predictions. The ionosphere is modeled with three parabolic layers. Ionospheric tilts and critical frequency gradients are taken into account by specifying the parabolic parameters at as many as 41 points along the path. These parameters are derived initially from the

*References are listed at the end of this paper.

Institute For Telecommunication Science* (ITS) coefficients and are then modified to incorporate the new features described in Sections 3, 4, and 5. If desired, actual measurements may be used in place of the parameters. The propagation analysis consists of a rapid, semianalytic, two-dimensional ray-tracing routine based on the Kift-Fooks method. Both topside and bottomside reflections from the normal ionospheric layers are allowed.

As originally developed, NUCOM computed propagation losses with a homing feature for evaluation of specific point-to-point communication circuits; binary error rates and signal-to-noise ratio were calculated. The new program now also has the option of evaluating the area surveillance capability of over-the-horizon (OTH) radar; signal-to-noise ratio is calculated and jammers may be introduced. Other features include homing from an elevated moving target and plotting of ray paths and wave fronts.

Several improvements have been made in the ionospheric model and loss mechanisms. These improvements include: a new model of the electron density profile in the high-latitude ionosphere; a model for computing auroral abosrption; and models for estimating reflection and obscuration losses for the E_s layer; both topside and bottomside reflections from the E_s layer are allowed. These improvements are especially useful for the evaluation of elevated, or ducted, modes of propagation across the auroral zone.

A number of different mechanisms that can result in elevated modes are simulated in AMBCOM. The chordal modes produced by ionospheric tilts, or electron density gradients, and the ducted modes that are successively reflected between the bottom of the F layer and the top of the normal E layer were both incorporated in the original NUCOM code. The improved code predicts, in addition, those ducted modes that are successively reflected between the F layer and the E_s layer.

In the next sections the new features are described in detail: The high-latitude ionosphere model, the auroral absorption model, and the sporadic E model. Finally, a few examples of the output capabilities are shown.

3. HIGH-LATITUDE IONOSPHERE MODEL

The new code represents auroral oval phenomena as functions of K_p, corrected geomagnetic latitude and time, and solar zenith angle. The oval expands and moves south with increased K_p, and the midlatitude trough is a feature on the nightside.

The auroral morphology is implemented by incorporating two auroral features that affect propagation significantly: A K_p-dependent F-layer critical frequency and a K_p-dependent auroral E critical frequency. The F-layer model is taken directly from the Rome Air Development Center (RADC) polar model developed by Elkins and co-workers (1973). The auroral E-layer

*Now called the National Oceanic and Atmospheric Administration

model was developed from Chatanika, Alaska incoherent scatter radar measurements of electron density profiles in the auroral ionosphere; this feature was added by SRI to the RADC-POLAR model (Vondrak et al., 1978), under contract to RADC. The auroral E is combined with the solar-controlled E to define a single "equivalent" layer at the E-layer height.* This method seems appropriate since the auroral E, unlike sporadic E, has a substantial semi-thickness (Vondrak et al., 1978).

No attempt was made to reproduce the unusual profile shapes found in the auroral zone (Vondrak et al., 1978) because of the requirement that profiles must be represented by parabolas to permit use of the analytic raytracing procedure. However, because the ionosphere generator for AMBCOM automatically generates an F_1 filler layer that is defined by E and F_2 parameters the resulting profiles are often reasonable approximations to auroral profiles. Modification of this filler algorithm to better represent a variety of shapes, would be a welcome improvement in the code.

For demonstration purposes, a sample path over the pole was chosen. Transmission from latitude 47°N, longitude 69°W to 50°N, 90°E was simulated using first the ITS ionosphere and then the AMBCOM auroral ionosphere with K_p values of 2.6 and 5.0. The case run was September 1200 UT, and a sunspot number of 100. Figure 1 shows the critical frequencies of the E- and F-layer along the path for each of the 3 cases. Figure 2 compares the mode structure for the ITS model with those modes that occur when the auroral model is used (two values of K_p are shown). Modes are shown schematically and are terminated after 5 hops; termination prior to 5 hops implies either penetration or a distance limit. Introduction of the auroral model causes the following unconventional modes to occur: (1) Topside reflections occur for a K_p of 2.6 at 10 MHz for a take-off angle ($\triangle$) of 25°, and at 12 MHz for $\triangle = 15°$; (2) A perigee ray occurs for a K_p of 2.6 at 14 MHz with $\triangle = 15°$. Figure 3 shows ray paths generated by the program for the three cases at a frequency of 12 MHz and increments in elevation angle of 5°.

Unconventional modes are often initiated by negative ionization gradients along the path; however, this occurs at a given frequency only over a limited range of elevation angles. For example, an elevated mode appears in Figure 3 for $\triangle = 15°$ for the case of $K_p = 2.6$ (center of plot); the corresponding gradient can be seen in Figure 1. It can also be seen from Figure 1 that the gradient is larger for $K_p = 5$, but no elevated mode occurred for the five take-off angles considered. A search on take-off angles would probably reveal a similar elevated mode in this case.

4. THE AURORAL ABSORPTION MODEL

The auroral absorption model is a function of K_p, season, solar activity, and corrected geomagnetic (CGM) latitude, longitude and time. It was developed from riometer measurements at approximately 30 MHz. Absorption values

*The E- and F-layer heights in the RADC-Polar model are sometimes inconsistent with heights generated by the ITS coefficients; for simplicity, the ITS heights were retained in the AMBCOM model.

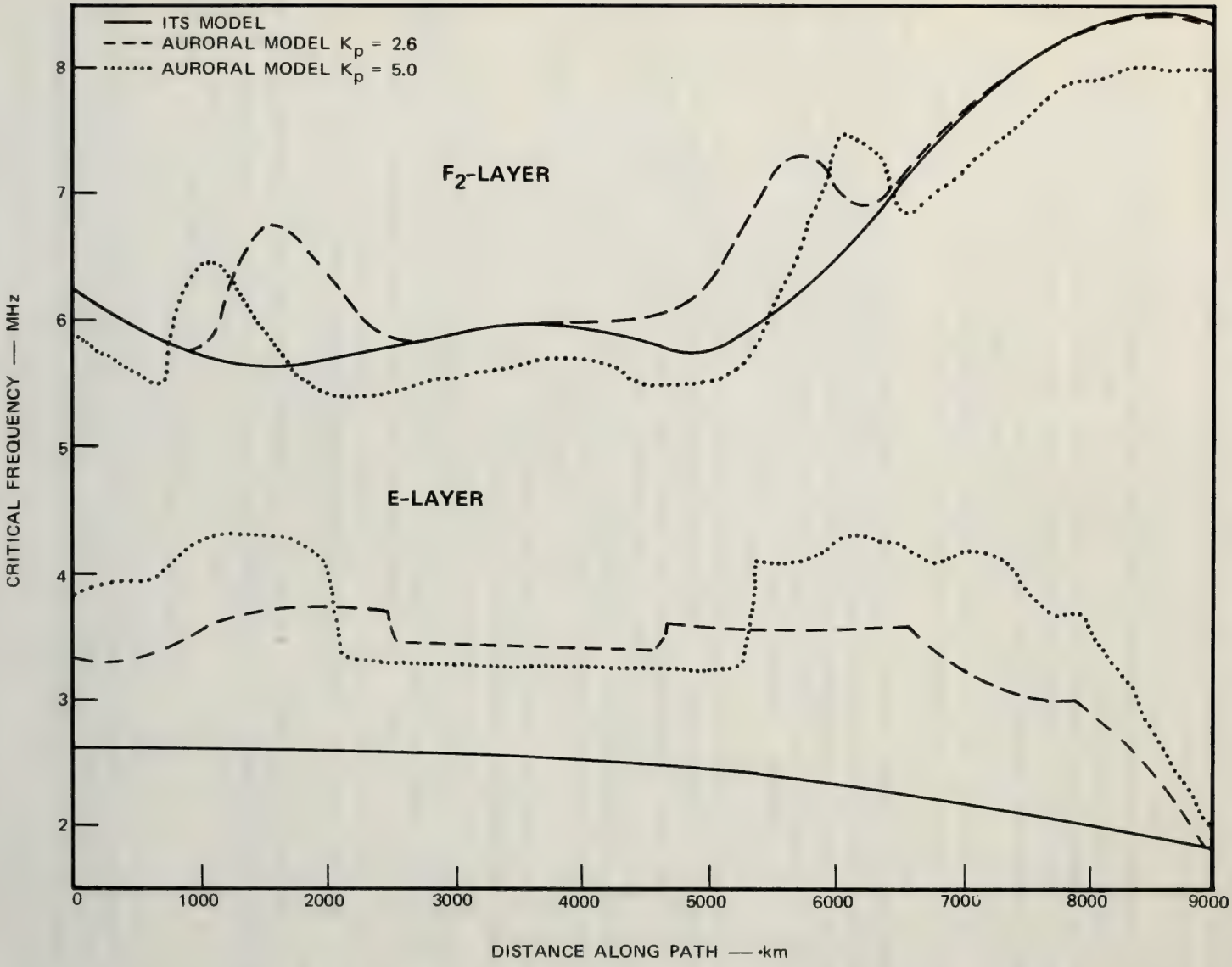
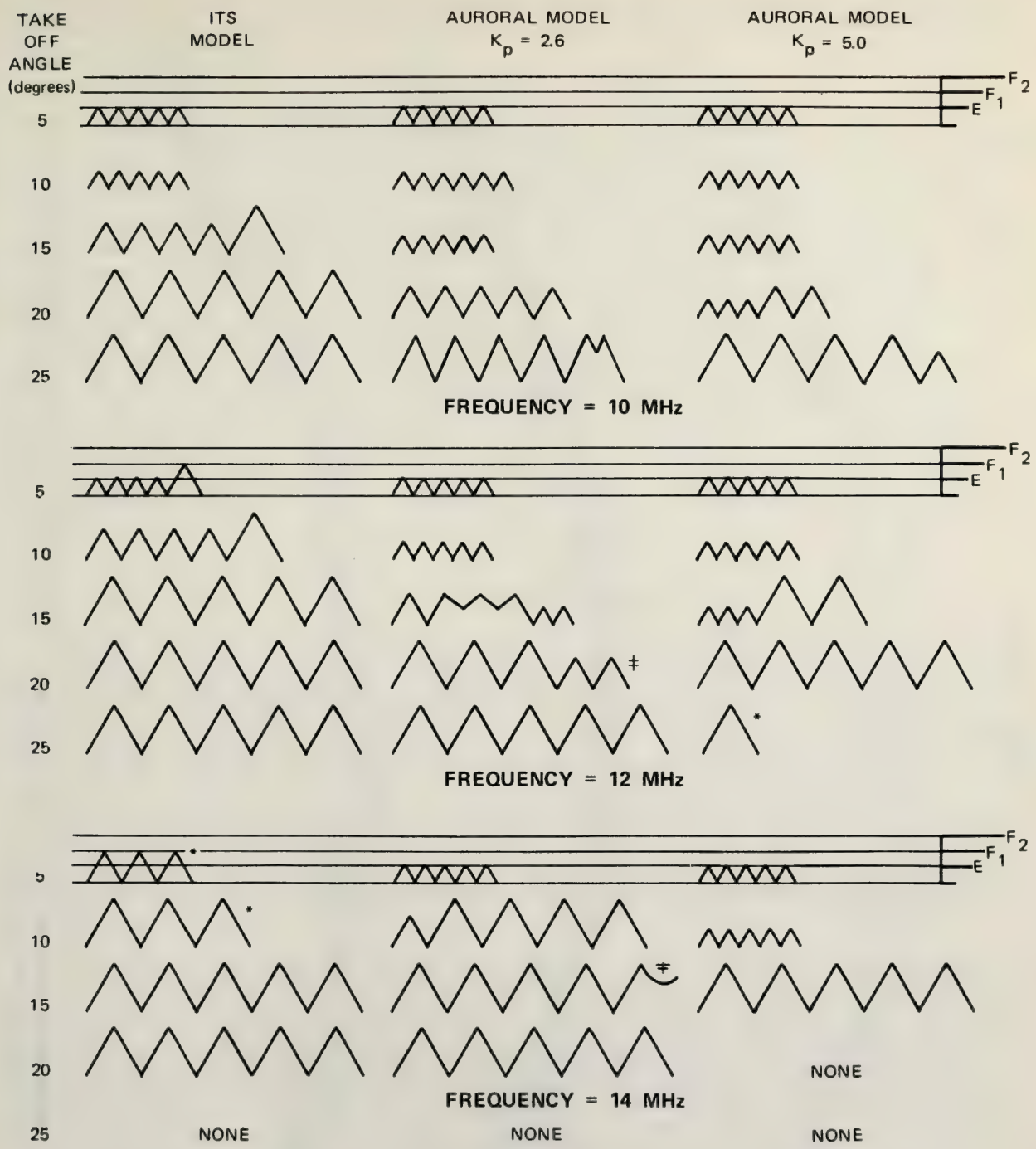


FIGURE 1 COMPARISON OF E- AND F-LAYER CRITICAL FREQUENCIES WITHOUT THE AURORAL IONOSPHERE (ITS MODEL) AND WITH THE AURORAL IONOSPHERE FOR K_p = 2.6 AND K_p = 5.0



NOTE: Calculations limited to five hops.

*Penetrated . ‡Distance cut off.

∓Perigee rays.

FIGURE 2 COMPARISON OF STYLIZED RAYPATHS AT VARIOUS TAKE-OFF ANGLES FOR ITS MODEL, AND AURORAL MODEL K_p = 2.6, AND K_p = 5.0

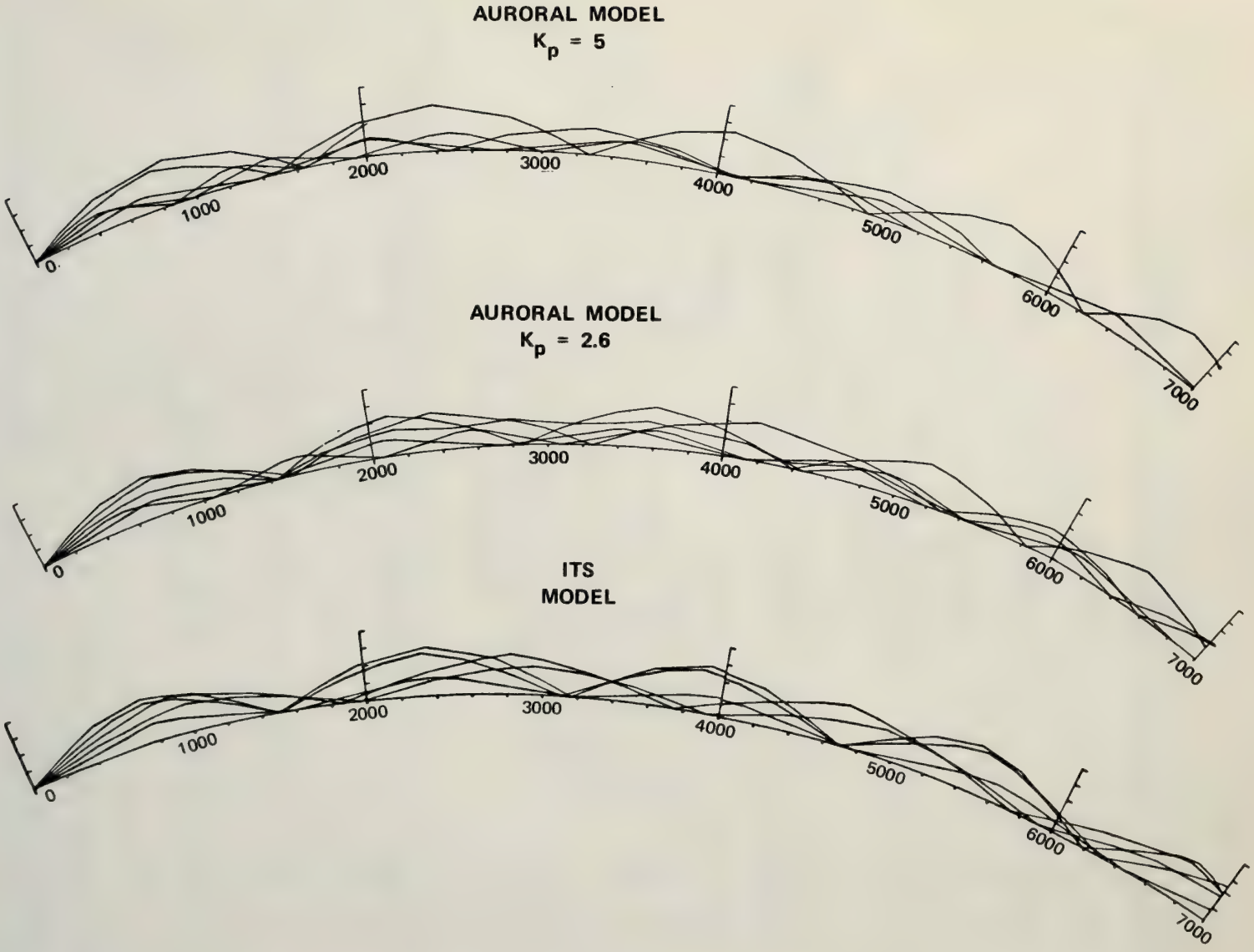


FIGURE 3 COMPARISON OF RAYPATHS FOR AURORAL MODELS, AND ITS MODEL AT A FREQUENCY AT 12 MHz FOR A DISTANCE OF 7000 km

given by the basic model of one-way-vertical absorption at 30 MHz are converted appropriately for the angle of passage through the D-region and the operating frequency.

The model in AMBCOM was developed on the RADC contract mentioned in Section 3 (Vondrak et al., 1978) and uses a method proposed by Foppiano (1975) as its basis (i.e., the formulation of the dependence on CGM coordinates, season, and solar activity). The K_p dependence was derived from averaged curves published by Hargreaves (1966). The final model was then calibrated with riometer data from College, Alaska, which had been used in developing the Basler (1963) model. Figures 4 and 5 show contours of one-way-vertical absorption at 30 MHz over the auroral zone for K_p = 2.6 and 1, respectively. The scale is CGM latitude versus CGM time; the longitude is constant. The figures show the expected variation in absorption as a function of time of day. Absorption effects of two kinds of particle precipitation (Hartz and Brice, 1967) can be seen in Figure 4. Around midnight there is a slight peak in absorption which is attributed to the "splash" type of precipitation; and, in the morning hours, there is a larger peak attributed to "drizzle" precipitation. All parameters in Figure 5 are the same as in Figure 4, except that K_p = 1.

5. SPORADIC E MODEL

Differences of opinion on how sporadic E (E_s) should be handled in a propagation prediction program have prompted us to provide several options. The user may choose the one that is most suitable for his problem. The options include rays that penetrate the E_s layer as well as ones that reflect. The specific options require that: (1) frequencies such that the equivalent vertical frequencies are less than f_oE_s always reflect, (2) equivalent vertical frequencies less than the blanketing frequency f_bE_s reflect, while greater frequencies penetrate, (3) all frequencies penetrate, and (4) no E_s is to be considered. Both reflection and obscuration losses are included in the first three options, with a choice of two methods of computing the losses.

Values of f_oE_s are obtained from median, upper, and lower decile values of the ITS coefficients. The median value of f_oE_s is normally used, but the user may override this with any percentage he desires. We consider E_s as being present if f_oE_s is greater than f_oE. This rule is based on the fact that the method used in compiling statistics for the coefficients substituted f_oE when no E_s was present.

The blanketing frequency, f_bE_s (in MHz) is calculated as a function of latitude (lat) and night or day from the following equation:

$$f_bE_s = f_bE_s^H = (.5 + .2\ (SSN/100))\ f_oE_s \qquad |lat| \geq 70$$

$$= f_bE_s^L = .65\ f_oE_s \quad \text{night} \qquad |lat| \leq 50$$

$$= .9\ f_oE_s \quad \text{day}$$

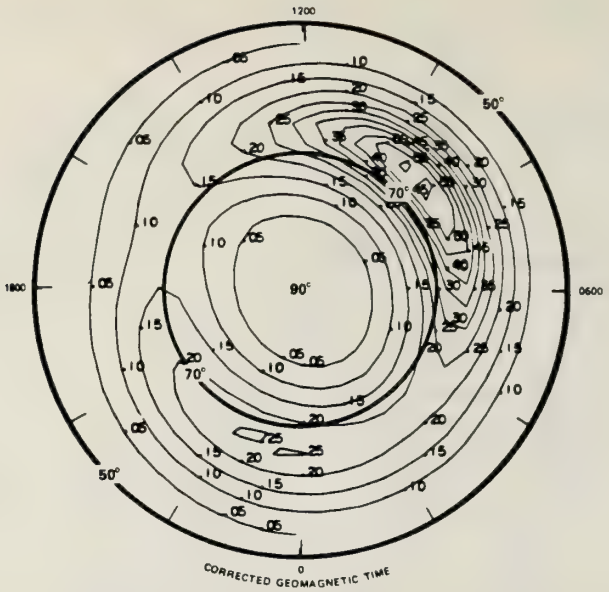


FIGURE 4 CONTOURS OF MEDIAN ONE-WAY VERTICAL ABSORPTION IN dB AT 30 MHz ON A PLOT OF CORRECTED GEOMAGNETIC LATITUDE vs. CORRECTED GEOMAGNETIC TIME, USING THE SRI ABSORPTION MODEL. Corrected geomagnetic longitude, 260°; sunspot number, 120; month, 12; K_p = 2.6.

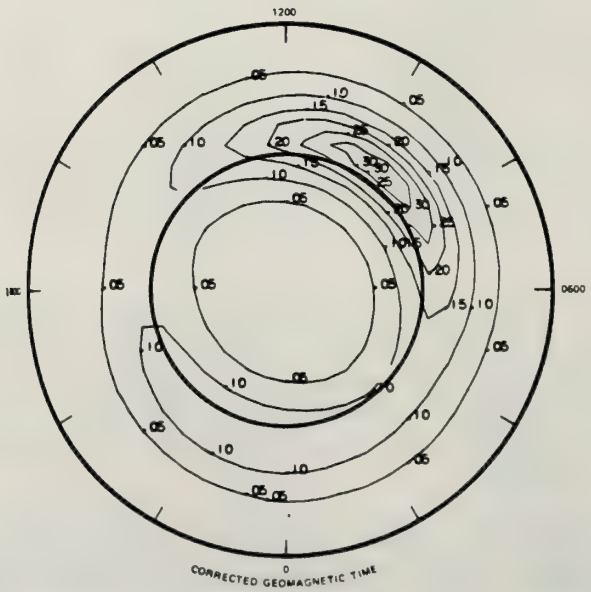


FIGURE 5 CONTOURS OF MEDIAN ONE-WAY VERTICAL ABSORPTION IN dB AT 30 MHz ON A CORRECTED GEOMAGNETIC LATITUDE-CORRECTED GEOMAGNETIC TIME GRID, USING A LOW K_p (K_p = 1). Corrected geomagnetic longitude, 260°; sunspot number, 120; SRI absorption model.

$$f_bE_s = f_bE_s^H(|\text{lat}|-50)/20 + f_bE_s^L(70-|\text{lat}|)/20 \qquad 50 < |\text{lat}| < 70$$

where the superscripts H and L refer to high and low latitude respectively. These estimates of f_bE_s are based on the data presented by Kolawole (1978).

The E_s model in AMBCOM is a thin layer (1 km semithickness) at a height of 110 km. This height is slightly below the height of the normal E-layer peak electron density (assumed to be 115 km in AMBCOM). This type of E_s is typical of temperate and low latitudes (Leighton et al., 1962). In this current implementation of the E_s option, upgoing rays that reflect from the E_s layer ignore the normal E-layer ionization below 110 km, while rays that penetrate are refracted in the normal E layer. Rays reflecting from the topside are first reflected from the normal E if possible. On penetration of the normal E the rays may still be reflected from the E_s layer. In this case the reflection is performed without refraction in the E layer.

Two methods are available for the loss calculations. One model is based on results published recently by Sinno and co-workers (1967); the other is that published in the early 1960s by Phillips (1963). In the absence of more extensive experiments measuring both reflection and obscuration loss, it is difficult to determine which method is the more accurate. Figure 6 compares the two methods for a sample case. The variable on the horizontal axis is $p = f \cos i/f_oE_s$; f is the operating frequency and i is the incidence angle. Reflection normally occurs for $p \leq 1$. Curves are labeled with the ratio of blanketing frequency f_bE_s/f_oE_s.

6. EXAMPLES OF OUTPUT CAPABILITIES OF AMBCOM

For communication planning, the new option that provides contour maps of signal-to-noise ratio (SNR) can be extremely useful. Contour maps of best SNR by frequency, or best SNR for all frequencies, can be generated by the program. Figure 7 shows contours of best SNR for all frequencies for an OHD backscatter site located at 42° latitude, 100°W longitude with the antenna pointing toward the west. Antenna patterns can be specified, but constant gain was assumed in this case. The maps are produced from propagation predictions made along radials extending from the OHD backscatter site at specified azimuthal directions. Figure 8 shows a sample of plots that can be made along each radial. The envelope of the best signal is used in the contour program (e.g., Figure 7). Azimuths are chosen at close enough increments so that significant changes in the ionosphere will not be missed. A capability for including jammer effects is also available. For this option propagation predictions are made at the azimuth of the jammer. The geographic outline map may be automatically generated to the specified scale for any desired location.

The option of raypath plotting is also a new feature. "Homed" rays between two sites or "ray sets" (shown in Figure 3) may be plotted. An option of plotting wave fronts at specified time delays is also available.

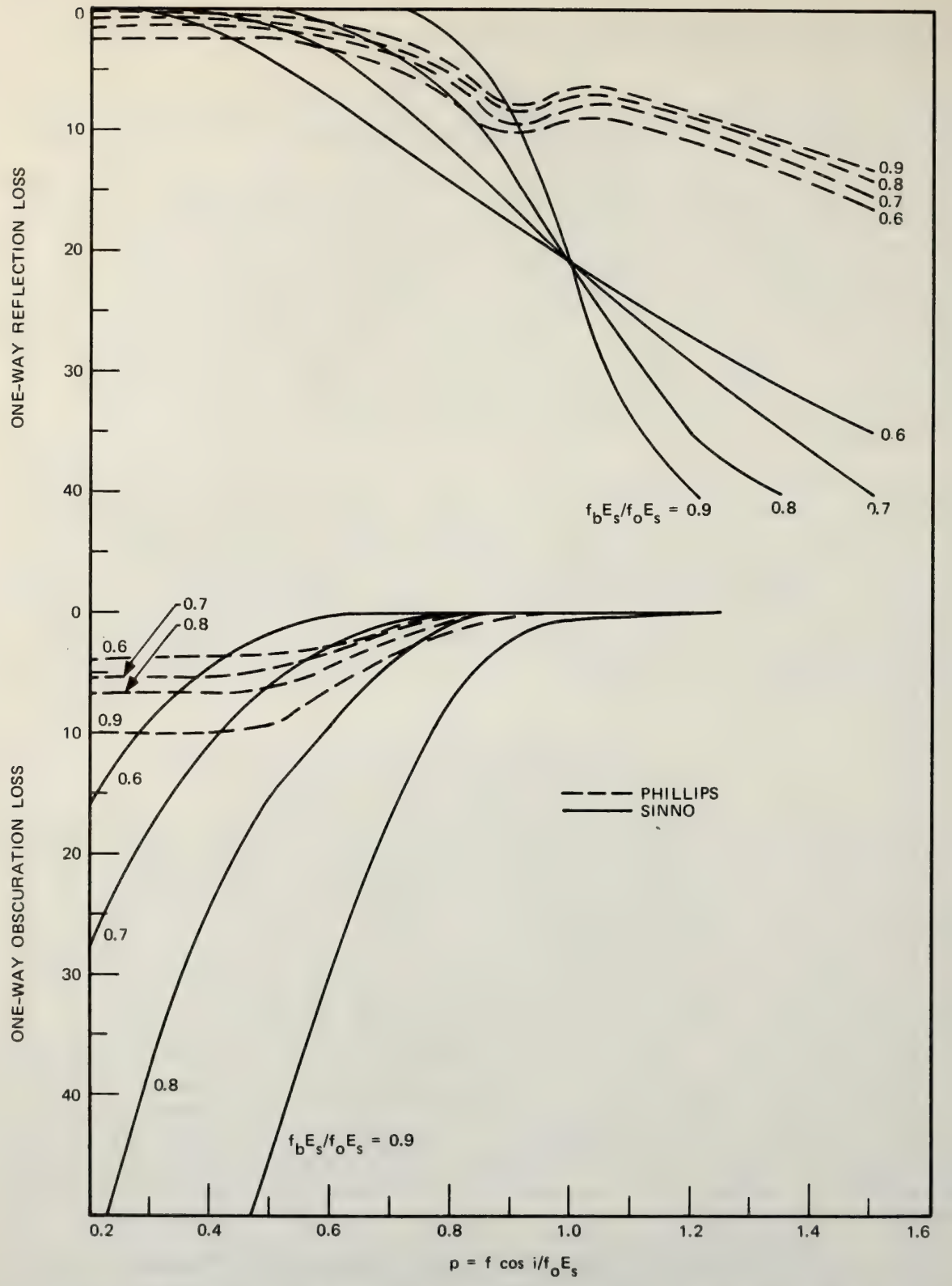


FIGURE 6 COMPARISON OF PHILLIPS AND SINNO E_s LOSS METHODS FOR SEVERAL BLANKETING FREQUENCY RATIOS (0.6, 0.7, 0.8, 0.9). Operating frequency 6 MHz; f_oE_s distribution; lower, median, and upper deciles = 3, 4, 7.

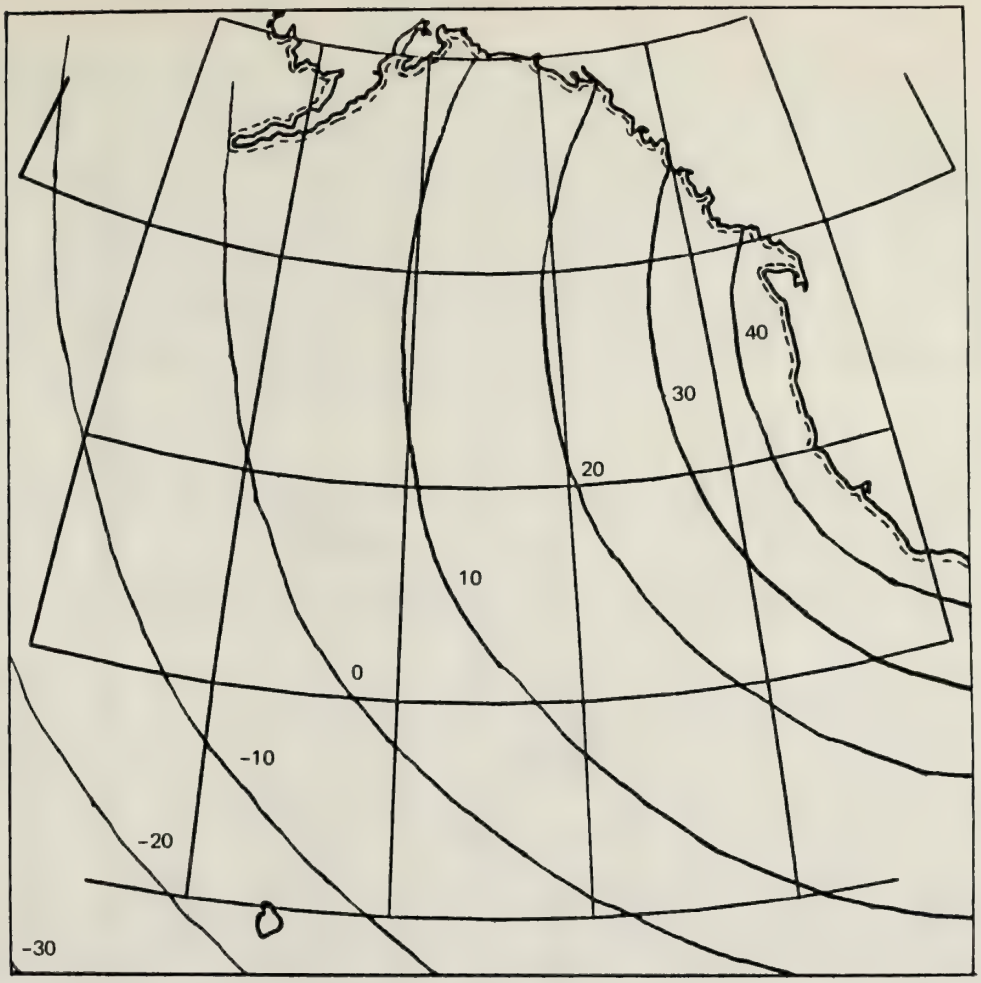


FIGURE 7 SIGNAL-TO-NOISE RATIOS FOR COMBINED FREQUENCIES (8, 12, 16 MHz). January; 20 UT; 75 SSN; site at 42° N, 110° W.

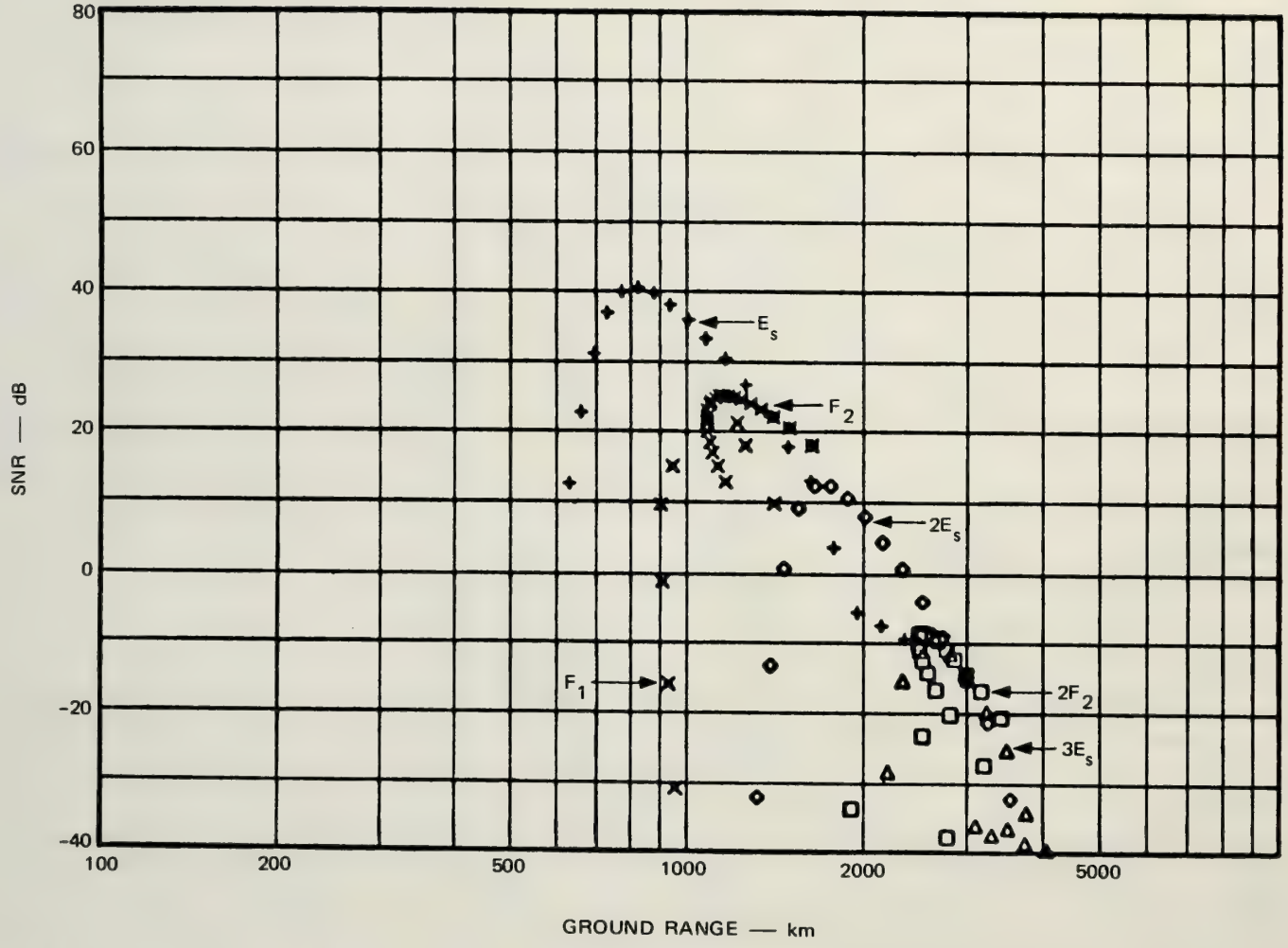


FIGURE 8 SIGNAL-TO-NOISE RATIO AS A FUNCTION OF GROUND DISTANCE FOR JUNE SSN 75; 16 UT; 12.0 MHz

7. COMPARISON OF AMBCOM PREDICTIONS WITH MEASUREMENTS

The ionosphere generator in AMBCOM consists of several parts, some of which have previously been verified against substantial quantities of data. For midlatitude paths the predictions remain the same except for optional E_s. Consequently, the comparisons presented in Nielson et al., 1967 remain applicable. Good agreement was reported between observed and predicted median MUFs and signal strengths for several midlatitude paths. Moreover, oblique ionograms synthesized by raytracing showed remarkably good agreement with observed mode structure. Similarly the models of the auroral F region and the polar cap ionosphere are essentially those developed by RADC from a large data base. The two sporadic E models were developed elsewhere and verified as well as possible by their originators.

Only the models of the auroral E-layer and the K_p-dependent auroral absorption are new. The former was developed by SRI from a limited set of data during low solar activity (all of the 24-hour Chatanika data available at the time). The absorption model was based on riometer data also from a limited set. Clearly further research is needed to verify and extend these models to a wider range of conditions.

As important as independent verification of all of the models themselves is verification of HF signal strength measurements on several long trans-auroral paths and on several paths where E_s effects may be assessed.

8. CONCLUDING REMARKS

Most of the available raytracing programs are either very time-consuming, as in numerical integration procedures, or too simplified to permit the introduction of large gradients such as those that occur in auroral and equatorial regions. The value of the AMBCOM program lies in its ability to incorporate tilts and topside reflections while still remaining economically attractive.

A comparison of running times and storage requirements for four specific programs used at SRI International is shown in Table I. The reader is cautioned that many variables affect the comparisons and the numbers shown are estimates based on a number of specific cases. The cost is normalized to that of AMBCOM.

Table I

Comparative Running Times and Storage Requirements Estimated From a Limited Set of Computer Runs on a CDC 6400 Computer

Program	Normalized Cost (Running Time)	Maximum Central Memory Required	Description
RADARC	.6	140000_8	SRIs Version of HMUFES (Barghausen 1969)
AMBCOM	1.0	146000_8	
CRT 1.43	10.0	137000_8	A 2-D incremental raytrace
AFCRL 3-D	100.0	106700_8	A 3-D incremental raytrace. March 1975 version

9. ADDENDUM

Recently (after the present paper had been submitted) a brief study was undertaken internally by SRI to further verify the RADC model, particularly within the polar cap. Predicted E and F-region critical frequencies were compared with VI ionosonde data from Fort Churchill (an auroral station) and Resolute Bay (a polar cap station). Good agreement was found for Fort Churchill and for f_oF_2 at Resolute Bay. However, significant differences were noted for f_oE inside the polar cap. On the basis of these results a modification was made in AMBCOM that results in significant changes within the polar cap. (These changes have not been made in Figures 1 and 2 of this paper.)

REFERENCES

Barghausen, A. L., J. W. Finney, L. L. Proctor, L. D. Schults (1969): Predicting long-term operational parameters of high-frequency sky-wave telecommunication systems. ERL 110-ITS, ESSA, Department of Commerce, Boulder, Colorado.

Basler, R. (1963): Radio wave absorption in the auroral ionosphere. J. Geophys. Res., 68:4665.

Elkins, T. and C. Rush (1973): A statistical predictive model of the polar ionosphere. In an Empirical Model of the Polar Ionosphere, AFCRL-TR-73-0331, Air Force Cambridge Research Laboratories, L. G. Hanscom Field, Bedford, MA.

Foppiano, A. (1975): A new method for predicting the auroral absorption of HF sky waves. CCIR, IWP 6/1, Docs. 3 and 10.

Hargreaves, J. (1966): On the variation of auroral absorption with geomagnetic activity. Planet. Space Sci., 14:991.

Hartz, T. R. and N. M. Brice (1967): The general pattern of auroral particle precipitation. Planet. Space Sci., 15:301.

Kolawole, L. B. (1978): The transparency characteristics of E_S types. Radio Sci., 13:159.

Leighton, H. I., A. H. Shapley, and E. K. Smith (1962): The occurrence of sporadic E during the IGY. In Ionospheric Sporadic E, Pergamon Press, London, 166-177.

Nielson, D. L., J. B. Lomax, and H. A. Turner (1967): The prediction of nuclear effects on HF communications. DASA 2035, Final Report, Contract No. DA-49-XZ-436, Stanford Research Institute, Menlo Park, CA.

Phillips, M. L. (1963): Auxiliary procedures used in theoretical evaluation of HF backscatter observations and other communications problems. External Technical Memorandum No. E14, ITT Electro-Physics Laboratories.

Sinno, K., M. Kan, and Y. Kirukawa (1976): On the reflection and transmission losses for ionospheric radio wave propagation via sporadic E. J. Rad. Res. Labs, Japan, 23:65.

Vondrak, R. R., G. Smith, V. E. Hatfield, R. T. Tsunoda, V. R. Frank, and P. D. Perreault (1977): Chatanika model of the high-latitude ionosphere for application to HF propagation prediction. Final Report, Contract F19628-77-C-0102, SRI International, Menlo Park, CA.

THE STATISTICAL PROPERTIES OF THE DISTURBED HIGH-LATITUDE IONOSPHERE IN RADIO WAVE PROPAGATION COMPUTATIONS

E. M. Kovalevskaya and E. M. Zhulina
Institute of Terrestrial Magnetism, Ionosphere and Radio Wave Propagation
of the Academy of Sciences of the USSR
Moscow Region, USSR

A practical method for taking into account statistical properties of the disturbed high latitude ionosphere in radio wave propagation computations is described. Material is presented as easily readable plots for various ionospheric conditions. This manual makes it possible to determine, apart from the reliable estimates of the boundaries of the examined characteristics, the range of their variations for a month and the variations due to disturbances. Calculations show that in high latitudes the confidence limit of one hop distance can be extended up to 1,000 km, while in middle latitudes these limits do not exceed 200-300 km. The confidence limits of azimuthal deviation may reach 1°.

Practical radio communication and studies of the problems of radio wave propagation often give rise to a need to know the confidence limits of variations in one or another characteristic. Existing practical instructions have usually been calculated for average conditions, and therefore additional calculations are required to find the intervals of variations in these characteristics. The present manual gives information relevant to variations of the hop distance and azimuthal deviations due to the statistical variations in the ionosphere. The material is set out in easily readable plots for the various ionospheric conditions (Figs. 1-4). It is possible to determine, apart from the reliable estimates of the examined characteristics, the range of their variations for a month and the variations due to disturbances. The manual can be used to calculate the radio links through high latitudes since the inhomogeneity and increased disturbance of the ionosphere in such regions result in a broad range of variations of the characteristics. The following input data should be set when using the manual: the height, h_mF2, and half-width, y_mF2, of the maximum of F2; the value of error, μ, or deviation of foF2 from the median due to disturbance; the values of the elevation angle Δ; and the operating-to-critical frequency ratio, f/fo.

The main concepts taken into account when writing the manual are considered below.

It has been shown by studying the statistical variability (SV) of the ionosphere (Zhulina and Kiseleva, 1974), using foF2 as an example, that in

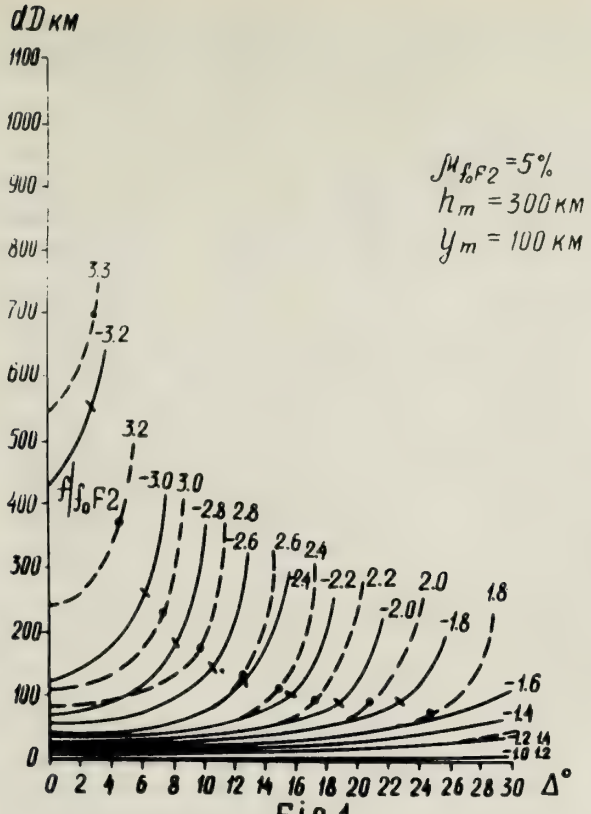


Fig.1

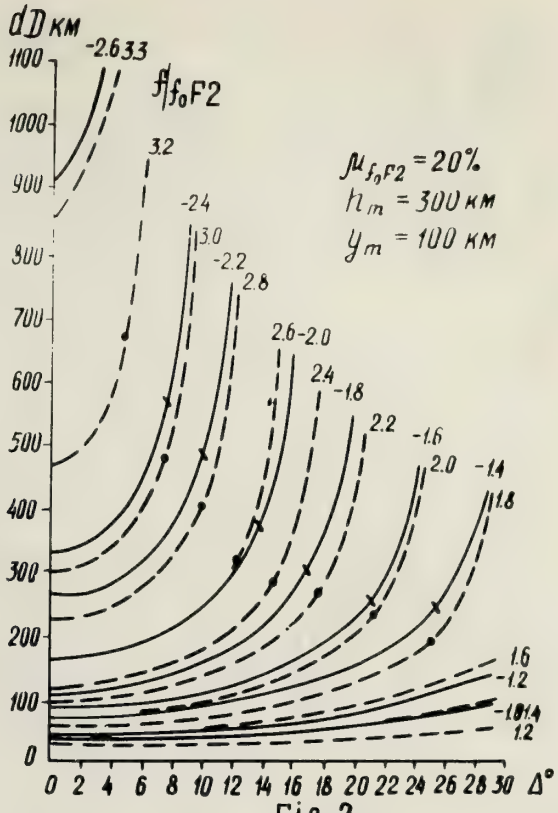


Fig.2

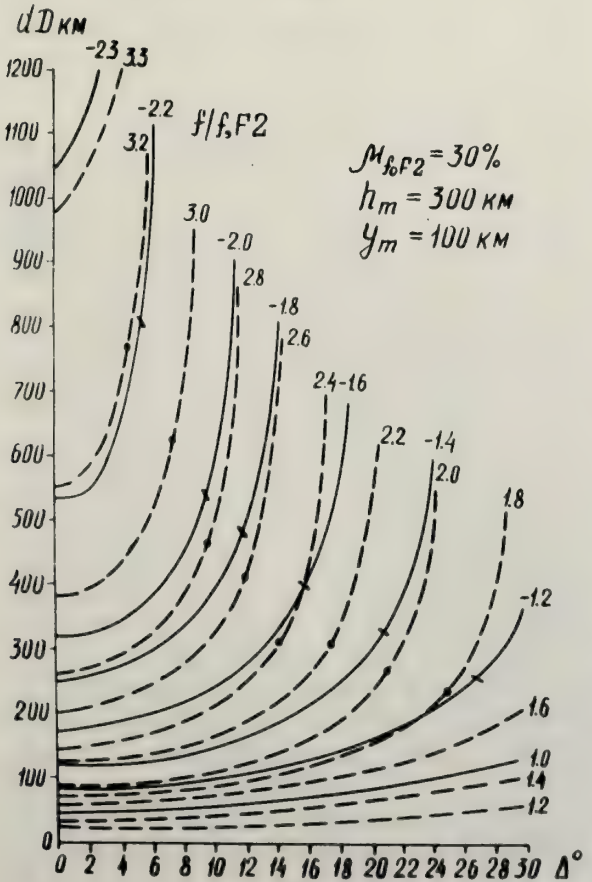


Fig.3

h_m=300км, y_m=100км, $\partial f_0/\partial x$=0.5·10^{-2} МГц/км

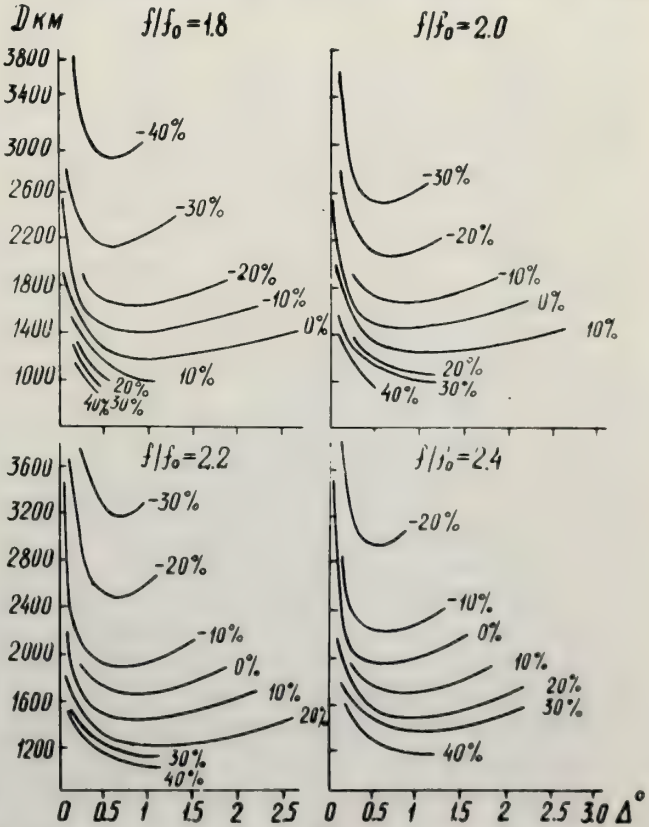


Fig.4

the middle and low latitudes, the normal law of distribution may be used in many cases to describe SV. The normal law of distribution is indicative of the random nature of the distribution of sampled values and their independence. In this case the median foF2 and the mean over the set, which form the basis of the calculations of all the characteristics of radio wave propagation, are representative estimates and can characterize, with sufficient reliability, a mean monthly state of the ionosphere. Although their determination as statistical values contains some error μ (which we shall call the natural error), if the normal law is satisfied, the error μ is of random nature.

The foF2 distribution in high latitudes is more complex (Zhulina and Kiseleva, 1974). Apart from the random component, the distribution comprises, as a rule, a systematic component, which is due to the dependence of the values on common nature. The latter is the source of the disturbance, namely the corpuscular penetrations resulting in ionospheric disturbances which last for many hours or even days. In middle latitudes, this component is of small value in most cases, whereas in high latitudes it is dominant. This circumstance affects the accuracy of the calculated value $X = \bar{x} \pm t\mu$, where t is the parameter in the student distribution determining the confidence limits ($t\mu$). In the general form, the error is the sum of two terms, namely, the independent (the first addend) and the dependent components:

$$\mu = \sqrt{\frac{\sigma_0^2[1 + (n - 1)\tau]}{n}}$$

where n is the number in the sample, σ_0^2 is the variance, and τ is the autocorrelation coefficient.

Calculations have shown that in the middle latitudes, and in the case of a normal distribution in high latitudes, the error μ is small (2-5 percent) and, correspondingly, the limiting error (for a 0.95 probability) is below 12 percent. In this case, the error in foF2 = x is usually much below the extrapolation error and the error due to the prediction of solar activity and, therefore, is usually neglected in practical calculations.

In high latitudes, the reliability in determining $\bar{x}$ is much lower. In some cases, the errors may reach 40 percent. Some results of the calculations of the natural errors are presented in Table 1. Included are the values of $\sigma_0 = (\overline{foF2} - foF2_i/\overline{foF2})$, τ, the coefficients of asymmetry and excess, and the character of the distribution for some stations located in various latitudes. It can be seen from the table that the errors in foF2 due to disturbances increase up to 20-40 percent (with the maximum in the center of the auroral zone) at high latitudes in winter and in equinox, excluding the evening hours. The significance of the variations in the propagation characteristics resulting from the foF2 natural errors can be determined. Further consideration was given to the variability (a) of the hop distance dD for reflections from the F2 region, disregarding the horizontal inhomogeneity in the plane of the great circle path, and (b) of the deviations of angles in the horizontal plane due to the horizontal inhomogeneity of the electron concentration of the F2 region. The calculations have been made for a one-layer parabolic ionosphere on the basis of the program published in Kerblay and Kovalevskaya (1974). The value of dD was determined as the difference in the hop distance in the presence and absence of the foF2 error:

$$dD = D_{foF2} - D_{foF2}(\mu)$$

Table 1. Values of parameters at various stations.

Station	Period of Observation		Year	σ_0	A	E	τ	$t\mu$	Distribution[1]
Kiruna	summer	day	1967	11.2	0.33	0.53	0.15	8.6	N
Murmansk	summer	morning	1964	12.8	0.53	0.3	0.03	4.4	N
Salekhard	summer	day	1969	13.2	0.86	-2.63	0.06	6.8	N
Sverdlovsk	summer	day	1964	8.2	-0.11	1.85	0.1	5.4	N
Murmansk	equin.	day	1968	15.6	-3.36	-3.19	0.14	11.4	N
Murmansk	equin.	night	1968	19.6	-0.16	0.6	0.41	25.0	B
Murmansk	equin.	day	1964	18.4	0.2	0.13	0.15	14.2	N
Dixon	equin.	day	1968	27.3	-1.13	3.03	0.27	18.0	AE
Salekhard	equin.	night	1968	23.8	0.06	-0.53	0.56	35.6	AE
Salekhard	equin.	night	1964	22.8	0.32	-0.32	0.46	28.0	AE
Leningrad	equin.	night	1968	23.7	0.17	-0.4	0.04	10.8	N
Resolute Bay	equin.	night	1958	20.2	0.21	2.58	0.2	18.2	N
Murmansk	winter	morning	1968	33.8	-7.96	-8.46	0.46	46.0	B
Murmansk	winter	night	1971	23.6	-0.26	-0.6	0.53	34.8	B
Dixon	winter	day	1968	25.9	-0.43	-0.43	0.46	35.4	B
Dixon	winter	morning	1964	21.9	12.7	14.1	0.54	32.2	B
Salekhard	winter	night	1971	32.2	0.2	-1.1	0.43	42.3	B
Salekhard	winter	day	1964	24.8	-6.8	-7.2	0.42	32.0	E
Leningrad	winter	night	1971	19.2	0.21	-0.43	0.2	17.4	N
Leningrad	winter	day	1971	12.4	1.01	4.11	0.2	11.2	N

[1]N = normal; B = bimodal; A = asymmetric; E = excessive distributions

The results of separate calculations of dD for the errors μ, which are 5, 20, 30 percent, are shown in Figures 1-3. The solid and dashed curves in the plots correspond to the negative and positive deviations of foF2, respectively. The numerals on the curves show the ratio of the operating frequency to foF2 (f/foF2). Also marked on the curves are the transitions of the low ray to the Pedersen ray. Figure 4 presents the plots of the lateral deviations $d\alpha$ for the errors μ equalling 0, 10, 20, 30, and 40 percent.

The plots presented in Figures 1-4 may be used also to estimate the dD and $d\alpha$ variations during negative or positive disturbances. In this case, the value of μ will denote the foF2 deviation due to disturbance. The negative and positive disturbances will result in an increase and decrease of the hop distance, respectively. It can be seen from Figures 1-3 that when the error in foF2 equals 30 percent, and propagation is by the usual ray, the value of dD usually fails to exceed 200 km even for the longest links. This value corresponds approximately to the accuracy of the calculations. The values of dD do not exceed 200 km even at μ = 10 percent in most cases up to f/foF2 = 2.6. At μ = 20 percent and higher, however, the value of dD can no longer be neglected. For example, in the links traversing the zones where μ is 30-50 percent, the dD variations may be 400-800 km. With regard to the Pedersen ray, when μ = 10 percent, the dD variations are larger than 200 km. A relevant specific example is as follows. Given the ionospheric parameters h_m = 300 km, y_m = 100 km, $\Delta = 4°$, f/foF2 = 2.0 in middle latitudes, when the error μ is small, the hop distance will be 2600 km. In high latitudes, due to the 30 percent statistical error, the hop distance will be 2600 + 340 km.

When the ratio f/foF2 = 2.2, the correction for one hop will be as much as 620 km.

The following example shows the degree of variation in the angle α of the azimuthal deviation as a function of the statistical error of the distance. For the initial conditions f/fo = 1.8, D = 1800 km, the value of α at μ = 0% will be about 0.1°. At μ = -20% or on the days with negative disturbances, α will increase up to $\simeq$ 0.3° and, in the case of the Pedersen ray, up to 1.8°. At positive μ or for positive disturbances resulting in an increase of foF2, α will decrease. The example presented above shows that the effect of the statistical error may be comparable with, and in some cases exceed, the calculated value of α proper.

Indicated above were only the errors in determining the median values of the hop distance and the angles of azimuthal deviations relevant to the statistical properties of the medium. The statistical variability of one or another parameter X as a whole (variations from day to day) must be described using the formula

$$X = \overline{x} \pm u\sigma_0$$

where u is the parameter of the normal distribution (u = 2 for P = 0.95).

In middle latitudes, the statistical scatter characterized by the term $u\sigma_0$ is, as a rule, significantly in excess of the confidence limit of the median estimates. In Leningrad, for example, in the equinox of 1968 at night, $t\mu$ = 10.8% and $u\sigma_0$ = 2 x 23.7 = 47%. In the disturbed medium (for example, in the high latitudes), the values of $t\mu$ and $u\sigma_0$ become comparable (see the same case for Murmansk, $t\mu$ = 25%, $u\sigma_0$ = 2 x 19.6 = 39%), which is indicative of low reliability in the median values. The calculations presented above show that in high latitudes, where errors in the median ionospheric parameters increase significantly due to their statistical nature, the main characteristics of propagation as well as the reliable limits should be calculated thereby permitting a higher accuracy of prediction of one or another feature of radio wave propagation.

REFERENCES

Kerblay, T. S., and E. M. Kovalevskaya (1974): Trajectories of Short Radio Waves in the Ionosphere. Nauka, Moscow.

Zhulina, E. M., and M. V. Kiseleva (1974): About features of statistical distributions of δfoF2 in high latitudes. In: Study of the F-Region and Outer Ionosphere, IZMIRAN, Moscow, 275.

PREDICTION OF HF COMMUNICATION DISTURBANCES BY PRE-SC HF FIELD INCREASES ON POLAR PATHS CROSSING THE AURORAL ZONE

T. ONDOH and K. OBU
Radio Research Laboratories, Tokyo, 184, JAPAN

Analysis of WWV field variations of the polar path received at Hiraiso, Japan shows that WWV field increases of about 10 - 20 dB are often observed at frequencies above 20 MHz for about 10 hours before geomagnetic storm sudden commencements. The pre-sc WWV field increases are accompanied with ionospheric f_oF_2 increases over approximate apexes around the noon on the polar paths. The pre-sc WWV field increases may be due to decreases of the ionospheric deviative absorption for HF waves associated with polar cusp f_oF_2 increases, which are caused by precipitations of enhanced polar cusp electrons with energy of 1 - 2 keV. Consequently, the pre-sc HF field increases on polar paths crossing the auroral zone are useful for the prediction of HF communication disturbances associated with geomagnetic storms in the solar quiet period.

1. Introduction

Since geomagnetic storms in the solar quiet period have no definite causal phenomena on the solar disc, a study on precursors of geomagnetic storms is important for the radio warning service, especially in the solar quiet period. At the Hiraiso Radio Warning Center, Japan, it has been experimentally known since the IGY that increases in the field intensity or receiving time of WWV 20 MHz propagating from Washington D. C., U. S. A. often occur before geomagnetic storms. The Washington-Hiraiso path traverses the northern auroral zone, and also the polar cusp region in geomagnetically disturbed periods. So, it is expected that particle precipitations through the polar cusp give some effect upon HF propagation on the Washington-Hiraiso paths. In this paper, we first analyse statistically storm-time variations of WWV 20 MHz field intensity received at Hiraiso, Japan and of f_oF_2 at approximate apexes of the Washington-Hiraiso path in order to elucidate the pre-sc field increases of WWV 20 MHz at Hiraiso. Secondly, we also derive statistically the storm-time variations of WWV field intensity on 25 MHz, 20 MHz, 15 MHz, and 10 MHz, and of f_oF_2 observed at Canadian ionospheric stations for the above purpose. Finally, applied results of the pre-sc field increase of WWV 20 MHz to the radio warning service at Hiraiso are reported in the solar quiet period for 1962 - 1965. All WWV field data used in this paper are of radio waves propagating from the transmitting station at Washington, D. C., although the WWV transmitting station was later transferred from Washington, D. C. to Fort Colins.

2. Ionospheric Stations Used and Method of Data Analysis

Ionospheric f_oF_2 and WWV field intensity data used in this paper were observed at ionospheric stations in Canada, Alaska, and Japan for 1957 - 1959. Table 1 gives geomagnetic co-ordinates of the stations used. We select 50 geomagnetic storms occurring during August,1957 to February,1959.

Table 1. Ionospheric stations used

Station	Geomag. Lat.	Geomag. Long.
Thule	88.0°N	1.1°
Eureka	86.5°N	236.4°
Alert	85.8°N	168.5°
Resolute Bay	82.9°N	289.3°
Baker Lake	73.7°N	315.1°
Ft. Churchill	68.7°N	322.7°
College	64.7°N	256.5°
Fairbanks	64.6°N	256.6°
Meanook	61.8°N	301.0°
Winnipeg	58.8°N	322.9°
Ottawa	56.9°N	351.3°
Washington	50.0°N	350.3°
Hiraiso	26.2°N	206.3°

Since WWV field intensities at Hiraiso include ZAN, we obtain the storm-time variation (D_{st}) of the medians of WWV 20 MHz field intensities observed at Hiraiso for the 50 geomagnetic storms. The storm-time T_{st} is reckoned from the occurrence time of geomagnetic storm sudden commencement (sc), and the storm-time variation (D_{st}) is derived by the superposed method at each storm-time from T_{st}= -24 hours to 31 hours. Storm-time variations of f_oF_2 and WWV field intensity at Canadian ionospheric stations are obtained by computing the average deviation of f_oF_2 or WWV field intensities from the monthly median over the 50 geomagnetic storms selected. The disturbance, D is expressed by $D = D_{st} + D_s$. The disturbance daily variation, SD is obtained by the superposed method of DS at each local time. We also compute the disturbance daily variation of f_oF_2 in the pre-sc stage for the 50 geomagnetic storms, in order to investigate an effect of the magnetospheric process on the pre-sc WWV field intensity in high latitudes.

3. Pre-sc WWV 20 MHz Field Increases Received at Hiraiso

Fig. 1 shows a typical example of WWV 20 MHz field increase and an extension of WWV 20 MHz receiving hours at Hiraiso before an sc of 0323 UT on July 27, 1958. Since no significant geomagnetic disturbance occurred before July 26, 1958, the record of WWV 20 MHz field intensity on July 26 represents the quiet-day propagation condition. The receiving hours of WWV 20 MHz before the sc of July 27 is about 4 hours longer than that on the quiet day (July 26). So, it seems that WWV 20 MHz waves propagate from Washington, D.C. to Hiraiso along the great circle path before the sc.

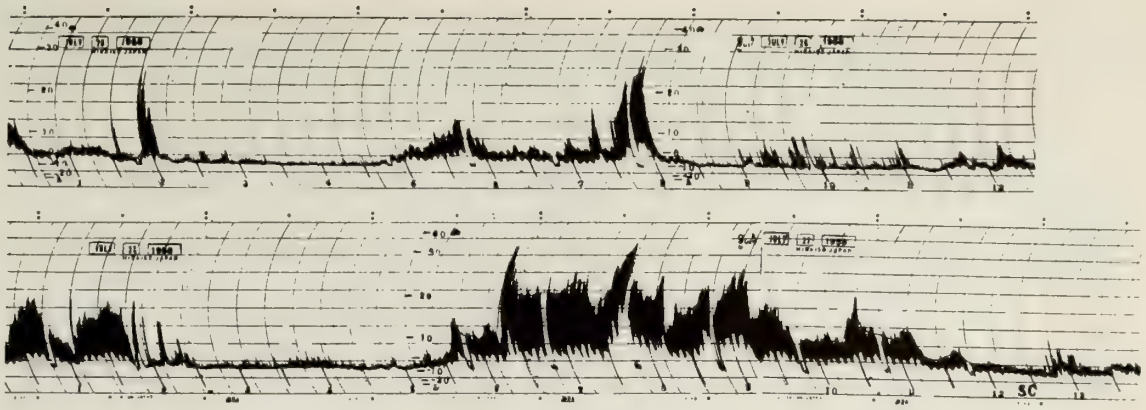


Fig. 1 Records of WWV 20 MHz field intensity received at Hiraiso showing field intensity increases before an sc of 0323 UT on July 27,1958.

Fig. 2 shows storm-time variations of the median of WWV 20 MHz field intensities received at Hiraiso over 50 geomagnetic storms which occurred without polar cap absorption during August, 1957 to February, 1959. An upper curve in Fig. 2 is the average storm-time variation of K-indices over the 50 geomagnetic storms at College, Alaska near an apex of the Washington-Hiraiso path. A pre-sc WWV 20 MHz field increase of about 10 - 20 dB above the quiet level is clearly seen from T_{st}= -12 hours to the sc. It is expected that an f_oF_2 increase at apexes of the propagation path causes an intensity increase of HF waves at frequencies near the F-layer penetration frequency. So, we derive storm-time average variations of f_oF_2 deviations from the monthly median over the 50 geomagnetic storms at Fairbanks, Meanook, and Winnipeg, where are near apexes of the Washington-Hiraiso path, in Figs. 3a, 3b, and 3c respectively. Figs. 3a - 3c clearly illustrate the pre-sc f_oF_2 increases at the above stations for T_{st}= -20 hours - T_{st}= -2 hours which are approximately the same storm-time interval as the pre-sc WWV 20 MHz field

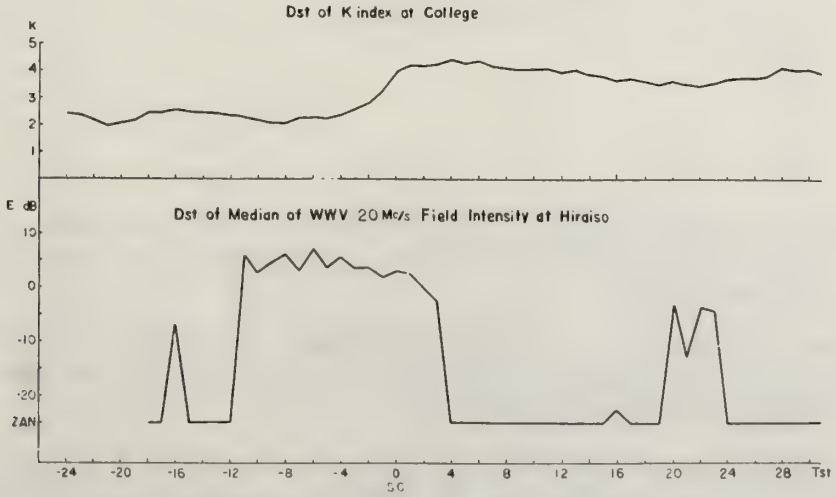


Fig. 2 Storm-time variations of K-indices at College, Alaska and of the median of WWV 20 MHz field intensities at Hiraiso,Japan over the 50 geomagnetic storms during August, 1957 to February, 1959.

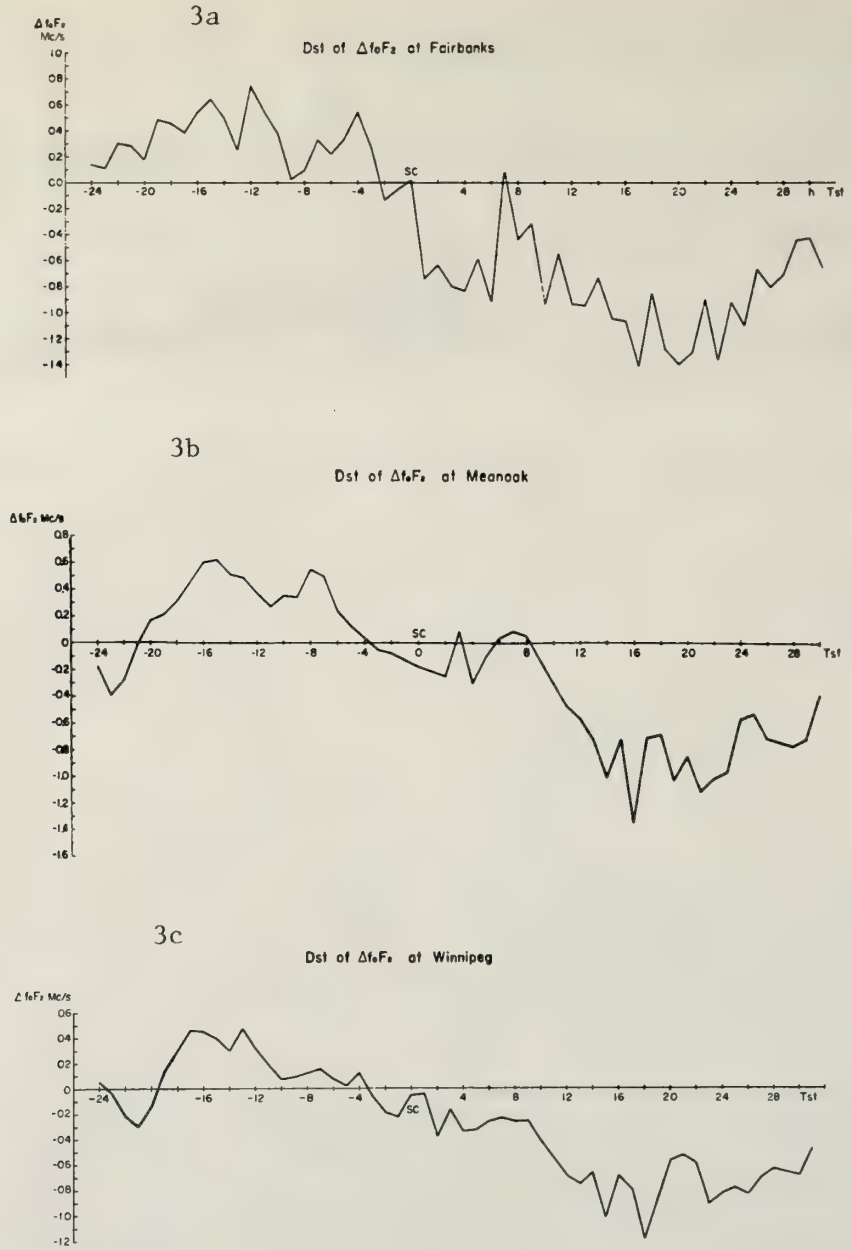


Fig. 3 Storm-time variations of f_oF_2 deviations from the monthly median over the 50 geomagnetic storms at Fairbanks (3a), Meanook (3b), and Winnipeg (3c).

increase received at Hiraiso. Thus, it becomes clear that the pre-sc WWV 20 MHz field increase is closely related to the pre-sc f_oF_2 increase at the apexes of the Washington-Hiraiso path.

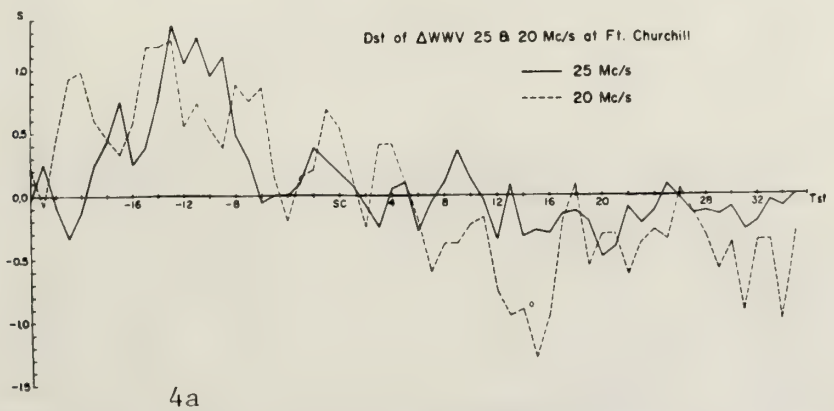
4. Frequency Band of The Pre-sc WWV Field Increase in High Latitudes

For the purpose of finding preferential frequency band of the pre-sc WWV field increase, we further analyse storm-time average variations of WWV field

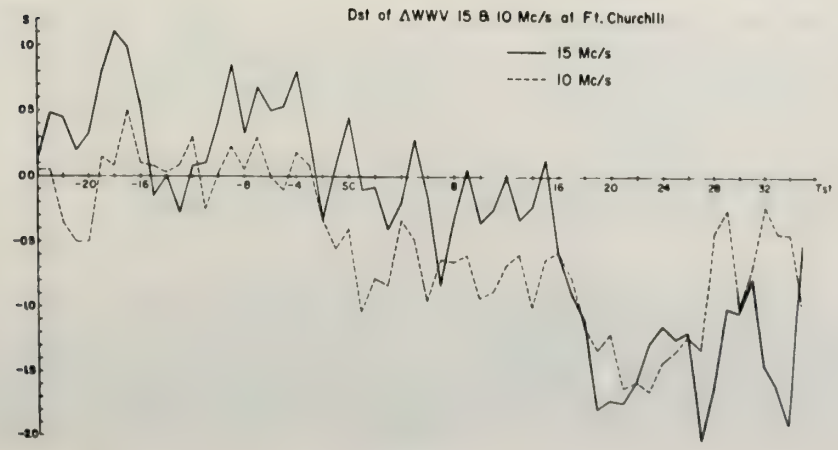
intensity deviations from the monthly median at 25, 20, 15, 10, 5, and 2.5 MHz over the 50 geomagnetic storms, using WWV data received at Ft. Churchill and Winnipeg during August, 1957 to February, 1959. Figs. 4a and 4b show storm-time average variations of WWV field intensity deviations from the monthly median scaled in the S-unit at Ft. Churchill and Winnipeg respectively. Pre-sc WWV field increases are clearly seen on 20 MHz and 25 MHz from T_{st}= -20 hours to -4 hours at Ft. Churchill, while there is no pre-sc field increase at frequencies below 15 MHz. However, any evident increase above $\Delta S \geq 1$ does not occur in the pre-sc stage on all WWV frequencies at Winnipeg, where is located at geomagnetic latitude below the auroral zone. Also, there is no systematic storm-time variation of 2.5 MHz field intensity at Ft. Churchill. Thus, the pre-sc WWV field increase occurs on frequency of 20 MHz and 25 MHz only at stations which have the WWV propagation path crossing the auroral zone.

Storm-time average variations of f_oF_2 deviations from the monthly median at Thule, Eureka, Alert, Resolute Bay, Baker Lake, Ft. Churchill, Ottawa, and Washington D. C. are shown in Fig. 5 for the same 50 geomagnetic storms during August,1957 to February, 1959. The storm-time variations in Figs. 3a -3c and 5 indicate that the pre-sc f_oF_2 increase occurs only at geomagnetic latitudes between about 83°N (Resolute Bay) and 57°N (Ottawa). But, even the storm time decrease of f_oF_2 does not occur at high latitudes above 85°N (Alert). The pre-sc f_oF_2 increase at Winnipeg, where is the approximate apex of the Washington-Churchill path, corresponds to the pre-sc WWV 20 MHz and 25 MHz field increases at Ft. Churchill.

4a



4a



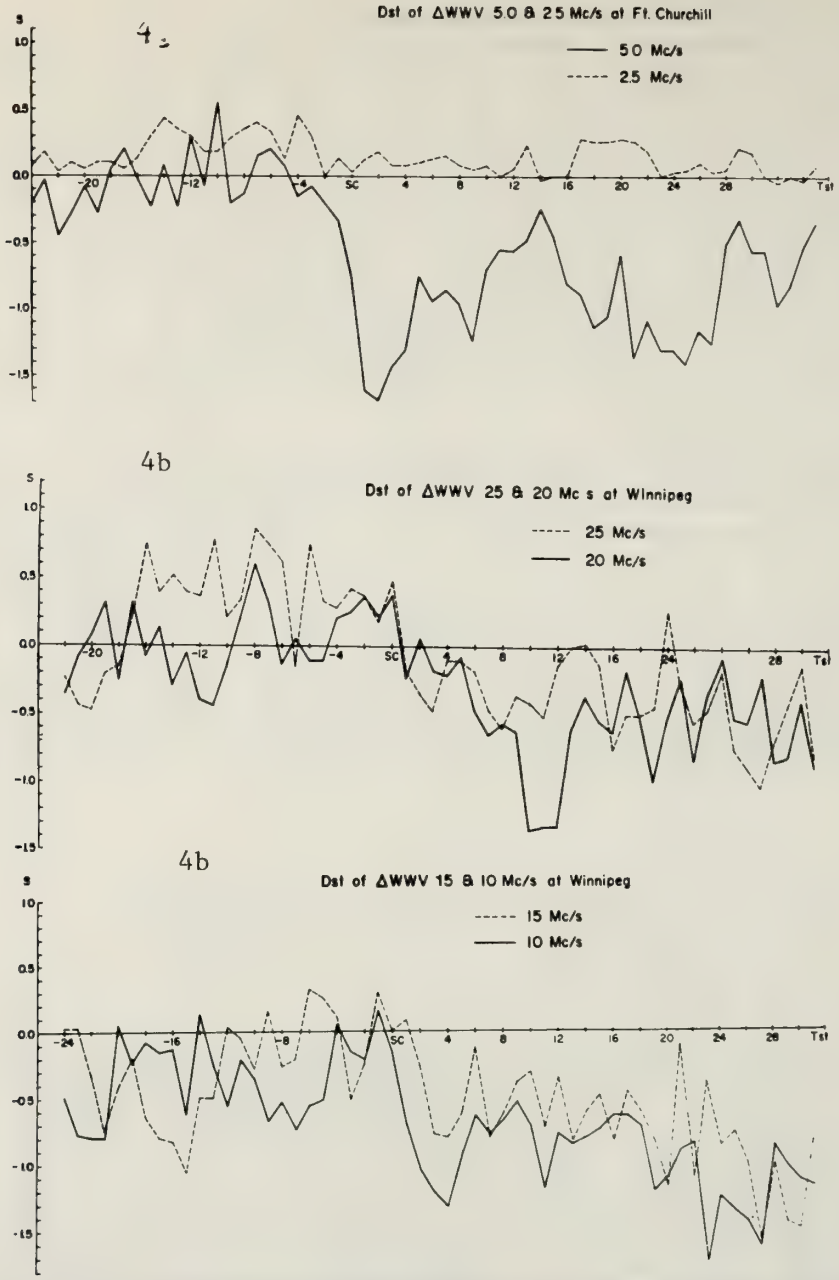


Fig. 4 Storm-time variations of WWV field deviations from the monthly median on 25, 20, 15, 10, 5, and 2.5 MHz at Ft. Churchill (4a) and Winnipeg (4b) over the 50 geomagnetic storms.

5. Effect of Dayside Polar-cusp Electrons on the Polar Ionosphere and Pre-sc HF Field Increases of Polar Paths

Disturbance daily variations (SD) of f_oF_2 in the pre-sc stage are obtained in Figs. 6a - 6f by superposing f_oF_2 deviations from the monthly median at each local time, using f_oF_2 observed at Resolute Bay, Baker Lake, Churchill, Fairbanks, Meanook, and Winnipeg during the 50 geomagnetic storms respectively. Figs. 6b - 6f show evident increases of the pre-sc SD component of

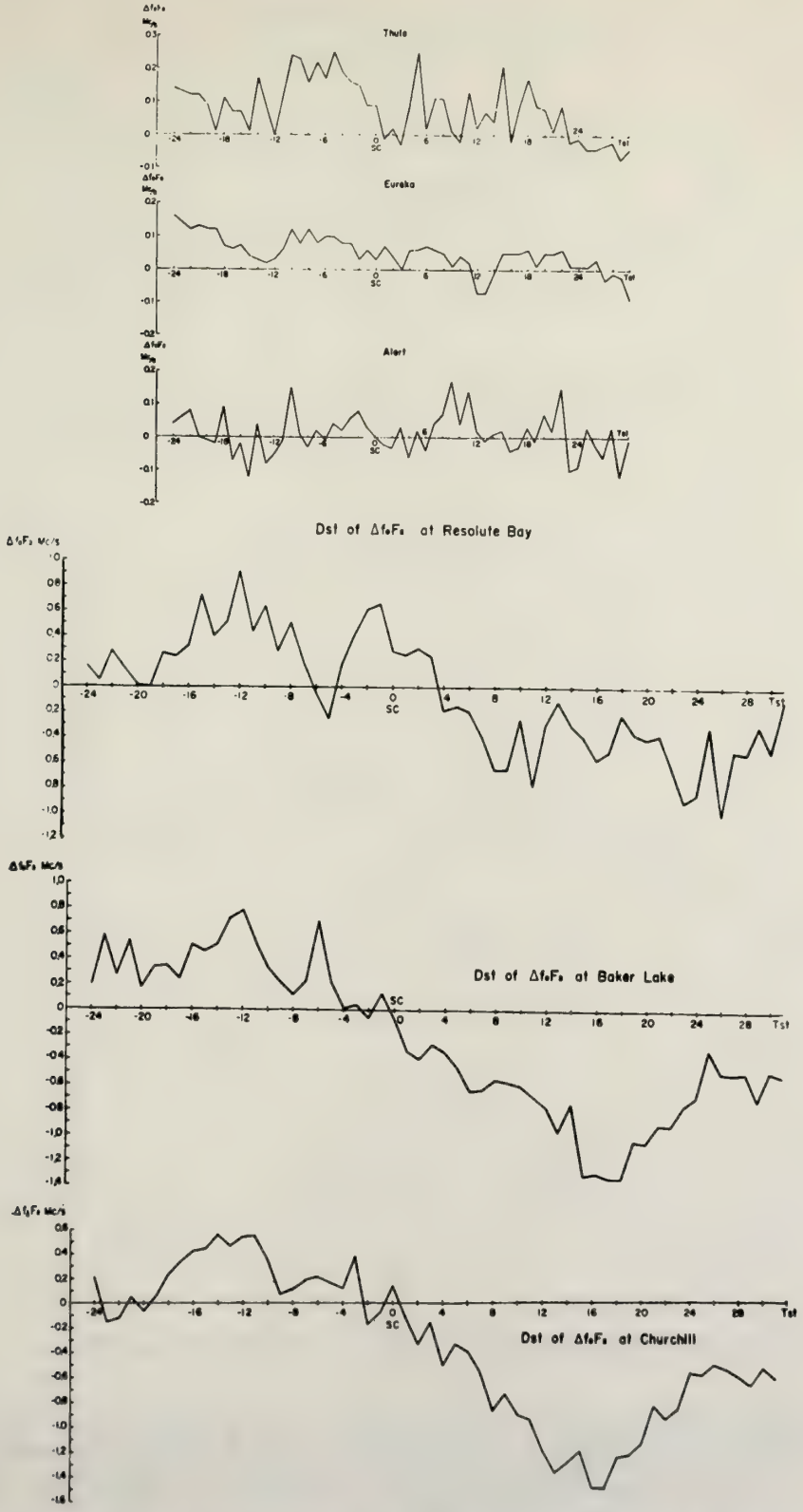


Fig. 5 Storm-time variations of f_oF_2 deviations from the monthly median over the 50 geomagnetic storms at Thule, Eureka, Alert, Resolute Bay, Baker Lake, Ft. Churchill.

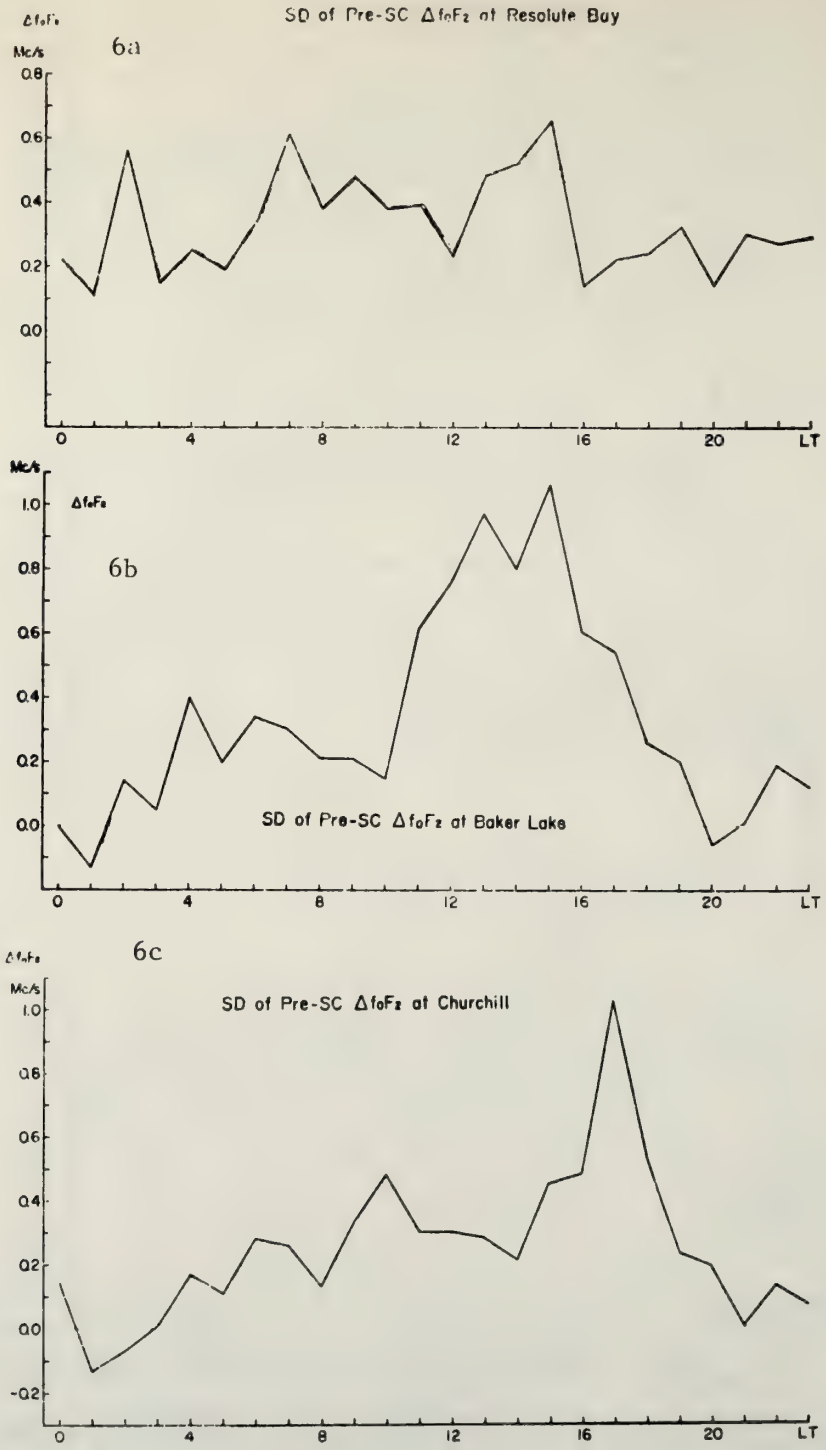
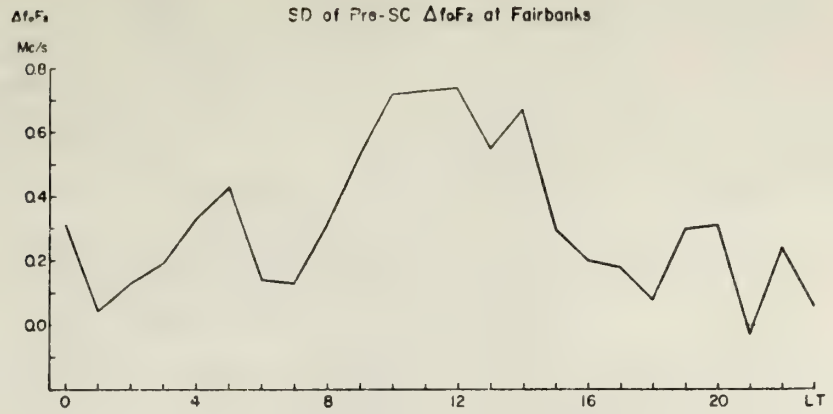


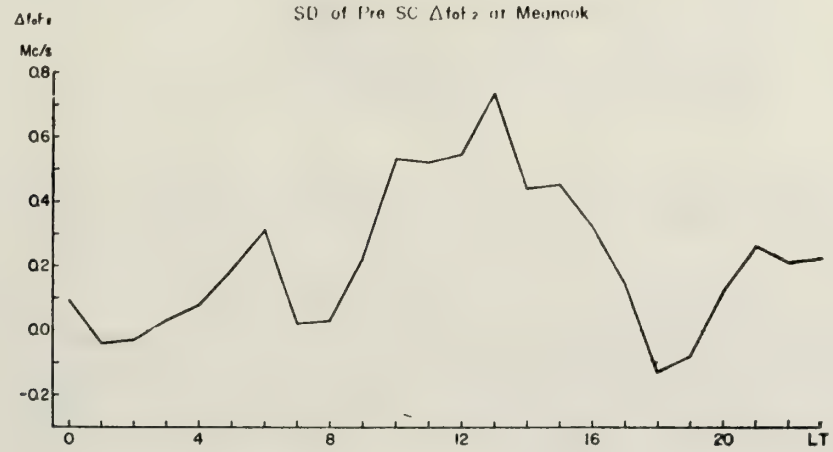
Fig. 6a - 6c Disturbance daily variations of f_oF_2 deviations from the monthly median in the pre-sc stage over the 50 geomagnetic storms at Resolute Bay (6a), Baker Lake (6b), Ft. Churchill (6c), and Fairbanks (6d).

f_oF_2 around the local noon in the auroral zone and higher latitudes below 82°N. The Ariel-4 observation indicates that polar-cusp electron (1 keV - 4 keV) intensities increase by a factor of 10 at 2 keV for magnetic local

6d



6e



6f

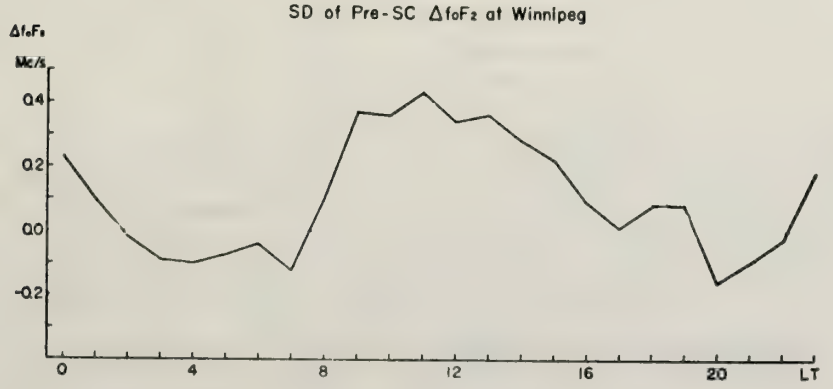


Fig. 6d - 6f Disturbance daily variations of f_oF_2 deviations from the monthly median in the pre-sc stage over the 50 geomagnetic storms at Meanook (6e) and Fairbanks (6f).

time of 11 - 13 hours during a period of northwardly directed interplanetary magnetic field (Craven and Frank, 1978). A flux of 1 - 2 keV electrons, 10^4 $cm^{-2}.sec^{-1}.eV^{-1}.ster^{-1}$ is required to account for the polar F-region at

the winter solstice by the particle impact ionization (Kamiyama, 1966). Therefore, the pre-sc increase of f_oF_2 around the local noon in high latitudes can be explained by the impact ionization of low energy (1 - 2 keV) polar-cusp electrons. Table 2 lists ranges of the pre-sc increase of f_oF_2. The pre-sc increase of f_oF_2 in Table 2 may cause a deviative-absorption decrease of the order of 10 - 20 dB for 20 - 25 MHz on polar paths. This produces the pre-sc HF field increase at 20 - 25 MHz and the prolonged receiving hours of WWV 20 and 25 MHz on polar paths.

Table 2. Ranges of the pre-sc f_oF_2 increases observed in high latitudes during August,1957 to February,1959.

Stations	Δf_oF_2
Resolute Bay	$\lesssim$ 5.5 MHz
Baker Lake	$\lesssim$ 5.5 MHz
Ft. Churchill	$\lesssim$ 5.0 MHz
Fairbanks	$\lesssim$ 4.5 MHz
Winnipeg	$\lesssim$ 4.0 MHz

6. Application of The Pre-sc HF Field Increase to The Prediction of HF Communication Disturbance in The Solar Quiet Period

One of the most reliable means for the HF communication disturbance in the solar quiet period is the 27-day recurrent geomagnetic disturbance. But, there are a few recurrent geomagnetic disturbances continuing more than three solar cycles. In this respect, the pre-sc HF field increases of polar paths are useful means for the prediction of HF communication disturbances in the solar quiet period. The HF communication disturbance associated with geomagnetic storm on March 4, 1964 was first warned by this method at the Hiraiso Radio Warning Center, though this storm was not predicted by the 27-day recurrent geomagnetic disturbances. Since then, the pre-sc WWV 20 MHz field increases have been successfully applied to the prediction of HF communication disturbances at Hiraiso Radio Warning Center.
Of 88 geomagnetic storms during January, 1962 to October,1965, 56 pre-sc (or sg) WWV 20 MHz field increases (64 %) were observed at Hiraiso, Japan. The occurrence rate of the pre-sc (or sg) WWV 20 MHz increases at Hiraiso in 1962, 1963, 1964, and 1965 is 64 %, 68 %, 57 %, and 66 % respectively. Thus, the pre-sc HF field increase on polar paths traversing the auroral zone is a useful means for the prediction of HF communication disturbances, especially in the solar quiet period.

References

Craven J. D. and L. A. Frank (1978) : Energization of polar cusp electrons at the noon meridian. J. Geophysical Research, 83 : 2127.

Kamiyama H. (1966) : Ionization and excitation by precipitating electrons. Report of Ionosphere and Space Research in Japan, 20:171.

MINICOMPUTER SIMULATION OF IONOSPHERIC RADIOWAVE PROPAGATION AT DECAMETRIC WAVELENGTHS

David D. Meisel
Department of Physics and Astronomy
State University College
Geneseo, New York 14454, U.S.A.

Basil Duke
Transmission Systems
Canadian Broadcasting Corporation
Engineering Headquarters
Montreal, Quebec, Canada

William D. Savedoff
Harvard University
Cambridge, Massachusetts 02138, U.S.A.

Initial experiments into the utilization of limited storage minicomputers for simulation of ionospheric propagation conditions on a worldwide basis are described with emphasis on prediction of received signal strength as a function of local time, calendar date, solar flux, and geomagnetic index. Comparison of the predictions with field strength measurements are made for several long-distance paths.

INTRODUCTION

As a part of a previous study of HF, VLF, and geomagnetic behavior during solar eclipses (Meisel, et al. 1976) a minicomputer program for simulation of oblique-incidence radiowave propagation behavior on one-hop and two-hop paths was developed. Based on this experience, it was decided to extend this program to long distance paths in order to see if solar eclipse effects could be detected from remote receiving stations. In particular it was of interest to see if the methods adopted by Haydon and others at the Institute for Telecommunication Sciences (ITS) [formerly the Central Radio Propagation Laboratory (CRPL)] (CRPL, 1948; Ostrow, 1962; Davies, 1965; Leftin, 1975; Roberts and Rosich, 1975; and Haydon, Leftin, and Rosich, 1976) could be modified to include the lower ionosphere details needed to simulate the observed solar eclipse changes while at the same time fit the whole program into the memory of a very modest sized electronic computer. Aside from the purely scientific applications of such a prediction program, there are some "commercial" possibilities which could materialize once quantitative reliability has been established.

The increased availability of electronic computers of moderate storage capabilities (minicomputers) has been one of the most dramatic developments of the last decade. Within the last year or so, ready-to-run "personal" minicomputers have become available at prices comparable to home video recorders. Thus, minicomputer simulation programs based upon those originally developed primarily for engineering studies of shortwave radio propagation would probably be useful in a wide variety of situations including use by governments of some third world countries, small broadcasting organizations and telecommunication companies and perhaps also by advanced radio amateurs, shortwave listeners, and radio engineering students.

COMPUTER REQUIREMENTS

In 1974, we started work on minicomputer ionospheric programs with a *slightly* modified 8K FOCAL compiler package using a standard 8K (12 bit words) memory Digital Equipment Corporation PDP-8/L computer belonging to the State University of New York-Geneseo (Physics and Astronomy Department) at Geneseo, New York. Two FOCAL programs are now available with corresponding BASIC versions in production. The first FOCAL program calculates the field strengths incident on the receiver location. The second FOCAL program inputs and uses incident field strength data generated by the first program to calculate the receiver input voltage. In FOCAL, both programs just fit into 8K memory computers. In BASIC somewhat larger memories appear to be required but the 16 bit words enable higher accuracy to be obtained. Adaptation of the FOCAL versions to minicomputers without FOCAL compilers also appears to be feasible, but no attempt has been made to actually do this yet. Although the minicomputer programs described here were developed independently of the latest NBS work, the input-output formats and purposes are remarkably similar.

In this paper, we describe only the ionospheric calculation part of the program set. The receiving antenna program has not been finalized so it will be described at a later date.

THE CALCULATIONS

As a starting point, we began with the CRPL methods described by Haydon in NBS Monograph 80 (Davies, 1965). Gradually the FOCAL program has evolved from strict application of the CRPL-1966 methods to unique algorithms which include semi-empirical corrections for a variety of effects not originally in the CRPL treatment but as a check on the calculation the CRPL-1966 path loss formula was originally used parallel to our own method. Since the program length must be kept within modest bounds, many approximations and linearizations have been made. Items included, at least to a first approximation, are:

(a) F2 critical frequencies - first order
(b) magnetionic effects - full polarization treatment
(c) ground reflections - full polarization treatment for land or sea (upon option)
(d) E, F1, and E_s cut-off effects - the E_s is optional
(e) deviative absorption - assuming parabolic layers

(f) F2 virtual height variations - calculated for path mid-point
(g) auroral absorption - includes general polar as well as "ring"
(h) magnetic storm effects - includes depression of F2 frequencies
(i) signal fading and polarization properties
(j) geometric focus effects - spherical earth approximation

Because of space limitations, the ionospheric program calculates the field properties for only one transmitting antenna lobe at a time. The input data required falls into three groups.

(a) Geophysical data - Transmitter and receiver locations, date, time, daily 10 cm solar flux value, and daily planetary magnetic index Ap.
(b) Full transmitter/antenna details - Frequency, input power, antenna gain above 1/2 λ dipole and parameters of one antenna lobe including vertical and/or horizontal directivities if required by the transmitting configuration.
(c) Options - Selection of sea or land reflectivities; selection of fractional E sporadic contribution.

The output information consists of the following for each F2 mode:

(a) the number of hops
(b) the azimuth
(c) the vertical angle of arrival
(d) the root-mean-square incident field computed using the semi-empirical model
(e) the limiting polarization ratio (vertical-to-horizontal) for two limiting situations--no fading and dominance by fading.

In setting up our computer programs we have made a synthesis of a variety of sources of geophysical, aeronomical, and radio engineering information. A number of empirical parameters for which no direct evaluation could be obtained from available physical measurements were set (by trial and error) using direct field strength measurements of Radio Japan (NHK), WWV, CHU, and Radio Ankara made at Geneseo, New York. These were previously obtained as a part of our solar eclipse propagation studies (Meisel et al., 1976).

As illustrative tests of the ionospheric simulation program, we present here results for three paths for which quantitative data were provided at our request by Radio Canada International, Radio South Africa and the Österreichischer Rundfunk.

(a) Meyerton, (Johannesburg, South Africa) to Ottawa, Canada - May 8-10, 1975
(b) Daventry, (United Kingdom) to Honeydew, (Johannesburg, South Africa) - Aug. 22-25, 1976
(c) Moosbrun, (Vienna, Austria) to Geneseo, (New York State), U.S.A. - May 08-31, 1976

Indirect signal evaluations of *all* ORF transmissions for 1976 based on detailed reception data were also made available to us together with extensive receiving antenna data but these cannot be fully evaluated until the

receiving station program is completed.

As might be expected the most important conceptual uncertainty involves the specification of the polar absorption and its correlation with solar and geomagnetic data. The role E_s plays in altering signal levels on some paths is likewise uncertain.

Because of memory space limitations, no *major* conceptual revisions can be contemplated and certainly no further major additions are possible. However, in the area of parameter *refinement* several items are of immediate interest:

(1) Better definition of D layer and auroral zone absorption and its dependence on geomagnetic index - observations of Radio Japan (NHK) will continue.
(2) Better definition of the solar cycle dependence of the properties of the geomagnetic index, in an effort to clarify what constitutes "average" or "normal" conditions.
(3) Definition of a *daily* E sporadic index which can be used to predict the average path E_s contribution--a parameter which functions as the F_{10} or Ap index is being sought.

In spite of the theoretical simplifications and the uncertainties in parameter values, we feel that the minicomputer program in its *present* 8K form adequately simulates ionospheric radio propagation. To demonstrate this we present results for several "problem" propagation paths. Other tests are planned in the future in conjunction with the receiver site program.

RESULTS

First, we considered the North American transmission of Radio South Africa using field strength measurements made at the Stittsville (Ottawa) Receiving Station of Radio Canada International. The original observations are given in the first table. For prediction purposes we adopted the following mean parameters.

Transmitter: Long. -28°.1, Lat. -26°.6 (Meyerton, South Africa)
Receiver: Long. +76°.0, Lat. +45°.5 (Stittsville, Ontario, Canada)
Date: 1975 May 8 *2800 MHz Solar Flux* = 70 (=F_{10})
Time: 2300 U.T. (GMT) *Ap Magnetic Index* = 15
Frequency: 9.5 MHz *Power:* 250 kilowatts
Beam Elevation Angle: 7.5°
Half-Power Full Width: 7°.8 (vertical)
26° (horizontal)
Gain: 20 dB over isometric dipole
Azimuth: 300° Sea Water Reflection

Observed Mean Field:

2300 GMT = 16 μV/m	maximum $\langle E \rangle \simeq$ 100 μV/m
$\langle E \rangle$ 3 days = 26 μV/m	minimum $\langle E \rangle \simeq$ 0 μV/m

FIELD INTENSITY MEASUREMENTS of RADIO SOUTH AFRICA (NORTH AMERICAN SERVICE).

9525 kHz
1975 May 8, 9, 10 - 2230 to 2320 GMT

Measurements taken at five minute intervals, expressed in dB/μV/m and μV/m.

	MAY 8		MAY 9		MAY 10	
	F_{10} = 71 Ap = 13 Low Normal SS No. Daily > 0		F_{10} = 69 Ap = 17 Below Normal SS = 0		F_{10} = 69 Ap = 17 Low Normal SS = 9	
Time (GMT)	Power dB/μV/m	μV/m	Power dB/μV/m	μV/m	Power dB/μV/m	μV/m
2230	30	31.6	15	5.6	40	100
35	33	44.7	12	3.98	38	79.4
40	38	79.4	16	6.31	34	50.1
45	36	63.1	16	6.31	25	17.8
50	36	63.1	10	3.16	23	14.3
55	30	31.6	14	5.01	20	10.0
2300	31	35.5	17	7.08	15	5.62
05	32	39.8	17	7.08	9	2.82
10	34	50.1	17	7.08	7	2.24
15	37	70.8	18	7.94	9	2.82
20	36	63.1	23	14.3	7	2.24
25	20	10.0	9	2.82	nil	nil
30	16	6.31	11	3.55	nil	nil
	$\langle E \rangle$ = 50.2		$\langle E \rangle$ = 6.2		$\langle E \rangle$ = 22.1	

Measurements were made with Stoddard F.I.-Meter model NM-25-T.

WWV recordings were made on C-60 cassette from 2310 to 2320 GMT each day.

Summary of Predictions

Since the prevailing E_s parameters are not known, three conditions E_s = 0, .25, and .5 have been assumed in the calculations.

E_s = 0 RSS* = 104 μV/m $f_{E_s} = f_E$

E_s = .25 RSS = 33 μV/m $f_{E_s} = f_E + 1.25$ MHz

E_s = .50 RSS = 40 μV/m $f_{E_s} = f_E + 2.5$ MHz

*RSS = root-squared-sum over all active modes

The E_s parameter used here is the fraction of 5 MHz that the E_s critical frequency is above the ordinary E-layer critical frequency. This parameter is not standard but will be used in future simulation programs until a standard E_s parameter is developed.

If Rayleigh fading statistics are assumed, the upper decile is 1.2 x RMS, the median is 0.8 x RMS, and the lower decile is 0.4 x RMS. Comparison of the individual values or the means shows the *best* agreement only if there is significant E_s present ($f_{E_s} \geq f_E + 1.25$ MHz). Since E_s is usually on the rise during May, it is not unreasonable to postulate that some E_s is present on all three test days.

As a *second* test, we chose the north-south United Kingdom/South Africa path using the early morning transmission of Radio Canada International (Daventry relay station) as monitored at the RSA receiving station at Honeydew (Johannesburg). The solar aspect in the August period was similar to the May period but the direction of propagation was reversed. Following the same format as above:

Transmitter: Long. +1°.1, Lat. 52°.3 (Daventry, G.B.)
Receiver: Long. -27°.9, Lat. -26°.2 (Honeydew, R.S.A.)
Date: 1975 Aug. 23 F_{10} = 69
Time: 0700 U.T. (GMT) *Ap* = 18
Frequency: 11.7 MHz *Power:* 100 kw
Beam Elevation Angle: 7°
Half-Power Full Width: 7°.8 (vertical)
26° (horizontal)
Gain: 20 dB
Azimuth: 170° Land Reflections

Observed Fields:

R.S.A.	1976 Aug. 22-25	0620-0640 GMT	∿5 μV/m
		0700-0720 GMT	∿2.5 μV/m
		0740-0800 GMT	∿2 μV/m

[There was considerable interference from a Russian transmitter on all days. The field measurements refer to values when the Russian station faded out.]

R.C.I. Technical Monitor - SIO (Signal strength, interference, overall merit) Reports - Inverted "L" NW-SE

1976 Aug. 24-28	S = 0 to S = 2	$\langle E \rangle$ 3 μV/m
1976 Aug. 31-Sept. 3	S = 0 to S = 2	0 < E < 20 μV/m

Summary of Predictions

As was done previously, we generated RMS field values at three E_s conditions E_s = 0, .25, and .5 representing $f_{E_s} = f_E$, $f_{E_s} = f_E + 1.25$ MHz and $f_{E_s} = f_E + 2.5$ MHz.

E_s = 0 4 μV/m = RSS*
E_s = .25 5 μV/m = RSS
E_s = .50 6 μV/m = RSS

*RSS = root-squared-sum over all active modes

Once again the agreement of observation within the limits of Rayleigh statistics must be considered satisfactory.

Next, measurements of the Austrian Radio (ORF) North American transmissions made by D. Meisel using an inverted trap dipole antenna were analyzed. These measurements are not as good as the previous ones because of the uncertainties of ground effects at the receiver particularly at 6 MHz. However using plausible attenuation assumptions, at least reasonable limits may be placed on the incident field values. The observations are gathered in a second table. The assumed parameters are:

Transmitter: Long. -16°.5, Lat. +48°.0
Receiver: Long. 77°.8, Lat. +42°.7
Date: 1976 May 19 F_{10} = 71
Time: 0010 U.T. (GMT) *Ap* = 7
First Frequency: 9.8 MHz *Power:* 100 kw
Beam El. Ang. = 14° *Half-Power Full Width:* 10°.5 (vert.)
Gain: 14.5 dB 10°.5 (horz.)
Azimuth: 303° Sea Reflection
2nd Frequency: 6.2 MHz *Power:* 100 kw
Beam El. Ang. = isotropic *Half-Power Full Width:* - vert.
Gain: 11 dB 50° (horz.)
Azimuth: 303° Sea Reflection

The F_{10} and Ap values given are interpolated from the daily values for the appropriate GMT of observation. Since the Austria-North America path is "trans-auroral" the magnetic field control of the signal strength is considerable as is demonstrated by comparing the minicomputer results for "average" conditions (F = 72, Ap = 10) with those prevailing at the time of the ORF transmission and our observations (F = 71, Ap = 7).

E-sporadic	Freq (KHz)	RSS (Ap = 7)*	RSS (Ap = 10)*
E_s = 0	9770	370 μV/m	230 μV/m
	6155	130 μV/m	70 μV/m
E_s = .25	9770	350 μV/m	230 μV/m
	6155	140 μV/m	70 μV/m
E_s = .50	9770	410 μV/m	270 μV/m
	6155	170 μV/m	80 μV/m

*RSS = root-squared-sum over all active modes.

The agreement for both frequencies is satisfactory within the limits set by Rayleigh statistics.

FIELD INTENSITY MEASUREMENTS of ORF AUSTRIAN RADIO (NORTH AMERICAN SERVICE).

(a) 9770 KHz - Inverted Dipole - SPR-4 Drake Receiver

1976	GMT	F_{10}	Ap	Input	MEAN-E*
May 08	0020	69	11	150 μV	110 μV/m
14	0120	72	4	1000	770
14	2319	74	4	150	110
15	0051	74	4	300	220
15	2345	76	5	600	460
17	0053	75	4	600	460
25	2355	68	7	300	220
29	2356	66	16	50	40
31	2349	67	10	300	220
Mean 19	0015	71	7	RMS = 360 μV/m	

*Based on pattern recalibration 4/15/77 and 0° to 30° range on the angle of arrival.

(b) 6155 KHz - Inverted Dipole - SPR-4 Drake Receiver

1976	GMT	F_{10}	Ap	Input	MEAN-E*
May 08	0020	69	11	300 μV	80 μV/m
14	0120	72	4	1000	260
14	2319	74	4	300	80
15	2345	76	5	300	80
17	0053	75	4	60	15
25	2355	68	7	70	30
29	2356	66	16	70	30
31	2349	67	10	100	30
Mean 20	0010	71	8	RMS = 100 μV/m	

*Based on pattern recalibration 4/15/77 and 0° to 30° range for the angle of arrival.

In order to check the program reliability at the higher shortwave frequencies as well as investigate the seasonal behavior of a transequatorial path, we generated predictions for the Canada-South Africa path at 1900 GMT for F_{10} = 70, Ap = 10 and for June 15 and December 15. Frequencies of 17.8 and 15.3 MHz were assumed and the known RCI antenna patterns were used. The results for E_s = 0 and receiver coordinates of lat. -28, long. -25 were:

Jun 15	17.8 → 160 μV/m	15.3 → 200 μV/m
Dec 15	17.8 → 650 μV/m	15.3 → 710 μV/m

In June, the field is contributed mainly by lowest mode (arrival angle less than 1°) and therefore the effective incident field will be considerably less than the amounts quoted. A summer (N. Hemisphere) fade-out is predicted by the simulation program and is in accord with past reports by RCI monitors. However, without an analysis of the receiving antenna pattern or without quantitative field measurements, it is difficult to assess how good such agreement really is. Further comparisons of other RCI or ORF paths will be postponed until the receiver program is available. Likewise propagation at lower shortwave frequencies remains to be explored. Although there is no reason to suspect that a computation failure would occur, the program has yet to be tested for frequencies below 6 MHz. Since a full polarization calculation is performed, however, no difficulties down to about 2 MHz are expected.

Extensive measurements at 15 MHz have been obtained using Radio Japan signals, but since some of these have been used for parameter adjustment they cannot properly be considered independent tests. Limited tests at higher frequencies have also been carried out and these are continuing in connection with further refinement of the F2 critical frequency algorithms. Once the receiving station program is finalized it will be possible to predict actual received total voltages directly and thereby refine the reception report comparisons considerably.

ACKNOWLEDGEMENTS

We gratefully acknowledge the contributions of the following people and organizations to this project. K. Kinsey, State University of New York, Geneseo, N.Y., for important FOCAL modifications; the Physics and Astronomy Department, SUNY, Geneseo, for the extended use of the PDP-8/L computer and associated equipment; J. R. Kearney, Transmission and Reception Research Department, South African Broadcasting Corporation for the Radio Canada International (Daventry, UK) measurements; Josef Jaschek and Herbert Kuhnle of the Austrian State Radio (ORF), Vienna, for details of their antenna characteristics as well as extensive SINPO report statistics; C. Uitzinger of Johannesburg, South Africa, for reception data bracketing the Daventry test period; E. I. Loomer, Division of Geomagnetism, Department of Energy, Mines and Resources, Ottawa, Canada for important historical geomagnetic data; the Canadian Broadcasting Corporation for making staff and equipment available for this project; and Judy Worden for particular care in typing the final copy of this paper as well as the many preliminary drafts.

REFERENCES

Central Radio Propagation Laboratory (1948): Ionospheric Radio Propagation. NBS Circ. 462, U.S. Dept. of Commerce.

Davies, K. (1965): Ionospheric Radio Propagation. NBS Monograph 80, U.S. Dept. of Commerce.

Haydon, G. W., M. Leftin, and R. K. Rosich (1976): Predicting the Performance of High Frequency Sky-wave Telecommunication Systems. Office of Telecommunications Report OTR-76-102.

Leftin, M. (1975): Ionospheric Predictions, Vol. 1. Office of Telecommunications Research and Engineering Report 13, OT-TRER 13.

Meisel, D. D., S. B. Duke, N. Goldblatt, and R. Aguglia (1976): Solar eclipse effects on HF and VLF propagation. J. Atm. and Terr. Physics, Vol. 38, 495-499.

Ostrow, S. M. (1962): Handbook for CRPL Ionospheric Predictions. NBS Handbook 90, U.S. Dept. of Commerce.

Roberts, W. M., and R. K. Rosich (1975): Ionospheric Predictions, Vols. 2, 3, and 4. Office of Telecommunications Research and Engineering Report 13, OT-TRER 13, U.S. Dept. of Commerce.

A SIMPLIFIED COMPUTER METHOD FOR LONG-TERM CALCULATION OF HF SKY-WAVE CIRCUITS

by: Armel A.E. Picquenard
Professor, Instituto Tecnológico de Aeronáutica - ITA
Centro Técnico Aeroespacial - CTA
12200 São José dos Campos - SP, Brazil

and: Eurico Rodriques de Paula
Research Assistant, Instituto de Pesquisas Espaciais - INPE
Conselho Nacional de Desenvolvimento Científico e Tecnológico - CNPq
12200 São José dos Campos - SP, Brazil

When planning a new HF station (Broadcast, AFTN, Coastal station, etc.), the frequencies, transmitter power, and antennas, must be selected to supply the required service during 10-20 years.

Consequently, previsions for the signal-to-noise ratio must be calculated for maximum and minimum solar activity, for various months of the year, for various hours of the day, and for the available frequencies, hence being interesting that the computation time be short.

After discussing most of the proposed computational methods, and evaluating the influence of various parameters, a simplified program has been developed, for the case of Brasil, and for short and medium ranges, till some 4,000 Km. In this case, in Brazil, the geomagnetic latitude is low, simplifying the problem.

Computational time, including signal-to-noise calculation, and for a complete solar cycle, is 3 - $3\frac{1}{2}$ minutes for three frequencies, with the B-6700 Burroughs computer.

1. INTRODUCTION

The program described in this paper is intended to supply the necessary information to the designer of HF radio stations, such as tropical wave or HF broadcast stations, airport stations, costal stations, etc.

An analysis of this type of problem has been made by Haydon et al., 1969, in a qualitative way. Our aim will be to transform those ideas in numerical values, to allow the designer to select frequencies, transmitter power and antenna types.

As the main factor of the service grade is the signal-to-noise ratio,

the program must compute the signal received power as well as the mean atmospheric noise power, which in Brazil is very high and is, generally, the dominant type of noise.

The transmitting stations will remain in operation during 10 to 20 years, therefore, calculations must be made for the extreme values of the Wolff number, stated in $R_{12} = 10$ and $R_{12} = 110$ respectively. For both values, the months of March, June, September and December are regarded as typical ones for the grade of ionization and for the atmospheric noise. Each of them is examined, and for each of the referred month calculations are made for each even hour (UT). If we study the circuit in 3 frequencies, we will need 288 calculations, hence the interest in having a fast program.

From another side, sophisticated programs are rather disappointing (CCIR, 1978b), so we can question the advantages of such sophistication, which requires a very extensive use of "loops", due to "cut-and-try" processes. This is peculiarly put in evidence in the 2nd CCIR Method (CCIR, 1978a), and increases the computation time very much.

Based on the above considerations, we attempted to build a program retaining only the strictly indispensable calculations to reach a reasonable accuracy, and without "loops". For this purpose, we have discussed the possible influence of the parameters involved, as will be explained later (item 2).

Another important consideration has been that more than 90% of the HF circuits installed in Brazil are less than 4,000 Km long, and, consequently, remain in low geomagnetic latitude. A circuit of rather short length means less propagation modes to be examined, and a low geomagnetic latitude permits the adoption of a constant "system excess loss" (CCIR, 1970), thus saving some computation. Consequently, we decided to limit our program to a length of 4,000 Km.

2. BASIS FOR OUR PREDICTION TECHNIQUE

The next point has been to discuss the actual importance of the computational processes used in the former methods (CCIR, 1970; Haydon and al. 1976; Laitinen and al., 1962; Lucas and al., 1966), and the grade of influence of the parameters involved, taking into account the limiting values they can have.

2.1. The deviation of the rays by the E-layer

In CCIR, 1970, an account is given of the deviation of the rays when going through the E-layer. (Figure 1).

With the geometry of Figure 1, using $R_0 = 6,371$ Km, $h_m E = 110$ Km, and making $\alpha = \alpha_E$, as suggested by Rawer, 1960, we find

$$\sin \alpha = 0.983 \cos \Delta \qquad (1)$$

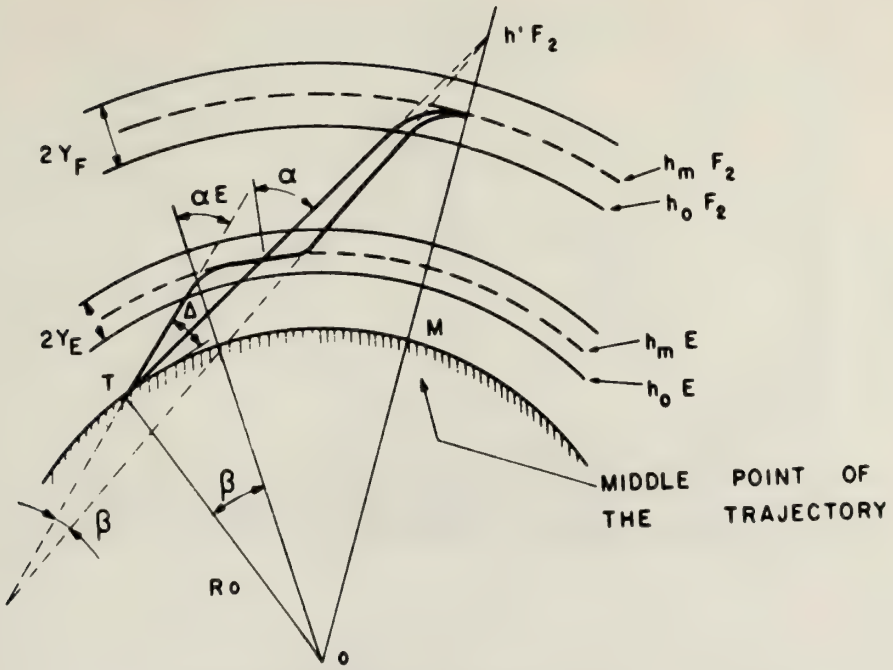


Fig. 1 - GEOMETRY FOR THE DEVIATION BY THE E-LAYER

Putting Z for the percent difference between the used frequency f and the maximum frequency that the E layer can reflect, we can write:

$$U = \frac{f_0 E \sec \alpha}{f} = \frac{1}{1 + 0.001Z} \qquad (2)$$

We can now calculate β versus Δ and Z. The result of this calculation is given in Figure 2.

As it is very difficult to use departure angles $\Delta < 5^0$, and as for $Z < 1$ we are very near of the reflection by the E-layer, we conclude that β will be always very small, and that we can neglect it in subsequent calculations.

It seems that the CCIR has reached the same conclusion, as CCIR, 1978a, does not more mention deviation by E layer.

2.2. Influence of $h'F,F_2$ on the calculation of signal received power

The virtual height of reflection by the F,F_2 layer depends on the frequency and on the geographic position of the reflection point. If we take into account the variation with frequency, the resultant computation is

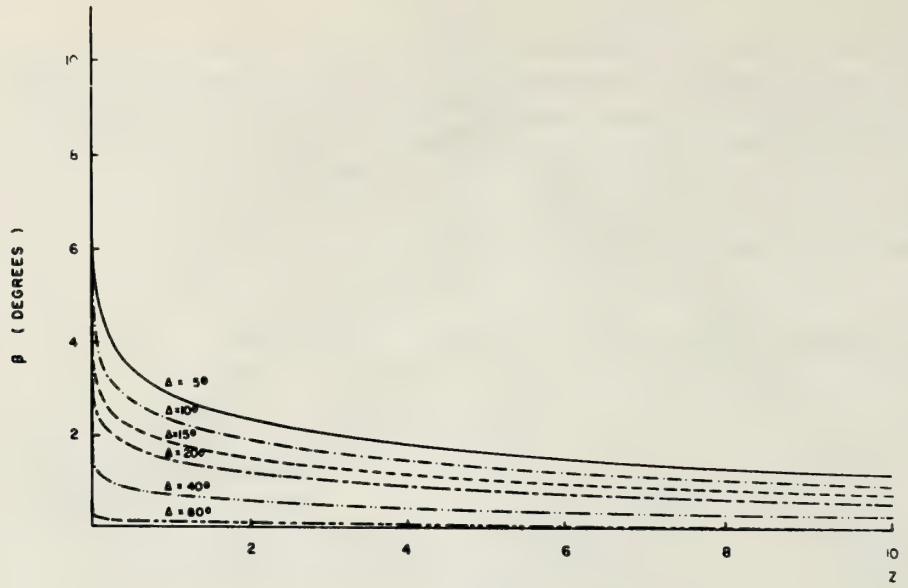


Fig. 2 - DEVIATION β VERSUS Δ AND Z

rather complex (CCIR, 1970; CCIR, 1978b). On the other hand, as we limit our circuit to a length of 4,000 Km, the reflection points in the case of the 2 x F mode, cannot be more distant than 2,000 Km, which limits the variation of $h'F,F_2$, between these points.

The variation of $h'F,F_2$ has two consequences: a variation of Δ, and hence of the gain of the antenna and, correlatively, a variation of the incidence angle on the D-layer, modifying the absorption. We shall examine the possible values of both effects.

2.2.1. Influence of $h'F,F_2$ on Δ

With the geometry of Figure 3, we obtain, for the case of 1 hop on the F,F_2 layer,

$$\frac{d\Delta}{dh'F_2} = \frac{1}{R_0} \frac{\sin\theta}{\left(1 + \frac{h'F_2}{R_0}\right)^2 - 2\left(1 + \frac{h'F_2}{R_0}\right)\cos\theta + 1} \qquad (3)$$

If we take R_0 = 6371 Km and $h'F_2$ = 350 Km, we have

$$\frac{d\Delta}{dh'F_2} = \frac{1}{6371}\left(\frac{\sin\theta}{2.1129 - 2.1099\cos\theta}\right) \qquad (4)$$

Differentiating for θ, we find that the maximum of $d\Delta/dh'F_2$ is reached for $\theta = 3{,}05^0$ (680 Km, value in agreement with the already published graphs) and

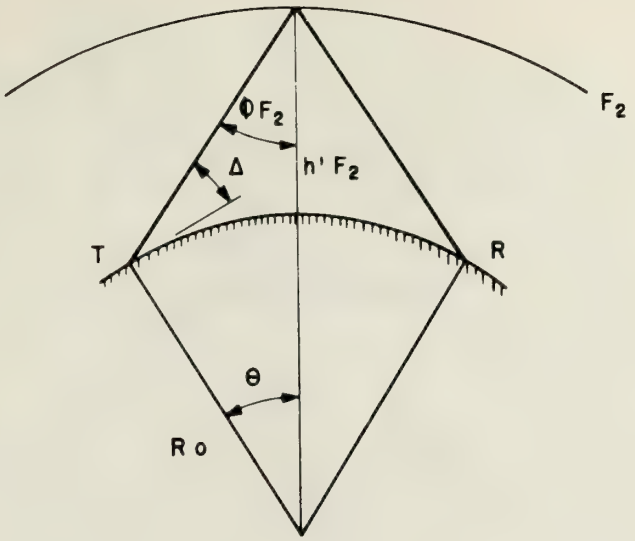


Fig. 3 - GEOMETRY FOR 1 HOP ON THE F-LAYER

that:

$$\left(\frac{d\Delta}{dh'F_2}\right)_{Max} = 0.0799^0 \text{ per Km}$$

This gives us $\pm 8^0$ for a variation of $\pm$ 50 Km of $h'F_2$.

In the case of 2 hops on the F,F_2 layer, we shall have the geometry of Figure 4.

Let us put $h_0 = (h_1 + h_2)/2$ and $h' = (h_2 - h_1)/2$, and assume that $h' << h_0$, using the subscript 0 for the values of the variables when $h' = 0$, and making $\Delta' = \Delta_0 - \Delta$.

After some approximations on the trigonometric functions, we find the following equations:

$$\begin{aligned} -R_0 \Delta' \sin \Delta_0 &= (R_0 + h_0 - h')(\phi_1 - \phi_0) \cos \phi_0 - h' \sin \phi_0 \\ &= (R_0 + h_0 + h')(\phi_2 - \phi_0) \cos \phi_0 + h' \sin \phi_0 \end{aligned} \qquad (5)$$

By means of these equations, and using again the geometry of Figure 4, we can calculate the difference Δ' between the true angle Δ and the angle Δ_0 calculated using $h_1 = h_2 = h_0$. For R_0 = 6371 Km, h_0 = 350 Km, h' = 25 Km and for a total distance of 4,000 Km, we find $\Delta' = 0.0049^0$.

In the same way, we can calculate the displacement $2R_0 (\theta_2 - \theta_0)$ of the

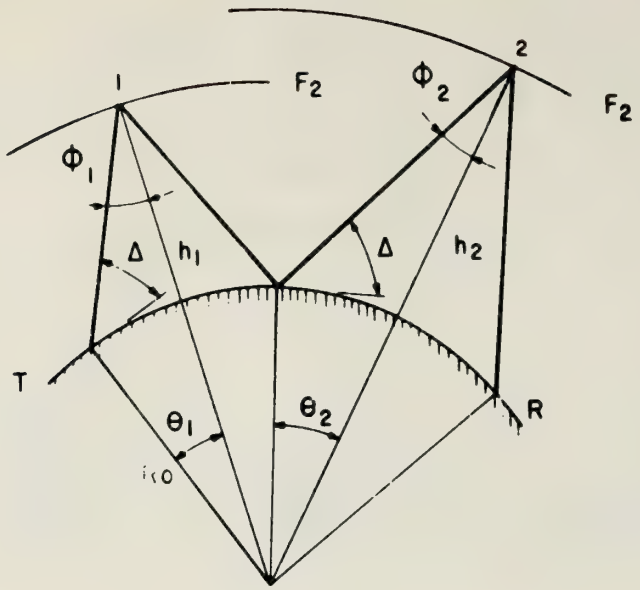


Fig. 4 - GEOMETRY FOR 2 HOPS ON THE F-LAYER

reflection point on the ground. With the same values of the data, we find 55 Km.

In view of these results, our conclusion is that we can use the mean value, h_0, of the virtual heights on both ionospheric reflection points, instead of the true values h_1 and h_2.

2.2.2. Influence of h' F,F_2 on the absorption

The angle of incidence on the D layer is a function of the angle of departure, which in turn varies with h'F,F_2, as seen in the preceding items. The figure 5 gives the geometry involved.

We have immediately:

$$\sin \phi_D = \frac{R_0}{R_0 + h_D} \cos \Delta$$

$$\tan \Delta = \frac{(h'F_2 + R_0) \cos \theta_{F_2} - R_0}{(h'F_2 + R_0) \sin \theta_{F_2}} \qquad (6)$$

$$D = 2 R_0 \theta_{F_2}$$

$$A \propto \sec \phi_D$$

These equations have been solved for h_D = 60 Km, and $250 \leq h'F_2 \leq 500$Km.

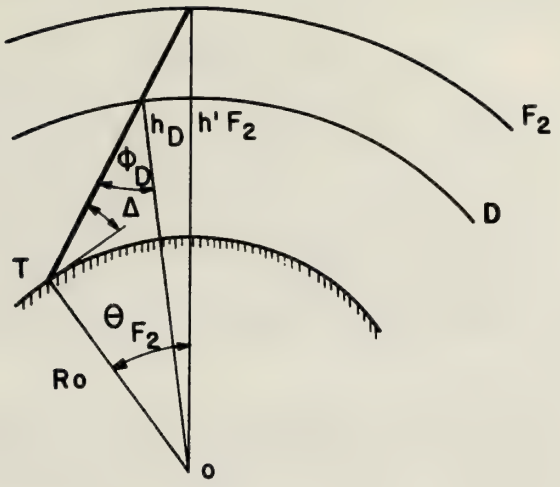


Fig. 5 - GEOMETRY FOR THE ANGLE OF INCIDENCE ON THE D-LAYER

The results are drawn, on the graph of the Figure 6, where sec ϕ_D is given as a function of D and $h'F_2$.

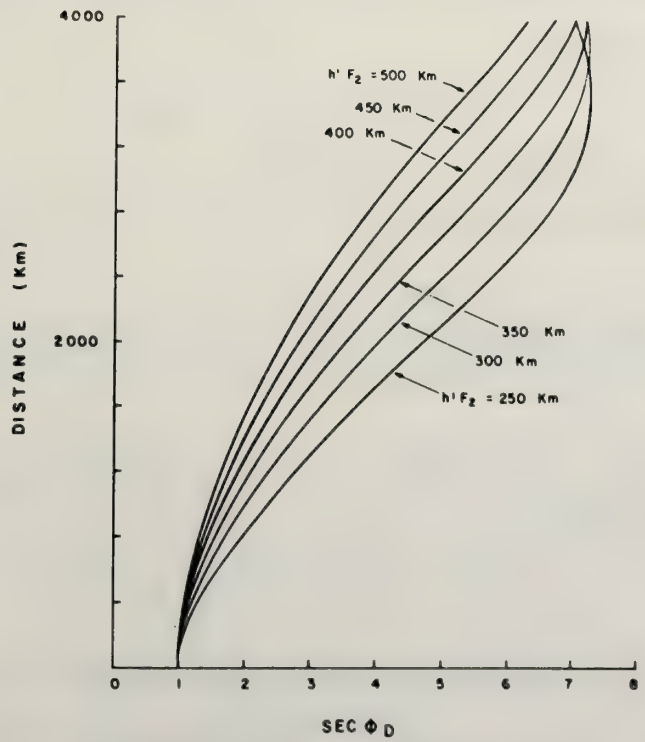


Fig. 6 - ABSORPTION AS A FUNCTION OF $H'F_2$ AND D

From this figure, we can conclude that, for a variation of $h'F_2$ of ± 50 Km, the variation of the absorption will be of the order of ± 15 %. As the calculation of the absorption is the weak point of all the methods, this inaccuracy is certainly tolerable.

2.3. Conclusions for our program

From the preceding discussion, we can draw the following conclusions:

a) The deviation of the ray by the E layer can be disregarded.

b) Due to the broad radiation diagram of the HF antennas, the values found for the error on Δ cannot substantially modify the gain of these antennas, for a variation of 50 Km of $h'F_2$.

c) In the case of 2 hops F,F_2, we can use the median of both values of $h'F,F_2$ without appreciable error.

d) The error on the value of the absorption for a variation of 50 Km of $h'F_2$ can be tolerated.

e) As the variation of $h'F_2$ with the frequency will be, in the worst case, of the order of 50 Km, we can use,without unacceptable errors, a fixed value of $h'F_2$, irrespective of the frequency.

3. OUTLINE OF OUR METHOD

As already mentioned, our method is intended to calculate MUF, signal received power, and mean atmospheric noise power for the following conditions:

- R_{12} = 10 and R_{12} = 110
- Months of March, June, September and December
- Even hours in UT

3.1. Propagation modes

We consider only the following modes:

- for $0 < D < 2000$ Km : 1E, $1F_2$, $2F_2$
- for $2000 < D < 4000$ Km : 2E, $1F_2$, $2F_2$

The possibility of existence of each mode is determined by the conventional method, examining the position of the used frequency in relation with the MUFs of the layers of interest, occultation of the F_2 layer by the E layer is also examined.

We don't consider the probability of existence of the various modes, however we calculate FOT and HPF. The signal received power is calculated for the strongest mode.

3.2. MUF

3.2.1. E-MUF

First, we calculate the MUF(2000)E by the formulas proposed in Lucas and Haydon, 1966.

$$MUF(2000)E = 3{,}41 + 38.431 - 68.071^2 + 89.971^3 - 70.971^4 + 29.511^5 - 4.991^6 \text{ MHz} \quad (7)$$

with:

$$I = J(1 + 0.0037\ R_{12})(\cos\ 0.881\ \chi)^{1,3} \qquad (8)$$

Where χ is the solar zenithal angle.

For $\chi > 102^0$, we take I = 0. We take J = 1.

The MUF(2000)E is transformed in MUF(D)E by means of the well-known nomogram (CCIR, 1967). No allowance is made for variations of the E-MUF with time.

3.2.2. F_2-MUF

The calculation of the monthly median value of F_2-MUF is made exactly as explained in the CCIR Report 340 (CCIR, 1967), except that the nomogram of page 396 of the referred document has been transformed into algebraic formulas.

Later, allowance is made for the statistical distribution of the MUF, by calculating the values of the deciles: FOT, with a probability of 90%, and HPF, with a probability of 10%. This is made by multiplying the monthly median values of the MUF, as calculated above, by the coefficients given in the Table 5.1 of CCIR, 1970.

3.3. Angles of departure

The virtual heights of reflection used are:

- for the E layer : 105 Km
- for the F_2 layer : those given by (Laitinen and Haydon, 1962), translated from a geographic map to a numerical matrix, for $+ 5^0 \leq \Phi \leq - 35^0$ and for the even hours in local time.

Using these data, simple geometrical reasonings give the angle of departure Δ for the various modes.

The angle Δ, for the modes F_2, allows us to calculate the skip-distance for the E layer and for this angle. The frequency of occultation by E is now deduced in the same way as in item 3.2.1.

3.4. Attenuation

The attenuation suffered by the waves is the sum of the free-space attenuation along the geometrical paths, the ionospheric attenuation, and the reflection loss on the ground.

3.4.1. Free-space attenuation

We use a method suggested by Laitinen and Haydon, 1962. First, the attenuation A_1, in free space and for the distance on the great-circle, is calculated. After this, the following formula, deduced from Figure 56 of the above reference gives the complement of atenuation due to the actual path

$$A_2 = 0.823733\ 10^{-1} + 0.808697\ 10^{-2}\Delta + 0.243386\ 10^{-2}\Delta^2$$
$$- 0.470163\ 10^{-4}\Delta^3 + 0.566952\ 10^{-6}\Delta^4 \qquad (9)$$

3.4.2. Ionospheric attenuation

This attenuation is calculated for each hop by the following formula (CCIR, 1970; Lucas and Haydon, 1966).

$$A_i = \frac{677{,}2 \sec \phi}{(f+f_H)^{1\cdot 98} + 10.2} (1 + 0.0037\ R_{12})\ [\cos(0.881\chi)]^{1\cdot 3} \qquad (10)$$

Where ϕ is the angle of incidence at a heigth of 100 Km. For $\chi > 102^0$, the product of the two last factors is taken as 0.1.

3.4.3. Reflexion loss on the ground

This loss is calculated as indicated in CCIR, 1970. A matrix covering the ranges $+ 15^0 \leq \Phi \leq - 55^0$ and $- 90^0 \leq \lambda \leq - 34^0$ discriminantes between "sea" and "ground".

3.4.4. Excess loss

As indicated by CCIR, 1970, an excess loss is added. For low geomagnetic latitude, this loss is given in 9 dB by the referred document.

3.5. Noise

The atmospheric noise factor, Fam, is calculated according to Zacharisen and Jones, 1970, and corrected for the actual passband of the receiver, b, by the formula:

$$P_N = Fam + 10 \log_{10} b - 204 \quad dBW \qquad (11)$$

3.6. Signal-to-noise ratio

As a rule, the discrimination gain of the receiving antenna can be disregarded, so the received power will be given by

$$P_R = 10 \log P_T - \Sigma A \quad dBW \qquad (12)$$

Where P_T is the EIRP of the transmitter, in Watts, and ΣA is the sum of the attenuations. This gives

$$S/R = P_R - P_N \quad dB \qquad (13)$$

Provision is made for calculating the gain of the transmitting antennas by the formulas given in Lucas and Haydon, 1966, thus deducing the power of the transmitter, P_T.

4. CONCLUSIONS

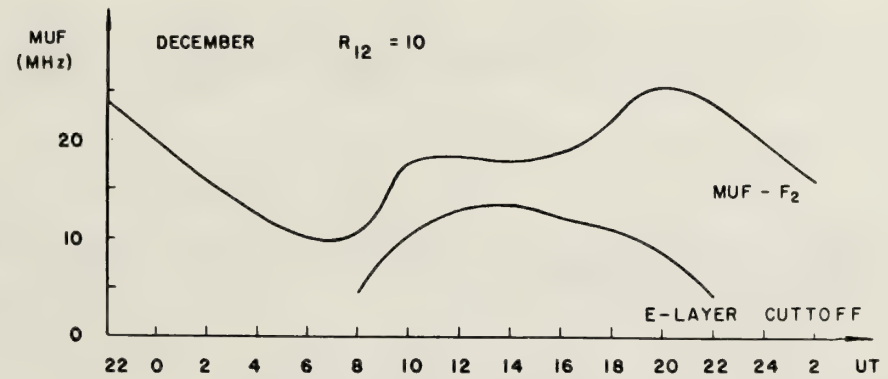
Limiting the range to 4,000 Km the area of utilization to the Brazilian region and discussing the type of calculation strictly needed to remain within a reasonable precision, we have developed a straightforward and fast program for the calculation of the performance of the HF circuits throughout a full solar cycle.

Comparing our results with those found by Barghausen, 1969 and by Lucas and Haydon, 1966 we have not found any significant difference.

5. SAMPLE CALCULATIONS

Figure 7 shows the MUFs for the path Rio de Janeiro (23.00^{0}S, 43.50^{0}W) to Belém (1.50^{0}S, 48.50^{0}W) for R_{12} = 10 e R_{12} = 110 on December.

Figure 8 shows the signal-to-noise ratio for the same path, R_{12} = 10 and R_{12} = 110, same month, for transmitting antenna gain of 1.8 dB, transmitting power of 1 Kw, receiver noise bandwidth of 100 Hz and operating frequencies of 13, 15 and 17 MHz. Those curves are interrupted for operating frequencies greater than the HPF and also for negative values of the signal-to-noise ratio. In this figure the symbols "+" represent points where the curves would be interruped for operating frequencies greater than the MUF and "0" points of interruption for operating frequencies greater than the FOT. The continuous line corresponds to 1F_2 mode and the dashed line the 2E mode.



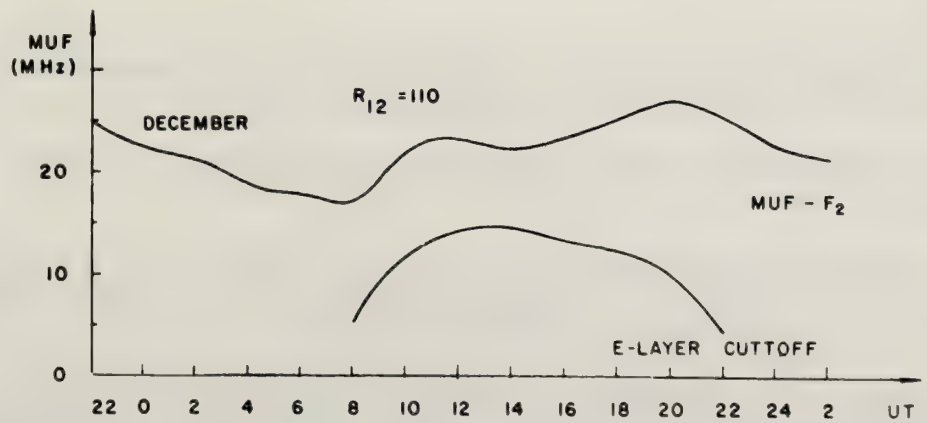


Fig. 7 - MUFs FOR THE RIO DE JANEIRO TO BELEM PATH FOR DECEMBER

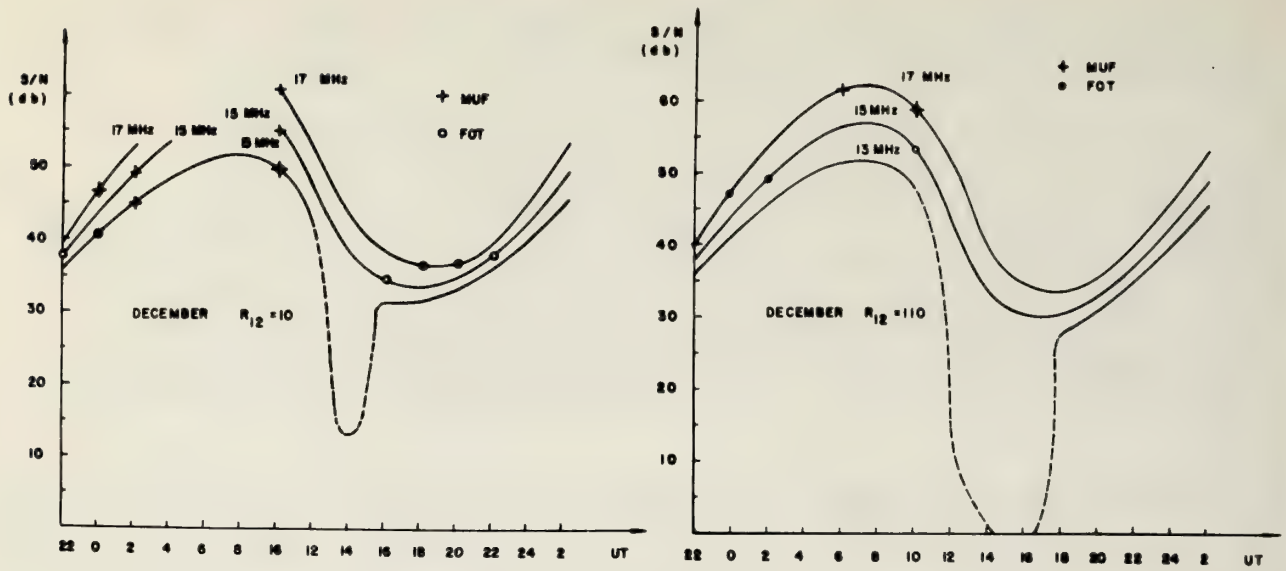


Fig. 8 - SIGNAL-TO-NOISE RATIO FOR THE RIO DE JANEIRO TO BELÉM PATH FOR DECEMBER, R_{12} = 10 and R_{12} = 110

6. REFERENCES AND BIBLIOGRAPHY

Barghausen, A.F., J.W. Finney, L.L. Proctor, and L.D. Schultz (1969): Predicting Long-term Operational Parameters of High-frequency Sky-wave Telecommunications Systems, ESSA Tech. Rept. ERL 110-ITS 78, Boulder, Col.

CCIR, 1964: World Distribution and Characteristics of Atmospheric Radio Noise, CCIR Rept. 322, ITU, Geneva.

CCIR, 1967: CCIR Atlas of Ionospheric Characteristics, CCIR Rept. 340, ITU, Geneva.

CCIR, 1970: CCIR Interim Method for Estimating Sky-wave Field Strength and Transmission Loss at Frequencies between the Approximate Limits of 2 and 30 MHz, CCIR Report 252-2, ITU, Geneva.

CCIR, 1978a: Draft Supplement to Report 252-2. Second CCIR Computer-based Method for Estimating Sky-wave Field Strength and Transmission loss at frequencies between 2 and 30 MHz, CCIR XIV th Plenary Assembly, Doc. 6/1070-E.

CCIR, 1978b: USA. Comparison of Methods used to Compute HF Sky-wave Field Strength, CCIR Special Preparatory Meeting (WARC-79), Doc. P/109-E.

Haydon, G.W., D.L. Lucas, and R.A. Hanson (1969): Technical Considerations in the Selection of Optimum Frequencies for High-Frequency Sky-wave Communication Services, ESSA Tech. Rept. ERL 113-ITS 81, Institute for Telecommunication Sciences, Boulder, Col.

Haydon, G.W., M.Leftin, and R. Rosich (1976): Predicting the Performance of High Frequency Sky-wave Telecommunication Systems (The use of the HFMUFES 4 Program) OT Report 76-102, Boulder, Col.

Jones, W.B., and R.M. Gallet (1962): Methods for Applying Numerical Maps of Ionospheric Characteristics, Journal of Research of the NBS, Vol.66 D, Nr. 6, pp. 649-662.

Jones, W.B. R.M. Gallet, and M. Leftin (1966): Advances in Ionospheric Mapping by Numerical Methods, NBS Technical Note 337, Boulder, Col.

Laitinen, P.O., and Haydon, G.W. (1962): Analysis and Prediction of Sky-wave Field Intensities in the High Frequency Band, Tech. Rept. 9, U.S. Army Signal Radio Propagation Agency, Fort Moumouth, N.J.

Leftin, M., S.M. Ostrow and C. Preston (1967): Numerical Maps of Monthly Median h'F,F_2 for Solar Cycle Minimum and Maximum, ESSA Tech. Memo. IERTM - ITS A69, Boulder, Col.

Lucas, D.L., and G.W. Haydon (1966): Predicting Statistical Performance Indexes for High Frequency Ionospheric Telecommunication Systems, ESSA Tech. Rept. IER. 1 -ITS A 1, Boulder, Col.

Lucas, D.L., and Harper, J.D.Jr. (1965) A Numerical Representation of CCIR Report 322 High Frequency (3-30 MC/S) Atmospheric Radio Noise Data,National Bureau of Standards Technical Note 318, Washington, D.C.

Picquenard, A.A.E. (1974): Radio Wave Propagation, McMillan, London.

Rawer, K. (1960): Radio Propagation between a Space Vehicle and the Earth in the Presence of the Ionosphere, Space Research, Proceedings of the First International Space Science Symposium,NICE, pp. 245-271.

Zacharisen, D.H., and Jones, W.B. (1970): World Maps of Atmospheric Radio Noise in Universal Time by Numerical Mapping,(draft) Boulder, Col.

PREDICTION OF foF2 BY THE MONTHLY RATIO(MR) METHOD

P. S. N. Murthy
All India Radio
Bhadravati, India

C. S. R. Rao
All India Radio
Jullundur, India

Mangal Sain
All India Radio
Research Department
Indraprastha Estate
New Delhi-110002, India

CCIR (Geneva, 1974) at present recommends (RED.371-2) the use of the R12 method, or the smoothed Sun Spot Number method, for predictions up to one year or more and the IF2 method or the Ionospheric Index method developed by U.K. for predictions up to 6 or 7 months. All India Radio (AIR) has so far been using the R12 method for predicting foF2. This method suffers from the "saturation effect". Both short and long-term predictions by this method have been shown to possess a considerable degree of error (Naismith et al, 1962).

The monthly ratio (for any month and hour) is the ratio of the monthly median foF2 for the month and hour to the corresponding value of the previous month. The ratios are calculated for at least one sun-spot cycle or preferably more, for any particular place. The median value of these ratios is taken to represent the value of MR for the particular month and hour for prediction purposes. The prediction now becomes a simple affair. One just has to take the observed foF2 for the latest available month and successively multiply this value by MRs of the succeeding months until the particular month for which the prediction is required, is reached. Predictions by the MR method are based on measured foF2 values and are free from the saturation effect. They do not entirely depend upon solar activity and do not use the twelve month running mean values of the index for the calculations.

Initial study on this method was done by All India Radio (AIR) in the early sixties (Rao and Sain, 1965). The study was intended mainly to find out the suitability of the method and was confined to noontime foF2. Madras, Delhi and Washington, representing low, middle and high latitude stations, were selected for the study. A more detailed investigation of the method has recently been made for the equatorial station at Kodaikanal (Geomagnetic latitude 0^{-o} 44'N), and the scope of the study was extended to eight hours instead of only midday.

Points of interest in the present study are: (i) MR predictions up to 3 months, including one-month and two-month predictions, had been considered in the earlier study, whereas every MR prediction is now for three months. (ii) R12 values based on measured Zurich Sun Spot numbers had been utilized earlier for prediction purposes. Now the latest predicted values of R12 (published by the Swiss Federal Observatory, Zurich) and IF2 (published by the Science Research Council, England), which would be available for the month for which the prediction by the MR method has been made, have been utilized. (iii) Data collected for a considerably long period of 16 years has been utilized for study (Radio Research Committe [India] - A Series, 1956-1972).

Table 1. Monthly Ratios for Kodaikanal.

Time IST	Year:	1956	1957	1958	1959	1960	1961	1962	1963	1964	1965	1966	1967	1968	1969	1970
	Month															
0800	Mar.	1.12	1.27	1.12	1.07	1.04	1.07	1.11	1.10	1.14	1.09	1.10	1.10	1.02	1.26	1.10
	June.	0.92	0.97	0.90	0.94	0.96	0.96	0.94	0.95	0.93	0.97	0.93	0.93	0.90	0.91	0.95
	Sept.	1.09	1.11	1.11	1.07	1.12	1.04	1.16	1.08	1.18	1.06	1.06	1.10	1.09	1.08	1.02
	Dec.	0.94	0.93	0.97	0.93	0.88	0.93	0.86	0.87	0.99	0.89	0.92	0.96	0.91	0.91	0.94
1300	Mar.	1.21	0.95	1.05	1.08	1.08	1.09	1,23	1.13	1.34	1,21	1.22	1.12	1.00	1.16	----
	June	0.90	1.03	0.97	0.94	0.98	0.96	0.94	0.94	0.88	0.98	0.87	0.96	0.93	0.99	0.94
	Sept.	1.04	1.00	1.08	0.99	1.04	0.99	1.15	1.06	1.07	1.05	1.02	1.04	1.00	1.17	1.09
	Dec.	0.92	0.88	0.97	0.94	0.90	0.94	0.85	0.89	0.91	0.88	0.96	1.11	1.01	---	0.81

IST = UT + 5½ hours

Table 2. Monthly ratios for Kodaikanal(median values).

Month	Time: IST	0000	0400	0600	0800	1200	1600	1800	2000
January		0.97	0.92	0.79	0.95	0.97	0.98	1.00	1.00
February		1.17	1.14	1.04	1.02	1.01	1.08	1.05	1.06
March		1.28	1.21	1.41	1.10	1.02	1.03	1.13	1.11
April		0.99	1.06	1.23	1.04	1.01	1.02	1.00	1.03
May		0.75	0.85	1.04	0.94	0.96	0.91	0.97	0.94
June		0.82	0.75	0.93	0.94	0.95	0.95	0.96	0.92
July		1.00	0.97	0.94	0.95	0.97	0.95	0.96	1.00
August		1.28	1.05	0.98	1.04	1.04	1.00	1.01	1.10
September		1.25	1.00	1.07	1.09	1.07	1.16	1.04	1.09
October		1.05	1.10	1.08	1.05	1.05	1.04	0.98	1.00
November		0.88	0.94	0.89	0.95	1.02	0.95	0.92	0.91
December		0.83	0.96	0.83	0.93	0.95	0.93	0.92	0.90

IST = UT + 5½ hours

The study has been made for the following 8 hours of the day, namely, 00, 04, 06, 08, 12, 16, 18 and 20 hours. Monthly ratios have been calculated for all the twelve months and for all the years. A few typical values of MRs so obtained are shown in Table 1. It may be seen from the table that the values of MRs vary around a mean or median and the range of variation is generally very small barring minor exceptions. Median values of MR required for prediction purposes have been arrived at from the calculated MRs for all the years. These are shown in Table 2.

To study the effect of sunspot numbers upon the values of MRs, calculated MRs were plotted against corresponding values of R12. During the period under study, R12 varied from 10 to 200. The best fit line for MRs for most of the cases was found to be parallel to R12 plotted as the abscissa. This shows that MRs are totally independent of sunspot numbers.

Predictions of foF2 by the three methods, MR, IF2 and R12, have been worked out for the five years, 1956, 1957, 1968, 1969, and 1970. Percentage deviation from measured values of foF2 have been calculated for all the predictions and the results are summarized in Table 3. It may be seen that MR method is comparable to IF2 method and better than R12 method.

Table 3. Percentage of predictions within 10% of observed values of foF2 at Kodaikanal.

	Year				
Method	1956	1957	1968	1969	1970
MR	70	62	65	63	68
IF2	68	61	72	70	61
R12	59	31	57	64	52

In an earlier study on IF2 undertaken in the Research Department of AIR, it was observed that IF2 is affected by the "saturation effect" during evening hours in the case of equatorial stations (for example Madras and Kodaikanal) when the values of R12 exceed 120 and are in the range of 150 to 200. During 1956, R12 rose from 80 to 160 and it reached a maximum of 200 during 1957. Predictions for evening hours only (16, 18, 20, and 00 Hours) for the years 1956 and 1957 were therefore picked and compared. The results are given in Table 4. It is seen that MR method gives better prediction compared to the other two methods during periods of high solar activity for low latitude stations.

Table 4. Percentage of predictions within 10% of observed values of foF2 at Kodaikanal (evening hours only).

	Year	
Method	1956	1957
MR	77	58
IF2	64	45
R12	60	13

Summarizing, the MR method is likely to become useful for making short-term predictions of foF2. Its greatest virtue is its simplicity. All one has to do is to take the latest observed foF2 (monthly median) and multiply this by MRs of the succeeding months. The other point in its favor is that it is free from the saturation effect noticed in the other two methods. The method appears promising and deserves, perhaps, a more thorough investigation and by different countries to assess its utility. The investigation made so far relates to one station and for 8 hours of the day only. Further work is in progress.

REFERENCES

Naismith, R., H. C. Bevan and P. A. Smith (1962): Proceeding of the Institution of Electrical Engineers , 109 125.

Rao, C. S. R., and Mangal Sain (1965): Prediction of Critical Frequency of F2 Layer., J. Institution of Telecommunication Engineers (India), Vol. 11, No. 8, pp 271-281.

HF COMMUNICATION PROBLEMS AT LOW LATITUDES DUE TO STEEP SPATIAL AND TEMPORAL GRADIENTS

D. R. Lakshmi, S. Aggarwal, P. K. Pasricha and B. M. Reddy
National Physical Laboratory
New Delhi - 110012, India

Very frequent degradation in ionosphere-supported communication occurs at low latitudes due to large temporal and spatial gradients. The dynamic situation during early morning hours and the horizontal gradients in F-region electron density associated with the equatorial anomaly cause unusual difficulties in the choice of operational frequencies. The magnitude and the morphology of these problems are discussed to keep the prediction users aware of the conditions.

1. INTRODUCTION

The tropospheric and ionospheric communication group at the National Physical Laboratory has been responsible for issuing predictions of the radio environment as well as for rendering advisory services for radio communication organizations in India for more than 15 years. During this period, several problems related to HF communications, which are particularly serious at low latitudes, have arisen. This paper describes the origin of these problems and suggests possible reasons and remedies.

Two most serious problems are caused by (a) large local time variations of critical frequencies (f_oF_2), especially during sunrise hours, and (b) large horizontal latitudinal gradients in the F-region electron densities associated with the geomagnetic anomaly. Similar problems may arise with respect to the gradients in the mid-latitude trough region at night; however, no discussion on this aspect is included here since this paper is restricted to low latitude issues.

2. PROBLEMS FROM STEEP TEMPORAL GRADIENTS

The local time gradients during sunrise hours are known to plague HF communications, particularly at low latitudes (Aggarwal et al., 1976). This problem is extremely important in countries where the mainstay of point-to-point communications continues to be the HF band supported by the ionosphere. Consider the following:

(a) HF link operators are expected to get their frequencies cleared from the appropriate governmental authority well in advance and it is usual practice to fix one frequency for the daytime and another for the nighttime. The use of the night frequency during sunrise will require much more power than is normally permitted while the frequency allocated for the daytime will be higher than the MUF during the transient period.

(b) Point-to-point links normally use inexpensive tuned directional antennas, and frequent change of operational frequency is deleterious from the point of view of antenna efficiency.

(c) In case of long distance circuits in the East-West direction involving multi-hop F-region propagation, the problem of the sunrise period will extend to a large number of hours, because the different F-region reflection points will fall in the transient location at different periods.

Figure 1 shows the diurnal variation in foF2 for Kodaikanal and Ahmedabad for winter during low solar activity. The normalized hourly percentage changes in foF2 are shown in the lower portion of the figure. The significance of the percentage changes is important because, even assuming that changes in the link frequency are permitted, antenna design considerations restrict such changes. The normalized percentage changes are calculated using the following relation:

$$\text{Normalized percentage change in } (foF2)_{\text{hour x}} = \frac{(foF2)_{\text{hour (X + 1)}} - (foF2)_{\text{hour x}}}{(foF2)_{\text{hour x}}} \times 100$$

The most important feature of this diagram is the extremely steep percentage increase in foF2, which is as high as 230 percent at 5 A.M. for Kodaikanal. Of course, the very low nighttime minimum values in foF2 at low latitudes are essentially responsible for these abnormally high percentage increases. It may also be noticed from the figure that the dusk changes are not so spectacular, especially when the percentage changes are considered.

Figure 2 shows variation of normalized percentage changes in foF2 at dawn for Kodaikanal and Brisbane during the years 1957 to 1967. The solar activity variations, modulated by seasonal variations as the running average sunspot number decreased from about 200 to 10, are very obvious. The magnitude of variations at Brisbane (Geo. Mag. Lat. 35.7^{0}S) during dawn are only marginal and show very little solar activity dependence. For Kodaikanal (Geo. Mag. Lat. 0.8^{0}N), however, the percentage changes are spectacularly large and the variation with solar activity is very significant. A very interesting feature is that during high solar activity the percentage values are larger at Brisbane, whereas at Kodaikanal the changes are insignificant. This figure convincingly demonstrates the seriousness of this problem at low latitudes for medium and low solar activities. The incidence of this problem at various stations combining seasonal and solar activity variations is depicted in Figure 3. The data employed for this study pertains to the year 1958, representing high solar activity, and the year 1965, representing low solar activity. The salient features that can be observed from these histograms are:

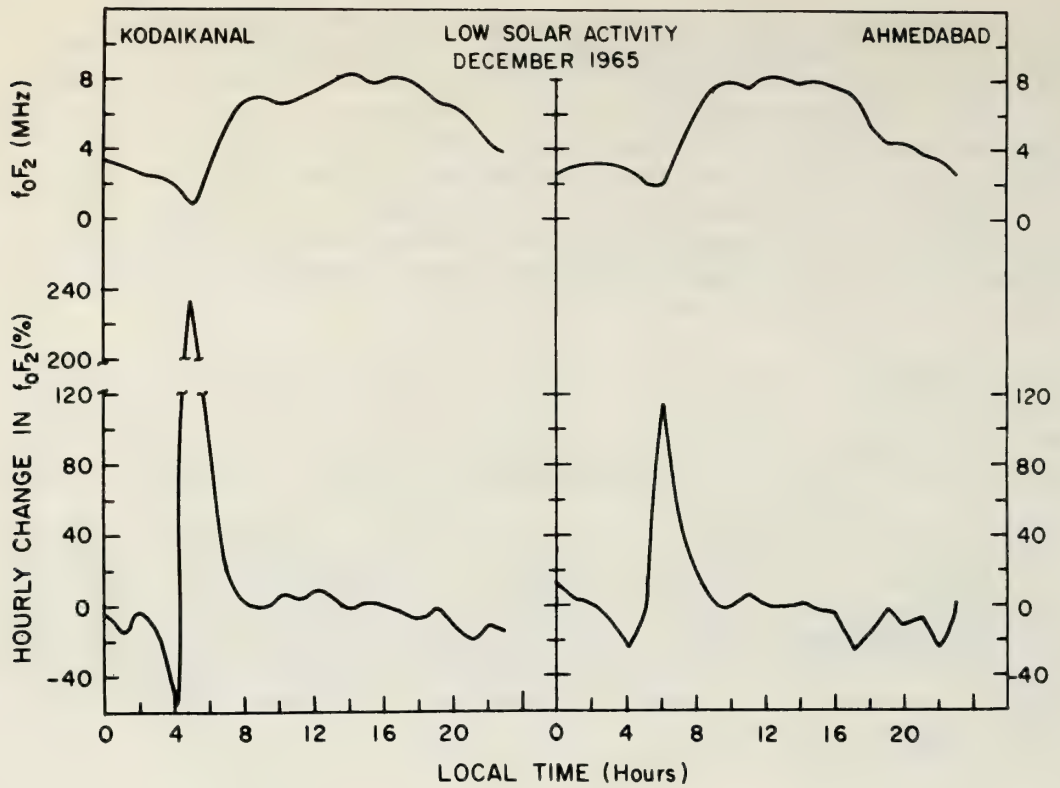


Figure 1. Diurnal variation of foF2 and the corresponding normalized hourly percentage changes in foF2 for Kodaikanal and Ahmedabad. A remarkably large percentage increase of 230% in foF2 for Kodaikanal at 0500 LT is an important feature to be noticed.

1. Percentage changes in foF2 are dependent on solar activity, especially at low geomagnetic latitudes.

2. The spectacularly large changes can be observed only at Kodaikanal which is almost on the geomagnetic equator. The changes gradually decrease with increasing geomagnetic latitude reaching very marginal values at latitudes around 30° and above. See Figure 3.

It may be repeated again that the main contribution for these apparently spectacular large percentage changes at very low geomagnetic latitudes is the very low nighttime electron densities in the F-region. However, as soon as the sun strikes the F1 layer level at dawn, the low latitude F2 region builds up much more rapidly than at middle latitudes. This is further accentuated by the fact that at low geomagnetic latitudes there is a steep decrease in foF2 even beyond midnight, bringing down foF2 to a very low value at 0400 hours local time. This problem is less serious during the dusk hours as may be seen from Figure 1. However, at middle and higher latitudes, gradients during dusk hours may be as large as during dawn hours partly because of an evening enhancement in foF2 followed by a sudden decrease after sunset (Evans, 1965).

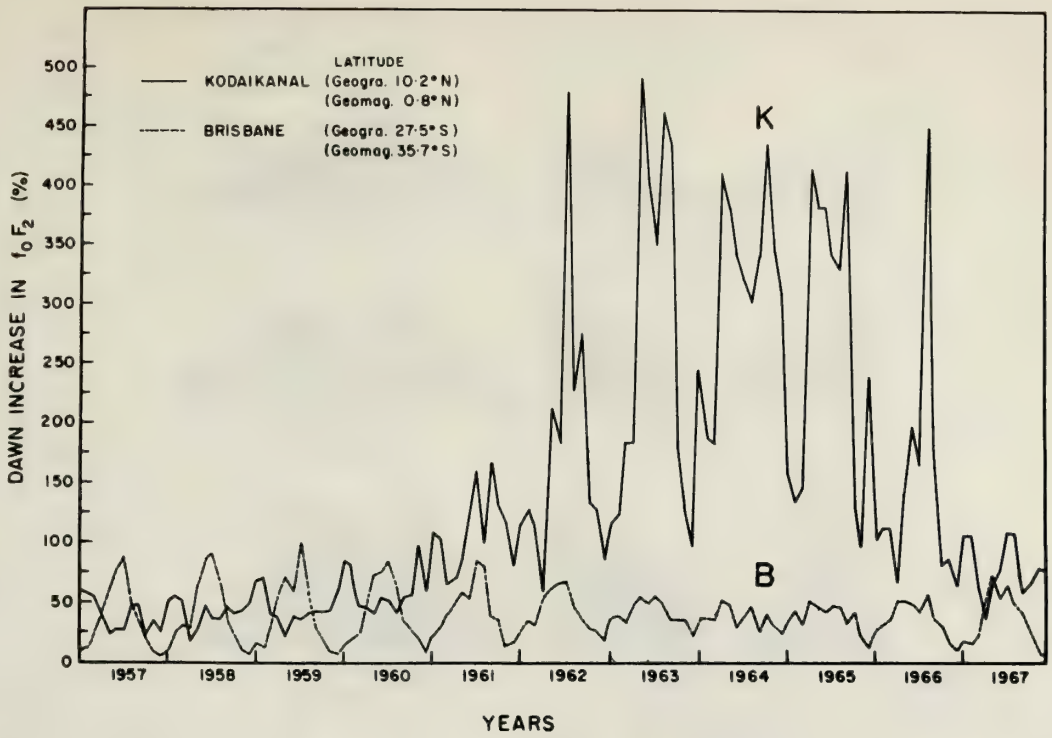


Figure 2. Spectacularly large values of percentage increase in foF2 for Kodaikanal during medium and low activity periods can be noticed here. The latitudinal dependence of foF2 changes near dawn can be appreciated by comparing Kodaikanal and Brisbane.

3. PROBLEMS DUE TO LARGE SPATIAL GRADIENTS IN THE EQUATORIAL ANOMALY REGION

The equatorial zone of approximately 30^0 wide centered at the geomagnetic equator exhibits several peculiar ionospheric properties, one of which is the large spatial gradients that affect ionospheric radio propagation in a number of ways. The phenomenon of trans-equatorial propagation, whereby frequencies as high as 100 MHz can be reflected by the ionosphere in trans-equatorial paths, has been studied in detail (McCue and Fyfe, 1965; Neilson, 1966; Bowen et al., 1968; Tao et al., 1970; Anastassiades and Antoniadis, 1972; McNamara, 1973; Neilson and Crochet, 1974). Several suggestions were made about the possible mode of this propagation, for example, ionosphere-to-ionosphere reflection such as $^nF2$ propagation, exospheric field guided propagation, etc. However, the problem discussed here does not concern trans-equatorial propagation, but propagation within one hemisphere itself where anomalous communication is possible, because of large horizontal latitudinal gradients. For example, if we consider the anomaly peak in the northern hemisphere to be at 15^0N geomagnetic latitude, if a north-south HF circuit is operating such that the reflection point is on either of the sides of the peak and if the frequency of the link is very close to the MUF, a peculiar situation arises. If the point of reflection is equator-ward of this

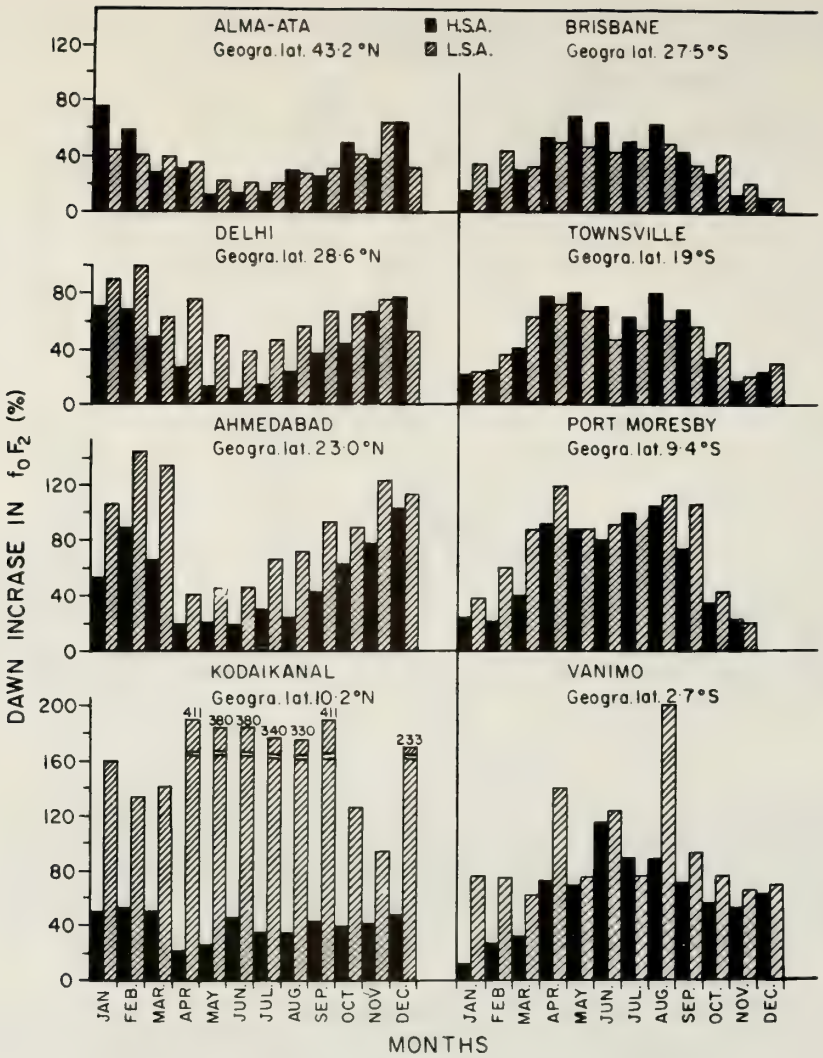


Figure 3. The seasonal variation of dawn enhancements at different latitudes during both high and low activity periods. The dawn time changes decrease with increasing latitude and increasing solar activity.

anomaly peak, the radio waves incident on the ionosphere for the northern circuit will continuously come across increasing levels of electron density on two counts (a) due to the vertical gradient as the radiowave penetrates higher into the ionosphere (b) due to the horizontal gradient as the wave progresses in the direction of increasing electron density. On the other hand for the same link in the return direction, the horizontal gradient is reversed. Thus the real MUF values for the two opposite directions in the same circuit can vary by a large margin depending on the angle of incidence and on the magnitude of the horizontal gradient. In fact, rather frequently, especially when the operating frequency is close to the MUF (calculated ignoring horizontal gradients), only one way communication would be possible. This has been one of the unusual complaints in the Indian Subcontinent.

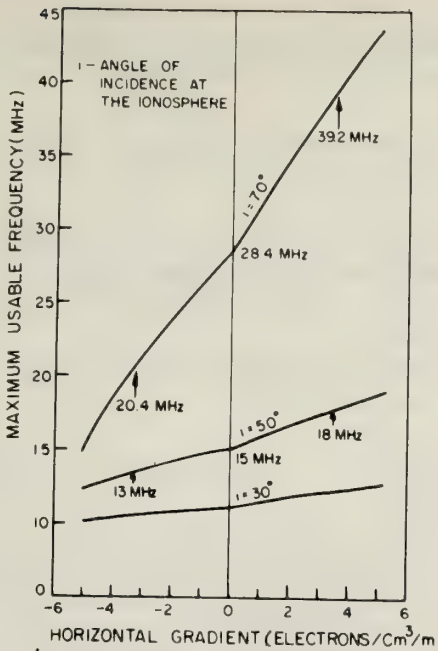


Figure 4. The effect of horizontal electron density gradients on maximum useable frequencies. The consequences can be serious for high angles of incidence - that is for long path distances.

To understand the magnitude of this problem, we have used the Alouette II data (fxF2), so that spatial resolution of the data can be high compared to ground based data. Assuming simple parabolic distribution, vertical electron density profiles are derived in the F2 region and the latitudinal gradients at fixed heights are computed. These horizontal gradients along the ray path are compounded with the vertical gradients to calculate the change in the real MUF for varying magnitudes of horizontal gradients (Lewis, 1953). Figure 4 shows some sample results of the change in MUF for different gradients for three angles of incidence. As expected, the shift in the MUF increases with increasing angles of incidence (at the ionosphere). It has been observed that gradients between 3 to 4 electrons per cubic centimeter per meter are usually prevalent in the equatorial anomaly region. Figure 4 is given only to illustrate the problem and results from more rigorous three dimensional ray tracing methods, which confirm this, are beyond the scope of this paper. However, the point to be noted is that even for modest angles of incidence such as 50^0 and electron density gradients of 3.5 cm^{-3} m^{-1}, the shift in actual MUF is from 15 MHz to 18 MHz while in the opposite direction the effective MUF will fall to 13 MHz. Thus, employing a frequency higher than 13 MHz will result only in one way communication.

CONCLUSION

Very obviously, the solution for both the problems discussed in this paper is to take these situations into account while predicting the link frequencies. It has been found practical to get a third frequency assigned for the dawn hours and use an antenna system with appropriate bandwidth. Predictions of operational frequencies for North-South two way links at low latitudes should take the anomalous gradients into account and a frequency lesser than the reduced MUF must be used.

REFERENCES

Aggarwal, S., D. R. Lakshmi and B. M. Reddy (1976): Some problems of HF communication at low latitudes and possible solutions. Indian J. Radio Space Phys.,5:302.

Anastassiades, M., and D. Antoniadis (1972): Time delay measurements in the Athens (Greece) - Roma (Lesotho) VHF trans-equatorial propagation circuit. J. Atmos. Terr. Phys., 34:1215.

Bowen, E. D., W. J. Fay and J. L. Heritage (1968): VHF characteristics of the transequatorial ionosphere. J. Geophys. Res., 73:2469.

Lewis, R. P. W. (1953): The reflection of radio waves from an ionized layer having both vertical and horizontal gradients. Proc. Phys. Soc. (London), 66:308.

McCue, C., and D. Fyfe (1965): Transequatorial propagation: Task Bridger introductory review. Proc. IREE Aust., 26:825.

McNamara, L. F. (1973): Evening-type transequatorial propagation on Japan-Australia circuits. Aust. J. Phys., 26:521.

Nielson, D. L. (1966): Oblique sounding of a transequatorial path, Spread-F and its effects on radio wave propagation. AGARDograph, 95:467.

Nielson, D. L., and M. Crochet (1974): Ionospheric propagation of HF and VHF radio waves across the geomagnetic equator. Rev. Geophys. Sp. Phys., 12:688.

Tao, K.F. Ochi., M. Yamaoka, S. Watanabe, C. Watanabe and K. Tanohata (1970): Experimental results of VHF transequatorial propagation. J. Radio Res. Lab. Jap., 17:83.

PREDICTION OF THE CHARACTERISTICS OF A RADIO SIGNAL REFLECTED FROM A HORIZONTALLY-INHOMOGENEOUS IONOSPHERE AND THE RELEVANT REQUIREMENTS FOR PREDICTION OF IONOSPHERIC PARAMETERS

T. S. Kerblay, E. M. Kovalevskaya, E. M. Zhulina, and L. M. Ishkova
Institute of Terrestrial Magnetism, Ionosphere and Radio Wave Propagation of the Academy of Sciences of the USSR
Moscow Region, USSR

This report deals with the research connected with the calculations and the prediction of the characteristics of radio signals reflected from a horizontally inhomogeneous ionosphere. The methods for estimating radio signal characteristics (MUF, hop distance, angles of arrival in the vertical and horizontal planes) and the prediction manuals developed in IZMIRAN are considered. The requirements for accurate predictions of ionospheric parameters are discussed.

Advances in the studies of the decameter band radio waves have resulted in significant changes in the approach to the problem of determining radio signal propagation conditions.

A more comprehensive prediction of the maximum usable frequency (MUF), including trajectory characteristics (angles of arrival in the vertical and horizontal planes, etc.) and time delays of particular propagation modes, requires (1) a mathematical formulation that ensures sufficient accuracy for practical purposes, and (2) prediction of the parameters of the ionospheric layers and the horizontal components of their gradients.

With the purpose of predicting the trajectory and temporal characteristics of radio wave propagation in an inhomogeneous ionosphere, the Laboratory of Short Radio Wave Propagation of IZMIRAN has developed methods for estimating radio signal characteristics using either predicted or measured ionospheric parameters.

A basic method (disregarding the effects of the Earth's magnetic field and charged particle collisions) developed by Kerblay and Kovalevskaya (1974, 1977) has been transferred to the computer and the program written in ALGOL-60 has been distributed to the communication services.

The effect of the horizontal inhomogeneity of the ionosphere is determined from the integral values

$$\int \frac{\partial n}{\partial \theta} \, dS \equiv \delta_1$$

and

$$\int \frac{\partial n}{\partial \chi} \, dS \equiv \delta_2$$

where $\partial n/\partial\theta$ and $\partial n/\partial\chi$ are components of the horizontal gradient of the refractive index with respect to the coordinates θ and χ at the current point of trajectory; θ is the angular distance of the current point of trajectory in the plane of the great circle arc between the transmitter and receiver; χ is the angular deviation of the current point of trajectory from the plane of the great circle arc.

In the model, δ_1 and δ_2 may be presented as

$$\delta_1 = \int_{S_E} \frac{\partial n}{\partial\theta}\, dS + \int_{S_{EF}} \frac{\partial n}{\partial\theta}\, dS + \int_{S_{F2}} \frac{\partial n}{\partial\theta}\, dS \qquad (1)$$

$$\delta_2 = \int_{S_E} \frac{\partial n}{\partial\chi}\, dS + \int_{S_{EF}} \frac{\partial n}{\partial\chi}\, dS + \int_{S_{F2}} \frac{\partial n}{\partial\chi}\, dS \qquad (2)$$

The first terms in equations (1) and (2) characterize the contribution of the horizontal inhomogeneity of the E layer (δ_E) to the integral value of the horizontal gradient of the refractive index; the second terms define the contribution of the interlayer region (δ_{EF}); the third terms determine the contribution of the F2 layer (δ_{F2}). The characteristics of radio wave trajectories (hop distance, arrival angles in the vertical and horizontal planes) can be obtained by solving the set of the ordinary differential equations and analytical expressions

$$d\delta_1 = \frac{\partial n}{\partial\theta}\,(1+\tan^2\psi+\tan^2\phi)^{1/2}\, dR$$

$$d\delta_2 = \frac{\partial n}{\partial\chi}\,(1+\tan^2\psi+\tan^2\phi)^{1/2}\, dR$$

$$d\theta_i = \frac{\tan\phi}{R}\, dR \qquad d\chi_i = \frac{\tan\Psi}{R}\, dR$$

$$\tan\phi = \frac{(c+\delta_1)(1+\tan^2\psi\,\cos^2\phi)^{1/2}}{\{n^2R^2 - [(c+\delta_1)(1+\tan^2\psi\,\cos^2\phi)^{1/2}]^2\}^{1/2}}$$

$$\tan\psi = \frac{\delta_2\,\tan\phi}{c}$$

where ϕ and ψ are the angles between a geocentric radius and the direction of the ray's trajectory in the $R\theta$ and $R\chi$ planes, respectively ($R\theta \perp R\chi$); c is a constant; $\chi = \chi_i + \chi_2$; χ_i is the angular deviation of the current point of the ray trajectory from the $R\theta$ plane in the ionosphere; χ_2 is the same beyond the ionosphere; $\theta = \theta_1 + \theta_i + \theta_2$; θ_i is the angular distance corresponding to the ray path in the $R\theta$ plane in the ionosphere; θ_1 and θ_2 are the same up to the ionosphere

$$\theta_{1(2)} = \pi/2 - \phi_{1(2)} - \arccos\left(\frac{R_{1(2)}\,\sin\phi_{1(2)}}{R_E}\right)$$

$$\chi_2 = \pi/2 - \psi_2 - \arccos\left(\frac{R_2\,\sin\psi_2}{R_E}\right)$$

The subscripts "1" and "2" relate respectively to the points of the ray's arrival to and escape from the layer; R_E is the Earth's radius; $R_{1(2)}$ is the altitude of the lower ionosphere boundary;

$$\theta_i = \theta_i E + \theta_i EF + \theta_i F2$$

$$\chi_i = \chi_i E + \chi_i EF + \chi_i F2, \quad \text{if} \quad \frac{\partial NE}{\partial \chi} \neq 0, \ \frac{\partial NEF}{\partial \chi} \neq 0, \ \frac{\partial NF2}{\partial \chi} \neq 0,$$

$$\chi_i = \chi_i F2, \quad \text{if} \quad \frac{\partial NE}{\partial \chi} = 0, \ \frac{\partial NEF}{\partial \chi} = 0.$$

The total hop distance, D, the angle of ray arrival in the vertical plane, Δ_2, and horizontal plane, α (the azimuthal deviation of the ray), are calculated using the formulas

$$d = \arccos(\cos\chi \cos\theta), \quad D = R_E d,$$

$$\Delta_2 = \arccos \frac{R_2 \sin \phi_2}{R_E},$$

$$\alpha = \arctan[(\sin d \operatorname{ctn} d_t - \cos d \cos A)/\sin A],$$

$$A = \left|\arctan\{\tan\chi/\sin[\arccos(\cos d/\cos\chi]\}\right.$$

$$\left. - \arctan\{\tan\chi_i/\sin[\arccos(\cos d_t/\cos\chi_i)]\}\right|,$$

$$d_t = \arccos[\cos\chi_i \cos(\theta_1 + \theta_i)].$$

Figure 1 shows the designations used in these formulas.

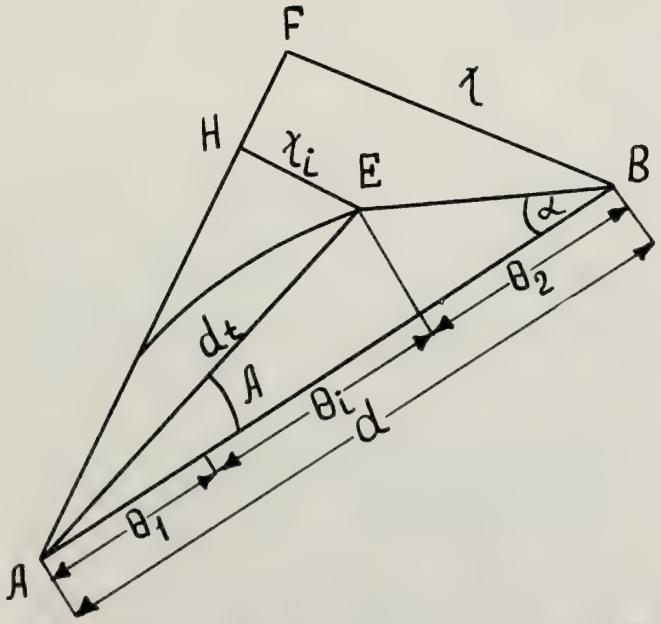


Figure 1. Diagram showing designations used in formulas. AB, AF, AE, EH, and BF are the arcs of great circles. AB is the arc connecting the transmission (A) and reception (B) points. AF is the arc in the plane in which there is the point of emission and the initial point of the trajectory in the layer. AE is the arc of the angle between the point of the ray escape from the layer (E) and the point of emission (A). EH and FB are the projections of the trajectory on the plane normal to the plane of the arc AF.

This method has been used to obtain the relationship between the magnitude and the direction of the horizontal projections of the gradients of N and the various characteristics of radio wave propagation. The effects of $\partial N/\partial\theta$ and $\partial N/\partial\chi$, i.e., the longitudinal and transversal gradients of the electron density may be treated as independent. The presence of $\partial N/\partial\theta$ will result in variations of MUF and hop distance and in the trajectory asymmetry, $\Delta_1 \neq \Delta_2$. When the gradient $\partial N/\partial\theta$ does not exceed the values (at sunrise and with longitude) characteristic of the regular gradients, the above mentioned characteristics do not vary but the trajectory escapes from the plane of the great circle and results in the azimuthal deviation, α. These factors were taken into account when developing the methods for calculating the azimuthal deviations in the presence of a gradient in the plane of the great circle arc (Ishkova and Kovalevskaya, 1977).

Development of the method has made it possible to separate the effects of gradients in different directions, permitting the effects of the horizontal gradients and statistical variability of the ionosphere to be estimated without using computer calculations. The prediction manual (Kovalevskaya and Kerblay, 1971) contains a set of graphs which make it possible to determine the hop distance for a given operating frequency, MUF, the arrival angles of the radio wave in the vertical plane (elevation angles) in case of reflection from the ionosphere with a longitudinal gradient of electron density, and from a spherically stratified ionosphere. To determine these characteristics, it is necessary to know the critical frequencies of the regular ionospheric layers and their longitudinal gradients as well as the geometric parameters of the layers using a parabolic approximation. It is possible to predict the characteristics of radio wave propagation (using computer programs based on the prediction manual) with the following ionospheric predictions: monthly predictions of MUF or many-year predictions of MUF (Chernyshev and Vasileva, 1973-1974) for determining the critical frequencies and the maps (Anufrieva and Shapiro, 1976) for determining h_mF2 and y_mF2. In Figure 2 is shown an example of $D(\Delta)$ from the manual (Kovalevskaya and Kerblay, 1971) for various values of $\partial f_0/\partial\theta$. The solid and dashed curves show the variations in the hop distance, MUF, and angles Δ with an increasing longitudinal gradient of f_0. Figure 3 presents the $\Delta_1(\Delta_2)$ diagram permitting the determination of the degree of trajectory asymmetry and the difference between the angles Δ_1 and Δ_2. It can be seen from the figure that the highest values of $\Delta_2 - \Delta_1$ can be observed near the MUF (the values of MUF are indicated by crosses in Fig. 3) and for the Pedersen ray. When $\partial f_0/\partial\theta = 0.75 \cdot 10^{-2}$ MHz/km exceeds the median value, which often occurs at sunrise, the difference $\Delta_2 - \Delta_1$ can reach 8-10° for the highest frequencies and the near-maximum hop distances.

The second prediction manual (Zhulina and Kovalevskaya, 1976) makes it possible to estimate the variations in the characteristics when the statistical properties and disturbances of the medium are included. The manual contains a set of graphs permitting the determination of the variations in the hop distances and deviations due to the statistical nature of the ionosphere. The manual makes it possible not only to obtain reliable estimates of the characteristics but also to determine the range of their monthly variations and variations due to disturbances.

This method for calculating the characteristics of radio signal trajectories has been modified for the E_s layer (Kerblay et al., 1977). In this case, the E_s layer is represented by a quasi-periodic model of large-scale structure (for more details see the report of T. S. Kerblay and G. N. Nosnova in these proceedings), the parameters of which are determined experimentally or on the basis of statistical predictions:

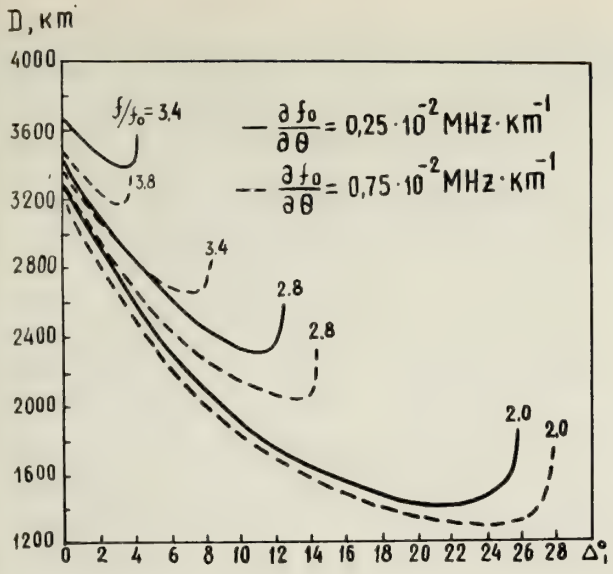


Figure 2. Distance versus elevation angle. h_m = 340 km; y_m = 140 km; f/f_0 is the relation of working frequency to critical frequency of the layer.

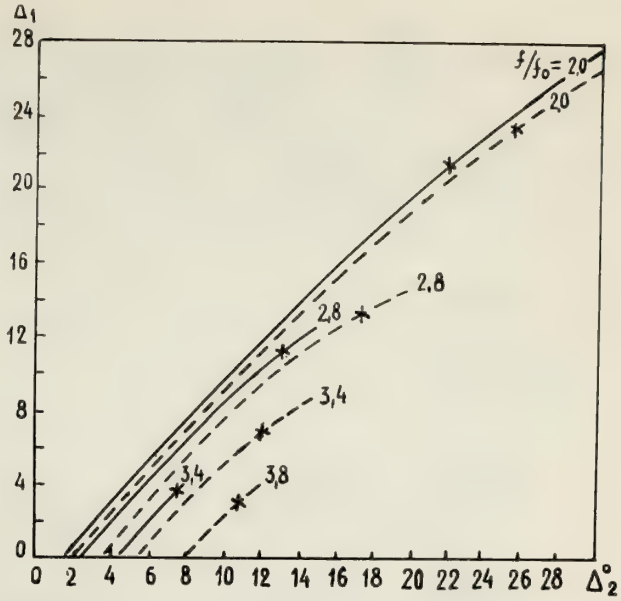


Figure 3. Angle of arrival versus angle of departure. h_m = 340 km; y_m = 140 km; f/f_0 is the relation of working frequency to critical frequency of the layer.

$$N(x,y,z) = 1.24 \cdot 10^4 f_c^2 \frac{4e^{\varkappa z}}{(1+e^{\varkappa z})^2} [1 - k \sin(2\pi x/l_1+\phi) \cos(2\pi y/l_2+\psi)]^2$$

The model of the N-distribution is in the Cartesian coordinate system, X, Y, Z. The Z, X, Y coordinate system for the ray path at the current point of trajectory is transformed into the R, θ, χ coordinate system using the following relations:

$$R \cdot \theta = x \cos\gamma + y \sin\gamma; \quad R \cdot \chi = -x \sin\gamma + y \cos\gamma; \quad R = R_m - z.$$

The angle γ characterizes the orientation of the periodical structure of N relative to the radio path direction.

The horizontal gradient of electron density is due to its periodical structure and the orientation of the Z, X, Y coordinate system relative to R, θ, χ. The expression for the component of the horizontal gradient of refraction index in the (Rθ) and (Rχ) planes is of the following form:

$$\frac{\partial n}{\partial \chi} = -\frac{4}{f^{1/2}} \frac{K \cdot e^{\varkappa z} f_c^2 [1-Kc_1c_2] \cdot A_1}{(1+e^{\varkappa z})^2 \sqrt{1 - \frac{4 f_c^2 [1+Kc_1c_2] e^{\varkappa z}}{f(1+e^{\varkappa z})^2}}}$$

$$A_1 = ac_3c_2 \sin\gamma + Bc_1c_4 \cos\gamma$$

$$c_1 = \sin(ax+\phi), \quad c_2 = \cos(by+\psi), \quad c_3 = \cos(ax+\phi), \quad c_4 = \sin(by+\psi)$$

$$a = \frac{2\pi}{l_1}, \quad b = \frac{2\pi}{l_2}$$

For the gradient $\partial n/\partial\theta$, A_1 is of the form

$$A_1 = bc_1c_4 \sin\gamma - ac_3c_2 \cos\gamma.$$

The gradients $\partial f_c/\partial x$ and $\partial f_c/\partial y$ are taken to be zero.

Presented below are the results of the calculations made for the parameters l_1, l_2, f_N, K taken from values published elsewhere. The following parameters of the E_s-model were used: l_1 = 100 km; l_2 = 25 km; f_c = 2 MHz; K = 0.5; $\varkappa$ = 0.87 km^{-1}; γ = 45°.

Some of the calculations of signal characteristics are shown in Figures 4 and 5 in the form of the functions $D(\Delta_1)$ and $D(\alpha_2)$ at f = 3, 5, and 7 MHz.

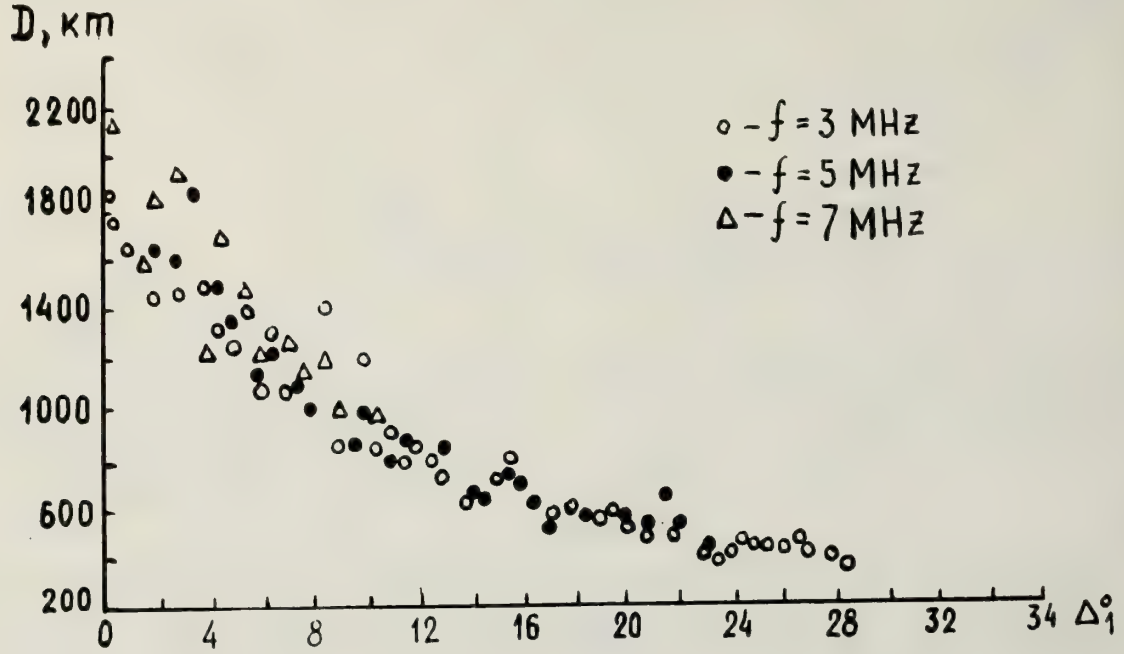


Figure 4. Distance versus elevation angle, E_s-reflections.

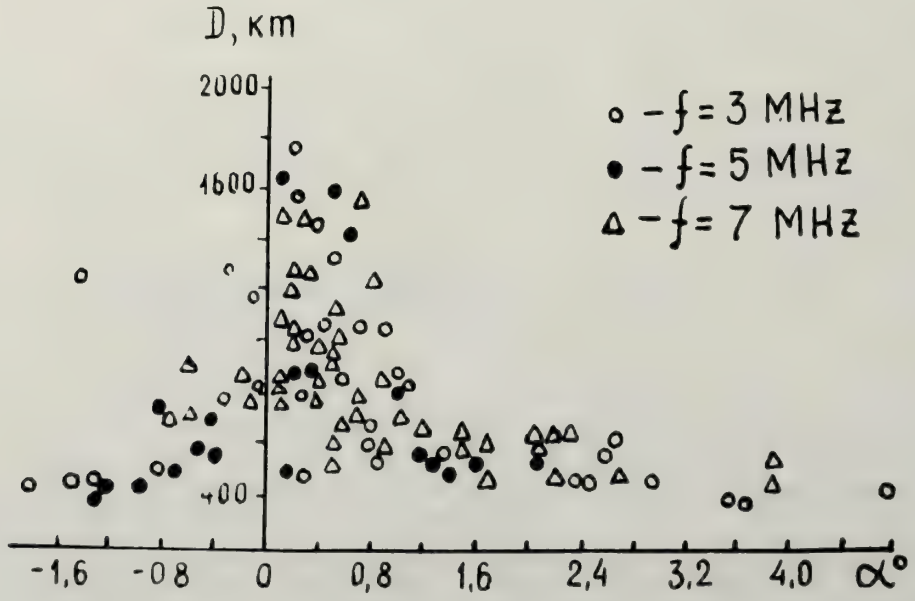


Figure 5. Distance versus azimuthal deviation, E_s-reflections.

It can be seen from Figure 4 that the inhomogeneous structure of the reflection region results in a significant variation of D for each angle Δ_1. The largest variance (some 500-600 km) is observed at elevation angles near zero. The mean mode of the variations is similar to that of the regular layers; the only difference being the absence of a clear dependence of D (for a fixed Δ_1) on the operating frequency and the absence of the separate branch of D (Δ) for the upper angles.

In Figure 5, the effect of a significant variation of the angles α_2 on $D(\alpha_2)$ can clearly be seen. The largest range of variations in α_2 (from -1.8° to +6.5°) is observed for small hop distances. The maximum distances corresponding to the elevation angles of 0-4° are characterized by a lesser variance of α_2.

It was of interest to compare (even if qualitatively) the above calculations with experimental data. The comparison was made using the measured angles Δ_2 and α_2 for reflection from the E_s-layer presented in Miya and Sasaki (1966) for two radio communication paths (D = 1480 and 2040 km) in the VHF band.

The experimental data show a decrease of the variance of α_2 with increasing path length and a shift of the center of the α_2 distribution, which coincides with the calculated results. A good quantitative agreement may be noted between the measured and calculated angles Δ_2 for D = 1480 km. Although the parameters used in the calculations were not coordinated with particular experimental conditions, in general, a quite satisfactory agreement is noted between the calculated and measured characteristics. The conclusion may be drawn, therefore, that the proposed method may well be used to calculate the characteristics of the signal reflected from the E_s-layer.

The above prediction materials in practice set forth definite requirements for the accuracy of the results obtained.

The accuracy of this method depends on a number of factors, namely, the approximations used in the physical formulation of the problem, the method of mathematical solution, and the accuracy of the input ionospheric parameters.

The first two factors (geometric-optical approximation neglecting charged particle collisions and anisotropy* and the numerical method of solution) introduce errors that are insignificant when compared with the errors due to insufficient accuracy of the ionospheric parameters and, therefore, only the latter source of the errors will be analyzed here. The analytical form is most convenient for presentation of the N(h)-profile in calculations. Selection of the analytical N(h)-profile model, which best represents the real N(h) distribution and is sufficiently simple to avoid undesirable difficulties in calculations, is a separate task.

The propagation characteristics of the F2 layer were intercompared for various analytical models (parabola, biparabola, linear layer, etc.) for fixed values of h_mF2 and y_mF2. The differences in the hop distances (Δ = constant) using a parabola (quasiparabola), biparabolic and quadratic

---

*It should be noted that the effects of the Earth's magnetic field are neglected when making massive calculations. There exists a version of the program that calculates separately the ordinary and extraordinary components, which is used when the effect of the magnetic field is expected to be significant.

sinusoid have been found to be 200-250 km at distances exceeding 3000 km (for the Pedersen rays and at low angles of elevation Δ). The differences are much smaller at the frequencies near the MUF. In the case of a linear (quasilinear) N(h) distribution, the hop distances are significantly in excess ($\Delta D \gtrsim 400$ km) of the corresponding values for other distributions.

In case of the regular altitude dependence of the lateral gradient of electron density, the differences in the azimuthal deviations of radio wave arrival (D = constant) are insignificant with the exception of the linear model. For the gradients of the ionospheric parameters, which are several times the median values, the differences in α are 0.3° for the lower rays and $\gtrsim$0.5° for the Pedersen rays. For gradients when the parameters are near the median values, the differences are but hundredths of a degree. In the linear model, such differences are much larger ($\Delta\alpha \simeq 1 - 1.5°$). From these results and considering that a near-linear distribution of N(h) occurs only at individual moments in the equatorial zone, the assumption has been made that the N(h)-profile may be presented as a combination of parabolas.

Table 1 indicates the magnitude of the error in the calculated characteristics resulting from inaccuracies in the parameters of a layer. Because the F2 layer has the greatest thickness and electron density and is the most variable, the calculations for this layer are used as an example. Examined separately will be the effects of the errors in determining the absolute values of the parameters f_0 , h_m, y_m and their longitudinal gradients.

Errors in determining the absolute values of the parameters will result in the following errors in the propagation characteristics. An error in the critical frequency, $\delta f_0 = 20\%$, leads to values of δD (at Δ_1 = constant) ranging from 100 to 700 km; the highest values have been obtained for the highest working frequencies and for the Pedersen ray. Table 1 lists examples of the numerical values.

Table 1. Examples of numerical values.

$\partial f_0/\partial\chi = 0.5 \cdot 10^{-2}$ MHz/km					
$\overline{f/f_0}$	$\bar{\Delta}$°	$\bar{D}$, km	δD, km	$\bar{\alpha}$°	$\overline{\delta\alpha}$°
2.0	10	1900	-100 +250	0.1	-0.05 +0.2
2.4	8	2250	-160 +650	0.2	-0.05 +0.25

Errors of the same order have been obtained for $\delta y_m = 40$ km (h_0 = constant). Somewhat smaller errors (by a factor of about 2) are due to $\delta h_m = 50$ km (y_m = constant). The variations in the azimuthal deviations are also largest for the upper ray and are not appreciable for the lower ray. When the layer parameters have been determined without error but the determination of the gradients involved some error, the inaccuracies in the characteristics (especially the angular parameters) are much larger. These calculations are exemplified in Table 2, which shows that, as $\delta f_0/\delta\chi$ and $\delta h_m/\delta\chi$ vary, α is changed by 0.1-0.8°. This is in excess of the values of $\delta\alpha$ presented in Table 1.

Therefore, not only do the requirements for accuracy of the input ionospheric data necessary to the calculations relate to the absolute values of

the N(h)-profile parameters, but also (to a considerable degree) to the accuracy of the representation of $\partial N/\partial\theta$ and $\partial N/\partial\chi$.

Table 2. Examples of numerical values.

$\alpha°$				$\alpha°$				
$\partial f_0/\partial\chi \cdot 10^{-2}$ MHz/km				$\partial h_m/\partial\chi \cdot 10^{-2}$ km/km				
D, km	f/f_0	0.25	0.5	D, km	f/f_0	-1.5	-3.0	-5.0
1000	1.6	0.2	0.4	1200	1.6	0.4	0.7	1.2
1400	2.0	0.1	0.2	1600	2.0	0.25	0.6	0.9
	2.0	0.7	1.4		2.0	0.6	1.2	2.0

REFERENCES

Anufrieva, T. A., and B. S. Shapiro (1976): Geometric parameters of the F2 ionospheric layer. Nauka, Moscow.

Chernyshev, O. V., and T. N. Vasilieva (1973-1974): Prediction of the maximum usable frequencies, W=10, 50, 100, 150. Nauka, Moscow.

"Collected programs for calculating the trajectory characteristics of short radio wave propagation" (1975). Nauka, Moscow.

Ishkova, L. M., and E. M. Kovalevskaya (1977): On the calculating method of the characteristics of short radio wave propagation in the equatorial ionosphere. In: Methods for Studying the Regularities of Radio Wave Propagation. Nauka, Moscow, pp. 65-71.

Kerblay, T. S., and E. M. Kovalevskaya (1974): Trajectories of short radio waves in the ionosphere. Nauka, Moscow.

Kerblay, T. S., and E. M. Kovalevskaya (1977a): Angular characteristics of a radio wave trajectory in a horizontally inhomogeneous ionosphere. Geomagn. i Aeron., 17:671.

Kerblay, T. S., E. M. Kovalevskaya, and G. N. Nosova (1977b): On a method of calculating trajectory characteristics of radio signals reflected from the E_s-layer. In: Diffraction Effects in Decameter Radio Waves in the Ionosphere. Nauka, Moscow, 82-89.

Kovalevskaya, E. M., and T. S. Kerblay (1971): Calculations of the hop distances, the maximum usable frequency, and the radio wave arrival angles including the horizontal inhomogeneity of the ionosphere. Nauka, Moskow.

Miya, K., and T. Sasaki (1966): Characteristics of ionospheric E_s propagation and calculation of E_s signal strength. Radio Science, 1:99-108.

"Monthly predictions of MUF." Gidrometeoizdat.

Zhulina, E. M., and E. M. Kovalevskaya (1976): Calculations of the radio wave propagation characteristics including the statistical properties of medium ionospheric disturbances. IZMIRAN, Moscow.

USING SOLAR FLUX INDEX PREDICTIONS TO FORECAST HF RADIO WAVE PROPAGATION

David Jacob Snyder
Brooklyn College
1137 E. 12th St., Brooklyn,
New York 11230, U.S.A.

A technique for predicting solar flux index numbers has been developed whereby the current solar flux cycle is correlated against the previous one. A future value of the current cycle can be predicted by the following formula:

$$yp = (r\ (sy/sx))\ (x-\overline{x}) + \overline{y},$$

where r is the correlation coefficient, sy and sx are the standard deviations of y and x, $\overline{x}$ and $\overline{y}$ are the means of x and y respectively, and yp is for long term and for short term predictions. The reliability of this technique is discussed on the basis of standard deviations of predicted values for both short term and long term predictions. Predictions of high frequency radio wave propagation based upon data compiled by correlations of the solar flux indices against various high frequency radio wave propagation paths are discussed. Examples of radio wave propagation predictions based upon the compiled data and the predicted solar flux index number are given.

1. INTRODUCTION

The solar flux index is a measurement of the overall level of solar activity. It is closely associated with the well known daily sunspot number and may soon be preferred to the sunspot number as a measurement of solar activity. While following the eleven year average cycle of solar activity, flux values vary from one day to the next in association with the activity on the sun. This activity influences the range of frequencies which will support ionospheric radio communications on specific circuits.

The solar flux index has been correlated with the temperature of the ionosphere in many studies. These studies show that the temperature of the isothermal region above the thermopause and the exospheric temperature show a variation associated with changes in the density of the ionosphere and in the solar flux index. The dependence of the variation of temperature on the intensity of solar ultraviolet radiation, as characterized by the solar flux index, apparently becomes more pronounced with increasing height.

The solar flux index measurements are gathered at the Algonquin Radio Observatory (ARO) of the National Research Council of Canada using a reflector of 1.8 meters in diameter, on a frequency of 2800 MHz. These radio emissions which originate from the solar disk and from any active regions are a continu-

ation of observations which were begun in Ottawa in 1947. Historically the measurement taken at local noon (about 1700 universal time) has been considered the "official" value for the day. The solar flux index is measured in units of 10^{-20} watts per square meter per cycle per second, and in general, have a range from about 60 to 400 units (Figure 1).

2. PREDICTION TECHNIQUE

A method for developing accurate predictions of future solar flux index values based upon previous observations was employed. In no sense is it believed that the past values are the cause of future values. Rather, some reliable indicator which will predict future values is desired.

The Pearson product moment correlation coefficient was used in order to employ the following two linear regression formula:

$$yp = (r\ (sy/sx))\ (x-\overline{x}) + \overline{y},$$

where r is the correlation coefficient, sy and sx are the standard deviations of y and x; $\overline{x}$ and $\overline{y}$ are the means of x and y, respectively; and yp is for long-term and short-term predictions.

3. BASIS FOR TECHNIQUE

The correlation coefficient (r) between the current and past cycles of the solar flux index at 10.7 cm is 0.762022 for 29 days, and 0.91251 for 766 days,

Tests of significance which can usually be applied to correlation studies (parametric tests) cannot be applied here because such tests fail to be applicable for a time series. These tests assume that samples are drawn from a stable and normally distributed universe, which does not exist in a time series such as the solar flux index. Therefore, the test used was a non-parametric test which ignores the limiting assumptions of the parametric tests. Such a non-parametric test is the Kendall-Mann test.

In Figure 2, the relationship between the current (designated by a circle) and past (designated by a square) monthly averages of the solar flux index is illustrated. When 25 monthly averages were correlated, the Pearson correlation was 0.95415, the Spearman correlation was 0.86692, and the Kendall-Mann tau b correlation was 0.70000. The correlation of the whole cycle differs little from that of the monthly averages: for 766 days the Pearson r was 0.91251, Spearman r was 0.80229, and Kendall-Man tau b r was 0.61651.

Figure 1.

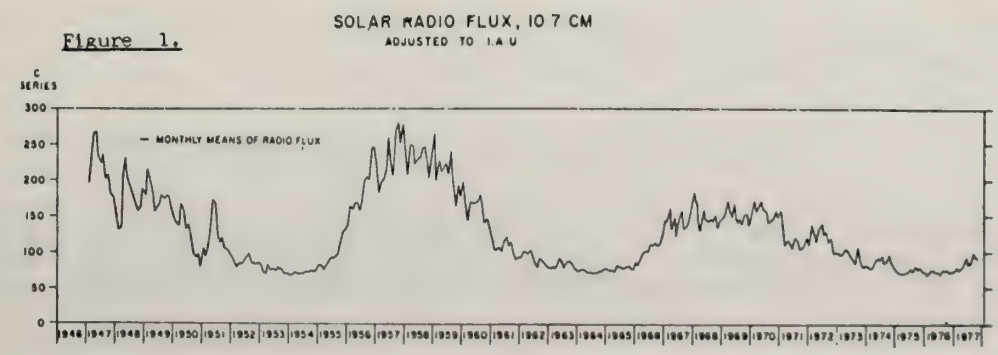


Figure 1. Solar radio flux, 10.7 cm, adjusted to I.A.U.

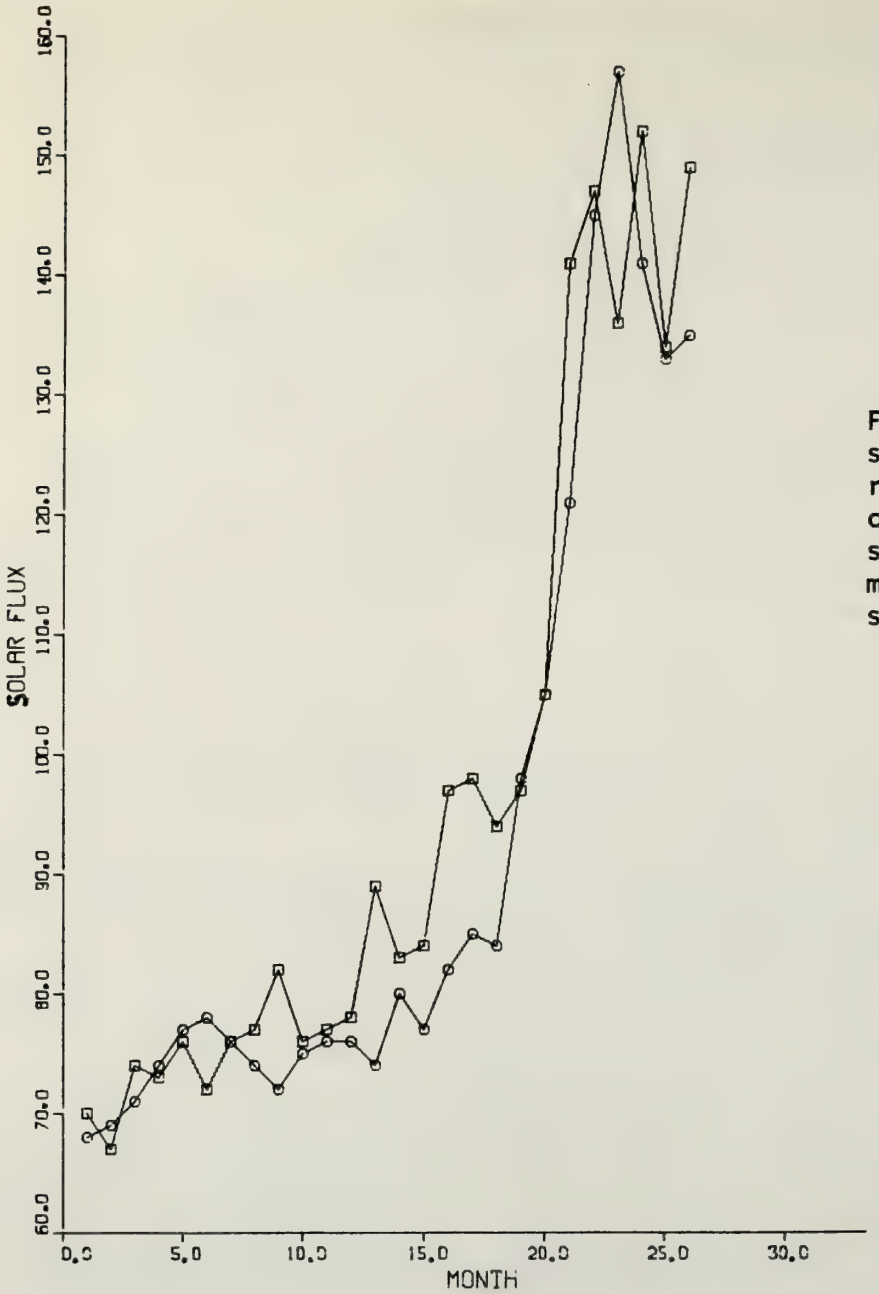


Figure 2. The relationship between the current (designated by a circle) and past (designated by a square) monthly averages of the solar flux index.

These correlations are all greater than the critical values for a two-tailed test at the 0.01 level of significance.

4. RELIABILITY OF PREDICTION TECHNIQUE

The reliability of the prediction technique is illustrated in Table 1 for monthly averages and in Table 2 for daily values. The measurement of reliability is based upon the standard deivations of predictions, using the following formula:

$$\sigma = \sqrt{\Sigma(YP-Y)^2/N}$$

Table 1. Standard deviations of monthly mean predictions for July 1976-August 1978.

Month(s) Predicted in Advance	Standard Deviation
1	5.7954
2	8.6790
3	10.2336
4	10.0157
5	10.8352
6	12.3184

Table 2. Standard deviations of daily predictions for August 1977-September 1978.

Day(s) Predicted in Advance	Standard Deviation
1	9.4011
2	9.4677
3	10.1373
4	11.6312
5	11.9235
6	12.1504
7	12.4472
8	12.5362
9	12.6182
10	12.7766
11	12.9796
12	13.3382
13	13.8213
14	14.3113

Figure 3 illustrates the comparison of observed (indicated by a circle) and predicted values (indicated by a square) for predictions made one month in advance.

5. RADIO PROPAGATION CHARTS

The various solar flux indices have been correlated with the radio transmission frequency, time in Greenwich mean time, and the location of the transmitter and receiver, in order to predict radio wave propagation. These charts (Tables 3a-3i) are a result of two years of collection and compilation of data. The data consisted of the stations that dxers (individuals who listen to distant transmissions on short wave radio) have heard from the start of the current cycle to date. An estimated 40,000 such reports have been evaluated from many radio hobby club publications. These clubs, whose membership is above 3,000, constitute the majority of listeners in the United States. Their equipment ranges from simple portable radios to highly expensive and sophisticated communications receivers.

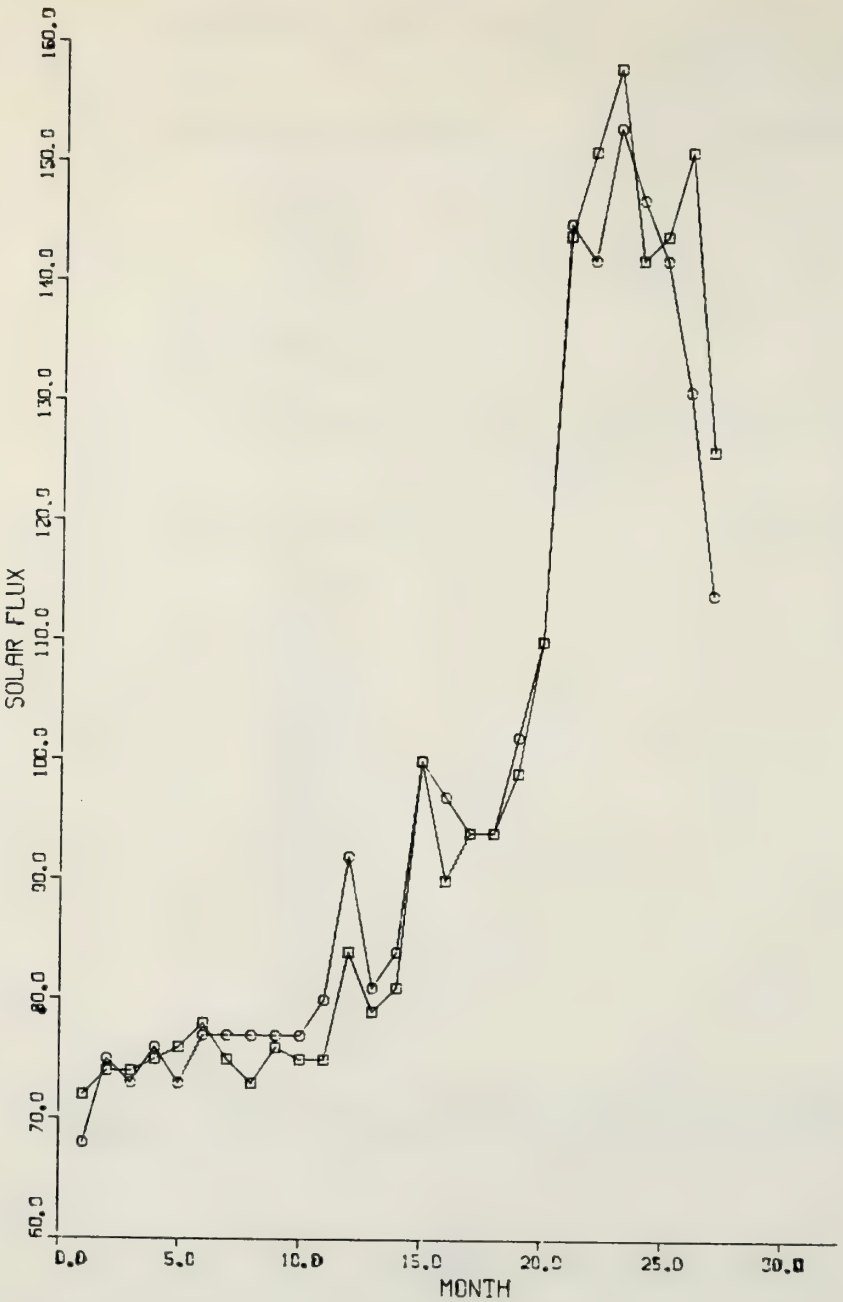


Figure 3. The comparison of observed (indicated by a circle) and predicted values (indicated by a square) for predictions made one month in advance.

The solar flux index of the previous day can be heard on radio station WWV from Fort Collins, Colorado. The station is on 2.5, 5, 10, 15 MHz and the announcements can be heard at 18 minutes after the hour. The current flux can be estimated by the prediction technique as much as two weeks in advance.

6. EXAMPLES OF PROPAGATION PREDICTIONS

The charts can be used to accurately predict ionospheric radio propagation on any given day if the flux is known. Here are a few examples of propagation predictions made by the chart versus what was actually heard:

"HOW TO PICK A BAND" BY DAVID JACOB SNYDER

Table 3a.

FOR EASTERN NORTH AMERICA JUNE 1978 ISSUE

SFI	EUROPE	SOUTH AMERICA	ASIA	OCEANIA	AFRICA	NORTH AMERICA
183		6 MHZ 1000-1100	9 MHZ 2200-2230	3 MHZ 1030-1130	9 MHZ 2030-2100	
180			15 MHZ 2200-2230		15 MHZ 2200-2230	6 MHZ 1100-1300
179		6 MHZ 1000-1100	9 MHZ 2200-2230		9 MHZ 2030-2100	
		9 MHZ 0930-1030				
178		3 MHZ 0000-0100				
		11 MHZ 0100-0130				
		15 MHZ 0100-0130				
172						2 MHZ 0300-0330
171			15 MHZ 0030-0100	15 MHZ 0330-0400		
170					4 MHZ 2330-0030	5 MHZ 0500-0630
168			15 MHZ 0230-0300			
165					3 MHZ 2300-2330	4 MHZ 0230-0300
					4 MHZ 0300-0600	
163		3 MHZ 0930-1000	4 MHZ 1130-1300		3 MHZ 2230-2300	
		4 MHZ 0330-0400			4 MHZ 0400-0500	
		5 MHZ 1030-1130				
162		3 MHZ 0200-0230			3 MHZ 2200-2330	
		4 MHZ 0400-0500				
					4 MHZ 2230-2330	
					6 MHZ 0230-0300	
161	6 MHZ 0130-0200		5 MHZ 2230-2300			
	21 MHZ 1630-1700		9 MHZ 0300-0330			
158		9 MHZ 0306-0330				4 MHZ 0330-0400
157		3 MHZ 0100-0200				
156			9 MHZ 2230-2300		4 MHZ 0330-0400	
			11 MHZ 2200-2230		1030-1200	
			0230-0300			
155		4 MHZ 0300-0330				
151			11 MHZ 2200-2230			
			15 MHZ 0000-0030			
149			9 MHZ 0030-0100		15 MHZ 1200-1400	
					1830-1900	
148			15 MHZ 2130-2200	3 MHZ 1200-1230		
146			9 MHZ 1130-1200			
145	21 MHZ 1630-1700		11 MHZ 0530-0600		5 MHZ 2200-2300	
					7 MHZ 0630-0700	
					11 MHZ 1030-1100	
143	12 MHZ 1200-1230		9 MHZ 1130-1200		15 MHZ 1130-1200	
			11 MHZ 1030-1100			
			17 MHZ 0430-0500			
142		3 MHZ 0830-0930			6 MHZ 0600-0630	2 MHZ 0130-0400
141			15 MHZ 0430-0500		15 MHZ 0400-0430	
140		3 MHZ 0830-1000	4 MHZ 1030-1230	4 MHZ 1130-1200	11 MHZ 1300-1400	3 MHZ 1100-1200
		5 MHZ 1100-1130	2330-0130		15 MHZ 1200-1400	0230-0300
			7 MHZ 1130-1200		2130-2200	
			9 MHZ 1130-1200			
			15 MHZ 1200-1230			
139		3 MHZ 0900-1000	4 MHZ 2330-0130			
			15 MHZ 2330-0000			
138		3 MHZ 0730-0900	4 MHZ 1000-1100;	15 MHZ 0630-0700	3 MHZ 0330-0400	13 MHZ 0430-0500
			2230-2300			
			11 MHZ 1130-1200		11 MHZ 0700-0730	

Table 3a. How to pick a band for Eastern North America June 1978 Issue

SFI	EUROPE	SOUTH AMERICA	ASIA	OCEANIA	AFRICA	NORTH AMERICA
137		15 MHZ 0130-0230	11 MHZ 2100-2200	3 MHZ 0830-0930	3 MHZ 0430-0500	
135	15 MHZ 0100-0130				3 MHZ 2200-2230	
			0700-0730,2000-2030			
134		4 MHZ 0100-0130				
133	11 MHZ 0130-0200		11 MHZ 2000-2030		11 MHZ 0130-0200	
			0100-0230			
132			15 MHZ 2330-0300			
131		5 MHZ 0330-0400	15 MHZ 2200-2230		4 MHZ 2230-2300	
		15 MHZ 2230-2300			15 MHZ 2200-2230	
130			11 MHZ 1930-2030			
129		3 MHZ 0730-0800	6 MHZ 0430-0500		4 MHZ 0500-0600	
					0630-0700	
					7 MHZ 0630-0700	
					9 MHZ 0630-0700	
128				11 MHZ 0700-0830		
127			15 MHZ 0130-0230			
125	6 MHZ 0330-0400	4 MHZ 0900-0930			3 MHZ 0100-0130	
		5 MHZ 1000-1130			4 MHZ 0330-0530	
		15 MHZ 2230-2300				
124					5 MHZ 2130-2230	
122			9 MHZ 0230-0300			
120	15 MHZ 1600-1630	4 MHZ 0300-0400		11 MHZ 0400-0500	4 MHZ 2130-2230	
119	21 MHZ 1700-1800		10 MHZ 1300-1400		3 MHZ 2230-2300	
			15 MHZ 1430-1500		4 MHZ 2230-2300,	
					0230-0300,0330-	
					-0400,0600-0630;	
					5 MHZ 2200-2230	
118		4 MHZ 0300-0330	10 MHZ 2030-2100		3 MHZ 2230-2300	3 MHZ 0330-0400
			15 MHZ 2030-2100		15 MHZ 2200-2230	6 MHZ 0930-1100
117					9 MHZ 1830-2200	
116					3 MHZ 2130-2230	
		4 MHZ 0300-0400			4 MHZ 2230-2300	
					2100-2130	
115		3 MHZ 0300-0330	11 MHZ 0100-0130		3 MHZ 0400-0430	
		4 MHZ 0230-0300			4 MHZ 0330-0400	
		6 MHZ 1000-1030			0500-0530	
113	15 MHZ 2300-2330,	3 MHZ 1030-1100	5 MHZ 1130-1200	3 MHZ 1100-1130	3 MHZ 0400-0430	
		4 MHZ 1000-1030	9 MHZ 1000-1030	5 MHZ 0730-1100	3 MHZ 0500-0530	
			11 MHZ 0900-0930	11 MHZ 0600-0700	4 MHZ 0130-0200	
		15 MHZ 2230-2300	15 MHZ 1100-1130	12 MHZ 0930-1000	0400-0600	
			0130-0200	15 MHZ 0630-0700		
			0230-0300			
111		3 MHZ 0130-0230	9 MHZ 1700-1730	15 MHZ 0600-0630	3 MHZ 2300-2330	4 MHZ 0300-0400
		4 MHZ 0430-0500			4 MHZ 0330-0430	
110						3 MHZ 0400-0430
109		6 MHZ 1000-1030		4 MHZ 1000-1400	4 MHZ 2200-2300	
		9 MHZ 0230-0300			0600-0700	
					9 MHZ 0500-0630	
					15 MHZ 2030-2230	
107		4 MHZ 0300-0400			4 MHZ 2230-2300	
106			15 MHZ 1230-1300		15 MHZ 1830-1900	
					2130-2200	
105	6 MHZ 0000-0100	9 MHZ 0430-0500	9 MHZ 2200-2300			
	9 MHZ 2200-2330					
	15 MHZ 1800-1830					
104	5 MHZ 2030-2130				3 MHZ 0530-0630	4 MHZ 0300-0400
103	11 MHZ 2300-2330	4 MHZ 0300-0400	9 MHZ 2230-2300	7 MHZ 1100-1130	4 MHZ 2100-2130	

Table 3b.

SFI	EUROPE	SOUTH AMERICA	ASIA	OCEANIA	AFRICA	NORTH AMERICA
102	11 MHZ 0100-0330		4 MHZ 1300-1330 12 MHZ 1800-1830	4 MHZ 1000-1400	11 MHZ 1900-1930 4 MHZ 2130-2300 0400-0430,0530-0630 9 MHZ 2030-2100	
101 100	11 MHZ 1400-1430	4 MHZ 0100-0500	15 MHZ 1130-1200 3 MHZ 1100-1200 5 MHZ 1100-1200 7 MHZ 0500-0530 15 MHZ 1830-2000	15 MHZ 0330-0400	6 MHZ 2030-2100	
99	6 MHZ 0330-0400	15 MHZ 2300-2330 17 MHZ 2300-2330	9 MHZ 1000-1100 1130-1200,1700- 1730,1800-1830 15 MHZ 2200-2300			4 MHZ 0430-0600 5 MHZ 0500-0530
98	5 MHZ 2130-2200 6 MHZ 0130-0200 15 MHZ 1330-1400		9 MHZ 2130-2200 2300-2330; 11 MHZ 2300-2330 15 MHZ 1200-1300 2200-2230		4 MHZ 1200-1230 0300- -0330,0430-0600 11 MHZ 1900-1930	
97			7 MHZ 2000-2030 15 MHZ 2230-2300		9 MHZ 0200-0230 0300-0330	
96		3 MHZ 2130-2200	9 MHZ 0000-0030 0500-0530 11 MHZ 0500-0530		3 MHZ 0500-0600 4 MHZ 2300-2330 11 MHZ 1530-1630, 1830-0030	
95	9 MHZ 1930-2030		9 MHZ 2130-2200 0230-0330		9 MHZ 0600-0630 11 MHZ 1900-1930	
94	6 MHZ 0030-0100 0230-0330; 9 MHZ 2130-2230	15 MHZ 0300-0330	7 MHZ 2200-2230 9 MHZ 2200-2230		6 MHZ 2230-2330 7 MHZ 0600-0630	
93		6 MHZ 2300-2330	9 MHZ 1300-1330	11 MHZ 0330-0530	4 MHZ 2130-2200 0600-0630; 7 MHZ 0530-0630; 15 MHZ 1800-1900	11 MHZ 0230-0300
92	9 MHZ 2200-2230 2300-0500 11 MHZ 2330-0500 0300-0330		11 MHZ 1200-1230 17 MHZ 0200-0230	4 MHZ 1030-1130 11 MHZ 0530-0600	5 MHZ 0400-0430 6 MHZ 0300-0330 7 MHZ 0400-0430 11 MHZ 2300-2330	
91		4 MHZ 0400-0430	9 MHZ 1800-1930 11 MHZ 0030-0100 15 MHZ 0130-0230 1930-200	9 MHZ 0530-0830 11 MHZ 0330-0500	9 MHZ 0430-0530 11 MHZ 2000-2030 2230-2330	15 MHZ 2200-2230
90	12 MHZ 2030-2100		5 MHZ 1130-1200 11 MHZ 1100-1130 12 MHZ 1730-1830	4 MHZ 1203-1300 15 MHZ 0430-0500	4 MHZ 0600-0630 15 MHZ 1900-2130	3 MHZ 0430-050
89	11 MHZ 1700-1730 0000-0030	11 MHZ 0330-0400	7 MHZ 2100-2200 9 MHZ 2200-2230 1830-1930 11 MHZ 1700-1900 2100-2130; 12 MHZ 1230-1300; 15 MHZ 2000-2030, 0430-0500,0200-0230	9 MHZ 0600-0630 11 MHZ 0130-0200	6 MHZ 2130-2300 15 MHZ 2100-2130	9 MHZ 1400-1430
88	6 MHZ 0300-0330 7 MHZ 0130-0200 11 MHZ 0600-0630		9 MHZ 1900-1930 11 MHZ 1500-0000 15 MHZ 0130-0200,2330 -0100,0400-0530; 17 MHZ 0100-0230	7 MHZ 0600-0630	4 MHZ 2200-2300, 0430-0600; 7 MHZ 0230-0300 9 MHZ 1830-2200	5 MHZ 2200-2300

Table 3c.

SFI	EUROPE	SOUTH AMERICA	ASIA	OCEANIA	AFRICA	NORTH AMERICA
			2300-0000		11 MHZ 0430-0500	
87		4 MHZ 0530-0600 6 MHZ 0900-1030	11 MHZ 1030-1100 12 MHZ 1700-1730 15 MHZ 0300-0330 17 MHZ 0300-0330	4 MHZ 0900-1330	3 MHZ 0400-0430 4 MHZ 0400-0700 5 MHZ 2230-2300 6 MHZ 2230-2330 9 MHZ 0400-0430 11 MHZ 2030-2100	
86	6 MHZ 0030-0100 11 MHZ 1100-1200 12 MHZ 1230-1300 1830-1900 15 MHZ 1400-1430		7 MHZ 1230-1300 9 MHZ 0530-0830 10 MHZ 1100-1130 11 MHZ 1200-13000 15 MHZ 1200-1230 17 MHZ 1530-1600	5 MHZ 0530-0700 7 MHZ 0800-1100	3 MHZ 2330-0000 4 MHZ 0700-0730,2230 -0000; 5 MHZ 2130- 000; 7 MHZ 0230-0300 0400-0430,0730-0800 9 MHZ 2200-2230 11 MHZ 1500-1700, 0200-0230; 15 MHZ 1500-1700	9 MHZ 1230-1300
85	6 MHZ 0200-0230 7 MHZ 0200-0230 9 MHZ 0200-0230 11 MHZ 0200-0230	3 MHZ 1030-1130	6 MHZ 2230-2300 9 MHZ 2200-2230 11 MHZ 1030-1100 1330-1400	15 MHZ 0400-0500	4 MHZ 2000-2230 2330-0000 9 MHZ 2130-2200	3 MHZ 0130-0200
84	9 MHZ 0000-0030 0130-0200 2130-2200 11 MHZ 0130-0200 12 MHZ 2100-2130	3 MHZ 1130-1200	9 MHZ 1330-1400 2200-2230 11 MHZ 1700-1800 1330-1400	9 MHZ 1500-1530	5 MHZ 2030-2100 6 MHZ 2230-2330 9 MHZ 2230-2330 15 MHZ 1300-1330 1800 -1900,1930-2030	3 MHZ 0000-0030 0200-0330 9 MHZ 1400-1500
83	9 MHZ 2130-2230 2330-0030		7 MHZ 0300-0330 0400-0430 9 MHZ 2030-2100 11 MHZ 1230-1300 15 MHZ 2330-0100 0200-0300	7 MHZ 0800-0830 11 MHZ 1630-1730 15 MHZ 0400-0430	3 MHZ 2200-2300 4 MHZ 2230-2300 0600-0630 6 MHZ 2100-2330 7 MHZ 2300-0030 0430-0500; 9 MHZ 0030-0100,0230-0330 0400-0430,1630-1730 11 MHZ 1900-2030 15 MHZ 2100-2200 0200-0230 21 MHZ 1330-1400	3 MHZ 0800-0300
82	5 MHZ 0100-0130 7 MHZ 0200-0230 9 MHZ 0000-0030	4 MHZ 2330-0000 0100-0200,0430 -0500,0600-0700; 6 MHZ 1100-1130 11 MHZ 2300-2330	4 MHZ 1130-1230 7 MHZ 0500-0530 1100-1200 9 MHZ 1930-2030 2200-2300,0200 0230; 11 MHZ 1130 -1200,2100-2130 15 MHZ 0200-0230 2000-2030	3 MHZ 0800-0830 15 MHZ 2000-0500	3 MHZ 0630-0700 4 MHZ 2000-2300 0300-0330,0400-0600 0630-0700 5 MHZ 0430-0500 0630-0700 6 MHZ 0630-0730 7 MHZ 0400-0430 0600-0730 9 MHZ 0530-0600 11 MHZ 2300-2330	3 MHZ 0100-0130 0330-0400 4 MHZ 0330-0400 0630-0700
81	6 MHZ 0000-0330 0900-0930 12 MHZ 1130-1200	4 MHZ 0700-0800 11 MHZ 0200-0230 15 MHZ 2100-2130 2230-2300	5 MHZ 1130-1300 7 MHZ 0430-0500 9 MHZ 1000-1230 1930-2300,0400 -0500; 11 MHZ 1700 -1730,2200-2230 0100-0130,1130- 1200; 15 MHZ 2330-	4MHZ 0830-0900 6 MHZ 0530-0600 7 MHZ 0800-1100 9 MHZ 0530-0600 11 MHZ 0600-0630	3 MHZ 0430-0500 0530-0600; 4 MHZ 0230-0300,0400 0530,2000-2030; 5 MHZ 0430-0500 7 MHZ 0400-0430,0530 0600; 9 MHZ 1800- 1900,1930-2000	4 MHZ 0300-0330 0630-0700 5 MHZ 0500-0600 15 MHZ 2000-0030

Table 3d.

SFI	EUROPE	SOUTH AMERICA	ASIA	OCEANIA	AFRICA	NORTH AMERICA
			0100,0400-0430		2300-2330,0330 -0400; 11 MHZ 1500 -1700,1900-2230 15 MHZ 1900-2000	
80	5 MHZ 0430-0500 6 MHZ 0200-0230 0900-0930 9 MHZ 0000-0030, 0130-0200; 11 MHZ 1630-1730 0100-0330 15 MHZ 1130-1200 1630-1800 17 MHZ 1230-1300 1530-1630 21 MHZ 1700-1730	4 MHZ 2330-0000 0300-0330,0500 0500-0530 5 MHZ 0700-0730 11 MHZ 0000-0030 0100-0200 15 MHZ 2100-2200 1230-1400	4 MHZ 1130-1230 0030-0130,0230 -0330; 6 MHZ 0500-0530,0800 0830; 7 MHZ 0230 0330; 9 MHZ 1200 -1300,1600-1730 1800-1830,1900 -1930,2100-2130 0900-1000,1030 -1100; 11 MHZ 1030-1100,1200 -1300,1600-1730, 1930-2030 15 MHZ 2200-2230 2330-0230,0300-0330 17 MHZ 1030-1100	3 MHZ 0900-1000 4 MHZ 0900-1330 7 MHZ 0700-0730 9 MHZ 0630-0700 11 MHZ 0400-0430 0630-0730 15 MHZ 0100-0430	3 MHZ 2130-2200 0330-0400; 4 MHZ 2030-2100,2200 2230,0200-0430, 0700-0730 5 MHZ 0330-0430 7 MHZ 2130-2200,0400 -0500; 9 MHZ 1830 -2130,2330-0300 0500-0530; 11 MHZ 1500-1700,1730 -1830,0530-0630 15 MHZ 1700-2000 2100-0030 17 MHZ 1700-1730	3 MHZ 0230-0330 0400-0530 9 MHZ 0400-0430 11 MHZ 1230-1330,0000 0000-0030 0100-0130
79	3 MHZ 0400-0430 6 MHZ 0300-0330 7 MHZ 0100-0430 9 MHZ 1930-2000 2230-2300,0300 0330; 11 MHZ 0000 0030,0100-0400	4 MHZ 0400-0430 5 MHZ 1030-1130 11 MHZ 2100-2200	3 MHZ 2130-2200 4 MHZ 1130-1200 2030-2130; 5 MHZ 1600-1630,2030 2130; 6 MHZ 2100 2130; 7 MHZ 0430 0500; 9 MHZ 1000 -1030,1100-1130 1200-1430,1600 1630,1900-1930 2000-2030,2100 2130,0000-0030 0200-0300; 11 MHZ 0930-1000,1330-1500 1730-1800, 2330-0200; 12 MHZ 1530-1630 15 MHZ 2300-0130 0200-0300,1200- 1230,1600-1630; 17 MHZ 1600-1630 0200-0300; 21 MHZ 1300-1330,1400- 1430;	3 MHZ 0900-1000 1030-1130 1200-12300 6 MHZ 0630-0700 11 MHZ 0100-0130 15 MHZ 1900-1930 0100-0430	3 MHZ 0600-0630 0330-0500 4 MHZ 2100-2200 2230-2300,0330 -0530,0600-0700 6 MHZ 1930-2300,0330 0400; 7 MHZ 2200-0100 11 MHZ 1200-1300 1830-1900 0630-0700 15 MHZ 1800-2100 2030-2200	3 MHZ 2330-0130 0200-0230 0500-0530 5 MHZ 2330-0000 11 MHZ 0000-0030
78	6 MHZ 0330-0400 0430-0700 9 MHZ 0000-0200 1830-1900 11 MHZ 1300-1330 2130-2200,0300 -0330; 15 MHZ 1230 1300,1430-1500 1600-1630 2200-2230	3 MHZ 0400-0430 4 MHZ 0200-0230 0530-0630 11 MHZ 2330-0230	4 MHZ 1030-1330 0400-0430 7 MHZ 1030-1300 1600-1900; 9 MHZ 1100-1130,2030 2100,2130-2230 0130-0300,0500 0530; 11 MHZ 1100 1600,1630-1900 2030-2200,2330 0000,0100-0130; 15 MHZ 1930-2130	3 MHZ 1230-1300 11 MHZ 0500-0700 15 MHZ 1830-1900 0200-0230, 0300-0530	3 MHZ 2130-2200 2230-2300,0230 -0700; 4 MHZ 2200 -2300,2330-0000, 0400-0530,0600 0630; 5 MHZ 2130 2300; 6 MHZ 0600 -0630,2230-2300 7 MHZ 0130-0200 0330-0400,0500 0600,0900-0930; 9 MHZ 1830-2230	3 MHZ 0230-0300 0330-0430,1030 1100; 6 MHZ 1930 2100; 11 MHZ 1530 1600; 15 MHZ 1800 -1830,2200-2230

Table 3e.

SFI	EUROPE	SOUTH AMERICA	ASIA	OCEANIA	AFRICA	NORTH AMERICA
			2200-2230,2300 0100,0130-0230 0500-0530 1130-1330		11 MHZ 1630-1700 1800-2000,2030 2100; 15 MHZ 1200 1300,1530-1600,1730 1800,1900-2200; 17 MHZ 1200-1230, 1400-1530	
77	5 MHZ 0100-0130 0530-0600 6 MHZ 0630-0700 9 MHZ 0000-0200 1830-1900 11 MHZ 1300-1330 2130-2200,0300 -0330; 15 MHZ 1230-1300,1430 1500,1600-1630 2200-2230	9 MHZ 1100-1130	3 MHZ 1130-1200 0500-0530 5 MHZ 1000-1030 1200-1230,2200 -2230; 7 MHZ 1800 1900; 0300-0330; 9 MHZ 1300-1330 1500-1730,2000 -2100,2130-2230 2330-0200,0300 -0330; 11 MHZ 1200 -1300,1630-1900 2200-2230,2330 0030; 15 MHZ 2300 -0230; 17 MHZ 1430-1600	3 MHZ 1200-1230 4 MHZ 0530-0630 7 MHZ 0600-0630 11 MHZ 0530-0630 0330-0430 15 MHZ 0200-0230 2300-0630	3 MHZ 2130-2200 2230-2300,0430 0600; 4 MHZ 2200 2300,0400-0430 0500-0530; 5 MHZ 2130-2300; 6 MHZ 0600-0630 7 MHZ 2330-0000,0330 7 MHZ 2330-0000 0430,0500-0630 0800-0830; 9 MHZ 1830 -2200,0230-0300, 0500-0530; 11 MHZ 1300-1330,1930 -2030; 15 MHZ 1500 -1630,1730-1800 2000-2200; 17 MHZ 1200-1230,1400-1500	11 MHZ 1530-1600 15 MHZ 1800-1830
76	6 MHZ 2300-2330 0000-0130,0230 -0300; 7 MHZ 2230 -2300,0100-0200 0600-0800; 9 MHZ 0400-0430 11 MHZ 2300-2330 0030-0130; 15 MHZ 1400-1430,1500 -1630,1700-1730 1900-1930 17 MHZ 1530-1600	3 MHZ 0330-0400 5 MHZ 0500-0530 9 MHZ 0430-0500 1100-1130 11 MHZ 2300-0230	2 MHZ 2200-2230 5 MHZ 1030-1100 6 MHZ 0900-0930 1030-1100; 7 MHZ 1130-1230,1930 2000; 9 MHZ 1100- 1130,1200-1230 1430-1530,1630 -1730,1800-2100 2200-0330; 11 MHZ 1030-1300,1330 -1400,1700-2030 2100-2200,2230- 2300,2330-0000 15 MHZ 1030-1100 1430-1530,2330 0330,1900-1930 17 MHZ 1200-1230	2 MHZ 1030-1100 1200-1230 7 MHZ 0530-0630 9 MHZ 1100-1230 11 MHZ 0600-0630 15 MHZ 0100-0630	3 MHZ 2330-0000 0300-0430,0530 -0630; 4MHZ 2200 -2300,2330-0000 0300-0430,0600 5 MHZ 2030-2200 0600-0630; 6 MHZ 2230-0000; 7 MHZ 0500-0530, 0600-0630,0730 -0800,0300-0330, 0400-0430; 9 MHZ 1830-2230,2330 0000,0200-0400 11 MHZ 2030-2100 2130-2230; 15 MHZ 1300-1700,1800 1830,1900-2230; 17 MHZ 1330-1400,1730 -1800,0100-0130; 21 MHZ 1300-1330	3 MHZ 0430-0530 1130-1200 5 MHZ 0200-0230 6 MHZ 0430-0500 9 MHZ 1200-1400 0330-0430 0330-0430 11 MHZ 0000-0030 0300-0330,0500- 0530; 15 MHZ 0030-0100 2030-2200
75	3 MHZ 0630-0700 6 MHZ 0100-0200 0330-0400,0700 0830; 7 MHZ 0230-0330 9 MHZ 2130-2230 0000-0030,0100 0130; 11 MHZ 1730-1800,0330 0430; 12 MHZ 1300 1330,2030-2100;	3 MHZ 0630-0730 0900-1030,1130 1130-1200; 4 MHZ 1130-1200 1230-1300,0000 0200,0330-0430 5 MHZ 0200-0230 9 MHZ 0430-0200 1130-1200 10 MHZ 0900-1030 11 MHZ 2300-0230	4 MHZ 1100-1130 1200-1230; 5 MHZ 1100-1130,1300 1330; 6 MHZ 2200 2230; 7 MHZ 1030 1230,1930-2000 2100-2300,0330 0400; 9 MHZ 1100 1130,1800-1830 2000-2330,0230 0300; 11 MHZ 1030	3 MHZ 1000-1130 4 MHZ 1230-1300 5 MHZ 0800-1200 7 MHZ 0600-1100; 9 MHZ 0130-0830 11 MHZ 0400-0430 15 MHZ 2300-0030 2300-0330,0600 0630;	3 MHZ 2200-0100 0330-0800; 4 MHZ 1930-2030 2100-0100,0330 0730; 5 MHZ 2130 0600,0500-0530; 6 MHZ 2100-2300 0400-0600; 7 MHZ 0130-0500; 9 MHZ 1830-0000 0300-0330; 11 MHZ	3 MHZ 0130-0200 0300-0430; 4 MHZ 0430-0500 6 MHZ 1130-1200 1930-2000 9 MHZ 1400-1430 2000-2030,2330 0000; 2100-2330;

Table 3f.

SFI	EUROPE	SOUTH AMERICA	ASIA	OCEANIA	AFRICA	NORTH AMERICA
	15 MHZ 1330-1400 1600-1630,2030 21 MHZ 1500-1630	15 MHZ 2100-2130 0000-0200	1230,1600-1630 1800-1830,2100 2130,2200-2230 15 MHZ 1900-1930 0000-0300,1100-1200		1930-2130; 15 MHZ 0800-1500,1530 1600,1800-1830 2130-2300 0000-0100	
74	5 MHZ 0100-0130 6 MHZ 2300-2330 0000-0030,0130 -0200,0230-0300 0430-0500; 9 MHZ 2130-2230 0100-0400 11 MHZ 0100-0400,1700 2030-2100 12 MHZ 1200-1230 15 MHZ 1300-1330	3 MHZ 0130-0300 4 MHZ 2330-0030 0100-0230,1100 -1130; 5 MHZ 0100 0130,0230-0300 6 MHZ 0900-0930 9 MHZ 0030-0100 0130-0200,0300 0400,2300-2330 11 MHZ 2300-0230	3 MHZ 1130-1200 2300-0000 4 MHZ 1130-1200 2230-2300,0100 -0200; 5MHZ 1100 1130,1300-1330 6 MHZ 1000-1200 7 MHZ 2100-2300 9 MHZ 1230-1330 2230-2330,0230 -0300; 10 MHZ 1300 1400; 11 MHZ 0430 0500,1200-1330 1630-1800,2100 2200,2300-2330 12 MHZ 1300-1330 1400-1430,1800 1800-1930,0100 -0130 21 MHZ 1400-1530	2 MHZ 0900-0930 3 MHZ 1000-1030 1130-1200 4 MHZ0900-1330 6 MHZ 1000-1300 7 MHZ 0730-0800 9 MHZ 1500-1530 11 MHZ 1100-1200 1930-2000; 15 MHZ 2030-2100,2300 0030,0230-0630	3 MHZ 2130-0000 0330-0430 4 MHZ 2030-0000 4 MHZ 2030-0000 0230-0700; 5 MHZ 2130-2230,0500 -0600; 6 MHZ 2130 2330,0330-0400 7 MHZ 2130-2330 9 MHZ 1630-1700 1800-2130,0300 0330; 11 MHZ 1430 1500,1730-2200 0600-0630 15 MHZ 1300-2300	3 MHZ 0100-0300 4 MHZ 2330-0100 0300-0330,0430 -0500,0630-0730 6 MHZ 0030-0100 9 MHZ 1130-1400 0400-0430 11 MHZ 0630-0700 1200-1230; 15 MHZ 2000-2030
73	5 MHZ 0100-0230 6 MHZ 0000-0030 0700-0730,0800 0815; 7 MHZ 0730 0800; 9 MHZ 1500 1530; 11 MHZ 1700 1600; 15 MHZ 1230 1330,1630-1630 1700-1800	3 MHZ 0630-0700 4 MHZ 2330-0000 0400-0430,0930 -1000; 5 MHZ 0400 0630-0700,1000 1030; 6 MHZ 1000 -1100; 9 MHZ 0400 0500,2000-2100 15 MHZ 1900-1930 2100-2130,0000 0200	4 MHZ 1130-1230 6 MHZ 1130-1330 0030-0100 7 MHZ 1100-1330 9 MHZ 1230-1200 1300-1400,1900 2030; 11 MHZ 1100 1230,1500-1530 1800-1830,0130 0200; 12 MHZ 1230 1300; 15 MHZ 1100 -1130,1200-1300, 1400-1500,1600 1700,1800-1830 2300-04000 17 MHZ 1430-1600	5 MHZ 0730-0900 0630-0900 1300-1330 9 MHZ 1200-1230 11 MHZ 2230-2330 0600,0630-0700	3 MHZ 2230-0000 0300-0400 4 MHZ 1100-1130 2100-0000,0300 0400-0500,0600 -0700; 5MHZ 0400 11 MHZ 1230-1400 6 MHZ 2130-2200; 6 MHZ 2130-2200 7 MHZ 0600-0700 9 MHZ 1900-1930 11 MHZ 1000-1030 1530-1800,1830 2030,2130-2200 15 MHZ 1530-1700 0000-0100 1800-1900	4 MHZ 0030-0530 0630-0700 5 MHZ 0430-0600 6 MHZ 0600-0630 1000-1030 1930-2100 0100-0130
72	5 MHZ 2130-2200 0100-0130 6 MHZ 2300-2330 0100-0130 0300-0330 7 MHZ 0100-0200 9 MHZ 2030-2130 2230-2330,0300 0030,0100-0200 0300-0330 11 MHZ 1630-1730 1930-2000,0130 0300; 15 MHZ 1330 1400,1600-1700 1730-1830	2 MHZ 1030-1100 3 MHZ 0000-0100 0130-0200,0700 0830,0900-0930 4 MHZ 2330-0000 0030-0100,0200 0230,0400-0430 0500-0530,1000- 1030; 5 MHZ 0200 0230; 6 MHZ 0700 0730,1000-1030 9 MHZ 0000-0200 10 MHZ 2300-2330 11 MHZ 2100-2130 2300-2330,0030	2 MHZ 2130-2200 4 MHZ 1030-1100 5 MHZ 1130-1230 2330-0000 9 MHZ 1100-1130 1700-1730,1930 2030,2100-2130 2200-2230 11 MHZ 1000-1030 1100-1500,1930 2030,2100-2230 12 MHZ 1200-1300 15 MHZ 1200-1300 17 MHZ 0200-0300	3 MHZ 1030-1200 4MHZ 0800-0900 1130-1200 7 MHZ 0600-0800 1000-1100 9 MHZ 0700-0730 1130-1200,1500 1600; 11 MHZ 0200 0230,0600-0730 15 MHZ 1830-1900 0130-0500	3 MHZ 2230-0000 0230-0400; 4 MHZ 2100-0000 0300-0500,0630 0700; 5 MHZ 2200 0000,0530-0700 6 MHZ 1930-2230 0000-0030,0 00 0330,0600-0630 7 MHZ 2300-2330 0630-0730 9 MHZ 1230-1400 1800-2100,2200 2230,2300-2330 0230-0300 11 MHZ	3 MHZ 2330-0000 0030-0100,0200 0230; 4 MHZ 2130 2200,0030-0500 5 MHZ 0330-0530 6 MHZ 1100-1200 0200-0230 9 MHZ 2130-2200 0130-0200,0330 0400,0430-0500 11 MHZ 0300-0330 15 MHZ 2000-2100 2200-0000
71	6 MHZ 2300-2330 0430-0500,0800 0830; 7 MHZ 0300-0330 9 MHZ 2300-0100 0130-0200 11 MHZ 0100-0300	2 MHZ 0130-0200 3 MHZ 0400-0430 1000-1030,2300 2300-2330; 4 MHZ 0330-0430 0500-0530 6 MHZ0530-0600 11 MHZ 0200-0230 15 MHZ 1300-1330 1400-1430 2200-2300	3 MHZ 1100-1200 4 MHZ 1100-1200 5 MHZ 1100-1200 2230-2300 6 MHZ 2230-2300 7 MHZ 0930-1000 1030-1130; 9 MHZ 0800-0830,0900 0930,1930-2100 11 MHZ 1130-1200 1330-1400,1730 1930,2000-2030 2100-2200,2330 -0000,0400-0430 15 MHZ 1600-1700 2030-2100,0230 0300,0400-0430	3 MHZ 1030-1130 4 MHZ 1030-1130 6 MHZ 0800-0830 9 MHZ 0600-0630 1130-1230 11 MHZ 0230-0300 0330-0400,0600 0630; 15 MHZ 0200 -0230,0500-0530	3 MHZ 2100-2200 2230-0000,0230 0330,0400-0530 4 MHZ 0400-0700 5 MHZ 0530-0700 6 MHZ 2200-2230 0330-0430; 7 MHZ 0230-0300,0530 0700; 9 MHZ 0600 -0630; 11 MHZ 1300 1330,1730-2200 15 MHZ 1400-1700 1800-2100,2130 -2200 17 MHZ 1500-1700	3 MHZ 0230-0300
70	7 MHZ 2130-2200 9 MHZ 2100-2130 15 MHZ 1400-1430 1700-1730	4 MHZ 0400-0430 15 MHZ 2200-2230	3 MHZ 1230-1300 4 MHZ 1130-1200 5 MHZ 1230-1300 7 MHZ 1130-1230 9 MHZ 1330-1400 11 MHZ 1830-1930 2100-2200,2330 -0000; 15 MHZ 1900-1930	3 MHZ 1100-1130 6 MHZ 0830-1030 9 MHZ 1100-1300	3 MHZ 2300-0000 0400-0530 4MHZ 2100-2300,2330 -0300; 5 MHZ 0530 -0630,1930-2230 6 MHZ 2230-2330 0300-0330,0500 0500-0600; 7 MHZ 0000-0030,0430 0630; 9 MHZ 0230-0300 11 MHZ 1930-2000, 2030-2100; 15 MHZ 1700-1830 2300-0030	3 MHZ 1000-1030 6 MHZ 1100-1130 9 MHZ 1130-1330 1600-1800,1830 1900,0300-0330 11 MHZ 2300-2330 15 MHZ 2000-2100
69	7 MHZ 0100-0130 0200-0230 9 MHZ 2300-2330 0000-0230 11 MHZ 2300-2330 0100-0230 15 MHZ 1700-1800 2100-2130,2200 -2300,0200-0230	4 MHZ 0000-0030 0400-0430 9 MHZ 0000-0300 0430-0500 11 MHZ 0000-0030	6 MHZ 1100-1230 2230-2330 7 MHZ 1200-1300 2100-2130,2300 2330,0400-0430 9 MHZ 1030-1100 1800-1830,1930 2200; 11 MHZ 1000 -1030,1100-1200 1230-1300,1730 -0030; 12 MHZ 0200 -0230; 15 MHZ 0000 -0200,1100-1130, 1700-20000 17 MHZ 0230-0330	3 MHZ 1000-1030 4 MHZ 0800-0830 1000-1030 5 MHZ 0730-0930 5 MHZ 1030-1130 7 MHZ 0500-0530 1030-1100 9 MHZ 1230-1300 0430-0500 11 MHZ 0130-0330 0500-0530 15 MHZ 0300-0330	3 MHZ 2230-2300 0330-0400,0430 -0500,0630-0730 4 MHZ 2200-2330 0330-0630 5 MHZ 2200-2330 0730-0930 7 MHZ 2130-2200 0330-0430; 9 MHZ 1830-1900,1930 2030,2200-2230 0230,2200-2230 2030,2200-2230 11 MHZ 1500-1830 1930-2230,0030 0100; 15 MHZ 1100- 1200,1330-1600,1730 1830,1900-2000,2300 2330,0130-0200 0530-0600	3 MHZ 0430-0530 5 MHZ 0530-0600 6 MHZ 0000-0030 9 MHZ 1230-1300 11 MHZ 2200-2230 0130-0230 15 MHZ 1330-1400 1930-2130
68	7 MHZ 0030-0100	4 MHZ 1000-1030	3 MHZ 0000-0030	4 MHZ 0830-0900	3 MHZ 2330-0000	3 MHZ 0400-0430

Table 3g.

Table 3h.

SFI	EUROPE	SOUTH AMERICA	ASIA	OCEANIA	AFRICA	NORTH AMERICA
	0700-0730 9 MHZ 2200-0030 0130-0230 11 MHZ 2200-0000 0030-0300 15 MHZ1400-1430	11 MHZ 2300-0000 15 MHZ 2200-2230 2300-2330 2300-2330	4 MHZ 1330-1400 0000-0030; 9 MHZ 1930-2030,2100 2130,2200-2230 11 MHZ 1300-1330 1700-1930,2000 2030,2130-2300 0000-0030,0100 0330; 15 MHZ 2230 0000-0130; 17 MHZ 1500-1530	7 MHZ 0730-0800 9 MHZ 0600-0630 0800-0830 11 MHZ 0130-0200 0330-0400 15 MHZ 0200-0230 0300-0330	0330-0400; 4 MHZ 2200-2230,0230 0400,0600-0630 6 MHZ 2100-2130 0330-0400 7 MHZ 0030-0130 9 MHZ 1630-2030 9 MHZ 1630-2030 2200-2230; 11 MHZ 0630-0700; 15 MHZ 1800-1900 2030-2100; 17 MHZ 1330-1400,1530-1600	5 MHZ 0530-0600 11 MHZ 1200-1300 0100-0130; 15 MHZ 2000-2130 15 MHZ 2000-2130 0400-0430
67	6 MHZ 0130-0200 9 MHZ 0000-0030 0130-0200 11 MHZ 1930-2100 0130-0200 15 MHZ 2100-2130	4 MHZ 0330-500 0900-0930 5 MHZ 0330-0500 0630-0730 11 MHZ 2300-2330 15 MHZ 1200-1230 2300-0000	4 MHZ 1030-1100 6 MHZ 1100-1200 2200-2230 9 MHZ 1930-2230 11 MHZ 1330-1400 1700-2000,2100 2200,0000-0030 15 MHZ 0000-0130 0330-0400,1600 1630,1830-1900	3 MHZ 0630-0730 0900-1330 4 MHZ 0700-1130 5 MHZ 0600-0630 9 MHZ 0430-0500 1200-1300 11 MHZ 0330-0430 0630-0700 15 MHZ 0230-0300 0330-0400 1700-1730	3 MHZ 2330-0000 0430-0530,0600 4 MHZ 2030-2100 2130-2230,0400 -0730; 5 MHZ 2230 2300,0430-0630 6 MHZ 2130-2230 0300-0330,0530 -0600; 7 MHZ 0300 0400,0430-0530 9 MHZ 1630-2030 11 MHZ 1500-1700 1900-2000,0400 -0430,0530-0600 15 MHZ 2030-2300 17 MHZ 1230-1300	3 MHZ 0130-0200 4 MHZ 0300-0430 0500-0530,1000-1030 6 MHZ 0530-0600 1030-1100 1030-1100 9 MHZ 0700-0730 11 MHZ 1130-1200 1300-1330,1500 -1530,0030-0100 0300-0330,0530-0600 14 MHZ 2200-2300 15 MHZ 0130-0200 0300-0330
66	5 MHZ 0130-0230 6 MHZ 0200-0230	3 MHZ 0830-0900 4 MHZ 0300-0400 11 MHZ 2300-2330	9 MHZ 0900-0930 1000-1030,2030 2200; 11 MHZ 1200 -1230,1600-1630 1700-1930,2100 2130,2300-0000 15 MHZ 2100-2130 0130-0200	4 MHZ 0830-0900 11 MHZ 0300-0500	3 MHZ 0300-0330 4 MHZ 2200-2230 0230-0300; 6 MHZ 2100-2130 7 MHZ 0400-0430 0600-0630 11 MHZ 0200-0230 0700-0730,1900 -1930,2330-0000 15 MHZ 2330-0030 0200-0230	15 MHZ 2000-2100 17 MHZ 1500-1530

Table 3i.

On 6 July 1976 the flux was 67. The chart indicates many openings, including: 4 MHz, Africa, 0400-0730 GMT; 4 MHz, Oceania, 0700-1130 GMT. The following was actually heard: Liberia on 4.770 MHz at 0635-0711; Ghana on 4.890 and 4.915 MHz at 0602-0700; Papua New Guinea on 4.890 MHz at 0705-0720; Australia on 4.920 MHz at 0700.

On 22 and 23 February and 7 March 1977 the flux was 78. Among the openings on the chart are: 3 MHz, North America, 0330-0430; 6 MHz, Europe, 0330-0400; 11 MHz, Africa, 1630-1700, 1800-2000; 15 MHz, Asia, 2200-2230, 2300-0100. These stations were heard with good reception: Guatemala on 3.300 MHz at 0340, Portugal on 6.025 at 0335, Malagasy Republic (Radio Nederland) on 11.730 at 1930, Liberia on 11.940 at 1657, and Japan at 2300, 0000, 0100 all on 15.105 MHz.

On 7 June 1977 the flux was 89. Among the openings predicted by the chart are: 9 MHz, Asia, 1830-1930; 11 MHz, Asia, 2100-2130; 15 MHz, Asia, 0400-0530. The following stations were heard with good reception: India on 9.525 MHz at 1850, Pakistan on 11.625 MHz at 2115-2125, and Japan on 15.310 MHz at 0458.

On 28 December 1977 the flux was 102 and the following openings were possible: 4 MHz, Africa, 2130-2300, 0400-0430, 0530-0630; 4 MHz, Oceania, 1000-1400; 9 MHz, Africa, 2030-2100; 4 MHz, Asia, 1300-1330; 12 MHz, Asia, 1800-1830. These stations were heard on that day: Liberia on 4.770 MHz at 2140, South Africa on 4.880 MHz at 0417, Papua New Guinea on 4.890 MHz at 1026-1400, Ghana on 4.915 MHz at 2200-2300, 0600-0615, Australia on 4.920 MHz at 1215-1234, Nigeria on 4.932 MHz at 0605, Malaysia on 4.950 MHz at 1329, Nigeria on 4.990 MHz at 2109 and 0558, Uganda on 9.730 MHz at 2031, Kuwait on 12.085 MHz at 1802.

On 27 February 1978 the flux was 140. The chart predicted: 3 MHz, North America, 1100-1200, 0230-0300; 4 MHz, Asia, 1030-1230; 4 MHz, Oceania, 1130-1200; 15 MHz, Asia, 1200-1230. The following stations were heard: Guatemala on 3.300 MHz at 1117-1130, 3.330 MHz at 0200-0300, and 3380 MHz at 1130; Mongolia on 4.763 MHz at 1030-1045; Sumatra on 4.768 MHz at 1135; Papua New Guinea on 4.890 MHz at 1139; Cambodia on 4.908 MHz at 1111; Vietnam on 15.012 MHz at 1201.

On 29 April 1978 the flux was 183. The chart shows 6 MHz, South America, 1000-1100; 9 MHz, Asia, 2200-2230; 3 MHz, Oceania, 1030-1130; 9 MHz, Africa, 2030-2100. The following were actually heard that day: Papua New Guinea on 3.335 MHz at 1059-1101 and Peru on 6.020 MHz at 1016-1033.

7. CONCLUSION

Thus a method to predict solar radiation levels and thereby radio wave propagation predictions has been developed for North America. With additional help and data, charts could be compiled for every part of the globe.

ACKNOWLEDGMENTS

I would like to thank my parents, Isaac and Rachel, for their patience and understanding with my work; my brother , Marc, for reveiwing much of the work and for his useful suggestions. A special thanks to Andrew Blumberg , Dov Banner , Michele Kitchner for their ideas and support , and to Morris Kitchner for his help and use of his dissertation. Thanks to all who have reveiwed this paper for their many and useful corrections. Last but not least thanks to G-d above who has guided me along this strange path.

REFERENCES

Dixon, Wilfred J., and Frank J. Massey (1969): Introduction to Statistical Analysis.

King, J. W., and W. S. Newman (1967): Solar Terrestrial Physics.

Kitchner, Morris (1955): Some Non-Parametric Tests for Time Series. Master of Arts dissertation, Department of Economics, New York University.

"Radio Propagation Forecast Information Via Radio Station WWV", U.S. Department of Commerce, Institute for Telecommunications.

Seber, G.A.F. (1977): Linear Regression Analysis.

Snodgrass, Joan G. (1977): The Numbers Game.

Solar Geophysical Data, explanation of data reports, U.S. Department of Commerce, National Oceanic and Atmospheric Administration.

Wonnacott, Thomas H., and Ronald J. Wonnacott (1977): Introductory Statistics for Business and Economics.

GRAFEX PREDICTIONS

J. F. Turner
Ionospheric Prediction Service
Australian Department of Science and the Environment
P.O. Box 702
Darlinghurst NSW 2010, Australia

A form of presentation of HF radio propagation predictions is described. This form contains the information needed for operational and short term planning, is compact and can be produced rapidly using a lineprinter.

1. INTRODUCTION

The Australian Ionospheric Prediction Service produces two types of predictions each intended to meet a specific need. The first type is intended for operational purposes which are mainly concerned with the selection of frequencies. The second type is for planning and design and involves calculation of quantities such as path loss. For convenience these are referred to as frequency and path predictions respectively. The availability of the world maps of basic ionospheric parameters in numerical form has made it possible to produce both type predictions using an electronic computer. Frequency type point-to-point predictions can be produced quickly and in large quantities. Although the path type predictions can also be produced reasonably quickly, they involve much more computing time. The bulk of communication prediction requirements are for operational purposes which can be satisfied by the frequency type predictions.

As the computing involved in producing a frequency type prediction can be performed very rapidly, there was a need for a way to display the results which was correspondingly rapid. The GRAFEX form was developed to meet this need. In addition to being fast the prediction computations produced a considerable amount of detail and the GRAFEX form attempts to show as much of this information as considered desirable in a reasonably compact form. (The name GRAFEX has no special significance; it was the name of the computer program which produced this form.)

2. FREQUENCY TYPE PREDICTIONS

The frequency type prediction information considered useful includes the upper decile, median and lower decile F-layer MUFs, the E-layer median MUF and the ALF for each hour (UT) for the first two possible modes. The MUF depends on the ionization density and height of a layer and an obliquity factor.

The F2 layer, because of its greater height and density and its persistence, is the most important layer for long-distance communication. However, because the angle of incidence of a signal on the lower layers is greater, the obliquity factor is greater for these layers and under certain conditions the MUF for a lower layer may be greater than that for the F2 layer. Consequently, in making predictions, the lower layers must be taken into account.

A signal propagated by the ionosphere may travel by one or more reflections from the ionized layer. If only one ionospheric reflection occurs this is referred to as single hop or more correctly as a 1F or 1E mode depending on the layer involved. There is a limit to the range at which a signal can be received by one ionospheric reflection. For the F layers this limit is between 3,000 and 4,000 kilometers and for the E layer it is about 2,000 kilometers. It should be noted that the F1 and F2 layers are treated together. The ALF is an estimate of the lowest usable frequency and is derived empirically from a combination of absorption and the E-layer cut-off.

Signals may travel between two terminals by more than one mode. Of course, the minimum number of reflections will use longer hops and have larger obliquity factors than the others. Thus the highest frequency which can be used is usually the MUF for the simplest mode. For higher modes the obliquity factor for the ALF will decrease and thus the lower limit of the range of usable frequencies will apparently decrease. However, other factors such as the loss of signal at each reflection, shielding by lower layers and poor aerial directivity, will tend to offset the lowering of the minimum by this decrease in the obliquity factor. Generally only the first two possible modes need to be considered.

3. PRESENTATION OF PREDICTION INFORMATION

The information could be displayed in tabular form but this is not easy to use; a diagram is preferable. Figure 1 shows the predictions in tabular form with appropriate headings. This form is only used for special purposes. A graph with time of day as the horizontal axis and frequency as the vertical axis showing the change in the various parameters through the day is a useful form. However, producing graphs either manually or using a computer plotter is slow and defeats the objective of having the output match the speed of the prediction computation. The GRAFEX form overcomes this by converting the predictions to a form which can be printed by the fast line printer but retains the diagramatic appearance.

By examining the numerical predictions for any desired hour it is possible, for a specific frequency, not only to determine whether the frequency will be received or not, but also to make some estimate of the probable quality of the received signal from the prediction information about the various modes. It has been found that the information in the predictions applied to a specific hour and frequency can be fitted into one of eleven categories.

NAME	SYDNEY	BRISBANE	LENGTH		731 KMS		AZIMUTHS		14.5		193.5	DATE			MARCH	100						
	0	1	2	3	4	5	6	7	8	9	10	11	12	13	14	15	16	17	18	19	20	21	22	23
FIRST MODE																								
UD	151	155	156	156	154	153	151	148	146	129	116	110	110	113	110	108	102	92	87	85	97	124	137	144
MED	137	140	142	141	139	137	136	133	128	111	100	95	91	89	87	85	83	77	73	71	85	112	124	131
LD	118	122	123	122	120	119	118	115	110	95	85	81	75	72	70	68	66	62	59	58	70	97	107	113
EMUF	121	126	129	127	123	115	103	86	63	30	0	0	0	0	0	0	0	0	0	22	62	86	102	113
ALF	49	50	51	50	49	46	42	35	18	0	0	0	0	0	0	0	0	0	0	0	25	38	43	47
SECOND MODE																								
UD	117	121	122	122	121	120	118	115	114	104	95	90	90	93	91	88	83	75	72	69	75	92	105	111
MED	106	110	111	111	110	108	106	104	101	91	83	79	75	74	73	71	68	64	61	59	66	84	95	101
LD	93	96	97	97	96	94	92	90	87	77	71	68	63	60	59	57	55	51	48	47	56	73	83	88
EMUF	67	70	71	71	68	64	57	48	35	16	0	0	0	0	0	0	0	0	0	12	34	47	56	62
ALF	36	37	37	37	36	34	31	26	15	0	0	0	0	0	0	0	0	0	0	0	19	28	32	35

UNIT 100KHZ

NAME	DARWIN	BRISBANE	LENGTH		2846 KMS		AZIMUTHS		129.2		301.5	DATE			MARCH	100						
	0	1	2	3	4	5	6	7	8	9	10	11	12	13	14	15	16	17	18	19	20	21	22	23
FIRST MODE																								
UD	345	366	375	375	379	381	387	379	350	325	291	275	268	275	286	275	268	250	223	197	202	254	298	316
MED	309	328	336	336	339	342	343	336	310	278	240	227	221	217	214	206	201	187	165	146	149	207	267	283
LD	273	293	308	308	311	309	307	301	278	239	202	191	185	178	171	164	160	144	123	109	111	169	235	250
EMUF	0	0	0	0	0	0	0	0	0	0	0	0	0	0	0	0	0	0	0	0	0	0	0	0
ALF	137	142	145	145	143	138	130	116	92	81	0	0	0	0	0	0	0	0	0	0	0	86	114	128
SECOND MODE																								
UD	220	239	240	236	241	239	243	234	232	206	181	171	173	178	179	176	175	162	146	126	120	139	189	219
MED	202	216	216	213	217	213	217	209	200	172	151	143	139	137	137	135	134	123	111	103	98	120	174	199
LD	175	192	199	196	198	192	196	189	175	147	129	122	116	112	113	110	107	96	87	82	78	100	150	173
EMUF	180	191	199	198	193	183	168	144	111	61	10	0	0	0	0	0	0	0	0	0	0	96	133	160
ALF	85	86	90	90	89	87	82	75	64	0	0	0	0	0	0	0	0	0	0	0	38	61	74	81

UNIT 100KHZ

Figure 1. Tables showing UD, median and LD F layer MUFs, E-layer MUF and ALF for two modes for two circuits.

Figure 1. Tables showing UD, median and LD F layer MUFs, E-layer MUF and ALF for two modes for two circuits.

4. GRAFEX SYMBOLS

These categories for the frequency (with the symbols) are as follows:

1. ( ) above all the normal MUF. (Of course the signal may be propagated by an unusual mode (e.g., sporadic E) or abnormally high ionization density.) This symbol is also used when the frequency is below the lowest ALF.
2. (.) below the first F mode upper decile MUF but above the median MUF. The frequency will be propagated on more than three days of the month but less than half the days.
3. (%) below the first F mode median MUF but above the lower decile MUF. The frequency will be propagated on more than half the days in the month but less than 90% of the days.
4. (F) below the first F mode lower decile MUF but above either MUF's. Communication on frequencies in this category should be usable on almost all days except, possibly, when an ionospheric storm is in progress.
5. (E) below the first E mode median MUF but above the first F mode median MUF. (The variation throughout the month about the E median MUF is very small so deciles are not quoted for this layer.) Propagation may still be possible by the F layer on a few days of the month.
6. (P) below the first E mode MUF and below the first F mode median MUF but above the F mode lower decile MUF. Propagation by first E mode is possible on all days and by the first F mode on more than half the days.

7. (B) below the first E mode MUF and below the first F mode lower decile MUF. Propagation is possible by both E and F modes on most days of the month.
8. (M) below the first F mode lower decile, below the second F mode median MUF and maybe also below the first E MUF. The mode by which the signal will be propagated in practice will depend on several factors including the aerial elevation angle and beamwidth used.
9. (S) below the second F mode median MUF and below the first mode ALF.
10. (A) very close to an ALF. (If the ALF is the first mode ALF the mixed mode symbol (M) overrides this.)
11. (X) below the second E mode MUF. Other modes such as mixed E and F and higher order F modes are also probable.

(Categories 2-7 must be above the first mode ALF and 8, 9 and 11 must be above the second mode ALF.)

5. COMMENTS ON THE SYMBOLS

In most cases these eleven categories are adequate to describe the propagation conditions but occasionally some unusual combination of numerical values will produce a peculiar classification. Some changes and additions to the categories have been made since the GRAFEX process was first used. These were introduced because it was found that the earlier categories were inadequate in enough cases to justify the increased complexity of additional symbols.

It should be noted that the second F mode upper decile and lower decile MUFs are ignored. The categories 8 and 9 use the median MUF. It is considered that including the extra categories using the second mode deciles would unduly complicate the resulting picture without much advantage. However, there is one very important case involving the second mode deciles. This is when no first mode F layer communication is possible. This can occur on circuits with hops between 3000 and 4000 kilometers length. If the F layer height is low the maximum length of the hop may be less than that required. In this case the highest frequencies that can be used are controlled by the second mode and Categories 2 and 3 are determined from the second mode deciles (Categories 4 to 8 are not possible).

6. FORMAT FOR PRINTING GRAFEX PREDICTIONS

The basic GRAFEX process involves determining, for a given frequency, the category for each hour using the numerical predictions, the appropriate symbol being printed in a tabulation (the 0 hour symbol is repeated for the 24th hour). The frequency is printed at the left hand end of the line.

The lines of GRAFEX symbols can be arranged in various ways but there are two forms commonly used.

If a user only requires predictions for specific frequencies a GRAFEX line can be produced for each of the frequencies. These can be printed with circuit name and date to give a very compact and complete prediction (Figure 2).

```
                    **KEY**

                .   USABLE LESS THAN 50% OF DAYS
                %   USABLE LESS THAN 90% OF DAYS
                F   FIRST F LAYER MODE ONLY
                E   E LAYER PROPAGATION POSSIBLE
                P   PROPN E (90%) OR F (50-90%) DAYS
                B   BOTH E&F MODES POSS. 90% OF DAYS
                M   MIXED FIRST AND SECOND F MODES
                S   SECOND F MODE BUT NO FIRST MODE
                A   HIGH ABSORPTION
                X   COMPLEX MODES

SYDNEY BRISBANE                                                 MARCH    100
FREQ  00  02  04  06  08  10  12  14  16  18  20  22  24
 MHZ   .   .   .   .   .   .   .   .   .   .   .   .   .
15.0   .   .   .   .   .   .   .                           .
12.5   %   P   P   P   %   %   %   %   %   .                   .   %   %
10.0   M   M   M   M   M   M   M   M   M   %   .   .   .   .   .   .   .   %   B   M   M
 7.5   M   M   M   M   M   M   M   M   M   M   M   M   M   %   %   %   %   %   .   .   %   M   M   M   M
 6.0   X   X   X   X   X   X   M   M   M   M   M   M   M   M   M   M   M   M   M   %   M   M   M   X   X
 4.0   A   A   A   A   A   X   X   X   M   M   M   M   M   M   M   M   M   M   M   M   M   X   X   A   A
       .   .   .   .   .   .   .   .   .   .   .   .   .   .   .   .   .   .   .   .   .   .   .   .   .
      00  02  04  06  08  10  12  14  16  18  20  22  24

DARWIN BRISBANE                                                 MARCH    100
FREQ  00  02  04  06  08  10  12  14  16  18  20  22  24
 MHZ   .   .   .   .   .   .   .   .   .   .   .   .   .
24.0   F   F   F   F   F   F   F   F   F   %   .   .   .   .   .   .   .   .   .   .   .   %   F   F
20.0   M   M   M   M   M   M   M   M   M   F   F   %   %   %   %   %   %   .   .   .   .   %   F   F   M
16.0   X   X   X   X   X   X   X   M   M   M   F   F   F   F   F   F   %   %   %   .   .   F   M   M   X
12.0   X   X   X   X   X   X   X   X   M   M   M   M   M   M   M   M   M   M   F   %   %   M   X   X   X
 8.0                           A   X   S   M   M   M   M   M   M   M   M   M   M   M   M   X   X
 6.0                               X   M   M   M   M   M   M   M   M   M   M   M   M
       .   .   .   .   .   .   .   .   .   .   .   .   .   .   .   .   .   .   .   .   .   .   .   .   .
      00  02  04  06  08  10  12  14  16  18  20  22  24
```

Figure 2. GRAFEX predictions for specific frequencies.

The second form (Figures 3 and 4) is the one more frequently used. This is the GRAFEX point-to-point circuit prediction. The GRAFEX lines are produced for a range of frequencies in fixed steps starting from the highest. When the full set of lines has been printed the result is a diagram which looks very like the graphical form but actually provides much more information about the various modes. A table is printed on the right of the GRAFEX diagram. This table lists the median hourly values of the F-MUF, EMUF and ALF for the first then the second modes. A short key giving the meanings of the symbols is printed under the GRAFEX diagram. Details of modes and number of hops are included. There is a heading at the top of the diagram giving the circuit name, the path length and the date to which the predictions apply. A GRAFEX circuit prediction will fit on a standard A4 page or half a line-printer page.

```
NAME  SYDNEY BRISBANE    LENGTH    731 KM  DATE        MARCH  100
VERT. ANG. IN DEGREES     1F 34-40   2F 54-59   1E12          2E25
FREQ 00      06      12      18      24          UT  FMUF  EMUF  ALF
MHZ  '       '       '       '       '
22.0                                          F  00  13.7  12.1  4.9
21.5                                          I  01  14.0  12.6  5.0
21.0                                          R  02  14.2  12.9  5.1
20.5                                          S  03  14.1  12.7  5.0
20.0                                          T  04  13.9  12.3  4.9
19.5                                             05  13.7  11.5  4.6
19.0                                          M  06  13.6  10.3  4.2
18.5                                          O  07  13.3   8.6  3.5
18.0                                          D  08  12.8   6.3  1.8
17.5                                          E  09  11.1   3.0  0.0
17.0                                             10  10.0        0.0
16.5                                             11   9.5        0.0
16.0                                             12   9.1        0.0
15.5  ...                                        13   8.9        0.0
15.0  .... ...                          .    0  14   8.7        0.0
14.5  .... ... ..                       .    N  15   8.5        0.0
14.0  ..%% ... ..                       ..   E  16   8.3        0.0
13.5  %%%% %%% ..                      ..%     17   7.7        0.0
13.0  %%%% %%% %.                      .%%  H  18   7.3        0.0
12.5  %PPP %%% %%.                     .%%  O  19   7.1   2.2  0.0
12.0  PBBB P%% %%.                     . %%P  P  20   8.5   6.2  2.5
11.5  BBBB BBF %%. .                    . %%B     21  11.2   8.6  3.8
11.0  BMMM MBF F%% ... ..              % %BB     22  12.4  10.2  4.3
10.5  MMMM MMM FF% ... ...             % FBM     23  13.1  11.3  4.7
10.0  MMMM MMM MM% ... ... .           % BMM     24  13.7  12.1  4.9
 9.5  MMMM MMM MM% %.. ... .        .F MMM
 9.0  MMMM MMM MMM %%% ... ..     .F MMM  S  00  10.6   6.7  3.6
 8.5  MMMM MMM MMM %%% %%. ... ..B MMM  E  01  11.0   7.0  3.7
 8.0  MMMM MMM MMM MF% %%% %.. .%M MMM  C  02  11.1   7.1  3.7
 7.5  MMMM MMM MMM MMM %%% %%. .%M MMM  O  03  11.1   7.1  3.7
 7.0  MMXX MMM MMM MMM MMM %%% %%M MMM  N  04  11.0   6.8  3.6
 6.5  XXXX XMM MMM MMM MMM M%% %MM MMX  D  05  10.8   6.4  3.4
 6.0  XXXX XXM MMM MMM MMM MMM %MM MXX     06  10.6   5.7  3.1
 5.5  XXXX XXX MMM MMM MMM MMM MMM XXX  M  07  10.4   4.8  2.6
 5.0  XXXX XXX MMM MMM MMM MMM MMM XXX  O  08  10.1   3.5  1.5
 4.5  XXXX XXX XMM MMM MMM MMM MMX XXX  D  09   9.1   1.6  0.0
 4.0  AAAA AXX XMM MMM MMM MMM MMX XAA  E  10   8.3        0.0
 3.5       AA XMM MMM MMM MMM MMX AA        11   7.9        0.0
 3.0          AXM MMM MMM MMM MXA           12   7.5        0.0
              '       '       '       '        13   7.4        0.0
    00      06      12      18      24    T  14   7.3        0.0
 .  USABLE LESS THAN 50% OF DAYS           W  15   7.1        0.0
 %  USABLE LESS THAN 90% OF DAYS           O  16   6.8        0.0
 F  FIRST F LAYER MODE ONLY                   17   6.4        0.0
 E  E LAYER PROPAGATION POSSIBLE              18   6.1        0.0
 P  PROPN E (90%) OR F (50-90%) DAYS       H  19   5.9   1.2  0.0
 B  BOTH E&F MODES POSS. 90% OF DAYS       O  20   6.6   3.4  1.9
 M  MIXED FIRST AND SECOND F MODES         P  21   8.4   4.7  2.8
 S  SECOND F MODE BUT NO FIRST MODE           22   9.5   5.6  3.2
 A  HIGH ABSORPTION                           23  10.1   6.2  3.5
 X  COMPLEX MODES                             24  10.6   6.7  3.6
```

Figure 3. GRAFEX circuit prediction for a short path length with 1E mode possible.

```
NAME  DARWIN BRISBANE    LENGTH   2846 KM  DATE        MARCH  100
VERT. ANG. IN DEGREES     1F 04-06   2F 18-21   1E 0          2E 4
FREQ 00      06      12      18      24          UT  FMUF  EMUF  ALF
MHZ  '       '       '       '       '
40.0                                          F  00  30.9        13.7
39.0                                          I  01  32.8        14.2
38.0                .                         R  02  33.6        14.5
37.0    .. ... .                              S  03  33.6        14.5
36.0   ... ... .                              T  04  33.9        14.3
35.0   ... ... ..                                05  34.2        13.8
34.0   .... .%% ..                         .  M  06  34.3        13.0
33.0  ..%% %%% %.                          .  O  07  33.6        11.6
32.0  .%%% %%% %..                         .  D  08  31.0         9.2
31.0  .%%% F%% %..                         .. E  09  27.8         8.1
30.0  %%FF FFF F%.                         .%    10  24.0         0.0
29.0  %FFF FFF F%. .                       ..%   11  22.7         0.0
28.0  %FFF FFF F%. .    .                  .%%   12  22.1         0.0
27.0  FFFF FFF FF% ..  ...               . .%F   13  21.7         0.0
26.0  FFFF FFF FF% ... ... .              %%F  O  14  21.4         0.0
25.0  FFFF FFF FF% ... ... ..    . %%F  N  15  20.6         0.0
24.0  FFFF FFF FF% ... ... ..    . %FF  E  16  20.1         0.0
23.0  FFFF FFF FFF %.. ... ..    . FFF     17  18.7         0.0
22.0  FFFF FFF FFF %%% ... ...   . FFF  H  18  16.5         0.0
21.0  FMMM MMM FFF %%% %%. ...   . FFF  O  19  14.6         0.0
20.0  MMMM MMM MMF F%% %%% %.. ..% FFM  P  20  14.9         0.0
19.0  MXXX XMM MMF FF% %%% %.. ..% FMM     21  20.7         8.8
18.0  MXXX XXM MMF FFF %%% %%. ..% FMM     22  26.7        11.4
17.0  XXXX XXM MMM FFF FF% %%. ..% MMX     23  28.3        12.8
16.0  XXXX XXX MMM FFF FFF %%% ..F MMX     24  30.9        13.7
15.0  XXXX XXX MMM MFF FFF F%% ..F MXX
14.0  XXXX XXX XMM MMF FFF FF% %%F MXX  S  00  20.2  18.0  8.5
13.0  XXXX XXX XMM MMM MMM MF% %%F XXX  E  01  21.6  19.1  8.8
12.0  XXXX XXX XMM MMM MMM MMF %%M XXX  C  02  21.6  19.9  9.0
11.0  XXXX XXX XXM MMM MMM MMM %FM XXX  O  03  21.3  19.8  9.0
10.0  XXXX XXX XXM MMM MMM MMM MFM XXX  N  04  21.7  19.3  8.9
 9.0  AAAA AAX XXM MMM MMM MMM MMX XXA  D  05  21.3  16.3  6.7
 8.0       AXS MMM MMM MMM MMX X           06  21.7  16.8  8.1
 7.0        XS MMM MMM MMM MMX             M  07  20.9  14.4  7.5
 6.0         X MMM MMM MMM MM              O  08  20.0  11.1  6.4
 5.0         X MMM MMM MMM MM              D  09  17.2   8.1  0.0
 4.0         X MMM MMM MMM MM              E  10  15.1   1.0  0.0
 3.0         X MMM MMM MMM MM                 11  14.3        0.0
 2.0         X MMM MMM MMM MM                 12  13.8        0.0
             '       '       '       '        13  13.7        0.0
    00      06      12      18      24    T  14  13.7        0.0
                                          W  15  13.5        0.0
 .  USABLE LESS THAN 50% OF DAYS           O  16  13.4        0.0
 %  USABLE LESS THAN 90% OF DAYS              17  12.3        0.0
 F  FIRST F LAYER MODE ONLY                   18  11.1        0.0
 M  MIXED FIRST AND SECOND F MODES         H  19  10.3        0.0
 S  SECOND F MODE BUT NO FIRST MODE        O  20   9.8        3.8
 A  HIGH ABSORPTION                        P  21  12.0   9.6  6.1
 X  COMPLEX MODES                             22  17.4  13.3  7.4
                                              23  19.9  16.0  8.1
                                              24  20.2  18.0  8.5
```

Figure 4. GRAFEX circuit prediction for a path longer than the maximum 1E mode.

8. USING GRAFEX PREDICTIONS

There are a number of ways communicators can use their frequencies. For example, the broadcaster will want to be sure that the broadcasts are on frequencies which can be received in the target area, while the radio amateur may wish to use frequencies above the median MUF on days when the MUFs are higher than normal. The GRAFEX predictions contain information to meet the needs of both these communicators. It is not possible to set down rules for using GRAFEX predictions which will completely meet the needs of all users but is is possible to set down a few general comments.

Use of a frequency during the hours when the GRAFEX symbol is 'F' should ensure that good communication is achieved most days of the month except when an ionospheric disturbance occurs.

Using a frequency when the symbol is '%' should be satisfactory on more than half the days of the month. In this case the operator should have a back up lower frequency available for those periods when the selected frequency is not propagated. A situation requiring the use of a frequency in the '%' region can arise around local nighttime when the MUF is falling rapidly and especially just after dawn when the frequencies are rising sharply.

It is not considered desirable to try to use frequencies when the symbol

is '.' except for special purposes.

It should be possible to maintain good communication during times when two modes are possible ('M' and 'B') provided that the signals by the two modes are not (almost) equal in strength. Generally signals by the first E mode ('B') and the second F mode ('M') are several dBs weaker than the signal by the first F mode. If the aerial favors the first F mode this will further reduce the possibility of interference. In some cases the aerial may favor the second F mode particularly on the lower frequencies. The vertical angle information printed below the circuit name and date may be helpful in resolving the problem.

Operation with frequencies at times when they are in the 'X' region is not considered desirable as there are likely to be several modes available at least one of which will interfere with the wanted mode.

It is not considered desirable to operate close to the ALF. The symbol 'A' indicates that the frequency is much too close to the ALF. However, even when the frequency is outside the 'A' region it may still be unsatisfactory. It is known that the absorption varies from day to day. Also there is often a small amount of sporadic E layer which may increase the E layer cut off frequency. These factors are not currently allowed for in IPS predictions.

9. CONCLUSION

The GRAFEX form of presentation of point-to-point frequency test predictions has evolved over several years of use and assessment of its usefulness. It has proved to be a far superior method of presenting such predictions than the earlier graphical methods or tabulations such as shown in Figure 1.

3. ABSORPTION, FIELD STRENGTH AND RADIO NOISE PREDICTIONS

PREDICTION OF RADIO WAVE ABSORPTION IN THE IONOSPHERE

J.O. OYINLOYE
Department of Physics
University of Ilorin
Ilorin, Nigeria

A new empirical formula of the form $L = F(U,x,I)$ has been found for predicting at a fixed frequency of 2.2 MHz both the temporal and spatial variations of radio wave absorption L in the ionosphere where U, x and I represent the ionizing flux, the solar zenith angle and the magnetic dip angle respectively. The new formula removes the necessity for having different absorption laws for the long-term (solar cycle) and short-term (diurnal and seasonal) temporal variations. It also incorporates latitude variation through the factor I.

INTRODUCTION

The variation with wave-frequency of radio wave absorption in the ionosphere, obtained at vertical incidence, has been treated in detail by GEORGE (1971) and SAMUEL and BRADLEY (1975). Once the absorption at one frequency (e.g. 2.2 MHz) is known, it is a straightforward matter to obtain the absorption at any other desired wave frequency. GEORGE and BRADLEY (1974) have also shown how to convert absorption observed at vertical incidence to equivalent absorption at oblique incidence.

The purpose of this paper is to obtain an equation of the form

$$L = F(U,x,I) \qquad (1)$$

that will predict 2.2 MHz absorption L at a given intensity level of the ionizing flux U, a given solar zenith angle x and at a given location having a magnetic dip I^{o}. Essential departures from the absorption laws hitherto used are (a) the introduction of U dependence into the diurnal and seasonal variations and (b) the explicit introduction of x into the long-term variation such as the solar cycle variation. It has been inferred from the time variations in the $1\text{-}8A^{o}$ solar X-ray flux measured by SATELLITE SOLRAD 9 - EXPLORER 37 that the ionizing flux could vary significantly during the course of a day, from day to day and from month to month and that these variations are usually accompanied by similar variations in observed radio-wave absorption (GNANALINGAM, 1974; OYINLOYE, 1978a). This observation shows that the influence of U on the time variation in absorption cannot be neglected even when considering the diurnal and seasonal variations. It has in fact been

shown by OYINLOYE (1978a) that by considering the factor U, the "equatorial seasonal anomaly" in absorption that has posed a problem for about two decades can be explained.

The experimental data required for the prediction work are the flux data U and the absorption data. It has been found from an earlier work by the author (OYINLOYE, 1978a) that time variations in the 1-8A^{o} solar X-ray is adequately representative of time variations in effective U at a large range of heights in the ionosphere. Also in the present work, time variations in the intensity of 1-8A^{o} solar X-ray measured by SATELLITE SOLRAD 9 - EXPLORER 37 have been used to represent the time variations in the effective U. The hourly values for 1969-1970 are taken from the 'Solar Geophysical Data, Part I' published by ESSA Research Laboratories.

Experimental data on absorption have been obtained from absorption bulletins issued by Colombo, Freiburg and Ibadan and also from "Absorption Data for the IGY/IGC and IQSY" issued by the World Data Centre A. Where there were no observed values at 2.2 MHz, absorption at this wave frequency has been deduced by the method described by GEORGE (1971) and SAMUEL and BRADLEY (1975). Information on the relevant stations is given in Table 1.

Table 1 INFORMATION ON STATIONS

Station	Geog.Lat. (deg.)	Geog.Long. (deg.)	Dip angle (deg.)	Year of Absorption Data Used
Ahmedabad	23.0N	32.2E	32N	1958
Bangui	4.6N	18.6E	13S	1958, 1959
Colombo	6.9N	79.9E	5S	1957-1959, 1964-1970
Freiburg	48.0N	7.8E	64N	1958, 1959, 1964-1966, 1969
Ibadan	7.4N	3.9E	6S	1957, 1958, 1966-1968
Singapore	1.3N	103.8E	17S	1964
Tokyo	35.7N	139.5E	49N	1958, 1959, 1964-1965
Tromso	69.7N	18.9E	78N	1957, 1958

PREDICTION FORMULA

The prediction formula of equation (1) can be written in the separable form

$$L = r(I)\Psi(U,x)$$

where r(I) is the latitude factor and $\Psi(U,x)$ is the time variation at a reference station where r(I) is unity. In this paper, Colombo is adopted as the reference station because several years of absorption dataare available at this station. Once $\Psi(U,x)$ is obtained for Colombo, it is an easy matter to

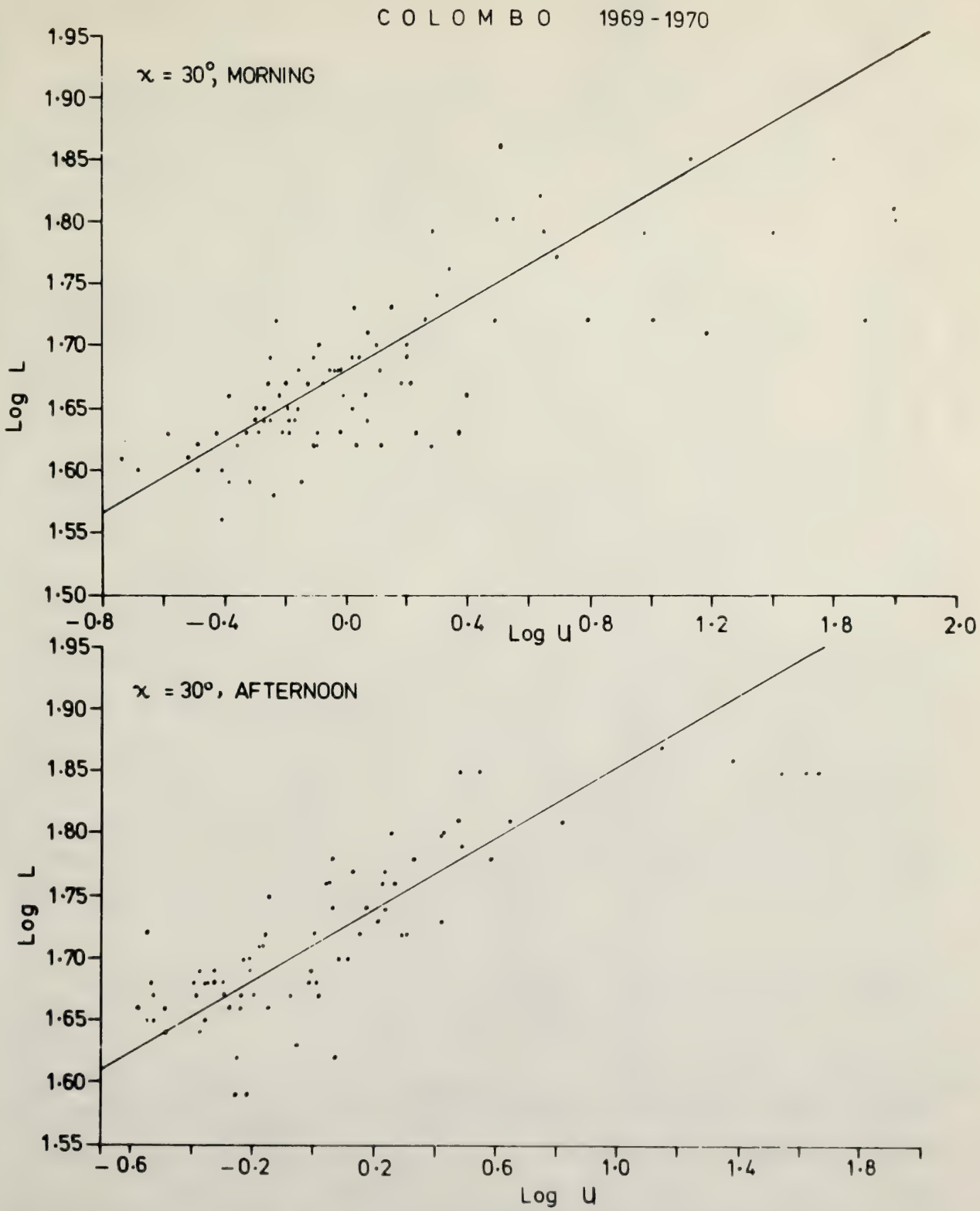


Fig. 1: DETERMINATION OF THE RELATIONSHIP BETWEEN 2.2 MHz ABSORPTION (dB) AND 1-8Å° SOLAR FLUX (MILLIERG CM^{-2} SEC^{-1}) FOR x=30° AT COLOMBO

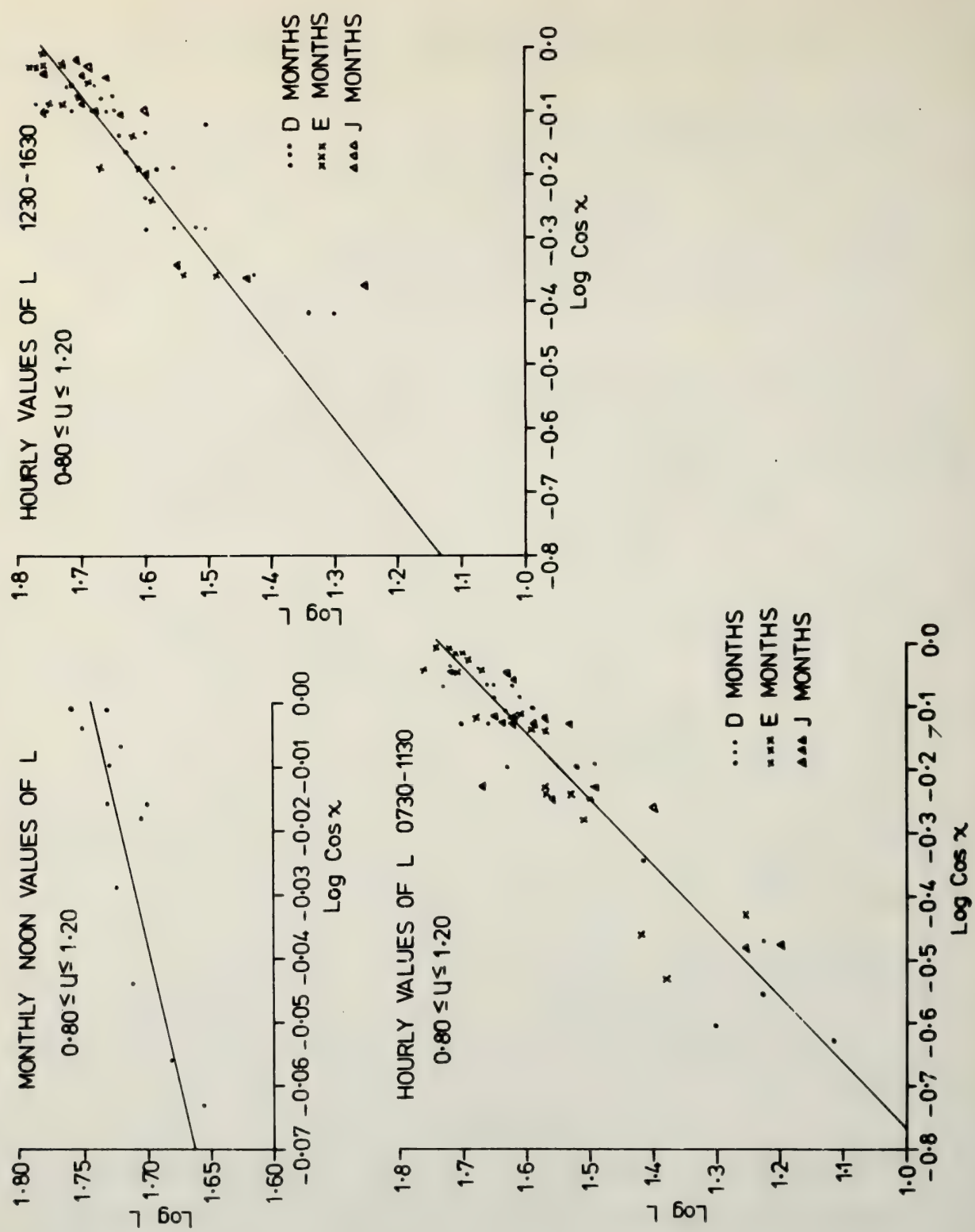


Fig. 2: DETERMINATION OF THE RELATIONSHIP BETWEEN 2.2 MHz ABSORPTION (dB) AND COS x FOR $0.80 \leq U \leq 1.20$ (MILLIERG CM^{-2} SEC^{-1}) AT COLOMBO

predict absorption for any other station using appropriate value of r(I) for that station.

Variation At Colombo At A Fixed Zenith Angle x=30°

2.2 MHz absorption data at Colombo for x=30° were obtained from the diurnal plots on regular world days during the period 1969-1970. From a plot of Log L against corresponding Log U shown as Fig. 1, it is found that the relationships between 2.2 MHz absorption L and 1-8A° solar X-ray U for x=30° are the following:

$$L = 48.0U^{(0.143\pm0.005)} \quad \text{Morning} \quad (2a)$$

$$L = 51.5U^{(0.143\pm0.005)} \quad \text{Afternoon} \quad (2b)$$

Though GNANALINGAM (1974) has suggested that at a fixed value of x, L is linearly related to $\sqrt{U}$, it has been found by the author (OYINLOYE, 1978b) that the L-$\sqrt{U}$ relationship is only approximate for a short range in the values of U. For a large range of values of U, the L-$\sqrt{U}$ plot is not linear.

Variation At Colombo At A Constant Level of U

Figure 2 shows the cos x dependence of 2.2 MHz absorption at Colombo at a constant intensity level of U given by $0.80 \leq U \leq 1.20$. From the plots the relationships between L and cos x are as follows:

$$L = 55.3(\cos x)^{1.13\pm0.20} \quad \text{For the monthly noon values} \quad (3a)$$

$$L = 55.1(\cos x)^{0.96\pm0.01} \quad \text{For 0730-1130 hours} \quad (3b)$$

$$L = 57.6(\cos x)^{0.78\pm0.02} \quad \text{For 1230-1630 hours} \quad (3c)$$

It is seen from equations (3a) and (3b) that within the limit of experimental errors, both the seasonal and morning hourly variations in L have the same cos x dependence once the influence of U is removed. That the afternoon cos x dependence of equation (3c) is different from (3a) and (3b) points to the reality of the existence of the asymmetry in the diurnal variation of L. Within the limits of experimental errors equations (3a), (3b) and (3c) tend to the same limit as the zenith angle x approaches zero. Because equation (3b) is derived from a wider spread in x values and a greater number of data points than equation (3a), a combination of equations (3b) and (3c) will be used in preference to a combination of equations (3a) and (3c) as input for the explicit determination of equation (1).

ψ (U,x) at Colombo

The combined influence of U and x on the time variations of 2.2 MHz absorption at Colombo can be put in the form:

$$L = L_o U^{0.143} \cos^m x \quad (4)$$

where L_o is the value of 2.2 MHz absorption at Colombo when U = 1.00 millierg cm^{-2} sec^{-1} and x = 0.0. Substituting equations (2) and (3) into (4) gives

$$55.1\ U^{0.143}\ (\cos x)^{0.96} \quad \text{Morning} \quad (5a)$$

$$57.6\ U^{0.143}\ (\cos x)^{0.78} \quad \text{Afternoon} \quad (5b)$$

Of course, within the limit of experimental errors, both equations (5a) and (5b) tend to the same value as x approaches zero. Equations (5a) and (5b) represent the time variations at Colombo given by $\psi(U,x)$.

Latitude Variation, r(I)

Absorption at any other station besides Colombo can be obtained by multiplying equation (4) by the factor r(I) to give the full equation of the type

$$L = r(I)L_o U^{0.143} \cos^m x \qquad (6)$$

where for a given zenith angle x, r(I) is the ratio of the 2.2 MHz absorption at a given station having dip angle I to that at Colombo and m takes the values 0.96 and 0.78 for the morning and afternoon hours respectively. The magnitudes of L_o for the morning and afternoon hours are given respectively by equations (5a) and (5b).

Figure 3 shows the latitude variation of r(I) with the dip angle I and this also constitutes the normalized latitude variation of noon absorption at 2.2 MHz. The stations from which were obtained the data used in Fig. 3 are listed in Table 1. The IGY and IQSY are regarded as high and low sunspot periods at all the stations except at Ibadan where 1966 data were used for the low sunspot period and 1967-1968 data for the high sunspot period. 1958 Ibadan data are subsequently used for validating the prediction formula of equation (6). It is to be noted from Fig. 3 that at low latitudes r(I) appears to be independent of the solar cycle while beyond about magnetic dip angle $I=30^o$, r(I) seems higher during low sunspot period than during high sunspot period. The error in r(I) is largest during winter at stations under the influence of the "winter anomaly in absorption".

VALIDATION OF PREDICTION FORMULA

In this section the prediction formula of equation (6) is first tested for the reference station of Colombo where r(I) is unity and then subsequently for other stations.

Figure 4 illustrates the good fit of observed data to the predicted calculated curves for short-term temporal variations at Colombo. Figures 4(a), 4(b) and 4(c) illustrate respectively the diurnal variations for the regular world days in 1969 and 1970 for the equinoctial month of April, the solsticial month of January and all the months of the year. The appropriate values of U for the diurnal variation in January are shown as Fig. 4(aii). For Figs. 4(b), 4(c) and 4(d) the observed time variations are for a constant level of U given by $0.80 \leq U \leq 1.20$ millierg cm^{-2} sec^{-1}. The vertical dashed lines in Figs. 4(a) and 4(b) indicate the times of minimum x. The time lag between the occurrence of minimum x and maximum absorption has been considerably discussed in another paper (OYINLOYE, 1978b). The diurnal variation shown in Fig. 4(c) covers a large range of x and the dashed line in this diagram is used to illustrate the continuity of equations (5a) and (5b) as x approaches zero.

Figure 4(d) shows the good fit of the observed seasonal variation to the predicted curve. The similarity in the seasonal variations of absorption and cos x is also noteworthy.

Figure 5 further illustrates that on a long term basis the observed data at Colombo have a good fit to the predicted variation of absorption with Sa which is the observed 10.7cm solar flux adjusted to 1 A.U. and measured in 10^{-22} W_m^{-2} Hz^{-1}. From a plot of $\log_e U$ against $\log_e S_a$, it has been

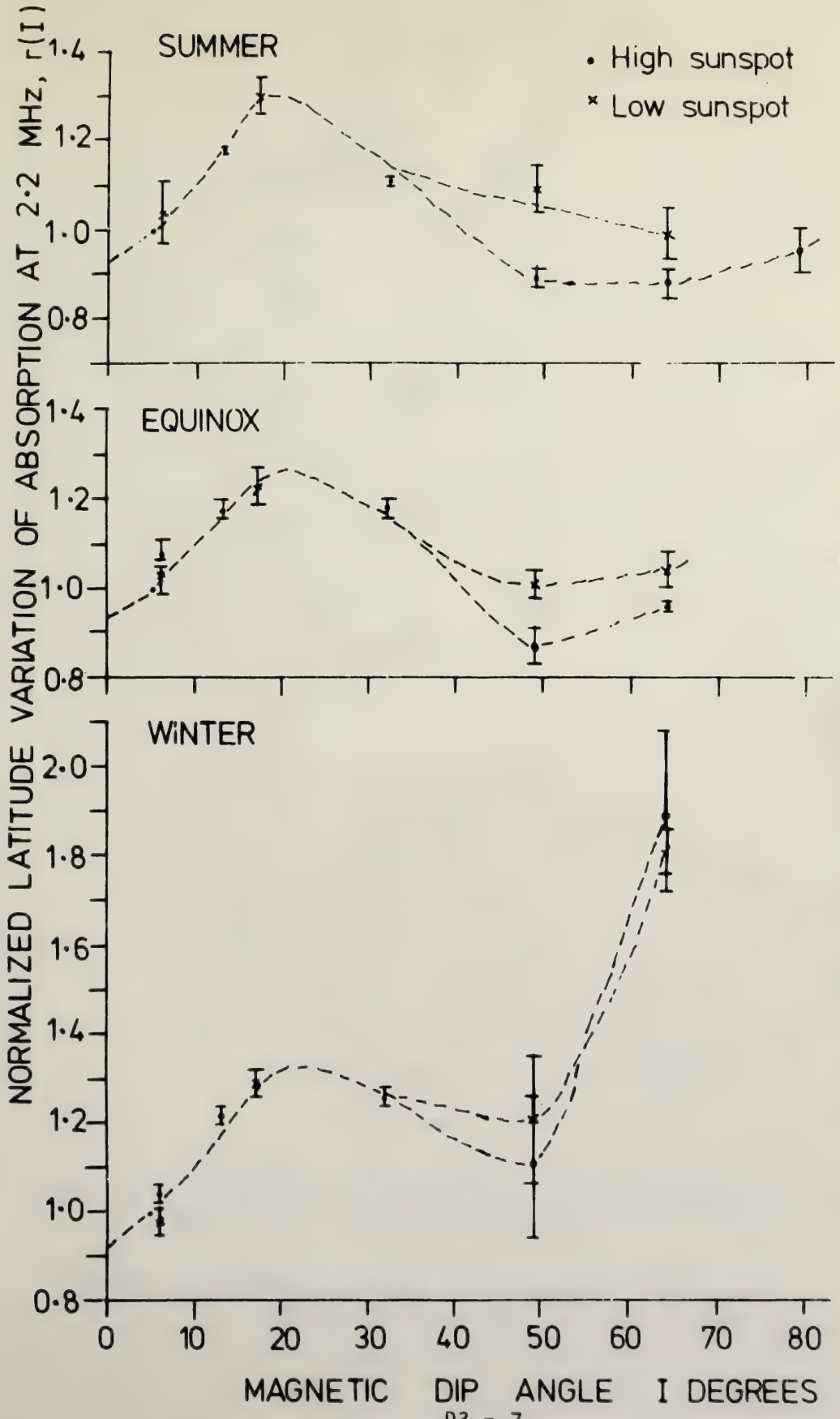


Fig. 3: NORMALIZED LATITUDE VARIATION OF 2.2 MHz ABSORPTION AT NOON WITH THE VALUE AT COLOMBO BEING UNITY

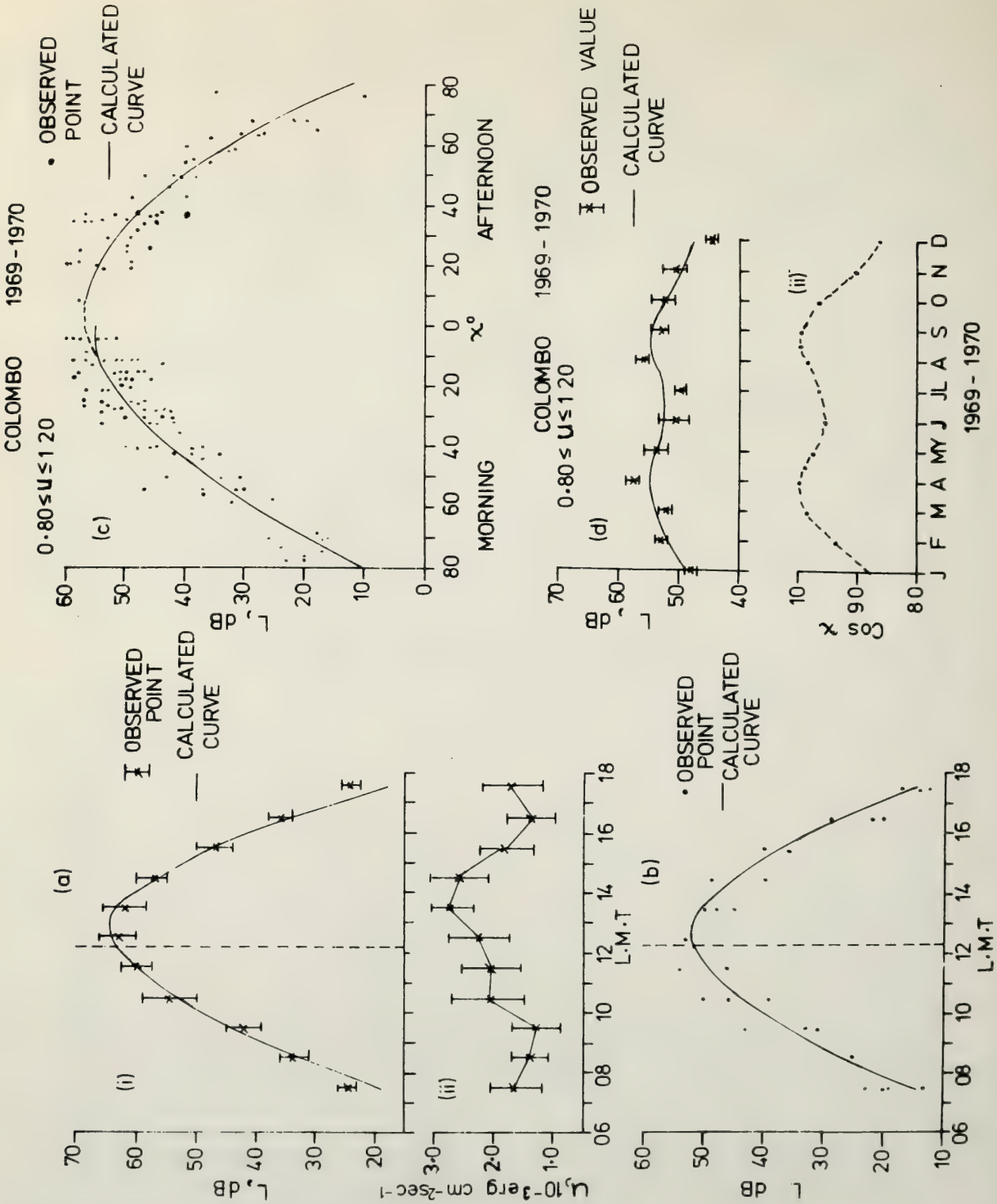


Fig. 4: A COMPARISON OF PREDICTED AND OBSERVED SHORT-TERM TEMPORAL VARIATIONS OF 2.2 MHz ABSORPTION AT COLOMBO

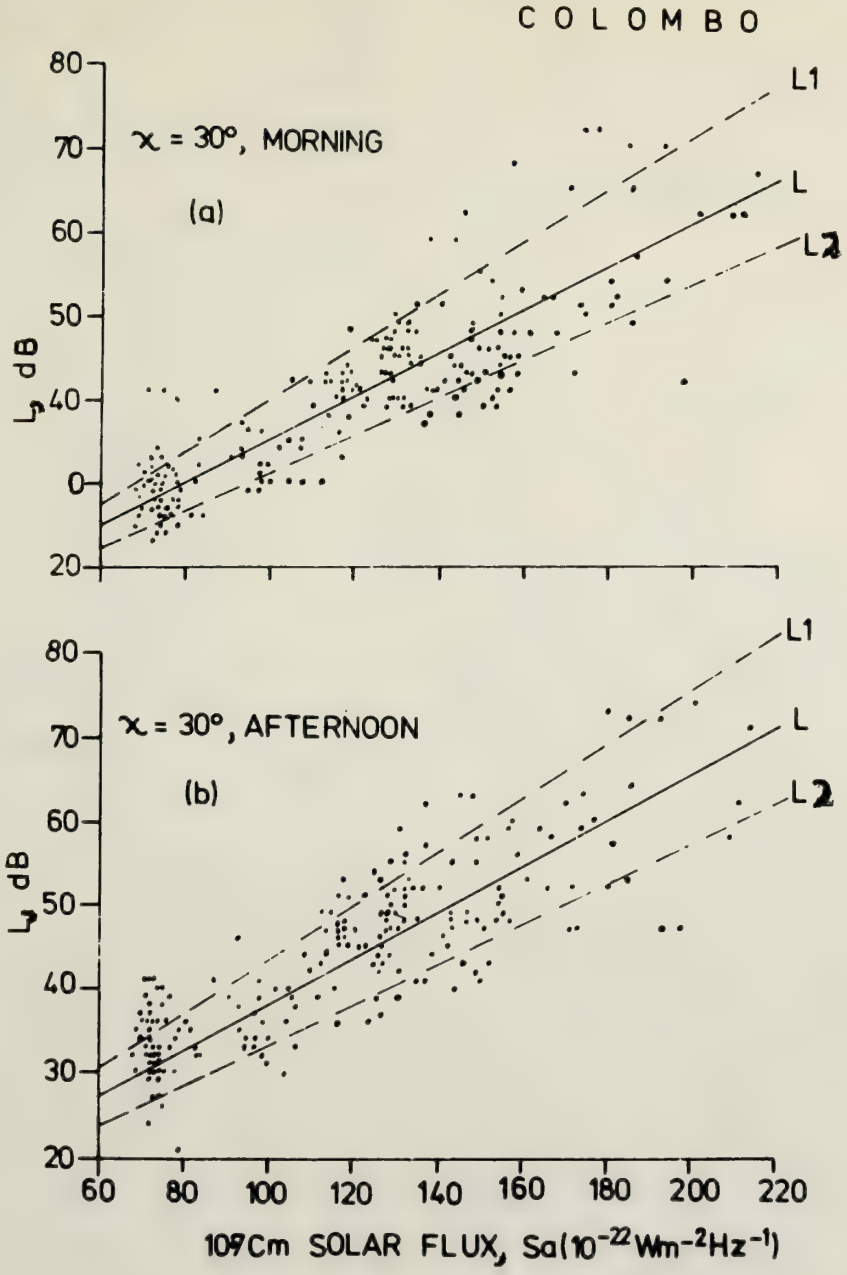


Fig. 5: A COMPARISON OF PREDICTED AND OBSERVED LONG-TERM TEMPORAL VARIATIONS OF 2.2 MHz ABSORPTION FOR x=30° AT COLOMBO

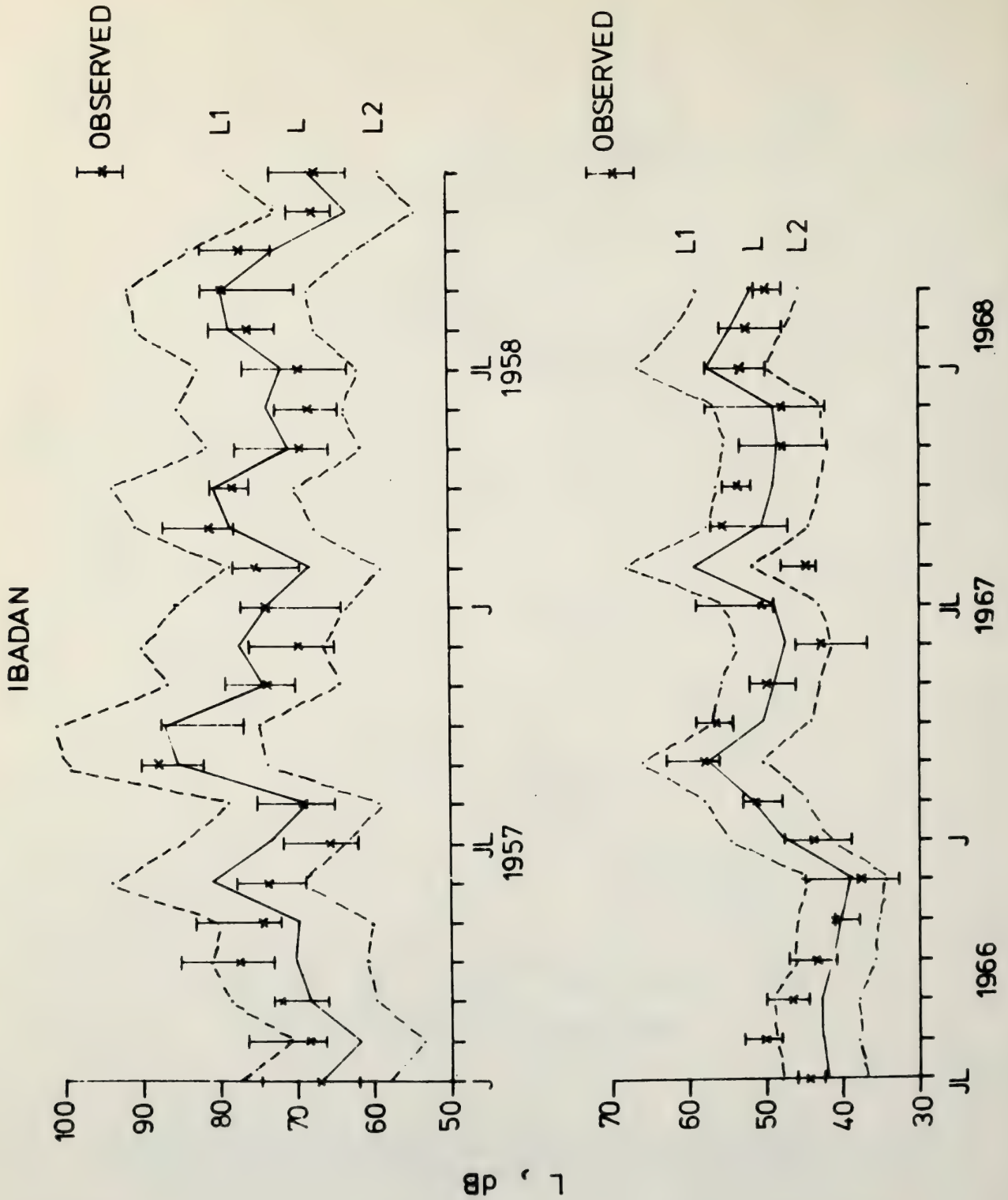


Fig. 6: A COMPARISON OF PREDICTED AND OBSERVED SEASONAL AND LONG-TERM TEMPORAL VARIATIONS AT IBADAN. ERROR BARS INDICATE THE QUARTILES ABOUT THE MEDIANS

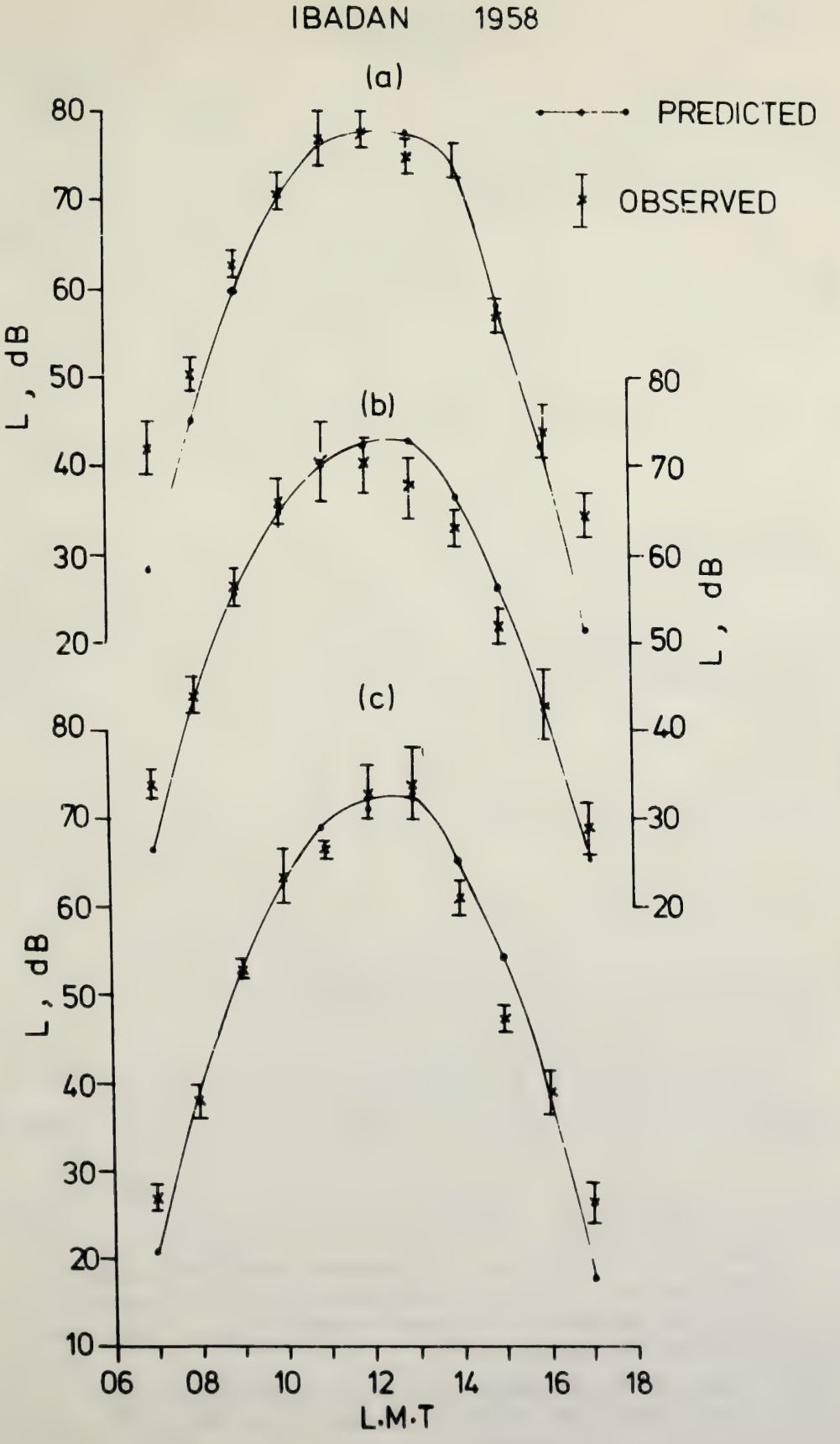


Fig. 7: A COMPARISON OF PREDICTED AND OBSERVED DIURNAL VARIATIONS OF 2.2 MHz ABSORPTION AT IBADAN DURING (a) EQUINOX PERIOD, (b) JUNE SOLSTICE AND (c) DECEMBER SOLSTICE. ERROR BARS INDICATE THE STANDARD ERRORS

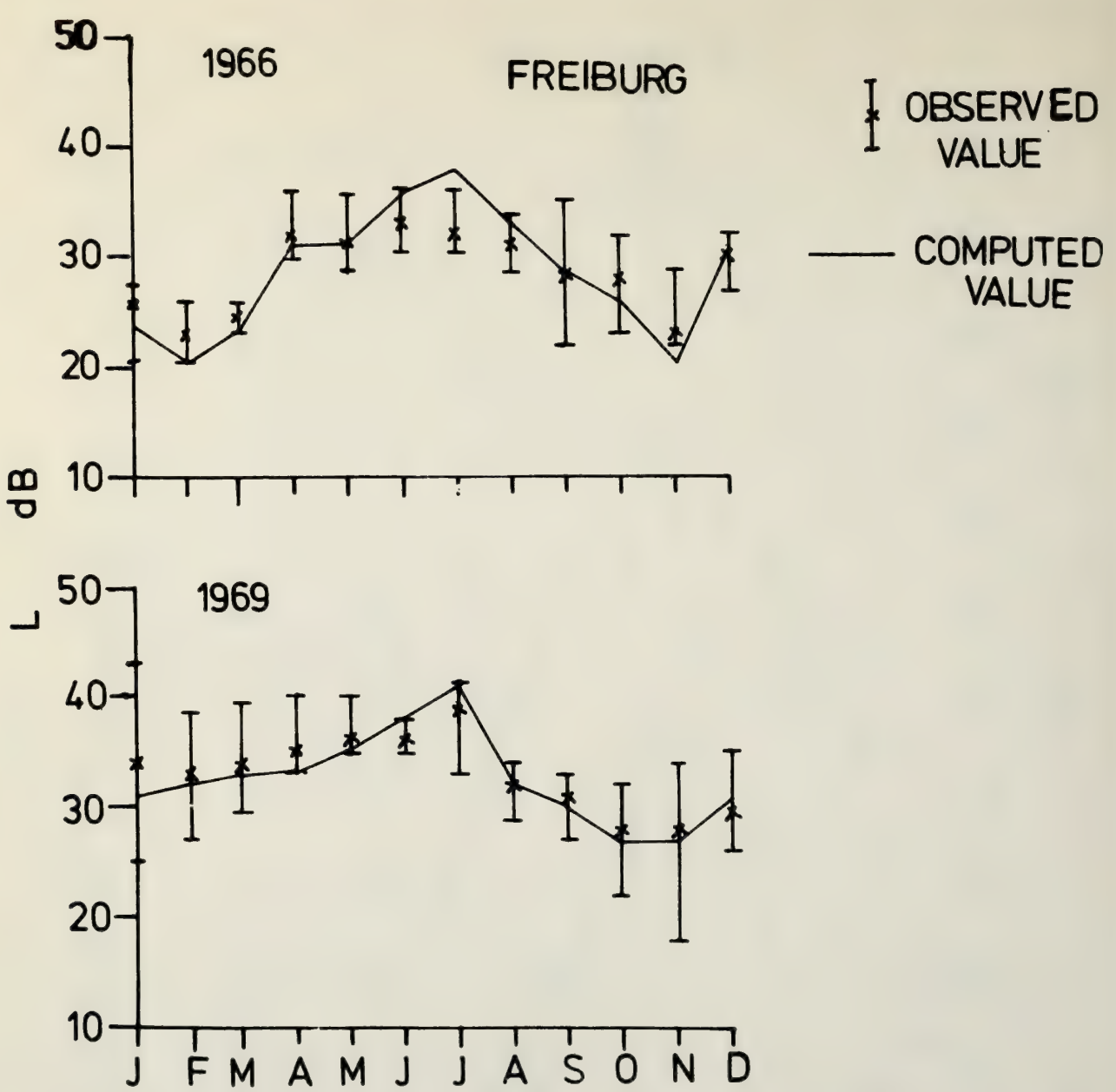


Fig. 8: A COMPARISON OF PREDICTED AND OBSERVED SEASONAL VARIATIONS OF 2.2 MHz ABSORPTION AT FREIBURG FOR BOTH LOW AND HIGH SUNSPOT CONDITIONS. ERROR BARS INDICATE THE QUARTILES ABOUT THE MEDIANS

found that

$$U = S_a^{(5.24 \pm 0.19)} e^{-26.11} \qquad (7)$$

L values for the continuous line in Fig. 5 have been calculated from equations (5a) and (5b) setting $x=30^o$ and substituting for U in equation (7). L1 and L2 for the broken lines correspond respectively to the upper and lower limits of U given by equation (7).

The predicted formula is also tested for Ibadan and Freiburg data. Ibadan and Freiburg are regarded as typical equatorial and non-equatorial

stations respectively. Furthermore, Freiburg is under the influence of the "winter anomaly" in absorption while Ibadan is not. For the purpose of comparison with observed absorption appropriate values of r(I) have been used in computing the predicted absorption. All the computed variations of absorption in Figs. 6, 7 and 8 except that for 1969 at Freiburg have been based on appropriate medians of the 10.7cm adjusted solar flux S_a. The curves shown as L1 and L2 in Fig. 8 give a measure of the uncertainty in calculated L arising from the uncertainty in the conversion equation (7) for U. The predicted 1969 variation of absorption at Freiburg is based on direct 1-8A^o solar X-ray data.

From Figs. 6, 7 and 8 a good agreement is evident between observed and predicted long-term seasonal and diurnal variations at Ibadan and seasonal variations at Freiburg during low and high sunspot conditions. It is also worth mentioning that a good agreement has been obtained for the predicted and observed diurnal variations at Tokyo for the years 1958-1959, averaged over each season. Diurnal data were not available for such a comparison at Freiburg.

CONCLUSION

A prediction formula for 2.2 MHz absorption has been obtained and tested. For prediction purposes at a given station, the parameters required are the 1-8A^o solar flux (or where not available the adjusted 10.7 solar flux), the normalized latitude factor r(I) and the zenith angle x. The present work further emphasizes one of the needs for X-ray monitoring for the purpose of short-term prediction in particular.

REFERENCES

George, P. L. (1971): The global morphology of the quantity $\int N\nu.dh$ in the D- and E-regions of the ionosphere. J.atmos.terr.Phys., 33: 1893

George, P. L., and P. A. Bradley (1974): A new method of predicting the ionospheric absorption of high frequency waves at oblique incidence. Telecomm. Journal, 41: 307

Gnanalingam, S. (1974): Equatorial ionospheric absorption during half a solar cycle (1964-1970). J.atmos.terr.Phys., 36: 1335

Oyinloye, J.O. (1978a): On the seasonal variation of absorption of radio waves in the equatorial ionosphere. J.atmos.terr.Phys., 40: 793

Oyinloye, J. O. (1978b): A new form of representation for temporal and spatial variations in radio wave absorption in the ionosphere. Accepted by J.atmos.terr.Phys.

Samuel, J. C., and P. A. Bradley (1975): A new form of representation of the diurnal and solar-cycle variations of ionospheric absorption. J.atmos.terr.Phys., 37: 131.

ON THE SHORT-TERM PREDICTION OF THE SPACE-TIME DISTRIBUTION OF AURORAL ABSORPTION

R. A. Zevakina, M. V. Kiseleva
Institute of Terrestrial Magnetism
Ionosphere and Radio Wave Propagation
of the USSR Academy of Sciences
Moscow, USSR

Instead of qualitative, short-term predictions of the absorption for the zone as a whole (Zevakina, 1975), we propose a method of quantitative prediction in decibels, taking account of the latitudinal and diurnal variation of absorption.

As the magnetic activity grows, absorption in the auroral zone increases and the zone itself widens. Driatskii (1974) and Hargreaves (1965) present empirical relations of the absorption on the magnetic activity (K_p and Δ H). However, these relations cannot take into account the large fluctuations of absorption values.

We have investigated the correlation of absorption with the auroral indices of magnetic activity - AE, K-indices and variations of the horizontal component (Δ H) of the geomagnetic field at auroral stations. Moreover, we have studied the variation of the statistical and latitudinal distributions of the auroral absorption for different levels of magnetic activity. The autocorrelation analysis of absorption has been carried out and, on the basis of autocorrelation and relation to the magnetic activity, a numerical method of prediction has been developed. Test cases are presented which demonstrate the accuracy of the method.

To this aim, we have used the tables of hourly values from riometric recordings made at four stations located at different latitudes: Heiss Isl. (corrected geomagnetic latitude, 73.8°N), Dikson (67.2°N), Murmansk (64.0°N), and Kiruna (64.3°N)-during the years of high (1968) and low (1964) solar activity. We have also used the charts of auroral absorption during 1964, 1965 and 1969 (World Data Center A, 1971). The absorption was measured at a frequency of 32 MHz at Heiss and Dikson Isls. and in Murmansk and at a frequency of 27 MHz in Kiruna.

The statistical distribution of auroral absorption has been examined for a quiet geomagnetic field (K = 0 - 2), and for weakly (K = 3 - 4), moderately (K = 5 - 6) and strongly (K > 6) disturbed states of the geomagnetic field, separately for the daytime (6-12 hrs LT) and nighttime (22-04 hrs LT) hours.

For each station, its own K-indices were used. Periods with polar-cap type of absorption were omitted from the analysis.

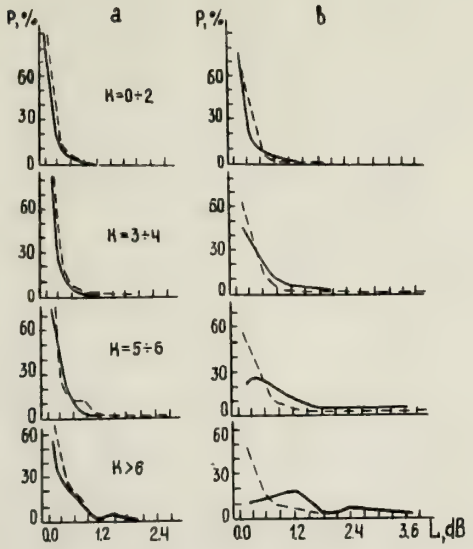


Figure 1. Probability (P, %) of different values of the auroral absorption (L, dB) at various levels of magnetic activity for Heiss (a) and Dikson (b). solid curve - day; dashed curve - night.

Figure 1 illustrates the statistical distribution of auroral absorption during 1968 from the data obtained on the Heiss and Dikson Islands. From figure 1 it follows that the character of the statistical distribution of absorption is about the same in the daytime and nighttime hours.

As the magnetic activity increases, the distribution changes at all stations, but more considerably in the middle of the absorption zone. On Heiss Isl., absorption is predominantly low. In 1968, it did not exceed 0.3 dB for 85% of the time during quiet and weakly disturbed conditions, 75% of the time during moderate conditions and 55% of the time during strongly disturbed conditions. Absorption equal to and over 1 dB was observed on the Heiss Isl. only 2% of the time during weak disturbances, 3% during moderate and 11% during strong disturbances.

In the middle of the zone (i.e. at Dikson Island) high absorption (> 1 dB) was registered much more often, especially during moderate and strong disturbances. On Dikson Isl., it was observed 4% of the time during quiet conditions, 13% of the time of weakly disturbed conditions, 19% under moderate and 27% under strong disturbances. At the other auroral stations, the maximum of the frequency of occurrence during quiet and weakly disturbed conditions is observed at low absorption values (at 0.3 dB), but under moderately and strongly disturbed conditions at high absorption values (> 1 dB). Over the solar activity cycle the absorption distribution does not change significantly.

The latitudinal distribution of the frequency of occurrence of auroral absorption exceeding 1 dB, has been considered by Driatskii (1974). In order to calculate the characteristics of radiowave propagation, apart from the frequency of occurrence, one should know the variation of the absorption value with latitude at different levels of the solar and magnetic activities.

In order to study the latitudinal absorption distribution, we have used the charts of absorption during substorms in 1964, 1965 and 1969, which have been compiled from the data of 36 stations situated on corrected geomagnetic latitudes ϕ' from 54.4^0N to 86^0N. Because two maxima can be observed in the diurnal dependence of auroral absorption, one in the pre-noon hours and the

other at midnight, the latitudinal distribution has been determined for noon and midnight values averaged over all substorm periods at the same magnetic activity. Figure 2 shows such distributions over magnetically quiet ($\Sigma K_p \leq 15$), weakly disturbed ($15 < \Sigma K_p \leq 25$) and also moderately and strongly disturbed ($\Sigma K_p > 25$) days during years of low and high solar activity. Strongly disturbed days were few; accordingly, the distribution at $\Sigma K_p > 25$ mainly characterizes moderately disturbed conditions. From the figure it follows that the latitudinal distribution varies with increasing magnetic activity considerably more during the nighttime than it does in the daytime. The zone width (absorption values > 0.5 dB) varied from 12^0 to 18^0, due to the displacement of its southern and northern boundaries. During 1969 the absorption was higher and the zone itself wider than during 1964-1965 only at $\Sigma K_p > 25$. For $\Sigma K_p < 25$, absorption during 1969 turned out to be lower than during 1964-1965. This result is somewhat unexpected. Possibly, it is associated with the limited amount of initial data or with a cyclic variation of absorption whose maximum does not coincide with that of solar activity (Zhulina, 1969).

It should be noted that the spread of values from the average latitudinal distribution is rather large. The root-mean-squared deviations (in dB) for the various latitudes at different levels of magnetic activity during 1964-1965 and 1969 are given in Table 1. It can be seen that the root-mean-square deviations are largest in the middle of the zone ($\phi' = 62\text{-}69^0$) at a high magnetic activity.

From the statistical and latitudinal distributions it is clear that the absorption increases with increasing magnetic activity. In order to estimate this dependence quantitatively, we have determined the correlation of the absorption with K-indices during the same interval, during the preceding interval, during the interval two intervals before and with hourly values of the horizontal component of the geomagnetic field (Δ H) with the shift from 0 to 6 hours.

Because the correlation may vary with the time of day, we considered the correlation coefficients separately for the midnight (00 hr LT), morning (10 hrs) and evening (18 hrs) hours at each station. From the data obtained at Dikson, Kiruna and Murmansk during 1968, these correlation coefficients

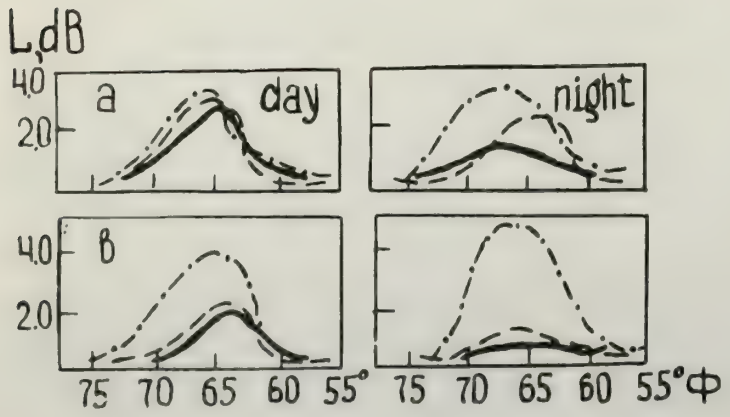


Figure 2. Latitudinal distribution of auroral absorption at different levels of magnetic activity during 1964-1965 (a) and 1969 (b). Dashed curve for $15 < \Sigma K_p \leq 25$, solid curve for $\Sigma K_p \leq 15$ and dash-dot curve for $\Sigma K_p > 25$.

Table 1. Root-Mean-Squared Deviations of Absorption in dB.

Corrected Geomagnetic Latitude ^{0}N	Day			Night		
	$\Sigma K_p \leq 15$	$15 < \Sigma K_p \leq 25$	$\Sigma K_p > 25$	$\Sigma K_p \leq 15$	$15 < \Sigma K_p \leq 25$	$\Sigma K_p > 25$
			1964 - 1965			
>70	0.75	1.08	1.62	0.29	0.69	0.27
62-69	1.26	1.76	1.79	1.22	1.76	0.27
55-61	0.40	1.30	0.15	0.27	1.06	0.18
55-75	1.05	1.54	1.39	1.00	1.48	0.22
			1969			
>70	0.00	0.51	1.19	0.00	0.18	0.50
62-69	0.95	1.61	2.73	0.23	1.16	2.49
55-61	0.50	0.34	0.38	1.15	1.25	1.78
55-75	0.10	1.22	2.07	0.14	1.02	2.02

are, on the average, the same at all three stations. During the nighttime and morning hours, correlation coefficients are equal to 0.5 using K-indices for the same interval, 0.6 for K-indices for the preceding interval and 0.4 with K-indices from two intervals before. During the evening hours, the correlation coefficients turned out to be about 0.3 for all three intervals of K-indices. Sometimes, they were nonrepresentative or not statistically significant. At equinox and in winter, the correlation coefficients were somewhat higher than in summer, sometimes reaching 0.7. In summer, they were sometimes nonrepresentative, which was also the case at the zone boundary.

The coefficients of correlation of absorption with hourly values of Δ H have been found to be equal to 0.3-0.4 when Δ H was shifted by 2-6 hours; they are somewhat lower when the values of Δ H during the same and nearest hours are employed. The correlation of absorption with hourly values of Δ H has turned out to be lower than with three-hour K-indices.

The correlation with both these indices indicates that absorption varies with magnetic activity, but with a delay of 2-6 hours. A delay of the same order has been found between the maxima of the diurnal dependences of magnetic activity and auroral absorption (Driatskii, 1966).

Since the coefficients of correlation of absorption with the indices of magnetic activity are low and not always representative, the correlation alone cannot serve as a basis for a quantitative prediction of absorption. In order to estimate the possibility of extrapolating absorption from day to day, taking into account the 27-day recurrence-tendency (the presence of recurrence-tendency of absorption was shown graphically), we have determined the autocorrelation coefficients for the mean midnight (during 22-02 hrs LT) and mean noontime (during 10-14 hrs LT) absorption with the values of absorption during the same hours on the previous day and also 2, 3, 26, 27, and 28 days before the given day during 1964-1965 from the data of Kiruna

and Murmansk and during 1968 from the data of Dikson and Murmansk. The coefficients of autocorrelation do not change appreciably from month to month; therefore, they are averaged over a year and are given in Table 2. From the table it follows that the autocorrelation of the nocturnal absorption is slightly higher than that of the daytime absorption. The autocorrelation is maximum with the absorption values for the previous day (0.59) and for 27 days before the given day (0.65). The autocorrelation coefficient for 1968 is higher than for 1964. Besides averaging over all days, the autocorrelation coefficients was also determined for the disturbed periods only (Table 2). These turned out to be usually higher than those averaged over all days.

Table 2. Autocorrelation Coefficients of Absorption.

Shift in time, days	1968		1964		Over disturbed days	
	Day	Night	Day	Night	Day	Night
-1	0.47	0.59	0.55	0.51	0.64	0.58
-2	0.55	0.57	-0.02*	0.45	0.48	0.48
-26	0.41	0.50	0.51	0.10*	0.30	0.85
-27	0.63	0.58	0.55	0.65	0.57	0.63
-28	0.43	0.45	0.57	0.10*		

*Nonrepresentative coefficients.

From the above, it follows that the absorption autocorrelation coefficients are the largest with the values for one, two and 27 days before the given day. Therefore, the extrapolation technique is applicable for the prediction of absorption. This method is commonly used to predict magnetic activity for a period of one to three days (Olson, 1969) and f_oF2, for a period of several hours (Lyakhova, 1973). The method makes it possible to determine the predicted value as a function of the previous values:

$$\Delta L_{pr} = a_1 \Delta L_1 + a_2 \Delta L_2 + a_{27} \Delta L_{27},$$

where ΔL is a difference between the observed and median values of L: $\Delta L = L_{obs.} - L_{med.}$, ΔL_1, ΔL_2, ΔL_{27} are the values for the previous days. To predict absorption one or two days ahead, we have determined the coefficients a_1, a_2 and a_{27} by the least-square technique for all days and, separately, only for disturbed conditions from the data obtained at Dikson during 1968 and at Kiruna during 1964-1965 (Table 3).

Making use of these coefficients, we have compiled forecasts of absorption for one or two days from the data of Dikson for 1968 and of Kiruna for 1964. The accuracy of such absorption predictions was about 70% under disturbed conditions and about 50% under magnetically quiet conditions.

The prediction of absorption for longer periods (to 27 days) can be made on the basis of forecasts of magnetic activity, using the statistical and

Table 3. Prediction Coefficients

Coefficient	Over all days				Over disturbed days	
	1968		1964			
	Day	Night	Day	Night	Day	Night
a_1	0.44	0.36	0.36	0.48	0.38	0.46
a_2	0.34	0.26	0.26	0.20	0.32	0.26
a_{27}	0.08	0.29	0.35	0.24	0.52	0.37

latitudinal distributions of absorption for different levels of activity. In this case, the value of absorption for the predicted level of magnetic activity is found from the latitudinal distribution, and the probability of this value at a given level of magnetic activity, from the statistical distribution. Forecasts made by this method for the Dikson Isl. for 1968 turned out to be true in 85% of all cases in the days characterized by $\Sigma K_p \leq 15$, in 95% for $15 < \Sigma K_p \leq 25$ when the absorption was estimated to within $^{p}50\%$.

REFERENCES

Brown, R. B. and J. K. Barcus (1963): J. Geophys. Res., 68:4175.

Driatskii, V. M. (1974): The nature of abnormal absorption of the radio emission from space to the lower high-latitude ionosphere. Leningrad. Ghidrometeoizdat.

Driatskii, V. M. (1966): Geomagnetism and aeronomy (Soviet), 6:1061.

Hargreaves, J. K. (1965): Planet. Space Sci., 13:1171.

Lyakhova, L. N. and L. I. Kostina (1973): Geomagnetism and Aeronomy (Soviet), 13:59.

Olson, R. H. (1969): Solar Phys., 8:240.

World Data Center A (1971): Temporal development of geographical distribution of auroral absorption for 30 substorm events in each of IQSY (1964-1965) and IASY (1969). Upper Atmosphere Geophysics, Report 16.

Zevakina, R. A., V. P. Kuleshova, E. V. Lavrova, and L. N. Lyakhova (1975): Methods of short-term prediction of magnetic activity and the state of the ionosphere. Instruction, Moscow, IZMIRAN.

Zhulina, E. M. (1969): In: Solar-terrestrial physics, iss. 1., Moscow, IZMIRAN, 177.

DETERMINATION OF THE SOLAR CYCLE VARIATION OF HF RADIO WAVE ABSORPTION AT LOW LATITUDE

K. M. Kotadia, A. Gupta and R. M. Kotak
Physics Department, Gujarat University
Ahmedabad 380 009, Gujarat, India

In this study, the prediction of ionospheric absorption measured by the A1 method at Ahmedabad (23^0N, 72.6^0E; magnetic dip 34^0N) is based on the solar activity represented either by the sunspot number or 10.7 cm solar radio flux, which can be reliably predicted from their existing long series of observations. Ahmedabad is a low latitude station situated at the well-known fully developed F2-peak of the Appleton anomaly. It is shown here that both the sunspot number and the 10.7 cm solar radio flux could serve on the average as equally reliable indices for the long-term prediction of radio wave absorption. Empirical formulae are established for the variation of absorption with solar activity from the available data over a half sunspot cycle. The constants involved in the linear relations are found to depend on radio frequency, time of day and the season. With the availability of data for one complete solar cycle, it would be possible to predict the seasonal influence on the variation of radio wave absorption with solar activity at fixed solar zenith angles, and the diurnal variation for each month at different frequencies.

SUNSPOT NUMBER AND 10.7 cm SOLAR RADIO FLUX

The 12-monthly running averages of sunspot number Rz and 10.7 cm solar radio flux $S_{10.7}$ (measured at Ottawa, Canada and standardized to a distance of 1 A.U.) are correlated for the 11-year period covering the years 1957-1968 from maximum to maximum of the solar cycle. A good linear fit is found between these two indices and it is empirically expressed as

$$S_{10.7} = 57.95 + 0.92\ Rz \qquad (1)$$

with a correlation coefficient of 0.998. Thus the $S_{10.7}$ flux remains at about 60 units (1 unit = 10^{-22} W/m^2/Hz) even at the solar minimum when Rz is zero and the slope of the line is almost unity. However, the day-to-day or instantaneous changes in the two quantities may not necessarily show so good a correspondence as seen in their yearly averages. Recently, attempts have been made to define a new index of solar activity in terms of the EUV radiation flux observed in satellites for modelling of the neutral atmosphere (Rawer et al., 1978).

VARIATION OF IONOSPHERIC ABSORPTION WITH SOLAR ACTIVITY

Measurements of ionospheric absorption of HF radio waves were made for nearly two solar cycles at mid-latitudes, particularly in Europe, and over short periods at other places. One such series over a cycle exists at an equatorial station, also, namely, Colombo in Ceylon (renamed as Sri Lanka). The gap at low latitude was filled by starting the work of Al-method absorption on 1.8, 2.2 and 2.5 MHz at Ahmedabad (23^0N, 72.6^0E; I = 34^0N) in April 1972 with objectives of studying various aspects of the lower ionosphere. In this paper, the prediction of ionospheric absorption as applied to communications is discussed.

From the data over a period of five years around the solar minimum when Rz varied from about 100 to 10, it has been possible to establish empirical relations showing how the ionospheric absorption changes with solar activity, i.e. with Rz and $S_{10.7}$. To remove the variation due to solar zenith angle in finding the changes due to solar activity alone, the values of absorption, L_{db}, at constant χ are taken from the monthly median curves of its diurnal variation. Here, the median values of L at cos χ = 0.6 and cos χ = 1 are chosen, the former being the value available in all months at Ahmedabad and the latter being taken from extrapolation of the linear graph of log L against log (cos χ). Figure 1 shows the mass-plot of monthly median L at cos χ = 0.6 and cos χ = 1 against the monthly mean Rz as well as $S_{10.7}$. A line of the form y = a (1 + bx) obtained by the least squared error method is drawn through the points. The scatter above and below the line does not show deviations by more than 5 dB. Similar line-fits were obtained for absorption on 1.8 and 2.2 MHz.

The linear graphs obtained in Figure 1 obey a formula of the form

$$L = a\ (1 + b\ Rz)\ dB, \text{ and} \qquad (2)$$

$$L = a\ \{1 + b\ (S_{10.7} - 60)\}\ dB. \qquad (3)$$

The empirical constants 'a' and 'b' in the above formulae for absorption on the three frequencies are given in Table 1 for cos χ = 0.6 and Table 2 for cos χ = 1.

Note from Table 2 that the value of 'a' decreases at higher frequencies, but that of 'b' increases. In contrast, at cos χ = 0.6, the values of 'a' and 'b' both decrease at higher frequencies. However, the slope, i.e. product 'ab' in the former case at cos χ = 1 turns out to be nearly the same within 10% for all the three frequencies, meaning that the rate of increase in total absorption with solar activity is nearly the same although the increase relative to the quiet-sun (solar minimum) value of absorption may differ. The value of 'b' given in the tables is the mean for all months, but it is found to change from month to month (Appleton and Piggott, 1954; Schwentek, 1971; Patel et al., 1973). We shall also be able to find these monthly values of 'b' on completion of our absorption measurements for one full solar cycle and then test if the product 'ab' remains nearly constant or not in all the months.

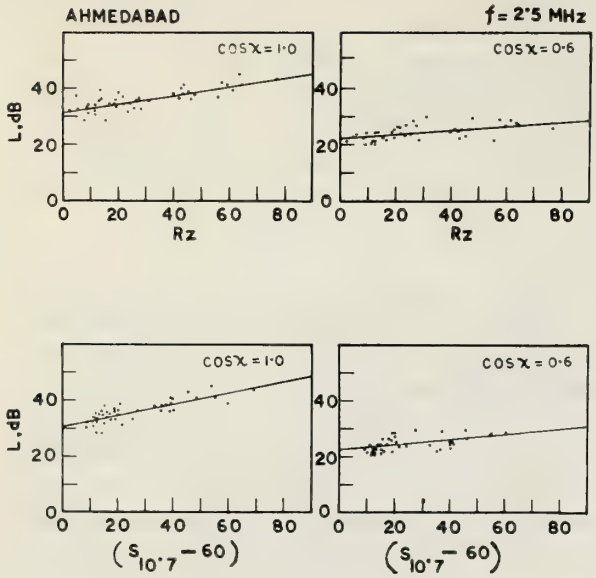


Figure 1. Variation of ionospheric absorption on 2.5 MHz with sunspot number and 10.7 cm solar radio flux.

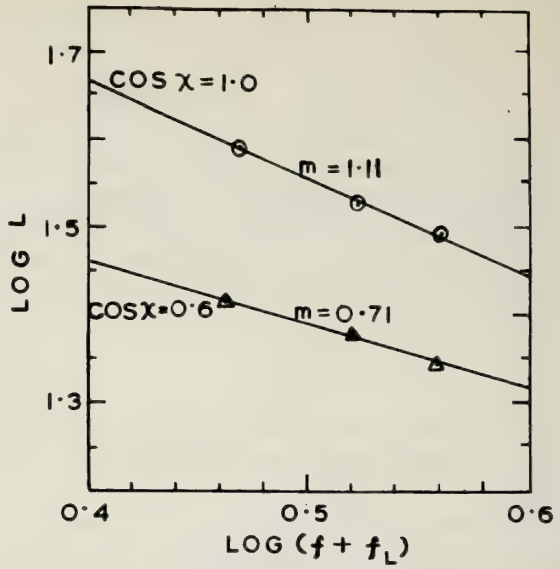


Figure 2. Frequency dependence of ionospheric total absorption at Rz = 0 for two fixed solar zenith angles.

FREQUENCY AND COS χ DEPENDENCE OF ABSORPTION

Absorption at Rz = 0 or $S_{10.7}$ = 60 seems to vary inversely as some power of the effective frequency $(f + f_H)$ where f_H is the electron gyromagnetic frequency. The exponent m in the inverse frequency variation of the total absorption may change depending on the proximity of the observing wave frequency to the E-layer critical frequency. This feature is clearly seen from the different slopes of the two lines in Figure 2, which gives the plot of log 'a' for cos χ = 1 and cos χ = 0.6 against log $(f + f_L)$ where L is longitudinal component of f_H equal to 1.12 MHz for Ahmedabad. The values of 'm' thus found are respectively 1.106 and 0.713, and the corresponding constants of proportionality found by extrapolation of the above plots are 127 and 66. Values of m for other stations are given by Gnanalingam (1969).

In prediction work for practical purposes, we are more interested in total absorption. However, for scientific studies on the structural changes in the D and E regions, one would attempt to separate the contributions of these regions to the total absorption and investigate in detail the dependence of these contributions on time of the day, season, solar activity and the operating frequency.

As regards the diurnal variation of absorption, it has been found that the absorption varies as $\cos^n \chi$. The mean value of n is found to remain

Table 1. Values of 'a' and 'b' for cos χ = 0.6.

Frequency	Rz		$S_{10.7}$	
MHz	a,dB	b	a,dB	b
2.5	22.22	0.0033	22.00	0.0040
2.2	23.91	0.0036	23.35	0.0049
1.8	25.96	0.0045	23.97	0.0060

Table 2. Values of 'a' and 'b' for cos χ = 1.

Frequency	Rz		$S_{10.7}$	
MHz	a,dB	b	a,dB	b
2.5	31.20	0.0052	30.60	0.0067
2.2	33.77	0.0054	33.08	0.0069
1.8	39.66	0.0043	38.81	0.0058

within 0.75 and 0.80 depending on the operating frequency (Gupta and Kotadia, 1976). However, it changes from 0.5 in winter to about 1.1 in summer during the course of a year. Empirical formulae incorporating all these effects have been given in different ways by different workers (Rawer, 1952; George, 1971; Lucas and Haydon, 1966; Samuel and Bradley, 1975). We shall also be able to fully evaluate them for a low latitude when our absorption data are completed over one solar cycle, i.e. in 1983.

OBLIQUE INCIDENCE ABSORPTION AT CONSTANT χ AND Rz = 100 EPOCH

The variation of vertical incidence absorption L explained above can be applied to the case of oblique incidence absorption L_{ob} for any angle of incidence i at the entry of the wave into the ionosphere for one hop reflection in the absence of any scattering irregularities over a given distance at appropriate frequency. Using the empirical relations derived for the variation of L with solar activity, L_{ob} can be calculated for different paths, angle i being known from the height of reflection and the distance on the earth of the intended communication circuit.

Suppose radio communication is desired over a distance of 1000 km by way of one-hop reflection from the E-layer over a low latitude, as that of Ahmedabad, under the following conditions: h = 100 km, i = 80^0, sec i = 5.73, f_v = 2.5 MHz, f_{ob} = 14.3 MHz, Rz = 100 or $S_{10.7}$ = 150, and cos χ = 0.6.

Then from the values given in Tables 1 and 2 for a and b, and using Martyn's Theorem, L_{ob} works out to be 5.2 dB. In solar minimum condition, this absorption comes down to 3.9 dB. However, at vertical incidence, the absorption on equivalent frequency 2.5 MHz comes down from 29.11 dB at Rz = 100 to 22.22 dB at Rz = 0. In both the cases the absorption increases by a factor of 1.33 from minimum epoch to Rz = 100 epoch of solar activity. But if we consider in terms of dB difference, it is much smaller at the high frequency used in actual communication over the surface distance of 1000 km. In the similar manner, we can work out other examples of absorption on different communication frequencies for the given operating conditions.

Superposed on the long-term regular variations of ionospheric absorption, there are short-term changes also associated with events like solar flares, PCA's, geomagnetic storms, Es and F-scatter irregularities and so on. It is difficult to evolve a method for prediction of ionospheric propagation conditions for such irregular changes. However, there have been attempts to predict the occurrences of solar flares and geomagnetic storms about 48 hours in advance, and changes in their frequency and intensity of occurrences with solar activity.

SUMMARY

In this paper, empirical relations are established to find the variation of HF radio wave absorption in the lower ionosphere over a low latitude station (23^0N) with solar activity at two fixed solar zenith angles. The prediction of absorption is based on the index of solar activity reliably available from the solar astronomers. It is shown that the vertical incidence ionospheric absorption at a constant solar zenith angle has a linear relation with solar activity of the form $L = a\ (1 + b\ Rz)$, but the constants involved in the empirical relation are functions of time of the day, season, operating radio frequency and its proximity to the critical frequency of the reflecting layer. An example is worked out to illustrate the method of predicting ionospheric absorption as applied to practical radio communication which shows that the ionospheric absorption on the average at $\cos \chi = 0.6$ for a surface distance of 1000 km from the transmitter through one-hop reflection in the E-layer over Ahmedabad at Rz = 100 would be 5.2 dB as against 3.9 dB for Rz = 0 condition. This prediction does not take into account the month-to-month seasonal changes in absorption and the additional effects due to scattering irregularities and other transient events. We have planned to continue the low-latitude ionospheric absorption measurements for one full solar cycle in order to enable us to predict diurnal variation of absorption for each month, seasonal variation at fixed solar zenith angles, dependence of index n on $\cos \chi$ and m for frequency-law on solar activity and other related studies for establishing a complete generalized relation between absorption and all factors affecting it. The normalized A-figure as studied by Samuel and Bradley (1975) will also be studied for Ahmedabad then.

REFERENCES

Appleton, E. V., and W. R. Piggott (1954): Ionospheric absorption measurements during a sunspot cycle. J. Atmosph. Terr. Phys., 5:141.

George, P. L. (1971): The global morphology of the quantity N dh in the D and E regions of the ionosphere. J. Atmosph. Terr. Phys., 33:1893.

Gnanalingam, S. (1969): Ionospheric absorption at low latitudes. 3rd International Symp. 'Equatorial Aeronomy', p-47 (PRL, Ahmedabad).

Gupta, A., and K. M. Kotadia (1976): Ionospheric absorption on 2.5 MHz at Ahmedabad. Ind. J. Rad. Space Phys., 5:211.

Lucas, D. L., and G. W. Haydon (1966): Predicting statistical performance indexes for high frequency ionospheric telecommunications system. ESSA Tech. Rpt. IER 1-ITSA 1.

Patel, B. M., J. C. Patel, and K. M. Kotadia (1973): Winter anomaly in ionospheric absorption of radio waves over half sunspot cycle. Ind. J. Rad. Space Phys., 2:219.

Rawer, K. (1952): Calculation of sky-wave field-strength. Wireless Engr., 29:287.

Rawer, K., G. Emmenegger, and G. Schmidtke (1978): Some features of EUV solar activity indices. XXI COSPAR Conf., W.G.IV, Paper A 2.6 at Innsbruck (Austria).

Samuel, J. C., and P. A. Bradley (1975): A new form of representation of the diurnal and solar cycle variations of ionospheric absorption. J. Atmosph. Terr. Phys., 37:131.

Schwentek, H. (1971): The sunspot cycle 1958-70 in ionospheric absorption and stratospheric temperature. J. Atmosph. Terr. Phys., 33:1839.

PREDICTION OF RIOMETER ABSORPTION FROM SOLAR FLARE RADIO BURST CHARACTERISTICS

Pradip Bakshi
Physics Department
Boston College
Chestnut Hill, MA 02167
and
William R. Barron
Air Force Geophysics Laboratory
Hanscom AFB, MA 01731

Earlier studies on radio-proton spectral correlations and proton-riometer absorption correlations are combined to propose a real time prediction scheme for the riometer absorption based on solar radio spectral information.

1. INTRODUCTION

We have shown elsewhere (Bakshi and Barron, 1979, Bakshi and Barron, 1978) the possibility of predicting the slope as well as the magnitude of the proton peak flux vs. energy profile by using as input certain characteristics of the U-shaped radio spectra. In another study (Bakshi and Barron, 1976) we have also shown that there is a very high correlation between certain features of the proton spectrum and the observed Riometer Absorption. Combining these results allows us to propose a real time, quantitative prediction scheme that relates the Riometer Absorption to the Radio Burst data. The above mentioned studies dealt with the major events of the twentieth solar cycle. The prediction scheme, based on these data can be tested by the coming events of the current cycle.

2. RADIO-PROTON CORRELATIONS

For the proton integral spectrum $I(>E\ MeV) = AE^{-\beta}$, we have shown (Bakshi and Barron, 1979) that the slope can be predicted from the real time radio data in the form

$$\beta = \frac{1.185}{\{\log_{10}(\omega_3/\omega_2)\}^{1.01}} \pm 0.45 \qquad (1)$$

where ω_3 is the frequency at which the high-frequency branch of the radio U spectrum attains its maximum flux density and ω_2 is the frequency at which the U spectrum attains its minimum flux density. The correlation coefficient for this power law form was $r \approx 0.77$.

The complete proton spectrum can now be obtained if we can predict the magnitude $I(>E_o MeV) \equiv I_{E_o}$ at any value of E_o. A convenient choice is E_o = 10 MeV. We have shown (Bakshi and Barron, 1978) that the time and frequency integrated radio energy ε is a good predictor of the proton flux magnitude I_{10}, after being corrected by a locational factor:

$$I_{10} = (0.115)\ \varepsilon^{1.77}\ e^{-3A}\ (5.14)^{\pm 1}, \qquad (2)$$

where ε, in units of 10^{-14} Joules m^{-2}, is obtained by a time integration of the incident radio flux density at various discrete frequencies, followed by a frequency integration over a standard range from 606 to 8800 MHZ, and A is the magnitude in radians of the angular distance of the flare location from the standard reference longitude 57^{o}W. The last factor in Equation (2) represents the standard deviation. The correlation coefficient for the data of the twentieth solar cycle which led to Equation (2) was $r \approx 0.80$. A slightly different formula can also be used (Bakshi and Barron, 1978), which relies in addition on the average proton energy factor $\rho = \beta/(\beta-1)$, where β is to be predicted by Equation (1).

3. PROTON-RIOMETER CORRELATIONS

Empirical connections between riometer absorption and solar protons during PCA events have been extensively studied. Most studies (Potemra, 1972, Cormier, 1973, Stroscio and Sellers, 1975) have considered a relation of the form $R = m[I(>E_o)]^{\frac{1}{2}}$, where R measured in dB is the observed riometer absorption (generally at 30 MH_z), $I(>E_o)$ is the corresponding flux of protons with energies greater than some specified energy E_o and m is an empirically determined proportionality constant, which assumes different values for different threshold energies E_o.

There is one obvious shortcoming in schemes such as these which rely entirely on the flux-magnitude of the protons. Consider, for instance, two events which give rise to the same flux $I(>E_o)$, but which have significantly different energy profiles, characterized by significantly different slopes β. It is reasonable to expect that the event with the harder proton spectrum (small β) will give rise to a larger riometer absorption, since its protons, on the average, carry more energy than is the case for the event with a softer spectrum (large β). The above mentioned schemes, however, cannot distinguish between such events. To rectify this, it is necessary to take into consideration the slope as well as the magnitude such as I_{10} for the proton profile. We have developed,

and tested (Bakshi and Barron, 1976), a simple empirical formula for the proton-riometer correlation along these lines.

The riometer absorption R is correlated with the proton variable $\log I_{10} + \alpha \log \rho$ where ρ is a measure of the average energy for the proton flux, and α is an adjustable parameter, varied to optimize the correlations. $\alpha = 0$ corresponds to ignoring the energy effects; $\alpha = 1$ corresponds to using the full energy flux rather than the number flux for the protons. The detailed selection criteria have been set forth in (Bakshi and Barron, 1976). Only the strong events with $I_{10} > 100$ protons cm^{-2} sec^{-1} $ster^{-1}$ were considered in this study. The riometer readings were generally greater than 2dB. If we assume that the proton profile is well represented by a single slope β, the energy factor ρ is given by $\rho = \beta/(\beta-1)$. For approximately a dozen events for the period 1967-72, characterizing the peak of the twentieth solar cycle, the best fit straight line is found (Bakshi and Barron, 1976) to be

$$R = a\{\log_{10} I_{10} + \alpha \log_{10} \rho\} + b, \qquad (3a)$$

with the best correlation coefficient ($r \approx 0.97$) obtained for $\alpha = 0.42$. The corresponding standard deviation is $\sigma = \pm 1.1$ dB and the coefficients a and b are given by

$$a = 7.81, \; b = -13.36, \; (\alpha = 0.42). \qquad (3b)$$

It should be noted that the correlation coefficient shows only a slight variation in the range $\alpha = 0.2$ to $\alpha = 0.6$. It is also interesting to note that the square root type formula, used in other studies (Potemra, 1972, Cormier, 1973, Stroscio and Sellers, 1975), would lead to almost twice as large a standard deviation $\sigma = 2.05$ dB and a significantly lower correlation coefficient ($r \approx 0.90$).

4. RADIO-RIOMETER PREDICTION SCHEME

It is now possible to combine Equations (1) to (3) to obtain a real time quantitative prediction for the riometer absorption R from various features of the radio spectrum. I_{10} is predicted by Equation (2) using the time and frequency integrated radio energy ε and the flare location A. $\rho = \beta/(\beta-1)$ is predicted by Equation (1), using the radio frequency ratio ω_3/ω_2. Then Equation (3) provides a prediction for R in terms of the real time flare parameters. It is necessary to observe the radio flux profiles at several different frequencies as a function of time in order to determine ε. It is also necessary to have real time integration routines to carry out the time and frequency integrations. By noting the peak flux density at each frequency, one can determine whether a U-spectrum has been achieved, and if so, what the peak (ω_3) and dip (ω_2) frequencies are. All of these operations are

within the present day technological capabilities, and in fact some of these operations are already being carried out at observatories like the Sagamore Hill Observatory. It should be noted that besides these radio observations, one also needs the flare longitude in order to correct for the attenuation effects according to Equation (2).

5. DISCUSSION

The prediction scheme described above rests on empirically established relationships, Equations (1) to (3). These ideas for using such relationships, which emphasize the radio-spectrum energy or the proton-spectrum energy as correlation variables are soundly based on general physical considerations, and thus do not depend on any particular, detailed theoretical models. Such models could lead to a more detailed understanding of why the relationships work and could also provide useful refinements that might improve the correlations.

Some of the limitations of the studies described above can be easily removed:

(i) The proton riometer correlation equation (3) is restricted to strong events, with $I_{10} > 100$ protons $cm^{-2}sec^{-1}$ $ster^{-1}$. Additional events with lower thresholds for I_{10} such as >50 or >10 protons $cm^{-2}sec^{-1}ster^{-1}$ should be examined to extend the range of applicability of Equation (3).

(ii) The radio-proton correlation in Equation (1) leads to slope values near or less than unity for radio frequency ratios $\omega_3/\omega_2 \geq 10$. The corresponding values of the energy factor $\rho = \beta/(\beta-1)$ are not meaningful, since the (ρ,β) relationship is valid only if the proton spectrum can be described in terms of a single slope for its entire energy range. Usually the spectrum softens for higher energies and if this is properly taken into consideration, a more meaningful energy factor for such events can be developed in terms of a two slope formula, as shown in Bakshi and Barron, 1976. An appropriate correction to Equation (1) has to be incorporated when $\omega_3/\omega_2 \geq 10$.

(iii) We have been concerned here with the peak riometer absorption for a given event. However, the proton-riometer relation holds even as a function of time, as the event unfolds. If one can develop a reliable prediction for the time development of the proton fluxes at various energies, it would, with the aid of Equation (3) provide a corresponding prediction for the riometer absorption. Further work on this topic is in progress.

REFERENCES

Bakshi, P., and W. Barron (1976): Predicting riometer absorption for solar radio bursts I. Correlations between proton spectra and riometer absorption, Rep. AFGL-TR-76-0166, Air Force Geophys. Lab., Hanscom Air Force Base, MA.

Bakshi, P., and W. Barron (1978): Prediction of proton flux magnitudes from radio burst data, Rep. AFGL-TR-78-0100, Air Force Geophys. Lab., Hanscom Air Force Base, MA.

Bakshi, P., and W. Barron (1979): Prediction of solar flare proton spectral slope from radio burst data, J. Geophys. Res. 84 131.

Cormier, R.J., (1973): Thule riometer observations of polar cap absorption events, AFCRL-TR-73-0060.

Potemra, T. A., (1972) Radio Sci. 7, 571.

Stroscio, M. A., and B. Sellers (1975): The calculation of riometer absorption and an approximate connection between riometer absorption and solar proton fluxes during nighttime PCA events, AFCRL-TR-75-0469.

A METHOD OF PREDICTING SKYWAVE FIELD STRENGTH IN HF BANDS IN TROPICAL ZONE

O. P. Sehgal
All India Radio
Simla, India
and
H. O. Agrawal
All India Radio
Research Department, Indraprastha Estate
New Delhi 110002, India

1. INTRODUCTION

The values of the field strengths measured in our region did not agree with the values estimated by well-known prediction methods such as those of CRPL and RPU-9 of the United States and SPIM of France. AIR therefore developed its own method, popularly known as the AIR method for the prediction of skywave field strength in HF bands in the tropical zone. The method was developed as a result of extensive measurements conducted over almost a full sunspot cycle of ionospheric absorption at New Delhi starting in 1954. The method can be used with both manual calculations and computer programming. A computer program has been written by J. A. Murphy (1969).

Of the many factors involved in the prediction of the skywave field strength, the most important is the ionospheric absorption, particularly the non-deviative absorption suffered by the wave in traversing the D region. Studies on the diurnal, seasonal and sunspot cycle variation of ionospheric absorption were made in the Research Department of AIR on the basis of vertical absorption measurements conducted on 5 MHz at New Delhi over a solar cycle (Rao et al., 1962). Based on practical observation, the formula for non-deviative absorption was determined and is given by the following expression:

$$L = \frac{635\, n\, (1 + 0.0017\, R_{12})\, \sec \phi}{(f \pm f_L)^2\ \mathrm{Ch}(\alpha, \chi)^{0.77}}$$

where L = ionospheric absorption
n = number of hops
R_{12} = 12 month running average sunspot number
ϕ = angle of incidence at the absorbing layer
f = wave frequency
f_L = longitudinal component of the gyrofrequency
$\pm$ = signs refer to ordinary (+) and extraordinary (-) wave components
$\mathrm{Ch}(\alpha,\chi)$ = Chapman function and is taken to be equal to $\sec \chi$ when $\chi \leq 80$.

On the basis of measurements of ionospheric absorption at night, a value

of 2.5 db for the deviative absorption has been taken into account for calculating the nighttime field strength and also a polarization loss of 3 db has been assumed. The AIR method (Rao, 1969) gives a set of ten nomograms and the skywave field strength of any circuit may be evaluated in an easy manner for different possible modes of propagation through the ionosphere.

Field strength measurements made on AIR's regional shortwave transmissions operating on 6-9 MHz bands indicate very good correlation between the observed values and the values estimated using the AIR method. The differences were within ±3 db.

2. RECENT STUDIES

Some recent studies, however, indicated that the AIR method gives higher absorption values on lower frequencies when the propagation is via the E region. Field strength measurements were therefore conducted on lower frequencies at New Delhi and the results were compared with those estimated by the AIR method and the CCIR first interim method. It was found that there was better correlation between the observed and the estimated values of field strength with the AIR method than with the CCIR first interim method when the transmissions were via the F region. But the field strength estimated by both methods did not agree with the observed values when the transmissions were via the E region. A document indicating these results was submitted to CCIR in 1975 (Doc. 10/56, 1974-78).

At the interim meeting of Study Group 6 of CCIR in Geneva in February/March 1976, Interim Working Party 6/1 proposed a second CCIR computer-based interim method which is described in detail in CCIR Report 252-2 (Rev. '76). This method is recommended for universal application and is based on a better understanding of ionospheric characteristics and the experience gained in using the first interim method. The main difference between this method and the other known methods is in the evaluation of basic transmission loss, in particular ionospheric absorption.

Field strength measurements were conducted by the Research Department of AIR on lower frequencies at New Delhi during 1974-75 and 1976. The observed values were compared with those estimated by the AIR method and the second CCIR method (using manual computation). It was found that there was good correlation between the observed values and those estimated using the second CCIR interim method when the propagation mode is via the E or F regions. Using the AIR method, the correlation was quite good when transmissions were via the F region. A document was submitted to CCIR in 1977 (Doc. 10/323, 1974-78) giving these results.

Further field strength measurements have been carried out at a number of places in India on different frequencies and the observed values, when compared to those estimated by the AIR method and the second CCIR method, indicate the same trend. The observed and estimated values are shown in a scatter diagram (see Figure 1). The results of the above studies on the comparisons between the AIR method and the second CCIR method for single hop propagation via F-region mode indicate that in a total of 61 cases of measurements taken at New Delhi, Gauhati, and Trivandrum, deviations are within ±3 db in about 50 percent of the cases by both the methods. However, the AIR method gave results within ±6 db in about 82 percent of the cases whereas the CCIR method gave results within ±6 db in about 67 percent of the cases.

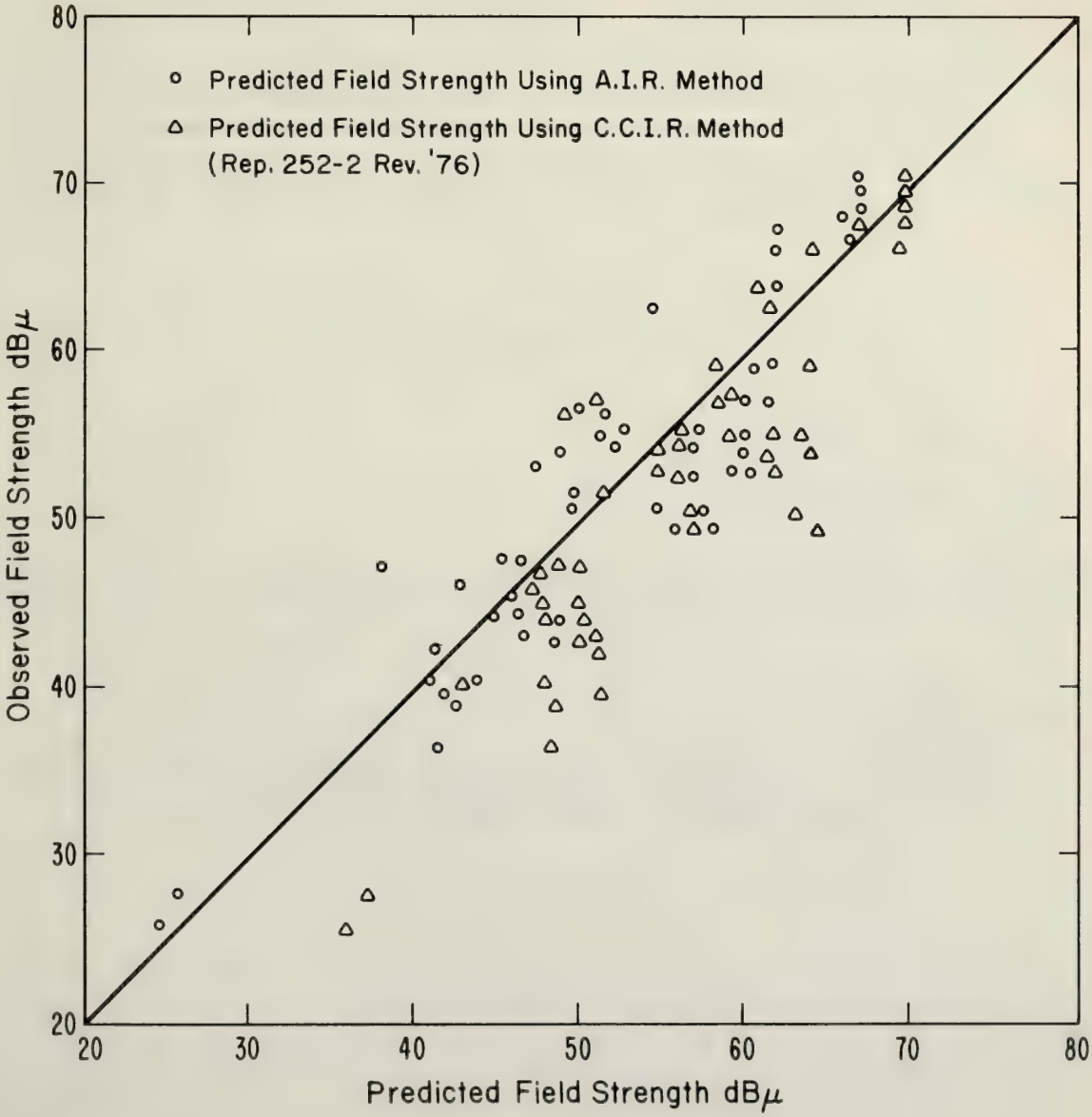


Figure 1. Observed and predicted field strength.

3. CONCLUSIONS

Regarding a suitable field strength prediction method, our view is that the method should be simple and easily applicable for day-to-day calculations particularly for countries in the tropical zone who are mostly economically weak and developing. The facilities of high speed computers are not generally available to most of them. Hence a method which is capable of being applied with simple aids like nomograms is most desirable. For propagation via F2 region the AIR method is quite appropriate due to its simplicity, proven accuracy and availability of nomograms. On the other hand the second CCIR method is cumbersome and requires the use of a high speed computer. The computer program is still not available. It has also to be put to elaborate practical tests for its applicability in tropical regions. In addition, nomograms, etc., are yet to be developed to apply this method for quick evaluation of field strength values.

REFERENCES

CCIR Doc. 10/56, 1974-78.

CCIR Doc. 10/323, 1974-78.

Murphy, J. A. (1969): Computer programme for the evaluation of field strength by AIR prediction method. Radio and Space Research Station, Slough, England.

Rao, M. K., Mazumdar, S. C., and Mitra, S. N. (1962): J.A.T.P., 24, pp. 245-256.

Rao, M. K. (1969): Nomographs for Calculation of Field Strength, Journal of Institution of Telecomm. Engrs (India), 15, p. 729.

UNPREDICTED VARIATIONS IN D-REGION RESPONSE TO SOLAR X-RAY EVENTS

R. H. Doherty

Seasonal and latitudinal changes in the D-region response to solar X-ray events have been observed using low frequency pulse propagation. These pulse signals (Loran-C) have been monitored over reciprocal paths. The once reflected sky wave signal is selected by sampling the pulse at the proper time. Also, the paths are long enough to greatly attenuate the ground wave signal.

The day time signals show considerable phase and amplitude sensitivity to sudden ionospheric disturbances (SID) produced by solar X-rays. The changes observed are not always the standard phase advance and amplitude increase normally seen on VLF cw signals. Three paths at roughly 25^0, 35^0 and 60^0N latitude have been statistically examined for a one year period. On a statistical percentage basis, phase advances are compared with phase retardations and amplitude increases are compared with amplitude decreases.

Two individual SID events occurring at different times on the same day are observed on four different paths to show how changes of solar zenith angle and latitude of the reflection point can influence the propagation effects observed.

The variations with latitude, the variation with season, and the variation with solar zenith angle all suggest that during a SID event the amplitude changes occur at a different ionospheric height than do the phase changes.

INTRODUCTION

Data from three reciprocal propagation paths were analyzed for the one year period from July 1, 1969 through June 30, 1970. The three paths chosen for this study were Hokkaido, Japan to Yap Island and reciprocal with a midpoint at 26^0N latitude; Jupiter Inlet, Florida to Nantucket, Massachusetts and reciprocal with a midpoint at 34^0N latitude; and Attu Island (in the Aleutian Islands of Alaska) to Port Clarence, Alaska and reciprocal with a midpoint at 60^0N latitude.

It has been recognized for some time (Doherty 1963) that although the usual observed effect for an SID as seen on VLF cw signals is a phase advance and an amplitude increase, LF pulse signals that are only once reflected from the ionosphere can show phase retardations or advances and amplitude increases or decreases in all possible combinations. The LF signals from

Tashkent to Delhi (Subrahmanyam, et. al., 1974) have been evaluated for these type of effects. The use of several paths at different latitudes all analyzed over a similar period has apparently not been previously reported.

The particular effect produced by a particular solar flare can be shown to depend on the intensity and wavelengths associated with the X-rays produced by that flare. A large flare can produce one effect and a small flare another effect on any given path for any given day. It was anticipated, however, that statistically over a season and for paths at different latitudes the variation of the intensity and wavelengths of flares could be averaged out. This should be particularly true if only the gross effects of the flares were considered.

Consequently, a study was made over a period of one year on the percentage of total number of SID's that produce phase advances or amplitude enhancements. The remainder of the flares in this study produced phase retardations or amplitude decreases or both. Actually, the phase and amplitude statistics are treated separately, but it is obvious from the results that there is a strong tendency for phase retardations and amplitude decreases to occur together.

1. STATISTICAL VARIATIONS FOR ONE YEAR OVER THREE PATHS

The statistical percentage variations presented in Figures 1 through 8 are arranged so that all of the phase information is presented in Figures 1 through 4 and all of the amplitude information is presented in Figures 5 through 8. A direct comparison of the phase effects to the amplitude effects can be obtained in each case by comparing Figures 1 and 5, 2 and 6, 3 and 7, or 4 and 8.

Figure 1 shows the seasonal variation in the percentage of phase advances for the three paths indicated above. This figure shows that there is a definite tendency for flares to produce retardations during winter months, particularly at the higher latitudes. This result suggests changes in the ionospheric D-region with latitude and season. Evidently the ionospheric D-region is reacting to the flare X-rays differently at some times than at others. In an attempt to determine if this effect was merely a manifestation of solar zenith angle changes, the percentages of phase advances were determined as a function of the solar zenith angles. In Figure 2 the data from all three paths were combined, but the percentages were evaluated for predominantly summer months (April through September) and predominantly winter months (October through March). The rapid drop off of the winter curve and the crossing of the summer and winter curves in Figure 2 appears to be primarily related to the fact that winter and summer conditions are quite different for the 60^{0}N latitude path. However, the difference in slope for the summer and winter periods may well be an indication of a smoothly changing D-region as a function of latitude, particularly in winter months, which is not just a manifestation of the larger solar zenith angles occurring at these times.

In Figures 3 and 4 the percentages were derived for each path separately

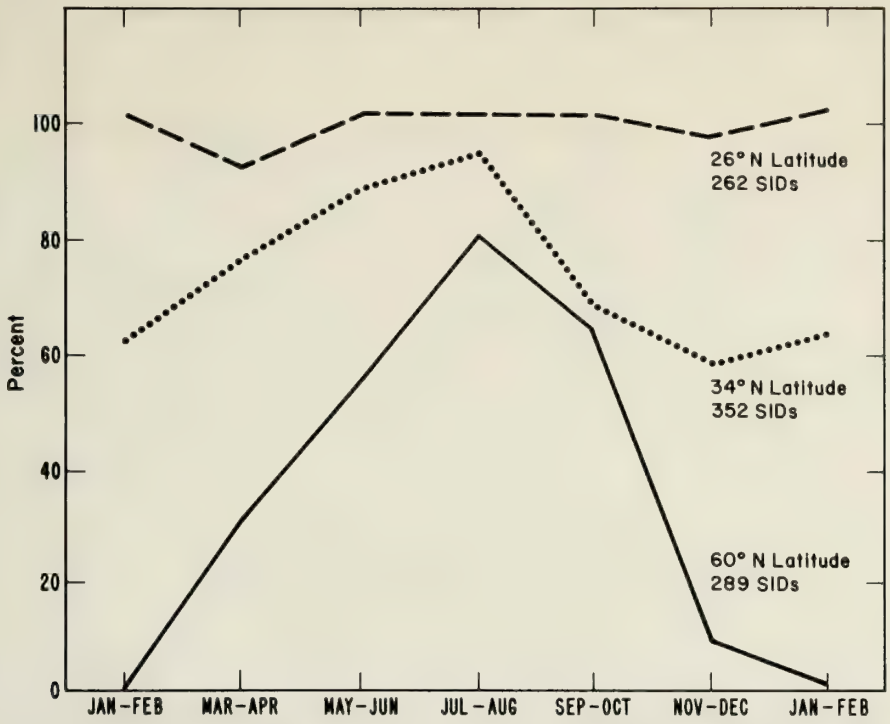


Figure 1. Percent of flare events with negative phase changes (phase advances) as a function of season.

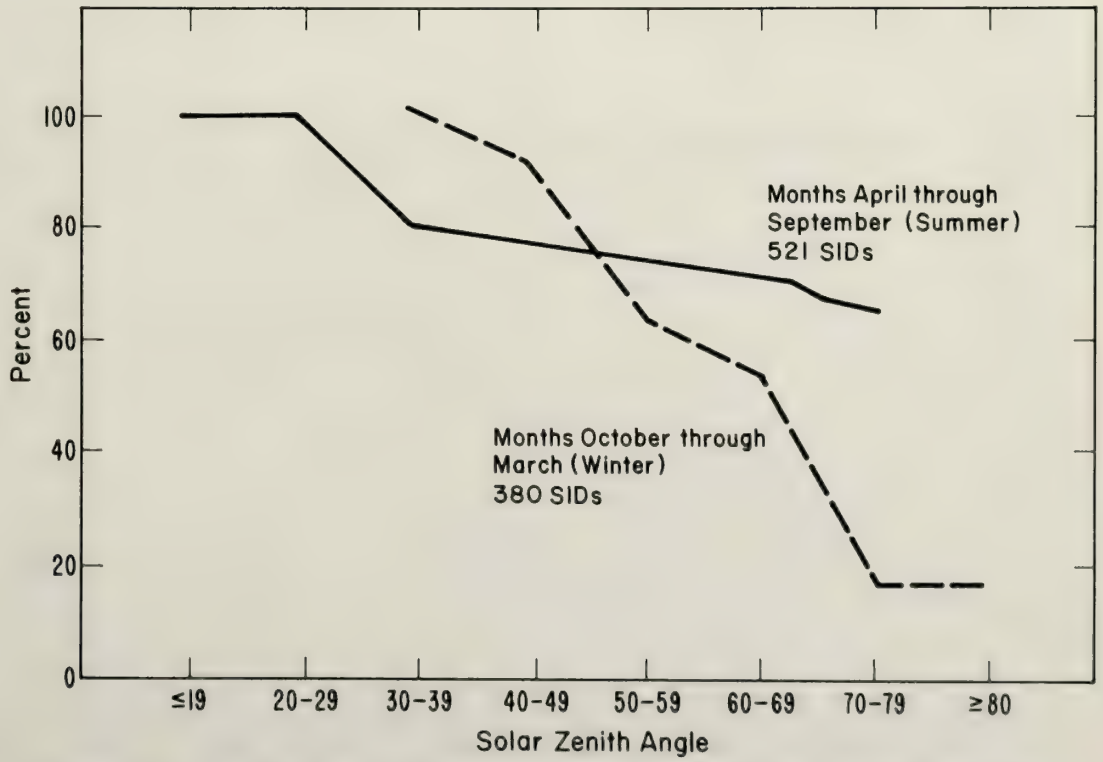


Figure 2. Percent of flare events with negative phase changes (phase advance) in the given solar zenith angle ranges for all three propagation paths.

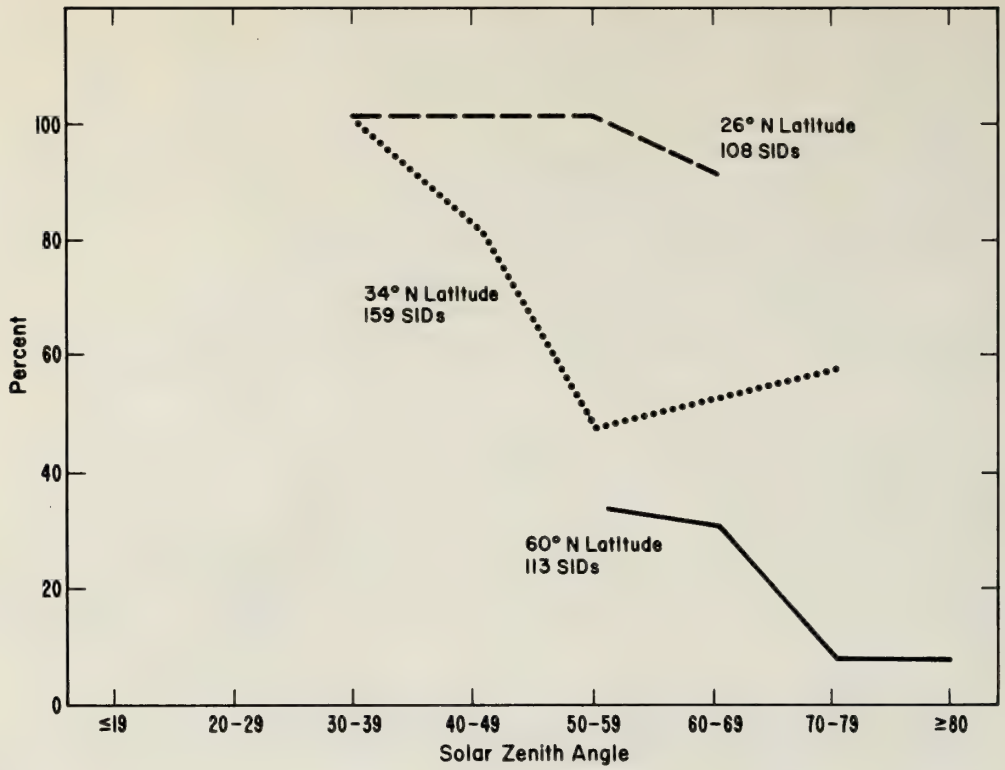


Figure 3. Percent of flare events with negative phase changes as a function of solar zenith angle for three paths at different latitudes for the winter months October through March.

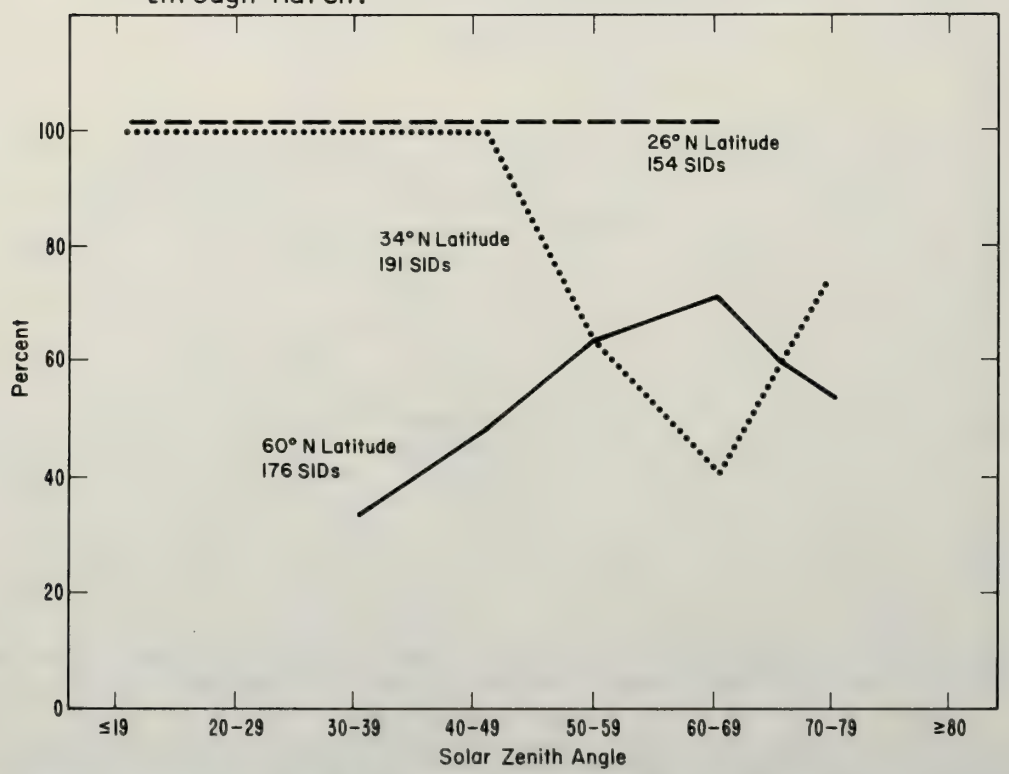


Figure 4. Like Figure 3 except for months April through September.

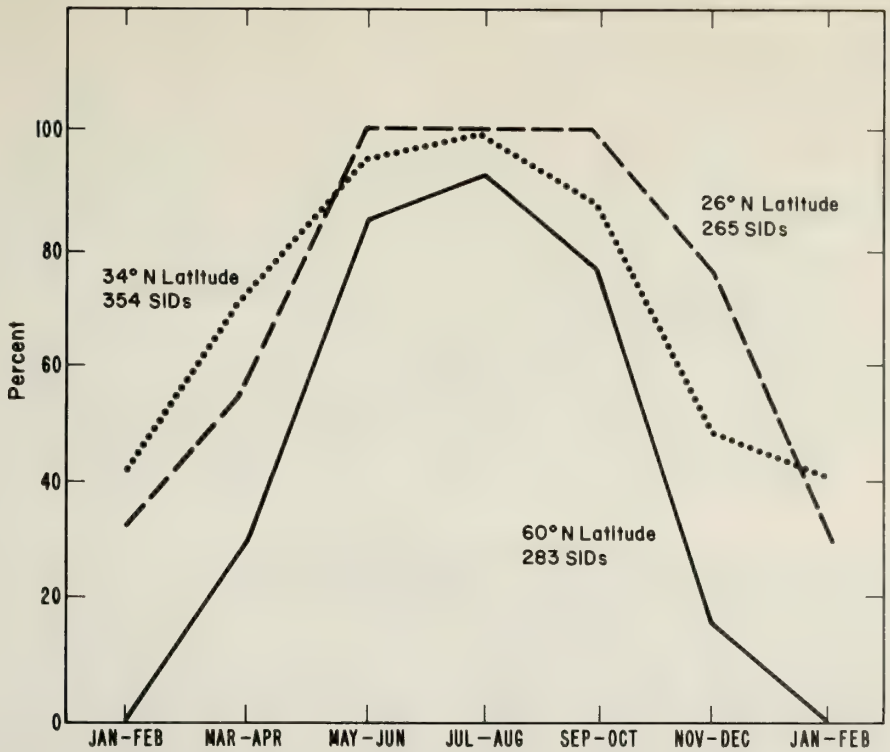


Figure 5. Percent of flare events with amplitude enhancements as a function of season.

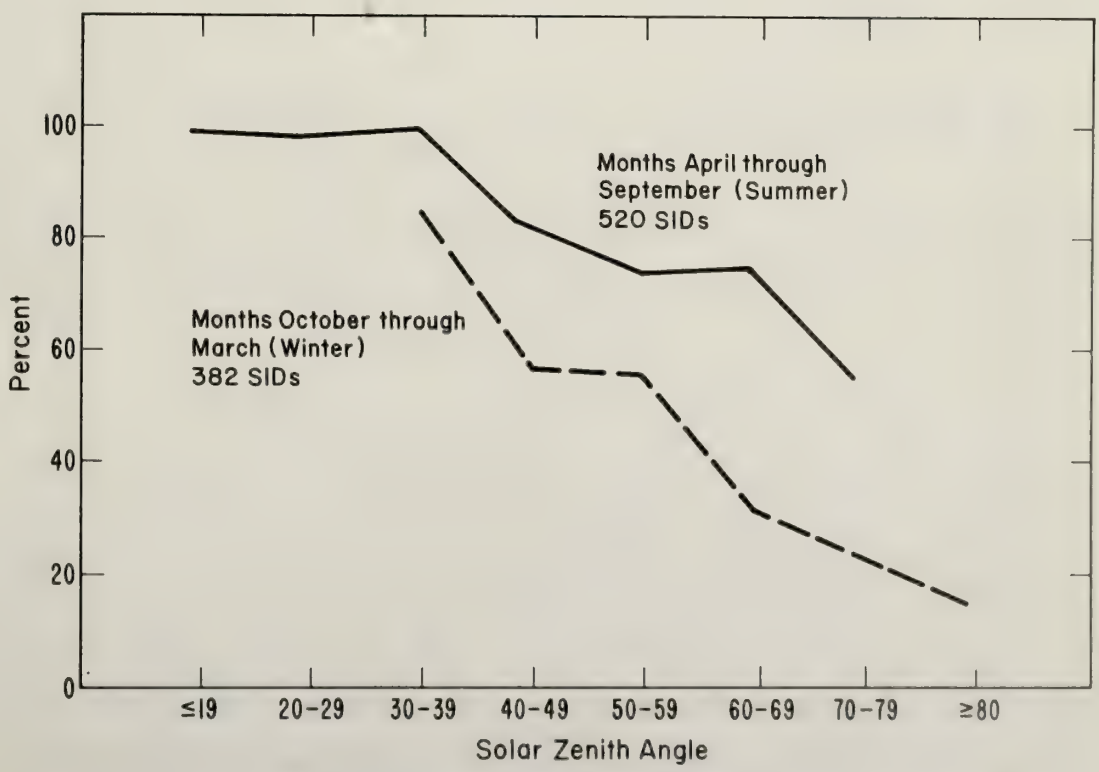


Figure 6. Percent of flare events with amplitude enhancements as a function of solar zenith angle.

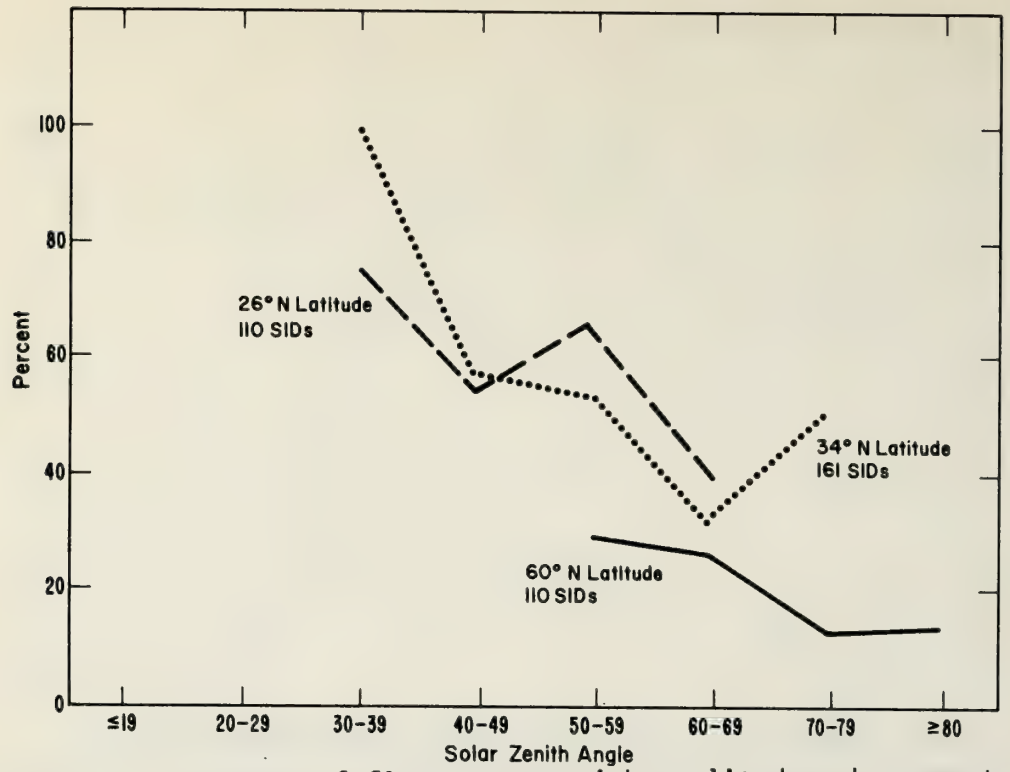


Figure 7. Percent of flare events with amplitude enhancements as a function of solar zenith angle for the months October through March (winter).

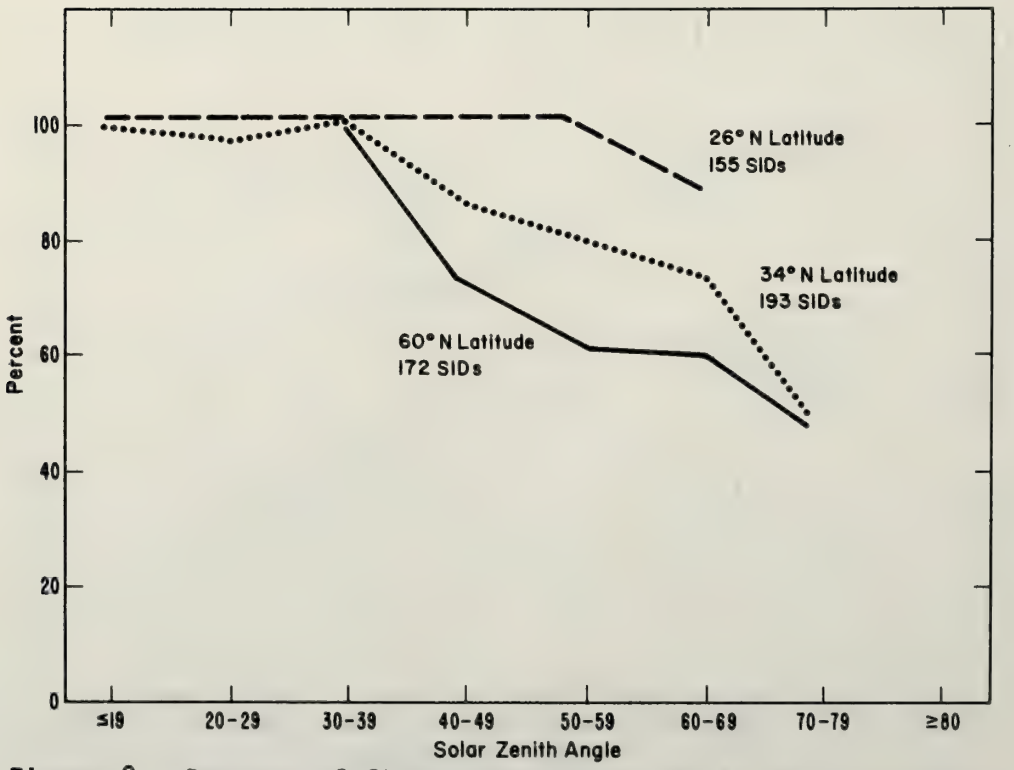


Figure 8. Percent of flare events with amplitude enhancements as a function of solar zenith angle for the months April through September (summer).

for both the winter and summer periods. The data plotted in these figures seem to emphasize the effects observed at 60°N latitude are considerably different from those observed at 26° and 34°N latitude, but this might be anticipated since the change in one case is only 8° whereas, in the other case, it is 26°. The analysis presented herein seems to be suggestive of D-region changes but inadequate in scope and number of paths analyzed to make quantitative statements about the D-region changes that may have occurred. The data particularly in Figure 3 and to a lesser extent in Figure 4 show that there appears to be a latitude effect for both the winter and summer periods. The data in Figures 2 and 3 suggest that there is a dependence on solar zenith angle in addition to latitude or season. This is true since there is nearly always a tendency for phase retardations to occur at higher zenith angles irrespective of the other factors. There is a suggestion in Figure 4 that at higher latitudes during the summer months this trend may reverse. This point should merit further study.

Figure 5 shows the results of an analysis similar to that presented in Figure 1. In this case the percentage of amplitude enhancements are plotted versus the seasonal periods. Again it can be seen that there is a strong seasonal variation. It is interesting to note that the seasonal variation of these amplitude percentages does not change as much with latitude as the phase percentages did. This is consistent with the previously reported fact that the diurnal amplitude variations do not change as much with latitude as the diurnal phase variations do (Doherty, 1968). These facts also suggest that there is a different region of the ionosphere controlling the signal amplitude than that controlling the signal phase. Figure 6 shows the amplitude effect versus the solar zenith angle for the three paths combined with the two periods similar to Figure 2 for the phase. The winter and summer curves do not cross in this case as they did in the phase analysis, again suggesting a different portion of the ionosphere influencing the phase and amplitude of the signals. Figures 7 and 8 again represent the results of the paths treated separately. In this case nearly all of the curves demonstrate a greater tendency for the amplitude to decrease as the solar zenith angle increases. The solar zenith angle changes, the changes in the latitude of the path, and the seasonal changes all seem to work consistently together in their effect on the percentage of amplitude events that show a signal enhancement.

2. SHORT TERM VARIATIONS OF SID SIGNATURES AND DIURNAL CHANGES

The statistical analysis described above suggests that there is a seasonal change, a latitudinal change, and a change in the D-region with solar zenith angle. It also suggests that at any one time there might be a trade off between latitude changes and solar zenith angle changes. Consequently, certain paths that lent themselves toward checking such effects were studied; and several events with this type of trade off were found. One such example is shown in Figures 9 through 16. On May 15, 1970, a solar flare occurred just after 1900 GMT (approximately noon at Boulder, Colorado). SID effects were observed on four paths as shown in Figures 9 through 12. The solar zenith angle from the midpoints of each of these paths was less than 35°. Figure 9 shows the effect observed for the path from Jupiter Inlet, Florida, to Nantucket, Massachusetts, where the latitude of the midpoint was 34°. The

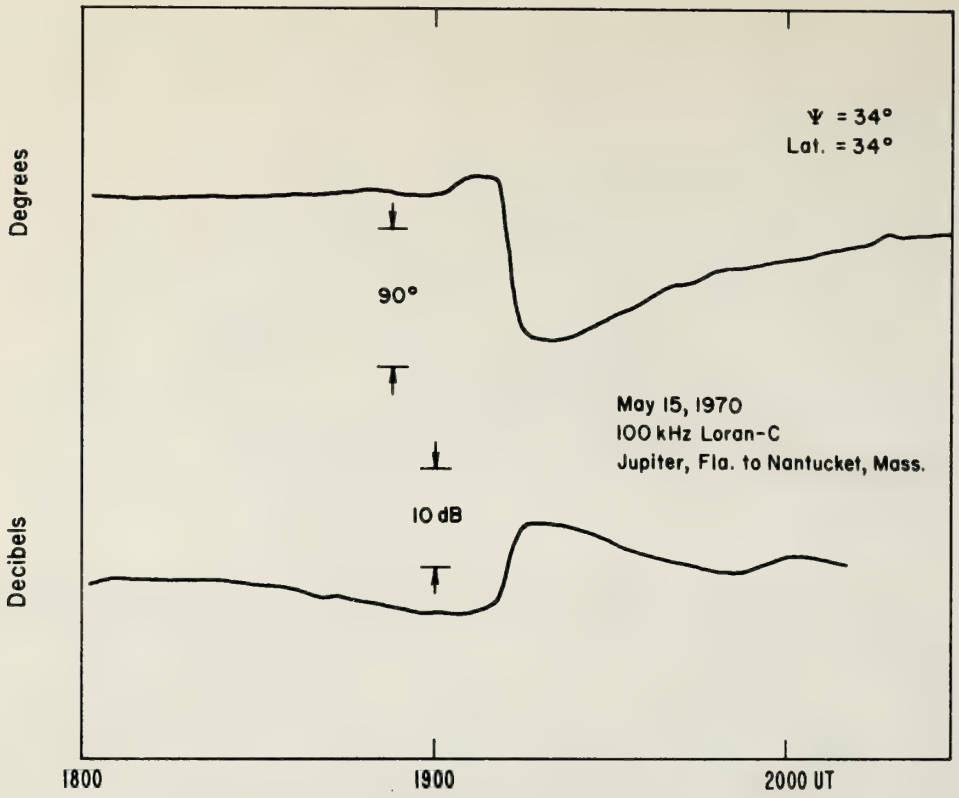


Figure 9.

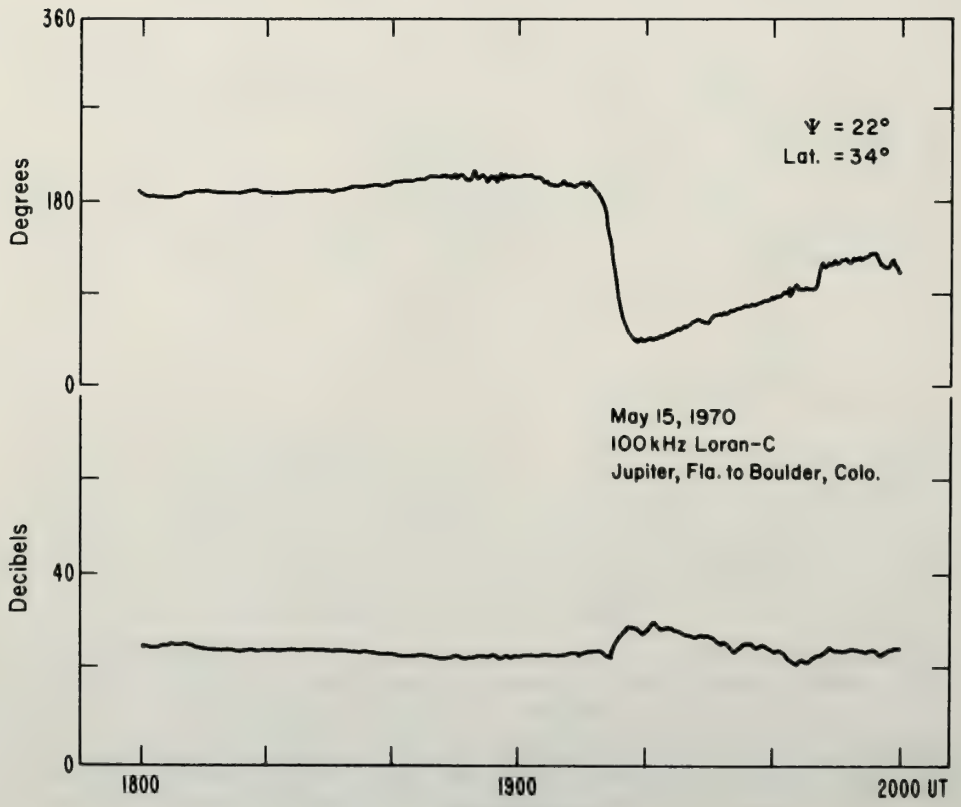


Figure 10.

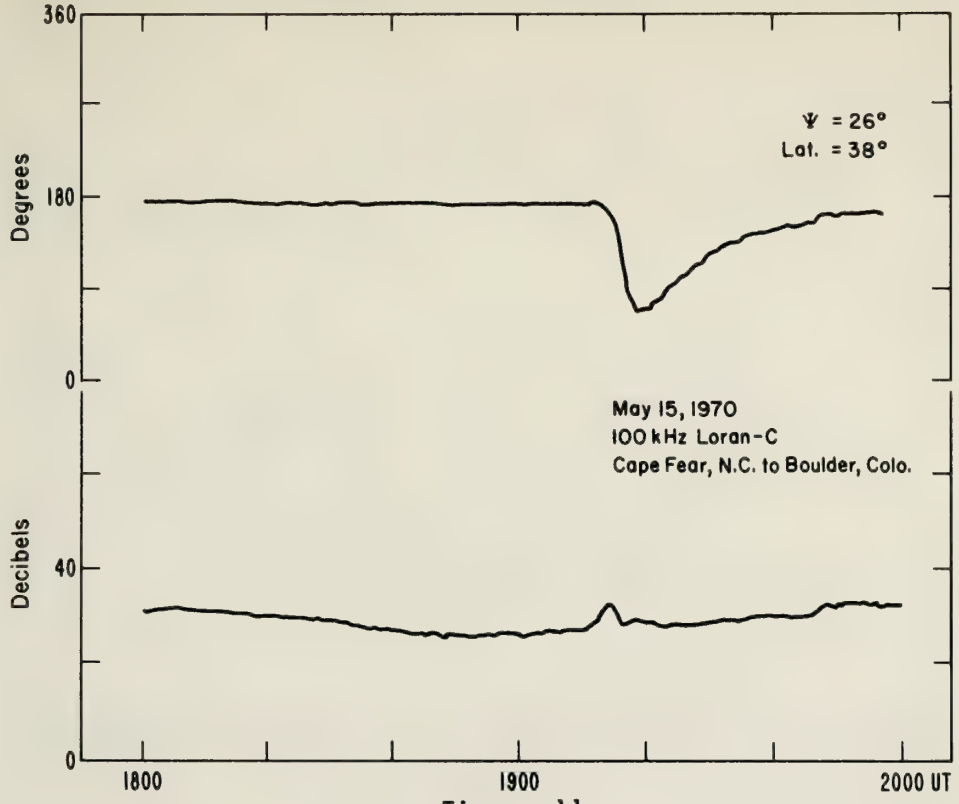


Figure 11.

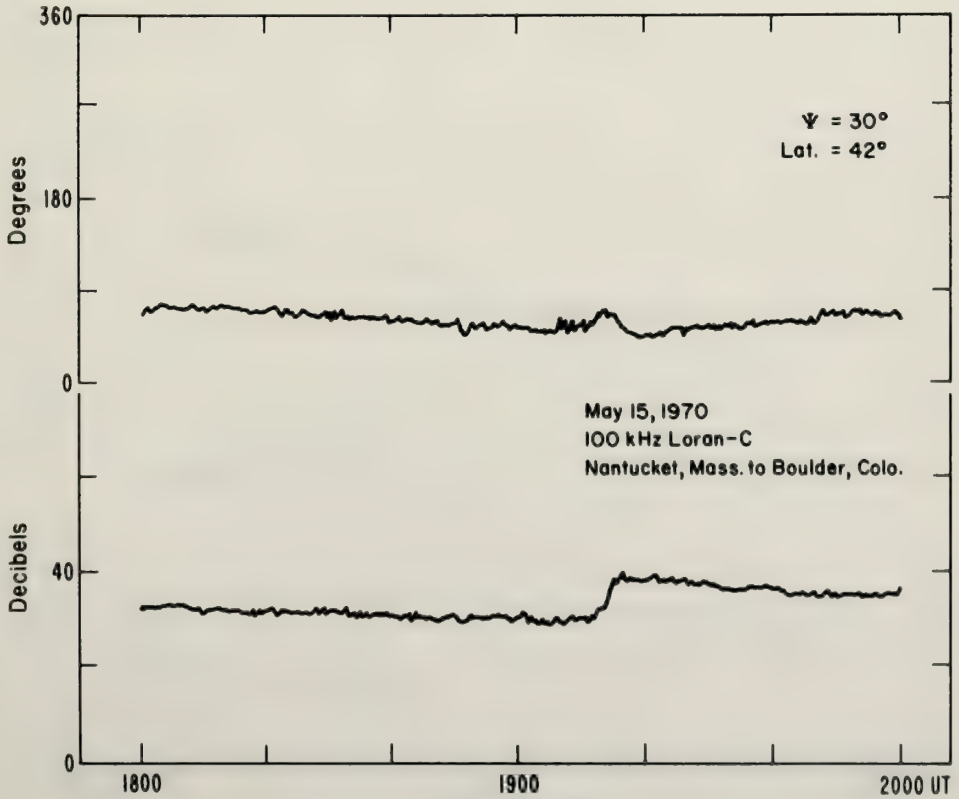


Figure 12.

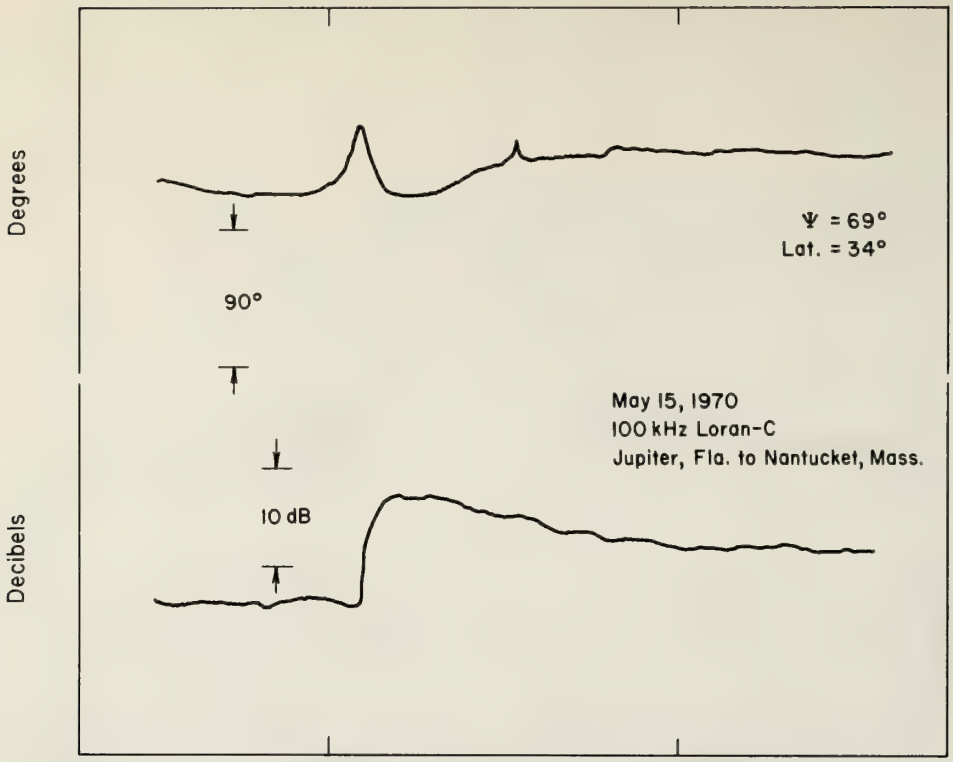


Figure 13.

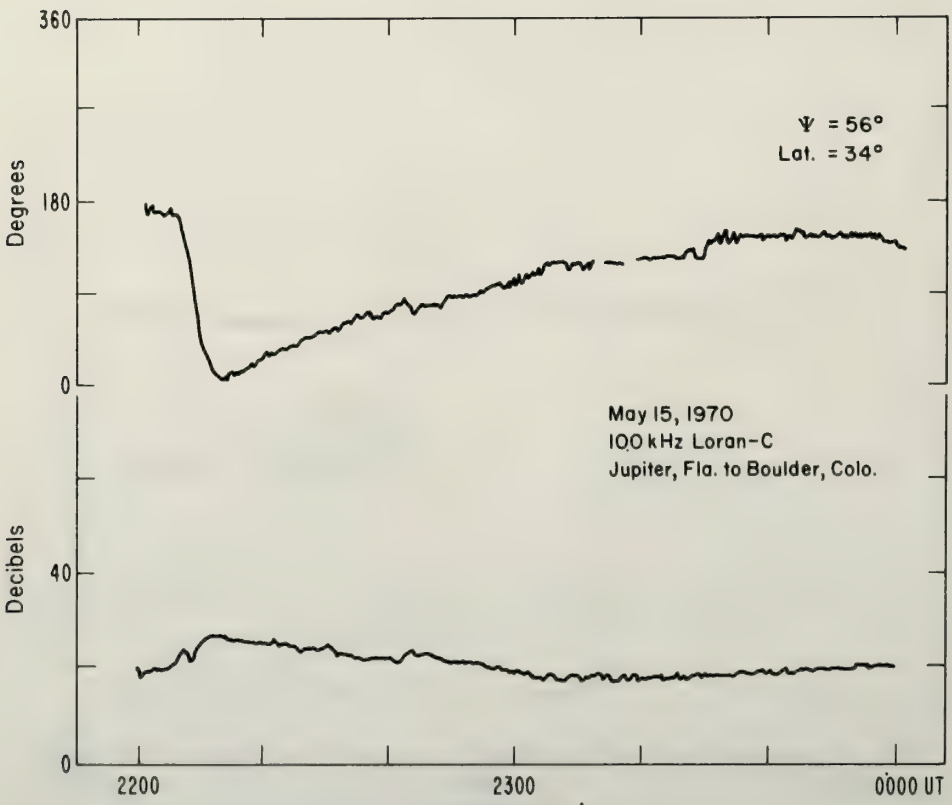


Figure 14.

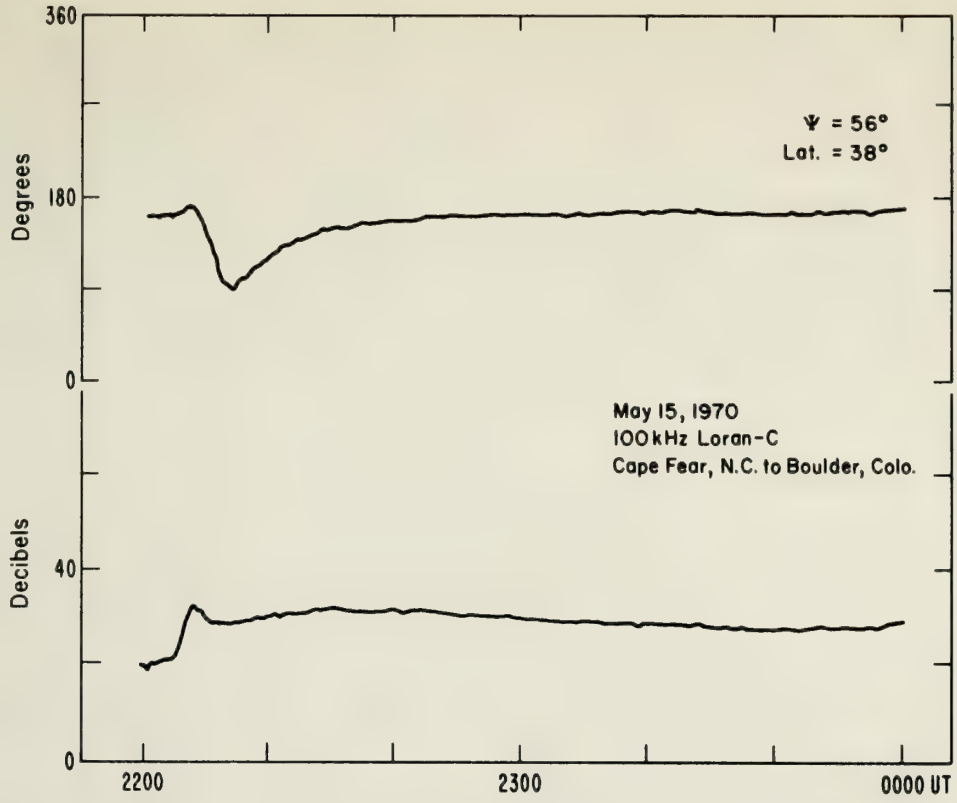


Figure 15.

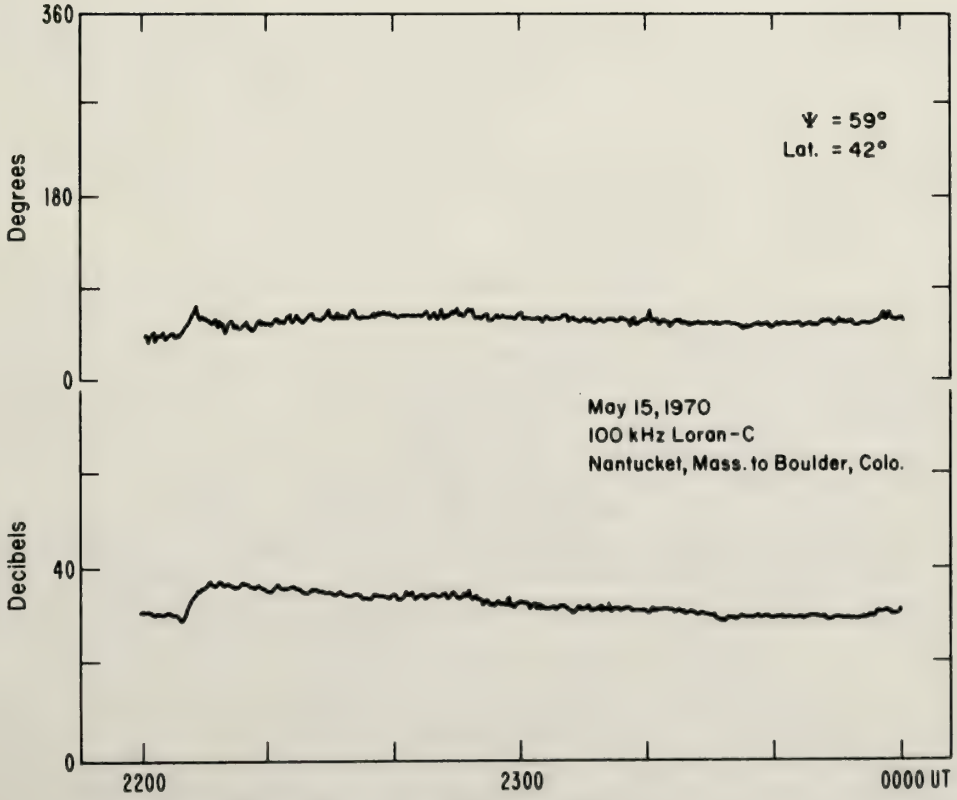


Figure 16.

phase advance and amplitude increase were comparable to those shown in Figure 10 for the path from Jupiter Inlet, Florida, to Boulder, Colo., with a midpoint latitude also equal to 34^0. (Note the difference in vertical scales between Figures 9 and 10). The signal observed between Cape Fear, North Carolina and Boulder, Colorado, where the latitude of the midpoint equaled 38^0, (Figure 11) showed a somewhat smaller effect; and the signal observed between Nantucket, Mass., and Boulder, Colo. (Figure 12), where the latitude of the midpoint equaled 42^0, showed a phase retardation rather than a phase advance. Three hours later when the solar zenith angle for the Jupiter Inlet, Florida, to Nantucket, Massachusetts, path was 69^0, a second flare occurred. Figure 13 shows a phase retardation was observed on this path, even though the latitude was 34^0. Figure 14 shows that a phase advance occurred on the path from Jupiter Inlet, Florida, to Boulder, Colorado, latitude = 34^0, where the solar zenith angle was only 56^0. Figure 15 shows a smaller phase advance on the path from Cape Fear, North Carolina, to Boulder, Colorado, latitude = 38^0, zenith angle = 56^0. Figure 16 shows a phase retardation again on the path from Nantucket, Massachusetts to Boulder, Colorado, latitude = 42^0, zenith angle = 59^0. It can be seen by referring back to Figure 13 that the effect observed over this 34^0latitude path is nearly the same as the effect observed for the 42^0latitude path (again note the difference in the vertical scales between Figures 13 and 16). This example gives a very graphic picture of the trade off between latitude changes and solar zenith angle changes that can occur at times.

In addition to the flare effects discussed above pronounced diurnal changes occur, primarily at sunrise and sunset, that are highly repetitive from day to day (Doherty 1967, 1968). These diurnal variations are different at different latitudes and change with season in a manner similar to the flare effects described above. Since there is little reason to anticipate that the night time D-region should change appreciably with season or latitude, it should be possible to relate the diurnal variations of the phase and amplitude with the solar flare observations to deduce a meaningful statistical model of what the daytime D-region looks like and how it changes with latitude, season, and solar zenith angle.

The diurnal variations that have been reported previously indicate that the phase of the LF pulse sky-wave signal follows a cosine chi pattern during the day at low latitudes for all seasons. At higher latitudes, it follows a cosine chi pattern in the winter, but a trapazoidial pattern with changes at sunrise and sunset in the summer. The measurements further show that the amplitude of the signals generally follow the trapazoidial pattern for all seasons and all latitudes. This again suggests a different portion of the ionosphere is controlling the phase and the amplitude. It is also interesting to note that the seasonal phase pattern shown in Figure 1 changes with latitude as does the diurnal pattern, but the seasonal amplitude pattern shown in Figure 5 does not change with latitude as is true of the diurnal amplitude pattern.

CONCLUSIONS

The results of this analysis suggests that any predicted D-region profiles will need a variation with season and latitude that can produce these

observed low frequency SID effects. The analysis shows that for the three northern latitude paths chosen, solar X-rays tend to attenuate the LF signals in the winter and enhance the signals in the summer. At the lowest latitude solar X-rays produce nearly 100% phase advances, whereas, at the highest latitude, phase retardations occur more than 50% of the total time, and nearly 100% during winter months. Seasonal variations are observed on all three of the paths with amplitude decrease and phase retardations more common during winter months. The non-correlation between the phase variations and the amplitude variations strongly suggest that a different part of the D-region is controlling the phase changes and the amplitude changes of these signals.

REFERENCES

Doherty, R. H. (1963): Oblique incidence pulse measurements at 100 k c/s. AGARD ograph 74, Pergamon Press, 133-147.

Doherty, R. H. (1967): Oblique incidence pulse measurements at 100 kHz pulses. Radio Science, Vol. 2 (new series). 645-651.

Doherty, R. H. (1968): Importance of associative detachment and dissociational attachment in the lower ionosphere as shown by LF radio measurements. J.C.R., 73. 2429-2440.

Subrahmanyam, C. V., Sastri, J. Hanumatr, and Desphande, S. D. (1974): Study of solar flare signatures on lf field strength over Tashkent-Delhi Path. Indian Journal of Radio and Space Physics, Vol. 3, 153-157.

SECULAR VARIATION OF OCCURRENCE RATE AND DISPERSION OF LOW-LATITUDE WHISTLERS DURING THE SOLAR CYCLE NOS.19 AND 20

Y.Tanaka, M.Hayakawa, J.Ohtsu and A.Iwai
Research Institute of Atmospherics, Nagoya University,
Toyokawa, Aichi, 442, Japan

On the basis of the measurement during the solar cycle Nos.19 and 20,the long-term variations of the occurrence rate and dispersion of whistlers at low latitudes are investigated in relation with the solar and geomagnetic activities. The whistler data used for the study were obtained at Wakkanai(geomag.lat.35.2°N),Moshiri (34.1°),Toyokawa(24.1°) and Sakushima(24.1°). First we find a very high correlation coefficient of ~0.9 between the dispersion at Wakkanai-Moshiri with the sunspot number,as in the case of the f_oF2. Then it is found that the occurrence shows a weak positive correlation with the geomagnetic activity,while it shows an obscure inverse one with the sunspot number. The occurrence is found to be well expressed by a linear equation of the geomagnetic activity and sunspot number based on the least square fit and then the correlation coefficients between the occurrence frequency at Wakkanai-Moshiri and Toydkawa-Sakushima and that expected from the equation are found to amount to rather high values of more than o.7, implying that the occurrence number can be determined by the joint influence of both activities.

1. Observation of whistlers in Japan

The routine-based observation of whistlers has been continued since 1957 at a low latitude station(Wakkanai,July 1957-Nov.1962;Moshiri,since Dec.1962) and also at a still lower latitude station(Toyokawa,July 1957-June 1966; Sakushima,since Feb.1967). The antenna site was changed from Wakkanai to Moshiri and also from Toyokawa to Sakushima so as to keep the observation in good conditions since we encountered the increase of artificial noises at the former sites. The observation had been made during two minutes starting from 20 and 50 min. every hour,but we are now carrying out the observation only during 50-52 min. every hour. The general view concerning the observation of low-latitude whistlers and their characteristics is given in the recent review paper by Hayakawa and Tanaka(1978).

2. Characteristics of occurrence number

Fig.1 shows the secular variation of the occurrence rate at Toyokawa-Sakushima. Dot marks in the figure indicate the daily average of the occurrence number per month. In obtaining the daily average per month we have excluded the whistlers which are clearly indentified as "long". To make clear the solar cycle variation in a more definite way we have attempted to exclude the seasonal dependence of the occurrence number and the effect due to different observing period as follows. The daily average in each month is normalized by the mean of the daily average for the relevant month at each site,Toyokawa or Sakushima,throughout the solar cycles 19 and 20(we call it the "normalized occurrence rate",although not shown in the figure). Then the running mean of normalized rate during 6 months before and 6 months after the relevant month is shown by a cross mark in the figure. Fig.2 is the similar result for higher latitude station(Wakkanai-Moshiri),which is drawn in the similar way as in Fig.1.

The exact estimation of the absolute value of occurrence number is,in most cases,very difficult because of the dependence of occurrence on the circumstances of radio noises at the observing site. So the simultaneous observation at both old and new sites in a certain overlapping period is highly required,even if there were not present the abrupt depletion in the observing conditions due to the increasing artificial noises at the old sites. We did not make such simultaneous observations,but we will be able to treat the running means at both stations quite equally since we notice a very smooth transition in the variation during the removal,as shown in Figs.1 and 2. In the case of Toyokawa-Sakushima stations in Fig.1,the observation was interrupted for seven months following the movement of the stations,but,nevertheless,it may be reasonable to imagine a relatively smooth transition in the normalized occurrence rate around that period with taking into account the transition at Moshiri in the same period. We have been monitoring,in a regular interval,the observing system including the antennas,pre- and main amplifiers and so we think that the observing conditions have been kept well in an isolated village of Moshiri as well as in a noise-free island of Sakushima up to date since the removal.

3. Characteristics of dispersion

Fig.3 shows the secular variation of the monthly mean(i.e. average per month) of dispersion and its running mean at Wakkanai-Moshiri.The range of dispersion is restricted to 25-90 $sec^{1/2}$. The difference in latitude between the two stations is too small to affect the results. The occurrence rate is found to show a great decrease in summer at Toyokawa-Sakushima as shown in Fig.1,and the available data are too few to determine the mean values at Toyokawa-Sakushima. So we study only the secular variation of dispersion at Wakkanai-Moshiri.

4. Secular variation of sunspot number,geomagnetic activity and f_0F2

Fig.4 illustrates the solar cycle variation of the daily average of sun-

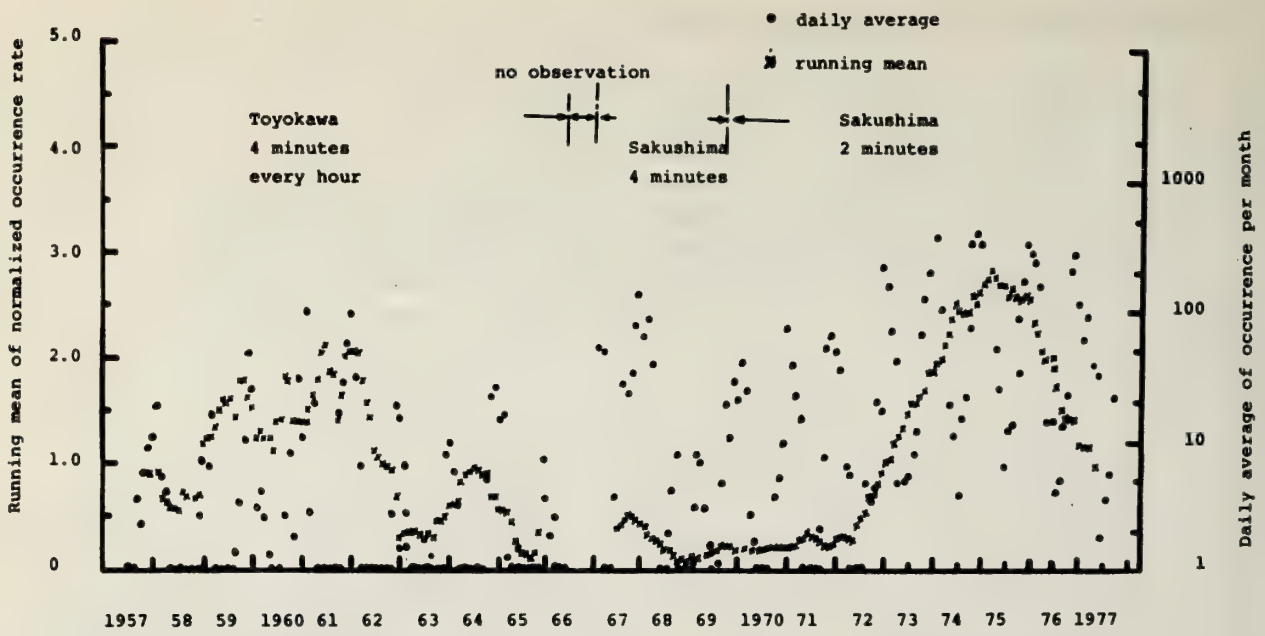


Fig.1 Secular variation of whistler occurrence rate at Toyokawa-Sakushima.

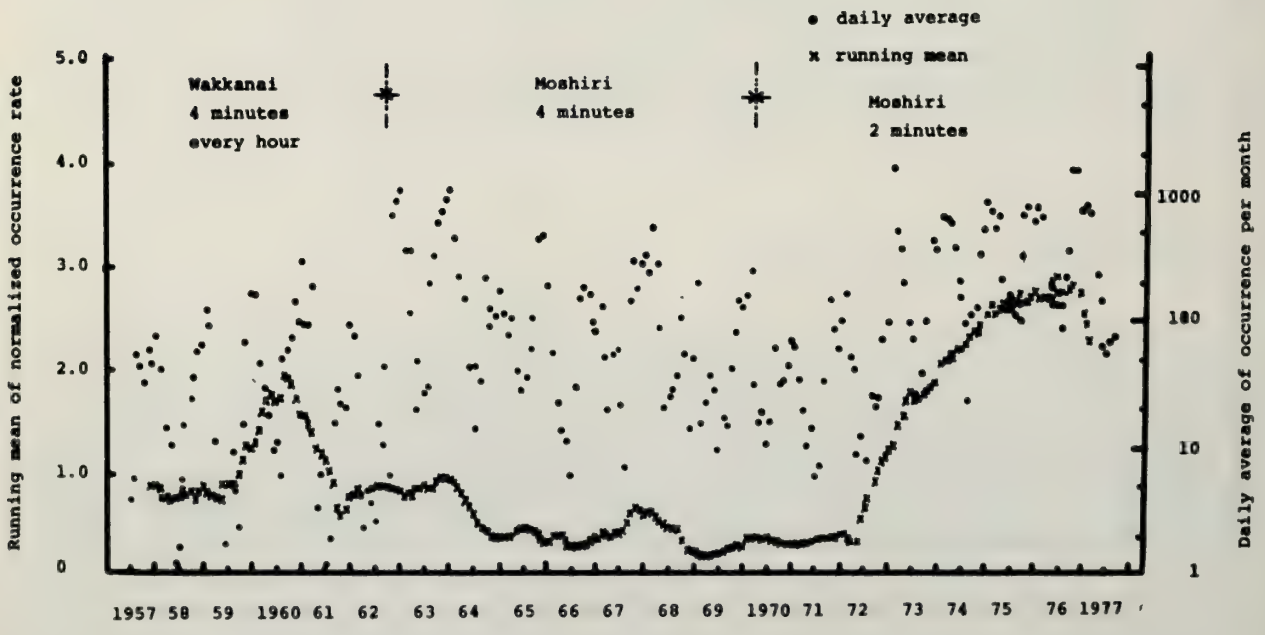


Fig.2 Secular variation of whistler occurrence rate at Wakkanai-Moshiri.

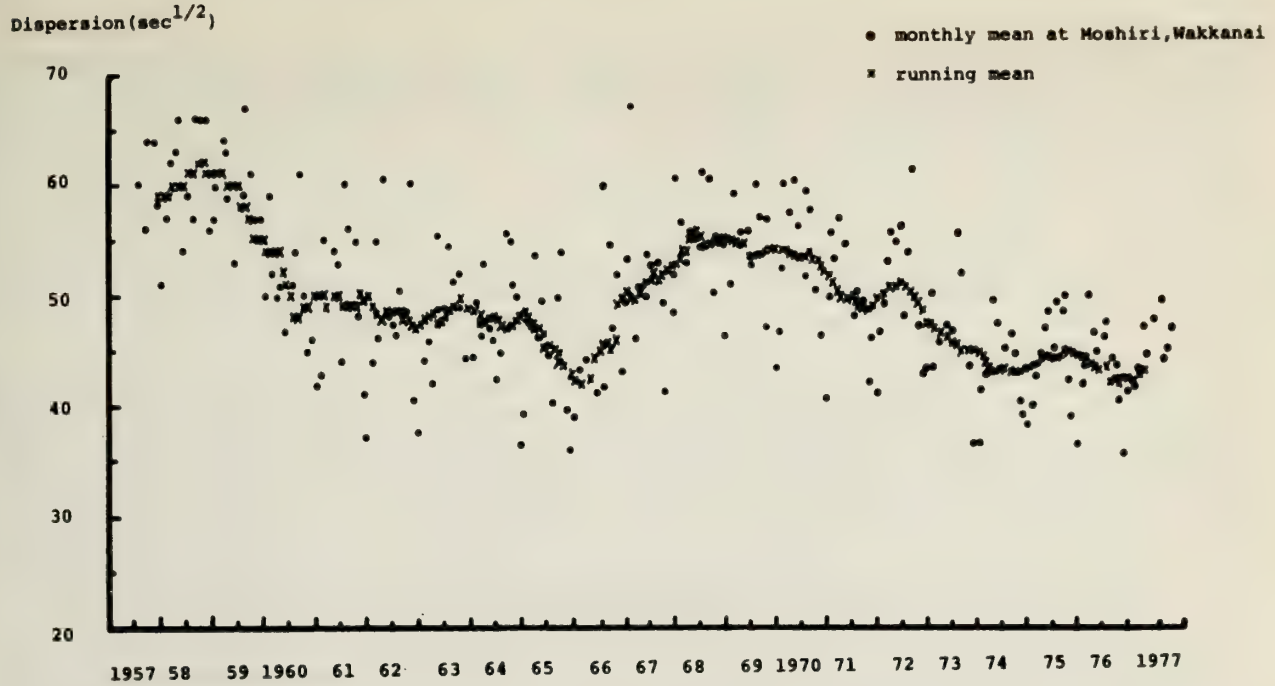


Fig.3 Secular variation of dispersion at Wakkanai-Moshiri

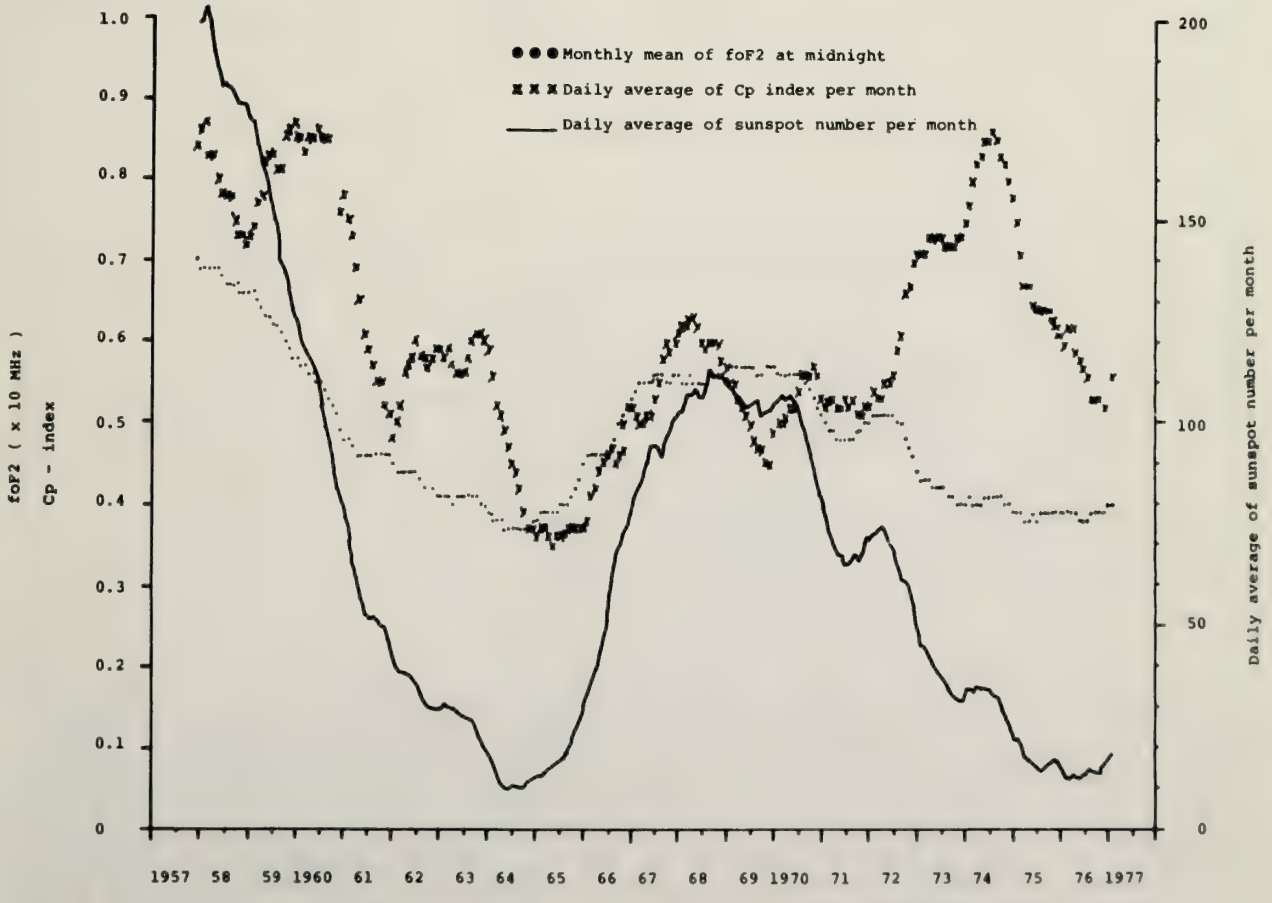


Fig.4 Secular variations of the monthly mean of daily sum of sunspot number, the monthly mean of Cp index and monthly median value of midnight f_oF2 at Wakkanai.

spot number per month,the daily average per month of the Cp index as a good measure of geomagnetic activity(Kane,1976), and the monthly median value of f_oF2 at midnight measured at Wakkanai. These three quantities are also expressed in the form of running means.

5. Correlation between the whistler characteristics and solar and geomagnetic activities

First we simply study discuss the association of the dispersion with solar activity. A comparison between Figs.3 and 4 shows that there exist very close relationships of the variations of the running means of dispersion and of foF2 with the sunspot number. We have found a surprisingly high correlation coefficient of 0.92 between the dispersion and solar activity and also a higher value of 0.98 between the foF2 and solar activity,as summarized in Table 1, implying that the magnetosphere is less sensitive to the long-term variation of solar activity than the ionosphere,as shown by Hayakawa et al.(1971). The similar positive correlation has already been found on the basis of whistler data at Wakkanai during the International Geophysical Years by Kimpara(1962a) and during the solar cycle 19 by Hayakawa et al.(1971). Based on the whistler data at Poitiers during the solar cycle 19,Bouriot et al.(1967) have investigated the solar cycle variation of the plasmaspheric electron density at middle latitudes,and obtained the positive correlation between them.

Table 1 INTER-CORRELATION BETWEEN VARIOUS PARAMETERS

Whistler Observation		Sunspot Number	Cp index	$\beta_1 Cp - \beta_2 SN$
Station	Data			
Toyokawa-Sakushima	Occurrence	-0.371	0.511	0.724
Wakkanai-Moshiri	Occurrence	-0.379	0.483	0.759
Wakkanai-Moshiri	Dispersion	0.917		
Wakkanai	foF2	0.977		

Now we discuss the variation of occurrence rate in more details. Whistler activity is specified either by the mean number of whistlers per unit time ("occurrence rate") or by the percentage pf periods containing whistlers("percentage occurrence"). Either measure of whistler activity includes the effect of thunderstorm activity as well as that of propagation conditions. Considering that if a propagation path existed for one whistler,then other nearby lightning discharges could also produce whistlers,the percentage occurrence seems to be a better measure owing to its less dependence on the thunderstorm activity. However,actually no significant difference was found between the two

measures(Allcock,1966). Then there is no evidence suggesting distinct correlation between the solar activity and thunderstorm activity around the conjugate region of our stations in the southern hemisphere(Markson,1971). Therefore it is thought that there is very little possibility to include the effect of thunderstorm activity during the process of obtaining the running means from the normalized occurrence rate. On this reasoning the secular variation of the occurrence rate shown in Figs.1 and 2 may be discussed only from the standpoint that such long-term solar cycle variations are attributed to the variations in the propagation conditions(Hayakawa and Tanaka,1978).

There are a few papers dealing with the association between the whistler activity and solar and geomagnetic activities. Kimpara(1962a) found a surprisingly high negative correlation over -0.9 on the basis of data during 4 years from July 1957, and later Hayakawa et al.(1971) have noticed a small inverse correlation ranging from -0.3 to -0.4 by making use of the data during the solar cycle No.19. A similar negative relation was found by Corcuff et al.(1966) between the whistler activity at Poitiers and sunspot as well as geomagnetic (Ap) activities using the data during 1957-1965.

Thus the general trend of inverse correlation between the occurrence rate and solar activity is apparently recognized over either a portion of the solar cycle No.19 or the whole one solar cycle. Such an inverse correlation may be understood in terms of the increase in ionospheric absorption of VLF waves during active solar periods(Hayakawa et al.,1971). A small negative correlation coefficient of -0.371 is obtained between the occurrence at Toyokawa-Sakushima and sunspot number(see Table 1) throughout the solar cycles 19 and 20. The corresponding value for Wakkanai-Moshiri is -0.379. These small correlations may suggest that the long-term variation of occurrence rate cannot be interpreted by the effect of solar activity alone and there exist some other factors contributing to the occurrence. It seems to us that the most promising factor is the geomagnetic activity. Enhanced whistler activity has been found during geomagnetic disturbances(Kimpara,1962b; Hayakawa et al.,1969; Tanaka and Hayakawa, 1973a,b). The secular variation of the geomagnetic activity represented by Cp index(Kane,1976) is given in Fig.4,which shows an oscillation whose period is roughly half of one solar cycle. Enhanced geomagnetic activities are seen to be nearly in phase with increased occurrence of whistlers as clearly seen from the comparisons of Figs.1,2 and 4. For example,we can identify the simultaneous enhancements in both occurrence and geomagnetic activity at 1959-1960,62-63, 67-68, and 72-74. Then we obtained the correlation coefficients of ~ 0.5 between them as shown in Table 1,which is higher than the correlation between the occurrence and solar activity. This may be understood as the consequence of the favoured condition of ducted propagation for low-latitude whistlers(Hayakawa et al.,1969; Tanaka and Hayakawa,1973a,b). The correlation coefficient between the solar activity and Cp index is found to be ~ 0.4, this suggesting a slight dependence of the Cp index on solar activity,as is quite reasonable. However,we ignore this week correlation between them and we think that the occurrence is resulted from the combined influence of the Cp index and solar activity as two independent factors. Now the occurrence is assumed to be expressed by a simple linear function of the Cp index(Cp) and solar activity(sunspot number,SN) as follows; the occurrence $=\beta_1$ Cp - β_2 SN,and an attempt is made to determine the constants of β_1 and β_2 by means of the least square method using the running means of the above three quantities in Figs.1,2 and 4, and also to deduce the correlation coefficients. As the results we obtained the following relationships; the occurrence at Toyokawa-Sakushima = 2.814 Cp -0.010 SN, and the occurrence at Wakkanai-Moshiri = 3.052 Cp - 0.012 SN, and moreover the correla-

tion coefficients between the occurrence rate observed and that predicted by the above equations amount to about 0.75. These high correlation coefficients seem to give us the support to the validity of our assumption that the occurrence rate of whistlers at low latitudes is accounted for by the joint effects of solar and geomagnetic activities considered to be independent of each other. The above equations we derived in the present paper will be the experimental basis of the forecast of occurrence of whistlers.

References

Allcock,G.McK.(1966) : Whistler propagation and geomagnetic activity. J.Inst. Telecom.Engrs., 12:158.

Bouriot,M., M.Tixier, and Y.Corcuff(1976) : Etude de l'ionisation magnétosphérique entre 1,9 et 2,6 rayons géocentriques au moyen des sifflements radioélectriques reçus à Poitiers au cours d'un cycle solaire. Ann.Géophys., 23:527.

Corcuff,Y., P.Corcuff, and M.Tixier(1966) : Evolution de l'occurrence des sifflements radioelectriques entre maximum et minimum d'active solaire, C.R.Acad.Sc.Paris, 263:584.

Hayakawa,M., J.Ohtsu, and A.Iwai(1969) : Occurrence and dispersion of whistlers during magnetically disturbed periods at lower latitudes, Rep.Ionos.Space Res.Japan, 23:9.

Hayakawa,M., J.Ohtsu, and A.Iwai(1971) : Characteristics of dispersion and occurrence rate of whistlers at low latitudes during one solar cycle, J. Geomag.Geoelect., 23:18.

Hayakawa,M., and Y.Tanaka(1978) : On the propagation of low-latitude whistlers, Rev.Geophys.Space Phys., 16:111.

Kane,R.P.(1976) : Geomagnetic field variations, Space Sci.Rev., 18:431.

Kimpara,A.(1962a) : Dispersion of whistlers, Nature, 193:667.

Kimpara,A.(1962b) : Whistlers and solar activity, Nature, 193:667.

Markson,R.(1971) : Consideration regarding solar and lunar modulation of geophysical parameters,atmospheric electricity and thunderstorms. Pageoph., 84:161.

Tanaka,Y., and M.Hayakawa(1973a) : The effect of geomagnetic disturbances on duct propagation of low-latitude whistlers. J.Atmos.Terr.Phys.,35:1699.

Tanaka,Y., and M.Hayakawa(1973b) : Storm-time characteristics of low-latitude whistlers. Planet.Space Sci., 21:1797.

ATMOSPHERIC RADIO NOISE MEASUREMENTS IN LF/MF BANDS

A. K. Bhatnagar and Mangal Sain
Research Department, All India Radio
Indraprastha Estate, New Delhi 110002, India

1. INTRODUCTION

Noise is an important parameter in the system planning of a broadcasting service as the minimum signal required for a certain grade of service depends directly upon the prevailing noise level at any location, in the absence of any other interference. In most of the tropical countries man-made noise is low, especially in rural areas, and the atmospheric radio noise which is of terrestrial origin emerges as the principal source of noise interference in the LF or other broadcast bands. The extraterrestrial or galactic noise becomes relevant only at very high frequencies.

In order to assess the acceptable requirement for primary grade sound broadcasting service in the LF band, the Research Department of AIR has been conducting atmospheric noise measurements for some time at certain typical locations in India like Delhi (28°35'N, 77°5'E), Trivandrum (8°29'N, 76°56'E) and Gauhati (26°N, 91°55'E).

2. ATMOSPHERIC RADIO NOISE MEASUREMENTS

Measurements of atmospheric radio noise were started at Delhi in 1975 at 155 kHz for a 6 kHz bandwidth, on a long-term basis. To cover some typical areas, the measurements were started at Trivandrum on 155 kHz, 225 kHz and 1630 kHz and also at Gauhati on 155 kHz and 525 kHz for a bandwidth of 6 kHz in 1977. Both Trivandrum and Gauhati, which represent southern and eastern parts of India, are known to have high thunderstorm activity. Standard field strength meter having charge and discharge time constants of 1 and 600 milliseconds, respectively, have been employed for noise measurements using a recorder with a response time of 400 milliseconds. American National Standard Institute (ANSI) has recommended the use of charge and discharge time constants of 1 and 600 milliseconds, respectively, for the quasi peak measurements of atmospheric radio noise (CCIR Report 227-1, 1974). On the basis of experience gained while analyzing the noise records collected at Delhi and elsewhere it has been realized that charge and discharge time constants of 1 and 600 milliseconds, respectively, give a better and more realistic assessment of impulsive type of noise prevailing in tropical areas when monitored with the sound program rather than using charge and discharge time constants of 10 and 600 milliseconds after Thomas and Burgess (1947), or even if measurements of noise are taken using the ARN-2 method of CCIR (CCIR

Report 322-1 and NBS Report 5545). Accordingly the noise records at Trivandrum, Gauhati and Delhi have been taken using charge and discharge time constants of 1 and 600 milliseconds in 1977-78. Each recording has been taken for 5 minutes at each frequency during every hour in the time blocks 1200-1600, 1600-2000 and 2000-2400 hours. A noise recording of 5-minute duration has been considered sufficient for correct evaluation of noise from the analysis of noise data.

3. ANALYSIS OF DATA AND DISCUSSION

Table 1 gives the comparison between the median values of the measured noise field at 155 kHz during different time blocks and those predicted from CCIR Report 322-1. It may be observed from Table 1 that in almost all cases the measured value of noise is less than the predicted one--the difference ranges from 3 dB to 20 dB considering all the three stations.

Table 1. Comparison between measured and CCIR predicted median values of atmospheric noise [dB(uv/m)] at 155 kHz for Delhi, Trivandrum, and Gauhati for 6 kHz bandwidth.

Season	Time Block (Hours) LMT	Delhi			Trivandrum			Gauhati		
		M	P	D(dB)	M	P	D(dB)	M	P	D(dB)
	1200-1600	12	5	-7	12	15	3	6.5	7	0.5
Winter	1600-2000	16	25	9	13	26	13	9.5	23	13.5
	2000-2400	22	30	8	16.5	32	15.5	14	28	14
	1200-1600	-	-	-	15	29	14	14	24	10
Spring	1600-2000	-	-	-	20	37	17	28	35	7
	2000-2400	-	-	-	29	38	9	31.5	37	5.5
	1200-1600	25	40	15	13	33	20	11	40	29
Summer	1600-2000	29	35	6	25	33	8	21	36	15
	2000-2400	31	38	7	31	34	3	32	41	9
	1200-1600	14	28	14	15	29	14	-	-	-
Autumn	1600-2000	22	36	14	22	36	14	-	-	-
	2000-2400	24	38	14	30	38	8	-	-	-

Note: M = Measured P = Predicted D = Difference (P-M)

In order to find the amplitude probability distribution of noise, the data collected at Delhi, Trivandrum and Gauhati during the different time blocks has been analyzed. The distribution has been found to be log normal with a standard deviation of 7 dB.

Satyam(1962), Laxshminarayana(1962), and other workers have investigated the short- and long-term amplitude probability distribution characteristics of atmospheric radio noise in India. They have found the distribution to be log normal. For such a distribution Norton has provided a theoretical formula

to determine the upper decile value of noise if its median value is known. If the standard deviation is σ, the upper decile value (UD) of noise may be found from the relationship; $UD = m + 1.282 \times \sigma$, where m is the median value of noise.

It may further be seen from Table 1 that the measured median value of noise of 32 dB (uv/m) at 6 kHz bandwidth (34dB at 10Khz bandwidth) has been observed at Gauhati in summer during 2000-2400 hours. Using Norton's formula, the upper decile value of the noise is 43 dB (uv/m) at 10 kHz bandwidth.

Upper decile values of noise have also been directly computed from the recordings made at Delhi, Trivandrum, and Gauhati on high local thunderstorm activity days during the months of July and August 1978. These values are given in Table 2. It may be noted from the table that these values range from 45 dB to 55 dB and that irrespective of the location, the magnitude of noise intensity is the same. The maximum upper decile value of noise is 55 dB.

Table 2. Measured upper decile values of atmospheric noise [dB(uv/M)] for localized thunderstorm activity days during July/August at 155 kHz for Delhi, Trivandrum, and Gauhati for 6 kHz bandwidth.

Month	Time Block Hours (LMT)	Delhi	Trivandrum	Gauhati
July	1200-1600	45	45	48
and	1600-2000	48	50	53
August	2000-2400	50	52	55

4. COMPARISON OF NOISE IN THE LF AND MF BANDS

As stated previously, the atmospheric radio recordings have been made at 155, 225/235, 525 and 1630 kHz at different locations in India. From these recordings the median values of noise have been worked out at each frequency. These values have been normalized for 200 kHz and 1 MHz in the LF and MF bands, respectively, knowing the values of noise at the lower and upper ends of each of these bands. The median values of the measured noise and those predicted from CCIR Report 322-1 are shown in Table 3 for both bands. It may be observed from the table that the CCIR predicted values of noise are mostly greater than the measured ones and generally the differences are quite large, amounting to 18.5 dB. From this analysis it is evident that CCIR Report 322-1, needs to be revised.

Table 3. Comparison between measured and CCIR predicted median values of atmospheric noise (dB) at 200 kHz and 1 MHz for Delhi, Trivandrum, and Gauhati for 6 kHz bandwidth.

Place	Season	Time Block Hours (LMT)	200 kHz			1 MHz		
			M	P	D(dB)	M	P	D(dB)
Delhi		1200-1600	34	37.3	+3.3	17.8	12.3	-5.5
	Summer	1600-2000	32.3	33.3	+1.0	16.9	14.3	-2.6
		2000-2400	36.8	34.3	-2.5	22.6	19.3	-3.3
		1200-1600	9.4	11.3	1.9	-	-	-
	Winter	1600-2000	11	24.3	13.3	2.4	9.3	+6.9
		2000-2400	16.4	30.3	13.9	6.2	16.3	10.1
		1200-1600	13	24.3	11.3	-	-	-
	Spring	1600-2000	18	30.3	12.3	8.2	14.3	6.1
		2000-2400	25	33.3	8.3	11.7	20.3	8.6
Trivandrum								
		1200-1600	10.0	30.3	20.3	3.8	4.3	0.5
	Summer	1600-2000	16.4	28.3	11.9	6.3	15.3	9.0
		2000-2400	27	32.3	5.3	14.0	17.3	3.3
		1200-1600	12	26.3	14.3	0.8	0.3	-0.5
	Autumn	1600-2000	18.4	31.3	12.9	7.2	14.3	7.1
		2000-2400	24.4	33.3	8.9	12.2	20.3	8.1
		1200-1600	5.6	8.3	2.7	-	-	-
	Winter	1600-2000	8.8	16.3	7.5	0	4.3	4.3
		2000-2400	13	25.3	12.3	1.9	10.3	8.4
Gauhati								
		1200-1600	11.6	19.3	7.7	-	-	-
	Spring	1600-2000	26	31.3	5.3	11.3	12.3	1.0
		2000-2400	30	33.3	3.3	20.3	20.3	0.0
		1200-1600	-	-	-	4.8	11.3	6.5
	Summer	1600-2000	18.8	33.3	14.5	9.8	14.3	4.5
		2000-2400	29.8	37.3	7.5	19.8	22.3	2.5

Note: M = Measured P = Predicted D = Difference (P-M)

5. CONCLUSION

The following conclusions can be drawn:

1. The measured median values of atmospheric radio noise in the LF and MF bands for the three typical locations (Delhi, Trivandrum and Gauhati) in India representing different typical thunderstorm activity regions, have always been found to be lower than those predicted from CCIR Report 322-1. As such the report needs revision.

2. The amplitude probability distribution of noise has been found to be log normal.

3. During high local thunderstorm activity days the upper decile value of atmospheric radio noise for three different locations in India has been found to range between 45 and 55 dB.

REFERENCES

CCIR Report 227-1, General methods of measuring the field strength and related parameters, Volume V (1974), Published by ITU, Geneva.

CCIR Report 322-1, World distribution and characteristics of atmospheric radio noise, Published by the ITU, Geneva.

NBS Report 5545, Instruction book for ARN-2 radio noise recorder, Published by N.B.S, Boulder, Colorado.

Norton, K. A.; Voglar, L. E.; Mansfield, W. V. and Short, P. J. (1955): The probability distribution of the amplitude of a constant vector plus a Raleigh distributed vector, Proc. I.R.E., 43, p. 1354-1361.

Satyam, M. (1962): Short term amplitude probability distribution of impulsive atmospheric radio noise, J.S.I.R. (India), 21D, 221-227.

Laxshminarayana, K. M. (1962): Short term time characteristics of impulsive atmospheric noise, J.S.I.R. (India), 21D, 228-232.

Thomas, H. A. and Burgess, R. E. (1947): Survey of existing information and data on radio noise over the frequency range 1 - 30 MC/S, Radio Research Special Report No. 15, H. M.'s Stationary Office, London.

PREDICTION OF WAVEGUIDE PROPAGATION OF RADIO WAVES USING THE EXTREMAL-PARAMETRIC METHOD BASED ON PREDICTED IONOSPHERIC PARAMETERS

A. G. Shlionsky
Institute for Terrestrial Magnetism, Ionosphere and
Radio Wave Propagation of the USSR Academy of Sciences
142092, Troitsk, Moscow Region, USSR

The concepts and the basic expressions of the mathematical formulation of the extremal-parametric method (EPM) for calculating the characteristics of radio waveguides is presented. EPM has been based on the analytical dependencies of the channel characteristics on the extrema of the modified refractive index and the latter's dependence on the extrema of the vertical gradient of electron density. In this case, predictions of the key ionospheric parameters (critical frequencies, geometric parameters, and the parameters of N_r^1 and interlayer valley) may be used to predict the waveguide characteristics.

After establishing the fact that radio waves may be rebounded in ionospheric waveguides (Krasnushkin, 1947), the theoretical studies have been directed toward a quantitative analysis including the variations of the real ionosphere. Several methods of calculation are possible, depending on the mathematical formulation, the physical factors included, the ionospheric data, the ionospheric models used, the determinable characteristics, etc. It is most important to analyze the experimental data obtained from long- and very long-distance link lines, in order to design a theoretical model that is a comparatively simple mathematical formulation. This should be combined with sufficiently accurate ionospheric models and available ionospheric data.

Presented below are some results of the systematic generalization of the formulation of the extremal-parametric method (EPM) for calculating ionospheric waveguides. Also presented are the analytical dependencies for some integral characteristics of the channels. The material set forth below supplements earlier works (Shlionsky, 1965-1977) that presented the concepts and a number of expressions for EPM.

The formulation for EPM consists of three basic sets of expressions:

1. the differential conditions for the extrema and the knee point $U(r) = r^2n^2(r)$ (where r is the geocentric distance and n is the refractive index) and for the limiting case of degeneration of the U(r) nonmonotonism and disappearance of the channel;
2. the analytical dependency of the parameters of the extrema $[U(r)]'_r$

on the parameters of the extrema $[f_N^2(r)]'r$ and on the working frequencies as obtained from the combined quadratic model $f_N^2(r)$, where f_N is the plasma frequency of the ionosphere;

3. the analytical dependency of the various characteristics of the channels (integral, etc.) on the parameters of the extrema $[U(r)]'r$ and $V = U_0 \sin^2 \phi_0$ (ϕ is the angle between the ray and the vertical; the subscript "0" denotes the initial conditions) obtained from the combined quadratic model $U(r)$.

The first set of EPM expressions will be written in the general form of the geometric-optical approximation as

$$n^2 + \frac{r}{2} (n^2)'_r = 0 \tag{1}$$

$$n^2 + 2r(n^2)'_r + \frac{r^2}{2} (n^2)''_r = 0 \tag{2}$$

$$(n^2)'_r + \frac{r}{3} (n^2)''_r = 0 \tag{3}$$

Here, condition (1) corresponds to $U'_r = 0$ for the extrema $U(r)$; condition (2) corresponds to $U''_r = 0$ at the $U(r)$ knee point; and condition (3) corresponds to the simultaneous satisfaction of conditions (1) and (2) at the level of the $U(r)$ nonmonotonism degeneration.

The equivalent set of expressions for $n^2 = 1 - f_N^2/f^2$ (i.e., disregarding the effect of the magnetic field, H, and of the number of charged particle collisions, ν, on the refractive index) is of the form

$$f_N^2(r) + \frac{r}{2} [f_N^2(r)]'_r - f^2 = 0 \tag{4}$$

$$[f_N^2(r)]'_r + \frac{r}{4} [f_N^2(r)]''_r - \frac{1}{2r} [f^2 - f_N(r)] = 0 \tag{5}$$

$$[f_N^2(r)]'_r + \frac{r}{3} [f_N^2(r)]''_r = 0 \tag{6}$$

The condition equivalent to equation (2) may also be presented as (Shlionsky, 1971):

$$[f_N^2(r)]'_r + \frac{r}{2} [f_N^2(r)]''_r + \frac{r}{4} \frac{[f_N^2(r)]'^2_r}{[f^2 - f_N^2(r)]} = 0 \tag{7}$$

Condition (4) has been used to obtain the following expressions for the maximum operating frequencies of rotation of the rays emitted horizontally from the initial level r and, in the extremum, from the degeneration level r_d satisfying condition (3) (Shlionsky, 1965 and 1971).

$$f_{max}(r) = \sqrt{f_N^2(r) + \frac{r}{2} [f_N^2(r)]'_r} \tag{8}$$

$$f_{max} = \sqrt{f_N^2(r_d) + \frac{r_d}{2} [f_N^2(r_d)]'_r} \tag{9}$$

It follows from condition (7) that $r_k > r_g$ [the indices k and g correspond to the knee levels $U(r)$ and $f_N^2(r)$] since the third term is positive and the first and second terms should be of different signs in the upper vicinity of r_g. It follows from condition (6) that $r_d > r_g$ since the signs of the first

and second terms should be of different signs in the upper vicinity of r_g.

The shift, $r_d - r_g$, may be obtained from condition (6) as

$$\frac{r_d - r_g}{r_g} = \sqrt{1.2 \frac{[f_N^2(r)]'_{r=r_g}}{[f_N^2(r)]'''_{r=r_g}} \frac{1}{r_g^2} + 0.04} - 0.2 \qquad (10)$$

A second set of EPM analytical expressions has been obtained (Shlionsky, 1965-1974) from condition (4) using the combined quadratic model, $f_N^2(r)$, satisfying the following basic requirements:

$$\text{for the extrema,} \quad [f_N^2(r)]'_r = 0$$

$$[f_N^2(r)]''_r > 0 \quad \text{below } r_g$$

$$[f_N^2(r)]''_r < 0 \quad \text{above } r_g$$

A sector of a parabola with vertex at the level $r_{max}F$ will be used above the r_g level:

$$f_N^2(r) = f_0^2 \left[1 - \frac{(r_{max} - r)^2}{y_m^2}\right]$$

Since the level r_d of channel degeneration is shifted above the level r_g, the upper boundaries r_A of the channels are above r_g in the altitude region approximated by this model. The channel axes, r_B, lie in the altitude region limited from below by r_μ, the minimum level of f_N^2 in the valley. In this altitude region, $f_N^2(r)$ is approximated by an inverted parabola with a vertex at the r_μ level:

$$f_N^2(r) = f_M^2 + \frac{f_g^2}{r_\mu^2} \frac{1}{p} (r - r_M)^2$$

$$p = \left(\frac{r_g}{r_M} - 1\right)^2 \Big/ (1 - f_M^2/f_g^2)$$

The second set of EPM expressions is of the form

$$\frac{r_A}{r_{max}} = 0.75 + 0.25 \left\{1 - 8 \frac{y_m^2}{r_{max}^2} [(f/f_0)^2 - 1]\right\}^{1/2} \qquad (11)$$

$$\frac{U_A}{r_{max}^2} = \left(\frac{r_A}{r_{max}}\right)^2 \left\{1 - \frac{f_0^2}{f^2} \left[1 - \left(\frac{r_{max}}{y_m}\right)^2 \left(1 - \frac{r_A}{r_{max}}\right)^2\right]\right\} \qquad (12)$$

$$\frac{r_B}{r_M} = 0.75 + 0.25 \{1 + 8p [\frac{f^2}{f_g^2} + \frac{f_M^2}{f^2}]\}^{\frac{1}{2}} \quad (13)$$

$$\frac{U_B}{r_M^2} = (\frac{r_B}{r_M})^2 \{1 - \frac{f_g^2}{f^2} [(\frac{f_M}{f_g})^2 + \frac{1}{p} (\frac{r_B}{r_M} - 1)^2]\} \quad (14)$$

The set may also include the expressions

$$r_k \simeq r_g \quad \text{and} \quad U_k \simeq r_g^2 (1 - \frac{f_g^2}{f^2})$$

As the difference $r_d - r_g$ (and hence $r_k - r_g$) is usually small, r_k may approximately (with some underestimation) be taken as r_g. Some characteristics are functions of the key parameters $f_N^2(r)$. Substituting the conventional parabola in equation (8) we get

$$\frac{f_{max}(r)}{f_0} = \{1 + (\frac{r_{max}}{y_m})^2 [3 \frac{r}{r_{max}} - 2 (\frac{r}{r_{max}})^2 - 1]\}^{\frac{1}{2}} \quad (15)$$

Consider now the third set of analytical expressions for the characteristics of the ionospheric channels. It is expedient to distinguish in the third set the small group of nonintegral characteristics (transverse altitudes of the channels, refraction-angle characteristics of radiowaves when they are trapped in and escape from the channel, etc.) that can be presented directly as functions of the V and U(r) extremum parameters. The limiting transverse altitude of the channel is

$$\Delta r \leq r_A - \sqrt{U_A}$$

where $\sqrt{U_A} = r_c n(r_c)$ and r_c is the lower boundary of the channel; $r_c \geq \sqrt{U_A}$ since $n(r_c) \leq 1$. The transverse altitudes of the channels corresponding to the low-sloping rays (reflected below r_g) are

$$\Delta r = \sqrt{U_B - V} [\frac{(r_k - r_B)}{\sqrt{U_B - U_k}} + \frac{(r_B - r_M)}{\sqrt{U_B - U_M}}]$$

The angles necessary for turning the rays trapped in a channel are

$$\Delta\phi_{min} = \text{arc sin}\sqrt{\frac{U_A}{U_B}} - \text{arc sin}\sqrt{\frac{V}{U_B}} \quad (16)$$

when the emitter is on the channel axis (Shlionsky, 1974c), and

$$\Delta\phi_{max} = \text{arc cos}\sqrt{\frac{V}{U_A}} \quad (17)$$

when the emitter is at the channel boundary, and

$$\Delta\phi = \arccos\sqrt{\frac{V}{U_B}} \tag{18}$$

when the rays glide along the channel axis.

When the absorption coefficient, γ, is a minimum for ionospheric ducting along the axis r_B, i.e.,

$$\frac{d}{df}\gamma(r_B(f)) = 0$$

(the collision frequency is nearly constant in the channel), we obtain an expression for the optimal frequency, f_{opt} (Shlionsky, 1977):

$$\frac{f_{opt}}{f_M} = \{1 + [(f_g^2/f_M^2) - 1]/[(r_g/r_M) - 1]^2\}^{\frac{1}{4}} \tag{19}$$

The majority of the EPM expressions of the third set correspond to the set of the integral characteristics of ionospheric channels. For these, the analytical expressions can be determined from a combined quadratic model U(r) (Shlionsky, 1974), which makes it possible to tabulate the corresponding integrals

$$\Theta = \sqrt{V}\int^{r_u} \frac{dr}{r\sqrt{U(r) - V}} \qquad \frac{c\Gamma}{\nu} = L_g - L_p$$

$$L_g = \int^{r_u} \frac{rdr}{\sqrt{U(r) - V}} \qquad T = \int^{r_A} \sqrt{U(r) - U_A}\, dr$$

$$L_p = \int^{r_u} \frac{U(r)dr}{r\sqrt{U(r) - V}} \qquad T_0 = \int^{r_u} \sqrt{U(r) - V}\, dr$$

where Θ is the interval of ray oscillations in the channel; L_g and L_p are the group and phase path; Γ is the absorption, T is the limiting volume of the channel in its given cross section; and T_0 is the adiabatic invariant or the initial volume of the channel for the ray (Gurevich, 1971).

The integrals are reduced to a tabular form using the combined quadratic model U(r). In this case, the U(r) dependence above and below r_k can be approximated by the various quadratic models that satisfy the following main requirements: $U_r' = 0$ in the extrema; U(r) and $U_r'' > 0$ above r_k; and $U_r'' < 0$ below r_k.

We use the model (Shlionsky, 1974a)

$$U(r) = U_B - (U_B - U_k)\frac{(r - r_B)^2}{(r_k - r_B)^2}$$

in the altitude region r_B, r_k and the model

$$U(r) = U_A + (U_k - U_A)\frac{(r_A - r)^2}{(r_A - r_k)^2}$$

in the altitude range r_k, r_A. The corresponding expressions for the levels

of the upper points of the turn are obtained from the condition $U(r) - V = 0$.

$$r_u = r_B + (r_k - r_B)\left(\frac{U_B - V}{U_B - U_k}\right)^{\frac{1}{2}}$$

$$r_u = r_A - (r_A - r_k)\left(\frac{V - U_A}{U_k - U_A}\right)^{\frac{1}{2}}$$

The combined quadratic model $U(r)$ is equivalent to the combined quasi-parabolic model $f_N^2(r)$.

In fact, we have from the equality

$$U(r) = r^2\left[1 - \frac{f_N^2(r)}{f^2}\right] = U_A + (U_k - U_A)\frac{(r_A - r)^2}{(r_A - r_k)^2} \quad (\text{for } r > r_k)$$

that

$$f_N^2(r) = f^2\left\{1 - \left[\frac{U_A}{r^2} + \frac{(U_k - U_A)}{r^2}\,\frac{(r_A - r)^2}{(r_A - r_k)^2}\right]\right\}$$

In this case, the level $r_A(f)$ is the upper limit of the altitude region $f_N^2(r)$ for a given f.

The characteristics of the rays reflected below r_k (low-sloping rays) are determined from only the first model of $U(r)$ by integrating from r_B to r_u.

The characteristics of the rays reflected above r_k (steep rays) are determined from both models of $U(r)$ by presenting the integral as the sum of two integrals in the corresponding altitude regions, i.e., r_B, r_k and r_k, r_u.

Presented below are the analytical dependencies obtained for some integral characteristics.

The expressions for the characteristics of the low-sloping rays ($V > U_k$, $r_u < r_k$) are of the form

$$\Theta = \sqrt{\frac{\beta_B}{\alpha_1 + \beta_B - 1}}\ \arccos\sqrt{\frac{1 - \beta_B}{\alpha_1}} \tag{20}$$

$$\alpha_1 = \frac{1 - U_k/U_B}{\left(\frac{r_k}{r_B} - 1\right)^2}; \qquad \beta_B = \frac{V}{U_B} - \sin^2\phi_B$$

$$L_g = \frac{\pi}{2}\frac{r_B(r_k - r_B)}{\sqrt{U_B - U_k}} + \frac{(r_k - r_B)^2\sqrt{U_B - V}}{(U_B - U_k)} \tag{21}$$

$$L_p = \frac{1}{\sqrt{V}}\left[U_B - \frac{(U_B - U_k)r_B^2}{(r_k - r_B)^2}\right]\Theta + \pi\frac{r_B\sqrt{U_B - U_k}}{(r_k - r_B)} - \frac{(U_B - U_k)}{(r_k - r_B)^2}L_g \tag{22}$$

$$\frac{c\Gamma}{\nu} = \left[1 + \frac{(U_B - U_k)}{(r_k - r_B)^2}\right]L_g - \frac{1}{\sqrt{V}}\left[U_B - \frac{(U_B - U_k)r_B^2}{(r_k - r_B)^2}\right]\Theta - \pi\frac{r_B\sqrt{U_B - U_k}}{(r_k - r_B)} \tag{23}$$

$$T_0 = \frac{\pi}{4} \frac{(r_k - r_B)}{\sqrt{U_B - U_k}} \sqrt{U_B - V} \tag{24}$$

Equations (22) and (23) show the determined link between the integral characteristics. They are the relatively invariant initial conditions of emission, V.

The expressions for the characteristics of the steep rays ($V < U_k$, $r_u > r_k$) are of the form

$$\theta = \frac{\sqrt{\beta}}{\sqrt{\frac{r_A^2}{r_k^2}\alpha - (\beta - \frac{U_A}{U_k})}} \ln \left[\sqrt{\frac{r_A^2}{r_k^2} \frac{(1-\beta)}{(\beta - \frac{U_A}{U_k})} - \frac{1-\beta}{\alpha}} + \frac{r_A \sqrt{1 - \frac{U_A}{U_k}}}{r_k \sqrt{\beta - \frac{U_A}{U_k}}} \right.$$

$$\left. - \frac{\sqrt{\beta - \frac{U_A}{U_k}}}{\sqrt{\alpha}} \right] + \frac{\sqrt{\beta_B}}{\sqrt{\alpha_1 + \beta_B - 1}} \arcsin \left[\frac{\sqrt{(1-\beta_B)}}{\sqrt{\alpha_1}} \frac{r_k}{r_B} + \frac{\sqrt{\alpha_1}\ (\frac{r_k}{r_B} - 1)}{\sqrt{1-\beta_B}\ \frac{r_k}{r_B}} \right]$$

$$- \frac{\sqrt{\beta_B}}{\sqrt{\alpha_1 + \beta_B - 1}} \arcsin \frac{\sqrt{1-\beta_B}}{\sqrt{\alpha_1}} ; \tag{25}$$

$$\alpha = (1 - \frac{U_A}{U_k}) \Big/ (\frac{r_A}{r_k} - 1)^2 \qquad \beta = \frac{V}{U_k} = \sin^2 \phi_k$$

$$L_g \equiv \frac{(r_k - r_B)^2 \ [\sqrt{U_B - V} - \sqrt{U_k - V}]}{(U_B - U_k)} - \frac{\sqrt{U_k - V}\ (r_A - r_k)^2}{(U_k - U_A)}$$

$$+ \frac{r_B (r_k - r_B)}{\sqrt{U_B - U_k}} \arcsin \frac{\sqrt{U_B - U_k}}{\sqrt{U_B - V}} - \frac{r_A (r_A - r_k)}{\sqrt{U_k - U_A}} \ln \left[\frac{\sqrt{V - U_A}}{\sqrt{U_k - U_A} - \sqrt{U_k - V}} \right] \tag{26}$$

$$L_p = \frac{[U_B - \frac{(U_B - U_k) r_B^2}{(r_k - r_B)^2}]}{\sqrt{\frac{(U_B - U_k) r_B^2}{(r_k - r_B)^2} - (U_B - V)}} \left\{ \arcsin \frac{(U_B - V)(r_k - r_B) + (U_B - U_k) r_B}{r_k \sqrt{U_B - U_k}\ \sqrt{U_B - V}} \right.$$

$$\left. - \arcsin \frac{\sqrt{U_B - V}(r_k - r_B)}{r_B \sqrt{U_B - U_k}} \right\} + \frac{r_B \sqrt{U_B - U_k}}{(r_k - r_B)} \arcsin \frac{\sqrt{U_B - U_k}}{\sqrt{U_B - V}} +$$

$$+\frac{\left[U_A+\frac{(U_k-U_A)r_A^2}{(r_A-r_k)^2}\right]}{\sqrt{\frac{(U_k-U_A)r_A^2}{(r_A-r_k)^2}-(V-U_A)}}\ln\frac{\sqrt{\frac{(U_k-U_A)r_A^2}{(r_A-r_k)^2}-(V-U_A)}\sqrt{U_k-V}+\frac{(U_k-U_A)r_A}{(r_A-r_k)}-(V-U_A)}{\frac{r_k\left[\frac{(U_k-U_A)r_A^2}{(r_A-r_k)^2}-(V-U_A)\right]}{\left[r_A-\frac{(r_A-r_k)\sqrt{V-U_A}}{\sqrt{U_k-U_A}}\right]}-\frac{r_k r_A(U_k-U_A)}{(r_A-r_k)^2}}$$

$$+\frac{r_A\sqrt{U_k-U_A}}{(r_A-r_k)}\ln\frac{\sqrt{U_k-U_A}-\sqrt{U_k-V}}{\sqrt{V-U_A}}-\sqrt{U_B-V} \qquad (27)$$

$$T=\frac{(r_k-r_B)}{\sqrt{U_B-U_k}}\frac{1}{2}\left[\sqrt{U_B-U_k}\sqrt{U_k-U_A}+(U_B-U_A)\arcsin\frac{\sqrt{U_B-U_k}}{\sqrt{U_B-U_A}}\right]$$

$$+\frac{1}{2}(r_A-r_k)\sqrt{U_k-U_A} \qquad (28)$$

$$T_0=\frac{(r_k-r_B)}{\sqrt{U_B-U_k}}\frac{1}{2}\left[\sqrt{U_B-U_k}\sqrt{U_k-V}+(U_B-V)\arcsin\frac{\sqrt{U_B-U_k}}{\sqrt{U_B-U_A}}\right]$$

$$+\frac{1}{2}\frac{(r_A-r_k)}{\sqrt{U_k-U_A}}\left\{(V-U_A)\ln\sqrt{V-U_A}+\sqrt{U_k-U_A}\sqrt{U_k-V}-(V-U_A)\ln\left(\sqrt{U_k-U_A}+\sqrt{U_k-V}\right)\right\} \qquad (29)$$

The above expressions for $\Theta(\phi_0)$ and the $U(r)$ are used to obtain the analytical dependence of the electric field in the waveguides.

The longitudinal focusing of the ray's energy in the propagation plane can be expressed in the general form by the factor (Rawer, 1952)

$$\sin\phi_0/[\cos\phi(r)\cdot d\Theta(\phi_0)/d\phi_0]. \qquad (30)$$

Considering $U(r)\sin^2\phi = U(r_0)\sin^2\phi_0$, we get

$$\frac{\sin\phi_0}{\cos\phi(r)}=\frac{1}{\sqrt{\csc^2\phi_0-\frac{U(r_0)}{U(r)}}} \qquad (31)$$

where $U(r)$ for any level r can be found using the quadratic model for a given altitude region:

$U(r) = r^2$ at levels below 100 km, where $n \simeq 1$
$U(r) = a^2$ at the Earth's surface (a is the radius)
$U(r) = U(r_0)$ at $r = r_0$. In this case

$$\sin \phi_0 / \cos \phi(r) = t_g \phi_0 \tag{32}$$

The analytical dependence for $\sin \phi_0 / \cos \phi(r)$ may be obtained by combining the $U(r)$ models for various regions corresponding to the altitudes of the emitter and receiver.

Differentiating the expressions for $\Theta(\phi_0)$ over ϕ_0, we get for the low-sloping rays:

$$\frac{d\Theta(\phi_0)}{d\phi_0} = \frac{\sin^2 \phi_0}{(\alpha_1 - \cos^2 \phi_0)} - \frac{(1 - \alpha_1) \cos \phi_0}{(\alpha_1 - \cos^2 \phi_0)^{3/2}} \arccos \left[\frac{\cos \phi_0}{\sqrt{\alpha_1}}\right] \tag{33}$$

The low-sloping rays are most important since, as ϕ_0 becomes lower, the probability of the ray retention in a channel decreases over a considerable length of the channel:

$$E(r,\Theta) = \frac{173\sqrt{P(\phi_0)}}{\sqrt{\sin \Theta}\, r \sqrt[4]{\operatorname{cosec}^2 \phi_0 - \frac{U(r_0)}{U(r)}}\, \sqrt{d\Theta(\phi_0)/d\phi_0}} \tag{34}$$

where P is the radiated power; E is the field intensity.

The factor $1/\sqrt{\sin \Theta}$ includes the ray beam divergence at $0 < \Theta < \pi/2$ and the subsequent convergence (focusing) up to the antipode at $(\pi/2) < \Theta < \pi$ in the direction of the propagation plane due to the sphericity of the medium.

By representing $U(r_0)$, $U(r)$, and $d\Theta(\phi_0)/d\phi_0$ corresponding to the various altitudes of emitter and receiver and the ranges of ejection angles, ϕ_0, we obtain a series of analytical expressions for $E(r,\Theta)$.

It follows from the EPM dependencies obtained that the max N_r' and the valley parameters are of great importance when forming the qualitative pattern of radio wave propagation and can significantly affect the majority of the channel characteristics.

For example, the limiting maximum frequencies of waveguides f_{max} are direct functions of the max N_r' parameters.

Figures 1 and 2 present the diurnal variations in f_{max} and f_{max}/foF2 calculated for medium-latitude models for winter, low solar activity W(a); summer, low and temperate W(b,c). The f_{max}/foF2 ratio varies between 5 and 10, i.e., 2 to 4 times MUF/foF2. The highest values are reached at night. The amplitude of the diurnal variation in summer is much larger than in winter. The absolute values of f_{max} vary within 20-60 MHz and increase with W.

The EPM formulas have been used to calculate the intervals of the ray oscillations, $\Theta(\phi_0)$. In the general case, $\Theta(\phi_0)$ is a nonmonotonic function with a high peak corresponding to the limiting steepest ray, an intermediate minimum for the ray reflected near r_g, and a weak second peak for the lowest-sloping gliding ray.

The rays reflected near the r_g level correspond with the maximum of the group part and with its decrease towards steeper and lower-sloping rays.

The max N_r' parameters also affect significantly the field distribution in a channel. As the angle, ϕ_0, increases when the ray approaches the channel axis, the focusing increases monotonically, whereas the absolute value of the field for a fixed ϕ_0 (depending on the parameters of the medium) increases

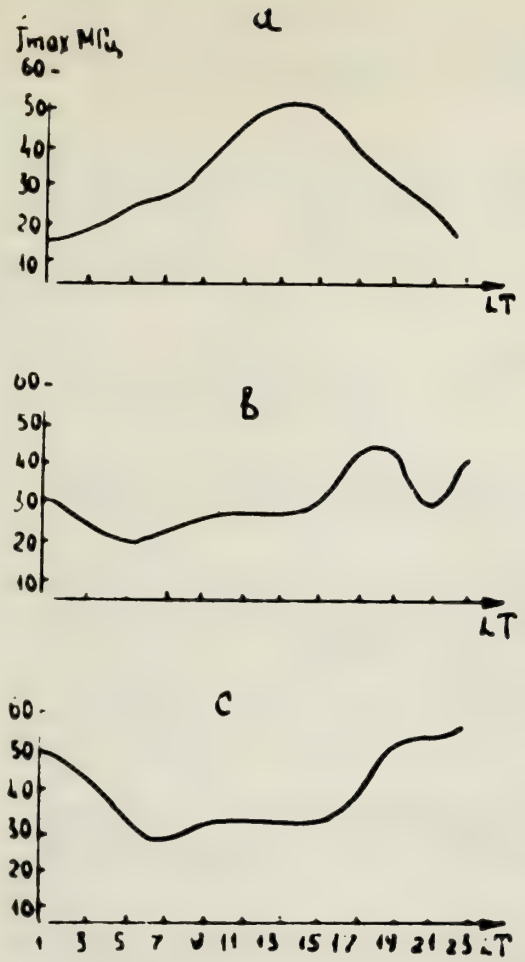


Figure 1. Diurnal variations in f_{max}.

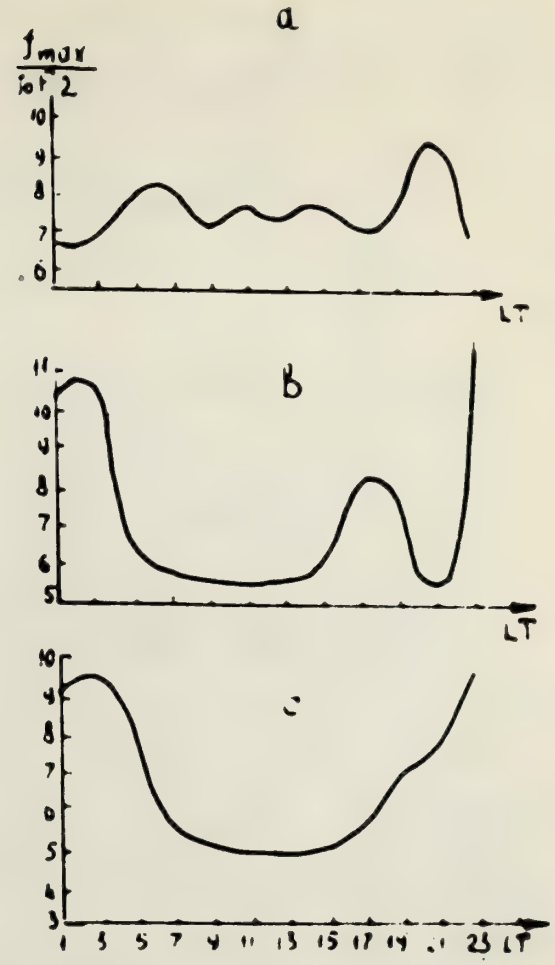


Figure 2. Diurnal variations in $f_{max}/foF2$.

with increasing $\alpha_1 \to 1$. For the extremely low-sloping rays reflected near r_g, $\sin \phi_0$ is significantly smaller than on the channel axis, although $d\Theta/d\phi_0$ exhibits a minimum. Therefore, the focusing is not as great.

At the upper boundary of the channel r_A, the field reaches its zero value since $d\Theta(\phi_0)/d\phi_0 = \infty$ for the extremely steep ray. The field maximum is located near the channel axis and corresponds to a gliding angle with $\phi_0 = \pi/2$ and $d\Theta/d\phi_0$ is small. The valley parameters affect directly the channel axis position, r_B, and U_B and all the characteristics depending on r_B and U_B.

Thus, the mathematical formulation of EPM consists of a set of expressions which, in combination, give the analytical dependencies of the various channel characteristics on the key parameters dN/dr. In other words, the available global predictions of critical frequencies, the geometric parameters of ionospheric levels, and the data for the parameters of the dN/dr maximum and the interlayer F/E valley may be used to determine EPM.

REFERENCES

Gurevich, A. V. (1971): Effect of nonlinearity on generation of round-the-world signals, Geomagn. i Aeron., 11:961-969.

Krasnushkin, P. E. (1947): Method of normal waves as applied to the problem of long-distance radio communication, Moscow State University, Moscow.

Rawer, K. (1952): Calculation of sky-wave field strength. Wireless Engineer, 29:287-300.

Shlionsky, A. G. (1965a): Some remarks concerning the ray methods of calculating the radio communication on short waves, Geomagn. i Aeron., 5:1052-1060.

Shlionsky, A. G. (1965b): Damping of satellite emissions for near-ground trajectories, Geomagn. i Aeron., 5:1061-1067.

Shlionsky, A. G. (1970): Dependence of the position of the rn(r)-function maximum on the altitude profile of ionization in "valley" and on the operating frequency, Geomagn. i Aeron., 10:147-148.

Shlionsky, A. G. (1971): About reflecting MUF of radio wave at over-Earth ionosphere wave propagation. Preprint No. 12, Moscow, IZMIRAN.

Shlionsky, A. G. (1974a): Some trajectory characteristics of radio wave ducting in the ionosphere. Collection IZMIRAN, The Questions of Short Radio Wave Propagation, part 2, 77-87.

Shlionsky, A. G. (1974b): The variations rn(r)-function maximum of the ionosphere. Collection IZMIRAN, The Questions of Short Radio Wave Propagation, part 2, 88-94.

Shlionsky, A. G. (1974c): The refractive characteristics of the seizure and going out from the ionospheric waveguide. Collection IZMIRAN, The Questions of Short Radio Wave Propagation, part 2, 95-100.

Shlionsky, A. G. (1977): The frequency dependence of the radio wave absorption in ionospheric channels. Collection, The Methods of the Research of Regularities in Radio Wave Propagation, Moscow, Nauka, 45-49.

Shlionsky, A. G. (1968): Determination of the extremum levels of the rn(r)-function and MUF under various ionospheric conditions, Geomagn. i Aeron., 8:367-368.

E. SATELLITE AND ELECTRIC POWER APPLICATIONS

ANOMALOUS SATELLITE DRAG AND THE GREEN-LINE CORONA

Richard C. Altrock
Air Force Geophysics Laboratory
Sacramento Peak Observatory*
Sunspot, New Mexico 88349

Satellite drag data for Skylab from Headquarters Aerospace Defense Command are compared with solar λ5303Å Fe XIV coronal scans from Sacramento Peak Observatory. During a short period in late 1977 and early 1978 there appears to be a distinct anti-correlation of anomalous drag with coronal intensity inferred at the center of the solar disk approximately two days earlier. The relation appeared at a time of a stable intensity pattern near the solar equator and evidently disappeared as the stable intensity pattern disappeared.

INTRODUCTION

It has been well established that coronal holes as observed in X-rays are the source of high-speed solar-wind streams. A number of studies have shown that streams emanating from holes near the sub-earth point impact on the geomagnetic field and cause disturbances in it (cf. Neupert and Pizzo, 1974). More recently, studies have shown that coronal holes may be identified in observations of λ5303Å of Fe XIV with sufficient precision to allow use of these data to predict recurrent geomagnetic disturbances during times of low solar activity (cf. Musman and Altrock, 1978). However, at best this technique results in a success ratio of approximately 80%. There are, therefore, times when an apparent low coronal emission at the sub-earth point does not result in a geomagnetic disturbance. This apparent lack of 100% correlation between regions of low emission in the green-line corona and high-speed streams has been confirmed by Kaufman (1978). This paper explores further the properties of these low-emission regions in their effect on another geophysical parameter.

* Operated by the Association of Universities for Research in Astronomy, Inc., under contract with the National Science Foundation

Recent Studies of satellite drag produced by density fluctuations in the atmosphere have resulted in inference of an anomalous drag that is uncorrelated with, among other parameters, geomagnetic disturbances (Lane and Hoots, 1978). Following a request from Headquarters Aerospace Defense Command, a preliminary comparison of these data with green-line data showed a favorable correlation with regions of low emissivity, and I have now found a subset of the observations that implies a direct connection between stable regions of low green-line emissivity and increases in satellite drag.

THE DATA

The observation and reduction of the green-line data are described in Musman and Altrock (1978). The data are basically coronal intensities at a given height above the limb obtained daily. I have utilized an equatorial average of the intensity in the latitude band $+15^{\circ}$ to -15°.

The satellite drag data are presented in the form of the total drag coefficient, B, having units of m^2/kg. The total drag is defined to be ρB, where ρ is density taken from the Jacchia 1964 model, which includes empirical corrections for geomagnetic index, a_p, and solar radio flux at 10.7 cm, $F_{10.7}$. Data are presented for Skylab (other data are being processed). The value of B is determined by comparison of the modelled motion with radar observations. Thus, variations in B represent unmodelled, or anomalous, variations in total drag.

The data are presented in Figure 1. The data set of B corresponding to unstabilized motion of Skylab ran from approximately DOY 340, 1977, to DOY 160, 1978. Data gaps of one day in $\bar{I}$ have been linearly interpolated over. $\bar{I}$ has been plotted increasing downwards.

RESULTS

Referring to Figure 1, we see that a stable coronal intensity pattern with a period of 27 days existed near the solar equator near the end of 1977. The intensity data became rather sketchy near the beginning of 1978, but at least four maxima can be inferred in this pattern (DOY 314, 341, 5, and 31). A fifth possible maximum near DOY 60 cannot be confirmed. After that, the intensity pattern can only be described as chaotic, with considerable difference between disk-center intensities inferred from east and west limbs and no clear recurrent features.

The satellite-drag data show many similarities to the shifted intensity values in the first half of the observation period. With an empirical value for the shift (or transit time from the center of the disk) of

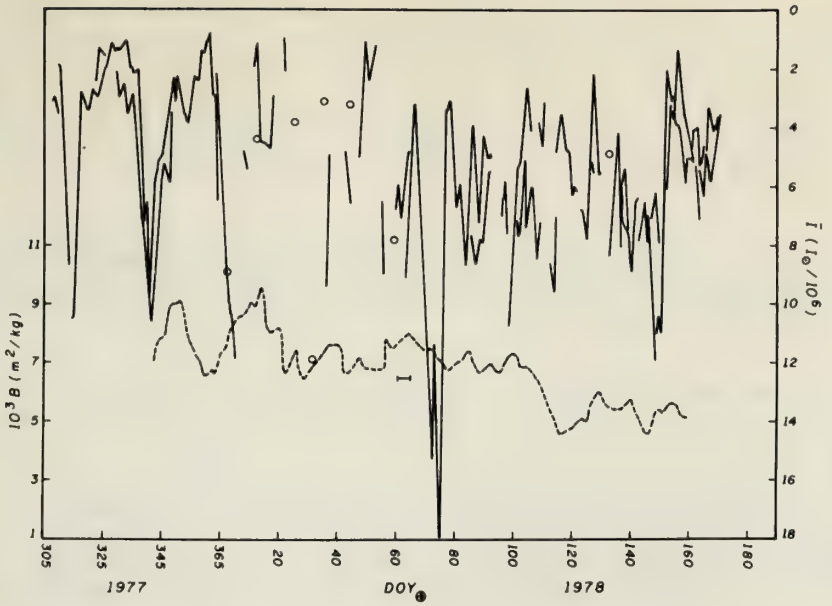


Figure 1: Total satellite drag coefficient for Skylab, B, (solid line) and average coronal λ5303Å intensity, $\bar{I}$, (dashed lines) as a function of day of the year at the earth, DOY⊕. Uncertainty bar near B represents the integration time of each point. The 30° latitude average of equatorial green-line intensity is plotted at the day of limb passage (LP) + 8.75 days for east-limb data and at LP-4.75 for west-limb data, or at CMP + 2 for either limb. No distinction is made on the graph between east and west limb data. Circles represent isolated data points of $\bar{I}$.

approximately two days, the maxima in $\bar{I}$ correspond well to the minima in B (DOY ∿ 342, 354-359, and 29). Other data, unavailable for publication at this time, show a similar pattern. The maxima in B at DOY ∿ 346 and 13 (and 37-40?) have associated minima in $\bar{I}$. As time progresses, the stationary pattern in the corona becomes chaotic, and no clear periodic signal is seen in the B curve. Another interesting feature in B is the decline in the average level, beginning about DOY 60 and bottoming out near DOY 117. This does not appear to be correlated with any particular event in the equatorial corona, although it does correspond, more or less, to the onset of the chaotic coronal intensity pattern.

The choice of a transit time (shift) of two days from CMP is arbitrary and uncertain. Digital data was unavailable at the time of writing, so a cross correlation was not performed. A transit time of zero (or 27 days) actually appears to fit this extremely limited data set better. Alternatively, a transit time of eleven days would align the maxima of $\bar{I}$ with the maxima of B. This transit time seems unlikely due to the low propragation velocity required (∿ 160 km s^{-1}) and the low probability that such a slow stream could maintain its coherence over that length of time. One might expect that such a stream would be disrupted by overtaking high-speed streams. However, one cannot completely discount the possibility that the periodic variation in B is due to low-speed streams emanating from regions bright in the green-line. Because a mechanism for this has not been identified, I prefer to conclude that the source of the increases in B lies in faint green-line regions; i.e., a (weak?) high-speed stream.

CONCLUSIONS

1. A clear 27-day period has been identified in a portion of total drag data for Skylab, after correction for geomagnetic disturbances and solar radio flux.

2. A good correlation of the periodic maxima in this anomalous drag has been found with a stable periodic low-intensity region in the equatorial corona as observed in λ5303Å Fe XIV.

3. The onset of unstable, rapidly-evolving conditions in the equatorial corona appears to coincide with the disappearance of periodic variations in corrected drag.

4. From these limited data, it appears that stable regions of low coronal intensity observed near the equator on the east limb may be used to predict anomalous increases in satellite drag up to nine days in advance.

ACKNOWLEDGEMENTS

I wish to thank Max Lane and Felix Hoots of the Office of Astrodynamic Applications, Headquarters Aerospace Defense Command, for supplying me with the satellite drag data and encouraging me to analyze it.

REFERENCES

Kaufman, J. J. (1978): The latitudinal structure of solar wind streams from radio scintillation observations, report No. 1, AFGL-TR-78-0169, Air Force Geophysics Laboratory.

Lane, M., and F. Hoots (1978): private communication.

Musman, S., and R. Altrock (1978): Recurrent geomagnetic disturbances and coronal holes as observed in Fe XIV λ5303Å, J. Geophys. Res., in press.

Neupert, W. M., and V. Pizzo (1974): Solar coronal holes as sources of recurrent geomagnetic disturbances, J. Geophys. Res. 79:3701.

EFFECTS OF MAGNETOSPHERIC DISTURBANCES ON THE GEOELECTRIC FIELD IN AURORAL AND SUB-AURORAL REGIONS, AND INTERACTIONS WITH HV-DC/AC ELECTRIC POWER LINES: *Large-scale man-made effects on the global aeronomic environment.*

Wolfgang-M. Boerner[1,2], James B. Cole[1], William R. Goddard[2]
(1)Communications Laboratory,SEL-1104, UICC, P.O.Box 4348, Chicago,IL 60680;
(2)AEM Laboratory, New Eng.Bldg., Univ. of Manitoba, Winnipeg, Canada R3T 2N2.

A basic study is proposed to advance research on how and to what extent geo-magnetic disturbances affect the geo-electric field in auroral, sub-auroral, and central latitudinal regions, and to assess their interaction with the electric fields and VLF noise radiated from HV-AC/DC power lines and other man-made systems.

1. INTRODUCTION

Until fairly recently the studies of geoelectricity and geomagnetism were largely separate endeavors; and except for highly localized effects of limited magnitude, man-made systems were thought to have no effect on the macro-geo-electromagnetic environment. It is now becoming apparent that not only are geomagnetic and geoelectric fluctuations intimately linked, but that they can interact with radiations from man-made systems (K.Bullough et al,1976). Although the total energy in atmospheric electrical disturbances is small vis-a-vis other geophysical parameters (it amounts to about 0.1% of the total kinetic energy of the atmosphere - H.Volland,1979), evidence is accumulating that they affect the weather. Helliwell et al (1977) and Park et al (1978) have presented evidence that relatively weak radiations from electrical power systems can be amplified by various natural mechanisms, especially in geoelectromagnetically active regions, and manifest themselves in effects on the magnetosphere thousands of kilometers away from their origin. The existence of this effect has been established clearly, yet its relative importance in influencing the electron distribution in the radiation belts was questioned in (Thorne and Tsurutani,1979) and requires further investigation.

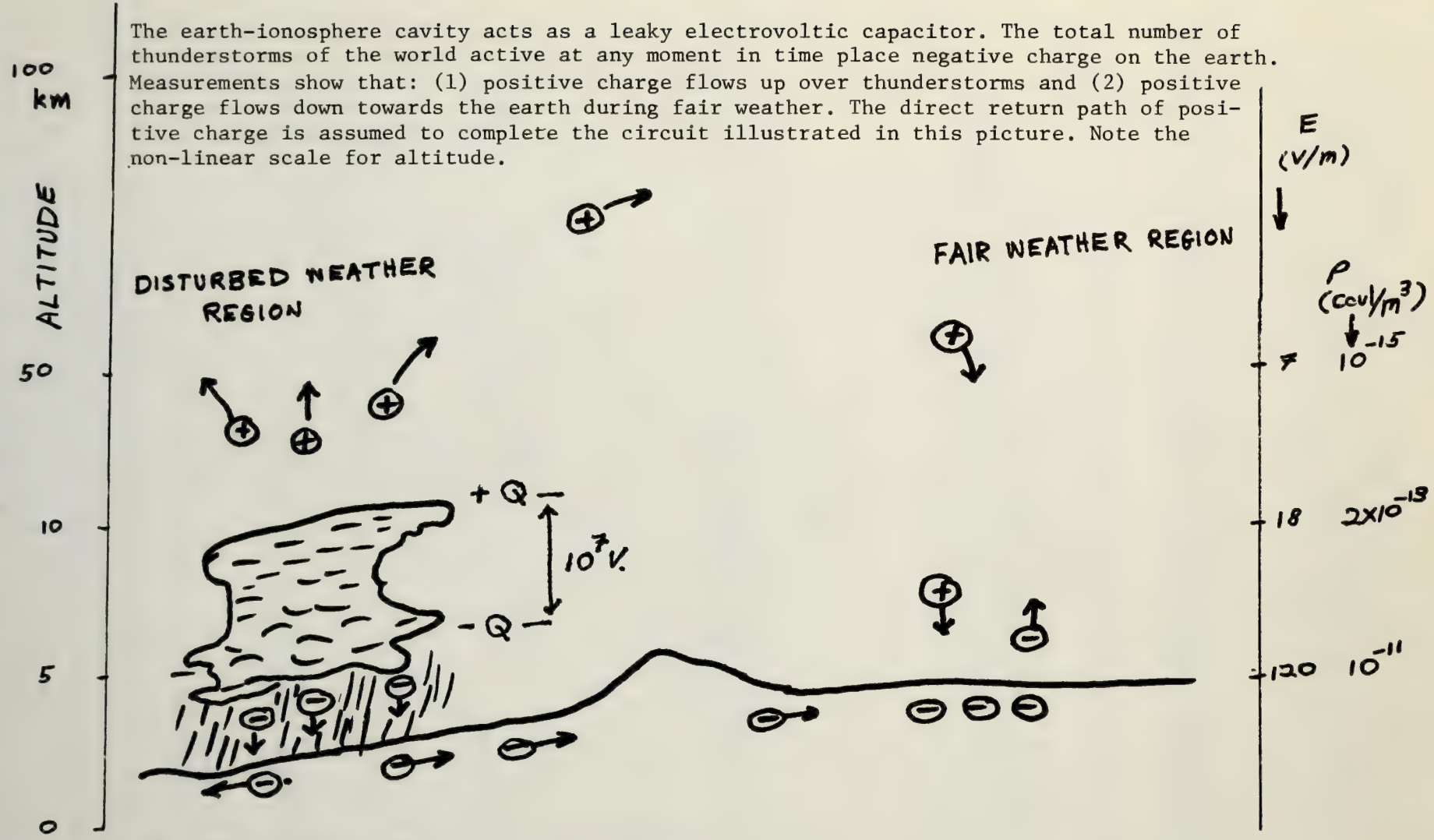
The existence of such effects and the possibility of others emphasizes the need to preface extension of man-made systems such as HV-DC/AC power and oil/gas pipelines into geoelectromagnetically active regions with careful investigation.

2. RELEVANT BASICS ON GEOELECTRICITY AND "LUFTELEKTRIZITÄT"

In the "classical" theory of geoelectricity, the terrestrial surface and →

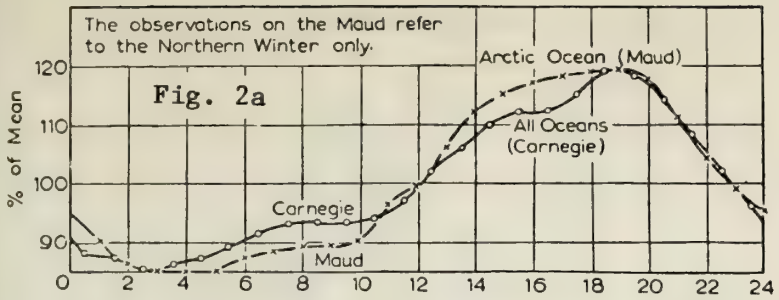
Since figures used have been chosen from references, they are not presented here but listed with title and proper reference at the end of this paper.

The earth-ionosphere cavity acts as a leaky electrovoltic capacitor. The total number of thunderstorms of the world active at any moment in time place negative charge on the earth. Measurements show that: (1) positive charge flows up over thunderstorms and (2) positive charge flows down towards the earth during fair weather. The direct return path of positive charge is assumed to complete the circuit illustrated in this picture. Note the non-linear scale for altitude.



(Eσ = I) is known as Ohm's law of the atmosphere: where σ = E/I
(σ) is the sum of the atmospheric polar conductivities, i.e., due to the positive and negative ions in the atmosphere
(ρ) = space charge density in the free atmosphere

Fig. 1 The classical or spherical capacitor model of the global electric circuit (Olson, 1978).



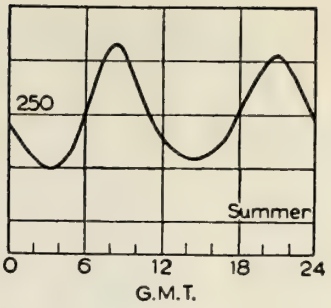
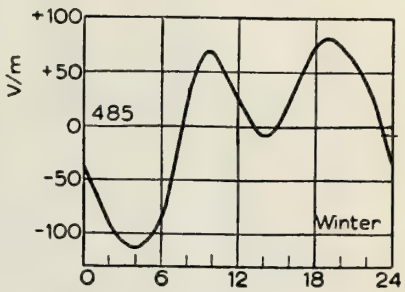


Fig. 2b



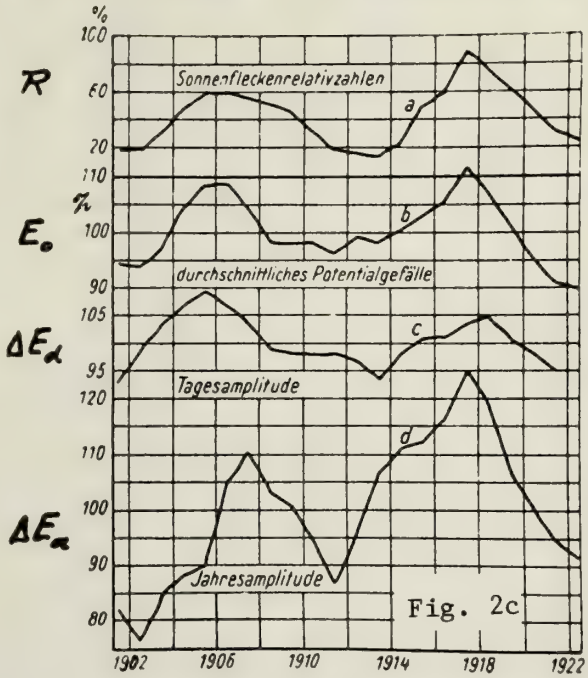


Fig. 2a Diurnal variation of potential gradient over oceans (Chalmers,1967, p. 164).

Fig. 2b Diurnal variation of potential gradient at Kew, winter and summer (Chalmers,1967, p. 162).

Fig. 2c Gegenüberstellung von Sonnenfleckenrelativzahlen und luftelektrischer Feldstärke an 5 Landstationen (Mühleisen,1969, p. 130).

the ionosphere are treated as ideal conductors between which there exists a potential difference of some 250 kV, the earth bearing negative charge. This potential gives rise to a vertical electric field at the earth's surface of approximately 130 V/m. The air is a leaky dielectric filling between the plates of this giant capacitor, passing a downward positive current estimated at between 600 and 1800 AMP (Chalmers,1967;Mühleisen,1971). Computing the total charge on earth from its measured surface electric field gives about 450,000 Coulombs (Fleming,1949). Clearly in the absence of some charging mechanism the earth-ionosphere capacitor would discharge within a few hours. According to the pioneering theory of C.T.R. Wilson (1909) thunderstorms are continuously at work - some 100 lightning flashes per second - pumping negative charge down to earth which leaks back to the ionosphere through fair-weather regions (Fig.1).

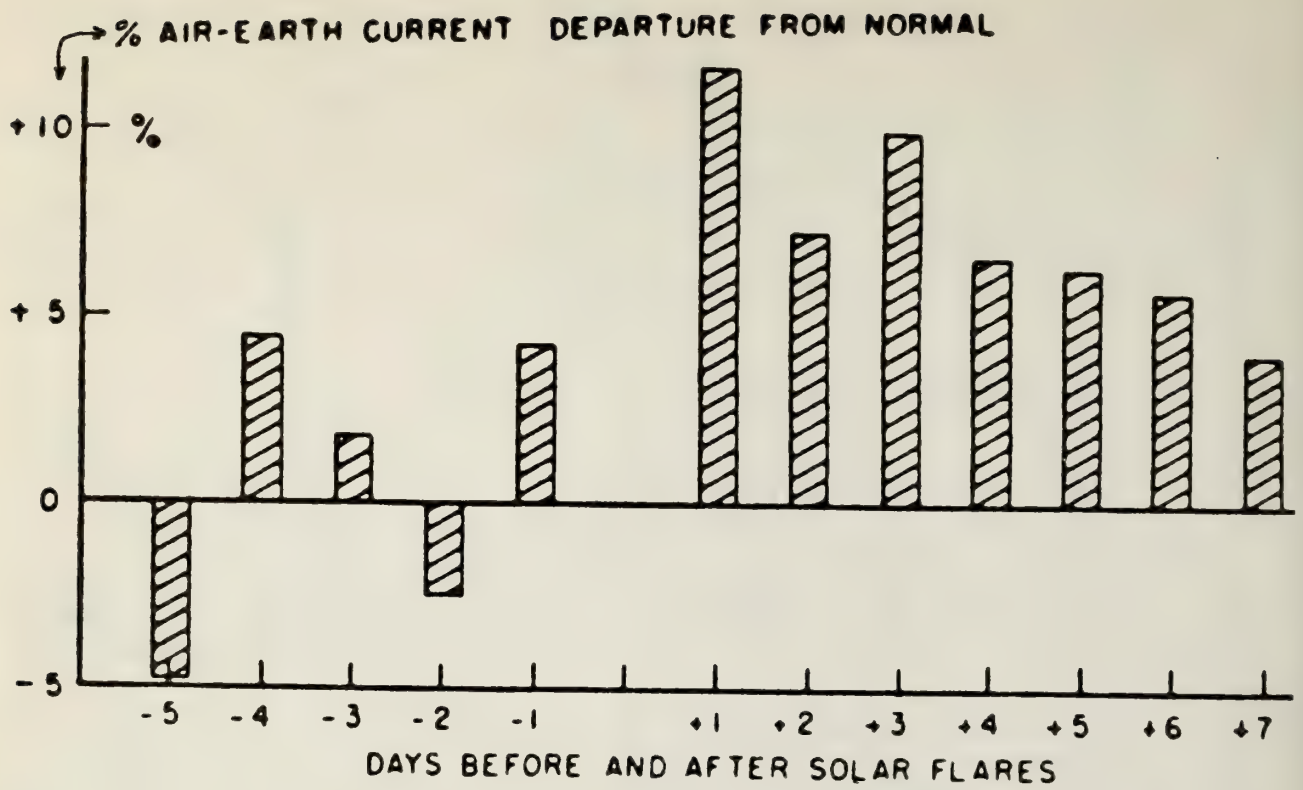


Fig. 3 Days before and after solar flares (Roble and Hays, p. 56).

This simple model however is not adequate to explain the dynamic nature of geoelectricity. The earth-ionosphere current and potential difference exhibit multi-cyclic behaviour with periods ranging from duirnal upwards through seasonal to eleven years, in apparent correlation with the sun-spot cycle (Fischer and Mühleisen,1972:Figs.2a,b,c); correlations are also observed with such events as solar flares (Reiter,1972:Fig.3) and the earth's passage across solar magnetic sector boundaries - where the sun's magnetic field changes from inwardly - to outwardly - directed (Reiter,1976;Herman and Goldberg,1978:Figs. 4,5). Thunderstorm activity has also been observed to correlate with solar magnetic boundary crossings (Lethbridge,1978). Localized variations in the atmospheric electric field and current density also occur which depend upon topography, meteorological conditions and local time. These can mostly be accounted for as arising from local variations in atmospheric conductivity in response to changes in ion production and dissipation rates (Israël,1969). On a shorter time scale and localized to auroral and near-auroral regions, dramatic geoelectric fluctuations including field polarity reversals are recorded in association with auroral activity (Olson,1971:Fig.6) and during geomagnetic storms (Lanzerotti,1977).

Observed correlations between solar events and fluctuations in atmospheric electrical parameters on the one hand and the theoretical link between atmospheric electricity and thunderstorms on the other might tempt one to postulate some relationship between solar events and terrestrial weatner. In fact hundreds of statistical correlations have been found between solar activity and weather - mainly rainfall and atmospheric vorticity (Herman and Gold-

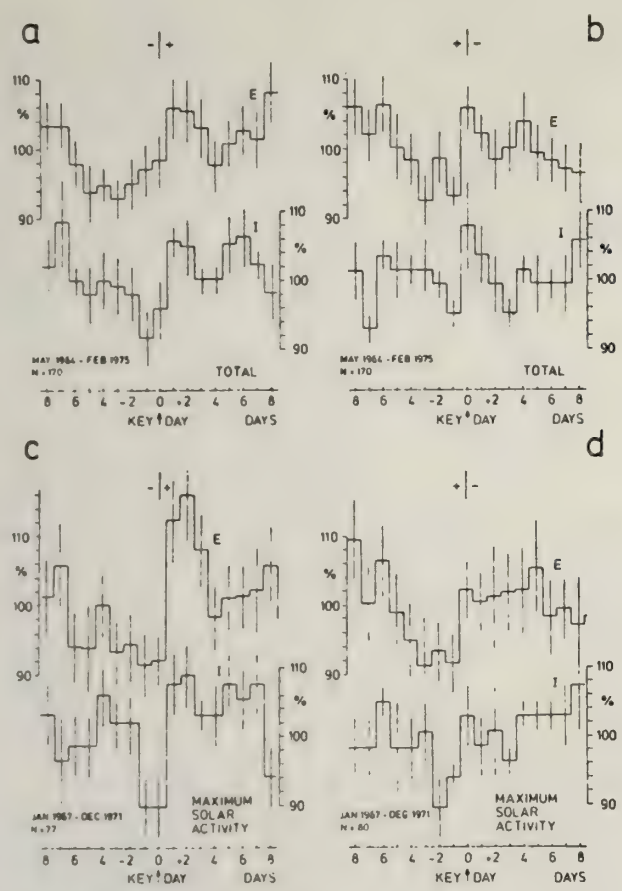
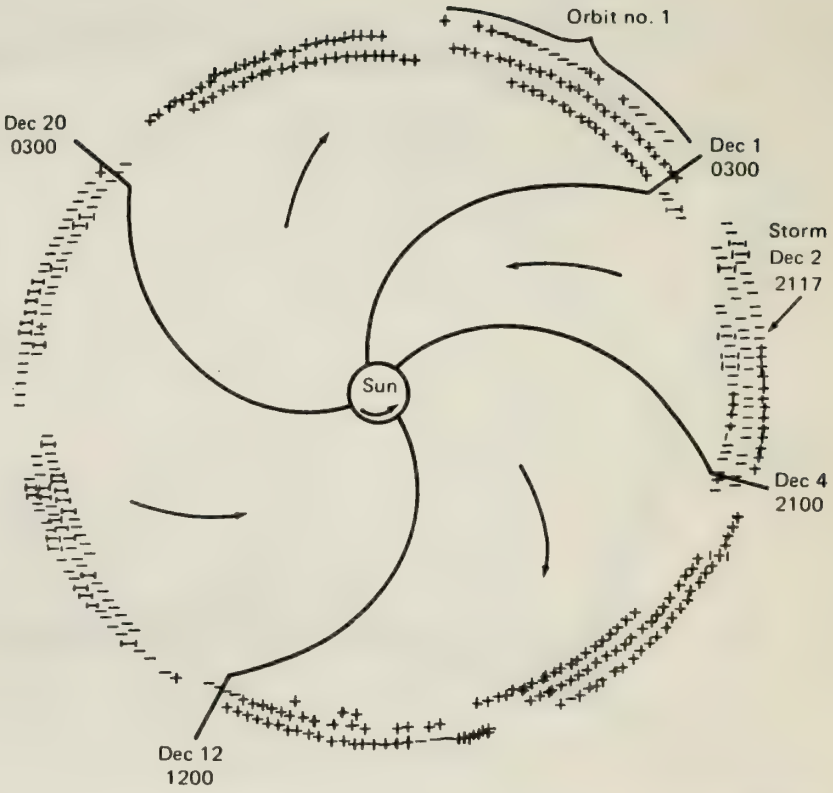


Fig. 4. Superposed epoch analysis of atmospheric electric field *E* and air-earth current density *I* (both recorded at Zugspitze peak observatory, 3 km a.s.l., above exchange layer on fine weather days), around days with passages of sector structure boundary of interplanetary magnetic field. −/+ : field direction changes toward/away from sun; +/− : vice versa. (a, b) Entire period from May 64 to Feb. 75, i.e., a complete solar cycle; 170 key days. (c, d) Period of maximum solar activity 1967–1971; 77/80 key days

Reiter, 1976, p. 192.



Solar magnetic sector structure as inferred from IMP 1 spacecraft observations (Wilcox and Ness, 1965). Plus signs (away from Sun) and minus signs (toward Sun) are 3-hourly measurements of interplanetary magnetic field direction, and arrows in the four sectors indicate predominant direction of the field.

Fig. 5; Herman and Goldberg, p. 77

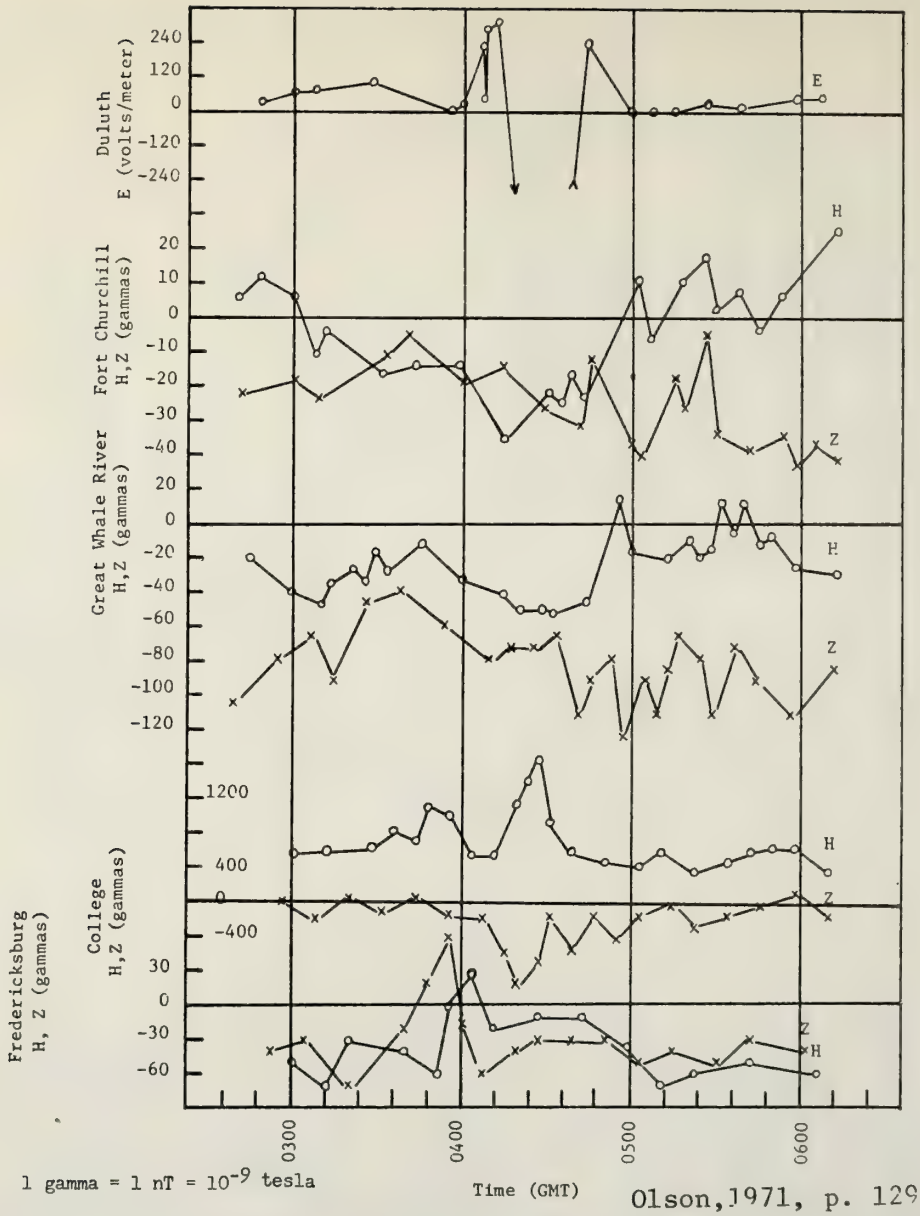


Fig. 6. Electric field and magnetometer measurements during an AEAE on 4 September 1966 GMT, Duluth, Fort Churchill, Great Whale River, and Fredericksburg (38.2°N, 77.4°W), College (69.9°N, 147.8°W).

berg,1978). However lacking an acceptable physical explanation such observations have been hitherto viewed with scepticism. The highly variable portion of the sun's spectrum accounts for only about 10^{-6} of its total luminosity which varies by no more than 1.0% over times measured in years (Livingston, 1978;Willis,1976). Thus the primary driving force for the earth's atmosphere, solar heating, is essentially constant. The total energy involved in atmospheric electrical disturbances is about 10^{-3} of its kinetic energy, while the average solar magnetic field in the neighborhood of earth is about 10^{-4} of its surface geomagnetic field (Dolezalek and Reiter,1974).

Recently a hypothesis to explain the apparent linkage between solar activity and terrestrial weather has been developed on the basis of a quantitative consideration of the ionosphere - earth - thunderstorm electric circuit in

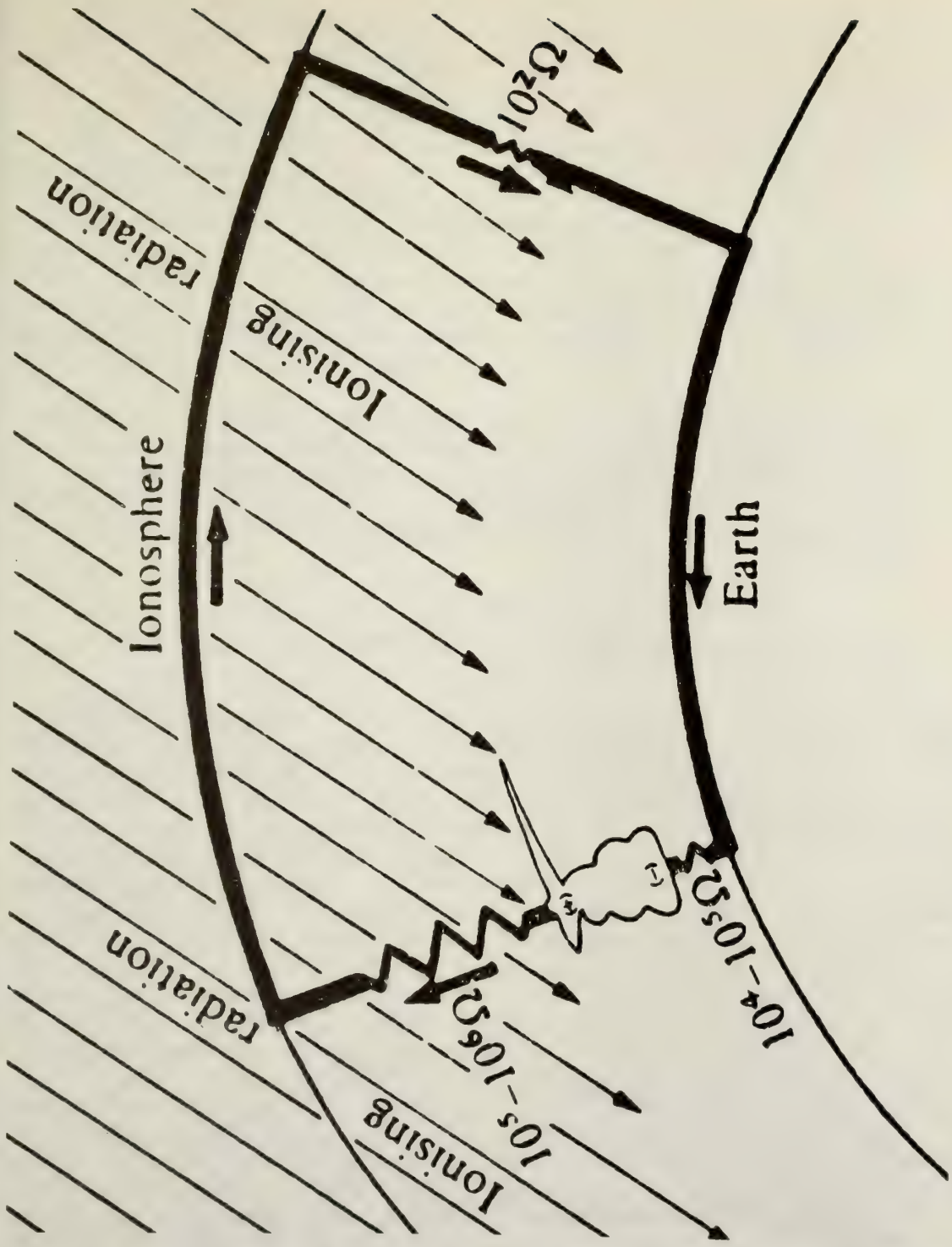


Fig. 7 The atmospheric global electrical circuit. Arrows indicate flow of positive charge; Markson, 1978, p. 104.

Wilson's model (Markson,1978:Fig.7). As shown in the figure some 90% of the circuit resistance is in the ionosphere to thundercloud-top portion, while thundercloud-bottom to ground accounts for 10%. Through fair-weather regions ionosphere-to-ground resistance is very small in comparison because of the relatively large cross-sections involved (analogous to many wires connected in parallel). The ionosphere-thundercloud resistance thus controls the current flow in the global atmospheric electrical circuit. According to the hypothe-

sis, it is this resistance which responds to solar activity and other events that alter the upper atmosphere conductivity between electric storm cloud-top and the ionosphere, affecting storm activity (Markson,1978). This also explains the observation that the correlation between solar activity and thunderstorm frequency generally increases with latitude, being greatest in auroral regions, where solar events more strongly perturb the atmosphere (Roble and Hays,1979). However these considerations alone cannot account for the magnitude (10-30%) of the changes in ionospheric potential observed in association with solar events. The observations can be explained by the existence in the mesosphere - between ionosphere and stratosphere - of a vertical electric potential about 100 kV in magnitude which can be "shorted" by radiation-induced ionization to add onto the lower atmosphere potential of about 300 kV. Experimental evidence supports the existence of such a field (Hale and Croskey, 1978).

This model cannot account for all the observed geoelectric fluctuations. A full understanding requires one to consider other voltage generating mechanisms in a circuit extending from ground up to the magnetopause (Hays and Roble,1979;Akasofu,1979:Fig.8). Neither the ionosphere nor the magnetosphere are actually isotropic homogeneous conductors. Electric potentials perpen-

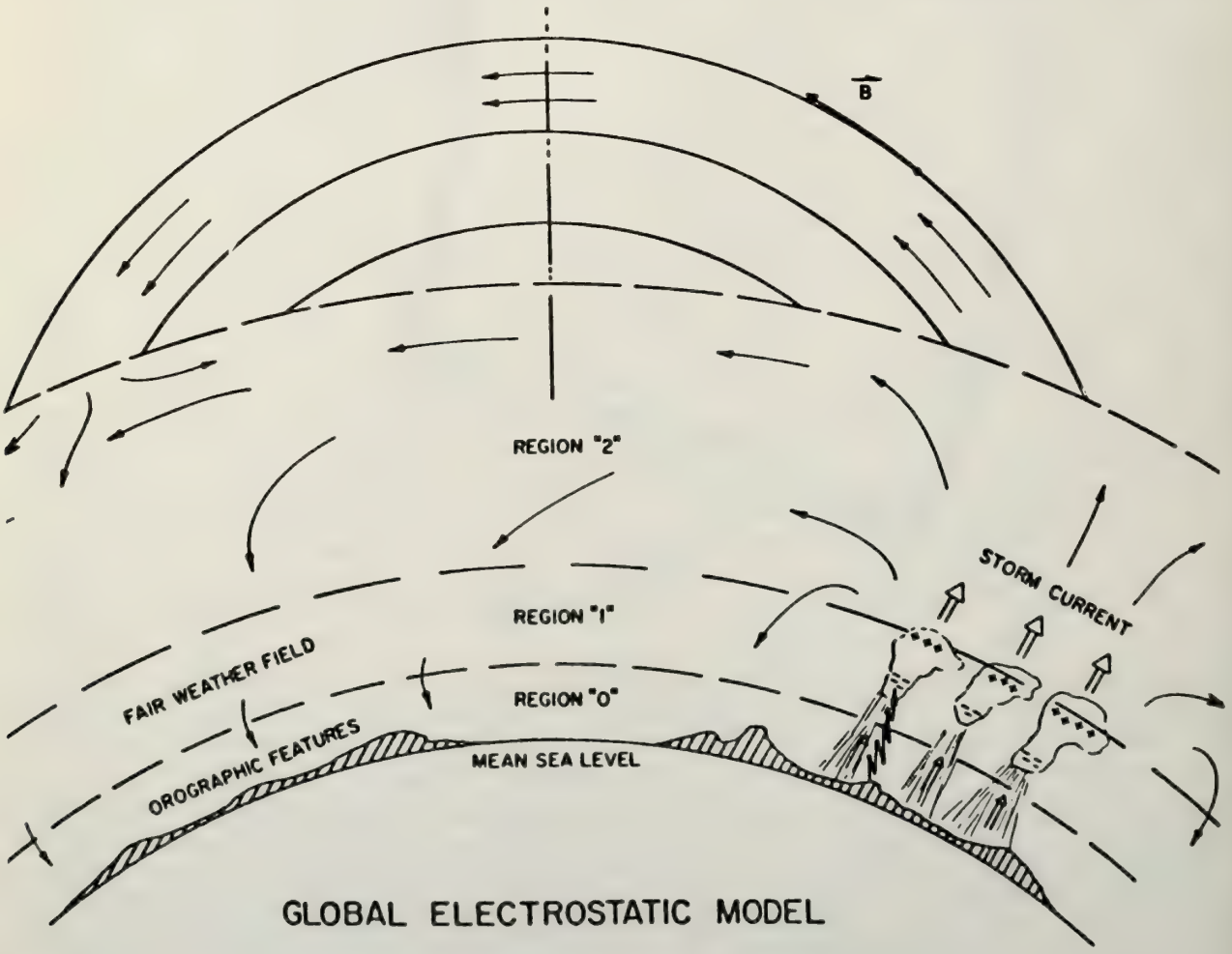


Fig. 8 Global electrostatic model (Roble and Hays,1979, p. 52).

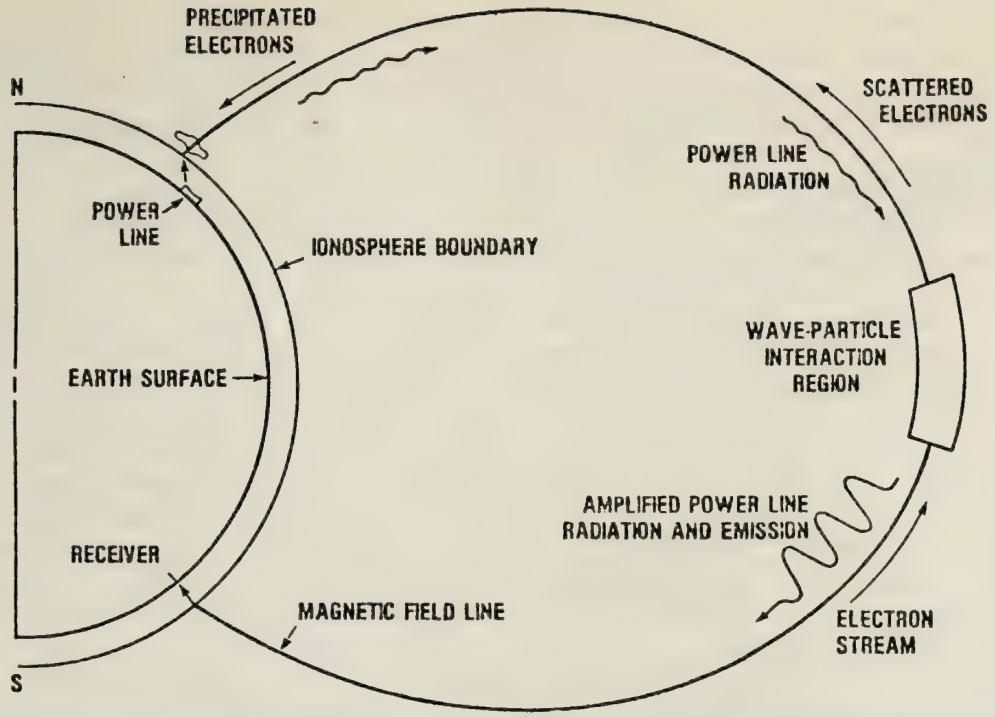


Fig. 9. VLF wave interactions with the magnetosphere (Park and Helliwell, 1978).

dicular to geomagnetic field lines are generated from motions of plasma inhomogeneities across the field lines (Goldberg and Herman,1979), and contrary to what one might suppose from the laws of motion obeyed by charged particles in magnetic fields, electric potentials exist along geomagnetic field lines as well (Kellogg and Weed,1969). The magnetospheric potential distribution can impress itself onto the ionosphere so that the latter is not an equipotential surface (Fälthamar,1969). It has been experimentally verified that ionospheric electric fields perpendicular to magnetic field lines can then map to low altitudes (Kelly and Mozer,1975). Further effects involve VLF spherics arising from both natural (e.g. lightning flashes) and man-made sources (powerlines harmonic radiation - see Sect. 5) which propagate along geomagnetic field lines and can produce electron precipitation fluxes 10^6 or more times the input wave power (Park and Helliwell,1978:Fig.9).

It increasingly appears that the mesosphere and stratosphere act as a buffer region between the troposphere and the upper atmosphere where small perturbations of local parameters in response to electromagnetic influences can be amplified into major effects on energy transport and conversion in the lower atmosphere. A quantitative description of the connection between geoelectromagnetic disturbances and terrestrial weather remains one of the major unresolved problems in contemporary geophysics.

3. GUIDELINES FOR EXPERIMENTAL WORK

In the evolving theories of sun-weather coupling the stratosphere and lower mesosphere act to amplify and transmit solar fluctuations down into the troposphere. The major impediment to the study of this mechanism is that the energy ration of extra-terrestrial corpuscular radiation (galactic and solar cosmic rays) to insolation is extremely small on the global scale. However

at high latitude, during local winter, this ration locally is significantly larger that the global mean, and sun-weather correlations are strongest in the poleward regions (Herman and Goldberg,1978).

There are several categories of energetic radiation which impinge on the upper atmosphere. Galactic cosmic rays, which are modulated by solar activity, are the dominant influences on atmospheric electrical properties between 5 and 30 km altitude. Solar proton events, though infrequent, can enhance ionization by several magnitude orders at the 30 km level. Relativistic electron precipitation is far more frequent and may possibly modulate stratospheric heating by inducing changes in ozone concentration. Finally in the auroral zone, frequent local electron precipitation events often produce significant *bremsstrahlung* X-rays. The conversion of electron energy to X-rays allows energy to penetrate to depths of atmosphere lower than the absorption height for the parent electrons (Goldberg,1978). In addition, electron precipitation can be affected by human electromagnetic activities, such as harmonics radiation arising from the transmission of electrical power (Sect. 5).

Thus experimental investigations into the "solar activity - atmospheric electricity - weather link" must concentrate on monitoring energy deposition in the atmosphere and concomitant effects on ozone concentration, conductivity and heating (Fig.10).

A complete description of global electrical response to solar and geomagnetic influences would require auroral zone measurements to be supplemented at lower latitudes as well. Because of the importance of mesospheric fields to the complete global electrical circuit, rocket as well as balloon measurements would be needed. The most efficient way to acquire the required data would be the use of low cost meteorological rockets such as are widely used for wind and temperature measurements equipped with electric field and charged particle sensors.

4. GEOELECTROMAGNETIC INFLUENCES ON MAN-MADE SYSTEMS

Electric and magnetic fields are not limited to the atmosphere, but penetrate into the solid earth as well. If one were to install two earthed electrodes separated by, say 200 m, and record the potential difference between them as a function of time, one would observe voltage fluctuations on the order of several millivolts ranging in period from a few seconds to several hours (Hessler,1976). Some of these "earth currents" are often called "geomagnetically induced currents", as they manifest themselves in conjunction with solar magnetic storms.

In the simplest picture of how solar activity affects the terrestrial fields, the solar wind carries charged particles to the earth which are deflected by its magnetic fields to form encircling sheet currents in the magnetosphere (Fig.11). Variations in the magnitudes of these currents in response to the fluctuating solar wind, and in their positions induce changing electric and magnetic fields (Levine,1966;Hermance,1978). Additionally, charged particles with sufficient energy can penetrate into the magnetosphere and become trapped in orbits about the geomagnetic field lines. Fields from these particles induce earth currents quite different in character (Figs. 12a,b) from those due to sheet currents (Fleming and Keller,1972). These particles are also affected by electromagnetic radiation from man-made systems. Such man-made effects will be discussed in the next section. The ionosphere,

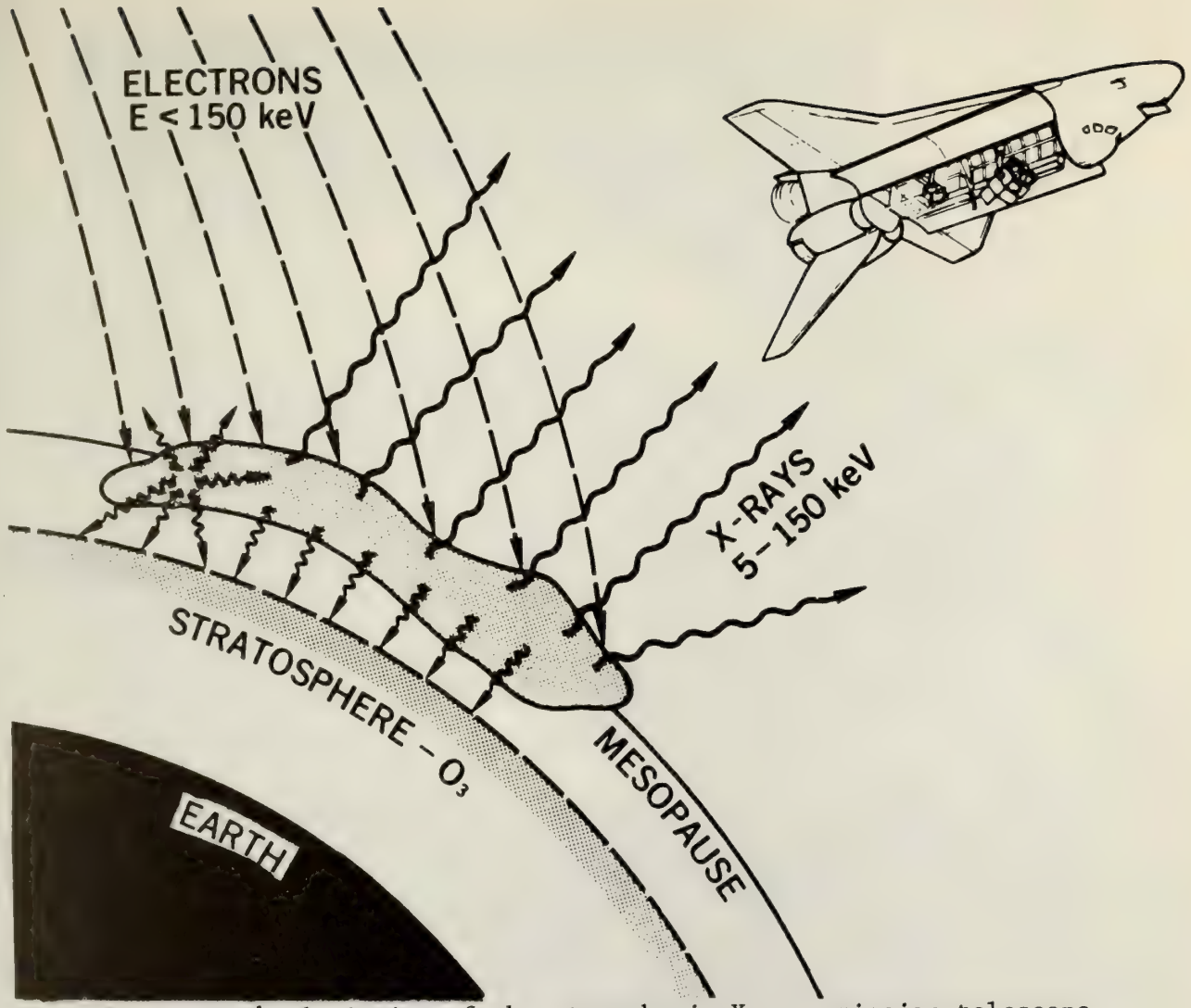


Fig. 10 Artist's depiction of the atmospheric X-ray emission telescope (AXET) concept and objectives (Goldberg,1978, p. 24).

being a conducting medium, serves to screen certain frequency components arising from the aforementioned magnetospheric currents. The ionosphere itself however is variable, so that the total field variability at the earth's surface is due both to magnetospheric current fluctuations and to ionospheric perturbations (Fleming and Keller,1972). Typical geomagnetic field fluctuations are about 2×10^{-5} of normal intensity, but go as high as 4×10^{-2} of normal (Bartels and Fanselau,1938).

In accordance with Faraday's law, changing magnetic fluxes induce electric fields, and thus currents in the conducting terrestrial surface. The frequency energy density spectrum of the induced terrestrial electric fields is given by $\frac{\partial E^2}{\partial f} = Z\frac{\partial H^2}{\partial f}$ where $E=|\bar{E}|$, $H=|\bar{H}|$, and f is the frequency. Z is the total impedance which depends both on frequency and local geology (Wait,1962; Goddard and Boerner,1979).

These induced electric fields can introduce currents in such systems as grounded electrical power and communications systems and pipelines (Lanzerotti, 1977;Acres Report,1975). Electric potentials of up to 7 V/km have been ob-

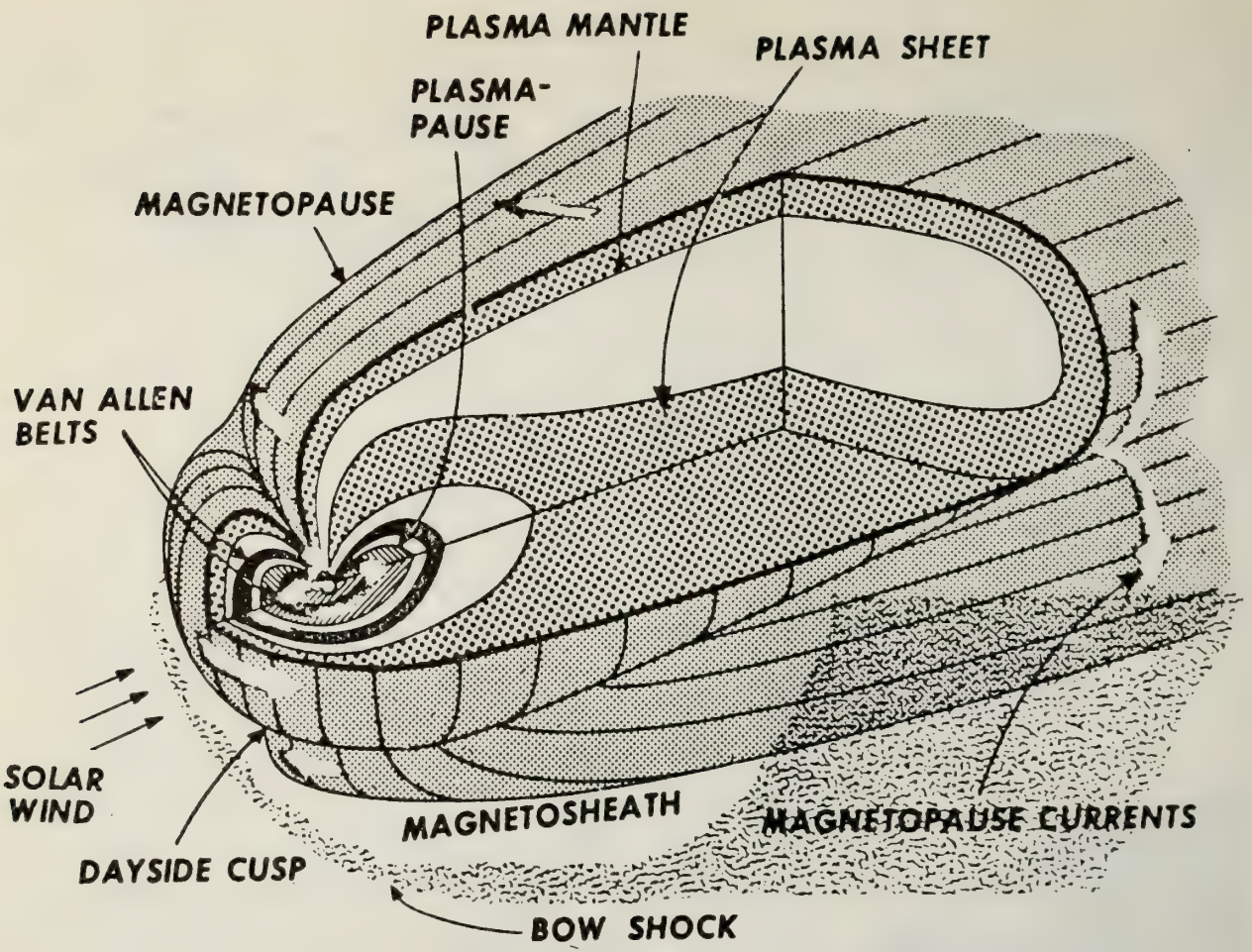
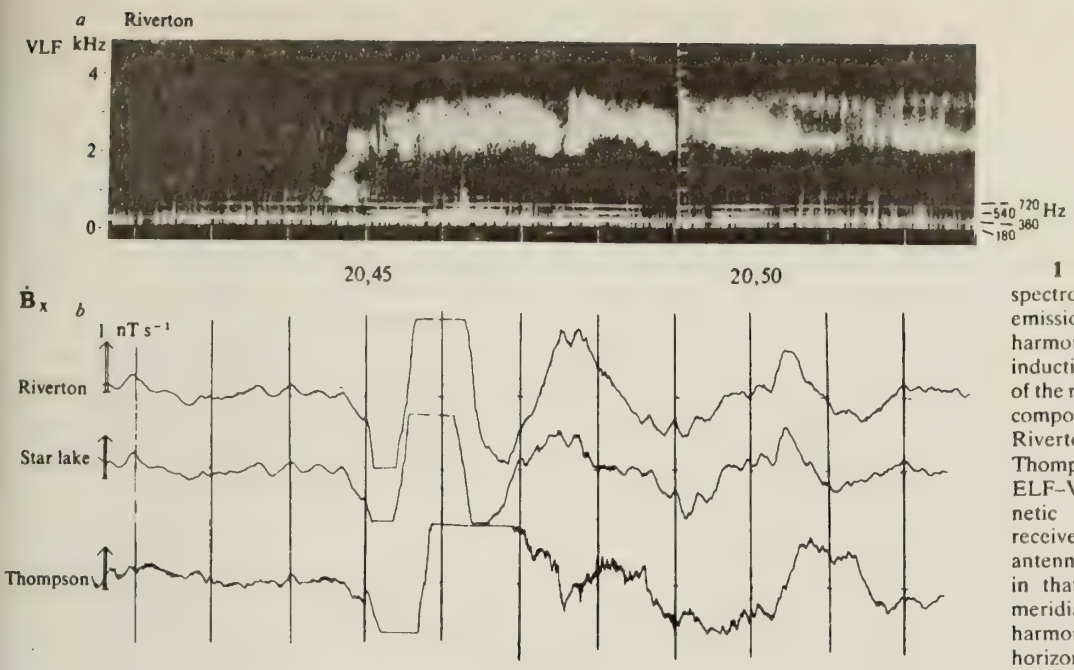


Fig. 11 Model of the earth's magnetosphere (Levine,1966, p. 47).

served, the effect generally being stronger with increasing latitude reaching maximum in the auroral belts (Albertson and VanBaelen,1970). Quasi direct currents amounting to hundreds of Amperes have been observed during solar disturbances on long systems such as pipelines and electrical transmission lines (Lanzerotti,1977;Akasofu and Merritt,1979;Goddard and Boerner,1978;Acres Report,1975:Figs.13a,b).

Principal effects are half-cycle saturation of magnetic devices such as power and current transformers, and misoperation of protective devices such as relays and circuit breakers. System shutdown is possible under extreme conditions (Albertson and Kappenmann,1978). The Alaska pipeline lies in a region which experiences geomagnetic disturbance energies up to 100 times greater than those which occur in most of the middle United States (Campbell,1978). Currents of up to several hundred Amperes have been observed which could considerably shorten its lifetime through enhanced corrosion as well as interfering with safety and control instrumentation (Procter,1976;Lanzerotti,1977; Akasofu and Chapman,1972).

It must be stressed that effects of solar induced currents are not proportional to current magnitude but increase rapidly above a certain threshold, e.g. when the half-cell potential oxidation potential is exceeded for pipeline corrosion, or when a shutoff current or voltage is reached for power system safety devices (Fleming and Keller,1972).



1 A frequency–time spectrogram of chorus emission and power line harmonics, (*a*), along with induction magnetograms of the magnetic horizontal component recorded at Riverton, Star Lake and Thompson (*b*). The ELF–VLF signals (magnetic component) were received on a loop antenna whose plane lay in that of the magnetic meridian. The power harmonics are seen as horizontal lines in the low frequency band below 1 kHz. Their enhancements start coincident with the initiation of the rapid negative deflection of the magnetic horizontal component.

Fig.12a; Hayashi, Oguti, Watanabe et al, 1978, p. 627.

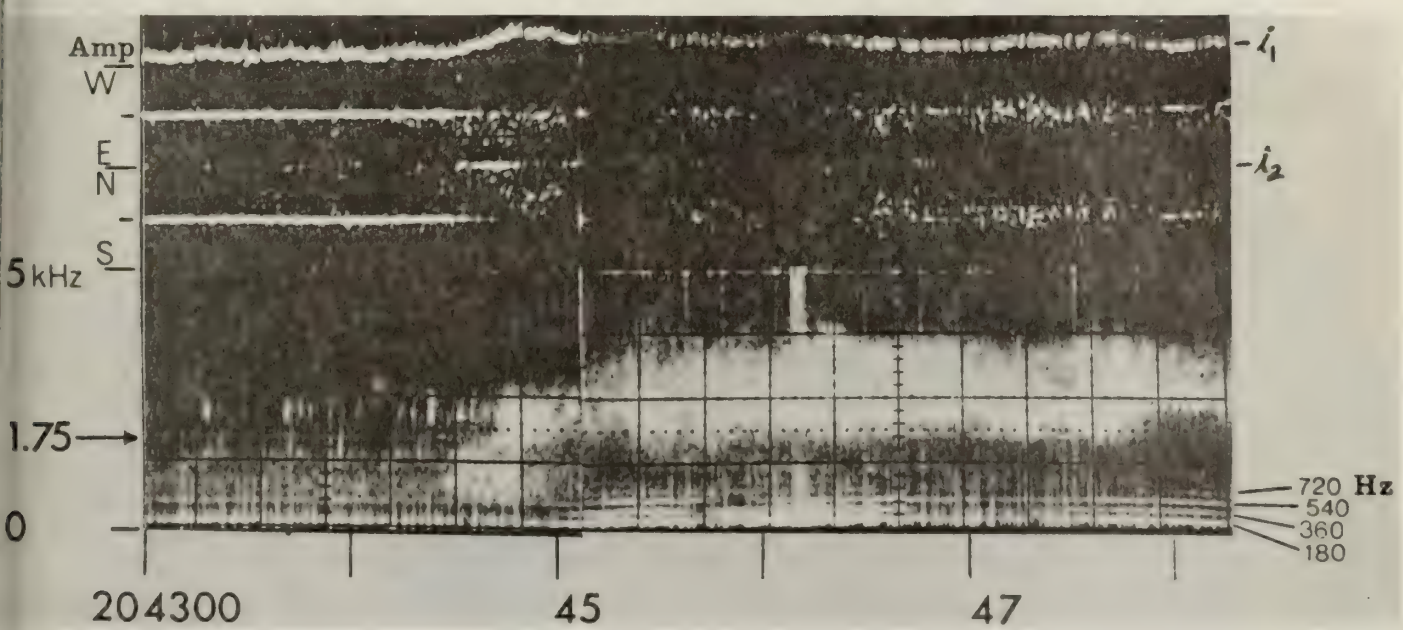
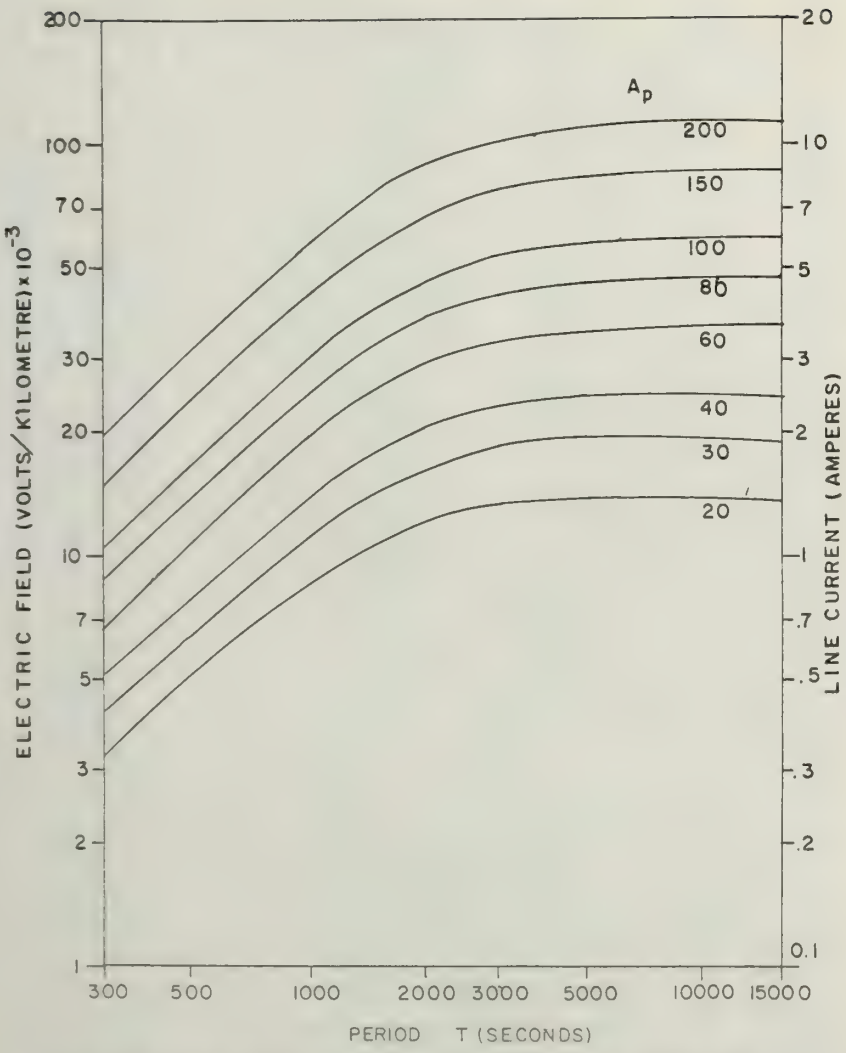


Fig.12b. Earth currents induced in the E-W direction (i_1) and N-S direction (i_2) with frequency time spectrograms of chorus emission and power line harmonics shown below; Hayashi, Oguti, Watanabe et al, 1978.



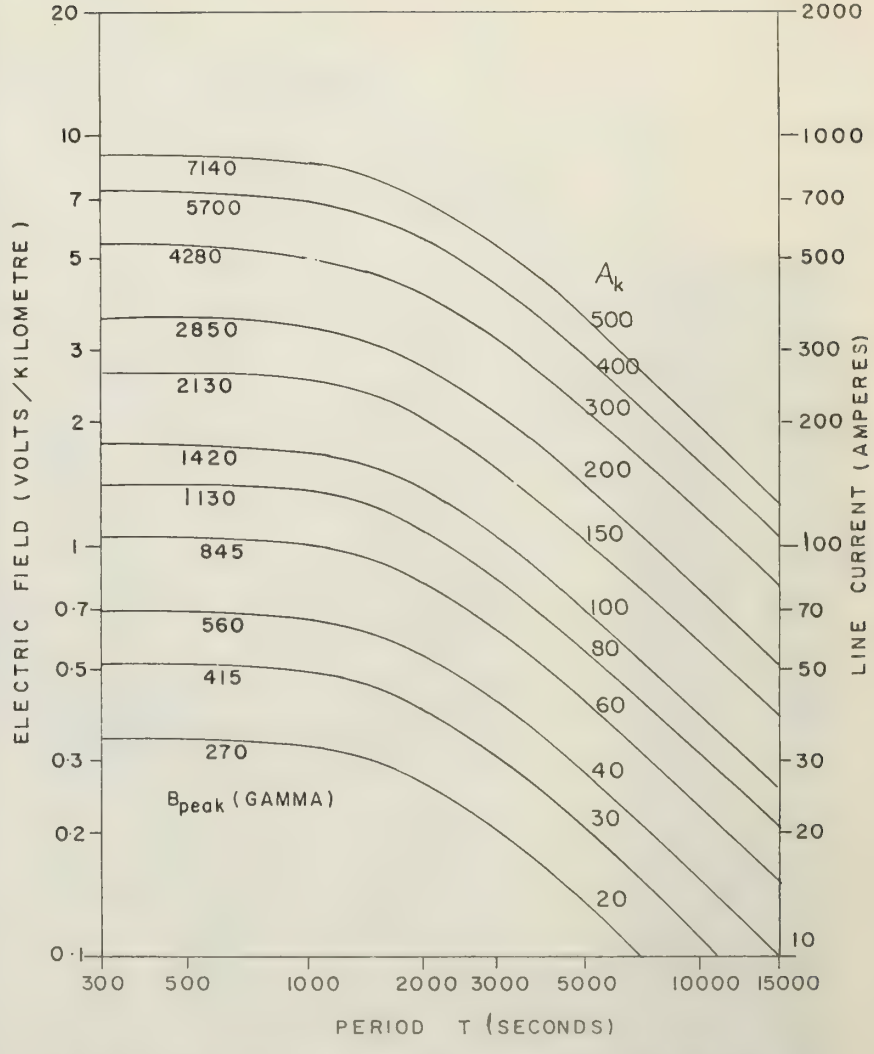
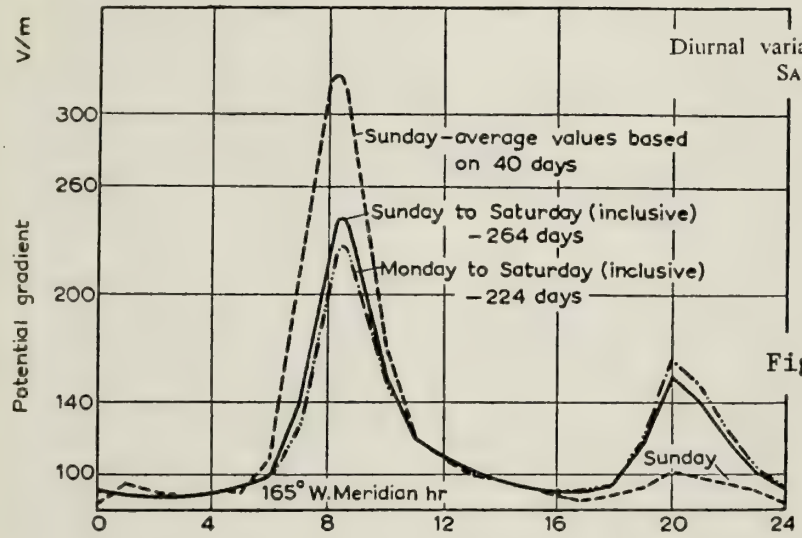


Fig. 13b Equivalent periodic induced electric field for surges in magnetic field and corresponding current (Cleland and Beamer, [illegible], p. 14).

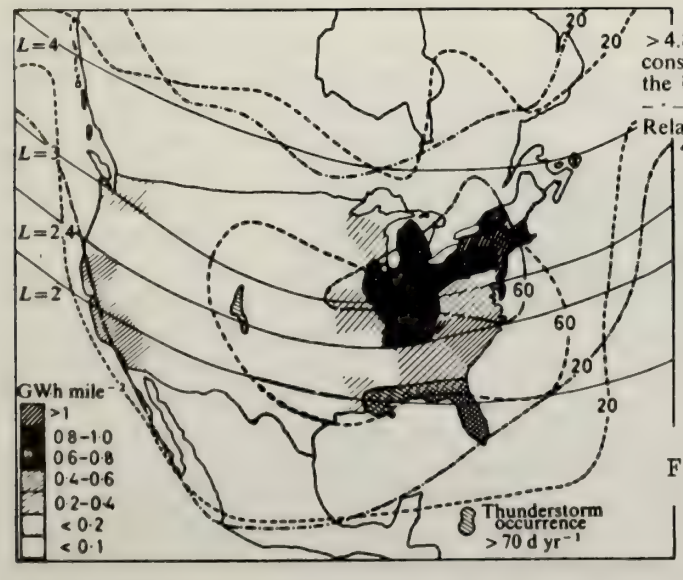
5. EFFECTS OF MAN-MADE SYSTEMS ON THE MAGNETOSPHERE: POWERLINE HARMONIC RADIATION (PLHR).

On the other hand, man-made systems can discernably affect the geoelectromagnetic environment. As can be seen from Fig.14 *human* electromagnetic influences on the environment are not always the product of advanced technology. The local custom of lighting bonfires on certain occasions gave rise to the observed Sunday variations. Chalmers (1952) and Mühleisen (1953) found the geoelectric field affected as far as 7 km distant from 133 kV electric power lines. Only rather recently however have the effects of human electromagnetic activities come to be observable on a global scale. Bullough, Tatnal, and Denby (1976) conclude that powerline harmonics originating in the earth's industrial regions are responsible, at least in part, for the formation of the 2<L<3 electron slot between the inner and outer radiation belts in the magnetosphere. Here L is the magnetic shell parameter, which in a



Diurnal variation of potential gradient in Samoa. (From SAPSFORD, 1937, Fig. 1, p. 157.)

Fig.14; Chalmers, 1967, p. 166.

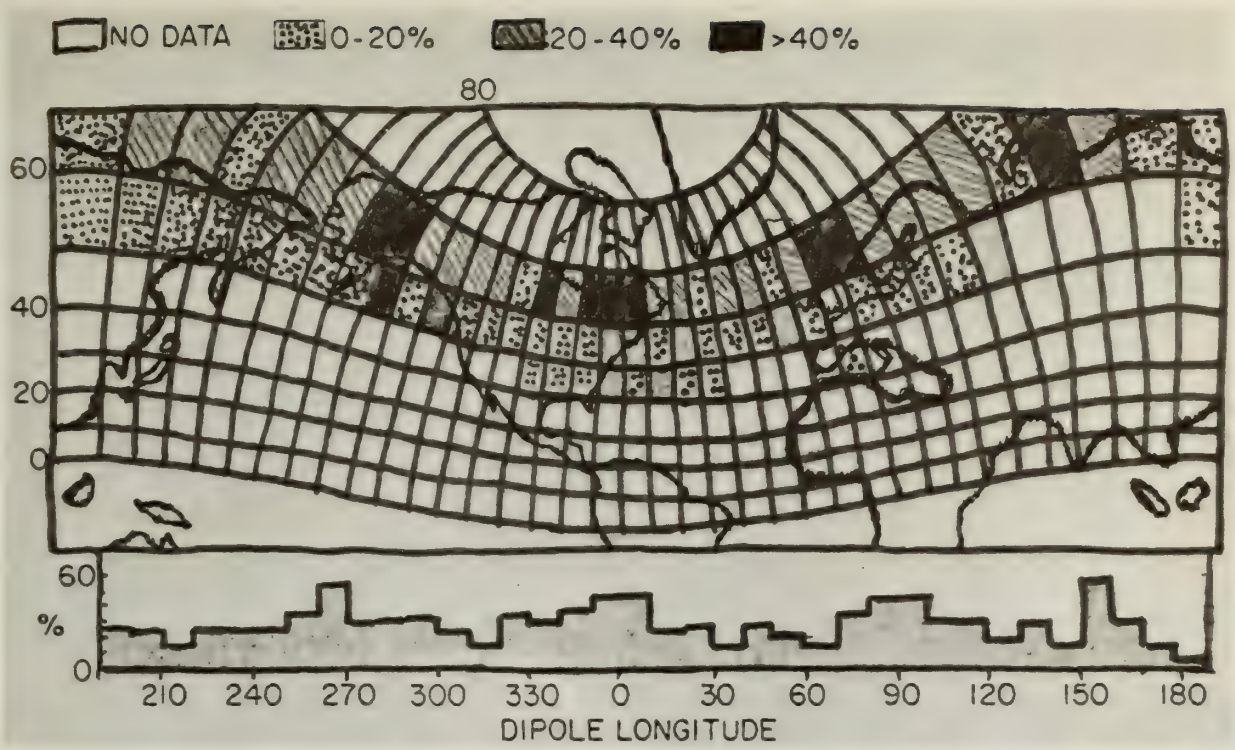


Percentage occurrence of emissions with intensity $>4.8\times10^{-15}$ W m^{-2} Hz^{-1} at 3.2 kHz, annual electric power consumption (in GWh mile^{-2}) and thunderstorm occurrence for the USA $K_p \leq 2+$. - - - - -, 1967 Summer (May, June, July). - · - · - · -, 1967 Autumn (August, September, October). Relative thunderstorm occurrence: summer/autumn = 4 (see

Fig. 15; Bullough et al, 1976, p. 402.

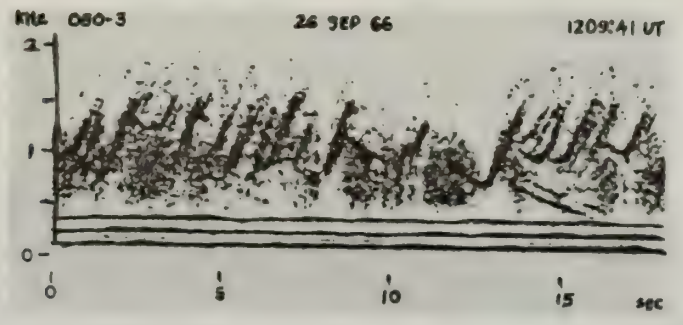
modified dipole model of the geomagnetic field gives the distance in earth radii where a field line crosses the equatorial plane. The intersections of these magnetic shells so defined with the terrestrial surface also specify a latitude-like coordinate (Egeland et al,1973). Helliwell, Park and Luette (1977) have found that VLF chorus activity has the highest probability of occurrence in regions which are threaded by geomagnetic field lines passing through industrial zones (Figs.15,16). These results have been explained as arising from powerline harmonics that leak into the magnetosphere and, after amplification up to 1000-fold by natural mechanisms, stimulate the recorded emission through cyclotron interaction with trapped electrons. In this way man-made radiation can manifest itself far out of proportion to its initial strength thousands of kilometers from its origin (Park and Chang,1978;Park and Miller,1979). However, according to Thorne and Tsurutani (1979) powerline harmonic radiation does not play any major role in the non-adiabatic dynamics of radiation belt electrons (Fig.16c). This finding will require well designed experiments of unbalancing HV-AC powerlines and forcing radiation of prespecified frequencies. We are going to carry out measurements of these design requirements during the forthcoming summer in Manitoba.

The distinction between man-made effects on nature, and natural effects on man-made systems is not always clearly defined. There is increasing evidence that powerline harmonic radiation can initiate or enhance thunderstorm activity (Bullough and Kaiser,1978). If Park and Helliwell's (1971) suggestion that thunderstorm electric fields create magnetospheric ducts proves correct, then powerline harmonics induced thunderstorm activity could lead to further enhancement of harmonic radiation in a self-sustaining cycle (Bullough et al,1976). Such an event may well have contributed to the July 1977 Northeastern U.S. blackout (Corwin and Miles,1978) which was preceded by geomagnetic and electric storm activity (Fig.17). Hayashi et al (1978) show how geomagnetic disturbances during the September 1977 storm have lead to excessive PLH radiation along one of Manitoba Hydro's extended HV-AC lines, an event which was concurrent with a substantial increase in electric storm activity along Lake Winnipeg and also extending into the Nelson River basin (Fig.18). These observations are corraborated by statistics provided by Manitoba Hydro and the Canada Department of Environment indicating that thunderstorm activity has increased coinciding with the increasing development of HV-DC/AC powerlines in Manitoba. In particular, there seems to be evidence that electric storm activity in the interlake region between Lake Manitoba and Lake Winnipeg has increased since the activation of a 450 KV (1.2 GW) DC powerline intertieing the Nelson River electric power generating base with Winnipeg over a distance of about 1000 km (Fig.18). It would be desirable to employ a network of spherics counters and integrators over the regions of interest. However, it should be noted that detection and monitoring methods of electric storms have been improved and careful re-investigation of these observations is required. In this context, we were made aware most recently of the statistics compiled in (Stringfellow,1974) which requires subtle re-examination. In case the statistics relating powerline outages due to lightning with the eleven year solar cycle are as definitive as shown in Fig.16c, such statistic should show up elsewhere. Definitely, basic statistical analyses of powerline outages due to geoelectromagnetic disturbances are warranted and we should draw particular attention to the research reported in (Lethbridge,1979) where statistical relationships between thunderstorm activity and solar magnetic boundary crossing events are discussed. Within this



Chorus occurrence frequency in invariant dipole coordinates. Each bin represents a magnetic flux tube extending from hemisphere to hemisphere with a cross-section of 10°x10° invariant latitude and longitude. The histogram shows longitudinal variations in percent occurrence averaged over invariant latitudes.

Fig. 16a; Helliwell et al, 1977, p. 277.



A spectrogram of chorus activity detected by the Ogo 3 satellite at L = 7.8, 38° dipole latitude, and 1210 local time. The geo magnetic activity was moderate (K_p = 4).

Fig. 16b; Helliwell et al, 1977, p. 276.

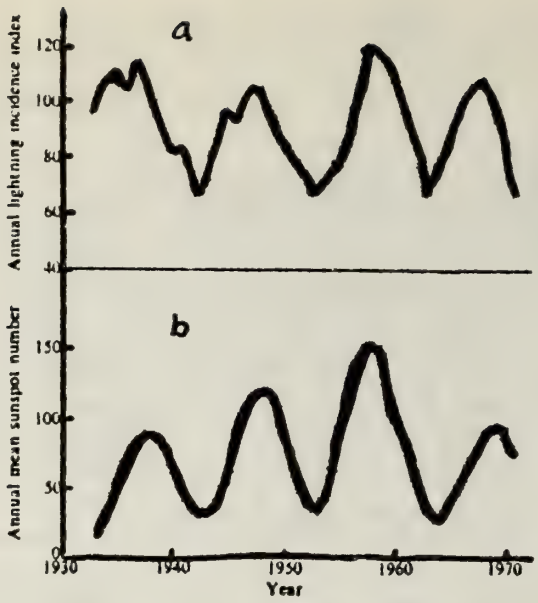


Fig. 16c Annual variation of: a)5-yr. running means of lightning; b)sunspot number (Stringfellow,1974).

auroral and sub-auroral region, effects of geomagnetic disturbances and PLH radiation compound along HV lines whose potentials range from about 230 KV to 1.2 MV comparable to or several times greater than the earth-ionosphere potential (250 KV). This gives rise to reversals in geoelectric field polarity, increases in local air conductivity influencing charge separation and build-up within clouds and leading to short range perturbations in the atmospheric electric environment within the localized region of the Agassiz-Nelson River basin which could serve as an ideal natural/man-made laboratory for controlled experiments. Further interdisciplinary studies are required to analyze these recent findings and to establish the relations with the geo-electromagnetic and aeronomic environment.

The utility of these proposed studies will be optimized if they are carried out on inter-regional basis in locations of different geological-geoelectromagnetic character as well as in a variety of urban/industrial regions: in the Golden Valley, Alaska; along the US West Coast (BPA); the Central USA (Commonwealth Edison of Illinois); the Agassiz-Nelson River Basin (Canada); the US East Coast (New York Consolodated Edison); the James Bay area, Canada (IREQ); and in New Foundland (Boteler,1979).

6. GEOELECTROMAGNETIC DISTURBANCE FORECASTING

Many adverse effects of geoelectromagnetic disturbances on man-made systems could be mitigated or averted given sufficient advance warning.

A major impediment to accurate geoelectromagnetic predictions is that the connection between solar events and terrestrial effects is seldom direct, but depends upon intermediate coupling mechanisms through the magnetosphere and upper atmosphere of which our knowledge is incomplete. For example, auroral effects on the terrestrial electromagnetic environment arise not only from the highly variable solar wind but also depend strongly upon the relative orientations of the solar and terrestrial magnetic fields with strong locality



Fig. 17 The New York black out of 14 July 1977 (US Air Force).

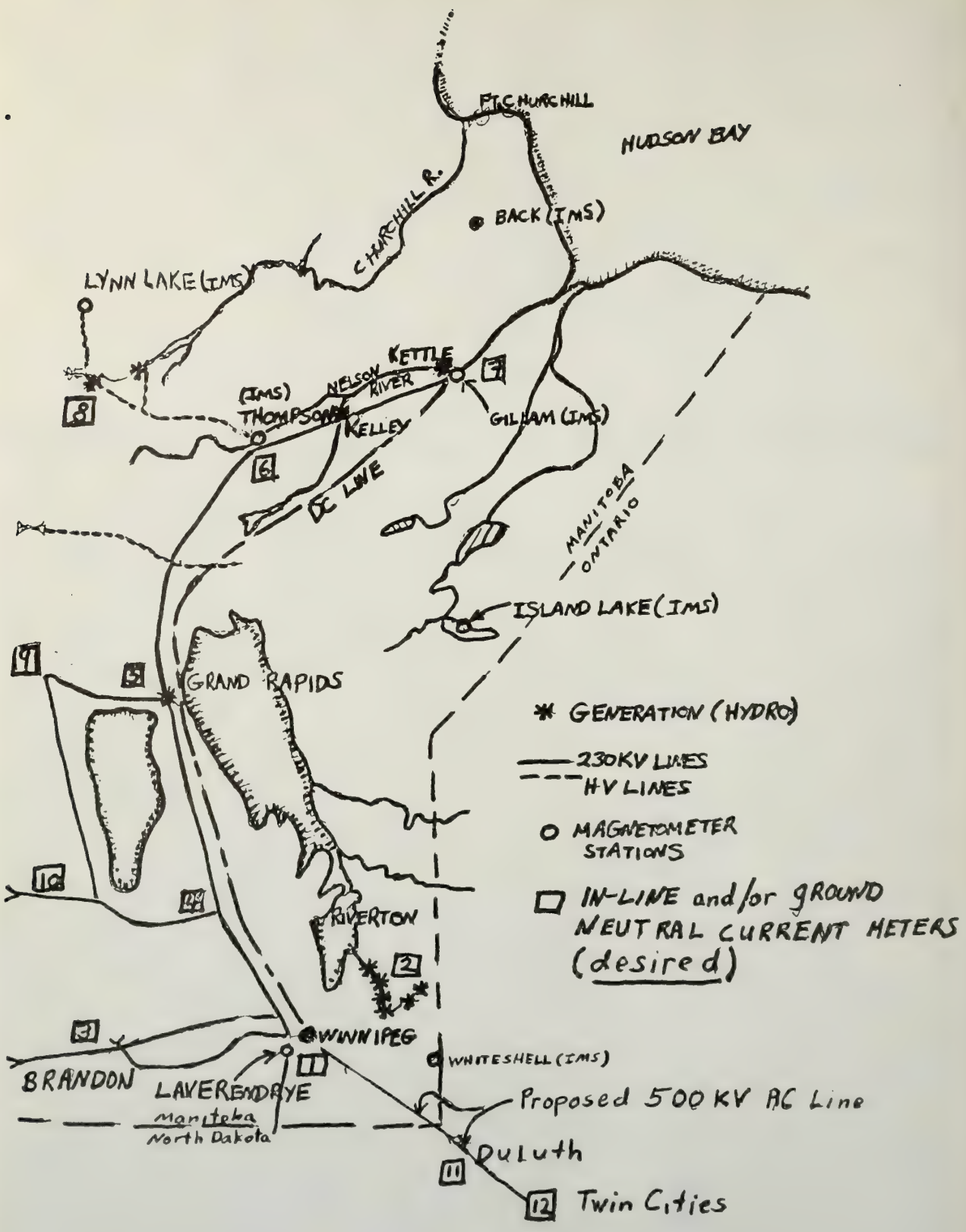


Fig. 18 Locations of desired and/or available monitoring stations (Goddard and Boerner, 1978, p. 10).



Fig. 19 View of the earth from above the N. pole showing N. America being brought into a "disturbed" zone by the earth's rotation (Boteler, 1979, p. 8).

dependence (Akasofu,1979). Nonetheless, for lack of more comprehensive data, most geoelectromagnetic forecasters base their predictions upon observable solar activity by extrapolating from previously deduced statistical correlations between solar events and subsequent terrestrial effects (Allen,1977). This approach yields reasonably accurate predictions for periods up to a few days, but is unreliable for longer periods. This is due in part to the fact that we cannot accurately predict of the birth and subsequent evolution of solar disturbances, and in part to the sun's rotation which can suddenly bring into view matured disturbances which formed on its unobservable side (Purple Mountain Observatory,1978). Despite the close connection between the terrestrial geoelectromagnetic disturbance cycle and the solar cycle there exist important differences as well (Feynman,1978) and even short term predictions based on solar observations alone become increasingly error prone with increasing latitude (Hruska,1979). As shown in Fig.20 certain types of disturbances are not global but manifest themselves through a band of local times. As the earth rotates different regions will successively pass through the disturbed zone. Specific quantitative predictions on disturbances of this sort must be based on more than simple statistical correlations between solar events and global means of geoelectromagnetic parameters.

Future progress in geoelectromagnetic forecasting will require detailed monitoring of the electromagnetic environment not only over the terrestrial

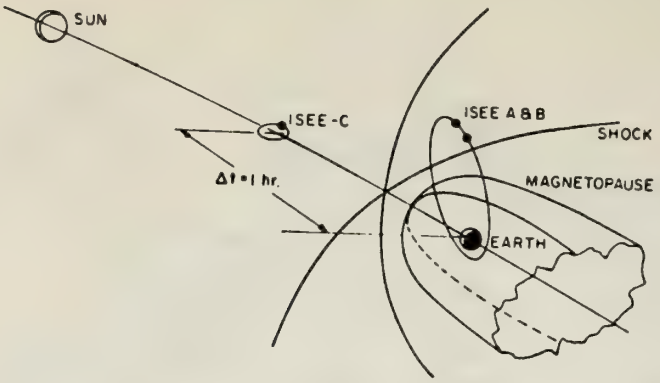


Fig. 20 A diagram showing ISEE-1 and -2 in orbit about the earth and ISEE-3 at the forward libration point (Ogilvie,1978, p. 151).

surface but extending outward to tens or hundreds of earth radii. This data would also serve as a basis to advance theoretical understanding of solar and magnetospheric electromagnetic processes which would allow more extended forecasts than are presently possible. In view of mounting evidence for geoelectromagnetic effects on weather and climate, the data might prove useful for weather forecasting as well.

A first approach in this direction was made with the launch of the International Sun-Earth Explorer (ISEE) satellites to monitor the solar wind and interplanetary magnetic field. One satellite (ISEE-3) will be orbited about an earth libration point situated at about 240 earth radii in the sunward direction (Ogilvie et al,1978:Fig.21). Akasofu (1978) has developed a formula to compute both the occurrence and magnitude of magnetospheric substorms observied in the zuroral zone, given the upstream values of solar wind velocity and interplanetary magnetic field direction and magnitude. As the solar wind requires about one hour to traverse the 240 earth radii from the ISEE-3, this satellite will permit quantitative predictions about one hour in advance.

The next step is to complement satellite monitors with a network of ground-based recorders across the auroral zone to measure geomagnetic fields, atmospheric electric fields and earth surface potentials. The ultimate objective is to monitor all important inputs into the sun-magnetosphere-earth system simultaneously with major geophysical outputs (geomagnetic field, atmospheric electric field, etc.) along with weather-related parameters. This will be the basis to construct cause-effect models from which can be derived quantitative advance prediction algorithms.

7. OVERALL RESEARCH ASPECTS

The possibility that man-made electrical systems, their radiation amplified in interaction with natural phenomena, might produce geo-electromagnetic perturbations on a global scale emphasizes the need for conclusive investigations well in advance of planned extensions of large-scale power transmission systems farther into the geo-electromagnetically active regions. Such investigations will require simultaneous recording of geomagnetic, geoelectric, and atmospheric electric parameters as well as currents induced in man-made systems at several locations spread over the Northern and Southern hemispheres.

The effects of powerline harmonics radiation and its interaction with the magnetosphere/magnetopause will require controlled experiments including imbalancing and forced radiation of powerline sections in regions accessible to ground-based, balloon, rocket and satellite borne instrumentation such as can be provided by Manitoba Hydro, BPA, Commonwealth Edison, etc. Detailed studies on how induced currents will affect ground-based transmission systems will have to be carried out simultaneously in collaboration with the utilities and manufacturers of HV DC converters and AC transformers. Research on many of these aspects has been initiated recently. Detailed outlines on specific projects are under preparation and will be presented separately.

8. LOCATIONS

There exist several prime locations to carry out the proposed research which requires the utilization of large-scale electric powerlines and oil/gas-pipelines for carrying out controlled experiments. *A nature-given laboratory is the Agassiz-Nelson River basin with extension into the Hudson Bay in central Northern America.* This region lies within the sub-auroral to auroral belts and large-scale HV-AC/DC powerlines of several Gigawatt power extending from about 58°N, to 45°N latitude are being developed by Manitoba Hydro and MAPP (Fig.18). Several geophysical laboratories can easily be set up by expanding recording stations of geomagnetic, geoelectric, and meteorological parameters.

Furthermore, the facilities of the Bonneville Power Administration as well as of Commonwealth Edison of Illinois are also located ideally and should provide two essential additional sites to carry out controlled PLHR experiments. Collaboration with Manitoba Hydro, MAPP, BPA and Commonwealth Edison have been established to initiate this research on a larger scale.

9. BENEFITS

The proposed international, interinstitutional and interdisciplinary research should be of immediate interest to the sciences of aeronomy, geophysics and geology as it should provide a host of hitherto unavailable factual data. It should also be of paramount importance to advancing the technology of electrical energy, oil and gas transmission in geo-electromagnetically active regions with the objective of reducing uncontrollable electromagnetic radiation and systems outages caused by transformer and relay malfunction or unwarranted corrosion. A byproduct of these studies will be an exhaustive spectral analysis of VLF background noise induced along supra-long conductor systems which should be of immediate interest for military communications. These studies will stimulate fruitful interchanges among various military, industrial and academic institutions.

10. ACKNOWLEDGEMENTS AND SUPPORT

The initiation of this research was and is supported in parts by Manitoba Hydro, NSP, EPRI, NSERC-Canada (Grant No. G 0087), the Space Research Facility Branch of NRC-Canada (particularly its newly established ballooning and

rocketing site at Gimli, Man.), and by a UICC Grant (No. RB 301-22-33-306). This interdisciplinary study will be carried out in collaboration with Professor Donald E. Olson, U. of Minn/Duluth; Professor Vernon D. Albertson, U. of Minn/Minneapolis; Professor Robert A. Helliwell, SU, Stanford; Professor Tomiya Watanabe, UBC, Vancouver, B.C.; Professor Takeo Yoshino, Univ. of Electrocomm., Tokyo. We are currently seeking active participation of other researchers involved in similar studies and we are seeking additional financial support.

REFERENCES

Acres Consulting Services Ltd., "Study of the disruption of electric power systems by magnetic storms", Report for Dept. of Energy Mines and Re-Sources, Ottawa, Canada, March 1975.

Akasofu, S-I., "Interplanetary energy flux associated with magnetospheric substorms", International STP Proceedings & Workshop, Boulder, Colorado, April 1979.

Akasofu, S-I. and Chapman, S., Solar Terrestrial Physics, Clarendon Press, Oxford, 1972.

Akasofu, S-I. and Merritt, R.P., "Electric currents in power transmission lines induced by auroral activity", To be published in Nature, 1979.

Albertson,V.D. and Kappenmann, J.G., "Magnetic storm effects in electric power systems and prediction needs", International Solar-Terrestrial Predictions Proceedings and Workshop Program, Preprint no. 77, November 30,1978.

Albertson, V.D., Kappenman, J.G., Mohan, N., Skarbakka, G.A., "Load-flow in the presence of geo-magnetically-induced currents", IEEE PES Meeting, Vancouver, B.C., July 15-20, 1979, Paper No. F79 702-2.

Albertson,V.D. and Van Baelen, J.A., "Electric and magnetic fields at the earth's surface due to auroral currents", IEEE Trans. on Power Apparatus and Systems, Vol. PAS-89, No. 4, April 1970.

Allen,J.H., "Relative magnitudes of major magnetic storms by the A_p^* measure, and their frequency distribution from 1932-76", presented at the IAGA/IAMP Symposium, Seattle, Wash., August 1977, 9 pages.

Anderson,C.W., Lanzerotti,L.J., et al, "Outage of the L4 system and the geomagnetic disturbances of 4 August 1972", Bell Syst.Tech.J.53(9), pp.1817-1837.

Bartels,J. and Fanselau,G., "Der erdmagnetische Sturm vom 16.April,1938", Naturwissenschaften 26(19), pp. 296-298, 1938.

Boteler,D.H., "The problem of solar induced currents", International Solar-Terrestrial Predictions Proceedings and Workshop Program, No. 150, 1979.

Bullough,K., et al, "Man-made elf/vlf emissions and the radiation belts", Nature 260(5550), pp. 401-403, 1976.

Bullough,K., Kaiser,T.R., "Ariel 3 and 4 studies of power line harmonic radiation", URSI, 1978 General Assembly, Helsinki, Finland.

Campbell,Wallace H., "Introduction of auroral zone electric currents within the Alaska pipeline", Pure and Applied Geophysics 116, pp.1143-1173,1978.

Chalmers,J.A., Atmospheric Electricity, Pergamon Press, London, 1967.

Chalmers,J.A., "Negative electric fields in mist and fog", J. Atmos. and Terr. Phys. 2, pp. 155-159, 1952.

Corwin,J.L. and Miles,W.T., "Impact assessment of the 1977 New York city blackout", Prepared for US Dept. of Energy by Systems Control,Inc., 1978.

Dolezalek,M. and Reiter,R., ed. Electrical Processes in Atmospheres, Proceedings of the 5th International Conference on Atmospheric Electricity held at Garmisch-Partenkirchen (Germany), 2-7 September 1974, Steinkopff Verlag GmbH & Co., K.G., Darmstadt.

Egeland,A., Holter, Ø., Omholt,A., Cosmical Geophysics, Scandinavian University Books, Universitetsforlaget, Oslo, 1973.

Fälthamar,G-G., "Electric fields in space - a survey", in Planetary Electrodynamics, S.C. Coroniti, J. Hughes, ed. Gordon and Breach, New York,1969.

Feynman,J., "The 21st solar cycle aa index of geomagnetic activity", International Solar-Terrestrial Predictions Proceedings and Workshop Program, Preprint No. 57, November 1978.

Fischer,H-J. and Mühleisen,R., "Variationen des Ionosphärenpotentials und der Weltgewittertätigkeit im 11-jährigen solaren Zyklus", Meteorologische Rundschau 25(1), pp. 6-10, 1972.

Fleming,D.B., Keller,G.V., "Research on the probability of occurrence of unusually large earth current storms", Final Report for the Bonneville Power Administration, Portland, Oregon and U.S. Bureau of Reclamation, Denver, Col., Submitted by Colorado School of Mines, Golden, Colorado, March 1972.

Fleming,J.A., ed. Terrestrial Magnetism and Electricity, Dover, New York,1949.

Goddard,W.R., Boerner,W-M., et al, "Effects of solar induced currents on electric power transmission systems of Manitoba Hydro in central Canada", Proc. of 21st Plenary Meeting ICSU-COSPAR 21, Innsbruck, Austria, 29 May-10 June, 1978, Paper no. 40-1.

Goddard, W.G., Boerner, W-M., "Prediction of Solar Induced Currents and Effects on Power Transmission Systems in Central Canada", International Solar-Terrestrial Predictions Workshop, April, 1979, Boulder, Co., 15 pages.

Goldberg,R.A., "An experimental search for causal mechamisms in sun/weather-climatic relationships. Symposium/Workshop on Solar-Terrestrial Influences on Weather and Climate, Ohio State University, Columbus, Ohio, July 24-28, 1978.

Goldberg,R.A. and Herman,J.R., "Coupling processes related to the sun-weather problem", Invited review for the International Solar-Terrestrial Predictions Workshop, Boulder, Colorado, April 23-27, 1979.

Hale,L.C. and Croskey,C.L., "Auroral effects on atmospheric electric fields", Oct., 1978. Submitted to Nature.

Hayashi,H., Oguti,T., Watanabe,T., Tsuruda,K., Kokubun,S., Horita,R.E., "Power harmonic radiation enhancement during the sudden commencement of a magnetic storm", Nature 275(5681), pp. 627-629, October 1978.

Hays,P.B. and Roble,R.G., "A quasi-static model of global atmospheric electricity I.The lower atmosphere",J.Geophys.Res.(Space physics),1979,in press.

Helliwell,R.A., Park,C.G., Luette,J.P., "Longitudinal variations of very-low-frequency chorus activity in the magnetosphere: evidence of excitation by electrical power transmission lines", Geophy. Res. Lett. 4, No. 7, pp. 275-278, July 1977.

Herman,J.R. and Goldberg,R.A., "Sun, weather and climate", NASA SP-46, Scientific and Technical Information Branch, NASA, Washington, D.C., 1978.

Hermance,J.F., "Electromagnetic induction in the earth by moving ionospheric current systems", Geophys. J.R. Astr. Soc. 55, pp. 557-576, 1978.

Hessler,V.P., "Causes, recording techniques and characteristics of telluric currents", Materials Performance, pp. 38-47, April 1976.

Hruska,J., "Forecasts of geomagnetic activity by Ottawa Magnetic Observatory: their reliability and application", International Solar-Terrestrial Predictions Proceedings and Workshop Program, No. 110, December 1978.

Israël,H., Einführung in die Geophysik, Springer-Verlag, New York, 1969.

Kellogg,P.J. and Weed,M., "Balloon measurements of ionospheric electric fields", in Planetary Electrodynamics, S.C. Coroniti, J. Hughes, ed. Gordon and Breach, New York, 1969.

Kelly,C.M. and Mozer,F.S., "Simultaneous measurement of the horizontal components of the earth's electric field in the atmosphere and in the ionosphere", J. of Geophysical Res. 80(22), pp. 3275-3282.

Lanzerotti,L.J., ed. Impact of ionopsheric/magnetospheric processes on terrestrial sciences and technology, SCOSTEP Survey, April 1977, Presented at the Solar Terrestrial Physics Conference, Innsbruck, Austria, June 1978.

Lethbridge,M.D., "Thunderstorm frequency and solar sector boundaries", Proc. of Ohio University Symposium on Solar Weather, July 1978.

Levine,M.A., "Plasmas in Space", IEEE Spectrum, pp. 43-47, November 1966.

Livingstone,W., "Solar input to the terrestrial system", Symposium on Solar-Terrestrial Influences on Weather and Climate, Columbus, Ohio, 1978.

Markson,R., "Solar modulation of atmospheric electrification and possible

implications for the sun-weather relationship", Nature 273(11), pp. 103-109, May 1978.

Mohan, N, Kappenman. J.G., Albertson, V.D., "Harmonics and switching transients in the presence of geo-magnetically-induced currents", IEEE PES Summer Meeting, Vancouver, B.C., July 15-20, 1979, Paper No. F79 694-1.

Mühleisen,R., "Die luftelektrischen Elemente im Großstadtbereich", Z. Geophys. 29, pp. 142-160, 1953.

Mühleisen,R., "New determination of the air-earth current over the ocean and measurements of ionosphere potentials", Pure and App. Geophy. 84, pp. 112-115, 1971.

Mühleisen,R., "Zusammenhänge zwischen luftelektrischen Parametern und Sonnenaktivität bzw. Nordlichtern", Kleinheubacher Berichte, Vol. 13, pp. 129-133, 1969.

Ogilvie,K.W. et al, "Descriptions of experimental investigations and instruments for the ISEE spacecraft", IEEE Trans. on Geoscience Electronics, Vol. GE-16, No. 3, July 1978. (SPECIAL ISSUE on missions of ISEE SPACE CRAFTS)

Olson,D.E., "The evidence for auroral effects on atmospheric electricity", Pure and Applied Geophysics 84, 1971 I, pp. 118-138, 1971.

Olson,D.E., "The measurement of atmospheric electrical parameters under AC and DC powerlines", September 1978, to be published.

Park,C.G. and Chang,D.C.D., "Transmitter simulation of powerline radiation effects in the magnetosphere", Geophys. Res. Lett. 5(10), pp. 861-864, October 1978.

Park,C.G. and Helliwell,R.A., "The formation by electric fields of field aligned irregularities in the magnetosphere", Radio Sci 6, pp. 299-304, 1971.

Park,C.G. and Miller,T.R., "Sunday decreases in magnetospheric VLF wave activity", To appear in J. of Geophys. Res., 1979.

Procter,T.G., "Pipeline telluric current as one phase of a wider interdisciplinary technological problem", Materials Performance, pp. 24-28, August 1975.

Purple Mountain Observatory, "Solar activity forecasting at the Purple Mountain Observatory", International Solar-Terrestrial Predictions Proceedings and Workshop Program, Preprint No. 4, September 1978.

Reiter,R., "Chromosphärische Eruptionen der Sonne beeinflussen atmosphärisch-elektrische Elemente in der unteren Troposphäre", Meteorologische Rundschau 25(1), pp. 1-6, 1972.

Reiter,R., "The electric potential of the ionosphere as controlled by solar magnetic sector structure", Naturwissenschaften 63, pp. 192-193, 1976.

Reiter,R., "Study to verify patterns of atmospheric potential gradient and air-earth current after solar flares based upon the geographic distribution of storm centers", Riv. Ital. di Geofis. 23(3/4), pp.193-197, 1974.

Reiter,R. and Littfass,M., "Stratospheric-tropospheric exchange influenced by solar activity", Results of a 5 Yeas Study. Arch. Met. Geoph. Biokl., Ser. A 26, pp. 127-154, 1977.

Roble,R.G. and Hays,P.B., "Solar-terrestrial coupling through atmospheric electric", To be published in NAS-Sun, Weather and Climate, 1979.

Rostoker,G., "Current flow in the magnetosphere during magnetospheric substorms", J. of Geophys. Res. 79(13), pp. 1994-1998, May 1974.

Stacey,F.D., Physics of the Earth, John Wiley and Sons, New York, 1969.

Stringfellow,M.F., "Lightning incidence in Britain and the solar cycle", Nature 249, May 24, 1974, pp. 332-333.

Tatnal,A.R.L., Matthews,J.P., Bullough,K., Kaiser,T.R., "Powerline harmonic radiation and the electron slot", Space Physics Group. Sci. Rep. 1978-1, Univ. of Sheffield, S. Yorkshire, England, March 1978.

Thorne,R.M. and Tsurutani,B.T., "Powerline harmonic radiation: Can it significantly affect the earth's radiation belt?", Science 204, 25 May 1979, pp. 839-841.

Volland,H., Schaefer,J., "Planetary waves and sun weather effects", Proc. and Workshop on Solar Terrestrial Predictions, April 23-27,1979, Boulder,Col.

Wait,James R., "Theory of magneto-telluric fields", J. of Res. of the NBS - D. Radio Propagaton, Vol. 660, No. 5, Sept.-Oct. 1962, pp. 509-541.

Willis,D.M., "The energetics of sun-weather relationship: Magnetospheric processes", J. of Atmos. Terr. Phys. 38 685, 1976.

Wilson,C.T.R., "On thunderstorm electricity", Phi. Mag. 17, pp. 634-641, 1909.

F. SUN-WEATHER PREDICTIONS

THE SOLAR PREDICTION OF CLIMATIC CHANGES

Hurd C. Willett
Solar Climatic Research Institute, Inc.
P. O. Box 20
Cambridge, Massachusetts 02142

The purpose of this paper is essentially threefold, namely:

1. To set forth in comprehensive form basic observed features of the hemispheric synoptic patterns of climatic change. It is to the explanation of these hemispheric patterns, so often lost sight of, that any specific hypothesis of physical solar control must be addressed.

2. To note significant statistical relationships between synoptic pattern sequences of climatic change and the cycles and specific manifestations of variable solar activity.

3. To offer some tentative suggestions as to possible physical linkage between disturbing solar impulse and atmospheric response. In conclusion are offered the author's suggestions as to the best research approach by which to establish that physical linkage. Only then can effective prediction models of climatic change be developed.

1. INTRODUCTORY REMARKS

The following discussion is based on more than 30 years of first hand experience by the author in the research of solar climatic relationships and their application to seasonal and longer-range weather prediction. Fortunately this long period of solar-climatic research was preceded by a 10-year study of the statistical-synoptic and physical-dynamic behavior of the general circulation of the northern hemisphere with Rossby and his colleagues at MIT. One practical result of this joint effort was the initial development of the 5-day forecasting technique which subsequently was established in the U.S. Weather Bureau as the Extended Forecast Section under Namias' direction.

As early as 1945 it became clear to the author as a result of this extensive physical-synoptic analysis of the development and prediction of current hemispheric weather trends, that major changes of the behavior pattern of the general circulation can <u>not</u> be explained primarily by the internal

dynamics of the earth-atmosphere system. Similar initial states of the system do not at all necessarily lead to similar subsequent states, and from time to time the usual or normal trends of development of the system suddenly are jolted into quite different and unusual trends.

It was this conclusion that decided the author around 1945 to look for extra-terrestrial sources of disturbance and control of large scale changes of the hemispheric pattern of the general circulation. Variable solar activity is the logical source of such disturbing impulses, and no evidence turned up to date indicates that we need look further.

Abnormality or change of climate is merely the mean weather expression of persistent anomaly or change of the pattern of the general circulation (GC). A climatic anomaly or trend is always associated causally with a correspondingly persistent anomaly or trend, usually of hemispheric or worldwide extent, of the mean state of the GC. Such anomalous mean states of the GC are seldom persistently present as a steady state over a long period of time, but rather persistently recurrent in a stronger state or more frequently than normal.

Basically the anomalous states or trends of the GC that set the climatic patterns fall into two distinct categories, the zonal and the meridional. Since these two forms or patterns of climatic change tend to be as distinctive in regime and probable cause as they are in form, to keep the discussion of a very complex problem as simple and clear as possible, each of the two basic categories of change is discussed in turn as to observed synoptic pattern, as to statistical relationship to cycles of solar activity, and as to possible solar cause. The zonal pattern is considered first as the simpler and probably more basic.

2. ZONAL PATTERNS OF CHANGE OF THE GC AND CLIMATE

2.1 Long Term Secular Changes

2.1.1 Synoptic

The general circulation of either hemisphere is said to be zonal in pattern when the two major zonal wind systems, the westerlies of middle latitudes and the compensating easterlies of lower latitudes are well developed and dominate the pattern.

The most important climatic contrast, that which is the basis of all long-term major climatic fluctuations or trends, depends on the progressive poleward or equatorward shift of the hemispheric zonal wind system from its normal latitude. The corresponding circulation patterns are referred to as the high latitude zonal (HLZ) and the low latitude zonal (LLZ) respectively. The severity of the climatic anomaly depends upon the degree and the persistence of the latitudinal shift.

A number of pertinent synoptic and dynamic features of this basic pattern of climatic change require brief mention, namely:

1. In terms of the hemispheric GC pattern, this fluctuation is best described as a contraction (HLZ) or expansion (LLZ) of the circumpolar cyclonic vortex (CPCV).

2. The expansion of the CPCV (LLZ) represents an expansion of the polar climatic zone, such that the maximum poleward gradient of temperature (latitudinal solenoid field) is shifted from higher to lower middle latitudes. Coldest winter temperatures in the arctic zone accompany a contracted rather than expanded CPCV.

3. Correspondingly the jet stream (-JS) or peak westerlies of the upper troposphere also shift with the solenoid field, and the strength of each correlates very highly negatively with the latitude (Willett, 1960), i.e., there is no tendency to conservation of angular momentum in the expansion or contraction of the CPCV.

4. The expanded CPCV forces the subtropical high pressure belt equatorward of its normal latitude into an intense narrow high pressure belt of strong subsidence bounded on the equatorward side by strong tropical easterlies (TE) at lower than normal latitude, i.e., high positive correlation exists between the strength and latitude of the ZW with those of the TE (Willett, 1960).

5. Corresponding to the strong low latitude jet of the expanded CPCV the LLZ circulation pattern is marked by an active belt of migratory lows at lower than normal latitudes, hence the climatic pattern is predominantly cool and wet in lower middle latitudes, cool and dry in higher middle latitudes, and warm and exceptionally dry in the narrow subtropical high pressure belt which imposes hot and dry conditions on regions normally watered by rains in the northern portion of the equatorial convergence belt. That belt in turn is exceptionally active producing heavy rains on the equatorial edge of the low latitude belt of abnormal heat and drought. This is par excellence the climatic pattern of a glacial as opposed to interglacial epoch.

6. The contraction of the CPCV (HLZ circulation) produces a pattern of climatic anomaly exactly the opposite of the glacial pattern of the expanded vortex, i.e., warm and wet in higher middle latitudes, a broad flat subtropical high pressure belt causing general warmth and deficiency of rainfall in lower middle latitudes, with a broad inactive intertropical convergence zone which spreads rain northward into the southern fringe regions of the normally dry belt of the subtropical high, but with less than normal rainfall in the tropical convergence zone. This is par excellence the climatic pattern of an interglacial as opposed to glacial epoch.

2.1.2 Relation to Long-Term Solar Secular Cycles

A. Observed Relationships

Figure 1 is introduced as the simplest means by which to convey briefly some picture of the observed secular solar climatic relationships which must be explained for best predictive application. Only the 80 or 100-year secular cycle is considered, because there are no statistically reliable samples of the longer cycles.

In Figure 1 the heavy sunspot number curve is after Eddy (1975), while the terminations of the secular cycles and the alternate positive or negative designation of the predominant polarity of the solar magnetic field during successive 11-year sunspot cycles are after Sleeper (1972). The periods of peak warmth (W- to W+) and of peak coldness (C- to C+) are designated after the following sources:

1. Since 1900, after Willett and Prohaska (1977), Willett (1978)
2. 1850-1900, Smithsonian World Weather Records, Willett (1950)
3. Previous to 1850, the masterful climatic treatise of Bruckner (1890)

The broken curve of predicted sunspot extrapolation and the warm and cold peaks of temperature departure following 1977 are noted briefly below.

The following features of Figure 1 merit attention and explanatory comment:

1. The prevalence of extreme coldness (and wetness) in middle latitudes (strong LLZ circulation) during prolonged periods of very low sunspot activity, notably the Maunder Minimum (1640-1710), and apparently likewise during the similar Sporer Minimum about 180 years earlier. These two periods constitute the backbone of the Little Ice Age, a period of active regeneration and growth of glaciers in middle latitudes. Ten thousand years of a climate no more severe than that of the Maunder Minimum would bring the northern hemisphere under an ice sheet like that of the Wurm (Wisconsin) glacial epoch.

LLZ climates less extreme than that of the Maunder Minimum, corresponding to less extremely low levels of sunspot activity, occurred during the first 25 years of the 80-year secular cycle starting in 1795, and the first 40 years of the 100-year cycle starting in 1875. A similar trend to cooler and wetter conditions in middle latitudes started in the late 1950's, exactly analogous to that in the 1770's, each time at the very active sunspot peak late in the 100-year cycle. This is the cooling trend frequently attributed to increased particulate matter in the atmosphere (Bryson, 1974). This trend was accurately predicted by Willett (1951) by solar analogy well in advance, to moderate slightly in the early 70's, and to continue to even lower extremes in the 80's and 90's like the analog period. Also accurately forecast by Willett (1955), as part of the predicted LLZ circulation pattern, was an abrupt decrease of severe hurricanes on the middle and north Atlantic coast of the U. S. in the 60's, to continue for the rest of the century (see 3 below).

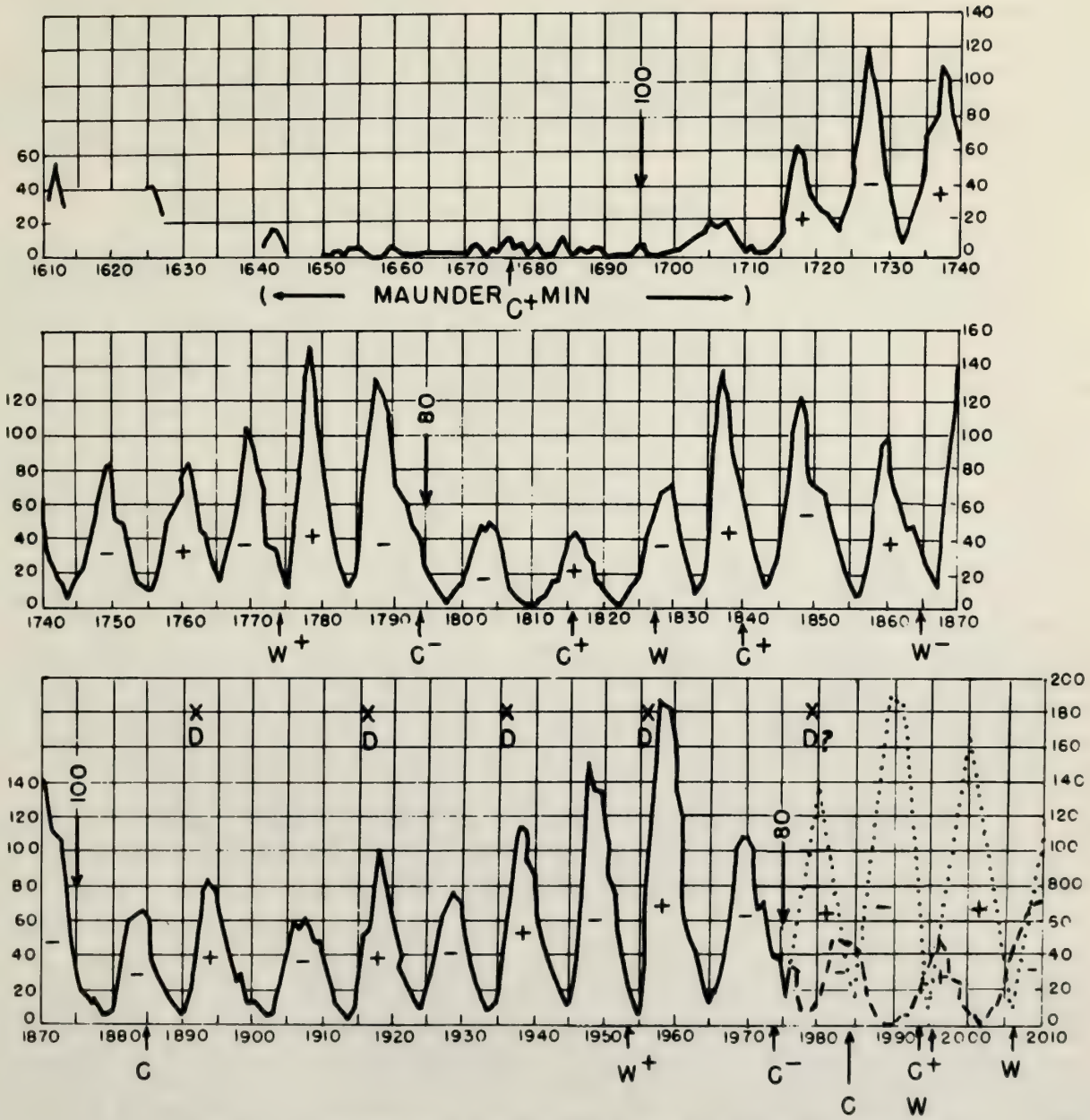


FIG. 1. SUNSPOT NUMBER AND CLIMATIC RECORD

2. Rising temperatures in middle latitudes (HLZ pattern) occurring during the period of most active increase of sunspots in the middle or later part of the secular cycles. Notably peak temperatures, the warmest since the Little Ice Age, occurred about 20 years before the end of each of the 100-year cycles, in each case some 4 or 5 years before the highest sunspot maximum since long before the Little Ice Age, warmer in the recent cycle of higher sunspot activity. In the 80-year cycle there were two equal sunspot peaks somewhat lower in number, one in the middle and one at the end of the cycle, preceded in each case by peak warmth correspondingly less extreme. The rising trend of temperature accompanying the rapid rise of sunspot activity following 1920 is that frequently attributed to CO_2 (Bryson 1974).

3. Dichotomy of the current sunspot trend (Figure 1 and Table 1).

The prediction by Willett (1978) in early 1977 of further intensification of the LLZ pattern beyond 1980 (peak of wetness and coldness in lower middle latitudes to occur in the 90's - Figure 1) was based on the assumption that sunspot activity as suggested by the heavy dashed line would continue analogously to that at the end of the 100-year cycle 180 years before. The upper line of C and W designations at the end of Figure 1 are taken from the analogous period.

Even by early 1977 it was apparent that sunspot activity was on a trend unprecedented in the early part of a secular cycle. After a record high minimum in 1976 (average RSS 12.5) the number has turned sharply upward towards a predicted strong positive maximum by the end of 1979 (light dotted curve in Figure 1). This trend is at complete variance with the marked sunspot inactivity, long 11-year cycles with low maxima and very low minima which initiated not only the analog 80-year cycle in 1795, but also the two 100-year cycles in 1695 and 1875. Is this sudden burst of sunspot activity merely a temporary aberration, or does it presage a return to the high activity and short 11-year cycles pertaining to the later active half of the two last 100-year cycles? The second alternative is suggested by the light dotted curve which portrays 1975 as a mirror point from which to retrace recent high sunspot activity with the normal reversal of the solar magnetic polarity of the successive 11-year cycles.

The solar climatic sequence suggested by the light dotted sunspot curve would radically alter the climatic predictions based on the early 19th century analog. It would call for a brief cold wet (LLZ) period in middle latitudes in the mid 80's, followed by a return to markedly warm dry (HLZ) conditions by the early 90's (at the time indicated to be of most severe coldness by the analog prediction), and a period of severe climatic stress (Section 2) by the late 90's. In this connection it should be noted that the last several years have been quite stressful climatically as required by a strong positive sunspot max in 1979-80. At any rate it is to be expected that the current tangent on which sunspot activity appears to be taking off, if long continued, will play havoc with the analog solar climatic predictions.

B. Tentative Suggestions as to Solar Explanation of Observed Relationships

There are three features of the observed long-term secular solar climatic relationships presented in Figure 1 of significance for this explanation by variable solar activity, namely:

1. In the long secular cycles by far the most statistically significant changes of temperature (and probably also of rainfall) occur in lower latitudes (25^{o}-35^{o}), during the summer season and in interior continental locations (predominantly continental as opposed to maritime climate), Willett, 1965a.

2. The periods of greatest coolness and wetness (LLZ climate) tend to coincide uniformly with the periods of lowest sunspot activity, but broad zonal warmth and dryness (HLZ climate) tends definitely to precede the periods of highest sunspot activity in the secular cycle, to coincide more with the period of most rapid rise of such activity from the quiet to the active part of the cycle.

3. The LLZ climatic patterns during the quiet portion of the secular cycle are more uniform and steady in middle latitudes with less short term fluctuation and geographical contrast than occurs in the HLZ patterns going into the active half of the cycle.

In the light of the above observational facts we may venture a few speculations as to how the sun may do it, as follows:

1. Prolonged periods of quiet sun must be periods of little solar wind or of high frequency u.v., whereas the black body radiation, including the low frequency u.v., retain full intensity or may even be enhanced by the clearness of the solar atmosphere (low activity of chromospheric eruptions).

2. The effective solar emanations must act, either directly or indirectly, to produce relative heating of the troposphere in subtropical latitudes and cooling in lower middle latitudes during long periods of very low sunspot activity, and the reverse during periods of strongly increasing sunspot activity.

3. The action of the effective solar emanations during the phase of the secular cycle of rapidly increasing sunspot number to increase the latitudinal gradient of temperature between lower middle latitudes and the subtropics terminates and apparently reverses well before solar activity reaches its peak.

In the light of these facts it might be suggested that the quiet sun permits a cooler atmosphere in the higher latitudes, probably by the strong reduction of outbursts of high frequency u.v. and of corpuscular radiation, hence the reduction of atmospheric ozone (particularly in winter) and of high level condensation nuclei (ci cloudiness). In addition, the elimination of strong corpuscular invasions (strong mid-latitude auroral activity) permits the CPCV to continue undisturbed without breakdown into a meridional

cellular pattern (see Section 2). On the other hand it is very interesting to note, using Feynman and Crooker's (1978) geomagnetic activity index for the strength of the solar wind, that the curve of hemispheric warming of the first half of the 20th century as given by Willett and Prohaska (1977) paralleled almost exactly their curve of the increase of the solar wind, rising slowly during the earlier decades, then more steeply to a pronounced peak in the early 50's, and then falling sharply during the following decade. This suggests an important indirect effect of the solar wind on the Greenhouse effectiveness of the earth's atmosphere from mid-latitudes poleward, perhaps through ozone or high tropospheric cloudiness (through condensation nuclei).

2.2 Short Term Changes of the Zonal Patterns

The short term climatic changes range in time period from those associated with successive phases of the DSS cycle through the quasibiennial year-to-year fluctuations of the seasonal climatic anomaly patterns within one phase of the DSS cycle, down to the monthly and sometimes even weekly sudden burst changes of the general circulation and attendant climatic pattern. The basic zonal patterns of circulation and climate HLZ and LLZ, may fluctuate in any period from the longest secular to the weekly sudden burst, but the meridional patterns treated in Section 2 have no significant association with the long secular cycles, but they do with all of the shorter periodicities from the DSS cycle to the sudden burst changes (sudden stratospheric warmings).

The basic zonal patterns of cirulation and climate, HLZ and LLZ, are similar in shape whether they are long term secular or the weekly very short term, but the latter, being single events, can be much sharper and more abrupt than the long term, which are statistical averages of a number of short term events. Hence the short term may be more illuminative of physical cause than the long term, so that synoptic and physical aspects of the short term fluctuations are combined in the following discussion.

Figure 2 presents the mean of the DSS cycle as it averaged from 1870-1970, approximately the years of the last 100-year secular cycle. The sunspot number graph is a smoothed curve drawn through the eight average phase numbers. The individual calendar years (1871-1981) entering into each phase of the DSS cycle, with an indication of the current dichotomy, are listed in Table 1.

In Figure 2 the average cycle year period of each of the eight phases is indicated across the middle of the graph. Across the top of the figure is indicated the tendency to GC pattern predominance during the cycle, and also the period of peak warmth W or coldness C, as well as of dryness (p-) or wetness (p+) of the mid-latitude climate.

The following synoptic features of the DSS cycle and even shorter term fluctuations of the zonal circulation (CPCV) from year to year, month to month and even week to week (see Section 2)are possibly significant for the explanation of the physical causation of fluctuations of the hemispheric zonal circulation (CPCV).

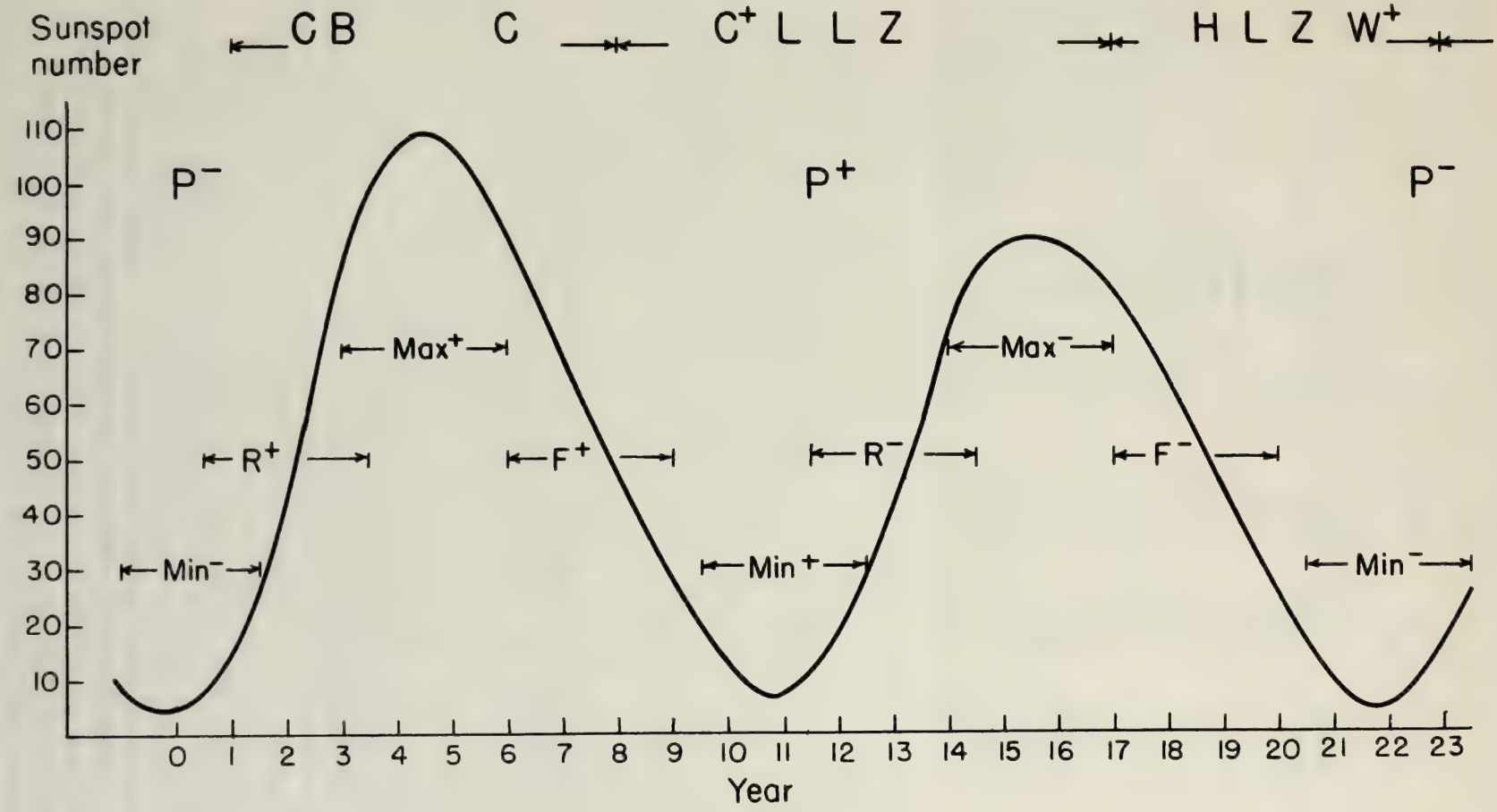


Fig. 2. The Double Sunspot Cycle as averaged 1870 – 1970

Eight Phases

Major (positive) half of cycle

1. R^+ Three years of most rapid increase
2. Max^+ Major (positive) maximum (three years)
3. F^+ Three years of most rapid decrease
4. Min^+ Following minimum (three years)

Minor (negative) half of cycle

5. R^- Three years of most rapid increase
6. Max^- Minor (negative) maximum (three years)
7. F^- Three years of most rapid decrease
8. Min^- Following minimum (three years)

Table 1. Classification of Years 1871-1981
by Phases of Double Sunspot-Cycle.

R^+	Max^+	F^+	Min^+	R^-	Max^-	F^-	Min^-	
1890	1871	1872	1877	1879	1882	1885	1888	
1891	1872	1873	1878	1880	1883	1886	1889	
1892	1892	1874	1879	1881	1884	1887	1890	
1915	1893	1895	1900	1903	1905	1908	1911	
1916	1894	1896	1901	1904	1906	1909	1912	
1917	1917	1897	1902	1905	1907	1910	1913	
1935	1918	1919	1922	1924	1927	1930	1932	
1936	1919	1920	1923	1925	1928	1931	1933	
1937	1937	1921	1924	1926	1929	1932	1934	
1955	1938	1940	1942	1945	1947	1950	1952	
1956	1939	1941	1943	1946	1948	1951	1953	
1957	1957	1942	1944	1947	1949	1952	1954	
1977	1958	1960	1963	1966	1968	1971	1975	1978 } from
1978	1959	1961	1964	1967	1969	1972	1976	1979 } secular
1979	1979	1962	1965	1968	1970	1973	1977	1980 } analog
	1980							
	1981							

1. Note in Figure 2 that whereas the peak of the LLZ cold and wet circulation pattern (expanded CPCV) is centered on the Min^+ phase of the DSS cycle, in line with the long term high preference of LLZ patterns for the periods of very low solar activity, the peak of the HLZ warmth and dryness is centered on the Min^- phase of the cycle, even lower in number than the Min^+ phase, at complete variance with the long term secular cycle record. The warmth and dryness of the Min^- ending in the late R^+ phase is statistically the most significant climatic anomaly of the DSS solar-climatic cycle. All of the major droughts since 1890 between the Rockies and the Mississippi Valley followed this pattern. The LLZ coolness and wetness of the Min^+ and R^- phases are the second most significant statistical fact of the cycle.

In this connection it may be noted that the reversal of the solar magnetic field is a known fact of the DSS cycle only during the last 100-year secular cycle, but there is no observational confirmation even of the existence of a DSS cycle during the previous 80-year secular cycle or earlier. However, the reversal of the solar magnetic field and of the sunspot pair magnetic fields certainly affect strongly the magnetic beaming of solar corpuscular radiation, i.e., the charged particle solar wind, towards the earth. That this is indeed a fact is confirmed by the observation that geomagnetic disturbance (C_i) which reaches significantly its highest peak level in the DSS cycle at Max^+ falls very sharply to much its lowest level of the cycle at Min^-. From there it recovers only to half of its Max^+ peak level by Max^-, but continues upward to a peak at F^- significantly below that of Max^+, and then to a bottom at Min^- much higher than that at Min^+ (Willett 1960b). More and more bits of evidence are pointing to the solar wind as a primary disturbing influence in fluctuations of the temperature and GC of our troposphere and lower stratosphere.

2. There is a normal seasonal sequence of the hemispheric zonal circulation (CPCV), although on occasion this normal sequence may be rudely interrupted by a complete breakdown or even reversal of the CPCV (Willett 1968). Normally a strong HLZ circulation, strongest in the lower troposphere, develops rapidly during the middle and late autumn, and trends towards a peak of LLZ (and JS) by mid or late January. Usually a sudden breakdown of the strong LLZ circulation and JS occurs in late winter. The CPCV rarely redevelops normal winter strength again during the spring and summer.

It may be remarked that the steady strengthening and equatorward expansion of the CPCV which is typical of autumn going into midwinter parallels the normal seasonal progression of the net loss of heat to space by the radiational heat balance, i.e., periods of strong LLZ circulation and CPCV are periods of conditions favorable to the relative cooling of the atmosphere in higher latitudes. Furthermore the tendency to sudden breakdown of the CPCV during the winter approaching March parallels the approach of the vernal equinox and peak geomagnetic disturbance (the solar wind again). This tendency is not present to the same degree at all during the southern hemisphere winter when the level of geomagnetic disturbance (solar wind invasion) is much lower (Willett 1968).

3. The climatic patterns which typefy respective phases of the DSS cycle are by no means always present nor do they represent averages, but rather a higher than average frequency of occurrence or intensity. There is a statistically significant tendency for such representative patterns to occur on alternate years, like the drought years 34-36, 54-56, 76-78, etc. This may be an expression of the quasi-biennial cycle, which probably is of solar origin, but this fact requires that solar-climatic seasonal prediction must at present, in our present lack of understanding of physical mechanisms, be based on a selection of analog years within the prevailing DSS cycle phase.

4. Major fluctuations of the hemispheric zonal wind system, or CPCV, sometimes referred to as the index cycle (index of the zonal westerlies), in a period of one to two months, is usually superposed on the normal seasonal sequence. Several features of this index cycle are instructive as to the behavior of the CPCV, e.g.:

a. The sequence of change is always the same as the seasonal, i.e., HLZ → LLZ → zonal breakdown → HLZ, probably to some extent an autogenetic system, whereas the phase preference sequence of the DSS cycle (HLZ → breakdown → LLZ → HLZ) is entirely imposed on the system from outside by the sequence of activity of the solar cycle.

b. The generation of the strongly zonal circulation, HLZ → LLZ, from an initial relatively resting or chaotic state, is a slow process requiring some weeks of undisturbed action by the radiational heat balance process, whereas the breakdown of the strong LLZ circulation usually occurs quite suddenly by a disturbance of the thermal, hence kinetic, symmetry of the CPCV.

c. There is no tendency to conservation of angular momentum in expansion or contraction of the CPCV, but rather the contrary, i.e., we note at the 500-mb level (Willett 1960, for 5-day means)

1) High negative correlation, 500-mb JS/latitude
2) Very high positive correlation, as required hydrostatically, 500-mb JS/Poleward gradient of temperature
3) Slightly negative correlation, 500-mb JS/sea level ZW
4) Predominantly negative correlation, 500-mb-JS/poleward transport of momentum at 30° and at 50°N.

All of this indicates strongly that the CPCV in its short term fluctuations is driven by the solenoid field in middle latitudes, i.e., by relative coldness in higher latitudes, not by momentum transport from the Maxwell cells in the lower latitudes. This probably is not true of the long term secular fluctuations.

d. Whereas the growth and expansion of the CPCV is a gradual process involving relative cooling of the atmosphere in the higher latitudes by radiational processes over a period of weeks without disturbance from a quiet sun, the breakdown of the strong LLZ circulation, the breakdown of the CPCV is a sudden process which may be accomplished in two or three days following a sudden outburst of solar activity, in extreme cases following strong geomagnetic disturbance, auroral and/or ionospheric disturbance, and quite typically a sudden stratospheric warming. The following facts suggest that a strong solar wind impulse is the primary motivating, if not direct, cause:

1) Sudden outbreaks of a quiet sun, along with sudden stratospheric warmings and the geomagnetic disturbance and zonal circulation breakdowns do not occur on Min^- or even Min^+ phase years (Labitzke, 1964). Such events are strongest during R and F years, particularly during R^+ years when periods of solar quiet and strong action alternate sharply (Willett 1968, Hanzlik 1930, 1931). Best guess is that sudden localized solar wind penetration of the upper atmosphere, as indicated by limited zones of auroral activity, disturbs directly the thermal, hence the isobaric, symmetry of the CPCV.

2) Roberts (1971) and his collaborators have long pointed out that sudden geomagnetic disturbance tends to be followed by deepening of the cold season trough at the 300-mb level over North America with the movement inland on the north Pacific coast of the next migratory trough. This undoubtedly is accompanied by ridging over the Pacific Ocean to the west, though Roberts does not state that, but this represents in the Pacific-North American sector the expected tendency toward breakdown of the zonal circulation. Furthermore, this phenomenon was particularly strong during the $Min^- \rightarrow R^+$ years in the 50's when first discovered, and weaker during subsequent years, as might be expected.

3) Major seasonal differences between the zonal structure of the arctic and antarctic circumpolar circulations parallel major seasonal differences in the pattern of geomagnetic disturbance, of auroral activity, of atmospheric ozone and of temperature in a manner entirely consistent with a solar wind explanation (Willett, 1968).

3. MERIDIONAL PATTERNS OF CHANGE OF THE GC AND CLIMATE

3.1 Synoptic Features

In synoptic terms it is the meridional, as opposed to the zonal, component of the GC, that controls the meridional component of the climatic pattern, just as the zonal component of the GC controls the zonal climatic pattern. This meridional component is seen most clearly in the upper level trough and ridge standing (Rossby) wave pattern, which rides the JS (zonal westerlies) of middle latitudes.

Fluctuations of this upper level wave pattern in wave length (or number), amplitude and meridional orientation define the fluctuations of the meridional component of the climatic pattern, which contribute equally with the zonal fluctuations to short term changes of climate (months, seasons and years), but are no part of the long term secular trends, except as they may be evident in the superposed DSS cycle when it is particularly strong.

When the climatic pattern is strongly zonal, either HLZ or LLZ, the wave pattern is small in amplitude and long in wavelength and the meridional climatic pattern is weak, i.e., the east-west contrasts are small and unimportant. However, as the wave pattern becomes larger in number and amplitude, the east-west climatic contrasts become sharper and larger, and the zonal weaker, i.e., the GC and climatic patterns trend from zonal to meridional, or the zonal pressure and wind belts break down progressively into north-south oriented cells. In the extreme case we no longer have a zonal circulation with its west to east storm tracks in middle latitudes, but rather a completely meridional circulation of northerly and southerly wind currents of polar and tropical air masses and strong fixed north-south oriented high and low pressure cells which block the normal eastward movement of migratory highs and lows, the so-called blocking pattern of the GC or climatic stress (CS) pattern of climate. This is the third basic pattern of the GC and climate, the one into which the HLZ and LLZ patterns break down when they become chaotic.

The climatic stress pattern is the one of greatest extremes of climate, of much more adverse climatic conditions even than the LLZ. It is not at all favorable to glaciation, because the tendency is to hot dry summers and cold dry winters over continents, hence it leaves little geological record for identification by epochs, but during historical times it has produced most human suffering and starvation. The Little Ice Age was a period of very benevolent climate for agriculture and many other human activities.

The location of heat and drought vs. warm and wet in summer, or severe cold vs. warm rain in winter, depends on the meridional orientation of the trough-ridge pattern. In the U. S. the CS pattern in summer is typically hot-dry in the midwest, and warm-wet (tropical disturbances) on the east coast (1934-1936, 1954-1956). In winter it is cold-dry in the midwest, northeast storms on the east coast. A westward displacement of the pattern has given severe cold in the far west, record floods in the Ohio-Mississippi Valley (1936-37), and an eastward displacement record cold in the northeast (1933-34).

We note from Figure 2 that the cellular blocking (CS) pattern tends to be centered squarely on the R^+ phase of the DSS cycle, although such patterns, representing the complete breakdown of the zonal patterns as discussed in Section 1, extend their influence through the Max^+ and into the F^+ phase. But all of the disastrously severe and prolonged CS periods have been in the R^+ phase (note dates in Table 1 above in reference to Figure 2). This is not meant to imply that this pattern may not arise during any phase of the DSS cycle, but merely that it develops more strongly, more frequently and of longer duration during or close to the R^+ phase.

Two additional synoptic features of the CS pattern, of some predictive significance, should be noted:

1. The statistically significant tendency for the DSS cycle phase extremes of weather to occur at two, occasionally 3-year intervals. This is true not only of extreme climatic stress conditions, e.g., see second paragraph , but also of HLZ or LLZ extremes. This probably is part of the significant hemispheric tendency for climatic autocorrelations to be negative at one year's lag and positive at two.

2. A significant tendency for the upper level standing wave pattern, i.e., the meridional component of the climatic pattern, to shift westward, never eastward, from the calendar season one year to the same calendar season the next year. This progressive westward displacement of a meridional sector of severe weather has been known to continue for as long as five years in sequence, e.g., a very severe winter over northern Europe 1946-47, east coast of the U.S. 1947-48, central U.S. 1948-49, along and east of our west coast 1949-50, and along an off our west coast 1950-51.

3.2 The Solar Explanation of Cellular Blocking

The sudden breakdown of a strong zonal circulation pattern into a cellular blocking (CS) pattern is probably prognostically the most significant large-scale long-range weather event. In Section 1 in the discussion of the breakdown of the zonal circulation it was pointed out how observations of Hanzlik, Duel and Duel, Willett, Labitzke and Roberts all implicate sudden solar wind as the primary direct cause of this phenomenon, including the sudden stratospheric warming which accompanies major occurrences.

The alternative explanation usually proposed is that the augmented and expanded CPCV eventually reaches a state of dynamic instability, imposed perhaps by continental or orographic barriers, and goes to pieces, the sudden stratospheric warming being generated dynamically, by forced subsidence, from the kinetic energy of the CPCV. However, this explanation offers no explanation of the following facts:

1. That sometimes a strong expanded CPCV continues undisturbed for weeks or months, other times is quickly terminated.

2. That the strongest and most frequent development of cellular blocking occurs during that phase of the DSS cycle when solar wind disturbance (geomagnetic activity) is strongest.

3. The very high coincidence between strong blocking (including sudden stratospheric warming) with strong bursts of solar geomagnetic disturbance.

4. That the thermal energy represented by a major stratospheric warming (such as that of February 1952) is several times the total KE of the initial CPCV (Willett 1968).

If there is any point in the whole gamut of solar climatic relationships where solar activity can be clearly predictive of major long-range weather trends, it is in the occasional prediction of the breakdown of a strong zonal into a severe CS pattern. The direct asymmetric supply by the solar wind of the thermal energy to the upper atmosphere appears to be the essential factor.

Limitation of space precludes any further speculation as to possible explanation of solar climatic physical linkage, but a well directed program of research certainly can come up with some answers. In conclusion a few suggestions are offered as to the direction that such a program should take.

Only when we have identified the specific manifestations of variable solar activity that affect the temperature and circulation of the atmosphere and can explain the physical linkage by which they do it will we be in a position to take full advantage of solar-weather or solar-climatic relationships for operational prediction.

To accomplish this we must begin with a thorough statistical analysis of the monthly mean departure patterns of atmospheric temperature and pressure in relation to the monthly mean departures of a number of indices of variable solar activity carefully selected as best representative of each of the manifestations of variable solar activity deemed capable, directly or indirectly, of affecting the state of the atmosphere, in order to pinpoint those aspects of solar variation which <u>do</u> affect the atmosphere significantly, and just where.

When the disturbing solar influences are identified to the best of our ability, we should select specific instances of strong outburst or high level action of each disturbing factor for a detailed synoptic analysis of atmospheric temperature and pressure, both at the ground and as high up as reliable observational data are obtainable, to study the time and space of atmospheric response to each disturbing influence.

Only then will we be in best position to explain the physical linkage from variable solar disturbance to direct or indirect atmospheric or weather response. And only when that is done will we be able to develop most advantageously long-range weather prediction models.

REFERENCES

Bruckner, E. (1890): Klima schwankungen seit 1700. Geographische Abhandlungen, Bd. IV, Heft 2, 1890 325 pp.

Bryson, R. A. (1974): A perspective on climatic change. Science 184 (4138): 753-760.

Duell, B. and Duell, G. (1948): The behavior of barometric pressure during and after solar particle invasions and solar ultraviolet invasions. Smithsonian Miscellaneous Collection, Vol. 110, No. 8, 34 pp.

Eddy, J. A. (1975): A new look at solar-terrestrial relationships. High Altitude Observatory, NCAR, Boulder, Co. 80303.

Feynman, J. and Crooker, N. U. (1978): The solar wind at the turn of the century. Nature, Vol. 275, October 19, 1978, p. 626.

Hanzlik, S. (1930, 1931): Der Luftdruckeffekt der Sonnenfleckenperiode. Mitteilung I and Mitteilung II, V28 and V29, Gerlands Beitrager zur Geophysik, pp. 114-125 and pp. 138-55.

Labitzke, K. (1964): On the mutual relation between stratosphere and troposphere during periods of stratospheric warmings in winter. Jour. Appl. Meteor., 4, pp. 91-99.

Rasool, S. I. (1964): The relationship of total atmospheric ozone to the sunspot cycle. J. Geophys. Res., Vol 67, pp. 661-670.

Roberts, W. D. and Olson, R. H. (1971): Study of lower stratospheric circulation over North America following geomagnetic disturbances. Procedings of the IUGG Symposium, Solar Corpuscular Effects on the Troposphere and Stratosphere, Moscow, August 1971.

Sleeper, H. P. Jr. (1972): Planetary resonances, bi-stable oscillation modes, and solar activity cycles. NASA Contractor Report - 2035, prepared by Northrop Service, Inc., Huntsville, Ala. 35807.

Willett, H. C. (1949): Solar variability as a factor influctuations of climate during geological time, from Glaciers and Climate. Geografiska Annaler, 1949 H 1-2, Stockholm, pp. 295-315.

Willett, H. C. (1950): Temperature trends of the past century. Centennial Proc. Roy. Meteor. Soc., London, 1950.

Willett, H. C. (1951): Extrapolation of sunspot-climate relationships. Journal of Meteorology, 8 (1), February, 1951.

Willett, H. C. (1955): Hurricanes of the Gulf and Atlantic coast of the United States. A report prepared for the Interregional Insurance Conference of New York, 1955, 63 pp.

Willett, H. C. (1960a): The statistical behavior of the general circulation of the northern hemisphere, October 1945 - March 1952. Scientific Report of the U. S. Weather Bureau - MIT Extended Forecasting Project, Cambridge, Mass., September 1, 1960.

Willett, H. C. and Prohaska, J. T. (1960b): Long-term indices of solar activity. Scientific Report No. 1, NSF Grant 5931, September 30, 1960, 39 pp.

Willett, H. C. (1965a): Solar-climatic relationships in the light of standardized climatic data. Jour. of the Atmos. Sciences, Vol. 22 No. 2, pp. 120-136, March 1965.

Willett, H. C. and Prohaska, J. T. (1965b): Further evidence of sunspot-ozone relationships. Jour. of Atmos. Sci., Vol. 22, No. 5, September 1965, pp. 493-497.

Willett, H. C. (1968): Remarks on the seasonal changes of temperature and of ozone in the arctic and the antarctic stratospheres. Jour. Atmos. Sci. Vol. 25, No. 3, May 1968, pp. 341-360.

Willett, H. C. and Prohaska, J. T. (1977): Patterns, possible causes and predictive significance of recent climatic trends of the northern hemisphere. Solar Climatic Research Institute, Inc., October 1977.

Willett, H. C. (1978): Prediction of climatic trends. Solar Climatic Research Institute, Inc., Cambridge, Mass., January 1978.

WEATHER AND CLIMATE PREDICTIONS IN THE NORTHERN HEMISPHERE BASED ON SOLAR - TERRESTRIAL RELATIONS

V. Bucha
Geophysical Institute, CSAS
141 31 Praha 4, Boční II, Czechoslovakia

Weather forecasts for periods of 14 - 28 days, particularly as regards predicting increased or decreased temperatures, sudden penetrations of Arctic air into Europe, occurrence of more substantial precipitation, generation of zonal flow and enhanced cyclogenesis in the region of the Atlantic, in Europe and part of North America, may be made by applying the proposed mechanism of relations between processes on the Sun, variations of geomagnetic activity and the change in distribution of temperature and pressure fields in the auroral oval and the north polar cap (Bucha 1976 a,b, 1977, 1978, 1979).

1. INTRODUCTION

The process of forecasting itself will be demonstrated on the possible mechanism of solar-terrestrial relations and on the development of meteorological situations in the Northern Hemisphere in the winter of 1974-75, beginning with the processes on the Sun and ending with a marked increase of temperature in Central Europe, which was reflected as the final consequence of the sequence of events that took place. Similar regularities will be demonstrated not only on six examples from 1974-75, but also on others, which likewise occurred in the winter of 1975-76, 1976-77 (four cases) and 1962-63 (six cases). An example of the forecast is given in the chapter 5.

The probable causes of long-range changes of climate will also be given, as well as an outline of the procedure for estimating the development of the climate from the determined relations as regards changes over an interval of 1 to 10^3 years, using the proposed hypothesis of the causes of alternation of periods of several years, climatically favourable and unfavourable, cold and warm winters in Europe and Alaska, the occurrence of minor glacial periods, the generation of glaciation and origin of interglacial periods.

2. ASSOCIATIONS BETWEEN GEOMAGNETIC AND METEOROLOGICAL PROCESSES, MECHANISM OF SOLAR-TERRESTRIAL RELATIONS

The comparison of certain changes of climate and temperature in the interval 12 to 10 thousand years ago (when the last period of glaciation terminated) with the marked changes in the positions of the geomagnetic pole, which had moved from the Pacific to the North American continent, displays striking agreement (Fig. 1) (Bucha 1976a, 1977b). It was first necessary to investigate whether there is an association between the position of the north geomagnetic pole (centre of the auroral oval) and its role in forming the climate and weather. As regards the short-term changes, we found a nearly unique dependence between the C_i-indices, characterizing geomagnetic activity, and the temperature variations (averages for the four winter months) in Prague over the last 25 years (Fig. 2). After a sudden increase in geomagnetic activity (indicating the corpuscular radiation), represented by the daily values of the K_p-indices, we observe a relatively sudden decrease of atmospheric pressure over the geomagnetic pole or in its neighbourhood at the 500 mb level, particularly during winter (Fig. 3a,b - 12 cases, Bucha 1976a).

If we look at the graphs representing gross agricultural production in some countries (Figs. 4abc), in years when an increased level of geo - magnetic activity was recorded in the month of May (representing the main critical period for the growth of cereals in Central Europe and Canada), the gross agricultural production will be seen to be higher on the average (e.g. in 1956-60, 1967-68, 1973-74). On the other hand, when the geomagnetic activity was low, there was a pronounced decrease in production (e.g. in 1954, 1962-65, 1970, 1972) (Bucha 1976b) (Fig.4abc). For Czechoslovakia a correlation coefficient was found 0.78.

As implied by the results of spectral analysis, applied to a set of diurnal data for a 4-year period (1962-65), Fig.5a displays statistically significant spectral density periods of 13.5, 9 and 6.7 days on the spectral curve of both, the geomagnetic activity represented by K_p-indices and atmospheric pressure over the geomagnetic pole ; this proves the relation between the periodicities, particularly at the time of solar minimum (Bucha 1976b). As an other example we investigated the positive correlations between the increase of geomagnetic activity and the decrease of pressure over the geomagnetic pole ; during the period of November 1962 - February 1963 (five-day gliding average), a correlation coefficient was found 0.56 under a time shift 2 days (Bucha 1978) (Fig.5b).

The results of studying the relations between geomagnetic activity (intensity of corpuscular radiation) and the changes in atmospheric circu - lation have indicated a positive dependence and enable a mechanism to be proposed, which would contribute to the elucidation of the causes of marked changes of the meteorological parameters, particularly the temperature (Fig.5c), pressure and air flow in the region of the auroral oval, over the geomagnetic pole and over the most of the Northern Hemisphere (Bucha 1976-1979).

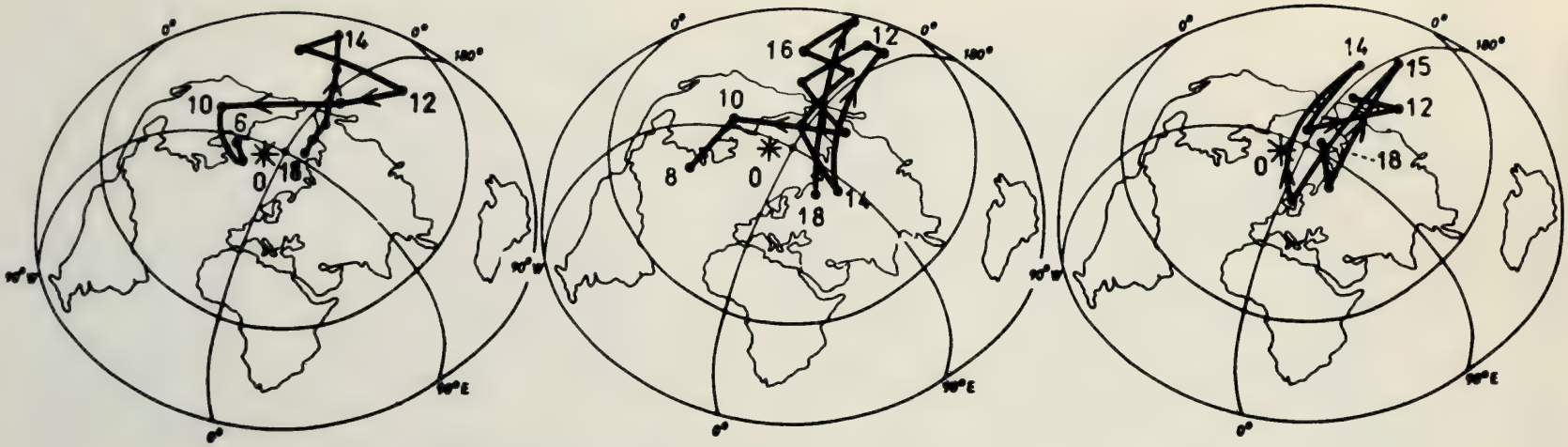


Figure 1. Position of the virtual geomagnetic pole 8 - 17 000 years ago : a) Czechoslovakia, (Bucha 1976a) b) Japan (Yaskawa 1974), c) U.S.A. (Easterbrook, Othberg 1977). ✳indicates the present pole position.

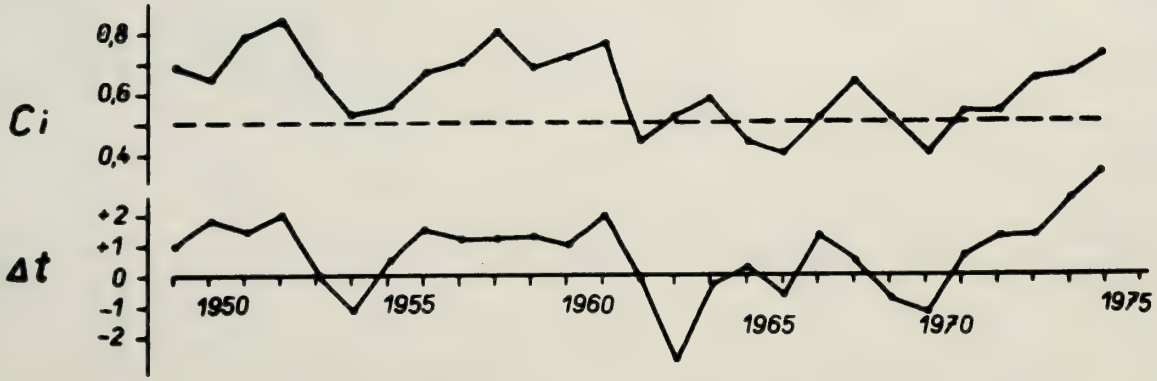


Figure 2. Correlation of geomagnetic activity (Ci-indices) and the deviations of the temperature from the standard in Prague for the months of November-February (mean values) and the period 1949-1975.

The solar-energy flux for meteorological phenomena is $P_{EM} = \pi r_E^2 F(1-A) = 8.9 \times 10^{16}$ W, if we assume the earth to have an albedo A = 0.5, r_E is the radius of the earth, F is the solar constant (Dessler 1974). The solar-wind energy flux strikes the geomagnetic field with a total energy flux P_S, but only less than 1% of it penetrates the geomagnetic field. Then we find that this value of corpuscular and magnetic energy flux $P_c = \pi r_M^2 \left(\frac{1}{2}\rho V_S^2 + \frac{B^2}{2\mu_0}\right) V_S \times 10^{-2} \doteq 5 \times 10^{10}$ W, where r_M is the radius of the magnetosphere, ρ is the mass density of the solar wind, V_S is its velocity, μ_0 is the permeability, and B is the strength of the interplanetary magnetic field. The available corpuscular energy flux is less than one millionth of the solar-electromagnetic energy flux absorbed by the earth.

During an intense magnetic storm, however, the corpuscular energy flux could increase to $P_{c(max)} = 10^{12} \div 10^{14}$ W, which might be enough to use

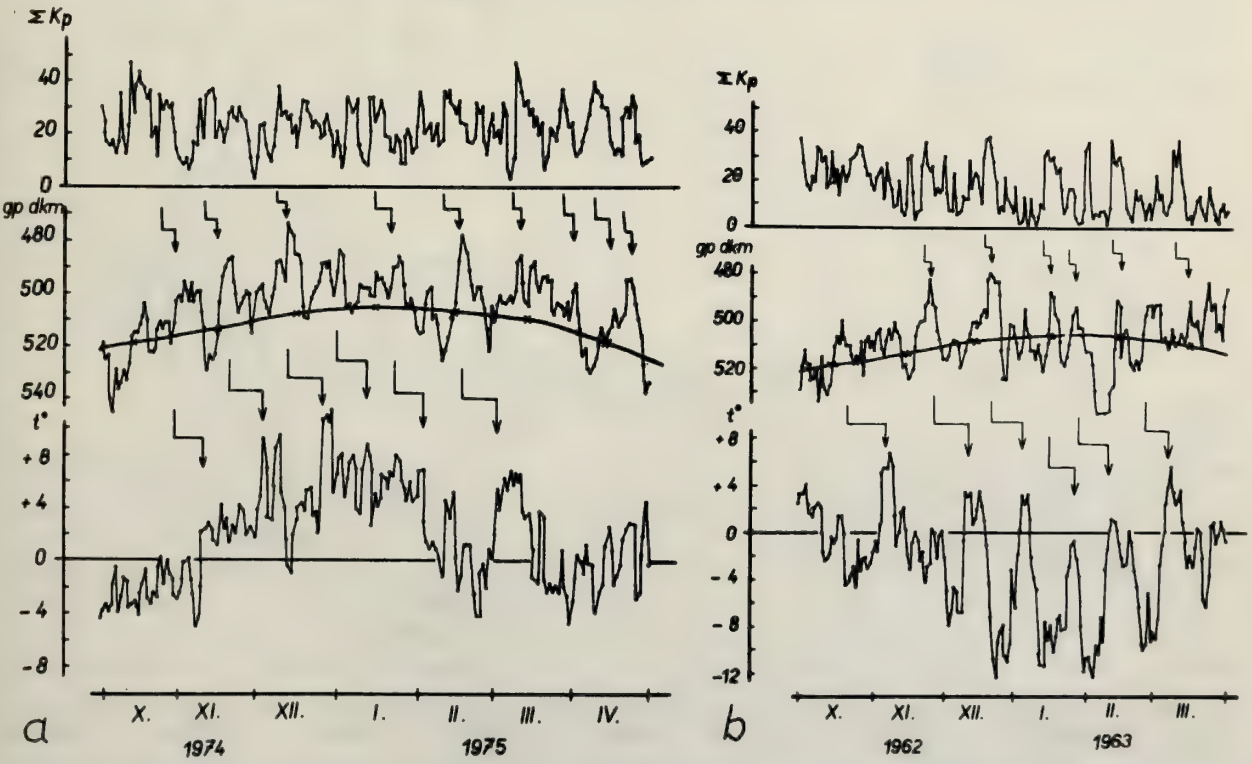


Figure 3a) Changes of the diurnal values of geomagnetic activity, represented by the sums of K_p-indices, daily values of the atmospheric pressure at the 500 mb level over the geomagnetic pole and of temperature deviations from the normal in Prague for the period Oct.1974-April 1975. The arrows indicate the correlation and the time lag between the increase of the K_p-indices, decrease of the pressure over the geomagnetic pole and the increase of temperature in Prague.

3b) Changes for the period Oct.1962-March 1963 ; refer to text in Fig.3a.

this energy as a trigger (Dessler 1974), mainly for the winter hemisphere, where P_{EM} might drop to 6 x 10^{15} W. According to Roberts and Olsson (1973) the energy of a typical rotating system of air U = 5.3 x 10^{17} J for the angular velocity w = 6 x 10^{-5} rad/s is comparable to the energy of a magnetic storm. Thus there appears to be enough power within the magnetosphere to cause such changes in vorticity of the lower atmosphere if the power can be directed and coupled effectively. Let us look for the coupling mechanism (Bucha 1977, 1979).

At the time of occurrence of magnetospheric sub-storms several parallel electric currents, 10^4 - 10^6 A in intensity, may be generated in the region of the auroral oval (Boström 1964). The electric conductivity in the

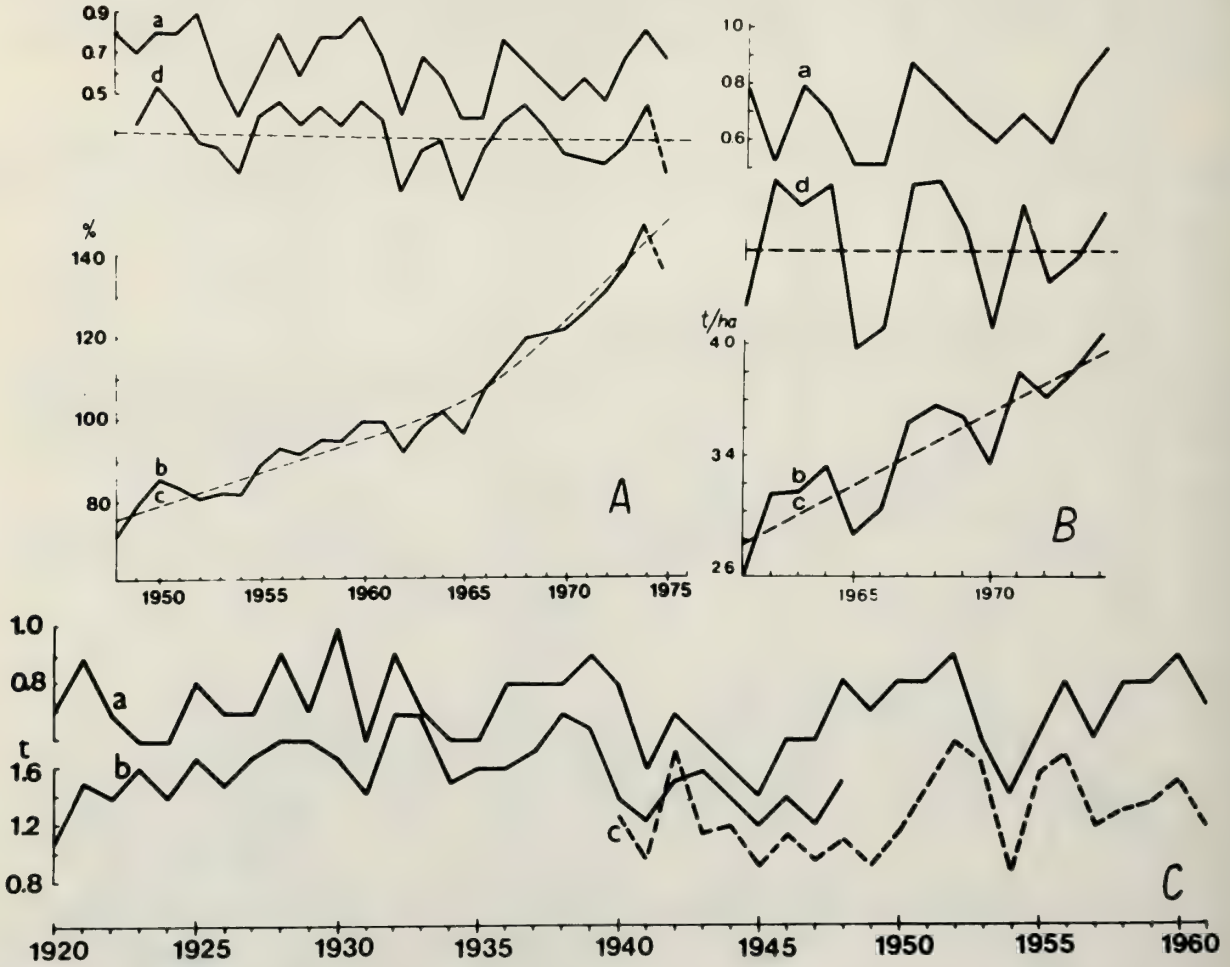


Figure 4a) Dependence of the gross agricultural production in Czechoslovakia on geomagnetic activity. Curve a represents the geomagnetic activity in May, curve b the actual gross agricultural pro - duction, curve c the average gross agricultural production, curve d the deviation of the gross agricultural production from the average. Correlation coefficient 0.78. B. Dependence of the average grain yields on geomagnetic activity in the FRG. C. Dependence of average grain yields on geomagnetic activity (curve a) in Czechoslovakia (curve b) and Canada (curve c).

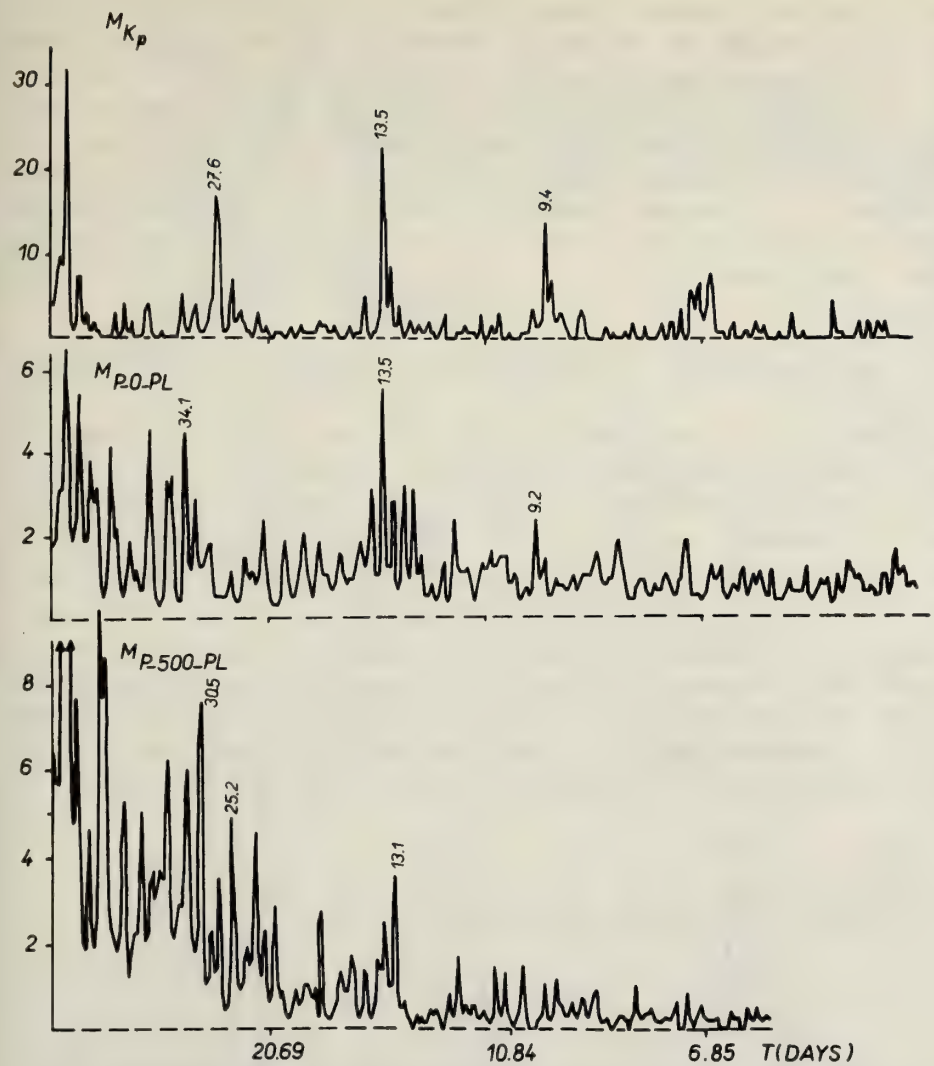


Figure 5a. Spectral function (maximum entropy) of geomagnetic activity M_{K_p}, of the atmo - spheric pressure over the geomagnetic pole at sealevel (M_{P-0-PL}) and at the 500 mb level ($M_{P-500-PL}$) for the period 1962-65. The most pro - nounced coinciding maximum was found for a period of 13.5 days and is evidence of the relation between geomagnetic activity and atmo - spheric pressure over the geomagnetic pole.

auroral oval is markedly increased (by as much as 5 orders of magnitude) (Akasofu 1968) which enables Hall and Pederson currents to be generated. Let us now speculate what the increase of temperature will be inside the auroral oval, as a result of the energy dissipation due to Ohmic losses. The overall energy in the centre of the oval generated as a result of the electric currents flowing within the oval is yielded by the integration (Bucha 1977). Under the assumption that the maximum currents of 10^6 A are considered, we would obtain a temperature increase in the centre of the auroral zone, i.e. over the geomagnetic pole, of 13°C, which corresponds to the anomalous temperatures actually observed at the Earth's surface in the region being considered during the geomagnetic storm (see four cases in Fig. 6 and eight cases in Figs. 7 - 9). As a result of this a low pressure area is generated over the geomagnetic pole and this, as implied by our positive correlations (Figs. 5a,b,c) affects the atmospheric circulation markedly. Even if the initial warming were 0.5 - 3°C only (during a less intensive geomagnetic storm), it seems to represent the first trigger enabling a rapid penetration of the warm air from the oceans into the auroral belt as an after-efect (see Figs. 10a,b and Bucha 1977, 1979).

Due to the energy of air masses coming from the Atlantic and Pacific Oceans to the north, the increase in energy of rotation in the cyclone over the polar cap (close to the geomagnetic pole) in 24 hours is 10^{17} - 10^{18} J. Thus there appears to be enough coupling force to set the whole process in the lower atmosphere in motion, starting in the formation of the cyclone over the geomagnetic pole as a second trigger modifying the direction of the air flow across the Atlantic to Europe (see Figs. 10a,b and twelve cases in Figs. 3a,b). As an after-effect seven cases of a sudden stratospheric warming were observed (see Figs.6 and 7).

3. THE SEQUENCE OF PHENOMENA AS A BASIS FOR PREDICTION TECHNIQUE

Relatively unstable active regions, in particular variable filaments occur at the centre of the solar disc just before the geomagnetic activity increases (Fig.6a,b). A marked increase in corpuscular radiation contributes to the generation of electric currents with intensities of as much as 10^6 A in the auroral region (Fig. 6c). This results in a considerable enhancement of geomagnetic activity (characterized by K_p-indices), as could have been observed, e.g., in October, November and December 1974 (Fig.6d). These severe geomagnetic storms result in sudden changes of the temperature in the auroral oval, as implied by meteorological observations at altitudes of up to 24 km (Fig.6d). Between 24 and 11 km (at the 30 to 200 mb levels) a decrease of average temperatures is observed (Fig.6d) in the region of

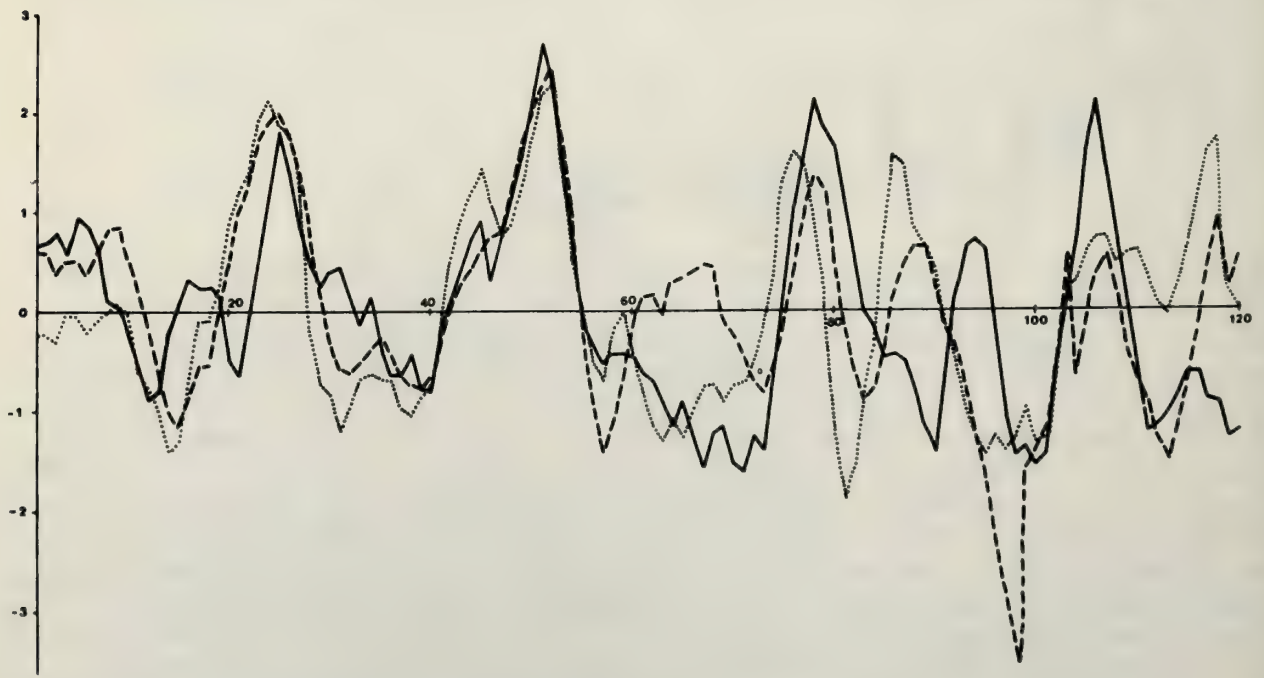


Figure 5b. Correlation between increased geomagnetic activity (———) and decrease of atmospheric pressure over the geomagnetic pole at the 500 mb level (- - - -) and at sea level (.....) for the interval 1 Nov.1962 to 28 Feb.1963, the geomagnetic activity preceding the pressure data by 2 days. Correlation coefficient 0.56.

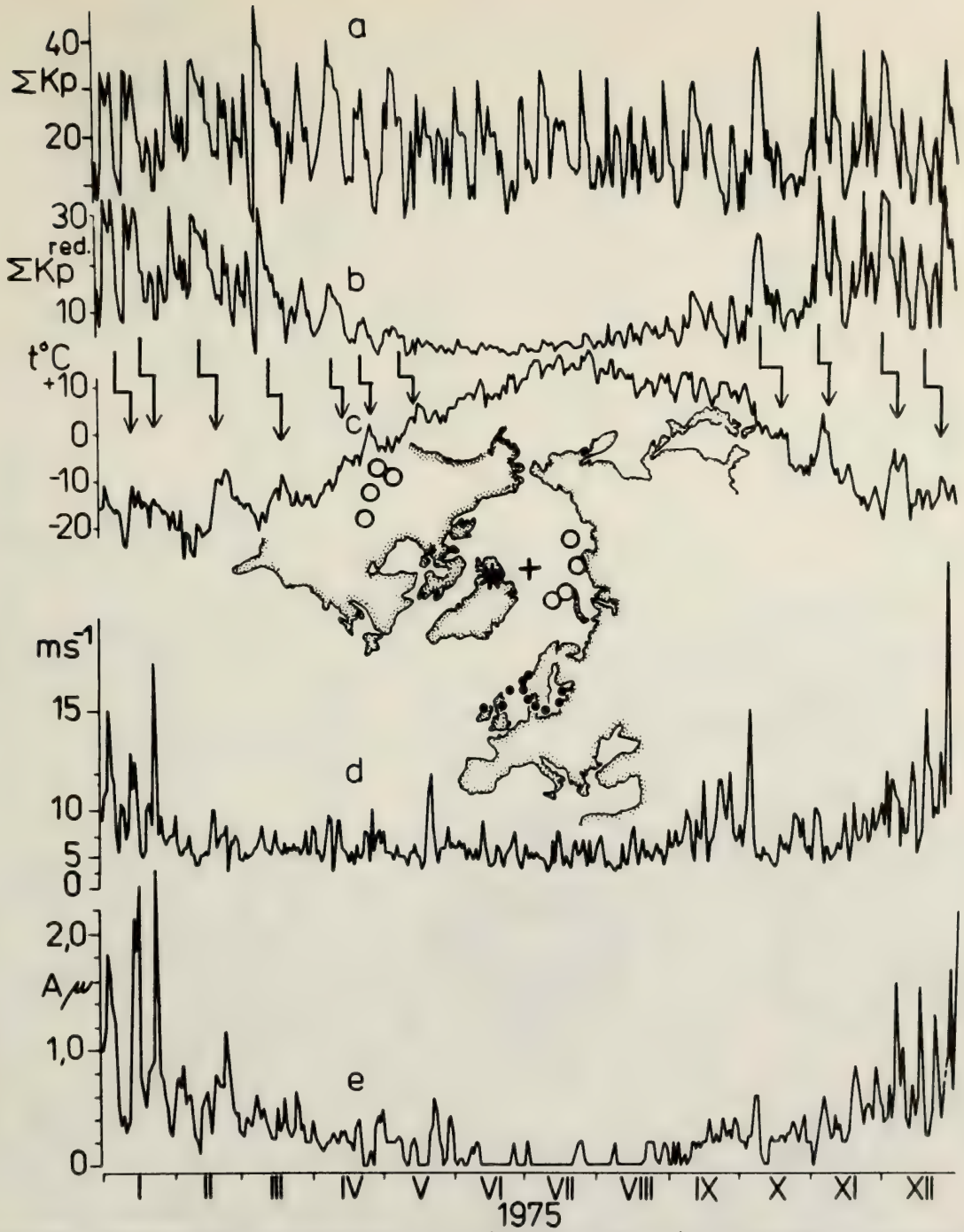


Figure 5c. Geomagnetic activity ΣK_p (1975-curve a), reduced corpuscular energy flux acting on the temperature changes in winter considerably (ΣK_p^{red} - curve b), temperatures along the auroral oval - north of Siberia, North America (averages from eight observatories marked O - curve c), wind velocity (averages from eleven observatories in Europe marked ● - curve d), amplitudes of microseismic activity (NS component) at the observatory Průhonice near Praque (curve e). Correlation coefficient between ΣK_p^{red} and $\Delta t^{o}C$ (curves b and c) is 0.65 (five-day gliding average - time shift of 4 days), between curves d and e 0.70, significance level 0.1 % .

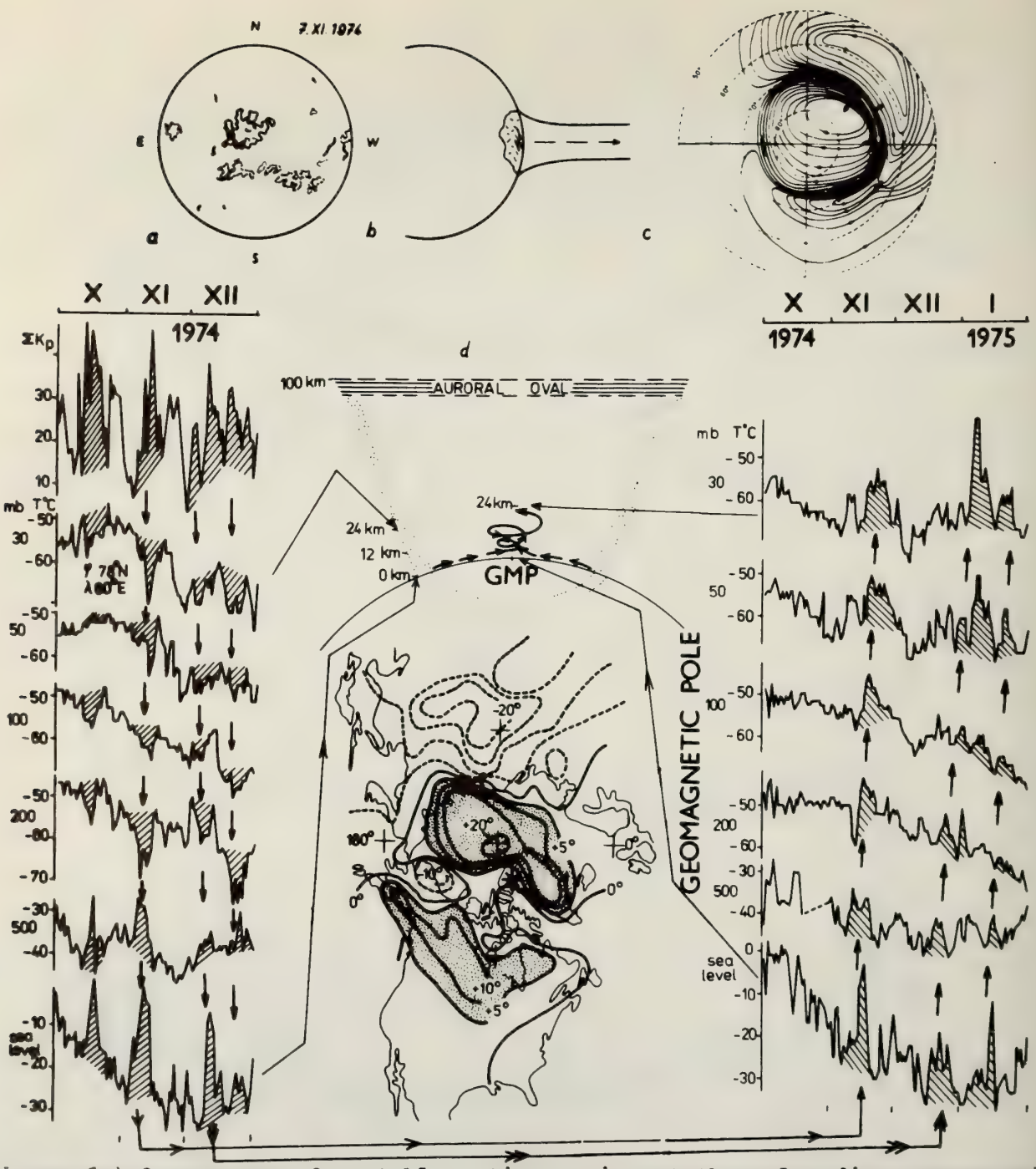


Figure 6a) Occurrence of unstable active region at the solar disc centre and of a filament to the left of the disc centre on Nov.7.1974, preceding a marked increase in geomagnetic activity. b) Schematic representation of coronal flow from unstable active region. c) Equivalent current system for an intense polar magnetospheric substorm. d) Geomagnetic activity (K_p), temperature changes in the auroral oval (observatory 78°N, 60°E-left-hand side), over the geomagnetic pole (right-hand side, where the sudden stratospheric warming is observed) and distribution of anomalous temperatures at sea level during the geomagnetic storm (Nov.9,1974 - in the middle).

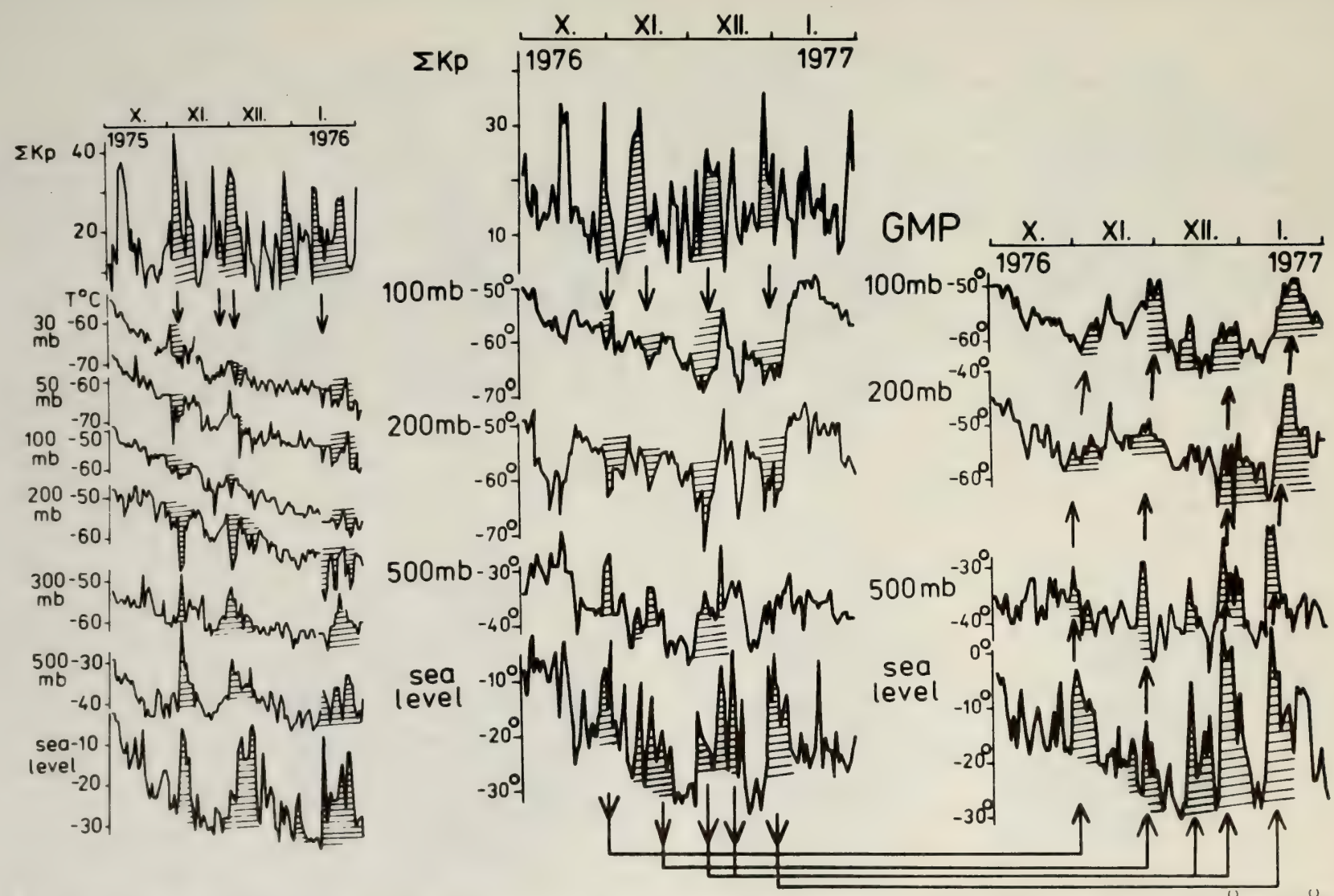


Figure 7. Geomagnetic activity (K_p), temperature changes in the auroral oval (observatory 78°N, 60°E, Oct. 1975-Jan. 1976 - left-hand side) ; geomagnetic activity (K_p), temperature changes (observatory 78°N, 60°E, Oct.1976-Jan.1977 and over the geomagnetic pole - right-hand side), showing temperature changes during several geomagnetic storms.

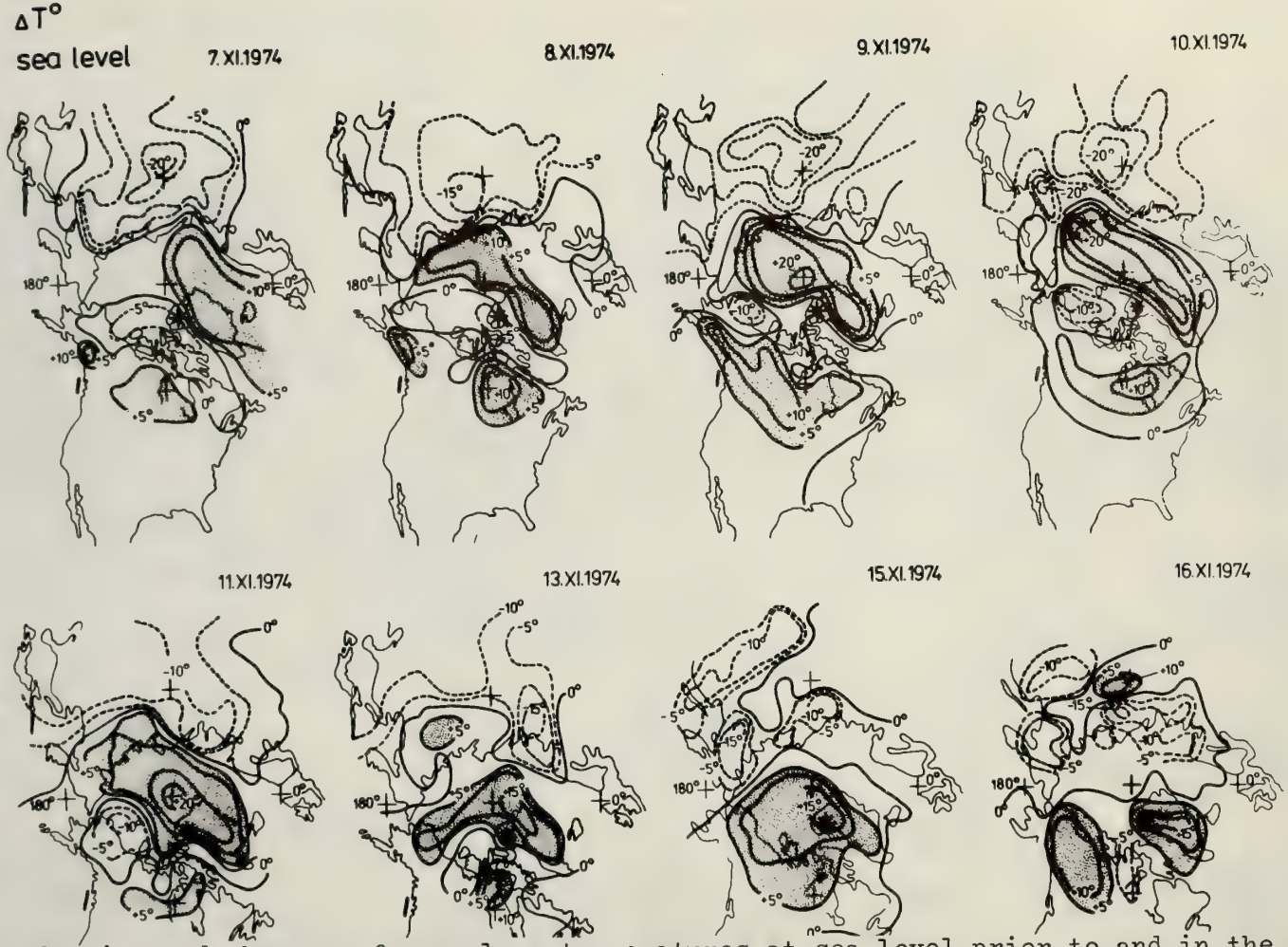


Figure 8. Distribution and changes of anomalous temperatures at sea level prior to and in the course of the geomagnetic storm (Nov.7-16,1974), showing the marked increase of temperatures during the geomagnetic storm, particularly in the region of the Arctic Ocean (north of Siberia) and Canada (Nov.9-11) and the gradual transfer of the region of high temperatures towards the geomagnetic pole (Nov.15-16), which creates conditions for the generation of a deep low over the geomagnetic pole (particularly at the 500 mb level).

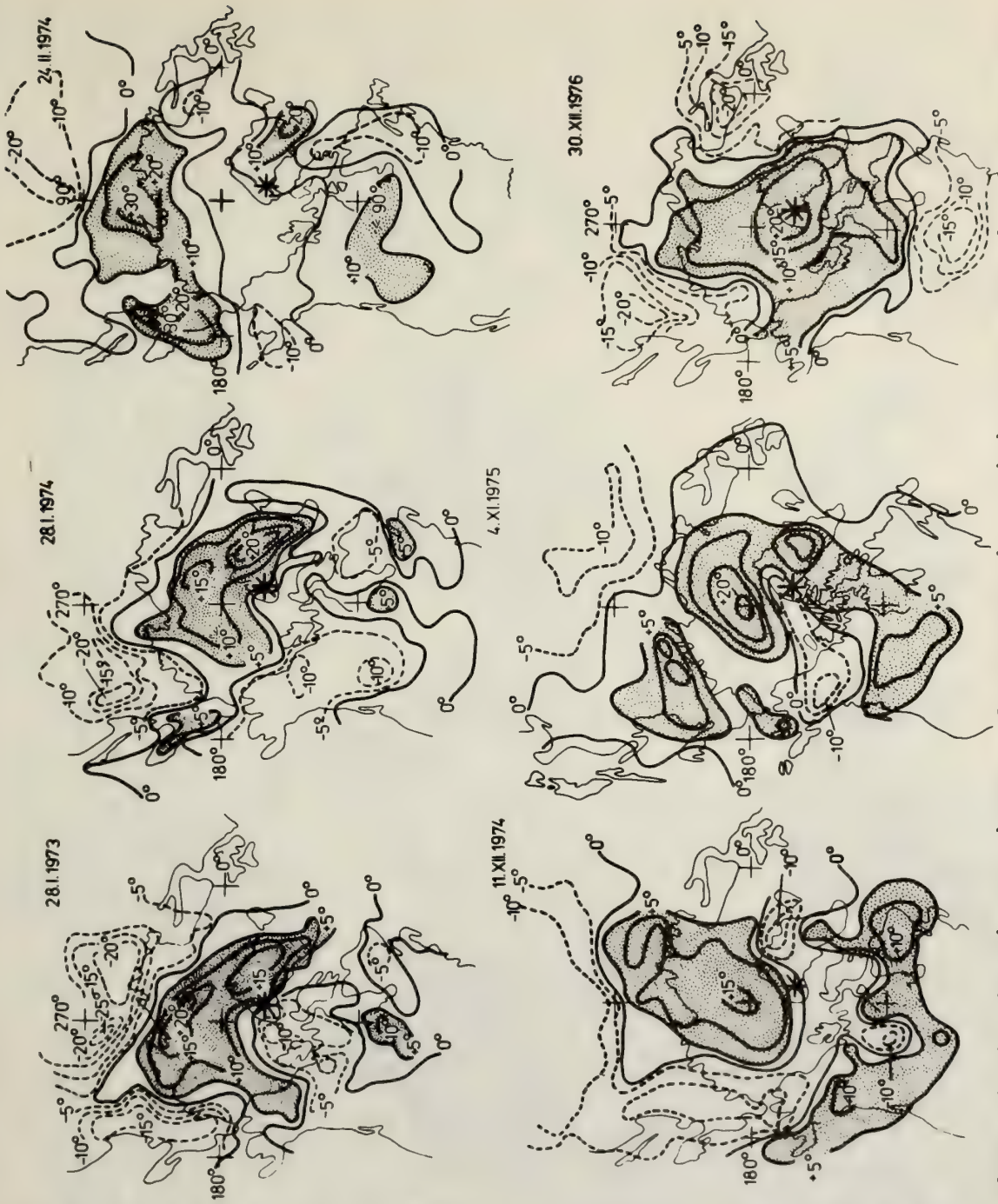


Figure 9. At the time of increased geomagnetic activity an expressive increase in temperature can be observed in the region of the auroral oval for six cases [anomalous temperatures (°C) observed at the Earth´s surface].

the Arctic Ocean (north of Siberia - observatory 78°N, 60°E in the auroral oval), whereas at an altitude of 5 km (500 mb) and on the Earth´s surface along the auroral oval temperature usually suddenly increases with values exceeding the standard at the Earth´s surface by as much as 30°C (Figs.5c,6d). The following hypothesis can be offered to explain these observations (Bucha 1978) : as a result of the marked heating at altitudes of around 100 km in the auroral oval, the velocities of the particles, propagating towards the Earth and concentrated into the auroral oval, increase ; here adiabatic ex - pansion of the rare medium takes place and this leads to the generation of planetary pressure waves and to their penetration through the auroral oval

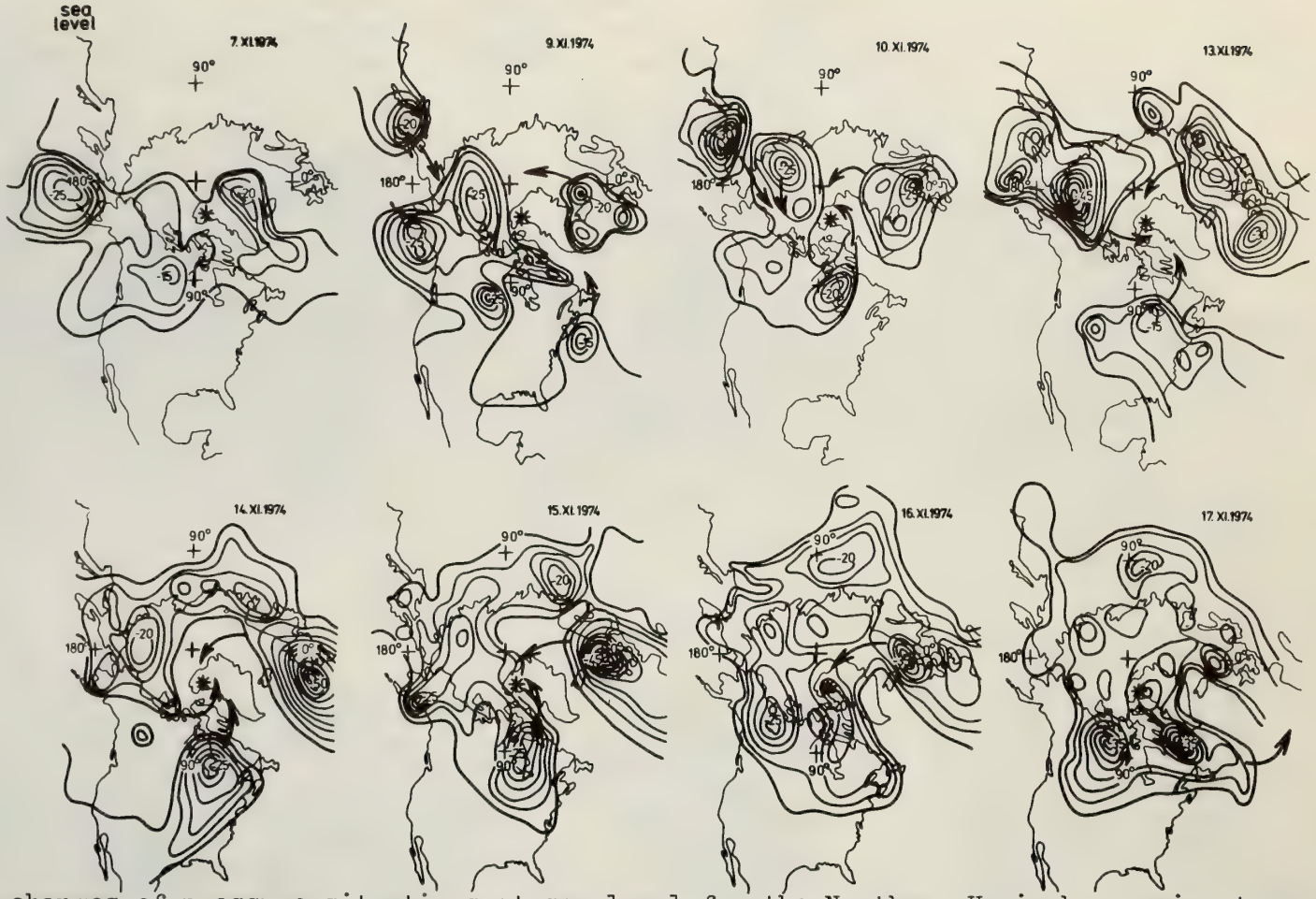


Figure 10a.

Distribution and changes of pressure situations at sea level for the Northern Hemisphere prior to and in the course of the geomagnetic storm (Nov.7-17,1974) showing the consequences of the marked increase in temperatures, as shown in Fig.8. After the commencement of the geomagnetic storm cyclogenesis intensifies considerably (Nov.9) and the cyclonal formations gradually move from the Atlantic and the Pacific Oceans at first to the regions where the temperatures had increased and then, as indicated by the arrows, to the geomagnetic pole (Nov.16) and from here to the south between Greenland and Canada (Nov.17).

into the troposphere (this is reflected in the increase or decrease of temperatures observed at altitudes of 24 - 11 km, ref. Fig. 6d and 7.) At altitudes below 6 km a direct transformation of kinetic into thermal energy apparently takes place as a result of the oscillations and collisional excitation of molecules in substantially denser air layers due to the planetary wave, propagating vertically downwards. This in turn leads to a marked warming of the ground layers of the atmosphere along the auroral oval, at first by between 3 - 10°C causing an intensified cyclogenesis which brings warm air masses to the north and leads to an additional warming up to 30°C (Figs.6d,7 - left-hand side). This marked increase in temperature can be observed especially in winter, whereas in summer it only represents one tenth (aproximately 3°C) (Fig.11). This follows from the ratio between the magnitude of the overall solar energy flux in the Northern Hemisphere in winter (6×10^{15}W) and from the corpuscular energy flux during a geomagnetic storm (as much as 10^{14}W), which amounts to about 10 : 1 (Dessler 1974, Bucha 1977a, 1978). The mentioned temperature manifestation in the auroral oval (Figs. 6-9) is considerably smaller in summer, because the solar energy flux (9×10^{16}W) in summer is more than 100 times the corpuscular energy flux (Fig.5c-curve a). Then the ratio of the corpuscular energy flux in summer acting on the atmospheric circulation (Figs.6-10) to the energy flux in the winter period is one tenth as indicated by K_p^{red} in Fig.5c (curve b).

A positive correlation between the corpuscular radiation indicated by geomagnetic activity and the temperature in the auroral oval (Fig.5c - curve c) was found (correlation coefficient 0.65). A correlation coefficient 0.70 shows a very close dependence of microseismic activity in Central Europe

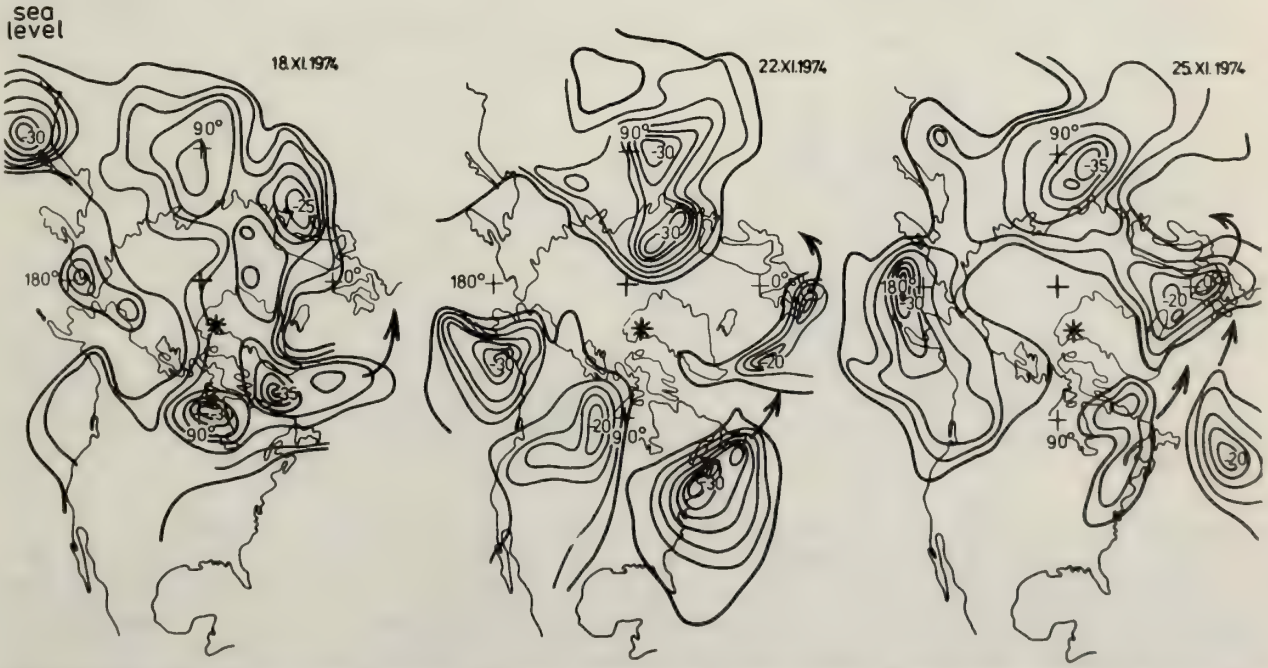


Fig.10b. The penetration of low-pressure areas from the geomagnetic pole to the south between Greenland and Canada (Nov.18,1974) and across the Atlantic towards SE (Nov.22) as far as Europe (Nov.25), resulting in a marked increase of temperatures in Europe (see Figs. 3a,b).

(curve e) on the wind velocity (curve d - Fig.5c, bottom). The increase in temperature over the geomagnetic pole lagged by 2 - 5 days and due to the cyclonal activity the masses of warm air penetrate gradually to higher layers and a sudden stratospheric warming can take place (Fig.6d,7 - right-hand side - seven cases).

In order to check that the mentioned occurrences of ascending currents (responsible for the gradual warming of the region around the geomagnetic pole upwards into higher levels - Fig.12 - several days after the increase in geomagnetic activity) were not singular, we compared the variations of

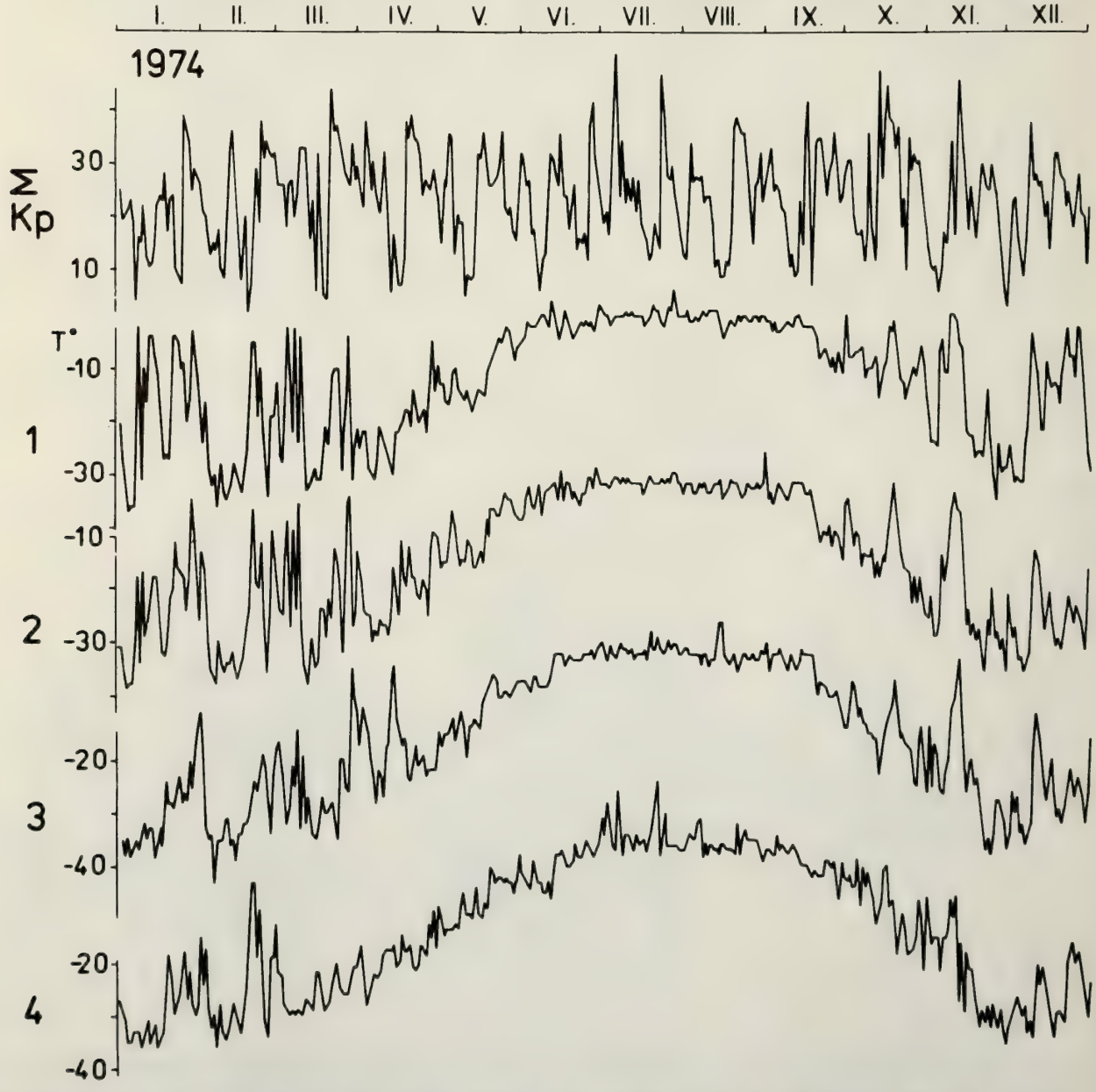


Figure 11. Geomagnetic activity (K_p) and temperature changes at the obser - vatories in the auroral oval (north of Siberia) showing expres - sive fluctuations of temperature in winter (up to 30°C) whereas in summer the temperature fluctuates by 3 - 5°C only.

geomagnetic activity (ΣK_p) with the variations of temperature at levels between 3 to 9 km, as observed at the Soviet drifting observatory SP-7 (top of Fig.12) and at the American observatory Resolute (bottom of Fig.12).

The marked increase in temperature along the auroral oval can be observed during a geomagnetic storm (Fig.13a) ; in case the geomagnetic activity is low, the increase of temperature is not observed or it does not follow the inexpressive geomagnetic storm immediately (Fig.13b).

The effect of the sudden increase of the corpuscular radiation can be observed in the overall development of the situations in the Northern Hemisphere (Fig.8-10). At the time of increased geomagnetic activity an expressive increase in temperature can be observed in the region of the auroral oval (Nov.9-11,1974, Fig.8); similar six cases (Fig.9) were observed after the increase in geomagnetic activity ; thus it can be shown that mainly in winter practically each stronger geomagnetic storm causes a similar increase in temperature and a similar distribution of this positive temperature effect in the region of the auroral oval.

The efect of the sudden increase of the corpuscular radiation after a longer period of geomagnetic calm can be observed in the overall development of the situations in the Northern Hemisphere. In Fig.8. which represents an anomalous distribution of temperature in the Northern Hemisphere (differences between the actual November temperatures and long-range temperature averages in November) we observe an irregular distribution of temperature anomalies at the time of low geomagnetic activity (Nov.7,1974) ; On Nov.8, i.e. on the day the geomagnetic storm commenced, there appears a band of high temperatures in the regions north of Siberia, which increase sharply within the next few days (Nov.9 - 11) to as much as 20°C above the standard value.

The warming takes place simultaneously along the whole auroral oval (Figs.6-9), however, particularly in the regions north of Siberia and in Canada, where the relatively low tropospheric temperatures enable the pla - netary wave, propagating into the troposphere as a result of corpuscular radiation, to penetrate more easily. Within the next few days (between Nov. 13 and 17) the temperatures in the auroral oval decreased gradually and the areas of increased temperatures moved towards the geomagnetic pole, where they culminated between Nov.17 and 20 (the temperature increase over the magnetic pole amounted to 20°C with gradual penetration into the higher levels, or even into the stratosphere, Figs.6d and 7).

The consequences of the sudden marked increase in surface temperatures in the region of the auroral oval are manifested with a lag of 1 - 2 days also in considerable changes of the pressure situations in the Northern Hemisphere (Fig.10a). We again employed anomalous values for the distribution of atmospheric pressure (by subtracting the actual values from the November average), because they provide a much more lucid idea of the events under way than the actual distribution of pressure, the constant effects of the continents and oceans and the dependence on geographic latitude being eliminated from them to a considerable extent. On Nov.7, 1974, prior to the beginning of the geomagnetic storm, the predominating well-known cy - clones (Icelandic, Aleutian) were observed over the Atlantic, the Pacific

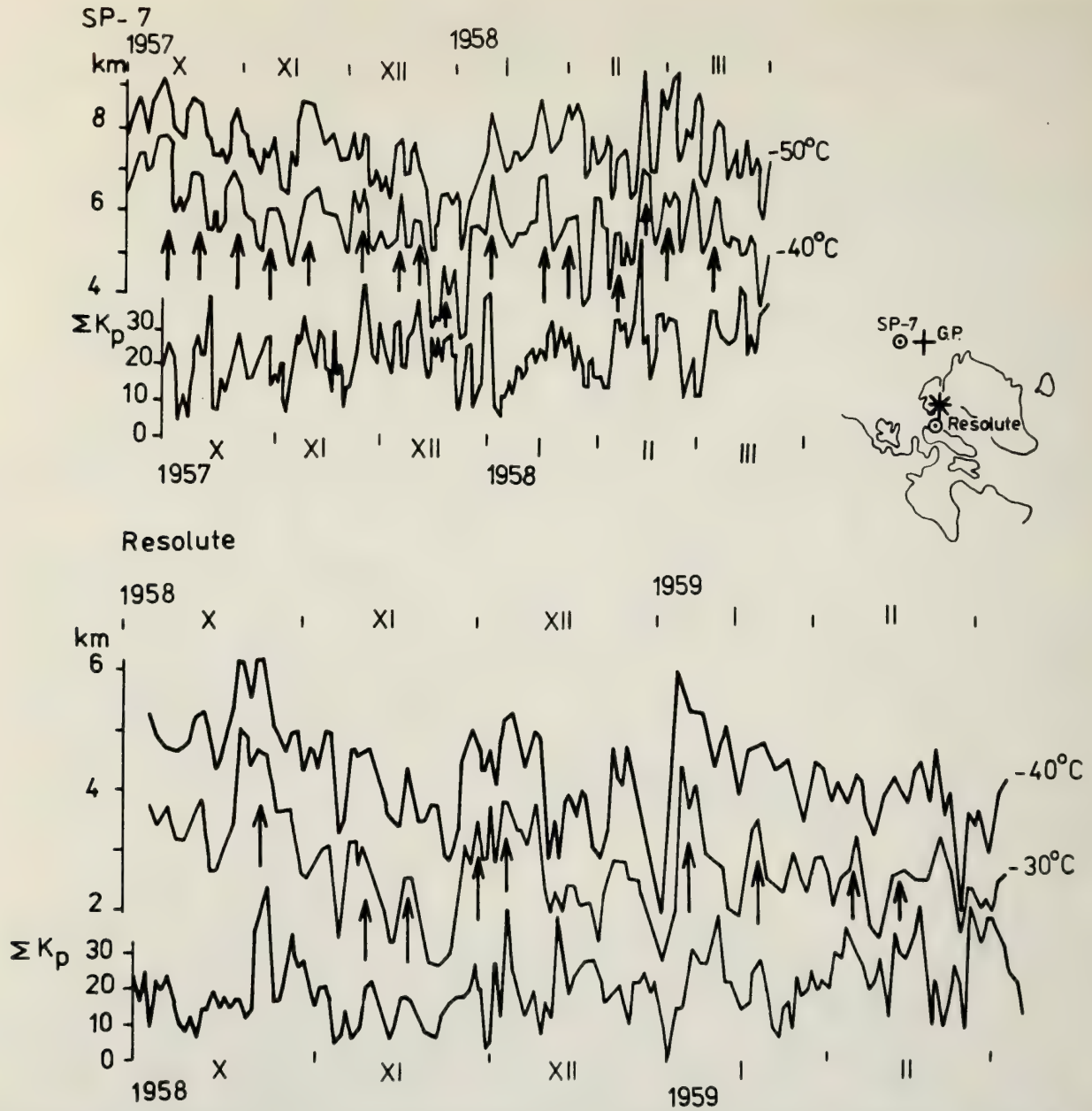


Figure 12. Comparison of temperature variations at levels between 3 and 9 km (height-section of temperature) for the interval October 1957 - March 1958 at the Soviet drifting observatory SP-7 (86°N, 180°E) (at the top) with the changes of geomagnetic activity, $\sum K_p$, shifted in time so that they precede the temperature changes by 9 days. Very similar periods of changes of the two parameters and identity between the increased values of geomagnetic activity and temperature can be observed. Comparison of temperature changes at levels between 1 and 6 km (height-section of temperature) for the interval October 1958 to February 1959 at the American observatory Resolute (74.5°N, 80°W) (at the bottom) with changes of the geomagnetic activity $\sum K_p$. The increased temperatures correspond to the increased $\sum K_p$-values displaced by 3 days and vice versa.

and partly over the North American continent, and a high pressure area over the whole Eurasian continent. This pattern is frequent in winter under low geomagnetic activity. On Nov. 9-12 a marked increase in geomagnetic activity was observed and, as its consequence, a marked increase in temperature in the region of the auroral oval, in the Arctic Ocean and Canada (Fig.8). This immediately resulted in a sudden and expressive intensification of cyclogenesis outside the auroral oval, simultaneously in the Atlantic and Pacific (Nov.10 - Fig.10a). Very active cyclones were generated here and moved towards the North-East. The predominating Icelandic low and an intensive cyclone, developing west of Scotland (Nov.13-15 - Fig.10a) moved relatively rapidly to the NE into the Arctic Ocean, into the areas where the marked temperature increase had occurred (to the north of Siberia - Fig.8). Also the Aleutian low moved across Canada to the NE (Fig.10a).

The air ascending to higher levels and towards the centre, the geomagnetic pole, allowed for a more intensive penetration of the warm masses from the south (Nov.12) ; this is also the reason why the low - pressure

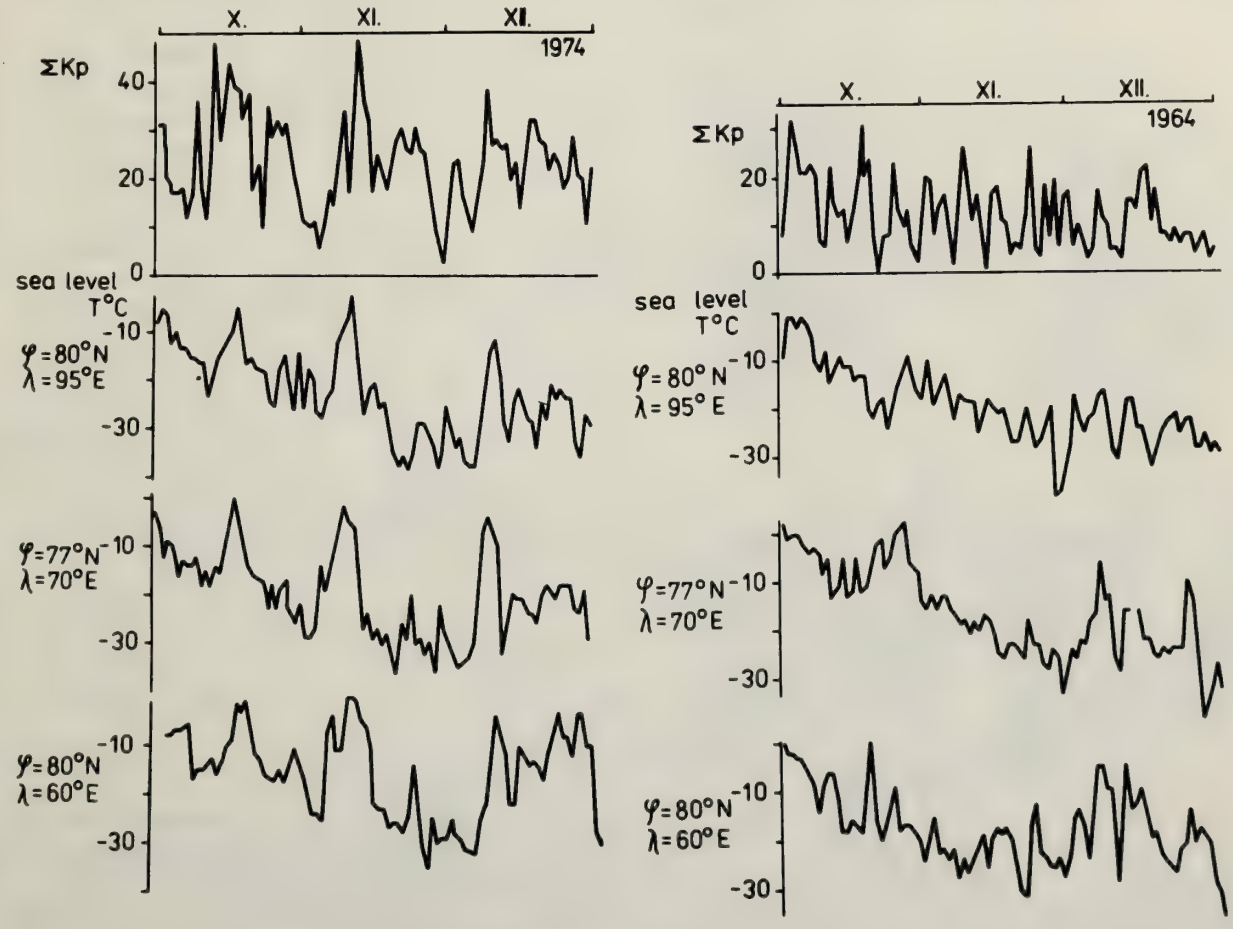


Figure 13. Positive correlation between high geomagnetic activity (Oct.-Dec.1974) and immediate warmings at three observatories north of Siberia, in the auroral oval (left-hand side). Low geomagnetic activity (Oct.-Dec.1964) is not followed by any expressive temperature effect (right-hand side).

formations move towards the regions north of Siberia (Nov.14) and of Canada, and gradually cover the whole polar cap (Nov.17-18 - Figs. 10a,b) in a prevailing poleward flow.

This development of the pressure situations is at first mainly reflected in the ground layers (Fig.10a). In the course of this process a flow of warm air enters this level from the West and East Atlantic, which takes over the main function of supplying warm air to the cyclone over the geomagnetic pole in this phase (Nov.18 - Fig.10b). The air flow from the Pacific along East Asia across Japan towards the NE and further across Alaska and Canada is also directed there. In thus contributes to the creation of a high cyclone over the geomagnetic pole, which is reflected in the gradual temperature increase at higher levels and, in winter, even by a sudden stratospheric warming (Figs. 6d, 7, 12, 14, 3a,b, 5c).

This cyclone over the geomagnetic pole, or in its neighbourhood, represents the main triggering mechanism in its further development with regard to affecting further the build - up of atmospheric circulation over the Northern Hemisphere and leading to gradual changes of the meridional flow into zonal. Masses of relatively warmer air from both oceans are concentrating into the cyclone over the geomagnetic pole and leaving it at higher levels. As the process develops, they push the Azores high to the south, penetrate along the west coast of Greenland to the south and move to the SE towards Europe, as indicated by the growing salient of low pressure between Greenland and Canada (Fig.10b - Nov.18, 22, 25,1974). This stops the flow of warm air from the Azores high to the north ; the warm flow (cyclones) proceeds from the Caribbean directly to the east, joins the lows, proceeding from the geomagnetic pole to the SSE (Nov.18-22 - Fig.4) and, after they have penetrated to Europe, we first observe



Figure 14.

Origin of regions of increased temperatures (top) of increased cyclogenesis along the auroral oval at sea level (middle) during the geomagnetic storm and their transport to the region of the geomagnetic pole where a central cyclone is generated over the geo - magnetic pole (✱) at the 500 mb level (Dec.11-12, bottom).

a decrease of pressure and then a marked increase of temperature by as much as 12°C (e.g., on Dec.3-9, 1974 - Figs 3a, 6, 8, in winter 1975-76, 1976-77 Fig.7, or several times in the winter of 1962-63 - Fig.3b). The marked decrease in the level of activity which follows the magnetic storm is reflected in Europe about 14 - 20 days later by the sudden penetration of Arctic air and an expressive drop in temperature in Central Europe after the cyclonal formations have passed over and before the high pressure has expanded into Europe (Figs.3a, 3b).

We have observed similar connections in more than ten cases investigated. However, the dependence is not always definitive. If several, particularly reccurent storms of several days duration follow one another, alternating with shorter calm intervals of a few days, it may happen that one cycle, lasting approximately 15 days, may overlap at a certain phase with a newly originating cycle, beginning with the penetration of the planetary pressure wave in the auroral oval into the troposphere (Fig.6d) and ending with the penetration of the low from the region of the geomagnetic pole into Europe (Figs. 10a, b, 3a, b).

Under low geomagnetic activity high pressure may be, as shown in Fig.4 in Bucha 1976b, generated over the geomagnetic pole, which, together with an extensive high pressure area over the Atlantic and possibly over

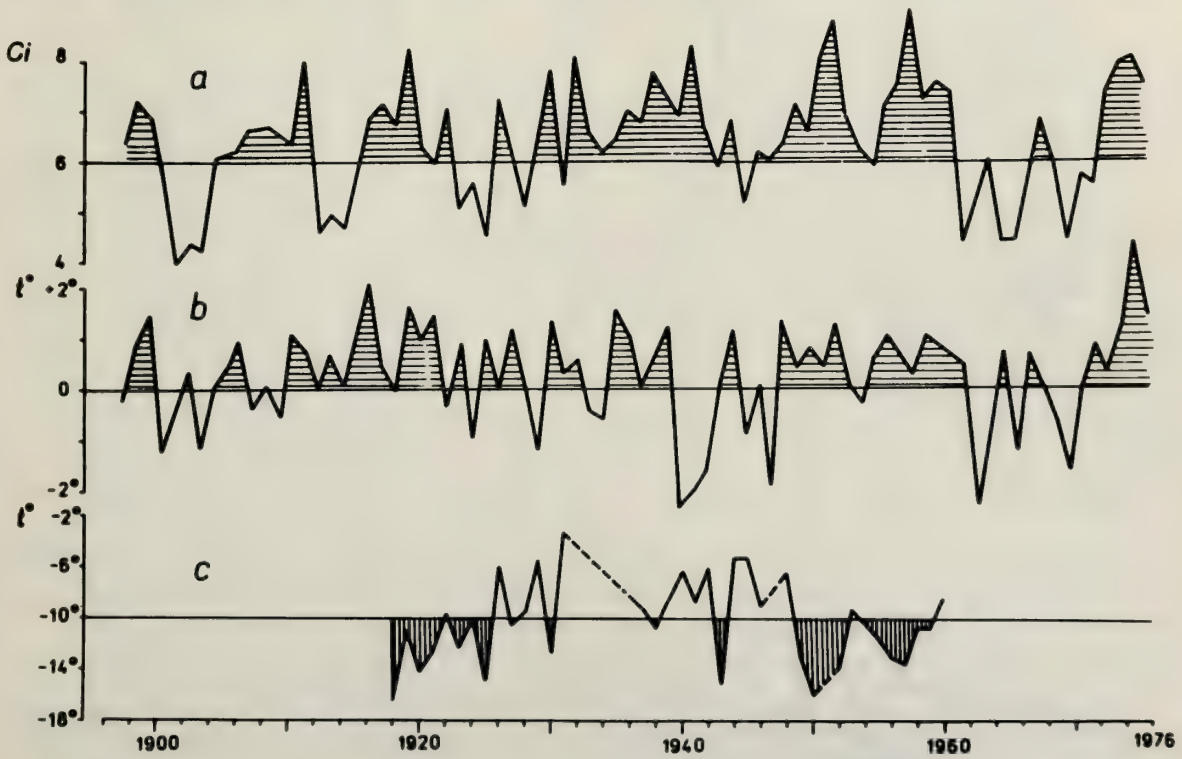


Figure 15. Correlation of geomagnetic activity (C_i-indices, curve a) and the temperature in Prague (curve b) and Matanuska (Alaska - curve c) for two months December - January (mean values) and the period 1897 - 1976. Increased geomagnetic activity and temperatures in Prague correspond to decreased temperatures in the region of Alaska (reversed correlation).

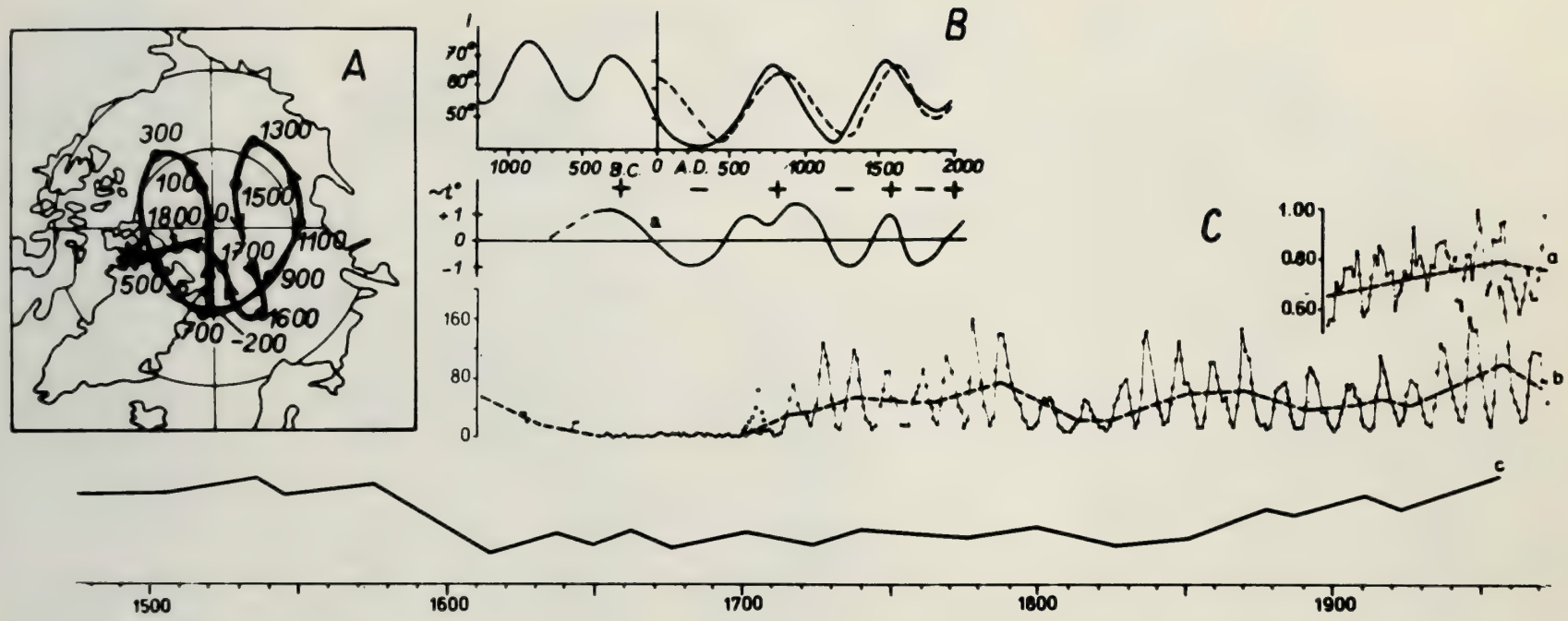


Figure 16.

A) Approximate position and wandering of the virtual geomagnetic pole between 200 B.C. and the present.
B) Variations of the geomagnetic inclination in the Caucasus (——) (Burlackaya 1965) and Bulgaria (----) (Kovaceva 1970) between 1 200 B.C. and the present. Curve a represents the temperature variation, + indicates increased temperatures, - decreased temperatures in Central Europe, based on historical data. The comparison clearly indicates that the temperature maxima are practically identical with the dip maxima ; the same holds for the minima of both quantities.
C) Changes of geomagnetic activity (curve a), solar activity (R numbers - curve b, Eddy 1976) and temperatures defined by changes in the distribution of Alpine glaciers (curve c, Le Roy Ladurie 1969). Expressive decrease of temperatures (by more than 3°C) occurred between 1580-1610, followed by successive warming after 1850.

North America, will hinder the penetration of cyclonal formations from the Caribbean to the NE, which is relatively slow. A typical example at the time of low geomagnetic activity is the development of the atmospheric disturbance over the Gulf of Mexico on June 18, 1972 (hurricane Agnes) (Bucha 1976b). The low pressure region was blocked from the NE and this resulted in extensive floods and damage in the eastern part of North Ame - rica. On the other hand the zonal flow has not penetrated into Central and Eastern Europe which was associated with long lasting draughts, e.g., in the summer of 1972.

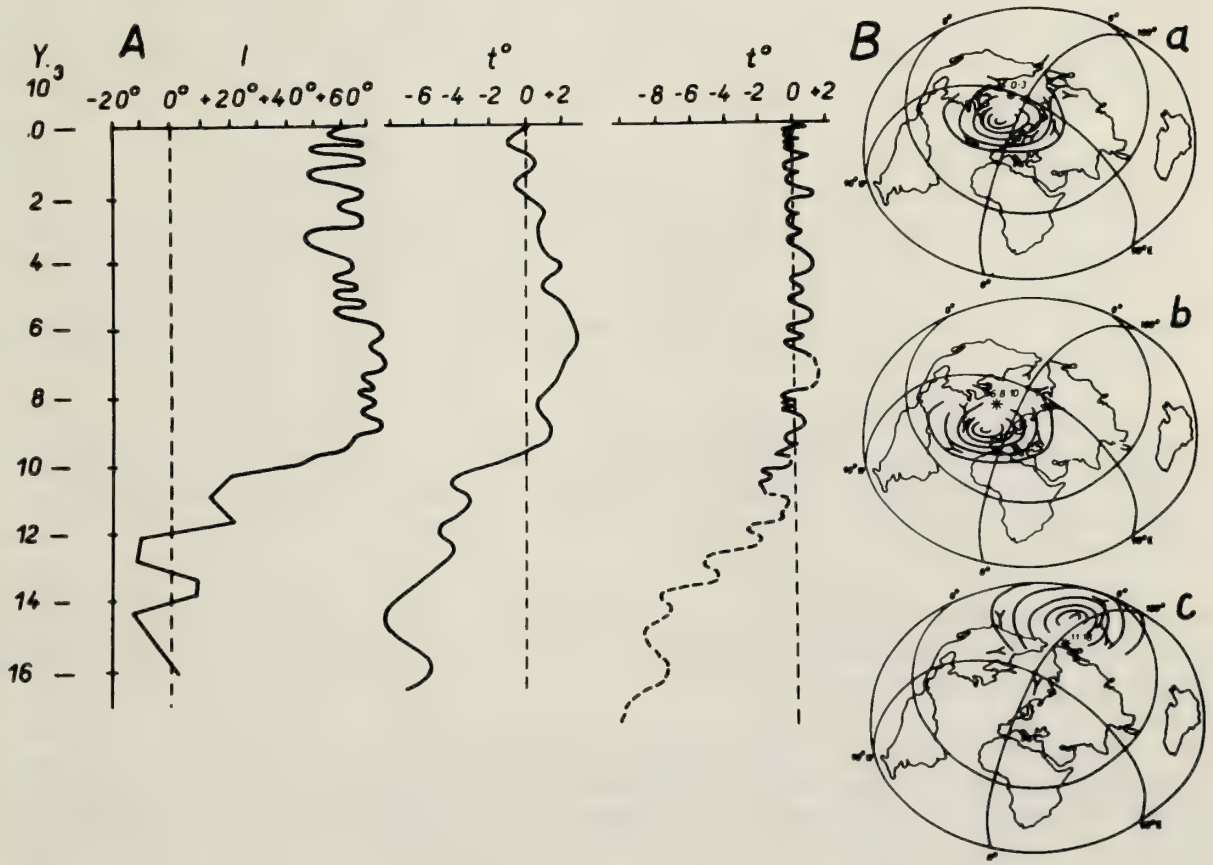


Figure 17. A) Variations of the geomagnetic dip I in Europe, on the left (Bucha 1976a, 1977a). Changes of air temperature in mid-latitudes based on paleobotanic data (Fairbridge 1967), in the middle. Temperature variations in the Eastern Alps (Patzelt, Bortenschläger 1976) on the right.
B) Schematic expression of the low pressure area which is formed as a result of the processes taking place over the polar cap. ✳ denotes the mean position of the geomagnetic pole which we investigated paleomagnetically : a) 0-3 for the last 3 000 years, b) 6-8-10 for the interval between 5 and 10 thousand years ago, c) 11-18 thousand years ago. The arrows indicate prevailing wind directions.

4. LONG - TERM CHANGES OF CLIMATE

As can be seen from the pattern of temperature variations in Central Europe and Alaska for the period 1918 - 1960 (averages of the months De - cember and January - Fig.15), decreased temperatures in Alaska correspond to increased temperatures in Central Europe and vice versa. This can be interpreted as follows : at the time of enhanced geomagnetic activity a cy - clone is generated over the geomagnetic pole (Fig.14) ; it gradually ex - pands over the whole of the North Atlantic preventing the cold masses of air from the Arctic from penetrating into Europe - zonal flow predominates, characterized by an increase in temperatures in Europe. Consequently, the flow of warm air from the Pacific to the North via Alaska is inexpressive - Alaska experiences subnormal temperatures.

After the geomagnetic disturbance is terminated, and zero or very low geomagnetic activity is in evidence, the cyclones along the auroral oval and over the geomagnetic pole decay. This change may result in the warm air flowing from the Pacific via Alaska to the North and in the cold Arctic air which penetrates at the rear of the cyclonal region relatively easily via Scandinavia to the south. This can explain the increased temperatures over Alaska and, simultaneously, a temperature decrease in Europe (Fig.15).

The above indicates that changes of climate and weather seem to be affected by changes in the corpuscular radiation (indicated by geomagnetic activity) and by changes in the positions of the geomagnetic pole (Fig.1, 16, 17). Higher inclinations in Europe correspond to warmer climate and vice versa.

It is known that the last interglacial period set on relatively sud- denly, approximately 10 500 years ago, and that it relieved the last glacial period in Europe and North America.

As given in Fig. 1 the geomagnetic pole together with the low - pressure area were according to paleomagnetic data (Bucha 1976a) located in the Pacific 11 - 16 thousand years ago where the zonal flow was intensified; Europe and eastern part of North America were under the influence of the cold northern flow (Fig.17). This could explain why these two continents were subject to glaciation. As opposed to the above, a relatively sudden change in climate took place in Europe and North America, for which period we found considerable change in the position of the north geomagnetic pole which moved from the Pacific to North America (Fig.1) (Bucha, 1976a, 1977) ; the climate changed to a very warm interglacial period.

In accordance with the approach and receding of the geomagnetic pole relative to Europe as well as with higher or lower geomagnetic activity the temperatures increased and decreased which seems to be the main cause of warmer or cooler ("minor" glaciation) periods (Fig.17) (Bucha 1977).

5. EXAMPLE OF USING THE HYPCTHESIS EXPLAINING THE SEQUENCE OF SOLAR-TERRESTRIAL-METEOROLOGICAL RELATIONS TO PRODUCE A 28-DAY FORECAST

If unstable active regions occur at the centre of the solar disc (Nov.7,1974 - Fig.6a,b), a marked increase in geomagnetic activity occurs 24 to 36 hours later (Nov. 8 - 12 - Fig.6d). As follows from the sequence of events, mentioned in the previous section and observed in 6 cases in 1974-75 (Fig.3a), in 6 cases in 1962-63 (Fig.3b) and also during the winters of 1975-76 and 1976-77 (Fig.7), immediately after the geomagnetic activity has increased we first observe a marked change in the temperatures at levels between 24 km and the Earth´s surface as a result of the planetary wave, penetrating the troposphere in the auroral oval (Fig.6d). This process is reflected in a marked increase of temperature in the auroral oval at the Earth´s surface, at first immediately by 3 to 10°C (Nov.8) and then during the next 2 - 3 days by as much as 30°C (Nov.9-11) due to the penetration of warm air from both oceans into the Artic regions (Fig.8). As a result of this increase of temperature towards the geomagnetic pole (Fig.8, bottom) the cyclogenesis in the auroral oval is enhanced substantially (Nov.9-16, Fig. 10a) and zonal flow sets in over the North Atlantic along the coast of Sweden due NE, as well as in the Pacific, over Canada due NE into the region of the geomagnetic pole ; this causes an outflow of air masses from the cyclone over the geomagnetic pole due south between Greenland and Canada (Nov.17, 18 - Fig.10a) and then accross the Atlantic towards Europe (Nov.22-28, Fig.10b). Here the zonal flow and penetration of a chain of cyclones across the whole of Europe towards the NE is reflected in a marked increase of temperatures by as much as 12°C (Dec.3-9, Fig.3a) at the end frequently associated with enhanced precipitation and, after the last cyclone has crossed Europe, in a sudden drop of temperature as a result of the penetration of Arctic air (Dec.10-12). The sequence of changes of geomagnetic activity, pressure over the geomagnetic pole and of temperatures in Central Europe can be seen in Fig. 3a,b. Therefore, depending on the situation on the Sun (on Nov.7, 1974) and particularly on the geomagnetic storm of Nov.8-12, 1974 one is able to forecast the weather in Europe as far as Dec.10, 1974. Fifteen other sequences, as can be seen in Figs. 3, 6-14 (Bucha, 1976a, b, 1977, 1978, 1979), were manifest in a similar way.

CONCLUSION

Wilcox et al. (1973) have presented results showing a correlation between geomagnetic storms and winds and pressure throughs. Positive correlations of geomagnetic and meteorological data (Figs.1-3), of geomagnetic activity and agricultural production (Fig.4), of geomagnetic activity, temperature, pressure and wind velocity were found (Bucha 1976-9) (Figs.5abc). Further the character of the actual meteorological processes confirms the proposed mechanism of solar-geomagnetic-meteorological relations (Fig.5c) and 11 cases of vertical propagation of temperature effects in the auroral oval and 7 cases of sudden stratospheric warmings (Figs.6,7), 7 cases of the warming in the auroral oval which immediately follow the increase of corpuscular (geomagnetic) activity (Figs.8,9) and 12 cases of dependence

between the changes in geomagnetic activity, decrease of atmospheric pres - sure at the 500 mb level over the geomagnetic pole and changes in tempera - ture in Central Europe - Figs.3a,b). The findings indicate the feasibility of 14 - 28 day weather predictions for Central Europe ; at the same time the suggested relations can be utilized for studying the corpuscular (geo- magnetic) effects on the changes in atmospheric circulation in other areas of the Northern Hemisphere.

The seasonal predictions of winter temperatures according to the correlations given in Fig.2 (mild or severe winters) can be made and the vegetation conditions for agricultural production may be tentatively pre - dicted according to the expected geomagnetic activity in May which, accord- ing to Fig.4, indicates favourable (high geomagnetic activity) or less favourable conditions (low geomagnetic activity) what concerns the prevail- ing types of atmospheric circulation including mainly temperatures and pre- cipitations during the main vegetation period (May to July).

REFERENCES

Akasofu, S. (1968): Polar and Magnetospheric Substorms. D.Reidel Publ.Comp., Dordrecht.

Boström, R. (1964): A Model of the Auroral Electrojects. J.Geophys.Res., 69:4983.

Bucha, V. (1976a): Variations of the Geomagnetic Field, the Climate and Weather. Studia geoph.et geod., 20:149.

Bucha, V. (1976b): Changes in the Geomagnetic Field and Solar Wind-Causes of Changes of Climate and Atmospheric Circulation. Studia geoph.et geod., 20:346.

Bucha, V. (1977a): Mechanism of Solar-Terrestrial Relations and Changes of Atmospheric Circulation. Studia geoph.et geod., 21:350.

Bucha, V. (1977b): Causes of Glaciations, Climate and Weather Changes. Project IUGS, UNESCO 73/1/24, Report No.4. Stuttgart-Prague.

Bucha, V. (1978): Possible Mechanism of Solar-Terrestrial Relations. Collection of Extended Summaries of Contributions Presented at Joint IAGA/IAMAP Assembly Seattle, Washington, IAMAP, Boulder, Colorado.

Bucha, V. (1979): Connections between Geophysical and Meteorological Processes. Studia geoph. et geod., 22:130.

Burlackaya, S.P. (1965): Archeomagnetizm. Nauka, Moskva

Dessler, A.J. (1974): Some Problems in Coupling Solar Activity to Meteorolo- gical Phenomena. Symp. Possible Relationships between Solar Activity and Meteorological Phenomena, Nov.1973,Nat.Aeronautics and Space Admin.

Easterbrook, D.J., Othberg, K. (1976): Paleomagnetism of Pleistocene Sedi - ments in the Puget Lowland. Project IUGS, UNESCO 73/1/24, Report No.3, Bellingham-Prague.

Eddy, J.A. (1976): The Maunder Minimum. Science, 198:824.

Fairbridge, R.W. (1967): The Encyclopedia of Atmospheric Sciences and Astro- geology. Reinhold Publ.Corp., New York, Amst., London

Kovaceva, M. (1970): Archeomagnitnye issledovanija v NR Bolgarii. Sb.tezisov dokl. VIII. konf. po post.geom. polju i paleomagnetizmu.

Le Roy Ladurie, E. (1969): Histoire du climat depuis l´an mil. Flammarion, Paris.

Patzelt, G., Bortenschläger, S. (1976): Spät-und Postglacial im Ötztal und im Inntal. Führer zur Exkursionstagung des IGCP Projektes 73/1/24, Stuttgart.

Roberts, W.O., Olson, R.H. (1973): New Evidence for Effects of Variable Solar Corpuscular Emission on the Weather. Rev.of Geophys. and Space Phys., 11:731.

Wilcox, J.M., Scherrer, P.H., Svalgaard, L., Roberts, W.O. and Olsson, R. (1973): Solar Magnetic Sector Structure : Relation to Circulation of the Earth´s Atmosphere. Science, 180:185.

Yaskawa, K. (1974): Reversals, Excursions and Secular Variations of the Geomagnetic Field in the Brunhes Normal Polarity Epoch. Paleolimnology of Lake Biwa and the Japanese Pleistocene, 2.

THE EFFECTS OF CHANGING THE SOLAR CONSTANT ON THE GENERAL CIRCULATION OF THE EARTH'S ATMOSPHERE

T. Asakura and Y. Tanaka
Longrange Forecast Division, Japan Meteorological Agency
Tokyo, Japan

Much statistical evidence of a solar-weather relationship is not necessarily accepted as universally true due to lack of understanding of the physical processes of solar-weather phenomena. This study is an attempt to clarify the physical processes in the atmosphere caused by changes of solar constant.

1. MODEL CALCULATION

1.1 The Model and Physical Processes Involved

The numerical model used in this study is the Statistical-Dynamical Model developed by Kurihara (1970, 1973), though the heating function has been revised. Despite many restrictions in the model, Kurihara (1973) successfully reproduced the seasonal change of the atmospheric circulation in his ocean-covered model.

The model atmosphere is divided into two vertical layers between the upper boundary, p=0, and the lower boundary, the earth's surface. In the meridional direction, the atmosphere between the north and the south poles is divided into 48 zonal rings having the same width.

By using the zonally averaged primitive equations, the first law of thermodynamics, the continuity equation, and hydrostatic assumption, we predict zonal mean wind components and eddy kinetic energy both at 250 and 750 mb, and zonal mean temperature and heat transport at 500 mb.

Precipitation is obtained as a difference between the water-vapor supply from the sea surface and the moisture flux divergence in an air column. The heat balance equation is solved at the land surface and land-surface temperature is obtained to estimate the sensible heat supply.

The long-wave radiation scheme used in this model is similar to that adopted by Smagorinsky (1963). In this study, the effects of land-sea distribution are incorporated by considering the area percentages of land and sea at each zonal ring.

The horizontal sensible heat transport is estimated using the equation derived assuming that the heat transport by baroclinic waves is performed only by a representative baroclinic wave determined by use of theoretical investigations. Concerning eddy transport of momentum, an assumption was made that the momentum flux divergence at the highest level is counterbalanced by frictional stress between the lowermost atmospheric layer and the earth's

surface. This model further assumes the earth's surface to be flat, thus so-called feedback mechanism is not incorporated.

1.2 Boundary Conditions, Changes in Solar Constant, and Time Integrations

The planetary albedo is taken from the table of Smagorinsky (1963) and is assumed to be symmetrical with respect to the equator. Sea-surface temperature and land-sea ice distributions are the same as those used in the Mintz-Arakawa Model (Gates et al., 1971). Those boundary conditions are kept fixed at their prescribed values throughout the time integrations.

Our preliminary run was begun with the atmosphere at rest and was continued up to the end of the second year with the seasonal march of solar insolation. The land-sea ice distribution was introduced on the last day of the preliminary run. Then the time integrations were carried out anew up to the 30th day of the fourth year.

The time integrations were made for three cases: the normal case (denoted as N-case hereafter) with a normal solar constant, 2.00 ly min^{-1}; the increased case (denoted I-case), with an increase in solar constant of 3%; and the decreased case (D-case), with a decrease in solar constant of 3%. We found that the time equilibrium was almost attained by the beginning of the third year, so the period from January to December in the third year was chosen for analysis. In the following, we mainly discuss the differences between N-case and D-case, namely the effect of the decrease in solar constant, especially on the characteristics of atmospheric motion and atmospheric temperature in the northern hemisphere.

According to Kondratyev (1969), a change in solar constant of about 3% is possible. A change in solar constant itself by +3% to -3%, in this study, may be too large; but when we consider the increase in aerosols in the atmosphere, a change in direct solar radiation to the top of the troposphere of about 3% may be possible.

2. DIABATIC HEATING AND MEAN TEMPERATURE

We first investigate the changes in heating functions, which are the driving forces of atmospheric circulation, due to the decrease in solar constant. Diabatic heating in this model is obtained as the net sum of short-wave radiative warming, long-wave cooling, sensible heat supply from the earth's surface, and release of condensation heat.

Figure 1(a) shows the seasonal march of monthly hemispheric averages of diabatic heating components for N-case. Figure 1(b) then is shown for D minus N case, that is, the changes due to the decrease in solar constant by 3%. Figure 2(a) shows the meridional distribution in these components for N-case, while Figure 2(b) gives the differences, D minus N case. Temperature at 500 mb is also depicted in these figures.

The precipitation seems to be influenced most by a decrease in solar constant. Figure 2(b) reveals that the decrease in solar constant brings about a large decrease in annual mean rainfall in the tropics of 6%, especially around 13°N; on the contrary, precipitation increases in the middle latitudes. In high latitudes around 60°N, the decrease amounts to 3%.

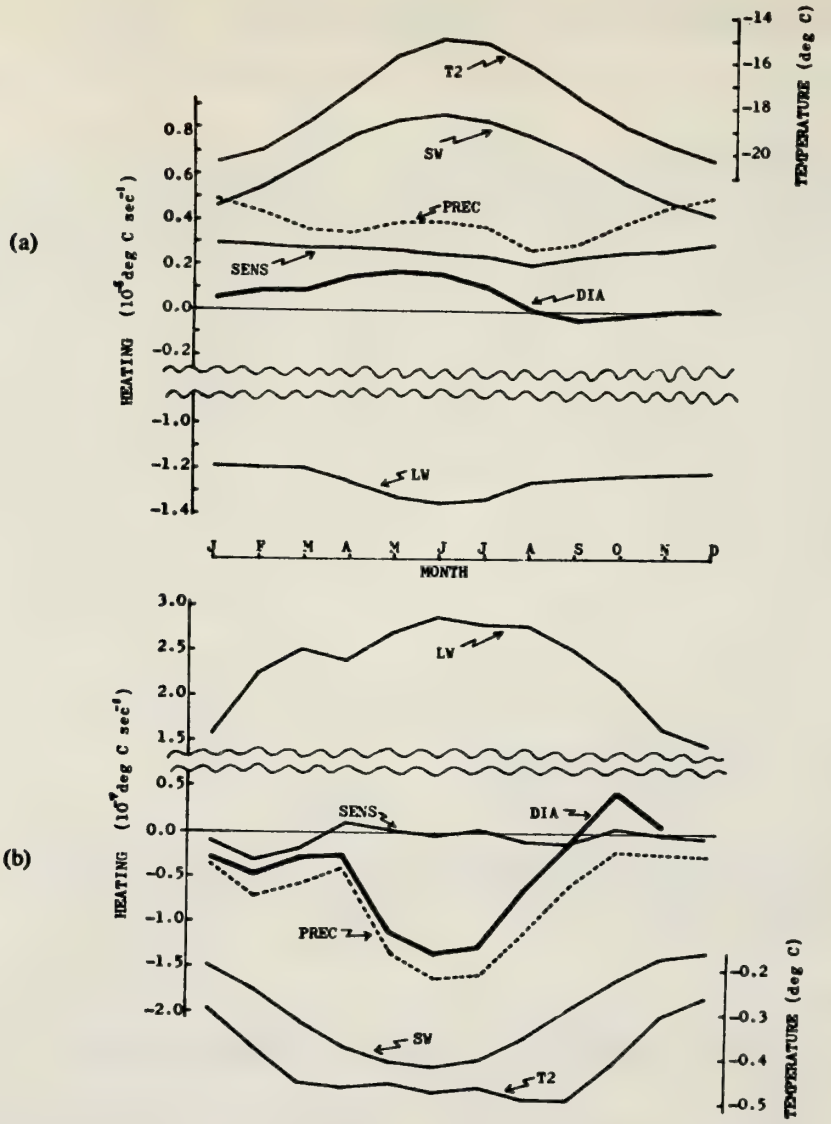


Figure 1. (a): The seasonal march of monthly northern hemispheric averages of diabatic heating (DIA) and its components; sensible heat supply from the earth's surface (SENS), short-wave radiative warming (SW), long-wave radiative cooling (LW) and release of condensation heat, or precipitation (PREC), and temperature at level 2 (T2) for N-case.

(b): Same as (a) except that the seasonal march of differences between D-and N-case is shown.

Figure 1(b) shows that, in the hemispheric average, the largest decrease appears in June, by 4%, with an annual mean decrease of 2%. It is noticeable that in figures 1(b) and 2(b) the precipitation and diabatic heating curves run almost parallel to each other, so the change in precipitation seems to play an important role on the change in diabatic heating. Figure 1(b) shows

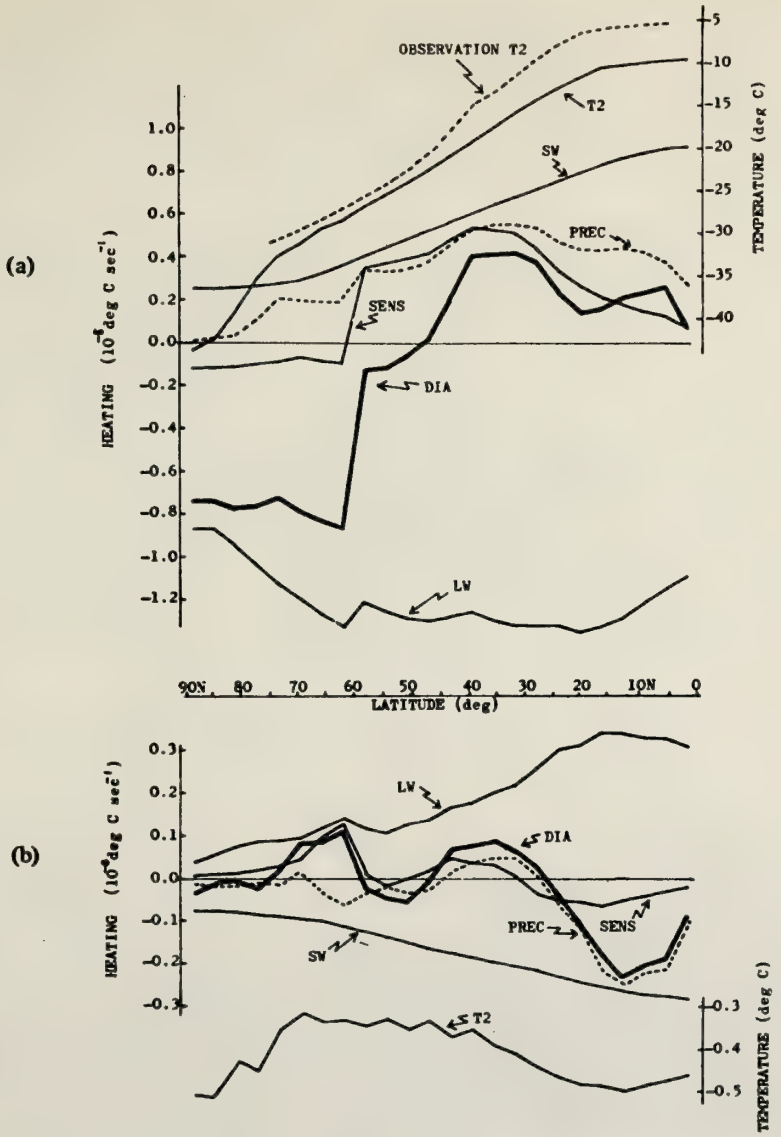


Figure 2. (a): The meridional distribution of annual latitudinal averages of diabatic heating and its components and temperature at level 2 for N-case. (See Figure 1 for notations).

(b): Same as (a) except that the distribution of differences between D- and N-case is shown.

that the hemispheric averages of changes in sensible heat supply from the earth's surface are very small; but, as is seen in Figure 2(b), they contribute to changes in diabatic heating in the tropics and middle latitudes.

The hemispheric mean temperature also falls and reaches its greatest decrease of about 0.5°C in summer, with an annual mean value of 0.4°C, as is shown in Figure 1(b). Figure 2(b) shows that in both the tropics and polar region, this decrease is large, while in higher latitudes the decrease is the smallest. Concurrent with the changes in temperature, the long-wave radiative cooling also weakens with a hemispheric annual mean decrease of 2%, as shown in Figure 1(b).

The change of diabatic heating in this model is equal to the net sum of the changes in the above constituents, so the diabatic heating weakens by about 8%, with its largest value in June while the annual mean decrease is about 7%, as is shown in Figure 1(b).

Figure 2(b) shows that the decrease in diabatic heating is most pronounced in the tropics, especially around 13°N, with a minimum of 11% mainly due to the decrease in precipitation. On the contrary, in middle latitudes around 35°N, the warming intensifies by 8% due to the increase in precipitation. So the changes in diabatic heating bring about the imbalance on the heating field between low and middle latitudes. The contrast of heating, or thermal gradient, weakens between low and middle latitudes while between middle and higher latitudes, it becomes large. Thus, these imbalances must be canceled out by means of changes in atmospheric circulation.

3. DIABATIC HEATING AND GENERAL CIRCULATION

Next we study how the changes in diabatic heating are balanced by the changes in atmospheric circulation. We estimate, in this model, the time derivative of atmospheric temperature as the net sum of eddy and mean horizontal sensible heat flux divergence, adiabatic heating due to eddy and mean vertical motion, heat diffusion, and diabatic heating.

Figures 3 and 4 show the variations of each component mentioned above. In Figure 3, the seasonal march of the monthly hemispheric averages of the components for N-case and those of differences in these components between the D- and N-cases are shown. In Figure 4, similar to Figure 2, the meridional distribution of the annual latitudinal averages for N-case and those of differences between the D- and N-cases are illustrated.

3.1 Vertical Motion

Figure 3(b) clearly shows that the decrease in diabatic heating is almost compensated for by the weakening of mean upward motion, or intensification of downward motion, so far as the hemispheric averages are concerned. The weakening is most remarkable in June; on the average the upward motion weakens by 15% over the year. The role of eddy vertical motion is very small compared with that of mean motion.

Figure 4(b) clearly shows that adiabatic cooling diminishes in low latitudes due to weakening in mean upward motion ; and that it counterbalances the decrease in diabatic warming there. Around 30°N, weakening in adiabatic warming is distinct, meaning a weakening in downward motion to balance with the increase in diabatic heating there. These changes in mean vertical motion in the tropics and around 30°N imply the weakening of Hadley circulation.

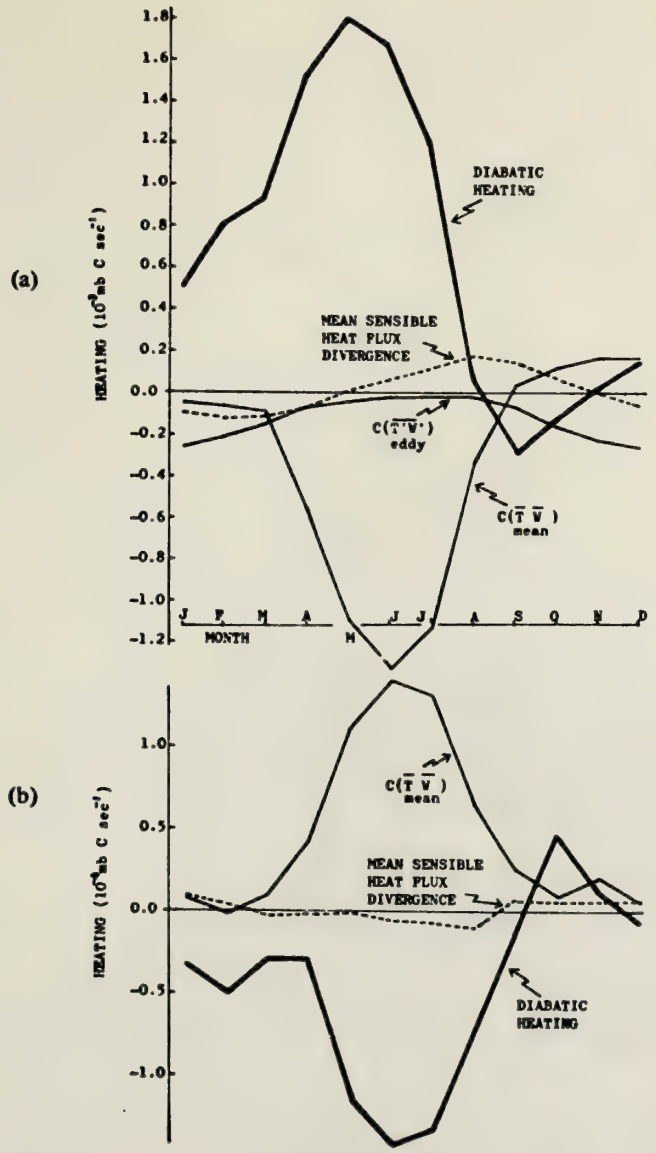


Figure 3. (a): The seasonal march of monthly northern hemispheric averages of energy conversion terms; diabatic heating, mean sensible heat flux divergence, conversion between potential and kinetic energy by eddies ($C(\overline{T'W'})$), and by mean flow ($C(\overline{T}\,\overline{W})$), where the notation W means vertical P-velocity, for N-case.

(b): Same as (a) except that the seasonal march of differences between D- and N-case is shown.

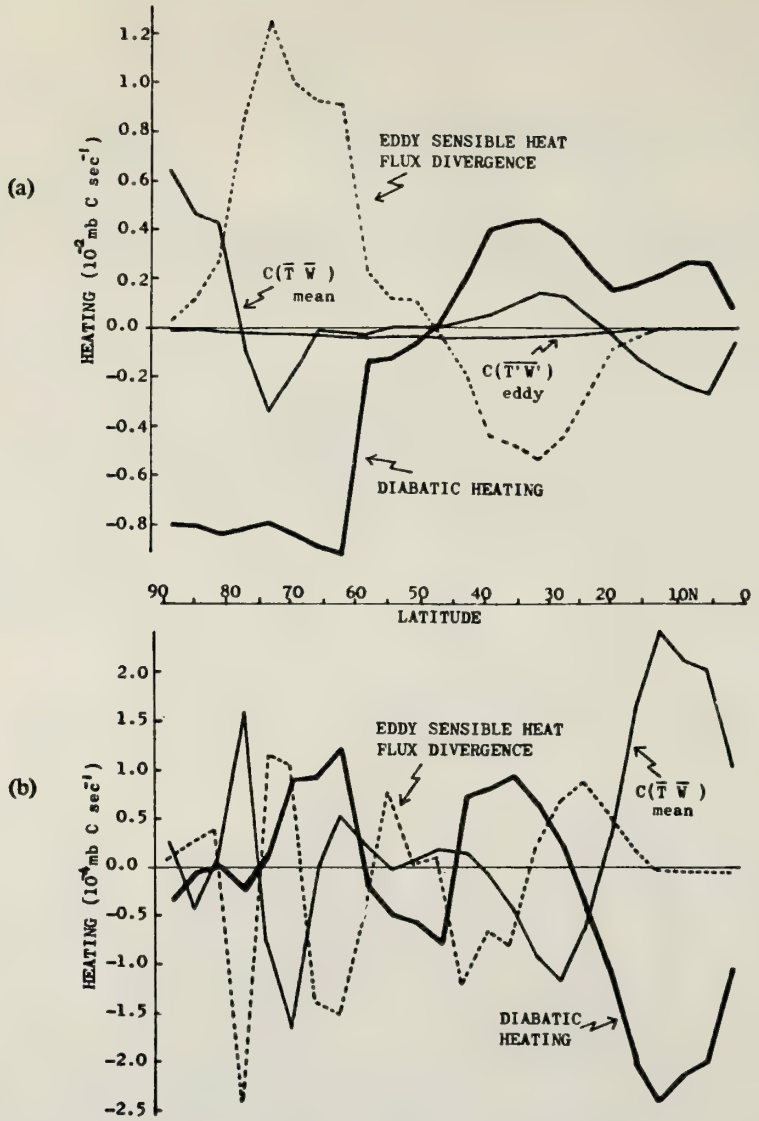


Figure 4. (a): The meridional distribution of annual latitudinal averages of energy conversion components for N-case. (See Figure 3 for notations.)
(b): Same as (a) except that the seasonal march of differences between D-and N-case is shown.

Around the tropics, the change in diabatic heating is almost compensated for by the change in mean vertical motion, but in middle and high latitudes, the sensible heat flux also plays a part to balance with the changes in diabatic heating.

3.2 Horizontal Sensible Heat Flux Divergence

We see in Figure 4(b) that around 25°N the cooling due to eddy sensible heat flux divergence weakens as the solar constant decreases; this means that the efficiency of sensible heat transport from low to middle latitudes lessens and corresponds with a weakening in Hadley circulation. Around 40°N, the decrease in solar constant causes an intensification in cooling by sensible heat transport by eddies, and this compensates for the intensification of diabatic heating due to the increase in precipitation there. Around 50°N, the heat flux warms the region. Thus the eddies transport more sensible heat from middle to higher latitudes due to the change in solar constant, and therefore the Ferrel circulation intensifies.

Since we assumed that sensible heat flux at the north and south poles is zero, the net hemispheric average in sensible heat flux divergence by mean flow is equal to an inflow, or outflow, of sensible heat to the other hemisphere. Figure 3 shows that the decrease in solar constant results in a weakening of sensible heat inflow in summer and a weakening of outflow in winter. This also means a weakening of hemispheric interaction due to a weakening in Hadley circulation at both hemispheres.

3.3 Temperature and Mean Zonal Wind

Figure 2(b) shows that the decrease in solar constant causes a weakening in baroclinicity between low and middle latitudes and a strengthening between high and polar latitudes. So the subtropical jet stream is weakened while the polar jet stream is strengthened. although their positions do not change remarkably.

4. SUMMARY AND DISCUSSION

Figure 5 shows our results schematically. As is seen, the decrease in solar constant results in the following effects in the atmospheric circulation:

1. Precipitation in summer decreases sharply in low latitudes, resulting in the weakening in diabatic warming which is balanced by a weakening of mean ascending motion in the southern branch of the Hadley cell.

Diabatic warming in middle latitudes is intensified by the increase in precipitation and sensible heat supply from the surface. In high latitudes around 55°N, diabatic cooling is intensified by the decrease in precipitation and sensible heat supply. An imbalance between these two latitudes is cancelled out by the enhancement of sensible heat flux in the Ferrel circulation. Wetherald and Manabe (1975) and MacCracken and Potter (1975) obtained similar results on the changes in precipitation.

2. Mean temperature of an air column decreases, especially in tropical and polar regions. However, the amount of decrease is about one-tenth of those in studies by Wetherald and Manabe (1975), MacCracken and Potter (1975), and Budyko (1969). The discrepancy may be due to ignoring feed-back mechanism in the present model.

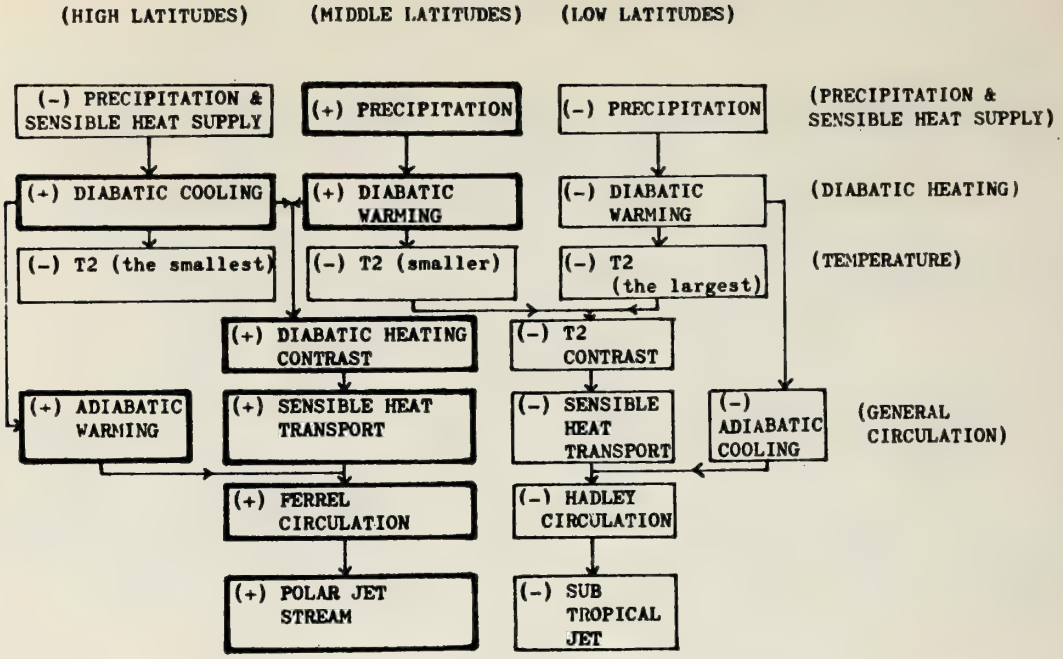


Figure 5. Schematic diagram of changes of components in atmospheric circulation caused by the decrease in solar constant. Bold-lined rectangles show intensifying (or increasing) phenomena, while thin-lined rectangles show weakening (or decreasing) phenomena.

3. In I-case, with an increase in solar constant, phenomena appear to be just the reverse of those in D-case, qualitatively and quantitatively.

In this paper, special emphasis should be placed on the fact that a change in solar constant brings about regionally and seasonally different effects on weather, and the differences are caused by a deformation of atmospheric motion. It is this deformation that makes our understanding of solar-weather evidence more difficult.

Acknowledgements

The authors express their hearty thanks to Dr. Y. Kurihara for giving them his excellent model, and Dr. A. Katayama for his helpful suggestions and discussions. They also thank the staff of Longrange Forecast Division, in the Japan Meteorological Agency, for their encouragement through this study.

REFERENCES

Budyko, M. I. (1969): The effect of solar radiation on the climate of the earth. Tellus, 21:5.

Gates, et al. (1971): A documentation of the Mintz-Arakawa two-level atmospheric general circulation model.

Kurihara, Y. (1970): Statistical-dynamical model of the general circulation of the atmosphere. J. Atmos. Sci., 27.

Kurihara, Y. (1973): Experiments on the seasonal variation of the general circulation in a statistical-dynamical model. J. Atmos. Sci., 30.

Kondratyev, Y. K. and Nikolsky, H. I. (1969): Solar radiation and solar activity. Quar. Jour. Roy. Met. Soc., 96.

MacCracken, M. C. and Potter, G. L. (1975): Comparative climatic impact of increased stratospheric aerosol loading and decreased solar constant in a zonal climate model. Proceedings of the WMO/IAMAP Symposium on Long-Term Climatic Fluctuation.

Smagorinsky, J. (1963): General circulation experiments with the primitive equations, I. The basic experiment. Mon. Wea. Rev., 91.

Wetherald, R. T. and Manabe, S. (1975): The effects of changing the solar constant on the climate of a general circulation model. J. Atmos. Sci., 32.

METEOROLOGICAL MICROSEISMS AND SUN-WEATHER RELATIONSHIPS

Jan Laštovička
Geophysical Institute, Czechosl. Acad. Sci.,
Boční II, 141 31 Prague 4, Czechoslovakia

The purpose of this paper is to show the usefulness of meteorological microseisms recorded at inland stations, inexpensive and less-known data, in sun-weather studies and predictions. The long-term variability of microseisms, their short-term variability, including response to geomagnetic storms and their response to the IMF sector boundary crossings are shown. Some possibilities of using them in a short-range weather forecasts are also shown.

1. INTRODUCTION - MICROSEISMS

Sun-weather relationships have been studied very extensively in various ways in recent years. The exploitation of meteorological microseisms for this purpose belongs to the less-known (perhaps even generally unknown) methods used. The purpose of the present paper is to summarize some older results of their use in sun-weather studies, to present some new results and to point at possibilities of exploiting them for predictions.

Besides earthquakes, the seismograph also records other motions, generally called "seismic noise". Seismic noise in the range of periods of about 1-10 sec is called "meteorological microseisms" (hereafter only microseisms). The microseisms reach the largest amplitudes at coastal seismic stations. These microseisms represent coastal effects or effects of close local sources. However, the microseisms recorded at stations, situated well inland like Prague, are of a different origin. Local and coastal effects are suppressed and background microseisms, which are a response to changes of atmospheric pressure fields and to cyclonal activity over large water areas (mainly over oceans), are recorded. The generation of microseisms is conditioned by rapid, intense changes in the pressure field pattern - even large stationary cyclones do not produce microseisms (Zátopek, 1976).

Source regions of microseisms observed at Prague (generally in Central Europe) are situated in the North Atlantic frontal zone, where the appearance of pronounced cyclonic activity is always connected with a sudden enhancement of microseisms. The region to the west, south-west and south of Iceland, surroundings of the Jan Mayen Island, the area off the coast of Central Norway, the northern Norwegian coast and the northern part of the Baltic Sea are these regions (Zátopek, 1964, 1976). On the other hand, there are some sourceless regions like the shallows off the coast of Greenland, the North Sea, the English Channel, the Mediterranean Sea, etc.

Meteorological microseisms, recorded at Prague, are strongly seasonally dependent. They are relatively large and well-developed in winter, whereas in summer they are often hardly detectable, perhaps due to different conditions of air-water interaction (Zátopek, 1966).

It is worth noting that the striking similarity, found in the regime of smoothed amplitudes of Northern Hemisphere microseisms (Europe and Japan) down to the latitudes of about 35°N, has been explained by the integral activity of the great polar vortex in the atmosphere (Zátopek, 1975). This finding together with the fact that the Central Europe microseisms are created in the key region of European weather and at latitudes high enough, where the sun-weather relationship is expected to be developed, indicate that it is suitable and necessary to exploit meteorological microseisms for investigating sun-weather relations.

2. IMF AND MICROSEISMS

The interplanetary magnetic field (IMF) belongs to the important phenomena which play a role in solar-terrestrial relationships. The relation between microseisms and the IMF sector boundary crossings and IMF radial component polarity was studied by Laštovička (1977, 1978). The results for the winter period (November 15 - March 15) are given in Fig. 1. All the values are presented in the form of I/I_o, where I_o is the crossing day value. The curves represent mean values over the period 1966-1973 (microseisms 1962-1968 - lack of data after 1968), regardless of the type of crossing. On one side of each curve the designation of the physical quantity and the scale are given, on the other side the +/- ratio and the number of crossings, n. The +/- ratio is the ratio of the 3-day average values observed in the away (+) sector to those in the toward (-) sector.

The same effect of sector boundary crossings, which consists in a more or less deep depression related to the boundary crossing, is observed in all the three types of quantities shown in Fig. 1. The values in the toward sector are a little higher than those in the away sector (+/- < 1). The statistical significance of the difference between extreme mean data points of the curves is between 75% (1178 kHz) and 99% (VAI 12 UT). The atmospheric vorticity area index at 500 mb characterizes the state of the troposphere northwards of 10°N. The radio-wave absorption data characterize the state of the daytime lower ionosphere over Central Europe (GDR). The less smoothed character of the microseismic curve is due to a lower number of data used.

Laštovička (1978) found another type of the IMF boundary crossing effect in the IMF magnitude, Ap, cosmic rays and in the nighttime radio-wave absorption in the lower ionosphere. It enables us to conclude that there are different types of the IMF sector boundary crossing effect depending on the altitude and, partly, on the phase of the day, and it represents further evidence of the usefulness of meteorological microseisms in studying extraterrestrial influence on the weather.

The sector boundary crossing effect in microseisms is similar for +/- and -,+ crossings in winter, but there is practically no such effect in spring and autumn. In contrast to a very weak winter tendency to higher microseismic activity in the toward sector, a slight but non-negligible opposite tendency is observed in spring and autumn (Laštovička, 1977).

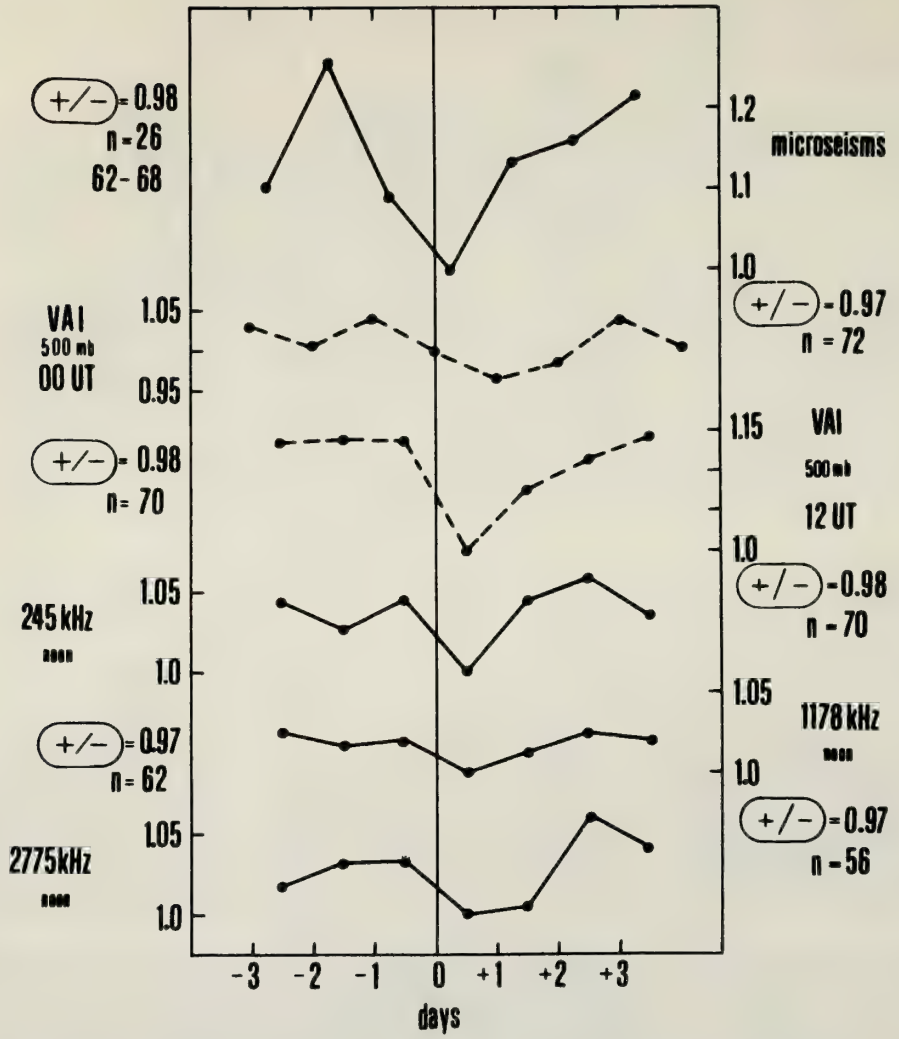


Fig. 1. The IMF sector boundary crossing effect in the amplitude of Prague meteorological microseisms, the Northern Hemisphere atmospheric vorticity area index (VAI) at the 500-mb level, and in radio-wave absorption (2775 kHz, 1178 kHz, 245 kHz) in the lower ionosphere at noon after Laštovička (1978). +/- ... the ratio of values observed in the away (+) sector to those observed in the toward (-) sector.

3. LONG-TERM VARIABILITY OF MICROSEISMS

The long-term variability of Prague microseisms was studied by Laštovička (1974), Zátopek (1975), Zátopek and Křivský (1974) and Zátopek et al. (1976) in relation to various phenomena associated with solar activity. They found a chain of interrelated phenomena (in the long-term sense) beginning at the sun and ending at the earth: the occurrence of solar flares, associated with type IV radio bursts (sun) - cosmic rays (interplanetary medium variability) - Ap (geomagnetic field) - radio-wave absorption (lower ionosphere) - microseisms (solid earth).

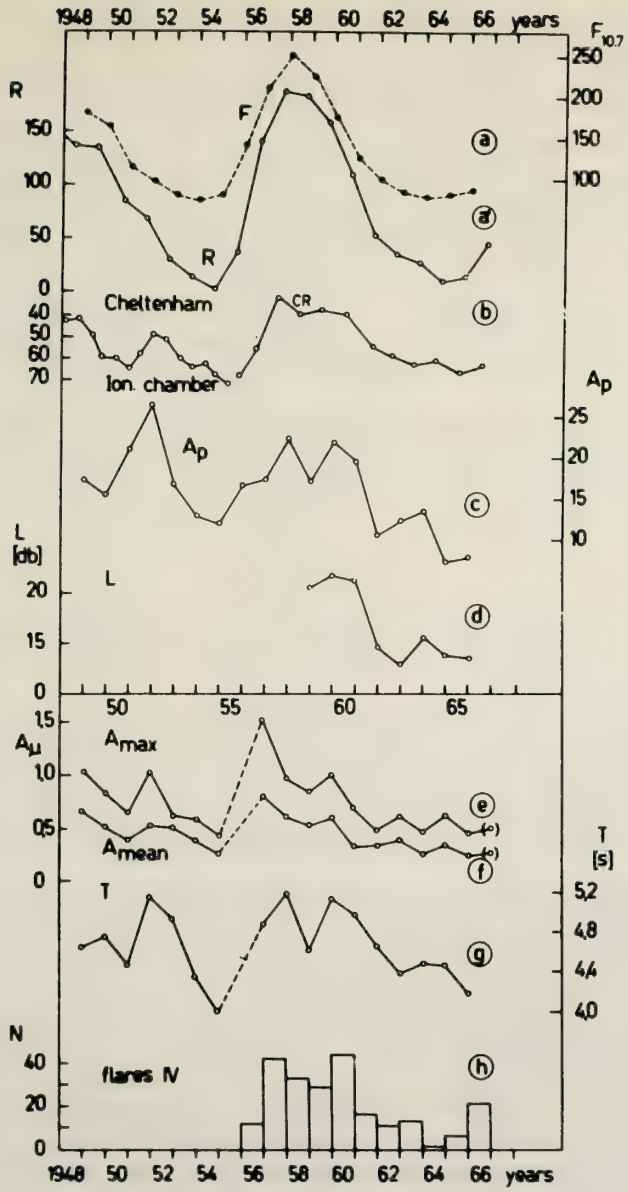


Fig. 2. Long-period (1948-1967) data on λ = 10.7 cm solar radio flux (a), sunspot numbers R (a'), cosmic ray intensity at Cheltenham (b), geomagnetic Ap indices (c), LF radio-wave absorption on 272 kHz at the Průhonice Observatory (d), maximum smoothed microseismic amplitudes at Prague (e), mean microseismic amplitudes at Prague (f), mean microseismic periods at Prague (g), and the occurrence of solar flares associated with type IV radio bursts (h). After Zátopek et al. (1976).

All these quantities together with the sunspot number R and solar radio noise $F_{10.7}$ are given in Fig. 2. All the quantities exhibit relatively strong secondary peaks in the solar cycle (1951/52, 1959/60), except R and F. Thus, those components of solar activity, which are associated with the geomagnetic activity (flares IV - CR - Ap) and not only with the solar wave radiation (F,R), seem to play the major role in sun-microseisms(weather) relations, as is expected (e.g.

King, 1975). As regards microseisms, the two-peak structure is developed particularly well for their periods. The best-fit lines are: $T(sec) = 0.039\ Ap + 0.0015\ F + 3.85$, $T(sec) = 0.040\ Ap + 0.0011\ R + 3.39$; correlation coefficients: $r(T,Ap) = 0.74$, $r(T,R) = 0.54$, $r(T,F) = 0.52$ (Laštovička, 1974).

The above chain of interrelated phenomena may be extended to the circumpolar vortex activity in the circumpolar pressure pattern, the variability of which is reflected by microseisms (Zátopek, 1975). These phenomena may be linked by a chain of associated processes, beginning with a particle and plasma cloud ejection during flares with type IV radio bursts, as suggested by Zátopek et al. (1976). Even if the chain of interrelated phenomena is not complete and some processes are not clarified, it is believed to provide a good initial basis for more profound studies of solar-terrestrial links.

The Prague meteorological microseisms form a long-period homogeneous series of data. As illustrated in this section, they represent a very convenient basis for studying various long-term effects in the lower atmosphere, particularly in the winter polar vortex.

4. SHORT-TERM VARIABILITY OF MICROSEISMS. PREDICTION POSSIBILITIES

The Prague microseisms are a response to the meteorological activity in the North Atlantic frontal zone, where most of the Central Europe weather (cyclones and frontal systems) is generated. Thus microseisms could be used for short-range (several days) qualitative weather forecast in Central Europe.

The short-term variability of microseisms and some other quantities are shown in Fig. 3 for the last quarter of 1974. The vertical lines in Fig. 3 indicate individual microseismic bursts. It follows from the strong seasonal dependence of microseismic amplitudes (Section 1) that even weak microseismic disturbances in October may indicate more significant meteorological activity than moderate or medium microseismic bursts in December.

The comparison of microseismic bursts with geomagnetic storms or activity enhancements displays a two-peak structure of microseismic response to geomagnetic storms. The direct effect of a geomagnetic storm is observed on the day of maximum ΣKp (within an interval $\pm$ 1 day), whereas the after-effect, which is comparable in magnitude with, and may be even larger than direct effect, is observed 2-4 days after the direct effect. The two-peak microseismic response strongly resembles the well-known two-peak effect of magnetic storms in the LF radio wave absorption in the midlatitude lower ionosphere. The occurrence and time-delay of the after-effect in Prague microseisms are consistent with a large decrease of the mean atmospheric pressure (about 10 mb) in the Iceland-Scandinavian region 3-5 days after strong sporadic geomagnetic bursts (Mustel et al., 1977). It is worth noting that the vorticity area index response to geomagnetic storms is less developed and besides a fairly sharp decrease in VAI a day or so following geomagnetic event, a 7 day delayed increase of VAI seems to appear. Only ΣKp is presented as a characteristic of magnetic activity, because daily values of auroral electrojet index (AE) yield the same general pattern as Kp.

A good response of the daily values of atmospheric temperature at the surface to magnetic activity was observed by Bucha (1977) for several high-latitu-

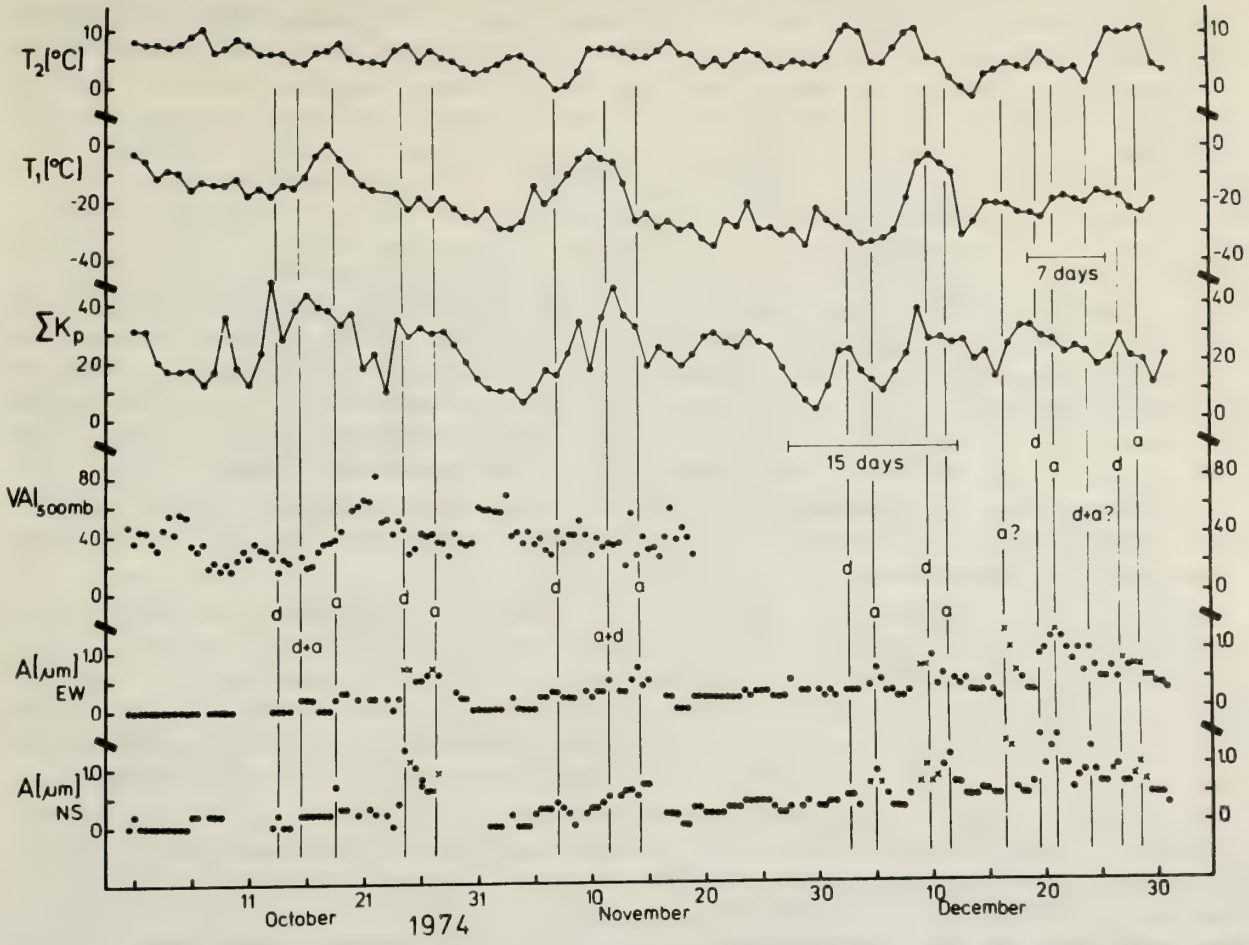


Fig. 3. Day-to-day variability of the amplitude A of Prague meteorological microseisms (separately NS and EW component; data points at 00 and 12 UT; crosses - long-period microseisms), the Northern Hemisphere atmospheric vorticity area index VAI at the 500-mb level, geomagnetic index ΣK_p, daily values of temperature T_1 at a meteorological station (80°N, 80°E), and daily values of temperature T_2 at Prague for the period October-December 1974. The VAI values since November 20 are missing. d,a - direct effect and after-effect in microseisms, respectively; ? - uncertain.

de stations in the period studied. The data of one of these stations are given in Fig. 3 as T_1. They correlate fairly well with geomagnetic activity, but the T_1-response (an increase with increasing magnetic activity) is different in individual events. There are two enhancements of geomagnetic activity (December 3 and the strongest one of October 13), accompanied only by a "microresponse" in the direct effect in microseisms. These two events display no effect in T_1. The moderately disturbed geomagnetic activity of the second half of December is associated with microseismic activity, whereas the same magnetic activity in mid-late November (16-26) is not. This results in significantly higher temperature in the former period (nearly by 10°C) contrary to the expected seasonal trend. These findings show that microseisms could probably be used as a check of the meteorological efficiency of individual geomagnetic storms.

There are two exceptions to the tendency above mentioned. On October 23-26 a strong microseismic burst and a medium enhancement of geomagnetic activity were observed, but no effect in T_1. The effect of December 16-17 (a?) is strong in microseisms, weak in T_1 (supports slightly enhanced temperature) and none or very weak (December 13) in geomagnetic activity. They are both long-periodic microseismic bursts (7-8 sec), i.e. their source regions are either Iceland, or Jan Mayen Is., or the Baltic region, but not the Norwegian regions (Zátopek, 1963). According to meteorological maps, quick passes of well-developed cyclones across the Icelandic microseismic region occurred on October 23 and October 26. The timing of the passes is consistent with microseismic timing. The same is true for the Icelandic and Jan Mayen Island regions as regards the December 16-17 event. Rapid decreases of microseismic activity are coincident with the movement of these cyclones over the Scandinavian part of the continent. Thus, we find meteorological causes of microseismic bursts in both events. As for the October event, no T_1 response is probably due to the T_1-station being located far to the east and to the non-global character of the event as a result of the observed development of geomagnetic activity. A similar situation existed during the December event. The effect is again probably non-global due to an insufficient geomagnetic precursor.

According to Bucha (1976), several days after an enhancement of geomagnetic activity a W-to-E circulation is established over Central Europe due to enhanced cyclonal activity in the North Atlantic frontal zone. This results in a decrease of the summer temperature and an increase of the winter temperature at Prague 7-12 days after the geomagnetic storm and, if geomagnetic activity continues, after another 5-7 days. The winter Prague temperature decreases significantly about 15 days after a decrease of geomagnetic activity (Bucha, 1976). The Prague temperature (upper curve T_2 in Fig. 3) really does not reflect geomagnetic and microseismic variability in the autumn months of October and November significantly, as expected. In winter we observe the predicted effects. The deep and well-expressed decline of geomagnetic activity in late November, associated with microseismic calm, is followed by a rapid decrease of Prague temperature 15 days later, as indicated in Fig. 3. The magnetic activity enhancement of early December is weak and the related microseismic burst only moderate. This results in no detectable effect in the Prague temperature (it is overlapped by the effect of the foregoing calm period). The temperature returns to normal (or a little higher) values on December 15, just 7 days after the enhancement of geomagnetic activity of December 8-10. However, this temperature is not as high as might be expected from geomagnetic data, because the associated microseismic burst is of medium importance only. The greatest increase of temperature in the studied period was observed after December 25, i.e. 7-10 days after another enhancement of geomagnetic activity, as indicated in Fig. 3. This enhancement of magnetic activity is a little smaller than the foregoing one, but is accompanied by a strong microseismic burst and, therefore, by a large increase of Prague temperature. Consequently, microseisms can also serve as a testing tool of geomagnetic storm efficiency in the weather of Central Europe.

The Prague and, generally, Central European meteorological microseisms can be used for studying meteorological responses to extraterrestrial influences connected with geomagnetic bursts and for estimating the efficiency of individual magnetic activity enhancements (bursts) in both high-latitude and Central European meteorology. They are useful for short-range (of the order of one week) forecasts of Central European weather. All the results are rather preliminary, because they are based on an analysis only covering three months, but they appear

to be reasonable and they do not contradict the findings of other authors. A prediction technique, based on geomagnetic and microseismic data, will be developed in future.

5. CONCLUDING REMARKS

It is worth noting the importance of the 35°N latitude. The general smoothed pattern of winter microseisms is the same down to about 35°N latitude in Europe and Japan (Zátopek, 1975). The 35°N latitude is also the approximate equatoward boundary of the occurrence of the winter anomaly (Wakai et al., 1970) and geomagnetic storm effects (Beynon and Williams, 1974 - 37°N) in radio-wave absorption in the lower ionosphere. This points out the importance of the region of 35°N latitude found earlier in global meteorological studies.

The Prague meteorological microseisms have been recorded continuously from 1948 to 1968. Later on the seismograph lost its quality and recording was stopped. When, some time ago, it was found that microseisms could be useful in solar-terrestrial studies, the microseismic data of the nearby (distance about 11.5 km) seismic station of Průhonice began to be evaluated back to 1968. This project will be finished completely in the near future. Based on the 1968 data, the relation between Prague and Průhonice microseisms was established by Procházková (1978) in order to provide a homogeneous series of data since 1948. We are now beginning to study these new microseismic data (e.g. Fig. 3).

Meteorological microseisms have various advantages and disadvantages. They are quite inexpensive to obtain as they are a by-product of seismic monitoring and the only effort and cost necessary consist in evaluating seismic records from a microseismic viewpoint. The Prague microseisms provide information about the North Atlantic frontal zone, which is very important for European weather. On the other hand, microseisms provide only indirect information, which is "contaminated" by their strong seasonal variation and which may sometimes be difficult to interprete due to the possible action of several different source regions.

Microseisms in different regions must first be carefully studied to identify their source regions, which are significantly affected by geological conditions of microseismic wave propagation. For example, the microseisms recorded on the Scandinavian Peninsula and Russian Platform have source regions different from those of Central Europe microseisms (Zátopek, 1961).

In conclusion it can be said that the meteorological microseisms, recorded inland, are an inexpensive and valuable additional tool for studying sun-weather relationships on both the long-period and short-period scale, as well as for improving weather forecasts on a time scale of the order of one week.

REFERENCES

Beynon, W. J. G., and E. R. Williams (1974): Magnetic activity and ionospheric absorption. J. Atmos. Terr. Phys., 36:699.

Bucha, V. (1976): Variations of the geomagnetic field, the climate and weather. Studia geoph. et geod., 20:149.

Bucha, V. (1977): Mechanism of solar-terrestrial relations and changes of atmospheric circulation. Studia geoph. et geod., 21:350.

King, J.W. (1975): Sun-weather relationships. Aeron. Astronautics, 13:10 (also Solar-Terrestrial Physics and Meteorology: A Working Document, SCOSTEP Secretariat, Washington 1975).

Laštovička, J. (1974): Relationship between microseisms, geomagnetic activity and ionospheric absorption of radio waves. Studia geoph. et geod., 18:307.

Laštovička, J. (1977): The interplanetary magnetic field sector structure and meteorological microseisms. Studia geoph. et geod., 21:168.

Laštovička, J. (1978): Lower ionosphere, lower atmosphere and IMF sector structure in winter. Presented on KAPG Symp. "Energy Content and Transfer in the Atmosphere", Sopron, Hungary (also J. Atmos. Terr. Phys. 41:995).

Mustel, E.R., V. E. Chertoprud, and V.A. Khvedeliani (1977): A comparison of changes of the surface atmospheric pressure field during periods of high and low geomagnetic activity. Astron. J., 54:682 (in Russian).

Procházková, D. (1978): Relation between microseisms recorded at seismic stations Praha and Průhonice. Studia Geoph. et Geod., 22:362.

Wakai, N., C. Ouchi, and C. Nemoto (1970): Winter anomaly of ionospheric absorption as observed in Loran-A signals. J. Radio Res. Labs. Japan, 17:185.

Zátopek, A. (1961): Sur la nature et l'origine des microséismes européens. Studia geoph. et geod., 5:51.

Zátopek, A. (1963) : Über einige Ergebnisse der statistischen Periodenerforschung von europäischen Mikroseismen. Studia geoph. et geod., 7:164.

Zátopek, A. (1964): Long-period microseisms generated in eastern part of Atlantic frontal zone. Studia geoph. et geod., 8:127.

Zátopek, A. (1966): Private communication.

Zátopek, A. (1975): On the long-term microseismic activity and some related results. Studia geoph. et geod., 19:14.

Zátopek, A. (1976): On the sources of meteorological microseisms observed in Central Europe. Acta Univ. Oul. A 43, Phys. 12:21 (also Sec. Rept. IASPEI Com. Microseisms).

Zátopek, A., and L. Křivský (1974): On the correlation between meteorological microseisms and solar activity. Bull. Astr. Inst. Czech., 25:257.

Zátopek, A., L. Křivský, and J. Laštovička (1976): Correlations between solar, interplanetary, geomagnetic, ionospheric, atmospheric circulation and microseismic phenomena. J. Interdisciplinary Cycle Res., 7:9.

" ON THE VARIATION OF THE ANNUAL MEAN SEA - LEVEL PRESSURE IN LATITUDE ZONES OF THE NORTHERN HEMISPHERE "

J. XANTHAKIS, B. TRITAKIS and B. PETROPOULOS
Research Center for Astronomy and Applied Mathematics
Academy of Athens
14, Anagnostopoulou street, Athens (136), Greece .

The mean annual sea-level pressure $\overline{P-P}_o$ within 10°-wide latitude zones of the Northern Hemisphere have been studied in relation to the 11-year solar cycle. A close correlation between $\overline{P-P}_o$ and the sunspot cycle in the Northern latitude zones 50°-60°N, 60°-70° N and 70°-80°N is obvious while no correlation was found in the zones lower than the 50° parallel of the earth. The extrapolation of the analytical expression for the mean annual sea-level pressure after 1960, which is the end of the time-series under consideration, shows an encouraging agreement with the observations of the few stations which have published more recent data. The latter conclusion is promising as a means of a rough prediction of the mean zonal sea-level pressure.

I N T R O D U C T I O N

In previous extended papers (Xanthakis 1973,1975) (Xanthakis et al. 1974) (Xanthakis and Tritakis 1977) we have made a global survey of the rainfall as well as a definition of the analytical expressions of the precipitation, within various latitude zones 10°-wide in relation to the solar activity. In the present paper we extend our previously described technique to the study of the sea-level pressure within the same latitude zones of the Northern hemisphere. Our data source, as in the previous papers, is the

" World Weather Records " which contains a large number of stations with observations available till 1960. To maintain the uniformity of the time-series we did not consider new stations after 1960. We only used data from the stations that were operative long before 1960, which were collected from microfiches published by the "World Weather Records ". Thus, an approximate forecasting of the quantity $\overline{P-P}_o$ is more reliable.

1. PREDICTION TECHNIQUE

For each station we calculate the differences :

$$P_i - P_o$$

where P_i are the annual mean sea-level pressure values and P_o is the minimum of the P_i-values during the whole period of observations at a given station. Next, the average of these departures at the different 10° latitude zones is calculated :

$$\overline{P-P}_o = \frac{1}{N}\sum(P_i - P_o)$$

where N is the number of stations located in a particular latitude zone. The correlations obtained between the annual values of $\overline{P - P}_o$ and two solar activity indices (area index I_α after Xanthakis (1970), and the Zurich relative sunspot numbers R_m) where found not to be statistically significant in the following latitude zones : 0°-10°N, 10°-20°N, 20°-30°N, 30°-40°N and 40°-50° N. These time series display only a long-term fluctuation (trend), which will be referred to as L_t, and sinusoidal fluctuations with short periods, between 3 and 7 years, and different amplitudes, which will be called as W. The W oscillations occur in a successive but irregular manner being sometimes superimposed and perhaps mutually complementary.

In the latitude zones confined by the equator and the 50°N parallel, the corresponding time series of the variable $\overline{P-P}_o$

can be represented for each 10° latitudinal zone by the analytical relation :

$$\overline{P - P_o} = C + L_t + W \qquad (1)$$

where C is the long-term averages of the above variable $\overline{(P - P_o)}$. The analytical expression of the L_t term is determined from the calculation of 11-year moving averages of the $(\overline{P - P_o})$. From conventional Power Spectrum Analysis we have also determined the short-term W -fluctuations. Their amplitudes and phases have been graphically inferred from the differences $(\overline{P-P_o}) - C - L_t$. Table 1 shows the number of stations used in the analysis as well as the values of C, L_t and W for each latitude zone (from 0° to 50°N) (fig.3).

Significant correlation coefficients between $(\overline{P-P_c}) - L_t$ and the solar activity indices I_α and R_m were found only in the high latitude zones (northern than 50°N) (see fig.1). As it can be seen from Table 2, and figure 1, these correlations changed sign during the period of records. Thus, in the zone 50°-60°N, the correlation was negative during the time interval 1885-1901, positive between 1902-1924, negative between 1924-1954 and again positive from 1955 onwards. The change in the sign of these correlations occurred more often in the latitude zone 60°-70°N while in the zone 70°-80°N the correlation changed sign only once in the period from 1889 to 1960. A similar change in the sign of the correlation has also been observed in zonal rainfall departures (Xanthakis, 1975).

Scherhag (1950) Köppen (1914) and Troup (1962) reported a similar change in the winter temperatures of Berlin and the temperature in the tropical zone.

It is noteworthy that although these correlations were not very strong they were statistically significant at the 0,01 level.

It is also interesting that the change of the correlation

T A B L E 1

CHARACTERISTIC PARAMETERS OF THE LATITUDE ZONES FROM $0^\circ - 10^\circ$ to $70^\circ - 80^\circ$N

ZONE $0^\circ - 10^\circ$ N

Long. $159^\circ,2$ W to $151^\circ,8$ E, Interval : 1890 - 1960

Number of Stations 5 ÷ 15, ST.DEV = $\pm$ 0,06 mb

$$\overline{P - P_o} = 1{,}95 - 0{,}40\sin\frac{2\pi}{0}(T-1870) - 0{,}20\sin\frac{2\pi}{22}(T-1886) + \alpha_n \sin\frac{2\pi}{\Psi_n}t$$

1870-1950; 1886-1919; 1919-1962; 1962-1995

where α_n varies between $-0{,}60 \div +0{,}80$ and $\Psi_n = 4$ or 6

ZONE $10^\circ - 20^\circ$N

Long. $99^\circ,2$ W to $123^\circ,$ E, Interval : 1886 - 1960

Number of Stations 9 ÷ 24, ST. DEV = $\pm$ 0,06 mb

$$\overline{P - P_o} = 1{,}95 - 0{,}55\sin\frac{2\pi}{80}(T-1864) - 0{,}50\sin\frac{2\pi}{40}(T-1918) + 0{,}70\sin\frac{2\pi}{40}(T-1958) \pm 0{,}30\sin\frac{2\pi}{22}(T-1908) + \alpha_n \sin\frac{2\pi}{\Psi_n}t$$

1918-1958; 1958-1998

$-$ 1908-1941
$+$ 1915-1937
$+$ 1937-1970

where α_n varies between $-0{,}50 \div +0{,}60$ and $\Psi_n = 4,5,6$ or 7.

ZONE $20^\circ - 30^\circ$N

Long. $157^\circ,8$ W to $49^\circ,1$ E , Interval : 1882 - 1960

Number of Stations 12 ÷ 22, ST.DEV. = $\pm$ 0,07 mb

$$\overline{P - P_o} = 2{,}23 + 0{,}50\sin\frac{2\pi}{36}(T-1886) + 0{,}40\sin\frac{2\pi}{36}(T-1866) \alpha_n \sin\frac{2\pi}{\Psi_n}t$$

1886-1904; 1922-1976; 1866-1938

where α_n varies between $-0{,}70 \div +0{,}50$ and $\Psi_n = 4,5,6$ or 8*

T A B L E 1 (continued)

ZONE 30° - 40° N

Long. 122°,4 W to 149°,0 E, Interval : 1883 - 1960

Number of Stations 25 ÷ 44, ST. DEV. = ± 0,08 mb

$$\overline{P - P_o} = 2,21 - 0,30\sin \frac{2\pi}{80}(T - 1860) + 0,30\sin \frac{2\pi}{80}(T - 1949) + \alpha_n \sin \frac{2\pi}{\Psi_n} t$$

1860-1980

where α_n varies between -0,50 ÷ +0,60 and Ψ_n = 4 or 8

ZONE 40° - 50° N

Long. 123°,3 W to 132°,8 E, Interval : 1882 - 1960

Number of stations 36 ÷ 52, ST.DEV. = ± 0,07 mb

$$\overline{P - P_o} = 3,71 + 0,45\sin \frac{2\pi}{90}(T - 1881) + \alpha_n \sin \frac{2\pi}{\Psi_n} t$$

where, α_n varies between -1,30 ÷ +1 and Ψ_n = 3,4,*6,7, or 8

ZONE 50° - 60° N

Long. 170°,2 W to 158°,7 E , Interval : 1885 - 1960

Number of Stations 21 ÷ 50, ST.DEV = ± 0,10 mb

$$\overline{P - P_o} = S\alpha + L_t + W, \text{ where}$$

$S_\alpha = 3,60 - 0,02\ I_\alpha$, (within the intervals 1885 - 1901, 1925 - 1954)

$S_\alpha = 2,30 + 0,02\ I_\alpha$, (within the intervals 1902 - 1924, 1955 -)

$$L_t = 0,10\sin \frac{2\pi}{80}(T - 1865) \pm 0,10 \sin \frac{2\pi}{40}(T - 1905)$$

- 1905-1945
+ 1945-1985

$$W = \alpha_n \sin \frac{2\pi}{\Psi_n} t$$

T A B L E 1 (continued)

Where, α_n varies between -0,50 +0,80 and $\Psi_n = 3^*$ or 6^*

ZONE 60°-70° N

Long. 165°,4 W to 177°,6 E , Interval : 1889-1960

Number of Stations 11-25, ST.DEV = ± 0,06 mb

$$\overline{P - P_o} = S_\alpha + L_t + W, \text{where}$$

$S_\alpha = 5,53 - 0,03\ I_\alpha$, (within the intervals 1889-1902, 1924-1933 1948-1954)

$S_\alpha = 3,70+0,04\ I_\alpha$, (within the intervals 1903-1923, 1934-1947, 1955-1960)

$$L_t = 0,25\sin \frac{2\pi}{80}(T - 1879) - 0,25\sin \frac{2\pi}{22}(T - 1880)$$

$$W = \alpha_n \sin \frac{2\pi}{\Psi_n} t$$

where α_n varies between -2,20 - +2,00 and $\Psi_n = 4$ or 6^*

ZONE 70°- 80° N

Long. 156°,0 W to 80°,4 E, Interval : 1889 - 1960

Number of Stations : 1-9, ST.DEV. = ± 0,06 mb

$$\overline{P - P_o} = S_\alpha + L_t + W, \text{ where}$$

$S_\alpha = 4,49 - 0,03\ I_\alpha$ (within the Interval 1889-1906)

$S_\alpha = 3,54 + 0,02\ I_\alpha$ (within the interval 1907-1960)

$$L_t = 0,50\sin \frac{2\pi}{80}(T-1884) - 0,50\sin \frac{2\pi}{33}(T-1912) \pm 0,50\sin \frac{2\pi}{22}(T-1880)$$

1912-1963 1869-1913, 1913-1957, 1957-2001

$$W = \alpha_n \sin \frac{2\pi}{\Psi_n} t$$

where, α_n varies between -1,00 +1,20

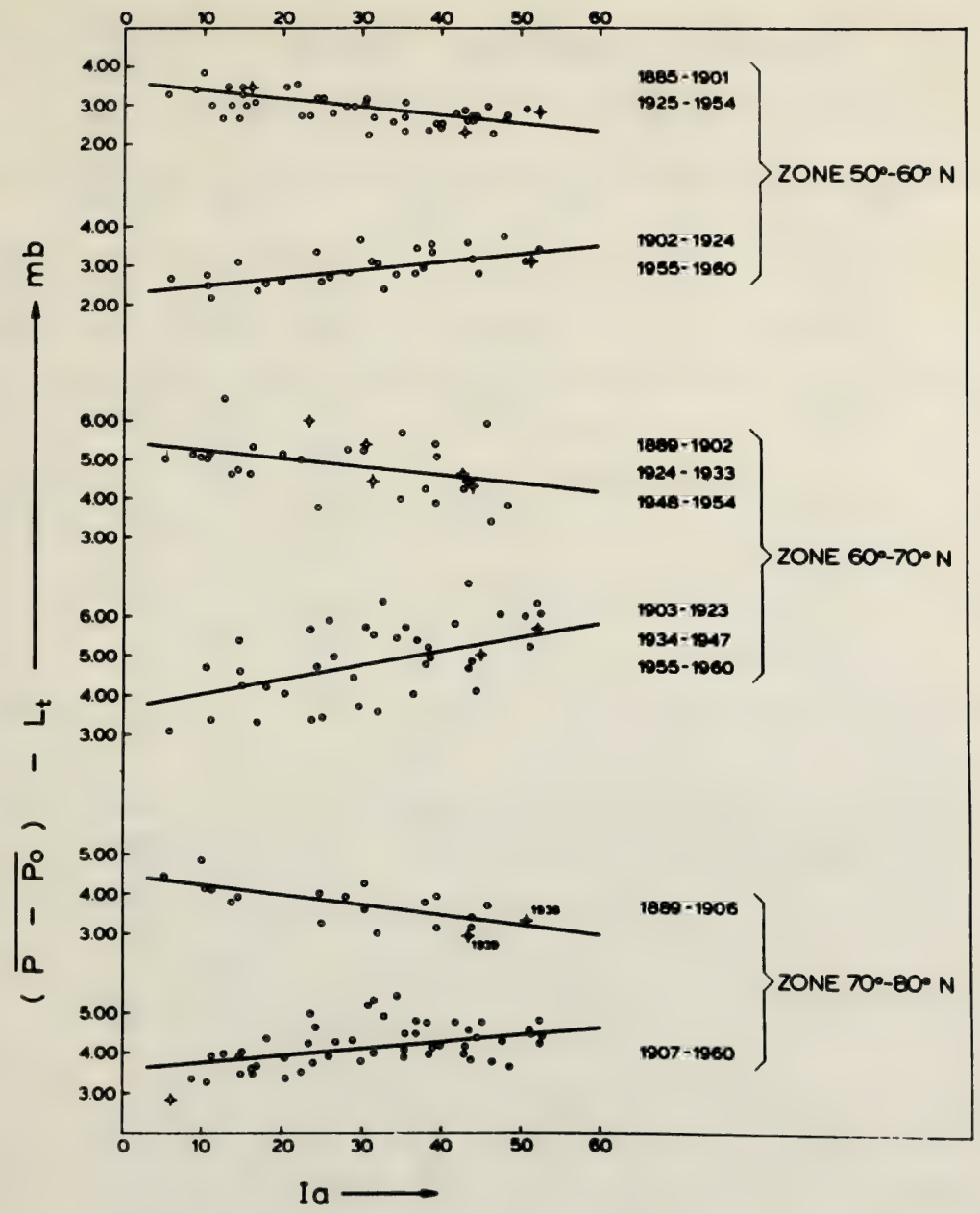


FIGURE 1: DISPERSION DIAGRAMS OF THE QUANTITY $\overline{(P - P_o)} - L_t$ AND I_α FOR THE LATITUDE ZONES 50°-60°N 60°-70°N AND 70°-80°N. ASTERIKS REFER TO THE VERY FEW CASES WHERE THE CORRESPONDING VALUES ARE TAKEN FROM 1:2:1 SMOOTHING.

TABLE 2

CORRELATION COEFFICIENTS BETWEEN $(\overline{P - P_o})$-L_t AND THE INDICES OF THE SOLAR ACTIVITY I_α , R_m

ZONE	$(\overline{P-P_o})$-L_t, I	$(\overline{P-P_o})$-L_t, R_m	TIME INTERVAL
50°-60°	-0,54	-0,48	1885 - 1901, 1925 - 1954
	+0,71	+0,49	1902 - 1924, 1955 - 1960
60°-70°	+0,46	+0,49	1903 - 1923, 1934 - 1947
			1955 - 1960
	-0,51	-0,60	1889 - 1902, 1924 - 1933
			1948 - 1954
70°-80°	-0,70	-0,54	1889 - 1906
	+0,50	+0,36	1907 - 1960

TABLE 3

LONG - TERM AND SHORT - TERM FLUCTUATIONS OF $\overline{P - P_o}$ IN THE 10° WIDTH LATITUDE ZONES OF THE NORTHERN HEMISPHERE

ZONES	FLUCTUATIONS																		
0°-10°			4			6*				22							80		
10°-20°			4		5	6		7		22						40	80		
20°-30°			4		5	6							36						
30°-40°			4						8								80		
40°-50°		3	4*			6		7								40			90
50°-60°		3*				6*										40	80		
60°-70°			4			6*				22							80		
70°-80°			4			6			8	22		33					80		

* statistically significant fluctuation at a confidence level lower than 0,05.

sign between $(\overline{P-P_o})$ $-L_t$ and I_α occurs near the extrema of the solar cycle.

In the high-latitude zones the time series of the $\overline{P-P}_o$ variable can be approximated by the analytical relation

$$\overline{P - P}_o = S_\alpha + L_t + W \qquad (2)$$

where S_α represents the regression line between $(\overline{P - P}_o) - L_t$ and the areas index I_α . The analytical expressions for S_α , L_t and W are given in Table 1 (zones 50° to 80° N). Table 3 below shows the "periods" of the oscillations L_t and W for all latitude zones. It is interesting that the long-term fluctuations diplay " "periodicities " of 22 and 80-90 years and sometimes multiples or submultiples of them. The fluctuations of 40 and 80-90 years can not be further discussed with respect to any "cyclic " behaviour because of the shortness of the record (less than 80 years).

This is not the case, however , with regard to the 22 year fluctuations which appear twice or three times sometimes changing their " phase " and thus displaying a " cyclic " behaviour.

The results from the calculations through the relations (1) and (2) are presented graphically in Figs. 2 and 3.

C O N C L U S I O N S

The variation in the zonal averages of annual mean sea-level pressures have in general small amplitudes of the order of 2 to 3 mbs. These fluctuations were not correlated with the solar activity indices I_α and R_m in the zones between the equator and the 50°N parallel. In the high latitude zones, however, there was an appreciable correlation, statistically significant at the 99% level, which changes sign at various times.

The fluctuations of the variable $\overline{P - P}_o$ can be represented with high accuracy through the relations (1) and (2) with corresponding standard deviations of the order of $\pm$ 0.05 to $\pm$ 0.08 mbs.

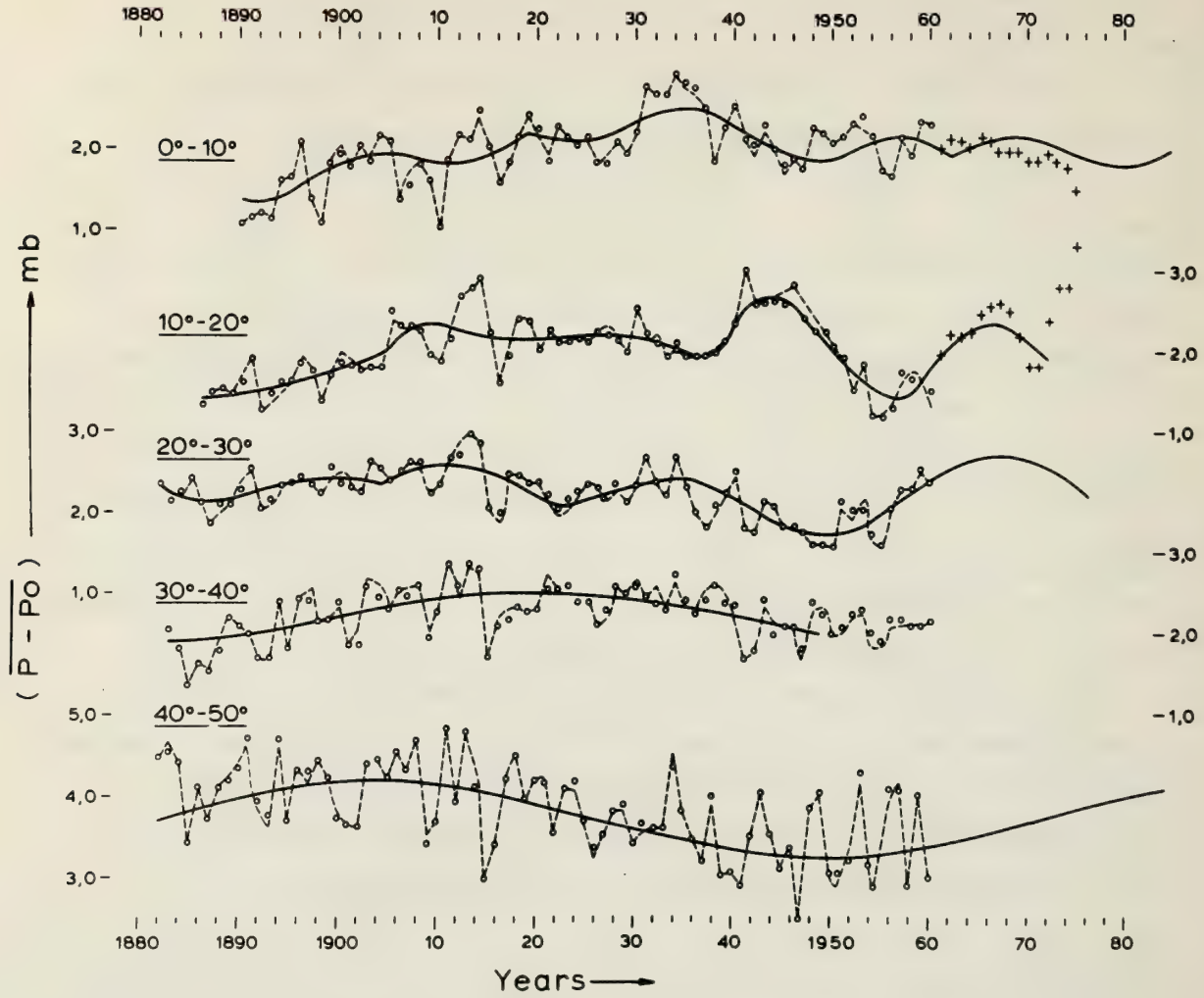


FIGURE 2 : ANNUAL VARIATION OF THE QUANTITY $C+L_t$ (CONTINUOUS LINE) AND THE CALCULATED VALUES OF $\overline{P-P_o}$ FROM THE RELATION (1) (DASHED LINE). THE CIRCLES REPRESENT THE OBSERVED VALUES OF $\overline{P-P_o}$ WHILE THE CROSSES CORRESPOND TO THE DATA OF A FEW STATIONS WE USE FOR CONFIRMATION OF THE PREDICTION.

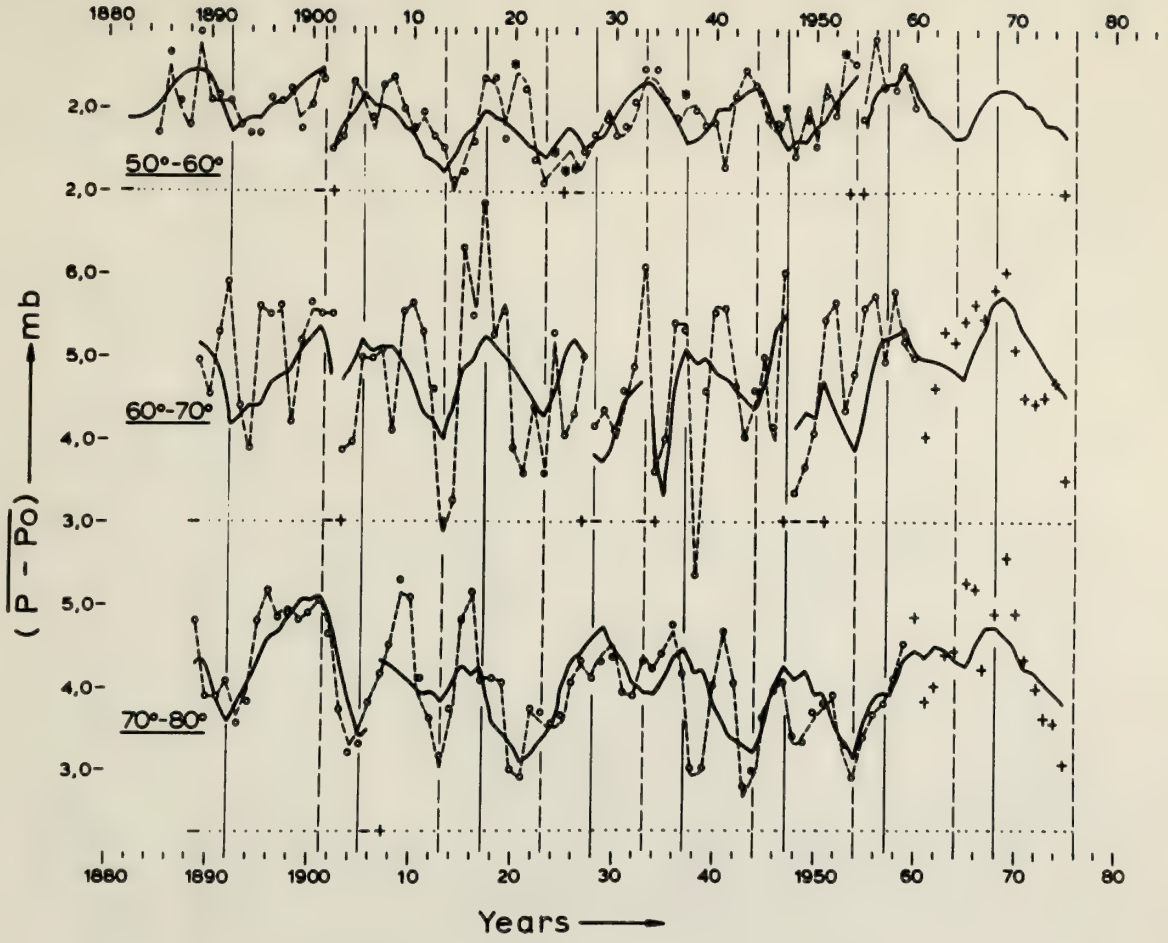


FIGURE 3 : ANNUAL VARIATION OF THE QUANTITY $S_\alpha + L_t$ (CONTINUOUS LINE) AND THE CALCULATED VALUES OF $\overline{P-P}_o$ FROM THE RELATION (2) (DASHED LINE).
THE VERTICAL CONTINUOUS LINES CORRESPOND TO THE MAXIMUM OF THE SOLAR ACTIVITY WHILE THE BROKEN ONES TO THE MINIMUM OF IT.
THE CIRCLES REPRESENT THE OBSERVED VALUES OF $\overline{P-P}_c$ WHILE THE CROSSES CORRESPOND TO THE DATA OF A FEW STATIONS WE USE FOR CONFIRMATION OF THE PREDICTION.

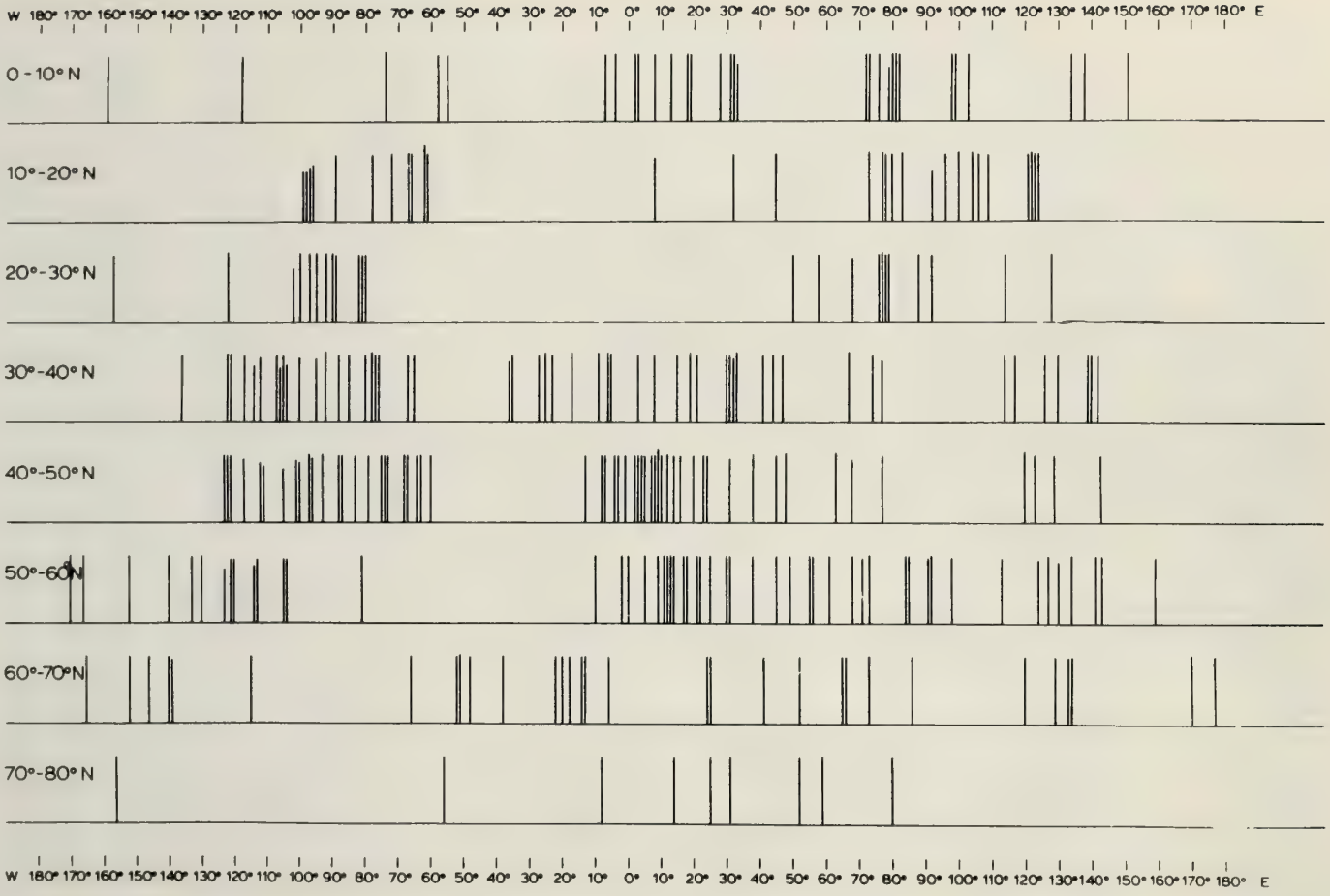


FIGURE 4. LONGITUDINAL DISTRIBUTION OF THE STATIONS UNDER CONSIDERATION AND THEIR RELATIVE SIZE of P_o.

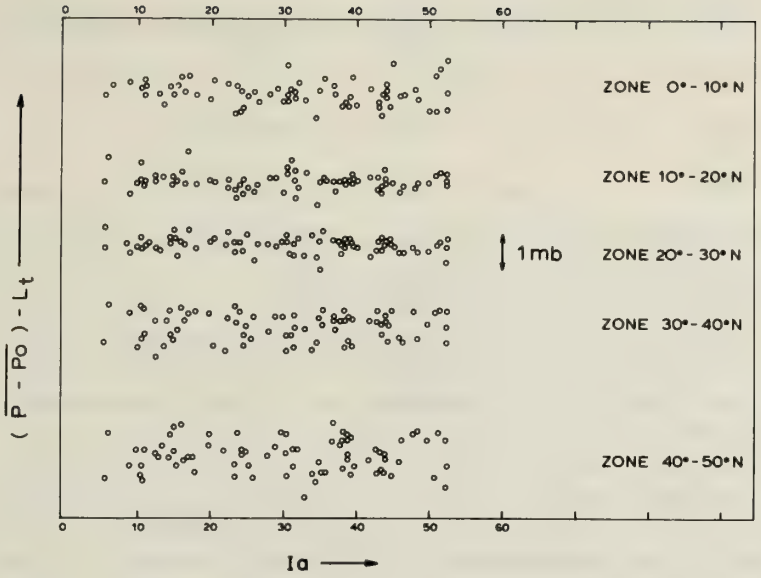


FIGURE 5 : DISPERSION DIAGRAMS OF THE QUANTITY $(\overline{P-P_o})-L_t$ AND I_α FOR THE 10° WIDE LATITUDE ZONES 0°- 50°N.

In view of the relative shortness of the record, no cyclic behaviour can be attributed at present to the long-term fluctuations component L_t. Finally, the encouraging agreement of the extrapolated analytical expression of $\overline{P - P_o}$ with the data of a few stations which continue their observations after 1960 in the latitude zones 0°-10°N, 10°-20°, 60°-70°N and 70°-80°N, indicates a simple way of prediction for the mean zonal sea-level pressure.

The extrapolated analytical expression of $\overline{P-P_o}$ after 1960 did not include short-term fluctuations W because of the difficulty to define their position and amplitude.

R E F E R E N C E S

Köppen, W. (1914) : Lufttemperaturen, Sonnenflecke und Vulkanausbruche, Met. Zeit., 31, 305-28.Braunschweig.

Scherhag, R. (1950) : Bestehen Zusammenhänge Zwischen der elfjährigen Sonnenfleckenperiode und der allgemeinen Zirkulation? Deutsche Hydr. Zeit., 3, 108-11. Hamburg.

Troup, A. J. (1962): A secular change in the relation between the Sunspot Cycle on temperature in the tropics, Geophisica pura e applicata, 51, 184-98. Milan.

Xanthakis, J. (1970) : On a relation between the indices of solar activity in the photosphere and the corona, sol.phys 10 : 168.

Xanthakis, J. (1973) : Solar activity and Precipitation. Proc. of the 1st European Astronomical Meeting, Athens, September 4th, 1972, vol. 1.

Xanthakis, J., C.Poulakos, and B, Tritakis (1974) : Solar activity and precipitation within the zones of latitude 0°-40°N. Praktika of the Academy of Athens 49 : 187

Xanthakis, J. (1975) : Solar activity and a global survey of the precipitation. Papers of the Academy of Athens No.37

Xanthakis, J., and B. Tritakis (1977) : Analytical expression of the mean annual variation of the precipitation within various latitude zones of the earth. J. interdisc.cycle Res. 8 : 226

THE 13.6-DAY OSCILLATION IN THE STRATOSPHERE

A. Ebel
Institute for Geophysics and Meteorology, University of Cologne
D-5000 Cologne 41, F.R.G.

A 13.6-d oscillation of zonally averaged height differences of the 10-mb surface, which is significantly correlated with solar activity fluctuations, is analyzed with respect to its statistical properties. The oscillation can be interpreted as a zonal wind perturbation in the northern hemisphere. The gain obtained by means of spectral analysis for the "10-mb surface" system appears to be relatively fixed in time. The latitudinal dependence of gain and phase resembles that of basic modes with zonal wave number zero for oscillating layers on a rotating sphere. The statistical model of a linear system with one input and output can be used to derive a "prediction" equation for a mean 13.6-d oscillation. The implications of the model concerning the temporal behavior of the stratospheric system are discussed showing that the 13.6-d oscillation is only one example—and a relatively simple one—of possible solar activity effects at 10 mb in a broader range of oscillation frequencies.

1. INTRODUCTION

Comparing daily values of the 10.7-cm flux of the solar radiation and zonal indices of the 10-mb circulation, a 13.6-d oscillation of the zonal mean wind responding to solar activity changes has been found at the height of the 10-mb surface in the northern hemisphere between 10°N and 80°N (Ebel and Bätz, 1977). The oscillation has been extracted from the 10-mb data applying the methods of spectral analysis of time series (Jenkins and Watts, 1968). Inherent in this form of bivariate time series analysis is the assumption of a linear system (the 10-mb surface) having one input (solar activity "processes") and one output (zonal index changes) determined by the response function of the system. Using this simple model of solar activity/stratosphere (10 mb) interaction it is easy to arrive at a prediction of the 13.6-d oscillation provided the response of the system and the input function are known or can be predicted for this oscillation period, as discussed in Section 3.

The phenomenon studied here and briefly described in the next section is certainly of minor importance compared to other meteorological effects in the stratosphere. In terms of wind it is a perturbation of less than 0.6 m/s

(Figure 1). Nevertheless, there are good reasons to study even such minor effects as far as the understanding of the physics of the stratospheric system and the application of statistical techniques to the analysis of this and similar systems are concerned:

1. Little knowledge and contradicting findings (e.g., Gerety et al., 1977; King, 1975; Olson et al., 1975; and Wilcox et al., 1976) and ideas exist with respect to the problem of how deep and how efficient solar activity effects, which are well established at least down to the mesopause, can penetrate to lower atmospheric layers.

2. The 13.6-d oscillation resembles some features found theoretically for oscillating layers on a rotating sphere (Longuet-Higgins, 1968); this gives some support to the assumption that statistics have helped to unravel some of the real behavior of the 10-mb surface.

3. There is good evidence that other oscillations with periods different from 13.6 d (which is approximately half the rotation period of the sun) are also correlated with solar activity oscillations; this may help to explore the variability of the stratospheric system and thus improve climatological studies.

4. The 13.6-d oscillation can be described with simple meteorological (physical) quantities and has a simple morphology. Therefore, it appears to be especially suited for the study of some principal problems concerned with the statistical methods used for investigating solar activity/weather relationships.

The purpose of this paper is therefore not so much the outline of a simple "prediction" technique for a single line in a broad spectrum of stratospheric oscillations as it is an attempt to clarify the assumptions necessary for progression from the (statistical) diagnosis of a sun-weather phenomenon to its prediction. This attempt is made in Section 4 where the stability of the "10-mb surface" system is analyzed. In terms of spectral analysis it is the frequency response function which is discussed. The present study is restricted to this topic, but it should be noted that the determination of the second component required for a prediction, namely, the input function "solar activity" might lead to similar problems like the evaluation of the response function.

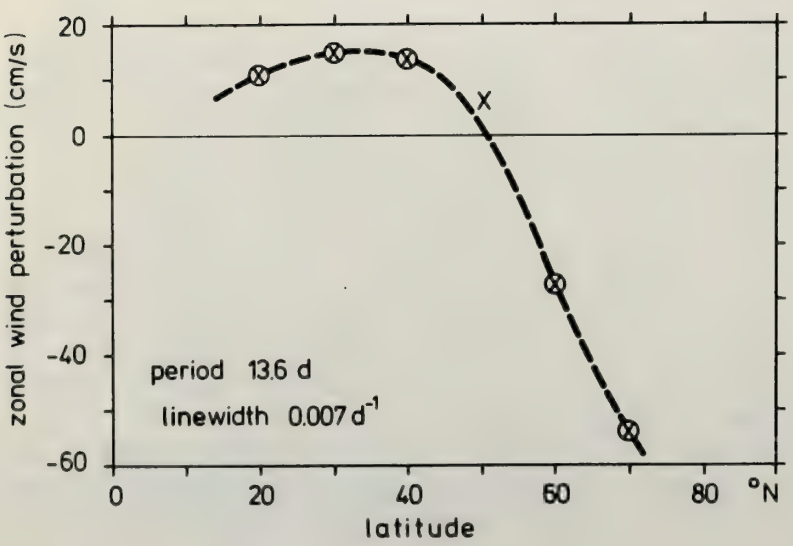


Figure 1. Perturbation of the mean zonal component of geostrophic wind correlated with solar activity oscillations at frequency 1/(13.6d). Encircled crosses: coherency estimate exceeds 95% confidence limit. Width of spectral line= 0.007 d^{-1}.

2. PHENOMENOLOGY OF THE 13.6-d OSCILLATION

For a detailed description of the 13.6-d oscillation of 10-mb indices and a complete discussion of its statistical significance, the reader is referred to Ebel and Bätz (1977). Only a brief summary of the applied data and final results is given here.

The zonal 10-mb indices (I) are defined as the zonally averaged height differences of the 10-mb surface for two latitude circles ϕ_1 and ϕ_2 separated by 20° ($\phi_2 - \phi_1 = 20°$):

$$I(\phi_1, \phi_2) = \frac{1}{n} \sum_{i=1}^{n} [h_i(\phi_1) - h_i(\phi_2)] \qquad (1)$$

where h_i is the geopotential height in gpm at n (normally 36) gridpoints on the latitude circles at 10°, 20°, ... 80°N. These data have been provided by the Meteorological Institute of the Free University of Berlin for the period November 1964-October 1971. The zonal 10-mb index can be interpreted as the zonally averaged geostrophic wind v (in m/s) using the relationship

$$v = 0.03\ I/\sin(\phi_1 + 10°) \qquad (2)$$

For monitoring the solar activity, daily values of the 10.7-cm flux of the solar radiation (briefly S10.7, in units of 10^{-22}W m^{-2} Hz^{-1}) have been chosen. Correlating the total time series of the 10-mb indices and of S10.7 a clearly significant coherence estimate was obtained at or near an oscillation period of 13.6 d, corresponding to half the rotation period of the sun. This is true for all latitude belts except for the index for 40°N-60°N. Coherence estimates, the gain for the 10-mb index, and its confidence limits are found in Table 1, part A, which also contains the phase estimates for the oscillation. Evidently, the oscillations at 10-mb are nearly in phase with the solar activity oscillations at latitudes below 50°N, and they are out of phase above 50°N (with a lag of roughly one day). Using the autospectral estimate for the indices at frequency f, $C_{II}(f)$, the coherence squared, $K^2(f)$, and an estimate of the bandwidth of the correlated signal, Δf, one arrives at an approximate amplitude $I'(f)$ of the oscillation of I given by

$$I'(f) = [K^2(f) C_{II}(f) \Delta f]^{\frac{1}{2}} \qquad (3)$$

Inserting the result into equation (2), an estimate is obtained for the amplitude of the quasiperiodic zonal wind perturbation at frequency f in a given latitude belt. The result for f = 1/(13.6 d) is shown in Figure 1, where in-phase oscillations are assigned to positive perturbations.

3. FREQUENCY RESPONSE

In principle, equation (3) is equivalent to the relationship

$$C^{+}_{II}(f) = G^2(f) C_{SS}(f) \qquad (4)$$

Table 1. Estimates of gain, squared coherency, and phase. [Gain in gpm/(10^{-22}W m^{-2}Hz^{-1}), phase in degrees (positive if S10.7 leads). Degrees of freedom 33 (part a) and 29 (parts B and C). Bandwidth 0.0067 d^{-1} (A) and 0.0133 d^{-} (B and C). Tukey window used. 95% confidence limit of coherency squared for prior selection 0.12. Solar activity spectral estimate C_{SS} in (10^{-22}W m^{-2}Hz^{-1})^{2}d. 95% confidence interval is (0.64, 1.7) x C_{SS}.]

Latitude (°N):	10-30	20-40	30-50	40-60	50-70	60-80
A. Period 11/64-10/71, sol. act. spectral estimate 1.6x10^5, f = 0.0738 d^{-1}.						
Gain	0.039	0.076	0.081	0.044	0.24	0.54
95% conf. interval, gain	±0.039	±0.055	±0.072	--	±0.20	±0.38
Squared coherency	0.15	0.27	0.25	0.06	0.22	0.22
Phase	36	2	27	88	201	235
B. Period 12/64-11/67, sol. act. spectral estimate 3.4x10^4, f = 0.0750 d^{-1}.						
Gain	0.048	0.023	0.093	0.16	0.13	0.63
95% conf. interval, gain	--	--	--	--	--	--
Squared coherency	0.07	0.02	0.06	0.11	0.02	0.08
Phase	106	161	179	125	-83	-53
C. Period 10/68-12/70, sol. act. spectral estimate 1.9x10^5, f = 0.0750 d^{-1}.						
Gain	0.054	0.071	0.094	0.046	0.24	0.43
95% conf. interval, gain	±0.028	±0.054	±0.087	--	±0.21	±0.43
Squared coherency	0.46	0.28	0.23	0.06	0.22	0.17
Phase	-8	-9	16	84	195	209

where G(f) is the gain function of the "10-mb$_+$surface" system, $C_{SS}(f)$ the autospectrum of solar activity (S10.7), and $C^+_{11}(f)$ a prediction of the output amplitude (10-mb index) which is only due to the input S10.7. Since $1'^2(f) = C^+_{11}(f)\Delta f$, the perturbation of the zonal index (equation (3)) or of the zonal mean geostrophic wind (equation (2)) with a given bandwidth can be derived with the aid of equation (4). The phase estimate F(f) (>0, if the oscillation of S10.7 leads that of the 10-mb index) completes the frequency response function

$$H(f) = G(f)\ \exp[iF(f)] \qquad (5)$$

The problem with the application of the "prediction equation" (4) for C^+_{11} is that the gain (and phase) estimates and C_{SS} have to be known. From now on we will concentrate on the first half of the problem, namely on the investigation of the frequency response characteristics of the 10-mb system around the oscillation period 13.6 d. The main assumption made for practical reasons for the derivation of the frequency response function concerns the stationarity of the stratospheric system at least for the time interval for which data have been available. If the system does not change in the future, H(f) should remain constant and the perturbation of the 10-mb index could be predicted from the input "solar activity (S10.7)". Besides, the hypothesis of a fixed system is implicitly inherent in most statistical studies of

atmospheric systems. No wonder that it causes so much trouble, especially in investigating solar activity-weather relationships.

Looking at the gain and phase estimates for the 10-mb index in Table 1, it seems that we are correct in concerning the 10-mb system around the oscillation period 13.6 d (though there is no guarantee for future stationarity). The data set has been split into two samples, one with low solar activity (part B), the other with higher solar activity (C). The gain exhibits nearly the same dependence as for the total period of observation (Table 1, A) in both cases, though it should be noted that the data for low solar activity do not result in coherency estimates significant at the 95% confidence limit. Yet it is evident that for weak input signals (low solar activity) difficulties in arriving at good estimates of the frequency response from the noisy 10-mb system have to be expected. The 95% confidence limits of the gain, which can be taken as a measure of the quality for a predicted response, always exceed the gain estimate in Table 1, part B. There is one indication in the gain estimate that the frequency response at period 13.6 d may change with time at certain latitudes. The 40°N-60°N belt shows an unexpectedly high value of the gain for low solar activity, which is approximately four times that for the period of high solar activity or for the total period. The coherency estimate exceeds the 90% confidence limit, whereas it is near zero in the other cases. It seems appropriate to study the temporal behavior of the 10-mb system in somewhat greater detail.

Before doing this it should be pointed out that the splitting of the data set into two separated periods made it necessary to increase the bandwidth of spectral computations to get the same degrees of freedom as for the total period (Table 1, headnote). Tests carried out by window broadening resulted in a decrease of the coherency peak showing that the solar activity effect on the zonal 10-mb indices is narrow banded.

4. "10-mb SURFACE" SYSTEM

The long-term variability of the stratosphere, which possibly also depends on solar activity (Naujokat, 1978) may affect the frequency response of the "10-mb surface" system—as given by the zonal indices, equation (1)—to solar activity oscillations. During the period 11/64-10/71, the system appeared to be relatively fixed near the oscillation period 13.6 d, i.e., half the rotation period of the sun. Yet there are other oscillation periods where strong correlations between the zonal indices and the solar activity can be found during shorter time intervals, e.g., individual summer and winter periods (Figure 2). They can be highly significant in the framework of statistical methods applied, but they disappear when longer time intervals are treated. For instance, a coherent 27-d oscillation of the zonal indices might be expected regarding the very strong power in the S10.7 spectrum due to solar rotation. Good correlation near the rotation period may occasionally appear during some time at some latitude. Yet it is completely suppressed in longer time series. The autospectra of the zonal indices may even show a strong minimum near the period 27 d. An example is shown in Figure 3.

The spurious appearance of large significant values in the coherency spectra derived from short time series of the zonal 10-mb index and S10.7

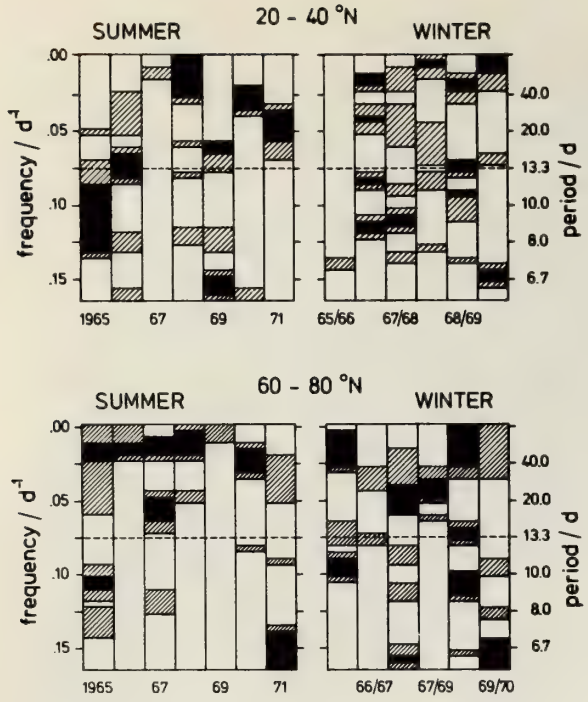


Figure 2. Coherency estimates (K) for 10.7-cm fluxes of solar radiation and zonal 10-mb indices of the latitude belts 20-40°N and 60-80°N.
Winter period: October-April.
Summer period: April-October.
Degrees of freedom of spectral estimates: 9.
Bandwidth: 0.0222 d^{-1}.
Hatched areas: K exceeds 95% confidence limit for prior selection.
Dark areas: 95% confidence limit for posterior selection exceeded.
Broken line at period 13.6 d.

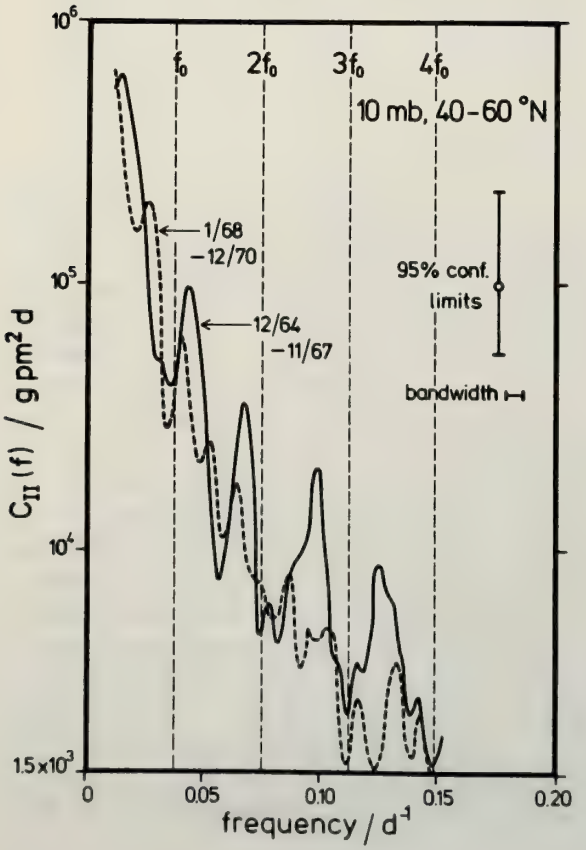


Figure 3. Autospectra of the zonal 10-mb index for 40-60°N.
Period of low solar activity: 12/64-11/67.
Period of higher solar activity: 1/68-12/70.
f_o = solar rotation frequency = 1/27.2 d.

points to the problem of stationarity or stability of the stratospheric system. One may distinguish three main causes for spurious significant results:

1. The applied statistical methods are not in agreement with the requirements of the physical system (nonstationarity, nonlinearity, etc.); in the case of the 13.6-d oscillation this has to be checked carefully with future observations.

2. The system may have more than one input leading to output signals, masking or pretending the expected output; in the case of the stratosphere one has to expect coupling with the troposphere—a problem still to be investigated by multivariate spectral analysis for the 13.6-d oscillation.

3. The system may have discrete and temporarily fixed states and the transition between these states might itself be a stochastic process. This point certainly involves the most serious complication in diagnosing and predicting a physical effect only on the basis of statistical methods in any atmospheric system or subsystem such as the 10-mb surface.

To illustrate this problem the coherency between the 10.7-cm flux and the zonal 10-mb index is compared in Figure 2 for periods larger than six days as obtained for individual summer and winter periods in two latitude belts. The coherency exceeds the 95%-confidence limit for prior selection in the hatched fields and the limit for posterior selection in the dark fields on Figure 2. These fields represent roughly 30 percent and 10 percent, respectively, of the total area. It seems difficult to explain this result just by inappropriate application of statistical methods. Rather, it appears that sporadic solar activity effects may show up at the 10-mb surface in a wide range of frequencies. With a few exceptions they disappear when longer time series are used. This can easily be explained by limited and irregular periods of efficiency of the solar activity input and by temporal changes of the phase relationship between input and output siganls. These are typical features of stochastic processes.

Further indications of the temporal variability of the stratospheric system in a broad frequency range (shown for $f < 0.15\ d^{-1}$ in Figure 3) are contained in the autospectral estimates of the zonal indices (or mean zonal geostrophic wind) for 40°N-60°N at 10 mb. The variance of the system increases during the period with low solar activity (12/64-11/67, continuous line). Apparently this occurs systematically concerning the spectral ranges between the solar rotation frequency and its higher harmonics. The reason for this is not yet understood.

5. CONCLUSIONS

The discussion in the last section shows that a comprehensive exploration of the relationship between solar activity and stratospheric weather and climate still requires the solution of numerous problems with respect to the statistics to be applied. The special case of the 13.6-d oscillation seems to indicate that, at least in some limited frequency intervals, certain fractions of the variance of stratospheric quantities can be determined with simple statistical techniques (spectral analysis) using solar activity parameters. "Prediction" in this case can only mean the estimate of an average signal or oscillation over longer periods and thus—for the present—

concerns the climate rather than the weather of the stratosphere. The verification of the findings for the 13.6-d oscillation in the sense of a prediction method requires 10-mb data at least up to the year 1978, which is not yet available.

The causes of the relationship between solar activity and the mean zonal wind at 10 mb near the oscillation period 13.6 d still must be explored. Speculations about the mechanisms (the role of ozone, connection with the full rotation period of the sun) are beyond the scope of this paper. They can be found in the paper of Ebel and Bätz (1977).

Acknowledgement. The 10-mb data have been provided by the Meteorological Institute of the Free University, Berlin. Valuable help by Professors K. Labitzke, G. Naujokat, and K. Petzold, Berlin, is gratefully acknowledged. Parts of this paper refer to a study supported by the Deutsche Forschungsgemeinschaft under Grant Eb 56/2.

REFERENCES

Ebel, A., and W. Bätz (1977): Response of stratospheric circulation at 10 mb to solar activity oscillations resulting from the sun's rotation. Tellus, 29:41.

Gerety, E. J., J. M. Wallace, and Ch. S. Zerefos (1977): Sunspots, geomagnetic indices and the weather: A cross-spectral analysis between sunspots, geomagnetic activity and global weather data. J. Atmos. Sci., 34:678.

Jenkins, G. M., and D. G. Watts (1968): Spectral Analysis and Its Applications. San Francisco: Holden Day.

King, J. W. (1975): Sun-weather relationships. Aeronaut. Astronaut., 13:10.

Longuet-Higgins, M. S. (1968): The eigenfunctions of Laplace's tidal equations over a sphere. Philos. Transact. Roy. Soc. London, A, 262:511.

Naujokat, B. (1978): Long-term variations in the stratosphere of the northern hemisphere during the last two sunspot cycles. Paper presented at International Symposium on Solar-Terrestrial Physics, Innsbruck, Austria, No. TA 8.6.

Olson, R. H., W. O. Roberts, and C. S. Zerefos (1975): Short term relationships between solar flares, geomagnetic storms, and tropospheric vorticity. Nature, 257:113.

Wilcox, J. M., L. Svalgaard, and P. H. Scherrer (1976): On the reality of a sun-weather effect. J. Atmos. Sci., 33:1113.

A CONSIDERATION OF THE POSSIBLE USE FOR WEATHER FORECASTING OF A PARTICULAR SUN-WEATHER RELATION

R. Gareth Williams and Michael J. Rycroft
Physics Department,
The University,
Southampton, England.

All sun-weather effects being discussed at present are based on statistical correlations and not on acceptable physical models. Therefore, it is appropriate to ask whether or not it is possible to improve meteorological forecasts by using these relations before we have a thorough understanding of the physics involved. A particular sun-weather relationship, involving the vorticity area index (VAI) and the solar sector boundaries (SSB), (Wilcox et al., 1974, 1976) is examined in order to consider this question for routine, daily weather forecasting. Wilcox et al. (1975) reported on the seasonal variations of the effect. Evidence is presented here showing that the effect is also inconsistent from year to year. The results of a study of the energetics of the VAI - SSB effect are also presented. It is concluded that we are, as yet, some way from using this particular sun-weather relationship as a predictive tool. It is suggested that the most productive way of moving towards this goal is to perform new statistical studies specifically designed to obtain a one-to-one sun-weather relationship and also to provide a detailed, overall picture of the meteorological effects. Such a relationship could probably be used as a predictive tool and would strongly focus the search for a physical mechanism.

1. INTRODUCTION

The "academic" aim of sun-weather relations is to improve our understanding of the complex interaction between solar activity, its effects on the interplanetary medium and changes in the terrestrial magnetosphere, ionosphere and atmosphere. The "economic" aim is to improve weather forecasting. Current understanding of what physical processes might be responsible for causing a sun-weather effect is somewhat limited. Indeed the difficulty experienced in finding such processes is one of the mainstays of arguments claiming that all sun-weather relations must be purely statistical flukes. Such arguments may or may not prove to be valid, but for the purposes of this paper it is assumed that physical links between transient solar phenomena and the troposphere do exist and are of a significant amplitude. Therefore, we must consider whether the "economic" goal can be

fulfilled without first achieving the "academic" one.

There seem to be two major problems to be surmounted before the "economic" aim can be attained. Firstly, it is necessary to have a one-to-one sun-weather effect, i.e. given a particular solar event, a particular tropospheric response must always be observed to occur. Such a relationship could also involve any dependence on ambient meteorological conditions and must allow for variations in the magnitude of the response caused, for example by variations of the amplitude of the solar impulse. Once an equation of this type has been found, a detailed description of the response of all the relevant tropospheric parameters must be obtained. It is not sufficient to know how the VAI responds; other, more conventional and physical parameters must be considered.

These two problems are discussed for the particular relationship between the VAI and the SSB.

2. ONE-TO-ONE RELATIONSHIP

Wilcox et al. (1974, 1976) have reported a significant statistical correlation between the VAI and the passage of the earth through the SSB. The correlation was obtained using a superposed epoch analysis and data covering the years 1963-73 inclusive. The solid lines in Fig.1a & b (Williams and Gerety, 1978) are reconstructions of the results of Wilcox et al. (1974, 1976) and characteristically show approximately a 10% decrease in the VAI a day or so after the passage of the SSB.

Wilcox et al. (1975) have also reported on the seasonal variations in the magnitude of the results. They show that the effect only appears in the months November through March. Thus it is clear that not all SSB cause the VAI to decrease. Nor is it sufficient to say that all the SSB occuring in winter cause an effect. The definition of winter may be lengthened or shortened by a week or two without seriously effecting the results. Therefore, we cannot claim as yet to have a one-to-one relationship.

Arguments along these lines become much more forceful when we further consider the results of Williams and Gerety (1978) as shown in Fig.1a & b. As mentioned above, the solid lines are essentially reproductions of the results of Wilcox et al. (1974, 1976). (For further details of the analysis techniques used, see Williams and Gerety (1978)). The dashed lines are the results of analysing new data covering January 1974 through March 1977. The results shown are for the months November through March. At 500 mb no effect at all is discernible, and at 300 mb the amplitude of the signal is at best seriously reduced.

This lack of response is not attributable to the solar minimum of 1976. Fig. 2 shows the result of analysing in identical fashion the 500 mb data for the similar $3\frac{1}{2}$ year period 1963-66 which covered the previous solar minimum. Nor is it attributable to variations in the distribution of key-dates: since a superposed epoch analysis is essentially a cross-correlation

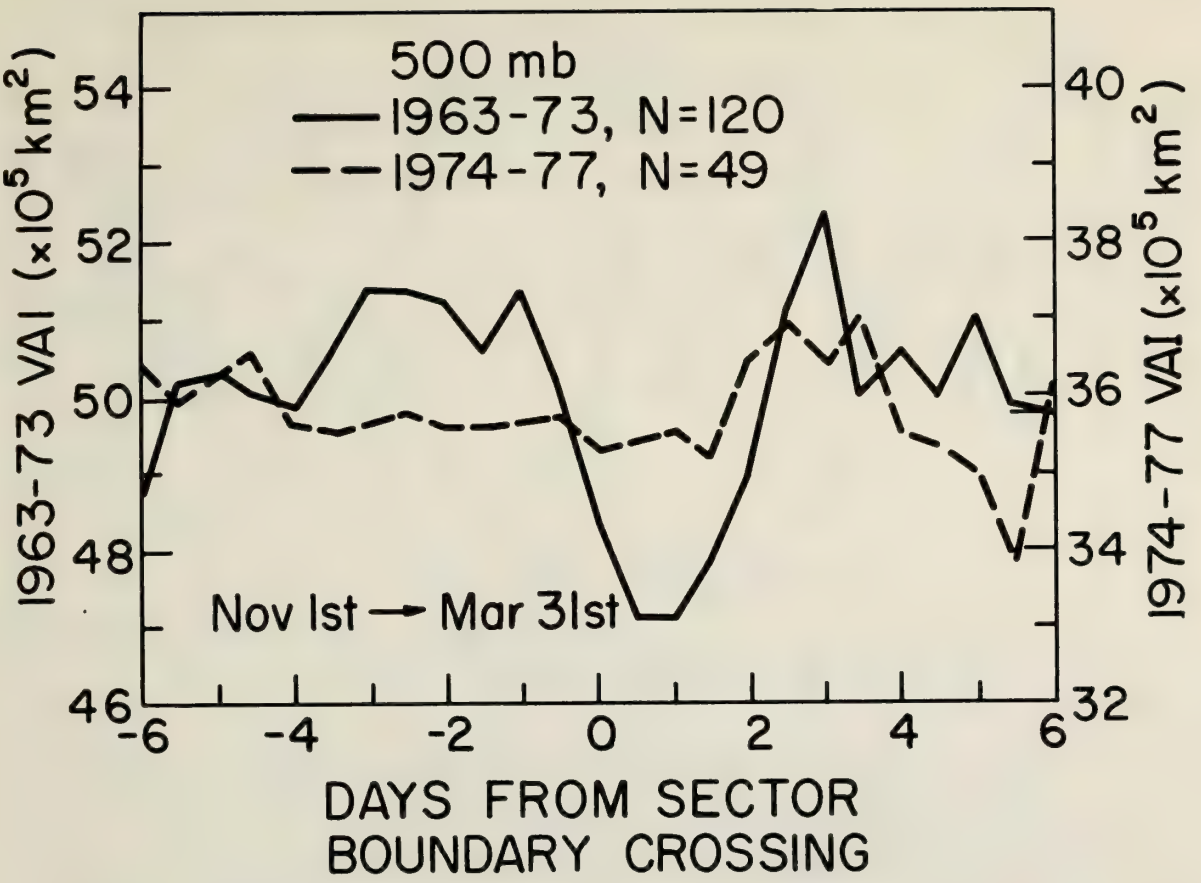


FIG. 1a: Results of Superposed Epoch Analysis of 500 mb VAI using SSB as keydates (from Williams and Gerety, 1978)

its result may depend on periodicities in either the keydates or the data being superposed. (Williams, 1978b) However Fig. 3 indicates that there are no marked differences in the properties of the keydates.

Since we are assuming that sun-weather effects do exist, this surprising result strongly suggests that many of the keydates used by Wilcox et al. (1974, 1976) may not have caused a tropospheric response. This implies that the 10% amplitude has been damped by some null results and that the true response of the VAI is even more marked. Thus, not only are we missing a one-to-one relationship, as yet, but also we consequently cannot be certain of the amplitude of the effect.

This one-to-one relationship, if it is found, will almost certainly not be simple. It is, perhaps, interesting to note that the typical winter values of the VAI were much lower during 1974-77 than from 1963-73 (see Fig.1) Also, the VAI is typically lower in summer than in winter. These two facts suggest that the explanation of both seasonal and inter-annual variations may lie in a dependence of the VAI response on the ambient meteorological conditions. (This possibility is currently under examination)

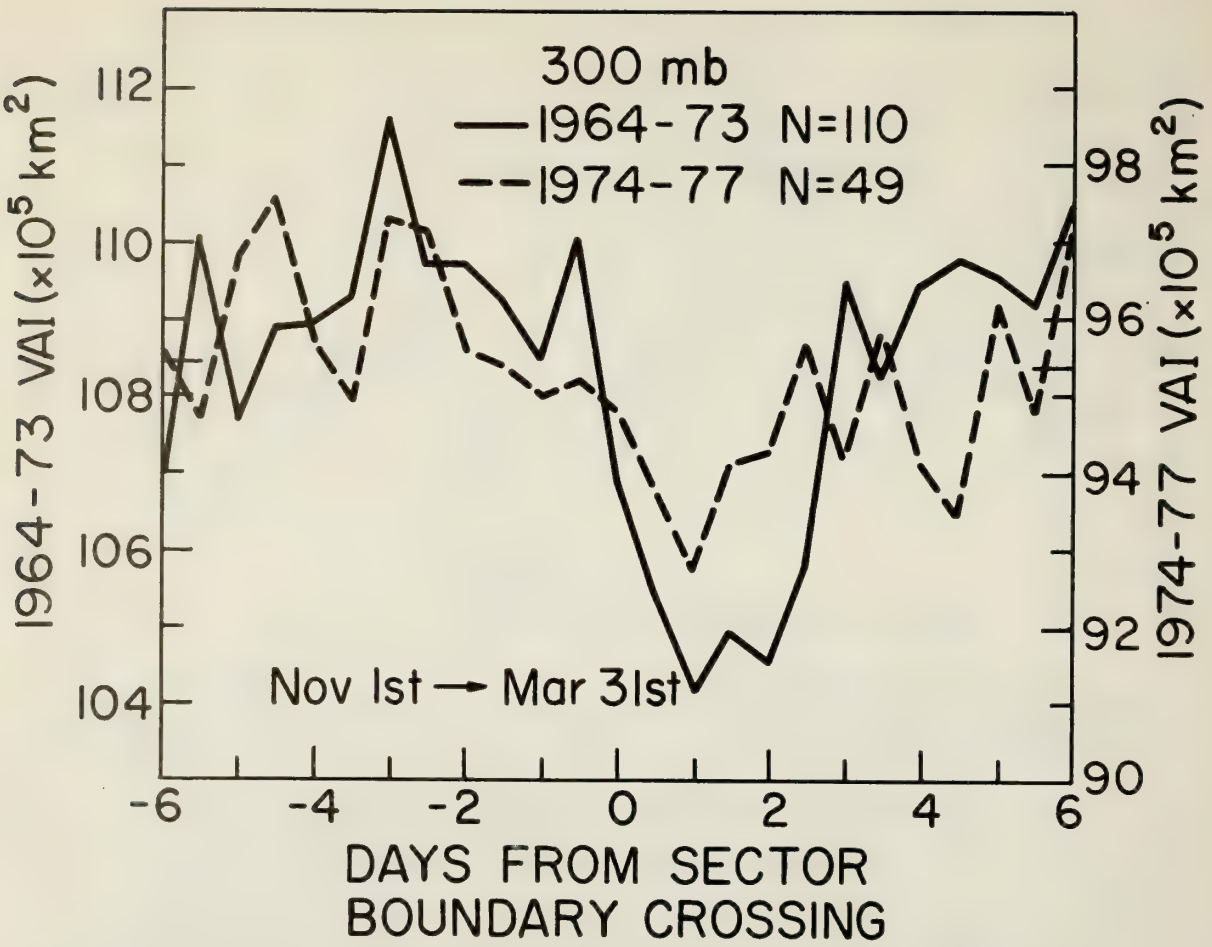


FIG. 1b: Results of Superposed Epoch Analysis of 300 mb VAI using SSB as keydates (from Williams and Gerety, (1978)

One final point deserves comment in this section. We have asserted that a one-to-one relationship is required before a predictive procedure can be established. On the other hand, Larsen and Kelley (1977) have shown that the ability of the Limited Fine Mesh prognostic model (Ramage 1976) to predict the VAI correctly, in its 12 hr. and 24 hr. weather forecasts, deteriorates after the passage of an SSB. This result was arrived at using the superposed epoch method for 47 keydates occuring during October through March 1972-74 and January 1975. This suggests that the statistical averages currently available to us may be used for predictive purposes. However, part of the data used overlaps with the period analysed by Williams and Gerety (1978). This not only implies that the result would have been more striking if these data had been omitted but also that predictions made during 1974 and 1975 would have been on the average, worsened by the inclusion of the VAI - SSB effect. Thus, we feel justified in making our assertion of the necessity of a one-to-one relationship.

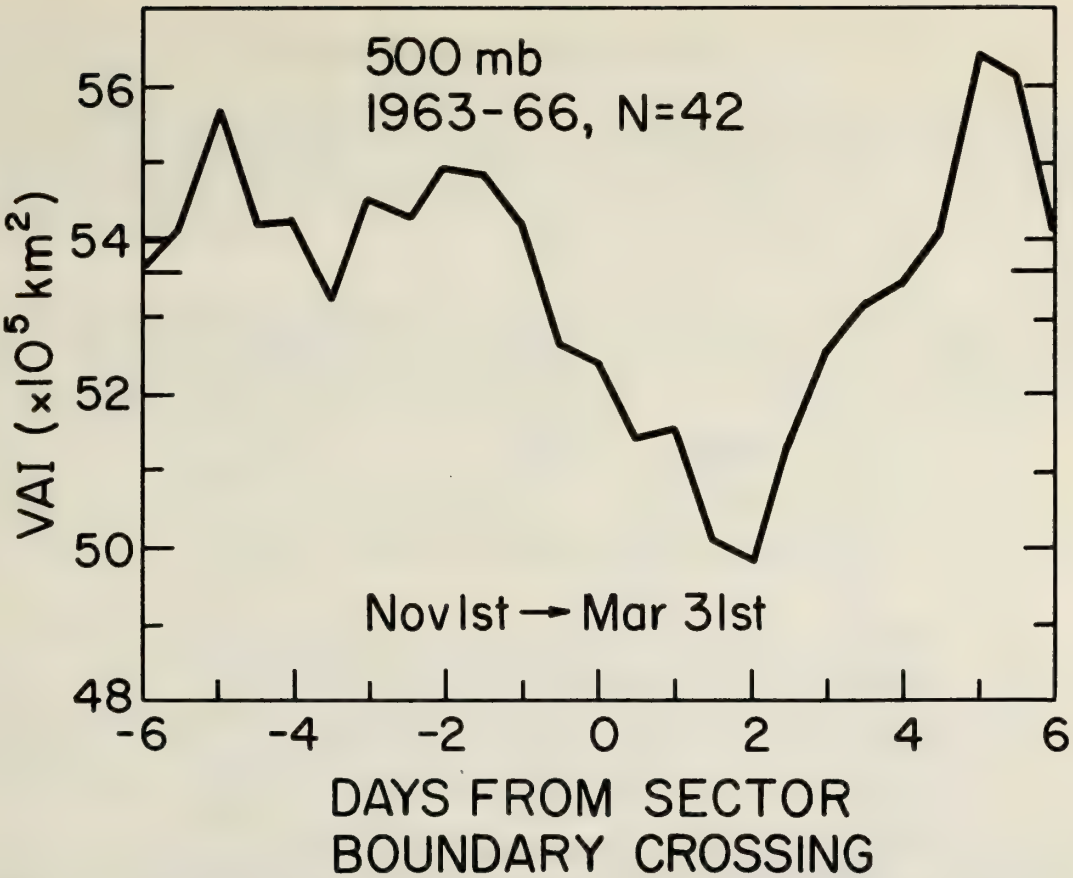


FIG. 2: Result of Superposed Epoch Analysis of 500 mb VAI using SSB as keydates for Solar 'Quiet' years 1963-66

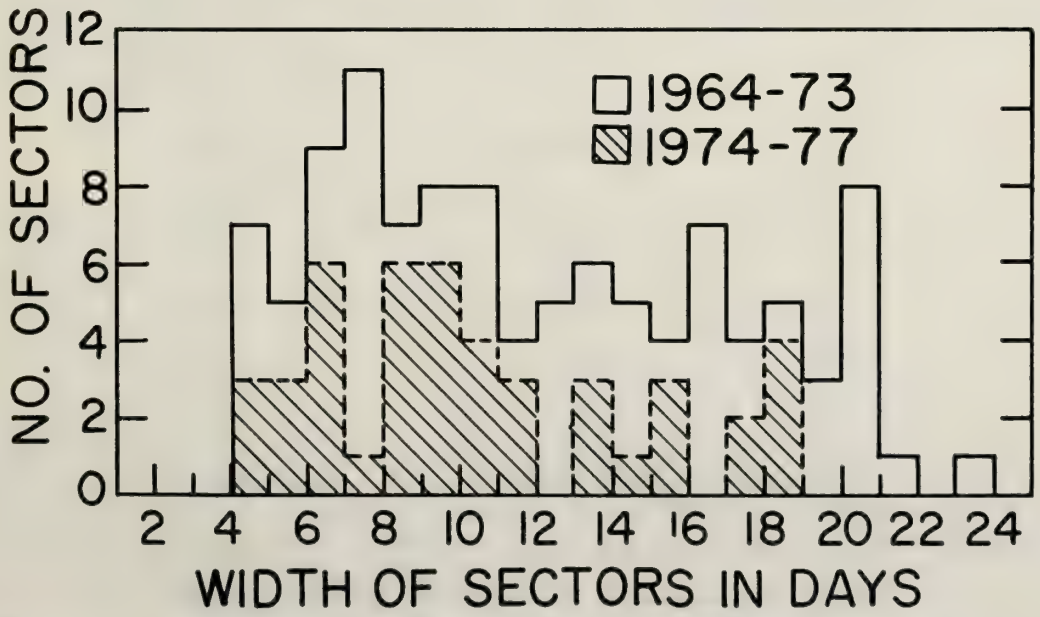


FIG. 3: Histogram of sector widths (from Williams and Gerety, 1978)

3. OTHER METEOROLOGICAL PARAMETERS

Once a one-to-one relationship is established, an overall understanding of the response of the troposphere is required. The VAI is not a conventional meteorological parameter and is not included in prognostic models. The major purpose of its definition seems to have been the establishment of a particular sun-weather effect.

Fig. 4 illustrates the results of one study aimed at understanding the VAI - SSB effect in terms of more conventional parameters. In this case, the parameters studied are the four components of the Lorenz energy cycle.

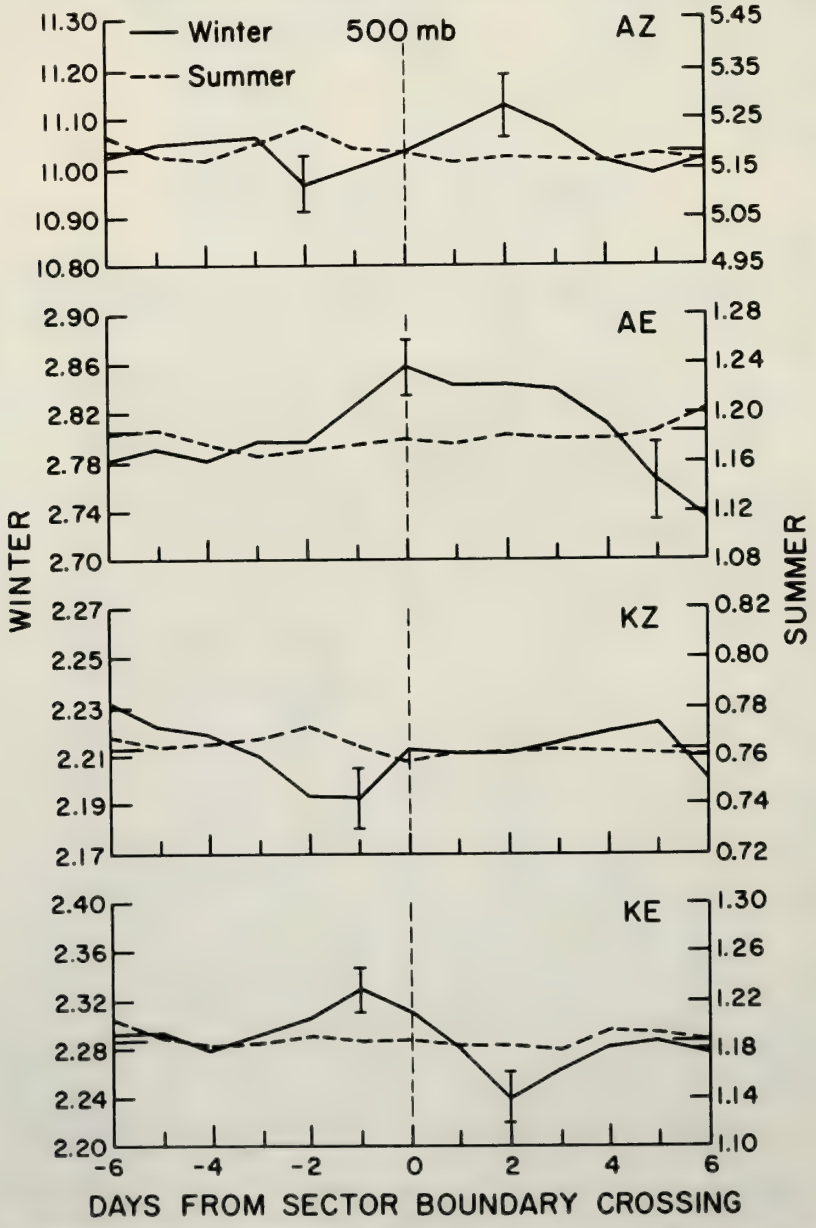


FIG. 4: Results of Superposed Epoch Analysis of Lorenz Energy parameters using SSB as keydates (from Williams 1978a)

These four parameters, viz. the eddy and mean zonal, kinetic (KE,KZ) and available potential (AE,AZ) energies (Dutton and Johnson, 1967) plus the rates of conversion between them, and their generation and dissipation, provide an overall description of the flow of energy through the atmosphere. Moreover, this formulation has the advantage that we may expect KE to be related to the VAI since each is, to some extent, a measure of large scale eddies in the atmosphere.

The results of performing a superposed epoch analysis on the four parameters at 500 mb are shown in Fig. 4 (Williams, 1978a) The keydates used are the SSB. The parameters were calculated using the National Meteorological Center dataset stored at the National Center for Atmospheric Research, Boulder, Colorado, U.S.A. The parameters are averages for the Northern Hemisphere, north of 20°N. and were calculated daily, from June 1963 to June 1976, using a computer program due to McGuirk and Reiter (1976). The error bars were calculated in identical fashion to that of Hines and Halevy (1977). Winter is defined as November 1st through March 31st.

The parameters AZ, AE and KZ do not show much response to the SSB. However, KE is interesting in that in winter it shows a variation similar to that of the VAI. The result is not as statistically significant as the VAI - SSB effect and the minimum occurs a day later; on the other hand, its annual and seasonal variation and its altitude dependence are similar to that of the VAI - SSB effect (see Williams, 1978a, for a fuller discussion).

In the context of this paper, this work illustrates a direction in which progress needs to be made. Firstly, it relates the behaviour of the eddy kinetic energy, KE, to the VAI and secondly it examines the response of other, related atmospheric parameters to the passage of an SSB. Thus, once the VAI has been used to establish the reality of the effects we must move towards the use of other meteorological parameters.

4. CONCLUSIONS

We have seen that it is dangerous to use the statistical sun-weather effects that are available at present as forecasting tools. Either a well understood physical mechanism or else a phenomenological, one-to-one relationship which satisfactorily allows for seasonal and longer term variations is needed. Since a satisfactory physical coupling has so far proved to be so elusive, it seems probable that such a one-to-one relationship is a necessary step towards establishing such a model. Therefore, it is concluded that further statistical studies are required before either the "academic" or the "economic" goal is achieved. These statistical studies must be well conceived in order to result in a detailed description of both the morphology of the results and the behaviour of such meteorological parameters as can be readily incorporated into prognostic models.

Therefore, we conclude that the answer to the question posed in the introduction is a qualified yes. The "economic" goal can, in principle be satisfactorily achieved without first fulfilling the "academic" goal completely, but not until further work has been performed. Moreover, it seems probable

that the "economic" goal provides the most likely route to the "academic" one. Finally, both goals are most likely to be achieved by a concerted effort aimed at fully understanding a particular sun-weather effect, such as the one considered in this paper.

ACKNOWLEDGMENTS

RGW wishes to thank the United States - United Kingdom Educational Commission whose financial support made much of this work possible.

REFERENCES

Dutton, J.A., and D.R. Johnson (1967): The theory of available potential energy and a variational approach to atmospheric energetics. Advances in Geophysics, 12:333.

Hines, C.O., and I. Halevy (1977): On the reality and nature of a certain sun-weather correlation. J. Atmos. Sci, 34:382.

Larsen, M.F., and M.C. Kelley (1977): A study of an observed and forecasted meteorological index and its relation to the interplanetary magnetic field. Geophys. Res. Lett., 4:334.

McGuirk, J.P., and E.R. Reiter (1976): A vacillation in atmospheric energy parameters. J. Atmos. Sci., 33:2079.

Ramage, C.S. (1976): Prognosis for weather forecasting. Bull. Amer.Meteor. Soc., 57:4.

Wilcox, J.M., P.H. Scherrer, L. Svalgaard, W.O. Roberts, R.H. Olson and R.L. Jenne (1974): Influence of solar magnetic sector structure on terrestrial atmospheric vorticity. J. Atmos. Sci., 31:581

Wilcox, J.M., L. Svalgaard and P.H. Scherrer (1975): Seasonal variation and magnitude of the solar sector structure-atmospheric vorticity effect. Nature, 255:539.

Wilcox, J.M., L. Svalgaard and P.H. Scherrer (1976): On the reality of a sun-weather effect. J. Atmos. Sci., 33,1113.

Williams, R.G. (1978a): A study of the energetics of a particular sun-weather relation. Geophys. Res. Lett., 5:519.

Williams, R.G., and E.J. Gerety (1978): Does the troposphere respond to day-to-day changes in the solar magnetic field ? Nature, 275:200.

Williams, R.G. (1978b): Comments on "Large amplitude standing planetary waves induced in the troposphere by the sun" by J.W. King et al. J. Atmos. Terr. Phys., 41:643.

G. MISCELLANEOUS PREDICTIONS

A PREDICTION OF THE INFLUENCE OF T, [NO] AND $q(O_2)$ ON THE POSITIVE ION COMPOSITION AT THE MESOPAUSE REGION

D.K. Chakrabarty and Purobi Chakrabarty
Physical Research Laboratory
Ahmedabad 380009, India

Using a currently known detailed positive ion chemical scheme, an attempt has been made to predict theoretically, the effect of the variation of T, [NO] and $q(O_2)$ on the positive ion composition at the mesopause region.

1. INTRODUCTION

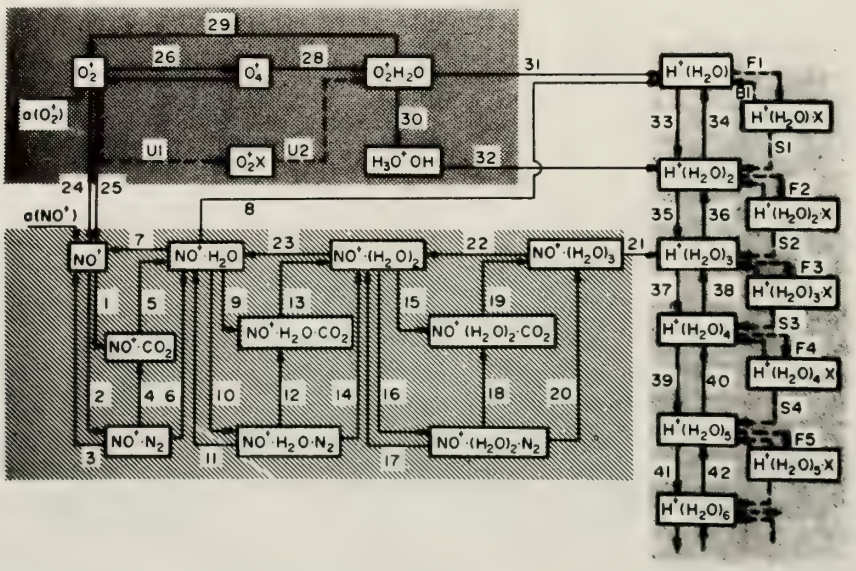
An accurate knowledge of electron density, Ne distribution with height in the D region is necessary to know the value of power and frequency of a transmitter that one has to employ for the long distance radio communication via the ionosphere. Several Government Departments like the Post Office, Over-seas Communication, Defence, etc. need this information. The simplest way to obtain the value of Ne is to use the well-known relation $q = \alpha N_e^2$ where q is the electron production rate and α is the effective electron loss coefficient. The accuracy of this method depends on how accurate are the values of q and α. While subject to certain conditions, one can calculate the value of q to a good degree of accuracy, the calculation of the value of α is not that simple. It depends critically on the relative densities of positive and negative ion species that exist in that condition in the D-region. In the height region of our interest, 80 - 90 km, it is the concentrations of positive ion species that are important.

Positive ion composition has been measured by several groups in different geophysical conditions (Meister et al., 1978; Goldberg and Witt, 1977; Arnold and Krankowsky, 1977; Narcisi, 1973). These observations have revealed the nature and extent of the variation of these ions. It has been found that a variation of either one or more of the following parameters viz. T, temperature, NO, nitric oxide density and $q(O_2)$, the electron-ion production rate due to ionization of O_2 takes place during these events (Offermann, 1977; Thrane et al., 1978). To predict the variation of these parameters with ion composition, one has to either use a simplified scheme or a detailed scheme. Although the simplified scheme has some basic

advantages, like fewer parameters, it does not give any indepth understanding. A detailed scheme is, therefore, always desirable. But, unfortunately the reaction rates for this situation are not fully known. Nevertheless, one can make a detailed study of the effect of the variation of these parameters on the D-region positive ion composition by assuming reasonable values for the unknown rate constants from the analogous reactions (Thomas, 1976; Reid, 1977). Such an attempt has been made in this report. The detailed ion chemical scheme which we have used here, has been able to satisfy the quiet time D-region features (Chakrabarty et al., 1978). By imposing different constraints on the scheme, we have predicted the variation of positive ion composition at the mesopause region. The constraints are a) an increase of T, b) an increase of $q(O_2)$ and c) an increase of NO density and hence q(NO).

2. TECHNIQUE

The ion-chemical scheme which we have used in this study is shown in Figure 1, alongwith the rates, the references of



$R1 = R9 = R15 = 2.5\times10^{-29}(200/T)^2\,[CO_2][N_2]$
$R2 = R10 = R16 = 2.0\times10^{-31}(300/T)^{4.4}\,[N_2][N_2]$
$R3 = 1.1\times10^{-8}(300/T)^{4.4}\exp(-2125/T)\,[N_2]$
$R4 = R12 = R18 = 1.0\times10^{-9}\,[CO_2]$
$R5 = R13 = R19 = 1.0\times10^{-9}\,[H_2O]$
$R6 = R14 = R20 = 1.0\times10^{-9}\,[H_2O]$
$R7 = 1.0\times10^{-16}\,[N_2+O_2]$
$R8 = 7\times10^{-12}\,[H]$
$R11 = R17 = 10R3$
$R21 = 3.3\times10^{-10}\,[H_2O]$
$R22 = R23 = 10R7$

$R24 = 4.4\times10^{-10}\,[NO]$
$R25 = 1.0\times10^{-17}\,[N_2]$
$R26 = 2.4\times10^{-30}(300/T)^{3.2}\,[O_2](O_2]$
$R27 = 3.0\times10^{-10}\,[O]$
$R28 = 2.2\times10^{-9}\,[H_2O]$
R29 = 0.6 (photodetachment)
$R30 = 1.9\times10^{-9}\,[H_2O]$
$R31 = 3.0\times10^{-10}\,[H_2O]$
$R32 = 3.2\times10^{-9}\,[H_2O]$
$U1 = 2.5\times10^{-31}\,[N_2+O_2]^2(300/T)^{4.4}$
$U2 = 1.0\times10^{-9}\,[H_2O]$

Figure 1. SCHEMATIC DIAGRAM OF POSITIVE ION CHEMISTRY

which are available from Chakrabarty et al. (1978). The continuity equations of all the ion species shown in this figure are solved simultaneously by a computer for a steady state condition with an arbitrary initial value of electron density, Ne. The equations are then iterated until N^+, the sum of all the positive ions (which is equal to Ne in the height region of our interest) stabilizes. The procedure is followed at all altitudes from 80 to 90 km in 2.5 km steps. The electron-ion production rates, the neutral concentrations, both major and minor, and the remaining all other input parameters used are as described in Chakrabarty et al. (1978). The computations are done in three phases. In the first, the temperature profile is changed by keeping NO density and $q(O_2)$ values constant. In the second, $q(O_2)$ is varied by keeping T and NO density values constant. And in the third, NO density is varied by keeping T and $q(O_2)$ constant. The results thus obtained are discussed below.

3. RESULTS AND DISCUSSION

3.1 Variation of T

A change in temperature at the mesopause level has been observed during conditions like winter anomaly, polar cap absorption, noctilucent cloud (Offermann, 1977; Thrane et al., 1978, Theon et al., 1967) as well as in quiet conditions (Schmidlin, 1976). In Figures 2A, B and C are shown the effect of variation of temperature on $[NO^+.H_2O]/[NO^+]$, $[NO^+]/[O_2^+]$ and $[H^+.(H_2O)_n]/([NO^+] + [O_2^+])$ (hereafter called f). It is seen that as the temperature increases, the values of $[NO^+.H_2O]/[NO^+]$ and f decrease and that of $[NO^+]/[O_2^+]$ increases. This is understandable because as the temperature increases, the rate R2 (see Figure 1) which is proportional to $T^{-4.4}$ decreases very fast. Consequently, more of $[NO^+]$ and less of $[NO^+.H_2O]$ will be formed. The increase of $[NO^+]/[O_2^+]$ with T at 90 km and after certain temperature, is marginal because at this altitude loss of NO^+ by dissociative recombination with electrons becomes the major loss process of NO^+. Since less number of $NO^+.H_2O$ is formed, less number of $H^+.(H_2O)_n$ will also be produced. The rapid decrease of f with temperature (Figure 2C) is due to two factors. Firstly, [NO] increases and secondly, fewer numbers of $H^+.(H_2O)_n$ ions are formed. Figure 2C also shows how the f=1 level goes down with the increase of temperature. This level lies at 85 km when T=175K, and slides to 80 km when T=207K.

3.2 Variation of $q(O_2)$

A change in the value of $q(O_2)$ takes place during events like PCA, aurora, solar flare and solar eclipse. The degree of change depends on the severity of the event. In Figures 2D,

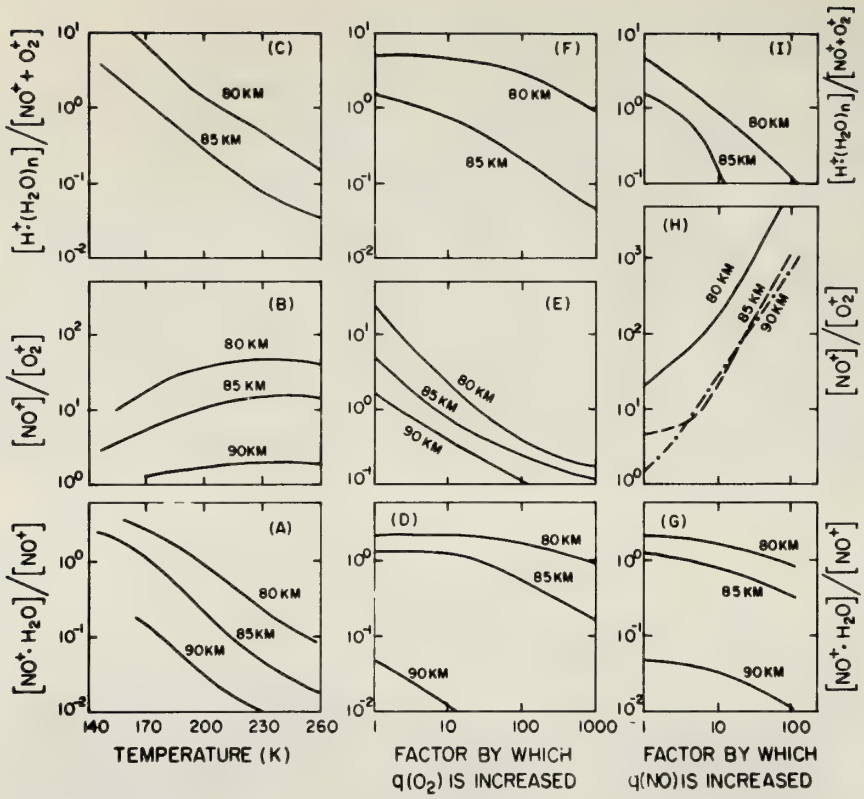


Figure 2. A,B,C: VARIATION OF $[NO^+.H_2O]$ / $[NO^+]$, $[NO^+]/[O_2^+]$ AND $[H^+.(H_2O)_n]$ / $([NO^+]+[O_2^+])$ RESPECTIVELY WITH TEMPERATURE WHEN $q(O_2)$ AND [NO] ARE CONSTANT.

D,E,F: VARIATION OF $[NO^+.H_2O]$ / $[NO^+]$, $[NO^+]/[O_2^+]$ AND $[H^+.(H_2O)_n]$ / $([NO^+]+[O_2^+])$ RESPECTIVELY WITH $q(O_2)$ WHEN T AND [NO] ARE CONSTANT.

G,H I: VARIATION OF $[NO^+.H_2O]$ / $[NO^+]$, $[NO^+]/[O_2^+]$ AND $[H^+.(H_2O)_n]$ / $([NO^+]+[O_2^+])$ RESPECTIVELY WITH $q(NO)$ WHEN T AND $q(O_2)$ ARE CONSTANT.

E and F are shown the effect of variation of $q(O_2)$ on $[NO^+.H_2O]/[NO^+]$, $[NO^+]/[O_2^+]$ and f. It is seen that the values of $[NO^+.H_2O]/[NO^+]$, $[NO^+]/[O_2^+]$ and f decrease as the value of $q(O_2)$ increases. This is understandable because with the increase of $q(O_2)$, more O_2^+ ions will be formed. As a result, there will be a decrease in the values of f and $[NO^+]/[O_2^+]$. An increase of $[O_2^+]$ will also increase $[NO^+]$ through the reaction R24 (see Figure 1) and hence $[H^+(H_2O)_n]$. Thus the $[NO^+.H_2O]/[NO^+]$ ratio should apparently remain constant. But from Figure 2D, at 80 and 85 km we find that this ratio remains constant upto the point when the value of $q(O_2)$ is increased by

a factor of 10 from that of normal value, beyond which this ratio starts decreasing. This happens because after this limit and at 90 km the loss of $[NO^+.H_2O]$ starts predominantly through the dissociative recombination with electrons instead of charge transfer through the reaction (10). A look at Figure 2F shows that the change in the f = 1 level takes place due to a change in the value of $q(O_2)$. But the magnitude of this change is less compared to that which takes place due to a change in the temperature (see Figure 2C). To lower the f = 1 level from 85 km to 80 km, an increase in the value of $q(O_2)$ by a factor of about 500 from that of normal value is necessary. In an event when such an increase in $q(O_2)$ takes place, the f = 1 level has been found to come down much below 80 km, almost to an altitude of about 70 km (Arnold and Krankowsky, 1977). Another interesting point to be noticed from Figure 2F is that at and below 80 km, f remains constant until $q(O_2)$ is increased by a factor of 10 from that of normal value, beyond which it starts decreasing probably due to the increased loss of this ion through dissociative recombination with electrons.

3.3 Variation of NO density

The density of NO at the mesopause has been found to change during conditions like aurora, winter anomaly etc. (Arnold and Krankowsky, 1977; Offermann, 1977) from that of quiet conditions. A change in the value of NO will also change the value of $q(NO)$. The effects of variation of $q(NO)$ on $[NO^+.H_2O]/[NO^+]$, $[NO^+]/[O_2^+]$ and $[H^+.(H_2O)_n]/([NO^+]+[O_2^+])$ are shown in Figures 2G, H and I. We find that the values of $[NO^+.H_2O]/[NO^+]$ and f decrease and that of $[NO^+] / [O_2^+]$ increase with the increase of NO density. As NO density increases, more NO^+ will be formed, hence an increase of $[NO^+]/[O_2^+]$ ratio and a decrease of f are understandable. The decrease of $[NO^+.H_2O]/[NO^+]$ ratio with increase of $[NO]$ is probably due to the increased effect of the loss of $NO^+.H_2O$ ions by dissociative recombination with electrons. Figure 2H shows that a 10 time increase in [NO] increases $[NO^+]/[O_2^+]$ ratio by almost the same factor. From Figure 2I it is seen that the f = 1 level goes down with the increase of NO density. An increase of NO density by a factor of 4 at 85 km can bring this level down to 80 km.

A comparison of Figures 2A, D and G shows that although $[NO^+.H_2O] / [NO^+]$ decreases with the increase of temperature, $q(O_2)$ and [NO], the ratio is more sensitive to changes in temperature than $q(O_2)$ and $q(NO)$.

A comparison of Figures 2B, E and H shows that $[NO^+]/[O_2^+]$ ratio increases with increase of temperature and nitric oxide density but decreases with increase in $q(O_2)$. The ratio is very much sensitive to changes in nitric oxide.

A comparison of Figures 2C, F and I shows that f decreases with the increase of T, $q(O_2)$ and NO density. But the magnitude of this decrease is more sensitive to T and NO variations than

$q(O_2)$. An increase of temperature by about 30K can bring the f = 1 level from 85 to 80 km. Similarly an increase of NO density by a factor of 4 can also bring the f = 1 level from 85 to 80 km. Does this indicate that there is a link between T and NO values?

4. CONCLUSION

The dependence of the positive ion composition on temperature, nitric oxide density and electron production rate due to the ionization of O_2 at the mesopause region is studied. It is shown that to predict the electron density in the mesopause region, effectively, there is an urgent need of more accurate and reliable measurements of temperature and nitric oxide density along with reliable electron production rates for different conditions of the ionosphere at all latitudes.

REFERENCES

Arnold, F., and D. Krankowsky (1977): Ion composition and electron-and ion-loss processes in the earth's atmosphere. Dynamical and Chemical coupling between the Neutral and Ionized Atmosphere,:93.

Chakrabarty, D.K., P. Chakrabarty, and G. Witt (1978): An attempt to identify the obscured paths of water cluster ions build-up in the D-region. J. Atmos. Terr. Phys., 40: 437.

Goldberg, R.A., and G. Witt (1977): Ion composition in a noctilucent cloud. J. Geophys. Res., 82:2619.

Meister, J., P. Eberhardt, U. Herrmann, E. Kopp, M.A. Hidalgo and C.F. Sechrist, Jr. (1978): D-region ion composition during the winter anomaly campaign on January 9, 1977. Space Res., XVIII:155.

Narcisi, R.S. (1973): Mass spectrometer measurements in the ionosphere. Physics and Chemistry of Upper Atmosphere,:171.

Offermann, D. (1977): Some results from the European winter anomaly campaign 1975/76. Dynamical and Chemical coupling between the Neutral and Ionized Atmosphere,:235.

Reid, G.C. (1977): The production of water cluster positive ions in the quiet daytime D-region. Planet. Space Sci., 25:275.

Schmidlin, F.J. (1976): Temperature inversion near 75 km. Geophys. Res. Lett., 3:173.

Theon, J.S., W. Nordberg, L.D. Katchen, and J.J. Horvath (1967): Some observations on the thermal behaviour of the mesosphere, J. Atmos. Sci., 24:428.

Thomas, L. (1976): Mesospheric temperatures and the formation of water cluster ions in the D-region. J. Atmos. Terr. Phys., 38:1345.

Thrane, E.V., W. Bangert, D. Beran, M. Friedrich, B. Grandal, O. Hagen, A. Loidt, K. Spenner, H. Schwentek, K.M. Torkar, and F. Ugletveit (1978): Ion production and effective electron loss rate in the mesosphere and lower thermosphere during the Western Europe Winter Anomaly Campaign 1975-76. J. Atmos. Terr. Phys., (in press).

ON PREDICTING THE PARAMETERS OF MEDIUM SCALE GRAVITY WAVES WITH THE ONSET OF TROPOSPHERIC JET STREAM

O. P. Nagpal
Department of Physics, University of Nairobi
P.O. Box 30197, Nairobi, Kenya

Dynamic instability of the wind shear layers in the tropospheric jet stream can generate short and medium scale gravity waves. Using the meteorological data and some reasonable models for the jet stream, various parameters of the generated gravity waves like speed, direction, period and horizontal wavelength can be predicted. No claim is made of the originality of the results presented here as several of these have already appeared in the recent literature. The emphasis has been to indicate that this analysis can be used as a prediction technique for the regularly occurring type of gravity waves both in the lower atmosphere and in the thermosphere.

1. INTRODUCTION

Earth's atmosphere is characterised by the presence of atmospheric gravity waves which occur with a wide range of periods, wavelengths and propagation speeds. Of the several phenomena of the atmospheric dynamics which these waves explain, the most established is the phenomenon of travelling ionospheric disturbances(TIDs). One of the interesting features of the gravity waves observed both in the neutral and ionised components of the upper atmosphere is their downward vertical phase propagation. Hines (1960) has pointed out that this sense of the phase progression implies that the wave sources must generally lie below the height of observation. Gossard (1962) confirmed Hines' suggestion and found that for an atmosphere without background wind, a window can exist at periods of about 10 min to 2 hr through which substantial amount of energy can leak out of the troposphere and this in turn may account for the frequent occurrence of the medium scale TIDs in the thermosphere. Since then, many investigators have turned their attention to meteorological sources of gravity waves which include weather frontal systems, severe thunderstorms, instabilities and distortions in the jet streams and penetrative cumulus convection. Once upper air data became routinely available, it was observed (e.g. Flauraud et al., 1954; Madden and Claerbout, 1968; Herron and Tolstoy, 1969; Herron et al., 1969) that many cases of gravity waves move with velocities that match the jet stream winds directly above. Based on these findings, Madden and Claerbout

(1968) and Tolstoy and Herron (1969) suggested that these waves can be produced by wind shear layers within the jet stream. Mechanisms include static instability (local convective activity) and dynamic instability (reduction in Richardson number within shear layers). Generation of wave spectra by both mechanisms has been examined by Tolstoy (1973). There is, however, a recent evidence that out of the two mechanisms, dynamic instability associated with vertical wind shear layers may be the chief cause for the generation of gravity waves (Keliher, 1975; Gedzelman and Rilling, 1978). Hence predictions may be made as to gravity wave period, speed and direction if the information concerning the wind shear layer is available.

Recently, evidence has also emerged by way of reverse ray tracing technique that some of the regularly occurring type of medium scale TIDs have their origin in the tropospheric jet stream (Cowling et al., 1970; Goe, 1971; Bertin et al., 1975, 1978; Sengupta et al., 1977; Sizun and Bertel, 1978) although the inferences are not free from difficulties. However, if each wave is considered separately and if efforts are made to get a complete wind profile upto the thermospheric heights, the characteristics of the observed TIDs can be matched with those predicted.

In the present paper, an attempt has been made to obtain information concerning the nature and characteristics of short and medium scale gravity waves (period, wavelength, speed and direction) generated by the onset of a tropospheric jet stream in the atmosphere. A brief description of the jet stream is given in section 2. The analysis given in section 3 is based on the previous studies of this kind by many investigators (e.g. Tolstoy and Herron, 1969; Keliher, 1975; Lalas and Einaudi, 1976; Mastrantonio et al., 1976). Section 4 gives the comparison of the predicted and observed gravity wave parameters.

As the tropospheric jet streams are regular features of the atmosphere, they would well account for the day to day observability of gravity waves both below and above the troposphere. Apart from whatever interest gravity waves attract in themselves or as a remote indicators of the other important geophysical phenomena, increasing attention is being paid to know how much energy and momentum these waves can carry when they propagate to upper atmosphere. This can be made possible by developing an ability to measure and model the various wave parameters originating from a given source. Also there is a current belief that clear air turbulence (CAT) is correlated with gravity waves observed at the ground level. However, the gravity waves that might be most effective in causing CAT have much smaller wavelengths than the ones either seen on microbarographs or higher in the atmosphere. Since, an unstable shear layer produces a spectrum of wavelengths the smaller of these might produce CAT and the larger of these might produce other effects.

2. DESCRIPTION OF JET STREAM

An atmospheric jet stream is described as a high speed air current in the form of a flattened, narrow core or tube, thousands of km in length,

a hundred or more km in width, and one or more km in vertical thickness. Although reports of maximum winds in the centre of the core reach 300 knots (150 m/sec) 100 to 200 knots (50 to 100 m/sec) is more typical of the maximum jet winds encountered. These maximum winds usually occur between 10-12 km but jet winds of lesser magnitude may be found at times above 6 km. There are two basic jet streams in the troposphere - the polar front jet stream (PFJ) and subtropical jet stream (STJ). The mean position of these jets for winter is shown in Fig. 1. During the winter, the STJ is

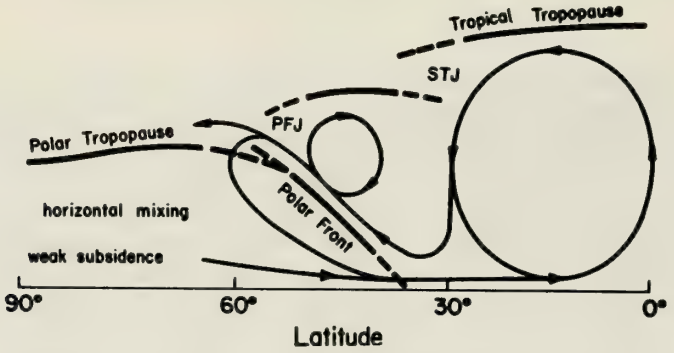


Fig.1. SCHEMATIC REPRESENTATION OF THE MEAN MERIDIONAL CIRCULATION IN THE NORTHERN HEMISPHERE DURING WINTER. HEAVY LINES= TROPOPAUSES AND POLAR FRONT. PFJ= POLAR FRONT JET STREAM AND STJ= SUBTROPICAL JET STREAM. (AFTER PALMEN, 1954).

relatively constant and continues in position and time and becomes broken and weak during the summer months. When well developed, winds of more than 150 knots (75 m/sec) are not uncommon. The PFJ is much more variable in location, continuity, wind speed and elevation. It is farthest south in mid winter and farthest north in summer, and its elevation decreases as it migrates northward. Both these jet streams are characterised by well-marked horizontal wind shears and strong vertical wind shears. Also wind speeds in the jet stream can build up only to a certain limiting value, beyond which cyclonic shears would be generated that produce dynamic instability (minimum Richardson number).

2.1 Jet Stream Associated Waves

One of the long established observations of surface pressure fluctuations interpreted as gravity waves is that the observed wave speeds and directions bear a relation to the speed and orientation of the upper atmospheric jet stream. Such correlations have been noted by many investigators (Flauraud et al., 1954; Madden and Claerbout, 1968; Herron and Tolstoy, 1969; Keliher, 1975; Essex and Love, 1978; Gedzelman and Rilling, 1978). The pressure oscillations tend to be of relatively low frequency (5-20 min periods) and the horizontal trace velocities are in the range of 20-60 m/sec

i.e. comparable to that of the jet stream. The association of these waves with the upper tropospheric jet stream now seems to be well documented, but the nature of connection remains unclear. However, there is recent evidence (Hooke and Hardy, 1975; Gedzelman and Rilling, 1978; Essex and Love, 1978) from surface pressure and clear-air radar observations which tend to confirm the suggestion by Madden and Claerbout (1968) that the wave generation mechanism in the troposphere may be dynamic instability associated with vertical wind shear in the neighbourhood of the jet stream. Goe (1971) inferred a casual connection between TIDs with periods of 12-15 min observed at Boulder and jet stream configurations with large horizontal wind shears. Cowling et al. (1970), and Bertin et al. (1975) using reverse ray tracing technique through windy atmosphere reported that weather disturbances and jet streams appeared as likely sources for the medium scale F region TIDs. Similar conclusions were drawn by Sengupta et al. (1977) who noted that the winter time medium scale TIDs correlated well with the westerly jet stream activity.

This correspondence has provided one of the principal form of evidence which supports the idea that the waves are generated by the dynamic instability of the jet stream winds.

2.2 Excitation of Gravity Waves

The excitation of gravity waves by shear flow instability has been investigated extensively. Drazin and Howard (1966) have presented a thorough review of the theoretical work in hydrodynamic stability of plane-parallel flow up to that time. The primary aim of these investigations is to specify, for given velocity and density or temperature profiles, the characteristics of the most unstable wave to be excited i.e. its wavelength, period, phase velocity and growth rate, as well as the range of horizontal wavelengths λ_x that are unstable for a given value of some characteristic Richardson number of the flow. Drazin and Howard (1966) show that for a homogeneous fluid with a monotonic velocity profile, a necessary condition for instability is that the velocity profile should have an inflection point. In such a fluid the waves will travel with a speed and direction matching that of the fluid at the inflection point. In a stratified fluid, however, there is no general expression for the wave speed although it is restricted to lie within the range of wind speeds by Howard's (1961) semi-circle theorem. The above analysis predicted the existence of one mode only which was connected with singular neutral solution.

More recently Jones (1968) discovered that there are other unstable modes which are not connected with the singular neutral solution. These new modes generally have longer wavelengths, are weakly dispersive and may not necessarily move with velocity of the fluid at the inflection point. These new modes have also been investigated by Lalas and Einaudi (1976), Davis and Peltier (1976) and Mastrantonio et al. (1976). Although these linear theories do suggest that an atmospheric shear layer can support a number of unstable modes in agreement with the observations (Hooke and Hardy, 1975), however, the generation of medium scale gravity waves which are observed at the F region heights is

forbidden in such linear theories. Paul (1977) and Bertin et al. (1978) point out that such waves may not be produced directly by shear instability but rather may result from non-linear interaction of two smaller, unstable waves. This theory has been able to account for certain of the observed characteristics of the internal gravity waves observed at the thermospheric heights.

3. PREDICTION OF GRAVITY WAVE PARAMETERS

3.1 Speed and Direction

The following method as outlined by Keliher (1975), will be used to predict the gravity wave speed and direction. The basic data required is the wind speed and direction as obtained by radiosonde and the temperature profile. It is first essential to identify the height at which the shear layers are present within the jet stream. This can be done by calculating the Richardson number which is given by

$$R_i = N_B^2 \; / \; \left(\frac{\partial u}{\partial z}\right)^2 \qquad \ldots\ldots\ldots\ldots\ldots (1)$$

where $\frac{\partial u}{\partial z}$ is the vertical shear of the wind in the horizontal direction and N_B is the Brunt Vaisalla frequency defined by

$$N_B^2 = (g/\theta)\,\frac{\partial \theta}{\partial z} \qquad \ldots\ldots\ldots\ldots\ldots (2)$$

where g is the gravitational acceleration and θ is the potential temperature. Knowing the data for two adjacent radiosonde sounding at levels z_1 and z_2, one can calculate the approximate Richardson number from the following:-

$$R_i = \left[\frac{2g}{T_1 + T_2}\;\left(g/c_p + \frac{T_2 - T_1}{z_2 - z_1}\right)\right]$$

$$\left[\left(\frac{u_2 \sin\alpha_2 - u_1 \sin\alpha_1}{z_2 - z_1}\right)^2 + \left(\frac{u_2 \cos\alpha_2 - u_1 \cos\alpha_1}{z_2 - z_1}\right)^2\right]^{-1} \qquad \ldots\ldots (3)$$

where T_1, u_1, α_1 are temperature, wind speed and direction at height z_1 and T_2, u_2, α_2 are corresponding quatities at level z_2. c_p is the specific heat at constant pressure. The height level where $R_i \leq \frac{1}{4}$ can then be chosen as the level where shear instability would be present (Chimonas, 1970). If $\hat{v}_1$ and $\hat{v}_2$ are the horizontal winds at two heights z_1 and z_2 immediately below and above the level where $R_i \leq \frac{1}{4}$ and assuming that wind varies in a linear manner between these levels, one may expect the gravity waves produced by such a region to travel with speed

$$\hat{v}_m = \tfrac{1}{2}(\hat{v}_1 + \hat{v}_2) \qquad \text{.....(4)}$$

relative to the ground and to have wave fronts perpendicular to

$$\hat{v}_s = \hat{v}_2 - \hat{v}_1 \qquad \text{.....(5)}$$

As the source is located at an average altitude z ($= \frac{z_1 + z_2}{2}$) the gravity waves over an array located at some horizontal distance x from the source will have an observed velocity $\hat{v}_o$ given by (Essex and Love, 1978)

$$\hat{v}_o = |v_m| \cos(v_m, v_s) \;/\; \cos \tan^{-1}(z/x) \qquad \text{.....(6)}$$

and azimuth given by

$$\alpha_s = \tan^{-1} \left(\frac{v_2 \sin\alpha_2 - v_1 \sin\alpha_1}{v_2 \cos\alpha_2 - v_1 \cos\alpha_1} \right) \qquad \text{.....(7)}$$

Equations (6) and (7) allow us to calculate the predicted apparent speed v_o and azimuth α_s of any wind shear generated wave.

Since radiosonde soundings are usually made every 12 hours, each sounding can be assumed to be a measure of meteorological conditions for 6 hours before and 6 hours after the time of release. As noted in section 2, STJ is relatively constant and continuous in position and time during winter months, the above equations can therefore be used to get the gravity wave speed and direction generated by STJ.

3.2. Period and Wavelength

To obtain the periods and expected horizontal wavelengths of the jet stream generated gravity waves, one has to resort to the modelling approach. Of the wind profiles utilised to model a shear layer, the simplest is the Helmholtz profile which has a background horizontal velocity $U_o(z)$ constant in each of two semi-infinite media and a sharp discontinuity at the separating interface. Other models in use are constant velocity layers and $U_o(z)$ given by a hyperbolic tangent profile (Drazin, 1958; Maslowe and Kelly, 1971; Thorpe, 1973). One then does the stability analysis of such an idealised model of a jet stream shear layer and the characteristics of the most unstable modes are calculated for minimum Richardson number of the flow. The stability investigations are usually supplemented by the general stability results of Miles (1961), Howard (1961) and Chimonas (1970) that provide bounds on the range of the phase velocities and growth rates of the unstable waves through the Howard's semi circle theorem.

Using the hyperbolic-tangent velocity profile for the atmospheric shear layer of the form $U_o(z) = V \tanh(z/h)$ shown in Fig. 2, where V is the maximum value of the background wind velocity U_o at z = h the height of the tropopause, and constant background temperature, Lalas and Einaudi (1976) and

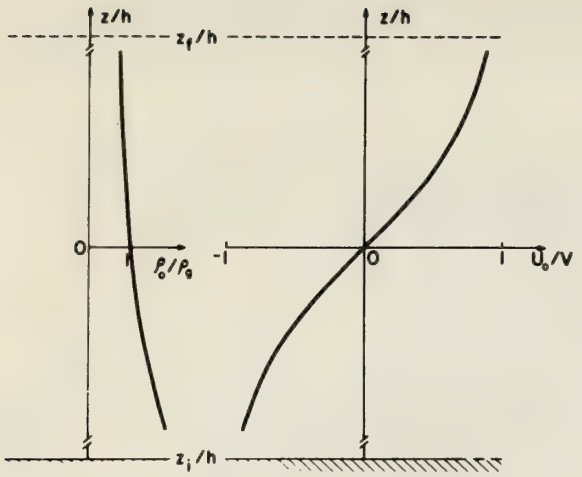


Fig.2. THE NORMALISED DENSITY AND VELOCITY PROFILES AND THE GEOMETRY OF THE BASIC FLOW IN THE TROPOSPHERIC JET STREAM (AFTER LALAS AND EINAUDI,1976).

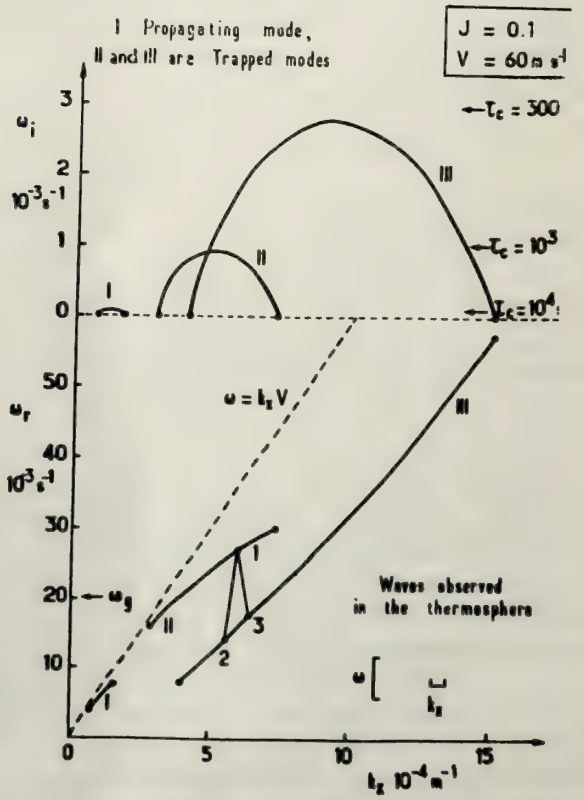


Fig.3. REPRESENTATION ON AN (ω,k_x) DIAGRAM OF THE UNSTABLE MODES ABLE TO DEVELOPE IN A JET STREAM WITH MAXIMUM VELOCITY V= 60 m/sec AND MINIMUM RICHARDSON NUMBER J=0.1. THE UPPER AND LOWER DIAGRAMS CORRESPOND TO THE IMAGINARY(GROWTH RATE) AND REAL PARTS OF ω. THE NON-LINEAR INTERACTION BETWEEN WAVES 1 AND 2 OR 1 AND 3 CAN YIELD WAVES WITH VALUES OF ω AND k_x WITHIN THE RANGES SHOWN FOR WAVES OBSERVED IN THE THERMOSPHERE (AFTER BERTIN et al., 1978).

Mastrantonio et al. (1976) find that the tropospheric jet stream can support a number of modes, some of which are essentially evanescent and others essentially free, propagating away from the shear zone. Figure 3 represents these unstable modes in an (ω,k_x) diagram calculated by Bertin et al. (1978) from the work of Lalas and Einaudi (1976) for a jet stream located at 12 km height and having maximum core speed of 60 m/sec. This gives us the expected horizontal wavelengths for a particular ω (or period) of a gravity wave mode. For example mode labelled I is a freely propagating mode capable of travelling upto thermospheric heights. The expected wavelengths would be 50 km or more. Wavelengths of the order of ten as well as few hundred kilometers have been recently detected by Uccellini (1975) which were thought to be responsible for triggering various kinds of atmospheric events along their path (e.g. convective thunderstorm). However, observations of medium scale gravity waves by Bertin et al. whose source origin was believed to be a jet stream, give characteristics which do not match with any of the modes shown in Fig.3. Thus they suggest that the observed wave could arise due to non-linear interaction of the two trapped modes labelled II and III. Similar analysis has been given by Paul(1977) who shows that the resulting wave from non-linear interaction of the smaller, unstable waves can account for certain of the observed characteristics of the power spectrum of the waves. The waves thus produced are internal waves which can travel freely through the fluid.

Similarly, in the lower atmosphere, pressure fluctuations at the ground, with periods of few minutes to several minutes and horizontal wavelengths of tens of meters to a few hundred kms were successfully explained by Tolostoy and Herron (1969) to originate in the jet stream. They computed the spectral distributions of gravity waves as would be expected on the ground due to disturbances of known spectra in the jet stream aloft. The input parameters were the wind velocity power spectra obtained by

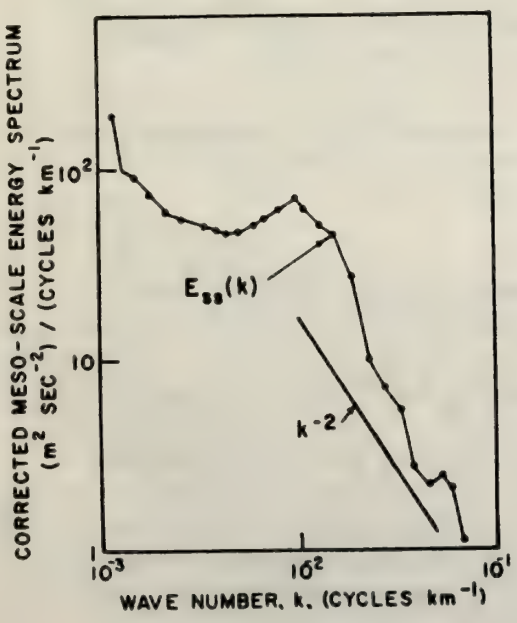


Fig.4. THE LONGITUDINAL POWER SPECTRUM FOR LONGITUDINAL WIND VELOCITY FLUCTUATIONS NEAR THE JET STREAM CORE AS DETERMINED BY KAO AND WOODS (1964).

aircraft measurements along jet stream axis by Kao and Woods (1964) and are shown in Fig. 4. Assuming thsese spectra to be stationary and as a frozen-in property of the wind system carried along by the jet core, Tolstoy and Herron showed that the power spectrum for ground level pressure perturbations P(p) can be computed by

$$P(p) = 0.2\ v^2 \frac{k_{zs}}{k_z} P(u) \qquad \text{.....(8)}$$

where P(u) is the power spectrum of the winds in the jet stream and is related to Ess(k) of Kao and Woods by P(u) = kEss with k in cycles/km, v is the jet core speed and k_z and k_{zs} are the vertical wavenumbers at the jet stream height and at the surface respectively. The spectrum thus calculated gives acceptable orders of magnitude for some of the observed properties of the mesoscale fluctuation fields (Hooke and Hardy, 1975). Although the primary purpose of the above analysis is to get the amplitudes of the surface pressure perturbations, nevertheless, the analysis does give the various periods of gravity waves reaching the ground.

4. COMPARISON OF OBSERVED AND PREDICTED PARAMETERS

Number of investigarors have made comparison of the observed wave phase

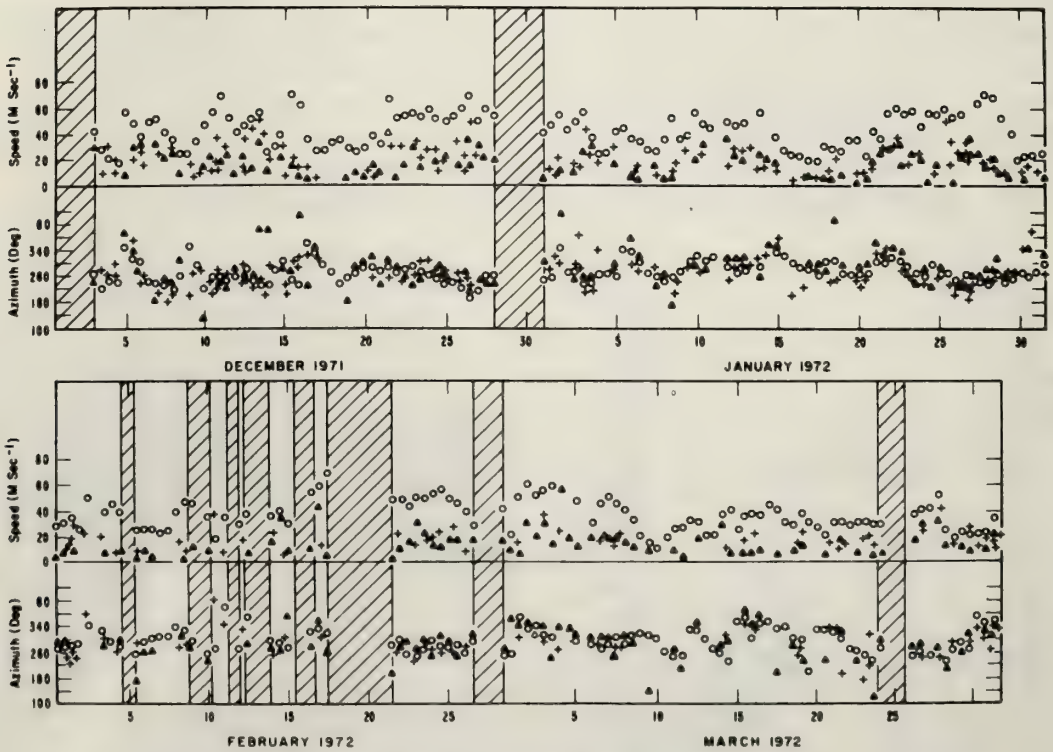


Fig.5. COMPARISONS IN SPEED AND AZIMUTH OF MICROBAROGRAPG-DETECTED GRAVITY WAVES (PLUSES),UPPER-TROPOSPHERE WIND MAXIMA (OPEN CIRCLES) AND PREDICTED WIND SHEAR INDUCED GRAVITY WAVES (SOLID TRIANGLES) FOR THE WINTER MONTHS, 1971-72 NEAR BOULDER, COLORADO. (AFTER KELIHER, 1975).

speed and direction with the wind speed and direction of the maximum tropospheric winds and good agreement has been reported. However, a comparison between the observed wave speeds and directions with those predicted by shear layer analysis has been attempted by a limited number of workers. Keliher (1975) noted that best correlation existed between gravity wave events and predictions from wind shear data during winter months (Fig.5) although the agreement was not too good for other months. The results of comparison indicated that one third to one half of his observed wave events were shear-induced. Gedzelman and Rilling (1978) and Essex and Love (1978) have presented a similar comparison. The procedure followed is much the same as described in section 3.1. Gedzelman and Rilling noted that about 37.5% of all the cases observed matched well both in speed and direction, though the discrepency was small for the other 60% of the cases. This they atrributed partly to the uncertainties involved in the radiosonde data. Their results are reproduced in Fig.6. From their results of comparison, these authors concluded that shearing instability is one of the more common generating mechanism of the waves. This conclusion was further supported by the fact that the observed waves were not very dispersive. Essex and Love

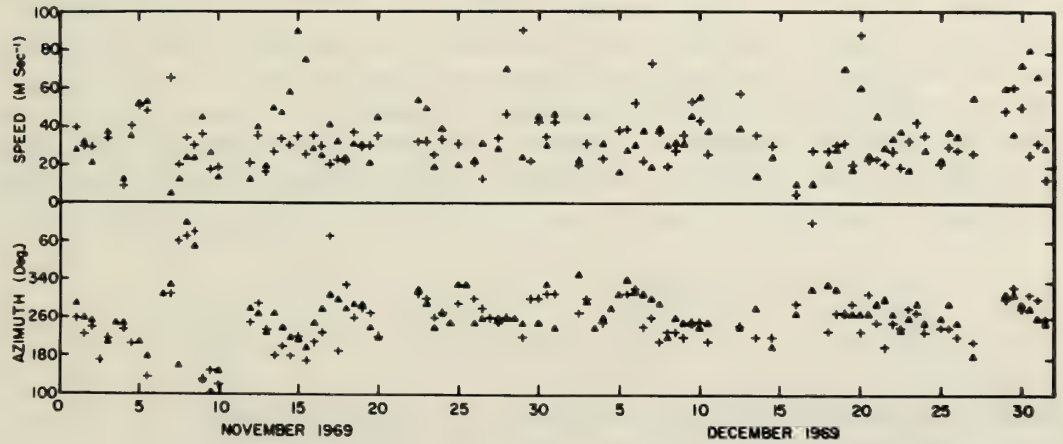


Fig.6. COMPARISONS IN SPEED AND DIRECTION OF MICROBAROGRAPH-DETECTED GRAVITY WAVES (PLUSES) AND PREDICTED WIND SHEAR INDUCED GRAVITY WAVES (TRIANGLES) FOR THE WINTER MONTHS, 1969 NEAR NEW YORK (AFTER GEDZELMAN AND RILLING, 1978).

noted that some of their observed gravity wave speeds had the right order of magnitude when compared with the predicted values provided that an assumption is made for the waves to originate in the lowest unstable layer in the jet stream.

A comparison of the observed spectra of surface pressure fluctuations and that derived from the wind velocity power spectra of the jet stream was made by Tolstoy and Herron (1969) who noted that a simple linear model predicts the correct order of magnitude and power spectra for surface pressure fluctuations in the 5-60 min period range.

We now carry out a comparison of the observed characteristics of the thermospheric medium scale gravity waves with those predicted theoretically by the jet stream model described in section 3.2. Such a comparison has been made by a rather limited number of investigators notable among them being Bertin et al. (1978) and Vidal-Madjar et al. (1978). A reverse ray tracing analysis is first employed to make sure that the wave path of the observed gravity wave can be followed down to the tropopause level. Figure 7 shows the characteristics of the medium scale gravity waves as measured by Bertin et al. (1978). The observed phase speeds lie in the range 80-250 m/sec with a maximum near 130 and 160 m/sec. The corresponding horizontal wavelengths are between 150-250 km and wave periods are between 17 and 40 min. Most of these waves could be traced back to the tropopause level thereby suggesting a jet stream to be the source. The predicted gravity wave modes which may develop in the jet stream are shown in Fig. 3. The main features of these unstable modes can be summarised as follows:-

(i) the horizontal phase velocity in all cases is smaller than the maximum speed in the jet, a consequence of the fact that modes are generated within their critical level.

(ii) the direction of propagation is colinear with the jet stream.

(iii) of the three modes, the two most likely to grow (II and III) are trapped modes propagating only inside the jet.

At first glance, all these characteristics are in contradiction to those of the waves observed in the thermosphere and traced back to the tropopause, where the horizontal phase velocities are at least two times that of the jet (taken 60 m/sec as maximum). However, it has been shown by Paul (1977) and Vidal-Madjar et al. (1978) that a non-linear interaction between two

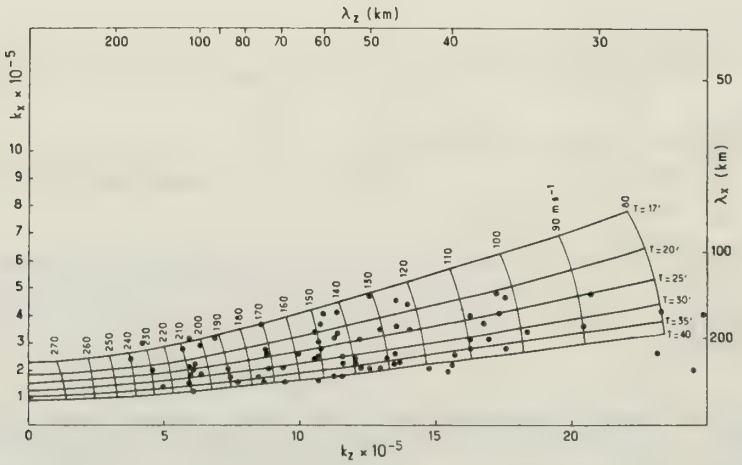


Fig. 7. SPECTRAL CHARACTERISTICS OF MEDIUM SCALE GRAVITY WAVES MEASURED BY BERTIN et al. (1978). EACH OF THE WAVE IS MARKED BY A POINT IN A (k_x,k_z) DIAGRAM. THE k_z IS THAT FOR THE WAVE AT 15 km ALTITUDE. THE HYPERBOLAS ARE CURVES FOR CLASSICAL DISPERSION. THE ESSENTIAL POINT IS THAT THE AVERAGE PHASE VELOCITY OF THESE WAVES IS AROUND 150 m/sec (AFTER, VIDAL-MADJAR et al., 1978).

waves with characteristics (ω_1,k_{x1}) and (ω_2,k_{x2}) belonging to modes II and III respectively in Fig. 3 can produce a secondary wave which then possesses a much larger phase speed. Table I taken from the work of Vidal-Madjar et al. shows the expected phase speeds and vertical wavelengths for the secondary waves formed as a result of non-linear interaction of four waves of mode II with four waves of mode III. The parameters thus obtained for the resulting waves are in broad general agreement with the observed characteristics shown in Fig. 7. It should, however, be noted that the observed spectral characteristics give only a very biased indication of the spectrum of real waves emitted by the jet stream. This is because of the atmospheric filtering between 10 and 250 km

Table - I

PHASE VELOCITY (V_p) AND VERTICAL WAVELENGTH (λ_z) FOR THE SECONDARY WAVE

Mode	$k_{x1} \times 10^{-4}, m^{-1}$	Mode	$k_{x2} \times 10^{-4}, m^{-1}$	λ_z, km	V_p, m/s
II	6.1	III	6.3	141	226
II	6.3	III	6.5	151	231
II	6.2	III	6.5	64	140
II	6.3	III	6.6	66.5	143

altitudes which helps the waves of higher phase velocities to reach the upper level.

5. CONCLUSION

As noted in the introduction, the tropospheric jet streams are regular features of the lower atmosphere. Once the information concerning their wind shear layers is available, one can predict the parameters of both up and down going gravity waves launched by these jet streams. In addition to explaining the day to day occurrence of mesoscale motions, the analysis given here can also be used to get some idea about the energy which these waves can carry into the thermosphere. Unfortunately, the tropospheric data are usually available every 12 hrs a day, so one has to assume that the jet stream does not move significantly during the time when a gravity wave is being launched. Also parameters like the tropospheric wind speed maximum and the exact position of the jet stream are difficult to determine with desired accuracy because the jet stream is snakelike rather than a clearly defined point source. In spite of these limitations, the technique presented here predicts the gravity wave parameters which agree reasonably well with those observed in the lower and the upper atmosphere.

REFERENCES

Bertin, F., J. Testud, and L. Kersley (1975): Medium scale gravity waves in the ionospheric F-region and their possible origin in weather disturbances. Planet. Space Sci., 23:493.

Bertin, F., J. Testud, L. Kersley, and P. R. Rees (1978): The meteorological jet stream as a source of medium scale gravity waves in the thermosphere: An experimental study. Accepted by J. Atmos. Terr. Phys.

Chimonas, G. (1970): The extension of the Miles-Howard theorem to compressible fluids. J. Fluid Mech., 43:833.

Cowling, D. H., H. D. Webb, and K. C. Yeh (1970): A study of traveling disturbances in the ionosphere, Tech. Rep. 38, Ionos. Radio Lab., Univ. of Ill. at Urbana-Champaign, 147 pp.

Davis, P. A., and W. Peltier (1976): Resonant parallel shear instability in stably stratified planetary boundry layer. J. Atmos. Sci., 33:1287.

Drazin, P. G. (1958): The stability of a shear layer in an unbounded heterogeneous inviscid fluid. J. Fluid Mech., 4:214.

Drazin, P. G., and L. N. Howard (1966): Hydrodynamic stability of parallel flow of an inviscid fluid. Advances in Applied Mechanics , Vol. 9, Academic Press, 1-89.

Essex, E. A. and G. B. Love (1978): The occurrence of ground level gravity waves in southeastern Australia as detected by microbarographs. J. Geophys. Res. , 83:1883.

Flauraud, E. A., A. H. Mears, F. A. Crowley, Jr., and A. P. Crary (1954): Investigation of microbarometric oscillations in eastern Massachusetts. Tech. Rep. 54-11, Geophys. Res. Pap. 27, Air Force Cambridge Res. Lab. Mass., U.S.A.

Gedzelman, S. D., and R. A. Rilling (1978): Short-period atmospheric gravity waves: A study of their dynamic and synoptic features. Mon. Wea. Rev., 106:196.

Goe, G. B. (1971): Jet stream activity detected as wavelike disturbances at mid-latitude ionospheric F region heights. Pure Appl. Geophys. , 92:190

Gossard, E. E.(1962): Vertical flux of energy into the lower ionosphere from internal gravity waves generated in the troposphere. J. Geophys. Res., 67:745.

Herron, T. J., and I. Tolstoy (1969): Tracking jet stream winds from ground level pressure signals. J. Atmos. Sci. , 26:266.

Herron, T. J., I. Tolstoy, and D. W. Craft (1969): Atmospheric pressure background fluctuations in the mesoscale range. J. Geophys. Res., 74:1321.

Hines, C. O. (1960): Internal atmospheric gravity waves at ionospheric heights. Can. J. Phys., 38:1441.

Hooke, W. H., and K. R. Hardy (1975): Further study of the atmospheric gravity waves over the Eastern Seaboard on 18 March 1969. J. Appl. Meteor.; 14:31.

Howard, L. N. (1961): Note on a paper of John W. Miles. J. Fluid Mech., 10:509.

Jones, W. L. (1968): Reflection and stability of waves in stably stratified fluids with shear flow: A numerical study. J. Fluid Mech., 34:609.

Keliher, T. E. (1975): The occurrence of microbarograph-detected gravity waves compared with the existence of dynamically unstable winds shear layers. J. Geophys. Res., 80:2967.

Kao, S. -K., and H. D. Woods (1964): Energy spectra of mesoscale turbulence along and across the jet stream. J. Atmos. Sci., 21:513.

Lalas, D. P., and F. Einaudi (1976): On the characteristics of gravity waves generated by atmospheric shear layers. J. Atmos. Sci., 33:1248.

Madden, T. R., and J. F. Claerbout (1968): Jet-stream-associated gravity waves and implications concerning jet stream stability. Proc. Acoustic Gravity Waves Symp., T. M. Georges, Ed., U.S. Govt. Printing Office. 121-124.

Maslowe, S. A., and R. E. Kelly (1971): Inviscid instability of an unbounded heterogeneous shear layer. J. Fluid Mech., 48:405.

Mastrantonio, G., F. Einaudi, and D. Fua (1976): Generation of gravity waves by jet streams in the atmosphere. J. Atmos. Sci., 33:1730.

Miles, J. W. (1961): On the stability of heterogeneous shear flow. J. Fluid Mech., 10:496.

Palmen, E. (1954): Uber die atmospharischen Strahlstrome. Meteorol. Abhandl. (Berlin), 2:35.

Paul, D. P. (1977): Nonlinear gravity wave-wind interactions and jet stream gravity wave generation. Ph. D. dissertation, MIT, 112 pp.

Sengupta, A., O.P. Nagpal, and C.S.G.K. Setty (1977): Travelling ionospheric disturbances and their possible correlation with jet stream activity. Ind. J. Radio Space Phys., September issue.

Sizun, H., and L. Bertel (1978): Observations of medium scale atmospheric waves from diverse measurements. Paper presented at the Symp. on Beacon Satellite Measurements of Plasmaspheric and Ionospheric properties, 22-25 May, 1978, Florence, Italy.

Thorpe, S.A. (1973): Turbulence in stratified fluids: A review of laboratory experiments. Boundary Layer Meteor., 5:95.

Tolstoy, I. (1973): Infrasonic fluctuation spectra in the atmosphere. Geophys. J. Roy. Astron. Soc., 34:343.

Tolstoy, I., and T.J. Herron (1969): A model for atmospheric pressure fluctuations in the mesoscale range. J. Atmos. Sci., 26:270.

Uccellini, L.W. (1975): A case study of apparent gravity wave initiation of severe convective storms. Mon. Wea. Rev., 103:497.

Vidal-Madjar, D., F. Bertin, and J. Testud (1978): Sur le jet stream de la tropopause en tant que source des ondes de gravité observées dans la thermosphere. Ann. Geophys. , 34:1.

SOLAR RELATIONSHIP AND PREDICTION OF SEISMIC ACTIVITY OF THE EARTH

Yu. D. Kalinin and V. M. Kiselev
L. V. Kirensky Institute of Physics
Siberian Branch of the Academy of Sciences of the USSR
Krasnoyarsk, Akademgorodok, 660036, USSR

Annual values of the planetary released seismic energy (E) for 1800-1974 were obtained on the basis of known earthquake catalogues. It was found that the principal components of the E-spectrum obtained by Burg's maximum entropy method correspond to time scales of about 180, 25 and 11 years. The prediction technique of the planetary seismic activity was developed on this basis.

1. GLOBAL SEISMIC ACTIVITY OF THE EARTH

The aim of this paper is the analysis and the prediction technique of seismic activity on the Earth. The knowledge of statistical regularities of the temporal variations of global seismic activity is necessary for understanding the causes of catastrophic earthquakes and for their time prediction.

We used annual amounts of released seismic energy (E) as the characteristic of planetary seismic activity. It is known that the majority of the annual seismic energy is released when great magnitude earthquakes occur. Therefore to obtain the series of E-values we used the data on earthquakes with magnitudes $M \geq 7.9$ (an earthquake with $M=7.9$ corresponds to a released energy $E=5 \times 10^{16}$ J). The known maximum value of E is equal to 3.43×10^{18} J for 1897.

Annual values of E for 1897-1974 were found from the earthquake data according to Richter (1958) and according to catalogues "Earthquakes in the USSR" (1963-1974). Before 1897 the instrumental measurements suitable for determination of E-values are absent. Therefore, we used the data on the number of earthquakes per year for 1800-1900 according to Lomnitz (1974) to find the E values for the nineteenth century. The time intersection of Lomnitz's data and instrumental data gave a conversion factor from the annual number of earthquakes to the amounts of released seismic energy. The continuous series of annual values of E was constructed for 1800-1974 in this manner.

Figure 1 represents the changes of planetary seismic energy for 1800-1974. The year-to-year changes of E are uneven and probably random, but there are also long-term variations. Note that the E series thus obtained differs from the E series obtained by Anderson (1974). This difference concerns the E-data for the nineteenth century especially. We verified our determination of E series for the nineteenth century by comparing the change of E with that of

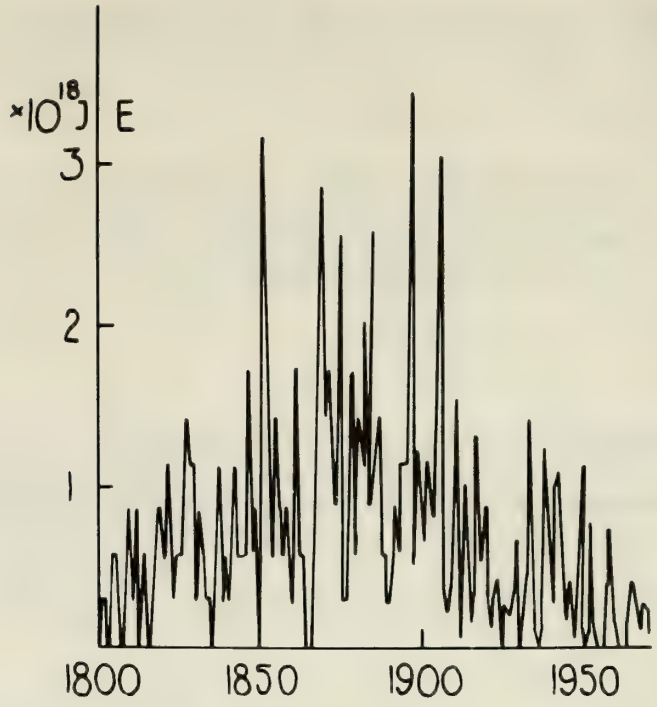


Figure 1. Changes of annual values of released seismic energy (in 10^{18}J) for 1800-1974).

the annual number (N) of volcanic eruptions. The N data were taken from Sapper (1927). Figure 2 shows the variations of E (upper curve) and N (lower curve) smoothed by 11-year sliding means. Figure 2 shows that the obtained changes of both E and N are in agreement for the nineteenth century.

2. SPECTRAL ANALYSIS OF E AND OF RELATIVE SUNSPOT NUMBERS

Spectral analysis of both relative sunspot numbers (R_z) and planetary seismic energy (E) was made by the maximum entropy method (Smylie et al., 1973). Power spectra of R_z (upper) and E are shown in Figure 3 as a function of period. The scale of the peak of the long-term component of E (with period equal to about 180 years) is placed to the right of Figure 3. We shall not discuss here either the origin of this component or the high-frequency components of E (with periods shorter than 10 years). Our emphasis is on components with periods of about 11 and 25 years in the E variations. These periods correspond to solar and solar magnetic cycles. It is necessary also to note that there are no long-term variations of E with a period of about 93 years, which take place in the changes of R_z.

It is interesting to make a comparison of the 11-year and 25-year variations of R_z and E, found by linear filtering of the initial series. For convenience, we shall mark these components as E(11), E(25), R_z(11) and R_z(25). They are presented in Figures 4 and 5, which show that the connection between E(11) and R_z(11) as well as between E(25) and R_z(25) is unstable.

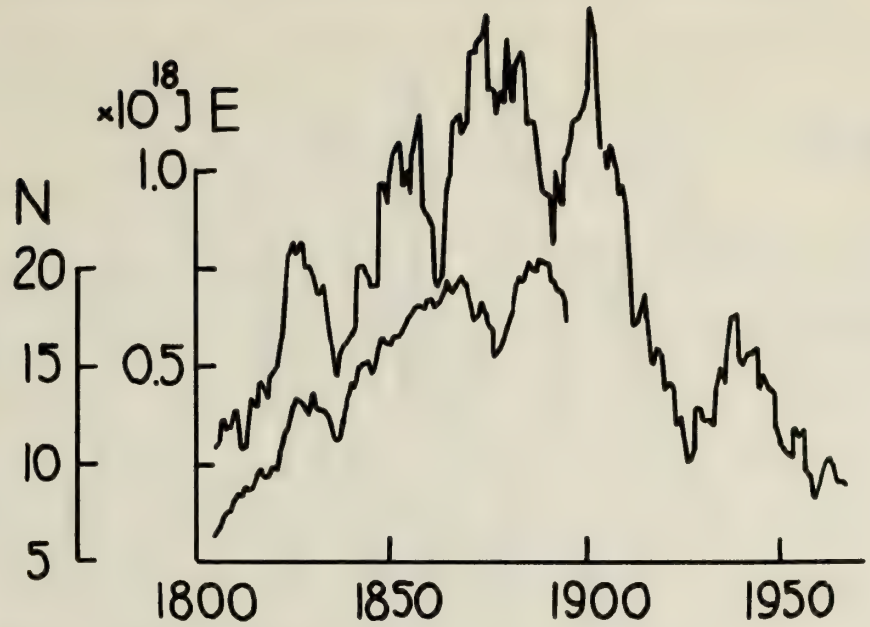


Figure 2. Changes of annual values (E) of released seismic energy (upper curve) and annual numbers (N) of volcanic eruptions. Both E and N are smoothed by 11-year sliding means.

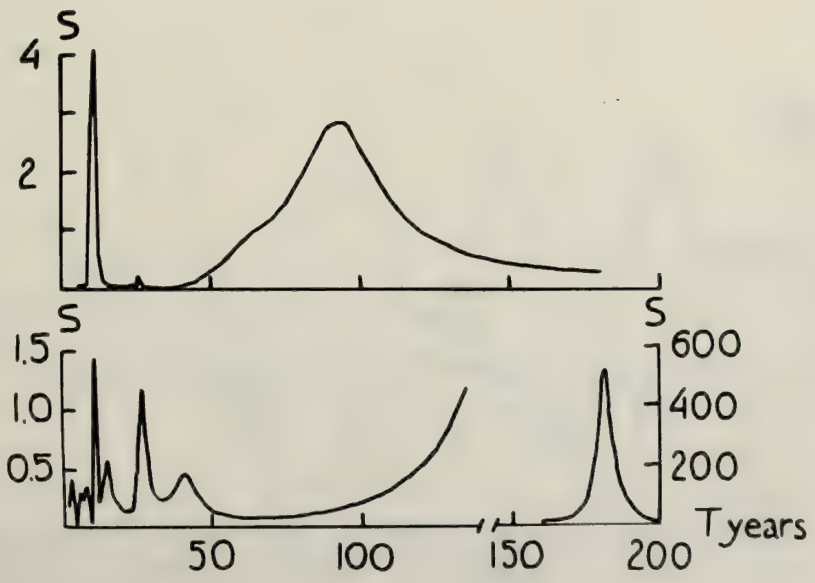


Figure 3. Power spectra of relative sunspot numbers R (upper curve) and of released seismic energy E (lower curve). The scale of the peak of the long-term variation of E is placed to the right.

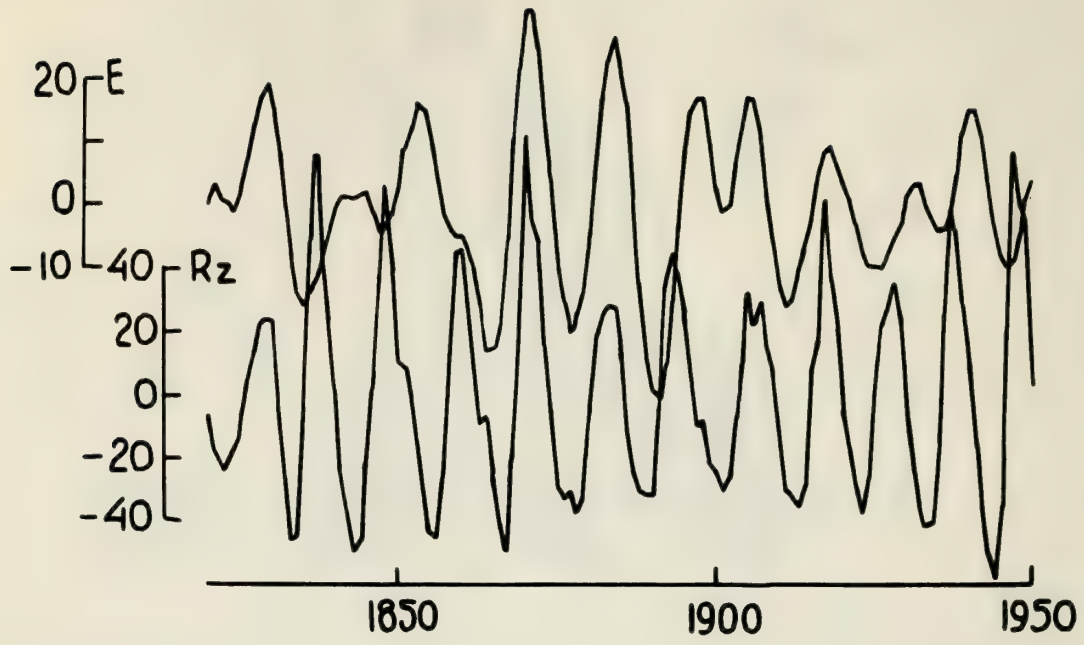


Figure 4. The 11-year variations of E (upper curve) and R_z (lower curve).

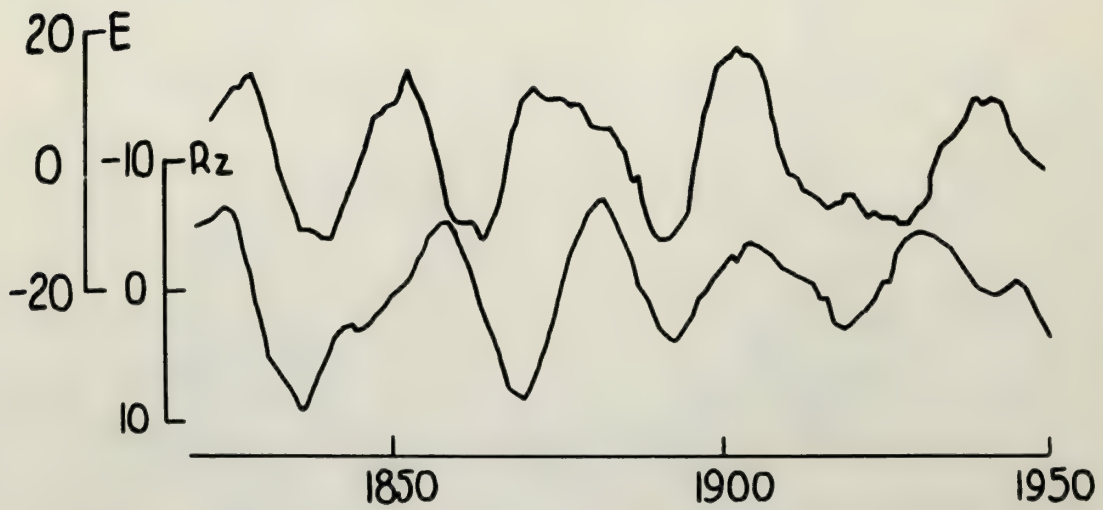


Figure 5. The 25-year variation of E (upper curve) and R_z (lower curve).

3. PREDICTION OF GLOBAL SEISMIC ACTIVITY OF THE EARTH

It is possible to make a statistical prediction of changes of released seismic energy using the presence of the 11-year and 25-year E variations and their connection with solar activity. We used the E data for the nineteenth century only. The E data for the twentieth century were used for verification of efficiency of the prediction technique. The prediction of E was made in two ways.

1. Mean curves of E(11) and E(25) were determined by a superposition method according to the nineteenth century data. The years of maxima of 11-year and 25-year cycles of R_z were taken as "zero years." Using the data on the maxima of $R_z(11)$ and $R_z(25)$ in the twentieth century the mean curves of E(11) and E(25) were superposed on the extrapolated curve of the 180-year cycle of E. In Figure 6 the initial E (solid line) and the predictive E (broken line) are shown. Both the initial and predictive E are smoothed by 3-year and 5-year sliding means and are presented as deviations from means. The correlation coefficient between them is equal to +0.59. A marked difference between the initial and predictive E after 1940 is probably due to the unstable connection of the 11-year and 25-year variations of R_z and E.

2. Mean curves of E(11) and E(25) were determined by the superposition method using the E-data for the nineteenth century only. The R_z data were not considered. The years of maxima of E(11) and E(25) in the nineteenth century were taken as "zero years." "Zero years" in the twentieth century were found by extrapolation. The predictive values of E for the twentieth century were obtained as in the previous case. Figure 7 shows the initial E (solid line) and the predictive E (broken line). In this case the correlation coefficient between the initial and predictive values of E is equal to +0.74.

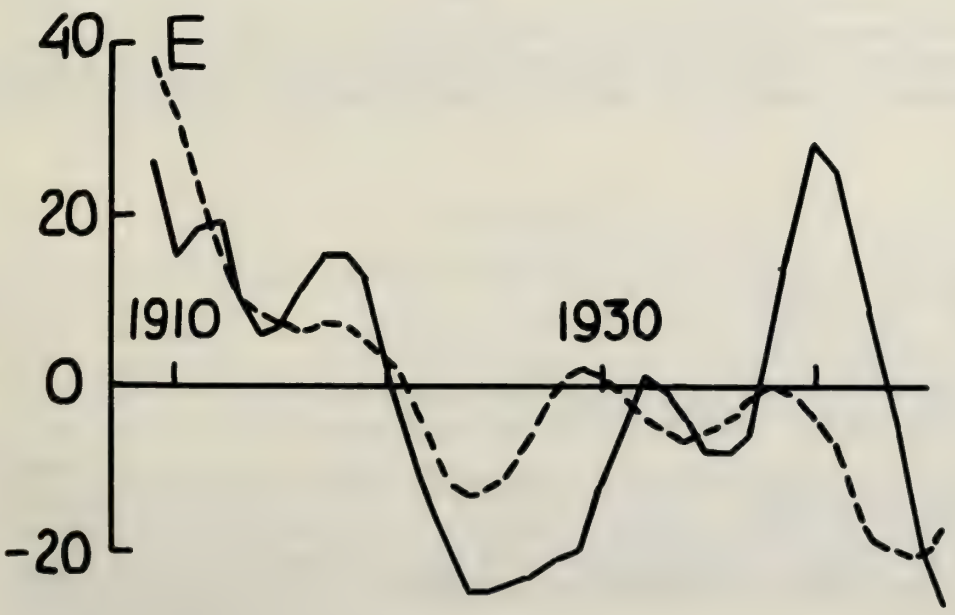


Figure 6. The initial (solid line) and predictive (broken line) changes of the released seismic energy, smoothed by 3-year and 5-year sliding means and represented as deviations from means, according to method 1 (see text).

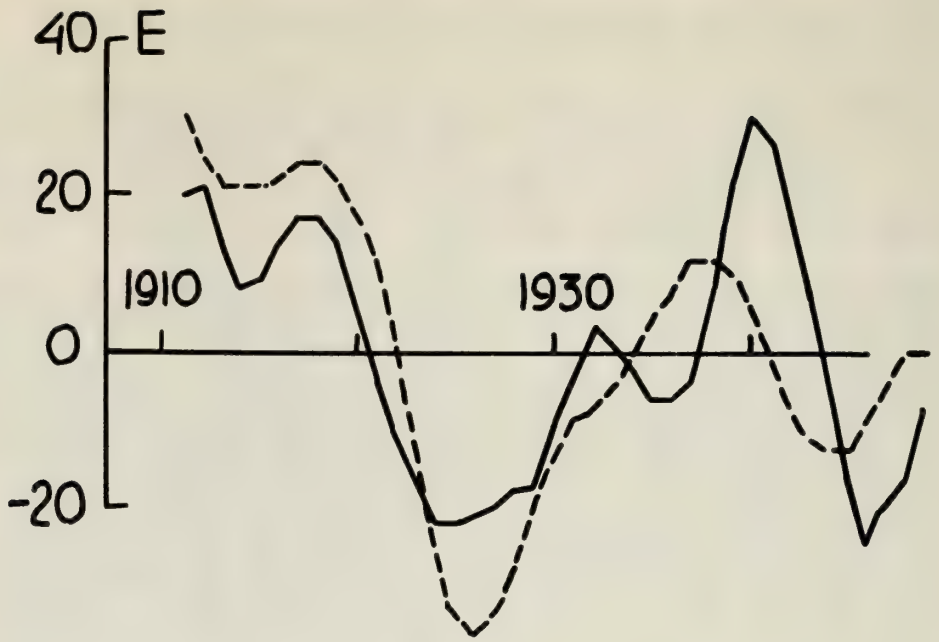


Figure 7. The initial (solid line) and predictive (broken line) changes of the released seismic energy, smoothed by 3-year and 5-year sliding means and represented as deviations from means, according to method 2 (see text).

4. CONCLUSION

Spectral analysis of the E and R changes give evidence for the solar dependence of the seismic activity variations having time scales in the range of 11-25 years. On this basis the suggested prediction technique may be useful for solving the prediction problem of the planetary released seismic energy.

REFERENCES

Anderson, Don L. (1974): Earthquakes and the rotation of the Earth. Science, 186:49.

Lomnitz, C. (1974): Global tectonics and earthquake risk. Elsevier Sci. Publ. Co., Amst.-London-N.Y.

Earthquakes in the USSR (1963-1974): Annual Reports, Acad. Sci. USSR. "Nauka" Publ. Co., Moscow.

Richter, Ch. F. (1958): Elementary seismology. W. H. Freeman and Co., San Francisco.

Sapper, K. (1927): Vulkankunde. Stuttgart, Germany.

Smylie, D. E., G. K. C. Clarke, and T. J. Ulrich (1973): Analysis of irregularities in the Earth's rotation. Methods of Computational Physics, 13:391.

SOLAR TERRESTRIAL PREDICTION: ASPECTS FOR PREVENTIVE MEDICINE.

Professor Eliyahu Stoupel,M.D.
Toor Institute of Cardiology, Beilinson Medical Center
Petah Tiqva, Israel.

A retrospective comparative study on total mortality and cardiovascular mortality was carried out among 3761 in-hospital deaths recorded at Beilinson Medical Center, Petah Tiqva, Israel, and 536 cardiovascular deaths out of hospital, from 1974-1977. The helio- and geophysical conditions prevailing were charted, and seven factors compared: monthly sumspots number (W), average of geomagnetic activity (K), sudden geomagnetic disturbances (SD), number of hours with negative and positive ionization and deviation in the solar gamma-wave propagation during the morning (fof_1) and afternoon (fof_2) hours - (minimal and maximal) from the monthly median of solar gamma wave propagation. The highest correlation between general and cardiovascular mortality with these seven factors was related to the sun gamma wave propagation (fof_1) in the early morning hours. During the geomagnetic periactive and peristormy periods, there were significant changes noted in the coagulation system, peripheral blood and diastolic blood pressure. These data can be important in understanding the etiology of cardiovascular deaths which occur with increased frequency during periods of increased geomagnetic activity, and may be of practical value in projecting plans for preventive therapy by advance interpretation of the cosmic data available.

This investigation is based on recognition of the factors cited below:

1. That the sun is the major "biological watch" regulator;
2. Recent advances in helio and geophysical monitoring systems, and the availability of more sophisticated interpretation of medical and physical data with advanced computer techniques (Gibson,E.G., and others).
3. Increasing international scientific co-operation;
4. The premise that cyclic or periodic changes observed in human physiology, epidemiology and pathology cannot be understood on the basis of only anatomical and morphological phenomena (Tchijevsky,AL., 1976, and others).

The goals of this study were: a) to check the influence of some geo- and heliophysical factors on general mortality and mortality from cardiovascular diseases in general and, in particular, from myocardial infarction

(MI), cerebral vascular accident (CVA) and other cardiovascular diseases occuring in and out of the hospital. b) to check the changes in coagulation system and arterial blood pressure that are closely connected with the mechanisms (pathogenesis) of a number of cardiovascular diseases. The study was conducted in Beilinson Medical Center (B.M.C. - 1000 beds) and 5 neighboring hospitals, from 1974-1977. The mortality data for the study of non-hospitalized cardiovascular accidents was obtained in the Abu-Kabir Institute for Forensic Medicine (Tel Aviv, 1974-1977, Vice Director Dr.B.Bloch). The cosmic information was provided by scientific institutions in the U.S.A. and the Academy of Science of the USSR.

MATERIALS AND METHODS

Daily and hourly index of hospital mortality in B.M.C. of 3761 hospital deaths in 1974-1977, included: 818 cardiovascular deaths, 239 deaths from MI. The cardiovascular deaths out of the hospital (determined by post-mortem examination) included 536 cardiovascular deaths (among them 164 from MI, 27 from CVA, 43 from coronary arteriosclerosis without signs of MI or coronarothrombosis, etc.). The study was performed on 1339 days, 683 non-active (quiet or unsettled) and 656 periactive (one day before, the active or stormy days and two days after them). In addition changes in quiet, unsettled, active stormy days, and particularly in pre-active (1 day before) and post-active (2 days after active) geomagnetic periods, were studied.
The activity gradation is demonstrated in Table 1.

GEOMAGNETIC ACTIVITY GRADATION - Table 1

STATE OF FIELD	QUIET		UN-SETT-LED	DISTURBED					
				ACTIVE	MINOR STORM		MAJOR STORM		
K	0	1	2	3	4	5	6	7	8	9
AMPLITUDE (gamma)	0-5	6-10	11-20	21-40	41-70	71-120	121-200	201-300	331-550	550

Arterial pressure of 550 healthy individuals was examined during different geomagnetical conditions and 870 hypertensive patients who were treated in the Hypertension Institute of B.M.C. (Dir.Prof.J.Rosenfeld), were also investigated. A study of peripheral blood and coagulation systems in connection with prevailing geomagnetic conditions was carried out in co-operation with Prof.H.Joshua (Clinical Laboratory Director of B.M.C.). The statistical analysis was performed in the Israel Institute for Productivity (Dr.J.Levy) and the Computer Center of Tel Aviv University. In all results the Student test was used (t,P.); in a part of results the null hypothesis method has used for the daily mortality index- "x^2" level (for analysis of the influence of geomagnetic activity on mortality), correlation coefficient (r) between various monthly heliophysical and geomagnetic parameters and mortality, correlation between geomagnetic activity and number of basophyles in the peripheral blood were investigated.

Table 2 presents the correlation between total mortality, cardiovascular and MI mortality and various mean monthly helio-and geophysical parameters: K - geomagnetic activity index; W - sunspots number; S - sudden geomagnetic disturbances; (+); (-) hours of positive or negative ionization, foF_1 - deviation from the median of Solary wave propagation in the morning hours; foF_2 - this parameter in the afternoon hours. There is a prominent rise in correlation coefficient between all parameters of mortality and foF_1 (min). S is the number of monthly geomagnetic disturbances based on the deformation of monthly cosmic data.

CORRELATION BETWEEN MONTHLY GEOPHYSICS PARAMETERS AND HOSPITAL MORTALITY (JAN. 1974 - MARCH 1977) - Table 2

	GEOPHYSIC. PARAM. / MORTALITY	K	IONIZATION +	IONIZATION -	W	S	foF_1 MIN.	foF_2 MAX.
1	TOTAL MORTALITY BEILINSON CENTER 2057* 76.18 11.3	0.27	0.043	0.312	0.008	-0.015	-0.583	0.245
2	TOTAL MORTALITY OTHER HOSPITALS 1704 63.11 13.0	-0.166	-0.107	0.189	-0.292	-0.294	-0.431	-0.034
3	TOTAL MORTALITY (1+2) 3761 139.30 21.2	0.04	-0.043	0.282	-0.174	-0.189	-0.575	0.109
4	CARDIOVASCULAR MORTALITY BEILINSON CENTER 818 30.3 10.7	0.026	0.029	0.228	-0.297	-0.318	-0.494	0.219
5	M.I. MORTALITY BEILINSON CENTER 239 8.85 3.35	0.224	0.025	0.289	-0.050	-0.038	-0.271	0.162

* TOTAL NUMBER OF OBSERVATIONS
MEAN STANDARD DEVIATION.

Six high and five low mortality months were chosen in B.M.C. and in five other hospitals among 27 monthly mortality figures (1974-1977).

Table 3 presents the mortality figures for the 27 months analyzed, and the Student test that confirms the statistically significant differences in high and low mortality during the months randomly chosen.

SELECTED MONTHLY HOSPITAL MORTALITY FIGURES Table 3
(Total and Cardiovascular) Jan. 1974 - March 1976.

CAUSE OF DEATH HOSPITAL NAME	MAIN FIGURES FOR 27 MONTHS	MAIN FIGURES IN 6 HIGH-MORTALITY MONTHS	MAIN FIGURES IN 5 LOW-MORTALITY MONTHS	DIFFERENCES SIGNIFICANT AT HIGH/LOW MORTALITY
CARDIOVASCULAR DISEASES/BEILINSON	30.259±10.668	44.666±4.633	16.600±3.209	P < 0.005
MYOCARDIAL INFARCTION/BEILINSON	8.852±3.494	13.833±1.722	4.200±0.837	P < 0.005
TOTAL/BEILINSON MEDICAL CENTER	76.185±11.279	91.50 ±2.81	61.000±2.738	P < 0.01
5 OTHER HOSPITALS	63.111±13.021	81.333±6.470	45.800±5.31	P < 0.005

Table 4 demonstrates the differences between various geomagnetic parameters in the high and low mortality months. The ± terms in tables 3 and 4 are standard deviations.

MONTHLY MAIN GEOMAGNETIC (G.M.) PARAMETERS IN HIGH AND LOW MORTALITY MONTHS
BEILINSON MEDICAL CENTER 1.1974 - III. 1976 Table 4

N	PARAMETER	6 HIGH MORTALITY MONTHS	5 LOW MORTALITY MONTHS	DIFFERENCES SIGNIFICANT AT:
1	ACTIVE G.M. PERIODS	2.833 ±0.408	2.000 ±0.707	P< 0.025
2	LOW G.M. ACTIVITY PERIODS	2.833 ±0.408	3.000 ±1.225	P> 0.05
3	HIGH G.M. ACTIVITY GRADIENTS	1.167 ±0.408	0.400 ±0.5478	P< 0.02
4	EXTREMELY G.M. PERIODS	5.667 ±0.8165	4.000 ±1.000	P< 0.02

Table 5 demonstrates the daily mortality indices and statistical significance between daily mortality in and out of hospital in different geomagnetic situations. In addition to Student test the differences in hospital cardiovascular mortality were confirmed with x^2 tests ($x^2 > x^2c$). For hospital cardiovascular mortality $x^2=12.449 : x^2c=11.070$. For cerebrovascular accidents (CVA) $-x^2-11.60 : xc^2=10.597$.

Table 5 BEILINSON MEDICAL CENTER

DAILY HOSPITAL MORTALITY INDEX IN DIFFERENT GEOMAGNETIC CONDITIONS 1974-1977.

	QUIET	ACTIVE	P
1. TOTAL CARDIOVASCULAR DEATHS IN HOSPITAL (n=818)	0.94	1.14	< 0.05
2. C.V.A. DEATHS IN THE HOSPITAL (n=269)	0.160	0.234	< 0.005
3. MYOCARDIAL INFARCTION DEATHS IN HOSPITAL (n=239)	0.284	0.294	> 0.05
4. TOTAL SUDDEN CARDIOVASCULAR DEATHS OUT OF HOSPITAL (n=27)	0.367	0.373	> 0.05
5. DEATHS FROM C.V.A. OUT OF HOSPITAL (n=27)	0.120	0.273	< 0.01
6. DEATHS FROM MYOCARDIAL INFARCTION OUT OF HOSPITAL (n=164)	0.096	0.161	< 0.02
7. DEATHS FROM CORONARY ATHEROSCLEROSIS WITHOUT M.I. OR CORONAROTHROMBOSIS. (n=43). OUT OF HOSPITAL	0.055	0.018	< 0.001

ELECTRICAL INSTABILITY?

Table 6 demonstrates the levels of systolic and diastolic arterial pressure investigated in healthy individuals and in treated (drug controlled) hypertensive patients - in different geomagnetic situations. We can see that in the two groups the increased geomagnetic activity coincided with increased diastolic pressure. The decrease in systolic pressure was significant only in geomagnetic storms, together with a tendency to pulse pressure (systolic-diastolic range) decreasing in active geomagnetic conditions.

ARTERIAL PRESSURE IN DIFFERENT GEOMAGNETIC CONDITIONS - Table 6

GEOMAGNETIC ACTIVITY	IN HEALTHY PERSONS (1)		IN HYPERTENSIVE (TREATED) (2)	
	SYST.	DIAST.	SYST.	DIAST.
1. QUIET	131.38 ±15.67	79.65 ±10.30	154.33 ±24.33	97.26 ±12.29
2. UNSETTLED	132.62 ±16.56	82.49 ±10.80	154.42 ±22.52	97.33 ±11.90
3. ACTIVE	131.01 ±16.22	83.01 ± 7.76	157.26 ±26.40	100.64 ±12.88
4. PERIACTIVE	131.86 ±16.40	82.70 ± 9.67	155.90 ±25.72	99.69 ±12.62
5. STORM			150.06 ±15.58	98.83 ±11.40
	n_1=550	n_2=870		

Tables 7 and 8 show the significant changes in various biochemical and coagulation system parameters.

GEOMAGNETIC ACTIVITY AND SOME PARAMETERS OF HOMEOSTASIS - Table 7

A. INCREASE

1. NUMBER OF THROMBOCYTES
2. PROTHROMBIN
3. PLATELETS AGGREGATION
4. FIBRINOLYTHIC ACTIVITY
5. DIASTOLIC ARTERIAL PRESSURE (PERIPHERAL RESISTANCE?)
6. HEMATOCRIT (IN COMPARISON TO THE PERIACTIVE DAYS)

B. DECREASE

1. NUMBER OF BASOPHILES (HEPARINOID PRODUCTION?)
2. TRIGLYCERIDES (IN GENERAL POPULATION)
3. CHOLESTEROL (IN GEOMAGNETIC STORM ONLY)
4. SYSTOLIC PRESSURE (IN GEOMAGNETIC STORM ONLY)

SIGNIFICANT CHANGES IN THE COAGULATION SYSTEM CONNECTED WITH GEOMAGNETIC ACTIVITY - Table 8

N	PARAMETERS	GEOMAGNETIC ACTIVITY			
		QUIET	PERIACTIVE	ACTIVE	STORMY
1.	PROTHROMBIN INDEX (n*=1331)	75.7 ± 7.10	78.5 ± 7.45	79.9 ± 8.16	79.9 ±11.92
2.	THROMBOCYTES (n=1053)	177.055 ±90.047	195.025 ±69.040 (POSTACTIVE- 213.056 ±85.005)	182.110 ±85.840	205.064 ±101.063 190.448 ±92.247
3.	BASOPHYLES (IN THE PERIPHERAL BLOOD) (n=1934)	0.55 ± 0.27		0.46 ± 0.21	0.20 ± 0.26
			UNSETTLED		
4.	PLATELETS AGGREGATION (n=162)	33.7 ± 15.4	34.0 ± 16.0	40.0 ± 17.0	47.0 ± 14.0 42.0 ± 16.0

*N - NUMBER OF TESTS

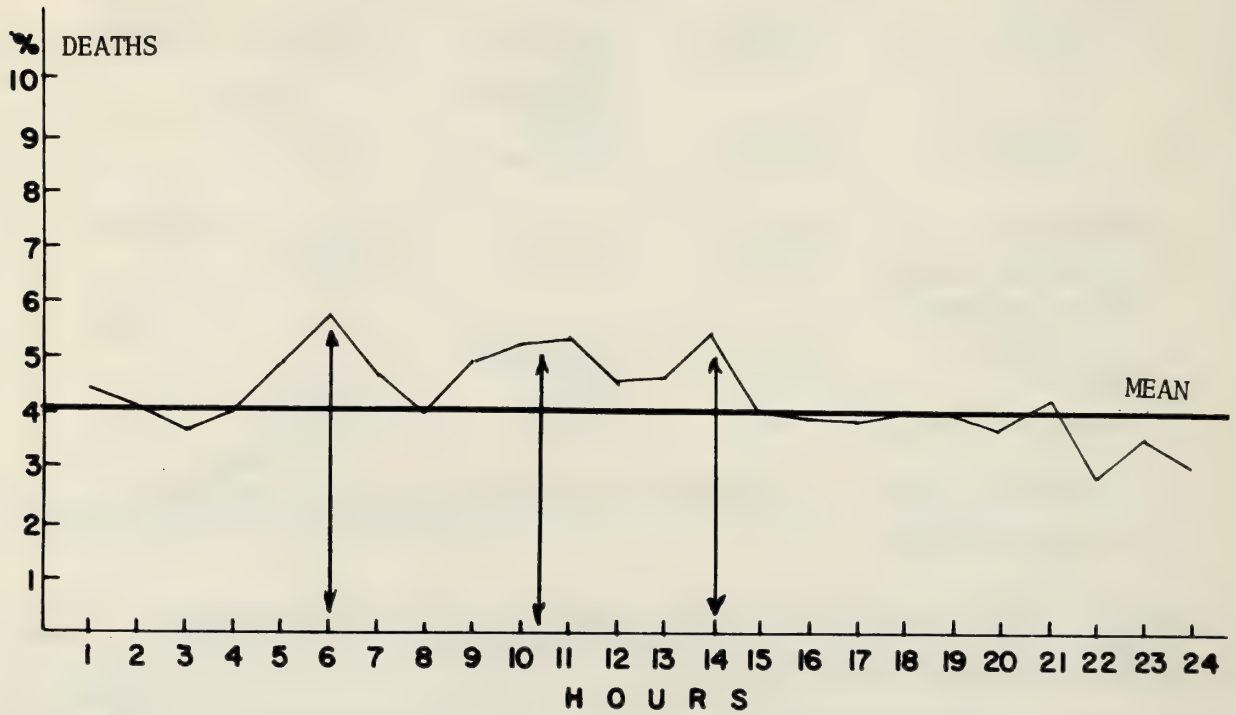
Table 9 demonstrates the parameters, that were proved, although without statistically significant changes.

NONSIGNIFICANT CHANGES Table 9

1.	ENGLOBULIN TIME / FIBRINOGEN /		
2.	BLOOD VISCOSITY	WITH TENDENCY TO	INCREASE
3.	BLEEDING TIME	"	
4.	CLOTTING TIME	"	
5.	PULSE PRESSURE	WITH TENDENCY TO	DECREASE
6.	TRIGLYCERIDES (IN ATHEROSCLEROTIC HEART DISEASE)		
7.	GLUCOSE		
8.	URIC ACID	WITH TENDENCY TO	INCREASE IN STORM

The most significant changes were in increased platelets aggregation, prothrombin index, thrombocytes count in the peripheral blood during increased geomagnetic activity, together with a decreased number of basophyles (anti-coagulant heparinoid productions); the fibrinolytic activity was changed conversely with a tendency to increase.

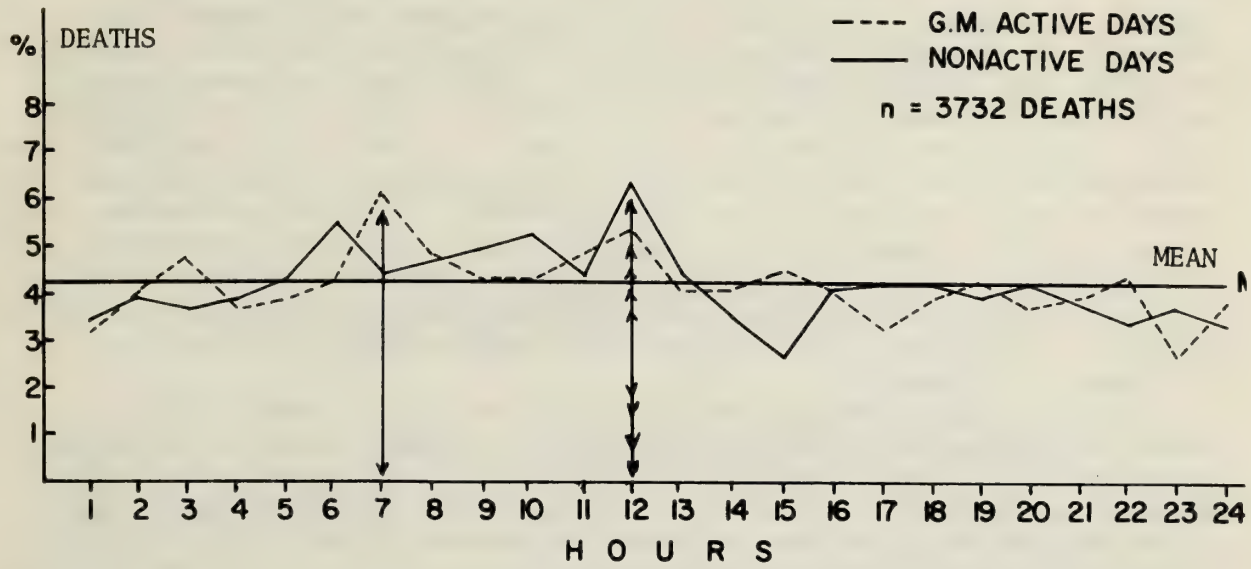
The hourly distribution of 3761 cases of hospital mortality is presented in Diagram 1.



There are two peaks in the 24-hour distribution: In the early morning hours (5 a.m.-7a.m.) and in the afternoon (1-2 p.m.). The relatively high correlation of monthly mortality index and sun wave propagation in the morning hours was the course for selected analysis of hourly mortality in the active and non-active days.

Diagram 2 demonstrates the two curves. There is a tendency to higher mortality figures in the morning hours in active days. On the non-active days the maximal hours were in the afternoon.

DIAGRAM 2



DISCUSSION

The influence of sun activity on a wide spectrum of biological processes was confirmed in the investigations of M.Faure, A.Tchijevski, G.Sardon, E.Budai et al. Tchijevsky wrote (1936) that human society will be ready to discuss the problem only 50 years hence. Recently a number of studies were performed to confirm the leading role of the central nervous system and particularly the hypothalamus in interaction with magnetic waves (M.Yiakovleva, C.Barnothy, I.Cholodov). Other studies confirm the importance of the central nervous system in the regulation of blood pressure, heart rhythm and coagulation factor (B.Lown, A.Myasnikov, J.Ganelina, E.Rozhdestuenskaya et al., I.Schwacabaya). Those together can explain the changes in coagulation factors (platelets aggregation and count, prothrombin index), diastolic pressure increase in the active geomagnetic periods. The fibrinolytic activity rose in general in active geomagnetic conditions (that can be a compensatory factor for increased other coagulation factors preventing thrombosis) and failed in patients with atherosclerotic heart and peripheral vascular disease. Recent evidence points to the greater role of thromboxan A_2 - a product of platelets aggregation in the tonus of smooth muscles of the small arteries (E.F.Ellis et al.). A higher level of thromboxan A_2 may be one of the factors affecting changes in micro-

circulation in general and in the myocardium and brain in particular. This together with the great influence of the hypothalamus on arterial pressure in general can act as a stimulant to diastolic pressure increase and predisposes to spasms of the coronary arteries (A.Maseri et al.). The influence of geomagnetic activity on diastolic pressure was confirmed in the healthy groups and the hypertensive patients in this study.

On the other hand the increase of sudden cardiac deaths out of the hospital in the quiet geomagnetic days requires further investigation (the group is only 43 persons). That contradicts the point of view that the complete isolation (A.Tchijevski et al.) of patients from geomagnetic influence can be helpful for general prevention of cardiovascular accidents connected with influence of cosmic factors. The absence of new myocardial infarctions or thrombotic changes in the increased number of sudden deaths from heart arteriosclerosis on quiet days is a factor which requires more investigation if one suspects that quiet geomagnetic conditions may predispose to electrical heart instability (B.Lown, L.Meltzer) and sudden death from arrythmias. Absence of any significant rise in hospital mortality from myocardial infarction can be attributed to improved cardiac care in intensive coronary care units in the last ten years. Previous investigations conducted in 1968 and in 1971, showed increased hospital mortality (I.Stupelis - E.Stoupel).

According to H.Jick, H.J.Weiss, Aspirin may play a useful role in preventive therapy connected with coagulation changes in its effect on anti-prostglandin activity (a group of prostglandins are precursors in blood platelets aggregation). This may have significance for regulating coagulation changes during periods of increased geomagnetic activity. It also explains the empiric tradition of the elderly population to use Aspirin for all ailments connected with weather changes. The hourly dynamics of the recorded deaths demonstrated the need for more care in the correct dosage of drugs, to prevent insufficient concentration of cardiac drugs in the blood and tissue in the early morning hours. The solar-terrestrial prediction data can be utilized to great advantage for: 1) increased readiness in the emergency medical services (ambulances, Intensive Coronary Care Units); 2) More efficient use of preventive therapy in high risk cardiovascular patients, K.Novikova, 1968;Y.Jushenaite, 1969; Y.Ganelina, 1969; E.Stoupel (I.Stupelis) 1970, 1976. The changes in hospital mortality (general and connected with geomagnetic activity) from myocardial infarction, confirm the progress in diminishing the number of sudden cardiac deaths occurring in hospital over the last 15 years.

A bright spectrum of possibilities exists for more studies about cosmic-biologic interaction for theoretical and practical biology and medicine.

REFERENCES

Barnothy, J.M. (1964), in: Biological Effects of Magnetic Fields.New York, 1:93.

Budai, E. (1931): Taches solaires et meningite cerebrospinale. Revue de Pathologie comparee et d'Hygiene Generale, 419.

Ellis, E.F., Oelr, O., Jackson Roberts, L., Payne, N.A., Sweetman, B.J., Dates, J.A. (1976): Coronary arterial smooth muscle contraction by a substance released from platelets. Evidence that it is Thromboxan A_2. Science 193:1135.

Faure, M. (1934-1935: Cosmobiologie. Nice.

Frishman, W.H., Weksler, B., Christodoulou, J.P., Swithen, C., Killipt, T. (1974): Reversal of abnormal platelet aggregability and change in exercise tolerance in patients with angina pectoris following oral propanolol. Circulation N. 4,50:887-896.

Frishman, W.H., Christodoulou, J.P., Weksler, B., Smithen, Ch., Killip, T., Scheidt, S. (1976): Aspirin therapy in angina pectoris: Effects on platelet aggregation, exercise tolerance and ECG manifestation of ischemia Am. J. Heart. 92, 1:3.

Gamelina, J. (1969): Sudden death in acute myocardial infarction and problems of resuscitation. Klin. Med. 11:111-119 (Russian).

Gibson, E.G. (1973): The quiet sum. Scientific and Technical Information Office. NASA, Washington, D.C.

Jick, H., Elwood, P.C. (1976): Aspirin and myocardial infarction. Am. Heart J. 91, 1:126.

Jushnaite, J. (1969): Solar activity and the pathology of circulation. Sveikatos Apsauga. 5:3-5 (Lithuanian).

Kholodov, I.A. (1966): The influence of electromagnetic and magnetic fields on the nervous system. IPRS-37102 (TT-66-33531). Washington, Joint Publication Research Service.

Lown, B., DeSilva, R.A., Lenson, R. (1978): Roles of psychologic stress and autonomic nervous system changes in provocation of ventricular premature complexes. Am. J. of Cardiology, 41, 6:979-958.

Maseri, A., Pesola, A., Marzilli, M., Severi, S., Parodi, O., L'Abbate, A., Ballestra, A.M., Biagiui, A. (1977): Coronary vasospasm in angina pectoris. Lancet, Vol. 1, 8014:713-719.

Meltzer, L.E., Dunning, A.J. (1972): Textbook of coronary care. Philadelphia & Amsterdam.

Myasnikov, A.L. (1954): Hypertonic disease. Megdiz Edition, Moscow.

Rozhdestvenskaya, E., Novikova, K. (1969): The influence of solar activity on the blood fibrinolytic system. Med. Ref. Journal, 10:65-69.

Sardon, G., Faure, M. (1927): Les taches solaires et la pathologie humaine. "La Presse Medicale" N. 18, Paris.

Searman, G.V.F. (1976): Electrochemical features of platelet interactions. Thromboses Res. 8(2) 235-246.

Schwacabaya, J.K. (1976): Actual problems of hypertensive crisis. Kardiologya 5:5-11.

Stupelis, I. (Stoupel, E.). Jushenaite, J., Labananskas, J., Stahaityte, N. (1970). The activity of the Earth's magnetic field, season, and risk of death from myocardial infarction. Abstracts of the 7th Conference of Internal Medicine, Latvia. Riga, pp 147-149 (Russian).

Stoupel, E. Forecasting in Cardiology. J. Wiley and Sons, New York, Toronto, Jerusalem (1976).

Tchijevsky, A.L.: Effect des facteurs physiques de la nature sur les elements nerveux et sur l'activite nerveuse des animaux et de .'homme rapport presente au laboratoire practique de Zoo psychologie V. 1925 Moscow. Traite de climatologie biologique et Medicinale V.1:672, Paris.

Tchijevsky, A.L. (1976): Terrestrial Echo of the Solar Storms, IInd Ed., Mislj Ed. Moscow. Introduction, O. Gazenko.

The Cosmic Data. Monthly of the Academy of Science of the USSR (1974-1977)

Weiss, H.J. (1976): Antiplatelet drugs - A new pharmacologic approach to the prevention of thrombosis. Am. Heart J., Vol. 92, 1:86-102.

Wovikova, K., Gnevishev, N., Tokareva, N. et al.(1978): The solar activity influence of the natural history of myocardial infarction. Cardiology 8, 4:109-112.

Yakovleva, M.I. (1973): Physiological mechanisms of effects of electromagnetic fields. (Leningrad)

☆ U. S. GOVERNMENT PRINTING OFFICE 1980 - 677-096/1242 Reg. 8

PENN STATE UNIVERSITY LIBRARIES
A00007094548S